Erol Tutumluer
Soheil Nazarian
Imad Al-Qadi
Issam I. A. Qamhia   *Editors*

Advances in Transportation Geotechnics IV

Proceedings of the 4th International Conference on Transportation Geotechnics Volume 2

Springer

Lecture Notes in Civil Engineering

Volume 165

Lecture Notes in Civil Engineering (LNCE) publishes the latest developments in Civil Engineering - quickly, informally and in top quality. Though original research reported in proceedings and post-proceedings represents the core of LNCE, edited volumes of exceptionally high quality and interest may also be considered for publication. Volumes published in LNCE embrace all aspects and subfields of, as well as new challenges in, Civil Engineering. Topics in the series include:

- Construction and Structural Mechanics
- Building Materials
- Concrete, Steel and Timber Structures
- Geotechnical Engineering
- Earthquake Engineering
- Coastal Engineering
- Ocean and Offshore Engineering; Ships and Floating Structures
- Hydraulics, Hydrology and Water Resources Engineering
- Environmental Engineering and Sustainability
- Structural Health and Monitoring
- Surveying and Geographical Information Systems
- Indoor Environments
- Transportation and Traffic
- Risk Analysis
- Safety and Security

To submit a proposal or request further information, please contact the appropriate Springer Editor:

- Pierpaolo Riva at pierpaolo.riva@springer.com (Europe and Americas);
- Swati Meherishi at swati.meherishi@springer.com (Asia - except China, and Australia, New Zealand);
- Wayne Hu at wayne.hu@springer.com (China).

All books in the series now indexed by Scopus and EI Compendex database!

More information about this series at http://www.springer.com/series/15087

Erol Tutumluer · Soheil Nazarian · Imad Al-Qadi · Issam I. A. Qamhia

Editors

Advances in Transportation Geotechnics IV

Proceedings of the 4th International Conference on Transportation Geotechnics Volume 2

Editors
Erol Tutumluer
Department of Civil and Environmental
Engineering
University of Illinois at Urbana-Champaign
Urbana, IL, USA

Imad Al-Qadi
Department of Civil and Environmental
Engineering
University of Illinois at Urbana-Champaign
Urbana, IL, USA

Soheil Nazarian
Department of Civil Engineering
The University of Texas at El Paso
El Paso, TX, USA

Issam I. A. Qamhia
Department of Civil and Environmental
Engineering
University of Illinois at Urbana-Champaign
Urbana, IL, USA

Contents

Subsurface Sensing for Transportation Infrastructure

About the Editors

Erol Tutumluer is Abel Bliss Professor in the Department of Civil and Environmental Engineering and the Director of International Programs at the University of Illinois at Urbana-Champaign, USA, where he is also the Paul F. Kent Endowed Faculty Scholar. He has research interests and expertise in characterization of pavement and railroad track geomaterials, i.e., subgrade soils and base/ballast unbound aggregates, soil/aggregate stabilization, geosynthetics, applications of artificial intelligence and deep learning techniques to transportation infrastructure, structural health monitoring of transportation facilities using sensors, modeling granular foundation systems using innovative techniques, sustainable use of foundation geomaterials and construction practices for transportation infrastructure, discrete element analysis of ballast, dynamic response measurement and analyses of track systems, and mechanistic analysis and design. Dr. Tutumluer has served as an investigator on over 100 research projects and graduated 21 PhD and 44 MS students, and authored/co-authored over 350 peer reviewed publications from his research projects. Dr. Tutumluer is a Founding Editor-in-Chief of the Transportation Geotechnics journal and the current Chair of the ISSMGE Technical Committee 202 on Transportation Geotechnics.

Soheil Nazarian is a Professor in the Department of Civil Engineering at the University of Texas at El Paso, USA. He has over 35 years of industry and academic experience in the area of transportation infrastructure, with an emphasis on structures materials, such as that of highways and bridges. His academic experience includes research and teaching positions at the Universities of Texas at Austin and El Paso, as well as the Director at the Center for Transportation Infrastructure Systems at UTEP. He holds a patent for the Moveable Seismic Pavement Analyzer, which is a nondestructive testing device used in evaluation of transportation infrastructure. Prof. Nazarian has been a contributor in over 100 research projects focused on nondestructive materials testing and materials applications, as well as the author of more than 300 industry related articles and publications.

Imad Al-Qadi is a Professor in the Department of Civil and Environmental Engineering and the Director of the Advanced Transportation Research and Engineering Laboratory (ATREL), the Illinois Center for Transportation (ICT), and the Smart Transportation Infrastructure Initiative (STII) at the University of Illinois at Urbana-Champaign, USA. He is also the President of the Transportation Engineering Solutions and Technologies, Inc. Al-Qadi's scholarly record features 700+ authored/co-authored publications, more than 400 of which are fully refereed papers (+280 in periodic journals). His research resulted in the development of new tests, testing specifications, advanced modeling and simulation of pavement loading, pavement layer interface and crack development, and analysis of radar electromagnetic wave interactions with civil engineering materials, roads, and bridges.

Issam I. A. Qamhia is a Postdoctoral research associate at the University of Illinois at Urbana-Champaign (UIUC). Dr. Qamhia holds a Ph.D. degree in civil engineering with transportation geotechnics specialization from UIUC, and M.S. and B.S. degrees in civil engineering from the University of Wisconsin Milwaukee and Birzeit University, respectively. He has over nine years of experience in aggregate characterization. His areas of expertise include repeated load testing, morphological shape characterization, tomography scanning, freeze-thaw testing, aggregate packing studies, as well as field characterization of bound and unbound aggregates through nondestructive and accelerated full-scale pavement testing. Dr. Qamhia has authored/co-authored more than 45 peer reviewed publications in prestigious international journals and conferences of repute, and is a frequent reviewer of journals and international conferences.

Rail Track Substructures, Including Transition Zones, and Transportation Geodynamics

Substructure Sensing in a Rail Bridge

Helsin Wang ⓘ**, Chih-Hsin Hu, Hsin-Chu Tsai, and Chung-Yue Wang** ⓘ

Abstract Lacking substructure information usually challenges bridge agencies when evaluating the flood or earthquake resistance of bridges in disaster-prone areas. Appropriate substructure inspection techniques are essential for bridge engineers to develop repair strategies efficiently and reasonably allocate maintenance funds. In this article, the electrical resistivity tomography technique was introduced to the foundation inspection of a rail bridge in Taiwan. Different survey layouts were chosen to inspect the pile bent substructures. Initially, the investigation line parallel to the traffic direction indicated an unexpected substructure pattern. Such a shallow low-resistivity anomaly crossing over more than ten pile bents severely interfered with the foundation depth inspection. Using two alternative investigation lines perpendicular to the previous survey direction successfully separated this low-resistivity zone into two single parts. One deeper low-resistivity contour located right below bridge position was identified as the foundation depths. Another shallow vertical-shape low-resistivity zone was identified as abandoned temporal sheet piles. This investigation case also reveals that two survey lines in different directions are suggested to separate the target substructure from unexpected embedded anomalies effectively.

Keywords Electrical resistivity tomography · Depth inspection · Pile bent · Rail bridge

1 Introduction

The as-built condition of foundations can affect the performance of existing bridges supported by these elements. Substructure information is crucial for bridge engineers

H. Wang (✉) · C.-H. Hu
HCK Geophysical, Taipei, Taiwan

H.-C. Tsai
Facility Management Research Center, CECI, Taipei, Taiwan

C.-Y. Wang
Department of Civil Engineering, National Central University, Chungli, Taoyuan, Taiwan

to maintain bridges. For example, lacking foundation dimension could impede rating the flood- or earthquake-resistant capacity of old bridges. Furthermore, materials deterioration, scour variation or cracking could also undermine the stability of a bridge.

The Taiwan Bridge Management System (TBMS), the most complete bridge database in Taiwan, archives the fundamental data for more than 28,000 vehicular bridges, viaducts, culverts and partial pedestrian bridges, with spans more than 6 m. This web-based bridge management and information system also provide a biennial official appraisal platform for the maintenance and management of bridge agencies in Taiwan.

The freeway, expressway, highway and railway bridges held by the central governments, which have sufficient budget, enough manpower and proficient experience, can sustain a better service level. However, the local governments managing a significant proportion about 60% of highway and pedestrian bridges usually face several quality uncertainty issues related to design, construction and data inventory, especially ageing bridges with almost 30 years on average.

The Federal Highway Administration (FHWA) defines the term "unknown foundation" associated with the existing bridges over waterways that cannot be evaluated for hydraulic vulnerability related to scour [3]. When coding the fundamental inventory of bridges, more than 50% of local bridges is classified to the "UNKNOWN" substructure category in the TBMS [11]. Consequently, lacking substructure information becomes the most severe challenge for bridge agencies when evaluating their flood or earthquake resistance in disaster-prone areas. Developing appropriate substructure inspection is essential for the governments in order to have more efficient repair strategies and more reasonable allocation of maintenance funds. It is of real importance to inspect unknown bridge foundations with proper inspection techniques.

Several non-destructive testing (NDT) methods have been developed to investigate the substructure conditions in bridges [2, 5, 7, 9, 14]. In 2013, a multidisciplinary task force was launched to build up appropriate methodology and practical techniques on unknown foundation assessment financially supported by the FHWA [3, 8]. A complete field NDT process was suggested on the Foundation Characterization Programme funded by the FHWA [1]. However, knowing complete substructure conditions is time-consuming and costly work if using all multiple inspection methods. Recently, an efficient and economical inspection strategy is, in practice, developed to non-destructively extract bridge substructure information in Taiwan [10–13]. These investigation cases indicate that the electrical resistivity tomography method can provide overall spatial distribution images of subsurface and point out possible embedded anomalies around the target bridge site in advance, especially for damaged river-crossing bridges [10, 11].

2 Description of Electrical Resistivity Tomography

The electrical resistivity tomography method is commonly used to identify geological layers, faults, groundwater pollutants, caves, mining, burial layers or landslide slip planes [4, 9]. The measured resistivity images provide useful information to identify the geological strata, rock/soil classification, groundwater table or anomalies, such as embedded pipelines, substructures or voids, in the geological formation [6]. On-site electrical resistivity is highly associated with the composition of the minerals, the size of the geomaterial particles, the configuration of the minerals and the water content in geological formations and the salinity in tidal reach rivers.

The principle of the conventional electrical resistivity tomography is to arrange the measurement points along a straight line through the target bridge site. Selecting one pair of current electrodes (current poles) in the ground surface creates an ideal electric field and forms one two-dimensional (2D) underground image profile, as shown in Fig. 1. Another pair of electrodes (potential poles) measure the potential difference of the electrical field. When anomalies, such as pipelines, substructures or cavities, exist underground, the electrical field will be distorted around these positions, and the locations and size of the anomaly could be identified in the 2D apparent resistivity image.

Figure 2 indicates a typical resistivity image around one single river-crossing bridge pier. The inspection resistivity values vary from 500 to less than 1 $\Omega \times$ m. The relatively high-resistivity values for sediments composed of gravel and rock are more than 150 $\Omega \times$ m, corresponding to the pink, red, orange or yellow zones. The reinforced bar content foundation usually forms an extremely low-resistivity zone, corresponding to the light blue and grey shades. The foundation type and pier depth are, respectively, identified as a shallow foundation and 6.5 m below the ground surface in this 2D resistivity image profile. The post-borehole exploration findings
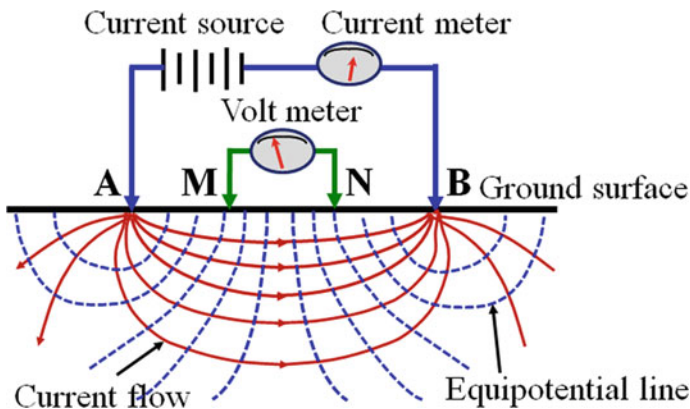
Fig. 1 Schematic representation for electrical resistivity tomography inspection
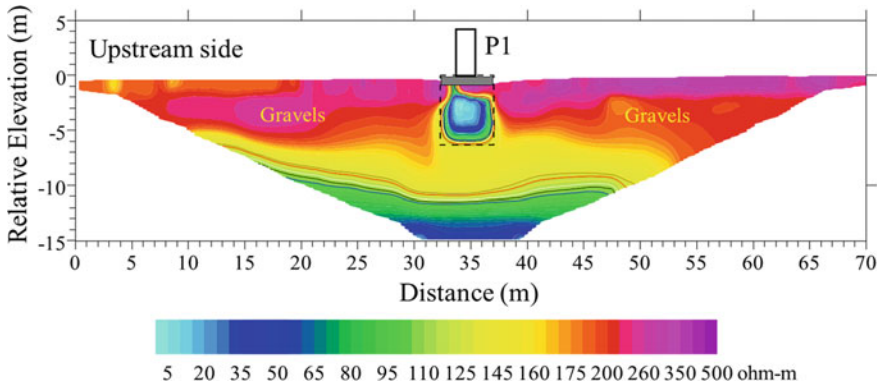
Fig. 2 Electrical resistivity tomography image on an unknown bridge pier inspection

confirmed the actual depth as 6.3 m, almost as the same as the investigation outcome (see Fig. 3).

In practice, the deployment of electrical resistivity tomography is highly associated with subsurface characterization and surface environment. Several setting parameters should be considered in the inspection process. The inspection depth and resolution of electrical resistivity tomography are dependent on both electrode spacing and layout length. The smaller the electrode spacing is arranged, the higher the image resolution and the shallower the inspection depth are. Accordingly, the larger the electrode spacing is used, the lower the image resolution and the deeper the inspection depth are. Both inspection depth and site geological characteristics determine the possible electrode spacing. A trial and error process is, in practice, suggested to determine the optimal layout deployment. A reliable inspection depth, in practice, is around 5–6 times of the electrode spacing. The optimal layout length is suggested to vary from 1.5 to 2 times of the foundation depth if possible [11, 13]. Two inspection modes, like a dipole–dipole array and a pole–dipole array, are suggested

Fig. 3 Borehole sampling on an unknown bridge pier inspection
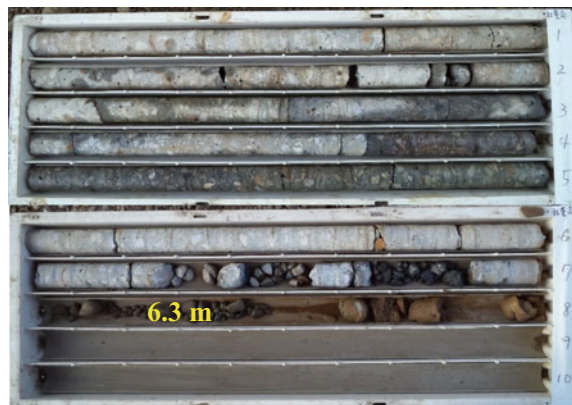
to obtain better cross-check image results [13]. Besides, if an extended workspace is available during the field testing, two different inspection directions are suggested to improve the inspection accuracy and effectively separate unexpected embedded anomalies from existing bridge substructures [10, 13].

3 Investigation of Substructure Depths

The electrical resistivity tomography technique inspected part of a 1.6-km-long twin-track railway bridge located at the Western Main Line of the rail transportation network in Taiwan (Fig. 4). Each 9.5-m-span deck is supported with two T-type-reinforced concrete (RC) girders and four RC piers. In order to avoid buckling of the slender RC pier and provide sufficient earthquake resistance of the rail bridge, extra horizontal RC rectangular beams were settled on the middle position of the bridge piers by linking every five spans. In addition, each pier is composed of two pile bents with two different diameters, including 1.2 m at the exposure portion and 2.0 m at the embedded part (Fig. 5). In the original design chart, the embedded depths of the pile bents are nominated as 25 m, and the exposure heights of the pile bents are various from 5 to 8 m, as shown in Fig. 5.

The electrical resistivity tomography was initially laid along the southbound track-side and kept a distance of 0.5 m away from the bridge piers (Fig. 6). The investigation length of 213 m in total ranged from Pier P46 to Pier P67 by using an electrode spacing of 3 m. It was expected that a longer investigation line could detect a deeper substructure and identify the bottom depths of these pile bents. However, the inspection results, shown in Figs. 7 and 8, present apparent resistivity images completely different from the expectation. The resultant images of two inspection modes, i.e., dipole–dipole array and pole–dipole array, indicated that vertical-shape low-resistivity closed zones, i.e. grey shades, regularly occurred at the pier positions, which usually represent reinforced steel re-bars in the bridge foundations.

Fig. 4 Rail bridge panorama images: **a** view from the northwest; **b** view from the southwest
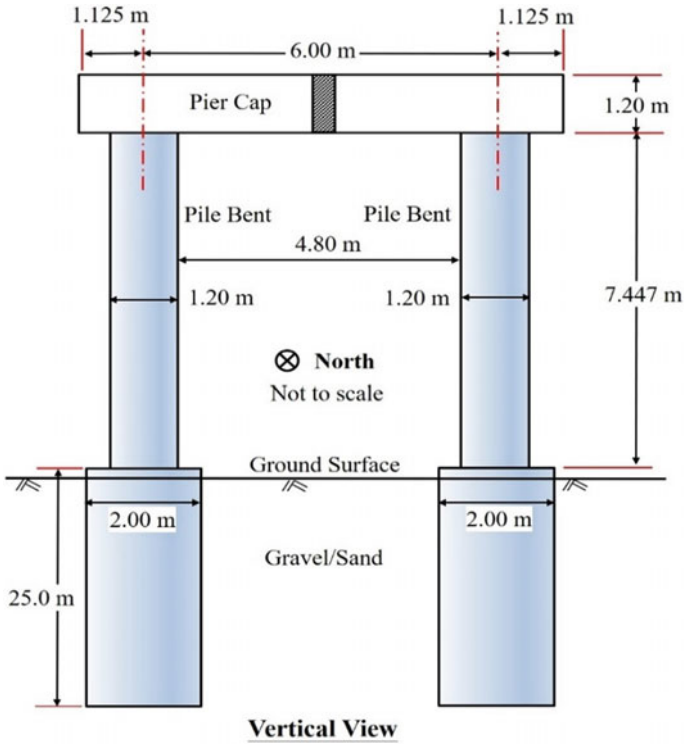
Fig. 5 Typical substructure profile of the bridge pier

Fig. 6 Inspection line of electrical resistivity tomography along the rail bridge
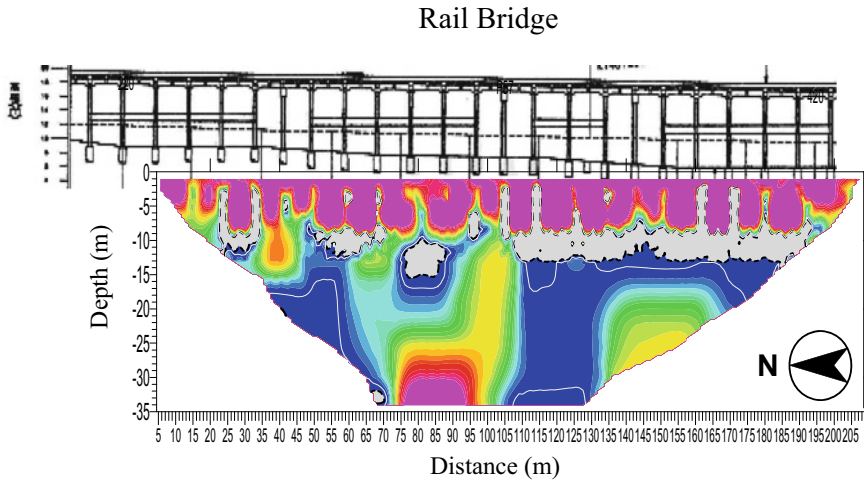
Fig. 7   Inspection results of electrical resistivity tomography: dipole–dipole array
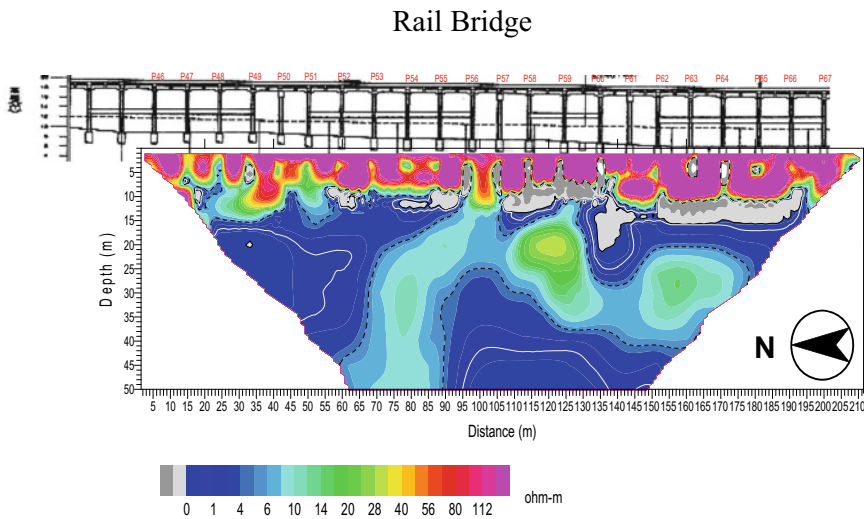
Fig. 8   Inspection results of electrical resistivity tomography: pole–dipole array

The electrical resistivity tomography can identify the pile bent locations. Still, the bottoms of the low-resistivity zones stop at depths around 8 ~ 12 m, much shorter than the nominal depths of 25 m, for both inspection modes. At the positions of 8 ~ 12 m deep, somehow an unexpected continuous low-resistivity zone was horizontally extended over ten pile bents, which were supposed to be separated from each other. The resulting images revealed that a layered anomaly, other than piles, with

low-resistivity values, obviously interfered with the electric field in the ground and blocked the inspection depth.

Another two survey lines, 200 m in length each, were then settled beside the locations of Piers P53 and P54 and chosen their alignments perpendicular to the previous survey direction, as shown in Fig. 9. The new investigation lines crossed over farmland, two RC drainage ditches, one small agriculture paved road and the rail bridge site. Using a larger electrode spacing of 5 m could improve the reliable inspection depth up to 30 m. The inspection results across Piers P53 and P54 are demonstrated in Figs. 10 and 11, respectively. Such modified survey deployment

Fig. 9 Inspection line of electrical resistivity tomography along pile bents
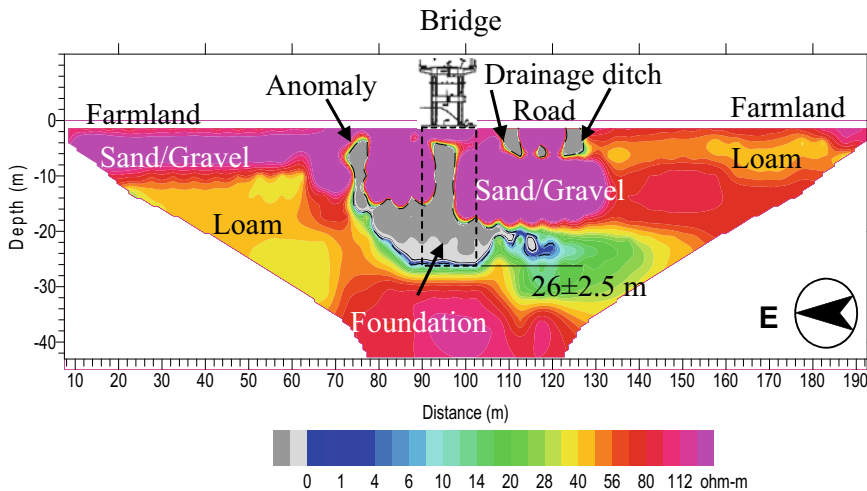
Fig. 10 Inspection results of electrical resistivity tomography across Pier P53
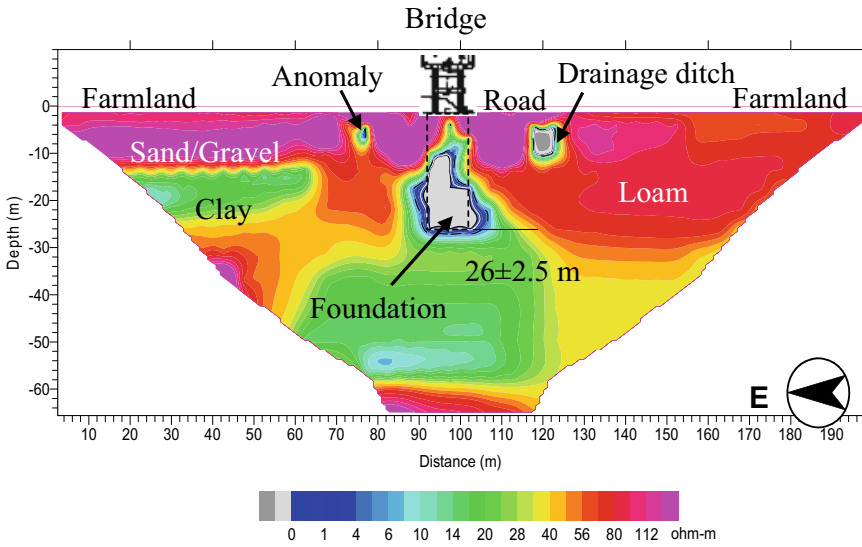
Fig. 11 Inspection results of electrical resistivity tomography across Pier P54

successfully separated the original continuous low-resistivity zone into two individual parts. For the zones existing right below the rail bridge site, the flat bottoms of the low-resistivity zones (grey shades) were significantly identified as 26 ± 2.5 m, which corresponded to the nominal depths, i.e. 25 m, of the pile bents. On the east side of the bridge, another vertical-shape low-resistivity closed-contour zone (grey shade) was identified as an unexpected anomaly, and its depth was located at the relatively shallow location, around 12 ~ 16 m. Besides, the remaining near-surface low-resistivity zones were located below the drainage ditches, which consisted of conductive-reinforced steel bars.

On the east side of the rail bridge, the unexpected vertical-shape low-resistivity anomalies cannot be appropriately interpreted based on the objects existing on the ground surface. Therefore, tracing back to the report of the rail bridge construction plan, the unexpected anomalies were located between the construction materials depot and the rail bridge construction site. The measured depth of the unexpected anomaly was around 12 m. Fortunately, this depth value met the geometrical dimension of the sheet piles, which are commonly used for the railway station excavation and relevant engineering projects. It is believed that the sheet piles could be used to temporarily mitigate the lateral displacement due to the heavy surcharge loading in the depot site for storing construction materials during the construction period. After finishing the rail bridge construction, parts of the temporal sheet piles, at least, were abandoned directly and remained under the ground surface on the rail bridge site. This cause could be the best possibility to explain the unexpected vertical-shape low-resistivity closed-contour zone found in the measured electrical resistivity images.

4 Conclusions

The electrical resistivity tomography technique was used to inspect the foundation depths of a rail bridge in western Taiwan. Different survey layouts were chosen to investigate the substructure conditions. Initially, an investigation line parallel to the traffic direction indicated an unexpected substructure pattern, a continuous horizontal-shape low-resistivity zone across over ten independent pile bents, by using two different inspection modes. Such an unreasonable horizontal low-resistivity zone located on shallow positions severely interfered with the inspection depths of the pile bents. Therefore, two alternative investigation lines perpendicular to the previous survey direction were chosen, and this new approach successfully separated this shallow low-resistivity zone into two single parts. Amongst, one deeper low-resistivity contour zone located right below the bridge pier site was identified as the foundation depths. The inspection depths are consistent with the nominal depth of 25 m. Another vertical-shape low-resistivity zone, as an unexpected anomaly, existed at the relatively shallow positions. According to the bridge construction information, the unexpected anomalies could be interpreted as the abandoned temporal sheet piles located between the rail bridge and a temporary depot site for stocking construction materials. Besides, this depth investigation case also suggests that using two inspection lines in different directions is a better approach, in practice, to separate target bridge substructures from other unexpected embedded anomalies effectively.

References

1. Boeckmann AZ, Loehr JE (2017) Current practices and guidelines for the reuse of bridges foundations. NCHRP-505. Transportation Research Board, National Academies, Washington, DC
2. Chinese Institute of Civil and Hydraulic Engineering (CICHE) (2010) Bridge inspection method and its application. Scientific and Technical Publishing Co., Ltd., Taipei (in Chinese)
3. Collin JG, Jalinoos F (2014) Foundation characterization program (FCP): tech brief #1-workshop report on the reuse of bridge foundations. Report No. FHWA-HRT-14-072. McLean, Virginia
4. Daily W, Ramirez A, Binley A, LaBrecque D (2005) Electrical resistance tomography—practice and theory. In: Butler DW (ed) Near-surface geophysics. Investigations in geophysics no. 13. Society of Exploration Geophysicists, Tulsa, pp 525–550
5. Hertlein BH, Davis AG (2006) Non-destructive testing of deep foundations. Wiley, Chichester
6. Loke MH (2000) Electric imaging surveys for environmental and engineering studies—a practical guide for 2-D and 3-D surveys. ABEM Instrument AB, Sundbyberg
7. Olson LD, Jalinoos F, Aouad MF (1998) Determination of unknown subsurface bridge foundations. NCHRP project no. E21-5. Olson Engineering, Wheat Ridge, CO
8. Schaefer VR, Jalinoos F (2013) Characterization of bridge foundations workshop report. Report no. FHWA-HRT-13-101. McLean, Virginia

9. Society of Exploration Geophysicists of Japan (2014) Application manual of geophysical methods to engineering and environmental problems. European Association of Geoscienists & Engineers (EAGE), Houten
10. Wang H, Hsieh S-C, Lin C, Wang C-Y (2014) Forensic diagnosis on flood-induced bridge failure. I: the determination of the possible causes of failure. J Perform Constr Fac 28(1):76–84. https://doi.org/10.1061/(ASCE)CF.1943-5509.0000419
11. Wang H, Hu C-H, Nguyen TV, Wang C-Y (2020) Depth evaluation on submerged pile bents. J Perform Constr Fac 34(1):06019003. https://doi.org/10.1061/(ASCE)CF.1943-5509.0001355
12. Wang H, Hu C-H, Wang C-Y (2015) NDT-based identification on an unknown bridge foundation. e-J Non-Destruct Test 20(1):888–896
13. Wang H, Wang C-Y, Hu C-H (2012) Bridge foundation inspection and its identification. In: Proceedings of the 36th national mechanics conference. National Central University, Chung-Li, Taoyuan, pp R-009-1–R-009-6 (in Chinese)
14. Wightman WE, Jalinoos F, Sirles P, Hanna K (2003) Application of geophysical methods to highway related problems. Report no. DTFH68-02-P-00083. Central Federal Lands Highway Division, Lakewood, CO

Mathematical Modeling of the Short-Term Performance of Railway Track Under Train-Induced Loading

Piyush Punetha and **Sanjay Nimbalkar**

Abstract The accurate prediction of the track deformation under train-induced repetitive loading is inevitable to assess the efficiency of a railway track. This paper presents an analytical technique to calculate the transient deformations in a railway track subjected to train-induced loading. The method considers the track substructure as multilayered media in which the behavior of an individual track layer is simulated using a mass-spring-dashpot model. Unlike existing approaches to model the track substructure as an equivalent single or double layer, the proposed analytical approach considers all the three layers of the ballasted track (i.e., ballast, capping or subballast and subgrade). The accuracy of the proposed technique is investigated by comparing the predicted values of track displacement with the published data available in the literature. The predicted results are found to be in good agreement with past studies. A parametric study on the substructure behavior revealed that the elastic modulus of track layers significantly influences the track response.

Keywords Mathematical model · Recoverable deformation · Railway track

1 Introduction

With an increase in demand for higher speed, the stress and deformations in the ballasted tracks have increased substantially [1]. To maintain an adequate level of passenger safety and comfort necessary for high-speed rail operations, the frequency of maintenance activities has increased manifolds. These maintenance operations are usually expensive due to poor understanding of the track behavior, inadequate planning, lack of time for the analysis of track inspection data or unavailability of an adequate database [2]. Thus, an accurate evaluation of the track substructure response is essential to plan the maintenance cycles and optimize track performance.

P. Punetha · S. Nimbalkar (✉)

School of Civil and Environmental Engineering, FEIT, University of Technology, Sydney NSW-2007, Australia

e-mail: Sanjay.Nimbalkar@uts.edu.au

The development of a reliable technique for the prediction of track response would lead to significant cost savings in the operation of the railways at elevated train speed.

The field studies, laboratory investigations, numerical and analytical simulations can be used to understand the behavior of a railway track. The field and reduced scale laboratory investigations with proper instrumentation are reliable approaches to understand the track response. They also provide valuable data that can be used for validating the numerical or analytical models. However, these investigations are usually time consuming and expensive. The numerical and analytical techniques are promising alternatives to analyze the track response. Consequently, several researchers have utilized numerical simulations to evaluate the response of the railway tracks subjected to train-induced repeated loads [3–12]. However, the numerical simulation of the railway tracks generally requires enormous computational time and resources.

The analytical techniques are relatively faster than the numerical simulations. Therefore, several researchers have developed analytical methodologies in an attempt to simulate the response of the railway track [13–16]. The track substructure in these methods is modeled using equivalent spring or dashpots, as a half-space (either homogenous or layered) or a combination of these two [17, 18]. Choudhury et al. [19] simulated the response of the railway track using a two degree of freedom mass-spring-dashpot model.

In this paper, a methodology is developed to calculate the transient (recoverable) response of the track substructure layers subjected to train-induced repeated loads. The present approach employs a mass-spring-dashpot model to capture the track behavior. The method includes the ballast, capping (also known as subballast) and subgrade layers and also considers the continuity of these layers in the longitudinal direction (i.e., the direction of train movement). The validity of the proposed technique is examined by comparing the model predictions with the published data available in the literature. Subsequently, a parametric investigation is carried out to study the effect of individual layer properties on the track behavior.

2 Development of Mathematical Model to Predict the Track Response

Figure 1 represents the schematic diagram of a ballasted railway track structure. It consists of two components: superstructure and substructure. The superstructure comprises the rails, ties (sleepers), rail pads and fasteners. The substructure is the geotechnical component which comprises ballast, capping (or subballast) and subgrade layers. To evaluate the transient response, the track substructure is modeled as a three degree of freedom (3DoF) system. Figure 2 shows the 3DoF mass-spring-dashpot model of the track substructure. Each substructure layer is composed of lumped masses that are supported by viscoelastic elements such as springs and dashpots.
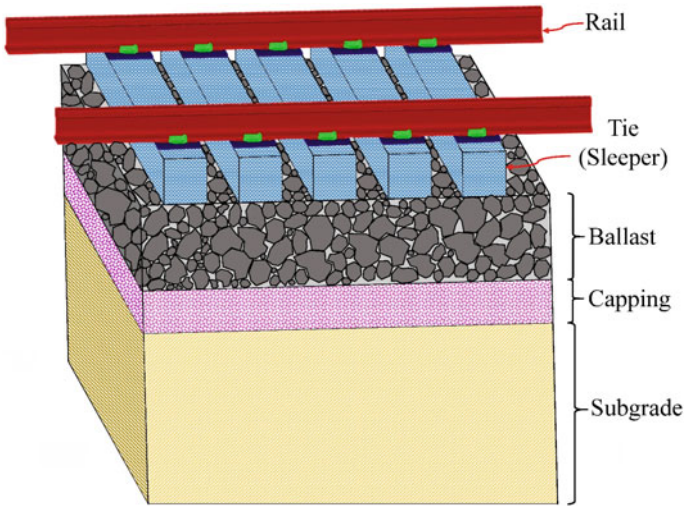
Fig. 1 Structure of a ballasted railway track

Fig. 2 Mass-spring-dashpot model of the track substructure
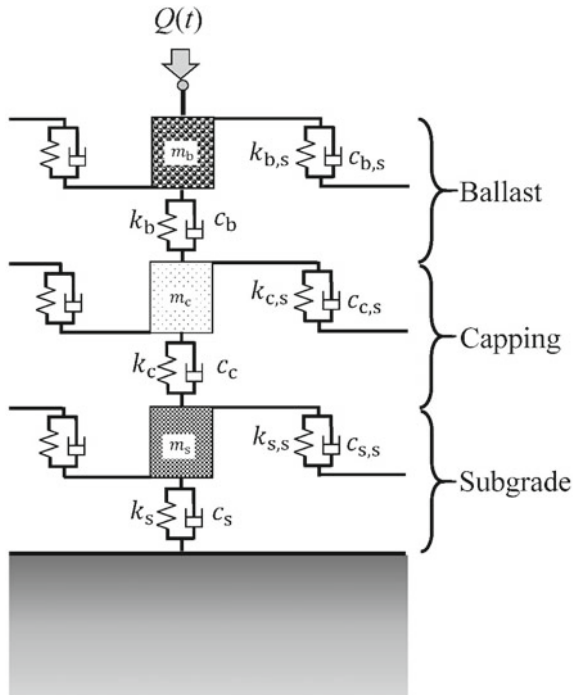
The equation of motion for the track below the nth tie point is derived by imposing the dynamic equilibrium condition:

$$M\ddot{Y}_{n} + C\dot{Y}_{n} + KY_{n} = F_{n} + C^{s}\left(\dot{Y}_{n+1} + \dot{Y}_{n-1}\right) + K^{s}\left(Y_{n+1} + Y_{n-1}\right) \quad (1)$$

where M, C, C^{s}, K and K^{s} are the mass, damping and stiffness matrices; $\ddot{Y}_{n}, \dot{Y}_{n}, Y_{n}$ and F_{n} are the acceleration, velocity, displacement and force vectors at the nth tie, respectively. The Newmark's implicit scheme is used to solve Eq. (1) and evaluate the transient response of the substructure layers in terms of displacement, acceleration and velocity-time histories. The mass, stiffness and damping matrices in Eq. (1) are defined as follows:

$$M = \begin{bmatrix} m_{s} & 0 & 0 \\ 0 & m_{c} & 0 \\ 0 & 0 & m_{b} \end{bmatrix} \quad (2)$$

$$C = \begin{bmatrix} c_{s} + c_{c} + 2c_{s,s} & -c_{c} & 0 \\ -c_{c} & c_{c} + c_{b} + 2c_{c,s} & -c_{b} \\ 0 & -c_{b} & c_{b} + 2c_{b,s} \end{bmatrix}; \quad C^{s} = \begin{bmatrix} c_{s,s} & 0 & 0 \\ 0 & c_{c,s} & 0 \\ 0 & 0 & c_{b,s} \end{bmatrix} \quad (3)$$

$$K = \begin{bmatrix} k_{s} + k_{c} + 2k_{s,s} & -k_{c} & 0 \\ -k_{c} & k_{c} + k_{b} + 2k_{c,s} & -k_{b} \\ 0 & -k_{b} & k_{b} + 2k_{b,s} \end{bmatrix}; \quad K^{s} = \begin{bmatrix} k_{s,s} & 0 & 0 \\ 0 & k_{c,s} & 0 \\ 0 & 0 & k_{b,s} \end{bmatrix} \quad (4)$$

where m_{s}, m_{c} and m_{b} are the vibrating mass of subgrade, capping and ballast, respectively; c_{s}, c_{c} and c_{b} are the damping coefficients of subgrade, capping and ballast, respectively; k_{s}, k_{c} and k_{b} are the stiffness of subgrade, capping and ballast, respectively; $k_{s,s}$, $k_{c,s}$ and $k_{b,s}$ are the shear stiffness of subgrade, capping and ballast, respectively; $c_{s,s}$, $c_{c,s}$ and $c_{b,s}$ are the shear damping coefficients of subgrade, capping and ballast, respectively. The mass and stiffness of the track layers are evaluated by using a pyramidal load distribution model incorporating the overlapping effect along both longitudinal and transverse directions [20, 21]. The damping coefficients for each layer are evaluated using the principle of vibrations as follows [22]:

$$c_{i} = \sqrt{\frac{E_{i}\rho_{i}}{(1 + v_{i})(1 - v_{i})}} \quad (5)$$

where $i = $ b, c and s for ballast, capping and subgrade, respectively; ρ_{i} and v_{i} are the density and Poisson's ratio of the ith substructure layer, respectively. The acceleration, velocity, displacement and force vectors are defined as follows:

$$\ddot{Y}_{n} = \begin{Bmatrix} \ddot{y}_{s,n}(t) \\ \ddot{y}_{c,n}(t) \\ \ddot{y}_{b,n}(t) \end{Bmatrix}; \quad \dot{Y}_{n} = \begin{Bmatrix} \dot{y}_{s,n}(t) \\ \dot{y}_{c,n}(t) \\ \dot{y}_{b,n}(t) \end{Bmatrix}; \quad Y_{n} = \begin{Bmatrix} y_{s,n}(t) \\ y_{c,n}(t) \\ y_{b,n}(t) \end{Bmatrix}; \quad F_{n} = \begin{Bmatrix} f_{s,n}(t) \\ f_{c,n}(t) \\ f_{b,n}(t) \end{Bmatrix} \quad (6)$$

where the subscripts s, c and b represent the subgrade, capping and ballast, respectively; $\ddot{y}$, $\dot{y}$ and y are the acceleration, velocity and displacement of the track layers, respectively; f is the external load acting on the substructure layer. The external load acting on the capping and subgrade layers at a tie point are taken as zero; whereas, the external load acting on the ballast layer is equal to the rail-seat load. The rail-seat load $[Q(t)]$ is evaluated following the approach given in Doyle [23].

The dynamic effects of the rail–wheel interaction are also incorporated in the analysis using an impact factor (IF) [24], which is a multiplier to the static axle (or wheel) load (Q_a) [1].

$$IF = 1 + \alpha_1 \left(\frac{V}{D_w} \right)^{\alpha_2} \tag{7}$$

where V and D_w are the train speed and wheel diameter, respectively; α_1 and α_2 are the empirical coefficients.

3   Verification of the Proposed Model

The validity of the proposed technique is examined by comparing the predicted results with the field investigation results reported by Takemiya and Bian [25] and Priest et al. [26]. Takemiya and Bian [25] presented the dynamic response of a high-speed ballasted rail track section located along the West Coast line in Sweden. The track at the test section comprised of 60 kg/m rails supported by rail pad, ties, ballast and subgrade layers. The track response was expressed in terms of the vertical displacement and acceleration generated during the passage of a Swedish X-2000 high-speed train.

Figure 3 compares the Fourier amplitude spectrum of the transient vertical ground displacement calculated using the present approach with the data recorded in the field investigations [25]. The values of the parameters used for the simulation are provided in Table 1. The thicknesses of the top (ballast), middle (capping) and bottom (subgrade) layers are taken as 1, 13.5 and 36 m, respectively. It is apparent that the response predicted using the proposed method is nearly identical to that observed in the field investigations. It can also be observed that the response is distributed over a frequency range of 0.1–9 Hz. The peaks are observed in the frequency range between 0.1 and 3 Hz (due to the combined effect of train geometry and speed) and at 3.2, 3.66, 4.12, 4.73, 5 and 6.7 Hz (associated with bogie positions).

Priest et al. [26] carried out extensive field investigations in a heavy haul track in South Africa. The track section comprised 60 kg/m rails supported by ties, ballast (0.3 m thick) and formation layers. They employed geophones to monitor the velocity and the corresponding displacement of individual track layers. Figure 4 compares the variation of transient displacement with time during the passage of 20-ton axle load wagons, calculated using the present approach with the data recorded in the field investigations. Table 1 provides the values of the parameters employed in simulations.
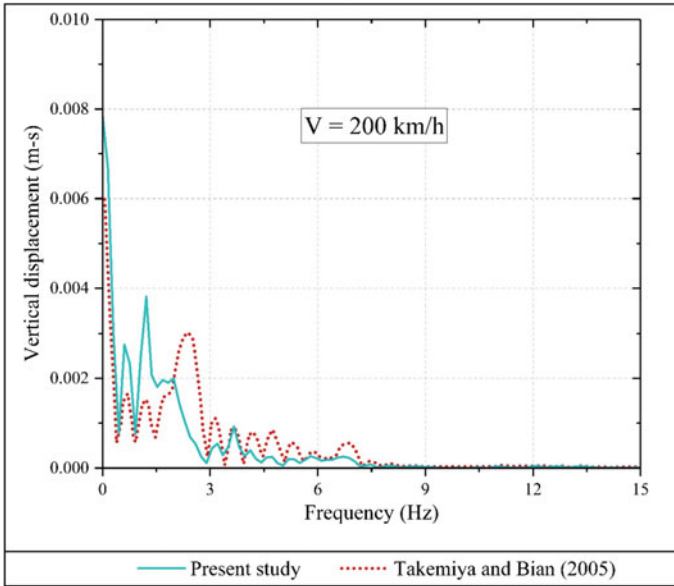
Fig. 3 Comparison of Fourier amplitudes of vertical ground displacement evaluated using the present approach with field data reported by Takemiya and Bian [25]

The model predictions slightly underestimate the magnitude of vertical displacement; however, the trend is similar to the field data.

Thus, the present approach can accurately evaluate the transient or short-term response of the track substructure layers. This method can be employed to optimize track performance, improve the efficiency and, consequently, reduce the operating cost of the railways. This approach may be of great interest to the practicing railway engineers owing to the simplicity and less computational power requirements.

4   Parametric Study

The proposed model is used to investigate the influence of elastic modulus on the transient response of track substructure layers. The elastic modulus of ballast (E_b), capping (E_c) and subgrade (E_s) is varied in the range of 138–551 MPa, 69–276 MPa and 14–276 MPa, respectively. A similar range of values has also been used by [27–29] in their parametric investigations. The track response is evaluated in terms of average recoverable vertical strain, which is the ratio of vertical deformation to the initial thickness of the substructure layer. The predictions are carried out for the Thalys high-speed train traveling at a speed of 150 km/h.

Figure 5 shows the variation of average recoverable strain in the ballast, capping and subgrade layers with elastic moduli E_b, E_c and E_s. The values of parameters

Table 1 Parameters for evaluating track response

Parameter	Symbol	Unit	Takemiya and Bian [25]	Priest et al. [26]	Parametric study
Wheel diameter	D_w	m	1.016	0.954	1.016
Axle load	Q_a	kN	118–180	196	250
Empirical coefficient	α_1	–	0.0065	0.0065	0.0058
	α_2	–	1	1	0.89
Ballast					
Elastic modulus	E_b	MPa	19	100	276 (138–551[a])
Poisson's ratio	υ_b	–	0.49	0.3	0.3
Density	ρ_b	kg/m^3	1500	1800	1760
Capping					
Elastic modulus	E_c	MPa	20	220	138 (69–276[a])
Poisson's ratio	υ_c	–	0.5	0.3	0.35
Density	ρ_c	kg/m^3	1430	2175	1920
Subgrade					
Elastic modulus	E_s	MPa	44	27,000	14 (14–276[a])
Poisson's ratio	υ_s	–	0.5	0.25	0.35
Density	ρ_s	kg/m^3	1475	2300	1920

[a]Values indicate the range used for the parametric study

used in the prediction are given in Table 1. The horizontal dashed line in the figure represents the strain when the parameters are assigned the nominal values. The downward (blue) and upward (red) arrows indicate a reduction and increment in strain, respectively. The results indicate that the average recoverable strain in the ballast and capping layers decreases by 77.9% and 7.9%, respectively, with a rise in E_b from 138 to 551 MPa. The subgrade layer showed a marginal effect. This reduction in resilient response is attributed to the increase in stiffness of the ballast layer (consequently, an increment in load distribution area) with a rise in the elastic modulus.

The recoverable strain in the ballast layer increases by 17% with a rise in E_c from 69 to 276 MPa; whereas, the strain in the capping layer decreases by 73% with an increase in E_c from 69 to 276 MPa. The capping modulus has an insignificant influence on the subgrade strain. The average recoverable strain in the subgrade layer decreases by 73% with a rise in E_s from 14 to 276 MPa. However, the recoverable strain in the ballast and capping layers increases by 69% and 70%, respectively, with
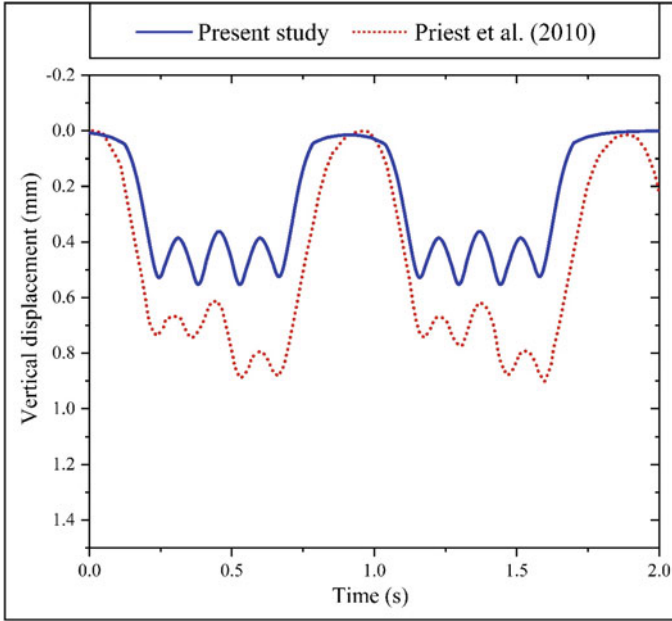
Fig. 4 Comparison of transient displacement evaluated using the present approach with field data reported by Priest et al. [26]

a rise in E_s from 14 to 276 MPa. This indicates that the presence of a stiff subgrade may increase the deformation in the granular (ballast and capping) layers.

Therefore, it is clear that the elastic modulus of the substructure layers plays a significant role in the transient response of the railway track. The present approach can be used to evaluate the track response for different train, track and substructure properties. Such analyses may provide the value of parameters that are required to achieve optimum track performance.

5   Conclusions

An analytical method is developed to predict the transient response of substructure layers in ballasted railway tracks. The approach evaluates the recoverable response using a three degree of freedom mass-spring-dashpot model. The validity of the technique is examined by comparing the predicted results with the field investigation results reported in the literature. A close agreement between the observed and predicted results demonstrates the accuracy of the proposed approach in evaluating the track substructure response. The parametric study on the track behavior shows that the elastic modulus of track layers significantly influences their response. The
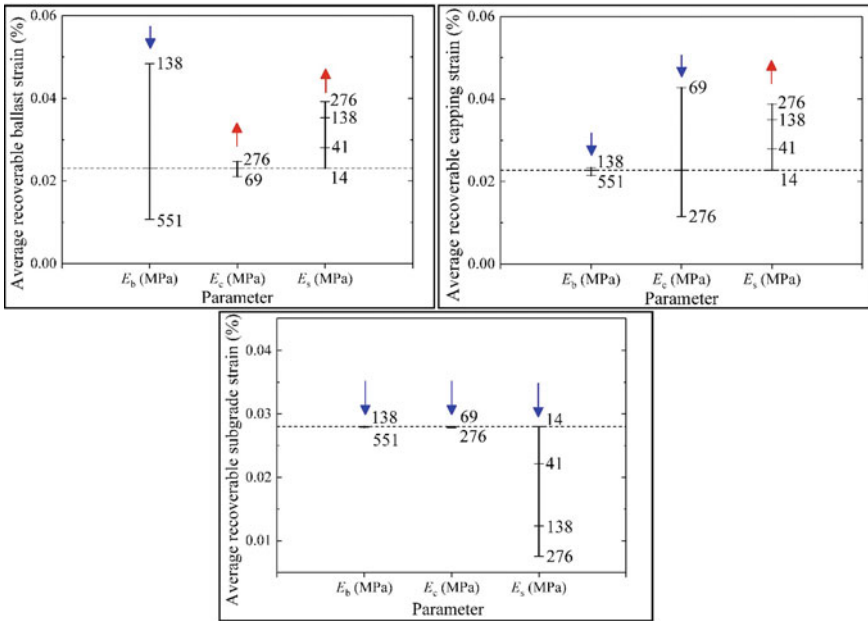
Fig. 5 Influence of elastic modulus on the average transient vertical strain in the track substructure layers

presence of stiff subgrade may increase the deformation in the granular substructure layers (ballast and capping). The present approach can be adopted by railway engineers to improve track performance.

References

1. Nimbalkar S, Indraratna B (2016) Improved performance of ballasted rail track using geosynthetics and rubber shockmat. J Geotech Geoenviron Eng 142(8):04016031
2. Nguyen K, Villalmanzo D, Goicolea J, Gabaldon F (2016) A computational procedure for prediction of ballasted track profile degradation under railway traffic loading. Proc Inst Mech Eng F J Rail Rapid Transit 230(8):1812–1827
3. Stewart H, Selig E (1982) Predicted and measured resilient response of track. J Geotech Eng Div 108(11):1423–1442
4. Yang YB, Hung HH (2001) A 2.5D finite/infinite element approach for modelling visco-elastic bodies subjected to moving loads. Int J Numer Methods Eng 51(11):1317–1336
5. Hall L (2003) Simulations and analyses of train-induced ground vibrations in finite element models. Soil Dyn Earthq Eng 23(5):403–413
6. Yang LA, Powrie W, Priest JA (2009) Dynamic stress analysis of a ballasted railway track bed during train passage. J Geotech Geoenviron Eng 135(5):680–689
7. Bian X, Jiang H, Chen Y (2010) Accumulative deformation in railway track induced by high-speed traffic loading of the trains. Earthq Eng Eng Vib 9(3):319–326

8. Galvín P, Romero A, Domínguez J (2010) Fully three-dimensional analysis of high-speed train–track–soil-structure dynamic interaction. J Sound Vib 329(24):5147–5163

9. Banimahd M, Woodward P, Kennedy J, Medero G (2013) Three-dimensional modelling of high speed ballasted railway tracks. Proc Inst Civ Eng Transp 166(2):113–123

10. Connolly D, Giannopoulos A, Forde M (2013) Numerical modelling of ground borne vibrations from high speed rail lines on embankments. Soil Dyn Earthq Eng 46:13–19

11. Chen J, Zhou Y (2018) Dynamic responses of subgrade under double-line high-speed railway. Soil Dyn Earthq Eng 110:1–12

12. Li L, Nimbalkar S, Zhong R (2018) Finite element model of ballasted railway with infinite boundaries considering effects of moving train loads and Rayleigh waves. Soil Dyn Earthq Eng 114:147–153

13. Metrikine AV, Popp K (1999) Vibration of a periodically supported beam on an elastic half-space. Eur J Mech A Solids 18(4):679–701

14. Chen YH, Huang YH (2000) Dynamic stiffness of infinite Timoshenko beam on viscoelastic foundation in moving co-ordinate. Int J Numer Methods Eng 48(1):1–18

15. Kaynia AM, Madshus C, Zackrisson P (2000) Ground vibration from high-speed trains: prediction and countermeasure. J Geotech Geoenviron Eng 126(6):531–537

16. Guo Y, Zhai W (2018) Long-term prediction of track geometry degradation in high-speed vehicle–ballastless track system due to differential subgrade settlement. Soil Dyn Earthq Eng 113:1–11

17. Dieterman H, Metrikine V (1997) Steady-state displacements of a beam on an elastic half-space due to a uniformly moving constant load. Eur J Mech A Solids 16(2):295–306

18. Sheng X, Jones CJC, Petyt M (1999) Ground vibration generated by a harmonic load acting on a railway track. J Sound Vib 225(1):3–28

19. Choudhury D, Bharti RK, Chauhan S, Indraratna B (2008) Response of multilayer foundation system beneath railway track under cyclic loading. J Geotech Geoenviron Eng 134(10):1558–1563

20. Ahlbeck DR, Meacham HC, Prause RH (1975) The development of analytical models for railroad track dynamics. In: Symposium on railroad track mechanics. Pergamon Press, Princeton University, pp 239–263

21. Zhai WM, Wang KY, Lin JH (2004) Modelling and experiment of railway ballast vibrations. J Sound Vib 270(4–5):673–683

22. Nimbalkar S, Indraratna B, Dash SK, Christie D (2012) Improved performance of railway ballast under impact loads using shock mats. J Geotech Geoenviron Eng 138(3):281–294

23. Doyle NF (1980) Railway track design a review of current practice. In: Bureau of Transport Economics (ed). Australian Government Publishing Service, Canberra

24. Esveld C (2001) Modern railway track. MRT-Productions, Delft

25. Takemiya H, Bian X (2005) Substructure simulation of inhomogeneous track and layered ground dynamic interaction under train passage. J Eng Mech 131(7):699–711

26. Priest JA, Powrie W, Yang L, Grabe PJ, Clayton CRI (2010) Measurements of transient ground movements below a ballasted railway line. Géotechnique 60(9):667–677

27. Selig ET, Li D (1994) Track modulus: its meaning and factors influencing it. Transp Res Rec 1470:47–54

28. Shahu J, Kameswara Rao N, Yudhbir (1999) Parametric study of resilient response of tracks with a sub-ballast layer. Can Geotech J 36(6):1137–1150

29. Li D, Hyslip J, Sussmann T, Chrismer S (2016) Railway geotechnics. Taylor and Francis, Boca Raton

A Deep Investigation into the Mechanisms and Factors Producing Mud Pumping

Stephen Wilk and Dingqing Li

Abstract Mud pumping is a common issue facing all railroads in which wet fines within the ballast pump up around the ties and onto the surface of the track during train loading. This often corresponds to poor drainage, loss in track geometry, reduced ballast strength and stiffness, and in the worst case leading to ballast failure. Despite the prevalence of this problem, the mechanisms behind mud pumping and the factors influencing it are not fully understood, although past investigations have determined that fines and water in ballast, as well as repeated dynamic wheel loads, need to act together to produce mud pumping. An improved understanding is to how it will allow for better prediction of mud pumping and the negative effects associated with it, along with improved maintenance planning and techniques. Transportation Technology Center, Inc. (TTCI) has further reviewed and investigated mud pumping situations from both its "rainy section" test zone at the Facility for Accelerated Service Testing (FAST) near Pueblo, Colorado, and multiple revenue service locations in attempt to understand the underlying mechanisms behind mud pumping. The rainy section at FAST and some revenue service sites suggested that some (and possibly most) mud pumping situations are purely surficial, originating from the wet regions just around the ties. However, other mud pumping situations have shown a seasonal or perched water table below the bottom of the ties that appears to cause moisture and fines to pump up to the surface from the subgrade or lower ballast layer. TTCI plans to continue to investigate different mud pumping situations with the end goals of developing ballast maintenance guidelines and improving track substructure-induced track geometry degradation forecasting models.

Keywords Mud pumping · Degraded ballast · Poor drainage · Repeated wheel loads

S. Wilk · D. Li (✉)
Transportation Technology Center, Inc., 55500 DOT Road, Pueblo, CO 81001, USA
e-mail: Dingqing_Li@aar.com

S. Wilk
e-mail: Stephen_Wilk@aar.com

1 Introduction

Ballast degradation is a common ballast issue faced by all railroads. Especially when wet, degraded ballast with fines can cause track geometry degradation, requiring increased maintenance. Improved identification of problematic or future degraded ballast locations can improve maintenance planning efficiency and reduce the need for reactive maintenance.

In an ideal track, the ballast layer should provide mechanical support to limit dynamic track movement in all three directions, prevent track geometry degradation, and also allow the drainage of excess water [1]. Excess moisture drains downward toward the sub-ballast and subgrade, which should have a 20:1–40:1 slope that causes excess moisture to run out of the track section. Drainage ditches along the track can then carry that excess moisture out of the right-of-way. The drainage in the ballast and sub-ballast is defined as internal drainage while the ditches are defined as external drainage.

Over time, both the internal and external drainage can become inhibited. For example, the ballast particles will mechanically break down from continual train loading producing fines that contaminate the ballast. In addition, fines can contaminate the ballast through surface infiltration or pump up from the subgrade. When enough fines contaminate the track section, the fines retain moisture and inhibit drainage of excess water. These are situations in which the internal drainage has been blocked. Another different example of blocked internal drainage is when the subgrade settles or heaves under the track creating pockets in which water can collect. Blocked external drainage is also a possibility in which ditches are blocked by brush or trash or are not large enough to handle excess water that then floods the track section. Reducing blocked internal and external drainage is important because they are the primary cause of ballast degradation and mud pumping, which is defined as when wet fines pump up onto the surface of the track. This mud pumping, and ballast degradation, is generally attributed to reduction in track performance, including but not limited to track geometry degradation, inhibited drainage, large track displacements, accelerated tie degradation, and increased rail wear and defects.

Multiple factors affect the performance of degraded ballast, including fine amount, fine type, fine distribution, moisture level, moisture source, and moisture distribution in the track section, along with many other variables such as climate and traffic [1, 2]. Fine levels above 20% by mass generally lead to increased maintenance activity and at 40% fines, and the majority of ballast voids are filled with fine particles. The type of fines present in the ballast will be dependent on location. They are primarily from ballast degradation, but may also result from surface infiltration, or may pump up from the subgrade when subsurface water is present. Smaller, more plastic fine particles are generally considered a greater issue than larger, but they are not the focus of this paper.

To investigate the influence of these variables, TTCI developed a "rainy section" test bed at FAST in 2017. This paper summarizes the previous two years of work (Phase I), explains the mechanism of mud pumping observed, discusses how the

findings from Phase I testing will guide the future testing at the rainy section, and compares the rainy section against other revenue service sites.

2 Rainy Section

The rainy section is a 20-foot-long section of track in Section 36 of FAST that contains upward of 40% fines by mass—primarily sand- and silt-size particles from natural ballast degradation (see Fig. 1)—and has an irrigation and drainage system that allows the replication of rainfall and control of drainage in the track. Figure 2 shows a photograph of the wetting process. This mimics a severe degraded ballast
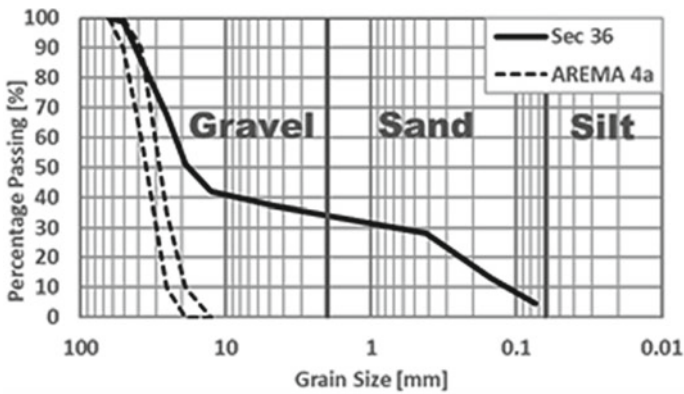
Fig. 1 Gradation curve of rainy section ballast material

Fig. 2 Photograph of irrigation system in the rainy section

condition in which the majority of ballast voids are filled by ballast degradation material and the fines are evenly distributed among the ballast section. The irrigation system replicates rainfall as the water source on the ballast. As a note, different fine level, fine type, moisture source, and fine distribution may significantly affect the results. Additional details of the rainy section setup can be found in previous publications [2–5].

3 Phase I Testing

The first phase of testing at the rainy section primarily involves quantifying how moisture affects track performance and the mechanism leading to surface mud pumping. A previous paper goes into more detail of the measurements and results [2].

To determine performance, multiple measurements were taken. Unloaded top-of-rail (TOR) elevations were collected after each night of FAST train operations (~2 MGT) to determine the elevation profile and unloaded settlement rates. Additional measurements were performed to determine track modulus at various stages of testing. Moisture sensors were installed at various locations in the rainy section to monitor moisture levels. Single-tie push (STP) tests were also conducted to determine the lateral tie resistance (resistance to lateral movement) under a variety of conditions. This quantified track settlement, track modulus, drainage, and lateral tie strength.

Multiple tests were conducted on the rainy section during Phase I, but they can be categorized into three main conditions: dry and no mud pumping (referred to as fine-degraded condition); wet and mud pumped (active mud pumping); and dry and mud pumped (no active mud pumping after dried). After surfacing, the fines were typically evenly distributed in the ballast section. During wetting (e.g., 10 mm/h of rain for 1 h) and train passage, the fines underneath the ties became saturated and had a state similar to a slurry consistency. As wetting (another hour at 10 mm/h) and train passage continue, the tie pressure would pump the mud slurry up around the ties and onto the track surface. This condition is commonly referred to as mud pumping. After being allowed to dry, the mud slurry remained at the surface but had dried out representing the dry and mud pumped condition.

Figure 3 shows how each of these three conditions, along with the clean ballast condition as a baseline, affects track performance at the rainy section. The results are presented conceptually (clean ballast represents the baseline condition of low settlement rate and high track modulus and drainage capacity) because of the variation between tests and dependence on specific measurements. However, Fig. 3 should give a general idea on the effect of moisture and fine distribution on performance. The specific results are presented in Table 1. The results also may vary for different situations.
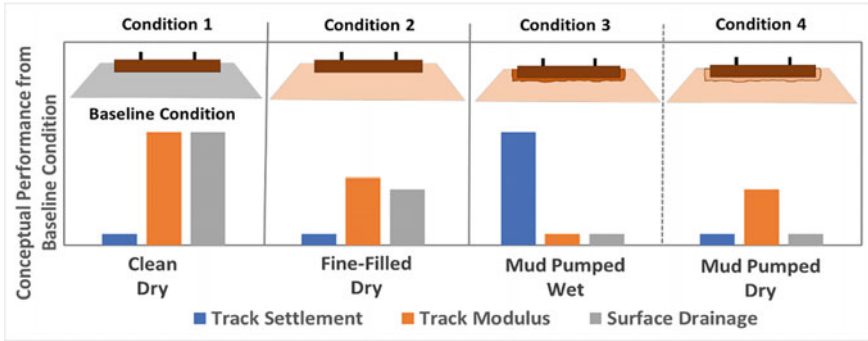
Fig. 3 Conceptual performance of four ballast conditions

Table 1 Rainy section performance metrics in a variety of conditions

Condition	Settlement rate [in/MGT]	Track modulus [lbs./in./in.]	Drainage time [Days]	Lateral tie resistance [kips]
Clean	0.03	4200	–	2.6
Degraded (dry)	0.03	3500	1	10+
Mud pumped (dry)	0.03	3000	5	6.0
Mud pumped (wet)	0.09	1500	5	2.9

The rainy section results show the following:

- *Clean Ballast*: This baseline condition typically shows small track settlement, track modulus value of about 4200 lbs./in./in. Excess water can drain within minutes and adequate lateral tie strength that is typical of previous measurements at FAST.
- *Dry Degraded Ballast*: This condition showed no visual signs of fines on the surface (typically a few inches of ballast cover), has similar settlement rates to clean ballast when dry, a slightly lower track modulus (3500 lbs./in./in.), inhibited drainage that took about a day to drain out excess water, and very high lateral resistance when dry due to strong shoulders.
- *Dry Mud Pumped Ballast*: This condition had visual signs of mud at the surface, similar settlement rates as the dry degraded ballast condition, a lower track modulus (3000 lbs./in./in.), and greater inhibited drainage that took about five days to drain out excess water. The lateral tie resistance likely had lower tie/ballast interface resistance, but the shoulder appeared to be still strong.
- *Wet Mud Pumped Ballast*: This condition had standing water and visual signs of mud at the surface, settlement rate much greater than the other conditions (~3× greater), a low track modulus (1500 lbs./in./in.), and inhibited drainage that took about five days to drain out excess water. The lateral tie resistance was similar to

clean ballast, but this value is likely dependent on the shoulder. If the shoulder is inadequate, the lateral tie resistance may be very low.

In summary, a few general remarks can be made from the results as follows:

- Increased settlement rate and decreased track stiffness are typically associated with wet ballast conditions. This means dry degraded ballast may not be a performance issue until heavy rainfall.
- Inhibited drainage is associated with fines in the track section and becomes more severe when the slurry surrounds the tie and forms a barrier. This means that mud pumping and surface fines keep the track in a more susceptible state for longer periods of time after wetting.
- From the first two points, it is logical that the performance of degraded ballast will be dependent on climate conditions (periods of moisture yearly and seasonally) and traffic (how many trains pass during times of moisture).

4 Mud Pumping Mechanism

A main objective of the ballast degradation research is to improve identification of potential problem regions and quantify the benefits of various maintenance and remediation action. In order to get to that stage, a thorough understanding of mud pumping and its causes is needed.

4.1 Rainy Section Specific

The observed process for mud pumping at the rainy section (see Fig. 4) is as follows and shown in Fig. 5. From the (a) dry initial condition, (b) rainfall (blue color) begins to wet the surface and upper ballast layer and ponds underneath the ties. After the rainfall has increased the moisture levels underneath the ties to a high enough level and train passage causes the ties to pump up and down, (c) the fines and water form a mud slurry (rust color) that is very soft and mobile. Continual train passage causes the tie to pump which pushes the mud slurry outward away from the tie, while sucking surrounding fines to the voids generated. This likely causes the slurry to move downward and outward, but the easiest escape path is upward around the tie. Eventually, the slurry coats the tie and track surface (d). The final cross section is shown in Fig. 6.

Multiple tests were run to determine the depth of the wet region (slurry). This involved moisture sensors, trenches, and PANDA® geoendoscopes (devices that can view downward into the ballast) [6]. All three methods agreed that the wet region in the rainy section is the top several inches below the bottom of the tie. This suggests that the moisture issue is primarily surficial and does not extend deep into the ballast section.

Fig. 4 Photograph of mud pumping with standing water
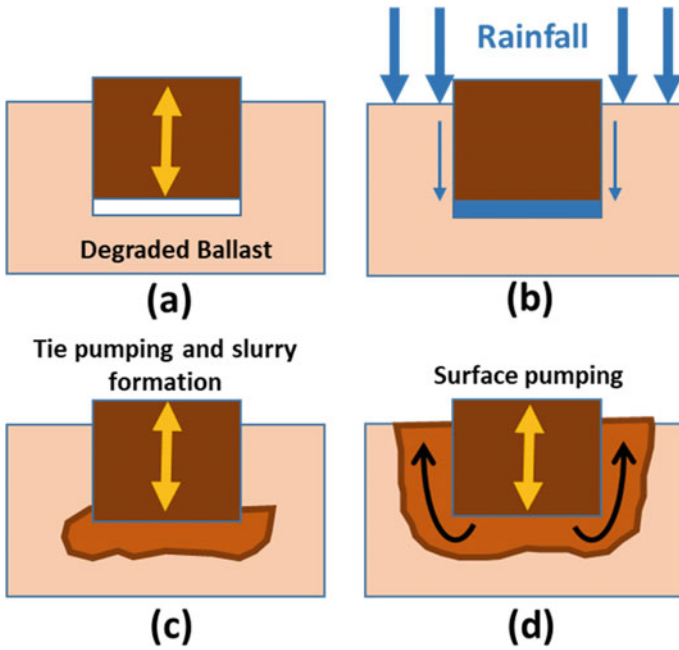
Fig. 5 Step-by-step of mud pumping in rainy section (blue—rain, light brown—degraded ballast with fines, rust—slurry, brown—tie yellow—time pumping due to train operations)
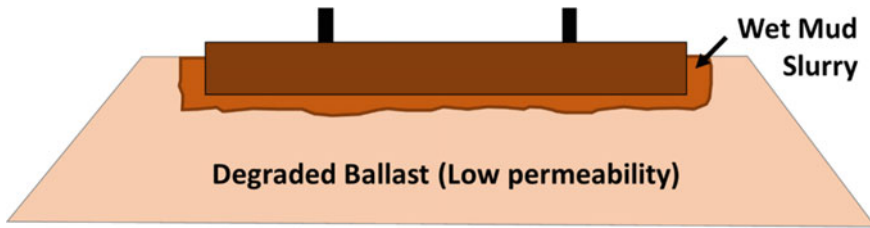
Fig. 6 Cross section of rainy section with surficial mud pumping

4.2 Other Mud Pumping Locations

One of the objectives of this research is to help prepare a field guide that allows railroad workers to properly identify root causes and perform maintenance in mud pumping situations. Therefore, TTCI has revisited past research [7] and made excavations at other mud pumping locations at FAST and revenue service locations to determine if other mud pumping situations resemble the rainy section and if any broad generalizations can be made.

From these investigations, the observation of mud pumping with just the slurry around the tie appears to be a common signature of surface issues. These locations often display higher levels of displacement, slurry a few inches below the tie, and likely have similar mechanisms as the rainy section. Example photographs are shown in Fig. 7. Figure 7a shows the surface of an active mud pumping track, and Fig. 7b shows the excavated cross section of the same track and the outline of the wet slurry with the moist, but not wet, degraded ballast underneath.

Therefore, the signature observations of surface mud pumping with slurry around the tie, ballast particles pushed away from the tie, and blocked internal drainage likely indicate a surficial issue in which the water source is rainfall. In these situations, maintenance should likely focus on improving drainage from the surface to below the tie. The details of this maintenance will be the subject of future research.

4.3 Subgrade Pumping

As opposed to the surface mud pumping discussed in the previous two Sects. 4.1 and 4.2, different surface mud pumping situations have also been widely observed. In these situations, the external drainage (i.e., ditches) appears to be blocked, and the track typically has a high-water table or is flooded. The surface mud pumping appears to be produced from the subgrade pumping up during train passage. This results in surface mud that appears more evenly distributed and is not localized around the ties. If the subgrade has settled or heaved under the track and trapped water, similar situations may be possible as well. Figure 8a, b shows examples of subgrade pumping.
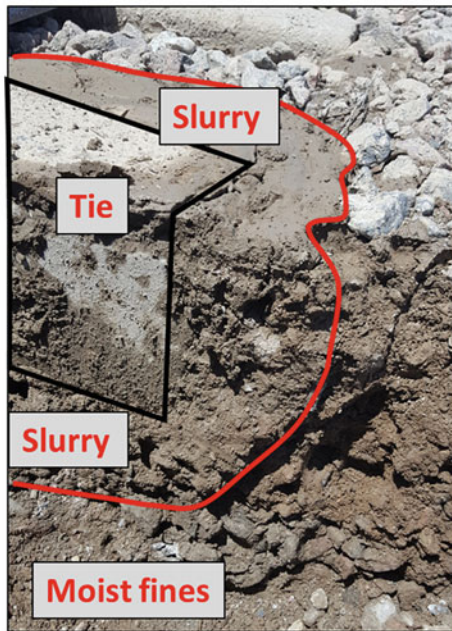
Fig. 7 Photographs of **a** surface mud pumping with a mechanism similar to the rainy section and **b** an excavation of the location

For these situations, the primary remediation focus should be unblocking or expanding ditches or setting up barrier layers between the subgrade and ballast. Previous studies conducted by TTCI have shown that these barrier methods to be helpful in reducing fines in the ballast section [8].

(a)

(b)
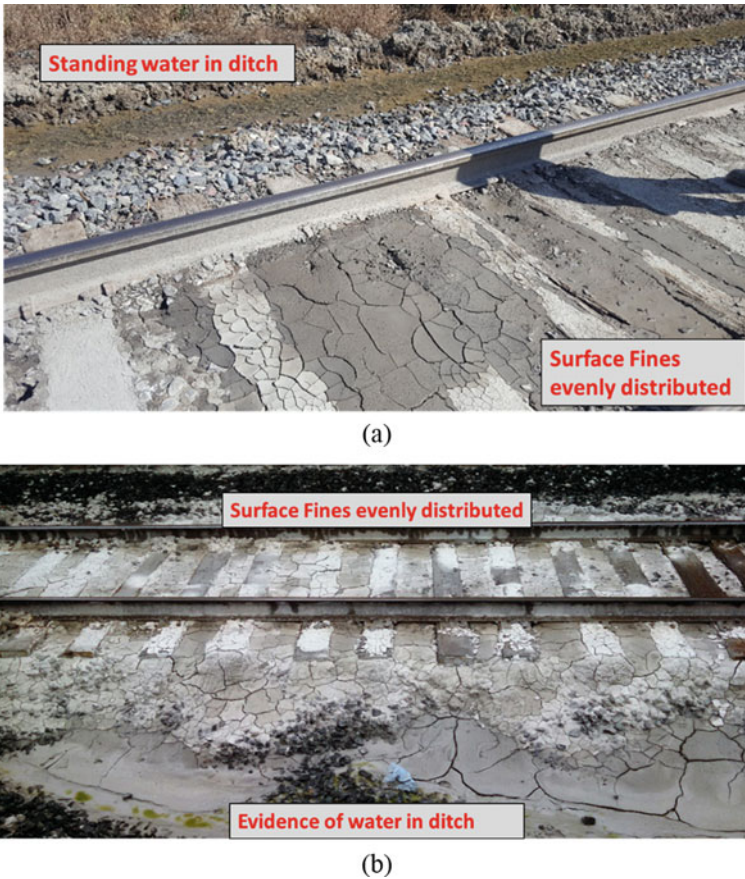
Fig. 8 Two examples of subgrade pumping with poor external drainage

4.4 General

From the previous three sections, it has been determined that there are three require-
ments for mud pumping: (1) degraded ballast, (2) water source, and (3) tie pumping
due to repeated wheel loads. These are expanded below:

- *Degraded Ballast*: Fines are an obvious precursor for mud pumping, but the influ-
  ence of fine level and fine type is likely significant. There should be a fine level
  threshold that is required for the slurry to form and different fine types will likely
  affect how the slurry acts. Distribution of fines in the track section will also play
  a role.
- *Water Source*: The source of water plays a significant role in mud pumping.
  At the rainy section and many FAST and revenue service sites (Sect. 4.2), the
  water source comes from rainfall that accumulates at the surface because the low

permeability of the degraded ballast inhibits drainage. This is known as blocked internal drainage. However, there have been other documented cases (Sect. 4.3) in which the water source is from a high-water table (subsurface water), often from blocked drainage ditches. This is known as blocked external drainage. This likely causes fines from the lower ballast section to pump upward to the surface. This suggests a deeper ballast layer problem and would require different remedial solutions.

- *Tie Pumping*: The tie moving up and down from train passage will not only help produce the slurry, but also push it upward around the ties to the surface. This indicates that the severity of mud pumping could be dependent on the amount of tie pumping.

5 Conclusion and Future Work

The main new finding from Phase I testing is that when ballast degradation is the fine type and rainfall is the water source, the moisture and slurry formation is a surficial issue. TTCI has reviewed other similar mud pumping locations that developed at FAST and previous revenue service investigations [5]; the observations agreed with the rainy section behavior. However, more investigations would be needed before any broad generalizations can be made and are the subject of future research.

This has implications on maintenance and remediation, because the results suggest maintenance should focus on ensuring the upper ballast layer which is drained (see Fig. 5). Phase II of the rainy section will test the effectiveness of potential maintenance methods by comparing settlement rates, drainage times, and visual observations. Initial options for testing are listed below:

- *Crib Trenching*: This maintenance method would be simplest and just requires localized work to remove the fines in the shoulder of the cribs of the muddy section. This will allow the drainage of any existing excess water and would hopefully allow additional drainage, until ultimately it is clogged by new slurry formation.
- *Shoulder Cleaning*: This will involve removing all the shoulder fine material and replacing with clean ballast.
- *Track Lift*: This maintenance method would lift the track 1 or 2 in. and could provide temporary separation between the fines and bottom of tie.
- *Undercutting*: This will involve removing all the fine material 6–8 in. below the bottom of the tie and replacing with clean material.

Revenue service investigations will also be important to verify that rainy section results are applicable to most revenue service conditions. These investigations should also allow the categorization of different mud pumping situations so these various situations can be identified and appropriate maintenance methods that address the root cause of the problem can be applied.

Additionally, all the work described will help to enhance detection methods, ground penetrating radar, for example, to better focus on important variables that correlate to track geometry degradation.

References

1. Li D, Hyslip J, Sussmann T, Chrismer S (2016) Railway geotechnics. CRC Press, Boca Raton, FL
2. Wilk S, Basye C, Brice M, Baillargeon J (2019) Influence of rain events on performance of fine-contaminated ballast. In: Larsson-Kraik PO, Ahmadi A (eds) Proceedings of the international heavy haul conference—2019, Narvik, pp 393–400
3. Wilk S, Basye C, Gao Y (2019) Influence of rain events on fine-contaminated ballast. Technology Digest TD-19-015, Aug 2019. AAR/TTCI, Pueblo, CO
4. Wilk S, Basye C, Gao Y (2018) Settlement of fine-contaminated ballast. Technology Digest TD-18-011, May 2018. AAR/TTCI, Pueblo, CO
5. Basye C, Gao Y, Wilk S (2018) Drainage properties of fine-contaminated ballast. Technology Digest TD-18-010, May 2018. AAR/TTCI, Pueblo, CO
6. Haddani Y, Benz Navarrete MA, Ranvier F (2019) Railroad substructure geotechnical characterization with dynamic penetration tests and geoendoscopy. In: Proceedings of geo-structural aspects of pavements, railways, and airfields (GAP 2019), Colorado Springs, CO
7. Read D, Hyslip J, McDaniel R, Li D (2010) Revenue service track substructure investigation. Technology Digest TD 10-006, Mar 2010. AAR/TTCI, Pueblo, CO
8. Wilk S, Basye C, Li D, Kerchof B (2019) Use of geosynthetics in diverse railroad applications. In: Proceedings of geo-structural aspects of pavements, railways, and airfields (GAP 2019), Colorado Springs, CO

A Multi-model Approach to Analyse Railway Track-Ground Dynamics and Soil Nonlinearity

C. Charoenwong, D. P. Connolly, K. Dong, P. Alves Costa, P. J. Soares, and P. K. Woodward

Abstract An increase in train speed generates amplified track deflection. With higher speed, larger strains are induced within the track and subgrade structures. This results in nonlinear behaviour of material properties, particularly the soil stiffness. In railway engineering, it is challenging to deal with these high levels of amplification because the deep wave propagation within the track and underlying soil structures is complicated. Therefore, this paper investigates the influential variables that cause a significant impact on the dynamic amplification of the railway. Four modelling strategies used to generate findings into the problems of railway track dynamics and track-soil nonlinearity. The four types of model are analytical, combined analytical–numerical, 2.5D finite element and 3D finite element. These four models are used to analyse the cases of homogenous half-space soils, homogenous soils above bedrock, layered soils, low-stiffness soil layers and track-soil nonlinearity. The analysis results provide a better understanding of wave propagation characteristics within the subgrade structures. This can be useful for consideration of the design or improvement of railway track structures and earthworks.

Keywords High-speed railway track · Analytical modelling · Numerical modelling · Railway track dynamics · Soil nonlinearity

C. Charoenwong · D. P. Connolly (✉) · P. K. Woodward
School of Civil Engineering, Institute for High Speed Rail and Systems Integration, University of Leeds, Leeds, UK
e-mail: d.connolly@leeds.ac.uk

K. Dong
Institute for Infrastructure and Environment, Heriot Watt University, Edinburgh, UK

P. Alves Costa · P. J. Soares
Faculty of Engineering, University of Porto, Porto, Portugal

1   Introduction

In recent decades, attempts have been made to increase the operational speed of trains for reducing journey times, increasing capacity on the network and supporting the economy. Higher speeds induce increased dynamic track-ground amplification and track displacements. These displacements can result in high strains within the track and subgrade structure, thus causing the stiffness of the material to behave in a nonlinear fashion. The propagation of energy occurs when the moving speed of a non-oscillating load reaches or goes higher than the wave propagate velocity of any layer in the supporting track-ground system [1]. This minimum threshold of this moving speed is defined as the "critical velocity" [2–5].

Since high levels of dynamic track amplification can lead to increased safety risks, accelerated track geometry degradation and the generation of high ground-borne vibration in the free-field [6–9], it is undesirable on railway lines. Therefore, an assessment of track dynamics is important, particularly for the design of high-speed lines where the dynamic stiffness of the system must be taken into account.

Existing railway standards consider the railway track behaviour as a combination of static and dynamic response using a basic function of the static response and speed [10]. If the types of train, track and soil are varied, the propagation of waves will become more complex. This approach thus is not able to accurately assess for those complexities.

To investigate dynamic behaviour due to moving loads, several models have been proposed in the literature. [11, 12] used analytical approaches to model the problem assuming a moving load on an elastodynamic medium. Apart from analytical methods, [13, 14] applied semi-analytical approaches to the railway problem which simulated the track using analytical expressions and modelled the 3D soil using Green's functions in terms of wavenumber–frequency domain. With semi-analytical models, a better understanding of the relationship between moving speed and amplification of dynamic displacement can be achieved with a relatively low computational demanding. However, they are still unable to cope with the complexity of the track.

Therefore, [6, 15, 16] used 2.5D approaches which assumed the track as an invariant structure in the direction of moving load and thus considering the problem in 2D before recovering to the 3D response. However, these 2.5D models cannot simulate ballast tracks which contain the sleeper spacing. [17, 18] applied periodic 3D models which discretised the track into various single 3D slides to overcome this problem. When dealing with the complexities of track properties and geometry, fully 3D models are useful despite a very high computational cost. With fully 3D models, the problem can be simplified and generally analysed in both frequency and time domains. Moreover, solving the problem in the time domain is attractive since more complex nonlinear track properties and wheel–rail interaction are allowed for the modelling [19, 20].

In this presented paper, railway track dynamics and track-soil nonlinearity are analysed using a multi-model approach which consists of analytical, semi-analytical,

2.5D numerical and 3D numerical. The remainder of this paper is organised as follows. In Sect. 2, the modelling approaches, which include the detail of four methodologies, are described. Section 3 shows the modelling analysis regarding soil layering and track-soil nonlinearity. Finally, the conclusions are drawn in Sect. 4.

2 Modelling Approaches

It is challenging to obtain a high-accuracy result and a low computational time from using only a single modelling approach to analyse the full range of railway track dynamic problems, particularly critical velocity issues. These issues are too complex to analyse using solely simplified approaches and consume a lot of time for using a single fully 3D model. Therefore, this paper considers the four most common methodologies of modelling for a study of railway track dynamics and links them to propose new findings into the problems of railway track dynamics and nonlinearity. The methodologies used in this paper are discussed in detail as follows.

Approach 1 (Analytical): As described in [21], the dispersion relationships between the track and ground are analytically computed. With this methodology, the critical velocity can be identified without creating dynamic amplification curves. The track and soil dispersion characteristics are analytically calculated in the wavenumber domain assuming the track structure to be 2D, infinite and invariant in the direction of train moving. For an example model of concrete slab track supported by two layers of soil, the dispersion relations in terms of phase velocity and wavenumber are illustrated in Fig. 1. The system of equations for slab track and the apparent phase velocity are described as given in Eqs. 2 and 4 in [21]. In both sub-figures, the critical velocity occurs at the point of intersection between the track dispersion line and the soil dispersion line.
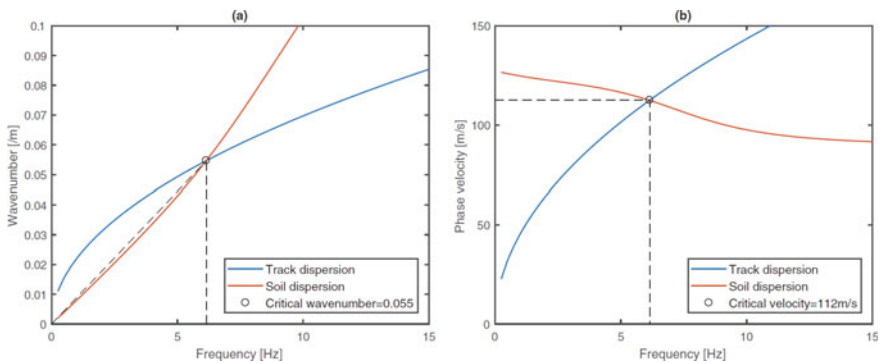
Fig. 1 Dispersion curves: **a** wavenumber, **b** phase velocity

Approach 2 (Semi-analytical): The second methodology is a combination of analytical and numerical approaches which is called a semi-analytical approach. As outlined in [22], the model consists of two main components. The track is modelled using an analytical approach, whereas the soil is modelled using the thin-layer method (TLM). This method allows the soil to be discretised in the vertical direction, but infinite and homogeneous along the horizontal direction. The quadratic three-node elements are used to increase the accuracy of propagation simulation within each soil thin layer. The soil stiffness is computed using the Green's function in the wavenumber–frequency domain and adopted within the track model to calculate the response of track-ground interface.

Approach 3 (2.5D numerical): The next methodology is a 2.5D numerical approach which both track and soil structures are defined as the 2D geometry using eight-node quadratic finite elements and solved in the frequency domain [16, 23]. To prevent reflection at boundaries, a perfectly matched layer (PML) [24] is used as an absorbing function at boundaries as shown in Fig. 2. With this approach, the structure is considered in 2D and the 3D response can be captured using Fourier transforms with respect to the spatial coordinate along the track.

Approach 4 (3D numerical): The last methodology is a fully 3D numerical approach which individual components of track and ground structures are simulated using ABAQUS with 20-node quadratic brick elements. The equations of motion are solved for moving loads in the time domain using implicit integration [25, 26]. The approach is able to provide high accuracy for the modelling of stress and strain fields.

Fig. 2 Simplified view of 2.5D track-ground mesh
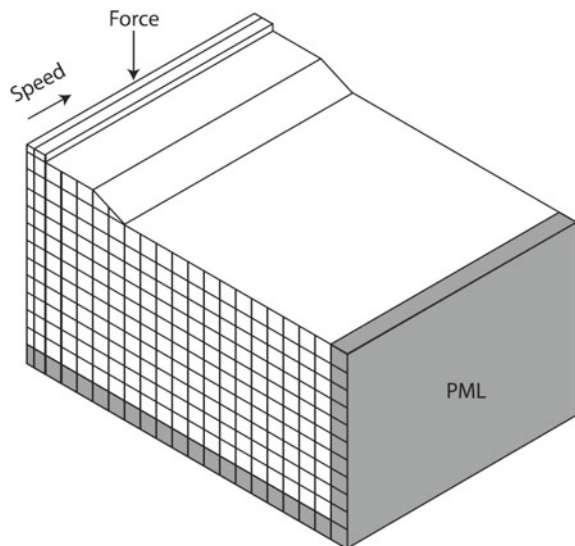
3 Modelling Analysis

When the train moves at high speeds, it induces deep wave propagation within the ground. The dynamic stiffness behaviours of the supporting subgrade, thus, become more influential. As shown in Table 1, parameters regarding track properties for both ballasted and slab tracks are considered in the modelling analysis. A wider range of track stratum is also included. Poisson's ratio and density of soil are 0.35 and 2000 kg/m^3, respectively. In this analysis, the four alternative types of model are used to explore homogenous half-space soils, homogenous soils above bedrock, layered soils, low-stiffness soil layers and track-soil nonlinearity, as described below.

3.1 Homogenous Half-Space Soils and Homogenous Soil Above Bedrock

Assuming a half-space is homogenous with infinite depth and uniform material properties. Since the properties, including stiffness and mass, are uniform, the phase velocity of P-SV waves is independent of excitation frequency, and thus, the critical velocity and the Rayleigh wave velocity are equal. To illustrate, a case of moving train load on a ballasted track (ballasted track properties in Table 1) supported by a homogenous half-space soil with 45 MPa stiffness is studied. The responses of a supporting homogenous half-space with two different speeds (50 and 100% of the critical velocity) are shown in Fig. 3. Based on the result of modelling, the low moving speed produces 2.5 mm while the high moving speed produces 3.9 mm

Table 1 Material properties of the ballasted and slab tracks

Component	Property	Ballasted track	Slab track
Rail	Bending stiffness (Nm^2)	1.29×10^7	1.29×10^7
	Mass (kg/m)	120	120
Rail pad	Stiffness (N/m)	5×10^8	5×10^8
	Damping (Ns/m)	2.5×10^5	2.5×10^5
Sleeper	Mass of sleeper (kg/m)	490	–
Ballast/slab	Height of ballast/slab (m)	0.35	0.35
	Young's modulus (MPa)	130	30,000
	Half-track width (m)	1.25	1.25
	Density (kg/m^3)	1700	2500

Fig. 3 Homogenous half-space soil contours: **a** low speed, **b** critical speed

of maximum rail displacement. It can be seen that the train load at higher moving speeds creates larger displacements. In addition to the amplitude of displacement, Fig. 3 also shows that the faster moving load generates a conical-type shape while the slower moving load generates a uniform response [27]. At speeds greater than the Rayleigh wave speed, this wave front angle is defined by: $\sin^{-1}(V_{\text{Rayleigh}}/V_{\text{train}})$. Another point is the generation of corresponding stress fields at 1 m depth from the surface, as illustrated in Fig. 4. It is apparent that the load at higher moving speed results in asymmetric growth and larger magnitude of the stress fields, particularly in the horizontal direction [28].

Typically, the stiffness increases with the depth of soil stratum. However, if a layer with a significantly higher stiffness than the supporting soils, for example, a rock layer, is found near the surface, the propagation at lower frequencies will be obstructed. An illustration of this case is shown in Fig. 5 which is a model of slab track overlying homogenous soils supported by stiff bedrock. Both homogenous saturated and unsaturated soils (40 MPa stiffness) are considered. Two different depths (5 and 15 m) of bedrock from the surface are also compared. As shown by the dashed lines,
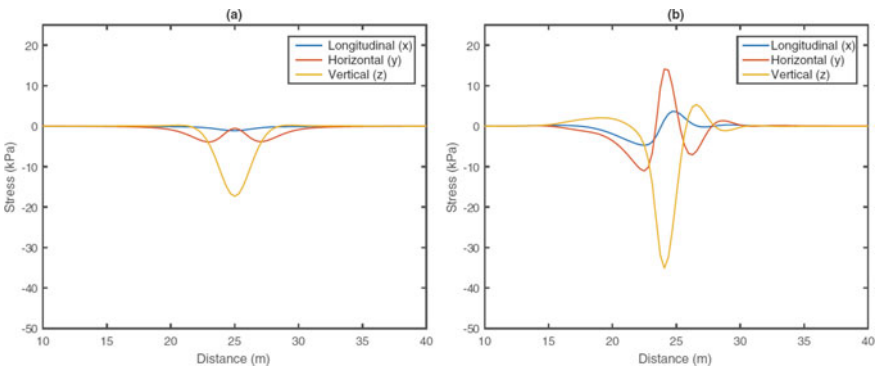
Fig. 4 Corresponding soil stresses fields: **a** low speed, **b** critical speed
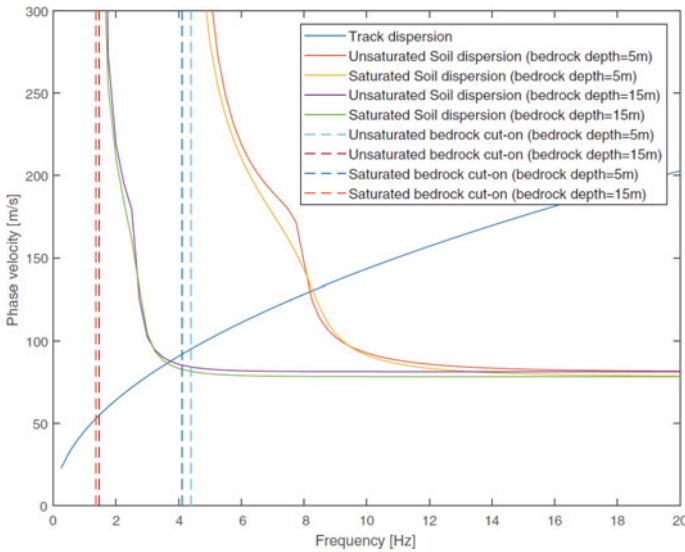
Fig. 5 Effect of bedrock depth on dispersion

the bedrock prevents the propagation of low-frequency waves. The graph also shows that significant dispersion occurs in the frequency ranges between 5 and 10 Hz for the case of 5 m depth and 1–3 Hz for the case of 15 m depth. Therefore, if the critical velocity lies within these frequency ranges, a slight change of track stiffness can lead to a big change in the critical velocity. On the other hand, if the critical velocity occurs at higher than these frequency ranges, changing the track stiffness will not affect the critical speed as seen by a constant relationship of phase velocity and frequency.

3.2 Layered Soils and Low Stiffness Soil Layers

To consider layered soils with infinite depth and varying stiffness, six cases of slab track resting on two-layered soils are analysed. The stiffness of the bottom soil layer is kept constant at 150 MPa, while the upper soil layer is changed with three values of stiffness (30, 75 and 100 MPa). For each stiffness, two different depths which include 12 m (thick) and 2 m (thin) are applied to the upper soil layer. Figure 6 illustrates the layered ground contours for the case of slab track resting on the top layer of soil with thick depth and 30 MPa stiffness. Two different speeds are applied as for the homogenous case. The resulting rail deflections are similar to the previous case, but it appears that there are trailing oscillations behind the faster train load. Figure 7 shows the analysis of track-ground dispersion for all six cases. For the case of the deep top layer, the critical velocity and the P-SV wave velocity of the upper layer are similar because the intersection point occurs within the range of a constant

Fig. 6 Layered soil contours: **a** low speed, **b** critical speed
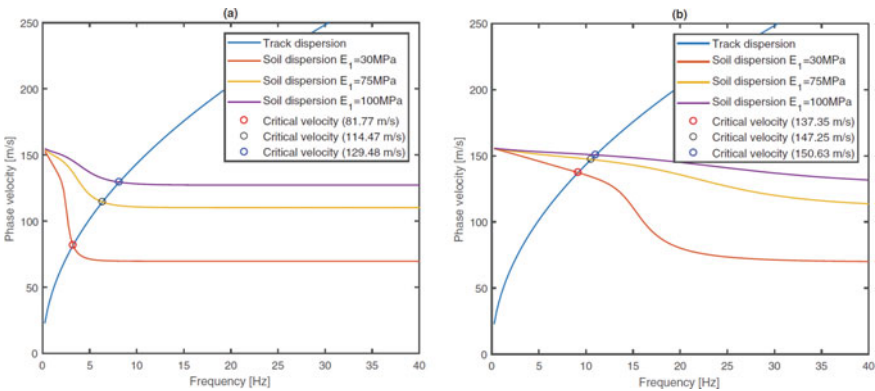
Fig. 7 Layered soil dispersion: **a** thick top layer-12 m, **b** thin top layer-2 m

relationship between phase velocity and frequency. Therefore, changing the track properties has a small influence on the critical speed. On the contrary, the critical velocity for the thin-layer case occurs between the P-SV wave velocity of the upper and lower soil layers. The critical velocity will deflect towards the wave speed in the bottom soil layer as the depth of the upper soil layer reduces.

Even though the soil stratum increases in stiffness with depth, low-stiffness soil layers can appear in the middle within the soil stratum resulting from natural processes [29] or engineering processes [22]. To illustrate, an example case of a soil layer with 100 MPa stiffness and 6 m depth overlying a softer soil layer with 50 MPa stiffness and infinite depth is created, and the result of the analysis is shown in Fig. 8. It can be seen that two peaks are generated and located at similar moving speeds to the shear wave velocities of these two soil layers. By definition, the first peak is defined as the critical velocity while the second peak is a train moving speed which produces the largest track amplification.
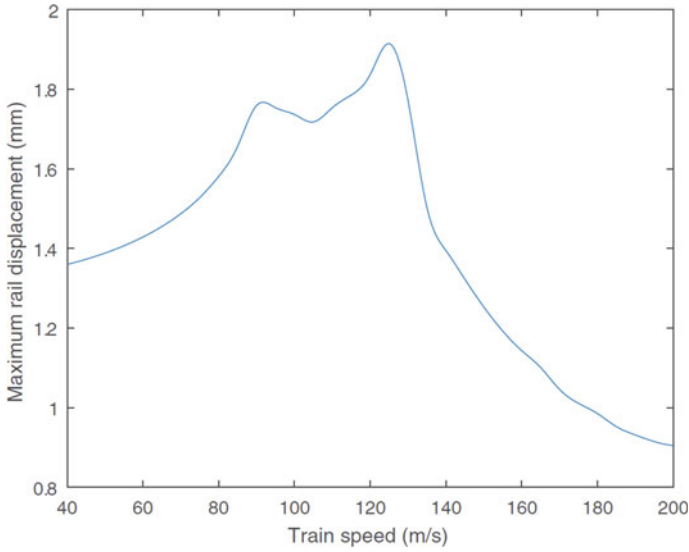
Fig. 8 Maximum vertical rail displacement curve

3.3 Track-Soil Nonlinearity

Elastodynamic waves propagate into the deeper soil layers as the train moving speed increases. This energy generates large strain levels and results in reduced soil stiffness in a nonlinear fashion which causes increased track displacements [30].

As an example, a case of a moving load on a homogenous soil with 45 MPa stiffness is considered. With regard to the curves of linear and nonlinear dynamic displacement shown in Fig. 9a, it can be seen that dynamic amplification increases, whereas the critical velocity reduces to approximately 85% of the linear case. This
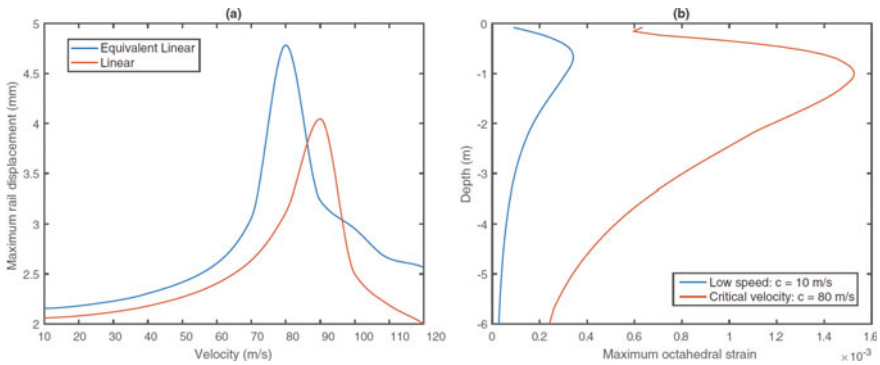
Fig. 9 Effect of nonlinearity: **a** maximum displacement versus velocity, **b** strain versus depth
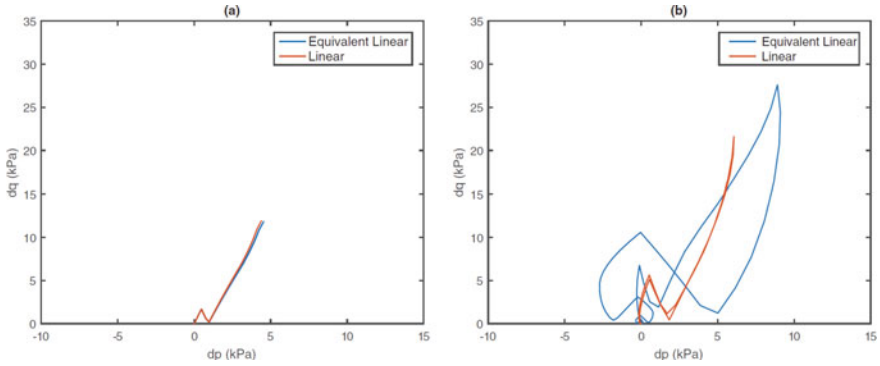
Fig. 10 p-q stress paths: **a** low speed (10 m/s), **b** critical speed (80 m/s)

can make a significant influence on high-speed train lines which often limit their operating train speeds to 70% of the critical velocity. Due to nonlinearity, operating trains at 70% of the critical velocity from the linear calculation can lead to the maximum possible track displacements or create a condition where displacements are extremely sensitive to small increases in speed. Therefore, avoiding designs close to this limit may reduce the risk of nonlinearity effects, particularly if the operating speed is expected to increase in the future. Moreover, the strain and depth relationship using the linear equivalent technique is presented in Fig. 9b. Two different speeds which include 10 m/s (low speed) and 80 m/s (critical speed) are considered. As a result, the strains due to the higher speed are obviously larger than the lower one, but the peak points of strain are located at similar depths. Finally, the p-q stress paths at 1 m depth below the track centre line are created for both low speed and critical speed, as shown in Fig. 10. In comparison, no sign of dynamic amplification occurs at the low speed, whereas the stress state turns into a turbulent shape and the magnitudes considerably increase at the critical speed.

4 Conclusions

This paper considers multiple types of models to analyse the railway track dynamics problems which involve soil layering and track-soil nonlinearity. The four models are analytical, semi-analytical, 2.5D numerical and 3D numerical.

The analysis shows that the relationship between track dispersion and soil dispersion has a strong influence on the critical speed. With a very thin top layer of soil, an improvement in the track structure can be taken into account for increasing the critical speed. Also, the depth of bedrock is considered as an important parameter since it can cause the critical velocity to become sensitive to small changes. In the case of low-stiffness soil layers, it is found that the soil wave dispersion, which affects the critical velocity, can become increasingly complex. Lastly, the investigation of

track-soil nonlinearity with linear and nonlinear methods is investigated. The results show that the difference in output from these two methods can cause a considerable impact on the critical speed.

References

1. Costa PA, Colaço A, Calçada R, Cardoso AS (2015) Critical speed of railway tracks. Detailed and simplified approaches. Transp Geotech 2:30–46. https://doi.org/10.1016/j.trgeo.2014.09.003
2. Connolly DP, Alves Costa P, Kouroussis G, Galvin P, Woodward PK, Laghrouche O (2015) Large scale international testing of railway ground vibrations across Europe. Soil Dyn Earthq Eng 71:1–12. https://doi.org/10.1016/j.soildyn.2015.01.001
3. Wang P, Wei K, Wang L, Xiao J (2015) Experimental study of the frequency-domain characteristics of ground vibrations caused by a high-speed train running on non-ballasted track. Proc Inst Mech Eng Part F J Rail Rapid Transit 1131–1144. https://doi.org/10.1177/0954409715577849
4. Connolly DP, Kouroussis G, Woodward PK, Alves Costa P, Verlinden O, Forde MC (2014) Field testing and analysis of high speed rail vibrations. Soil Dyn Earthq Eng 67:102–118. https://doi.org/10.1016/j.soildyn.2014.08.013
5. Costa PA, Soares P, Colaço A, Lopes P, Connolly D (2020) Railway critical speed assessment: a simple experimental-analytical approach. Soil Dyn Earthq Eng 134:106156. https://doi.org/10.1016/j.soildyn.2020.106156
6. Galvín P, Mendoza DL, Connolly DP, Degrande G, Lombaert G, Romero A (2018) Scoping assessment of free-field vibrations due to railway traffic. Soil Dyn Earthq Eng 114:598–614. https://doi.org/10.1016/j.soildyn.2018.07.046
7. Kouroussis G, Vogiatzis KE, Connolly DP (2018) Assessment of railway ground vibration in urban area using in-situ transfer mobilities and simulated vehicle-track interaction. Int J Rail Transp 6:113–130. https://doi.org/10.1080/23248378.2017.1399093
8. López-Mendoza D, Romero A, Connolly DP, Galvín P (2017) Scoping assessment of building vibration induced by railway traffic. Soil Dyn Earthq Eng 93:147–161. https://doi.org/10.1016/j.soildyn.2016.12.008
9. López-Mendoza D, Connolly DP, Romero A, Kouroussis G, Galvín P (2020) A transfer function method to predict building vibration and its application to railway defects. Constr Build Mater 232:117217. https://doi.org/10.1016/j.conbuildmat.2019.117217
10. Van Dyk BJ, Edwards JR, Dersch MS, Ruppert CJ, Barkan CPL (2017) Evaluation of dynamic and impact wheel load factors and their application in design processes. Proc Inst Mech Eng Part F J Rail Rapid Transit 231:33–43. https://doi.org/10.1177/0954409715619454
11. Frýba L, Steele CR (1976) Vibration of solids and structures under moving loads. Noordhoff International Publishing, Groningen
12. Lamb H (1904) On the propagation of tremors over the surface of an elastic solid. Philos Trans R Soc A Math Phys Eng Sci. https://doi.org/10.1098/rsta.1904.0013
13. Dieterman HA, Metrikine A (1996) Equivalent stiffness of a half-space interacting with a beam. Critical velocities of a moving load along the beam. Eur J Mech A/Solids 67–90
14. Lombaert G, Degrande G, Kogut J, François S (2006) The experimental validation of a numerical model for the prediction of railway induced vibrations. J Sound Vib 297:512–535. https://doi.org/10.1016/j.jsv.2006.03.048

15. Hung HH, Chen GH, Yang YB (2013) Effect of railway roughness on soil vibrations due to moving trains by 2.5D finite/infinite element approach. Eng Struct 254–266. https://doi.org/10.1016/j.engstruct.2013.09.031

16. Alves Costa P, Calçada R, Silva Cardoso A, Bodare A (2010) Influence of soil non-linearity on the dynamic response of high-speed railway tracks. Soil Dyn Earthq Eng 30:221–235. https://doi.org/10.1016/j.soildyn.2009.11.002

17. Arlaud E, Costa D'Aguiar S, Balmes E (2016) Receptance of railway tracks at low frequency: numerical and experimental approaches. Transp Geotech 9:1–16. https://doi.org/10.1016/j.trgeo.2016.06.003

18. Chebli H, Othman R, Clouteau D, Arnst M, Degrande G (2008) 3D periodic BE-FE model for various transportation structures interacting with soil. Comput Geotech 35:22–32. https://doi.org/10.1016/j.compgeo.2007.03.008

19. Shih JY, Thompson DJ, Zervos A (2017) The influence of soil nonlinear properties on the track/ground vibration induced by trains running on soft ground. Transp Geotech 11:1–16. https://doi.org/10.1016/j.trgeo.2017.03.001

20. Woodward PK, Laghrouche O, Mezher SB, Connolly DP (2015) Application of coupled train-track modelling of critical speeds for high-speed trains using three-dimensional non-linear finite elements. Int J Railw Technol 3:1–35. https://doi.org/10.4203/ijrt.4.3.1

21. Mezher SB, Connolly DP, Woodward PK, Laghrouche O, Pombo J, Costa PA (2016) Railway critical velocity—analytical prediction and analysis. Transp Geotech 6:84–96. https://doi.org/10.1016/j.trgeo.2015.09.002

22. Dong K, Connolly DP, Laghrouche O, Woodward PK, Alves Costa P (2018) The stiffening of soft soils on railway lines. Transp Geotech 17:178–191. https://doi.org/10.1016/j.trgeo.2018.09.004

23. Colaço A, Costa PA, Connolly DP (2016) The influence of train properties on railway ground vibrations. Struct Infrastruct Eng 12:517–534. https://doi.org/10.1080/15732479.2015.1025291

24. Connolly DP, Giannopoulos A, Forde MC (2014) A higher order perfectly matched layer formulation for finite-difference time-domain seismic wave modeling. Geophysics 80:T1–T16. https://doi.org/10.1190/GEO2014-0157.1

25. Connolly D, Giannopoulos A, Fan W, Woodward PK, Forde MC (2013) Optimising low acoustic impedance back-fill material wave barrier dimensions to shield structures from ground borne high speed rail vibrations. Constr Build Mater 44:557–564. https://doi.org/10.1016/j.conbuildmat.2013.03.034

26. Connolly D, Giannopoulos A, Forde MC (2013) Numerical modelling of ground borne vibrations from high speed rail lines on embankments. Soil Dyn Earthq Eng 46:13–19. https://doi.org/10.1016/j.soildyn.2012.12.003

27. Connolly DP, Costa PA (2020) Geodynamics of very high speed transport systems. Soil Dyn Earthq Eng 130:105982. https://doi.org/10.1016/j.soildyn.2019.105982

28. Yu Z, Woodward PK, Laghrouche O, Connolly DP (2019) True triaxial testing of geogrid for high speed railways. Transp Geotech 20:100247. https://doi.org/10.1016/j.trgeo.2019.100247

29. Madshus C, Kaynia AM (2000) High-speed railway lines on soft ground: dynamic behaviour at critical train speed. J Sound Vib 231:689–701. https://doi.org/10.1006/jsvi.1999.2647

30. Dong K, Connolly DP, Laghrouche O, Woodward PK, Alves Costa P (2019) Non-linear soil behaviour on high speed rail lines. Comput Geotech 112:302–318. https://doi.org/10.1016/j.compgeo.2019.03.028

Performance of Jointed S&C Bearers

A. S. Khan, E. Ferro, L. Le Pen, and W. Powrie

Abstract Long bearers are used at switches and crossings (S&C) to maintain the gauge and prevent relative lateral movement between the rails for all possible routes a train may take. Traditionally, these bearers are formed of continuous timber or pre-tensioned steel reinforced concrete beam, up to 6 m or more in length. However, restrictions on the availability and cost of access time for track works have led to the development of new jointed bearers. These allow modules of S&C to be pre-constructed and loaded onto road/rail vehicles for joining on site, reducing the track access time required and saving money. Jointed bearers have elements that are not much longer than plain line ties (<3.0 m). However, joining the bearer elements presents challenges. Two types of solution are currently available: (1) flexible joints—which allow some relative rotation and vertical movement between the connected ends of the bearer parts; (2) rigid joints, which may give a bending stiffness close to that of a continuous beam. The type of joint has implications for crossing performance, and the existence of alternative designs suggests that a universal solution has not been identified. This paper presents results from a laboratory study carried out to evaluate the effect of joint type on performance. In testing, repeated loading representative of >1 million cycles of a 20 tonne (20,000 kg) axle load was applied to the railseats of bearers supported on a ballast bed. Settlements and resilient movements at locations along the bearers were measured and analysed. The results show that the type or absence of a joint significantly affects the settlement and resilient deflections along the bearer length.

Keywords Bearers · S&C · Ballast · Switches and crossings · Railroad · Railway · Joints · Modular

A. S. Khan (✉) · E. Ferro · L. Le Pen · W. Powrie
Infrastructure Research Group, University of Southampton, Building 178, Burgess Road, Southampton SO16 7QF, UK
e-mail: a.s.khan@soton.ac.uk

1 Background

Railway switches and crossings (S&C) make the rail network flexible by allowing tracks to cross and converge/diverge. UK railways have an S&C density of just over 5 units per 10 km of mainline track [1]. Traditionally, a relatively large proportion (24% of the total maintenance budget) is spent on S&C, which accounts for only 5% of the total track mileage [2]. In the financial year 2017/2018, network rail (NR) spent £195 M on S&C renewals and refurbishments out of a total track renewal cost of £764 M [3]. Similarly, disproportionate maintenance and renewal costs are incurred in Europe, e.g. 13% of total track maintenance cost in Sweden is spent on S&C less than 5% of track mileage [4] and 25% in Switzerland [5]. Amtrak, the primary passenger service operator in the USA, has a similar level of S&C complexity with approximately the same density per unit length of track as network rail in the UK [6].

An S&C is conventionally divided into three main segments (Fig. 1): the switch panel, the closure panel and the crossing panel. The switch panel allows vehicles to traverse from the stock rail via the switch blade to the closure panel. The closure panel leads to the crossing panel where the tracks fully diverge.

S&C have a number of complicating features compared with plain line. The variation in geometry leads to non-symmetric loading [8], while discontinuities in the rails changes in lengths/masses of the bearers, and other variations along the running length give rise to different responses to loading. Significant impact forces occur at the transfer from the stock rail to switch blade owing to the change in height [9] and over the gap between the wing rail and the crossing nose [10]. Other complicating factors include variations in track system stiffness, differential settlement and mass distribution of the rails, irregularities in wheel-rail contact, and dipped rail joints between the switch and closure rails.

Bearers at S&C have the same primary roles as plain line ties, which are to maintain gauge and transfer loads from trains onto the ballast and substructure. However, at
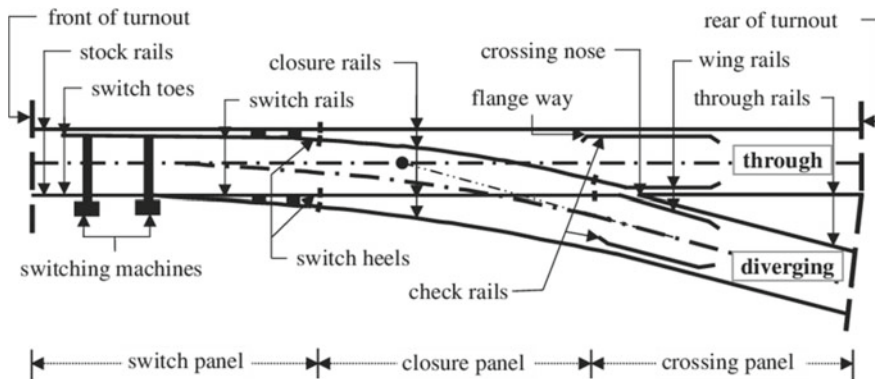
Fig. 1 Schematic of a typical S&C and its components [7]

S&C, bearers may need to maintain gauge over multiple lines and link two or more tracks together. Thus, S&C bearers support multiple rails. Loads on a pair of rails at one end of a continuous or rigid jointed bearer supporting two adjacent lines can cause the bearer to rotate downward under the loaded track, lifting the unloaded track at the far end [11, 12]. Owing to the combination of factors described, S&C are more prone to differential settlement and require more frequent maintenance and renewal.

Track maintenance or renewal is carried out in time slots known as possessions, during which the track being maintained and possibly adjacent track(s) are blocked to traffic. Railway operators have introduced modular S&C as a way to reduce possession durations. Traditionally, S&C are assembled in a manufacturing yard for quality and tolerance checks, then disassembled, transported to site, and re-assembled again at the site for installation. Modular S&C reduces the steps, and therefore, the installation time needed for S&C renewal by enabling pre-assembled segments to be transported and then joined together on site. However, a mechanical joint between the long bearer sections is required.

The type and location of the joints along the bearers may significantly affect the mechanical behaviour of S&C both in the short term, when accumulated ballast settlement is small but its rate potentially large, and in the long term, when the track geometry has changed due to permanent deformation of the ballast bed after repeated train loading. Several types of bearer joints have been designed by bearer manufacturers and are currently in use with different solutions adopted in different countries. These joints fall into two main types: (1) forming a near-rigid connection and (2) allowing relative vertical movement and rotation between the bearer parts. Figure 2 shows one type of flexible joint and one type of rigid joint in current use. In the UK, the national railway manager, network rail, uses joints formed of a metal shroud bolted to the ends of the bearer sections to be joined (Fig. 2b). This type of
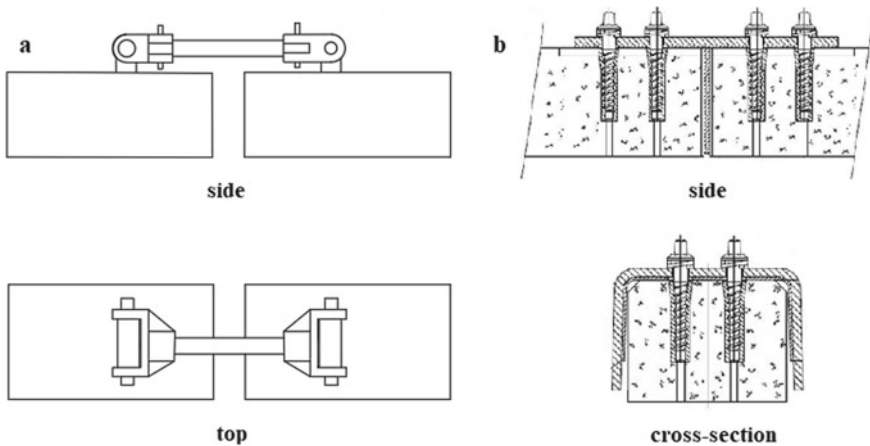
Fig. 2 Schematic representation of **a** flexible bearer joint (Progress Rail) and **b** rigid bearer joint (Network Rail [13])

joint is intended to provide a more rigid connection, so that a modular bearer behaves as closely as possible to its continuous counterpart.

The flexible joint shown in Fig. 2a consists of a pinned–pinned connection that allows relative rotation and vertical movement between the connected bearer parts. The particular type of joint shown is not intended for use in modular construction, and this type of flexible joint is intended to be used for joining adjacent tracks (i.e. the joint is not to be placed between the main route running rails). However, other types of flexible joints are available, and their placement may not be so restricted. The rigid joint shown in Fig. 2b has been specifically developed for modular S&C construction and may be placed in almost any location along a bearer length (e.g. between running rails and between main tracks).

The fact that joints with very different mechanical behaviours are used on railway networks suggests that there is not yet a consensus on the mechanical characteristics needed for optimal performance, although there is some recognition among manufacturers that the location of the joint is significant in the restrictions that some suppliers place on this. Nevertheless, there remains a lack of understanding of the effect of joint type on S&C performance at both a bearer element and system level. Jointed bearers of either kind could potentially give rise to undesirable relative track movements, if the characteristics of the joints are not carefully selected or their behaviour understood. Maintenance procedures also need to account for actual jointed bearer characteristics and behaviour. A recent derailment at an S&C in the UK [13], where the presence of jointed bearers may or may not have been coincidental, has prompted a detailed evaluation of the performance of the type of rigid joints used in the UK (Fig. 2b).

In contrast to a rigidly jointed or continuous bearer, flexibly jointed bearers are expected to reduce lifting of the adjacent line during train passage. They may also reduce the impact loading on the ballast, and the maximum positive bending moment within bearers [14].

This study compares the performance of two different bearer joints (Fig. 2) and a continuous bearer, by means of full-scale laboratory tests. In the tests in this paper, the joint was placed between the running rails of the through route and loading applied only to the through route to give a comparison of behaviour for this particular circumstance. The work contributes to an improved understanding of the interaction between long bearers and the underlying ballast, and the influence of joint type or lack of a joint, in both the short and the long term. Future work will evaluate relative performance of joint types that are located outside of the running rails and possibly also consider other loading arrangements.
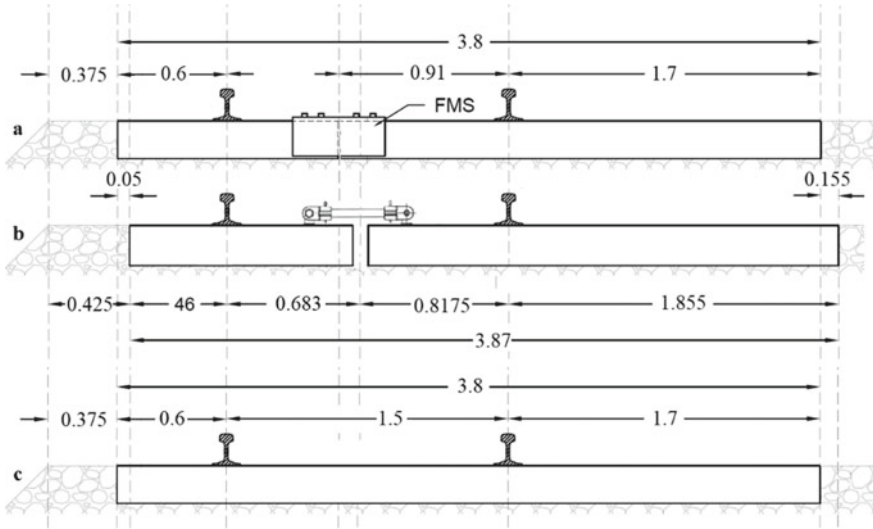
Fig. 3 Dimensions of bearers (m): **a** rigid jointed, **b** pinned jointed, **c** continuous

2 Materials and Methods

2.1 Bearers and Ballast

Ballast was sourced from Mountsorrel quarry (UK). Its particle size distribution lies within the range specified by the relevant British Standard (CAT. A, BS EN 13450:2002). It has a grain specific gravity (G_s) of 2.66, an average grain size (D_{50}) of 41 mm, a coefficient of uniformity ($C_u = D_{60}/D_{10}$) of 1.4, and a coefficient of gradation ($C_g = D_{30}^2/(D_{30}D_{60})$) of 1.0.

The bearers were formed of pre-tensioned steel reinforced concrete. Three different types of bearer were tested: a modular bearer with near-rigid connection (Fig. 3a), a pinned jointed modular bearer (Fig. 3b), and a continuous bearer (Fig. 3c). The joint and bearer configurations tested are summarised in Table 1.

2.2 Test Preparation

The tests were carried out in the Southampton Railway Testing Facility (SRTF), a laboratory representation of a single bearer bay of track in plane strain conditions. A schematic of the test arrangement is shown in Fig. 4 and as a photograph in Fig. 5.

Figure 4 shows how the load has been applied equally to the rails on one side of the bearer using a spreader beam for one possible route referred to as the mainline route, rails for the diverging route are absent from the laboratory assembly.

Table 1 Summary of the tests carried out

Test no	Joint type	Joint description	Bearer cross-section (m)
1	N/A	Joint absent/continuous bearer	3.8 × 0.27 × 0.21
2	Rigid	Metal shrouded 8 bolt joint with rubber layer between the joining ends of the bearer segments and between the metal joint and concrete bearer (Fig. 2b)	3.8 × 0.27 × 0.21
3	Flexible	Pinned–pinned 'dog bone' joint offering relative rotation and vertical movement between the joining sides of the bearer segments (Fig. 2a)	3.8 × 0.28 × 0.205
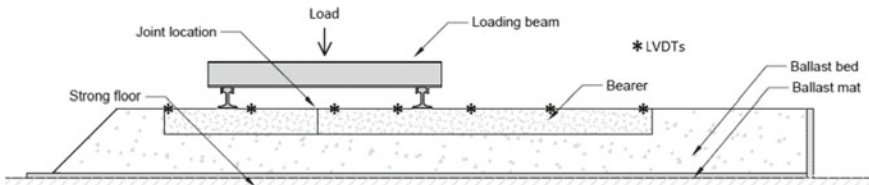
Fig. 4 Schematic of test set-up

Figure 6 shows an extract from an S&C layout plan indicating the placement of the rigid type of joint used in the UK. The shaded bearer has dimensions and a joint position similar to those tested in the laboratory. However, there are some slight differences in dimensions between the laboratory bearers, owing to variations in the sizes provided by different suppliers (Fig. 3). For the flexible joint, a special bearer section was made specifically for this testing comparison because the joint was in a non-standard location.

The SRTF was originally used for testing plain line railway ties [15, 16] and was modified to accommodate long S&C bearers. For the tests reported in this paper, a medium soft subgrade was simulated by the placement of a 19 mm under-ballast mat (UBM Sylomer® D 1519, supplied by Getzner) overlain by two, 3 mm thick neoprene rubber layers. A 300 mm depth of ballast, the bearer, and the crib ballast was placed on top of the neoprene layers. The neoprene rubber layers protected the ballast mat, which was re-used.

The tests were prepared following established standard procedures described in detail in [17] and summarised below:

1. Ballast was manually placed, newly for each test, to a depth of 300 mm, then carefully levelled and compacted using a plate vibrator.
2. The bearer was placed on the levelled ballast surface.
3. At one end of the testing rig, the ballast was placed to form a shoulder of horizontal extent 375 mm then a 1:1 slope.
4. The other end of the test box was closed at a distance of 1.9 m from the other bearer end, to simulate the support at the middle of a wide ballast trackbed.
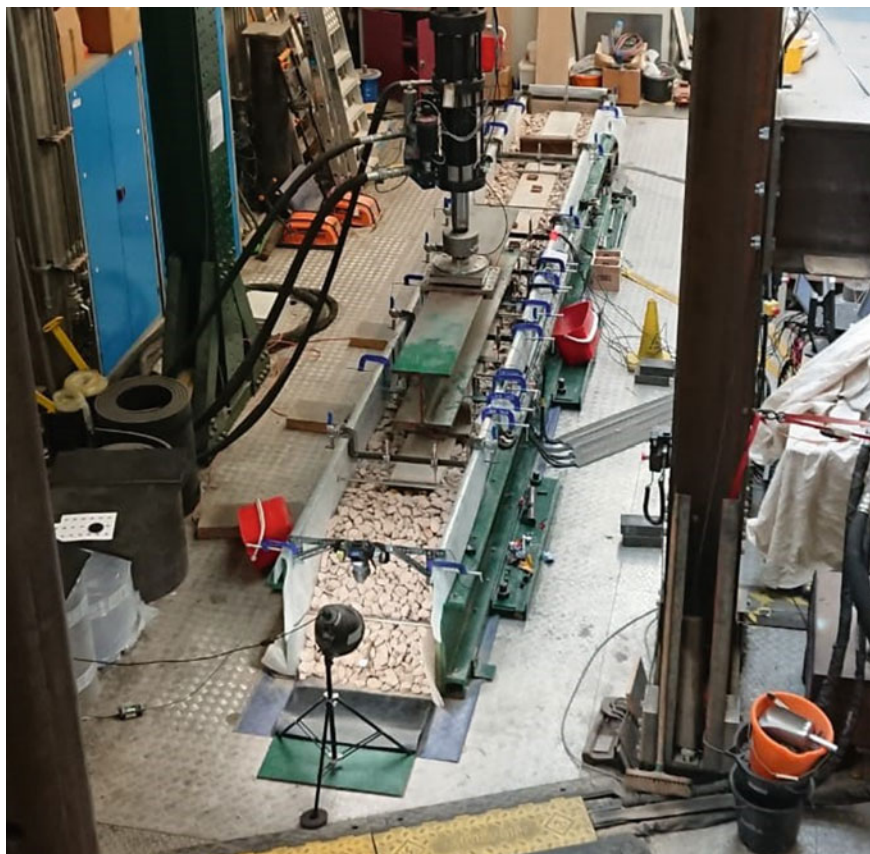
Fig. 5 Photo of test set-up
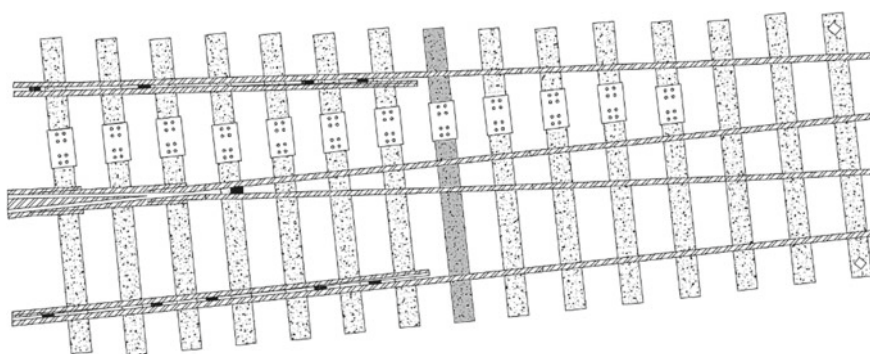
Fig. 6 Plan view of S&C part where two lines merge/diverge (test bearer shaded)

5. Crib ballast was placed by pouring from buckets to the top level of the bearers sides.

In each test, 1 million cycles of a sinusoidal load ranging between 5 and 98.1 kN were applied to the rails on the (left) side of the bearer, nearer the shoulder, at a frequency of 4 Hz. 98.1 kN is equivalent to a 20 tonne axle load, assuming that load spreading by the rails results in the transfer of 50% of the load to the bearers on either side. 1 million cycles represent 20 million cumulative tonnes. The selection of a 20 tonne axle load is somewhat arbitrary; some freight vehicles are heavier, while passenger vehicles can be lighter. The application at 4 Hz is pseudo static in that accelerations over the amplitude of movements present are much less than gravity. The selection of 4 Hz is a practical decision to allow a large number of load cycles to be applied in a relatively brief time period and is not intended to correspond to any particular train speed. The field loading at S&C is more complex with significant dynamic effects.

The loading set-up (Fig. 4) represents an S&C with the through line much more heavily trafficked than the diverging line. This commonly occurs, for example, at S&C where the diverging route exists only for trains to temporarily divert onto an alternate route while maintenance is carried out.

Given the necessary simplifications to the testing arrangements compared with the greater variability of field conditions, these tests should be viewed as supplementing knowledge by taking advantage of the greater ability to provide controlled conditions in a laboratory set-up to gain insights into relative performance.

2.3 Instrumentation

Linear variable displacement transducers (LVDTs) were positioned along the bearer to monitor the vertical movements (Fig. 4). Data were sampled at 100 Hz. The measurements were used to calculate the bearer permanent settlement (taken as the deflection at the minimum load) and also the resilient movement as the difference between the deflections at the maximum and minimum load, within each cycle. The settlement measurements were zeroed after the first 10 loading cycles, to minimize variability from laboratory bedding in of the ballast under initial loading from the comparison.

3   Results and Discussion

Figures 7, 8, and 9 show the permanent settlement along the bearers for the continuous (no joint), rigid jointed, and flexible jointed bearers, respectively, at logarithmic increments of load cycles.
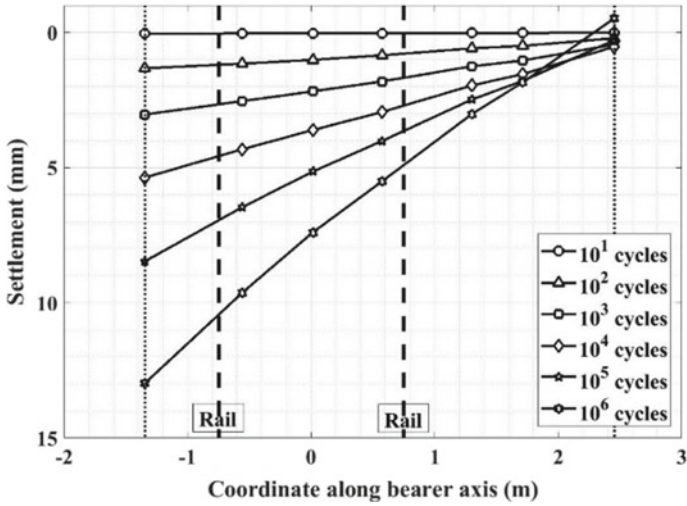
Fig. 7 Permanent settlement along the continuous bearer at different numbers of load cycles
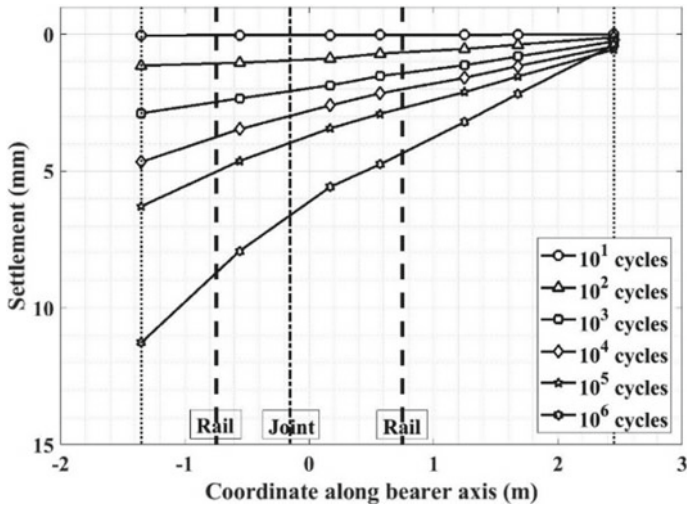
Fig. 8 Settlement along the near-rigid jointed bearer at different numbers of load cycles

In the short term, an initially high rate of settlement reduces as the ballast densifies. Uneven settlement becomes apparent along the length of each bearer. The degree of unevenness depends on the type of joint. The flexible jointed bearer undergoes significantly more settlement over its shorter section, towards the unconfined ballast shoulder. At the opposite bearer end, the variation in settlement is less, with all the bearers settling almost the same small amount and a small amount of uplift at the extreme (inner) end of the continuous bearer. In the longer term, the settlements
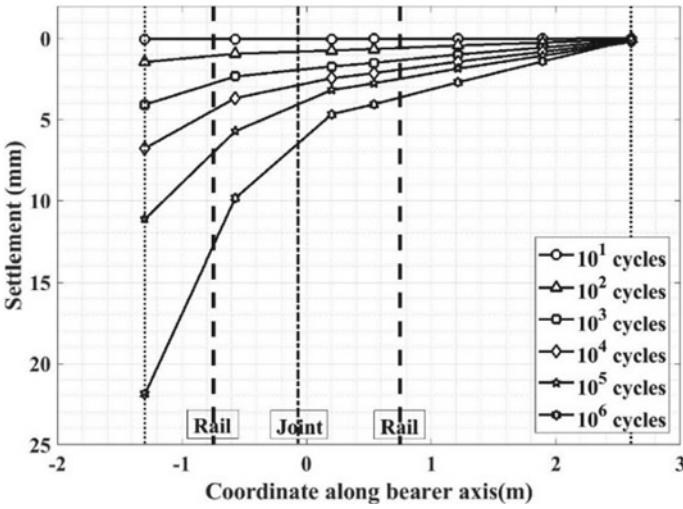
Fig. 9 Settlement along the pinned jointed bearer at different numbers of load cycles
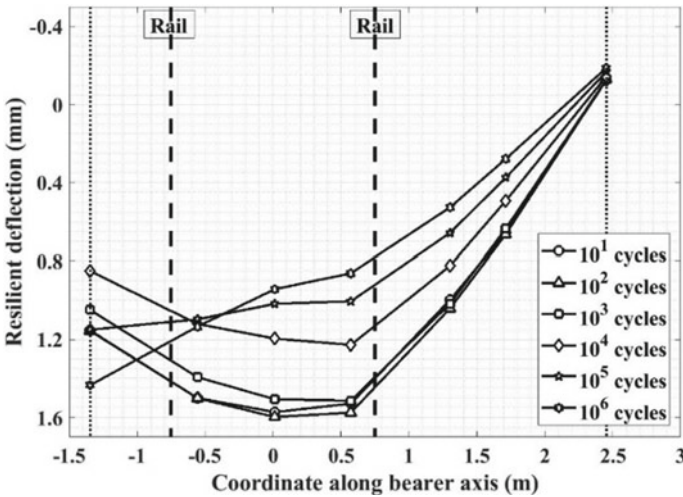
Fig. 10 Resilient deflection along the continuous bearer at different numbers of load cycles

continue to develop at reducing rates, with the trends in variations along the bearer length, and differences between the bearers becoming more pronounced.

The discontinuity introduced by the flexible joint leads to a larger difference between the rail levels. However, in absolute terms, the difference in permanent settlement is less than 8 mm, and because this is a test on an isolated bearer, it is not necessarily what would happen in the field.

Figures 10, 11, and 12 show the resilient deflections at the same numbers of cycles as Figs. 7, 8, and 9 for permanent settlement.

In the short term, the continuous bearer showed the greatest resilient deflections, concentrated in the region between the loaded rails. The rigid jointed bearer deflected less than the continuous bearer, but there is a similar trend in distribution of resilient deflections along its length. Resilient deflections were smallest for the flexible jointed
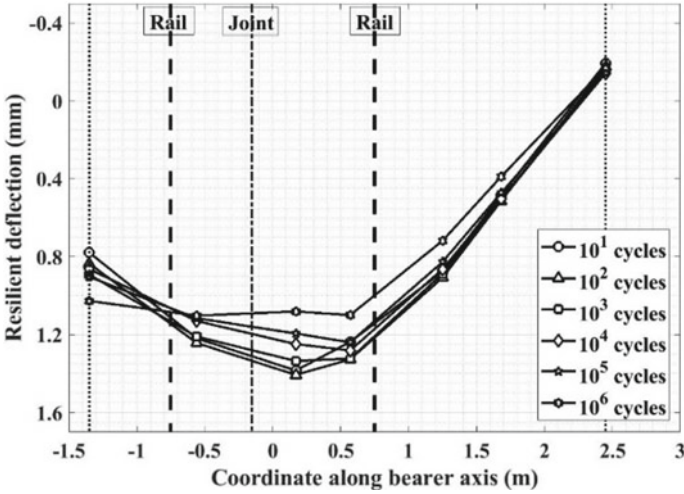
Fig. 11 Resilient deflection along the rigid jointed bearer at different numbers of load cycles
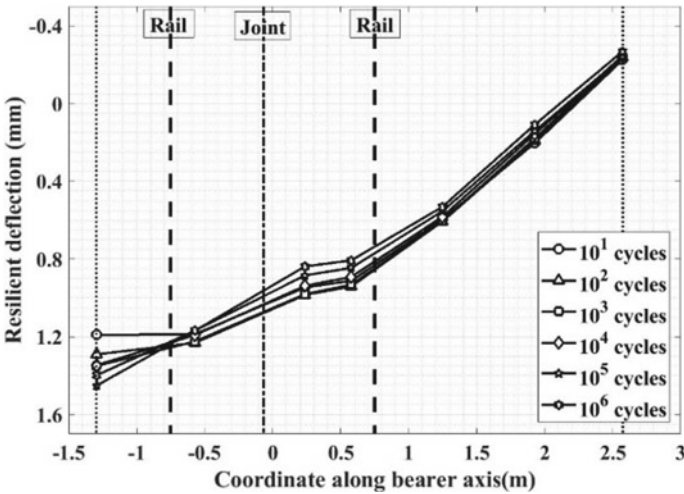
Fig. 12 Resilient deflections along the flexible jointed bearer at varying load cycles

bearer, which tended to deflect more closest to the ballast shoulder. There was a small amount of uplift at the far (inner) end of all bearers.

In the longer term as the ballast compacts and/or spreads laterally, the bearer resilient shape changed depending on joint type or absence thereof. For the continuous and rigid bearers, the location of maximum resilient movement migrated from the railseat in the short term to the bearer end (nearest the unconfined ballast shoulder). Both bearers exhibited this tendency (Figs. 9 and 10), although the rigid jointed bearer was only just doing so at 10^6 cycles, whereas it was apparent at 10^5 cycles for the continuous bearer. This is considered to be a result of outward movement of the ballast shoulder and possible voiding in that particular location. For the flexible jointed bearer, the resilient shape remained broadly similar to that in the short term.

4   Summary

The tests have shown that the distribution and evolution (with number of load cycles) of permanent settlement and resilient movement along the length of a bearer were significantly influenced by the type or absence of joints placed between the rails.

– The modular bearer with the flexible joint showed significantly greater permanent settlement and rotation over its shorter part, closer to the ballast shoulder, uncoupling the behaviour of the bearer parts.
– A small resilient uplift of the unloaded end of the bearers occurred in all cases.
– For the rigid jointed and continuous bearers, the distribution of the resilient deflections changed significantly with the number of loading cycles, with the deflections of the end closer to the shoulder increasing. This was attributed to the outward movement of the ballast shoulder and possibly the formation of a small gap between the bearer and the ballast at the shoulder end.
– For the flexible jointed bearer, changes in resilient deflections with increasing number of load cycles were minimal, as the relative vertical movement and rotation between the bearer parts allowed the bearer base to remain conformal to the ballast.

The tests have shown modular bearer behaviour is affected by the type of joint. A flexible joint, which uncouples the behaviour of the two bearer parts, provides a very consistent resilient response over time. However, the flexibly jointed parts undergo greater relative permanent rotation and vertical settlement. This is perhaps why the manufacturer recommends at least a pair of rails on each jointed bearer part.

The tests represent a likely worst case on an isolated bearer, with a minimal ballast confinement from the shoulder end. In the field, behaviour will be more complex. At locations where tracks are in cuttings and/or the ballast shoulder is confined with additional measures, the differential settlement would be reduced. Further testing is currently in progress at the University of Southampton to investigate the effect of joint location along the bearer and a fuller range of conditions. The results of these

tests may be used with numerical modelling of full S&C to better understand the system properties taking account of the rails and vehicle dynamic loading.

References

1. ORR (2017) Strategy for regulation of health and safety risks—chapter 6a: track. Office of Rail and Road, London
2. Network Rail (2013) Annual returns 2013, a technologyenabled future. Network Rail Kings Place, 90 York Way, London
3. Network Rail (2019) Our information and data. [Online]. Available: https://cdn.networkrail.co.uk/wp-content/uploads/2019/06/Annual-expenditure-2017-18.pdf. Accessed 7-10-2018
4. Nissen A (2005) Analys av statistik om spårväxlars underhållsbehov. Doctoral dissertation. Samhällsbyggnad, Avdelningen för drift och underhåll, Lulea tekniska universitet
5. Zwanenburg WJ (2009) Modelling degradation processes of switches & crossings for maintenance & renewal planning on the Swiss railway network. Doctoral dissertation. École polytechnique fédérale de Lausanne
6. ORR (2012) Efficient expenditure benchmarking of network rail against North American railroads. Office of Rail Regulation, Derby
7. Pålsson BA, Nielsen JC (2012) Wheel–rail interaction and damage in switches and crossings. Veh Syst Dyn 50(1):43–58
8. Lau A, Hoff I (2018) Simulation of train-turnout coupled dynamics using a multibody simulation software. Model Simul Eng 1–10
9. Zhu JY (2006) On the effect of varying stiffness under the switch rail on the wheel–rail dynamic characteristics of a high-speed turnout. Proc Inst Mech Eng Part F J Rail Rapid Transit 220(1):69–75
10. Alfi S, Bruno S (2009) Mathematical modelling of train-turnout interaction. Veh Syst Dyn 47(5):51–574
11. James Sae S, Olivia M, Sakdirat K (2017) Torsional effect on track-support structures of railway turnouts crossing impact. J Transp Eng 143(2):1–10
12. Le Pen L, Watson G, Hudson A, Powrie W (2017) Behaviour of under sleeper pads at switches and crossings—field measurements. Proc Inst Mech Eng Part F J Rail Rapid Transit 1049–1063
13. RAIB (2018) Freight train derailment at lewisham, south-east London. Derby
14. Zhu J, Thompson D (2009) Characterization of forces, dynamic response, and sound radiation from an articulated switch sleeper in a turnout system. Proc Inst Mech Eng Part F J Rail Rapid Transit 53–60
15. Le Pen L (2011) Track behaviour: the importance of the sleeper to ballast interface. Proc Inst Mech Eng Part F J Rail Rapid Transit 225(2):113–128
16. Abadi T, Le Pen L, Zervos A, Powrie W (2016) Improving the performance of railway tracks through ballast interventions. Proc Inst Mech Eng Part F J Rail Rapid Transit 232(2):337–355
17. Abadi T, Le Pen L, Zervos A, Powrie W (2019) The effect of sleeper interventions on railway track performance. J Geotech Geoenviron Eng 1–14

Asphalt/Ballast Trackbeds for Improved Clearance Beneath Historical Bridges for Electrification Works

Taufan Abadi and **Louis Le Pen**

Abstract Electrification of existing railway lines offers the potential to operate more sustainably with zero carbon emissions at the point of use by eliminating the need for diesel multiple units, diesel locomotives and/or dual electric/diesel vehicles. However, many existing lines are not suitable for placing overhead electrical lines continuously along the route because of low clearance beneath historical overbridges. These can be replaced, but unless the bridge is already life expired this is not usually economically viable. An alternative approach is to lower the track under the structure. However, this may have structural implications. To mitigate these, the engineered trackbed thickness could be reduced so that less material is dug out during the lowering works. This research investigates the potential for reducing the trackbed thickness by using an asphalt layer with an overlying low thickness ballast layer. A series of tests were carried out using the Southampton Railway Testing Facility (SRTF), a laboratory representation of a single sleeper bay of track. Different thicknesses of ballast and asphalt with varied ballast gradations were placed into the apparatus for evaluation. Tests were carried out by applying a cyclic load representing a 20-tonne axle load at 4 Hz for up to 3 million cycles (60 million cumulative tonnes). It was found possible to reduce the trackbed thickness; however, there remained minimum required thicknesses for both the asphalt and ballast layers needed to prevent stress localization, which manifested as damage to the asphalt surface and non-even resilient response along the sleeper length with cycles.

Keywords Asphalt trackbed · Ballast gradation · Electrification · Bridge gauge

T. Abadi · L. Le Pen (✉)
Infrastructure Research Group, University of Southampton, Boldrewood Innovation Campus, Southampton, Hampshire SO16 7QF, UK
e-mail: louis.lepen@soton.ac.uk

1   Introduction/Background

Approximately 25% of the cost of electrification schemes is for civil engineering-related works, of which the bulk is for bridge reconstruction [1]. Changes to railway systems, which would allow the volume of bridge reconstruction to be reduced, have the potential to generate significant cost savings and ultimately benefit the fare-paying public. A potential method to reduce bridge reconstruction for electrification is to modify and lower the track form creating the space for electric lines to pass beneath existing bridges.

On ballasted track, it is already possible to change the sleeper type to reduce the trackbed height requirement. However, this alone does not provide sufficient gains in clearance. A further height reduction is only possible by adjusting the engineered trackbed thickness.

Asphalt has conventionally been used for highways with its application to railways growing steadily in the USA [2]. Various studies have shown that asphalt track systems offer benefits in modern railway construction, where asphalt is able to provide high-quality and longer-lasting track support [3]. The asphalt layer can be inserted as a sealant layer between subgrade and ballast to block water penetration and acts as a flexible layer able to improve load distribution and reduce stress onto the subgrade [4, 5]. Asphalt is also expected to reduce track irregularities [6–8].

There may be various arrangements for an asphalted track system [3, 9, 10]. The most common is probably to introduce an asphalt layer onto a suitable formation and lay standard grades of ballast directly on top to a thickness suitable for tamping (e.g. >150 mm). This arrangement combines the benefits of conventional ballasted track (the ability to maintain with mechanized tampers and to realign the geometry) with the potential benefits of a more uniform and durable support. In the longer term, asphalt/ballast systems may lead to reductions in the frequency and cost of maintenance, although the evidence base for this requires more work.

This research investigates, through laboratory experiments, the potential for reducing the trackbed thickness by using an asphalt layer with an overlying low thickness of ballast. In the asphalt/ballast trackbed, the asphalt is expected to strengthen and stiffen the trackbed support and withstand the trainload transferred from a thinner ballast layer. However, the gradation of ballast to be used requires alteration so that a suitable number of grain diameters are present to distribute the stresses evenly onto the asphalt. In this localized and specialist type of application, the ballast thickness is potentially too small for mechanized tampers to be used. However, the cost saving in avoiding bridge reconstruction would potentially justify local manual packing operations to maintain geometry when needed.

2 Methods

The Southampton Railway Testing Facility (SRTF) was used for testing. The SRTF is a laboratory representation of a single sleeper bay of track. It has previously been used to investigate the influence of different sleeper and ballast arrangements on their long-term performance [11–13]. In this research, the SRTF was modified by inserting a steel frame containing a pre-prepared asphalt layer within the walls of the apparatus. The asphalt frame or "tray" also contained fixings to confine the ballast at either end of the sleeper using steel plates to model a condition under a bridge where the bridge piers/abutments would constrain the trackbed. The SRTF side walls were narrowed above the asphalt tray by the placement of wooden spacers on top of the trays steel sides. This provided for a representation of the intended in field sleeper spacing of 500 mm, and this is narrower than most track. Figure 1 shows the installation of asphalt into the tray frame, and Figs. 2 and 3 show the general arrangement of the SRTF for these tests.

A combination of ballast, sleeper and asphalt trackbeds of four different ballast thicknesses and two different gradations was tested. Cyclic tests were carried out using a 10-tonne cyclic load (approximately equivalent to a 20-tonne axle load allowing for 50% transfer to a supporting sleeper) at a frequency of 4 Hz for 3 million loading cycles. This is approximately equivalent to a cumulative load of 60 million tonnes or an interval between maintenance interventions (tamping) on conventional ballasted track. The test bed was set to a width of 500 mm allowing for a locally closer spacing compared with a more usual 600–700 mm on plain line. The closer spacing for this testing was intended to reproduce a locally closer spacing of sleepers passing beneath a bridge to help distribute the load more evenly at this sensitive location.

Fig. 1 Asphalt tray being loaded with asphalt and compacted
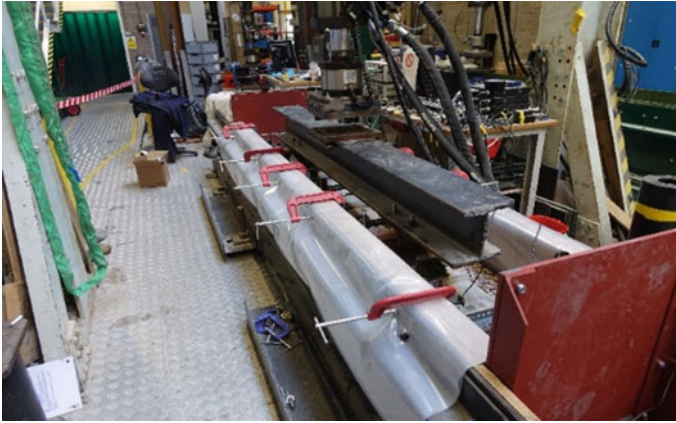
Fig. 2 Photograph of the SRTF laboratory tests
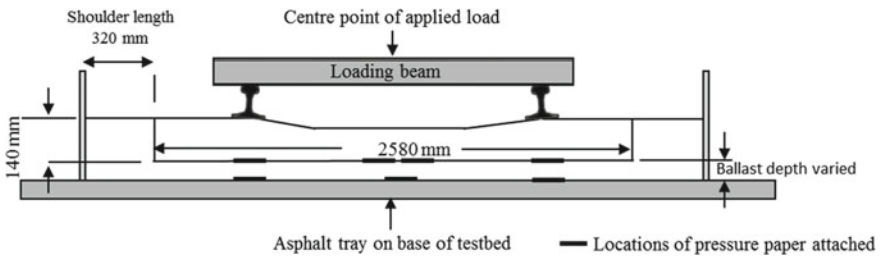
Fig. 3 Cross section through test

Common procedures were followed for each test:

(1) The steel tray was prepared off site with a 15 mm thick ballast mat, 50 mm of type 1 fill and a 100 mm thickness of asphalt giving a height of 165 mm (Fig. 1), and this is just lower than the internal maximum height of the tray which was 180 mm.

(2) The tray was inserted into the test apparatus, the end panels were bolted into position, and wooden spacers placed against the rig internal sides on top of the steel sides of the asphalt tray so that the internal width of the test arrangement was the same as the asphalt width (500 mm).

(3) Pressure-sensitive paper was placed onto the sleeper soffit and the asphalt surface directly below each rail seat and the sleeper centre (Fig. 3).

(4) A chosen type and height of ballast was placed compacted and levelled with a total of 22 passes of a 400 mm × 320 mm, 26 kg plate vibrator giving a 5 kN compaction force, and the surface levelled at the same time.

(5) Sleeper, crib ballast, loading beam and linear variable displacement transducers (LVDTs) were placed. Each test was started no longer than 24 h after test preparation had been completion.

(6)   A vertical cyclic compression force with a minimum of 5 kN and a maximum of 98 kN was then applied to 3 million cycles at 4 Hz.

The sleeper vertical displacement was monitored by an array of LVDTs. The sensors were positioned at the sleeper ends, on the internal sides of the rail seats and in the middle of the sleeper. Data were recorded at 100 Hz.

3   Material

The EG47 mono-block concrete sleeper was selected for use in these tests owing to its relatively small height dimension. The base of this sleeper type has dimensions of 2580 mm length × 290 mm width × 140 mm depth. The sleeper mass is approximately 260 kg.

An under sleeper pad (USP) of type Sylomer SLB 3007G was attached onto sleeper soffit for every test. This type of USP has a thickness of 7 mm and static bending modulus, C_{stat}, of 0.36 N/mm³ [14].

Ballast used in the tests was red granite sourced from Cloburn quarry, Lanark, South Lanarkshire, Scotland, ML11 8SR [15]. The ballast was supplied in 14–20 mm (stone blowing aggregate) and 8–11 mm gradings.

The ballast density and specific gravity were measured. The results are presented in Table 1. The minimum and maximum density was measured within a 300 mm-sided cubic box. Loose specimens were prepared by placing ballast gently into the box without allowing grains to fall from any height. Dense specimens were placed in three layers, with each layer vibrated after placement by mounting the box onto the base of a heavy-duty sieve shaker. After vibration of the last layer, further ballast grains were added manually to obtain a level surface.

The particle size distribution (PSD) of each ballast grading used was measured and is shown in Fig. 4 with selected key values of grain sizes also shown in Table 1.

The asphalt bed was prepared by project partners Network Rail (NR) and AECOM (Fig. 1). The tray was loaded first with a 15 mm thick ballast mat at the base and then 50 mm of type 1 fill before being overlain with 100 mm of asphalt.

The under ballast mat (UBM) was a Sylomer SR110 with a thickness of 15 mm [14]. It has c_{stat} value of 0.11 N/mm² from tests to DIN ISO 1827 [16]. Theoretical calculations were used to select the ballast mat with the intention that it would behave as a relatively soft subgrade and oblige the asphalt layer to operate in a relatively onerous condition.

Table 1   Ballast properties

Ballast grading (mm)	Density (kg/m³)		Specific gravity (G_s)	Grain size (mm)		
	Loose	Dense		D_{90}	D_{50}	D_{10}
14–20	1397	1507	2.62	21.1	16.6	14.2
8–11	1329	1454		11.5	9.9	7.8
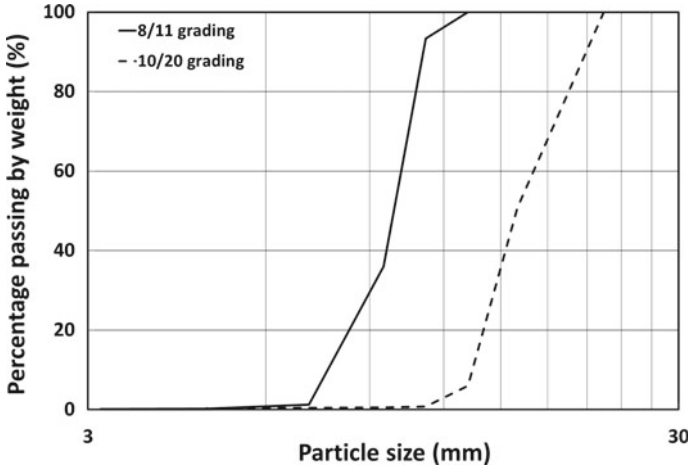
Fig. 4 PSD of ballast gradings used for the tests

The type 1 fill provided thermal isolation to prevent heat from the asphalt placement from damaging the ballast mat. Type 1 fill is a specification used by the UK highways agency (BS EN 13285 in combination with the specification for highway works: SHW, series 800). The key characteristics of this type of fill are that it is a granular predominantly sandy material.

4 Instrumentation (LVDTs and Pressure Paper)

Vertical LVDTs to measure ballast permanent settlement and resilient behaviour were placed on either side of the sleeper, near the rail seats and in the middle (Fig. 5).

To determine the average settlement, each LVDT reading was weighted in proportion to the area of sleeper closest to it (Fig. 5).

To investigate the contact at sleeper/ballast and ballast/asphalt surface interface, pressure paper was used. Pressure paper is a thin film consisting of micro-encapsulated colour forming and colour developing materials [17, 18]. The pressure paper turns red with the intensity of the colour proportional to the magnitude of the
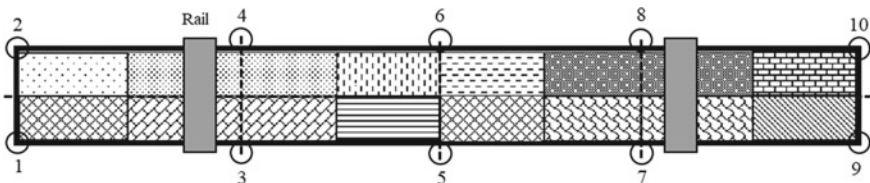
Fig. 5 LVDT locations on the sleeper and shading/hatching to show the area weighting

Table 2 Test conditions

Components	Thickness (mm)			
	Test 1	Test 2	Test 3	Test 4
Asphalt below the ballast (constant)	100 (not counting type 1 and ballast mat which would be the subgrade in the field)			
Aggregate (variable)	50 (stone blower)	100 (stone blower)	150 (stone blower)	75 (8–11 mm)
Component above ballast layer	350 (USP, EG47 sleeper and 60 kg/m rails)			
Thickness of trackbed and sleeper/rails	500	550	600	525

pressure [11–13, 19]. Pressure paper with sensitivities in the ranges 2.5–10 MPa and 10–50 MPa was used. Sheets of the pressure paper measuring 200 mm × 250 mm were placed at key locations on the asphalt surface and at the sleeper soffit (Fig. 3). At the end of the test, the paper was carefully recovered and provided a cumulative record of the contact area over the whole loading history.

5 Parametric Study

Four tests are shown in Table 2. The overall thickness of the trackbed was varied by changing the thickness of the ballast layer while maintaining the overall thickness of other components, giving a study range of rail top to bottom of trackbed thickness of between 500 and 600 mm. Tests 1 to 3 investigate the performance of increasing ballast thicknesses from 50 to 150 mm using a stone blower aggregate in 14–20 mm grain size range. Test 4 used a finer gradation (8/11 aggregate) from the same parent rock to investigate whether a finer graduation would improve relative performance and also allow further reductions in trackbed thickness.

6 Test Results and Discussion

6.1 Settlement and Resilient Deflection

Figure 6 shows the results of permanent settlement (area-weighted method) against the number of loading cycles on a log scale with the results zeroed after ten loading
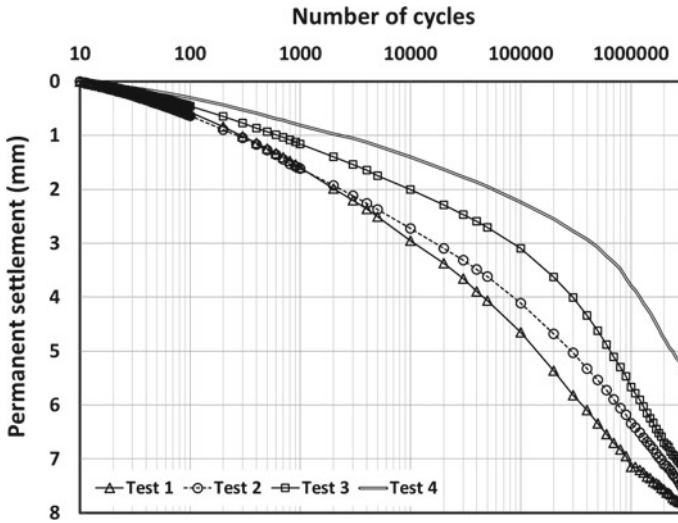
Fig. 6 Permanent settlement found using the area-weighted LVDT measurements

cycles to allow for bedding in. Each test showed a similar trend of vertical permanent settlement evolution with cycles.

Figure 7 shows the resilient range of movement per cycle on the primary *y*-axes. In most of the tests, the range was within 1.0–1.5 mm. The resilient deflection range is likely to be dominated by contributions of movement from the USP and UBM. However, the largest resilient deflection occurred for test 1 and was greater than
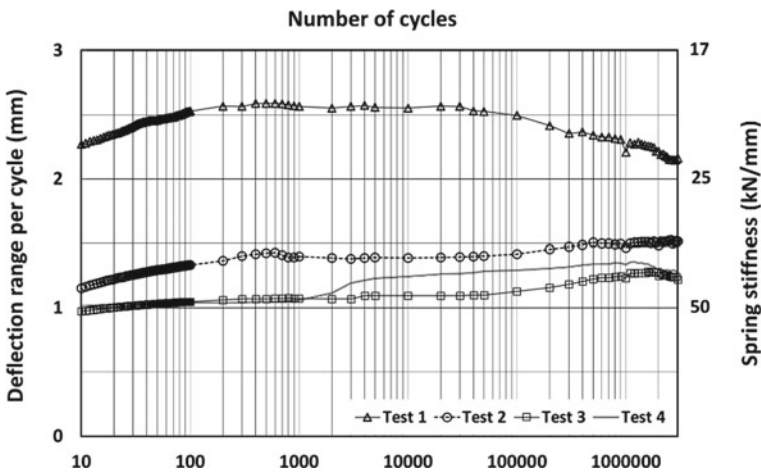
Fig. 7 Deflection range and spring stiffness found using the area-weighted LVDT measurements

2 mm. This occurred as a result of an unstable ballast layer which was too thin (50 mm), for the ballast grain size ($D_{50} = 17$ mm).

The secondary *y*-axes of Fig. 7 indicates approximately the equivalent spring stiffness for the major grid lines calculated/inferred from the deflection of the sleeper and the known load—these values have been placed as an approximate guide although the increments are not linear. Towards 3 million loading cycles, the spring stiffness per sleeper end (or per rail) of all the tests was between 20 and 40 kN/mm (i.e. rail load of 50 kN divided by deflection). This is a relatively soft support as was the intention from using the USP and UBM.

The support from the ballast is greatest below the rail seats for sleepers on freshly laid or just tamped ballast and is often idealized as a w- or m-shaped distribution (e.g. [20]). However, the pressure distribution may change with traffic loading. After many cycles of loading, gaps can develop below the sleeper ends, creating a condition known as centre binding. Centre-bound sleepers are supported mainly by the ballast below the sleeper centre and tend to bend about their middle. This can lead to sleeper failure. To investigate the tendency towards centre binding, the deflection data were compared for measurements at the sleeper ends and at the middle (Figs. 8 and 9).

Figures 8 and 9 show that although there were some differences present early on and the development of increased sleeper corner deflection, the sleepers retained a generally consistent deflection range throughout the test. The general uniformity of sleeper deflection and lack of any tendency to centre bind may be due to the inclusion of the USPs which have been found to mitigate against centre binding in other research [11].
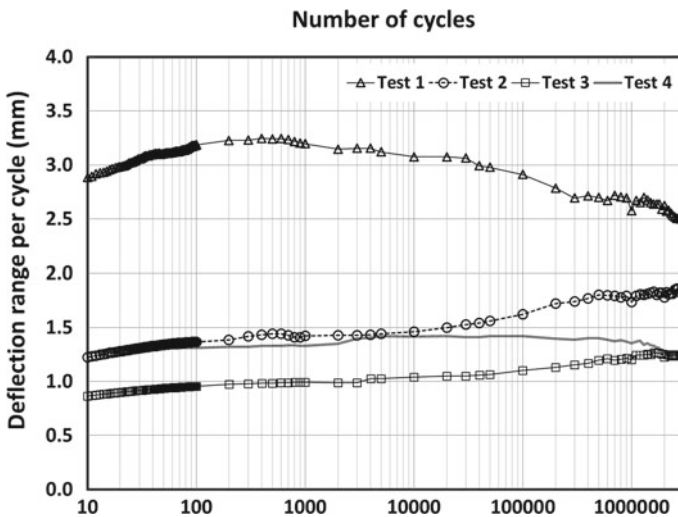
Fig. 8 Average deflection at sleeper corners
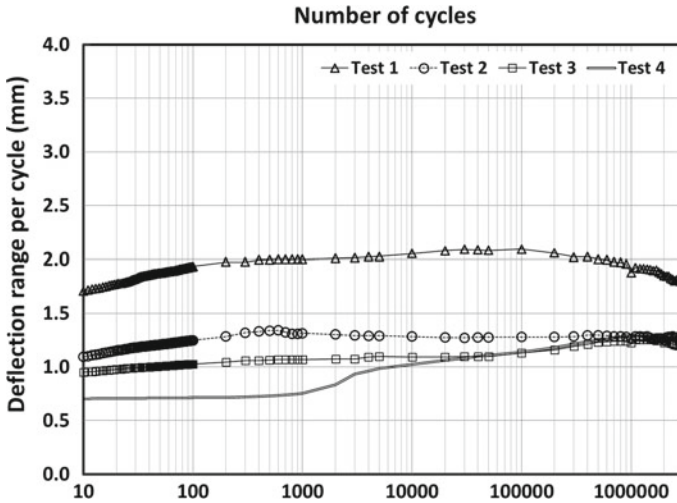
Fig. 9 Average deflection at sleeper middle

6.2 Contact Area

The percentage of contact area at sleeper/ballast and ballast/asphalt surface interfaces was calculated using an image thresholding technique (Adobe Photoshop CS6 software). The results are summarized in Table 3.

Tests 1 to 3 used the same ballast gradation, and their contact areas onto the asphalt follow in order of ballast thickness (more contact for thinner layers). This may be interpreted as thinner layers being less stable over the loading history resulting in increased cumulative contact areas as ballast grains move about.

Test 4 used a finer gradation, and this showed a relatively high contact area at >2.5 MPa but a relatively low result for >10 MPa. This may be interpreted as more individual contacts from the greater number of finer grains, but each of these contacts was of a lower stress owing to greater stress distribution through the greater number of grains.

Table 3 Percentage of contact area at sleeper/ballast and ballast/asphalt surface interfaces

Test	Percentage (%) contact area at interface of			
	Sleeper/ballast, measured by pressure paper range of		Ballast/asphalt, measured by pressure paper range of	
	>2.5 MPa	>10 MPa	>2.5 MPa	>10 MPa
1	16.1	8.3	56.4	44.6
2	17.6	8.5	20.9	14.7
3	13.0	7.0	15.8	3.5
4	12.9	5.4	53.3	10.0
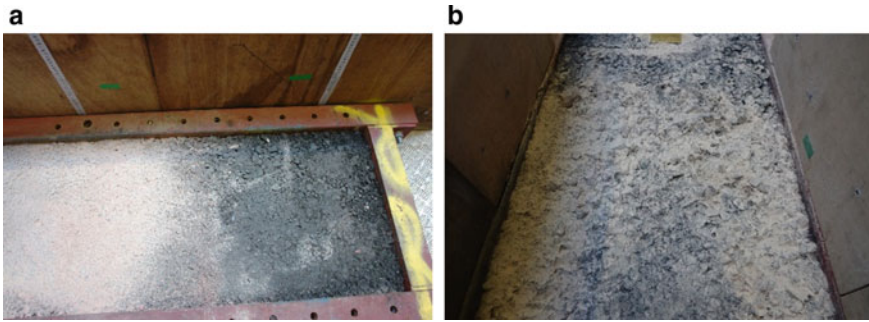
Fig. 10 Asphalt surface after testing with **a** no damage and **b** damage from a too thin and too large grain-sized ballast (test 1)

At the sleeper/ballast interface, the contact areas recorded were relatively close for each of the tests at between 12.9 and 17.6% for the higher threshold and 5.4–8.5% for the lower threshold. Near the sleeper soffit, the stresses have not had the opportunity to dissipate with depth. The small variation that is present could be a consequence of differences in ballast gradation and localization of stresses (so that the paper was not necessarily representative of the whole sleeper/ballast contact area).

6.3 Asphalt Surface Condition

At the end of each test, the asphalt surface was visually evaluated. Most of the asphalt used showed no obvious signs of damage. The exception to this was test 1, which had the thinnest ballast layer (50 mm).

Figure 10a shows a smooth asphalt surface, although there has been generation of dust locally from the red granite ballast which has fixed to the asphalt surface discolouring it. Figure 10b shows pitting damage on the asphalt surface below test 1. This illustrates the damage caused by stress localization resulting from using a too thin ballast layer with a too great grain size.

7 Conclusion

Research has demonstrated the feasibility of using an asphalted shallow depth track form to support electrification on the railway network and avoid the need for bridge reconstruction. These results also provide insights that may be more widely applicable.

In the testing, it was found that a reduced trackbed thickness can perform well; however, there are minimum required thicknesses for the ballast layer needed to prevent stress localization, which manifested as damage to the asphalt surface and

non-even resilient response along the sleeper length with cycles. The minimum thickness of a ballast layer is also influenced by its grain size. Finer gradations are required for thinner ballast layers. Further research is required to determine optimum configurations over a wider range of test conditions.

References

1. Govan C, Brough M, Hasnayn M (2018) Shallow-depth asphalt trackform development. Permanent Way Inst J 136(2):36–40
2. Rose JG, Lee HM Jr (2008) Long-term assessment of asphalt trackbed component materials' properties and performance. In: AREMA annual conference 2008, Salt Lake City
3. Rose JG, Souleyrette RR (2015) Asphalt railway trackbeds: recent designs, applications and performances. In: AREMA annual conference, Minneapolis
4. Esmaeili M, Amiri S, Jadidi K (2012) An investigation into the use of asphalt layers to control stress and strain levels in railway track foundations. Proc Inst Mech Eng Part F J Rail Rapid Transit 228(2):182–193
5. Cardona DR, Benedetto HD, Sauzeat C, Calon N, Saussine G (2016) Use of a bituminous mixture layer in high-speed line trackbeds. J Constr Build Mater 125:398–407
6. Khairallah D, Blanc J, Cottineau LM, Hornych P, Piau J-M, Pouget S, Hosseingholian M, Ducreau A, Savin F (2019) Monitoring of railway structures of the high speed line BPL with bituminous and granular sublayers. J Constr Build Mater 211:337–348
7. Khairallah D, Blanc J, Cottineau LM, Hornych P, Piau J-M, Pouget S, Hosseingholian M, Pouget S, Ducreau A, Voigner P (2018) Monitoring of railway structures HSL BPL with bituminous layer. In: Proceedings of seventh transport research arena TRA 2018, a digital era for transport solution for society, economy and environment, Vienna, 16–19 Apr 2018
8. Momoya Y, Sekine E (2005) Performance-based design method for railway asphalt concrete reinforced roadbed. In: Seventh international conference on the bearing capacity of roads, railways and air-fields, Trondheim, 25–27 June 2005
9. Rose JG, Hensley MJ (1991) Performance of hot-mix-asphalt railway trackbeds. Transp Res Rec 1300:35–44
10. Rose JG, Brown ER, Osborne ML (2000) Asphalt trackbed technology development: the first 20 years. Transp Res Rec J Transp Res Board 1713(1):1–9
11. Abadi TC, Le Pen LM, Zervos A, Powrie W (2019) Effect of sleeper interventions on railway track performance. J Geotech Geoenviron Eng 154
12. Abadi TC, Le Pen LM, Zervos A, Powrie W (2018) Improving the performance of railway tracks through ballast interventions. Proc Inst Mech Eng Part F J Rail Rapid Transit 232(2):337–355. https://doi.org/10.1177/0954409716671545
13. Abadi TC (2015) Effect of sleeper and ballast interventions on rail track performance. Thesis of doctor of philosophy, PhD thesis, Thesis of doctor of philosophy, Faculty of Engineering and the Environment, University of Southampton, Southampton
14. Getzner (2018) https://www.getzner.com/en/downloads?downloadTags=Data%20Sheet,en,Sylomer. Accessed 15 Oct 2019
15. Cloburn Quarry Company Ltd. (2019) Engineering rock. www.cloburn.co.uk. Accessed 22 Oct 2019

16. ISO: ISO 1827:2016 (2016) In rubber, vulcanized or thermoplastic—determination of shear modulus and adhesion to rigid plates—quadruple-shear methods. International Organization for Standardization, Vernier, Geneva
17. A J P Automotive Ltd. (2011) Pressure measurement film prescale
18. Fuji Film (2013) Fuji film prescale pressure measurement film. Available: http://www.fujifilm.com/products/prescale/prescalefilm/
19. Abadi TC, Le Pen LM, Zervos A, Powrie W (2015) Measuring the area and number of ballast particle contacts at sleeper-ballast and ballast-subgrade interfaces. Int J Railw Technol (IJRT) 4(2):45–72
20. Zakeri JA, Sadeghi J (2007) Field investigation on load distribution and deflections of railway track sleepers. J Mech Sci Technol 21(12):1948–1956

Settlement of Ballasted Track with Large Sleeper Spacing

Yoshitsugu Momoya, Kazuki Ito, and Shuhei Kikkawa

Abstract Maintenance of low annual tonnage ballasted tracks for local railway lines is an important consideration in Japan. To improve safety, deteriorated wooden sleepers are replaced with concrete sleepers. However, the cost of concrete sleepers is higher. To reduce the cost of the replacement, it is effective to increase the sleeper spacing and reduce the number of sleepers. In this scenario, the applied load on each sleeper will increase. In this study, the applied load on each sleeper was calculated by FEM analysis and verified by measuring the rail seat load at the site. The full-scale cyclic loading tests on single sleeper ballasted track models were carried out to investigate the settlement of sleeper. In the tests, the effects of roadbed stiffness and fine contents of ballast material on the settlement of sleeper were investigated. From the tests conducted, the threshold sleeper spacing that would not considerably increase the settlement was determined.

Keywords Ballasted track · FEM analysis · Full-scale test

1 Introduction

In recent years, sustainable operation of local railway lines became an important management issue for railway operators in Japan. In many local lines, operating expenses including maintenance costs are larger than income obtained by passenger fare. However, keeping safety for train operation is the most important subject for railway operators.

Y. Momoya (✉) · K. Ito
Railway Technical Research Institute, 2-3-38, Hikari-cho, Kokubunji-shi, Tokyo, Japan
e-mail: momoya.yoshitsugu.29@rtri.or.jp

K. Ito
e-mail: to.kazuki.29@rtri.or.jp

S. Kikkawa
West Japan Railway Company, 2-4-24, Kita-ku, Shibata, Osaka-shi, Osaka, Japan
e-mail: syuuhei-kikkawa@westjr.co.jp

77

To ensure safe operations of trains, railway operators are replacing old wooden sleepers with concrete sleepers. In the case of local lines in Japan, to minimize the maintenance cost, some railway operators are replacing one sleeper out of three wooden sleepers with concrete sleepers. In those kinds of ballasted tracks, two old wooden sleepers have remained between concrete sleepers. Generally, the spacing of the sleepers is approximately between 600 and 700 mm. When the wooden sleepers are replaced with concrete sleepers with one sleeper out of three sleepers, the spacing between the replaced concrete sleepers becomes approximately 2000 mm. In the future, the remaining wooden sleepers will deteriorate and the replacement of these sleepers will become necessary. To cope with that, to reduce the cost of sleeper replacement, the ballasted track design to replace two wooden sleepers with one concrete sleeper was investigated in this study. In this situation, when remained two wooden sleepers are replaced with one concrete sleeper, finally, the distance of concrete sleepers becomes approximately 1000 mm (Fig. 1).

When the sleeper spacing or distance increases in the ballasted track, the applied trainload on each sleeper will increase. In this study, the applied load on each sleeper was calculated by FEM analysis and verified by measuring the rail seat load at the site. FEM is one of the valid and generally used methods to obtain the deformation of ballasted track [1–3]. Then the full-scale cyclic loading tests on single sleeper ballasted track models were carried out to investigate the settlement of sleeper. Full-scale testing is an effective method for the evaluation of ballasted track deformation

(a) Wooden sleepers

(b) One concrete sleeper out of three sleepers

(c) Concrete sleepers with large distance
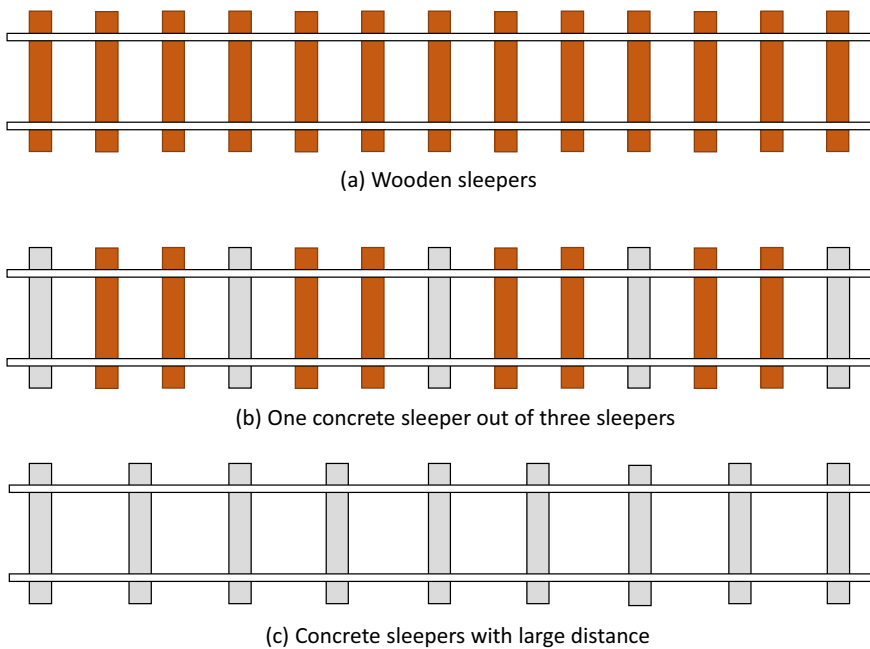
Fig. 1 Replacement of wooden sleepers to concretes sleepers with large distance
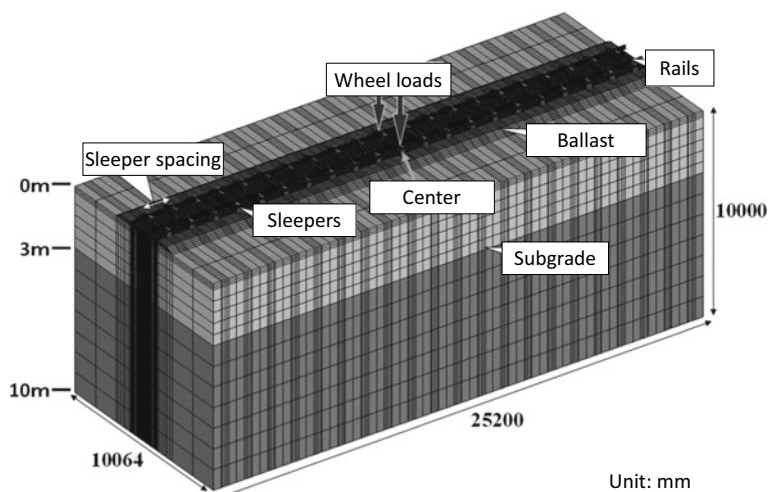
Fig. 2 FEM analysis model

characteristics [4, 5]. In the tests, the effect of the roadbed stiffness and the fine contents of ballast material on the settlement of sleeper was investigated. From the series of tests, the envelope line of the sleeper distance that the settlement becomes rapidly increase was obtained.

2 Sleeper Load Obtained by FEM Analysis

To obtain the load applied to the sleeper with different spacing, linear elastic FEM analysis was carried out. The spacing of the sleepers in the FEM models was set to 600, 800, 1000, and 1200 mm. Rails were JIS 50 kgN rail, the thickness of the ballast layer was 200 mm. The applied wheel load on the rail was 80 kN each on both rails, which are the standard wheel load used in Japanese railway design. Figure 2 shows the analysis model and Table 1 lists the physical properties of the components. Figure 3 shows the analysis results. The load distribution ratio was obtained by rail seat load divided by wheel load when the sleeper is just under the wheel position. The load distribution ratio increased linearly with the increase of sleeper spacing.

3 Measurement of Sleeper Load at the Site

To measure the sleeper load (rail seat load) at the site, loading tests were carried out by using RFWD (Railway Falling Weight Deflectometer) [6] at the site. Figure 4

Table 1 Physical property of the components

Component	Type	Young's modulus (MN/m²) Spring coefficient (MN/m)	Poisson's ratio	Note
Rail	Solid	210,000 MN/m²	0.3	
Rail pad	Spring	110 MN/m	–	
Concrete sleeper	Solid	35,000 MN/m²	0.2	
Ballast	Solid	100 MN/m²	0.3	
Subgrade	Solid	30.5 MN/m²	0.3	0–3 m
Ground	Solid	60.9 MN/m²	0.3	3–10 m

Fig. 3 Relationship between sleeper spacing and load distribution ratio
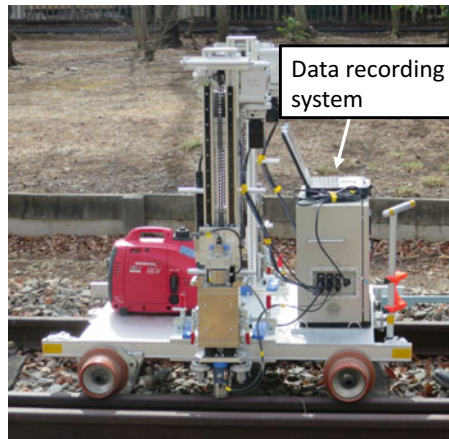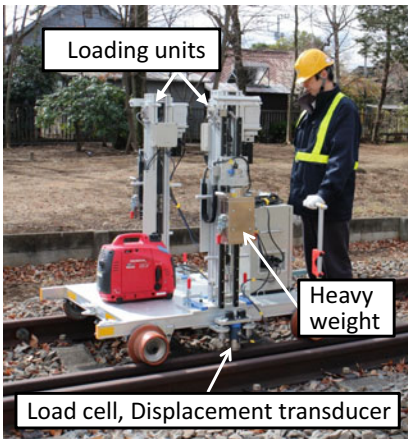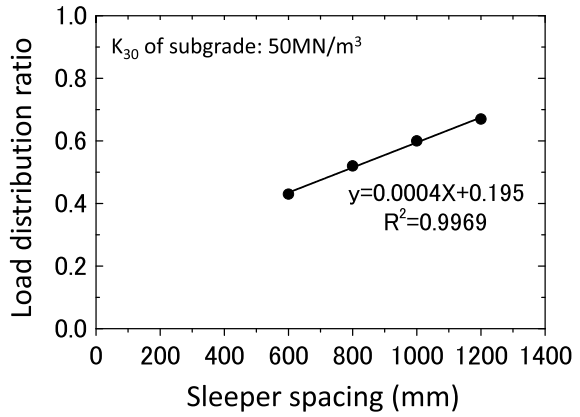
Fig. 4 RFWD (Railway Falling Weight Deflectometer)

shows the configuration of RFWD. RFWD is equipped with two loading units and a maximum load of 20 kN is applied by each unit simultaneously.

RFWD tests were carried out in two sections where the sleeper spacing was 740 and 1041 mm. Before the RFWD test, the ballasted track was tamped to correct track irregularity to eliminate the effect of floating sleeper. Rail seat load was measured by the sensor pads installed between rail and sleeper as shown in Fig. 5. The sensor pads are the track pad installed with piezoelectric load sensor.

Figure 6 shows obtained load distribution ratio by measured rail seat load. The calculated load distribution ratio by FEM is also indicated in the figure. In the test section with sleeper spacing of 1041 mm, the load distribution ratio became larger than in the test section with 740 mm. The measured value at the site corresponded well with the value obtained by FEM analysis.
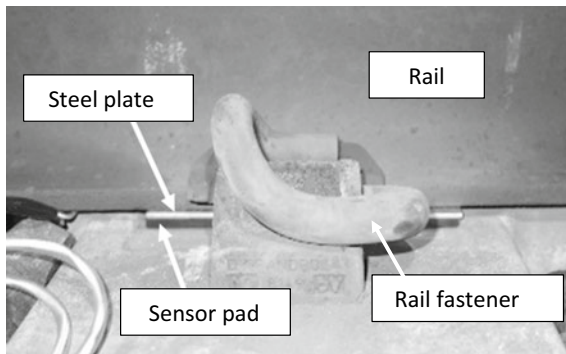
Fig. 5 Sensor pad to measure the rail seat load

(a) Sleeper spacing: 740mm (b) Sleeper spacing: 1041mm
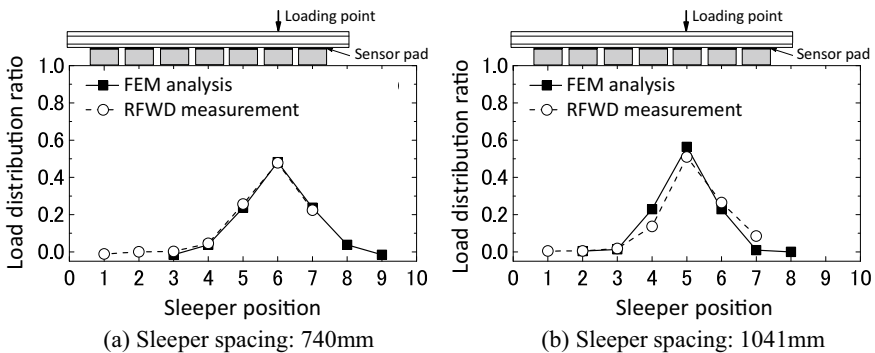
Fig. 6 Measured load distribution ratio

4   Full-Scale Cyclic Loading Test

4.1   Test Condition

Based on the FEM analysis and field measurement, to evaluate the effect of load distribution ratio on the sleeper, full-scale cyclic loading tests were carried out by using full-scale cyclic loading apparatus in RTRI. The test model was a single sleeper ballasted track model. Figure 7 shows the plane view of the ballasted track model. The wooden sleeper model and concretes sleeper model were simultaneously loaded by two hydraulic actuators. Figure 8 shows the cross-section of track and subgrade.

Fig. 7 Plane view of the ballasted track model

Wooden sleeper   Concrete sleeper
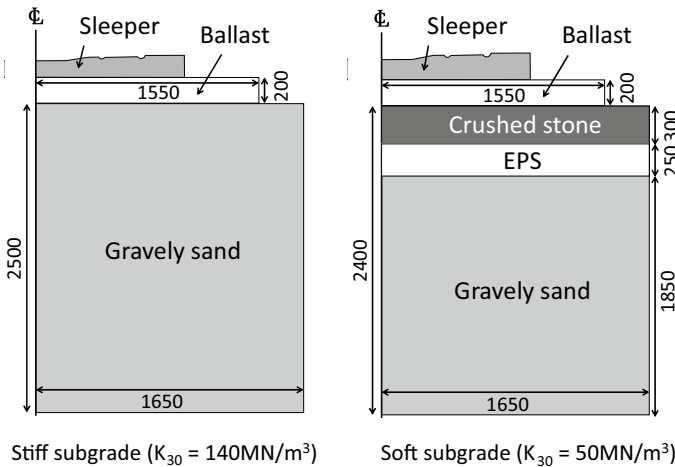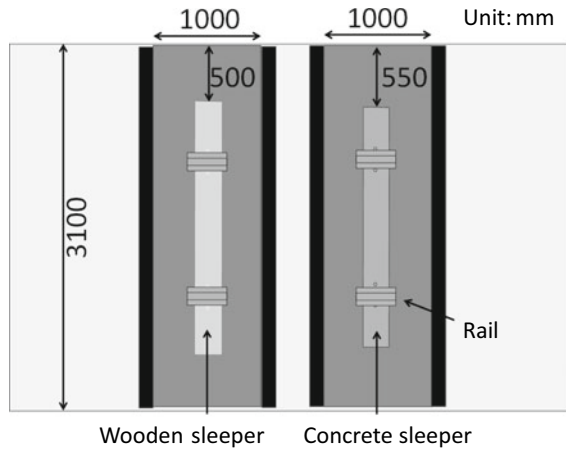
Fig. 8 Cross-section of ballasted track and subgrade model

Table 2 Loading condition

Loading step	Load distribution ratio	Min load (kN)	Max load (kN)	Total amplitude (kN)
Pre-loading	0.4	5	69	64
Step 1	0.4	5	69	64
Step 2	0.6	5	101	96
Step 3	0.8	5	133	128
Step 4	1.0	5	165	160

Full-scale tests were carried out with the stiff subgrade with K_{30} of 140 MN/m^3 and soft subgrade with K_{30} of 50 MN/m^3. On the soft subgrade, cyclic loading tests with a ballasted track containing fine contents were also carried out.

Table 2 presents the loading sequence. The applied cyclic load was increased stepwise assuming the increase of load distribution ratio by the increase of sleeper spacing. Before each loading step, tamping for the ballasted track was carried out to initialize the condition of the ballast layer. For each step, 300 thousand times cyclic loading was carried out.

4.2 Test Results

Figure 9 shows the test result of the case with a concrete sleeper ballasted track on the stiff subgrade. Vertical displacement of sleeper became large as applied load increased. The increment of settlement clearly became large at Step 4. Figure 10 shows the test result of the case with a concrete sleeper ballasted track on the soft subgrade. Displacement of the sleeper became significantly larger than the case
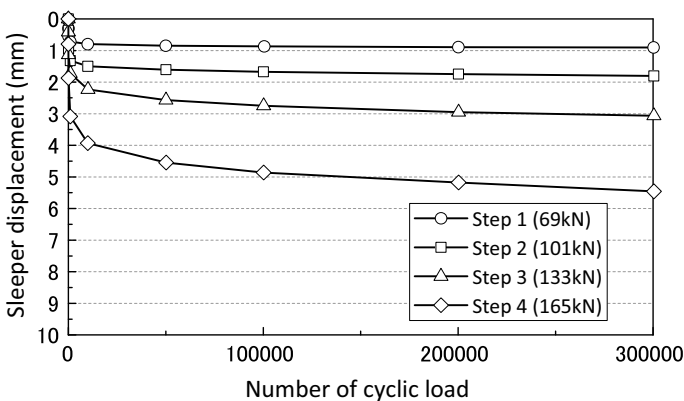
Fig. 9 Sleeper displacement with stiff subgrade and concrete sleeper
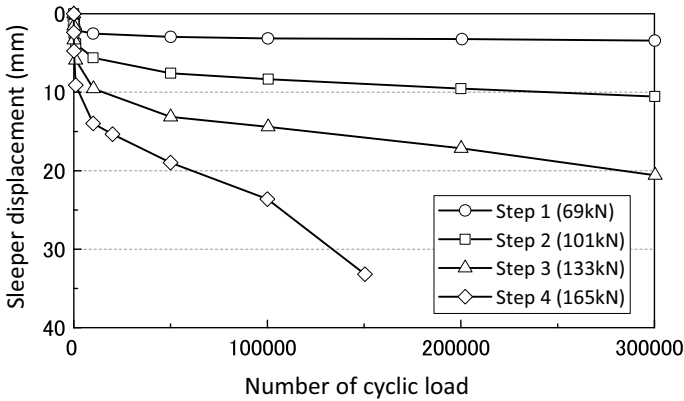
Fig. 10 Sleeper displacement with soft subgrade and concrete sleeper

with the stiff subgrade. Particularly, in Step 4 with a total amplitude of 160 kN, the settlement of the sleeper became significantly larger than Step 3.

Figure 11 shows the relationship between sleeper displacement and applied load on the sleeper. In the case with stiff subgrade, in the load up to 160 kN, displacement of the sleeper became larger approximately linearly with the increase of applied load. On the other hand, in the case with soft subgrade, displacement of the sleeper became non-linearly larger by the increase of applied load. In both subgrades, the displacement of the sleeper became larger in the case with a wooden sleeper than in the case with a concrete sleeper.
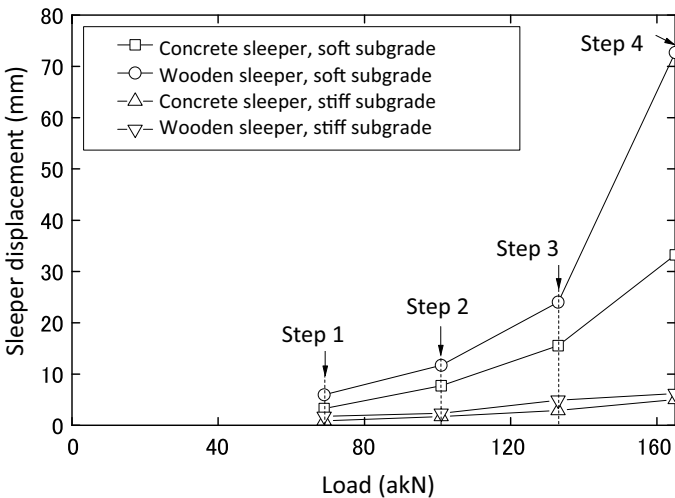
Fig. 11 Relationship between sleeper displacement and applied load
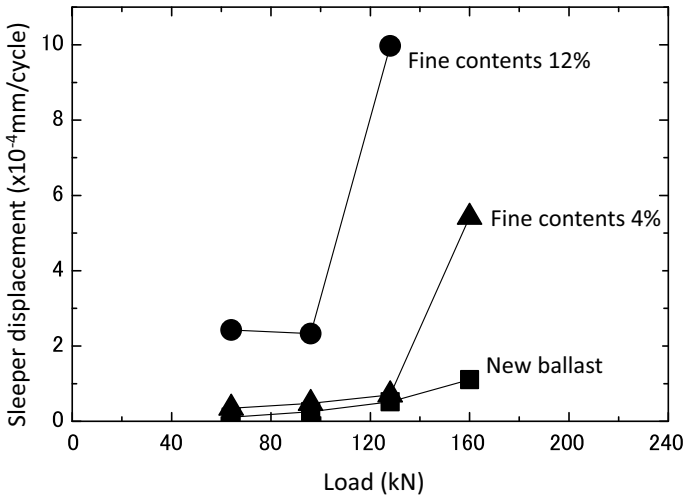
Fig. 12 Effect of fine contents in ballast on sleeper displacement

Figure 12 shows the increment of displacement of the sleeper after the initial deformation in the case with the soft subgrade. In the case with fine content (small particle under 0.075 mm) of 4%, displacement of the sleeper became significantly large under 165 kN loading. In the case with fine content of 12%, the displacement of the sleeper was already very large under 69 and 96 kN, the displacement became catastrophically large under 128 kN loading. The test result showed that a large ratio of fine contents significantly increases the displacement of sleepers under repeated loading.

Here, 1×10^{-4} mm displacement per cycle means 10 mm displacement by 100 thousand cycles. In the case with an axle load of 160 kN, 100 thousand cycles correspond to an annual tonnage of 1.6 million tons per year. That is to say 20 mm displacement with 3.2 million tons per year. In the local railway lines in Japan, 3–4 million tons are general annual tonnage. For the local railway line as such, around 1×10^{-4} mm displacement per cycle seems to be an appropriate threshold value.

Based on the FEM analysis and field measurement, with the sleeper spacing of 1041 mm, the load distribution ratio was approximately 0.6 and the sleeper load is around 100 kN under axle load of 160 kN. Under this condition, the sleeper displacement becomes smaller than 1×10^{-4} mm with new ballast and ballast with fine contents of 4%. Therefore, it is considered that the sleeper spacing of 1041 mm is practically acceptable.

5   Conclusion

In this paper, the settlement of sleepers in ballasted tracks with large sleeper spacings was discussed based on FEM analysis, field measurement, and full-scale cyclic loading tests. The results indicated that a sleeper spacing of 1041 mm is practically acceptable for local railway lines with low annual tonnage.

References

1. Indraratna B, Nimbalkar S, Ngo N, Neville T (2016) Performance improvement of rail track substructure using artificial inclusions—experimental and numerical studies. Transp Geotech 8:69–85
2. Jing H, Bian X, Jiang J (2016) Critical velocity of high-speed train running on soft soil and induced dynamic soil response. In: Advances in transportation geotechnics 3. The 3rd international conference on transportation geotechnics
3. Paixão A, Varandas J, Fortunato E, Calçada R (2016) Non-linear behaviour of geomaterials in railway tracks under different loading conditions. In: Advances in transportation geotechnics 3. The 3rd international conference on transportation geotechnics
4. Abadi T, Le Pen L, Zervos A, Powrie W (2016) A review and evaluation of ballast settlement models using results from the Southampton Railway Testing Facility (SRTF). In: Advances in transportation geotechnics 3. The 3rd international conference on transportation geotechnics
5. Momoya Y, Ito K, Nakamura T (2014) Reuse of degraded ballast to roadbed improvement. In: Proceedings of the second international conference on railway technology: research, development and maintenance
6. Momoya Y, Tanigawa H, Nakamura T, Ito K (2018) Development of FWD system to measure the stiffness of railway track. In: Railways 2018 (the fourth international conference on railway technology)

Dynamic Response of Subgrade in a Bridge Transition Along the Qinshen High-Speed Rail

Tengfei Wang , Qiang Luo, Liang Zhang, and Jun Yao

Abstract Transition zones spanning between the bridge and open track require special attention for the safe operation of high-speed trains. To evaluate the service-ability of transportation substructure, an extensive dynamic monitoring program was undertaken on railway bridge transition of the Qinhuangdao–Shenyang Passenger-dedicated Line (Qinshen PDL) to assess the dynamic properties of subgrade under train moving loads. Accelerations, displacements, and dynamic stresses of the subgrade in response to trains' passage were measured through geotechnical instrumentation. Following this, the field measurements were statistically analyzed and interpreted. The attenuation of dynamic stress along the depth below the ballasted track was presented and fitted by an empirical formula. The dynamic amplification coefficient of soil stress was obtained using the induced soil stress at train speed of 5 km/h as a reference value. Dynamic stress, displacement, and acceleration were examined with respect to their spatial distributions. The measurements of track levels were also adopted for revealing the mechanism. Given that design codes of rail track substructures gradually evolve from empirical design to mechanical–empirical design, an in-depth and comprehensive understanding of the dynamic response of subgrade soil under moving train loads can provide a reference for infrastructure serviceability assessment.

Keywords Transition zone · Field monitoring · Dynamic response · Subgrade

T. Wang · Q. Luo (✉) · L. Zhang
MOE Key Laboratory of High-Speed Railway Engineering, Southwest Jiaotong University, Chengdu 610031, P.R. China
e-mail: lqrock@swjtu.edu.cn

School of Civil Engineering, Southwest Jiaotong University, Chengdu 610031, P.R. China

J. Yao
DMY Engineering Consultants, Inc., 217 Perry Pkwy, Suite 12, Gaithersburg, MD 20877, USA

1   Introduction

Transition zones are generally used for reducing the abrupt changes in substructure stiffness that frequently occurs between a railway track underlain by earth structure and the track over support having a high stiffness, such as tunnel, bridge, and culvert. A significant difference in support stiffness results in increased dynamic wheel loads and accelerated rate of track geometry degradation. The dynamic issues associated with transition zones are generally recognized and have received detailed investigations. An extensive monitoring program was undertaken to reveal the fundamental causes of poor performance of a railway transition zone [1]. For the design of a transition zone, it is necessary to investigate the local geotechnical conditions, identify where movements are likely to arise, and understand the conceptual basis on which substructure in transition zone will operate. A comprehensive field test [2] has been conducted on a heavy-haul railway line to explore the dynamic response of subgrade in a transition zone. The findings indicate that two bogies from adjacent wagons should be treated as one loading unit for design. Palese et al. [3] tried to interpret the variation of dynamic stress collected from pressure transducers placed in transition subgrade based on track geometry measurements, which improves our understanding regarding the role of substructure quality on track geometry degradation. Bian et al. [4] reviewed the recent research advances in geodynamics of high-speed rail subgrade, including dynamic stress distribution within soil and dynamic amplification with increasing train speed. Field observations were carried out by Li et al. [5] to collect the embankment vibrations under passages of heavy-haul train, suggesting that different suspension modes would contribute to a higher vibration level for locomotive than a wagon.

More attention has recently been paid to the slab track dynamic in transition zones through field testing or numerical modeling, e.g., [6–11]. In contrast, in-depth insights into the behavior of transition subgrade under passage of trains are minimal. Been added to the China railway network in 2003, the Qinhuangdao–Shenyang Passenger-dedicated Line (i.e., Qinshen PDL) is the first newly built high-speed rail (top speed of 250 km/h) in China. Given the insufficient investigations on subgrade dynamics at bridge approach, field monitoring was conducted at a bridge transition of Shahe Grand Bridge (Fig. 1) within a trial section (specially designed for localized higher speed, 350 km/h), in order to assess the dynamic response of subgrade under trial train operation.

2   Monitoring Program

The instrumentation site for monitoring program was chosen on a bridge-subgrade transition, and a detailed description is provided in Fig. 2. The inverted trapezoid transition (slope gradient = 1:2) comprises geogrid-reinforced soil (0.3 m in thickness for

Fig. 1 Overview of the bridge-subgrade transition zone (DK 43+578)
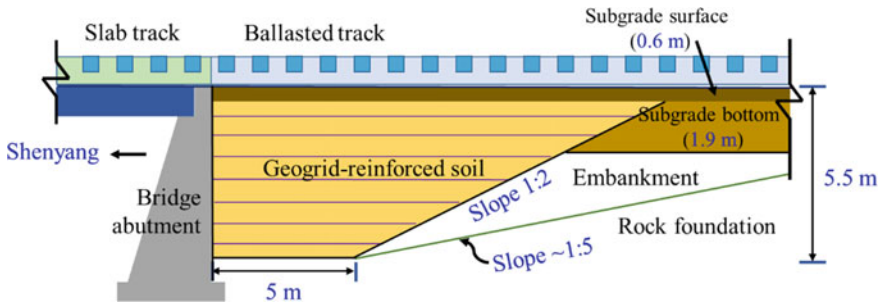
Fig. 2 Schematic of the studied railway earthworks at bridge approach of Shahe Grand Bridge

each layer, 25 kN/m for geosynthetics) of 16 m in length and 5.5 m in height, consistent with Chinese design code for high-speed railway (TB 10001-2016). The open track, away from the bridge approach, is on a 5.5 m high earth structure (subgrade and embankment) underlain by inclined rock foundation. The subgrade surface was constructed using well-graded gravels, while the subgrade bottom primarily consists of Class-A fill. The granular layer thickness in ballasted track was 35 cm.

As specified in Fig. 3, measurements of dynamic stress, acceleration, and vertical displacement were made during trial train operations, using earth pressure cells (range: 100 kPa; accuracy: ±0.1% F.S.; vibrating wire), accelerometers (range: 2 g; accuracy: 0.02 g), and displacement transducers (range: ±2 mm; linearity: ±0.2% F.S.). Earth pressure cells were mounted beneath both the left and right rails; all the displacement transducers and accelerometers were located beneath the left rail. Please also note that earth pressure cells have been placed at three depths during earth structure construction, while all the accelerometers and displacement transducers were mounted on the surface of subgrade. The subgrade dynamic responses
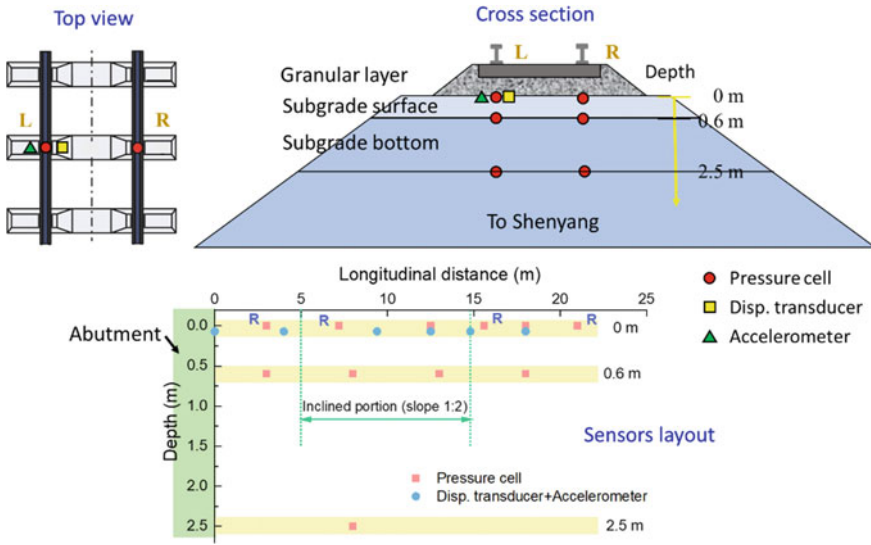
Fig. 3 Instrument configuration for field monitoring. Displacement transducer and accelerometer were all mounted beneath the left rail; all the pressure cells were mounted beneath left and right rails, except for four marked "R" that were only below right rail

to train operation were collected over one week, incorporating 29 passages. Table 1 summarizes the train's geometric and mass specifications, revealing that 12 bogies and 24 axles were considered. The total combined wagon length is 158.4 m.

Before field testing commenced, a geotechnical site investigation was performed to evaluate the quality of field compaction within the transition zone. The filed unit weight for the soil after compaction was determined by the sand cone method. Porosity and K_{30} value (i.e., modulus of subgrade reaction = reaction pressure sustained by the soil sample under a rigid plate of 300 mm in diameter per unit settlement measured at 1.25 mm settlement) have been used for the site assessment. Statistical results in Table 2 demonstrate that the upper 95% confidence interval for porosity is 17.37% (<20%) and the lower 95% confidence interval for K_{30} is 168.2 MPa/m, satisfying the standard requirements (150 MPa/m).

Table 1 Geometric and mass characteristics of the high-speed train

	No. of wagons	No. of axles	Inter-bogie spacing (m)	Inter-axle spacing (m)	Total axle spacing (m)*	Average weight per axle (kg)
Locomotive	4	4	18	2.5	152	13,090
Wagon	2	4	18	2.5		

Note It denotes the spacing between the foremost and end axles

Table 2 Summary statistics for field compaction evaluation

	Sample size	Max	Min	Mean	Std. Dev	C.V
γ (kN/m^3)	62	22.89	21.10	22.25	0.402	0.018
M.C. (%)	62	9.40	3.60	6.48	1.535	0.237
γ_d (kN/m^3)	62	21.23	20.48	20.91	0.133	0.006
n (%)	62	18.80	16.00	17.26	0.496	0.029
K_{30}(MPa/m)	14	210.0	148.8	174.9	14.26	0.081

Note Std. Dev. = standard deviation, C.V. = coefficient of variation, γ = unit weight, M.C. = moisture content, γ_d = dry unit weight, n = porosity, K_{30} = modulus of subgrade reaction

3 Data Processing and Analysis

Track geometry data was collected and evaluated at eleven fixed points, with a longitudinal distance of −9.6, −4.8, 0.0, 4.8, 9.6, 14.4, 19.2, 24.0, 28.8, 33.6, and 38.4 m from the bridge abutment (negative value denotes a position on the bridge). Figure 4 reports the effect of length interval on the assessment of track geometry, and its determination, where track level difference serves as an indirect assessment of the differential settlement of substructure experienced in transition zones. It appears that maximum difference occurs for a point at 19.2 m of longitudinal direction, for both predefined lengths. The overall track level difference first increases then decreases with the distance from the abutment.

The raw data was processed to extract the peak dynamic stresses, peak vertical displacements, and peak accelerations to provide desired values for correlation and
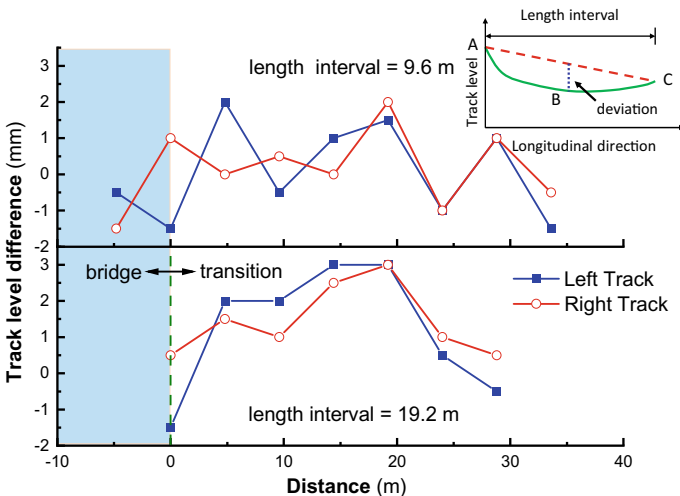
Fig. 4 Plots of track geometry versus longitudinal distance during level surveys using two lengths. Track levels are identified for points A, B, and C, from which the difference is calculated

Fig. 5 Measured dynamic soil stress attenuation along with the depth
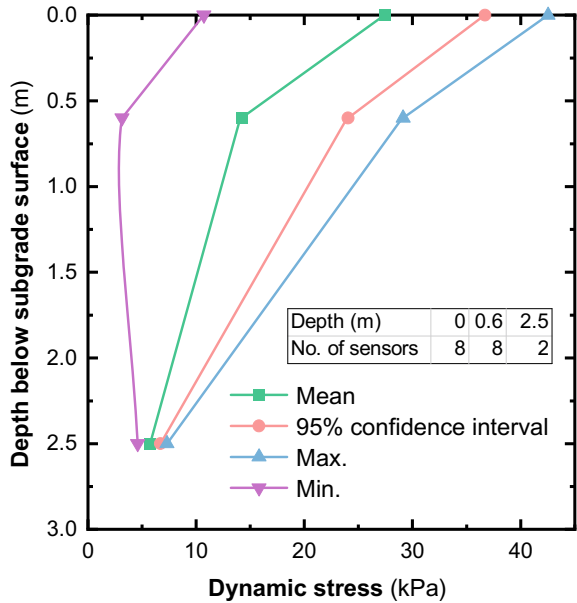
further analyses. As shown in Fig. 5, the dynamic soil stress dissipates rapidly with the depth, e.g., 50% off as depth increases to 0.6 m from surface, which can be normalized by an attenuation coefficient to explore the general attenuation law. The train-induced dynamic stress of subgrade is not intense due to the axle loads applied.

The train-induced dynamic stress at the top of subgrade is used as a reference value. Then, the attenuation coefficient (η) is defined as a ratio of dynamic stress at a certain depth to the reference value. Figure 6 demonstrates the variation of attenuation coefficient with depth for the measured ballasted track. At a depth of 2.5 m below subgrade surface, corresponding to the bottom of subgrade, the dynamic stress is observed to dissipate 80% off, compared with the reference value. Based on dynamic soil stress profile, an empirical formula is proposed to characterize the attenuation law of dynamic stress with depth as follows:

$$\eta = 1 - \frac{z}{a + b \cdot z} \tag{1}$$

where η denotes the normalized attenuation coefficient; z refers to the depth beneath the top of subgrade; a and b represent fit coefficients. In this case, the envelope can be fitted by Eq. (1) with $a = 0.64$ and $b = 1.01$.

Besides the dynamic stress attenuation law with depth, the dynamic stress intensity on the top of subgrade is also a major factor for the design of railway subgrade. For most scenarios, the dynamic stress distribution on ballasted track is less uniform than that in slab track [4]. The field monitoring and model tests suggest that the dynamic surface stress ranges 50–100 kPa for the ballasted track, while just 13–20 kPa for

Fig. 6 Attenuation coefficient of dynamic stress (η) in soil

$$\eta = 1 - z/(0.64 + 1.01 \cdot z)$$
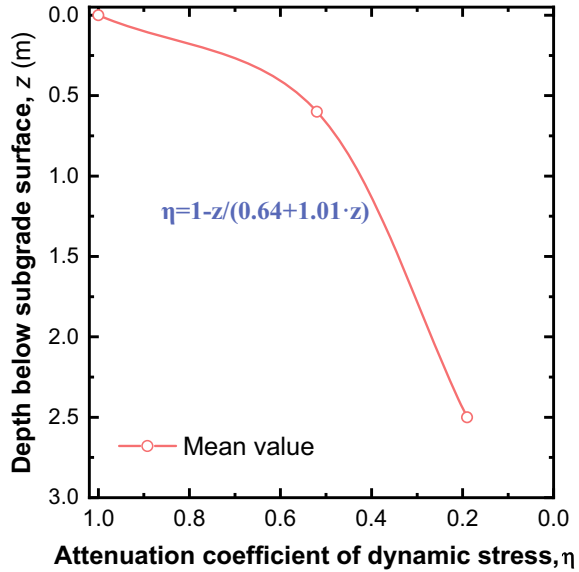
ballastless track. An empirical formula is proposed to identify the maximum dynamic stress at the top of subgrade with granular layer thickness of 35 cm, σ_{dl}, as follows [4]:

$$\sigma_{dl} = 0.26 \times P \times (1 + \alpha v) \tag{2}$$

where P denotes the static axle load of vehicle (kN); $(1 + \alpha v)$ represents an impact coefficient associated with train speed, and $\alpha = 0.003$ (km/h)$^{-1}$ for target speed of $300 \sim 350$ km/h, and $(1 + \alpha v) \leq 1.9$ when the speed is larger than 300 km/h.

In this study, we primarily investigated the mean values of induced soil stress, displacement, and acceleration. Figure 7 reveals the changes in average dynamic soil stress with different train speeds. An average of the dynamic stress is 24.74, 16.77, and 5.87 kPa for the depth of 0, 0.6, and 2.5 m. By introducing the reference value at train speed of 5 km/h to Eq. (2), the calculation produces that $\alpha = -0.00011$ at the top of subgrade, $\alpha = 0.00067$ at 0.6 m in depth, and $\alpha = 0.00057$ at 2.5 m in depth. What interests us most is that the dynamic soil stress at the surface even decreases under high-speed conditions, indicating that there was no statistically clear link between the mean values and the train speeds. Also, the stress fluctuation is predictably less significant as the depth increases.

The dynamic soil stress is plotted against longitudinal distance in Fig. 8 for a train traveling at a velocity of 250 km/h. It suggests that the dynamic stress is the lowest adjacent to the bridge abutment and gradually rises with an increase in the longitudinal direction. Unlike other common trends reported in the literature, the relatively low structure stiffness is deemed responsible for such a dynamic stress response under train operation in this study.
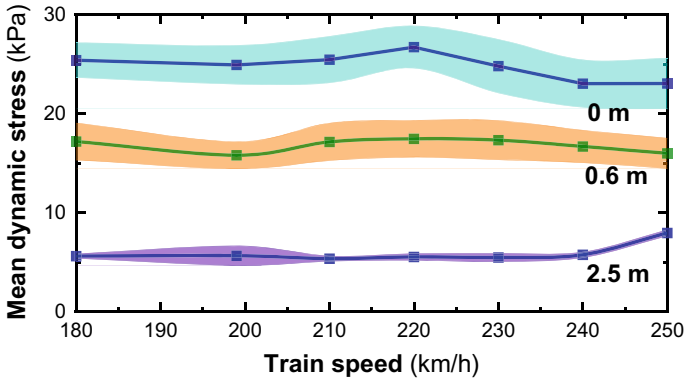
Fig. 7 Variation of dynamic soil stress with train speed at different depths. Right track, 8 m away from the bridge abutment; each filled area represents corresponding error bar

Fig. 8 Plots of measured dynamic stress versus distance from the bridge abutment at a train speed of 250 km/h. Colored area marks error bar
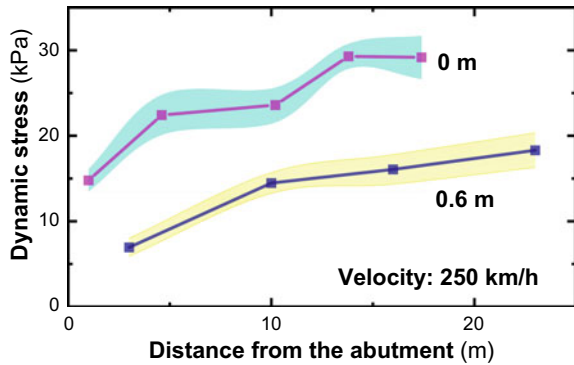
The average vertical displacements (both upward and downward displacements were considered) were obtained and plotted against various train speeds for three locations, as shown in Fig. 9. From the data for the displacement transducers at different depths, two major observations can be made. First, the effect of train speed on the mean vertical displacement is not significant for soil located at the abutment. In contrast, displacement amplitudes at 9.4 and 14.8 m in the longitudinal direction fluctuate considerably with velocities. Second, the surface soil near the abutment produces the smallest vertical displacement. In general, the train speed has a great influence on the maximum values as reported by other researchers, while this effect is statistically minimal for mean values.

As illustrated in Fig. 10, soil at the top of subgrade varied in a similar manner with distance from abutment under two velocities, including three distinct segments (0 ~ 9.4 m; 9.4 ~ 12.4 m; 12.4 ~ 17.8 m). In general, the average vertical displacement yields approximately 0.35 mm (peak) at 9.4 m longitudinally and reaches 0.1 mm (minimum) at the abutment. It is likely that the data collected at 9.4 m is abnormal
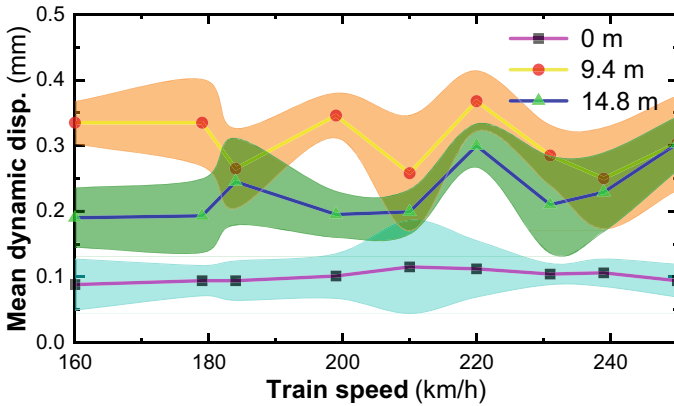
Fig. 9 Mean vertical displacement at subgrade surface varying with train speed. 0, 9.4, and 14.8 m refer to the distance from bridge abutment; colored area marks error bar

Fig. 10 Mean vertical displacement at subgrade surface varying with distance from abutment under two train speeds. Colored area marks error bar
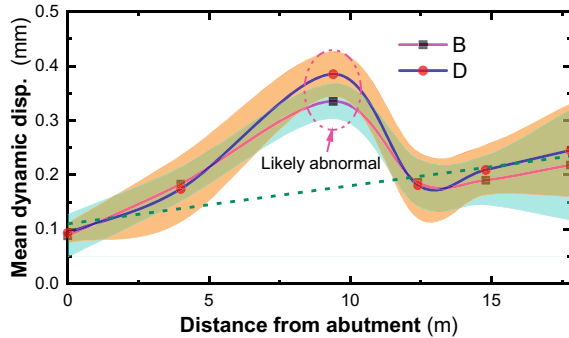
due to sensor issues. The rest data points showed a general increasing trend with distance.

High variability can be observed in the measured mean acceleration on the top of subgrade as shown in Fig. 11. Similar to the results of vertical displacement, acceleration at 9.4 m longitudinally yields the largest value, while the least at the abutment. A positive correlation between the mean acceleration and train speed can be obtained for different locations along the railway lines. Under a high traveling speed (e.g., > 230 km/h), accelerations collected from different locations trend toward a constant, approximately 5 m/s^2.

The variation of acceleration of subgrade surface with longitudinal distance was demonstrated in Fig. 12. Most locations produced similar values at a certain speed, except for the surface acceleration at 12.4 m longitudinally. It can be inferred from Fig. 2 that an abrupt change occurs because of the discontinuous transition structure, which should be carefully dealt with during routine maintenance. Nevertheless, the dynamic stress (<100 kPa), vertical displacement (<1 mm), and acceleration
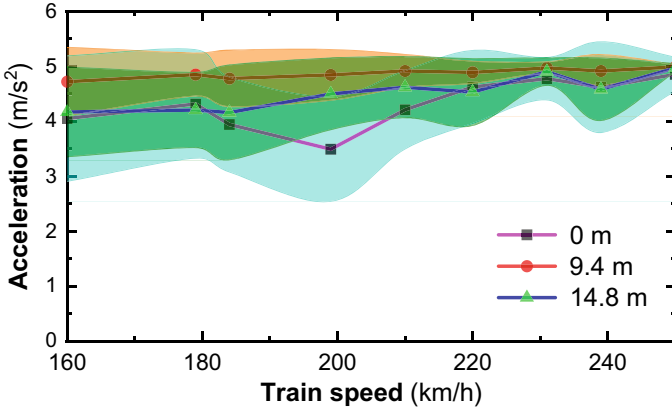
Fig. 11 Plots of train-induced acceleration at subgrade surface against train speed for different distances away from the abutment. Colored area marks error bar
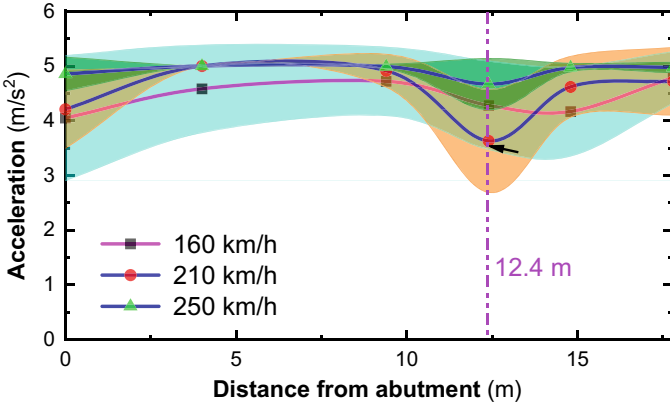
Fig. 12 Train-induced acceleration at subgrade surface varying with distance from abutment under train speeds of 160, 210, and 250 km/h. Colored area marks error bar

(<10 m/s^2) yield satisfactory values, indicating that the standard design for earth structure at bridge approach is reasonable.

The implication of statistical analyses on the train-induced dynamic stress, vertical displacement, and acceleration for simulating dynamic behavior of subgrade in a transition zone is summarized as follows. In numerical modeling, probability-based random events (e.g., dynamic stress) are applied to subgrade to assess its dynamic response. The performance of constructed transition zones should be assessed against the specification requirements, providing reference for other scenarios involving transition zone design. Nevertheless, it requires extensive investigations to achieve this goal in future.

4 Conclusions

Field monitoring was carried out at a bridge transition of high-speed rail to explore the dynamic response of track substructure. Analysis and interpretation of the instrumentation data reveal the following:

1. The collected data from measurements suggests the dynamic response of subgrade did not exceed expectations, with upper 99% confidence intervals of 40.54 kPa, 0.13 mm, 13.55 m/s^2 for dynamic soil stress, peak vertical displacement, acceleration at the top of subgrade, respectively. In general, the current design of transition zone proves to be rational.
2. The dynamic soil stress dissipates rapidly in depth, and the dynamic attenuation coefficient (η) has a value of approximately 0.2 at a depth of 2.5 m (i.e., the bottom of subgrade).
3. In this case, the profound effect of train speed on accelerations was evidenced, while train speed has limited influence on the mean values of dynamics stress and displacement.
4. The variation patterns of dynamic stress, displacement, and acceleration in the longitudinal direction are similar under different train speeds.

References

1. Coelho B, Hölscher P, Priest J et al (2011) An assessment of transition zone performance. Proc Inst Mech Eng Part F J Rail Rapid Transit 225:129–139. https://doi.org/10.1177/09544097J RRT389
2. Mei H, Leng W, Nie R et al (2019) Experimental research on the dynamic response characteristics of the transition subgrade induced by heavy-haul train passage. Proc Inst Mech Eng Part F J Rail Rapid Transit 233:974–987. https://doi.org/10.1177/0954409718822924
3. Palese JW, Zarembski AM, Hartsough CM et al (2017) A study on subgrade pressure differential over regions of known substructure transition as it relates to track geometry. In: Joint rail conference. ASME, pp 1–10
4. Bian X, Li W, Hu J et al (2018) Geodynamics of high-speed railway. Transp Geotech 17:69–76. https://doi.org/10.1016/j.trgeo.2018.09.007
5. Li P, Ling X, Zhang F et al (2017) Field testing and analysis of embankment vibrations induced by heavy haul trains. Shock Vib 2017. https://doi.org/10.1155/2017/7410836
6. Li D, Davis D (2005) Transition of railroad bridge approaches. J Geotech Geoenviron Eng 131:1392–1398. https://doi.org/10.1061/(ASCE)1090-0241(2005)131:11(1392)
7. Shan Y, Albers B, Savidis SA (2013) Influence of different transition zones on the dynamic response of track-subgrade systems. Comput Geotech 48:21–28. https://doi.org/10.1016/j.com pgeo.2012.09.006

8. Shan Y, Shu Y, Zhou S (2017) Finite-infinite element coupled analysis on the influence of material parameters on the dynamic properties of transition zones. Constr Build Mater 148:548–558. https://doi.org/10.1016/j.conbuildmat.2017.05.071

9. Hu P, Zhang C, Wen S, Wang Y (2019) Dynamic responses of high-speed railway transition zone with various subgrade fillings. Comput Geotech 108:17–26. https://doi.org/10.1016/j.compgeo.2018.12.011

10. Stark TD, Wilk ST, Rose JG (2016) Design and performance of well-performing railway transitions. Transp Res Rec 2545:20–26. https://doi.org/10.3141/2545-03

11. Mishra D, Qian Y, Huang H, Tutumluer E (2014) An integrated approach to dynamic analysis of railroad track transitions behavior. Transp Geotech 1:188–200. https://doi.org/10.1016/j.trgeo.2014.07.001

An Alternative Approach to Track Settlement Prediction

G. Ognibene, L. Le Pen, J. Harkness, A. Zervos, and W. Powrie

Abstract Many empirical equations have been formulated in an attempt to model the settlement of ballasted railway track at an individual sleeper. Some equations have been used with vehicle track interaction models (VTI) to predict the development of differential settlement along the track iteratively and hence maintenance requirements, over potentially millions of cycles of load. For settlement equations to be suitable in such simulations, they require as an input a VTI model output that varies along the track, such as the force on the sleeper or the current resilient deflection range. For computational economy, these VTI simulations are usually run in large steps with the settlement predicted forward over many cycles. There is, however, no one generally applicable settlement equation, and it remains unclear whether the loss of accuracy that ensues from stepping the VTI analyses is acceptable. A realistic settlement equation needs to incorporate both stress- and load history-dependent behaviour. This paper proposes a new settlement model that allows for stress history and has the potential to be applied at every cycle within an iterative VTI simulation. The ballast layer is modelled by combining a nonlinear visco-elastic element to simulate the resilient response with a plastic-hardening element for permanent settlement. This leads to the calculation of permanent settlement without recourse to an explicit empirical equation. The parameters used in the model are determined using data from cyclic laboratory tests on a single sleeper. The effect of different loading histories on the model is considered.

Keywords Ballast · Ballast settlement · Settlement equations · Cyclic plastic model · Densification · Lateral spreading · VTI · Trackbed · Railway track

G. Ognibene (✉) · L. Le Pen · J. Harkness · A. Zervos · W. Powrie
Infrastructure Research Group, University of Southampton, Boldrewood Innovation Campus, Southampton, Hampshire SO16 7QF, UK
e-mail: G.Ognibene@soton.ac.uk

1 Ballast Settlement

Ballast settlement may occur as a result of a number of mechanisms, viz. densification or compaction, lateral spreading, ballast degradation, ballast foundation interpenetration, and fouling [1–3]. Ballast foundation interpenetration and fouling may be considered as secondary, as they depend on external factors and are more easily preventable by good design and operation.

Ballast settlement due to repeated loading is commonly characterized by two (Fig. 1) or possibly three phases [1, 4]. In each phase, different mechanisms of settlement dominate. When a railway track is new or freshly tamped, the initially relatively loose ballast settles rapidly under train passage as grains rearrange and reorient to form a denser and more compact structure. This process is characterized by a reduction in void ratio. Some authors suggest that during this stage, ballast degradation (i.e. particle breakage and abrasion) also occurs. However, such degradation is likely to be significant only for weak rock materials [3] or when the ballast is subjected to abnormally high impact forces (e.g. below a hanging sleeper).

Once the ballast has achieved a denser, stable state, further settlement is probably largely a result of lateral spreading. Some authors have proposed a third stage of settlement [5], dominated by ballast grain degradation, but it is not clear how significant this is for strong, high-quality ballasts under normal loading conditions.

The relative importance of the various mechanisms of settlement and their associated stages depends on the characteristics of the individual grains, the bulk properties of the granular assembly, the stress state, and the loading conditions at a particular site [6]. The evolution of settlement with an increasing number of load cycles varies with the amplitude and possibly frequency of the applied loads [7].

A clear distinction between the two primary phases of settlement is difficult to identify in practical tests. Some authors [1, 8] have suggested that the cross-over between the two primary phases could be identified as the second inflection point on a graph of settlement against the logarithm of the number of cycles of a uniform load, as shown in Fig. 2.
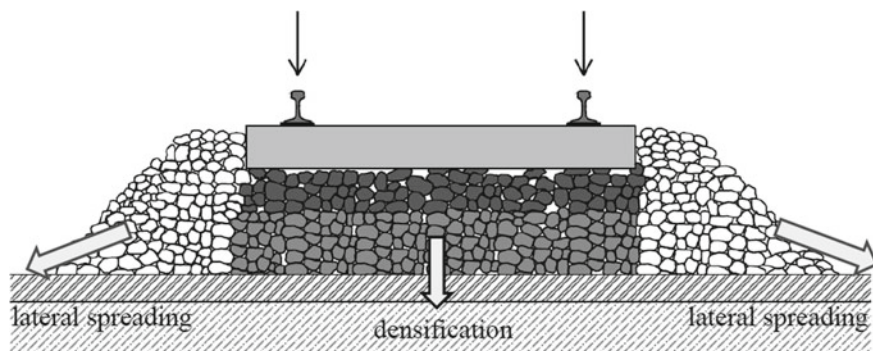
Fig. 1 Two main settlement stages of railway ballast: densification and lateral spreading
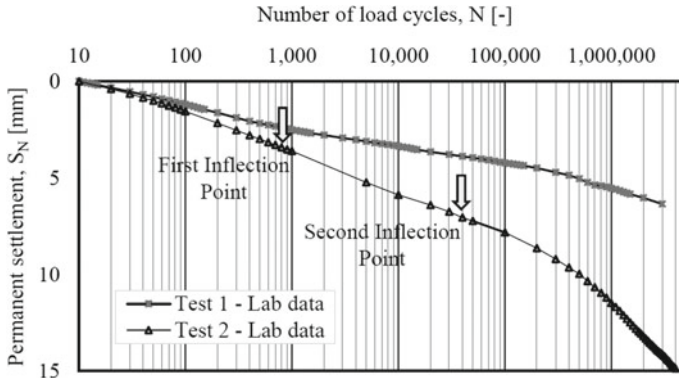
Fig. 2 Ballast permanent settlement after ten cycles against the logarithm of the number of load cycles: data for the two tests considered in this study [8]

However, most equations that have been proposed to predict settlement do not reproduce such inflection points. Many are log-linear (e.g. [9, 10]) or exponential (e.g. [7, 11]) relationships between accumulated settlement, S_N, and the number of loading cycles, N, for a uniform load. They are essentially curve fits and are only even approximately correct for the conditions under which they have been derived.

Some equations are more complex with terms that dominate in either the short or longer term, for example, Eqs. (1) [7] and (2) [12]:

$$S_N = \alpha\left[1 - \exp(-\beta N)\right] + \gamma N \tag{1}$$

$$S_N = S_\infty \left[1 - \frac{1}{1 + \alpha \log\left(1 + \frac{N}{N_0}\right)}\right] \tag{2}$$

These equations, or variations thereof, show greater potential for matching observed settlement curves and their inflexion points. However, most existing settlement equations, including those with multiple terms, are not suited for predicting track geometry deterioration in iterative VTI simulations because their only input is the number of loading cycles, which would lead to a uniform settlement along the length of the track.

There are some equations whose input variables include the stress [13, 14] or the current deflection range [4], which can be applied in iterative VTI simulations. However, these equations have yet to be validated. This paper proposes a new settlement model, which takes as an input the stress at a given location and can be applied implicitly within a VTI simulation.

Table 1 Ballast materials used in the settlement tests

	Test 1	Test 2
Rock	Granite	Gabbro
$G_s \, [\text{Mg/m}^3]$	2.66	2.96
D_{50} [mm]	41	38
$C_u = D_{60}/D_{10}$	1.40	1.60
$C_c = D_{30}^2/(D_{30} D_{60})$	1.0	0.9
F [kN]	5–98	5–157
Quarry	Mountsorrel (U.K.)	Saif Bin Darwish (U.A.E.)

2 Southampton Railway Testing Facility

Results from tests in the Southampton Railway Testing Facility (SRTF) are used for calibration of the model. The SRTF consists of a sleeper placed on top of a 300 mm layer of ballast underlain by a 12 mm neoprene rubber mat, which replicates the support provided by the soil (for full details, see [15]). A vertical load is applied by a hydraulic actuator, via a steel beam, to two short sections of rail installed on the sleeper. The load is applied as a sinusoidal force, which oscillates between a minimum value of $F_{\min}$ and a maximum of $F_{\max}$ at a frequency of 3 Hz.

Results from two tests (summarized in Table 1) are considered in this paper, selected because they show the influence of a change in load. Results from measurement locations along the sleeper were combined to give the average permanent settlement with the number of load cycles shown in Fig. 2.

3 Proposed Settlement Model

3.1 Overview

The model comprises three masses m_r, m_s, and m_b, representing the rail, sleeper, and ballast, respectively (Fig. 3). The railpad, which connects the rail with the sleeper, is characterized by a linear Kelvin–Voigt unit having stiffness k_{rp} and damping c_{rp}. The ballast layer is simulated using a bespoke cyclic visco-elastic-plastic unit, described later. The rubber mats, which represent the support provided by the foundation layer, are characterized by a linear Kelvin–Voigt model having stiffness k_f and damping c_f. A harmonic force, $F(t)$, is applied on the top of the rail to simulate cyclic wheel loads. An implicit nonlinear Newmark algorithm is used to solve the resulting system of nonlinear equations.

Fig. 3 Single sleeper system model
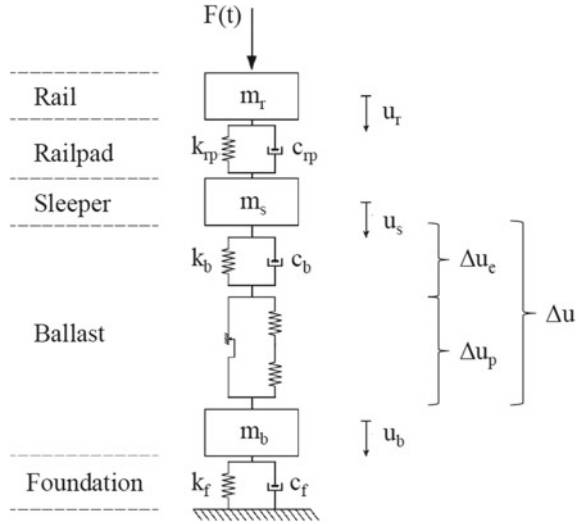
The bespoke unit representing the ballast layer (Fig. 3) comprises a linear Kelvin–Voigt unit in series with a plastic-hardening unit. The Kelvin–Voigt unit consists of a spring of stiffness k_b in parallel with a dashpot of damping c_b. The plastic-hardening unit consists of a slider in parallel with two hardening springs, with the frictional element defined by a threshold force F_y and the springs by stiffnesses H_d and H_s. These units reproduce both the resilient and plastic deformation of the ballast. The governing equations of the model are given in Sect. 3.2. In Sect. 3.3, the user-defined functions that quantify behaviour are explained, and possible physical descriptions and justifications are given.

3.2 Governing Differential Equation

The total deformation Δu is given by the sum of the resilient (elastic) deformation Δu_e and irreversible (plastic) deformation Δu_p:

$$\Delta u = \Delta u_e + \Delta u_p \tag{3}$$

Plastic deformation will develop only when the slider is activated, that is, when the force applied to the ballast layer F_b exceeds the threshold force F_y, and only during loading (i.e. not during unloading), defined as $\dot{u}_b > 0$:

$$F_b - F_y = \begin{cases} F_b - F_y & \text{for } F_b > F_y \text{ and } \dot{u}_b > 0 \\ 0 & \text{for } F_b \leq F_y \text{ or } \dot{u}_b \leq 0 \end{cases} \tag{4}$$

Thus, if the total force F_b applied to the ballast layer is less than the yield force F_y, the unit is equivalent to Kelvin–Voigt and gives visco-elastic behaviour. The total force F_b is given by the sum of the force acting on the spring (characterized by k_b) and the dashpot (c_b):

$$F_b = k_b \Delta u_e + c_b \Delta \dot{u}_e \tag{5}$$

Because in this case the total deformation Δu corresponds to the resilient deformation Δu_e, the differential equation governing the force–deformation relationship of the model is

$$\Delta \dot{u} + \frac{k_b}{c_b} \Delta u = \frac{F_b}{c_b} \tag{6}$$

If the total force F_b applied to the ballast layer is greater than the yield force F_y, the slider will cause some irreversible deformation, Δu_p, within the ballast layer, proportional to the excess applied force $(F_b - F_y)$ and the hardening parameter H:

$$\Delta u_p = \frac{F_b - F_y}{H} \tag{7}$$

where the total hardening spring stiffness H is given by

$$H = \left(\frac{1}{H_d} + \frac{1}{H_s} \right)^{-1} \tag{8}$$

Because the Kelvin–Voigt and the hardening plastic units are in series, both experience the total force F_b being applied to the ballast layer, which is equal to the sum of the forces passing through each of the constituent in-parallel elements:

$$F_b = k_b \Delta u_e + c_b \Delta \dot{u}_e = H \Delta u_p + F_y \tag{9}$$

The governing equation is obtained by differentiating Eq. (3) and substituting $\Delta \dot{u}_e$ and $\Delta \dot{u}_p$. The elastic deformation rate $\Delta \dot{u}_e$ is obtained by combining Eqs. (3), (7), and (9) and $\Delta \dot{u}_p$ from differentiating Eq. (7):

$$\Delta \dot{u}_e = \frac{F_b}{c_b} - \frac{k_b}{c_b} \left(\Delta u - \frac{F_b - F_y}{H} \right) \quad \Delta \dot{u}_p = \frac{\dot{F}_b}{H} \tag{10}$$

The governing differential equation then becomes

$$\Delta \dot{u} + \frac{k_b}{c_b} \Delta u = \left(1 + \frac{k_b}{H} \right) \frac{F_b}{c_b} + \frac{\dot{F}_b}{H} - \frac{k_b}{H} \frac{F_y}{c_b} \tag{11}$$

In a time stepping analysis, the force applied to the ballast layer, $F_b^{N,k+1}$, at a time step $k + 1$ and at a load cycle, N, can be computed using the backward Euler method as

$$F_b^{N,k+1} = \alpha F_b^{N,k} + \alpha \Delta t \left\{ H^N \Delta \dot{u}^{N,k+1} + \frac{k_b}{c_b} H^N \Delta u^{*N,k+1} + \frac{k_b}{c_b} F_y^N \right\} \qquad (12)$$

In Eq. (12), the accumulated settlement developed up to the previous load cycle, S_{N-1}, is subtracted from the total deformation, $\Delta u^{N,k+1}$, to obtain the in-cycle deformation, $\Delta u^{*N,k+1}$:

$$\Delta u^{*N,k+1} = \Delta u^{N,k+1} - S_{N-1} \qquad (13)$$

where α is defined as

$$\alpha = \frac{c_b}{c_b + \Delta t \left(k_b + H^N \right)} \qquad (14)$$

The plastic strain accumulated within the ballast layer from the beginning of load step N, up to time step $k + 1$, is given by

$$\Delta u_p^{N,k+1} = \Delta u_p^{N,k} + \left(\frac{F_b^{N,k+1} - F_b^{N,k}}{H^N} \right) \quad \text{with } \Delta u_p^{N,1} = 0 \qquad (15)$$

The accumulated plastic settlement after N loading cycle is

$$S_N = S_0 + \Delta S_N = S_0 + \sum_{i=1}^{N} \Delta u_p^{i,k_{max}} \qquad (16)$$

where S_0 is the settlement after ten cycles measured in the laboratory (see Sect. 4.2), and ΔS_N is the net accumulated plastic settlement computed as the sum of the plastic deformation developed at the end of load cycle i, $\Delta u_p^{i,k_{max}}$.

3.3 Functions

To assign functions and/or coefficients to F_y, H_d, and H_s and ultimately to calculate Δu_p, several assumptions are made on the basis of the laboratory test results (Fig. 2) and the wider literature. These are

- The plastic deformation of the ballast layer, Δu_p, is governed by the force applied to the ballast layer, F. A threshold value of this force, F_y, delineates the change from elastic to plastic behaviour of the ballast layer.

- The yield force, F_y, is always less than the maximum force applied to the ballast layer, F_{max}: the laboratory tests have shown that permanent settlement always develops, even though it may be almost imperceptible per cycle.
- The two hardening parameters, H_d and H_s, control the components of settlement due to densification, Δu_{pd}, and lateral spreading, Δu_{ps}, respectively. The first causes most of the settlement during the initial stage, while the latter governs the longer-term (second stage) behaviour.
- The hardening parameters, H_d and H_s, increase exponentially with accumulated plastic settlement S_N.

At the end of each load cycle N, the plastic parameters F_y^N, H_d^N, and H_s^N are updated depending on the maximum ballast force during that loading cycle, $F_{b,max}^N$, and the accumulated settlement up to that cycle, S_N. The plastic unit is defined by a total of seven parameters (F_{y0}, α_y, S_0, H_d^0, H_s^0, α_d, α_s), which are determined for each laboratory test to reflect the different ballast mechanical and physical properties, loading conditions, etc., and will now be described in detail.

Evolution of the hardening springs

The hardening springs H_d and H_s represent the plastic deformation from densification and lateral spreading, respectively. They have been defined such that initially (for low values of S_N), the combined hardening spring H, defined by Eq. (8), will be equal to H_d and then (for higher values of S_N) to H_s. Both hardening parameters grow exponentially (but at different rates) with the accumulated plastic settlement:

$$H_d^N = H_d^0 \cdot \exp(\alpha_d \cdot rx); \quad H_s^N = H_s^0 \cdot \exp(\alpha_s \cdot rx) \tag{17}$$

where r represents the growth rate, and x defines the time variable. r and x depend on the accumulated plastic settlement S_N and are defined as

$$r = \log\left(\frac{S_N}{S_0}\right) \quad x = \Delta S_N \tag{18}$$

Evolution of the threshold force

The equation defining the evolution of the threshold force F_y^N with respect to the accumulated plastic settlement S_N at the end of each load cycle N is a reformulation of the Chicago density relaxation law [16] and shares similarities with settlement Eq. (2):

$$F_y^N = F_{y0} + \left(F_{b,max}^N - F_{y0}\right)\left[1 - \frac{1}{1 + \alpha_y \cdot \log\left(\frac{S_N}{S_0}\right)}\right] \tag{19}$$

where $F_{b,max}^N$ is the maximum force applied to the ballast during the Nth load cycle. F_{y0} is the initial yield force (at the first load cycle), and a_y is a parameter governing

Table 2 Parameters used in the modelling

Parameter	Value		Unit	Source
	A	B		
Rail mass, m_r	60	60	[kg/m]	UIC60 (or E 60)
Railpad stiffness, k_{rp}	230	230	[MN/m]	Pandrol [20]
Railpad damping, c_{rp}	75	75	[kNs/m]	Pandrol [20]
(Half) sleeper mass, m_s	160	160	[kg]	Mono-block G44
Ballast stiffness, k_b	210	210	[MN/m]	Based on literature [17–19]
Ballast damping, c_b	0.12	2	[MNs/m]	Based on literature [17–19]
(Half) ballast mass, m_b	300	300	[kg]	Based on literature [17–19]
Foundation stiffness, k_f	750	750	[MN/m]	Assumed
Foundation damping, c_f	0.15	2	[MNs/m]	Assumed

the growth rate of the yield force F_y. The model architecture could be adapted to accommodate a different stress threshold function, should this be required.

4 Calibration of the Model

4.1 Resilient Deformation Calibration

The values adopted for the various model parameters, with alternatives denoted *A* and *B* having different levels of material damping, are shown in Table 2. Figure 4a, b compares the average force–deflection relationships measured on the sleeper during Test 1 with those calculated using the model with parameter value sets *A* and *B* in Table 2.

The measured sleeper deflection exhibits stronger damping than calculated using the parameter set *A*, which shows almost perfect elasto-plastic behaviour. The energy losses in the measured data are explained partly by the presence of the rubber mat beneath the tested ballast and partly by the ability of ballast stones to dissipate energy though inter-grain friction. Increasing the damping assigned to both the ballast and the foundation layer (c_b and c_f), using the *B* values of Table 2, results in a better fit to the data (Fig. 4b), although the values used are not consistent with those reported in the literature (e.g. [17–19]).

4.2 Plastic Deformation Calibration

The five plastic parameters of the model (α_y, H_{d0}, H_{s0}, α_d, α_s) were obtained on the basis of giving an adjudged best-fit with the experimental settlement curves (shown
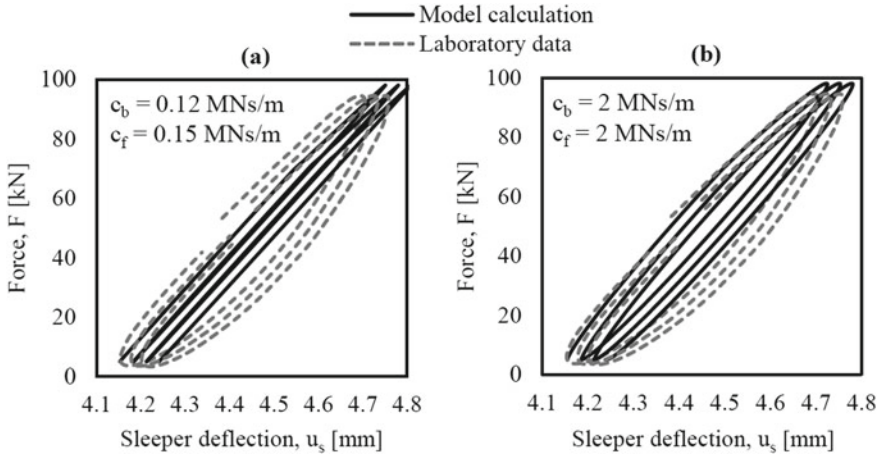
Fig. 4 Comparison of force–deflection at the sleeper measured in the laboratory and calculated using the model, with **(a)** low (values *A*) and **(b)** high material (values *B*) damping

in Fig. 2). F_{y0} and S_0 represent the yield force and the settlement after ten load cycles, respectively (the first ten load cycles are neglected to eliminate the initial variability in the laboratory data, which occurs as a result of the sleeper bedding in). The initial yield force, F_{y0}, was determined so as to match the measured force–deflection relationship in the tenth loading cycle (Fig. 2). The settlement at the tenth cycle, S_0, was obtained from the settlement laboratory data. The resulting calculated settlements are shown in Fig. 5.
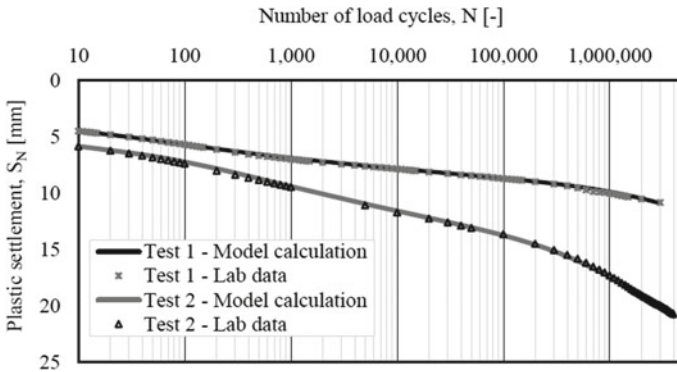
Fig. 5 Comparison between measured and calculated plastic settlement, S_N, as a function of the logarithm of the number of loading cycles, N

5 Application of the Model

A common approach used by practitioners to simulate cumulative plastic deformation of ballast (e.g. [21]) involves shifting the settlement curve when the load changes to a new one intended to represent the plastic deformation rate associated with the new loading. A similar approach has been adopted here, updating the plastic parameters $(S_0, \alpha_y, H_{d0}, H_{s0}, \alpha_d, \alpha_s)$ at the end of each load cycle according to the peak stress currently applied to the ballast (F_{max}). In this paper, only the values of F_{max} used in the laboratory tests (98 and 157 kN) have been considered, together with the corresponding model parameters (Table 3).

5.1 Application 1—Change in Load Condition

Figure 6a shows, on a semi-logarithmic scale, the calculated ballast settlements for a change in the applied load to the rail, F, from 98 to 157 kN after 100,000 cycles using the model parameters for Test 1 (Table 3) at the lower load and for Test 2 at the higher load. No other account was taken of the change in ballast type. As might be expected, the settlement curve changes from its initial trajectory following Test 1 to that of Test 2.

5.2 Application 2—Comparison Between Different Loading Histories

Figure 6b compares calculated settlement curves for two different hypothetical loading histories. Three loading steps (a, b, and c) have been applied in two scenarios labelled x and y. In the first simulation (x), the maximum forces applied during steps a, b, and c were 98, 157, and 98 kN, while in the second simulation (y), the maximum applied loads were 157, 98, and 157 kN.

The model suggests that the highest stresses dominate the development of plastic settlement. For example, in Fig. 6b, it can be seen that even if the lower stress loading forms the majority of the stress history (scenario x), an increase to a higher stress results in a rapid adjustment in ballast settlement towards that calculated if the higher load had been applied from the outset (as observed by [22]). Conversely, when the

Table 3 Ballast materials used for the settlement tests

	F_{y0} [kN]	a_y [–]	H_{d0} [GN/m]	a_d [–]	H_{s0} [GN/m]	a_s [–]
Test 1	70.0	12.0	0.6	2.8	0.7×10^3	0.40
Test 2	80.0	20.0	1.4	1.0	0.2×10^3	0.16
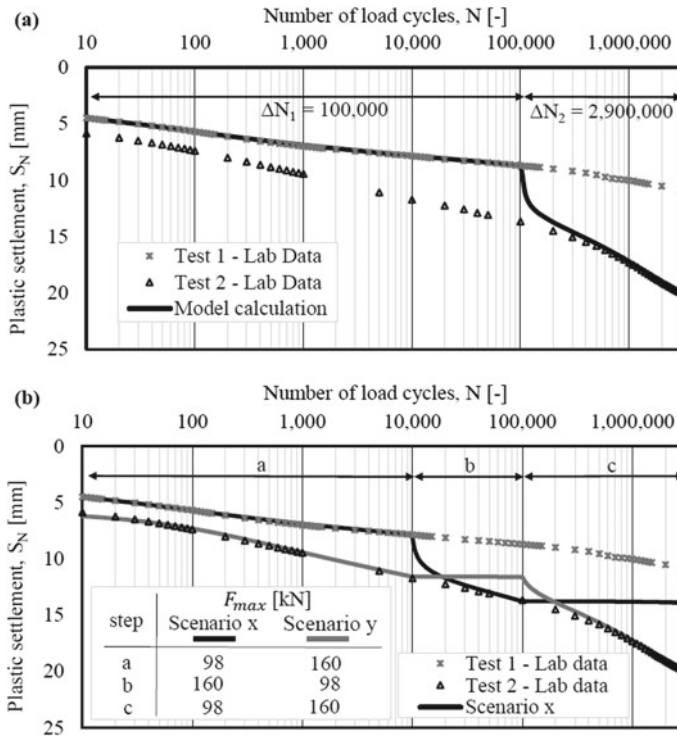
Fig. 6 Application of the model to calculate ballast settlement versus the logarithm of the number of load cycles for the load histories indicated in parts (**a**) and (**b**)

stress level was reduced (scenario y step b or scenario x step c), the settlement rate reduces almost to zero (as noted by [23]).

6 Conclusion

A novel conceptual model for calculating railway ballast settlement during trafficking has been proposed, which uses a combination of a nonlinear visco-elastic and plastic-hardening elements to capture both the resilient and plastic response. The model has been tested in single sleeper loading but has the potential to be integrated into a VTI model for calculation of along track differential settlement.

The settlement has been subdivided into two components, attributable to (i) densification and (ii) lateral spreading of the ballast. The first causes most of the settlement during an initial stage, with the second becoming predominant after the ballast has reached a stable volumetric state. The model was able to reproduce accurately the ballast settlements measured in two full-scale laboratory tests with different ballasts

and axle loads, up to 3 million cycles. Different loading conditions can be accounted for by adjusting the parameters. Model calculations show that a high stress loading regime is disproportionately damaging in terms of the settlement caused. In future work, the proposed settlement model will be integrated into a full VTI analysis.

References

1. Dahlberg T (2001) Some railroad settlement models—a critical review. Proc Inst Mech Eng Part F J Rail Rapid Transit 215:289–300. https://doi.org/10.1243/0954409011531585
2. Suiker ASJ, Selig ET, Frenkel R (2005) Static and cyclic triaxial testing of ballast and subballast. J Geotech Geoenviron Eng 131:771–782. https://doi.org/10.1061/(ASCE)1090-0241(2005)131:6(771)
3. Ferro E (2018) The mechanical behaviour of fibre reinforced railway ballast. PhD thesis. https://eprints.soton.ac.uk/428625/
4. Guérin N, Sab K, Moucheront P (1999) Identification expérimentale d'une loi de tassement du ballast. Can Geotech J 36:523–532. https://doi.org/10.1139/cgj-36-3-523
5. Indraratna B, Nimbalkar S (2013) Stress-strain degradation response of railway ballast stabilized with geosynthetics. J Geotech Geoenviron Eng 139:684–700. https://doi.org/10.1061/(ASCE)GT.1943-5606.0000758
6. Lekarp F, Isacsson U, Dawson A (2000) State of the art. II: permanent strain response of unbound aggregates. J Transp Eng 126:76–83. https://doi.org/10.1061/(ASCE)0733-947X(2000)126:1(76)
7. Sato Y (1995) Japanese studies on deterioration of ballasted track. Veh Syst Dyn 24:197–208. https://doi.org/10.1080/00423119508969625
8. Abadi T, Le Pen L, Zervos A, Powrie W (2016) A review and evaluation of ballast settlement models using results from the Southampton Railway Testing Facility (SRTF). Procedia Eng 143:999–1006. https://doi.org/10.1016/j.proeng.2016.06.089
9. ORE (1970) Deformation properties of ballast. Laboratory and track tests
10. Shenton MJ (1985) Ballast deformation and track deterioration >. In: Track technology. Thomas Telford, pp 253–265
11. Selig ET, Waters JM (1994) Track geotechnology and substructure management. Thomas Telford, London
12. Saussine G, Quezada JC, Breul P, Radjai F (2014) Railway ballast settlement: a new predictive model. In: Railway 2014. Civil-Comp Press, Ajaccio, p 12
13. Sato Y (1997) Optimization of track maintenance work on ballasted track. In: Proceedings of the world congress on railway research (WCRR '97), Florence, Italy, pp 405–411
14. Varandas JN, Hölscher P, Silva MAG (2010) A settlement model for ballast at transition zones. In: Proceedings of tenth international conference on engineering computational technology. https://doi.org/10.4203/ccp.93.19
15. Abadi TC (2015) Effect of sleeper and ballast interventions on rail track performance. PhD thesis. https://eprints.soton.ac.uk/id/eprint/388080
16. Knight JB, Fandrich CG, Lau CN, Jaeger HM, Nagel SR (1995) Density relaxation in a vibrated granular material. Phys Rev E 51:3957–3963. https://doi.org/10.1103/PhysRevE.51.3957
17. Ferrara R (2013) A numerical model to predict train induced vibrations and dynamic overload. PhD thesis. https://tel.archives-ouvertes.fr/tel-00842993v2

18. Bezin Y, Iwnicki SD, Cavalletti M, de Vries E, Shahzad F, Evans G (2009) An investigation of sleeper voids using a flexible track model integrated with railway multi-body dynamics. Proc Inst Mech Eng Part F J Rail Rapid Transit 223:597–607. https://doi.org/10.1243/09544097J RRT276
19. Zhang S, Xiao X, Wen Z, Jin X (2008) Effect of unsupported sleepers on wheel/rail normal load. Soil Dyn Earthq Eng 28:662–673. https://doi.org/10.1016/j.soildyn.2007.08.006
20. Pandrol. Fastclip FC—rail fastening system—technical specification. https://www.pandrol. com
21. Ford R (1995) Differential ballast settlement, and consequent undulations in track, caused by vehicle-track interaction. Veh Syst Dyn 24:222–233. https://doi.org/10.1080/004231195089 69627
22. Stewart HE (1986) Permanent strains from cyclic variable-amplitude loadings. J Geotech Eng 112:646–660
23. Shenton MJ (1978) Deformation of railway ballast under repeated loading conditions. In: Railroad track mechanics and technology. Elsevier, Princeton University, USA, pp 405–425

Evaluation of Ballast Particle Degradation Under Micro-Deval Testing Using Photogrammetry

André Paixão , **Carlos Afonso, Bruno Delgado** ,
and Eduardo Fortunato

Abstract Railway ballast plays an important role in the economic efficiency and sustainability of the rail transport. In this context, the morphology of its particles, in what regards the shape, angularity and surface texture, is critical and affects the mechanical performance of this aggregate material. Minimum mechanical resistance requirements ensure that the material undergoes limited degradation and preserves optimal morphological parameters throughout its field use. Many current technical specifications require the characterization of the morphology of ballast particles which is performed according to well-established and extensively validated empirical and manual testing approaches that were developed in the past. However, some of these approaches are subjective, prone to human error, reductive of the three-dimensional aspects of the particles and do not take advantage of more recent knowledge and currently available automated methods and image analysis approaches to fully characterize these aggregates. In this work, the authors present the application of a photogrammetry method for 3D reconstruction of ballast particles, as an alternative to other significantly expensive approaches. Ballast samples were submitted to micro-Deval abrasion testing, and the evolution of the morphology of a set of particles was analyzed at different stages of that test. Recent and automated image analysis techniques were applied to evaluate changes in the particle morphology. This work demonstrates that close-range photogrammetry for the 3D scanning of ballast particles is a cost-efficient approach to study these aggregates.

Keywords Railway ballast · Particle morphology · Abrasion · Photogrammetry

A. Paixão (✉) · E. Fortunato
National Laboratory for Civil Engineering (LNEC), Av. Do Brasil, 101 Lisboa, Portugal
e-mail: apaixao@lnec.pt

A. Paixão · B. Delgado
Faculty of Engineering, CONSTRUCT, University of Porto, R. Dr. Roberto Frias s/n, Porto, Portugal

C. Afonso
Faculty of Engineering, University of Porto, R. Dr. Roberto Frias s/n, Porto, Portugal

1   Introduction

The ballast layer is one of the most important elements of conventional railway tracks. Its functions include the transmission and dissipation of the cyclic loads resulting from the passage of trains to the underlying layers, maintaining the position of the track and providing proper drainage. Throughout its life cycle, the ballast layer densifies, and its particles degrade, mainly as a result of those successive impact loads. Consequently, the position of the rails may become inadequate and track defects are generated, thus reducing the performance of this infrastructure and eventually leading to the need to perform maintenance interventions to reestablish proper rail geometry. This deformation behavior of the ballast layer, as well as its stability, largely depends on the particle morphology [1]. It is consensual to consider three subscales in the analysis of particle characteristics: shape, angularity and texture. A rough analysis of particle morphology can lead to inconclusive or even erroneous results.

The mechanical and geometric properties usually require that ballast particles are defined in specific regulations, considering well-established characterization procedures [2, 3]. However, some of these procedures are based on empirical analysis approaches, are highly operator dependent and therefore subject to human error, such as manual measurement of the dimensions that are traditionally used to morphologically classify particles [4, 5].

Recent advances in the analysis of digital images, supported by advanced technical means, have made measurements more reliable and allowed for in-depth knowledge of various aspects, including [1]: particle size distribution; volume and surface area; shape (sphericity (Ψ); shape factor (F)); angularity (angularity index); texture (texture index). Various methods and equipment are currently available for particle morphology scanning and analysis, but most are very expensive and difficult to use. In addition to two-dimensional particle morphology characterization methods based on automatic image processing techniques such as the aggregate image measurement system (AIMS) [6] or the University of Illinois Aggregate Image Analyzer (UIAIA) [7, 8], studies have been performed using three-dimensional particle digitization methods that, for example, either use mechanical probes or stylets [9], or take advantage of LASER technology [9–12], or resort to X-ray computed tomography [13, 14]. The method used in this study—previously validated and described by the authors [15]—also allows the three-dimensional digitization of ballast particles but uses photogrammetry, in a low cost and easy implementation process, when compared to the other methods mentioned above.

In Europe and in other countries, researchers have studied the evolution of particle morphology using the micro-Deval test—EN 1097-1 [16]—simulating an accelerated process of aggregate degradation [7, 17, 18]. Synthetically, this test consists of evaluating the generation of fines from an aggregate by the rolling action of a certain amount of this material within a metallic drum of predefined dimensions and to which a rotation speed of 100 revolutions/min is applied until it reaches 14,000 revolutions. Herein, to be able to compare the results with those of previous studies,

the authors considered appropriate to also use this test procedure to simulate rail ballast degradation.

2 Material and Sample Preparation

The specimens tested in this work were prepared according to the procedure established in the European Standards EN 1097-1 for the micro-Deval test [16], using a sample of granite aggregate that met the regulation requirements in Portugal for railway ballast application [2, 19]. Thus, three specimens of 10 kg ± 100 g were prepared, each consisting of two fractions of about 5 kg retained in sieves 31.5 mm and 40.0 mm, respectively, totaling 30 kg. From this material, 30 particles were selected (10 from each specimen) with the concern to obtain a heterogeneous representation of the particle shapes. The mass evolution of these particles was monitored throughout the work in the various stages of the micro-Deval test using a high precision balance (0.0001 g).

3 Three-Dimensional Scanning and Reconstruction of Particles

3.1 Image Capturing—Photographic Session

As mentioned above, the photogrammetry digitization process used in this work was based on that previously validated and presented by Paixão et al. [15]: Each particle is placed on a pedestal, painted with matte paint to prevent reflections, which is attached to a turntable (Fig. 1); images are captured around the particle sequentially in 10° increments up to 360°. This process is repeated for each of the three camera positions in height as depicted in Fig. 1. Thus, $3 \times 36 = 108$ images are captured to obtain overall coverage of each particle. The following equipment was used: Canon EOS 80D, 24.2 Megapixel camera, with 22.3 mm × 14.9 mm CMOS image sensor; Canon EF 50 mm f/1.8 STM lens; polarizing filter; iPhone 6 with Canon Camera Connect application for camera remote control; articulated lamps with diffused light; tripod; rotating tray with 10° marking and built-in pedestal; white paper background.

3.2 Digital Reconstruction of 3D Particle Models

The procedure proposed by Paixão et al. [15] for the digital reconstruction of the particles uses two distinct programs: In the first, *VisualSFM* [20–22], a dense point cloud is generated from the 108 images of each particle; later, in the second program,
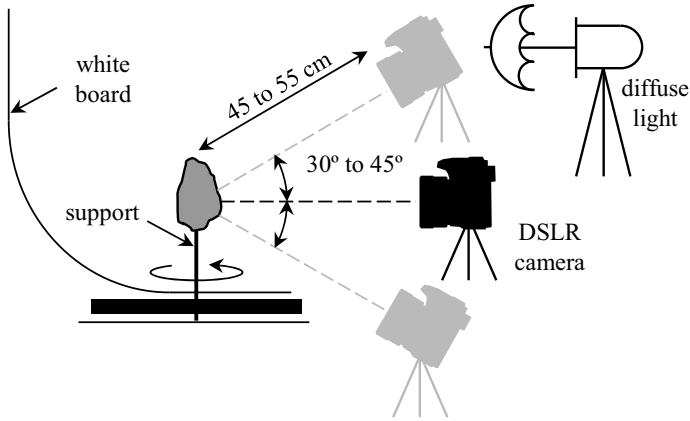
Fig. 1 Setup of the photography session and workflow of the photogrammetry approach

the *MeshLab* [23], that cloud is cleaned (when necessary), appropriate scale is applied and a 3D triangular mesh is generated, as described in greater detail by Afonso [24]. Figure 2 presents examples of the steps of the application of this procedure in the generation of the point cloud of one of the studied particles.

Compared to other three-dimensional scanning methods, this is relatively fast and significantly less expensive. Still, the average time taken for the digitization, the three-dimensional reconstruction and the model analysis of each particle was about 1 h [24]. It should be noted that due to the phasing implemented in the micro-Deval test, a total of 3×30 digital models were constructed (averaging around 270,000 vertices and 540,000 faces), using a total of 9720 captured images. To elucidate on the detail of the scans achieved with this method using the described equipment, on average, the density of the obtained cloud points was above 80 points/mm^2 of surface area and the density of the meshes was above 30 vertices/mm^2. Another important aspect was the possibility of estimating the specific density value, γ, of each particle, since its real weight and digital volume were known. The average value of the specific
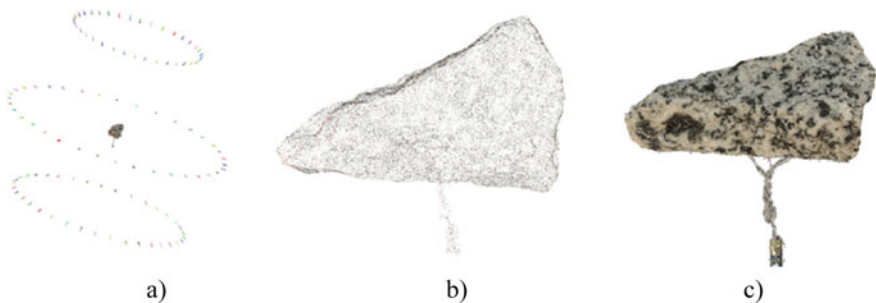
Fig. 2 Point cloud generation: **a** position of the 108 image captures; **b** point cloud; **c** densified point cloud with color information [24]

density of the analyzed particles thus obtained was 2.74 g/cm^3. Using the density determination test for that selected particle set using the submerged basket method as laid down in the European Standard EN 1097-6 [25], a value of 2.73 g/cm^3 was obtained, which corresponds to a difference of only 0.4% from the previous value.

4 Micro-Deval Abrasion Testing

As mentioned above, the accelerated simulation of ballast particle degradation was performed using the micro-Deval test. However, two changes were made to the procedure of Annex A of the European Standard EN 1097-1 [16] as regards rail ballast testing. As in previous studies [18], the first change was the non-addition of water to the specimen during the test, i.e., by performing the dry test in the light of Annex B of the same standard. This change aimed to simulate the real situation as faithfully as possible and to be able to compare the results with future numerical modeling work using the discrete element method. The second difference was that the tests were interrupted at an intermediate stage (after 2000 revolutions out of a total of 14,000 revolutions) to weigh and digitize the selected particles. Thus, this change resulted in three moments of photogrammetry digitization of the particles: (i) in their initial state, before the test; (ii) at an intermediate stage of the test, after 2000 revolutions; (iii) and upon completion of the test. At the end of the tests, the specimen fractions were weighed to determine the dry ballast micro-Deval value: $M_{DS,RB}$. To distinguish the particles in the various stages of the procedure, given the high wear conferred by the test, they were painted with spray.

After the completion of the micro-Deval tests, the photogrammetry sessions, and the particle reconstruction, for all phases, it was possible to evaluate the evolution of their morphology by analyzing and comparing the three-dimensional models that were constructed. In this task, the *GOM Inspect* software was used, which allows comparing three-dimensional meshes and contains some features for automatic alignment and distance calculation between meshes that facilitate their handling (Fig. 3a), making it a particularly useful tool for comparison of the generated meshes and, consequently, for the analysis of particle wear during the test. Comparisons were made for each particle between the initial situation (0 revolutions) and after 2000 revolutions (0 vs. 2000); between this state and the final situation after 14,000 revolutions (2000 vs. 14,000); and between the initial and the final (0 vs. 14,000). Figure 3b depicts an example of the inspection performed by the program, mapping the distances between the starting particle and the final particle (Fig. 3c).
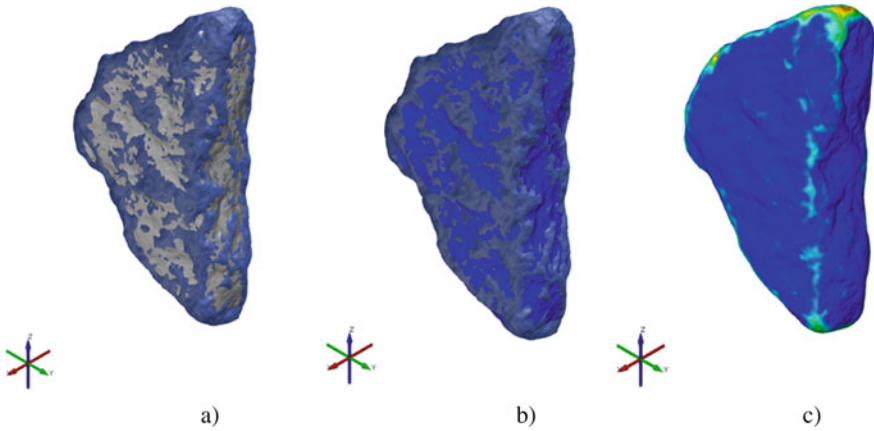
Fig. 3 Alignment of the 3D models (**a**); particle inspection (**b**); evaluation of morphology evolution (**c**) [24]

5 Results and Discussion

5.1 Results of the Micro-Deval Abrasion Tests

The dry micro-Deval value, $M_{DS,RB}$, obtained in the three specimens was 3. To give a reference of the influence of the presence of water, a fourth test was also performed following the normal procedure of the European Standard [16] to determine the value of wet micro-Deval for ballast, $M_{DE,RB}$, i.e., by adding (2 ± 0.05) l of water to the specimen during the test. In the latter, a higher value of $M_{DE,RB} = 7$ was obtained, which was expected and was close to that obtained by Jerónimo [9], concerning Portuguese granite ballast material similar to the one studied in this work.

Regarding the results of the three dry tests, the cumulative mass of particles smaller than 1.6 mm is shown in Fig. 4a, where a higher rate of production of smaller material can be observed in the first phase (0.0497 g/rev.) than in the next phase (0.0183 g/rev.), which is in agreement with the results obtained by other authors [17] and is a characteristic result of this test procedure [18, 26]: Initially, the particles have protruding vertices and edges and some roughness that are first removed at the beginning of the test. The particles that were analyzed showed analogous degradation behaviour. By way of example, Fig. 4b shows the percentage of lost mass of 10 screened particles from one of the tests performed.

Figure 5 shows examples of digital model comparisons, regarding one of the particles, where a color map is superimposed on the mesh corresponding to the wear suffered by that particle in each stage (the color scale corresponds to the distance between two meshes relative to different phases of the test). Figure 6 shows the real aspect of this particle in the respective phases, identifying the areas that suffered significant wear.
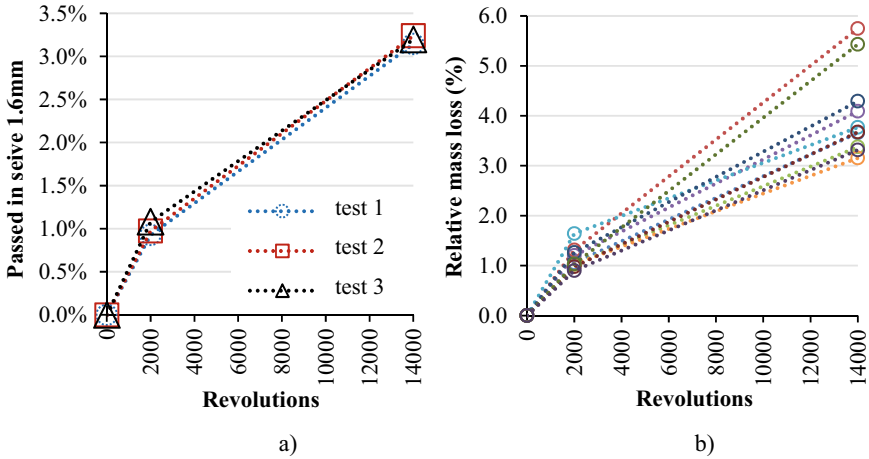
Fig. 4 Production material passing sieve 1.6 mm (% by mass) by each specimen (**a**) and relative mass loss of 10 particles from the 1st test (**b**) (each color represents one particle)
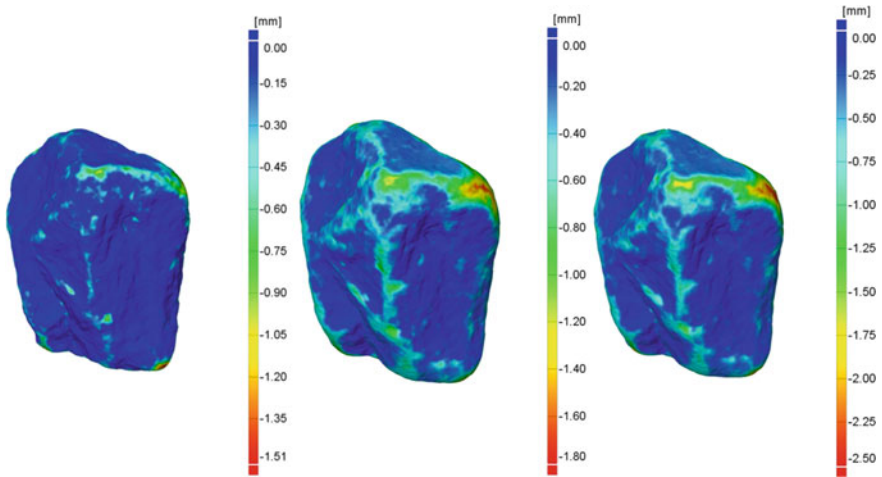
Fig. 5 Differences between meshes of particle 1 (0 vs. 2000; 2000 vs. 14,000 and 0 vs. 14,000) [24]

5.2 Evolution in Particle Morphology

Traditionally, particle morphology is evaluated using several classification criteria proposed by different authors that were mostly presented over the last century. In this work, due to the large number of manual measurements that would have to be performed on the 30 particles, for each of the three phases, and in order to eliminate the typical errors introduced in these types of measurements [5], a digital measuring

Fig. 6 Aspects of particle 1 after 2000 (left) and 14,000 (right) revolutions [24]

tool developed in a MATLAB environment was used, which guarantees automated measurement, without user intervention, of various parameters. Among other parameters, this tool determines the maximum (L), intermediate (I) and smallest (S) dimensions [27], volume (V), surface area (A), sphericity parameter (Ψ—as defined by Wadell [28], considering the volume and surface area of the digital particle model) and the flattening ratios $p = S/I$, elongation $q = I/L$, equidimensionality S/L and the form $F = p/q$. Figure 7 presents the example of the analysis of particle 1 using this tool. To classify the particles according to their morphology, the proposal of Blott and Pye [4] was considered, showing in Fig. 8 the evolution of the morphology of all selected particles in a modified Zingg diagram.

From the analysis of Fig. 8, it can be seen that most particles did not significantly change their morphological classification, and, in general, the same level of particle classification heterogeneity was maintained, i.e. from moderately elongate and moderately flat to non-elongated and not flat and from very non-equant to equant, with form factors between 0.49 and 1.78. However, six particles (20%) were identified that showed a relatively longer paths with respect to the migration of ratios p and q and that changed their classification throughout the micro-Deval test. Visually, this evolution would be difficult to identify, and the possible manual measurement of the dimensions L, I, and S could lead to quite different classifications, since these are traditionally determined using a caliper. Thus, using an automatic digital particle measurement tool, it was possible to determine those dimensions and other parameters more precisely and without operator intervention, avoiding the introduction of human error in the measurements.

Regarding the sphericity (Ψ) of the particles, this parameter varied within the following ranges: [0.64; 0.85] at initial assessment; [66; 0.87] after 2000 revolutions; [0.69; 0.89] after 14,000 revolutions. Thus, after completing the test, the range amplitude decreased but the respective range values increased. This increase was due
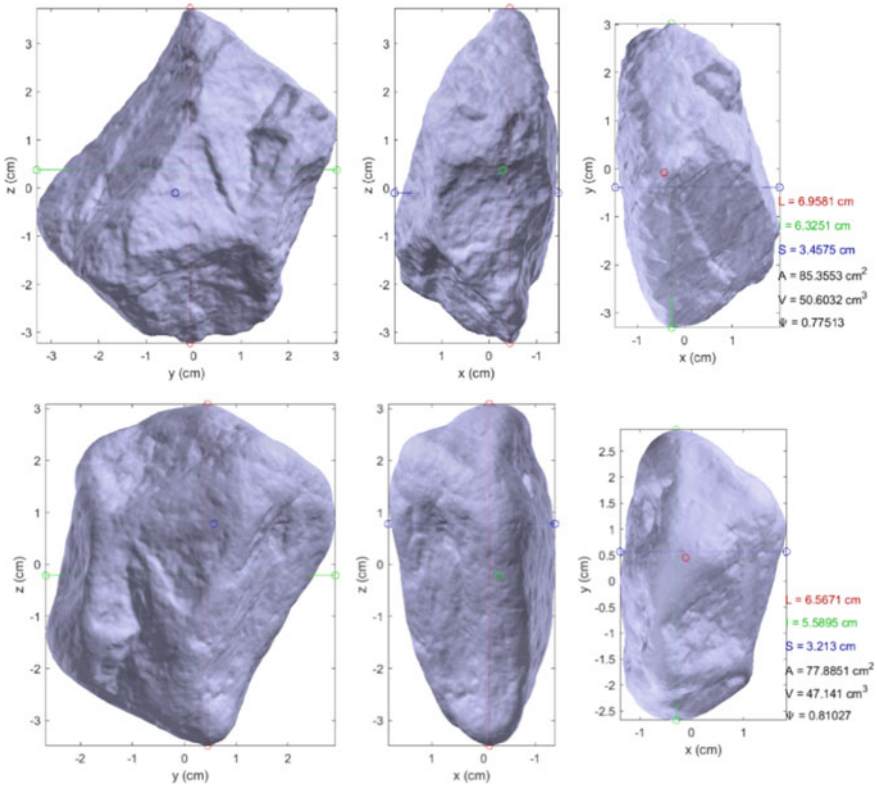
Fig. 7 Analysis of particle 1 (initial configuration above and final configuration below)

to wear inside the drum which led to particle shapes increasingly close to the shape of a sphere (hence sphericity values closer to the unit value). This type of evolution is characteristic of the effect of erosion of rolling aggregates.

It was also found that the evolution of the flatness ratio was higher than the evolution of the elongation ratio. The range of variation of the flatness ratio was [−0.15; 0.13], and the elongation ratio range was [−0.08; 0.05]. These variations were obtained by calculating the difference between the final and initial ratio values.

6 Conclusions

The presented work was developed in the scope of a M.Sc. dissertation [24] which aimed to study the morphological evolution suffered by rail ballast particles when subjected to accelerated wear. The followed methodology was based on micro-Deval tests on specimens of a granite aggregate, using the dry procedure, and performing photogrammetry scans for three-dimensional reconstructions [15] of a set of 30
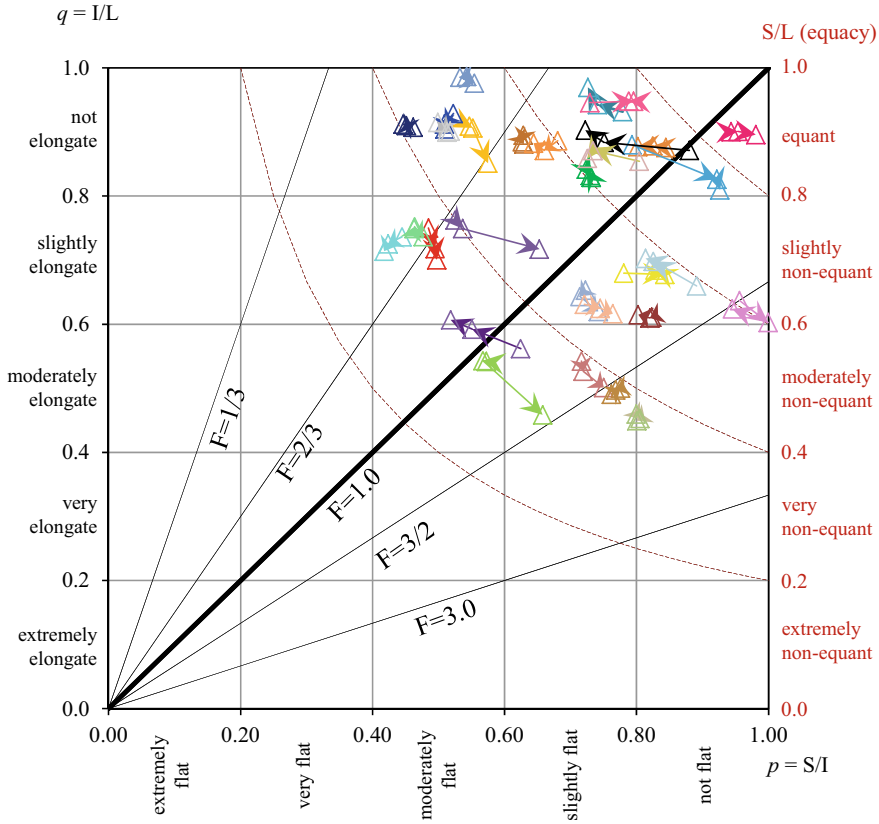
Fig. 8 Evolution and respective modified classification [4] of the studied particles (each particle is represented by a different color; the arrows identify the evolution path between the three different stages denoted by triangles)

selected particles at three stages: (i) before the start of the test; (ii) after 2000 revolutions of the micro-Deval equipment drum, with interruption of the test; (iii) and at the end of the test. The following main conclusions were drawn:

- From the morphology analysis, it was found that for the thirty analyzed particles, only six (20%) changed their classification, as established by Blott and Pye [4]. The use of an automatic digital particle measurement tool allowed to perform measurements more precisely and without operator intervention, avoiding the introduction of human errors.
- The analysis of the sphericity parameter (also automatically determined and using the actual tridimensional shape of the particles) revealed a growing tendency toward the unit value—a behavior that was expected as the particle's angularities were smoothed and rounded, approximating to the shape of a sphere.

- Regarding the evolution of the flatness and elongation ratios, no evident correlation with the evolution of the sphericity was identified.

It should be noted that close-range photogrammetry has several advantages compared to other methods for digital reconstructing of particle models, such as ease of handling and adaptation to the objects to be scanned; significant lower cost; digital models can retain the colour of scanned points; does not require changing particle positions during the image capture process; and is relatively fast (roughly 1 h for digitally reproducing a particle, including photograph session, preprocessing, and mesh generation). However, it also has some disadvantages, such as: It may require careful preprocessing of the point cloud (i.e. locally, where the particle rests on the vertical support), it strongly depends on the lighting conditions and some knowledge of photography concepts is required for best results.

Concerning the other scales of morphological evaluation of ballast particles, namely on a smaller scale (texture and angularity), it was not possible to address them in the present work. However, in the future, it is intended to take advantage of the digital particle library to perform more advanced three-dimensional analyzes using, for example, Fourier series, Spherical Harmonics or Proper Orthogonal Decomposition (POD), as explored by Deiros et al. [18] and Ouhbi [29], which would deepen the morphological characterization approach presented in this work.

References

1. Guo Y, Markine V, Zhang X, Qiang W, Jing G (2019) Image analysis for morphology, rheology and degradation study of railway ballast: a review. Transp Geotech 18:173–211
2. CEN: European Standard EN 13450:2013 (2013) Aggregates for railway ballast. CEN TC 154—Comité Européen de Normalisation, Brussels
3. AREMA (2010) Manual for railway engineering. American Railway Engineering and Maintenance-of-Way Association, Lanham, MD
4. Blott SJ, Pye K (2008) Particle shape: a review and new methods of characterization and classification. Sedimentology 55(1):31–63
5. Folk RL (1955) Student operator error in determination of roundness, sphericity, and grain size. J Sediment Res 25(4):297–301
6. Gates L, Masad E, Pyle R, Bushee D (2011) Aggregate image measurement system 2 (AIMS2): final report. Federal Highway Administration (FHWA), U.S. DoT, Washington, DC
7. Moaveni M, Mahmoud E, Ortiz EM, Tutumluer E, Beshears S (2014) Use of advanced aggregate imaging systems to evaluate aggregate resistance to breakage, abrasion, and polishing. Transp Res Rec 2401(1):1–10

8. Rao C, Tutumluer E (2000) Determination of volume of aggregates: new image-analysis approach. Transp Res Rec 1721(1):73–80
9. Jerónimo P (2014) Caraterização Mecânica, Digitalização Volumétrica e Modelação Numérica de Partículas Rochosas para Balastro Ferroviário. M.Sc. thesis, University of Porto, Faculty of Engineering, Porto
10. Anochie-Boateng JK, Komba JJ, Mvelase GM (2013) Three-dimensional laser scanning technique to quantify aggregate and ballast shape properties. Constr Build Mater 43:389–398
11. Lanaro F, Tolppanen P (2002) 3D characterization of coarse aggregates. Eng Geol 65(1):17–30
12. Sun Y, Indraratna B, Nimbalkar S (2014) Three-dimensional characterisation of particle size and shape for ballast. Géotech Lett 4(3):197–202
13. Erdogan ST, Quiroga PN, Fowler DW, Saleh HA, Livingston RA, Garboczi EJ et al (2006) Three-dimensional shape analysis of coarse aggregates: new techniques for and preliminary results on several different coarse aggregates and reference rocks. Cem Concr Res 36(9):1619–1627
14. Garboczi EJ (2002) Three-dimensional mathematical analysis of particle shape using X-ray tomography and spherical harmonics: application to aggregates used in concrete. Cem Concr Res 32(10):1621–1638
15. Paixão A, Resende R, Fortunato E (2018) Photogrammetry for digital reconstruction of railway ballast particles—a cost-efficient method. Constr Build Mater 191:963–976
16. CEN: European Standard EN 1097-1:2011 (2011) Tests for mechanical and physical properties of aggregates—part 1: determination of the resistance to wear (micro-Deval). CEN TC 154—Comité Européen de Normalisation, Brussels
17. Deiros I, Combe G, Emeriault F, Toni J-B, Voivret C, Ferellec JF (2017) Wear of sharp aggregates in a rotating drum. EPJ Web Conf 140:07009
18. Deiros I, Combe G, Emeriault F, Voivret C, Ferellec J-F (2019) X-ray CT analysis of the evolution of ballast grain morphology along a micro-Deval test: key role of the asperity scale. Granular Matter 21(2):30
19. REFER: IT.GEO.001 (2008) Fornecimento de Balastro e Gravilha. Rede Ferroviária Nacional, EPE, Lisboa
20. Wu C, Agarwal S, Curless B, Seitz SM (2011) Multicore bundle adjustment. In: 2011 IEEE conference on computer vision and pattern recognition. IEEE Computer Society, Colorado Springs, pp 3057–3064
21. Wu C (2013) Towards linear-time incremental structure from motion. In: 2013 international conference on 3D vision (3DV 2013). IEEE Computer Society, Seattle, pp 127–134
22. Furukawa Y, Curless B, Seitz SM, Szeliski R (2010) Towards Internet-scale multi-view stereo. In: 2010 IEEE computer society conference on computer vision and pattern recognition (CVPR). IEEE Computer Society, San Francisco, CA, pp 1434–1441
23. Cignoni P, Callieri M, Corsini M, Dellepiane M, Ganovelli F, Ranzuglia G (2008) MeshLab: an open-source mesh processing tool. In: Scarano V, Chiara RD, Erra U (eds) 2008 eurographics Italian chapter conference. The Eurographics Association, Salerno, pp 129–136
24. Afonso C (2019) Caracterização mecânica e digitalização tridimensional na análise de partículas granulares de geomateriais. M.Sc. thesis, University of Porto, Faculty of Engineering, Porto
25. CEN: European Standard EN 1097-6:2013 (2013) Tests for mechanical and physical properties of aggregates—part 6: determination of particle density and water absorption. CEN TC 154—Comité Européen de Normalisation, Brussels
26. Bach H (2013) Evaluation of attrition tests for railway ballast. Ph.D. thesis, Graz University of Technology, Graz
27. Krumbein WC (1941) Measurement and geological significance of shape and roundness of sedimentary particles. J Sediment Res 11(2):64–72
28. Wadell H (1932) Volume, shape, and roundness of rock particles. J Geol 40(5):443–451
29. Ouhbi N (2017) Une description morphologique précise des grains pour l'étude numérique des propriétés mécaniques du ballast ferroviaire. Ph.D. thesis, Université Paris-Est

Importance of Bending Stiffness of Different Track Forms

Toshan Rampat [ID], **Louis Le Pen** [ID], **William Powrie** [ID], **and John Harkness** [ID]

Abstract The most common form of railway track construction is still discrete sleepers on ballast. However, other types of track, sometimes referred to as ballastless, hybrid and/or slab track, may in some circumstances be more cost effective over their life cycle despite their higher initial cost. Current trackbed design methods for different types of superstructure generally specify a trackbed/subgrade support stiffness in terms of an "E_{V2}" value, i.e. the stiffness evaluated from the second load step in a plate bearing test. Specifying the same E_{V2} value regardless of the track system superstructure creates over-conservative designs that fail to make use of the higher longitudinal bending stiffness of ladder or slab track systems compared with ballasted track. This paper reports the results of computer analyses carried out to understand better the influence of the longitudinal bending stiffness of the track system superstructure on trackbed response. Three-dimensional models of three types of railway track superstructure system (conventional sleepers, ladder and slab track) were set up in finite element simulations. The models were validated against closed-form solutions for a beam on an elastic foundation. Parametric studies were then undertaken to understand how changes in support stiffness influenced peak trackbed deflections and stresses, for the different track superstructures. The results show that, with increasing bending stiffness of the track superstructure, peak deflections are decreased, and the longitudinal extent of the deflection bowl is increased. There are also significant reductions in stresses being transferred into the trackbed. Slab and ladder tracks are also shown to be better at spanning regions of poor/reduced support.

Keywords Bending stiffness · Ladder track · Slab track · Ballasted track · FEM · Trackbed stiffness · Railway · Railroad · Ties · Sleepers

T. Rampat (✉) · L. Le Pen · W. Powrie · J. Harkness
University of Southampton, Southampton, UK
e-mail: T.C.Rampat@soton.ac.uk

1   Introduction/Background/Problem Statement

The primary function of a railway track system is to transmit wheel loads to the subgrade in a way that does not damage the track or the formation. The most common type of railway track is the conventionally ballasted system, in which sleepers or ties placed at intervals beneath the rails are supported on a ballast layer, typically 300 mm thick, overlying a prepared subgrade. However, there are alternative designs of railway track systems; for example, ladder and slab track incorporate longitudinal beams beneath the rails, giving the track system superstructure much greater longitudinal bending stiffness than conventionally ballasted track.

Ladder track consists of two longitudinal beams supporting the rails, with transverse connections at suitable intervals. Research into track systems with longitudinal rail support in Japan, Russia and France in the mid-twentieth century [1] led to the construction and testing of ladder tracks. Potential hoped for advantages included lowering the life cycle cost and reducing maintenance requirements. However, to date, ladder tracks have not gained widespread adoption.

In Japan, excessive maintenance requirements for traditional ballasted track on embankments on the Tokaido line (opened in 1964) led to the development of slab track [2]. Slab tracks have subsequently been used in various forms [3]. Early applications amounted to little more than casting the sleeper to rail baseplate mounting onto a wet-poured concrete slab. However, over time different proprietorial systems have been developed and gained acceptance for use on various types of railway line, including at high speed. Slab track systems may be classified by their means of construction; precast, cast in situ/slip formed or combinations thereof. Precast systems are formed by joining slab elements together on site; cast in situ and slip formed types have the potential to provide a more continuous beam support. One system currently in common use is Rheda 2000 [4]; this is cast on site with the potential to provide continuous, unjointed beam support [5]. It was developed on the basis of experience with highway pavements [6, 7].

The means of joining slab elements together will have a major influence on the way in which a slab system will perform. The current European (EU) specification/standard for slab track [8], which appears to have been partly developed with existing systems in mind, requires the slab to be supported on the top of a frost protection layer having $E_{v2} = 120$ N/mm^2 (measured at the surface), where E_{v2} is the modulus of elasticity evaluated from the second load step in a plate bearing test [7–9]. The substructure should also have a sufficient bearing stiffness, $E_{v2} \geq 60$ MPa measured at the upper surface for newly constructed track and $E_{v2} \geq 45$ MPa for existing track [7]. These are relatively onerous requirements that are unlikely to be met by the natural soils present. Such specifications will usually therefore require the in situ soils to be improved and/or replaced with high-quality granular fill. The requirement for the high support stiffness is in part explained because the steel reinforcement within the slab is placed along the neutral axis, hence does not provide tensile resistance in bending, making the slab prone to cracking. A high E_{v2} value means that large settlements are unlikely [10], but leads to a conservative design in

which the benefits of a potentially stiffer track form are not realized. If slab track systems were reinforced above and below the neutral axes, it might be possible to use them at sites with lower and/or more variable support stiffnesses.

A further consideration for slab or ladder systems on lower stiffness ground support is the presence of joints. Many slab/ladder track systems are formed of panels that require jointed connections between them. These connections may give rise to a locally reduced bending stiffness. Discontinuous slab track systems may have dowel bars or plates to minimize any discontinuity of displacement and possibly rotation between adjacent panels [11]. Previous experimental and numerical investigations have shown that dowel connections attract significant local stresses [12], with the interface strength between the joint and the slab influencing damage at this location [13].

To gain an improved understanding of the role of the bending stiffness of the track superstructure on the maximum deflections and stresses transferred into the substructure, finite element computer simulations have been carried out on idealized representations of three different types of track: conventional discrete sleeper supported ballasted track, ladder track and continuous slab track. The geometry of each track type has been created to represent generic types rather than specific systems. The three track-type models were subjected to loads associated with a typical rail bogie for different substructure support conditions, intended to reproduce stiff, soft and variable supports. For the initial evaluation, track superstructure systems with continuous (unjointed) bending stiffness were considered.

2   Methods

2.1   General Principles

The superstructure was modelled using proprietary software [14], with a combination of general-purpose brick, wedge and tetrahedral elements (C3D8I, C3D6 and C3D4) and a mesh seed size of ~ 80 mm. The support stiffness was represented using elastic foundation elements [14] characterized by a foundation modulus, with the foundation pressure acting directly on the surface of the structure it supports. The equivalent spring stiffness is the product of the elastic foundation modulus and the area to which it is applied. The foundation modulus may also be converted to a track modulus, which is a common way of defining the support to a railway track system [15]. For convenience, these definitions are given in Table 1.

In the units column of Table 1, the length term L sometimes appears twice. In all cases, the first occurrence relates to the downward deflection and the second, where present, to the length of track or area of trackbed. A further complicating feature with the use of a foundation modulus or indeed any of the types of support stiffness specified in Table 1 is that they do not directly convert to E_{v2}. An E_{v2} value is an

Table 1 Track stiffness definitions

Parameter	Units	Conversion from foundation modulus
Foundation modulus	$F\,L^{-1}\,L^{-2}$	N/A
Spring stiffness	$F\,L^{-1}$	Multiply by area (e.g. area per sleeper spacing or per metre of track)
Track modulus	$F\,L^{-1}\,L^{-1}$	Multiply by effective width of foundation (e.g. by length of sleeper)

estimate of Young's modulus over the depth of soil influenced by the bearing plate—in effect, a lumped average material and geometric response to a specified load. In this paper, values of foundation modulus have been selected based on measured ballasted track performance (e.g. [16, 17]) rather than specific subgrade responses to plate bearing tests.

2.2 Support Stiffnesses and Allowance for Rail Pad

Railway tracks run over a range of different subgrade soils and earthwork types. Three cases of support stiffness were investigated as shown in Fig. 1. The hard support is defined as having an equivalent track modulus of 60 N/mm/mm and the soft of 10 N/mm/mm selected on the basis of the literature [18]. Cases (a) and (b) have a uniform support stiffness; case (c) represents a variation of hard and soft regions along the track in 10 m lengths. The intention is to evaluate performance over a range of plausible subgrade supports that do not necessarily meet the slab track requirements for E_{v2} values (for which a direct conversion is not in any case possible).

The equivalent track moduli, shown in Fig. 2, were applied for the three superstructure geometries using the principles of conversion defined in Table 1. This is a conservative assumption in terms of the calculated deflection for the ladder and slab tracks as it takes no benefit from the increased substructure contact areas. The ratio of contact areas is shown in Table 2.

The track moduli proposed represent the effective support seen by the rail. To assign a suitable value to the foundation below the sleeper, ladder or slab support requires an allowance to be made for the compliance of the rail pad. This can be
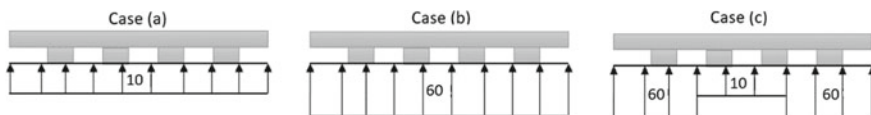
Fig. 1 Track modulus (N/mm/mm) evaluated along 26 m track lengths applied to the rail
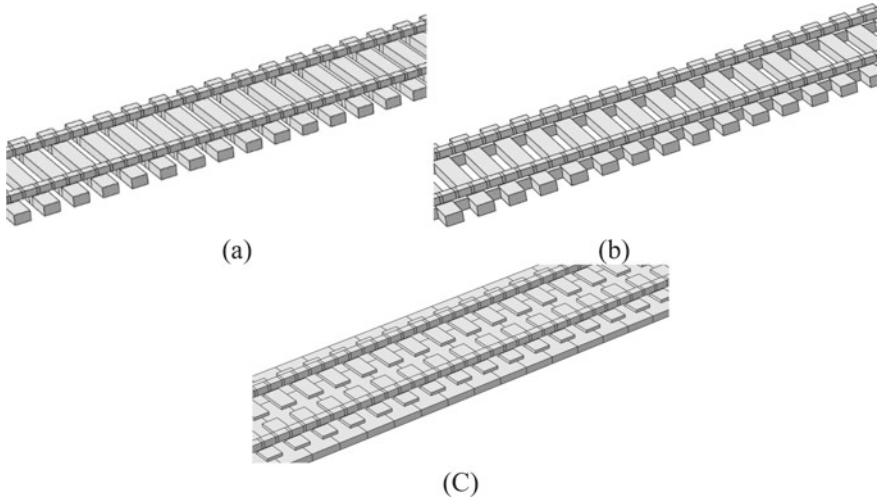
Fig. 2 Track types. **a** conventional ballasted track, **b** ladder track, **c** slab track

achieved by considering them as springs in series, with a total stiffness given by $1/k_{total} = 1/k_{trackbed} + 1/k_{railpad}$.

2.3 Loading and Boundary Conditions

Two vertical loads, each of 75 kN, were applied at a distance of 2.75 m apart, corresponding to an approximate axle spacing on a single bogie, on each rail near the centre of each model (i.e. four loads in total). Loads were applied over individual sleepers to ensure symmetrical deflection. A 26 m length of track was modelled. The rails were fixed in all directions at both ends. Taking advantage of symmetry, half of the geometry across the track was modelled using appropriate boundary restraints.

2.4 Geometry

The dimensions, properties and assumptions used in modelling each of the generic track forms shown in Fig. 2 are summarized in Table 2.

The sleeper spacing, sleeper depth, slab depth and overall dimensions were chosen to be representative of a range of systems currently available, but some of the shapes were simplified for ease of modelling. The height of the full slab was reduced so that, together with the rail mounting plate, the overall track form height matched that of the sleeper and ladder tracks. Also, the spacing of sleepers was set to a likely minimum to maximize the area in contact with the elastic foundation. (The

Table 2 Model parts dimensions and properties

Track form	Sleeper	Ladder	Slab	Reference/justification
Spacing (mm) of rail supports	550	550	550	Minimum recommended spacing on Network Rail
Major dimensions of support structure (mm) (W × L × H: sleeper) (W × L × H: ladder cross-ties + W × L × H: per ladder beam), (L × H: continuous slab)	300 × 2500 × 200	300 × 2500 × 200 250 × 300 × 200	2800 × 140	B30 sleeper [16], slab [4] W: along the track/rail major axes, L: across the track, H: vertical height. Ladder dimensions in two parts for the cross-ties and the additional beam parts per rail along the track length (see Fig. 2)
Rail support structure at given spacing	N/A	N/A	300 × 1000 × 60	Support per rail, per spacing (see Fig. 2)
Elastic modulus of concrete (N/mm^2)	30,000			
Elastic modulus of rail steel (N/mm^2)	205,000			[19]
Equivalent rail dimensions (mm)	150 × 134.5			Vignole 60 kg/m rail converted to a rectangular section of equivalent I
Elastic modulus of pads (N/mm^2)	16			Equivalent to a spring support of 60 kN/mm for pad specified (see next row)
Rail pad dimensions (mm)	150 × 300 × 12			Equivalent to the rail width and sleeper width
Poisson's ratio (all)	0.3			[17]
Bending stiffness, EI (Nmm^2)	6.2×10^{12}	1.2×10^{13}	1.7×10^{13}	Weighted average by volume, not including rails
Contact area ratio	1	1.2	2.05	Relative to sleeper/ballasted track

minimum recommended centre-to-centre distance between two sleepers on network rail is 550 mm.) The track modulus was distributed between the rail pads and the trackbed. These simplifications retain the general characteristics of each track form, but facilitate comparison on an equitable basis.

Table 3 Simulations carried out

Name	Track type	Track modulus (N/mm/mm) (case)	Trackbed modulus (allowing for rail pad) (N/mm/mm)	Foundation modulus (allowing for rail pad) (N/mm/mm^2)
C10	Conv	10 (a)	11	0.0161
C60	Conv	60 (b)	133	0.196
L10	Ladder	10 (a)	11	0.0135
L60	Ladder	60 (b)	133	0.163
S10	Slab	10 (a)	11	0.00786
S60	Slab	60 (b)	133	0.095
C6010	Conv	60 and 10 (c)	Combinations of above	Combinations of above
L6010	Ladder	60 and 10 (c)		
S6010	Slab	60 and 10 (c)		

2.5 Simulations Carried Out

Table 3 summarizes the simulations carried out, and the values of trackbed modulus converted to foundation modulus are applied making allowance for a rail pad with a spring stiffness of 60 kN/mm.

2.6 Loading

Loading was applied in a ramped pseudo-static manner at the central portion of each track length by means of two pressures applied over conveniently located vertically facing rail elements. The application of the wheel loads as pressures for these simplified simulations avoids stress localization and obviates the need for a computationally expensive finer mesh.

2.7 Calculation Outputs

In each simulation, stresses and deflections are presented along a suitable calculation path as follows:

- *Longitudinal paths*: Two paths were placed: One directly below the rails (above the pads) and the other one below the track support (above the trackbed).
- *Transverse paths*: under each sleeper or cross-tie, or 550 mm apart for the slab track.

As an example, the calculation paths for the ladder track are shown in Fig. 3.
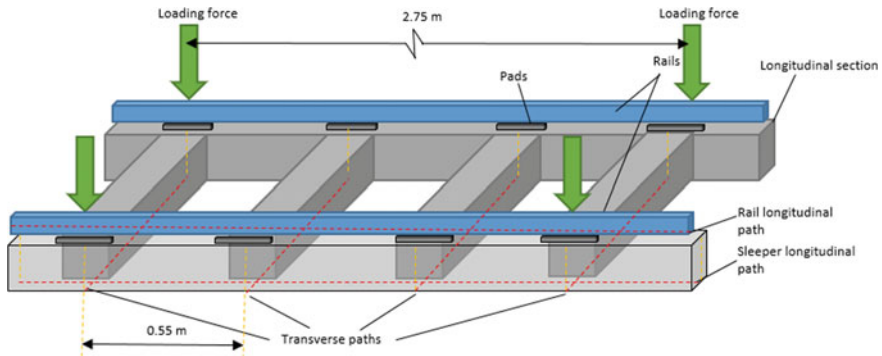
Fig. 3 Calculation paths for output data (not to scale)

Comparative performance was then evaluated considering the stress and deflection profiles.

3 Validation

The models were compared with results from a closed-form beam on an elastic foundation (BOEF) solution [18] using the track moduli indicated in Table 3. Figure 4 compares the BOEF analyses deflections with those calculated below the rails in the numerical simulations, for the three track types and different support stiffnesses.

For the conventional (sleeper) track system, the calculated deflected profiles are in close agreement (Fig. 4a). The increased bending stiffness of the ladder and slab track reduces the maximum deflections and increases the extent of the deflection bowl (Fig. 4b, c). Minor discrepancies arise as a result of the more complex material modelling and boundary conditions in the FEM analyses.

4 Results and Discussion

4.1 Deflections

The calculated deflections below the track structure are shown in Fig. 5. The "W" shape of the deflected profile is more pronounced for conventional track, where the sleepers are relatively free to rotate. Deflections for the ladder and slab track forms are very close to each other.

Figure 6 shows the transverse deflections of each track form. As might be expected, the range in deflection is reduced as the stiffness of the track form is increased, and it is reduced with increasing foundation stiffness.
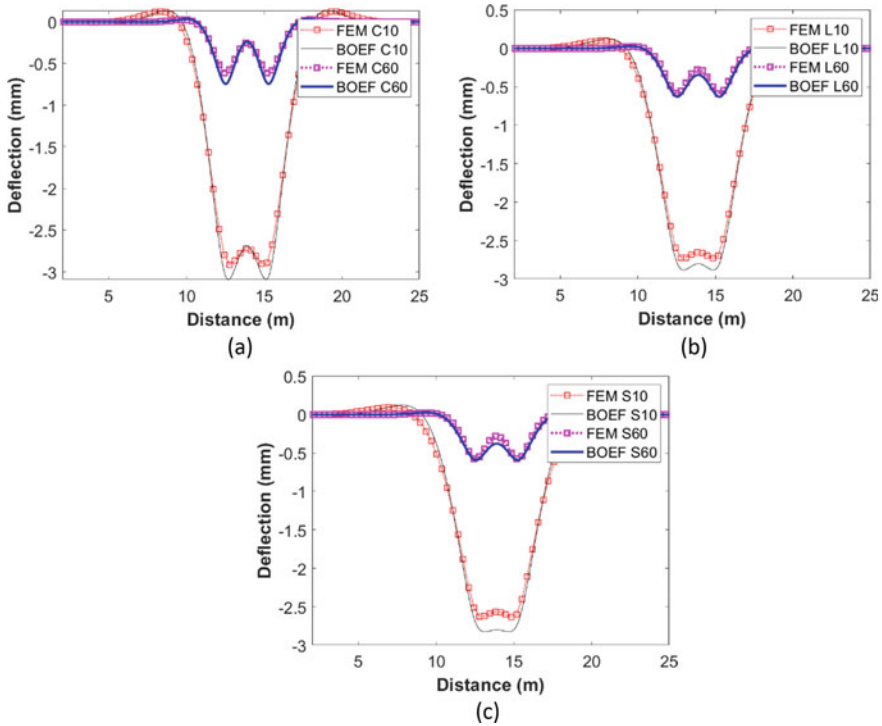
Fig. 4 Comparison of FEM and BOEF analysis results: **a** conventional ballasted, **b** ladder and **c** slab track

Figure 7 shows the longitudinal profile of peak stress transmitted to the foundation (the top surface of the trackbed) for the three track forms and different support conditions.

Stresses were determined along the paths indicated in Fig. 3 and were calculated as the products of the calculated deflections and the specified foundation moduli. Because the slab and ladder tracks have much greater trackbed (foundation) contact areas than the conventionally ballasted track system (see Table 2), the reduction in peak stress for these systems is very significant. Peak stresses are approximately $^1/_3$ and $^1/_2$ of those for conventional track for the slab and ladder systems, respectively, for the stiffest support case. Peak stresses tend to increase with increasing foundation stiffness. If the support stiffness is non-uniform, the slab track distributes the loads more evenly, giving more uniform distribution of foundation pressure with significantly lower peaks. In these simulations, the effective track modulus was kept constant between the simulations; this will give conservative results in terms of deflection but may exaggerate the reductions in stress achieved.
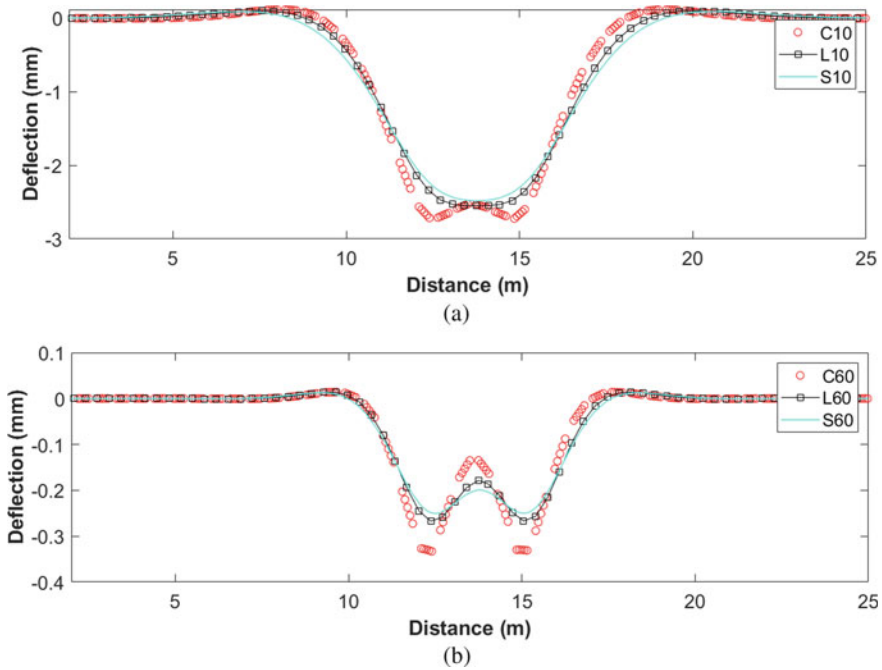
Fig. 5 Deflections at the base of the track, for a trackbed modulus of **a** 10 N/mm/mm and **b** 60 N/mm/mm. Note the vastly different vertical scales
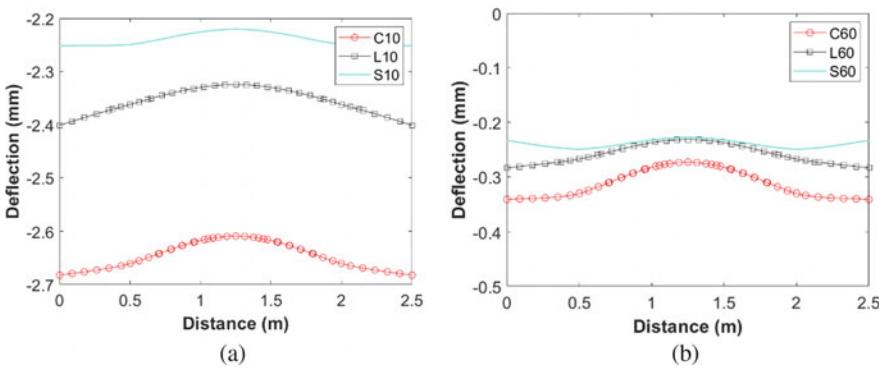
Fig. 6 Transverse deflection (across the track) at the top of the trackbed, for a foundation stiffness of **a** 10 N/mm/mm, **b** 60 N/mm/mm. Stress transfer onto the trackbed

5 Summary

In total, nine simulations were carried on three different types of railway tracks using 3D finite element analysis. The aim was to assess the importance of longitudinal
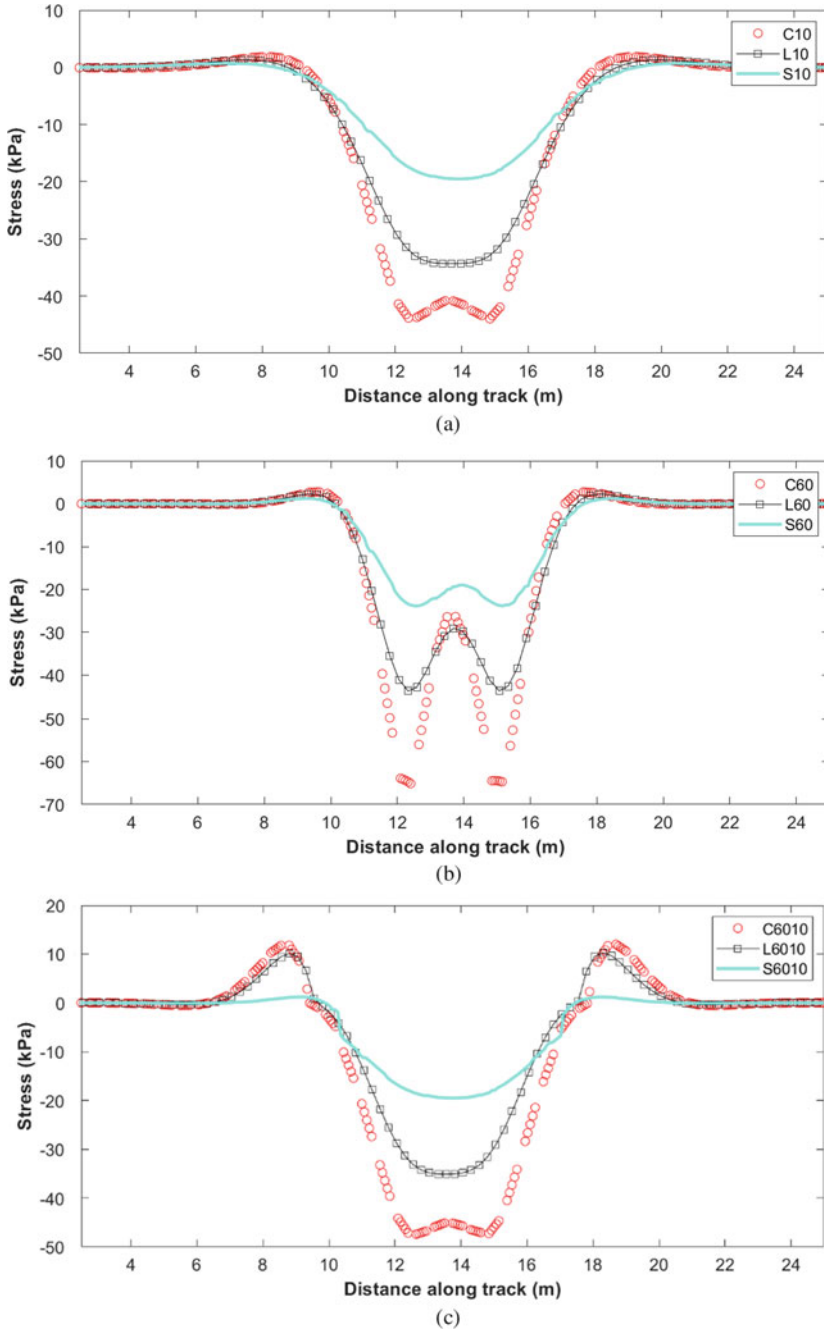
Fig. 7 Peak stresses transmitted to the trackbed surface for different track types and **a** uniform soft (10 N/mm/mm), **b** uniform hard (60 N/mm/mm) and (c) non-uniform support conditions

bending stiffness on stresses and deflections, for different track support conditions. It was found that slab tracks distribute pressures more uniformly. Where the support is non-uniform, slab tracks show better load distribution and more uniform foundation stresses. The deflection profiles of all the track forms were similar in shape, with differences mainly in the magnitude of the deflection in both the longitudinal and transverse directions. In quantitative terms, the results show that for the cases analyses the peak trackbed stresses can be reduced by as much as factors of 3 and 2 for the slab and ladder systems, respectively, compared with conventional track for a given track modulus. The ladder and slab tracks also gave a more uniform distribution of stress, when spanning over a locally softer support.

References

1. Wakui H, Matsumoto N, Inoue H (2005) Technological innovation in railway structure system with ladder track system. Tokyo Railway Technical Research Institute
2. Hillig J (1994) Erdbautechnische Anforderungen ain eine schotterlose Fahrbahn. Der Eisenbahningenieur 45(5):324–334
3. Gautier PE (2015) Slab track: review of existing systems and optimization potentials including very high speed. Constr Build Mater [Internet]. 92:9–15. Available from: https://doi.org/10.1016/j.conbuildmat.2015.03.102
4. Railone (2011) Rheda 2000 Ballastless Track System
5. FIB (2006) Precast concrete railway track systems. International Federation for Structural Concrete, 41p
6. Zhao X, Li Z, Liu J (2011) Wheel-rail impact and the dynamic forces at discrete supports of rails in the presence of singular rail surface defects. Proc Inst Mech Eng Part F J Rail Rapid Transit. 226(2):124–39. Available from: https://doi.org/10.1177/0954409711413975
7. Esveld C (2001) Modern railway track.MRT-Productions, vol 53, p 160
8. International Union of Railways (2008) UIC Code 719—Earthworks and track bed construction for railway lines
9. BSI Standards (2018) BS EN 16432–2:2017—Railway applications—Ballastless track systems
10. Esveld (2016) Interview
11. Chen L, Chen J, Wang J (2018) Applied sciences calculation of reasonable tension value for longitudinal connecting reinforcement of CRTSII Slab Ballastless track
12. Chung W, Kwon K, Jang SY (2014) Deflection-based load transfer efficiency of floating slab track. KSCE J Civ Eng 18(2):616–624
13. Liu X, Qin H, Xiao J, Liu X, Zhang W (2019) Effects of interface strength on damage to railway slab—track joints under temperature rise, pp 1–12
14. Simulia (2014) Abaqus User's Guide
15. Timoshenko S (1927) Method of analysis of statical and dynamical stresses in rail. Proceedings of 2nd international congress for applied mechanics, pp 1–12
16. Railone (2014) Concrete sleepers
17. Roylance D (2008) Mechanical properties of materials

18. Powrie W, Le Pen L (2016) TSWG. A guide to track stiffness. Cross Industry. Available from: https://www.thepwi.org/technical_hub/technical_hub_files/a_guide_to_track_stiffness_final_reviewr11

19. Le Pen L, Milne D, Thompson D, Powrie W (2016) Evaluating railway track support stiffness from trackside measurements in the absence of wheel load data. Can Geotech J. 53(7):1156–66. Available from: https://eprints.soton.ac.uk/391563/

Track Geomechanics for Future Railways: Use of Artificial Inclusions

Buddhima Indraratna [ID], **Trung Ngo** [ID], **Yujie Qi** [ID],
and Cholachat Rujikiatkamjorn [ID]

Abstract Given that current ballasted tracks cannot support faster and heavier Australian heavy freight trains, the need to develop innovative and sustainable ballasted tracks for transport infrastructure is crucial. This paper reviews and discusses the use of artificial inclusions such as recycled rubber mats, end-of-life tyres, and geogrids to stabilize ballasted rail tracks overlying soft formation soil. It also presents a novel solution for increasing the stability and resiliency of track structure by energy-absorbing recycled rubber tyres. This study confirms that a capping layer confined by tyres will actively reduce ballast breakage within the track substructure. Numerical simulations employing discrete element method (DEM) are also carried out to study the micro-mechanical aspects of ballast aggregates and the interaction between the particles and inclusions. This study shows that waste rubber products and geosynthetics will eliminate the need for a capping layer in certain terrain and help to decrease the thickness of the ballast layer. The outcomes of this study will lead to a better understanding of the performance of ballast tracks reinforced with artificial inclusions and also help to improve the design and cost-effectiveness of ballasted tracks, with a view to enhancing passenger comfort and safety.

B. Indraratna
Civil Engineering, Transport Research Center and ARC Training Centre for Advanced Technologies in Rail Track Infrastructure (ITTC-Rail), School of Civil and Environmental Engineering, University of Technology Sydney, Sydney, NSW 2007, Australia
e-mail: buddhima.indraratna@uts.edu.au

T. Ngo (✉) · Y. Qi
School of Civil and Environmental Engineering, University of Technology Sydney, Sydney, NSW 2007, Australia
e-mail: Trung.Ngo@uts.edu.au

Y. Qi
e-mail: yujie.qi@uts.edu.au

C. Rujikiatkamjorn
Civil Engineering, School of Civil and Environmental Engineering, University of Technology Sydney, Sydney, NSW 2007, Australia
e-mail: cholachat.rujikiatkamjorn@uts.edu.au

Keywords Track geomechanics · Artificial inclusions · Numerical modelling

1   Introduction

Australian railways offer an efficient mode of transportation for freight and passengers across all the States. However, the dynamic impact loads induced by heavy haul trains cause breakage, lateral spreading, and settlements of ballast which leads to rail-tie misalignment and decreased load bearing capacity, all of which compromises safety and entails frequent track maintenance [1, 2]. For these reasons, conventional ballasted rail tracks should be enhanced so they can deal with the increased demand for heavier freight trains.

Artificial inclusions such as geo-composites (e.g. geogrids) and energy absorbing inclusions (rubber mats) produced from recycled tires are becoming more popular worldwide because they eliminate the hard interfaces between ballast aggregates and concrete sleepers. This increases contacts of surface area of the ballast and reduces ballast stresses [3–8]. Moreover, some of these artificial inclusions can be obtained through recycled materials such as waste tyre, which in a way reduces the stockpiling of waste materials and the cost of using natural aggregates.

However, since the number of studies that analyse how well synthetic inclusions actually improved performance of tracks is still limited, this paper reviews current research done at the University of Wollongong Australia (UOW) using large-scale test facilities and computational modelling to evaluate the ability of artificial inclusions (i.e. under-ballast mats, tyre cells, granular waste mixtures, and geogrids) to eliminate ballast degradation and associated deformation.

2   Large-Scale Laboratory Testing

2.1   Use of Under-Ballast Mat for Improved Performance of Ballast

The track process simulation testing apparatus (TPSTA) was used to study the effect that under-sleeper pads (USPs) have on the load deformation of ballast. The testing chamber of this TPSTA is based on the unit cell of a standard gauge track (800 mm × 600 mm × 600 mm). It has four moveable walls connected by hydraulic jacks placed on ball bearings and hinges (Fig. 1a), so the walls can be fixed or moved laterally. The cyclic loading frequency can be applied up to 30 Hz, and the axial load can simulate a train up to 40-tonne axle load. There are pressure plates and settlement pegs (Fig. 1b, c) in the TPSTA placed on top of the ballast layer to measure the stress and ballast deformation during testing. A concrete sleeper with rail is placed on top of the test specimen to simulate the field condition. Around the concrete sleeper is filled with shoulder ballast. Further details of the instrumentation and the placement
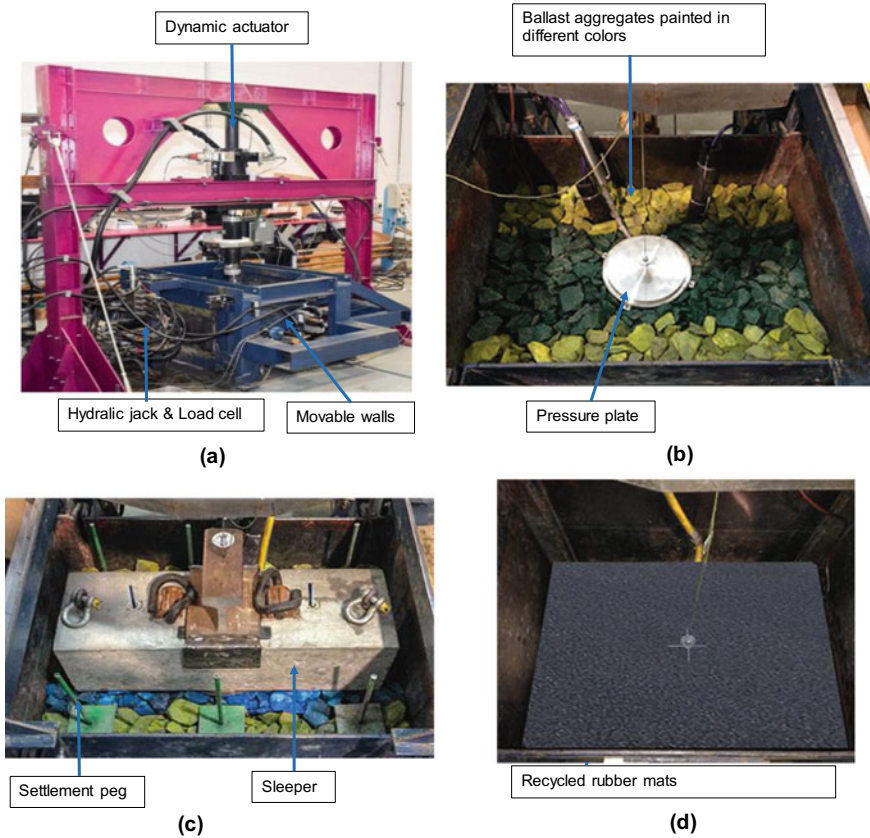
Fig. 1 TPSTA: **a** 3D view; **b** Ballast aggregates and pressure plate; **c** Settlement pegs; and **d** Recycled rubber mat

of track substructure layers, including a plan view and cross section of the TPSTA, can be found elsewhere [9, 10].

The ballast is ordinary igneous rock aggregates collected from a quarry in Wollongong and crushed to comply with Australian standard AS:2758.7: (2015). The capping layer (sub-ballast) is a mixture of sand and gravel, and the soft subgrade is a mixture of sandy-clay soil. There is a 10 mm-thick under-ballast mat (UBM) made from recycled rubber tyres to be placed beneath the ballast layer (Fig. 1d) to investigate its performance under cyclic loading. The stiffness of the tested UBM at 5–05 Hz was measured in laboratory, the average C_{stat} from the three samples is 0.20 N/mm³, and the C_{dyn} ranged from 0.46 to 0.59 N/mm³ for the UBM made from recycled shredded tyre waste. Tests took place under 25 and 35-tonne axle loads (assumed 40% per sleeper) at varied frequencies ($f = 15$–25 Hz), during which the vertical and lateral displacement of the ballast assemblies were monitored at given time intervals [4]. The thickness of ballast, capping, and subgrade layers typically
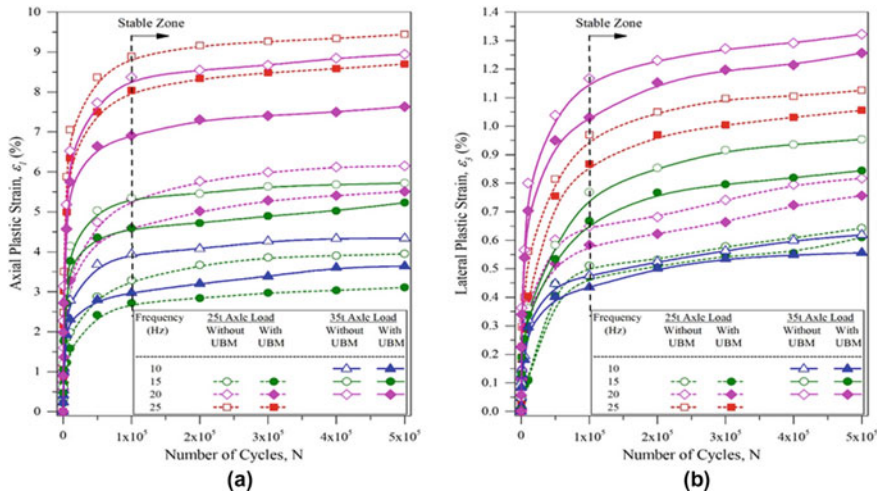
Fig. 2 Measured laboratory test data: **a** axial strain, ε_1 versus load cycles (N); and **b** lateral strain, ε_3 v.s N (modified after Navaratnarajah et al. [4]-with permission from ASCE)

used for the tests was 300, 150, and 150 mm, respectively. The ballast aggregates were sieved after each test to determine the amount of breakage. The wall could be moved outward during the tests, and the associated displacements (i.e. strains) were measured by potentiometers.

Figure 2 shows the accumulated vertical and lateral deformations and the corresponding strain of ballast (with/without UBM). Under a given axle load and frequency f, the UBM reduced the vertical and lateral strain in the ballast by up to 21 and 12%, respectively. Moreover, the overall ballast degradation (breakage) had decreased by 35%, and there was an almost 19% reduction in vertical stress at the base of the ballast–concrete interface.

2.2 Use of Scrap Rubber Tyres for Capping Confinement

Scrap tyres have been trialled at the UOW to confine the capping (sub-ballast) layer because they provide additional cellular confinement to the infilled aggregates and also increase the strength and stiffness of the railway track. Indraratna et al. [11] proposed using rubber tyres as a base for the capping layer where one side wall was cut and the tyres were infilled with aggregates. A geotextile was placed between tyres and the subgrade as a separator. Previous studies revealed that from an engineering perspective, a tyre cell has three main effects: (i) extra confinement provided by the tyre will increase the stiffness; (ii) it provides more uniform stress distribution onto the subgrade; (iii) the tyres will also increase the damping of the track and its ability to attenuate dynamic forces. The TPSTA used to carry out cyclic tests of recycled
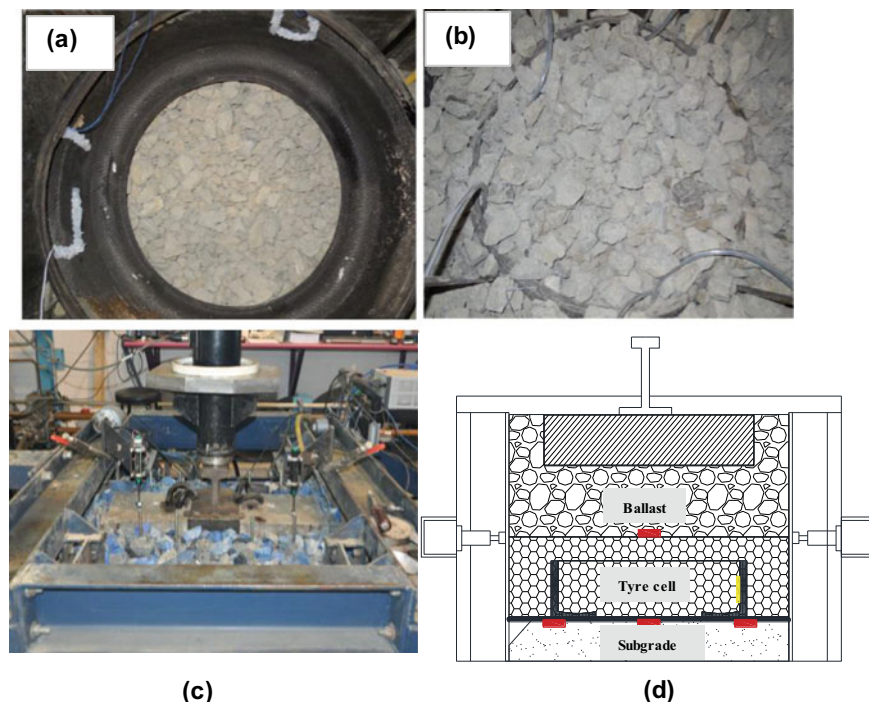
Fig. 3 **a** Recycled tyres before installing the strain gauges, **b** tyres filled with capping aggregate, **c** TPSTA test set-up, **d** schematic showing the placement of tyre in capping

tyres and confined capping layer is presented in Fig. 3. The cyclic loading frequency was 15 Hz, and the maximum vertical pressure was 385 kPa to simulate the track field condition of a heavy haul with 40-tonne axle load running at 115 km/h. The cyclic loading test continued until 500,000 cycles were achieved.

Measured test results show that having a tyre in the capping layer vastly improved lateral confinement of infills, thus mitigating the lateral spreading and degradation of ballast, while improving the damping properties of the system (Fig. 4a). It also reduced the track modulus (Fig. 4b), which may be of some benefit for sections of track over rigid foundations such as transition zones and concrete bridge decks where vertical stiffness should be reduced to avoid abrupt changes in stiffness along railway embankments.

Finite element modelling (FEM) was carried out to study the beneficial effect that recycled tyres have on track embankments, as shown in Fig. 5. Details of the FEM model, including the loading and boundary conditions and the model parameters, can be found in Indraratna et al. [11]. The simulations showed that with waste tyres, the stress imparted onto the subgrade was almost 12% less than where there are no tyres (Fig. 6). In summary, they showed that a capping layer stabilized with rubber
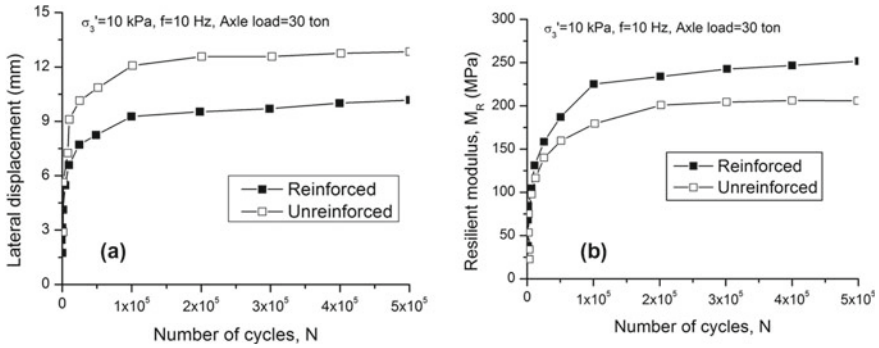
Fig. 4 **a** Measured lateral displacement; **b** measured resilient modulus (modified after Indraratna et al. [11])
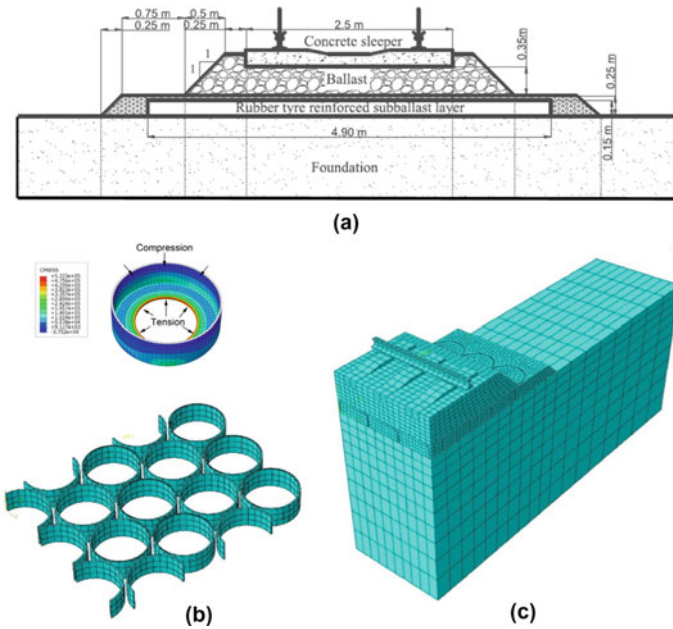
Fig. 5 **a** Track geometry with recycled rubber tyre, **b** FEM mesh for recycled rubber tyres, and **c** Simulated track section with tyres (modified after Indraratna et al. [11])

tyres reduces the stress transferred onto the ballast and subgrade layers, mitigates ballast breakage and particle displacements, and enhances damping of the system.
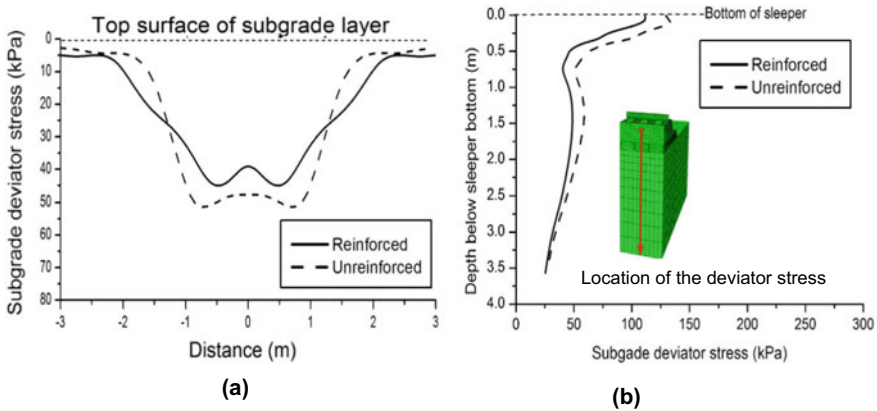
Fig. 6 Role of recycled rubber tyres on: **a** distribution of subgrade stress, and **b** distribution of stresses against depth (modified after Indraratna et al. [11])

2.3 A Synthetic Energy-Absorbing Layer for Railway Sub-ballast

It has been reported that recycled rubber crumbs (RC) have higher energy-absorbing property compared to natural aggregates [7, 12–17]. To extend the usage of mining waste such as steel furnace slag (SFS) and coal wash (CW) in dynamic loading project (i.e. rail tracks), Indraratna et al. [15] have introduced RC into the blends of SFS and CW to develop a synthetic energy-absorbing layer (SEAL) for railway sub-ballast. The rubber crumbs obtained through shredding of waste tyres having sizes (0–2.3, 0.3–3, and 1–7 mm) were utilized. The optimal waste mixture to be used as sub-ballast has been optimized as SFS:CW = 7:3 with 10% RC mixing by weight (i.e. SEAL10), and through a series of comprehensive laboratory tests, the advantages of adding 10% RC into the mixture of SFS and CW have been identified as (i) reducing the swelling potential of SFS and the particle breakage of CW, and (ii) increase the ductility and energy-absorbing properties of the waste mixtures [12–18]. Qi et al. [17] also proposed an energy-absorbing concept and concluded that installing the SEAL10 to the rail track will help to reduce the ballast degradation and minimize the track deformation as more energy input will be absorbed in the SEAL rather than go to other layers. To verify this, large-scale cubical triaxial tests using the TPSTA at the University of Wollongong have been carried out to examine the deformation behaviour and ballast degradation of the track specimen with and without SEAL10.

Figure 7a illustrates the schematic of the large-scale test specimen, where the SEAL (150 mm thick) is placed between a layer of 200 mm-thick ballast and a layer of 100 mm-thick structural fill, and a concrete sleeper with rail is installed on top of the test specimen. Around the concrete sleeper is filled with the shoulder ballast (in red). Figure 7b-c shows the procedure for preparing the test specimen. To check
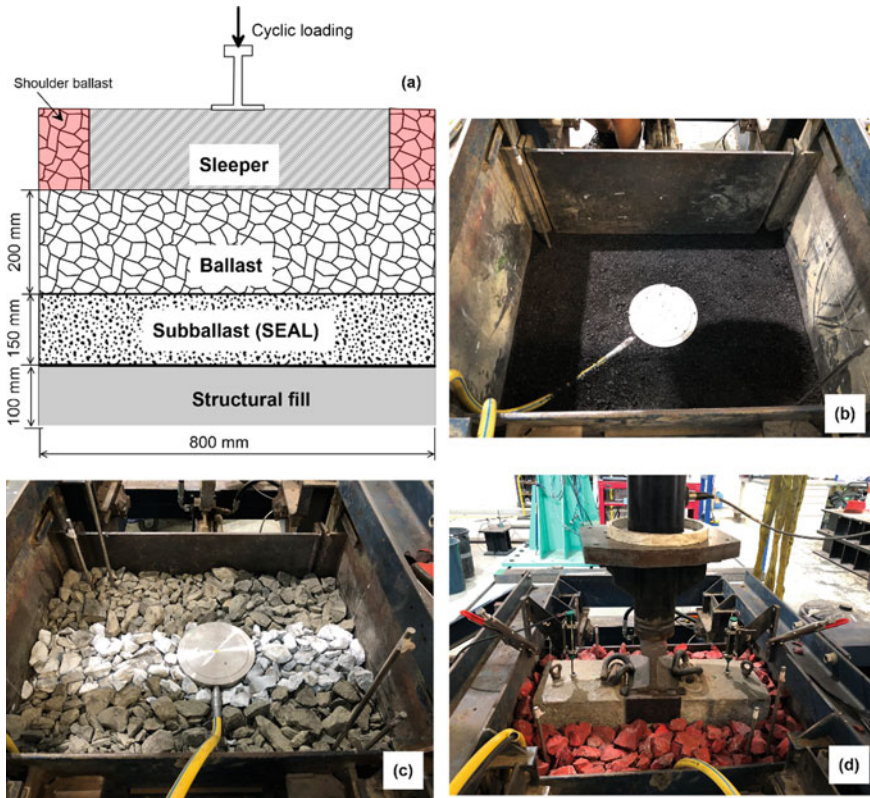
Fig. 7 **a** Schematic showing the track specimen incorporating SEAL, **b** installing the SEAL, **c** compacted ballast on top of SEAL, and **d** install the shoulder ballast and the concrete sleeper

the ballast breakage, the ballast directly under the sleeper was coloured in white and re-sieved after each test. The cyclic loading test was conducted with frequency $f =$ 15 Hz, and the vertical stress under the sleeper is 230 kPa to simulate a train with a 25-tonne axle load running at 115 km/h. The effective confining pressure was 15 kPa to simulate the field condition. Each test was completed when 500,000 cycles were achieved.

The vertical and lateral deformation varying with the loading cycles of the track specimen incorporated with SEAL10 are shown in Fig. 8. To compare its performance with that of a traditional track, the test results from previous studies [4, 9] with traditional track materials under the same loading conditions are also shown in Fig. 8. Note that the settlement and the lateral deformation (dilation) accumulate rapidly before 50,000 cycles due to the initial densification and particle rearrangement, and then, the accumulation rate gradually decreases to the end of the test. Comparing to the test results with traditional materials, the test specimen with SEAL10 shows a promising performance with less settlement and lateral deformation.

Fig. 8 Settlement and lateral deformation of the large-scale cubical triaxial test with and without SEAL (modified after Qi and Indraratna [20])
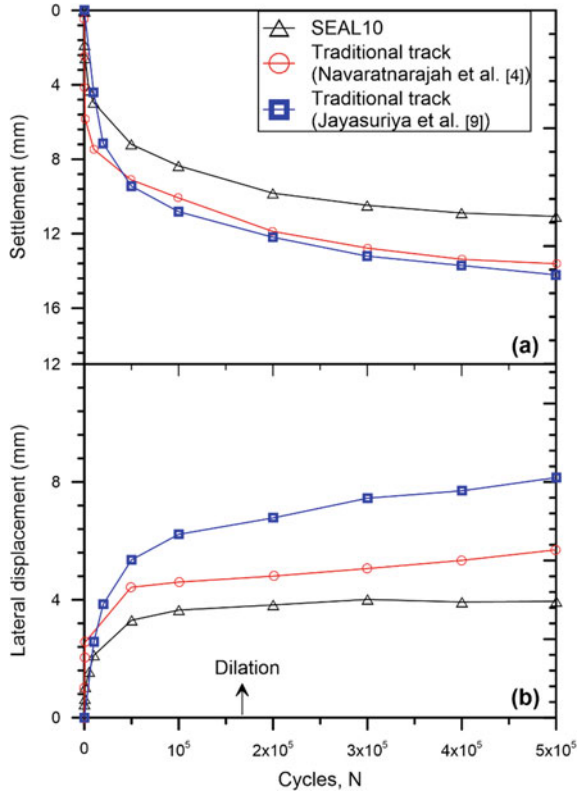
The ballast breakage is evaluated using the ballast breakage index (BBI) initially proposed by Indraratna et al. [19] by comparing the particle size distribution curve of ballast before and after each test:

$$\mathrm{BBI} = A/(A + B) \tag{1}$$

where A denotes the area enclosed by the particle size distribution curves of ballast before and after the test, and B denotes the area enclosed by the initial particle size distribution curve and the arbitrary boundary of maximum breakage. The detailed definition of BBI is shown in Fig. 9a. Figure 9b shows the BBI of the test specimen with and without SEAL10, where the BBI of the track specimen with traditional track materials is around 0.6, while the one with SEAL10 is 0.31, indicating that the inclusion of SEAL10 can significantly reduce the ballast degradation. This further verifies the energy-absorbing concept proposed by Qi et al. [17].
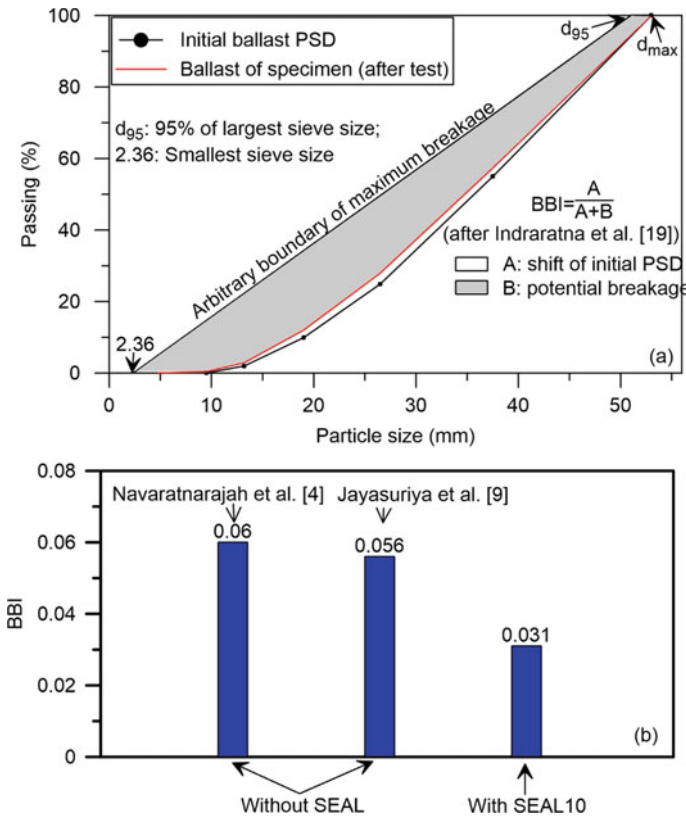
Fig. 9 **a** Definition of the ballast breakage index (BBI, modified after Indraratna et al. [19]) and **b** BBI of the large-scale cubical triaxial test with and without SEAL (modified after Qi and Indraratna [20])

3 Discrete Element Modelling for Ballast

While the discrete element method (DEM) developed by Cundall and Strack [21] has been widely used to study the mechanical behaviour of granular aggregates, it has also been used to simulate ballast grains as it can capture the discrete nature which contains arbitrarily shaped discrete particles [22–28]. The DEM approach can simulate ballast particles of various sizes and shapes by bonding many spheres to represent the actual shape and angularity of ballast (Fig. 10a). A biaxial geogrid with a 40 mm × 40 mm aperture was modelled by connecting a number of small spheres, and similarly, the geogrids tested in the laboratory (Fig. 10b). The DEM for a large-scale direct shear test of geogrid-reinforced fresh and fouled ballast is shown in Figs.10c-d. Micro-mechanical parameters used to simulate ballast, geogrid, and coal-fouling material to obtain these parameters can be found in Ngo et al. [24]. DEM simulations for large-scale direct shear box tests were implemented for fresh
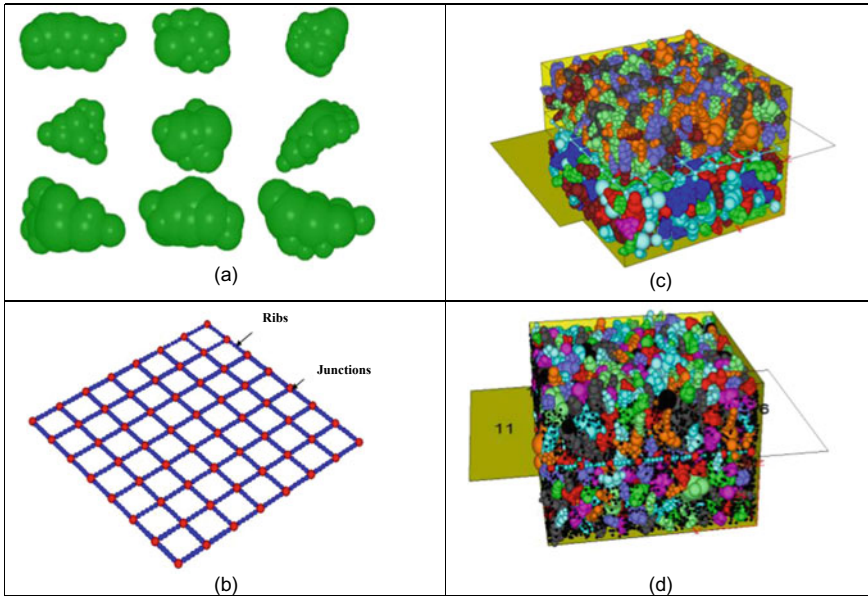
Fig. 10 Simulated large-scale direct shear test for geogrid-reinforced ballast (Ngo et al. [24])

ballast and 40%-VCI-fouled ballast (with/without geogrid). The VCI stands for void contaminant index, and it has been introduced earlier by Tenakoon et al. [29].

Figure 11 shows a comparison of the predicted shear stress–strain with those measured in the laboratory (with/without geogrid). Note that this simulation agrees quite well with the laboratory data from Indraratna et al. [30]. The strain softening and volumetric dilatancy of ballast shown in all the simulations indicate that the higher σ_n the greater the shear strength and the smaller the dilation. This can be explained by the interlocking effects that occur between the ballast particles and geogrid [31].

4 Selected Case Studies for Research Impact

4.1 New Ballast Gradation for Australian Rail Tracks

Other than adopting a subtle modification of British Standards, the standards and specifications for ballast in Australia have not changed for many decades. Ground conditions in Australia are completely different from other parts of the world which is why there is no international ballast design which considers the rate and extent of particle breakage. Particle breakage caused by the passage of trains has been considered in the development of new ballast gradations AS:2758.7 [32], which is why the
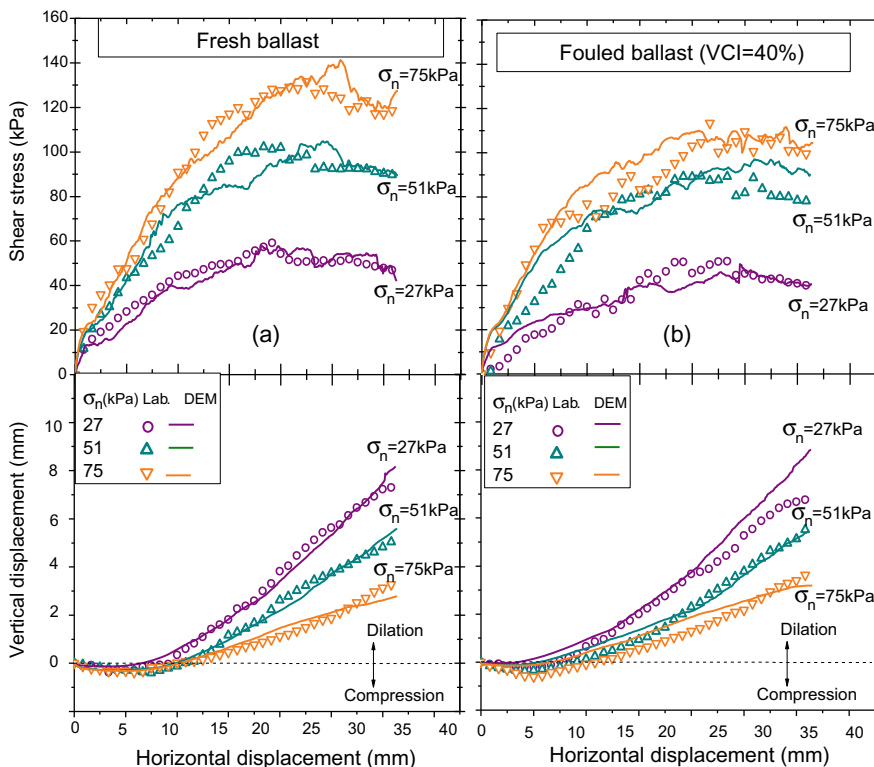
Fig. 11 Comparisons between DEM and laboratory test results: **a** fresh ballast, and **b** 40% VCI-fouled fouled ballast (Ngo et al. [24])

60-Graded gradation has been adopted by Sydney Trains (previously, RailCorp) for the design of new tracks. This new gradation has enhanced the capability for track upgrades, while allowing greater loads to be carried at increased speeds by utilizing existing infrastructure with minimum maintenance costs.

4.2 The Use of Geosynthetics with Recycled Ballast

The use of degraded ballast (i.e. recycled ballast from the spoil tips of Sydney Trains) strengthened with artificial plastic grids increased the internal stability by reducing the movement of aggregates. By using this technique to move from theory to practice, the novel track built at Bulli (north of Wollongong) via a joint collaboration between RailCorp and the University of Wollongong (UOW) has resulted in a resilient track that will bear greater train loads with less settlement; this track has been tested and monitored over a period of two years. This method has proved to be an excellent

solution for the need to quarry fresh ballast, while proactively contributing to reducing environmental degradation and saving the Australian rail industry millions of dollars.

4.3 New Design Software

Practicing engineers still prefer to develop simplified software that will provide solutions that are accurate enough for ballasted track design rather than sophisticated numerical modelling. The salient research outcomes that have evolved at the Centre for Geomechanics and Railway Engineering (CGRE), UOW, over the past two decades have resulted in a software: *Supplementary Methods of Analysis for Rail Track* (SMART) based on MATLAB subroutines, as the main user interface shown in Fig. 12. The SMART is unique and more comprehensive for preliminary track design and analysis because it is expected to revolutionize the current state-of-the-art of track design.
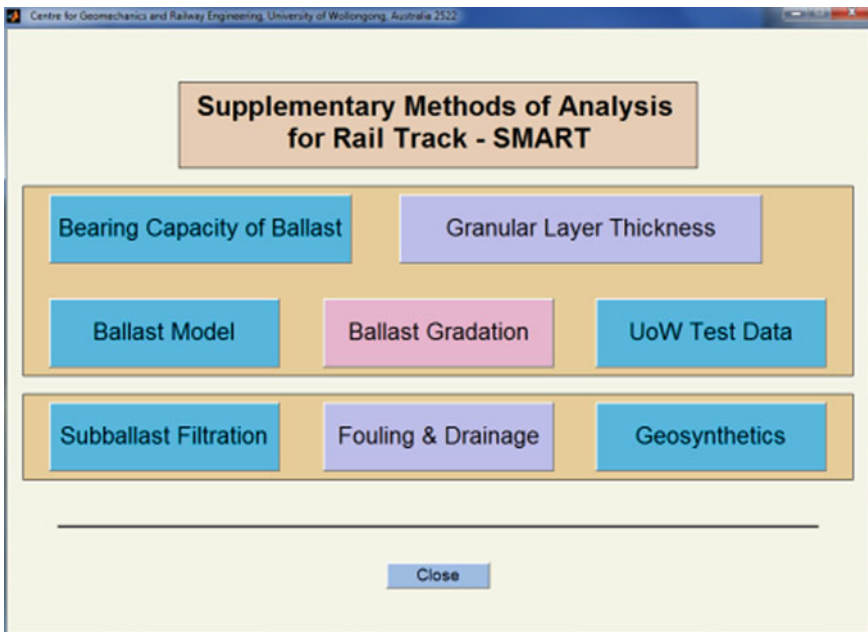
Fig. 12 Snapshot of SMART design software developed at UOW

5 Conclusions

This paper reviews recent studies carried out at the University of Wollongong Australia to examine the ability of artificial inclusions to minimize ballast deformation and associated breakage induced by heavy haul freight trains. The following conclusions can be drawn:

- The laboratory tests showed that the inclusion of under-ballast mats (UBMs) reduced the permanent deformation of ballast and decreased particle breakage by up to 50% because their energy-absorbing properties reduced the dynamic amplification of train loads.
- An approach of confining the capping layer with recycled rubber tyres for increased stability and resiliency of track substructure was tested using large-scale TPSTA tests under cyclic loading conditions. FEM simulations on the use of tyres to provide additional confinement to ballasted tracks were also implemented. The laboratory and FEM results proved the role of recycled rubber tyre by reducing the stress transmitted to the subgrade that could effectively decrease the required ballast thickness.
- The performance of the track specimen incorporated with a proposed synthetic energy-absorbing layer (SEAL10) was investigated through a large-scale cubical triaxial test. The test results showed that the inclusion of SEAL10 reduces the vertical and lateral deformation of the track, as well as reducing the ballast degradation by almost 50% compared to test specimen with traditional materials.
- Laboratory tests and DEM simulations on ballast reinforced by geogrids proved that the geogrid reinforcement plays a substantial role in increasing the shear strength and controlling the permanent deformations of the ballast. This is attributed to the aggregate-geogrid interlock mechanism, which contributes to improved stability of the granular assembly leading to a more uniform distribution of the internal loads.
- There is no doubt that rubber tyres improved the geogrid–ballast interaction and increased the confinement of the capping layer, and moreover, the use of rubber products, particularly on harder subgrades, resulted in improved resilient tracks with enhanced longevity and stability with significant implications for the ongoing cost of track maintenance.

Sun, as well as others that contributed to the contents, as cited in respective publications. Salient contents from these previous studies are reproduced herein with kind permissions from the original sources. The authors are also grateful to Cameron Neilson, Duncan Best, Richard Berndt, and other CME technician for their assistance during the laboratory and field tests. The authors also thank Robert Clayton (English editor) for proofreading and professionally editing the manuscript.

References

1. Selig ET, Waters JM (1994) Track geotechnology and substructure management. Thomas Telford, London
2. Indraratna B, Ngo NT, Rujikiatkamjorn C (2013) Deformation of coal fouled ballast stabilized with geogrid under cyclic load. J Geotech Geoenviron Eng 139(8):1275–1289
3. Abadi T, Pen L, Powrie W (2019) Effect of sleeper interventions on railway track performance. J Geotech Geoenviron Eng 145(4):04019009
4. Navaratnarajah SK, Indraratna B, Ngo NT (2018) Influence of under sleeper pads on ballast behavior under cyclic loading: experimental and numerical studies. J Geotech Geoenviron Eng 144(9):04018068
5. Indraratna B, Sun Q, Ngo NT, Rujikiatkamjorn C (2017) Current research into ballasted rail tracks: model tests and their practical implications. Aust J Struct Eng 18(3):204–220
6. Biabani MM, Ngo T, Indraratna B (2016) Performance evaluation of railway subballast stabilised with geocell based on pull-out testing. Geotext Geomembr 44(4):579–591
7. Sol-Sanchez M, Thom NH, Moreno-Navarro F, Rubio-Gamez MC, Airey GD (2015) A study into the use of crumb rubber in railway ballast. Constr Build Mater 75:19–24
8. Tutumluer E, Huang H, Bian X (2012) Geogrid-aggregate interlock mechanism investigated through aggregate imaging-based discrete element modeling approach. Int J Geomech 12(4):391–398
9. Jayasuriya C, Indraratna B, Ngo TN (2019) Experimental study to examine the role of under sleeper pads for improved performance of ballast under cyclic loading. Transport Geotech 19:61–73
10. Indraratna B, Ngo NT, Rujikiatkamjorn C (2017) Improved performance of ballasted rail tracks using plastics and rubber inclusions. Procedia Eng 189:207–214
11. Indraratna B, Ngo NT, Sun Q, Rujikiatkamjorn C, Ferreira FB (2019) Concepts and methodologies for track improvement and associated physical modelling and field monitoring: geotechnics for transportation infrastructure. Lecture Notes in Civil Engineering vol 28, pp 219–246. Springer, Singapore
12. Qi Y, Indraratna B, Heitor A, Vinod JS (2019) The influence of rubber crumbs on the energy absorbing property of waste mixtures. In: Sundaram R, Shahu J, Havanagi V (eds) Geotechnics for transportation infrastructure, vol 29. Lecture Notes in Civil Engineering. Springer, Singapore, pp 271–281
13. Qi Y, Indraratna B, Vinod JS (2018) Behavior of steel furnace slag, coal wash, and rubber crumb mixtures, with special relevance to stress-dilatancy relation. J Mater Civ Eng ASCE 30(11):04018276
14. Qi Y, Indraratna B, Coop MR (2019) Predicted behaviour of saturated granular waste blended with rubber crumbs. Int J Geomech ASCE 19(8):04019079
15. Indraratna B, Qi Y, Heitor A (2018) Evaluating the properties of mixtures of steel furnace slag coal wash, and rubber crumbs used as subballast. J Mater Civil Eng ASCE 30(1):04017251
16. Indraratna B, Qi Y, Ngo TN, Rujikiatkamjorn C, Neville T, Ferreira FB, Shahkolahi A (2019) Use of geogrids and recycled rubber in railroad infrastructure for enhanced performance-laboratory and computational study. Geosci Spec Iss 9(1)

17. Qi Y, Indraratna B, Heitor A, Vinod JS (2018) Effect of rubber crumbs on the cyclic behaviour of steel furnace slag and coal wash mixtures. J Geotech Geoenviron Eng ASCE 144(2):04017107

18. Qi Y, Indraratna B, Heitor A, Vinod JS (2019) Closure to "effect of rubber crumbs on the cyclic behaviour of steel furnace slag and coal wash mixtures". J Geotech Geoenviron Eng ASCE 145(1):07018035

19. Indraratna B, Lackenby J, Christie D (2005) Effect of confining pressure on the degradation of ballast under cyclic loading. Géotechnique 55(4):325–328

20. Qi Y, Indraratna B (2019) Performance of recycled rubber/mining waste mixtures based on energy analysis. J Mater Civil Eng ASCE, Accepted 19th Dec 2019

21. Cundall PA, Strack ODL (1979) A discrete numerical model for granular assemblies. Géotechnique 29(1):47–65

22. McDowell GR, Li H (2016) Discrete element modelling of scaled railway ballast under triaxial conditions. Granular Matter 18(3):66

23. Tutumluer E, Qian Y, Hashash YMA, Ghaboussi J, Davis DD (2013) Discrete element modelling of ballasted track deformation behaviour. Int J Rail Transport 1(1–2):57–73

24. Ngo NT, Indraratna B, Rujikiatkamjorn C (2014) DEM simulation of the behaviour of geogrid stabilised ballast fouled with coal. Comput Geotech 55:224–231

25. O'Sullivan C, Cui L, O'Neill C (2008) Discrete element analysis of the response of granular materials during cyclic loading. Soils Found 48(4):511–530

26. Huang H, Tutumluer E, Hashash YMA, Ghaboussi J (2009) Discrete element modeling of aggregate behavior in fouled railroad ballast. Geotech Spec Publ 192:33–41

27. Bian X, Li W, Qian Y, Tutumluer E (2019) Analysing the effect of principal stress rotation on railway track settlement by discrete element method. Géotechnique 0:1–19. https://doi.org/10.1680/jgeot.1618.P.1368

28. Lobo-Guerrero S, Vallejo LE (2005) Discrete element method evaluation of granular crushing under direct shear test condition. J Geotech Geoenviron Eng 131(10):1295–1300

29. Tennakoon N, Indraratna B, Rujikiatkamjorn C, Nimbalkar S, Neville T (2012) The role of ballast-fouling characteristics on the drainage capacity of rail substructure. Geotech Test J 35(4):1–11

30. Indraratna B, Ngo NT, Rujikiatkamjorn C (2011) Behavior of geogrid-reinforced ballast under various levels of fouling. Geotext Geomembr 29(3):313–322

31. Brown SF, Kwan J, Thom NH (2007) Identifying the key parameters that influence geogrid reinforcement of railway ballast. Geotext Geomembr 25(6):326–335

32. AS:2758.7 (2015) Aggregates and rock for engineering purposes, Part 7. Railway Ballast. Standard Australia, Australia

Studying Railway Vibration Projects with a Focus on Environmental Aspects

Agnes van Uitert, Saeed Hosseinzadeh, Peter Schouten, and Otto Heeres

Abstract As the railway authorities increasingly demand more and faster railway transport, the existing railway networks are likely to be modified or rebuilt. For this purpose, an environmental impact assessment is needed. Processing the relevant data along railway tracks is among the most challenging tasks in ongoing railway vibration projects. This data includes the types and structural characteristics of buildings along the track, various ground conditions and vibration characteristics of the railway line. All GIS-related information concerning the buildings located along the track is being processed. Moreover, the superstructure and ground conditions are characterized along the railway track. Thus, cooperation of geotechnical-, railway-, environmental- and GIS experts is required. In parallel, measurement campaigns are performed to assess the vibration strength generated by passenger or freight trains along and perpendicular to railway tracks. After having processed all GIS-related information as well as measurement data, one should address issues with annoyance due to vibrations. For this purpose, through analytical and empirical methods, along with numerical approaches, maximum vibration levels at buildings along railway track are determined and identified. Subsequently, the vibration levels are assessed against the threshold levels. An abatement measure is to be performed, if need be. In this paper, a methodology is introduced where the whole aforesaid process is elaborated. For this purpose, a case study of a project in the Netherlands involving data along the railway track is presented and discussed. This methodology can be employed for similar railway vibration projects worldwide taking environmental aspects into account.

A. van Uitert · S. Hosseinzadeh (✉) · P. Schouten · O. Heeres
Arcadis, 6814 DV Arnhem, The Netherlands
e-mail: saeed.hosseinzadeh@arcadis.com

A. van Uitert
e-mail: agnes.vanuitert@arcadis.com

P. Schouten
e-mail: peter.schouten@arcadis.com

O. Heeres
e-mail: otto.heeres@arcadis.com

155

1 Introduction

Studying railway-induced ground-borne vibrations, due to economic and environmental concerns, has gained enormous attention over the past few decades. Examples of adverse consequences of railway-induced vibrations are contained in (e.g. [1, 2]). The generated ground-borne vibrations may also result in ground-borne noise in the buildings located in the vicinity of the railway tracks. The theoretical background of ground-borne vibration and noise is provided in [3].

In the last few decades, several researchers have studied ground-borne vibrations and noise, generated by railway traffic, namely using numerical methods (e.g. [4–7]), analytical and theoretical approaches (e.g. [8, 9]), experimental and empirical methods (e.g. [10, 11]) or a combination of numerical and experimental approaches (e.g. [12]). These studies include railway vibration generated in underground railway tunnel or a surface railway track (e.g. [13, 14]) and in different geotechnical conditions (e.g. [15]).

Several standards and regulations have been developed for buildings so as to define target values for vibration and noise generated by railway traffic. Examples of these standards and guidelines include, but are not limited to, FTA-VA-90-1003-06 in the USA [16], DIN 4150-2 and DIN 4150-3 [17, 18] in Germany, BS 6472-1 [19] in the UK, SS 460 4861 [20] in Sweden, NS 8176 [21] in Norway, SBR vibration directive B by the Building Research Foundation (in Dutch: SBR-B; [22]) and Dutch policy rules of track vibration (in Dutch: Bts, [23]) in the Netherlands.

Predicting railway vibrations is an inherently complex task involving numerous uncertainties, especially when performing such analysis over a large area of train trajectory (e.g. a railway track of tens of kilometres in length). Processing data sets along the railway track is among the most challenging tasks in existing projects. This data includes the types and structural characteristics of buildings along the railway track, various ground conditions and vibration characteristics of the railway track. A cooperation of geotechnical-, railway-, environmental- and GIS experts is required so as to address the possible adverse effects with respect to railway-induced vibrations. In the present paper, the authors aim to present a methodology taking environmental aspects into account for assessing railway vibration projects worldwide involving the relevant data along kilometres of railway track.

2 Data Compilation and Analysis

Assessing vibration-related problems along a railway track of tens of kilometres includes collection and analysis of all related information. Table 1 gives a summary of

Table 1 Required data for railway vibration assessment studies

Input information	Processing	(Possible) Outputs
Site investigations	Archival research Interpretation of soil and rock types and characteristics Interpretation of geohydrological data	Geotechnical profiles and parameters as well as groundwater table along track
Measurement campaigns	Existing tracks: Measuring velocity and acceleration signals from trains New Tracks: Performing further investigations (e.g. falling weight test for measuring shear wave speed, seismic CPTs, etc.)	Vibration strength along different locations/receivers
GIS-data processing	Information related to buildings/dwellings along track Cadaster information related to the impact area of project	Structural characteristics of buildings and dwellings along track Foundation characteristics Distance from buildings/dwellings to track
Environmental aspects	Land use information	Determination of availability of areas for applying abatement measures
Railway line characterization	Investigation of superstructure along railway track	Type of superstructure including rails and sleepers along track Presence of railway level crossing and turn out and track circuit
Railway traffic information	Investigation of train characteristics, train speeds and frequency	Number, type and speed of trains Geometry and configuration of trains
Underground utilities information	Information related to depth and position of underground utilities	Type and level of cable and pipelines Presence of underground objects
Structural properties of buildings positioned along railway track	Function of the buildings (e.g. a dwelling), types of floors and foundations, floor areas, years of construction, rigidity of construction	Categorization of buildings based on different aspects

required data for railway vibration assessment studies. The required data mentioned in Table 1 is separately elaborated in the next subsections.

2.1   Site Investigation

As for site investigation, archival research is carried out in the first place. For instance, in the Netherlands, DINOloket [24] can be used to retrieve site investigation data conducted in the project area. However, depending on the uncertainty involved, additional geotechnical laboratory testing as well as CPT or SPT and boreholes along and within the location of railway tracks are to be carried out. This should be accompanied by monitoring of groundwater levels.

Additional site investigation is needed allowing both to determine the stratigraphy as well as the dynamic characteristics of ground layers at the considered track location.

2.2   Measurement Campaigns

The in situ vibration measurements are to be performed along and perpendicular to railway track within the area of train trajectory. This helps practitioners determine the ground-borne vibration levels as well as damping characteristics of ground layers along railway track. For this purpose, several measurement points are chosen based on the location of considered buildings in a project as well as different distances to the centre of the railway track. The number of measurement points is highly dependent on the number of profiles considered in a project. The duration of measurements along the existing lines is usually a couple of days in order to acquire an insight into the damping characteristics of the ground along the railway track for different types of trains as well as to establish the variation in excitation due to different train configurations.

For conventional railway traffic, the measured data is divided into freight and passenger trains and different vibration strength depending on speed and types of trains. The latter may affect the magnitude of source vibration strength and the dominant vibration frequency. After having collected the needed measurement data, a filtering process is performed to provide the input data in terms of the characteristic sets of induced vibrations and damping characteristics for an analytical/empirical model.

2.3 GIS-Data Processing

In order to pinpoint all the spatial information related to buildings positioned along railway track, cadastral information is needed. This information includes, among others, number of inhabitants per dwelling, distance to the railway track, construction year, building function (e.g. housing, office, etc.) and building size. Based on archive data, the types of buildings including floor type (e.g. wood or concrete), foundation type (e.g. shallow foundation or founded on piles) and number and area of floors are determined and coupled to the GIS-model.

2.4 Environmental Aspects

While commencing a vibration project with data acquisition, one also needs to collect environmental land use-related data including, but not limited to, presence of green areas, position of trees along railway track of project area, building with sensitive function in the vicinity of the railway track, etc.

Along with predicting vibration levels at buildings positioned along railway track, one also needs to assess annoyance due to vibrations. Moreover, an additional analysis may be required to assess the risk of damage to structures (including dwellings) due to vibration as well as the chances of exceeding the allowable values of low-frequency ground-borne noise in the buildings. The first requires an insight into the ground conditions where layers sensitive to vibratory compaction are present. Both of them require an insight into structural properties of the buildings.

2.5 Railway Line Characterization

Railway line is to be characterized depending on the types of superstructure. This includes types of track, i.e. ballastless or ballasted tracks, type of rails and sleepers, type of fasteners, presence of dampers, track layout and configurations, level crossing, track circuit (i.e. a device showing if a train is present on the track), etc. In effect, all unevenness in the track–train interaction system would affect vibration levels. It has been observed in Arcadis projects that a defect in railway track circuit would lead to significant changes in measured ground-borne vibration levels.

2.6 Railway Traffic Information

In order to assess the vibration strength, the number of trains as well as types of trains (e.g. freight or passenger trains) need to be evaluated. This will define the train

speed and dominant frequency generated at different locations. For a measurement assessment, the train geometry and configuration are also needed.

2.7 Underground Utilities Information

In case of a track on embankment, the presence of any fixed underground object may locally affect the vibration strength. Therefore, it is of importance to pinpoint all the underground utilities before defining the measurement campaign. Underground utilities include cables, pipelines, etc. It has been observed in Arcadis projects that a pipeline present at the site location in the vicinity of railway track would lead to significant changes in measured ground-borne vibration levels.

3 Approaches

3.1 Prediction Model

After collection and analysis of the above-mentioned data, the vibration prediction model through analytical/empirical approach can be built up so as to predict vibration levels considering the relevant frequency ranges as well as different distances from the track. A data analysis is conducted to process data sets including GIS-related data coupled to the above-mentioned model over the entire length of the project which is incorporated in the prediction model. Field measurement data is used to calibrate the prediction model. The model is employed for predicting vibration levels at each location along the track considered in a project both for reference and future situations.

In some projects, numerical analyses are used in the first place to predict vibration levels. Examples of such cases are design of new tracks, when the track is constructed in a tunnel or underpass or an underground station as well as complex geometries and soil–structure interactions in different directions along the track (e.g. presence of railway structures). Other examples include the locations where the allowable vibration levels exceed threshold values according to national standards and where an "abatement measure assessment" must be carried out. In spite of advantages of numerical modelling, they can be quite time consuming compared to analytical models.

In the common practice, a combination of analytical and empirical methods along with numerical approaches is used. Examples of numerical techniques employed for this purpose are displacement-based FEM (e.g. [25]), infinite elements, finite elements in which an analytical solution is incorporated and finite difference method. The focus of this paper is not on numerical analysis.

3.2 Assessment Against National Directive

After having predicted the ground-borne vibrations, a comparison is made between the obtained results and the allowable threshold values defined by the standards and regulation at the considered location. In the Netherlands, the threshold vibration levels for each single property positioned along the railway track are determined based on national regulations (Bts). This is carried out based on the determination of the maximum vibration level (V_{max}) recorded at the location of a property and the average vibration level (V_{per}) based on measurements during a certain period of time through the passage of trains. Vibration assessment according to Bts [23] is shown in Fig. 1. Once the allowable levels of V_{max} or V_{per} as defined in Bts [23] are exceeded, an abatement measure assessment has to be performed. The allowable vibration levels are shown in Table 2.

The assessment is performed for existing tracks in case of planned modifications of alignment of the tracks or train operations. For this situation, an increase of 30% in the maximum vibration level is accepted provided that the upper threshold value is not exceeded, as such an increase is considered not to be noticeable for human beings.
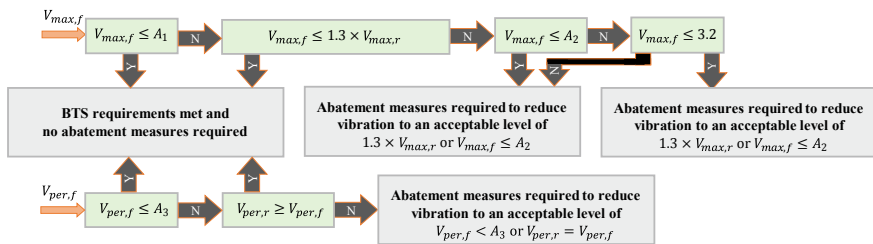
Fig. 1 Vibration assessment according to Bts [23] in which $V_{max,f}$ and $V_{per,f}$ denote vibration levels for future situation; whereas, $V_{max,r}$ and $V_{per,r}$ imply vibration levels for reference or current situation

Table 2 Allowable vibration levels according to Bts [23]

Building/dwelling function (−)	Day and evening period (07:00–23:00)				Night period (23:00–07:00)			
	V_{max}		V_{per}		V_{max}		V_{per}	
	A1		A2	A3	A1		A2	A3
Dwellings and health centres	0.2		0.8	0.1	0.2		0.4	0.1
Offices and educational centres	0.3		1.2	0.15	0.3		1.2	0.15

Fig. 2 Map of the
Netherlands with
approximate project location.
Inset: the section considered
in this study (adapted from
Google Earth)
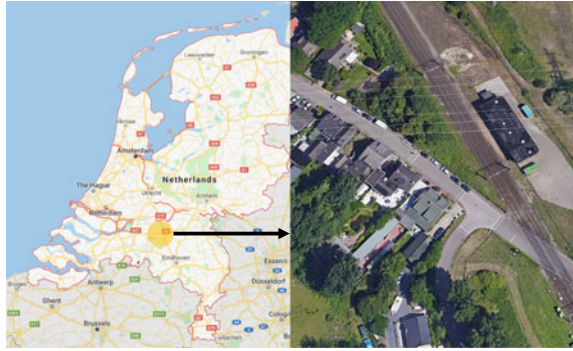
4 Case Study and Discussions

In this paper, a project in the Netherlands is discussed as an illustration of the above-
mentioned aspects which need to be considered in the assessment of railway-induced
vibration and noise. In this paper, the focus is given to vibration only.

4.1 Project Description

The project comprises an approximately 40-km-long existing railway track. At two
locations, additional tracks are planned as well as two viaducts, some underpasses and
a tunnel construction in order to increase the number of passenger and freight trains.
In this project, more than 25 reference locations were chosen in which measurements
were performed. At each location, 2–3 geophones were employed. In addition, video
cameras and microphones were employed throughout the measurement period in
order to identify the type of the trains as well as disturbances. A section of approxi-
mately 200 m is considered in this paper. The approximate location of the project is
shown in Fig. 2.

   At this location, railway traffic includes both passenger (both local and intercity
trains) and freight trains. The speed of trains (both for reference and future situations)
is within a range of 80 km/h to 140 km/h. That is, for freight trains, the speed increases
from 80 km/h to 100 km/h while no speed changes to the passenger trains are applied.

4.2 Ground Conditions and Measurements

Ground conditions consist mostly of loosely to medium sand with intermediate thin
soft layers such as clay or peat. The in situ vibration measurements were performed
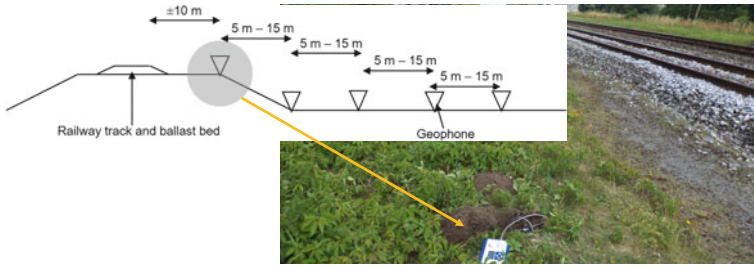
Fig. 3 Schematic layout of measurement points along the railway track. Inset: a geophone placed perpendicular to the railway track at the project location

for the considered location to determine the ground-borne vibration levels along the railway track as well as to determine the damping characteristics of the soil layers.

For this purpose, several measurement points were chosen based on different distances from the centre line of the railway track as shown schematically in Fig. 3.

Dominant frequency was determined based on the measurements performed at the site location. The representative frequency is in a range between 16 Hz and 31.5 Hz.

Damping factors (α and n, based on Barkan's equation [26], Eq. 1) for passenger and freight trains were determined based on the measurement data. Equation 1 implies the relationship between the effect of damping factors on vibration strength against the distance from the source of vibration:

$$C_{\text{Ground}} = \left(\frac{r_0}{r}\right)^n e^{-\alpha(r-r_0)} \tag{1}$$

where C_{Ground} is a factor considered for geometric transformation in the ground (considering both spatial and physical damping), α is the material damping factor ranging from 0.01 to 0.05 for both passenger and freight trains for different frequencies, n is the geometrical factor for attenuation ranging from 0.1 to 0.2 for both passenger and freight trains for different frequencies, r is the distance between the vibration source and receiver, and r_0 is the reference distance from the source (i.e. 5 m).

4.3 Abatement Measures

For selecting a suitable measure, a cost–benefit analysis was performed for those locations where threshold values are expected to be exceeded based on analyses. Application of abatement measures at the location of receivers (e.g. a building) requires permission from the owners and may also be quite costly, especially in case the structural or functional characteristics of the building are subsequently subject to adjustments; which is why these measures are usually not preferred. As at the

relevant locations more than four tracks will be present in the future situation, it was also not be economically feasible to propose measures on the track at these locations. Therefore, measures in the propagation path, namely stiff barriers, were studied. For this purpose, the effectiveness of stiff wave barriers using diaphragm wall and jet grouting techniques were studied through numerical modelling. The characteristics of both methods are summarized in Table 3. These measures with similar thickness and depth of the walls, however costly and intrusive they seem, are common in Dutch practice and have been applied to several projects. This is due to the favourable ground conditions and limited working space.

In practice, different criteria such as effectiveness, suitability, practical application, maintenance, robustness and costs of the abatement measure are considered in an abatement measure assessment. For this location, a sensitivity analysis was performed through numerical modelling with respect to the effectiveness of the measures. However, the measurements were first used to validate the reference simulations performed by dynamic FEM analysis [25] in the time domain. An example of the loading plan used in FEM analysis is shown in Fig. 4. This is determined based on the geometry, type and speed of the passing trains.

Table 3 Characteristics of both diaphragm wall and jet grouting techniques

Technique (−)	Diaphragm wall	Jet grouting wall
Construction method	Bentonite stabilized excavation of approx. 1-m-wide trenches that are filled with concrete	Injected cylindrical column of approx. 1.5 m diameter
Young's modulus (GPa)	Up to 30 GPa	From 2 GPa to almost 5 GPa depending on soil structure
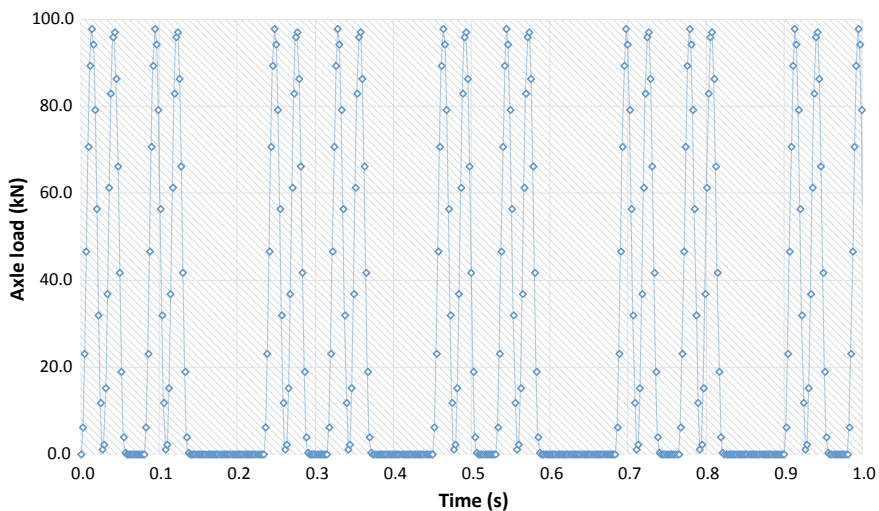
Fig. 4 Example of a loading plan employed for numerical modelling for a train speed of 80 km/h

Fig. 5 Comparison between the numerical analyses performed for the considered location (without measure) and the freight train vibration measurement data with dominant frequencies
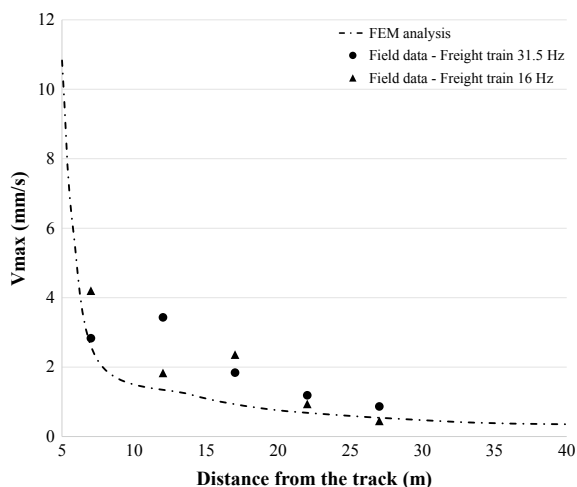
Viscous boundary conditions were used at the boundaries of the model so that the model absorbs the seismic waves avoiding wave reflections. Undrained condition is considered in cohesive soils, and fully drained conditions are assumed only for non-cohesive layers. Dynamic geotechnical parameters were obtained via site investigations (see Table 1).

Figure 5 shows a comparison between the results of numerical modelling (with a train speed of approximately 80 km/h corresponding to the upper bound dominant frequency) and in situ vibration measurements of the freight trains. Two dominant frequencies (i.e. 16 Hz and 31.5 Hz) were employed in this comparison. As seen in Fig. 5, the numerical analysis for this location underestimates the vibration level at short distances from the track. This can be possibly attributed to the simplification in FEM analysis with respect to the ground behaviour during dynamic loading, material damping characteristics and interaction between the vibration source and the railway track system. That being said, a good agreement is observed between the measurement data and FEM analysis results between the average distances of 20 m and 30 m from the track.

The location of the considered dwellings in which the measurements were conducted is about 20–25 m away from the track. This implies that the FEM analysis results correspond to the measurements for the considered location.

The model was further used to calculate the effectiveness of the measure, which is determined as the ratio between the calculated vibration level with the application of stiff wave barrier and the reference situation (where no stiff barrier is modelled). The following are the key points from these analyses:

- A reduction of 6–7 dB is achievable by applying a 15 deep and 0.5-m-wide diaphragm concrete wall at 6 m distance from the railway track. By considering an 18-m-deep jet grouting barrier with an average thickness of 1.0 m, the same

effectiveness as that of a diaphragm concrete wall could be achieved at the same location.

- Jet grouting differs from diaphragm wall in terms of the stiffness of the barrier material as well as its installation process. This implies that the contrast between the stiffness of the jet grout barrier and the surrounding soil is less compared to that of a diaphragm concrete wall barrier in the same strata. This, in the authors' view, has significant impact on the effectiveness of the measure.
- From the results at this location, it was concluded that increasing the width of the stiff wave barrier for both jet grouting and diaphragm wall techniques has a minor impact on the effectiveness of the measure. However, it was observed that a decrease in the depth of barrier leads to a significant change in the performance of barrier.
- It was observed that not only the dimensions of the barrier and its stiffness affect the effectiveness of the barrier, but also the position of the wave barrier relative to the tracks and the receptor buildings. It was observed that, at this location, the closer the position of the wall to the track, the greater the effectiveness will be. It was also observed that a good effectiveness is realized with the barrier close to the receiver.

5 Conclusions and Recommendations

In this paper, a methodology for assessing environmental impact of railway vibration on thousands of buildings along tens of kilometres of railway track was put forward as shown in Fig. 6. This includes the prediction of vibration level at each individual building along the railway track in the project area as well as an abatement measure
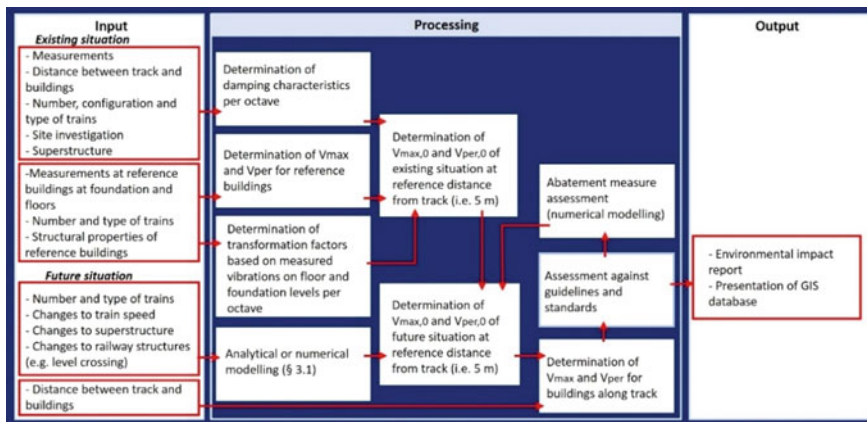
Fig. 6 Methodology for assessing environmental impact by railway vibrations—a reference building is the location in which measurements on foundation and floor levels are carried out

assessment based on a cost–benefit analysis. This can also be applied to other projects worldwide.

From a practical perspective, a few aspects are recommended to be considered as follows:

(1) The effect of changes in groundwater table on ground-borne vibration measurements.
(2) The effect of railway structures including railway turn outs (points) and level crossings on ground-borne vibration levels.
(3) The effect of thickness of embankment on ground-borne vibration levels especially in far distances from railway track.

Further study will contribute to a better understanding of railway vibration impact as support to railway authorities and practitioners in planning of future railway projects.

References

1. Janssen S, Coelho BZ, Koopman A, Peris E, Groll W, Wisniewska K (2015) Annoyance due to vibration from freight railway lines in the Netherlands and Poland. In: Proceedings 10th European congress and exposition on noise control engineering, EuroNoise. The Netherlands, pp 595–598
2. Connolly DP, Marecki GP, Kouroussis G, Thalassinakis I, Woodward PK (2016) The growth of railway ground vibration problems—a review. Sci Total Environ 568:1276–1282
3. Thompson D (2008) Railway noise and vibration. Mechanisms, modelling and means of control. Elsevier Ltd, Oxford
4. Kaynia AM, Madshus C, Zackrisson P (2000) Ground vibration from high-speed trains: prediction and countermeasure. J Geotech Geoenviron 126(6):531–537
5. Hall L (2003) Simulations and analyses of train-induced ground vibrations in finite element models. Soil Dyn and Earthq Eng 23:403–413
6. Lombaert G, Degrande G (2009) Ground-borne vibration due to static and dynamic axle loads of InterCity and high speed trains. J Sound Vib 319(3–5):1036–1066
7. El Kacimi A, Woodward PK, Laghrouche O, Medero G (2013) Time domain 3D finite element modelling of train-induced vibration at high speed. Comput Struct 18:66–73
8. Karlström A, Boström A (2006) An analytical model for train-induced ground vibrations from railways. J Sound Vib 292(1):221–241
9. Sheng X, Jones CJC, Thompson DJ (2004) A theoretical model for ground vibration from trains generated by vertical track irregularities. J Sound Vib 272(3–5):937–965
10. Bahrekazemi M (2004) Train-induced ground vibration and its prediction. PhD Dissertation, Royal Institute of Technology, Stockholm, Sweden
11. Zhai W, Wie K, Song X, Shao M (2015) Experimental investigation into ground vibrations induced by very high-speed trains on a non-ballasted track. Soil Dyn and Earthq 72:24–36
12. Kouroussis G, Vogiatzis K, Connolly DP (2017) A hybrid numerical-experimental assessment of railway ground vibration in urban area. In: Zhai W, Wang KCP (eds) ICRT 2017: Railway Development, Operations, and Maintenance, China
13. Forrest JA (1999) Modelling of ground vibration from underground railways. PhD Dissertation, University of Cambridge, The UK
14. Kouroussis G, Connolly DP, Verlinden O (2014) Railway-induced ground vibrations—a review of vehicle effects. Int J Rail Transport 2(2):69–110

15. Eitzenberger A (2008) Train-induced vibrations in tunnels: a review. Technical Report, Lulea University of Technology, Sweden
16. Hanson CE, Towers DA, Meister LD (2006) Transit noise and vibration impact assessment. No. FTA-VA-90-1003-06
17. Deutsches Institut für Normung (1999) DIN 4150-2. Structural vibrations—Part 2: Human exposure to vibration in buildings
18. Deutsches Institut für Normung (1999) DIN 4150-3—Structural vibrations—Part 3: Effects of vibration on structures
19. British Standards Institute (2008) BS 6472-1—Guide to evaluation of human exposure to vibration in buildings. Vibration sources other than blasting. British Standards Institute
20. SIS: SS 460 4861 (1992) Vibration and shock—measurement and guidelines for the evaluation of comfort in buildings. Standard, SIS Förlag AB, Stockholm, Sweden
21. Norwegian Council for Building Standardization (1999) NS 8176—Vibration and shock—measurement of vibration in buildings from land-based transport and guidance to evaluation of its effects on human beings
22. Building Research Foundation (SBR) Directive (B) (in Dutch) (2003) Annoyance to people in buildings, measurement and assessment
23. Staatscourant (2014) Dutch policy rules of track vibration (in Dutch: Bts). No. 8251
24. DINO Homepage. https://www.dinoloket.nl. Last accessed 6 Oct 2019
25. Brinkgreve RBJ, Kumarswamy S, Swolfs WM, Zampich L, Ragi Manoj N (2019) Plaxis 2D 2019 User's Manual. Plaxis BV, The Netherlands
26. Barkan DD (1962) Dynamics of basis and foundations. McGraw-Hill, New York

Receptance Test Performed on a Laboratory Ballasted Track Section

Ana Ramos ⓘ, Alexandre Castanheira-Pinto, Ahmet Esen ⓘ, António Gomes Correia ⓘ, Pedro Alves Costa ⓘ, Rui Calçada ⓘ, Peter Woodward, and Omar Laghrouche ⓘ

Abstract A receptance test was performed in a ballasted track section with three sleepers after cyclic loading tests. This physical model is installed in the laboratory of *Heriot-Watt University*. The ballasted track is resting on a compacted substructure that is characterized by a frost protection layer (FPL), subgrade and geosynthetic-reinforced soils (GRS). A geogrid TX190L was placed between the ballast and FPL. The ballasted track is characterized by BS113A continuous rails, elastic pads and three G44 sleepers (spaced 0.65 m) embedded on the ballast layer. The receptance test is a helpful tool in the identification of the resonant frequencies that characterize the dynamic behavior of the track, and the results can be used in a calibration process of a numerical model. The response of the track was evaluated through the accelerometers placed on the head and web of the two rails and on the sleepers. The experimental tests were performed over the three sleepers, and the obtained results were compared taking into account the coherence function. Furthermore, the identification of the main resonant frequencies (full-track resonant frequency, anti-resonant frequency of the sleepers and rail resonant frequency) was also analyzed considering the accuracy of the obtained results in terms of coherence (only values higher than 0.9 were considered).

Keywords Ballasted track · Experimental tests · Receptance test

A. Ramos (✉) · A. G. Correia
University of Minho, ISISE, Department of Civil Engineering, Guimarães, Portugal
e-mail: id6629@alunos.uminho.pt

A. Castanheira-Pinto · P. A. Costa · R. Calçada
CONSTRUCT - LESE, Faculty of Engineering, University of Porto, Porto, Portugal

A. Esen · O. Laghrouche
Institute for Infrastructure and Environment, Heriot-Watt University, Edinburgh, UK

P. Woodward
Institute for High Speed Rail and System Integration, University of Leeds, Leeds, UK

169

1   Introduction

The receptance tests allow identifying the resonant frequencies of a railway structure. As expected, the response of the ballasted track is influenced by the stiffness of the structure [1]. Indeed, the ballast and the subgrade properties have an important role in the performance of the ballasted track and also have a significant influence on the dynamic response of the track when solicited by an impulse [2].

The behavior of the railway track varies according to the characteristics of the applied load. Indeed, the response of the structure can be divided into three main groups: low frequency (0–40 Hz), medium frequency (40–400 Hz) and high frequency (400 Hz until 1500 Hz) [3]. Considering this range, many studies state that the low frequencies are dependent on the mechanical properties of the substructure (mainly the foundation), while the ranges of the medium and high frequencies are related to the properties of the materials of the track such as the rails, rail pads, sleepers and ballast layer.

The receptance tests allow minimizing the uncertainty associated with the properties of the elements of the railway's track (since the dynamic response of the track depends on these properties). Indeed, the receptance test has been widely used in the numerical calibration. For example, this method was used to explain the rail roughness growth [4], the railway rolling noise emission from wheel and track [5], to obtain the track parameters in the scope of the environmental impact of ground-borne vibration from railway traffic [6, 7] and also used as a tool in the study of possible mitigation measures such as the use of a stiff wave barrier in the soil [8]. Furthermore, the hammer test was also used to evaluate and monitor the dynamic properties of the rail pads [9, 10] and more recently the dynamic properties of the rail ballast [11]. Moreover, the hammer test was also performed to study the propagating wave types in railway tracks at high frequencies [12]. More lately, the receptance test was used as a tool to calibrate and describe the dynamic behavior of the train-track system [13]. Thus, from the receptance curves, the numerical model can be calibrated by an inversion procedure in order to obtain a reasonable fit between the computed and measured receptance values [14].

This work aims to explore the resonant frequencies of a ballasted track section placed at the laboratory of *Heriot-Watt University* and understand the influence of the cyclic tests performed previously, which can cause asymmetries since the railway structure is submitted to more than 3 million load cycles (increasing its degradation).This physical model is a special structure because it is a "finite" structure with the development of only 2.2 m (three sleepers spaced 0.65 m). This was the main challenge of this work since the regular/traditional receptance tests are performed on a ballasted track with infinite extent. The tests were performed in a partnership between an extensive team.

2 Receptance Test

In this case study, the receptance test was performed in a ballasted track section ($L = 2.2$ m) at the laboratory of *Heriot-Watt University*, following the similar procedures described in [15].

In order to obtain the dynamic behavior of the track, an impulse load was applied by an instrumented hammer to the rails and sleepers. The head of the hammer is instrumented with force transducer and the track (rail and/or sleeper) with accelerometers. The range of the excited frequencies is defined according to the characteristics of the hammer. From the performance of the receptance test on this ballasted track, three main resonant frequencies are expected to identify:

- A: full-track resonant frequency;
- B: anti-resonant frequency of the sleepers;
- C: rail resonant frequency.

In this case, it is not probable to identify the *pin-pin* resonant frequency because it occurs, generally, for higher frequencies (between 400 and 1200 Hz). This frequency depends on the support spacing, and on the bending, and shear properties of the rail.

In order to understand the shape of the vibration modes identified previously, a schematic representation is depicted in Fig. 1.

The full-track resonant occurs for frequencies within 40–140 Hz. The vibration mode shape is characterized by a vertical vibration of the rail and sleepers over the supports. This resonant frequency is highly influenced by the properties of the ballast and foundation soil.

The anti-resonant occurs between a pair of resonant frequencies. An anti-resonant frequency is observed in discretely supported tracks (as in this case) with two elastic layers and occurs in frequencies between 80 and 300 Hz.
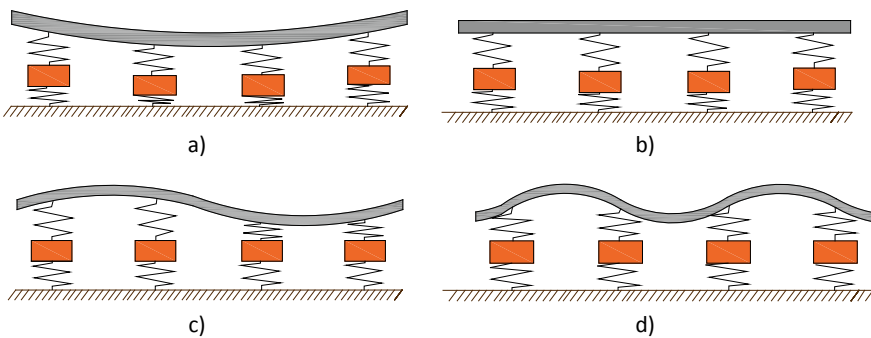
Fig. 1 Resonant frequencies: **a** full-track resonant frequency; **b** anti-resonant frequency of the sleepers; **c** rail resonant frequency; **d** pin-pin resonant frequency (adapted from [3])

The vertical vibration of the rail over the supports is highly dependent on the rail pads properties (stiffness and damping) and rail properties. This resonant occurs in frequencies between 250 and 1500 Hz.

3 Laboratory Testing

3.1 Ballasted Track—Description

The traditional ballasted track is composed of the superstructure and substructure. The superstructure includes the rails, rail pads, fastening system and sleepers. The substructure is composed of the ballast, sub-ballast and subgrade.

The substructure of the tested ballasted track is composed of frost protection layer (FPL), subgrade and geosynthetic-reinforced soils (GRS). Between the ballast and FPL (in order to reduce the penetration of ballast to the substructure), a geogrid TX190L was placed.

The ballast consists of micro-granite with a moisture content of 0.5%. This material was placed considering four layers of 100 mm until reaching the 400 mm measured to under the sleeper. The bulk density after compaction was equal to 16 kN/m³ [15].

In these experimental tests, G44 sleepers (embedded on the ballast layer) were placed at 0.650 m spacing and lower elastic pads from a slab track tests (used during the static and cyclic) were used as rail pads [15]. The static stiffness of the lower elastic pad was approximately 22.5 kN/mm, and the dynamic stiffness was approximately 40 kN/mm. The Pandrol fastening system was used to lock the rails to the sleepers. Regarding the rails, three segments (Fig. 2) of BS113A (56E1) were adopted during the cyclic tests. However, before the receptance tests, the segment rails were replaced by the continuous rails since the bending stiffness of the rail influences the results of the test. A perspective of the experimental ballasted track is depicted in Fig. 3.

Fig. 2 Example of segments of rails (three) in a ballastless track used in the cyclic tests [15]

a)

b) c)
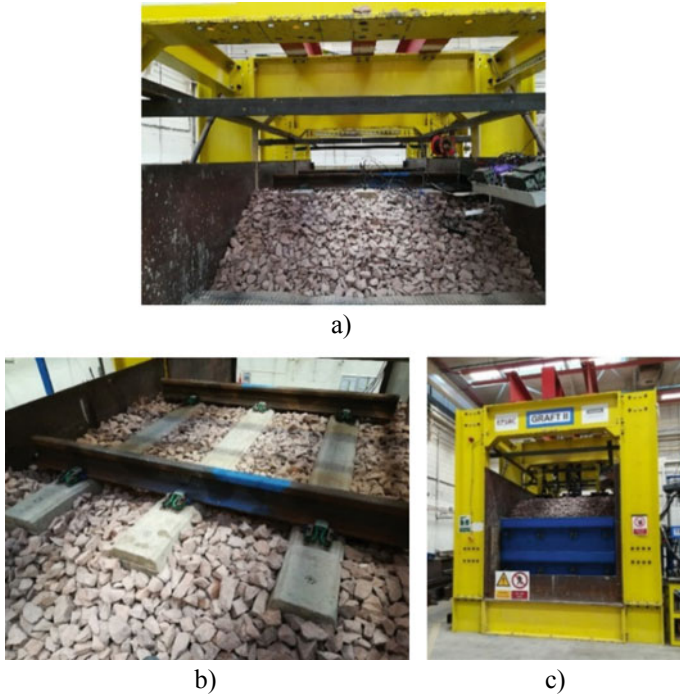
Fig. 3 **a**, **b** Experimental ballasted track; **c** Perspective of the experimental structure

3.2 Setup of the Receptance Test

The analysis of the dynamic response is usually performed in the frequency domain using a transfer function (receptance) that relates the frequency content response with the frequency content impulse. The receptance represents the inverse of the dynamic flexibility of the track:

$$\text{receptance}(m/N) = \text{displacement/force} \tag{1}$$

To apply this transfer function, it is necessary to determine the dynamic displacement of the track. During the performance of the receptance test, the track is excited by an impulse through the use of the instrumented hammer—model 086D50—and the response of the track is evaluated through the accelerometers placed on the rails and sleeper. In this case, the impulse was applied to three points (Fig. 4): (1) head of the right rail; (2) head of the left rail; (3) middle of the sleeper.

The large-sledge impulse hammer from PCB Piezotronics has a mass equal to 5.5 kg, a measurement range $\pm$ 5000 lbf pk ($\pm$22,240 N pk) and a sensitivity equal to ($\pm$15%) 1 mV/lbf (0.23 mV/N).

Fig. 4 Setup of the receptance test: **a** representation; **b** general perspective of the structure and setup

The response was evaluated on the rails and on the sleepers considering the position of the accelerometers. The setup of the experimental test, depicted in Fig. 4, is characterized by the instrumentation of four points on the rails and two points on the sleeper. The accelerometers are fixed on the rail and on the sleeper by magnets, angle brackets and metal plates. In this work, two accelerometers of 5G (Acc2 and Acc3) and two accelerometers of 50G (Acc13 and Acc14) were used to measure the displacements of the rails. The 5G accelerometers were placed on the head of the rails and 50G on the web of the rail profile. Furthermore, two 5G accelerometers were placed on the edge of the sleeper (Acc0 and Acc1), as depicted in Fig. 4.

The signal of the hammer and of the accelerometers is acquired and conditioned through a system composed of the modulus NI CDAQ-9172 that is equipped by plates IEPE and controlled by a portable computer.

Throughout the receptance test, the accelerometers (Acc0, Acc1, Acc2, Acc3, Acc13 and Acc14) were moved from one sleeper to another, keeping the same setup. In the analysis of the results of the sleepers placed at the extreme positions (sleeper 1 and 3), some difficulties were found on the interpretation of the tests because of the results of the coherence function.

After acquiring the signals of the accelerometers and the instrumented hammer, the transfer function between the impulse and the displacements of the observation points is determined considering a certain number of events (in this receptance test, the number of events is between 50 and 100). The number of events corresponds to the number of impulses applied by the hammer. The obtained signals consist of a set of impulses applied, as depicted in Fig. 5. The separation of the several impulses in isolated events was performed through an algorithm that allows identifying each one of the peaks and events. The analysis of the results was performed for each event. After this procedure, the final receptance curve consists of the average of the whole set of events treated previously.

Thus, a significant number of events allows evaluating the coherence of the acquired signals. The experimental receptance function is determined by the following expression:
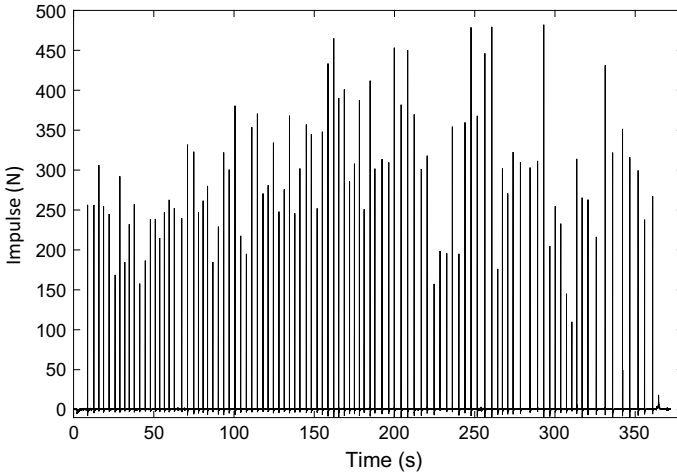
Fig. 5 Temporal register of the force applied by the hammer on the head of the rail

$$H_{\exp}(\omega) = \frac{x_i^m(\omega)}{\omega^2 x_m^m(\omega)} \tag{2}$$

where $x_i^m(\omega)$ and $x_m^m(\omega)$ are the mean acceleration of a certain observation point and the mean of the impact force, respectively (in the frequency domain). These values are obtained by the following expressions:

$$x_i^m(\omega) = \frac{1}{N} \sum_{k=1}^{N} x_i^k(\omega) \tag{3}$$

$$x_m^m(\omega) = \frac{1}{N} \sum_{k=1}^{N} x_m^k(\omega) \tag{4}$$

where N corresponds to the number of events.

From the number N of events of the receptance tests, the coherence between the excitation and the response is determined in order to evaluate the quality of the acquired signals.

3.3 Experimental Results and Analysis

The experimental tests show good results on the middle sleeper (no. 2). However, as mentioned previously, in the sleepers placed on the extreme positions (no. 1 and 3),

the coherence results are very poor and it may not be possible to use the receptance results in a calibration process, as depicted in Fig. 6.

This fact can be justified by the rigid boundaries and also asymmetries of the structure due to the cyclic tests performed as described in [15]. Indeed, during the cyclic tests, segment rails were used, which means that it is not possible to justify the poor coherence results with the possible bending of the rail since the continuous rails were only placed after the cyclic tests.

In Fig. 7, an example of the experimental hammer impulse is presented in the time and frequency domain. This particular impulse was applied to the head of the rail to obtain the receptance function.

Thus, a significant number of events allow evaluating the coherence of the acquired signals. The coherence function—$\gamma(\omega)$—varies between 0 and 1. The coherence equal to one means a good coherence of the results (signal with high quality). This
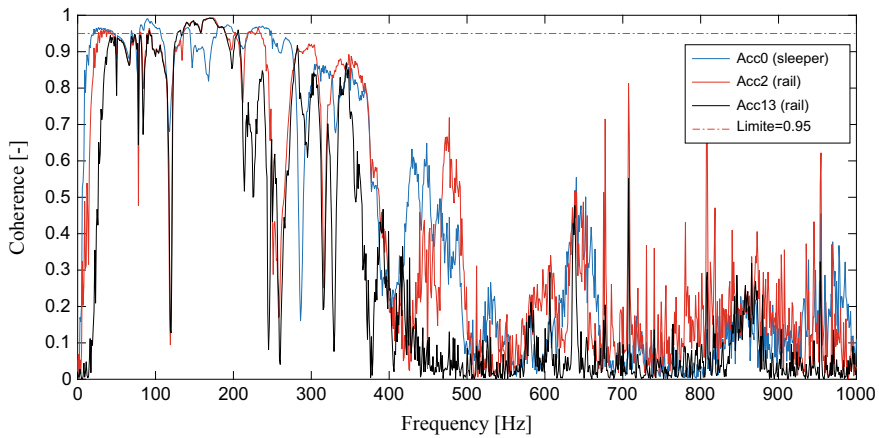
Fig. 6 Results of the coherence tests: impulse on the right rail of sleeper 3
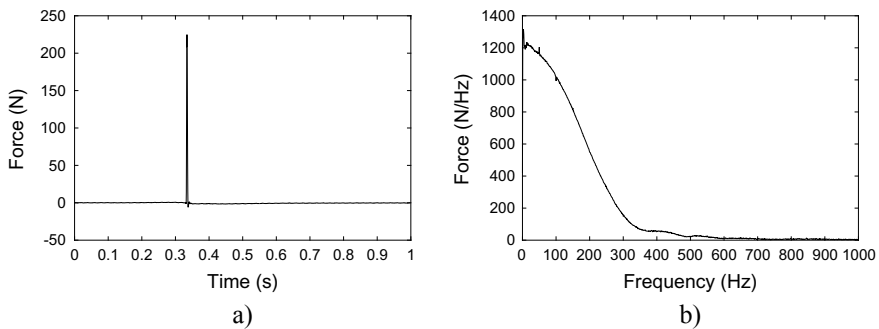
Fig. 7 Impulse applied on the track to obtain the receptance functions: **a** time domain; **b** frequency domain

value is hard to obtain due to some noise of the signal. Experience shows that values of less than 0.9 of coherence should be ignored. The coherence function is determined by the following expression:

$$\gamma^2(\omega) = \frac{S_{mi}^m(\omega)\overline{S}_{mi}^m(\omega)}{S_{mm}^m(\omega)\overline{S}_{ii}^m(\omega)} \tag{5}$$

where S_{ii} corresponds to the power spectrum. The dash represents the conjugate of the variable.

Figures 8 and 9 presented the coherence and receptance results for the sleeper no. 2 considering the application of the impulse on the head of the rail and middle of the sleeper, respectively. The results include the response of the accelerometers 5G and 50G placed on the rail.

Analyzing the results of both impulses, the coherence results show that it is only possible to use the results for frequencies below 400 Hz. Above this value, the coherence is very low. Furthermore, the receptance results allow identifying very well
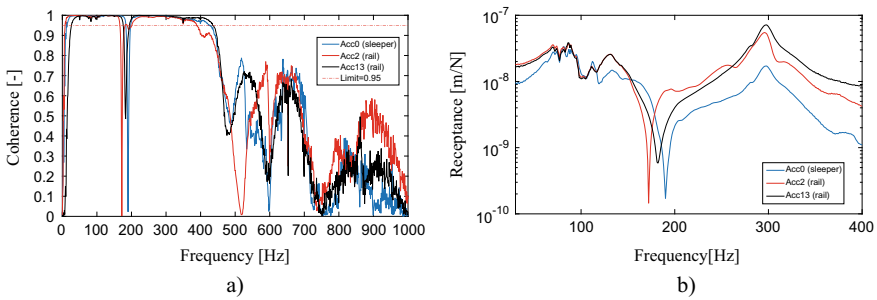
Fig. 8 Results of the receptance tests (impulse applied on the head of the rail): **a** coherence results; **b** receptance results
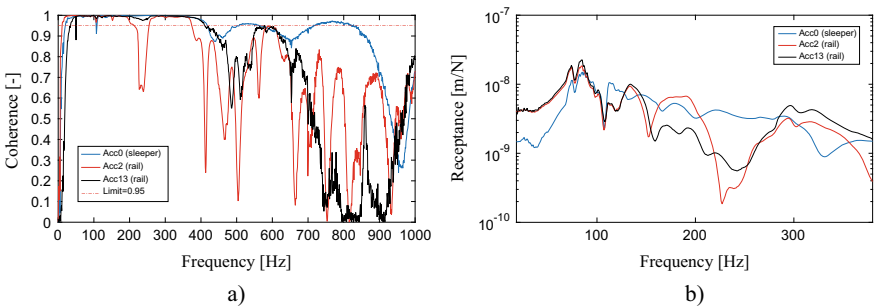
Fig. 9 Results of the receptance tests (impulse applied in the middle of the sleeper): **a** coherence results; **b** receptance results
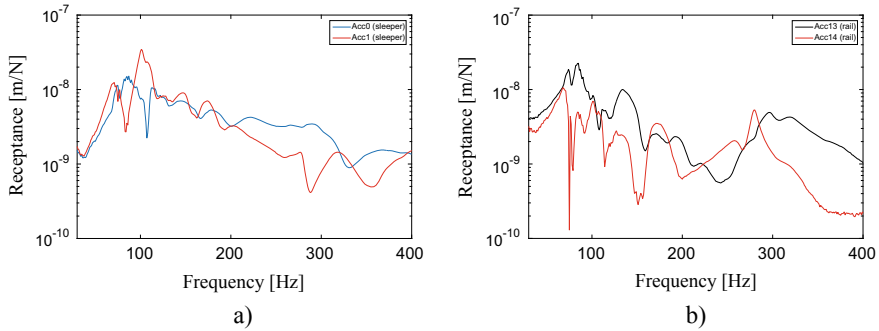
Fig. 10 Comparison of the receptance tests (impulse applied at the middle of the sleeper): **a** sleeper results; **b** rail results

the full-track resonant frequency (around 50–100 Hz) and the rail resonant frequency (around 300 Hz). The anti-resonant rail is probably occurring around 200 Hz. The pin-pin frequency was not identified since it occurs for higher frequencies.

In order to evaluate the influence of the performance of cyclic tests before the receptance tests, the symmetry of the structure was analyzed comparing the receptance results of both rails and sleepers from both sides. Considering the impulse applied in the middle sleeper, the receptance results were compared. In Figs. 10a, b, the response of the sleepers and the rails is compared, respectively. Due to a fault on the accelerometer 3, the 50G accelerometers were used instead of 5G.

The results depicted in Fig. 10 show that the dynamic behavior of the integral structure may not be performed in symmetric conditions since the experimental curves are not overlapping.

4 Conclusions

A receptance test campaign was carried out in a ballasted track section installed in the laboratory of the *Heriot-Watt University*. This physical model has several advantages when compared to the real-field ballasted track (linear structure) since the tests are performed in a controlled environment, which means that it is easier to characterize/parameterize the materials. Indeed, there is control over the used materials, its quality, compaction conditions, etc. However, the geometry of the laboratory physical model, and consequently the boundary conditions, can have an influence on some test results as has been pointed out for the receptance tests. Additionally, in this receptance tests setup, this track section was previously submitted to more than 3 million loading cycles which can lead to the degradation of the structure. These constraints inherent to the laboratory ballasted track section influenced the receptance test results and analysis, which are summarized as follows:

- the test results show that there is not a total overlap of the experimental curves from tests in symmetric conditions, which means that the dynamic behavior of the integral structure may not be totally symmetric, probably due to the compaction conditions of the substructure and the differential settlements induced by the cyclic loadings;
- only the receptance tests on the middle sleeper show results above the coherence limit (0.9) until 300–400 Hz.

Further research is necessary to investigate the influence of boundary conditions in the receptance curves and also the heterogeneity of the structure under testing.

References

1. Aggestam E, Nielsen JCO, Bolmsvik R (2018) Simulation of vertical dynamic vehicle-track interaction using a two-dimensional slab track model. Int J Veh Mechan Mob 56:1633–1657
2. Knothe K, Wu Y (1998) Receptance behaviour of railway track and subgrade. Arch Appl Mechan (Ingenieur Archiv) 68:457–470
3. De Man AP (2002) A survey of dynamic railway track properties and their quality. PhD thesis, Delft University of Technology, Delft, The Netherlands
4. Hiensch M, Nielsen JCO, Verheijen E (2002) Rail corrugation in the Netherlands—measurements and simulations. Wear 253:140–149
5. Hartung CF, Frid A, Nielsen JCO (2003) Railway rolling noise emission from wheel and track—simulations and full-scale test rig measurements. In: Proceedings of the tenth international congress on sound and vibration, pp 1673–1680
6. Verbraken H, Veirman N, Cuellar V, Lombaert G, Degrande G (2015) The prediction of vibration transfer for railway induced ground vibration. Notes on numerical fluid mechanics and multidisciplinary design
7. Dos Santos NC, Colaço A, Costa PA, Calçada R (2016) Experimental analysis of track-ground vibrations on a stretch of the Portuguese railway network. Soil Dyn Earthq Eng 90:358–380
8. Coulier P, Cuéllar V, Degrande G, Lombaert G (2015) Experimental and numerical evaluation of the effectiveness of a stiff wave barrier in the soil. Soil Dyn Earthq Eng 77:238–253
9. Kaewunruen S, Remennikov AM (2007) Response and prediction of dynamic characteristics of worn rail pads under static preloads. In: 14th international congress on sound and vibration 2007, ICSV 2007, pp 61–68
10. Kaewunruen S, Remennikov AM (2008) An alternative rail pad tester for measuring dynamic properties of rail pads under large preloads. Exp Mech 48:55–64
11. Kaewunruen S, Tang T (2019) Dynamic behaviour of railway ballast exposed to flooding conditions. Int J Geomate 16:101–108

12. Ryue J, Thompson DJ, White PR, Thompson DR (2008) Investigations of propagating wave types in railway tracks at high frequencies. J Sound Vib 315:157–175
13. Alves Ribeiro C, Calçada R, Delgado R (2017) Experimental assessment of the dynamic behaviour of the train-track system at a culvert transition zone. Eng Struct 138:215–228
14. Costa PA, Calçada R, Cardoso AS (2011) Experimental validation of a 2.5D FEM-BEM model for the assessment of vibrations induced by traffic. In: Papadrakakis M, Fragiadakis M, Plevris V (eds) COMPDYN :3rd ECCOMAS thematic conference on computational methods in structural dynamics and earthquake engineering. Corfu, Greece
15. Čebašek TM, Esen AF, Woodward PK, Laghrouche O, Connolly DP (2018) Full scale laboratory testing of ballast and concrete slab tracks under phased cyclic loading. Transport Geotech 17:33–40

Investigation Into the Mechanical Behavior of Track-Bed Materials with Different Grain Size Distributions of Coarse Grains

Shuai Qi, Yu-Jun Cui, and Ren-Peng Chen

Abstract In French ancient railway substructure, the interpenetration of ballast and subgrade soils formed a new layer, namely interlayer. Along the depth, a decreasing trend of ballast content was identified in field investigation. In this study, the effect of C_u of coarse grains on the mechanical behaviors of interlayer soils was investigated by carrying out monotonic triaxial tests. Five volumetric contents of coarse grains f_v (5, 10, 20, 35, and 45%) and three C_u values were considered. Also, X-ray μCT scans were performed on representative samples to visualize the grain distributions. Results show that: (a) at each C_u value, from the variation trend of q_{max} with f_v, a characteristic volumetric content of coarse grains $f_{v\text{-cha}}$ was identified, defining two soil fabrics (namely fine-fine contact structure and grain-grain contact structure). When C_u decreased, $f_{v\text{-cha}}$ increased since fewer grain contacts were developed at smaller C_u; (b) in the case of grain-grain contact structure, the decrease of C_u increased the maximum deviator stress q_{max}, friction angle, Poisson's ratio and dilatancy angle, since more large grains were involved at smaller C_u; (c) in the case of fine-fine contact structure, the C_u decreasing led to decreases in q_{max}, friction angle, Poisson's ratio and dilatancy angle due to smaller quantity of coarse grains; (d) for two soil fabrics, the variations of Young's modulus and cohesion with C_u shared the same pattern: the smaller the C_u, the larger Young's modulus and the cohesion.

Keywords Monotonic triaxial tests · Grain size distribution · X-ray microcomputed tomography (μCT) scans

S. Qi · R.-P. Chen
Department of Civil Engineering, Zhejiang University, Hangzhou 310058, China

S. Qi · Y.-J. Cui (✉)
Laboratoire Navier/CERMES, Ecole Des Ponts ParisTech (ENPC), Champs-sur-Marne 77455, France
e-mail: yu-jun.cui@enpc.fr

S. Qi
School of Civil and Transportation Engineering, Beijing University of Civil Engineering and Architecture, Beijing 102616, China

1 Introduction

In France, conventional railway lines constitute 94% of the total railway network. Unlike the new lines, the conventional ones were built by directly putting ballast on the subgrade without setting a separation layer. Under the effect of train circulations, the ballast and the subgrade soils interpenetrated into each other, creating a new layer, namely interlayer. Field investigation showed that the ballast content decreased with depth. This decreasing trend roughly defined two soil fabrics: a ballast grain skeleton for the upper part and a fines matrix with ballast drowned in it for the lower part. The dry density of the interlayer was pretty high (2.4 Mg/m^3), defining a favorable mechanical behavior. Thus, during the renewable program for conventional lines, the interlayer was kept in the railway substructure.

As the grain size distribution (characterized by the coefficient of uniformity C_u) of the ballast contained in the interlayer can vary from one site to another, the mechanical behaviors of the interlayer can change accordingly. The effect of C_u was investigated in this study by performing monotonic triaxial tests on a microballast/fines mixture with five volumetric contents of coarse grains (5, 10, 20, 35, and 45%). Three C_u values (2.72, 2.01, and 1.12) of coarse grains were considered. In addition, X-ray micro-computed tomography (μCT) scans were carried out on representative samples to visualize the distributions of coarse grains. Based on the testing results, the effect of C_u on mechanical behaviors was analyzed.

2 Materials and Methods

Considering the difficulty of obtaining enough interlayer soils from the field, the constitutive fine soils and coarse grains were fabricated in the laboratory. For the preparation of the fine soils, a method proposed by Lamas-Lopez [8] was used, in which nine different commercial sands and clays were mixed at a global water content of 4%. Their mass proportions were determined according to the grain size distribution of the fines at "Sénissiat site" (Fig. 1a). After mixing, the grain size distribution of the fabricated fines was measured (see Fig. 1a), which agreed well with the in situ one. The liquid limit and the plasticity index of this fine material were identified as 32.0 and 20.0%, respectively. According to the standard of American Society for Testing and Materials D2487-11 [1], this fines material was lean clay (CL).

The maximum grain size of the field ballast can reach 63 mm, which was too large to be tested in the triaxial cell with 100 mm diameter adopted in this study. To eliminate the sample size effect, the ratio between sample diameter and maximum grain size was controlled to be 5, following the suggestion proposed by Nitchiporovitch [10] and Pedro [11]. This ratio was also widely adopted by many researchers [2–4, 15–17]. Indeed, as recommended by Vallerga et al. [13] and Chen et al. [5, 6], the ratio of 3 to 4 times is large enough for the triaxial tests. Thereby, the selected ratio
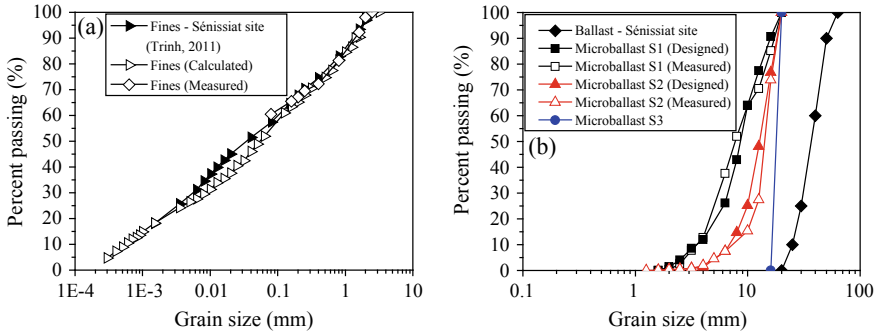
Fig. 1 Grain size distribution curves of **a** fines and **b** microballast materials with three different C_u values

of 5 can be considered to be reasonably sufficient to reflect the real behavior of the studied soils. In Wang et al. [16], a microballast material was designed (termed as S1 in this study), with its grain size distribution (Fig. 1b) determined based on that of the field ballast at "Sénissiat site" (Fig. 1b) by using the parallel gradation method [9]. To fabricate S1, three commercial grains were mixed with a mixing machine. The mass proportions of these three coarse grains were determined according to the grain size distribution of S1.

To study the effect of C_u, by reducing the proportion of smaller grains as compared to S1, another two microballast materials were designed and fabricated, which were termed as S2 and S3. The designed grain size distributions of S1, S2, and S3 are put together in Fig. 1b, their C_u values being 2.72, 2.01, and 1.12, respectively. As can be observed, when C_u decreased, the curve became steeper and the grain size range became narrower, defining a more uniform pattern. The fabricated grain size distributions of S1, S2, and S3 were also measured and plotted in Fig. 1b, which showed good agreements with the designed ones.

In order to quantify the coarse grains in a sample, a parameter, namely volumetric content of coarse grains f_v was adopted, defined as the ratio of the volume of the coarse grains V_c to the total sample volume V_{total}. The total sample volume can be calculated by the sample dimension (100 mm diameter and 200 mm height). For a certain f_v value, the volume of the coarse grains can be determined easily. Then, the dry mass of the coarse grains can be obtained with the dry unit mass of the coarse grains ($\rho_{s-c} = 2.68$ Mg/m^3). For the fine soils, its volume V_f was obtained by subtracting the coarse grain volume V_c from the total volume V_{total}. Note that all the pores are assumed to be included in the fines volume. The fines soils in all samples were kept at the optimum state defined by the optimum water content $w_{opt-f} = 13.7\%$ and the maximum dry density $\rho_{max-f} = 1.82$ Mg/m^3. With these two parameters, the dry mass of the fines and the water can be calculated accordingly.

In this study, five f_v values (5, 10, 20, 35, and 45%) and three C_u values (2.72, 2.01, 1.12) were considered. Note that the case of $C_u = 2.72$ has been studied by Wang et al. [16] and the relevant testing results were taken for comparison. For the

sample preparation, water was firstly sprayed to the fines to achieve the optimum water content of 13.7%. Then the wetted fines were stored in a hermetic container for 24 h for moisture homogenization. Afterward, these fines soils were mixed with the dry coarse grains. Finally, the mixture was compacted into a mold in three layers to obtain a sample with dimensions of 100 mm diameter and 200 mm height.

Monotonic triaxial tests were carried out with drainage valves open. No saturation procedure was applied, and the water contents in all samples were kept constant. Three confining pressures of 30, 60, and 120 kPa were considered, and a shearing rate of 0.5 mm/min was used. The test ended after the deviator stress reached a peak value or when an axial strain of 15% was attained.

X-ray μCT scans were performed on samples with $C_u = 1.12$ and four f_v values (5, 20, 35, and 45%). For each sample, the middle part (100 mm height) was scanned. The X-ray source's parameters were 170 kV and 10 μA. The voxel size that can be detected was 58.4 μm.

3 Results and Discussions

3.1 Changes of Shear Behavior with Volumetric Content of Coarse Grains

To illustrate the effect of f_v on shear behavior, the results of the samples with $C_u = 1.12$ under $\sigma_3 = 120$ kPa were used, as shown in Fig. 2. For the maximum deviator stress q_{max} (Fig. 2a), it increased slightly when f_v increased from 5 to 20%. By contrast, when f_v was larger than 35%, increasing f_v led to a significantly increase of q_{max}. When it came to the volumetric strain ε_v (Fig. 2b), the increase of f_v favored the dilatancy behavior. For $C_u = 1.12$ under $\sigma_3 = 30$ and 60 kPa, and for $C_u = 2.72$ and 2.01 under $\sigma_3 = 30$, 60 and 120 kPa, similar phenomena were observed.
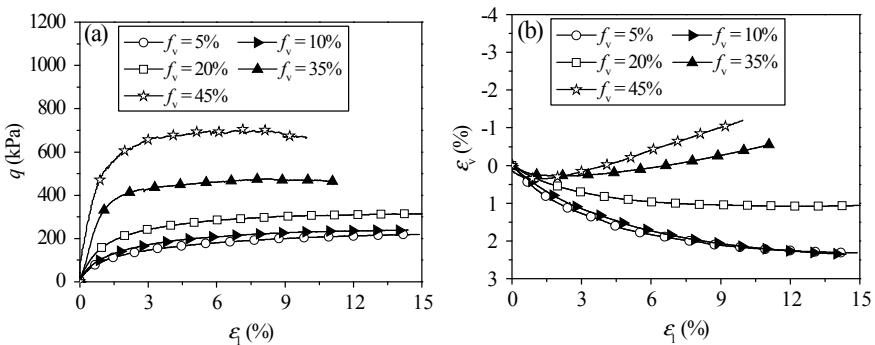
Fig. 2 Shear behavior of soils with $C_u = 1.12$ and different f_v values under $\sigma_3 = 120$ kPa

The maximum deviator stress q_{max} of all three C_u values is plotted against f_v in Fig. 4. At each C_u, q_{max} increased with the increase of f_v and a bilinear increasing trend of q_{max} was observed, with the slope at $f_v \geq 35\%$ distinctly larger than that at $f_v \leq 20\%$. At the intersection points of the two fitting lines passing through $f_v \geq 35\%$ and $f_v \leq 20\%$, a characteristic volumetric content of coarse grains $f_{v\text{-cha}}$ was identified. It can be suspected that the soil fabric at $f_v \leq f_{v\text{-cha}}$ was dominated by a fine-fine contact structure, while a grain-grain contact structure dominated the soil fabric at $f_v > f_{v\text{-cha}}$. To verify this point, three-dimensional (3D) views of the coarse grain distributions were built based on the two-dimensional (2D) μCT slices. Figure 5 shows the results of $C_u = 1.12$. As can be observed, when $f_v = 5$ and 20% (smaller than $f_{v\text{-cha}}$), the coarse grains floated in the fines matrix, while when $f_v = 35$ and 45% (larger than $f_{v\text{-cha}}$), the coarse grains were in contact with each other. Similar observations were made by Wang et al. [16] for the case of $C_u = 2.72$. To further clarify this aspect, the coarse grain contacts were quantitatively characterized with the average coordination number N_c of the 2D slice. For a given grain, its coordination number N_{ci} was defined as the total number of its neighboring grains [7]. For example, the coordination number N_{ci} of the gray grain in Fig. 3a is 4 (Fig. 3b). The coordination number N_c of a certain 2D slice was determined by averaging the coordination numbers of all grains [7]:

$$N_c = \frac{\sum N_{ci}}{Q} \tag{1}$$

where N_{ci} is the coordination number for a certain inclusion grain; Q is the quantity of the inclusion grains in a slice.

Twenty slices were selected for each sample. Figure 6 shows the coordination number of three C_u values against f_v. For a certain sample, the coordination number
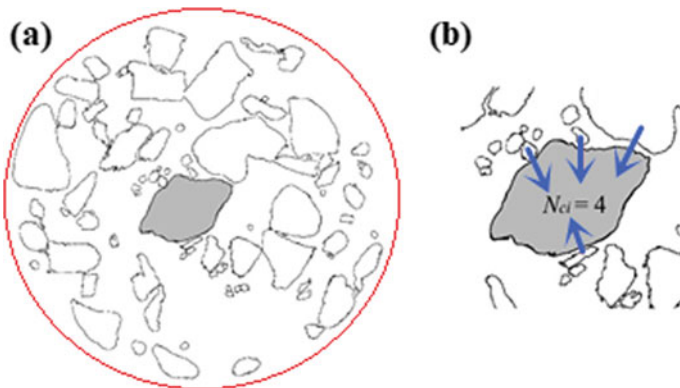
Fig. 3 Illustration of the definition of coordination number N_{ci} for a given grain ($f_v = 35\%$, $C_u = 2.72$) (after Wang et al. [15]): **a** processed slice showing only inclusions; **b** definition of coordination number for a given grain
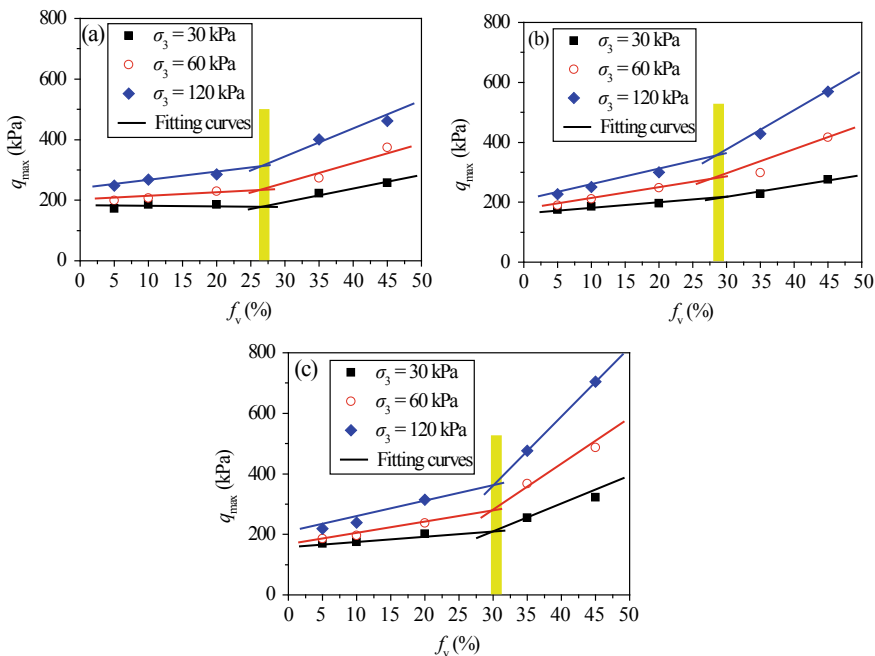
Fig. 4 Peak deviator stress versus f_v for: **a** $C_u = 2.72$; **b** $C_u = 2.01$; **c** $C_u = 1.12$
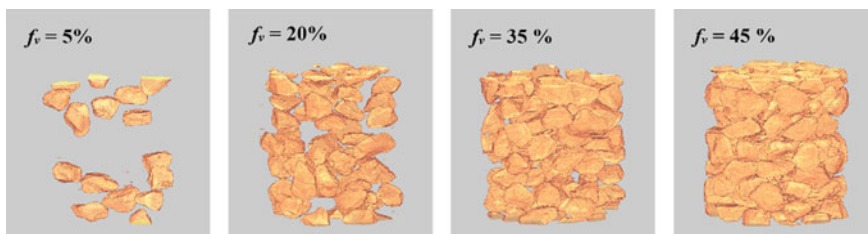
Fig. 5 Three-dimensional views of the coarse grain distributions inside samples with $C_u = 1.12$

Fig. 6 Coordination number versus f_v for three C_u values
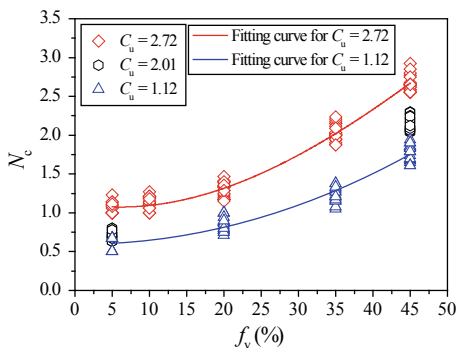
varied in a narrow range. In addition, for both cases of $C_u = 2.72$ and 1.12, N_c did not change significantly with the increase of f_v from 5 to 20% (smaller than $f_{v\text{-cha}}$) but increased drastically after $f_v = 35\%$ (larger than $f_{v\text{-cha}}$). For the case of $C_u = 2.01$, the N_c increasing was expected to follow the same pattern. This increasing trend of N_c suggests that the coarse grains were rarely in contact when $f_v \leq 20\%$, while the grain contacts were well developed when $f_v \geq 35\%$.

3.2 Effect of C_u on Characteristic Volumetric Content of Coarse Grains

As can be observed from Fig. 4, the decrease of C_u gave rise to an increase in $f_{v\text{-cha}}$: The $f_{v\text{-cha}}$ values for $C_u = 2.72$, 2.01, and 1.12 were 27.0, 28.8, and 30.5%, respectively. This suggests that to form a grain-grain contact structure at smaller C_u, more coarse grains were needed. This can be explained as follows: The N_c values of smaller C_u were smaller (Fig. 6) (due to smaller grain quantity in this case), suggesting that the grain contacts developed at smaller C_u were fewer. To some extent, $f_{v\text{-cha}}$ can be considered as a value where a certain number of coarse grain contacts were developed. Thus, to form a grain skeleton, more grains were needed, resulting in a larger $f_{v\text{-cha}}$.

3.3 Effect of C_u on Shear Behavior in the Case of Grain-Grain Contact Structure

The shear behavior of the soils with $f_v = 35\%$ under $\sigma_3 = 120$ kPa is shown in Fig. 7. It was observed that the decrease of C_u increased the q_{max} (Fig. 7a) and made the volume change more dilative (Fig. 7b). Similar phenomena were observed for $f_v =$
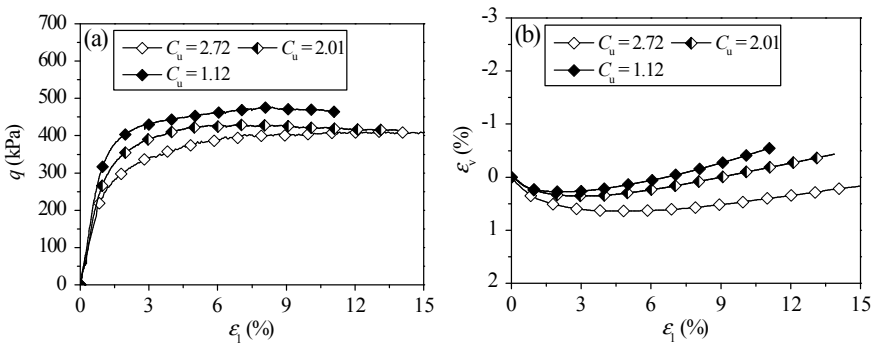
Fig. 7 Shear behavior of soils at $f_v = 35\%$ and three C_u values under $\sigma_3 = 120$ kPa

35% under $\sigma_3 = 30$ and 60 kPa, and for $f_v = 45\%$ under $\sigma_3 = 30$, 60 and 120 kPa, which can be explained as follows: With the maximum grain size set as the same value (namely 20 mm as shown in Fig. 1b), a smaller C_u corresponded to more large grains. During shearing, the rearrangement of large grains was harder. As a result, a larger q_{max} was obtained. As for the volumetric change, the more pronounced dilative behavior at smaller C_u can also be attributed to the involvement of more large grains, which favored the dilatancy. This mechanism can be termed as "large or small" of coarse grains in terms of grain size.

3.4 Effect of C_u on Shear Behavior in the Case of Fine-Fine Contact Structure

From the stress–strain behavior of the soils at $f_v = 5$ and 10% under $\sigma_3 = 120$ kPa (Fig. 9a), it can be observed that the smaller the C_u, the smaller the q_{max}. A similar phenomenon was observed for $f_v = 5$ and 10% under $\sigma_3 = 60$ kPa. However, q_{max} of three C_u values was similar under $\sigma_3 = 30$ kPa (Fig. 8a). This is possibly because q_{max} reflected the friction at failure, which was dominated by two factors, namely the soil property mainly related to the quantity of coarse grains involved in the friction process (e.g., in the shear band zone) and the confining pressure corresponding to the normal stress in the friction process. It seemed that $\sigma_3 = 30$ kPa was too small to reveal this C_u effect. The decrease of q_{max} with C_u decreasing observed at $\sigma_3 = 60$ and 120 kPa can be attributed to smaller quantity of coarse grains at smaller C_u, which caused less coarse grains to present along the shear band, resulting in a smaller q_{max}. This mechanism can be termed as "more or less" of coarse grains in terms of grain quantity.

As for volumetric strain ε_v (see Fig. 8b and Fig. 9b for the cases of $f_v = 5$ and 10% under $\sigma_3 = 30$ and 120 kPa), the increasing C_u made the dilatancy more pronounced. A similar phenomenon was observed under $\sigma_3 = 60$ kPa, which can be explained by
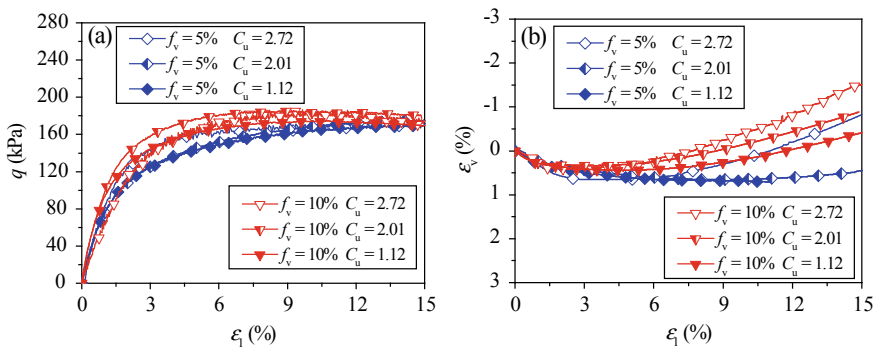
Fig. 8 Shear behavior of soils at $f_v = 5$ and 10% and three C_u values under $\sigma_3 = 30$ kPa
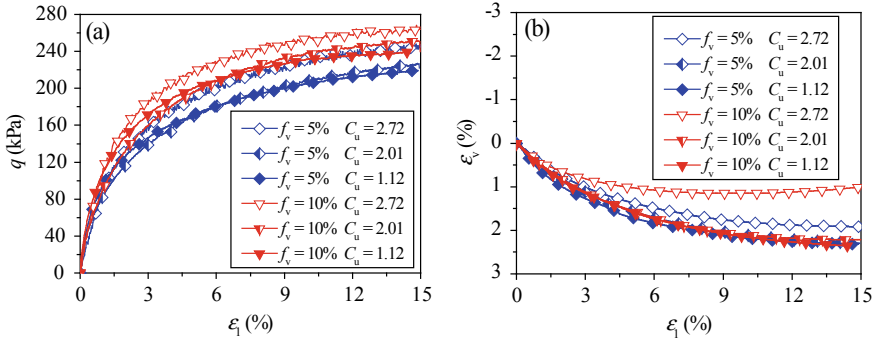
Fig. 9 Shear behavior of soils at $f_v = 5$ and 10% and three C_u values under $\sigma_3 = 120$ kPa

the increase of grain quantity, increasing the amount of the grain-grain contacts and thus producing a larger dilatancy.

For $f_v = 20\%$, the results of the soils sheared under $\sigma_3 = 60$ kPa are taken as an example and shown in Fig. 10. The q_{max} and ε_v were almost the same for the three C_u values. This phenomenon was also observed under $\sigma_3 = 30$ and 120 kPa. This independence feature with respect to C_u can be explained as follows: In this case, the grain-grain contact skeleton was not well developed with only parts of the coarse grains in contact with each other. Thus, both the mechanisms of "large or small" and "more or less" took part in the shear process, the effects of which were opposite, leading to a shear behavior independent of C_u value.
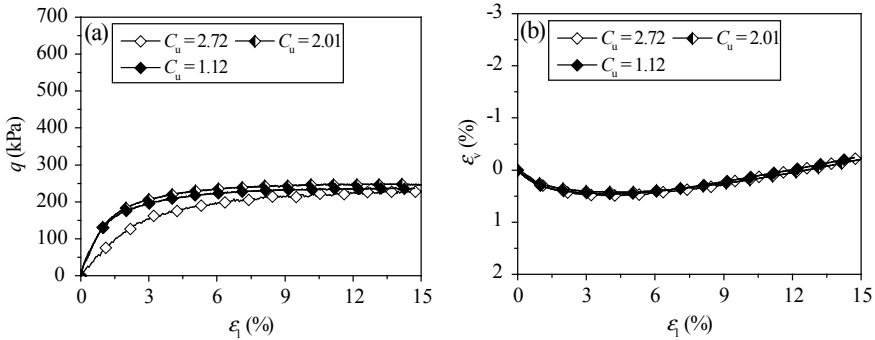
Fig. 10 Shear behavior of soils at $f_v = 20\%$ and three C_u values under $\sigma_3 = 60$ kPa

Fig. 11 Young's modulus versus f_v for different C_u and σ_3 values
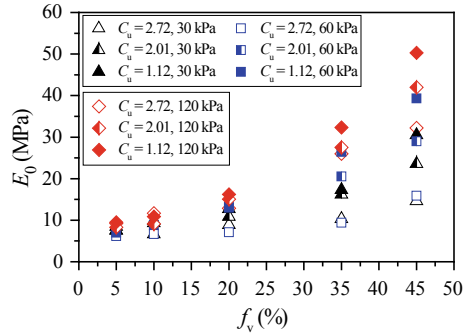
3.5 Effect of C_u on Young's Modulus

For the sake of simplicity, in this study, Young's modulus E_0 was defined as the ratio of deviator stress q to axial strain ε_1 when $\varepsilon_1 = 1\%$. Figure 11 presents the variations of E_0 with C_u at different f_v values. It can be observed that the C_u effect became more pronounced when f_v increased. At each f_v value, E_0 increased with C_u decreasing. This phenomenon can be explained as follows: The resilient modulus was determined by the resilient strain under a certain stress level, which mainly occurred at the contacts between grains. When C_u decreased, the grain quantity decreased due to the involvement of less small grains. As a result, less grain contacts were created, implying less grain interactions. Thus, a larger M_r was obtained.

3.6 Effect of C_u on Poisson's Ratio and Dilatancy Angle

Poisson's ratio v and the dilatancy angle ψ were calculated based on the volumetric strain–axial strain relationship. More details for the calculation of these two parameters can be found in Wang et al. [16]. In Fig. 12a, Poisson's ratio of all C_u values is plotted against f_v. For $f_v = 5$ and 10%, Poisson's ratio of smaller C_u was smaller, suggesting that the lateral strain decreased with less coarse grains dispersed in the fines matrix. For the grain-grain contact structure ($f_v = 35$ and 45%), Poisson's ratio increased when C_u decreased. Note that for $f_v = 20\%$ the soil fabric of which was identified as fine-fine contact structure, the variation trend of Poisson's ratio with decreasing C_u was the same as the one at grain-grain contact structure. This can be attributed to the fact that at $f_v = 20\%$ parts of the coarse grains were in contact with each other. This increasing trend of Poisson's ratio with decreasing C_u can be explained by the involvement of more large grains, which enlarged the lateral strain at a given axial strain, giving rise to a larger Poisson's ratio.

Figure 12b presents the dilatancy angle of all C_u values against f_v. At grain-grain contact structure, the dilatancy angle increased when C_u decreased, whereas
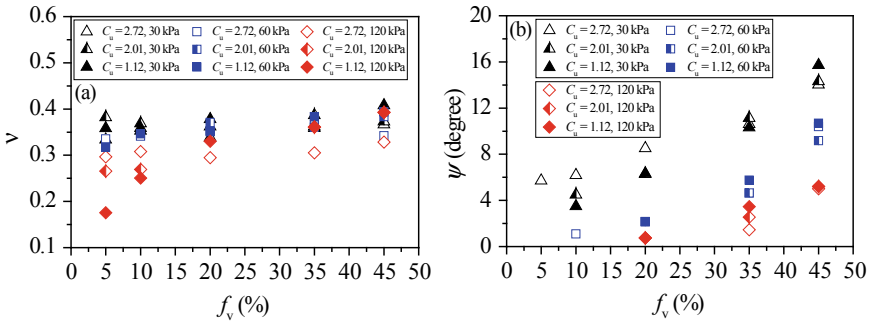
Fig. 12 **a** Poisson's ratio and **b** dilatancy angle versus f_v for different C_u and σ_3 values

an opposite trend was observed at fine-fine contact structure: The C_u decreasing led to a decrease in dilatancy angle.

3.7 Effect of C_u on Cohesion and Friction Angle

The cohesion and the friction angle were determined based on the failure line in the p–q plane. More details about the calculation process can be found in Wang et al. [16]. The variation of cohesion with C_u at different f_v values is plotted in Fig. 13a. Generally, for all f_v values, when C_u increased, the cohesion decreased. This can be explained as follows: The quantity of coarse grains increased with the increase of C_u, creating more grain-grain contacts and correspondingly decreasing the quantity of fine-fine contacts. As a result, a smaller cohesion was obtained.

For friction angle, as shown in Fig. 13b, an increasing trend of friction angle with decreasing C_u was observed for grain-grain contact structure ($f_v = 35$ and 45%) and for the case of $f_v = 20\%$, which can be explained by the fact that the rearrangement of coarse grains in the case of smaller C_u was more difficult since more large grains
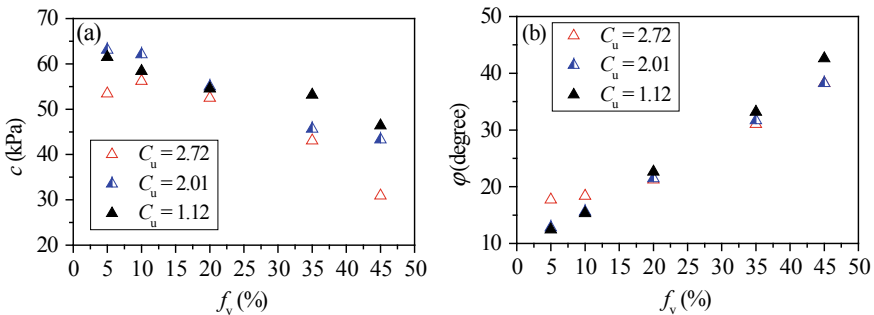
Fig. 13 **a** Cohesion and **b** friction angle versus f_v for different C_u values

were involved. As for the fine-fine contact structure, the friction angle of smaller C_u was smaller. This was because fewer coarse grains were presented along the shear band in this case.

4   Conclusions

This study investigated the effect of C_u of coarse grains on the mechanical behaviors of a microballast/fines mixture representing interlayer soils, by performing monotonic triaxial tests and X-ray micro-computed tomography (μCT) scans. Five volumetric contents of coarse grains (5, 10, 20, 35, and 45%) and three C_u values (2.72, 2.01, and 1.12) were considered.

For each C_u, peak deviator stress q_{max} increased with the volumetric content of coarse grains f_v increasing. Based on the increasing pattern of q_{max}, a characteristic volumetric content of coarse grains f_{v-cha} was identified, with which two soil fabrics can be defined, namely fine-fine contact structure and grain-grain contact structure. The f_{v-cha} of smaller C_u was larger, because in this case the formation of the grain-grain contact structure needed more coarse grains.

In the case of grain-grain contact structure, the overall soil behaviors were dominated by the amount of large coarse grains. When C_u decreased, the peak deviator stress increased and so did the friction angle. This could be explained by the involvement of more large grains, the rearrangement of which was more difficult during shearing. The C_u decreasing increased Poisson's ratio and dilatancy angle. This was also owing to the involvement of more large grains, enlarging the lateral strain at a given axial strain and favoring the dilatancy.

In the case of fine-fine contact structure, the soil behaviors were controlled by the amount of total coarse grains. Smaller q_{max} and smaller friction angle were observed for smaller C_u corresponding to smaller amount of total grains, since the coarse grains presented along the shear band were fewer in this case. The decrease of C_u led to decreases in Poisson's ratio and dilatancy angle, which can be attributed to fewer grain contacts at smaller C_u.

The two soil fabrics shared the same varying trend in terms of Young's modulus: Young's modulus increased when C_u decreased. This can be explained by the involvement of more large grains. In addition, when C_u increased, the cohesion decreased at both two soil fabrics, since the cohesion was expected to result from the fine-fine contacts and the increase of the grain quantity decreased such contacts.

References

1. ASTM D2487-11 (2011) Standard practice for classification of soils for engineering purposes (unified soil classification system). ASTM International, West Conshohocken, PA, USA

2. Cai YQ, Chen JY, Cao ZG, Gu C, Wang J (2018) Influence of grain gradation on permanent strain of unbound granular materials under low confining pressure and high-cycle loading. Int J Geomech 18(3):04017156

3. Cao ZG, Chen JY, Cai YQ, Zhao L, Gu C, Wang J (2018) Long-term behavior of clay-fouled unbound granular materials subjected to cyclic loading with different frequencies. Eng Geol 243:118–127

4. Cerni G, Cardone F, Virgili A (2012) Characterisation of permanent deformation behavior of unbound granular materials under repeated triaxial loading. Conctruct Build Mater 28(1):79–87

5. Chen WB, Yin JH, Feng WQ, Borana L, Chen RP (2018) Accumulated permanent axial strain of a subgrade fill under cyclic high-speed railway loading. Int J Geomech 18(5):04018018

6. Chen WB, Feng WQ, Yin JH, Borana L, Chen RP (2019) Characterization of permanent axial strain of granular materials subjected to cyclic loading based on shakedown theory. Constr Build Mater 198:751–761

7. Jouannot P, Jernot JP, Lantuejoul C (2006) Particle determination of the coordination number in granular media. Image Anal Stereol 25:55–61

8. Lamas-Lopez F (2016) Field and laboratory investigation on the dynamic behaviour of conventional railway track-bed materials in the context of traffic upgrade (Ph.D. thesis). Ecole Nationale des Ponts et Chaussées, Université Paris-Est, Marne-la-Vallée, France

9. Lowe J (1964) Shear strength of coarse embankment dam materials. In: Proceedings of the 8th international congress on large dams 3, pp 745–761. International commission on large dams, Paris

10. Nitchiporovitch AA (1969) Shearing strength of coarse shell materials. In: Proceedings of the 7th international conference on soil mechanics and foundation engineering, pp 211–216. Sociedad Mexicana de Mecanica, Mexico

11. Pedro L (2004) De l'étude du comportement mécanique de sols hétérogènes modèles à son application au cas des sols naturels (Ph.D. thesis). Ecole Nationale des Ponts et Chaussées, Université Paris-Est, Marne-la-Vallée, France

12. Seif El Dine B, Dupla JC, Frank R, Canou J, Kazan Y (2010) Mechanical characterization of matrix coarse-grained soils with a large-sized triaxial device. Can Geotech J 47:425–438

13. Vallerga BA, Seed HB, Monismith CL, Copper RS (1956) Effect of shape, size and surface roughness of aggregate particles on the strength of granular materials. In: Symposium on road and paving materials, pp. 63–76. American Society for Testing and Materials, America

14. Wang HL, Cui YJ, Lamas-Lopez F, Dupla JC, Canou J, Calon N, Saussine G, Aimedieu P, Chen RP (2017) Effects of inclusion contents on resilient modulus and damping ratio of unsaturated track-bed materials. Can Geotech J 54:1672–1681

15. Wang HL, Cui YJ, Lamas-Lopez F, Dupla JC, Canou J, Calon N, Saussine G, Aimedieu P, Chen RP (2018) Permanent deformation of track-bed materials at various inclusion contents under large number of loading cycles. J Geotech Geoenviron Eng 144(8):04018044

16. Wang HL, Cui YJ, Lamas-Lopez F, Calon N, Saussine G, Dupla JC, Canou J, Aimedieu P, Chen RP (2018) Investigation on the mechanical behavior of track-bed materials at various contents of coarse grains. Constr Build Mater 164:228–237

17. Wichtmann T, Rondon HA, Niemunis A (2009) Prediction of permanent deformations in pavements using a high-cycle accumulation model. J Geotech Geoenviron Eng 136(5):728–740

Stress–Strain Analysis of Heavy Haul Rail Track with Steel Slag Ballast by Laboratory Tests and Numerical Simulations

Bruno Guimarães Delgado ⓘ**, António Viana da Fonseca** ⓘ**, and Eduardo Fortunato** ⓘ

Abstract The resilient response of the ballast layer is a key aspect for stress–strain behavior of rail track lines. This paper presents part of an extensive research that has been evaluating the possibility of using, with operational benefits, Inert Steel Aggregates for Construction (ISAC) as heavy haul railroad ballast material. Stress–strain analyses were performed by finite element method (FEM) whose pseudo-elastic parameters for nonlinear constitutive laws were obtained from resilient modulus tests by Method B from European Standard EN 13,286-7 (CEN: Unbound and hydraulically bound mixtures—Part 7: cyclic load triaxial test for unbound mixtures. EN 13,286–7, Brussels (2004) [CEN (European Committee for Standardization) (2004) Unbound and hydraulically bound mixtures—Part 7: cyclic load triaxial test for unbound mixtures. EN 13286-7, Brussels]) for 'higher stress levels' carried out under scaled down ballast specimens in a ratio of 1:2.5 from ballast standard AREMA N. 24 (AREMA, Manual for railway engineering, vol I–IV. Lanham (2015) [AREMA (American Railway Engineering Maintenance-of-way Association) (2015) Manual for railway engineering, vol I–IV. Lanham, USA]). The numerical simulations were carried out at two loading levels (32.5 and 40 t/axle) increased by dynamic impact coefficient of 1.4. The results showed that the structure with ISAC ballast has lower levels of vertical displacements and moments on the rails and was able to concentrate more stress in the ballast layer decreasing slightly the stress level on the top of platform in comparison with what was observed for the structure with a well-known-granite ballast, commonly used in rail track lines around the world.

Keywords Steel slag ballast · Resilient modulus · Numerical simulations

B. G. Delgado (✉) · A. Viana da Fonseca
CONSTRUCT-GEO, Faculty of Engineering, University of Porto, Rua Dr. Roberto Frias S/N, Porto, Portugal
e-mail: up201502655@fe.up.pt

A. Viana da Fonseca
e-mail: viana@fe.up.pt

E. Fortunato
National Laboratory for Civil Engineering, Av. do Brasil 101, Lisboa, Portugal
e-mail: efortunato@lnec.pt

1   Introduction

The circular economy concept has driven the use of industrial by-products in several construction industry applications. Some researchers indicate that steel slags can be used, for example, in bound and unbound granular layers for transport substructures, provided that steel slag is previously stabilized to ensure its chemical and environmental stability [3, 4]. Regarding the possibility of using steel slag as railway ballast material, there are interesting studies available, but most focus is on evaluating this material just from environmental point of view, its electrical resistance or mechanical properties based on index parameters expressed in ballast specifications. This has included correlations with Los Angeles and micro-Deval tests results, or even based on particle crushing strength test results [5, 6]. However, few studies have been carried out to evaluate this material under loading and boundary conditions compatible with the application in question, especially regarding the high cyclic loading provided by passage of heavy haul trains.

In Portugal, for example, the aggregate from electrical arc furnace steel slag, after processing by steel companies, is classified as an inert aggregate, in terms of expansibility and environmental issues, having given rise to the trade denomination 'Inert Steel Aggregate for Construction (ISAC)' [4]. In the medium term, it is estimated that in Portugal, approximately 400×10^3 tonnes per year of steel slag will be produced [4], which, if used as ballast material, will allow to the construction of approximately 250 km of railway tracks per year.

Nowadays, a target for the main heavy haul freight rail companies in the world is to increase the freight capacity from about 25–32.5 to 40 tonnes per axle, sometimes under extreme weather conditions, such as in Brazilian Amazon region [7]. In Brazil, four heavy haul railway lines account for 82% of the total demand for freight railway transport. The ballast layer of these railway tracks uses natural crushed rocks, mainly granite, basalt and gneiss, with particle size distribution (PSD) curve framed in the standard gradation AREMA N. 24 [2].

Recent laboratory studies have shown that under axle loads of 40 tonnes, the ISAC ballast presented superior performance compared to traditional granite aggregate ballast with regard to long-term plastic behavior [7] due to, possibly, the highest angularity and crushing strength of its particles [8].

Thus, an extensive study has been carried out at Laboratory of Geotechnics (LabGEO) of the Faculty of Engineering of the University of Porto (FEUP) in partnership with the National Laboratory for Civil Engineering (LNEC) to evaluate the possibility to apply ISAC as railway ballast material in terms of stress–strain behavior under heavy cyclic loading conditions. Therefore, resilient modulus tests were carried out to obtain pseudo-elastic parameters aiming to simulate the railway track response from nonlinear elastic constitutive laws using a numerical solution.

2 Laboratory Tests

2.1 Overview

In order to maintain the specimen representativeness in triaxial tests, several researchers have recommended that the ratio between the maximum particle size and the diameter of specimen needs to be about 1/6. This ratio is also specified by American Standard ASTM D5311 [9] for soils. However, some results shown that a ratio of 1/5 has lead to good results [10]. Moreover, Bishop and Green [11] recommend that the ratio between height (H) and diameter of sample (D) should approach two, being this recommendation adopted almost universally in geotechnical laboratories. These restrictions imply the need of 'extra-large' (and expensive) triaxial apparatus for ballast laboratory studies [12, 13].

With the purpose to perform triaxial tests with granular materials at lower costs, Lowe [14] proposed to carry out tests with the material on scaled down specimens by parallel gradation technique, where a smaller PSD curve, but composed of the same material, can be used in triaxial cells (large but not 'extra-large') if the scaled PSD curve is parallel to the full-scale PSD curve of the material.

The scale reduction techniques of triaxial specimens to evaluate the geomaterials mechanical behavior are not consensual among the researchers. However, regarding deformability parameters, Sevi and Ge [15] conducted studies that pointed to the possibility of carrying out triaxial tests with scaled down specimens by parallel gradation technique, when the characteristics of constituting particles are similar (e.g., size, shape, surface roughness, particle crushing strength, resistance to attrition). This would ensure that the material at the same compaction level (relative density) would attain similar physical indices on full or reduced scale.

Rosa [16] correlated resilient modulus values obtained from full-scale ballast against values obtained from scaled down ballast. Ballast materials with similar particles morphology were used, both full and reduced scale, for different genesis and PSD curves, and a good correlation between modulus values were found, concluding favorably to the use of resilient ballast parameters from scaled down specimens for stress–strain analysis, since the modulus values either full-scale or scaled down had the same order of magnitude and also because the stress distribution is not so sensitive to small resilient modulus values variations.

For the studies in this paper, scaled down ballast specimens were used, obtained by parallel gradation technique in a ratio of 1:2.5 from the full-scale ballast standard AREMA N. 24 (Fig. 1a). This scaling down ratio was established as the minimum necessary to meet the 1/5 restriction between the maximum particle size and the diameter of specimen, as specimens of 150 mm diameter and 300 mm height were used. These specimens were molded by vacuum (usual procedure for non-cohesive granular materials) which was only possible due to completely dry ballast specimens. After molding, the specimens were instrumented with three axial linear variable differential transducers (LVDTs), at 120° from each other, fixed along the entire
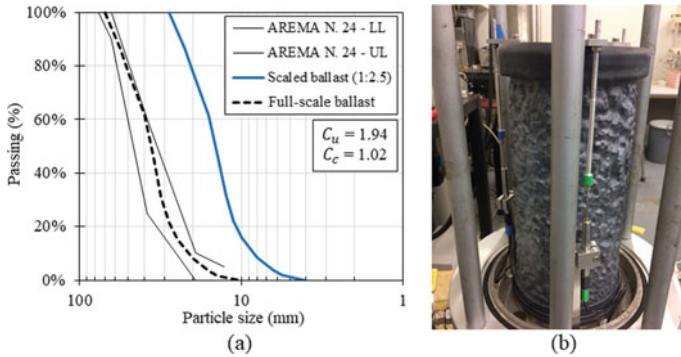
Fig. 1 **a** Particle size distribution of scaled ballast from AREMA N. 24 limits; and **b** example of scaled ballast specimen with LVDTs

height of the specimens; for this, a screw system was fixed at triaxial cell base and at top-cap of specimens tested (Fig. 1b).

The tests to determine the resilient modulus were carried out according to the method B (constant confining pressure) by European Standard EN 13,286-7 [1], applying the 'higher stress level' protocol. Figure 2 shows the stress paths, in the $p' - q$ plane, applied during triaxial tests to define the resilient modulus values of the studied materials, in which 100 cycles per path are applied (resilient modulus test). More details about the triaxial apparatus can be seen in Delgado et al. [7]. The tests strictly follow the standard procedure, after specimen conditioning with 20,000 cycles of deviatoric stress application with 340 kPa and a constant confining pressure of 70 kPa.

Fig. 2 Cyclic stress paths for resilient modulus test in the high stress level (HSL) with constant confining pressure (method B by EN 13,286-7 [1])
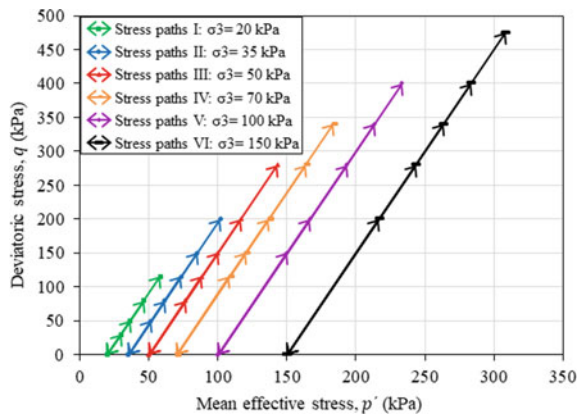
2.2 Resilient Parameters

Figure 3 shows the resilient modulus values obtained by laboratory triaxial tests. The results are presented both against confining pressure and cyclic deviatoric stress (q_{cyc}). For all applied stress paths, it can be seen that the ISAC presented higher values of resilient modulus than the granite aggregate. It is important to note that in both materials, as expected for non-cohesive granular materials, the values of resilient modulus were more sensitive to variation of the confining pressure than to variation of the deviatoric stress, at least for the low-to-moderate stress ratios (q_{cyc}/p').

It should be noted that all resilient modulus tests were considered satisfactory, since the accumulated permanent deformation during the tests was less than 0.2%.

The stiffness parameters obtained by regression analyses for the models of resilient behavior that take into account the variation of the resilient modulus (RM) against the confining pressure and against the cyclic deviatoric stress, as well as the model that takes into account the variation of the RM against the first invariant of stresses (θ), are shown in Table 1, for the resilient modulus tests performed. For triaxial tests under axisymmetric stress conditions, we have:

$$\theta = \sigma_1 + 2.\sigma_3 = q_{cyc} + 3.\sigma_3 \tag{1}$$
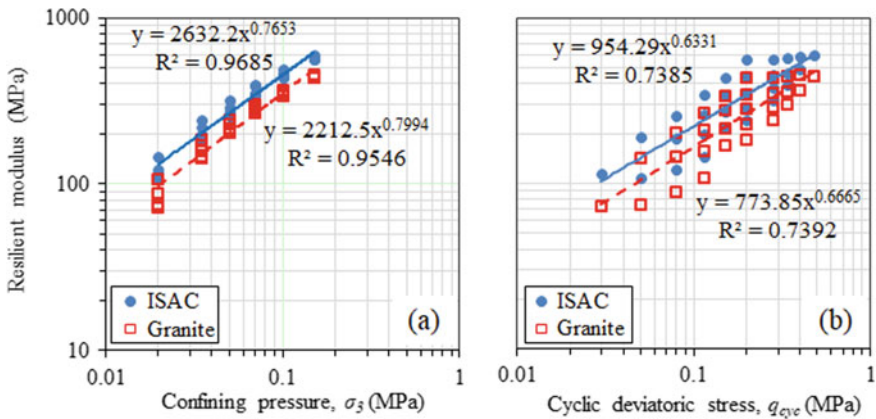
Fig. 3 Variation of resilient modulus for the ballast materials against: **a** confining pressure and **b** cyclic deviatoric stress

Table 1 Resilient parameters of nonlinear elastic ballast models

Material	Model		
	RM $= K_1 \sigma_3^{K_2}$	RM $= K_1 q_{cyc}^{K_2}$	RM $= K_1' \theta^{K_2'}$
ISAC	K_1=2632.2 K_2=0.7653 $(R^2 = 0.9685)$	K_1=954.3 K_2=0.6331 $(R^2 = 0.7385)$	K_1'=1692.4 $K_2' = 0.7986$ $(R^2 = 0.9531)$
Granite	K_1=2212.5 K_2=0.7994 $(R^2 = 0.9546)$	K_1=773.9 K_2=0.6665 $(R^2 = 0.7392)$	K_1'=1368.1 K_2'=0.8269 $(R^2 = 0.9466)$

Note $q = \sigma_1 - \sigma_3$, being σ_1 the major principal stress (vertical cyclic loading) and σ_3 is the minor principal stress (usually the constant confining pressure in the triaxial cell)

3 Numerical Simulations

3.1 Finite Element Analyses

Four scenarios were simulated: (i) Scenario 1–32.5 t/axle loading with ISAC ballast; (ii) Scenario 2–32.5 t/axle loading with granite aggregate ballast; (iii) Scenario 3–40 t/axle loading with ISAC ballast; and (iv) Scenario 4–40 t/axle loading with granite aggregate ballast. The *SysTrain* (version 1.63) software was used, which was developed at the Military Institute of Engineering (IME) from Brazil. The software models both superstructure (rails, sleepers and fastening system) and substructure (ballast, sub-ballast and subgrade) by finite element method (FEM) and presents as major attractions for users: (i) a 3D graphical interface based on the *MS-Windows®* platform; (ii) parametric modeling from a predefined rail track geometry; (iii) constitutive models and some materials with parameters already pre-registered, with the possibility, however, of alteration or inclusion of new models and/or materials; and (iv) a relatively fast and reliable stress–strain analysis in elastic regime (under static loading).

Silva Filho [17] provides a detailed description of the discretization, parameterization, numerical integration and convergence methods adopted by *SysTrain*. He was a member of the software development team and reports also that the software has undergone several calibration processes, both by field instrumentation and by comparison with another numerical model (*ANSYS®* v.15), ensuring analyzes with a good reliability level.

The software is three-dimensional and allows several possibilities regarding the number of sleepers, number of substructure layers, types and position of loading (on the symmetry axis of sleepers or on the gap between them), substructure layers geometry, etc. About the constitutive models for the rail track components, both superstructure and substructure, the software has nine predefined models.

The boundary conditions define a lower rigid boundary and null displacements in the normal direction to the model's vertical boundary planes.

| GDT = | 183 cm | 353 cm | 183 cm | 254 cm | 183 cm | 353 cm | 183 cm |
| GDU = | 185 cm | 445 cm | 185 cm | 234 cm | 185 cm | 445 cm | 185 cm |
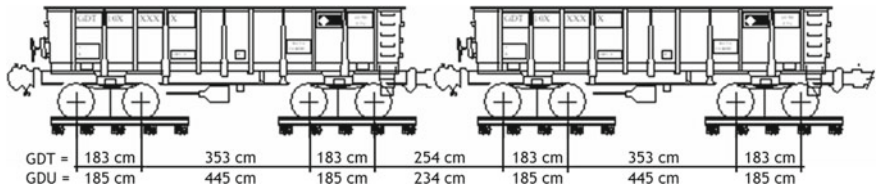
Fig. 4 Scheme of two consecutive gondola wagons (GDT/GDU—not to scale) [18]

The most severe condition for stress–strain analysis of heavy haul rail tracks is given by the bogies between adjacent wagons [18]. Thus, the loading for simulations was defined as being imposed by two bogies between couplings of two consecutive gondola wagons (GDT type for 32.5 t/axle loading and GDU type for 40 t/axle loading) (Fig. 4), applied to a structure with nineteen sleepers (same spacing). More details about these wagons can be seen in Santos et al. [19].

Figure 5 shows a cross section of the rail track structure, with dimensions of the components and layers used to the numerical simulations. Figure 6a shows the load distribution applied by GDU wagons used to simulate 40 t/axle loading (the loads
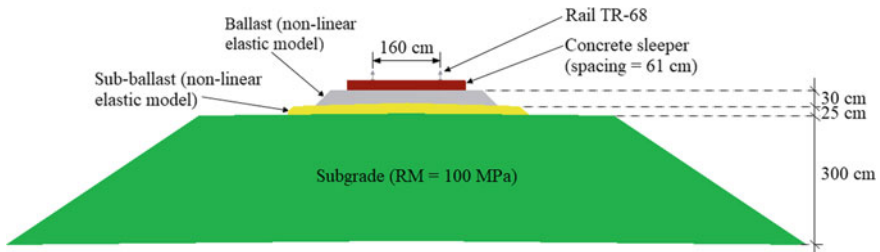
Fig. 5 Cross section with simulated rail track structure (not to scale)
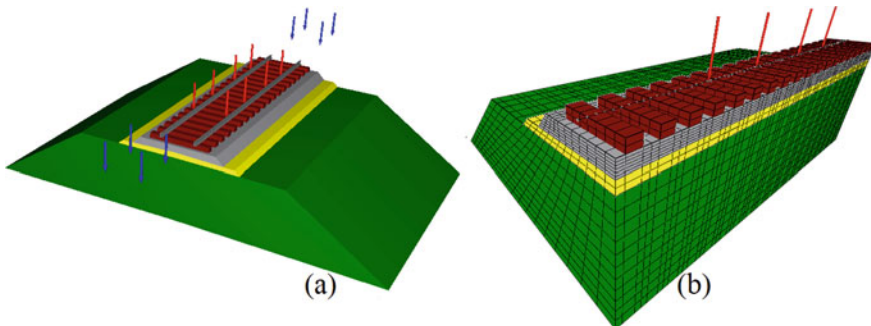
Fig. 6 3D rail track structure used to FEM simulations with GDU wagons: **a** geometric and load distribution model (red arrows represent the wheels loading the model; the blue arrows represent only geometric positions of the extreme wheels of wagons) and **b** finite element mesh

corresponding to the two extreme axles, blue vectors, were not considered in the simulations). Figure 6b shows the three-dimensional finite element mesh employed in the analysis for this loading level, which is transversely symmetrical with respect to a vertical axis located midway between rails.

Considering that the *SysTrain* software only simulates static loading under the structure and assuming a dynamic coefficient of 1.4, estimated by empirical equations [2], the 32.5 t/axle loading was converted into a GDT wagon with a total gross weight of 182 tonnes. Similarly, the 40 t/axle loading was increased with the same impact factor, resulting in a total gross weight of 224 tonnes per GDU wagon.

The parameters used to the simulations are presented in Table 2. For the ballast, the parameters were obtained by linear regression taking into account the variation of the resilient modulus against the confining pressure, due to the good fit of this model for studied materials. For the sub-ballast, the parameters were obtained from Delgado [18]. The other parameters were obtained from the software library.

In addition, four additional simulations were carried out, considering the same load levels, materials and boundary conditions, but with a unit load applied to the vertical centerline of a central sleeper under a structure with nine sleepers. This loading framework is the critical condition for sleeper–ballast contact stress.

3.2 Results

Figure 7 shows the 3D deformed meshes with the node vertical displacements for the four simulated scenarios.

For all carried out simulations, the negative result values indicate compressive stresses and downward displacements and the positive result values indicate tensile stresses and upward displacements.

As expected, the maximum displacements occur in the regions immediately below the load application points. For both studied materials, both for the 32.5 t/axle (scenarios 1 and 2) and the 40 t/axle (scenarios 3 and 4), the maximum displacements on the rail top level were similar for both materials under the same loading level.

For axle load of 32.5 tonnes, the maximum displacements obtained were below the tolerance limit recommended by AREMA [2], which is 6.35 mm, but slightly lower for ISAC (5.87 mm) in comparison to the granite aggregate ballast (6.05 mm), implying that the rail track structure with ISAC ballast is stiffer for this loading level.

However, for 40 t/axle loading the maximum displacements obtained were already above the tolerance limit [2]. Nevertheless, the values were again slightly lower for the ISAC (7.41 mm) in comparison to the granite aggregate (7.64 mm), showing again the higher stiffness of the rail track structure with ISAC ballast also for this loading level, as can be compared in Fig. 8 for the four simulated scenarios.

The maximum vertical stress values in the ballast layer for both studied materials were reached, as expected, at the base of sleepers. Figure 9 shows sleeper–ballast interface contact stress for all additional simulated scenarios, in a semi-cross section

Table 2 Material parameters adopted in FEM analysis

Rail track component	Parameter	Value			
		Scenario 1	Scenario 2	Scenario 3	Scenario 4
Rails	Density (kg/m^3)	7850	7850	7850	7850
	Elastic modulus (Pa)	210×10^9	210×10^9	210×10^9	210×10^9
	Poisson's ratio	0.30	0.30	0.30	0.30
Sleepers	Density (kg/m^3)	2400	2400	2400	2400
	Elastic modulus (Pa)	32×10^9	32×10^9	32×10^9	32×10^9
	Poisson's ratio	0.25	0.25	0.25	0.25
Fastenings	Spring stf. K_x (N/m)	7×10^6	7×10^6	7×10^6	7×10^6
	Spring stf. K_y (N/m)	7×10^6	7×10^6	7×10^6	7×10^6
	Spring stf. K_z T (N/m)	70×10^6	70×10^6	70×10^6	70×10^6
	Spring stf. K_z C (N/m)	70×10^6	70×10^6	70×10^6	70×10^6
Ballast	Bulk density (kg/m^3)	1800	1550	1800	1550
	Coefficient K_1'	67,378.12	35,357.64	67,378.12	35,357.64
	Coefficient K_2'	0.7653	0.7994	0.7653	0.7994
	σ_3 minimum (Pa)	20.7×10^3	20.7×10^3	20.7×10^3	20.7×10^3
	σ_3 maximum (Pa)	137.9×10^3	137.9×10^3	137.9×10^3	137.9×10^3
	Poisson's ratio	0.20	0.20	0.20	0.20
Sub-ballast	Bulk density (kg/m^3)	1730	1730	1730	1730
	Coefficient K_1'	131.22×10^6	131.22×10^6	131.22×10^6	131.22×10^6
	Coefficient K_2'	-0.232	-0.232	-0.232	-0.232
	σ_d minimum (Pa)	1×10^3	1×10^3	1×10^3	1×10^3
	σ_d maximum (Pa)	206×10^3	206×10^3	206×10^3	206×10^3
	Poisson's ratio	0.40	0.40	0.40	0.40
Subgrade	Bulk density (kg/m^3)	1800	1800	1800	1800
	Coefficient K_1'	100×10^6	100×10^6	100×10^6	100×10^6

Table 2 (continued)

Rail track component	Parameter	Value			
		Scenario 1	Scenario 2	Scenario 3	Scenario 4
	Poisson's ratio	0.40	0.40	0.40	0.40

Notes stf. Stiffness, *T* Tensile, *C* Compression

Units expressed in the International System of Units (*SI*) except Spring St.

For ballast layer, the coefficient K_1' was obtained from experimental parameter K_1 (RM test). Considering the 'Granular Resilient 1' model from the software, this coefficient is given by: $K_1' = K_1.10^{\alpha(1-K_2)}$ and $K_2' = K_2$, being for K_1 given in MPa: $\alpha = 6$.
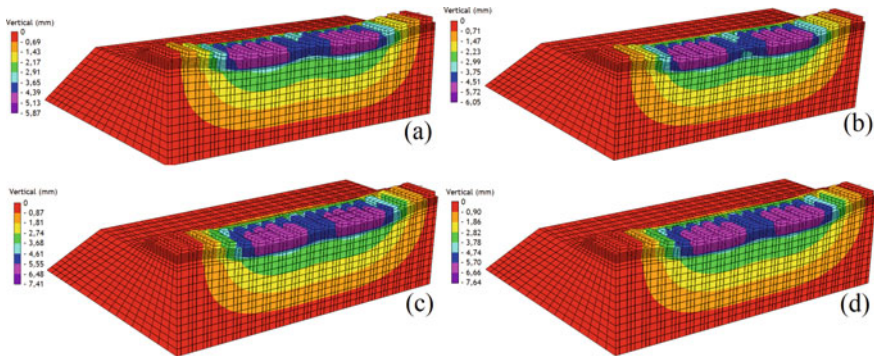
Fig. 7 Total vertical displacements of the rail track structure: **a** Scenario 1 (ISAC—32.5 t/axle), **b** Scenario 2 (Granite—32.5 t/axle), **c** Scenario 3 (ISAC—40 t/axle) and **d** Scenario 4 (Granite—40 t/axle)
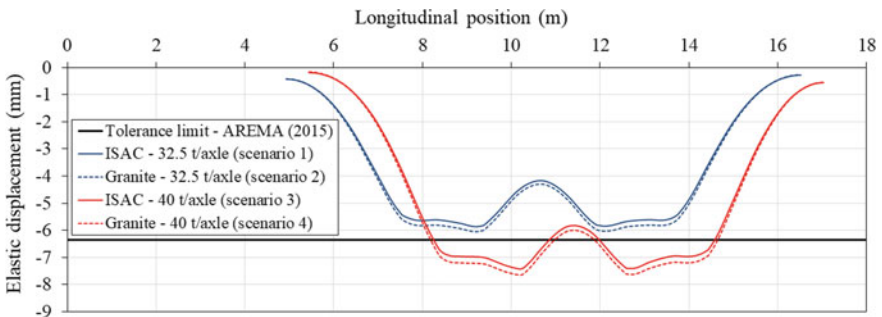
Fig. 8 Vertical elastic displacements of rail track on the rail top level

(*Y*-axis) of a sleeper, for both GDT (32.5 t/axle) and GDU (40 t/axle) wagons, from the centerline of the loaded sleeper (critical condition).

It was observed that in the rail track structure with ISAC ballast, the contact stress with the sleeper was higher than to the granite aggregate ballast structure, mainly
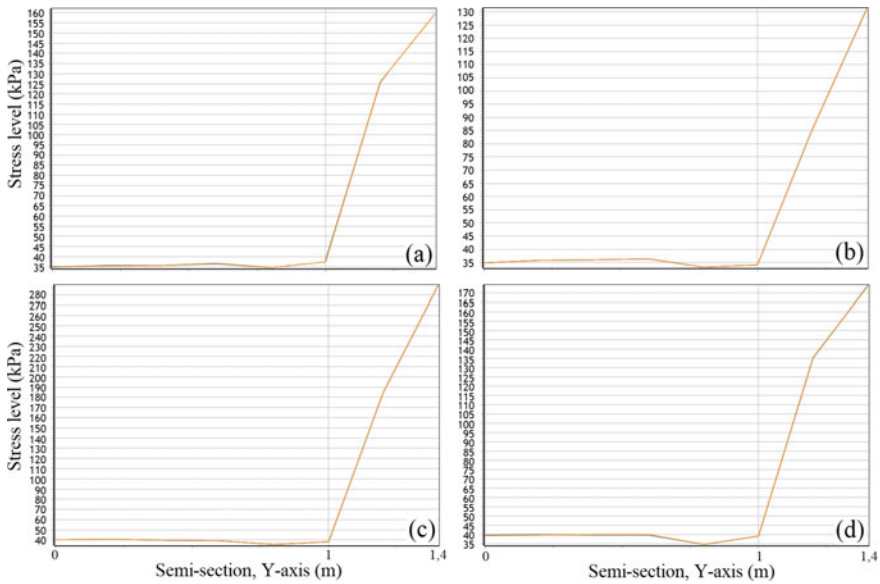
Fig. 9 Sleeper–ballast contact stress: **a** Scenario 1 (ISAC—32.5 t/axle), **b** Scenario 2 (Granite—32.5 t/axle), **c** Scenario 3 (ISAC—40 t/axle) and **d** Scenario 4 (Granite—40 t/axle)

at sleeper extremity. In the sleeper centerline, both materials showed very similar contact stress and not much higher when loading increased from 32.5 to 40 t/axle. The maximum stress values in the sleeper–ballast contact for all simulated scenarios were observed at the sleeper extremity, being 159 kPa for ISAC and 133 kPa for granitic aggregate, considering axle load of 32.5 tonnes; and 288 kPa for ISAC and 174 kPa for granite aggregate when 40 t/axle loading was applied. For all simulated scenarios, the maximum stress values at the sleeper–ballast contact are well below the most restrictive limit recommended by AREMA [2], which is 448 kPa.

Table 3 summarizes the vertical compression stress levels obtained in each layer of the rail track for all simulated scenarios

Regarding the vertical stress level transferred to the sub-ballast, it was found that for 32.5 t/axle loading the maximum value obtained for the rail track structure with ISAC ballast (scenario 1) was slightly higher than for the structure with granite aggregate ballast (scenario 2). However, probably due to the higher stiffness mobilized in

Table 3 Maximum vertical tress levels on top of substructure layers

Top of layer	Maximum vertical stress (kPa)			
	Scenario 1	Scenario 2	Scenario 3	Scenario 4
Ballast	159	133	288	174
Sub-ballast	121	117	133	139
Subgrade	70	73	110	120

the structure with ISAC ballast when the axle load level has increased to 40 tonnes, the maximum value obtained for the rail track structure with ISAC ballast (scenario 3) was slightly lower than the obtained for the structure with granite aggregate ballast (scenario 4). Nevertheless, the materials showed very close vertical stress transferred to the sub-ballast, and both materials were able to transfer to this layer stress values below the 172 kPa limit suggested by AREMA [2] as limit stress in platform.

On top of the subgrade, the maximum vertical stresses obtained were also very close considering the different materials. However, for 40 t/axle loading relatively high stress values were observed. Thus, for this loading level some rail track design approaches, such as sleepers spacing reduction or sub-ballast thickness increasing, can be useful to control the induced subgrade stress, improving the rail track performance.

About the maximum bending moment on the rail top level, for axle load of 32.5 tonnes the obtained value for the ISAC ballast structure was 46.05 kN m, slightly lower than for the granite aggregate ballast structure whose was 46.74 kN m. Both values are below the maximum allowable for the rails considered in the analyses (TR-68), which is 67.98 kN m. Considering the axle load of 40 tonnes, the value obtained for the ISAC ballast structure was 58.66 kN m, still lower than those verified when simulating the granite ballast structure (59.46 kN m), both again below allowable value.

4   Conclusions

Although the performance of both materials is similar, when considering 40 t/axle loading the rail track structure with ISAC ballast performs better than the granite aggregate ballast according as its higher stiffness can decrease the rail track platform stress.

The fact that none of the rail track structures met the maximum vertical displacement criterion for axle load of 40 tonnes [2] does not make the application of this load level permanently unfeasible, as this limit of 6.35 mm, which was not defined from rail tracks with operations under this loading level, can be reviewed. Thus, further studies are needed to assess of long-term effects on both rail track and vehicle components. In addition, both materials met the other design criteria for this loading level.

References

1. CEN (European Committee for Standardization) (2004) Unbound and hydraulically bound mixtures—Part 7: cyclic load triaxial test for unbound mixtures. EN 13286-7, Brussels
2. AREMA (American Railway Engineering Maintenance-of-way Association) (2015) Manual for railway engineering, vol I–IV. Lanham, USA
3. Mathur S, Soni S, Murty A (1999) Utilization of industrial wastes in low-volume roads. Transp Res Rec 1652(1):246–256
4. Gomes A, Roque A, Ferreira S, Fortunato E (2012) Case study to promote the use of industrial byproducts: the relevance of performance tests. J ASTM Int 9(2):1–18
5. Morata M, Saborido C (2016) Slag aggregates with enhanced performance for railway track bed layers. In: Proceedings of the third international conference on railway technology: research, development and maintenance, pp 1–17. Cagliari, Italy
6. Kuo C, Lin C (2017) Engineering performance of steel slag as railway ballast. In: Proceedings bearing capacity of roads, railways and airfields, pp 1859–1864. Athens, Greece
7. Delgado B, Viana da Fonseca A, Fortunato E, Maia P (2019) Mechanical behavior of inert steel slag ballast for heavy haul rail track: laboratory evaluation. Transport Geotech 20(100243): 1–10
8. Delgado B, Viana da Fonseca A, Fortunato E, Motta L (2019) Particle morphology's influence on the rail ballast behaviour of a steel slag aggregate. Environ Geotech https://doi.org/10.1680/jenge.18.00203
9. ASTM (American Society for Testing Materials) (2004) Standard test method for load cyclic triaxial strength of soil. D5311, USA
10. Skoglund K (2002) A study of some factors in mechanistic railway track design. PhD Thesis, Norwegian University of Science and Technology, Norway
11. Bishop A, Green G (1965) The influence of end restraint on the compression strength of a cohesionless soil. Géotechnique 15(1):243–266
12. Fortunato E, Pinelo A, Matos Fernandes M (2010) Characterization of the fouled ballast layer in the substructure of a 19th century railway track under renewal. Soils Found 50(1):55–62
13. Indraratna B, Salim W, Rujikiatkamjorn C (2011) Advanced rail geotechnology—ballasted track. Taylor & Francis Group, London
14. Lowe J (1964) Shear strength of coarse embankment dam materials. In: Proceedings of 8th Congress on Large Dams, Transactions, Vol. III, International Commission on Large Dams, pp 745–761. Paris, France
15. Sevi A, Ge L (2012) Cyclic behaviors of railroad ballast within the parallel gradation scaling framework. J Mater Civ Eng ASCE 24:797–804
16. Rosa A (2019) Effect of granulometry and lithology on ballast behavior by laboratory and computational analysis. Master thesis, Federal University of Rio de Janeiro, Brazil (in Portuguese)
17. Silva Filho J (2018) Contribution to development of a mechanistic-empirical method for rail track design focusing tropical soil substructures. PhD thesis, Military Institute of Engineering, Brazil (in Portuguese)
18. Delgado B (2012) Deformability assessment of a tropical soil from western Maranhão state as sub-ballast material for Carajás Railroad. Master thesis, Federal University of Ouro Preto, Brazil (in Portuguese)
19. Santos G, Barbosa R, Shu X, Urban C, Joy R (2014) Characterization and modelling of a new heavy axle load freight wagon for wheel rail wear prediction. J Mechan Eng Technol 2(3):17–28

Railroad Ballast Movements Pattern Recognition by Using "SmartRock"

Kun Zeng and Hai Huang

Abstract Ballast is an important part of railroad infrastructure. It is used as a support base for bearing the track load and facilitating drainage of water from the track. Unfavorable ballast performances (e.g., ballast fouling, loss of lateral confinement) can contribute to damage and deterioration of rail structures such as the rail, tie and fastening components. Therefore, accurate and timely monitoring of ballast condition is critical for rail safety operation and effective maintenance. This paper presents a series of ballast box tests to investigate the ballast particle movement pattern inside railway ballast under different ballast, loading, moisture and shoulder confinement conditions. Eight wireless devices, SmartRocks, were embedded in different locations in the ballast box to monitor individual ballast particle movements. The results indicate that (1) load magnitude and frequency have apparent effect on ballast particle movements. (2) The difference of particle movements in fouled ballast under dry versus wet condition is more dramatic than the difference in clean ballast. (3) Lack of shoulder confinement would cause failure of interaction between the shoulder ballast with tie and surrounded particles, which could generate more space for ballast particles away from the shoulder translation and rolling above other particles. (4) This study also demonstrates that SmartRock is capable of recording the particle translational accelerations and particle angular rotations information under different ballast and load conditions.

Keywords Ballast box test · Ballast fouling · Lateral shoulder confinement · SmartRock

K. Zeng
Department of Civil and Environmental Engineering, The Pennsylvania State University, University Park, PA, USA

H. Huang (✉)
Department of Rail Transportation Engineering, The Pennsylvania State University, Altoona, PA, USA
e-mail: huh16@psu.edu

1   Introduction

Rail ballast, as it is known, is an important part of railway infrastructure. Unfa-
vorable ballast performances can contribute to damage and deterioration of above
structures such as the rail and tie [1–4]. There are several factors can be taken into
consideration on the effect of the ballast failure (e.g., load magnitude, load frequency,
moisture content and shoulder stability). To sustain proper and long-time usage of
railway, it is crucial to maintain ballast to be relatively clean. Both laboratory and
numerical studies have been conducted to study ballast performance under fouled
ballast condition [5, 6]. Fouling of ballast makes the granular mass effectively less
angular and decreases its shear strength [7]. In addition, lateral loads are transferred
from the rails through the fastenings to the sleepers, then into the ballast. Railway
track is conventionally considered to have a sufficient resistance to lateral loading [8].
However, in-service failure of the ballast is not a well-understood or well-documented
phenomenon. In field conditions, ballast behavior, e.g., ballast lateral movement and
ballast migration, is commonly hard to monitor as traditional measuring devices,
such as accelerometer, LVDT, strain gage, force cell, have not been successfully
used [9, 10]. Zhai et al. [11] inserted accelerometers into the ballast layer to measure
ballast particle movement. All these instruments are not a realistic ballast particle
shape, and therefore do not reflect the movement a normal ballast particle would have
experienced, and being able to accurately measure real ballast particle movement is
important for studying ballast failure mechanism. This paper aims to study the ballast
particle movements under different load and ballast conditions. A series of labora-
tory ballast box tests was conducted for this purpose in a controlled environment.
A wireless device—"SmartRock"—was installed in the ballast box to record indi-
vidual ballast particle movements under cyclic axle loading conditions. Conclusions
are reached on the effect of different load conditions and ballast conditions.

2   Test Preparation

2.1   Experimental Setup

A ballast box with a dimension of 3.96 m (long) × 3.36 m (wide) × 1.22 m (high)
manufactured by Altoona Pipe and Steel as well as an advanced loading system was
used as the main equipment in the laboratory study stage, as shown in Fig. 1.

Clean angular limestone aggregates and fouled were used in this study as clean
ballast condition. The gradation of the ballast, as shown in Fig. 2, conforms
to the No.4A gradation requirements of the American Railway Engineering and
Maintenance-of-Way Association (AREMA). Fouled ballast was prepared by mixing
of the finer particles with No.4A limestone. As the result of sieve analysis, the fouling
index of the fouled ballast we used in our test is 20.05% which falls into the fouled
ballast category.

Fig. 1 Photo of advance ballast box

Fig. 2 Gradation properties of clean ballast, fouled ballast and subgrade
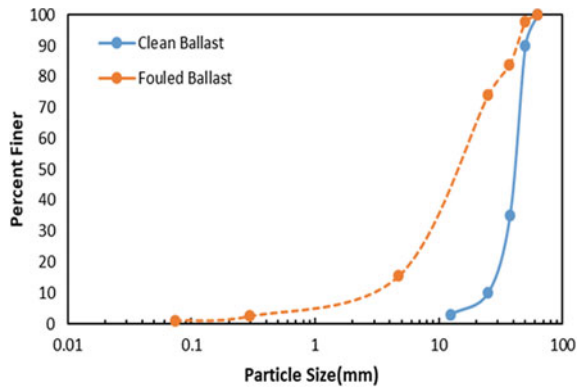
2.2 Instrumentation—"SmartRock"

A proprietary wireless device—"SmartRock", as shown in Fig. 3—was utilized to monitor ballast particle movement under rail train loading. It can sense, record and transmit its movement, including rotation, translation and orientation in 9 degrees of freedom, respectively, in real time. The SmartRock is capable of sending raw data to a base station for visualization and analysis via the Bluetooth. 3D printing technology was employed to form the shell of the SmartRock to make it into a real ballast shape. The development of the SmartRock was explained in detail in Liu et al. [10].

Fig. 3 Photos of
SmartRock: **a** angular
SmartRock and **b** cubic
SmartRock

(a)   (b)
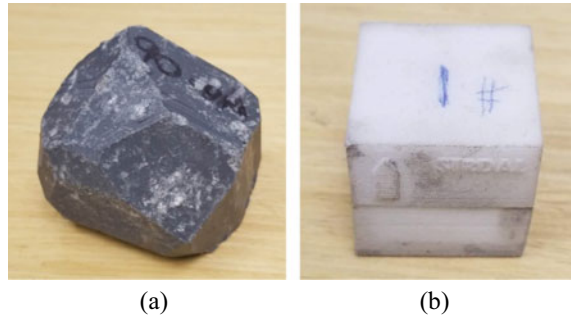
2.3 Laboratory Test Setup

A full-scale railway track structure consisted of a ballast layer (36 cm thick) and a
subgrade layer (30 cm thick). Detailed plan can be found in [12] (Fig. 4).

The magnitude and frequency of the load are within the range of a typical train
wheel load [13–15]. The following testing matrix, Table 1, including different loading
and environmental combinations has been applied:

3 Result and Discussion

Particle motions of the embedded SmartRocks can reflect motions of the surrounding
ballast particles during cyclic loading under different ballast or load conditions as
shown in testing matrix. Figure 5 shows the recorded transitional accelerations of the
two SmartRocks under different load frequency ($f = 0.2$, 1 and 2 Hz) in both clean and
fouled ballast testing conditions. It is shown that acceleration of the SmartRocks was
apparently increased by comparing the 0.2 Hz accelerations with 1 Hz accelerations.
And there is a little bit increase in magnitude as well as increase in fluctuations by
comparing the recorded accelerations under 2 Hz with 1 Hz load frequency.

For different load magnitude, 35.5 Kips as the passenger load and 65.5 Kips as
the freight load have been used in the test. Figure 6 shows the recorded transitional
accelerations of the two SmartRocks under passenger load and freight load. It is
shown that movements of the SmartRocks under passenger load were apparently
smaller than the corresponding value of the SmartRocks under freight load. It appar-
ently shows that load magnitude has a significant influence on the ballast particle
individual movement. In addition, by comparing Fig. 6a versus Fig. 6b, movements
of the SmartRocks were with fewer fluctuations in fouled ballast condition than in
clean ballast condition due to finer particles and less void ratio in fouled ballast.

Several tests have been done under different moisture contents in the clean ballast
versus fouled ballast, and angular rotation data has a very interest result. Figure 7
shows the recorded accumulated rotations of the SmartRocks 5 cm beneath the rail

(a)

(b)
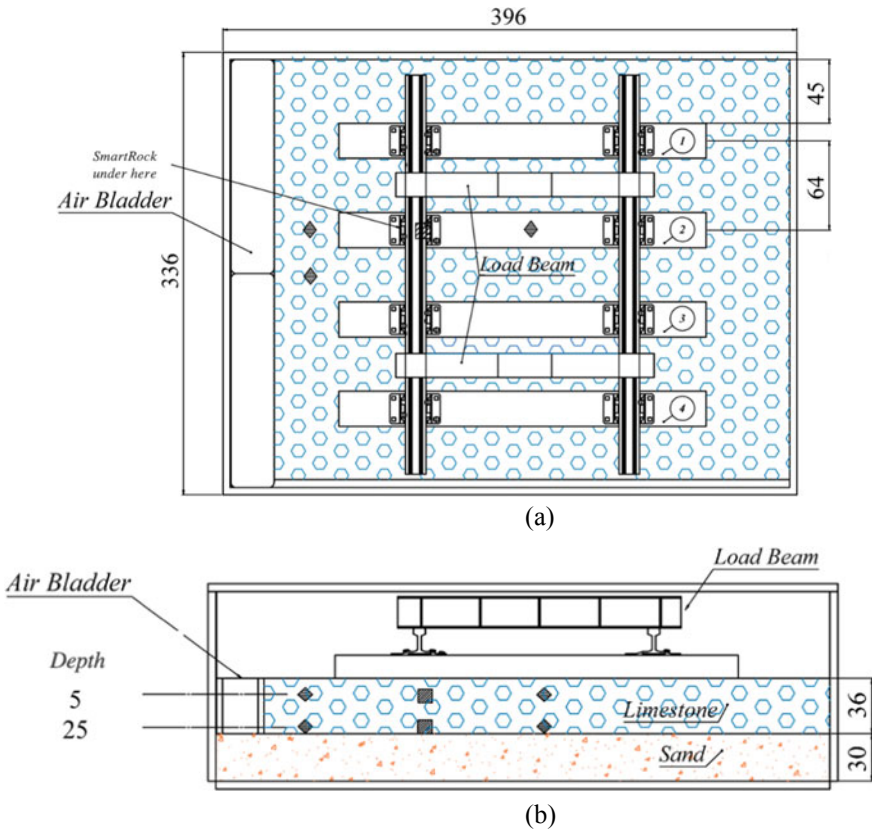
Fig. 4 Geometry of track structure and location of SmartRocks in ballast box: **a** top view and **b** side view of test setup (all unit in cm)

Table 1 Test matrix for ballast box test

Test group	Action item #	Ballast condition	Moisture condition	Shoulder confinement	Load	Load frequency (Hz)
I	1	Clean	Dry	Y	Passenger	1
	2	Clean	Dry	Y	Freight	0.2, 1, 2
	3	Clean	0.9%	Y	Freight	1
	4	Clean	0.9%	N	Freight	1
II	1	Fouled	Dry	Y	Passenger	1
	2	Fouled	Dry	Y	Freight	0.2, 1, 2
	3	Fouled	10.1%	Y	Freight	1
	4	Fouled	10.1%	N	Freight	1
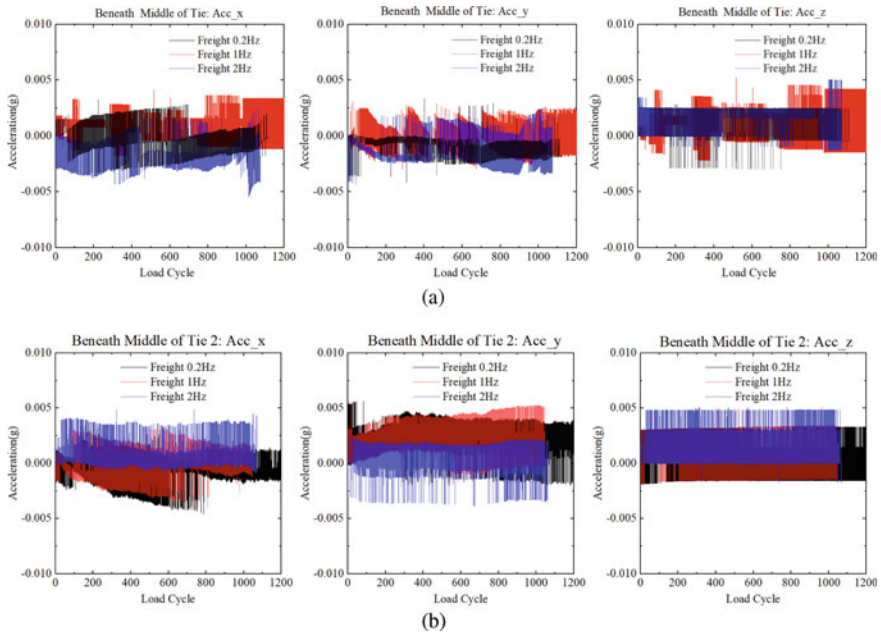
Fig. 5 Particle translational acceleration 5 cm below top of ballast under 0.2, 1 and 2 Hz three different loading frequencies: **a** beneath middle of tie: clean ballast and **b** beneath middle of tie: fouled ballast

seat and middle of Tie 2 in both clean and fouled ballast under dry versus wet conditions. A comparison between Fig. 7a versus Fig. 7b and Fig. 7c versus Fig. 7d shows that for clean ballast, there is no significant difference in the particle rotations of the SmartRocks under dry and wet conditions, but the rotation direction is more fluctuated. For the fouled ballast, the SmartRock experienced higher accumulated rotation in the wet condition than in the dry condition. In addition, the rotation direction is more constant than in the clean ballast test. This is because the intrusion of fine particles in fouled ballast reduces the drainage capacity of the ballast and water was held inside the ballast would serve as a lubricant causing a reduction in internal friction, which makes the ballast particles easier to rotate.

Another test is study on the effect of shoulder confinement. Figure 8 shows the result of a comparison of the SmartRock accumulated rotations under with shoulder confinement condition versus without shoulder confinement condition. Due to the lack of confinement from the shoulder, ballast particles should be more likely to slide and roll over each other. In the shoulder removal, the accumulated rotations are little bit larger than with the shoulder confinement in both clean and fouled ballasts.
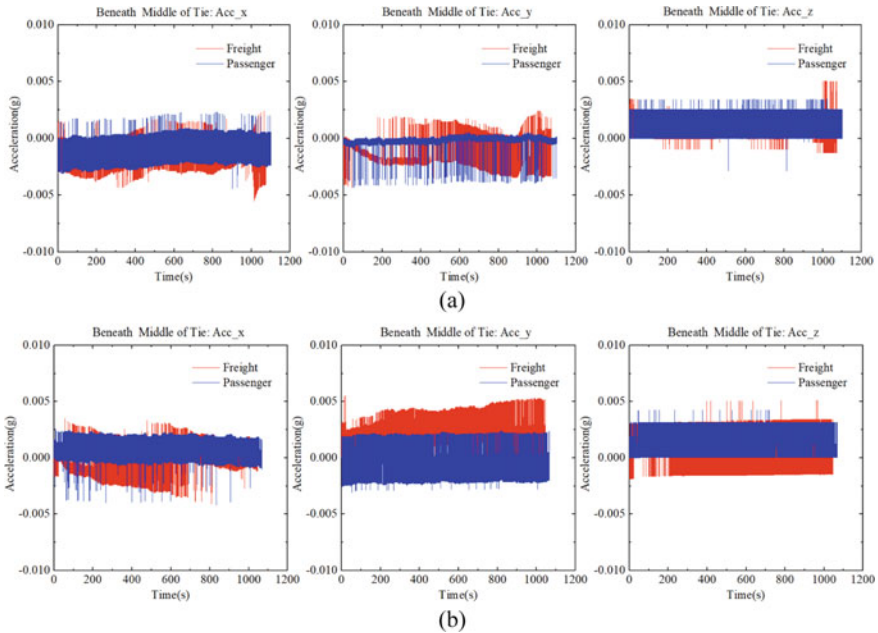
Fig. 6 Particle translational acceleration 5 cm below top of ballast under passenger load and freight load: **a** beneath middle of tie: clean ballast and **b** beneath middle of tie: fouled ballast

4 Conclusion

This paper presents a series of ballast box tests to investigate ballast particle movement pattern inside railway ballast under different load frequency, load magnitude, moisture conditions and shoulder confinement. A wireless device—"SmartRock"— was installed in different locations in the ballast box to monitor ballast particle movements under different conditions. Two different ballast conditions have been considered: clean and fouled ballasts. In this study, although unreproducible initial conditions, e.g., ballast particle shape, particle arrangement, etc., could cause the marginal differences in magnitude, it is interesting to note that the results obtained using SmartRock instrumentation showing some trends could be used as a benchmark to evaluate ballast conditions.

Based on the results of the ballast box tests, conclusions specific to the test conditions (e.g., load frequency, loading, moisture content) can be summarized as follows:

- SmartRocks installed in the ballast box are capable of recording the particle translational accelerations and particle angular rotations information of ballast particles under different ballast and load conditions. SmartRock can serve as a potential monitoring tool to monitor the ballast behavior and performance in field.
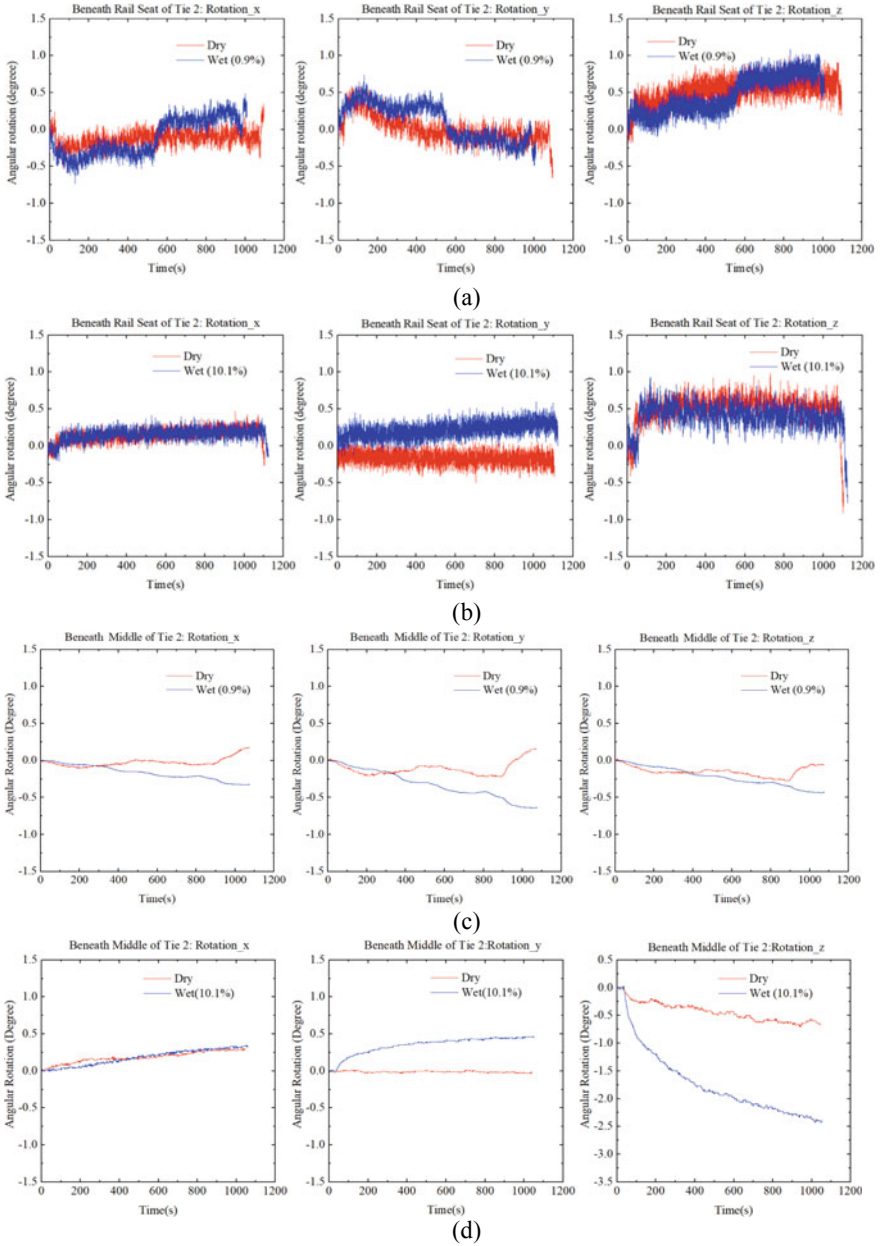
Fig. 7 Particle angular rotations of top SmartRock under dry versus wet conditions beneath Tie 2: **a** rail seat of tie: clean ballast; **b** rail seat of tie: fouled ballast; **c** middle of tie: clean ballast; **d** middle of tie: fouled ballast

(a)

(b)
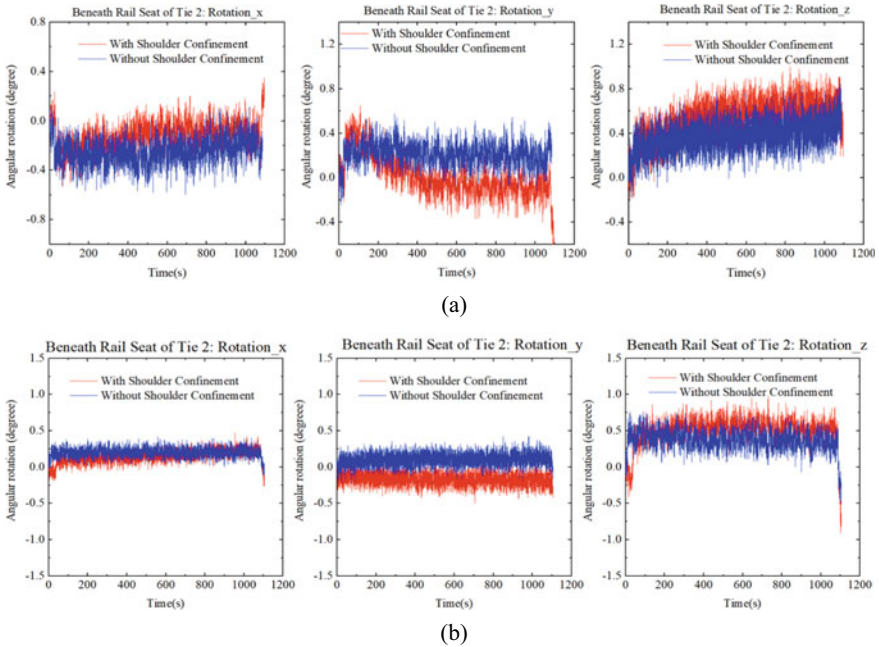
Fig. 8 Particle angular rotations of top SmartRock beneath rail seat of Tie 2 with/without shoulder confinement under **a** clean ballast and **b** fouled ballast

- Particle translational movement and rotation were different under different frequency. From the results, higher frequency could cause more dramatically particle movements. But influence on the increase in magnitude still needs to be study in future.
- Load magnitude has an apparently effect on ballast particle movements. The peak magnitude of translational accelerations under freight load is higher than that under passenger load. And the difference is much bigger in clean ballast than fouled ballast due to finer particles and less void ratio in fouled ballast.
- The different of movement of particles between dry condition and wet condition behaves quite different in clean ballast and fouled ballast. The intrusion of fine particles in fouled ballast affects the hydraulic conductivity by reducing the drainage capacity of the ballast. Water held inside the ballast would serve as a lubricant causing the reduction internal friction of the ballast particles. So in fouled ballast, the result shows particle movements are more dramatic as water content increases.
- Lack of shoulder would cause different effects on the movements of ballast particles in different location. When shoulder was removed, due to the lack of confinement from the shoulder, ballast particles should be more likely to slide and roll over each other. Thus, the ballast particles at the middle and the rail seat of the

Tie 2 show more dramatic rotational movements in without shoulder than in with shoulder confinement condition.

References

1. Raymond GP (2002) Reinforced ballast behavior subjected to repeated load. Geotext Geomember 20(1):39–61
2. Saussine C, Cholet C, Gautier PE, Dubois F, Bohatier C, Moreau JJ (2006) Modeling ballast behavior under dynamic loading. Part 1: A 2D polygonl discrete element method approach. Comput Methods Appl Mech Eng 195(19–22):2841–2859
3. Tutumluer E, Huang H, Hashash Y, Ghaboussi J (2006) Aggregate shape effects on ballast tamping and railroad track lateral stability. In: Proceedings of 2006 annual AREMA, annual conference, Louisville, KY
4. Tutumluer E, Huang H, Hashash Y, Ghaboussi J (2007) Discrete element modeling of railroad ballast settlement. In: Proceedings of 2007 AREMA, annual conference, Chicago
5. Chiang CC (1989) Effect of water and fines on ballast performance in box tests. MS Project Rep. No. 89–366P, University of Massachusetts, Amherst, MA
6. Han X, Selig ET (1997) Effects of fouling on ballast settlement. In: Proceedings of 6th international heavy haul railway conference. International Heavy Haul Association, Virginia Beach
7. Tennakoon N, Indraratna B, Nimbalkar S, Impact of ballast fouling on rail tracks, Second International Conference on Railway
8. Le Pen L, Bhandari AR, Powrie W (2014) Sleeper end resistance of ballasted railway tracks. J Geotech Geoenviron Eng 140(5):04014004
9. Ngo NT, Indraratna B, Rujikiatkamjorn C (2014) DEM simulation of the behaviour of geogrid stabilised ballast fouled with coal. Comput Geotech 55:224–231
10. Liu S, Huang H, Qiu T (2015, March) Laboratory development and testing of "SmartRock" for railroad ballast using discrete element modelling. In: 2015 joint rail conference, pp V001T01A019–V001T01A019. American Society of Mechanical Engineers
11. Zhai WM, Wang KY, Lin JH (2004) Modeling and ex- periment of railway ballast vibrations. J Sound Vibr 270(4–5):673–683
12. Zeng K, Qiu T, Bian X, Xiao M, Huang H (2019) Identification of ballast condition using SmartRock and pattern recognition. Constr Build Mater 221:50–59
13. Huang H, Tutumluer E, Dombrow W (2009) Laboratory characterization of fouled railroad ballast behavior. Transp Res Rec 2117(1):93–101
14. Huang H (2010) Discrete element modeling of railroad ballast using imaging based aggregate morphology characterization. Ph.D. dissertation, Department of Civil and Environmental Engineering, University of Illinois at Urbana-Champaign, Urbana, IL
15. Gao Y, Qian Y, Stoffels SM, Huang H, Liu S (2017) Characterization of railroad crosstie movements by numerical modeling and field investigation. Constr Build Mater 131:542–551

Effect of Degraded Subgrade Stiffness on Rail Geometry and Train Vibration in High-Speed Railways

Hongguang Jiang, Shun Liu, Yixin Li, Haoran Chi, Jizhe Zhang, Ming Liang, and Zhanyong Yao

Abstract The degradation of railway subgrade stiffness will cause the acceleration of track degradation and deteriorate ride comfort and safety. It is hard to foresee these problems because both track substructure and subgrade are not visible to inspect. To study the influence of subgrade stiffness degradation on high-speed train and track system, 3D FEM analyses of the Fuxing trains and ballastless tracks were conducted to simulate different degradation conditions of roadbed stiffness. Firstly, the numerical model was verified by the field measurement of vibration velocity at the concrete base in the Beijing–Tianjin high-speed railway. Then, the influences of the degradation of roadbed stiffness on the rail displacements and train dynamics were analyzed. It is found that since the ballastless track had quite high rigidity, the uneven degradation of roadbed stiffness did not result in obvious additional increase of rail displacement. However, the uneven degradation of roadbed stiffness resulted in larger vibrations of train wheels. Particularly, the wheel accelerations were more sensitive to the uneven degradation of roadbed modulus amplitudes than the wavelengths.

Keywords High-speed train · Ballastless track · Roadbed degradation · Uneven modulus · Rail displacement · Train acceleration

1 Introduction

High-speed railway has attracted much attention in many countries due to its advantages of high speed and comfort. Smooth tracks are necessary to reduce the dynamics of wheel-rail system. Since substructure defects, such as settlement and degraded stiffness, are easily mapped to the rail surface and are known to cause rail irregularities, ballastless tracks with better integrity and high rigidity are widely used by many countries. Strict standards have been specified to limit uneven subgrade settlement and control the rail irregularities. However, it has been measured in the field that uneven roadbed stiffness with modulus reduction up to 80% has occurred

H. Jiang · S. Liu · Y. Li · H. Chi · J. Zhang · M. Liang · Z. Yao (✉)
School of Qilu Transportation, Shandong University, Jinan, China
e-mail: zhanyong-y@sdu.edu.cn

in high-speed railways. The effects of decreased and non-homogeneous substructure stiffness should also be evaluated in ballastless tracks in high-speed railways.

The influence of uneven subgrade settlement on track geometry and vehicle dynamics is a focus of research for ballastless railways. Guo et al. investigated the influences of subgrade uneven settlement on the rail geometry and dynamic responses caused by moving train and predicted the development of long-term track settlement of ballastless track in high-speed railways [1, 2]. Jiang et al. pointed that the settlement mapping characteristics from the subgrade surface to the rail were largely dependent on the track equivalent flexibility, and proposed a unified formula to describe the geometry mapping relationship [3]. Besides the track degradation caused by subgrade uneven settlement, the initial uneven distribution of subgrade stiffness is mainly due to the variability of filling materials and compaction variability during construction. Subgrade with high degree of compaction and low moisture content has larger modulus [4]. Through field sample testing in high-speed railways, moisture contents and fine contents of roadbed were found severely exceeding the specification limits [5]. With the rising moisture content caused by rainfall and cyclic loadings caused by moving train, subgrade soil would soften and fine particles might migrate into the aggregate, which accelerated the degradation of subgrade stiffness. Higher fine contents resulted in lower subgrade resilient modulus and showed early tendency of collapse [6]. Based on the triaxial tests, Chen obtained the soil resilient modulus under different conditions of moisture contents, which reduced by 72.6% with higher moisture content as opposed to that at the optimum moisture content [7]. Wang et al. pointed that the migration of fine particles greatly reduced the resilient modulus up to 60% [8]. Cui et al. found that after cyclic loading, a considerable amount of fine particles migrated into the roadbed or ballast layer. The fine particles in roadbed increased with the loading cycles. With the decrease of volumetric content of coarse grains, the friction angle and resilient modulus also decreased [9]. More fine particles were deposited in the interface with the development of interlayer and severe mud pumping existed in low compactness and saturated state [10, 11]. In order to investigate the effects of mud pumping on the vibration responses of high-speed railways, Li et al. assumed that the concrete base lost support from the underlying subgrade within the mud pumping area, which is similar to the simulations of subgrade uneven settlement [12]. However, for most situations of mud pumping, weakened subgrade support with reduced soil modulus still existed for the track structure.

For traditional railways, the track substructure condition is generally evaluated by static track stiffness. But the field measurement of static stiffness consumes large amount of times and resources. Dynamic track stiffness determined by track loading vehicle (TLV) and rolling stiffness measurement vehicle (RSMV) was reported capable of measuring track stiffness for a train speed of up to 60 km/h [13]. Kaynia et al. pointed that measurement of track stiffness was a useful tool for detection of anomalies and possibly defects in the track substructure system, and a solution that could allow processing of the vehicle vibration data for the purpose of identifying track defects [14]. This paper presents an attempt to explore the effect of degraded subgrade stiffness on rail geometry and train vibrations in high-speed railways. A 3D FEM including the Fuxing trains and ballastless tracks was conducted to

simulate different degradation conditions of roadbed stiffness. The influences of the degradation of roadbed stiffness on the rail displacements and train dynamics were analyzed.

2 Numerical Model

2.1 Three-Dimensional Finite Element Model (3D FEM) of Ballastless Track

The new Fuxing-type high-speed train with axle load of 170 kN was used in the numerical model, and the dimensions and the parameters of the train are presented in Fig. 1 and Table 1. The car body, bogie frame and the wheelset are simulated as rigid element, and the primary and secondary suspensions were simulated as spring-damping elements.

According to the construction specification of Chinese high-speed railway, a 3D FEM of CRTSII slab ballastless track subgrade system was built using ABAQUS software, as shown in Fig. 2. This model was 189 m long, 89.7 m wide and 23.5 m deep, comprising two UIC60 rails, a 2.6 m wide × 0.2 m thick track slab, a 2.6 m wide × 0.05 m thick cement asphalt mortar (CAM) layer, a 2.6 m wide × 0.3 m thick concrete base, a 0.4 m thick roadbed, a 2.4 m thick embankment and a 20 m thick foundation. Table 2 presents the parameters of linear elastic elements used to simulate the railway infrastructure components. The rails were modeled as two continuous Euler beams, and the fasteners were modeled as spring elements with stiffness of 28.5kN/mm. Interfaces among the track slab, CAM layer, concrete base and the roadbed were allowed relative movement. Hard contact was applied to simulate the interface interactions in the ABAQUS software. The tangential contact behaviors contained the relative slip between the surfaces and the frictional shear stress. The surfaces would not show slippage (i.e., the tangential displacement is zero) before the shear stress reached its Coulomb critical value. The foundation bottom was fixed in all directions, and only vertical movements were allowed in other boundaries of the foundation. The waves caused by train movements could be absorbed by multiple damping boundaries verified by Liu and Quek [15].

2.2 Validation of FE Model with Field Measurements

Song carried out field measurements of vibrations at concrete base on the Beijing–Tianjin Intercity Passenger Line during its trial operation [16]. The distances between the wheelsets and the axle load were the same to the Fuxing-type high-speed train. Since this railway was built according to the high-speed railway construction specification, it had the same track structure type and parameters to the numerical model.
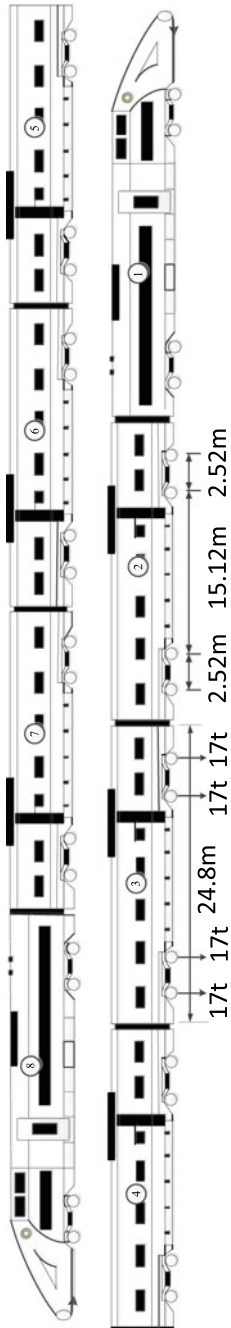
Fig. 1 Configuration of Fuxing bullet train in China

Table 1 Parameters of the Fuxing-type high-speed train

Components	Value	Units
Car body mass	5.2×10^4	kg
Bogie frame mass	3.2×10^3	kg
Wheelset mass	1.2×10^3	kg
Primary suspension vertical stiffness	1.04×10^6	N/m
Primary suspension vertical damping coefficient	5×10^4	N s/m
Secondary suspension vertical stiffness	4×10^5	N/m
Secondary suspension vertical damping coefficient	6×10^4	N s/m
Distance between bogie centers	17.64	m
Bogie wheelbase	2.52	m
Speed	100	m/s
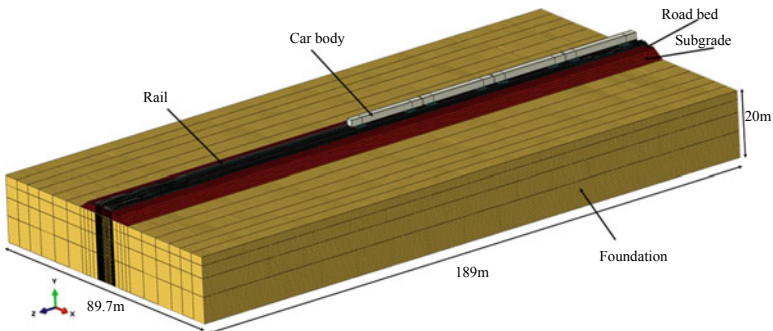
(a) 3D finite element model
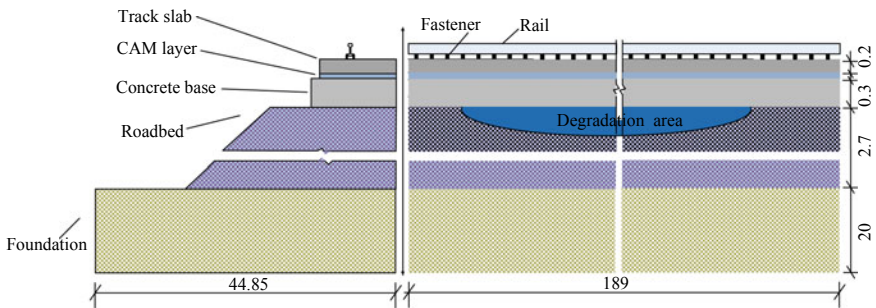
(b) Cross and Longitudinal section of CRTS II ballastless track (unit: m)

Fig. 2 3D finite element model of CRTSII slab ballastless railway system

Table 2 Parameters used in the 3D numerical model

	Density (g/cm^3)	Elastic modulus (MPa)	Poisson's ratio	Damping	
				Alpha	Beta
Rail	7.83	210,000	0.3	–	–
Track slab	2.7	35,000	0.167	0.24	0.00021
CAM layer	1.8	315	0.3	0.61	0.00051
Concrete base	2.7	24,000	0.167	0.24	0.00021
Roadbed	2.3	240	0.25	1.52	0.00128
Embankment	1.92	120	0.3	1.52	0.00128
Foundation	1.82	100	0.35	1.52	0.00128
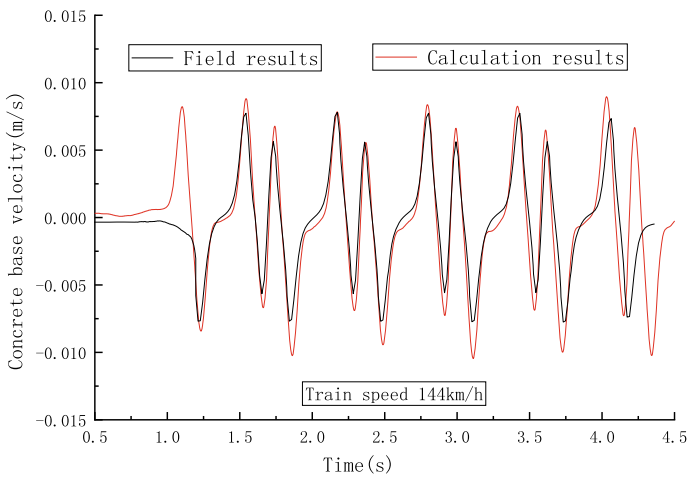
Fig. 3 Comparisons of velocity between field measurement and numerical simulation

Figure 3 compares the calculation results with the field results in terms of the concrete base's velocity responses at train speed of 144 km/h. It can be seen that the positive peaks in the velocity–time curves corresponded to the positions of train bogie. Both the curve pattern and peak values obtained from the numerical simulation were close to those of field measurements. Therefore, it is reliable to describe the dynamic responses of the ballastless track structure with the proposed 3D FE model.

2.3 Description of Roadbed Degradation

To investigate the influence of roadbed degradation on the dynamic responses of the high-speed train–ballastless track structure, even and uneven degradations of roadbed stiffness were set in the FE model. For the even degradation of roadbed

Fig. 4 Uneven degradation
of roadbed stiffness
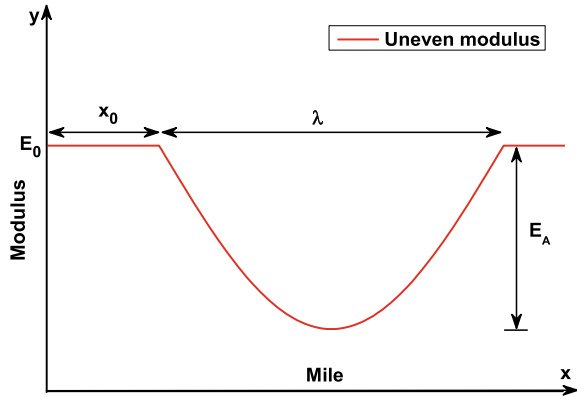
stiffness, the values of elastic modulus E were chosen as 240, 192, 120 and 48 MPa, representing the uniform reductions by 0, 20, 50 and 80%, respectively. For the uneven degradation of roadbed stiffness, cosine curves in terms of amplitude and wavelength were applied in the FE model as illustrated in Fig. 4.

The cosine roadbed stiffness profiles were obtained as follows:

$$E(x) = \begin{cases} E_0, x \leq x_0 \\ E_0 - E_A\left[\cos\frac{2\pi(x-x_0)}{L}\right], x_0 < x < L + x_0 \\ E_0, x \geq x_0 + L \end{cases} \quad (1)$$

where $E(x)$ is the elastic modulus of roadbed along the longitudinal direction; E_0 is the initial elastic modulus before roadbed degradation, equal to 240 MPa; E_A and λ are the amplitude and wavelength of stiffness degradation areas at the roadbed; E_A was chosen as 48, 120 and 192 MPa, which represented the maximum modulus reduction (MR) ratios were 20, 50 and 80% from the initial elastic modulus; λ was chosen as 20, 40 and 100 m; and x_0 is the starting position where the roadbed stiffness begins to degrade. The assignment of elastic modulus in the roadbed degradation areas was implemented using the reprogrammed subroutine USDFLD in the ABAQUS software.

3 Results and Discussion

3.1 Mapped Geometry of Ballastless Track Structure

Railway roadbed supplies enough stiffness to support the superstructure. When the roadbed softens, additional displacement would occur caused by self-weight of

Fig. 5 Additional rail displacement caused by degradation of roadbed stiffness under self-weight of the superstructure

(a) λ=20m

(b) λ=40m
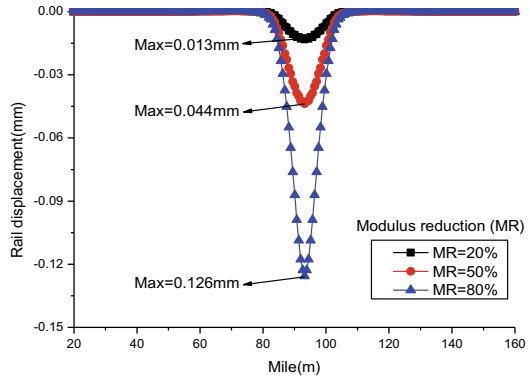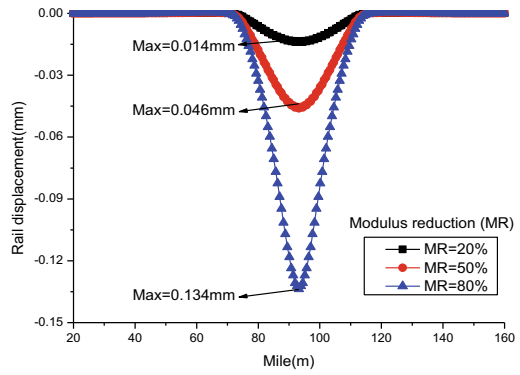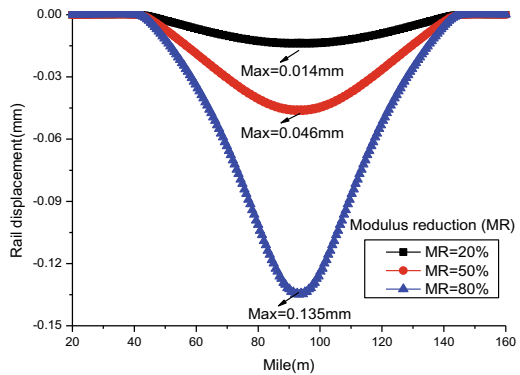
(c) λ=100m

Fig. 6 Additional rail displacement caused by degradation of roadbed stiffness under train loads
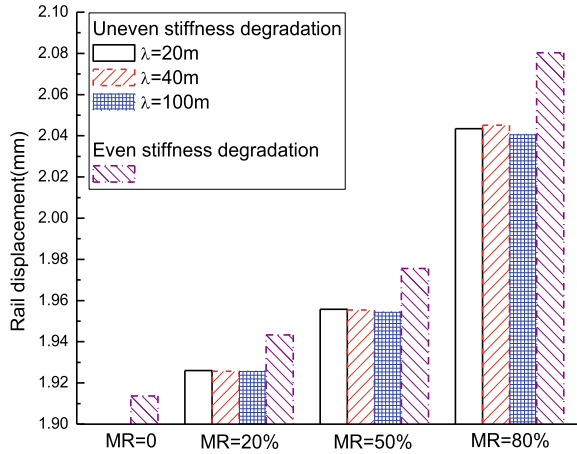
the superstructure and train loads. Figure 5 presents the additional rail displacement under self-weight of the superstructure caused by the uneven degradation of roadbed stiffness, where the initial rail displacement before roadbed degradation was balanced. For the uneven wavelength $\lambda = 20$ m, the maximum rail displacement increased by 0.013, 0.044 and 0.126 mm corresponding to the roadbed modulus reductions (MRs) of 20, 50 and 80%. The additional rail displacement almost displayed the same shape to the pattern of uneven stiffness as shown in Fig. 4, and it increased with the reduction of the roadbed stiffness. The increase of uneven wavelength also resulted in a little growth of the maximum rail displacement. It indicates that although the ballastless track had very high rigidity, the degradation of roadbed stiffness could map to the rail surface under self-weight of the superstructure, resulting in track irregularities. Therefore, it is possible to evaluate the roadbed stiffness based on the rail geometry.

Figure 6 presents the additional rail displacement when the train passed by the stiffness degradation areas of railway roadbed. For the high-speed railway without roadbed degradation, the maximum rail displacement was 1.913 mm. The increments of rail displacement caused by moving train loads were 0.012, 0.042 and 0.13 mm when the roadbed modulus reduced by 20, 50 and 80% with the wavelength of 20 m. These values were quite similar to the additional rail displacements caused by self-weight of the superstructure. It indicates that although the roadbed softened by 80%, train loads did not result in obvious additional increase of rail displacement at the degraded areas. The increments of rail displacement were mainly contributed from the geometry mapping under self-weight of the superstructure. Compared to the uneven stiffness degradation, the additional rail displacement was larger at the situations of uniform stiffness degradation.

3.2   Dynamic Responses of High-Speed Train

Figure 7 shows the accelerations of train wheels and car bodies under the uneven degradation of roadbed stiffness. It can be seen from Fig. 7a that the wheel accelerations were quite sensitive to the modulus reduction. Although the increments of rail displacement were only 0.012, 0.042 and 0.13 mm with the roadbed modulus reduction of 20, 50 and 80% at wavelength $\lambda = 20$ m, the wheel accelerations increased to 5.92, 29.8 and 204.7 mm/s^2, respectively. However, the influence of

Fig. 7   Train acceleration caused by uneven stiffness degradation
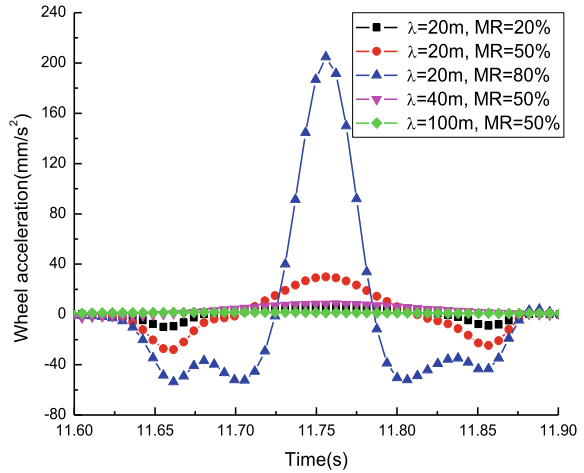
(a) Wheel acceleration
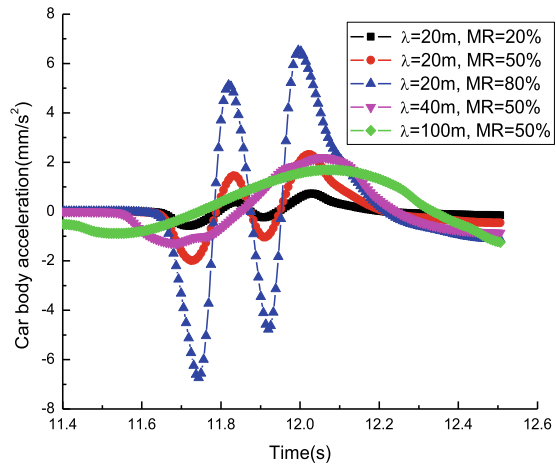
(b) Car body acceleration

wavelength on the wheel accelerations was quite minor, which were at low levels with the wavelengths increased from 20 to 40 m and 100 m. Due to the effects of bogie-wheel and car body–bogie suspensions, the car body accelerations reduced sharply as shown in Fig. 7b. The development of car body accelerations was similar to that of train wheels caused by uneven degradation of roadbed stiffness. Larger decrease in roadbed modulus resulted in higher accelerations of car body. The allowable accelerations were 30 m/s^2 for train wheel in Spain and 1 m/s^2 for car body in China. The maximum accelerations of train wheel and car body were 204.7 and 6.5 mm/s^2 caused by the roadbed degradation, which were within the limits for train comfortable running.

4 Conclusions

A 3D finite element model was established to analyze the influence of roadbed degradation on the rail displacements and vehicle dynamics. The numerical model was validated by the comparison with the field measurement in the Beijing–Tianjin high-speed railway. Accordingly, the following conclusions can be drawn:

(1) The uneven degradation of roadbed stiffness is mapped to the rail geometry and resulted in rail irregularities under the self-weight of the ballastless track. Compared to the wavelength of uneven modulus, the reductions in modulus amplitudes played more important role in the rail displacement.

(2) For the degraded roadbed area in ballastless railways, train loads did not result in obvious additional increase of rail displacement, which were mainly contributed from the geometry mapping under self-weight of the superstructure.

(3) The uneven degradation of roadbed stiffness resulted in large vibration of high-speed trains. For the conditions modeled, the wheel accelerations were more sensitive to the uneven degradation of roadbed modulus amplitudes than the wavelength. Due to the effects of bogie-wheel and car body–bogie suspensions, the car body accelerations reduced sharply.

(4) For the given conditions of uneven degradation of roadbed stiffness, the maximum accelerations of train wheel and car body satisfied the allowable limits for riding comfort. It is possible to evaluate the roadbed stiffness-based train wheels' dynamics. More situations will be calculated in the following research.

References

1. Guo Y, Zhai W, Sun Y et al (2017) Mechanical characteristics of modern tramcar–embedded track system due to differential subgrade settlement. Aust J Struct Eng 18(3):1–12
2. Guo Y, Zhai W (2018) Long-term prediction of track geometry degradation in high-speed vehicle–ballastless track system due to differential subgrade settlement. Soil Dyn Earthq Eng 113:1–11
3. Jiang H, Li X, Xin G et al (2019) Geometry mapping and additional stresses of ballastless track structure caused by subgrade differential settlement under self-weight loads in high-speed railways. Transport Geotech 18:103–110
4. Liu K, Yang G, Xu J (2015) Trixial tests on dynamic elastic modulus of subgrade fillers under high-speed railway loading. J Disaster Prev Mitig Eng 35(05):666–673
5. Linghu Y (2018) Reasons analysis of frost heaving of HSR subgrade and its treatment. Chinese Railways 10:52–56 (in Chinese)
6. Wang C (2015) Dynamic triaxial tests on completely weathered quartz monzonite soil samples with minimal confining pressures. Soil Eng Found 29(02):109–112 (in Chinese)
7. Chen X (2009) Subgrade strength based on the attenuation of the road under the conditions of structural mechanics analysis and recommendation of a typical structure. Shandong University, Master (in Chinese)
8. Wang Y, Mao X, Li W (2019) Effects of resilience modulus decay of phyllite packing embankment caused by water migration on the mechanical properties of pavement structure. Sci Technol Eng 19(12):344–352
9. Cui Y-J (2018) Mechanical behavior of coarse grains/fines mixture under monotonic and cyclic loadings. Transport Geotech 17:91–97
10. Duong TV, Cui Y-J, Tang AM et al (2014) Effect of fine particles on the hydraulic behavior of interlayer soil in railway substructure. Can Geotech J 51:735–746
11. Duong TV, Cui Y-J, Tang AM et al (2014) Investigating the mud pumping and interlayer creation phenomena in railway sub-structure. Eng Geol 171:45–58
12. Li T, Su Q, Shao K et al (2019) Numerical analysis of vibration responses in high-speed railways considering mud pumping defect. Shock Vib 2019(2):1–11
13. Berggren EG, Kaynia AM, Dehlbom B (2010) Identification of substructure properties of railway tracks by dynamic stiffness measurements and simulations. J Sound Vib 329(19):3999–4016
14. Kaynia AM, Park J, Norén-Cosgriff K (2017) Effect of track defects on vibration from high speed train. Procedia Eng 199:2681–2686
15. Liu G, Quek JS (2003) A non-reflecting boundary for analyzing wave propagation using the finite element method. Finite Elem Anal Des 39(5–6):403–417
16. Song H (2011) Theoretical and field test analysis of high-speed train and slab track coupling interaction. Zhejiang University, Master (in Chinese)

Can One Exclude Track and Rolling Stock Stiffness for the Assessment of Dynamic Impact Forces Due to Variations in Track Profile?

Erdem Balcı and **Niyazi Özgür Bezgin**

Abstract The geometric quality of a railway track is an important indicator of track performance and ride quality. European Norms (EN) recommends intervals of geometric values for the plan and profile geometries of railways, and AREMA has recommendations for geometric maintenance. Nevertheless, these recommendations frequently exclude an explicit understanding for the track stiffness and the primary and secondary stiffness values of the rolling stock. However, the authors suggest that track and rolling stock stiffness values affect the dynamic impact forces that develop on railway tracks. Therefore, it is the authors' opinion that the recommendations for the limits of variability of the track vertical profile must include recommendations for the track and rolling stock stiffness. An analytical method introduced by the authors can explicitly assess the effect of track and rolling stock stiffness on the dynamic impact forces that develop due to variations in track profile, track and rolling stiffness and wheel roughness. This paper will evaluate the AREMA and EN recommendations for the track profile variations. The paper will then introduce the developed method and the analytical equations developed by the method and use these equations with the track profile variation intervals recommended in the EN to show the necessity of specifying track and rolling stock stiffness value intervals along with the recommendations for interventions due to profile variations to reduce train speeds or correct the track profile.

Keywords Track profile · Track stiffness · Track geometric quality · Dynamic impact forces · Bezgin method

E. Balcı (✉) · N. Ö. Bezgin
Civil Engineering, Istanbul University-Cerrahpaşa, 34320 Istanbul, Turkey

1   Introduction

The significance of the evaluation of tracks' geometric quality came into prominence in the twentieth century. Development of track recording vehicles allowed European infrastructure companies to measure track geometry and thus develop their own evaluation standards (EN). EN 13,848-5 [1] is European Standard for railway applications and track and track geometric quality. In Part 5 of the Standard, geometric quality levels for plain line are examined in detail and wavelength intervals are recommended for the assessment of limit cases. Implementation of these given recommendations is necessary for 31 European countries according to CEN/CENELEC Internal Regulations. There is a variety of studies that recommend track quality levels [2, 3]. Track geometric quality recommendations presented by European Standard take three previous studies into account as much as possible [3–5]. Even though their suggestions differ from the others, they also do not take track and rolling stock stiffness into consideration. According to the standard, depth and amplitude of the isolated defects for a specific train speed determine track's geometric quality.

Variations in the track profile cause dynamic impact forces in railways. However, irregularity type of the profile (i.e., "ascend" or the "descend") is not the only parameter that determines the amount of dynamic forces transferred to the track. Previous studies show that track and rolling stock stiffness are also important in the assessment of dynamic impact loads [6–8]. An analytical method introduced by Bezgin [9] takes track roughness, track stiffness and rolling stock stiffness into consideration to estimate dynamic impact forces that develop due to variations in track profile, track and rolling stock stiffness and wheel roughness. One can easily use this method to understand the effects of track and rolling stock stiffness on the dynamic impact forces for a given track profile and train speed conditions [9, 10].

In this work, dynamic impact factors are calculated for EN's recommended values for limit cases. It is shown that when all parameters held constant for a given track profile, variation in the track stiffness causes different dynamic loadings [9]. Firstly, track quality levels and recommendations of EN and AREMA are explained. Later, the Bezgin method and sets of equations developed by the method are introduced. Finally, dynamic impact factors are estimated according to the limits specified in EN. It is found that both track and rolling stock stiffness play a crucial role in occurrence of dynamic forces. Therefore, both should be taken into consideration for track geometry recommendations to avoid excessive values of dynamic impact forces.

2   Evaluation of Track Quality in EN and AREMA Manual

In order to bring a harmonized track quality standards that can be applied in Europe, European Standard defines three quality levels:

- **Alert Limit (AL)**: Limit that if exceeded, it is necessary to analyze track geometry and carry out a regularly planned maintenance.
- **Intervention Limit (IL)**: Limit that if exceeded, corrective maintenance must be carried out to prevent immediate action limit to be reached before the next inspection.
- **Immediate Action Limit (IAL)**: Limit that if exceeded, immediate action (such as closing the line or reducing the speed) must be taken to lower the derailment risk to an acceptable level.

There are recommendations of values for track gauge, longitudinal level, alignment and twist to determine these limits. However, only recommendations for longitudinal level will be examined in this work. Longitudinal-level differences for these limits are addressed for three wavelengths. Wavelengths (λ) show the length of the track that track irregularity continues. This value is equal to twice of the transition length (L). These wavelengths are:

- D1: 3 m $< \lambda \leq$ 25 m
- D2: 25 m $< \lambda \leq$ 70 m
- D3: 70 m $< \lambda \leq$ 200 m

The last wavelength is related to passenger comfort rather than safety. Thus, longitudinal-level differences in limit cases are specified for D1 and D2 wavelengths. Table 1 shows the isolated defect recommendations for AL, IL and IAL and for mean to peak values. The mean stands for the calculation over a length that is equal or higher than twice of the wavelength in D1 or D2. Since it is close to zero in practice, zero to peak values are used. One can notice that the effects of track and rolling stock stiffness are not explicitly considered within these recommendations.

In AREMA Manual [11], track geometry is described by various parameters and elements. These can be found by the projection of track geometry onto different planes (i.e., horizontal or longitudinal planes). Thus, track geometry is described in four different ways: horizontal track geometry, longitudinal track geometry, track geometry in transverse vertical plane and track geometry in the track plane. Irregularity measurements may be performed by a track geometry measuring vehicle (TGMV). An example of the output of a TGMV is shown in Table 2. TGMV gives

Table 1 Longitudinal alignment differences for limit cases specified in European Standard

Speed (km/h)	AL (mm)		IL (mm)		IAL (mm)	
	Wavelength		Wavelength		Wavelength	
	D1	D2	D1	D2	D1	D2
$v \leq 80$	18	–	21	–	28	–
$80 < v \leq 120$	16	–	19	–	26	–
$120 < v \leq 160$	15	–	17	–	23	–
$160 < v \leq 230$	12	20	14	23	20	33
$230 < v \leq 300$	10	18	12	20	16	28

Table 2 Priority defect report sample (AREMA)

Defect name	From post/feet	To post/feet	Length (feet)	Maximum value	Threshold	Speed	Track type
LPROFILE	47 + 678	47 + 685	7	3/4″	58″	60	T
RPROFILE	47 + 678	47 + 685	7	3/4″	58″	60	T

a strip chart as an output, showing overall track geometry in one picture. "From post" shows where the signal value exceeds the threshold, and "to post" is where signal value falls below the threshold. Length is the difference between these two, and maximum value is the largest measured signal value. Aim of the chart is to find the listings of priority defects where threshold is exceeded. A threshold value must be predetermined for the evaluation of the results of the strip chart. Points where geometric defects exceed their threshold are evaluated as priority defects or exceptions. Thresholds are set by considering railroad's standards.

Besides, there are special priority defects that do not fit into description of basic priority defects, such as maximum allowable speed defect. This type of defect can be found only in curves. Maximum speed in the curve is usually set by the railroad's standards using the following formula.

$$V = \sqrt{\frac{(E + U)}{0.0007D}} \tag{1}$$

V Maximum allowable speed (mph)
E Actual curve superelevation (inches)
U Allowable unbalanced superelevation (inches)
D Curve degree.

AREMA suggests corrective action in points where threshold is exceeded. This threshold is usually based on the operational speed. The formula used in the curves is a combination of allowable speed, superelevation and curve parameters.

However, track stiffness is one of the main indicators of the track quality and rolling stock stiffness is an effective parameter on dynamic forces generated by train. In order to investigate their effects, dynamic impact forces must be calculated for different stiffness values within the limits that is specified in EN. One can use the Bezgin method to assess dynamic impact forces in a track with track profile irregularities.

3 Bezgin and Extended Bezgin Equations Used for the Estimations of Dynamic Impact Forces

Extended Bezgin equations are formed by the implementation of Bezgin method, and they can be used to estimate dynamic impact forces generated by train's passage over

track irregularities [9, 10, 12]. These equations consider the effects of primary and secondary spring stiffness values of the rolling stock in addition to the track stiffness. The method is based on the principle of energy conversation, kinematics and a new concept of impact reduction factor. A previous study [12] shows the development of Bezgin equations to obtain $K_{B,a}$ and $K_{B,d}$ which are the dynamic impact factors for ascending and descending track profiles, respectively.

While Bezgin equations take track stiffness (k), train speed (v), variation in track profile (h) and transition length (L) into consideration, extended Bezgin equations consider the bogie stiffness (k_b), wheel spring stiffness (k_w), Hertzian contact stiffness (k_h) and damping quality of the train (s) in addition. A system stiffness is used as a combination of these stiffness values. One can find the details of the application of this method to yield the extended Bezgin equations elsewhere [10]. However, four of the equations developed by the method are shown in Eqs. 2, 3, 4, 5 and 6 that estimate dynamic impact force factors for ascending track profile variation ($K_{B,a}$ and $K'_{B,a}$), descending track profile variation ($K_{B,d}$ and $K'_{B,d}$) and the secondary impact (K_j) that occurs due to an ascending track profile, respectively.

$$K_{B,a} = 2\sqrt{\left[\frac{h}{2a}(1-f)+1\right]} - 1 \tag{2}$$

$$K_{B,d} = 1 + \sqrt{\frac{2h}{a}(1-f)} \tag{3}$$

$$K'_{B,a} = 2\sqrt{\left[\frac{h}{2a'}(1-f-s)+1\right]} - 1 \tag{4}$$

$$K'_{B,d} = 1 + \sqrt{\frac{2h}{a'}(1-f-s)} \tag{5}$$

$$K_J = \frac{a_v}{g} \text{ where } a_v = 2h\left(V/L\right)^2 \tag{6}$$

One can benefit from the presented Bezgin and extended Bezgin equations to estimate the dynamic impact forces occurring over a rough length of track where the track profile changes. While a wheel of the train passes over the irregularity in D1 or D2 wavelength, it is first exposed to a descending and then ascending track profile as shown in Fig. 1. Throughout the first half of the wavelength, $K_{B,d}$ and $K'_{B,d}$ dynamic impact factors can be used for estimations. Since the second half of the wavelength is an ascending profile, wheel accelerates beyond the transition length and reaches a certain speed. When the track irregularity ends, vertical acceleration diminishes and the wheel leaps onto and drops on the track, causing an additional dynamic impact factor (K_J). Therefore, effects of the ascending wheel acceleration must be added to the existing dynamic impact factors in the ascending profile. Total dynamic impact forces in the ascending profile can be estimated by $K_{B,a} + K_J$ or $K'_{B,a} + K_J$.

Fig. 1 Dynamic impact
factors due to descending
and ascending track profiles
[11, 13]
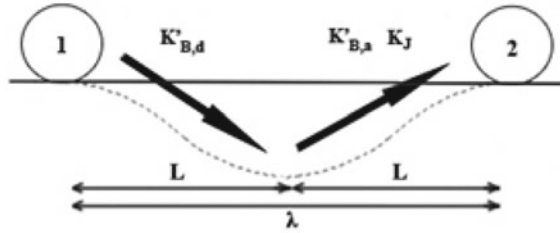
4 Dynamic Impact Forces Due to Longitudinal-Level Differences in EN Quality Limits

EN Standard has recommendations for five intervals of train speeds:

- $v \leq 80$ km/h
- 80 km/h $< v \leq 120$ km/h
- 120 km/h $< v \leq 160$ km/h
- 160 km/h $< v \leq 230$ km/h
- 230 km/h $< v \leq 300$ km/h

In order to calculate dynamic impact force factors, this paper considers train speed values of 50, 100, 150, 200 and 250 km/h. Each of these five values represents the value intervals specified in the EN. There are two wavelengths (D1 and D2) and two track irregularity types (ascending and descending profile). EN determines the longitudinal alignment difference in the alert, intervention and immediate action limits for a certain speed and a certain wavelength. Dynamic impact force factors are calculated for each train speed, wavelength and longitudinal alignment difference but with the inclusion of track and rolling stock stiffness.

Calculations are done by using ALLTRACK v1 [14], a program that calculates dynamic impact factors for given track characteristics by the implementation of Bezgin and extended Bezgin equations. Dynamic impact force factors are calculated for track stiffness of 20, 40, 60, 80 and 100 kN/mm. Bogie stiffness of 5 kN/mm, wheel spring stiffness of 10 kN/mm, Hertzian contact stiffness of 200,000 kN/mm, damping factor of 0.01 and wheel force of 125 kN are used. Rough track length values are chosen closer to the minimum limits. For instance, D1 wavelength covers the irregularities between 3 and 25 m. In calculations, D1 wavelength is picked as 5 m and thus transition length is obtained as 2.5 m. For D2, wavelength of 30 m and, thus, transition length of 15 m are used. Dynamic impact factors that are obtained via Bezgin and Extended Bezgin Equations are calculated. However, only dynamic impact factors of Bezgin equations are shown in the graphs. In order to help readers to compare the graphs of different limit cases, same dynamic impact factor scale is used in all figures (Fig. 2).
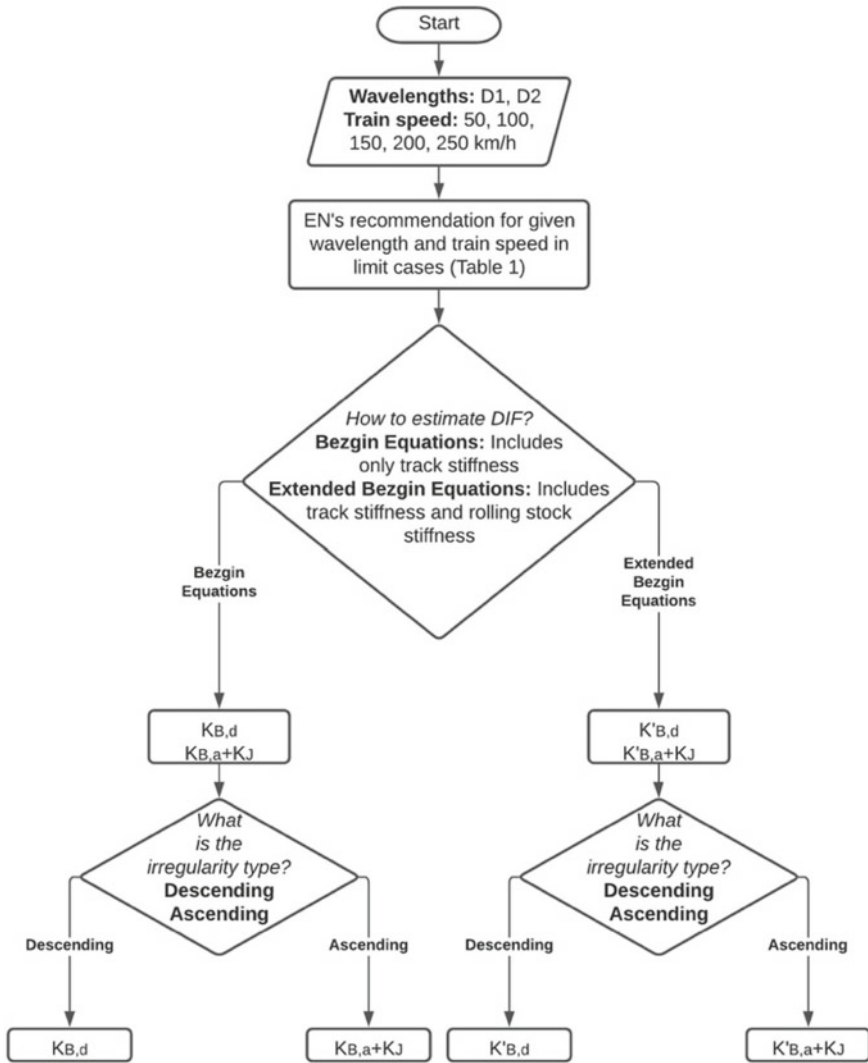
Fig. 2 Flowchart of the determination of dynamic impact factors for limit cases

4.1 Dynamic Impact Force Factors in Ascending Profile

Calculations are done for recommended longitudinal-level differences at alert limit (AL), intervention limit (IL) and immediate action limit (IAL), respectively. Variation of the dynamic impact factors with the track stiffness for AL is shown in Fig. 3.

$K_{B,a}$ factor does not take rolling stock stiffness value into consideration and relates to the track stiffness values. This factor reaches very high values because
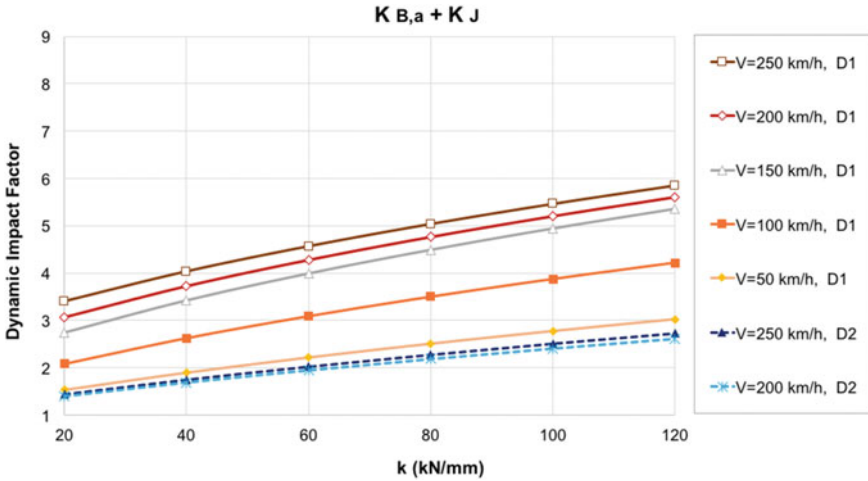
Fig. 3 Dynamic impact force factors due to ascending profile in AL [13]

train's suspension abilities are not considered. It can be seen from the figure that dynamic impact factors increase with the increasing track stiffness. Especially in higher speeds, dynamic loading in $k = 120$ kN/mm is remarkably higher than the loading in $k = 20$ kN/mm. Additional dynamic impact due to wheel's vertical acceleration is also an effective parameter to be considered. Its value is related to transition length and train's speed. While $K_{B,a}$ is almost equal for train speeds $v = 200$ km/h and $v = 250$ km/h, total dynamic load is different because of the K_J. This gap between dynamic loadings due to K_j gains importance especially in higher speeds and longitudinal differences and lower transition lengths.

$K'_{B,a}$ factor includes train's suspension abilities and is affected much less by the increase in the track stiffness. From $k = 20$ kN/mm to $k = 120$ kN/mm, maximum increase in $K'_{B,a}$ is %1.6 for given train speeds and wavelengths. Since equivalent system stiffness, which is a combination of track stiffness, wheel spring stiffness, bogie spring stiffness and Hertz contact stiffness, is used in the determination of $K'_{B,a}$, the relative effect of track stiffness becomes much less. In other words, rolling stock stiffness and damping quality of a train are very important to reduce the effects of track stiffness on dynamic impact forces.

Figure 4 illustrates the change of impact factors with the increasing track stiffness in IL, and it is similar to the change in AL. In IL, $K_{B,a} + K_j$ factor reaches nearly 7 times of the static wheel force, while it reaches nearly 6 times in AL. Because longitudinal profile variations are higher for this limit. One can see that there is more difference between the estimated factors with different train speeds. While total dynamic impact load is 4 for track stiffness of $k = 20$ kN/mm, it is near to 7 when $k = 120$ kN/mm. This shows the potential difference in the dynamic loads for given EN recommendations.
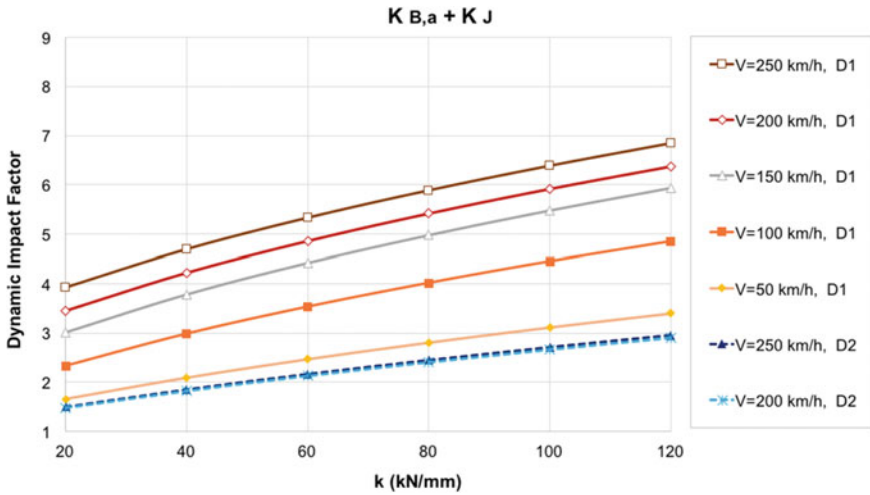
Fig. 4 Dynamic impact factors due to ascending profile in IL [13]

Distinction between D1 and D2 wavelengths is significant. Since D1 has a shorter length of track irregularity than D2, it is seen that dynamic impact force factors estimated for D1 and $v = 50$ km/h are higher than the factors estimated for D2 and $v = 250$ km/h.

In Fig. 5, dynamic factors are calculated for IAL, representing poor track conditions. When track quality decreases, track stiffness' importance on impact factors increases. Due to K_j, train speed is more effective on loading in IAL. Inequality
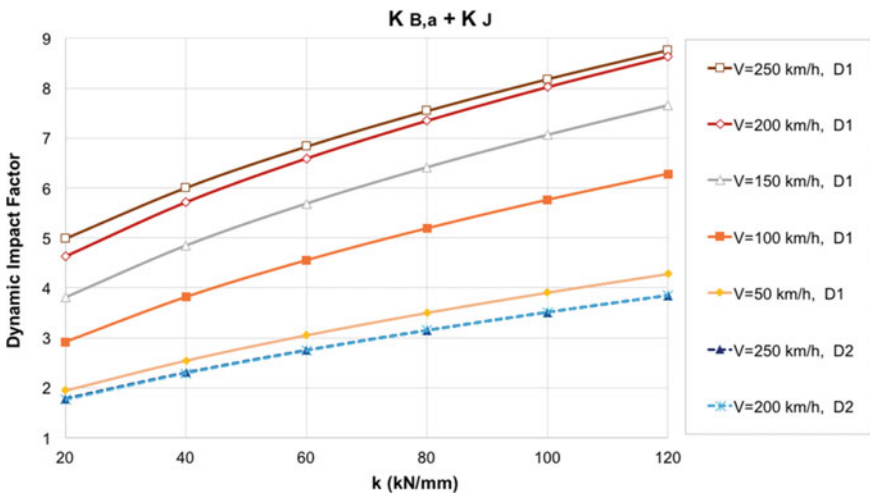
Fig. 5 Dynamic impact factors due to ascending profile in IAL [13]

between different track stiffnesses is more obvious for this case. While transferred forces into the track are 5 times of train's static wheel force for $k = 20$ kN/mm, it is 9 times for $k = 120$ kN/mm. One must note that AL is the first of these three limits, and thus the estimated dynamic impact force factors for this limit are the least. IAL is the worst-case scenario limit for the railway track, and the estimated dynamic impact force factors can be much higher than those estimated for AL and IL.

4.2 Dynamic Impact Forces in Descending Track Profile

For descending track profile, dynamic impact forces occur due to wheel's descent from "h", depending on its speed. Secondary impact will not occur in this case. Variation of the dynamic impact forces due to descending profile with the track stiffness for AL is shown in Fig. 6. $K_{B,d}$ curves are plotted for D1 and D2 wavelengths and for AL, IL and IAL, respectively.

Change of $K_{B,d}$ factors with track stiffness is similar to the change in $K_{B,a} + K_j$ factors. When train speed is high, dynamic loads in high track stiffness become twice of the loads in the low track stiffness. For IL, $K_{B,d}$ factor is the same for $v = 150, 200$ and 250 km/h. For this specific case, track stiffness is the key in the determination of occurred dynamic loads. Loads in $k = 120$ kN/mm can be more than twice of the loads in $k = 20$ kN/mm for IL and IAL. Transferred dynamic load to the track depends heavily on the track stiffness. Therefore, given recommendation according to wavelengths and specific train speeds is not sufficient solely. $K_{B,d}$ dynamic impact factors for IL and IAL are shown in Figs. 7 and 8, respectively.
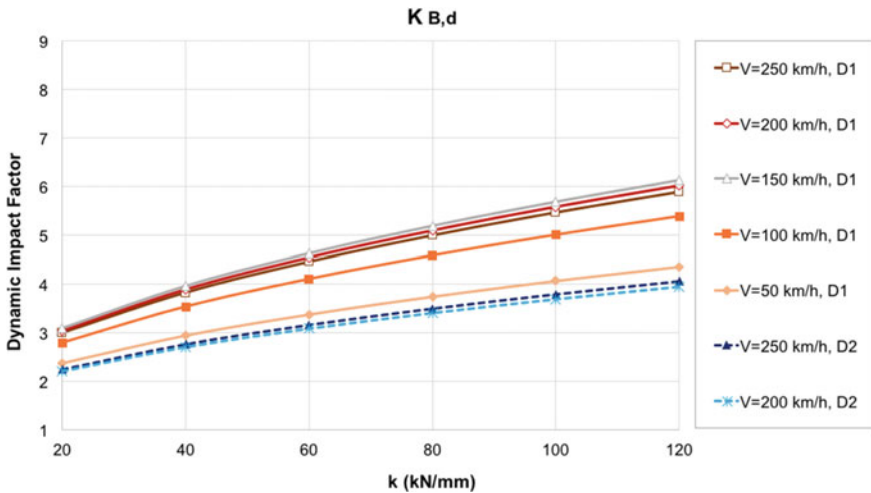
Fig. 6 Dynamic impact factors due to descending profile in AL [13]
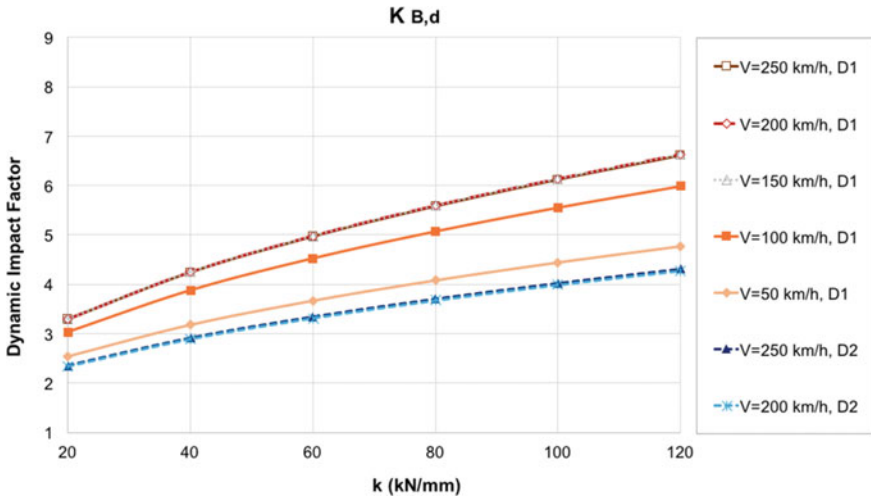
Fig. 7 Dynamic impact factors due to descending profile in IL [13]
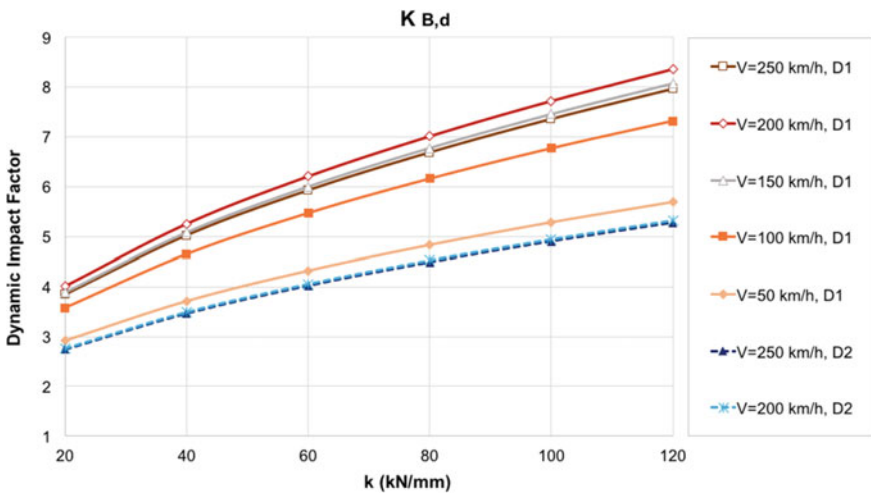
Fig. 8 Dynamic impact factors due to descending profile in IAL [13]

$K'_{B,d}$ dynamic impact factor, on the other hand, is affected less by the variation of track stiffness. From $k = 20$ kN/mm to $k = 120$ kN/mm, maximum increases in the $K'_{B,d}$ are %2.8, %3 and %3.3 for AL, IL and IAL, respectively.

5   Conclusions

This study investigated the importance of track and rolling stock stiffness in the assessment of dynamic impact loads. EN's intervals of geometric value recommendations and AREMA's method to determine a track's quality exclude the understanding of track's and rolling stock's stiffness. However, change in the stiffness values affects the dynamic impact forces occurred in a track. Possible change of track stiffness in frost-prone regions requires a thorough assessment of the effects of the variations in track stiffness on dynamic impact forces that occur due to variations in track profile.

The Bezgin method is an analytical method, which correlates dynamic impact forces to the track and rolling stock stiffness. Through the resulting equations that come with the implementation of this method, variation in the dynamic loads is shown for changing track stiffness. It is found that dynamic loads are affected by track stiffness to varying degrees. Especially when the primary wheel suspensions are damaged or malfunctioning, dynamic impact force factors can reach excessive values. It is also shown that stiffer tracks lead to higher dynamic impact forces. The study is repeated for AL, IL and IAL cases specified in EN. From AL to IAL, the track condition worsens and dynamic forces transferred to the track get higher. When train applies higher wheel forces, deterioration of the track accelerates and track's condition becomes worse.

When equivalent system stiffness is used in the equations, effect of the track stiffness was negligible. Instead, stiffness of the rolling stock elements took part covering the effect of the variation in track stiffness over dynamic loading. However, one must be cautious about the possibility of the absence or malfunctioning of the rolling stock stiffness elements.

In IAL, dynamic impact factor of a train without suspension can be anywhere between 4 and 9, depending on the track stiffness. EN's recommendations with the exclusion of track and rolling stock stiffness can lead to excessive dynamic impact forces and, thus, poor track performance, rapid deterioration of the track elements and shorter service life. AREMA's method for the inspection of the track is based on TGMV's priority defect chart which is evaluated by a predetermined threshold. Since all maintenance tasks must be done according to output of the proposed method, it is very important to determine the threshold carefully. However, determination of the threshold is usually based on the railroad's standard and it is mostly done by considering operational speed.

In conclusion, both track and rolling stock stiffnesses are very important parameters that require consideration in the assessment of track geometric threshold values.

References

1. EN 13848-5:2008+A1:2010 railway applications—track—track geometry quality, 2008—Part 5: geometric quality levels
2. EN 13848-1, Railway applications—track—track geometry quality—Part 1: Characterisation of track geometry
3. EN 14363:2005, Railway applications—testing for the acceptance of running characteristics of railway vehicles—testing of running behavior and stationary tests
4. ORE B 55, Prevention of derailment of goods wagons on distorted tracks: RP 8 (April 1983), Conditions for negotiating track twists—Recommended values for the track twist and cant—calculation and measurement of the relevant vehicle parameters—vehicle testing (final report)
5. TSI Hs Infrastructure (2002) Technical specification for interoperability (TSI) relating to the infrastructure subsystem of the trans-European high-speed rail system. EU Commission, Brussels
6. Yau J-D, Yang Y-B, Kuo S-R (1999) Impact response of high speed rail bridges and riding comfort of rail cars. Eng Struct 21(9):836–844
7. Li MXD, Berggren EG (2010) A study of the effect of global track stiffness and its variations on track performance: simulation and measurement. Proc Instit Mechan Eng Part F: J Rail Rapid Transit 224(5):375–382
8. Lei X, Zhang B (2010) Influence of track stiffness distribution on vehicle and track interactions in track transition. Proc Inst Mechan Eng Part F: J Rail Rapid Transit 224(6):592–604
9. Bezgin NO (2017) Development of a new and an explicit analytical equation that estimates the vertical impact loads of a moving train. Procedia Eng 189:2–10
10. Bezgin NÖ, Wehbi M (2019) Advancement and application of the Bezgin method to estimate effects of stiffness variations along railways on wheel forces. Transp Res Rec 2673(7):248–264
11. AREMA (American Railway Engineering and Maintenance-of-Way Association) (2016) Manual for railway engineering, vol 4
12. Bezgin NO (2018) Application of a new concept and a method to estimate the vertical impact forces on railway tracks due to track profile irregularities. In: 97th transportation research board meeting, Paper No.: 18-00407, Washington DC
13. Balcı E (2019) Investigation of the effects of railroad stiffness changes on the vertical wheel forces, MSc Thesis
14. Bezgin NÖ (2019) ALLTRACK v1 January 2, 2019. Researchgate. https://doi.org/10.13140/RG.2.2.32548.94083

The Influence of Local Irregularities on the Vehicle–Track Interaction

Aditi Kumawat, Ullrich Martin, Sebastian Bahamon, and Sebastian Rapp

Abstract Local track irregularities such as mud spots generally cause a sudden variation in track stiffness, which leads to the track geometry degradation in a short period. The interaction of the moving train with such track defects induces additional dynamic stresses in the track system that may prove harmful for the structural health of the track structure. In this paper, an analytical approach is proposed to simulate the vertical track acceleration caused by a local track irregularity when subjected to a uniformly moving load. The railway track is modeled as an infinitely long continuous Euler–Bernoulli beam lying over a Pasternak-type viscoelastic foundation track model. At any given location along the rail beam, the stiffness and thickness of the considered foundation model, respectively, denote the track substructural stiffness and track geometry. To simulate the effects of local irregularities, a pre-defined variation of the stiffness and thickness is considered in a particular section of the foundation model. The time-domain deflection/acceleration responses are obtained for the railway track subjected to a uniformly moving (a) point load and (b) two-mass oscillator system. The results show that the local irregularities may cause significant damage to track structure, which may lead to poor ride comfort or in some cases, even derailment.

Keywords Local track irregularity · Railway track · Analytical model

1 Introduction

The interaction of the moving train with the vertical imperfections (wheel flats and railhead corrugations), rail discontinuities (crossings, switches, turnouts), or local irregularities (mud spots) results in unstable vibrations [1, 2]. These vibrations

---

A. Kumawat (✉)
Department of Civil Engineering, Indian Institute of Technology Kanpur, Kanpur 208016, India

U. Martin · S. Bahamon · S. Rapp
Institute of Railway and Transportation Engineering, University of Stuttgart, Pfaffenwaldring 7, 70569 Stuttgart, Germany

are detrimental for the long-term performance of the track structure, and to ensure passenger safety, continuous track monitoring is essential.

Track stiffness and vertical track geometry are the two crucial parameters that are often implemented for the quality assessment of in-service railway tracks. The track stiffness is defined as the ratio of the train load to the rail deflection. The track geometry data includes the longitudinal profile, alignment, track gauge, cross-level, and twist. Both the track stiffness and geometry may vary along the length of the track at the transition zones, switches, and crossings [3]. However, local irregularities such as mud spots cause a sudden variation in track stiffness and geometry, which leads to track degradation in a short period. The interaction of the moving train with such track defects induces additional dynamic stresses in the track system that may prove harmful for the structural health of the track.

Track recording vehicles are often used for continuous measurement of stiffness and vertical profile along the length of the railway track [4, 5]. Additionally, acceleration sensors mounted on in-service trains are also employed to recognize the track irregularities along the railway tracks. However, continuous monitoring of railway tracks is costly, disrupts the regular operations, and has not been implemented yet for a vast length of railway networks across the world. Therefore, prior knowledge of the typical acceleration signals due to various track defects under the dynamic train loads is essential to detect the track failures as early as possible [6].

Several studies have simulated the acceleration/displacement response of the rail beam under moving train loads using various analytical and numerical methods [7–9]. However, most of these methods analyze the track assuming a constant track stiffness. Only a few theoretical studies are available in the literature which consider the variation of track stiffness along the track length [10]. Moreover, none of those studies take into account track geometry degradation.

The present study is performed in three parts (see Fig. 1). In this first part of this research, an analytical approach is proposed to simulate the vertical track deflection/acceleration caused by a local track irregularity. In the second part, the track acceleration data is collected via (1) an experimental study performed on a 1:87
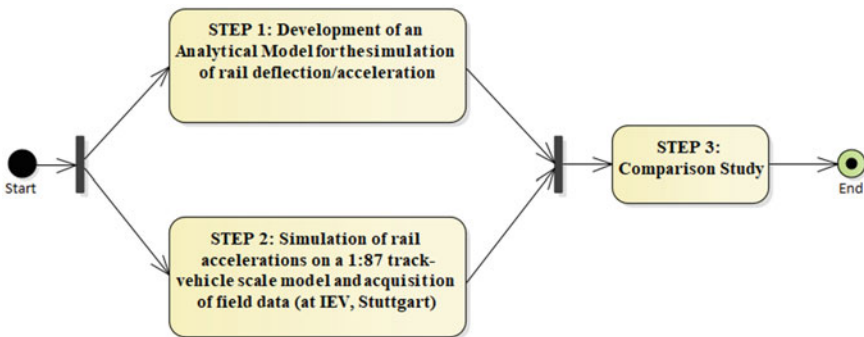
Fig. 1 Activity diagram showing the steps of the study

track–vehicle scale model and (2) field measurements. In the third part, the reliability of the proposed approach will be assessed by comparison with the collected data. In this paper, however, we only present the first part of this study. A subsequent article (under preparation) will focus on the second and third parts based on results of ongoing research.

The railway track is modeled as an infinitely long continuous Euler–Bernoulli beam lying over a Pasternak-type viscoelastic foundation track model. At any given location along the rail beam, the stiffness and thickness of the considered foundation model denote the track substructural stiffness and track geometry, respectively. For simulating the effects of local irregularities, a pre-defined variation of the stiffness and thickness is considered in a particular section of the foundation model. An analytical approach is employed to analyze the response of a vehicle moving over the local irregularity. The results comprise the time-domain deflection/acceleration response of the rail beam and vehicle system for various train velocities.

2 Analysis

Figure 2 represents the railway track model used to analyze the behavior of railway track system under motion-induced dynamic loading. The rail beam is idealized as an infinite Euler–Bernoulli beam with x denoting the space coordinate along the length of the rail beam. The track structure beneath the rail beam is idealized via a viscoelastic Pasternak layer. The viscoelastic component of this layer comprises viscous dampers superimposed with a spring layer. The viscoelastic layer accounts for the stiffness $K(x)$ and damping $c(x)$ associated with various track components (rail pads, sleepers, ballast, and subgrade). Further, the Pasternak layer (of thickness $H_P(x)$) takes into account the shear behavior of the substructure components (ballast
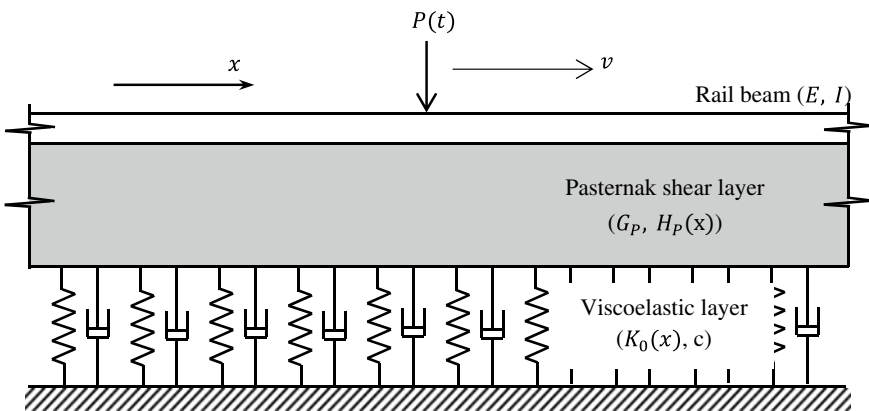
Fig. 2 Definition sketch of the considered railway track model

and subgrade) via the shear parameter $G_P(x)$. In addition to this, the Pasternak shear elements introduce the interaction between the viscoelastic spring elements.

Thus, the considered track model idealizes the railway track system in a simplistic manner through its stiffness, damping, and shear parameters. Ideally, a proper model of the railway track should account for the sleepers, rail pads, and rail fasteners. Further, the model for ballast and subgrade should account for effects such as inter-particle friction, particle angularity, and nonlinear deformation behavior. However, the primary goal of this study is to propose a computationally inexpensive analytical model that, at the cost of certain simplifications, can still yield reasonable results for the reference of practicing engineers.

Under these idealizations, the equation of motion of the rail beam is given by [9]

$$EI\frac{\partial^4 w}{\partial x^4} - G_P(x)H_P(x)\frac{\partial^2 w}{\partial x^2} + K(x)w + c(x)\frac{\partial w}{\partial t} + \rho\frac{\partial^2 w}{\partial t^2} = F(x,t) \quad (1)$$

where $w(x,t)$ is the transverse deflection of the rail beam (considered positive downward), E is Young's modulus of rail beam material, I is the moment of inertia of the rail beam cross section about the axis of bending, ρ is the mass per unit length of the beam, and $F(x,t)$ is the load applied per unit length of the beam. In this case, $F(x,t)$ is given by

$$F(x,t) = P(t)\delta(x - vt) \quad (2)$$

where δ represents Dirac's delta function and $P(t)$ is the time-varying vertical load moving over the rail beam with uniform velocity v. Further, as mentioned in the introduction, the effect of local irregularity (mud spot) is simulated via the variation of stiffness $K(x)$ and height $H_P(x)$ of the Pasternak layer along x. However, it is assumed that the shear parameter $G_P(x)$ and damping values $c(x)$ remain constant along the length of the railway track. Considering that, and using Eq. (2). Equation (1) can be rewritten as:

$$EI\frac{\partial^4 w}{\partial x^4} - G_P H_P(x)\frac{\partial^2 w}{\partial x^2} + K(x)w + c\frac{\partial w}{\partial t} + \rho\frac{\partial^2 w}{\partial t^2} = P(t)\delta(x - vt) \quad (3)$$

Denoting $\iota = \sqrt{-1}$ and $\widehat{f}(\omega)$ as the Fourier transform of an arbitrary function $f(x)$ of the space coordinate x, we have

$$\widehat{f}(\omega) = \int_{-\infty}^{\infty} f(t)e^{-\iota\omega t}\, dt \quad (4)$$

and

$$f(t) = \frac{1}{2\pi} \int\limits_{-\infty}^{\infty} \widehat{f}(\omega) e^{\iota \omega t} \, d\omega \tag{5}$$

Further, on taking the Fourier transform of Eq. (3) using Eq. (4) we can write

$$EI \frac{\partial^4 \widehat{w}}{\partial x^4} - G_P H_P(x) \frac{\partial^2 \widehat{w}}{\partial x^2} + K(x)\widehat{w} + \iota c\omega\widehat{w} - \rho\omega^2\widehat{w} = P\left(\frac{x}{v}\right) e^{-\iota\omega\left(\frac{x}{v}\right)} \tag{6}$$

where $\widehat{w}(x, \omega)$ denotes the Fourier transform of $w(x, t)$. On simplifying the above equation, we can obtain the solution for $\widehat{w}(x, \omega)$ as:

$$\widehat{w}(x, \omega) = \left(\frac{P(x/v)v^3}{EI\omega^4 + G_P H_P(x)\omega^2 v^2 + v^4 K(x) - \rho\omega^2 v^4 + \iota c\omega v^4} \right) e^{-\iota\omega\left(\frac{x}{v}\right)} \tag{7}$$

To obtain the rail beam deflection $w(x, t)$ in time domain, one needs to evaluate the inverse Fourier transform of $\widehat{w}(x, \omega)$ using Eq. (5) as:

$$w(x, t) = \frac{1}{2\pi} \int\limits_{-\infty}^{\infty} \left(\frac{P(x/v)v^3 e^{-\iota\omega\left(\frac{x}{v}\right)} e^{\iota\omega t}}{EI\omega^4 + G_P H_P(x)\omega^2 v^2 + v^4 K(x) - \rho\omega^2 v^4 + \iota c\omega v^4} \right) d\omega \tag{8}$$

Furthermore, to determine the rail beam deflection below the moving load $P(t)$ we can substitute $x = vt$ in the above equation:

$$w_0(t) = \frac{1}{2\pi} \int\limits_{-\infty}^{\infty} \left(\frac{P(t)v^3}{EI\omega^4 + G_P H_P(vt)\omega^2 v^2 + v^4 K(vt) - \rho\omega^2 v^4 + \iota c\omega v^4} \right) d\omega \tag{9}$$

where $w_0(t)$ represents the rail beam deflection at the location $x = vt$, i.e., $w_0(t) = w(vt, t)$.

3   Results and Discussion

In this section, the response of the railway track system to the local irregularity is evaluated using the above formulation presented. The parameters used for the calculations are listed in Table 1. The variations of the track stiffness from a constant stiffness K_0 (see Table 1) and that of the Pasternak layer thickness H_P (see Table 1) assumed to simulate the local irregularity are shown in Fig. 3a, b, respectively.

Table 1 Railway track and oscillator parameters [2, 8, 9]

Parameters	Symbol	Values
Rail beam		
Mass per unit beam length	ρ	60 kg/m
Modulus of elasticity	E	210 GPa
Central area moment of inertia	I	3055 cm^4
Shear layer		
Shear modulus	G_P	43.3 MPa
Height	H_P	0.5 m
Viscoelastic layer		
Stiffness per unit beam length	K_0	40 MPa
Damping ratio	ζ	0.05
Point load		
Load magnitude	P_0	100 kN
Oscillator		
Mass	m_0	880 kg
	m_1	745 kg
Stiffness	k_1	0.735 MN/m
Coefficient of viscous damping	c_1	9.36 kN-s/m

Figure 4 shows the deflection response $w_0(t)$ of the rail beam subjected to a uniformly moving load $P(t) = P_0$ (see Fig. 2 and Table 1), at the location $x = vt$, where v denotes velocity. It may be noted that the positive value of deflection indicates the downward deflection (i.e., settlement). The deflection is obtained at four different velocities. It may be observed from Fig. 4 that initially, at all the considered velocities, the rail beam deflections are constant. Those constant values are equal to $w_0(t) = w_v$, obtained by inserting the constant stiffness K_0 and thickness H_P in Eq. (9), at the given velocity. However, as the load approaches the local irregularity, the deflection values gradually increase, and respective maximum values are attained at $x = 15$ m. As the load moves beyond the local irregularity, those deflections decrease and again reach the constant value w_v. The increase in deflections (by up to 360%) at the location of local irregularity shows that the stiffness and track geometry degradation may adversely affect the track performance.

Further, it may also be observed from Fig. 4 that as the velocity increases, the maximum deflection at $x = vt$ also increases. To better understand the effect of velocity on the rail beam deflection, Fig. 5 presents the maximum deflections $w_0(t)_{\max}$ observed for the velocities ranging from 0 to 500 m/s. It may be seen that $w_0(t)_{\max}$ increases with velocity, with the maximum amplification occurring at $v = 447$ m/s. This velocity is referred to as the critical velocity of the track. The maximum train velocities for ballasted tracks are much lesser than the observed critical velocity. However, the critical velocity value depends on the overall track stiffness and high
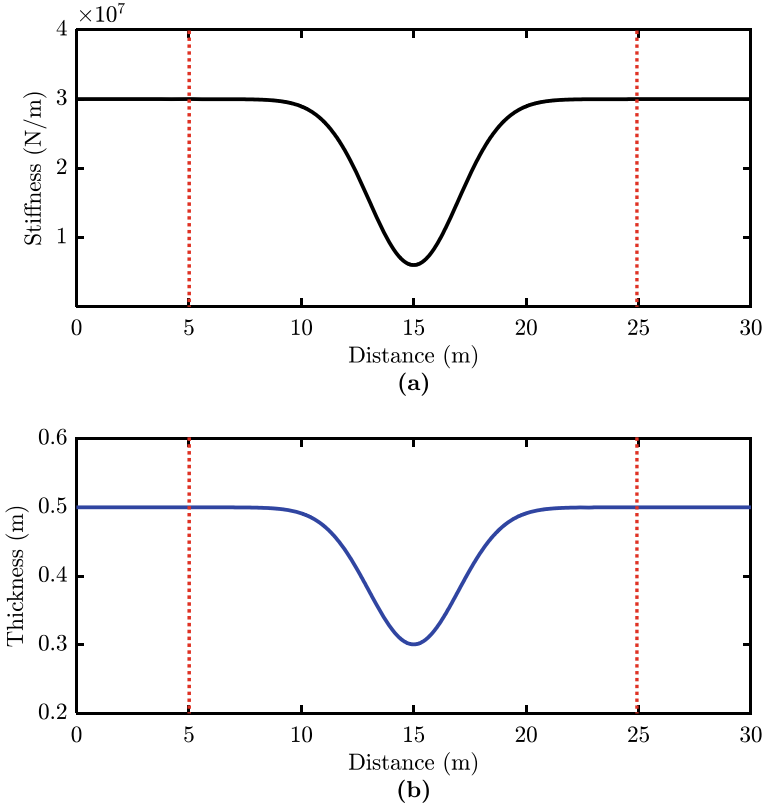
Fig. 3 Variation of track parameters along the railway track. **a** Stiffness. **b** Thickness (the dotted vertical lines specify the location of local irregularity)
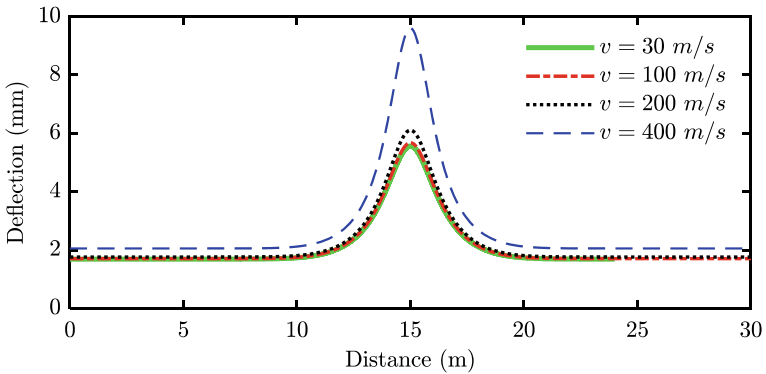
Fig. 4 Deflection response of the rail beam subjected to a uniformly moving load, at the location $x = vt$, for $v = 30, 100, 200,$ and 400 m/s
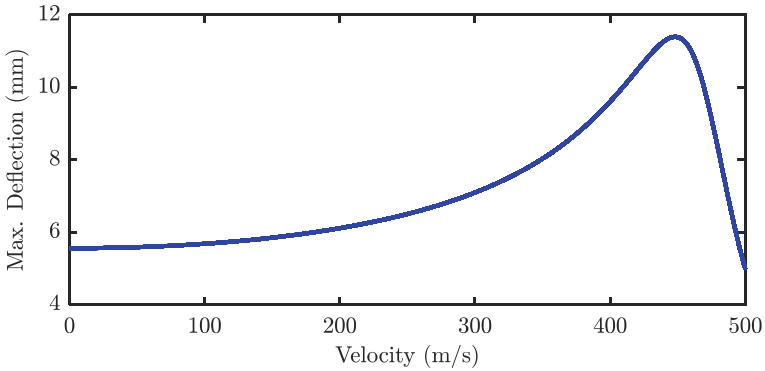
Fig. 5 Maximum rail beam deflections observed for the velocities ranging from 0 to 500 m/s

amplifications in deflections may be observed for a soft subgrade even at velocities of magnitudes comparable with the train velocities [8].

In this section, we analyze the effect of the considered local irregularity on vehicle–track interaction. Figure 6 shows a two-mass oscillator moving uniformly (with velocity v) over the Pasternak viscoelastic model (with varying thickness $H(x)$ and stiffness $K(x)$). The oscillator system comprises masses m_0 and m_1 connected via a spring (with stiffness k_1) and dashpot (with viscous damping coefficient c_1). The parameters defining the oscillator system are listed in Table 1. It is assumed that the moving oscillator system is in constant contact with the rail beam, and therefore, the absolute displacement of mass m_0 is equal to that of the rail beam, i.e., $w_0(t)$. $w_1(t)$ represents the absolute displacement of mass m_1. The force exerted by the moving oscillator system on the rail beam $P(t)$ (see Eq. (9)) is derived in using an approach given in the study [9].
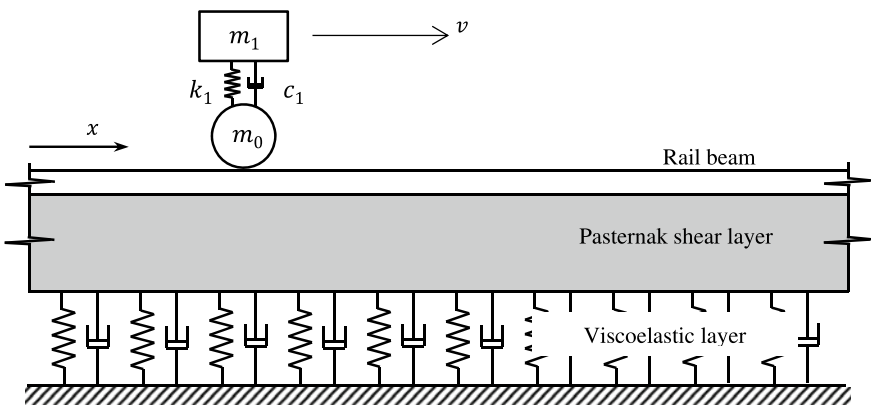
Fig. 6 Railway track model with two-mass oscillator

Figure 7 shows the deflection response of the masses m_0 (or of the rail beam) and m_1 at the location $x = vt$ for three different velocities, $v = 30, 100,$ and 200 m/s. It is assumed that both masses are at rest at location $x = 0$ and time $t = 0$.

It may be observed that the deflections $w_0(t)$ and $w_1(t)$ oscillate about a constant value. This value is equal to the deflection observed at the contact point when a point
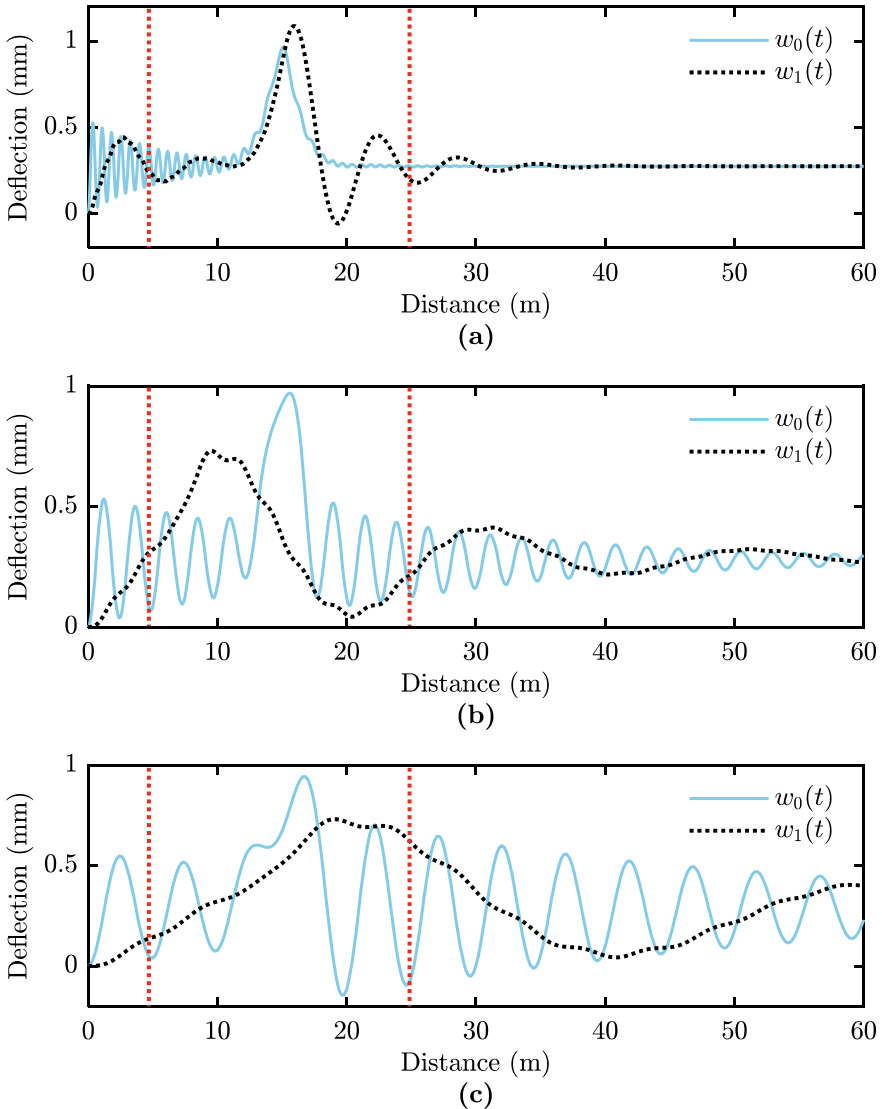
Fig. 7 Deflection responses of the masses m_0 ($w_0(t)$) and m_1 ($w_0(t)$), at $x = vt$, for three different velocities, **a** $v = 30$ m/s, **b** $v = 100$ m/s, and **c** $v = 200$ m/s (the dotted vertical lines specify the location of local irregularity)

load of magnitude $(m_0 + m_1)g$, where g is acceleration due to gravity, traverses the track model. The oscillatory vibrations of the deflection $w_0(t)$ have a much higher frequency than those for the deflection $w_1(t)$. Also, the frequency of vibration for both $w_0(t)$ and $w_1(t)$ decreases with the increase in velocity. Further, the effect of oscillator damping is evident in Fig. 7 where at all the considered velocities, as the oscillator moves away from initial location, the magnitude of deflections $w_0(t)$ and $w_1(t)$ decays with every cycle of vibration. The rate of vibration decay, however, decreases with the increase in velocity.

Further, in Fig. 7, as the oscillator approaches the local irregularity section ($x = $ 5–25 m), an increase (by up to 250%) in $w_0(t)$ can be clearly observed at all velocities. In addition to this, a significant increase (by up to 290%) in $w_1(t)$ may be observed for the velocity $v = 30$ m/s. However, the effect of the local irregularity is negligible on $w_1(t)$ at higher velocities ($v = 100$ and 200 m/s). The low value of deflection observed at higher velocities may be attributed to the local irregularity's length along the rail track. It has been found that for an irregularity of longer length, significant changes in deflections may be observed even at higher velocities. Lastly, as the oscillator moves beyond the local irregularity, the deflection values dampen to the constant value. Thus, it may be concluded that, the local irregularities may cause a significant damage to track structure which may lead to poor ride comfort or, in some cases, derailment.

Figure 8 shows the acceleration responses of the masses m_0 and m_1 along the length of the railway track. The comparison of these responses with the field acceleration data will be able to test the reliability of the presented approach. However, the data acquisition is still in process, and the subsequent article will focus on the comparison study.

4   Summary and Conclusions

In this paper, an attempt was made to simulate the effect of local irregularities in the railway track. The railway track is idealized via a Pasternak viscoelastic foundation model. A pre-defined stiffness and geometry variation are incorporated in a particular section of this foundation model to simulate the local irregularity. Further, an analytical approach is used to analyze the rail beam deflection/acceleration responses under dynamic train loading for the cases of uniformly moving (a) point load and (b) two-mass oscillator system.

For both considered loading types, a significant increase in the rail beam deflections is observed (by up to 360 and 250%, respectively) as the load approaches the simulated local irregularity position. The maximum amplification in the rail beam deflection is observed at the so-called critical velocity value. Lastly, it is found that the oscillator damping brings the rail beam response closer to that observed for the case of constant moving load idealization.
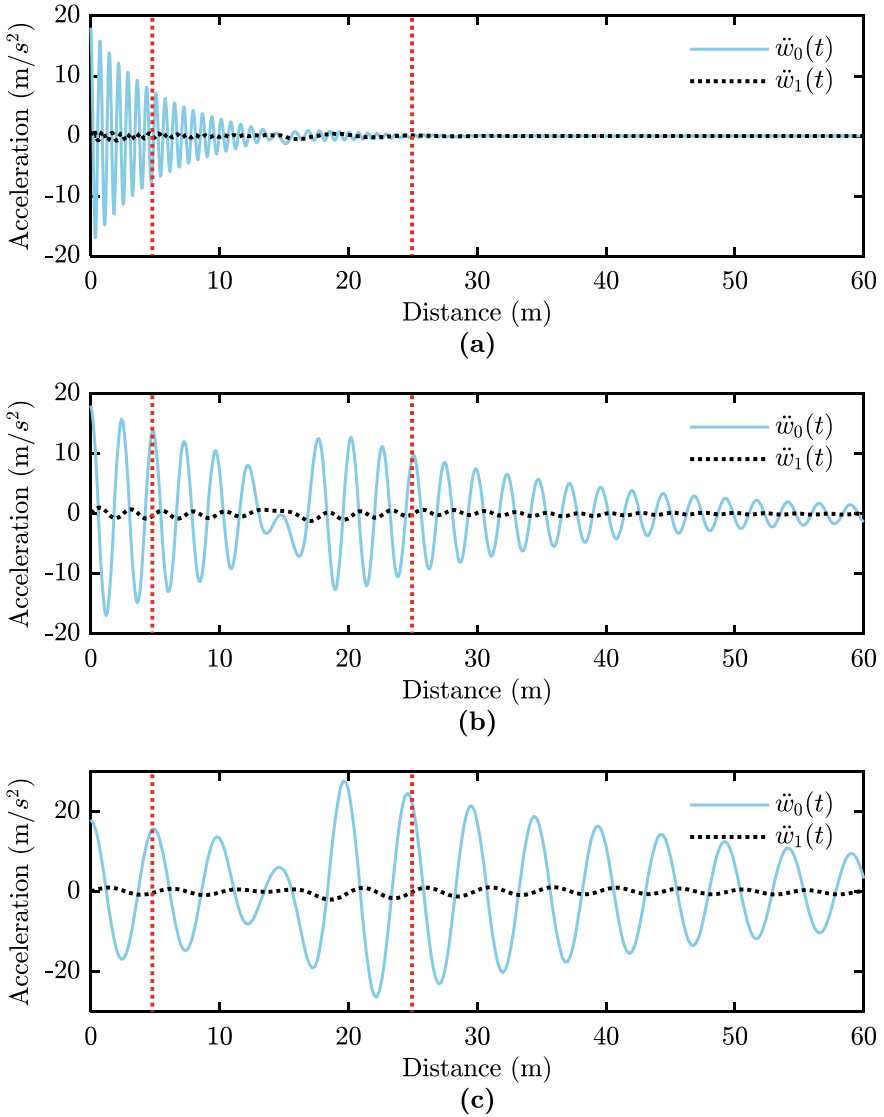
Fig. 8 Acceleration responses of the masses m_0 ($\ddot{w}_0(t)$) and m_1 ($\ddot{w}_1(t)$), at $x = vt$, for three different velocities, **a** $v = 30$ m/s, **b** $v = 100$ m/s, and **c** $v = 200$ m/s (the dotted vertical lines specify the location of local irregularity)

References

1. Knothe KL, Grassie SL (1993) Modelling of railway track and vehicle/track interaction at high frequencies. Veh Syst Dyn 22(3–4):209–262

2. Esveld C (2001) Modern railway track, 2nd edn. Delft University of Technology, MRT-Production
3. Iwnicki S (2006) Handbook of railway vehicle dynamics. CRC Press, Boca Raton
4. Norman C et al (2006) Design of a system to measure track modulus from a moving railcar. US Department of Transportation, Federal Railroad Administration, Office of Research and Development
5. Berggren EG, Kaynia AM, Dehlbom B (2010) Identification of substructure properties of railway tracks by dynamic stiffness measurements and simulations. J Sound Vib 329(19):3999–4016
6. Rapp S et al (2019) Track-vehicle scale model for evaluating local track defects detection methods. Transp Geotech
7. Basu D, Kameswara Rao NSV (2013) Analytical solutions for Euler-Bernoulli beam on visco-elastic foundation subjected to moving load. Int J Numer Anal Meth Geomech 37(8):945–960
8. Kumawat A, Raychowdhury P, Chandra S (2019) Frequency-dependent analytical model for ballasted rail-track systems subjected to moving load. Int J Geomech 19(4):04019016
9. Kumawat A, Raychowdhury P, Chandra S (2019) A wave number-based approach for the evaluation of the Green's function of a one-dimensional railway track model. Eur J Mechan A/Solids 103854
10. Quirke P et al (2017) Drive-by detection of railway track stiffness variation using in-service vehicles. Proc Inst Mechan Eng Part F J Rail Rapid Transit 231(4):498–514

Repeatability of Minimum and Maximum Density Testing on Clean and Fouled Ballast

M. W. Jones, E. K. Akey, C. L. Ho, and A. J. Rubin

Abstract Ballast material is a critical part of the safety of railways, such as padding tracks to prevent dynamic vibrations from causing trains to derail. The effectiveness of this material is closely tied to the percentage of fouling that is intermixed with the material. Generally, ballast is placed as compact as practical, but overtime, fouling of the ballast changes the composition of the placed material. Relative density could provide insight into the relative compactness and strength of the material. Unfortunately, the results of minimum or maximum density tests are not well documented in the existing literature. Although ASTM D4254 and D4253 do provide guidelines for minimum and maximum density testing of large particle diameters, there is minimal discussion in the literature regarding the anticipated error when testing with ballast and fouling. Tests to attempt to characterize this behavior, minimum and maximum density tests were run using Connecticut Granite ballast with granite stone dust used as a fouling material. The samples contained fouling at intervals of 0, 15, 30, 45, and 60% by mass and were placed in a 12-inch interior diameter cylinder mold in accordance with the ASTM standards. For each fouling condition, two operators each conducted 10 minimum density and 5 maximum density tests for a total of 100 minimum density tests and 50 maximum density tests. The effect of fouling, density, and operator, on the repeatability of the tests on ballast, is discussed.

Keywords Ballast · Minimum density testing · Maximum density testing · ASTM standards

M. W. Jones (✉) · E. K. Akey · A. J. Rubin
Smith College, Northampton, MA 01063, USA
e-mail: jone3247@umn.edu

C. L. Ho
University of Massachusetts Amherst, Amherst, MA 01003, USA

1 Introduction

ASTM standards D4254 and D4253 outline proper methods for performing maximum and minimum density tests on soils; however, research on the applicability of said standards to large particle soils such as railroad ballast is limited. Ballast material, the padding used on tracks to prevent dynamic vibrations from passing trains, is majorly composed of coarse gravel. Because the ASTM standards, particularly the minimum density, require approximations from the human eye, the error arising from this process may increase when dealing with the coarser soil. To test this effect, samples of AREMA #4 ballast mixtures containing 0, 15, 30, 45, and 60% fouling by mass were tested using each of the standards. 100 minimum density tests and 50 maximum density tests are used to discuss the effects of fouling, density, and operator on the repeatability and accuracy of these tests on the ballast material.

2 Background

Relatively speaking, the volume of research on the ASTM minimum and maximum density standards is very small for ballast-sized particles. Previous studies that do exist have been focused primarily on the methods when sands/silt mixtures are considered. The extent of the repeatability on larger particle materials does not extend far beyond the ASTM publication itself [1]. The ASTM publication specifies that all minimum density tests should be as follows for samples with particles over ¾ -in in diameter [2]:

> 9.2.3.1 Fill the mold to overflowing but no more than 1 in (25 mm) above the top. For solids where the maximum particle size passes the ¾-in. (19.0-mm) sieve, use the steel straightedge (and the fingers when needed) to level the surface of the soil with the top of the mold. For soils with a large maximum particle size, use the fingers in such a way that any slight projections of the larger particles above the top of the mold shall approximately balance the larger voids in the surface below the top of the mold.

The latter allows for a large degree of human error and variation from test to test. Acceptable range and standard deviation were assessed by ASTM when the standards were published in 2016, but only on USCS classification SP soil types, nothing as coarse as the ballast materials (with particles up to 60 mm) tested in this project. They found that in both single- and multi-laboratory results, the average value tests were the same, but standard deviation was significantly lower for the single-operator tests. The average value found when triplicate tests were conducted also varied slightly from the single-test results. The precision and accuracy are still untested for coarser samples.

The ASTM standard for maximum density testing using a vibrating table cites the procedure as such [3]:

> 11.1.4 Attach the mold to the vibrating table.

11.1.5 Firmly attach the guide sleeve to the mold and lower the appropriate surcharge weight onto the surcharge base plate.

11.1.7 Vibrate the mold assembly and specimen for $8 \pm \frac{1}{4}$ min at 60 ± 2 Hz or for $12 +/- \frac{1}{4}$ min at $50 +/- 2$ Hz. Remove the surcharge weight and guide sleeve from the mold. Check that the surcharge base place is firmly and uniformly in contact with the surface of the soil.

The surcharge weight is determined to give a surcharge stress of $2.00 \pm 0.20 \, \text{lb/in}^2$ on the sample. The mass of the sample should be no less than $M_r = 0.0024 * V_m$ where V_m is the volume of the mold.

Examinations of the maximum density standards are slightly more common. A group of researchers in Italy published a paper in 1992 comparing the results of the ASTM standard and the pluviation technique to calculate the maximum dry density of soils ranging up to $D_{max} = 9.5$ mm[3/8″] [4]. Their project shows some variation in the maximum standard but does conclude that the pluviation technique is more desirable. Furthermore, the pluviation technique is likely impractical for large particles, such as ballast. Similarly, a project done by researchers at Johns Hopkins University used both the maximum and the minimum techniques to determine the effects of non-plastic fines on the void ratios of sands. This examination was done on a much smaller scale (~800 g sample size), to minimize the amount of particle breakage during the tests of non-plastic fines on the void ratios of sands [5].

3 Methods

3.1 Minimum Density

The fouling material used in this experiment was defined as anything passing a 3/8″ sieve. The fouling, therefore, can be smoothed from the surface of the sample using a straightedge, but the ballast requires a human eye to estimate the projections above and below. This somewhat complicates the ASTM minimum density standard.

Samples of granite ballast from Connecticut were used to construct an AREMA #4 gradation/fouling mixtures for the minimum and maximum density tests. A grain-size curve for each mixture is shown in Fig. 1. The minimum tests were run ten times by two different operators at fouling percentages of 0, 15, 30, 45, and 60% by mass. Each mix was prepared by measuring out dry ballast and fouling separately according to a target mass, thoroughly mixed, and then placed into the testing mold. Each specimen was prepared in a 12″ × 12″ cylinder mold to constrain movement along the horizontal axis. For each test, the ballast/fouling mixture was placed in an 8″ tube that was centered in the mold. Once full, the tube was removed, and ballast allowed to pour out into a minimum density configuration. The excess mixture was then removed in conjunction with the ASTM standard outlined above, and density values are calculated.
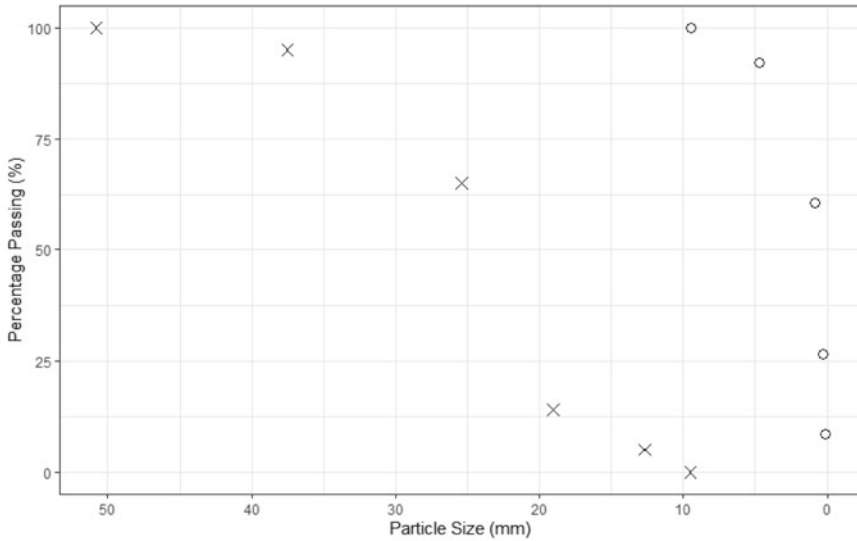
Fig. 1 Grain-size curve displaying percentage passing for AREMA #4 ballast mixture (*X*) and fouling materials (*O*)

3.2 Maximum Density

Maximum density tests were run on the same AREMA #4 Connecticut Granite ballast at fouling percentages of 0, 15, 30, 45, and 60% by mass. Five trials by two different operators were run to compare the human influence on data. Samples were placed in the cylinder mold and bolted to a shaker table. A surcharge weight of 200 kg, approximately 10 times the sample mass, was secured to the sample on top of a plate. Figure 2 shows a picture of the setup including the filled cylinder and surcharge load.

Samples were then run in general accordance to the ASTM standard outlined in the background section. From the completed samples, depth measurements were taken to analyze the skew of the plate, and density was computed for each sample.

4 Results

4.1 Minimum Density Analysis

Data from the minimum density tests, shown in Fig. 3, demonstrates an unevenness between the two operators' results across each fouling percentage. While certain

Fig. 2 Maximum density setup with cylinder, surcharge weights, and shaker table
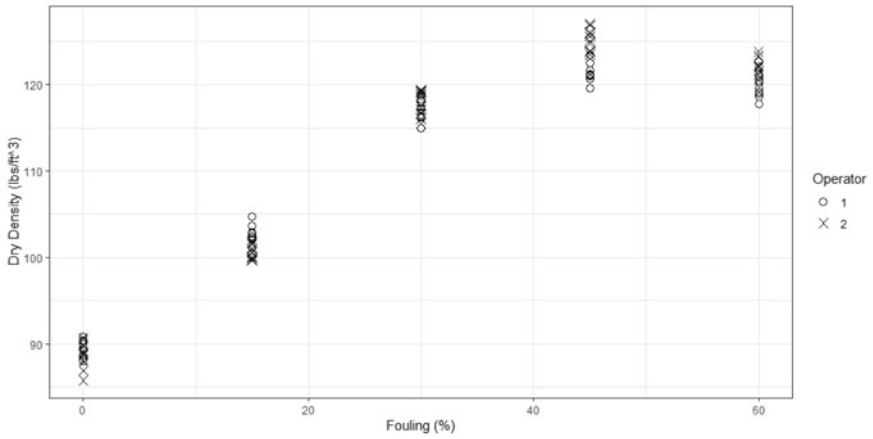
Fig. 3 Data from minimum density tests. Operator 1 shown in 'X' and Operator 2 in 'O', ten tests conducted by each operator

values, like those at 0 and 30% fouling show nearly indistinguishable values, others are distinct.

The data from the two operators was taken, and using a paired two-tailed t-test, the sample means were compared. At the 5% significance level, the 0 and 30% fouling tests showed equivalent means for the two operators, but the other three fouling percentages failed to satisfy this test. This indicates that there is a statistically significant difference in results from the operator on the dry density value for certain mixtures.

Under the Section 'Precision and Bias', of ASTM standard D4254—16, it specifies that for any replicate test of three or more trials performed by the same operator using the same equipment and material in the same time period should differ by no more than the single-operator d2s limit defined as $sd * 1.96\sqrt{2}$. For replica tests performed by multiple operators, the values should differ by no more than the multiple operator d2s limit, defined similarly but using the multiple operator standard deviation. Corresponding values for the minimum tests are shown in Table 1.

A similar limit is set for single tests performed by multiple laboratories. While the ASTM uses 12 different laboratory tests to determine the standard deviation of the single-laboratory tests, the two operators collected in this project are not enough to make an accurate prediction of the acceptable range for single tests. But, a comparison of the mean over 20 tests and the first dry density test by each operator shows an average error over the five fouling levels of 2.14% with the range from 0.03 to 3.00%. Within each fouling dataset, there are no trends, such as later tests approaching the sample mean, to suggest that the operator is getting better with each iteration.

4.2 Maximum Density Analysis

Similar to the minimum density tests, the maximum density standard also specifies that for any replicate test of three or more trials performed by the same operator using the same equipment and material in the same time period should differ by no more than the single-operator d2s limit defined as $sd * 1.96\sqrt{2}$.

The empirical maximum data, shown in Fig. 4, at the 5% significance level shows the same mean for both Operator 1 and Operator 2 data at all fouling levels. Unlike the minimum data, the values at each fouling increment show similar accuracy and only slight variations in precision.

Data in Table 2 shows the summary of the acceptable ranges for the maximum ballast tests. Single tests, using the first run from each operator, show an average margin of error of 1.9%, ranging from 0.55 to 5.09% maximum fluctuation from the sample mean on the first test. Once again, within each fouling dataset there are no trends such as tests 8, 9, 10 approaching the sample mean to suggest that the operator is getting better with each iteration.

Table 1 Summary of results from minimum density tests

	Average value (lbf/ft³)	Standard deviation (lbf/ft³)	Acceptable range of two results (lbf/ft³)	Average value (lbf/ft³)	Standard deviation (lbf/ft³)	Acceptable range of two results (lbf/ft³)
Single-operator results						
	Operator 1			Operator 2		
0	89.647	0.812	2.249	88.460	1.342	3.720
15	102.632	1.423	3.945	100.659	0.737	2.042
30	117.365	1.192	3.305	117.864	1.386	3.842
45	121.672	1.174	3.253	125.230	1.186	3.288
60	119.8617	1.242	3.444	122.296	0.924	2.561
Multiple-operator results						
0	89.085	1.248	3.461	–	–	–
15	101.633	1.505	4.170	–	–	–
30	117.614	1.317	3.651	–	–	–
45	123.483	2.148	5.953	–	–	–
60	121.110	1.623	4.499	–	–	–
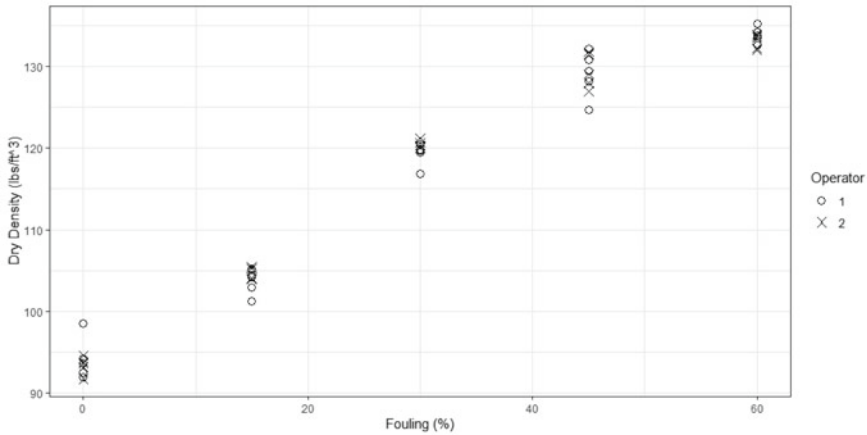
Fig. 4 Data from maximum density tests. Operator 1 shown '*X*' and Operator 2 in '*O*', five tests conducted by each operator

5 Discussion

In order to conclude on the effectiveness of the ASTM minimum and maximum standards with respect to density testing, the influence of fouling, density, and operator on the variability of the data needs to be discussed.

For the minimum tests, 100 data points were collected, the most to date on such a material, at 0, 15, 30, 45, and 60% fouling by mass. Among the data collected by the two operators, only two sets, at 0 and 30, were found to be statistically similar. This shows variation between the two operators, and those tests performed by the different laboratories may not necessarily be concluded to have the same mean. In the summary of triplicate tests from the minimum density ASTM record, both single-operator and multi-laboratory results on SP soil types showed the same average value to 4 significant figures.

When examining the range of the minimum density data for a single operator, the 'Acceptable Range of Two Results' from the ASTM standard was set at 1.4 lbf/ft^2 for an average density value of 98.17 lbf/ft^2. Across all fouling percentages for single operators, the ballast data shows a range of nearly twice that. See Table 1. However, the acceptable range for the multi-laboratory results from the ballast is well under that listed in the ASTM standard for the same test (6.9 lbf/ft^2). Therefore, we see that there is a change in accuracy and a general increase in precision when the standard is applied to larger grains.

Within the minimum density tests, the amount of fouling and the mean dry density have no visible effect on the accuracy of the data. The maximum density data shows very little trend as well but does show clear peak variability (high standard deviation) with the peak average density value at 45% fouling.

Table 2 Summary of results from maximum density tests

	Operator 1			Operator 2		
	Average value (lbf/ft^3)	Standard deviation (lbf/ft^3)	Acceptable range of two results (lbf/ft^3)	Average value (lbf/ft^3)	Standard deviation (lbf/ft^3)	Acceptable range of two results (lbf/ft^3)
Single-operator results						
0	93.426	0.942	2.611	94.202	2.333	6.467
15	104.58	0.705	1.957	103.637	1.376	3.813
30	120.42	0.458	1.269	119.27	1.242	3.442
45	129.42	1.912	5.300	129.04	2.578	7.147
60	133.09	0.791	2.193	133.84	0.836	2.317
Multiple-operator results						
0	93.814	1.821	5.048	–	–	–
15	104.11	1.190	3.299	–	–	–
30	119.84	1.098	3.044	–	–	–
45	129.23	2.278	6.313	–	–	–
60	133.47	0.896	2.482	–	–	–

For the maximum density data, only 50 data points were collected, so no firm conclusions can be drawn due to the smaller sample size. However, using the same methodology as for the minimum tests, it is shown that the acceptable range of two results is larger for ballast material for both single- and multi-laboratory tests. In the case of Operator 2 results, the range for 0 and 45% fouling is four times that found for SP soils in the ASTM standard. Unlike the ASTM standard, which suggests greater variability in minimum tests when compared to maximum tests, the data for ballast shows a greater variability in maximum than minimum tests.

The data from the maximum density two operators is statistically similar for all fouling points. Therefore, any maximum density tests run by different laboratories are likely to achieve the same mean.

6   Conclusion

Tests to attempt to characterize this behavior, minimum and maximum density tests were run using Connecticut Granite with granite stone dust used as a fouling material and compared to ASTM standards D4254 and D4253 completed for SP soil types. A total of 100 data points from minimum density tests concluded that multi-laboratory results will find an average value within 2% of each other and have a higher precision between operators than the SP types. Single tests by each operator show an average error range from the five fouling levels of 2.14% from the population mean with the range from 0.03 to 3.00%. For maximum density testing, sample size was not large enough to conclude, but trends show that ballast data is both less accurate and less precise then on SP soil types. Average values for each fouling level were within 2% of the mean value for each operator, even though the corresponding acceptable range is significantly larger than the one in the ASTM standard. Single tests show an average margin of error of 1.9%, ranging from 5.09 to 0.55% maximum fluctuation from the sample mean on the first test.

Although the results showed a greater variability than those deemed acceptable by the ASTM standard, it is worth considering if the variability from the minimum and maximum density test would be suitable for ballast applications. In future, it would be worthwhile to consider what level of accuracy would be required for testing on ballast. If the current ASTM methodology is not capable of achieving those results, an improved methodology should be developed for large diameter particles.

In future, more maximum density tests will help solidify the tentative conclusion about the variability of the tests. Additionally, using more operators would provide more insight into the variability of the samples. The ASTM standard uses 12 different operators in their single-test analysis and 8 in their triplicate-test analysis. Completing the range of fouling percentages from 0 to 100 would help illustrate the comparison of the density tests for coarser grains (lower fouling) to finer grains (higher fouling).

Additionally, data on the elastic modulus of the AREMA #4 mixtures was taken at the same time as the described data. For further description, see "Measuring Railroad

Ballast Modulus of Elasticity Using Light Weight Deflectometer" by E. Akey et al. (Paper ID #266).

References

1. Rohrman A (2019) Laboratory Study of the Geotechnical Properties of Abraded Railway Ballast with Natural and Clay Mix Fouling. Doctoral Dissertation
2. D 4254—16 Standard Test Methods for Minimum Index Density and Unit Weight of Soils and Calculation of Relative Density, ASTM. Published September 2016
3. D4253-00 Standard Test Methods for maximum Index Density and Unit Weight of Soils Using a Vibratory Table, ASTM. Reapproved, Published 2006
4. Lo Presti DCF, Pedroni S, Crippa V (1992) Maximum dry density of cohesionless soils by pluvation and by ASTM D 4253–83: a comparative study. Geotech Test J GTJODL 15(2):180–189
5. Lade PV, Liggio CD Jr, Yamamuro JA (1998) Effects of non-plastic fines on minimum and maximum void ratios of sand. Geotech Test J GTJODJ 21(4):336–347

Measuring Railroad Ballast Modulus of Elasticity Using Light Weight Deflectometer

Emily Katherine Akey, Mariel W. Jones, Carlton L. Ho, and Aaron J. Rubin

Abstract Light weight deflectometers (LWDs) are used to rapidly determine the modulus of elasticity and spring constant of granular materials and pavements. The LWD can be operated by one person making it incredibly efficient to collect this important data. It is primarily used in the field to determine the properties of soils or paving materials, but also has the potential to be used on railroad ballast. However, to date, there have been minimal studies using LWDs on railroad ballast. The goal of this current study was to investigate the repeatability of LWD testing on prepared cylindrical ballast specimens. To use the LWD on ballast, we conducted minimum and maximum density tests in accordance with ASTM D4254 on 12-inch interior diameter by 12-inch interior height cylinder specimens at different percentages of fouling ranging from 0 to 60% by mass. Then, the LWD measurements were taken on the top of the specimen using a 12-inch-diameter plate. In total, 100 measurements were made on minimum density mixtures and 50 maximum density mixtures. The effect of density and fouling on test repeatability and procedural best practices for LWD testing on cylindrical ballast specimens are discussed.

Keywords Railroad · Ballast · Light weight deflectometer · Geotechnical properties

1 Introduction

Railroad ballast is an essential component of many railway structures. Ballast is uniformly graded crushed stone that rests under railway ties to facilitate water drainage and support the load of trains [1]. Over time, this ballast breaks down

E. K. Akey (✉) · M. W. Jones · A. J. Rubin
Smith College, Picker Engineering, Northampton, MA, USA
e-mail: ekatherineakey@gmail.com

C. L. Ho
Civil and Environmental Engineering Department, University of Massachusetts Amherst, Amherst, MA, USA
e-mail: ho@umass.edu

into small fragments called fouling which fills in the void space between ballast aggregate. When all of the void space of the ballast is filled with fouled materials, this interferes with the function of the ballast, contributing to problems such as train derailment [1].

Inspecting ballast beds is primarily done visually without machinery or instrumentation, which allows ballast to become highly fouled before it can be seen. The material properties of fouled ballast are important for engineering evaluation of the structure–ballast–soil system. However, measuring the engineering properties of ballast is often time consuming and may require the rail service to be temporarily halted to collect in situ measurements. The LWD is a fast and convenient non-penetrating method to collect structural properties of geotechnical materials, but its effectiveness on larger particles such as ballast is not well documented in the literature. This study focuses on the effectiveness of LWD measurements to collect modulus of elasticity data on different percentages of dry fouled ballast. The data collected was analyzed to determine the repeatability of using an LWD on fouled ballast at both maximum and minimum dry densities.

This study was conducted at Smith College with funding from the Summer Undergraduate Research Fellowship (SURF) program.

2 Background

Estimating the elastic modulus of railroad ballast can be challenging both in the field or laboratory. Traditionally, in the laboratory, the primary method for calculating the modulus of elasticity for ballast is performing a triaxial test, which can take several days to complete and requires large molds and high capacity systems to accommodate the ballast. In this study, the possibility of using an LWD to collect modulus of elasticity data was considered. In contrast to triaxial testing, the LWD is quick and portable, allowing the same data to be collected in minutes rather than days. However, the effectiveness of the LWD on larger particles such as railroad ballast has not been well documented in the literature.

The main components of an LWD include a falling mass, load cell, and deflection plate [2]. The LWD was first invented in 1980s in Germany by the Federal Highway Research Institute and HMP as an in situ test to determine soil elasticity [3]. The typical loading plate diameter is eight inches. However, most LWD devices have detachable plates to allow other plate sizes, such as the twelve inches plate used in this study.

The entire LWD is, by name, lightweight and able to be used by one or two people, allowing for wide uses in the geotechnical/transportation engineering fields. The LWD is primarily used to test pavements and soils in the field. One of the reasons the LWD has not been used for rougher materials in previous studies is because the plate must be level and in full contact with the sample [4]. LWD measurements are typically conducted on compacted specimens because the LWD creates an impact on the sample during testing. If the impact causes additional settlement during testing,

the sample's properties have changed and thus the test may be inaccurate. The manufacturer suggests that for each LWD test, the mass is released without recording data as a settling drop to seat the plate onto the surface of the sample.

3 Methods

The procedure for using an LWD begins with raising the mass to a preset height and clicking it into place. Once the deflection plate of the LWD is resting flat against the sample, the mass is released and allowed to free-fall guided by a central rod onto the load cell attached to the deflection plate. Once the mass has rebounded, it must be caught and relocked into the handle at the top. The deflection of the plate is measured and can be used in conjunction with the force from the falling mass to estimate the spring constant (the spring constant is provided as an output by the proprietary LWD software). The modulus of elasticity within the cylinder can then be calculated from the spring constant of the sample as shown in Eq. 1 [5]:

$$E = \left(1 - \frac{2v^2}{1-v}\right)\frac{4H}{\pi D^2}k \tag{1}$$

where v = Poisson's ratio (assumed $v = 0.3$ in this study), H = height of the mold, D = the diameter of the plate or mold, and k = spring constant as calculated by the LWD device [5].

To understand the repeatability of using an LWD on different percentages of fouled ballast, we used a 12-inch interior diameter by 12-inch interior height cylinder with dry ballast specimens prepared to different percentages of fouling ranging from 0 to 60% by mass. The tests were conducted at approximately 0% water content. We conducted these tests at both minimum dry density and at maximum dry density. For each minimum density fouling percentage, we performed 20 trials, and for each maximum density fouling percentage, we performed ten trials. Both the minimum and maximum trials were split between two operators. We did not notice a significant difference between samples made by different operators. Each trial consisted of loading the cylinder with the correct mix of fouling and ballast and operating the LWD with a 12-inch plate to find modulus of elasticity. These data will be used to determine the best practices for using a LWD on ballast.

To create each sample, we air-dried the ballast and fouling to near 0% water content (confirmed with oven measurements). We then mixed together fouling and ballast to either 0%, 15%, 30%, 45%, or 60% fouling. The material used was Connecticut Granite ballast prepared to AREMA #4 gradation specifications and the same Connecticut Granite stone dust for fouling. Minimum and maximum density samples were prepared in accordance with ASTM D4254 and ASTM D4253 [6] (Figs. 1, 2 and 3).

Typically, while using an LWD, it is suggested by the manufacturer to place the instrument on the sample and do a few "seating drops" as to establish good contact

Fig. 1 Minimum density samples are prepared by removing a soil filled tube, thus releasing the sample into the mold at an approximate minimum density

Fig. 2 Minimum density 60% fouling and 40% railroad ballast cylinder samples. On the left is the sample after being placed into the cylinder mold, and the right is after the excess is removed to the approximate correct volume

between the plate and the test material. However, with the minimum density trials, this was not possible as we did not want to change the density of the sample with the pressure from the LWD drop. During testing, it was observed that the drop weight did result in compaction of the specimen. This compaction was quantified for future analysis.

Fig. 3 Minimum density 60% fouling and 40% railroad ballast cylinder sample with LWD placed on top

4   Results

It is generally understood that the modulus of elasticity of ballast changes according to fouling percentage and water saturation percentage. This study was interested in the functionality of the LWD at different fouling percentages that might occur. Figures 4 and 5 display the modulus of elasticity measurements for the different fouling mixes at approximately maximum and minimum density. These plots show that there is no significant difference between the operators of different trials.

Table 1 shows the summary of average elastic modulus data taken from both relative minimum and maximum densities. As this study is one of the first to look at minimum and maximum densities of ballast, it is not certain whether the densities used are exactly minimums or maximums. However, the samples are prepared in accordance with the ASTM standards for minimum and maximum density soil samples. In addition, the corresponding standard deviation is also calculated. This table also shows that, as expected, the maximum modulus values are higher than the minimum modulus values. For the most part, the modulus of elasticity decreases as fouling percent increases for the minimum density trials. This trend is not clear for the maximum density trials. It was observed that the standard deviation values
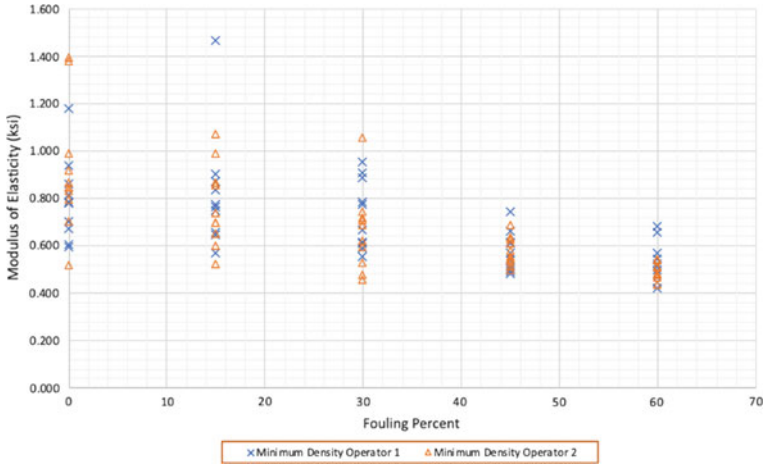
Fig. 4 Modulus of elasticity of ballast samples at different fouling percentages for all minimum density trials conducted contrasting operators
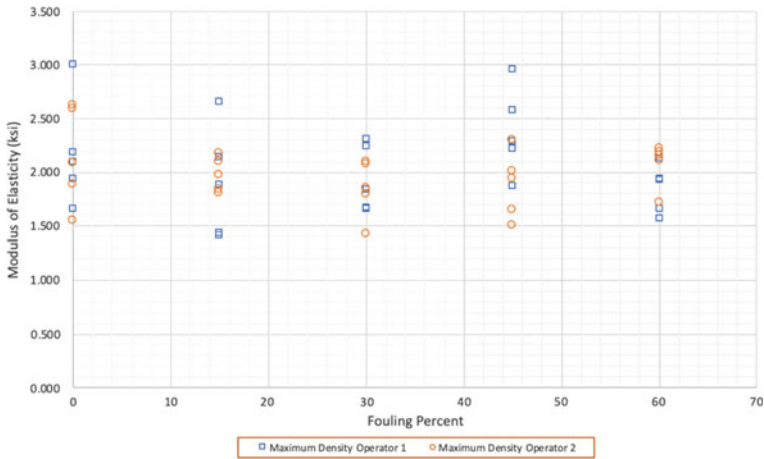
Fig. 5 Modulus of elasticity of ballast samples at different fouling percentages for all maximum density trials conducted contrasting operators

decrease as the fouling percent increases. This is expected because when the fouling percentage increases, the contact between the ballast/fouling mixture and the LWD plate also increases and therefore decreases the variability of contact pressure on the plate caused by different formations the particles (ballast and fouling) can form.

Table 1 Summary of average values for minimum and maximum densities for all trials performed on each fouling percentage along with standard deviation and acceptable range between two results

Fouling percent	Average E value (ksi)	Standard deviation (ksi)
Minimum density, all trials (20)		
0	0.857	0.234
15	0.796	0.211
30	0.696	0.160
45	0.575	0.072
60	0.515	0.065
Maximum density, all trials (10)		
0	2.161	0.457
15	1.942	0.363
30	1.895	0.280
45	2.131	0.433
60	1.960	0.237

5 Discussion

To determine the repeatability of using an LWD on railroad ballast, LWD tests were performed on different mixes of ballast and fouling at both minimum and maximum dry densities. The minimum density data shows a clear trend of decreasing modulus with increasing fouling. The maximum density data does not appear to show a clear trend.

For example, to see if the average modulus values from five trials would be significantly similar to the average modulus value for all 20 trials.

Above in Fig. 6, the minimum density trials have been split into five tiers: highest, middle highest, middle lowest, and lowest. These correspond to the values within each fouling range. Figure 6 illustrates that the spread of the minimum density data becomes smaller as we increase fouling. If the highest and lowest five values were removed, the data would be more consistent and less variable. While there is still a small range of data for the middle values, the overall trend of modulus still decreases as fouling increases. We can also see that the highest five values have a much larger spread. It was observed that in this dataset, that when large deviations from the mean occurred, the deviations tended to be overestimations.

Figure 7 is similar to Fig. 6, except with maximum density trials. The five highest, five from the middle of the data, and the five lowest average values are shown on this plot. The maximum data is trickier to understand. The modulus data is relatively consistent and does not have a clear negative or positive trend as fouling increases. Based on the data collected, assuming dry conditions, it does not appear that the modulus of elasticity is sensitive to the percentage of fouling present (up to 60% fouled).

In the results outlined above, it is clear that our data is fairly repeatable, but errors of ±25% are typical. Although this potential error is relatively large, it can
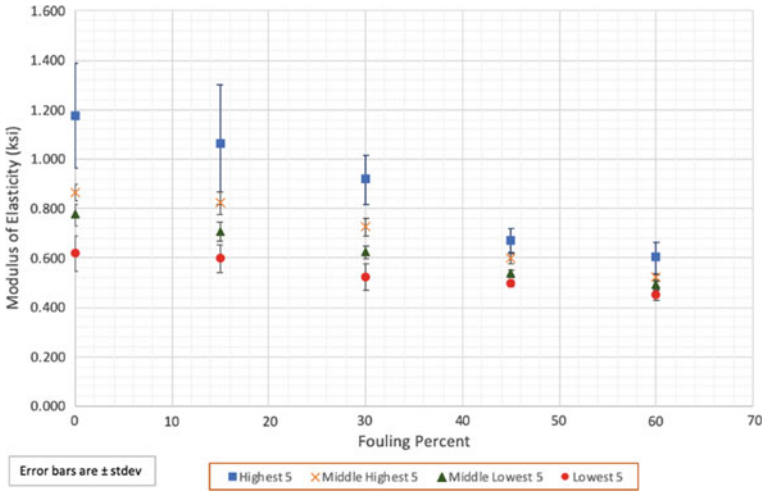
Fig. 6 Modulus of elasticity for minimum density trials separated by averages from five highest, five highest middle, five lowest middle, and five lowest values split by fouling percentage
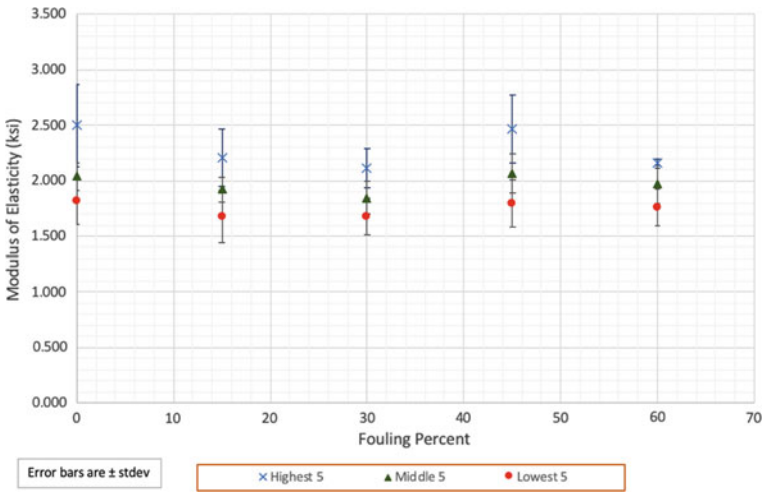
Fig. 7 Modulus of elasticity for maximum density trials separated by averages from five highest, five middle, and five lowest values split by fouling percentage

be observed that this is due to outlier data points that, individually, deviate from the mean much more than the majority of test values for a particular fouling percent. In the present study, 10–20 tests appear to produce a relatively reliable mean, but it is difficult with the current sample size to estimate how few trials could have been conducted while still maintaining a statistically significant mean. In future studies,

this should be further investigated so that the process of estimating elastic modulus from LWD measurements can be streamlined.

In the minimum density trials, standard deviation decreases as fouling percent increases, leading us to believe that LWD data becomes more repeatable as fouling increases. The maximum data seems to be consistent as fouling increases, and the repeatability does not change as fouling increases.

Overall, using an LWD on railroad ballast to estimate modulus of elasticity appears to be feasible, but to fully quantify repeatability, more test data on dry samples as well as test data on saturated samples will need to be collected.

6 Conclusions

In this paper, LWD testing on railroad ballast mixed with fouling was discussed. An array of testing samples at both minimum and maximum densities and at various fouling percentages was completed in order to get an idea about how the LWD device would react with the material and to estimate whether it is feasible to use in further testing. One of the benefits of the LWD is that it can be used in the field and also on molded samples.

It is important to be mindful of the differences in support between a molded ballast sample and ballast found in real conditions under railway tracks. The laboratory conditions used in this study confined the ballast from lateral movement and also vertically confined the sample from the bottom. These constrictions differ from the conditions found in reality, where ballast has minimal confinement, and the support from the bottom is less stiff than in the cast iron cylinder. Due to the containment differences between the laboratory conditions used in this study and in situ railroad ballast, it is anticipated that there likely are systemic differences in measured moduli between the LWD, other laboratory measured moduli such as triaxial testing, and field conditions. These differences should be researched and characterized further.

The next steps for future research on using LWD devices with railroad ballast and fouling are on saturated samples. Adding water changes strength characteristics and is an important aspect in rail bed maintenance. Knowing the effects of water on railroad ballast strength would be incredibly useful, as precipitation and bad weather are the main causes of derailment. A start to that problem is characterizing the material properties of the ballast.

References

1. Huang H, Tutumluer E, Dombrow W (2009) Laboratory characterization of fouled railroad ballast behavior. Transp Res Rec. https://doi.org/10.3141/2117-12
2. ASTM E2835—11 (2011) http://insitutest.com.au/wp-content/uploads/ASTM_E2835-11.pdf. Last accessed 2019/9/26

3. Elhakim AF, Elbaz K, Amer MI (2014) The use of light weight deflectometer for in situ evaluation of sand degree of compaction. HBRC J 10:298–307
4. Siekmeier J et al (2009) Using the dynamic cone penetrometer and light weight deflectometer for construction quality assurance
5. Schwartz C, Afsharikia Z, Khosravifar S (2017) Standardizing lightweight deflectometer modulus measurements for compaction quality assurance. 147 https://www.roads.maryland.gov/OPR_Research/MD-17-TPF-5-285-LWD_REPORT.pdf
6. D18 Committee. Test methods for minimum index density and unit weight of soils and calculation of relative density. http://www.astm.org/cgi-bin/resolver.cgi?D4254-16 https://doi.org/10.1520/D4254-16

The Effect of Elastic Pads and Mats on the Stress–Strain State of Railway Subgrade

Andrei Petriaev [ID]**, Anastasia Konon** [ID]**, and Vladimir Egorov**

Abstract High substructure stiffness leads to an increase in rail pressure on the sleeper. As a result, the track settlement is accelerated, and the dynamic component of the wheel load increases as well. Reducing the vibrational dynamic effect on the subgrade and ballast is the most effective reserve for improving railway track reliability. Field studies were conducted to evaluate the effect of using elastic geosynthetic materials on top of the subgrade on the strain state. These materials help reduce and level stiffness of subballast and subgrade. To assess the values of the track elastic deformations, Getzner Werkstoffe mats, Colbond Enkadrain pads and porous rubber pads were placed on top of the subgrade. The influence of axle loads on the elastic deformations of rail has been investigated, and a comparison with typical control track sections has been made. The effects of using the elastic geosynthetic materials on rail elastic strains were obtained under varied axial and linearly increasing loads.

Keywords Stiffness · Settlement · Under sleeper pads

1 Introduction

In terms of high-speed operation and regarding the trend to the increase in maintenance periods, additional measures are needed for railway track stability. This task is solved by increasing the stiffness of under-rail bed and reducing the detrimental impact of a rolling stock on the environment.

When reconstructing railway lines for the high-speed operation, techniques for ballast strengthening are widely used [1]. They are, for example: geogrid reinforcement and stabilization [2–7], elastomer polyurethane ballast coatings [8, 9], random fibre reinforcement of ballast [10], bitumen injection into ballast to improve stiffness

A. Petriaev · A. Konon (✉) · V. Egorov
Emperor Alexander I St. Petersburg State Transport University, Moskovsky pr., 9, St. Petersburg 190031, Russian Federation

V. Egorov
e-mail: vegorov@pgups.ru

[11] and rubber crumbs adding into ballast to reduce particle wear [12]. The use of under-sleeper pads [13] and asphaltic layer [14] can also improve railway track performance. These techniques make it possible to ensure the operational reliability of the subgrade active zone. On the other hand, a stiff track base leads to high-level stresses and increases vibration and noise.

One of the most effective reserves for track reliability improving is the reduction of vibrational dynamic effects on the substructure [15, 16]. In such cases, the optimal solution is to place a resilient (elastic) layer under the ballast to reduce vibrations and noise from rolling stock and allows changing the stiffness of the under-rail bed. The high stiffness of the base leads to an increase in rail stress on the sleeper, to an accelerated track settlement, the appearance of unequal elasticity (i.e. transition zones close to bridges and culverts [17]) and an increase in the dynamic component of the wheel load.

An effective solution to both reduces the vibrational dynamic effect on the sleepers and substructure and significantly decreases the level of noise, and vibration from passing trains is to lay an elastic layer in the form of pads in subballast. The elastic layer is a geosynthetic material that reduces and levels stiffness of subballast and subgrade.

World's operating experience and the results of experimental application on domestic railways show that the installation of an elastic material in the ballast can reduce the level of vibration by 50% and reduce sound pressure by 10 dB. To reduce the level of noise and vibration, the elastic subballast pads can be used in the following cases:

- on reinforced concrete bridges and trestles with the ballasted track;
- on railway tracks in the city area operated with freight trains at a speed of at least 80 kmph and passenger trains at a speed of at least 140 kmph;
- in tunnels to reduce the level of secondary noise and reduce the vibrational dynamic effects on the structural elements of the tunnel lining;
- on track sections, situated close to residential and administrative buildings or industrial facilities, which are sensitive to vibrational dynamic effects.

Ensuring optimal vibration and noise isolation is achieved due to the elastic interlayer between the superstructure and the subbase, made by laying elastic pads/mats under the ballast.

2   Materials and Methods

To assess the influence of geosynthetics on the strain state of the subgrade, it is necessary to measure the magnitude of the resulting elastic deformations during the passage of a moving load. To assess the values of the track elastic deformations, field tests were carried out with laying Getzner Werkstoffe mats, Colbond Enkadrain pads and porous rubber pads on top of the subgrade. Three test sections and a control

Fig. 1 Test site cross section
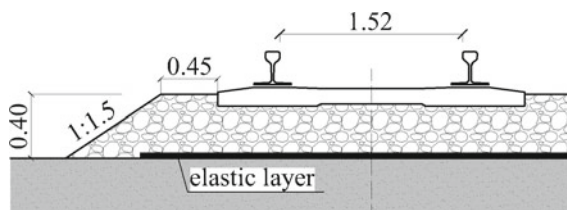
section were made, each 20 m long. Test sections were situated consequently without any spacing. Cross section of the site is shown in Fig. 1.

Rail elastic deformation was measured with deflectometer. Materials' properties are given in Table 1.

The experimental sections have superstructure with reinforced concrete sleepers and continuously welded rails laid on a stabilized subgrade. The sections are located on a straight line. It is a continuous welded track with 65 kg/m rails, and the gauge is from 1519 to 1522 mm. The subgrade is constructed from medium sand.

Locomotives were chosen as test moving units in our studies. Locomotives types and properties are given in Table 2.

The results obtained during the test on each section are compared among each other and with the data of the control section.

Table 1 Test materials' properties

Material type	Size, mm	Thickness, mm	Material	Static stiffness, N/m m^3	Other properties
Sylomer D 619 mats by Getzner (**geosynthetic A**)	4000 × 1500	25	Composite: polyurethane and geogrid	0.03	$C_{stat} =$ 0.06 N/mm^3
Enkadrain pads by Colbond (geosynthetic B)	Roll cut to 4000 × 1500	2 × 12	Composite: core—PA, geotextile—PP	–	Ultimate tensile strength (lengthwise and broadwise) 5 kN/m
Geosynthetics test production (**geosynthetic C**)	1200 × 500	25	Rubber	0.06	

Table 2 Test locomotive operation characteristics

Locomotive type	Axle load, kN	Speed range at test, kmph	Function
CHS-6	201	70–140	Passenger
CHS-2T	205.9	70–140	Passenger
VL10	225.6	40–70	Freight

3 Results and Discussion

The data presented in Fig. 2 indicate a different effect of the moving load on the deformability of subgrade.

The elastic settlement from the impact of the CHS-2T locomotive is 80–85% relative to the VL-10 locomotive and the CHS-6 locomotive is 75–82%, respectively. The elastic settlement during the passage of the CHS-2T locomotive and the CHS-6 locomotive, in the section with the geosynthetic A subballast pads, is 83–88% and 79–85%, respectively. As a rule, the ratio of elastic settlement increases slightly with the increasing speed of the rolling stock. In our opinion, this fact occurs due to the redistribution of the load along the sleepers when subgrade stiffness changes.

Subballast pads can significantly reduce the subgrade stiffness and thereby decrease the actual stresses on the subgrade top due to the stress redistribution to more sleepers. The results of this test are shown in Fig. 3.

Data analysis indicates a change of rail elastic deflection in the under-rail section depending on types of subballast pads laid on the subgrade top. The greatest elastic settlement is recorded for geosynthetic A pads, the smallest one is for 2 layers of geosynthetic B pads, and the intermediate position is for porous rubber pads. The increase in the rail elastic settlement compared with the control section is 1.92, 1.12 and 1.72 times, respectively.

Figure 4 shows the approximation results of elastic settlement in the under-rail section versus train speed for the passage of passenger locomotive CHS-2T.

Graph analysis indicates the direct proportion of elastic settlement on the speed of trains. The presented dependences differ in settlement absolute values and different growth rates with train speed increasing. The growth rate of rail elastic settlement is 0.071 mm/10 kmph in terms of an increase in the train's speed in the control section.

● VL10 at test section
● VL10 at the section with geosynthetics A
● CHS-2T at control section
● CHS-2T at section with geosynthetics A
● CHS-6 at control section
● CHS-6 at section with geosynthetics A
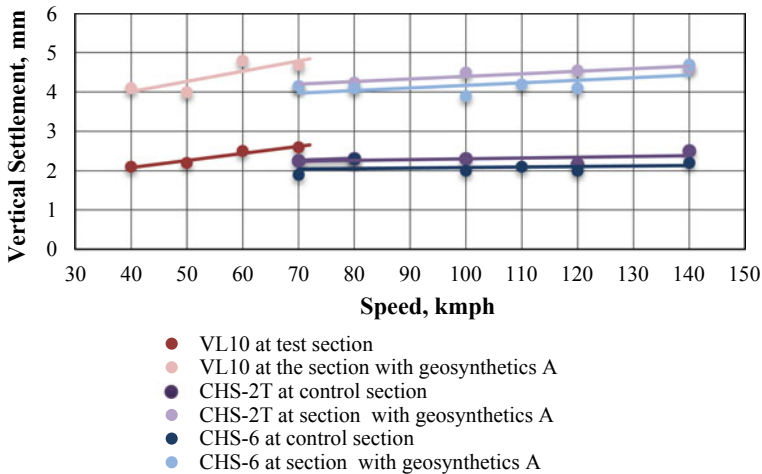
Fig. 2 Vertical rail deflection dependence on locomotive speed
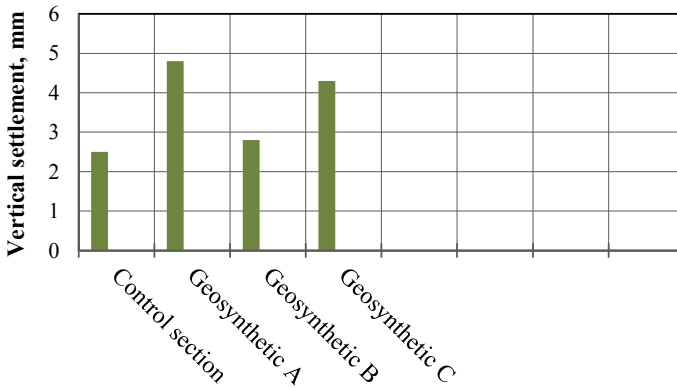
Fig. 3 Vertical rail deflection in the under-rail section during the passage of the VL10 locomotive at a speed of 60 kmph
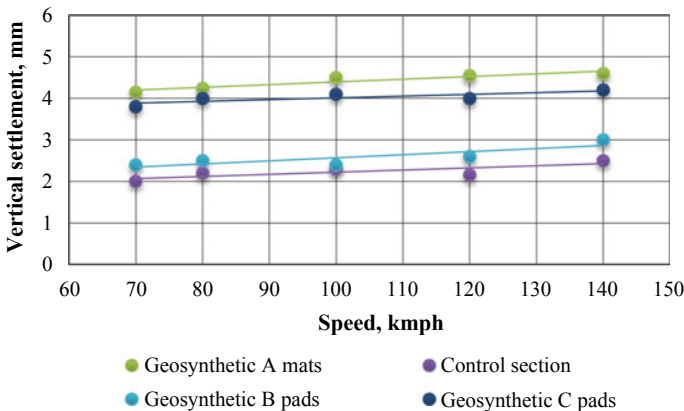
Fig. 4 Dependence of the rail vertical settlement on CHS-2T passenger locomotive speed

Placement of 2 layers of geosynthetic B pads at a depth of 0.4 m under the sleeper does not lead to a significant change in elastic strain growth.

Use of geosynthetic A subballast pads at the subgrade top gives an elastic settlement increase of 0.064 mm for every 10 kmph, which is 11% less compared to the control section of the track. The lowest strain growth rate in the under-rail section in terms of train speed increasing is observed in the section with the geosynthetic C subballast pad. In this case, the rate of elastic strain growth is 0.057 mm/10 kmph, which is 25% less compared to the control section of the track.

The use of two-layered geosynthetic B pads does not affect the sensitivity of the subgrade top area. It does not give positive results in the change in elastic deformations with speed increasing, while the use of a geosynthetic C subballast pad reduces

the elastic strain growth by 25% compared to the control section. The use of geosynthetic A subballast pad in the track structure reduces the intensity of elastic strain by 11%.

From the performed studies, it can be concluded that the use of subballast pads in the subgrade top reduces the effect of train speed on the growth of track elastic settlement. The obtained dependence of the rail elastic settlement under the axial and linear loads is shown in Figs. 5 and 6. In the studied range of acting loads, both dependencies are described by the linear Eq. (1).

$$\delta = \delta_i + K * (P_i - P_l) \tag{1}$$

where δ_i are initial elastic deformations arising in the cross section of the embankment during the passage of rolling stock with a load of P_i, mm;
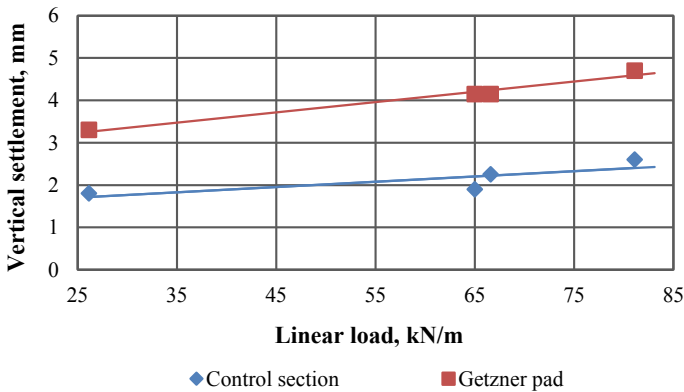
Fig. 5 Dependence of vertical rail deflection on a linear load at 70 kmph
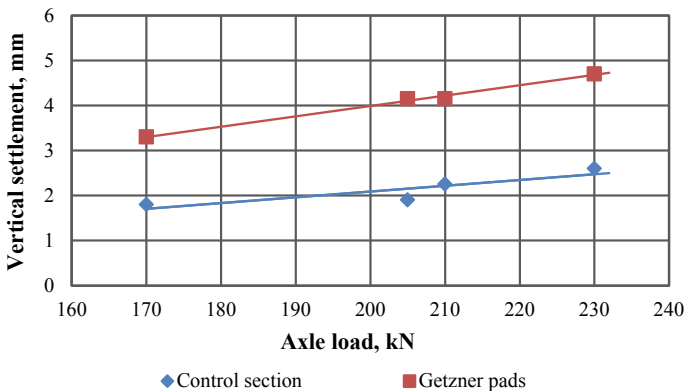
Fig. 6 Dependence of the rail vertical strain from the axle load at 70 kmph

K is the coefficient of elastic strain increase with load rise, mm/kN;

P_i is the linear or axial load at which the value of elastic deformations, kN, is determined; and

P_l is the initial value of the load interval at which the dependence $\delta = f(P)$, kN, is determined.

For this dependence, the coefficient K is indicative. Its value varies significantly depending on the type of under ballast pad. Laying the geosynthetic A ballast mat at the subgrade top gives an increase in elastic strain from the linear load of 0.14 mm for every 10 kN. In the control section, the same value reaches 0.25 mm per every 10 kN increase in linear load. Thus, the laying of a ballast mat leads to a 78% increase in the influence of linear load on the elastic deflection of the rail compared to the control section of the track. A similar dependence is observed for axle load (see Fig. 6).

For the geosynthetic A subballast mat, the rate of elastic strain growth from the axial load is 0.23 mm for every 10 kN, while in the control section the same value reaches 0.13 mm for every 10 kN. The presented data show that the laying of a subballast mat leads to a 77% increase in the effect of the increase in axial load on the elastic strain of the rail compared to the same value in the control section.

4 Conclusions

The conducted field studies allowed to evaluate the effect of the elastic geosynthetic materials placed on top of the subgrade on the measured strain state. The influence of axle loads on the rail elastic deformations has been investigated, and a comparison between sections with and without the elastic geosynthetic materials was performed. The effects on the rail elastic strains were evaluated and obtained under axial loads that were varied linearly.

References

1. Zhai W, He Z, Song X (2010) Prediction of high-speed train induced ground vibration based on train-track-ground system model. Earthq Eng Eng Vib 9(4):545–554
2. Petriaev A (2017) Stress response analyses of ballasted rail tracks, reinforced by geosynthetics. Procedia Eng 189:660–665
3. Rakowski Z (2017) An attempt of the synthesis of recent knowledge about mechanisms involved in stabilization function of geogrids in infrastructure constructions. Procedia Eng 189:166–173
4. Grygierek M, Kawalec J (2017) Selected laboratory research on geogrid impact on stabilization of unbound aggregate layer. Procedia Eng 189:484–491
5. Petriaev A, Konon A (2019) Tests of geosynthetics-reinforced ballast stressed state under heavy trains. MATEC Web Conf 265:01004
6. Aursudkij B, McDowell GR, Collop AC (2009) Cyclic loading of railway ballast under triaxial conditions and in a railway test facility. Granular Matter 11(6):391–401
7. Buyn Y-H, Tutumluer E (2019) Local stiffness characteristic of geogrid-stabilized aggregate in relation to accumulated permanent deformation behavior. Geotext Geomembr 47(3):402–407

8. Indraratna B, Hussaini SKK, Vinod JS (2013) The lateral displacement response of geogrid-reinforced ballast under cyclic loading. Geotext Geomembr 39:20–29

9. Woodward PK, Kennedy J, Laghrouche O, Connolly DP, Medero G (2014) Study of railway track stiffness modification by polyurethane reinforcement of the ballast. Transp Geotech 1(4):214–224

10. Ajayi O, Le Pen L, Zervos A, Powrie W (2017) Scaling relationships for strip fibre—reinforced aggregates. Canadian Geotech J 54(5):710–719

11. D'Angelo G, Thom NH, Lo Presti D (2016) Bitumen stabilized ballast: a potential solution for railway track-bed. Constr Build Mater 124:118–126

12. Sol-Sánchez M, Moreno-Navarro F, Rubio-Gámez M (2014) The use of deconstructed tires as elastic elements in railway tracks. Materials 7:5903–5919

13. Lakušic S, Ahac M, Haladin I (2010) Experimental investigation of railway track with under sleeper pad. In: Drmota E (ed) Proceedings of 10th Slovenian road and transportation congress. Slovenia, pp 386–393

14. Rose JG, Teixeira PF, Veit P (2011) International design practices, applications, and performances pf asphalt/bituminous railway trackbeds. In: Proceedings of GeoRail 2011, Paris, France

15. Ngo T, Idraratna B, Rujikiatkamjorn C (2019) Improved performance of ballasted tracks under impact loading by recycled rubber mats. Transp Geotech 20:01706514

16. Kolos A, Romanov A, Shekhtman E, Akkerman G, Konon A, Kiselev A (2020) Bearing capacity of high embankment clay soils in terms of heavy axle load operation. In: Petriaev A, Konon A (eds) Transportation soil engineering in cold regions, vol 1. Lecture notes in civil engineering 49. Springer, Singapore

17. Serebryakov D, Konon A, Zaitcev E (2017) The study of subgrade operating conditions at bridge abutment approach. Procedia Eng 189:893–897

Ballast Fouling Identification Through Statistical Pattern Recognition Techniques on Ballast Particle Movement

Saharnaz Nazari, Hai Huang, and Tong Qiu

Abstract Ballast fouling is one of the most common undesirable conditions in tracks that adversely impact ballast performance. Poor performing ballast can cause rough track geometry and accelerate the deterioration rate of other track components such as rail, tie, and fasteners. Real-time monitoring of ballast condition can assist in providing responsive maintenance planning and safe train operation. Several studies have been done till date with the aim of providing an automatic and continuous monitoring of ballast. SmartRock is a wireless sensor that has proven capable of serving as a continuous monitoring system for ballast condition. This sensor closely resembles the ballast particle, and while embedded in the ballast layer, it can provide information regarding ballast particle movement under the load of passing trains in real time. In this study, a field experiment was conducted on a clean and a mud spot section with the same traffic and weather conditions. Four SmartRocks were placed in each of these sections, and data recorded was analyzed using statistical pattern recognition technique. Linear discriminant analysis (LDA) is the algorithm deployed in this study to predict fouling of ballast through SmartRock data. The results of this study are encouraging toward the use of the SmartRock system together with LDA algorithm as a monitoring tool on the state of track ballast.

Keywords Ballast fouling · Railway · SmartRock · Statistical analysis · Pattern recognition

S. Nazari (✉) · T. Qiu
Department of Civil and Environmental Engineering, The Pennsylvania State University,
University Park, PA 16802, USA
e-mail: sun51@psu.edu

H. Huang
Department of Rail Transportation Engineering, The Pennsylvania State University, Altoona, PA
16601, USA

1 Introduction

The ballast plays a key role in track stability and maintaining track geometry. Ballast can get fouled over time mainly due to particle abrasion, breakage, and intrusion of subsoil into its top layer [1]. Fouling compromises ballast's performance in providing proper support for track superstructure and undermines track safety. Therefore, maintenance of ballast is of paramount importance to railroad operations. With traditional methods of ballast inspection being both labor intensive and time consuming, focus of recent studies has been on incorporation of cameras, sensors, and information technologies into a system that delivers continuous information regarding the state of ballast in a real-time manner. While some technologies such as light detection and ranging (LIDAR) and ground penetrating radar (GPR) are useful inspection tools as they allow mapping of the track substructure and aid detection of inadequate or degraded ballast, they do not have a proven capability of automatic and continuous monitoring of the track system [2–5]. The SmartRock system is an innovative sensor that can capture the behavior of ballast particles under train load under different conditions [6]. This paper focuses on the use of SmartRock sensors to collate data from the track ballast, process the same through statistical pattern recognition techniques, and apply algorithms to detect a change in the ballast condition.

The SmartRock is a wireless, battery-operated sensor designed to resemble a ballast particle in terms of shape, weight, size, and strength. The design of the main body or the shell of SmartRock was incorporated using discrete element method (DEM), while its manufacture was carried out through 3D printing. This shell houses the internal measurement unit (IMU) which is the heart of the SmartRock system. Figure 1a shows SmartRock shell, and Fig. 1b shows SmartRock IMU.

This IMU consists of a triaxial gyroscope, a triaxial accelerometer, and a triaxial magnetometer that record rotation, translation, and orientation, respectively. Previous studies by Liu et al. [6, 7] have proven that SmartRock is capable of realistically
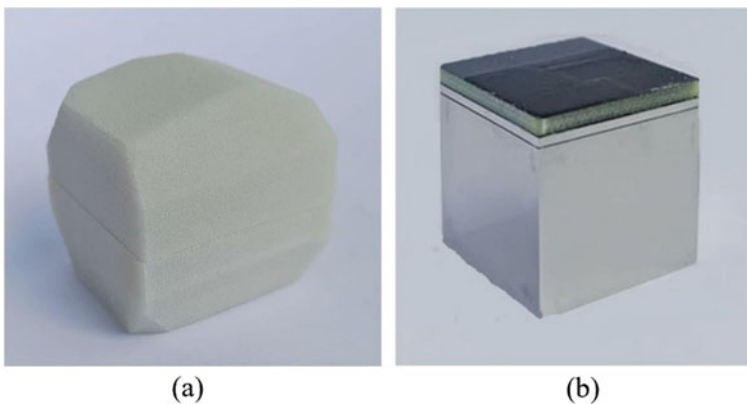
Fig. 1 SmartRock components; **a** 3D-printed shell and **b** IMU inside the shell

capturing the movement of individual ballast particles. The SmartRock works in conjunction with several other components that make the SmartRock system a potential real-time and continuous monitoring instrument of the state of the ballast. The working of this system will become clearer in the succeeding sections of this paper.

Incorporating these emerging technologies as a structure, health monitoring system generates massive amounts of data. Managing this data and extracting the required knowledge regarding the health condition of the structure is a challenge. Statistical pattern recognition (SPR) is a technique that is increasingly being put to use in damage detection in the field of structural health monitoring (SHM) [8, 9]. In this approach, as large amounts of data are collected through sensors placed in the considered structures, SPR helps distinguish, locate, as well as evaluate damage occurrence using advanced machine learning algorithm [10]. SPR is concerned with discovering regularities in the incoming data through the use of computer algorithms and then evaluating the structure's condition by applying these algorithms to the future data.

The objective of this paper is to demonstrate an algorithm, developed on SPR techniques, that can aid identification of fouling in the ballast layer with real-time data collected from SmartRock. In the following sections, the field tests conducted to collect the data are first briefly described, followed by a presentation of algorithm development. The developed algorithm is applied to analyze the field data, and the results are discussed at the end.

2   Field Work

The field work for this study was undertaken in Bellwood, Pennsylvania. A class 4 ballasted track with wooden ties which runs freight as well as passenger trains was selected. Freight and passenger trains' speed was around 40 km/h and 115 km/h, respectively. The two sections, one clean and one mud spot, chosen for the study were in proximity on the same track and hence identical on traffic load, time of passing of trains, and environmental factors. Figure 2a shows the clean spot with the ballast in good condition, while Fig. 2b shows the mud spot section where waterlogging is the result of intrusion of subsoil into the ballast.

Data was collected using identical processes and instrumentation in the sections. The instrumentation comprised a battery-powered wireless system consisting of SmartRocks, a data acquisition box (DAQ), a remote monitoring device, a Wi-Fi hotspot, a solar panel, a battery, and a power inverter. The DAQ box functions as a trackside host to communicate with the SmartRocks [6]. The remote monitoring device empowers the SmartRocks to start collecting and transmitting data. Next, the hosts pass the SmartRock data to a cloud-based computing center using Wi-Fi. Figure 3 shows a comparison between SmartRocks and ballast particles in the field.

Four SmartRocks were installed on each of the two sections. Two SmartRocks were placed in the crib 10 cm below the ballast surface with one under the rail seat and the second besides the end of the tie. The third SmartRock was embedded underneath
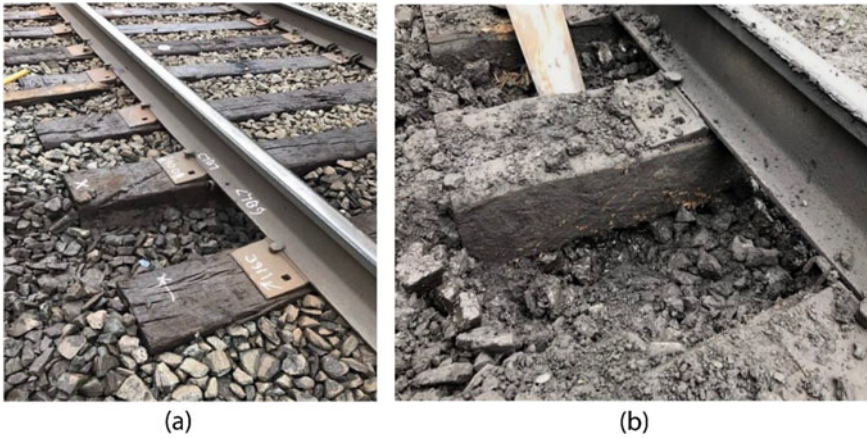
Fig. 2 Comparison of two sections: **a** clean section and **b** mud spot section

Fig. 3 SmartRocks and ballast particles

the tie. For monitoring the tie movement, another SmartRock was stripped of its outer shell and its internal unit was fixed to the surface of the tie itself. The reason for choosing this placement for SmartRock sensors was that the ballast placed under the outer section of the tie, under the rail seat and tie end, is experiencing higher load and vibration due to train passage [11]. The SmartRock underneath the tie encountered technical problems. This SmartRock was not sending any signal to the data acquisition system resulting in no data being collected from this spot. Figure 4 illustrates the instrumentation plan in this study, and Fig. 5 shows the actual image from the site.
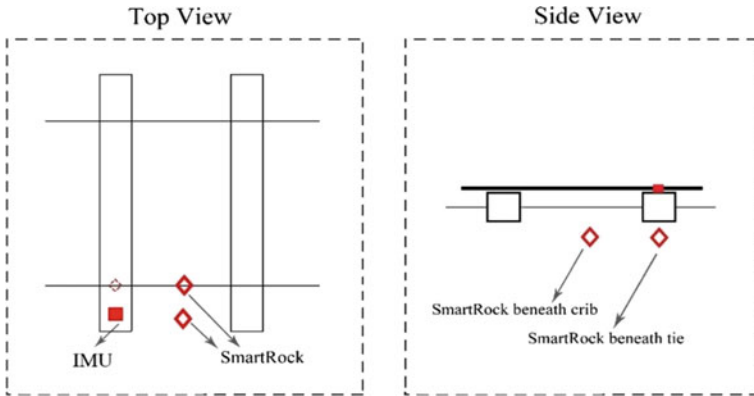
Fig. 4 Instrumentation plan for each section

Fig. 5 Field instrumentation installation

3 Statistical Pattern Recognition

SPR has been investigated in SHM studies with the aim of developing an efficient algorithm to analyze the data generated by monitoring systems for damage detection [9]. For the first time, Farrar et al. [8] defined SHM problems in the context of SPR techniques. During this process, the system's responses are recorded over numerous time intervals. Then, the condition of the system is evaluated by analyzing the recorded data. Damage identification with pattern recognition entails four stages [8]:

1. Operational evaluation
2. Data acquisition, fusion, and cleansing
3. Feature selection and information condensation
4. Statistical model development for feature discrimination.

The primary focus of this study is applying Steps 3 and 4 on SmartRock data for detection of fouling in ballast. Defining the damage-sensitive feature is arguably one of the most crucial steps for damage detection. In time series data, a review of relevant literature suggests indicators such as coefficient of the autoregressive model (AR) as one of the most common features that can be employed to detect damage [12, 13]. The AR model tries to predict one variable using a linear combination of past values of the variable. In the AR(n) model, "n" is the order of the regression which represents the number of previous data points used to model the current data point. The general p order form of AR is given as:

$$x(t) = \sum_{j=1}^{p} \varphi_{xj} x(t - j) + e_x(t) \tag{1}$$

where $x(t)$ represents the data point collected at time t, e is the random error, and φ is the AR coefficient [14].

After defining the damage-sensitive feature, the next step is statistical model development to discriminate the features extracted from different structural conditions. In this study, an algorithm named linear discriminant analysis (LDA) was applied to the extracted features.

LDA, also known as Fisher's discriminant, is one of the common group classification approaches for structural damage identification [15]. LDA tries achieving the most separability between various classes in the feature space by determining the best linear classifier [16]. To that end, we first assume a set of observations (x) with two classes of data. The mean of each class is $\vec{\mu}_1$ and $\vec{\mu}_2$. We assume $\vec{w}$ as the matrix projects the x data into scalar y as:

$$y = w^{\mathrm{T}} x \tag{2}$$

The mean of these projected features would be equal to $\vec{w} \cdot \mu_i$. The next step is to define the ratio of the variance between the classes to the variance within the classes:

$$F\{w\} = \frac{(\mu_1 - \mu_2)^2}{S_1^2 + S_2^2} \tag{3}$$

where S_i is the within-class variance of the projected data, which is calculated:

$$S_i^2 = \sum (y_n - \mu_i)^2 \tag{4}$$

Based on w, Eq. (3) can be written as:

$$F\{w\} = \frac{w^T S_B w}{w^T S_w w} \tag{5}$$

where S_B is the between-class covariance matrix as:

$$S_B = (\mu_1 - \mu_2)(\mu_1 - \mu_2)^{\mathrm{T}} \tag{6}$$

and S_w is the within-class covariance matrix as:

$$S_w = \sum (X_n - \mu_2)(X_n - \mu_2)^{\mathrm{T}} + \sum (X_n - \mu_1)(X_n - \mu_1)^{\mathrm{T}} \tag{7}$$

Furthermore, it can be demonstrated that with the maximum separation the proper $\vec{w}$ is proportional to:

$$\vec{w} \propto S_w^{-1} \cdot (\mu_1 - \mu_0) \tag{8}$$

At the end, the classification methods for data with categorical response variable attempt to assign an individual observation to one of the defined categories. The results of these analyses are summarized in the following section.

4 Analysis Result

The data used in this study is the vertical accelerations recorded by the SmartRocks in the field. Figure 6 compares the vertical acceleration time histories collected from the SmartRocks installed in crib and on the tie. This visual comparison of raw time series data gives initial insights into the signal.

A comparison of the data from the two sections shows higher peak vertical acceleration as experienced by the SmartRocks in the mud spot section than the acceleration observed in the clean section, for both passenger and freight train load. Moreover, the plots in Fig. 6 illustrate we had higher vertical acceleration at the tie area compared
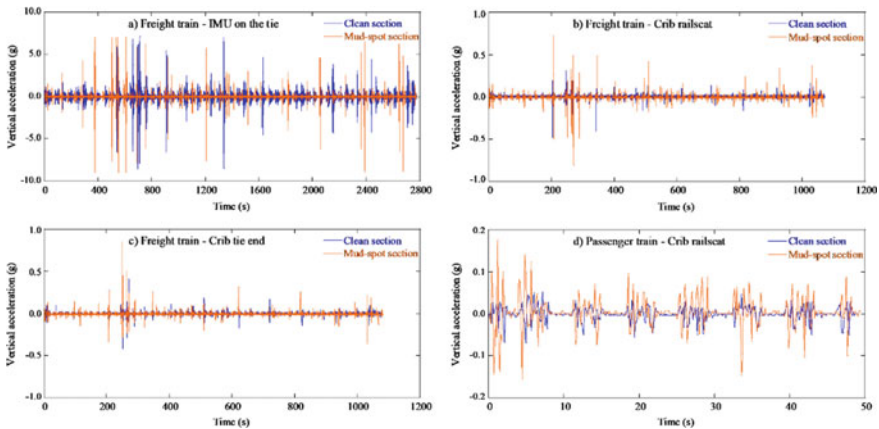
Fig. 6 Comparison of vertical accelerations recorded from the SmartRocks

to the vertical acceleration experienced by the SmartRocks in the crib. Pattern recognition technique was employed in this study to develop an algorithm to differentiate between the data from these two sections.

In the operational evaluation step of pattern recognition technique, it was assumed that the variation caused by environmental and operational condition change would be negligible since each data set (the data collected for one train) consisted of data collected over a short time period. Therefore, the focus of our data analysis is on extracting features and building statistical models for detecting the damage.

Before extracting a damage-sensitive feature, each data set (coming from one train) was divided into smaller time windows for statistical analysis. A closer look at the plotted raw time series in Fig. 6 reveals three patterns in recorded acceleration from the clean sections, including "the group effect of four closely spaced wheels, impulse-like peak accelerations caused by dynamic impact from the wheel load, and small or no accelerations from the middle of each car" [6]. As a preliminary step, each group effect was separated for further analysis. In preprocessing the data, since the weight of each car was different in a train set, each group effect was scaled between -1 and 1. Further, all the signals were standardized by subtracting the mean from individual data and dividing by the standard deviation.

In this study, the coefficients of autoregressive (AR) models were selected as damage-sensitive features to distinguish between data collected from undamaged and damaged structures. In applying the AR model, the efficient order for AR model is defined with the partial autocorrelation function (PACF) plot of the data [12]. In time series data, the PACF describes the partial correlation of a single value with its own lagged values when removing the effect of the other values between these two lags. PACF plot of the data (Fig. 7) showed a cutoff after the third lag which means the third order is the best for the AR model. Therefore, a third-order AR model was applied on vertical acceleration signals recorded by the SmartRocks from the field.

Prior to applying the AR, the data was divided into ten-point time windows, a third-order autoregressive model was then built for each of them, and the coefficients of AR models were selected as damage-sensitive features. Following this procedure, a set of AR coefficients were obtained for subsequent damage diagnoses. In conclusion,
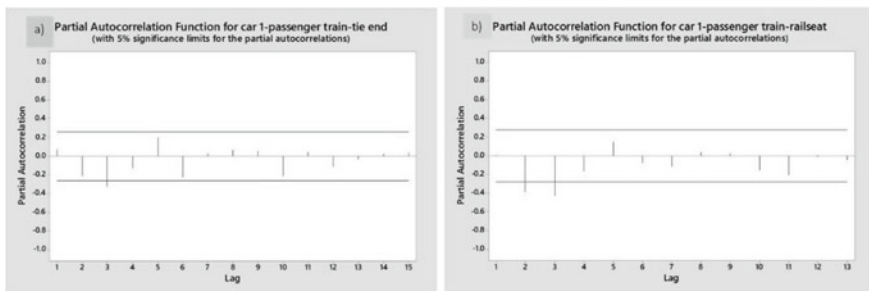
Fig. 7 Partial autocorrelation function plot for the first car; **a** tie end SmartRock and **b** rail seat SmartRock

Table 1 Confusion matrix of LDA on extracted features: (1) SmartRock on the tie; (2) SmartRock at crib tie end; and (3) SmartRock at crib rail seat

	True clean	True mud spot
1. IMU on the tie		
Predicted clean	492	17
Predicted mud spot	4	84
2. Crib at tie end		
Predicted clean	163	124
Predicted mud spot	4	5
3. Crib at rail seat		
Predicted clean	107	186
Predicted mud spot	40	40

from each window, we extracted three features—the AR coefficients. Thus, each time window was encoded by a three-dimensional feature vector and labeled as either clean or mud spot.

After selecting the damage-sensitive feature, with the purpose of damage detection, LDA was applied to the feature vector. In this study, we had two sets of features obtained from the reference data and the mud spot. After applying the third-order AR model and labeling the features as clean and mud spot, 70% of the features were randomly selected as the training data, and the remaining 30% were considered as the test data. The model was initially fitted on the training data set and then applied to the test set in order to evaluate the capability of the model in predicting the class of the coming data. The data utilized as the input of LDA algorithm is from the SmartRocks placed in the crib ballast in two areas: at the tie end and the rail seat as well as the IMU attached on the tie. The standardization process was performed on the AR features prior to applying the LDA algorithm by subtracting the mean and dividing by the standard deviation of the features [14]. The results of the LDA classification algorithm are provided in a confusion matrix, Table 1.

In the confusion matrix, each represents the predicted class for the test data set, while each column represents the actual class of this data. Therefore, with comparison of the actual class of each data point with the predicted class, the performance of the classification model can be evaluated by defining the number of false positives, false negatives, true positives, and true negatives. By constructing this matrix, it is possible to compare the LDA predictions and the true classes and define the type of errors in prediction.

The parameter used in this study to evaluate the classification model is specificity or true-negative rate. This is a statistical parameter that is being widely used to assess prediction models. It measures the proportion of test data that was labeled as mud spot and identified correctly as mud spot with the LDA algorithm. It can be calculated by dividing the proportion of data points which correctly predicted as mud spot by the total number of data points which are actually mud spot.

Considering the confusion matrixes above, the LDA model resulted in 83.2% specificity for the IMU mounted on the tie, while for the crib area the algorithm

could predict the damage with the specificity of 3.9% and 31.7% at the tie end and rail seat, respectively. These results show that LDA working together with the SmartRock data was able to detect damage at a good accuracy level. Also, from the results it can be concluded that SmartRock data recorded from the tie area was more indicative of damage, and therefore, this place is better for capturing the damage.

5   Conclusion

The primary objective of this study is the development of a mechanism for identifying ballast fouling in real time. A wireless network of SmartRock sensors was used to collect data from one undamaged and one damaged section of a rail track, and pattern recognition algorithms designed to recognize the two sections were put to test. The SmartRock is a battery-powered remote sensor that can provide insight into the structural condition of ballast by capturing the translational and rotational movement characteristics of ballast particles. These SmartRocks were installed within the ballast layer, and data was acquired by monitoring two track sections—one clean and one mud spot. Algorithms based on statistical pattern recognition techniques were then employed to analyze the rotational and translational movement of ballast particles measured through the SmartRock sensors. The analysis approach applied to the data was LDA, which is a classification algorithm. Applying this approach to the data collected from three different spots of railroad track section, crib in the rail seat area, crib at the end of the tie, and the tie movement proved that the tie area is the suitable place for monitoring fouling damage to the track as the LDA showed high accuracy in predicting the features extracted from the mud spot section by the IMU. The results prove that LDA is the statistical approach that together with SmartRock data can predict the mud spot in ballast conditions.

References

1. Selig ET, Waters JM (1994) Track geotechnology and substructure management. Thomas Telford
2. Zarembski AM, Grissom GT, Euston TL (2014) On the use of ballast inspection technology for the management of track substructure. Transp Infrastruct Geotechnol 1(1):83–109
3. McHenry MT, Brown M, LoPresti J, Rose J, Souleyrette R (2015) Use of matrix-based tactile surface sensors to assess fine-scale ballast–tie interface pressure distribution in railroad track. Transp Res Rec 2476(1):23–31
4. Al-Qadi IL, Xie W, Roberts R (2008) Scattering analysis of ground-penetrating radar data to quantify railroad ballast contamination. NDT E Int 41(6):441–447
5. Qian Y, Dersch MS, Gao Z, Edwards JR (2019) Railroad infrastructure 4.0: development and application of an automatic ballast support condition assessment system. Transp Geotech 19(January):19–34
6. Liu S, Huang H, Qiu T, Gao L (2016) Comparison of laboratory testing using SmartRock and discrete element modeling of ballast particle movement. J Mater Civ Eng 29(3):D6016001

7. Liu S, Huang H, Qiu T, Kerchof B (2018) Characterization of Ballast particle movement at mud spot. J Mater Civ Eng 31(1):04018339
8. Farrar CR, Duffey TA, Doebling SW, Nix DA (1999) A statistical pattern recognition paradigm for vibration-based structural health monitoring, p 10
9. Sohn H, Farrar CR, Hemez F, Czarnecki J (2001) A review of structural health. Library.Lanl.Gov, pp 1–7
10. Somwanshi SS, Gawalwad BG (2016) Monitoring civil structures with a smart wireless sensor network. Int J Eng Appl Sci 2(3)
11. Li D, Hyslip J, Sussmann T, Chrismer S (2015) Railway geotechnics. CRC Press
12. Gul M, Necati Catbas F (2009) Statistical pattern recognition for structural health monitoring using time series modeling: theory and experimental verifications. Mech Syst Signal Process 23(7):2192–2204
13. (2001) Damage diagnosis using time series analysis of vibration signals. Smart Mater Struct 10(3):446–451
14. Sohn H, Czarnecki JA, Farrar CR (2000) Structural health monitoring using statistical process control. J Struct Eng 126(11):1356–1363
15. Farrar CR, Nix DA, Duffey TA, Cornwell PJ, Pardoen GC (1999) Damage identification with linear discriminant operators (No. LA-UR-98-4702). Los Alamos National Lab., NM (US)
16. Bishop CM (2006) Pattern recognition and machine learning springer mathematical notation Ni. Springer, New York

Study of the Track Dynamics for Optimizing the Railway Superstructure

J. C. Silva Filho , **A. M. Skwarok** , **and R. L. Witiuk**

Abstract Brazil is currently experiencing an expansion of the rail freight modal participation in the national transportation matrix, so that different strategies of capacity increase have been discussed in the country. One of the main strategies refers to the increase of axle load of the railway vehicle, in which the study of the railway pavement becomes essential to verify its capability to resist the new load as well as to understand the impacts in terms of track stress–strain. Thus, the present paper used a finite element method (FEM) to calculate the variation of the track module, rail bending stress and subgrade normal stress in 184 arrangements of pavement structure simulations. For each track element arrangement, a material property or a geometry property variation of the studied layer was performed in order to identify the track behavior. In this study, Systrain was used, a railway pavement analysis software developed by Silva Filho (Contribuição para o desenvolvimento de um método de dimensionamento mecanístico-empírico de pavimentos ferroviários com foco nos solos tropicais. Curso de doutorado em engenharia de defesa, Instituto Militar de Engenharia, 2018 [1]) Contribuição para o desenvolvimento de um método de dimensionamento mecanístico-empírico de pavimentos ferroviários com foco nos solos tropicais. Curso de doutorado em engenharia de defesa, Instituto Militar de Engenharia). As a result, it was verified that the influence of the ballast shoulder and ballast geometry on the stress–strain behavior of the track is low. On the other hand, the foundation layers, especially the subgrade layer, had shown a great influence on the support conditions of the railway pavement.

J. C. Silva Filho (✉) · A. M. Skwarok · R. L. Witiuk
Rumo Logística, Curitiba, PR 82920-030, Brazil
e-mail: jose.filho@rumolog.com

A. M. Skwarok
e-mail: aldrei.skwarok@rumolog.com

R. L. Witiuk
e-mail: rafael.witiuk@rumolog.com

1   Introduction

Brazil is today the ninth largest economy in the world leveraged by commodities production which represents about 62% of the country's added value in exports [2, 3]. In the year of 2018 commodities, exports generated about $150 billion for the Brazilian trade balance, of which about 22% was soybean exports and almost 14% corresponded to iron ore exports. Both products have the particularity of being extracted in the Brazilian countryside and must be transported more than a thousand kilometers on average to the main harbor of Santos, Tubarão, Itaqui and Paranaguá in the country coast.

To ensure a sustained economic growth as well as maintain its commodities production competitiveness in the international market, Brazilian railway infrastructure capability must increase to guarantee their market advantage. Increasing the railway operation capacity demands continued investments in infrastructure of the major's rail freight exports corridors of iron ore and soybeans productions.

Among the strategies to enhance the railways productive capacity can be emphasized the increase of the axle load and the operational train length. This increasing capacity demand can be observed in the main Brazilian railways, such as Rumo Logística, Estrada de Ferro Carajás, Malha Regional Sudeste (MRS) and others.

Therefore, it is important to identify the impacts of increasing the loads intensity and their application cycle on the railway pavement, using computational tools for develop stress–strain analysis in the railway pavement layers. Moreover, it is also emphasized the importance of studying variations in the types of materials that compound each layer, in order to optimize its life cycle and interlayer stress.

Thus, the present paper aims to identify the railway pavement behavior for different layers arrangements of rail, sleepers, ballast, subballast and subgrade. The geometric variation as well as the material proprieties variation of these layers and elements was evaluated in terms of track deflection (track module), bending stress and normal subgrade stress in order to identify the most effectiveness elements in the pavement performance. Finally, this project issue is to optimize the railway pavement structure by identifying the main elements variation that impacts track the most and verify its intensity.

1.1   An Empirical Mechanistic Pavement Design

In order to evaluate the structural behavior of each track component, a finite element method (FEM) was used. The FEM adopted for this analysis was the Systrain software developed by Silva Filho [1] to allow the determination and evaluation of stresses and strain caused by the train transient loading. Moreover, there are several tools developed to perform this type of analysis, such as the Geotrack [4], Illitrack [5] and Kentrack [6] softwares, that were not available for this study.

These analytics methods based on FEM have been widely used for design and evaluation of railway pavements including for the characterization of railway track formation as studied by Gräbe et al. [7].

1.2 Railway Formation

This paper evaluates the track structural properties due to the use of different type of railroad elements formation as rail, sleepers, ballast cushion and subballast cushion. It will be defined below the different properties and settings of each element and layer of the railway pavement.

The Rail. Rails can be considered as one of the most important components in the track structure, having as their function to receive and distribute the wheel loads over the sleepers, to guide the wheels in a lateral direction, to provide adherence in rail/wheel traction, distribute accelerating and braking forces and conduct signals and electrical current. Given this diversity of functions and importance, the rail is also the costliest element of the track.

The first studies related to rail section optimization were performed by American Railroad Engineering Association—AREA [8] and Zarembski and Abbot [9]. The results of these studies do not indicate substantial opportunities for the rail cost—strength ratio improvement in the perspective of rail section.

According to Sadeghi apud. Doyle [10, 11], the rail has been modeled as a beam element on an elastic basis from stress–strain criteria due to the axle loads over the rail, the temperature variation in the environment, the rail/wheel contact stress and the side shift stress.

The model developed by Silva Filho [1] departs from the same premises and considers the structural element defined by two nodes and six independent variables given by the translation and rotation in the three axes. Thus, it is possible to evaluate the different types of stresses acting on the rail from the stiffness matrix solution defined according to local coordinates, global coordinates and the variables of interest mentioned. That model is calculated according to the model defined by Timoshenko—which considers the shear stress and effects on the rail.

The main types of rail commercially used in Brazil are TR-57, UIC-60 and TR-68 with critical loads enforced from 200 to 400 kN as presented by Rangel et al. [12]. In this paper, the simulation was performed using UIC-60 and TR-68 whose technical specifications are presented in Table 1.

The Fastening. The fastening systems correspond to the various elements which together form the connection that join the rail and the sleeper. According to Delft [13] exists, a wide variety of fastenings available and even more being added to the market in view of the variety of new materials, and the sleepers structure evolution. Despite this diverse scenario of possible fastening systems to be used on the track structure, in Brazil predominates, the use of Deenik, Fast Clip and E-Clip presented in Fig. 1.

Table 1 Rail specifications

Gauge (m)	1.6	Gauge (m)	1.6
Section	TR-68	Section	UIC-60
H—height (mm)	185.7	H—height (mm)	172
B—width of foot rail (mm)	152.4	B—width of foot rail (mm)	150
$C1$—width 1 of head rail (mm)	0	$C1$—width 1 of head rail (mm)	70
$C2$—width 2 of head rail (mm)	74.6	$C2$—width 2 of head rail (mm)	74.3
S—thickness of web rail (mm)	17.4	S—thickness of web rail (mm)	16.5
$K1$—thickness of head rail (mm)	0	$K1$—thickness of head rail (mm)	51
$K2$—height of head rail (mm)	0	$K2$—height of head rail (mm)	37.5
F—height of foot rail (mm)	0	F—height of foot rail (mm)	31.5
D—thickness of foot rail (mm)	0	D—thickness of foot rail (mm)	11.5
A—rail area (mm^2)	8617	A—rail area (mm)	7687
Yh—neutral line (mm)	0	Yh—neutral line (mm)	80.69
Ix—moment of inertia (mm^4)	3950	Ix—moment of inertia (mm^4)	3055
Iy— moment of inertia (mm^4)	395	Iy—moment of inertia (mm^4)	305.5
T—polar moment of inertia (mm4)	79	T—polar moment of inertia (mm^4)	61.1
Wx—module of section (mm^3)	391.6	Wx—module of section (mm^3)	335.5

Source Silva Filho and AREMA (2018)

Fig. 1 Deenik, Fast Clip and E-Clip fastening, respectively [14, 15]

Fastening is composed mainly by the baseplate and the clip—or elastic fastening which have different functions, being the steel baseplate responsible for distributing the stress from the vertical loading, besides anchoring the rail in response to horizontal forces. Elastic fastening, on the other hand, guarantees durability and deflection in the connection between the rail and the sleeper, being indispensable for concrete ties.

The Systrain software resorts the fastening model as defined by Silva Filho [1], being expressed by 3 nodes with 3 degrees of freedom, each node allows the translation in the x, y and z axes. The structural behavior is defined according to the scheme shown in Fig. 2, and the stiffness matrix solution derived from the respective model is given by the Newton–Raphson method.
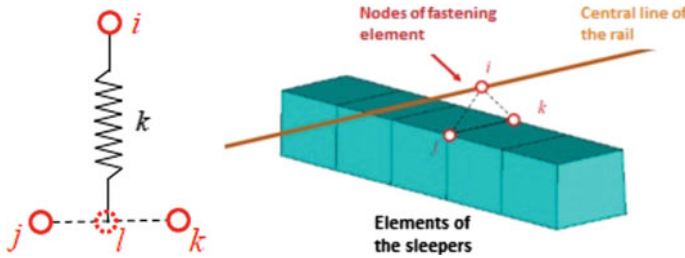
Fig. 2 Fastening model used by Silva Filho [1]

Table 2 Fastening premises

Rigidity	Values
Stiffness of spring Kx (kN/m)	7000
Stiffness of spring Ky (kN/m)	7000
Stiffness of spring Kz (traction) (kN/m)	70,000
Stiffness of spring Kz (compression) (kN/m)	70,000

Source SPADA (2003)

For the simulations performed in this article, the fastening premises were adopted as shown in Table 2, which consists of steels baseplates for wooden sleepers and polymeric rail pads for concrete sleepers, with elastic moduli and Poisson's ratios constants.

The Sleepers. In ballasted track, the sleeper has the important objective of distributing the rail stresses evenly on the ballast surface. The sleeper is also responsible for supporting the fastening baseplate and the rail foot, preserving the track gauge and rail inclination, providing adequate electrical insulation between the rails and to resist the influence of the weather.

The study on the different types of sleepers is based mainly on Talbot's [16] experience about the effective contact surface between the ballast and the sleeper. For him, despite the durability advantages of the concrete sleeper, the wooden sleeper presents a better distribution of the stresses in the ballast since it allows the crimping of the gravel, which maximize the area of contact with the ballast, preserving it.

In the model developed by Silva Filho [1] for Systrain analysis, the sleeper is approximated to a hexahedral mesh defined by 8 nodes at its vertices. The degrees of freedom assigned to the model consist in a three-dimensional translation, representing the x, y and z axes. To solve the deformation matrix of the hexahedral model, the B-bar method was used as presented by Silva Filho and Bower (2010) [10] in order to treat the volumetric and the deviation deformations separately.

This research considered concrete and wooden sleepers with constant elasticity modulus and Poisson's ratio in the simulation. Regarding the distance between the sleepers, the adopted values are presented in Table 3 as well as other sleepers specifications.

Table 3 Sleepers specifications

Specifications	Values
Spacing (cm)	55–60
Length (m)	2.8
Height (cm)	20
Under width (cm)	30
Upper width (cm)	28

Source Silva Filho [1]

The Ballast Layer. According to Selig and Waters [17], the ballast is considered a granular material of hard stone and rock origins on which sleepers distribute the stress from the rail and sleepers loads. Traditionally, this layer is formed by granular material uniformly graduated, free of dirt and dust, not prone to cementation. The main issues related to the ballast choice material have economic origin.

In this case, there is a need to evaluate the elements in terms of support capacity, size, shape, hardness, abrasion and composition aiming to the use of the material with best properties to resist from the stress of the railway operation. Among the main functions of the ballast, the most important are the vertical, lateral and longitudinal resistances that retain track in it required position [17].

In addition, the resilience and energy absorption promoted by this layer can be highlighted, as well as its capacity to allow the passage of particulate material through its formation, the practicality of maintenance, the immediate drainage to the next layer and the dissipation of energy and stresses to the subsequent layers.

For the case of study, it will be used the elements according to Table 4 with ballast thickness set in 30–40 cm, and their resilience module and Poisson's ratio vary from 200 and 300 MPa, respectively.

The Subballast Layer. This layer is located between the subgrade and ballast. The subballast applies some similar functions with the ballasted layer, such as reduce the stress at the subgrade in comparison with the bottom of the ballast and contribute with the subgrade frost protection [17]. The second subballast function presented does not have a mayor importance for a tropical region as Brazil; for these regions,

Table 4 Ballast specifications

Specifications	Values
Height (cm)	25–30
Ballast shoulder (m)	25–40
Declivity of the slope (H:V)	1
Under declivity (%)	3
Type of under declivity	Right
Covering of sleeper	Yes

Source Silva Filho [1]

the main subballast function is to increase the resistance of the subgrade to erosion and water penetration [18].

According to Indraratna et al. [19] to evaluate the subballast layer, the leading aspects to be regarded are related to its drainage and foundation properties. These drainage criteria are associated with the ballast open surface that permits water to flowing down through the underlying layers. To ensure the properties of the layers, AREA standardizes the distribution for the particle size limits of the layers.

However, in Brazil, the most part of soils can be identified as thin sands, silts or clays, which means that normally these soils do not meet the requirements of AREA. Even so Gomes [20] had shown in his research that the resilience moduli of Brazilian fine soils located in the country side nearly always exceed 200 MPa, so that the adequate support strength of the undercarriage is confirmed. In the present study will be assumed values of stress state and Poisson coefficient to calculate de resilient modulus as presented in Table 5.

The Subgrade Layer. The subgrade layer is usually understood as the foundation layer of the track. However, according to Selig and Waters [17], SPADA [21] and Silva Filho [1], this understanding can be considered simplistic since the track structure must be assumed as a multilayer system in which each element responds to a part of the tensions dissipation arising from the train loads. In this perspective, each layer contributes individually to stress dissipation, acting as part of the track foundation, and impacts directly throughout its structure.

In the present study will be assumed values of resilient modulus and cohesion observed in a tropical soil as presented in Table 6.

Table 5 Subballast specifications

Specifications	Values
Specific mass (kg/m^3)	1200
Coefficient $K1$ (MR. Arg) (MPa 1.37)	93.1
Coefficient $K2$ (MR. Arg) (–)	−0.37
Minimum stress of diversion (MPa)	0.021
Maximum stress of diversion (MPa)	0.206
Poisson coefficient (–)	0.4

Source Silva Filho [1]

Table 6 Sleepers specifications

Specifications	Values
Specific mass (kg/m^3)	1800
Coefficient $K1$ (MR. Eln.) (MPa)	80–100
Poisson coefficient (–)	0.4

Source Silva Filho [1]

2   Case of Study: Railway Superstructure Optimization Using Finite Element Method Systrain

As described, the track presents the structural behavior of a multilayers system whose each layer properties directly impact on the capability of entire pavement to resist the cycle load application. In order to evaluate the track behavior due to component alterations, 184 simulations were performed using Systrain software. Each simulation considered a different elements type arrangement; Table 7 presents the type of variation for each component.

2.1   The Variation of the Railway Elements

To evaluate the results of tracks performance obtained from the Systrain software, the rail deflection and the interlayer stress data were exported from the software in order to develop comparative matrices. These matrices allow to identify the patterns on stress and deflection variations due to track element changes.

Along this project, the simulations were developed in two phases. The first phase treated the combination of two variations of each element presented in Table 7, totalizing 128 simulations. Those simulations results provided an intensity and range of impact overview caused by the modification of each component singly in terms of stress and deflection.

The second step comprises a further consequences investigation on track simulated behavior due to the components whose variation generated the greatest impact on pavement properties.

Table 7 Rail specifications

Track elements	Variations	Quantity
Rail section	UIC-60 and TR-68	2
Sleeper	Concrete and wood	2
Spacing between sleepers (cm)	55 and 60	2
Ballast shoulder (cm) [h. ballast]	25 and 40	2
Ballast height (cm) [h. b.]	25 and 30	2
Subballast height (cm) [h. sb.]	20 and 25	2
Subgrade resilient moduli (MPa)	80 and 100	2
Wx—module of section (mm^3)	391.6	

3 Results

3.1 Phase 1: Overview of Components Impact on Track Behavior

The results of the general simulations are presented below. The ballast shoulder augmentation did not present significant improvement in relation to the stress–strain variables evaluated, performing improvements of less than 0.40% on track deflection as shown in Table 8.

Regarding the sleepers spacing, it was observed that the variation in the intensity of the rail bending stress around 2.88–3.18% and a greater impact was observed for concrete sleepers than wooden sleepers. In addition, it was identified that the bending stresses will be higher the thicker the ballast and subballast will be. In none of the 169 simulations, the rail type section exceeds the limit of acceptable tension, remaining less than a half of this value.

In the case of the UIC-60 rail section, a smaller variation in bending stress ratio was observed due to the spacing of the sleepers from 55 to 60 cm. The variance of the increasing ending stress for the UIC-60 rail results is 36%, which is lower than the variance of the TR-68 rail results as can be seen in Tables 9 and 10.

Table 8 Maximum variation rate on track module due to shoulder enlargement—from 25 to 40 cm

		h. ballast = 25		h. ballast = 30	
Sleepers dist	R.M. subgrade	h. sb = 20 cm (%)	h. sb = 20 cm (%)	h. sb = 20 cm (%)	h. sb = 20 cm (%)
55	80	0.36	0.36	0.36	0.36
55	100	0.40	0.40	0.40	0.00
60	80	0.35	0.35	0.35	0.35
60	100	0.39	0.39	0.39	0.39

Considering concrete sleepers and TR-68 rail

Table 9 Variation rate on bending stress due to sleeper spacing—from 55 to 60 cm

TR-68		h. ballast = 25		h. ballast = 30	
Sleeper	R.M. subgrade	h. sb = 20 cm (%)	h. sb = 20 cm (%)	h. sb = 20 cm (%)	h. sb = 20 cm (%)
Concrete	80	2.97	3.02	3.06	3.11
Concrete	100	2.88	2.93	2.93	2.98
Wood	80	2.94	3.03	3.03	3.09
Wood	100	2.86	2.95	2.95	3.00

Considering TR-68 rail section

Table 10 Variation rate on bending stress due to sleeper spacing—from 55 to 60 cm

UIC-60		h. ballast = 25		h. ballast = 30	
Sleeper	R.M. subgrade	h. sb = 20 cm	h. sb = 20 cm	h. sb = 20 cm	h. sb = 20 cm
Concrete	80	3.03	0.36	0.36	0.36
	100	3.01	0.40	0.40	0.00
Wood	80	3.01	0.35	0.35	0.35
	100	2.99	0.39	0.39	0.39

Results for UIC-60 rail section

Comparing the rail bending stress and the track module variation occurred because of the section variation from UIC-60 to TR-68, it is possible to verify an inverse relation between these variables in Table 11.

Comparing the rail bending stress and the track module variation occurred because of the section variation from UIC-60 to TR-68, it is possible to verify an inverse relation between these variables in Table 11.

In terms of subgrade resilient module alteration, it is possible to identify an important impact of this feature on the track module, in view of the variation observed in Table 12 that exceeds 10%. For all arrangements of track elements, the impact of subgrade resilient module was almost the same, ranged from 9.86 to 10.75% of variation as presented in Table 12. In the other hand, the ratio of resilient module impact in the bending stress ranged from 1.69 to 2.31%.

There were not observed an important variation on bending stress and track module as a result of ballast height augmentation as stated on Table 13. However, the relative range of variation according to the track arrangement was from 0.40 to 1.04% for track module and from 0.32 to 0.56% for bending stress.

3.2 Phase 2: Further Evaluation of Some Element Proprieties

In the phase one of the study, it was verified that exists some main features that impact the most in the track performance. These characteristics were the tie spacing and the resilient module of the underlayers—subgrade and subballast. To better understand the effect of the ballast resilient module, the ballast height and subballast height, it was also managed more simulations of these characteristics. The results are presented in Figs. 3, 4 and 5.

Table 11 Variation rate on bending stress (B.S.) and track module (T.M.) due to rail section change from UIC-60 to TR-68

Sleeper	Tie Spacing	h. ballast = 25 cm				h. ballast = 30 cm			
		h. sb = 20 cm		h. sb = 25 cm		h. sb = 20 cm		h. sb = 25 cm	
		B.S (%)	T.M (%)	B.S (%)	T.M (%)	B.S (%)	T.M (%)	B.S (%)	T.M (%)
Concrete	55	7.01	−1.79	6.98	−1.81	6.98	−1.81	6.94	−1.82
	60	6.95	−2.08	6.92	−2.10	6.92	−2.10	6.88	−2.11
Wood	55	7.02	−2.08	6.99	−1.75	6.99	−1.75	6.95	−1.76
	50	6.96	−2.01	6.93	−2.03	6.93	−2.03	6.89	−2.05

Results for concrete sleepers

Table 12 Variation rate bending stress (B.S.) and track module (T.M.) due to subgrade resilient module increase from 80 to 100 MPa

Rail	Tie	h. ballast = 25 cm				h. ballast = 30 cm			
		h. sb = 20 cm		h. sb = 25 cm		h. sb = 20 cm		h. sb = 25 cm	
Section	Spacing	B.S (%)	T.M (%)	B.S (%)	T.M (%)	B.S (%)	T.M (%)	B.S (%)	T.M (%)
TR-68	55	2.23	10.75	2.09	10.47	2.09	10.47	1.95	10.55
	60	2.31	10.73	2.17	10.14	2.21	10.14	2.07	9.86
UIC-60	55	2.00	10.56	1.84	10.64	1.85	10.64	1.69	10.36
	50	2.01	10.51	1.91	9.93	1.94	9.93	1.80	10.00

Results for concrete sleepers

Table 13 Variation rate on bending stress (B.S.) and track module (T.M.) due to ballast height increase from 25 to 30 cm

Rail	Tie	R.M. subgrade = 80 MPa				R.M. subgrade = 100 MPa			
Section	Spacing	h. sb = 20 cm		h. sb = 25 cm		h. sb = 20 cm		h. sb = 25 cm	
		B.S (%)	T.M (%)	B.S (%)	T.M (%)	B.S (%)	T.M (%)	B.S (%)	T.M (%)
TR-68	55	0.56	0.72	0.56	0.72	0.42	0.40	0.42	0.81
	60	0.47	1.04	0.47	0.70	0.37	0.39	0.37	0.39
UIC-60	55	0.52	0.70	0.52	0.71	0.37	0.79	0.37	0.40
	50	0.43	1.02	0.43	0.68	0.36	0.38	0.32	0.76

Results for concrete sleepers
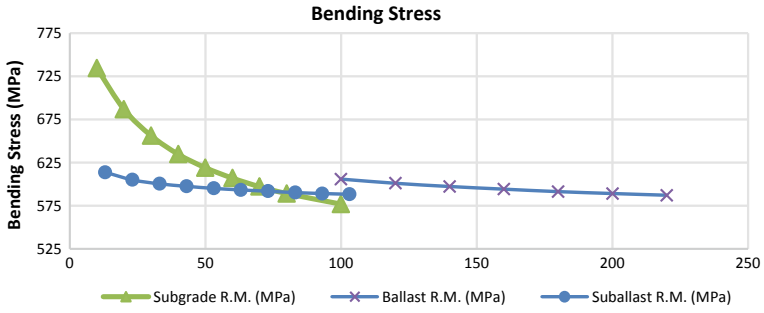
Fig. 3 Under layers and ballast proprieties influence in the rail bending stress
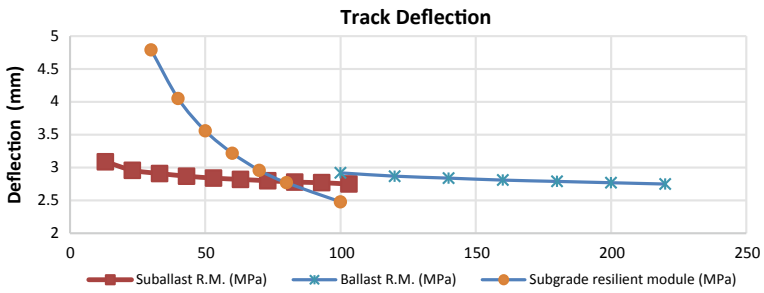
Fig. 4 Under layers and ballast proprieties influence in the track deflection

Fig. 5 Sleepers spacing, ballast and suballast height proprieties influence in the track deflection

4   Conclusion

Having developed the 184 railway pavement simulations in Systrain software and managed the analysis of track deflection, bending stress and subgrade stress results, some conclusions as presented below:

- It was observed that the most effective variation on the track performance is related to the improvement of the proprieties of the substructure layers, such as the subballast and the subgrade. However, the variation in the subballast thickness did not yield significant results in terms of increasing track module, bending stress decrease on the rail, nor in the tension of the subballast.
- The same geometrical aspects and resilient module properties of the material were studied for the ballast layer. For this layer, a low variation impact was identified on both characteristics—resilient module and track deflection—for the stress parameter points to a low influence of this layer on the pavement's ability to withstand the loads imposed on it.
- Among the geometric characteristics studied, the sleeper spacing stands out as one of the items with the greatest impact on pavement performance for all evaluated parameters. Negligible influence was also identified of shoulder increase for the parameters of deflection, bending stress and subgrade stress evaluated in the present paper.

Thus, it is concluded that the most important elements and characteristics for railway pavement optimization are the properties of the infrastructure layers, especially the subgrade, and the spacing between the sleepers.

References

1. Silva Filho JC (2018) Contribuição para o desenvolvimento de um método de dimensionamento mecanístico-empírico de pavimentos ferroviários com foco nos solos tropicais. Curso de doutorado em engenharia de defesa, Instituto Militar de Engenharia
2. Mdic. http://www.mdic.gov.br/comercio-exterior. Last accessed 2019/10/05
3. World Bank. https://data.worldbank.org/indicator. Last accessed 2019/10/05
4. Chang CS, Adegoke CW, Selig ET (1980) Geotrack model for railroad track performance. J Geotech Eng Div 106(GT11):1201–1218
5. Tayabji SD, Thompson MR (1976) Program Illi-track: a finite element analysis of conventional railway support system. User's manual and program listing (No. FRA-OR&D-76–257 Final Rpt.)
6. Liu S (2013) KENTRACK 4.0: a railway trackbed structural design program. Theses and Dissertations-Civil Engineering
7. Ruiz HAM, Gräbe PJ, Maina JW (2019) A mechanistic-empirical method for the characterisation of railway track formation. Transp Geotechn, 18, 10–24
8. Kerr AD (1978) Thermal buckling of straight tracks, fundamentals, analyses, and preventive measures. Bull Am Railway Eng Assoc, Bulletin 669, 80, 16–47
9. Zarembski A, Abbott R (1978) Fatigue analysis of rail subject to traffic and temperature loading. 202–215
10. Sadeghi J (1997). https://ro.uow.edu.au/cgi/viewcontent.cgi?article=2249&context=theses. Last accessed 2019/11/30
11. Sadeghi J (1997) Investigation of characteristics and modelling of railway track system
12. Rangel GWA, Aragão FTS, Motta L (2015) Avaliação computacional da rigidez da fixação pandrol e-clip para utilização em simulações do pavimento ferroviário. 44ª Reunião Anual de Pavimentação. Foz do Iguaçu–PR
13. Esveld C, Esveld C (2001) Modern railway track (Vol. 385). Zaltbommel: MRT-productions
14. BRRailparts. http://www.brrailparts.com.br/grampos.php. Last accessed 2019/11/20

15. Railway fastenings. http://portuguese.railwayfastenings.com/sale-7194726-railway-fast-clip-quick-clamp-system-60si2mna-painting-in-subway.html. last accessed 2019/11/20
16. Talbot AN (1933) Stresses in railroad track. Sixth Progress Report of the Apecial Committee on Stresses in Railroad Track. In: Proceedings of AREA (Bulletins) American Railway Engineering Association (AREA), 45, 68–848
17. Selig ET, Waters JM (1994) Track geotechnology and substructure management, 1st edn. Thomas Telford Services, Londres
18. Brina HL (1988) Estradas de Ferro. Ed. UFMG, Belo Horizonte, MG
19. Indraratna B, Salim W, Rujikiatkamjorn C (2011) Advanced rail geotechnology—Ballast Track. CRC Press, London
20. Gomes (2018) Proposta de classificação de solos lateríticos concrecionados para Pavimento Ferroviário. Mestrado em Engenharia de Transportes, Instituto Militar de Engenharia
21. Spada JLG (2003) Uma abordagem de mecânica dos pavimentos aplicada ao entendimento do mecanismo de comportamento tensão-deformação da via férrea. Universidade Federal do Rio de Janeiro

Update and Case Studies of Geotrack™: A Software for Railway Track and Subgrade Analysis

Yin Gao, Patti Schreiber, Stephen Wilk, Amanda Hanson, Taifeng Li, and Dingqing Li

Abstract Geotrack™ is a software for railroad track and subgrade analysis originally developed in the 1980s and is owned by Transportation Technology Center, Inc. (TTCI), a subsidiary of the Association of American Railroads (AAR). Geotrack™ provides validated analytical solutions under vertical wheel loads, with ballast, subballast, and subgrade layers fully characterized with geotechnical properties. This paper presents the latest update to this software, including execution on modern computers, a new user interface, new output visualization, and more importantly enhanced capabilities in terms of dynamic factor analysis and a permanent deformation prediction. In addition, this paper will present case studies to illustrate how Geotrack™ can help engineers understand the performance of multi-layer railway tracks under various loading, track, and subgrade conditions.

Keywords Track analysis · Subgrade analysis · Geotrack™ upgrade

1 Introduction

Railway transport is one of the most important ways to transport freight in the US, which has the largest rail freight network in the world [1]. To provide safe and efficient railway operations, the design of tracks, as well as track maintenance practices, needs to be improved and optimized. Railway track models simulating the interaction between track components and vehicle traffic can help to understand the track structure responses.

Geotrack™ is a pioneered computer model for track analysis. It was originally developed in the 1980s by the University of Massachusetts and is currently owned

Y. Gao (✉) · P. Schreiber · S. Wilk · A. Hanson · D. Li
Transportation Technology Center, Inc., Pueblo, CO 810001, USA
e-mail: yin_gao@aar.com

T. Li
China Academy of Railway Sciences Corporation Limited, Beijing, China

by Transportation Technology Center, Inc. (TTCI), a subsidiary of the Association of American Railroads (AAR). Geotrack™ is a three-dimensional, multi-layer analytical model for the analysis of conventional railway track structures under quasi-dynamic vertical wheel loadings. The model can determine track and subgrade responses under given wheel loads, track, and subgrade conditions. Up to four super-imposed axles can be analyzed in the model. The trackbed layers are treated as linear elastic materials. A descriptive schematic is shown in Fig. 1. The detailed algorithm has been documented in other publications [2–6].

Other than Geotrack™, there are other multi-layer track models that have been developed for analyzing track component performance (rails, fasteners, sleepers), stress and deformation of ballast, and subgrade layers [e.g., 7–8]. Finite element modeling (FEM) has also been used by many to evaluate track performance [e.g., 9].

Table 1 is a summary of the input and output parameters for the Geotrack™ model. This model can be used for a number of track types, such as wood tie track, concrete tie track, slab track, track with standard gage, wide gage, or narrow gage, for applications including:

- Analyzing the effects of loads on-track component performance

Fig. 1 Forces and components in Geotrack™ model
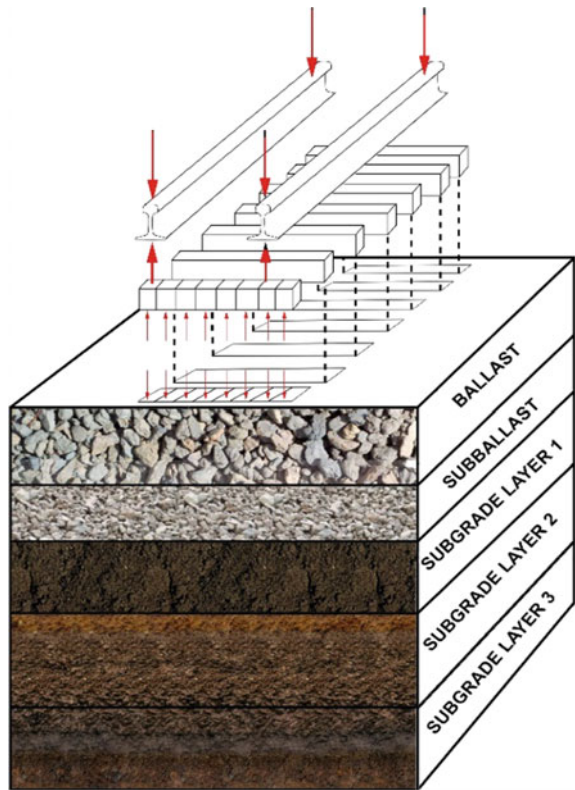
Table 1 Input and output parameters in Geotrack™

Input	Output
• Rail—gage, weight, Young's modulus, moment of inertia, and cross-sectional area • Fastener/pad—vertical stiffness • Ties—tie spacing, length, height, width, Young's modulus, and moment of inertia • Substructure layers—modulus, Poisson's ratio, layer thickness, unit weight, and coefficient of lateral earth pressure • Wheel loads—magnitudes and spacings of up to four-wheel loads	• Rail—deflections and rail seat load at all tie locations, maximum bending stress • Ties—deflections and tie-ballast reactions at ten segments along each tie, bending moments at tie center and at rail–tie seats • Substructure layers—vertical deflections, complete 3D stresses, and strains at any location • Track modulus

- Analyzing the effects of rail and tie properties on track behavior and performance
- Analyzing the effects of pad stiffness and ballast stiffness on-track behavior and performance
- Analyzing the effects of track subgrade conditions on-track behavior and performance
- Conducting track granular layer thickness design
- Conducting track modulus/stiffness analysis.

The original version of Geotrack™ was developed in 1980s using the FORTRAN programming language. To make Geotrack™ more user-friendly and compatible with modern computer platforms, an upgrade of the software has been developed. The latest version uses a user interface that much improves the input function and the visualization of results, while keeping the same core algorithm of the original version which was validated.

The original version of Geotrack™ was developed in the 1980s using FORTRAN programming language. Since this time, the program has been updated to improve the compatibility to modern computer operating systems. To make Geotrack™ more user-friendly and practical to users, an executable for Windows® with expanded features has been developed in the last several years by TTCI researchers. The latest version uses a user interface that greatly improves the input function and the visualization of results, while keeping the same validated core algorithms of the original version. This paper will present case studies to show the enhancement and capabilities of this "reborn" Geotrack™.

2 Software Upgrade Objectives

This software upgrade includes several objectives: (1) develop an executable version of Geotrack™ in modern computers; (2) enhance the capabilities of Geotrack™ with new functions and better visualization tools; and (3) perform testing and case studies to verify the new release.

3 Software Upgrade

The previous section of this paper summarizes the key features of the earlier version of Geotrack™. However, the earlier version of Geotrack™ was only executable on the old Windows platforms (98, 2000). Through obsolescence of Windows user interface libraries and 16-bit emulators, the early version of the software no longer executes on modern Windows platforms. Beginning in 2016, TTCI has been making efforts to allow the software to run on modern Windows systems and expand the technical functionality of Geotrack™ such as.

- Compatible to run on the modern Windows platforms
- A new user interface to the Geotrack™ integration engine

  - Allowing a user to intuitively enter inputs for track analysis
  - Visualization tools of the outputs

- New technical functions to the integration engine and user interface

  - Dynamic speed factor
  - Plastic deformation calculations
  - Capability of interfacing with TTCI's vehicle dynamics software (NUCARS®).

3.1 New User Interface

A new user interface has been introduced as shown in Fig. 2. The input tab contains all the input parameters (including loads, rails, ties, layer information) for the Geotrack™ model. Seven subgroups are included within the inputs tab: (1) general; (2) load; (3) rails; (4) tie; (5) layers; (6) cumulative modulus depths; and (7) additional depths. Each subgroup can be expanded or collapsed for easier input, using the small up arrow on each subgroup label. This new user interface uses TTCI's software development standards and is more efficient for users to enter inputs since the early version only displayed one subgroup on screen.

The new interface has features to visualize the three-dimensional subgrade stresses (Fig. 3a: "soil stress heatmaps") and plot track responses including the reaction loads at rail–tie and tie-subgrade interfaces, as well as deflections of rail and tie. The soil stress heatmaps are generated at each layer interface by extracting the results of stresses and displacements from the output file. This feature provides a direct view of the track responses at the layer interfaces. Depending on which slice orientation of subgrade is being selected, the options for selecting the output data for the plot and the output heatmap plot will change. Superimposed track responses will be linearly added from each wheel if multiple wheel loads are selected. As shown in Fig. 3b, wheel loads were applied at ties #1 and #8 and generated the plots as a result.
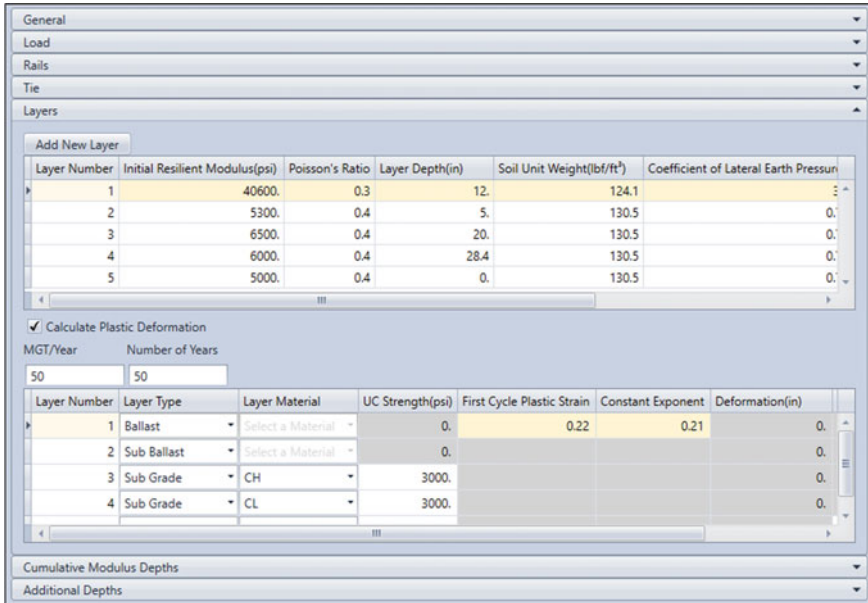
Fig. 2 User interface for model inputs

3.2 New Technical Functionality

To provide more analysis tools, several new functions have been incorporated into the software, as listed at the beginning of this section. These new functions have undergone initial testing and have been validated. Additional debugging and testing will be performed to improve the robustness of each function.

Dynamic Factor

To introduce a dynamic factor of the load, train speed and wheel diameter are considered in the model. The dynamic factor can be calculated using the following equations provided in the American Railway Engineering and Maintenance-of-Way Association (AREMA) manual for railway engineering [10]:

> **Talbot dynamic factor:** $\phi = 1 + \frac{33S}{100D}$
> ϕ: dynamic factor, S: train speed (mph), D: wheel diameter (in).
> **Dynamic loading**: $P_{\mathrm{dyn}} = P_{\mathrm{stat}} \times \phi$
> P_{dyn}: dynamic wheel load (lbs), P_{stat}: static wheel load (lbs).

(a)

(b)
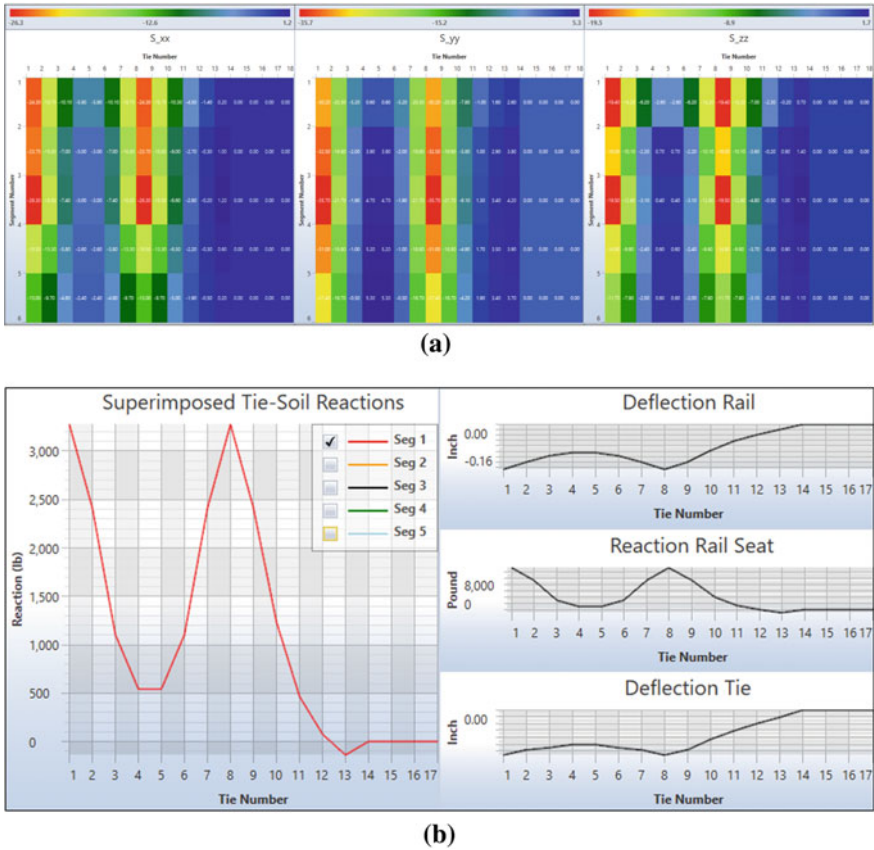
Fig. 3 New visualization tools: **a** heatmaps of soil stresses; **b** plots of track responses

Permanent Deformation of Ballast, Subballast, and Subgrade Layers

The model can now calculate permanent or plastic deformation of the substructure layers. The Li-Selig model [12–14] and Chrismer's model [15] are used in the algorithms. The software can calculate the plastic deformation of each layer, depending on the material type assigned to the layer. The software allows for each layer type to be ballast, subballast, subgrade, or a user-defined deformation value to account for other subgrade materials. Depending on the layer type, the required inputs vary from first cycle plastic strain and exponent coefficient, layer material, unconfined compressive strength, or user-selected deformation with maximum layer depth. This deformation calculation focuses on the plastic strain of the substructure layers and currently does not directly calculate the ballast breakage. Also, the effect of water content on the subgrade layer is not considered in the current model. The total permanent deformation is calculated using the maximum stress of each layer and then summed up across the layer depths.

Interface with NUCARS®

Geotrack™ outputs the characteristics of the track system into a format that can be used as input to the NUCARS® track model (A multi-body vehicle dynamics model developed by TTCI) for users interested in modeling vehicle responses to track inputs. The force–displacement at tie-soil interface can be saved to a text file which can be used as input in NUCARS® track models for the tie-ground connection. By doing this, one can take full advantages of the track model (Geotrack™) and the vehicle dynamics model (NUCARS®).

Unit Conversion

Users have the option to change the input and output display units between the US Customary and International systems of units. This feature will help users to quickly toggle back and forth between the two-unit systems. The written input and output files, however, will remain in US Customary units.

4 Case Studies

Two case studies were performed to validate Geotrack™ analyses by comparing model outputs against actual track measurements.

4.1 Track Modulus Analysis

Track modulus is the vertical stiffness of the rail foundation, meaning "modulus of rail support." It is an important measure of the track performance, indicating such aspects as track deflection. Geotrack™ can calculate the track modulus by given track parameters, which helps to optimize track design and describe the track performance. Table 2 gives the input values of material properties, for example, Geotrack™ track modulus analysis. Accordingly, the track modulus calculated by the Geotrack™ model is 2837 lb/in/in.

In order to validate the simulated track modulus, track modulus measurements were taken using a light car—182,725 lb (22,784-lb wheel loads)—and a heavy car—319,800 lb (39,975-lb wheel loads)—measuring the relative top of rail vertical deflection when the wheel load was over a tie. A total of eight ties in a tangent wood tie zone were measured.

Figure 4 shows the track modulus measurements at the eight ties. The average track modulus of eight ties was 2507 lb/in/in. which is about 13% less than the calculated modulus (red horizontal line). However, these ties have accumulated more than 1,000 MGT, and exact ballast and subgrade conditions are unknown. Therefore, the model can provide an acceptable estimate.

Table 2 Nominal track and subgrade parameters for Geotrack™ analysis

Variable	Value	
Rail properties		
E—GPa (ksi)	207 (30,000)	
I—m^4 (in^4)	3.95e−5 (94.9)	
Cross section area—m^2 (in^2)	8.61e−3 (13.4)	
Gage—m (in.)	1.435 (56.5)	
Rail weight—kg/m (lb/yd)	67.7 (136.2)	
Tie and fastener	**Wood**	
Base width—m (in.)	0.229 (9.0)	
Base length—m (in.)	2.59 (102)	
Cross section area—m^2 (in^2)	4.06e−2 (63)	
E—GPa (ksi)	10 (1500)	
I—m^4 (in^4)	1.07e−4 (257)	
Weight—kg (lb)	114 (250)	
Spacing—m (in.)	0.50 (19.5)	
Fastener stiffness—kN/mm (kips/in.)	50 (285)	
Granular layers	**Ballast**	**Subballast**
Density— Mg/m^3 (pcf)	1.76 (110)	1.92 (120)
Poisson's ratio	0.3	0.35
Modulus—MPa (ksi)	276 (40)	138 (20)
K_o– (unitless)	1.0	1.0
Thickness—m (in.)	0.3 (12)	0.15 (6)
Subgrade and bedrock	**Subgrade**	**Bedrock**
Density—Mg/m^3 (pcf)	1.92 (120)	2.24 (140)
Poisson's ratio	0.35	0.1
Modulus—MPa (ksi)	41 (6)	6890 (1000)
K_o—(unitless)	1.0	1.0
Thickness—m (in.)	Infinite (for last layer)	

4.2 Earth Pressure at a Bridge Approach

A bridge approach test zone was established on the high tonnage loop (HTL) at TTC. The test used a lightweight foam concrete (LWFC) structure to replace the in situ subgrade in order to remediate differential settlement at the bridge approach. The LWFC transition zone (in red, Fig. 5) was designed and constructed at three steps (32
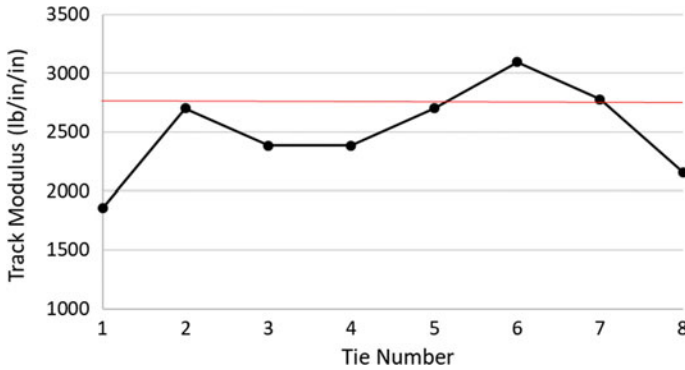
Fig. 4 Track modulus from in-track measurement and simulated value
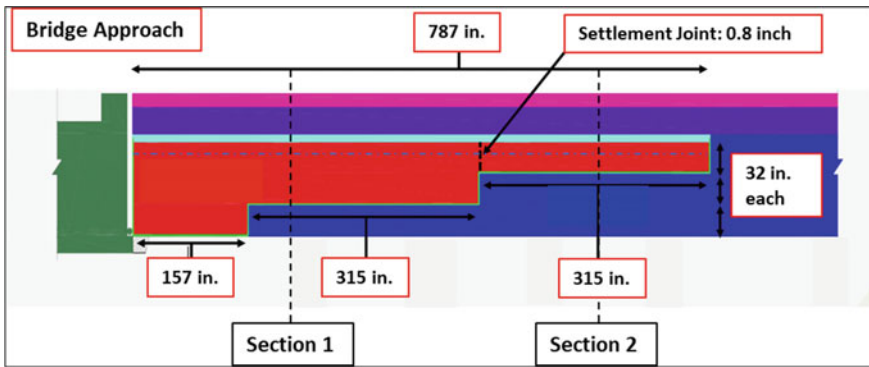
Fig. 5 Profile of LWFC test setup

inches for each step) to transfer the trainload gradually and minimize the differential settlement from the top surface of the embankment. The dimensions of the LWFC structure are shown in Fig. 5. As a part of the test program, earth pressure cells were installed on the top surfaces of the LWFC and subballast at Sections 1 and 2 as shown in Fig. 5. The pressure data measured in this test was used to compare to the results from Geotrack™.

The test zone is supported by wood ties with cut spikes. Therefore, typical properties of a wood tie track system (19.5-inch tie spacing, wood tie dimension, etc.) were assumed in the modeling. Table 3 shows the material properties of the track components that were used in the model.

The dynamic earth pressure cells were installed in Sects. 1 and 2. In addition, cars with different axle loads (88.2, 82.7, 77.2 kips) were used to provide vertical forces in the test. The depth of each layer is shown in Table 4.

Table 5 shows the comparison of the in-track earth pressure measurements and the simulated results using Geotrack™. Generally, Geotrack™ can produce similar

Table 3 Material properties for the model input

Track component	Modulus (ksi)
Rail	30,000
Wood	1450
Ballast	40
Subballast	20
LWFC	25
Subgrade	6
Foundation	1000

Table 4 Layer depth of two sections

Layer	Section 1		Section 2	
	Individual layer depth (in)	Cumulative layer depth (in)	Individual layer depth (in)	Cumulative layer depth (in)
Ballast	14	14	14	14
Subballast	36	50	36	50
LWFC	64	114	32	82
Subgrade	32	146	64	146
Foundation	0	146	0	146

Table 5 Earth pressure comparison of simulated results and in-track measurements

Test section	Axle load (kips)	Location	Geotrack™ (psi)	In-track measurements (psi)	Diff. %
Section 1	77.2	Subballast	16.11	15.56	3.51
		LWFC	7.20	11.08	−34.99
	82.7	Subballast	17.31	16.37	5.78
		LWFC	7.81	11.63	−32.86
	88.2	Subballast	18.41	17.33	6.25
		LWFC	8.31	12.10	−31.37
Section 2	77.2	Subballast	15.21	17.87	−14.88
		LWFC	6.51	7.44	−12.58
	82.7	Subballast	16.31	18.09	−9.82
		LWFC	6.90	8.01	−13.85
	88.2	Subballast	17.41	18.37	−5.20
		LWFC	7.40	8.56	−13.48

results for the subballast layer. In addition, the results matched well for Section 2. Less than 15% of the difference between the measured results and Geotrack calculated results was seen at all locations for different wheel loads. The results at Section 1 on

the top surface of the LWFC did not correlate well. Some localized factors can cause the difference, such as unstable pressure cells and uneven surface of LWFC which were not considered in this model. More investigation will be made to understand the reason to cause the difference in the results.

5   Conclusions

This paper summarizes the new upgrade in the latest version of Geotrack™. The legacy software has been updated to run on modern Windows® platforms. A new user interface that provides convenient input for users and offers modern visualization of outputs has been incorporated with the Geotrack™.

Moreover, several new technical functions have been added to the software to improve the capabilities of track analysis. These functions include dynamic speed factor of input wheel loading, plastic deformation calculations for substructure layers, an interface with TTCI's vehicle dynamics software (NUCARS®) and automated conversion of model between US Customary and International systems of units.

Furthermore, this paper presents case studies to compare simulated earth pressure and track modulus results by Geotrack™ to the actual in-track measurements at FAST. The results showed that Geotrack™ can predict reasonable track responses for various track conditions.

References

1. U.S. Department of Transportation, Federal Railroad Administration
2. Chang CS, Adegoke CW, Selig ET (1980) GEOTRACK model for railroad track performance. J Geotech Eng Div 106(11):1201–1218
3. Alva-Hurtado JE (1980) A methodology to predict the elastic and inelastic behavior of railroad ballast. Ph.D. Dissertation, University of Massachusetts, Department of Civil Engineering, Amherst, MA
4. Stewart HE, Selig ET (1982) Predicted and measured resilient track response. J Geotech Eng Segment ASCE 108(GT11):1432–1442
5. Stewart HE (1982) The prediction of track performance under dynamic traffic-loading. Ph.D. Dissertation, University of Massachusetts, Department of Civil Engineering, Amherst, MA
6. Li D, Hyslip J, Sussmann T, Chrismer S (2015) Railway geotechnics. CRC Press, Book
7. Huang YH, Lin C, Deng X, Rose J (1984) KENTRACK, a computer program for hot-mix asphalt and conventional ballast railway trackbeds. Research Report No. RR-84-1. The Asphalt Inst.
8. Robnett QL, Thompson MR, Knutson RM, Tayabji SD (1975) Development of a structural model and materials evaluation procedures. Report No. DOT-FR-30038 Report. To FRA, Ballast and Foundation Materials Research Program, University of Illinois Champaign, Illinois

9. Indraratna B, Nimbalkar S (2011) Implications of ballast breakage on ballasted railway track based on numerical modeling. Comput Methods Geomech Front New Appl
10. The American Railway Engineering and Maintenance-of-Way Association Manual for Railway Engineering (2018)
11. Li D, Selig ET (1996) Cumulative plastic deformation for fine grained subgrade soils. J Geotech Geoenviron Eng ASCE 122(12):1006–1013
12. Li D, Selig ET (1998) Method for railroad track foundation design. I: Development. J Geotech Geoenviron Eng ASCE 124(4):316–322
13. Li D, Selig ET (1998) Method for railroad track foundation design. II: Applications. J Geotech Geoenviron Eng 124(4):323–329
14. Mishra D, Sharma S, Shrestha A, Li D, Basye C (2016) Geotrack-2015: an upgraded software tool for railroad track analysis. In: 2016 Joint Rail Conference, Columbia, South Carolina, USA
15. Chrismer SM (1984) Mechanics-based model to predict ballast-related maintenance timing and costs. Ph.D. Dissertation, University of Massachusetts, Department of Civil Engineering, Amherst, MA

Railway Subgrade Characterization Through Repeated Loading Triaxial Testing

Gino Calderon Vizcarra ⓘ **, Luiz Muniz** ⓘ **, Thatyane Gonçalves** ⓘ **, and Sanjay Nimbalkar** ⓘ

Abstract Currently, the improvement of means of transportation is a great challenge. Brazil has a large ore production, which will continue in the next decades, and seeks to reduce the transportation times between production and export centers, as well as reduce the emission of contaminants to the environment. In this sense, railways are a more efficient and environmentally friendly means of land transportation, and their proper conservation and operability affect the net gains that Brazil receives from the export of commodities. The implementation of this program proposed in the engineering practice would allow taking more precise decisions regarding the activities of maintenance of railroads, generating significant savings. The first step of the research is the analysis and interpretation of results of repeated load triaxial tests carried out in Brazil on railway subgrade soils. An engineering methodology is presented considering the geotechnical properties of the foundation soil obtained through field and laboratory tests for performing of geotechnical analysis. To ensure the railway stability, criteria of bearing capacity, elastic deflection and permanent deformation for the railway substructure must be met. A prediction model of permanent deformation is used, as well as the influence of moisture on the behavior of the foundation soil. This study aims to contribute to the finding of a comprehensive methodology for evaluating the useful service life of the track substructure so that the most appropriate material can be selected for use as a railroad formation material in order to limit stresses on the railway subgrade, which in turn cause progressive loss of geometric profile of the railway, and to maintain a safe operation of the trains. This will allow significant savings in the periodic maintenance of the substructure, which are one of the activities to restore the track geometry of railways.

Keywords Permanent deformation · Railway subgrade · Triaxial testing

G. C. Vizcarra (✉)
Universidad Catolica San Pablo, Arequipa, Peru

L. Muniz · T. Gonçalves
Muniz and Spada Engenheiros Consultores, Rio de Janeiro, Brazil

S. Nimbalkar
University of Technology Sydney, Sydney, Australia

1 Introduction

Permanent deformation is the accumulated plastic strain under repeated loading. One of the criteria for railroad subgrade design is to prevent excessive permanent deformation due to repeated loading. A big part of maintenance expenditures is directed to give a soft alignment to track which is affected by ballast, sub-ballast and subgrade, it means geotechnical components of track. In many cases, the settlements are not uniform, and this produces track misalignment. In the same way, the understanding of plastic strain accumulation mechanism is essential for an appropriate design of track foundation. A railway subgrade must not present excessive permanent deformation caused by repetitive loading.

The project goal is to identify the lane 2 capacity to bear loads to 325 kN/axle. For this, three study stages were performed. The first one was the field visit and DCP testing, the second one was the geotechnical analysis of railway subgrade, and the third one was the bearing capacity evaluation for railway sections.

2 Experimental Program

2.1 Materials

Samples were collected in two stages. In the first stage, five disturbed samples were collected to perform physical characterization. For the execution of repeated loading triaxial tests, three undisturbed samples measuring 400 × 400 mm were collected from 10 cm below the ballast bottom. The samples were prepared in the field in accordance with the Brazilian Standard NBR 9604/2016 and kept in a humid chamber to preserve its natural water content. Two cylindrical specimens with dimensions 100 mm × 200 mm were obtained from each undisturbed sample by carefully cutting of excessive soil with a sharp knife. In addition, DCP tests were performed at these locations. Figures 1, 2, 3, 4, 5 and 6 show the samples collecting at the field which is a tropical soil.

| (a) | (b) |

Fig. 1 404 + 840 section **a** general view **b** sample collecting

(a)   (b)

Fig. 2 405 + 890 section **a** sample collecting **b** sample preparation

(a)   (b)

Fig. 3 407 + 090 section **a** general view **b** sample collecting

(a)   (b)   (c)
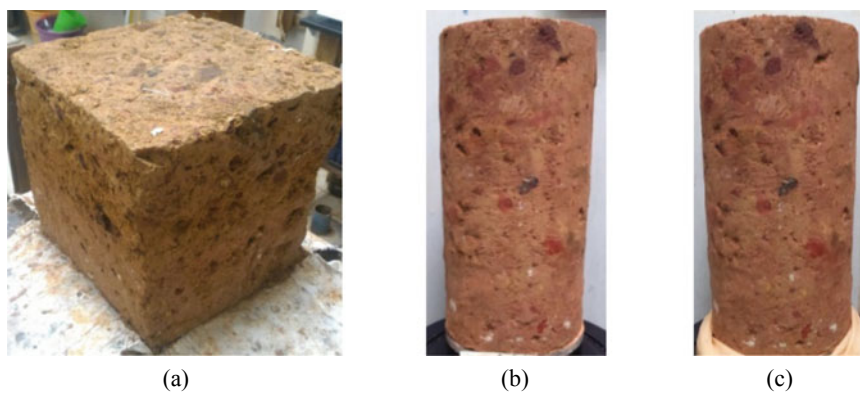
Fig. 4 404 + 840 section **a** 40 cm × 40 cm sample **b** specimen before the test **c** after the test

(a)   (b)   (c)
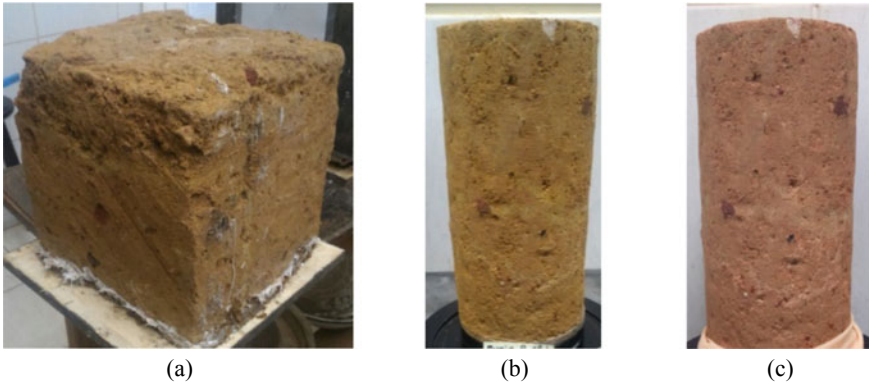
Fig. 5 405 + 890 section **a** 40 cm × 40 cm sample **b** specimen before the test **c** after the test

(a)   (b)   (c)
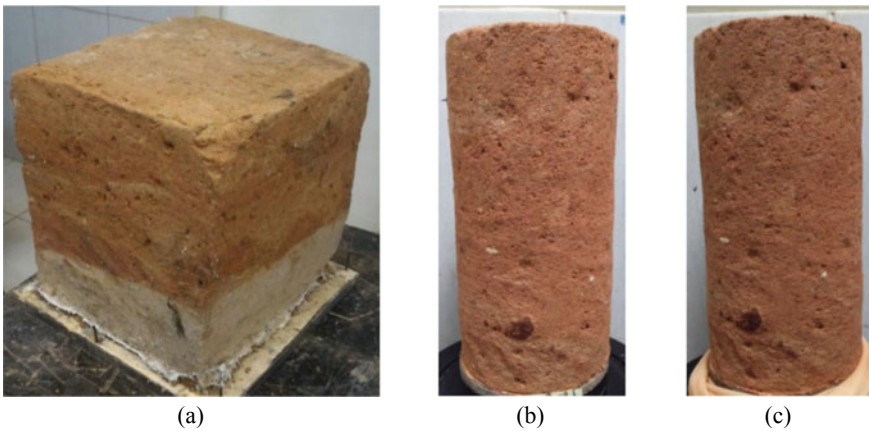
Fig. 6 407 + 090 section **a** 40 cm × 40 cm sample **b** specimen before the test **c** after the test

2.2 Methods

A set of physical characterization tests was performed on disturbed samples. DCP tests were performed at three locations, and repeated loading triaxial tests were carried out on undisturbed samples. The tests list is shown in Table 1.

To obtain the resilient modulus (MR) corresponding to each section, a correlation equation published by Angelone [1] was applied. After that, stress and strain analysis considering a 325 kN/axle load using computational software Ferrovia 3.0 [2].

$$M_R(\text{MPa}) = 201.0 \times (\text{DN})^{-0,44} (\text{mm/blow}) \tag{1}$$

where:

Table 1 Tests list

Stage	Test	Section
1	Particle-size-distribution Atterberg limits SUCS classification HRB classification	404 + 800, 405 + 900, 407 + 100
2	Dynamic cone penetrometer (DCP)	404 + 840, 405 + 890, 407 + 090
3	Repeated loading triaxial	404 + 840, 405 + 890, 407 + 090

DN—value obtained in DCP test (mm/blow);

M_R—resilient modulus.

Cyclic long duration triaxial tests were performed to evaluate the plastic mechanical behavior of a subgrade layer submitted to cyclic stresses equivalent to railroad traffic. The triaxial apparatus used for the permanent deformation test is composed by three main segments: load structure, triaxial cell and pressure gages. Complementary, LVDTs (Linear Variable Transducers) are used to record the displacements. All the electronic components are controlled by an on-board computer with an acquisition system named SICAEO (Fig. 7a).

Confining and deviator stresses between 30 and 150 kPa are applied, as a result of calculations done in the software Ferrovia 3.0 which would be the in situ stresses acting in the sampling point. This range covers stresses values that commonly act in the track subgrade layers. It must perform two tests as a minimum requirement for each material with different stresses pairs, with the objective to obtain an adequate correlation between strain and cycles number. Also, it is recommended to perform tests on samples with different moisture to study the influence in permanent deformation of soil due to moisture variations happen along each year.

Fig. 7 a Specimen in triaxial chamber; **b** specimen under wetting by capillarity [3]

(a)   (b)
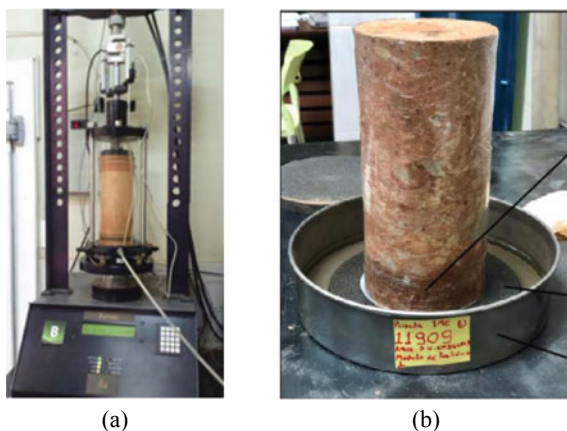
Table 2 Triaxial testing conditions

Sample	km	Water content (%)	σ_1 (kPa)	σ_3 (kPa)	σ_d (kPa)	σ_1/σ_3	N
P25A1	404.840	9.6	100	35	65	2.85	150,000
P25A2	405.890	9.84	110	40	70	2.75	150,000
P25A2	405.890	11.4	110	40	70	2.75	150,000
P25A3	407.090	9.1	100	35	65	2.85	150,000

The cylindrical specimens were tested with 150,000 load cycles at 2 Hz frequency under natural water content condition without conditioning loading. The testing principal stresses are shown in Table 2. After 150,000 load cycles, only the specimen P25A2 was retired from the chamber and placed above a porous stone in a container of a small level of water for 48 h (Fig. 7b); the specimen was wetted by capillarity and increased its weight, which was measured every 12 h until the specimen did not have more weight increments, according to procedure described by Campos [3]. The estimation for permanent deformation was based on a daily traffic composition with a typical convoy with three hundred thirty 4-axle wagons and three 6-axle locomotives. The annual cycle estimated for the fleet is 5.372.070 load cycles. There are many models to predict permanent deformation as Monismith et al. [4], Tseng and Lytton [5] and others.

3 Results

Characterization tests indicate that the subgrade layer is essentially composed by clayey sand (USCS). Results are shown in Table 3. Table 4 shows DCP test results for each section correlated to CBR and resilient modulus (MR) values which allowed us to assign layer thickness and resilient values to a typical section (Fig. 8).

Subgrade stresses calculated with software Ferrovia 3.0 [2] were higher than maximum allowed value, and so it was decided to check permanent deformation through repeated load testing. Figure 9 shows repeated load triaxial results for this section. The evolution of accumulated permanent deformation versus the cycles

Table 3 Physical characterization test results

km	Depth	Gravel (%)	Sand (%)	Fines (%)	LL (%)	LP (%)	IP (%)	USCS	HRB
404+ 800	0.00–0.20	33	38	29	21	13	9	SC	A-2-4
	0.20–1.50	10	56	34	23	14	10	SC	A-2-4
405 + 900	0.05–0.20	39	35	25	20	12	9	SC	A-2-4
	0.20–1.50	11	57	33	22	13	9	SC	A-2-4
407 + 100	0.10–0.35	25	46	29	25	15	10	SC	A-2-4

Table 4 DCP test results

km	Layer	DN (mm/blow)	CBR	MR (MPa)
404 + 840 L2	0.00–11.00	10.5	17	58
	11.00–31.70	19.3	8	42
	31.70–86.70	10.0	18	60
405 + 890 L2	0.00–10.20	10.0	18	60
	10.20–41.70	20.6	8	40
	41.70–75.40	11.7	15	55
407 + 090 L2	0.00–7.40	10.8	17	58
	7.40–17.70	27.1	6	35
	17.70–25.60	3.9	55	102
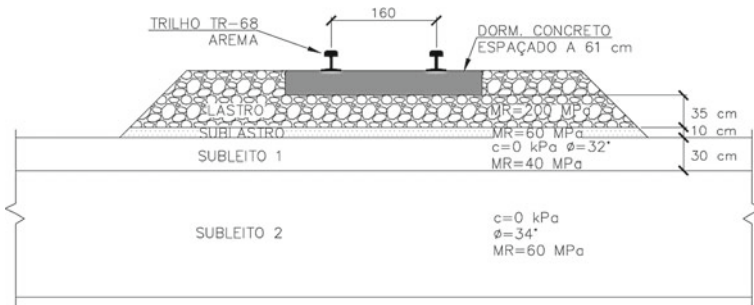
Fig. 8 Railway cross section
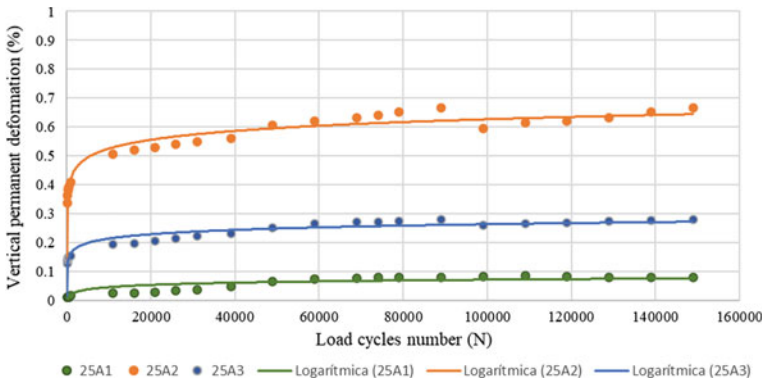
Fig. 9 Vertical permanent deformation vs. load cycles number
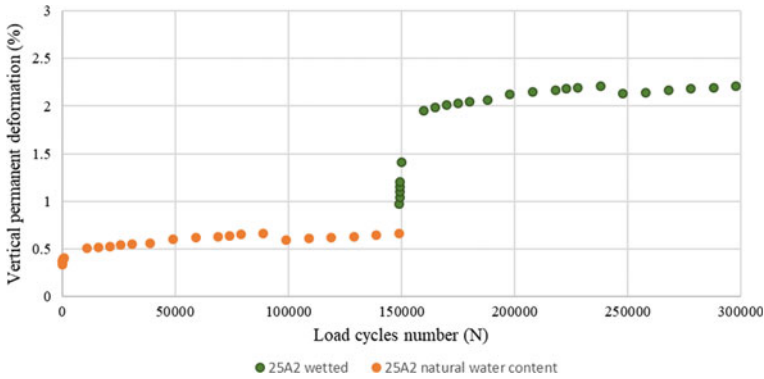
Fig. 10 Influence of water content on vertical permanent deformation

number for a same soil under three stress states is shown. In this case, it is observed that the soil reaches a Shakedown state or vertical plastic strain stabilization for considered stress state. Figure 10 shows the influence of wetting on permanent deformation where an increment of 1.56% in water content induces an associated increment of 1.54% in vertical permanent deformation.

4 Conclusions

A novel evaluation methodology for subgrade permanent deformation was described and evaluated. To obtain reliable results, repeated load testing was performed on undisturbed samples which allowed us to take into consideration soil structure influence. In the same way, the influence of water content was an important parameter for permanent deformation.

References

1. Angelone S, Tosticarelli J, Martinez F (1991) El Penetrometro Dinâmico de Cono. Su Aplicación al Control y Diseño Estructural de Pavimentos. In: Congresso Ibero-Latinoamericano del Asfalto, vol 6, 19 p (in Portuguese)
2. Rodrigues RM (1994) Um Modelo para Análise Estrutural de Vias Permanentes Ferroviárias sobre Lastro. Anais do X Congresso Brasileiro de Mecânica dos Solos e Engenharia de Fundações - COBRAMSEF, vol 3, pp 755–762, Foz do Iguaçu (in Portuguese)

3. Campos P (2019)—Avaliação do efeito de variação de umidade no comportamento mecanístico de um trecho da Estrada de Ferro Carajás. Master Dissertation. Instituto Militar de Engenharia. Rio de Janeiro. Brazil (in Portuguese)
4. Monismith CL, Ogawa NE, Freeme CR (1975) Permanent deformation characteristics of subgrade soils due to repeated loading. Transportation Research Record, No. 537, pp 1–17
5. Tseng KH, Lytton RL (1989) Prediction of permanent deformation in flexible pavements materials, implication of aggregates in the design, construction, and performance of flexible pavements. ASTM STP 1016, ASTM, West Conshohocken, pp 154–172

Investigation into Ground Vibration Responses of High-Speed Rail Slab Tracks Considering Train-Track-Soil Interactions

Ting Li, Qian Su, and Sakdirat Kaewunruen

Abstract Slab tracks are widely adopted in high-speed railway networks. Based on a critical literature review, most previous studies related to ground vibrations have been carried out with the traditional ballasted track. In order to highlight the ground vibration responses of high-speed railway with slab tracks induced by the wheel-rail dynamic interactions under the roughness of rail surface, a novel 3D coupled train-track-soil model is developed based on the multi-body simulation (MBS) principle, finite element modeling (FEM) theory, and perfectly matched layers (PML) method using LS-DYNA. This model has been validated against the field test results. The maximum displacement of the rail is obtained with various train speeds to investigate the critical speed of high-speed railway system. The vibration displacements and velocities of soils are then analyzed under normal and critical speeds. The train-track interactions are also presented. This study could provide new insight into the ground vibrations of high-speed railway with slab tracks in practice.

Keywords Ground vibration · Critical speed · Slab track · Train-track-soil interactions

1 Introduction

High-speed railway has been developed rapidly all over the world [1–3]. The French TGV has reached a record speed of 574.8 km/h. The Chinese 'Fuxing' train is traveling at a speed of 350 km/h in numerous rail networks in China. These high-speed trains can impart greater dynamic forces to infrastructures and result in an elevated

T. Li · Q. Su (✉)
School of Civil Engineering, Southwest Jiaotong University, Chengdu 610031, China
e-mail: suqian@126.com

Key Laboratory of High-Speed Railway Engineering, Ministry of Education, Southwest Jiaotong University, Chengdu 610031, China

T. Li · S. Kaewunruen
School of Engineering, University of Birmingham, Birmingham B15 2TT, UK

vibration level for grounds [4–6]. Therefore, the assessment of ground vibration is getting increasingly crucial for high-speed railways in practice.

According to previous studies, high-speed trains traveling on soft soils can significantly increase the vibration level, particularly when the train moves at the so-called 'critical speed', at which the train induces a resonance-like phenomenon [7–9]. The measured soil displacements from the well-known railway site at Ledsgard, Sweden show that the amplified displacement will be around three times the static value when the train speed is close to the Rayleigh wave velocity [4, 10]. It is noted that most previous studies have normally investigated the ground vibration under ballasted track [7, 11–14]. However, the use of slab track is getting prevailing in high-speed railways because of its advantages of higher stability, lower deformation, and easier maintenance compared with ballasted track [3, 6, 15]. The study of ground vibration responses of high-speed railway with slab track is rather limited.

Additionally, a lot of previous methods just simplified the train loads as moving quasi-static loads, and the dynamic wheel-rail interaction under the roughness of rail surface has been ignored [8]. However, the dynamic loads play an important role in the train-induced ground vibrations and should be taken into consideration when the ground vibration is investigated [4].

In order to investigate the critical speed of high-speed railway with slab tracks considering the wheel-rail dynamic interactions under the roughness of rail surface, a novel 3D-coupled train-track-soil interaction model is developed based on the multi-body simulation (MBS) principle, finite element modeling (FEM) theory, and perfectly matched layers (PML) method using LS-DYNA. The critical speed is investigated firstly. The dynamic responses under various train speeds are also presented. This study could bring an insightful and new understanding of the ground vibration of high-speed railway with slab tracks in practice.

2 Development of the Numerical Model

A 3D coupled train-track-soil interaction model is developed using LS-DYNA to investigate the ground vibration responses of high-speed railway system with slab tracks. The high-speed train is simulated based on the MBS principle, and the slab track is developed based on the FEM theory. Besides, the subgrade and ground are simulated based on the FEM theory together with the PML method.

2.1 Modeling of the Train and Track

The vehicle in this model is the China Railway High-speed (CRH) 380 Electric Multiple Unit (EMU) train. The vehicle consists of one car body, two bogies, four wheelsets, and two stage-suspension systems, as shown in Fig. 1. The car body, bogies, and wheelsets are simplified as the rigid-bodies with shell and beam elements.
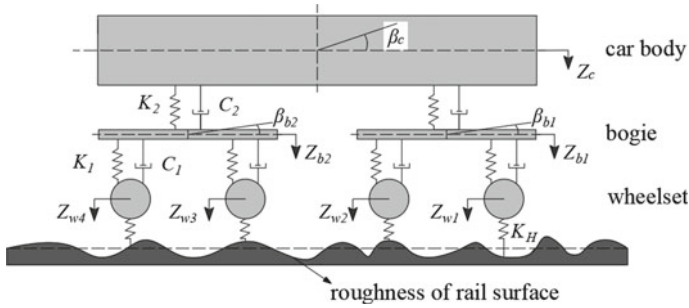
Fig. 1 Simulation of the vehicle

These multi-rigid-bodies are connected by the springs and dashpots. As the vertical vibration is the primary excitation to the infrastructures, the ten vertical degrees of freedom of the vehicle are considered in this model.

The track in the model is the China Railway Track System (CRTS) II slab track, which consists of rail, rail pads, concrete slab, cement asphalt (CA) mortar layer, and concrete base. The rail is simulated as the Euler beam, which is supported by discrete springs and dashpots to represent the rail pads. The concrete slab, CA mortar, and concrete base are simulated as solid elements.

The contact between the wheel and rail is simulated based on the Hertz contact theory. The roughness of Germany high-speed low disturbance irregularity is used to excite the wheel-rail dynamic interactions [15]. In LS-DYNA, the keywords: *Rail_Track and *Rail_Train are used to define the parameters of the wheel-rail contact. The properties of the CRH EMU 380 train and CRTS II slab track are shown in Table 1 [15–17].

2.2 Modeling of the Soil

The soil is simulated based on a typical cross section of Beijing-Shanghai high-speed railway in China [18]. The subgrade consists of three layers: Surface layer, bottom layer, and subgrade body. The ground consists of two layers of clay.

The soils are simulated as solid elements based on the FEM theory. In order to model the infinite boundary around the soil, the PML method, which is the most efficient form for absorbing dynamic energies, is used to attenuate the dynamic wave propagations, as illustrated in Fig. 2.

The material properties of the soils are measured from the section of the Beijing-Shanghai high-speed railway, as shown in Table 2. In order to describe the damping effect of the soil, the coefficients of the Rayleigh damping are used. In this model, $\alpha = 0$ and $\beta = 0.0002$ [19].

Table 1 Properties of train and track

Properties	Values
CRH380 EMU train	
Mass of the car body (kg)	40,000
Mass of the bogie (kg)	3200
Mass of the wheelset (kg)	2400
Inertia of pitch motion of the car body(kg m^2)	5.47×10^5
Inertia of pitch motion of the bogie(kg m^2)	6800
Primary suspension stiffness (N/m)	1.04×10^6
Secondary suspension stiffness (N/m)	4×10^5
CRTS II slab track	
Mass density of the rail (kg/m^3)	7830
Modulus of elasticity of the rail (Pa)	2.059×10^{11}
Poisson's ratio of the rail	0.3
Stiffness of the rail pads (N/m)	5.0×10^7 (dynamic stiffness)
Damping of the rail pads (N s/m)	7.5×10^4
Mass density of the concrete slab (kg/m^3)	2500
Modulus of elasticity of the concrete slab (Pa)	3.6×10^{10} (reference static value, strain-rate dependent)
Poisson's ratio of the concrete slab	0.2
Mass density of the CA mortar (kg/m^3)	1900
Modulus of elasticity of the CA mortar (Pa)	7×10^9 (reference static value, strain-rate dependent)
Poisson's ratio of the CA mortar	0.2
Mass density of the concrete base (kg/m^3)	2400
Modulus of elasticity of the concrete base (Pa)	2.55×10^{10} (reference static value, strain-rate dependent)
Poisson's ratio of the concrete base	0.2

Fig. 2 Absorbing boundary of PML
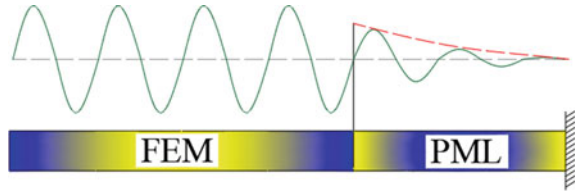
Table 2 Properties of Soils

Components	Depth (m)	Density (kg/m³)	Modulus of elasticity (MPa)	Poisson's ratio	c_R (km/h)
Surface layer of subgrade	0.4	2300	200	0.25	616.08
Bottom layer of subgrade	2.3	1950	150	0.35	567.58
Subgrade body	2	2100	110	0.3	473.24
First layer of ground	2.4	1900	42	0.3	307.43
Second layer of ground	13.1	2010	83	0.36	415.00

2.3 Numerical Solution

The dimension of the whole model is set as 120 m × 130 m × 15.5 m. The model has 399,386 elements, including beam elements, shell elements, solid elements, springs, and dashpots, as shown in Fig. 3. It is noted that the Beijing-Shanghai high-speed
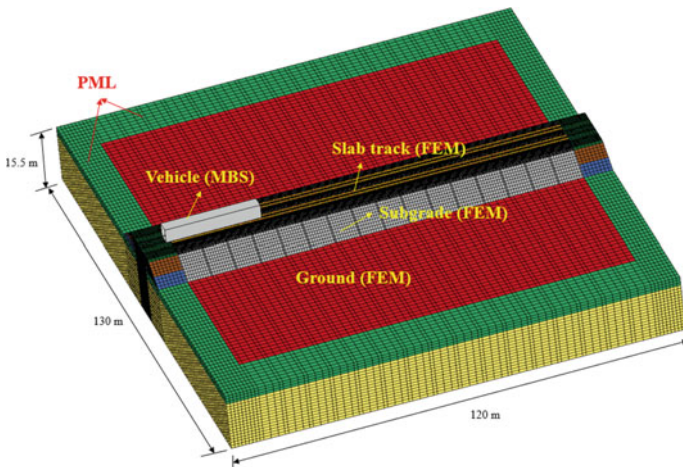
Fig. 3 Numerical model in LS-DYNA

railway is a double-line railway, indicating the model cannot be developed as a half model from the center of the railway since the dynamic train load is asymmetric.

The vehicle is set to move at a constant speed over the rail after the dynamic relaxation. The explicit central difference method is used to integrate the motion equations of the coupled train-track-soil model by LS-DYNA with a time step of 1.23×10^{-5} s.

3   Results and Discussion

In order to investigate the critical speed of high-speed railway with slab tracks, the maximum displacement of the rail with train speed is firstly obtained. The displacement of soils, the peak particle velocity of soils, and the wheel-rail contact force are then investigated at various train speeds.

3.1   Critical Speed

The train speed is varied from 0 to 650 km/h to investigate the critical speed of the high-speed railway with slab tracks. Although a speed of 650 km/h is much higher than the normal operational train speed ($\leq$400 km/h), this study aims to obtain the critical speed of this railway (Fig. 4).

The critical speed of the railway is around 440 km/h. Unlike the amplification phenomenon in the ballasted track, the increased displacement at critical speed is not significant in this railway. The displacement is increased by 18.4% from 1.03 mm (0 km/h) to 1.22 mm (440 km/h). It is likely that the slab track exhibits a global

Fig. 4 Maximum displacement of rail with train speed
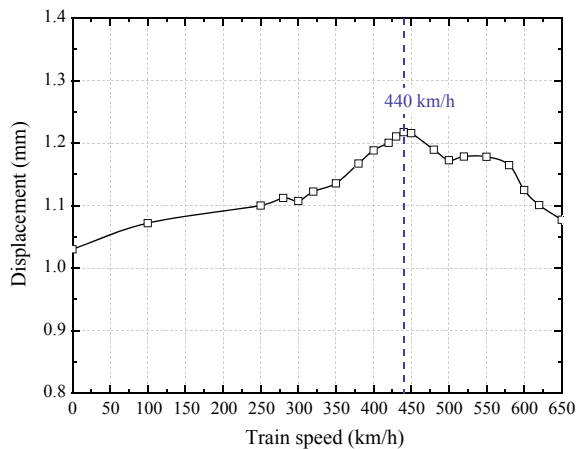
higher stiffness than the conventional ballasted track, leading to a smaller amplification of resonance-like phenomenon. Also, the critical speed, 440 km/h, is not close to the Rayleigh wave velocity of soils from Table 1. It is noted that the subgrade is normally simplified as one layer in previous studies, and the critical speed is therefore determined by the Rayleigh wave velocity of the subgrade or the first layer of ground. However, there are five layers of soils based on the cross section of Beijing-Shanghai high-speed railway. The trapezoidal subgrade, together with five types of soil properties, makes the propagation and dispersion of both surface and body waves complex.

3.2 Displacement of Soils

The contours of the displacement of soils at three train speeds (300, 440, and 580 km/h) are shown in Fig. 5. When the train speed is 300 km/h, the contours of the displacement are concentrated in a small range of soils. The maximum upward displacement at this moment is 0.04 mm, and the downward displacement is 0.52 mm, as shown in Fig. 5a.

When the train speed is 440 km/h, which is the critical speed of this railway, the Mach cone phenomenon can be observed. This phenomenon is analogous to a boat moving through the water, as shown in Fig. 5b. The maximum upward displacement is 0.21 mm, which is higher than the value at 300 km/h. The downward displacement, 0.73 mm, is also higher than that at 300 km/h.

(a) 300 km/h   (b) 440 km/h
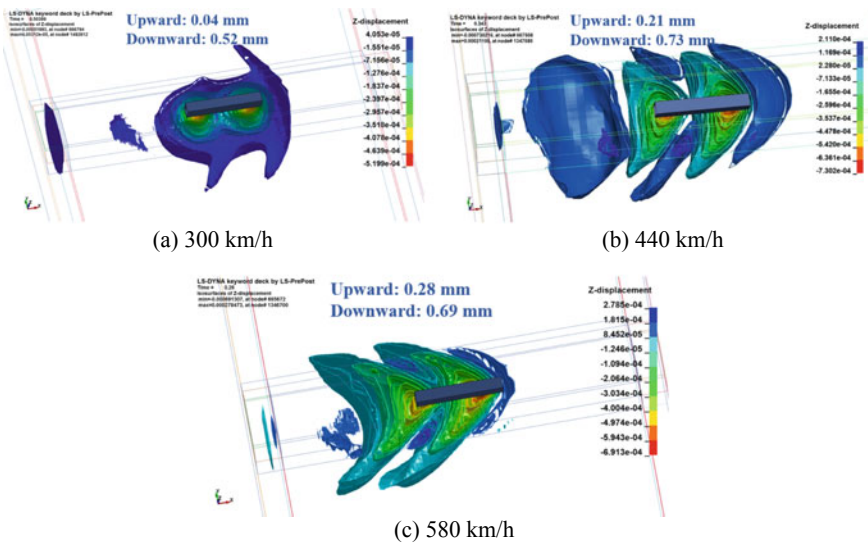
(c) 580 km/h

Fig. 5 Contours of the displacement of soils
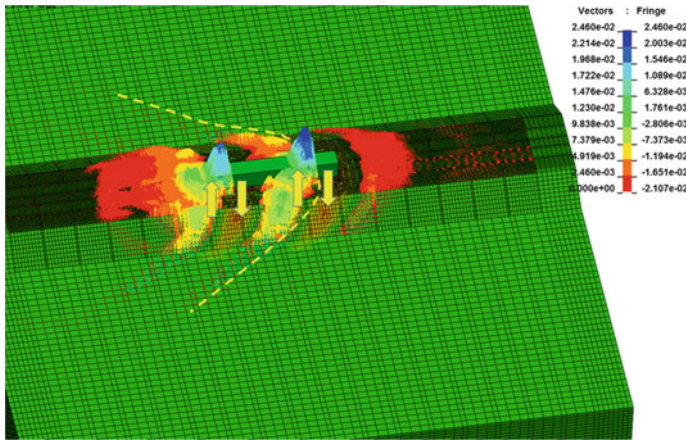
Fig. 6 Vector of the velocity of soils at 440 km/h

When the train travels at a speed of 580 km/h, the Mach cone phenomenon can still be observed. The downward displacement is lower than that at 440 km/h, but the upward displacement still exhibits a relatively high value (0.28 mm), as shown in Fig. 5c.

3.3 Peak Particle Velocity

The vector of the velocity of soils at 440 km/h is shown in Fig. 6. The Mach cone phenomenon is evident. The velocity of the soils tends downward-upward-downward-upward, which corresponds with the positions of four wheelsets.

The peak particle velocities of soils with lateral distance at three train speeds are shown in Fig. 7. The peak particle velocity decreases rapidly in the range of subgrade, and the values are lower than 10 mm/s in the range of ground. Also, train speed has an evident influence on the peak particle velocity. The vibration velocities of soils increase with train speed.

3.4 Train-Track Interactions

The time history of the wheel-rail contact force is shown in Fig. 8a. The train speed exhibits an evident influence on the wheel-rail contact force. The maximum force increases significantly with train speeds. Also, when the train speed is super high (580 km/h), the contact force at several moments decreases to 0 kN, indicating the contact-loss occurs [20, 21].

Fig. 7 Peak particle velocities of soils along with lateral distance

Fig. 8 Train-track interactions
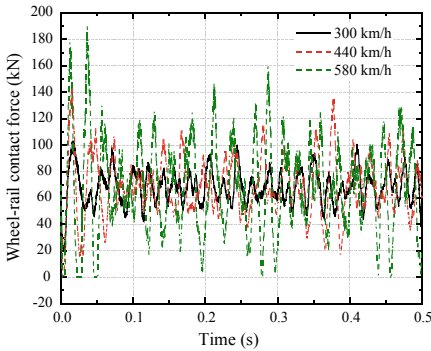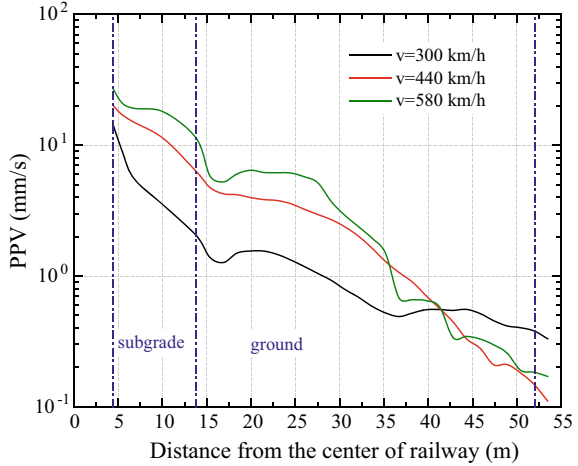
(a) time history
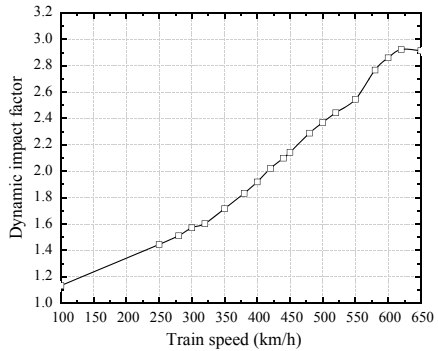
(b) dynamic impact factors

The dynamic impact factor increases rapidly from 1 to 2.9 when the train speed is increased from 0 to 650 km/h, as shown in Fig. 8b.

4   Conclusions

Considering most previous studies related to ground vibrations have been carried out with the traditional ballasted track, a novel 3D coupled train-track-soil interaction model is developed based on MBS principle, FEM theory, and PML method, to investigate the ground vibration responses of high-speed railway with slab tracks. Based on the ground vibration responses, the following conclusions can be drawn:

(a) The high-speed railway with slab tracks exhibits a critical speed of 440 km/h in this study, but the amplification effect of displacement of rail is insignificant at critical speed.

(b) The Mach cone phenomenon is evident in the contours of vibration displacements and velocities of soils at critical speed.

(c) The train-track dynamic interaction forces increase significantly with the train speed.

References

1. Zhai W, Han Z, Chen Z et al (2019) Train–track–bridge dynamic interaction: a state-of-the-art review. Veh Syst Dyn 57(7):984–1027
2. Remennikov AM, Kaewunruen S (2008) A review of loading conditions for railway track structures due to train and track vertical interaction. Struct Control Health Monitoring: The Official Journal of the International Association for Structural Control and Monitoring and of the European Association for the Control of Structures 15(2):207–234
3. Li T, Su Q, Shao K et al (2019) Numerical analysis of vibration responses in high-speed railways considering mud pumping defect. Shock Vibr, Article ID 9707909
4. Connolly DP, Kouroussis G, Laghrouche O et al (2015) Benchmarking railway vibrations—track, vehicle, ground and building effects. Constr Build Mater 92:64–81
5. Kaewunruen S, Martin V (2018) Life cycle assessment of railway ground-borne noise and vibration mitigation methods using geosynthetics, metamaterials and ground improvement. Sustainability 10(10):3753
6. Kaewunruen S, Wang Y, Ngamkhanong C (2018) Derailment-resistant performance of modular composite rail track slabs. Eng Struct 160:1–11
7. Huang H, Chrismer S (2013) Discrete element modeling of ballast settlement under trains moving at "Critical Speeds." Constr Build Mater 38:994–1000
8. Costa PA, Colaço A, Calçada R et al (2015) Critical speed of railway tracks. Detailed and simplified approaches. Transp Geotec 2:30–46
9. Gao Y, Huang H, Ho CL et al (2017) High speed railway track dynamic behavior near critical speed. Soil Dyn Earthq Eng 101:285–294
10. Kouroussis G, Connolly DP, Verlinden O (2014) Railway-induced ground vibrations–a review of vehicle effects. Int J Rail Transp 2(2):69–110
11. Shih JY, Thompson DJ, Zervos A (2017) The influence of soil nonlinear properties on the track/ground vibration induced by trains running on soft ground. Transp Geotech 11:1–16
12. Kouroussis G, Verlinden O, Conti C (2012) Influence of some vehicle and track parameters on the environmental vibrations induced by railway traffic. Veh Syst Dyn 50(4):619–639
13. Kouroussis G, Conti C, Verlinden O (2013) Investigating the influence of soil properties on railway traffic vibration using a numerical model. Veh Syst Dyn 51(3):421–442

14. Olivier B, Connolly DP, Alves Costa P et al (2016) The effect of embankment on high speed rail ground vibrations. Int J Rail Transp 4(4):229–246
15. Li T, Kaewunruen S, Su Q et al (2019) Effects of static and dynamic material properties on vibration responses of slab tracks in high speed railways. In: Acoustics 2019. Proceedings of the Institute of Acoustics, Milton Keynes, UK, pp 246–254
16. Xin T, Wang P, Ding Y (2019) Effect of long-wavelength track irregularities on vehicle dynamic responses. Shock Vibr, Article ID 4178065
17. Wang M, Cai C, Zhu S et al (2017) Experimental study on dynamic performance of typical nonballasted track systems using a full-scale test rig. Proc Inst Mech Eng Part F: J Rail Rapid Transit 231(4):470–481
18. Feng SJ, Zhang XL, Wang L et al (2017) In situ experimental study on high speed train induced ground vibrations with the ballast-less track. Soil Dyn Earthq Eng 102:195–214
19. Kouroussis G, Verlinden O, Conti C (2011) Free field vibrations caused by high-speed lines: measurement and time domain simulation. Soil Dyn Earthq Eng 31(4):692–707
20. Du Kim K, Warnitchai P (2009) Dynamic analysis of three-dimensional bridge–high-speed train interactions using a wheel–rail contact model. Eng Struct 31(12):3090–3106
21. Fujii Y (2004) Simulation of contact loss for trains with high voltage bus cables under DC feeding system. IJTIA 123(5):568–574

Analysis of Contact Stress at Ballast Bed-Soil Subgrade Interface Under Cyclic Loading Based on Coupled DEM-FEM

Junhua Xiao, De Zhang, and Xiao Zhang

Abstract The discrete element method (DEM) and finite element method (FEM) coupling algorithm were introduced into the analysis of interface stress between railway ballast bed and soil subgrade. The point cloud data of irregular shape ballast sample were obtained by 3D-laser scanning. A new particle shape simplification method based on local curvature was proposed to simplify the point cloud and retain the main properties of edges and angularities, which can improve the calculation efficiency in DEM. Then, interface element was established between the interlayer boundaries of ballast bed and subgrade, and consequently the DEM and FEM were dynamically coupled through exchanging the data of forces and velocities between those two layers within each time step. Thus, the DEM-FEM coupling model of ballasted track-subgrade was established, and it had been validated with the indoor model test results measured by tactile sensor. The calculation results were also compared with those got by the earth pressure cell. The results show that: The distribution of contact stress between ballast and subgrade was highly discrete. The average value of interface stress obtained by the tactile sensor and the DEM-FEM coupling model were close, and they were both about two times larger than that measured by the earth pressure cell. According to the result of the coupling model, the high-concentrated interface stress of the subgrade decreased rapidly with the depth. When it was over 0.1 m below the subgrade interface, the interface stress could decay by more than 80%.

Keywords DEM-FEM coupling · Local curvature · Ballast · Subgrade · Contact stress

J. Xiao (✉) · X. Zhang
Shanghai Key Laboratory of Rail Infrastructure Durability and System Safety, Tongji University, Shanghai 201804, China
e-mail: jhxiao@tongji.edu.cn

J. Xiao · D. Zhang · X. Zhang
Key Laboratory of Road and Traffic Engineering of the Ministry of Education, Tongji University, Shanghai 201804, China

D. Zhang
Shanghai Road and Bridge (Group) Co. Ltd, Shanghai 200433, China

1 Introduction

Due to economic and technical limitations in the past, the underlying structure of ballasted tracks, which occupies a fairly large proportion in the old existing ordinary railways of China, consists of a ballast bed of crushed stone and a subgrade bed of fine-grained soil. When the subgrade soil is contact with gravel ballast directly, significant stress concentration on the subgrade surface could be induced in these old ballasted beds without subballast. As a result, some issues of subgrade deterioration emerged, such as settlement, ballast pockets, and mud pumping, which brought unfavorable influences on railway operations. With the growing demand of heavy-haul freight transportation on existing conventional railway lines, the research on the cause and treatment of ballasted railway subgrade defects has become a hot spot in recent years.

It is generally known that interface stress between ballasted and subgrade is formed by the diffusion and transmission of train load through rail, sleeper and ballasted bed. With the increase in train load, interface stress between ballasted bed and subgrade soil may exceed the original design strength of the subgrade. Then, the ballast particles and subgrade soil would intrude into each other, and subgrade surface deformation and progressive damage would occur, thus causing various subgrade defects [1]. One of the main reasons for above phenomenon is the stress concentration caused by the angularity of ballast.

At present, the methods of quantifying interface stress between ballast and subgrade include empirical method based on diffusion angle [2], theoretical analysis method based on Boussinesq formula combined with Odemark theory [3], and dynamic finite element method based on elastic–plastic theory [4], etc. However, none of these methods can reflect the mesoscopic contact behavior of ballast layer. And through the traditional earth pressure cell, the results are only the uniformly distributed stress level in a certain area of subgrade surface and local high stress will be ignored. In order to understand the actual stress conditions of the ballasted railway subgrade as well as investigate the information mechanism of subgrade deterioration more accurately, it is necessary to conduct a refined research by novel testing and simulation methods.

With the development of sensor technology, some researchers have developed new testing technology to obtain more detailed response information of track structure. McHenry [5] introduced a new type of tactile sensor (Tekscan) to measure the contact stress between ballast and sleeper in-situ test, and revealed the discrete distribution of it. Liu [6] measured the contact stress between wooden sleeper and ballast by hydraulic granular material pressure cell. Aikawa [7] used intelligent sleepers with a large number of impact force sensors arranged at the bottom of sleepers to measure the dynamic pressure distribution at the bottom of the sleepers. It can be seen that the testing methods for the railway subgrade and track structure become more refined and intelligent.

The discrete element method (DEM) has been widely used in the study of the mechanical behavior of the interaction between ballast [8]. Indraratna [9] used two-dimensional bonded disk particles by program PFC2D to simulate the breakable

irregular ballast gravels, and studied the accumulated deformation caused by particle breakage of ballast under cyclic load. Based on the real projection profile of ballast particles, Huang [10] and Tutumluer [11] used the three-dimensional visual reconstruction method to generate ballast particles, and established a sample database of considerable number of irregular ballast particle models for DEM simulation. Jan [12] used polyhedron to make a simulation of the ballast compression with irregular shape. Aikawa [7] used the block discrete element software 3DEC to establish a discrete element model of ballast, rail rubber pad, sleeper and subgrade, and they studied the dynamic response of sleeper and ballast by applying sinusoidal load on the rail bearing groove. However, the cost of DEM simulation would be so high if the model is large, which results in difficult in engineering application. Therefore, researchers began to explore coupling methods to solve engineering problems. Shao [13] used discrete element model to simulate discontinuous ballast bed and simulated sleeper, subgrade and foundation by finite element method (FEM), then use the DEM-FEM coupling method to carry out interactive calculation to study the long-term cumulative deformation of sleeper and ballast under train load. Xiao [14] established a DEM-FDM coupling model of sleeper, ballast and subgrade by PFC/FLAC, and analyzed the distribution and attenuation depth of subgrade surface stress.

One main reason for the uneven distribution and stress concentration of the interface stress between ballast and subgrade is the irregular shape of ballast particles. So it is necessary to describe the shape of ballast particles accurately to calculate the interface stress more correctly. Therefore, in this paper, 3D-laser scanning technology was used to obtain the sets of point cloud of real ballast particle shape. And based on local curvature distribution on particle surface, a new simplification method was proposed to reduce the number of contour points of each particle to no more than 31, which could retain the morphological features of particles and improved the efficiency of numerical simulations. A rectangular area under the rail was selected as the research object for indoor model test, and tactile surface sensor was introduced to test the contact stress between railway ballast bed and subgrade. Then, a DEM-FEM coupling algorithm was used to analyze the interface stress.

2 DEM-FEM Coupling Method and Simplification Method of Ballast Particle Shape

In this paper, the soil foundation bed was considered as a continuum medium, which was calculated by the finite element method. Nevertheless, the mechanical behavior of ballast was simulated by the discrete element method. Therefore, the DEM-FEM coupling method was introduced to calculate the contact stress between ballast and soil foundation bed. As shown in Fig. 1, the following was a brief introduction to the coupling method. Firstly, the geometric characteristics of the FEM surface mesh
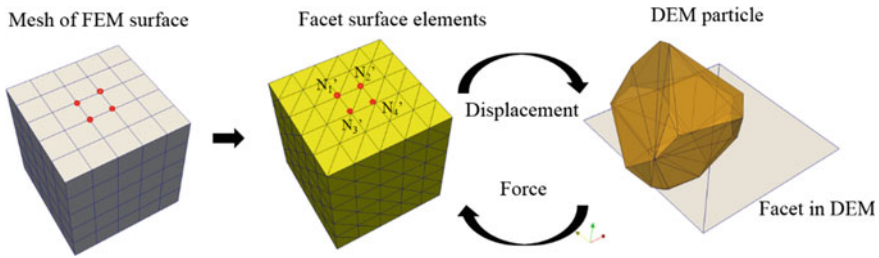
Fig. 1 DEM-FEM coupling principle

element were copied as facet interface elements into the DEM. Then, the displacements of the FEM mesh nodes were transferred to the DEM through the interface elements as the particle boundary condition. At the same time, the interaction forces between the particles and facet interface elements in the DEM were transferred to the FEM as the coupling interface forces, so as to calculate the stress at each point and complete the coupling procedure.

The random irregular shape and non-uniform arrangement of the ballast particles are the main reasons for the "discrete" distribution of the contact stress between the ballast bed and subgrade soil. In this paper, 3D-laser scanning was used to obtain the set of point cloud data of railway ballast particles. The gradation of cleaned ballast sample was controlled according to the regulation for the first-class gravel ballast [15], so that the weight ratio of the gravel particles with the size of 0–16 mm, 16–25 mm, 25–35.5 mm, 35.5–45 mm, 45–45 mm, 56–63 mm can meet the standards, as shown in Fig. 2.

Tutumluer et al. [16] used 45.9 kg ballast particles to carry out large-scale direct shear test. Many researchers [17, 18] used the crushed stone ballast with a mass of about 52–60 kg in the triaxial test for large-scale ballast. Therefore, in order to reduce the cost of scanning and ensure the typical samples of test, 50 kg ballast particles

Fig. 2 Grading curve of ballast 3D laser scanning sample
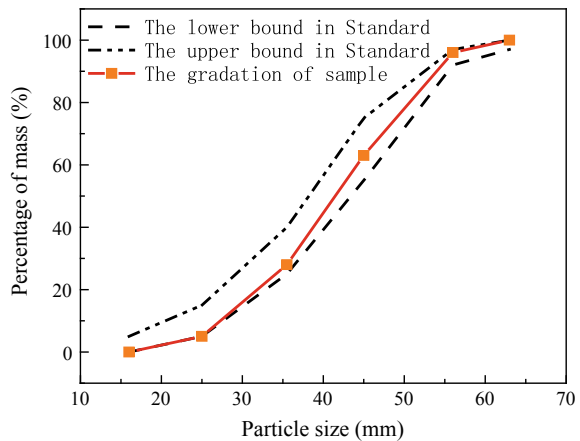
Fig. 3 Partial ballast particles used for scanning and particle scanning process

(584 particles in total) meeting the grading requirements were randomly selected for scanning to obtain the point cloud data. Figure 3 shows the partial ballast particles for scanning.

The point cloud data of 3D scanning particles were very huge, which even contained the grain surface texture information. These costs were extremely high in the DEM simulation. Thus, to improve the efficiency of DEM calculation, the main features of particle edges and angularities should be retained, while the redundant information such as grain surface texture and tiny edge features were eliminated. On the surface of particles, the local curvature at edges and angularities is obviously larger than that at other locations, so it is an effective method to recognize edges and angularities from the particle point cloud by using the local curvature. In order to calculate the local curvature at these points, the surface normal of each point should be determined first, and then the rate of change in normal direction of their neighborhood could be used to characterize the local curvature.

Taking any contour point P as an example, the tangent plane at P is named T and the normal vector is $\vec{v}_0$. According to the principle that the sum of the squares of the distance from adjacent points to T is the smallest, $\vec{v}_0$ can be obtained by weight fitting. The covariance matrix $\mathbf{C}$ and its eigenvalues λ corresponding to T can be written as Eqs. (1) and (2):

$$C = \frac{1}{k} \sum_{i=1}^{k} (P_i - \overline{P})(p_i - \overline{P})^{\mathrm{T}} \tag{1}$$

$$C \cdot \vec{v}_j = \lambda_j \cdot \vec{v}_j, \quad j \in \{0, 1, 2\} \tag{2}$$

where k is the number of adjacent points of P_i (in this paper, $k = 9$). $\overline{P}$ represents the 3D centroid of the nearest neighbor element. λ_j is the jth eigenvalue of covariance matrix. $\vec{v}_j$ is the jth eigenvector. λ_j measures the change of P_i along $\vec{v}_j$ direction. Labeling eigenvalues makes $\lambda_0 \leq \lambda_1 \leq \lambda_2$ so that the plane $T(x)$:$(x - p) \cdot \vec{v}_0 = 0$ can be minimized to the sum of the square distances of the adjacent points around
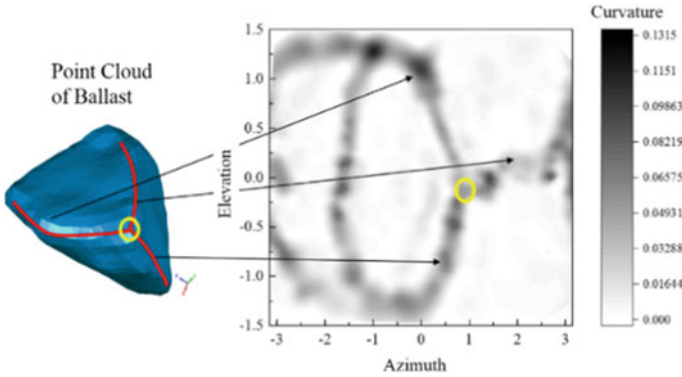
Fig. 4 The correspondence between the morphology and the curvature distribution

P. Therefore, $\vec{v}_0$ is approximately the surface normal at P. In turn, λ_0 quantitatively describes the variation along the surface normal. So, at point P, the local curvature is defined as Eq. (3):

$$\sigma_k(p) = \frac{\lambda_0}{\lambda_0 + \lambda_1 + \lambda_2} \qquad (3)$$

Taking one particle for example, the correspondence between their outline shapes and curvature distributions were shown in Fig. 4. The local curvature distribution of particle surface can be obtained from the two-dimensional plane expansion with azimuth and elevation as horizontal and vertical axes, respectively.

The darker the color, the higher the local curvature of the point valued. The dark continuous strips indicates edges on the surface, corresponding to the area marked by the red lines on the grain, and the intersection of the edges indicates an angularity, corresponding to the area marked by yellow circle. Therefore, it can be concluded that the local curvature and the distribution of discrete points of particle point cloud can effectively describe and identify the edge and angularities characteristics of ballast.

When the local curvature distribution of particles is calculated, the region is divided into $n \times n$ rectangles (this paper sets $n = 5$), and the points with the largest local curvature in each region are retained. The black marked points in Fig. 5a were the points reserved after simplification (only 25 dots were finally selected), and the red marked points in Fig. 5a were 6 axial points corresponding to global morphological features for three axis including long axis, middle axis and short axis [19]. The simplified particles can be obtained by restoring these selected points (31 points) to the 3D spherical coordinate system, as shown in Fig. 5b. Compared with the initial reconstructed particle, the simplified particle omitted the surface texture information, but retained the global and local morphological features. And the number of the contour points of the simplified particle was significantly reduced to no more than 31, therefore the calculation efficiency in DEM could be effectively improved.

(a) Initial ballast particle point cloud

(b) Simplified ballast particle
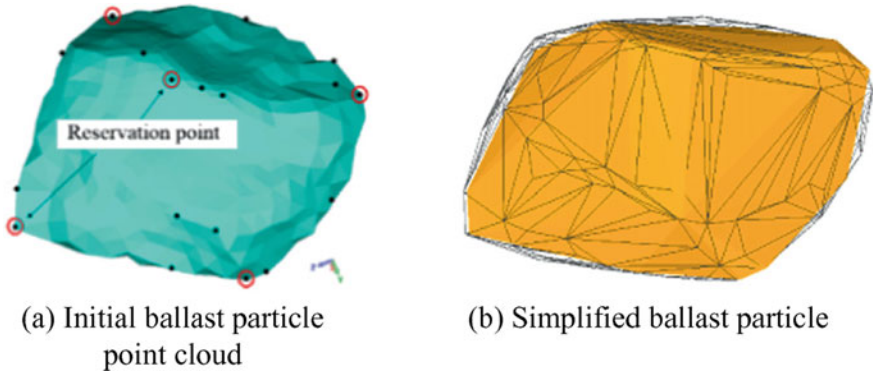
Fig. 5 Initial point cloud of particle and simplified particle shape

3 Laboratory Test and DEM-FEM Coupling Model

Considering that the maximum dynamic stress of subgrade generally appears beneath the rail, a rectangular area of 1.00 m × 0.57 m below the rail was defined in this experiment to study the contact stress between the ballast and subgrade, as shown in Fig. 6a. An indoor model test was carried out and the model box had inner dimensions of 100 × 57 × 100 cm (length × width × height). The Vaseline was smeared on the inner surface of the model box during testing to eliminate the boundary friction effect. The model box was filled with 60-cm thick compacted soil and 35-cm thick ballast bed. A Type III sleeper was used in the test, with a length of 55 cm, a height of 23 cm and a width of 30 cm (see Fig. 6b).

(a) Diagram of study area

(b) Diagram of model test
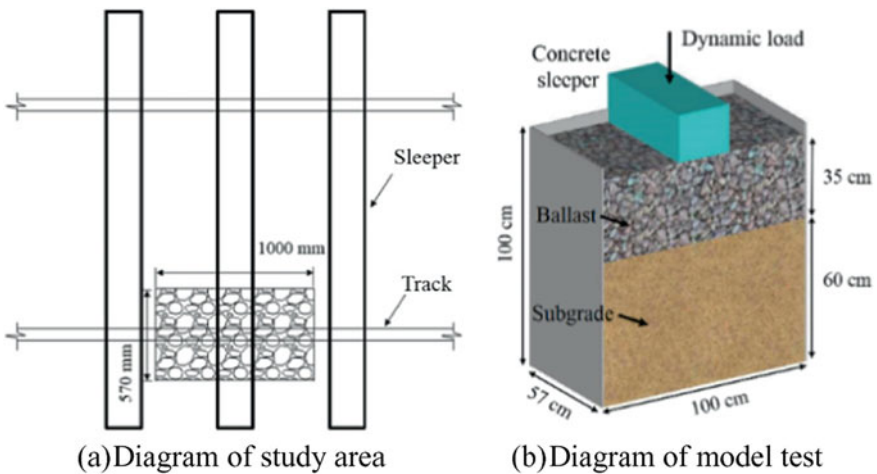
Fig. 6 Diagram of study area and illustration of laboratory model test

Fig. 7 Tactile sensor
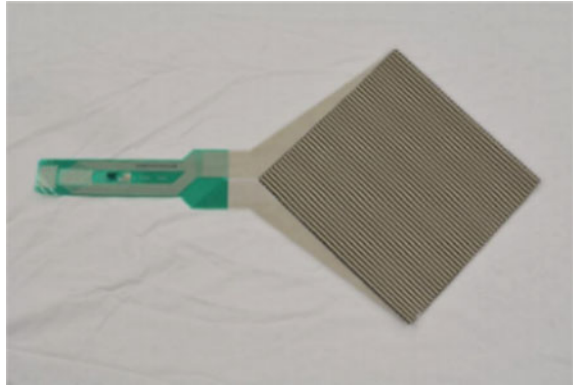
In order to detect the contact stress between ballast and subgrade, the Tekscan tactile sensor with a thickness of 0.1 mm was adopted. The sensor was placed on the interface between ballast and subgrade below the center of sleepers, whose active area was a rectangular area of 24.59 × 24.59 cm in length and width. The sensor was filled with 1,936 pressure-sensitive elements (i.e., 44 × 44 matrices) and the unit test area was 1 cm^2, with maximum test range of 3000 kPa, as shown in Fig. 7.

Cyclic loading was applied to the steel plate fixed onto the upper surface of the sleeper by the actuator of the multichannel electro-hydraulic servo testing system, as shown in Fig. 8a. The load form was a half-sine pulse shape to simulate the repeated train load. Considering the on-site train load conditions and the loading capacity of
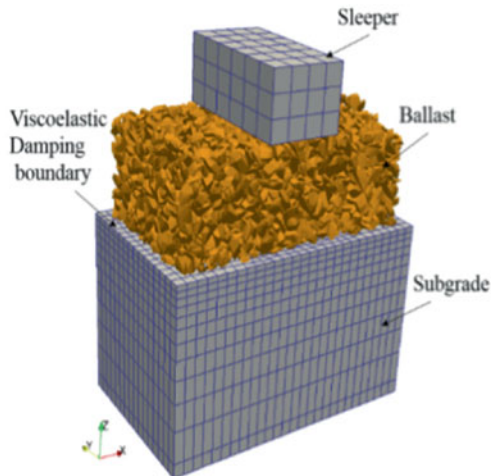
(a) The model test   (b) The DEM-FEM coupling model

Fig. 8 The scene of model test and DEM-FEM coupling model

the electro-hydraulic servo testing system in the laboratory, the loading amplitude was controlled between 3 and 24 kN, which was divided into 7 levels, 3 kN, 6 kN, 9 kN, 12 kN, 15 kN, 18 kN and 21 kN, respectively, and the load frequency was 1 Hz.

Then, according to the laboratory test, the DEM-FEM model was established (see Fig. 8b) to simulate discrete ballast particles and continuum subgrade soil, which was implemented by DEM program Yade [20] and FEM program OOFEM [21]. Polyhedral particles were randomly generated in a 1.0 m × 0.57 m cube with walls composed of facets, which were piled by gravity and compacted by loading plate in layers. On the basis of the 3D-scanning particles, the irregular shapes of ballast were simplified by the simplification method in Sect. 2 and generated in DEM model. The sizes of the sleeper and subgrade were the same as those of the indoor model test. In order to reduce the reflection of stress wave under cyclic loading, the viscoelastic damping boundary with the grid elements (normal stiffness was 1.2×10^8 N/m and damping coefficient was 0.6) of 5-cm thick were set around the model.

In order to capture the peak value of interface stress at ballast-soil interface accurately, the minimum size of the finite element mesh size of the subgrade soil under the sleeper was 1 cm. The mesh size of that gradually increased outside the sleeper width range and the maximum mesh size of the interface layer was 4 cm. The sleeper was simulated with linear elastic material and the material of subgrade soil adopted Drucker-Prager constitutive model. The mesoscopic parameters of the discrete element model and material parameters of each part of finite element model were shown in Tables 1 and 2. The simulations were carried out on the workstation with the operating system environment of Ubuntu 16.04. The processor of this workstation is a dual-core Inter Core i7-8700 CPU @3.20 GHz 3.19 GHz, and the internal memory is 32 GB. A whole loading cycle of this simulation cost 14 h.

Table 1 Mesoscopic parameters of discrete element model of ballast and wall

Mesoscopic parameters	Density ρ/(kg m^{-3})	Normal volumetric stiffness k_n/(N m^{-3})	Shear stiffness k_s/(N m^{-3})	Friction coefficient	Damping coefficient c	Time-stepping Δt/(step s^{-1})
Ballast	2680	1.82×10^{10}	1.6×10^{10}	0.65	0.3	1×10^{-6}
Surrounding wall	2680	1.82×10^{10}	1.5×10^{10}	0.2		
Bottom wall	1950	1.2×10^8	4.0×10^7	0.5		

Table 2 Material parameters of sleeper and subgrade

Material parameters	Density ρ/(kg m^{-3})	Modulus E/Pa	Poisson's ratio μ	Friction coefficient	Damping coefficient c	Time-stepping Δt/(step s^{-1})
Sleeper	2500	3.0×10^{10}	0.20	0.5	0.03	1×10^{-6}
Subgrade	1950	1.2×10^8	0.33	0.23	0.3	

4   Analysis of Contact Stress Between Ballast and Subgrade

Figure 9a, b showed the contact stress at the interface between ballast and soil subgrade from the model test result and the coupling model calculation under the condition of dynamic load amplitude of 21 kN and load frequency of 1 Hz. From the results, it can be seen that the measured and calculated interface contact stresses were both in discrete distribution. The maximum contact stress in the rectangular area tested by the tactile sensor in the indoor test was 1476.9 kPa, whereas the maximum contact stress calculated by the coupling model was 1752 kPa, which also occurred in the area beneath the sleeper.

At the same time, the traditional test method by earth pressure cell was also used in this paper to compare the test results of tactile sensor and from the coupling model. The resistance strain type earth pressure cell with a diameter of 10 cm and a thickness of 2 cm was selected and placed at the interface between the ballasted layer and the soil subgrade, which was also directly below the sleeper for testing. The test result of the earth pressure cell was the average stress of the single point force in the test area. Hence, the interface stress results (as shown in Fig. 10a, b) in the approximate area (9 × 9 cm) of tactile sensor and the coupling model were selected, and the average values were compared with the test result of the traditional earth pressure cell, as shown in Table 3.

The average interface stress results in the test area (9 cm × 9 cm) calculated by coupling model and measured by tactile sensor were compared with the results of the earth pressure cell (The results are shown in Table 3). It can be seen that the average value of the interface stress calculated by the coupling model was close to that measured by the tactile sensor, which were more than two times larger than that measured by the earth pressure cell. Therefore, it indicated that the dispersion and irregular shapes of the ballast particles in the ballast bed would cause greater stress concentration.

According to the coupling model, the results of several large interface stress (6 points) varying with the depth of subgrade were shown in Fig. 11a. It can be seen that

(a) Results of tactile sensor   (b) Results of DEM-FEM coupling model
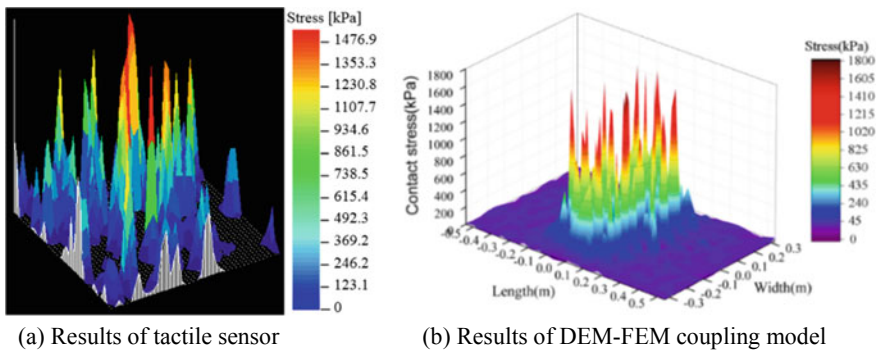
Fig. 9 Results of surface stress measured by tactile sensor and calculated by coupling model

(a) Results of tactile sensor

(b) Results of coupling model
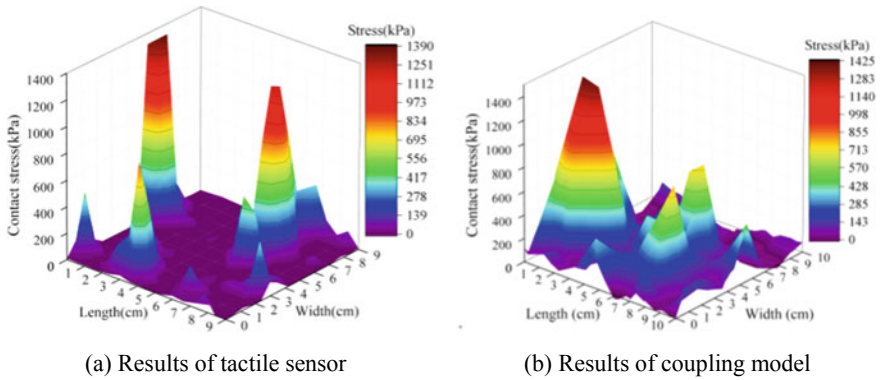
Fig. 10 Results surface stress measured by tactile sensor and calculated by coupling model in the range of 9 × 9 cm

Table 3 Comparison of test results of tactile sensor, coupling model and earth pressure cell

Test or model calculation	Average value of interface stress (kPa)
Tactile sensor	98.6
Coupling model	116.6
Earth pressure cell	47

(a) Stress varying with subgrade depth

(b) Stress distribution of subgrade at 0.1m depth
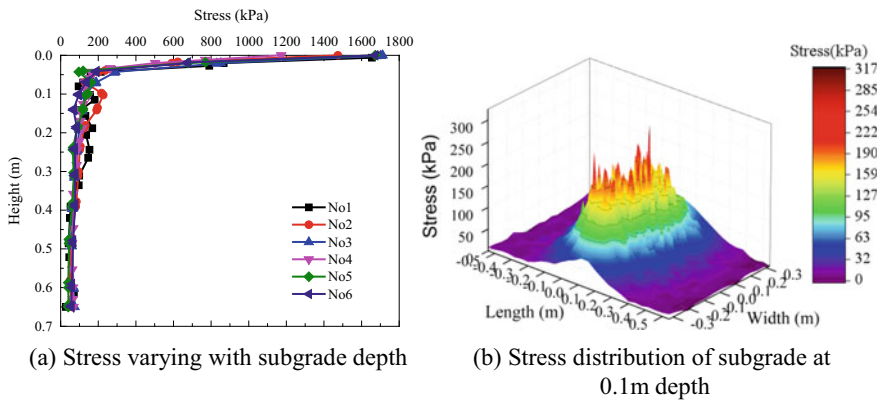
Fig. 11 The results of stress varying with the subgrade stress

when it was over 0.1 m below the subgrade interface, the interface stress basically decreased by more than 80%. Figure 11b showed the calculation results of subgrade bed stress at the depth of 0.1 m, the stress distribution of subgrade became more uniform than that of interface, and the dispersion of stress distribution of subgrade was significantly reduced.

5 Conclusion

In this paper, considering the dispersion of ballast particles and the characteristics of irregular edges and angularities, the DEM-FEM coupling method was introduced to calculate the interface stress between ballast particles and subgrade soil. Then, the indoor model tests of ballast and subgrade were carried out. The new tactile sensor was used to measure the interface stress between ballast and the subgrade. The interface stress results obtained by the coupling model and the tactile sensor were also compared with those measured by the earth pressure cell. The main conclusions were as follows:

- The local curvature of particles could be effectively used to identify the features of particle edges and angularities. According to the local curvature, it could not only simplify the scanned particle point cloud, but could also retain the morphological features of the particle, which could improve the calculation efficiency in DEM.
- The distribution of contact stress between ballast and subgrade was highly discrete, and there was an obvious stress concentration phenomenon. The average values of interface stress obtained by the tactile sensor and the DEM-FEM coupling model were similar, and they were both about two times larger than that measured by the earth pressure cell.
- According to the result of the coupling model, the high-concentrated interface stress of subgrade decreased rapidly with depth. When it was over 0.1 m below the subgrade interface, the interface stress could decay by more than 80%.

Therefore, it is necessary to take certain measures to improve the contact state of the ballast particles with the subgrade surface, such as laying the subballast between the ballast and subgrade layers, in order to reduce the contact stresses.

References

1. Duong TV, Cui YJ, Tang AM, Dupla JC, Canou J, Calon N, Robinet A (2014) Investigating the mud pumping and interlayer creation phenomena in railway substructure. Eng Geol 171:45–48
2. Liu G, Luo Q, Zhang L, Jiang LW (2015) Analysis of the design load on the high-speed railway ballasted track subgrade. J Railway Sci Eng 12(03):475–481
3. Han ZL, Zhang QL (2005) Dynamic stress analysis on speed-increase subgrade of existing railway. China Railway Sci 26(5):1–5
4. Xiao JH, Guo PF, Zhou SH (2016) Dynamic stability of existing railway subgrade under the effect of heavy axle load trains. J Tongji Univ (Nat Sci) 44(6):884–891
5. Mchenry MT, Brown M, Lopresti J, Rose J, Souleyrette RR (2015) Use of matrix-based tactile surface sensors to assess fine-scale ballast–tie interface pressure distribution in railroad track. Transp Res Record J Transp Res Board 2476(2476):23–31
6. Liu Q, Lei X, Rose JG, Purcell ML (2017) Pressure measurements at the tie-ballast interface in railroad tracks using granular material pressure cells. In: Proceeding of the 2017 Joint Rail Conference. ASME, Philadelphia, pp 1–9
7. Aikawa A (2015) Dynamic characterisation of a ballast layer subject to traffic impact loads using three-dimensional sensing stones and a special sensing sleeper. Constr Build Mater 92:23–30

8. Lu M, Mcdowell GR (2007) The importance of modelling ballast particle shape in the discrete element method. Granular Matter 9(1/2):69–80
9. Ngo NT, Indraratna B, Rujikiatkamjorn C (2014) DEM simulation of the behaviour of geogrid stabilised ballast fouled with coal. Comput Geotech 55(1):224–231
10. Huang H, Tutumluer E (2014) Image-Aided element shape generation method in discrete-element modeling for railroad ballast. J Mater Civ Eng 26(3):527–535
11. Tutumluer E, Huang H, Hashash YMA (2006) Aggregate shape effects on ballast tamping and railroad track lateral stability. In: AREMA conference, USA, pp 1–23
12. Eliáš J (2014) Simulation of railway ballast using crushable polyhedral particles. Powder Technol 264(264):458–465
13. Shao S, Yan Y, Ji S (2017) Combined discrete-finite element modeling of ballasted railway track under cyclic loading. Int J Comput Methods 14(5), 1750047-1-1750047-18
14. Xiao JH, Zhang D, Wang YH, Guo JQ (2018) Study on interface stress between ballast and subgrade for traditional railway based on coupled DEM-FDM. Eng Mech 35(9):170–179
15. Railway Ballast, TB/T 2140-2008. Ministry of Railway, Beijing
16. Huang H, Tutumluer E (2011) Discrete element modeling for fouled railroad ballast. Constr Build Mater 25(8):3306–3312
17. Suiker AS, Selig ET, Frenkel R (2005) Static and cyclic triaxial testing of ballast and subballast. J Geotech Geoenviron Eng 131(6):771–782
18. Indraratna B, Thakur PK, Vinod JS (2010) Experimental and numerical study of railway ballast behavior under cyclic loading. Int J Geomech 10(4):136–144
19. Xiao JH, Zhang X, Zhang D, Xue LH, Sun SQ, Stránský J, Wang YH (2020) Morphological reconstruction method of irregular shaped ballast particles and application in numerical simulation of ballasted track. Transp Geotech 24, 100374-1-12
20. Smilauer V, Catalano E, Chareyre B, Dorofeenko S (2012) Yade documentation, 2nd edn. http://yade-dem.org/doc/. The Yade Project
21. Patzak B, Bittnar Z (2001) Design of object oriented finite element code. Adv Eng Softw 32(10–11):759–767

Mud Pumping in Ballastless Slab Track of High-Speed Railway and Its Remediation

Zhangbo Wan, Shuhao Li, Xuecheng Bian, and Yunmin Chen

Abstract Mud pumping is an increasing subgrade distress in ballastless slab track of high-speed railway, which heavily affects the driving comfort and even threatens the driving safety. However, the existing researches mostly focused on the water-induced distress in ballasted railway, and little attention was paid on the mud pumping in ballastless slab track. In this paper, both in-situ investigation and discussion of the conventional grouting remediation method were carried out. It can be observed that mud pumping mainly occurred at the expansion joint located at the ends of concrete base and then expanded to both sides of the expansion joint from 1–2 m. The defects in railway structure and the standing water stored in the roadbed layer were the two main factors contributing to mud pumping. In addition, based on the traditional chemical glue injection (CGI) remediation method (the shallow grouting repair method), a modified polyurethane grouting remediation method (the deep grouting repair method) was put forward to treat mud pumping in ballastless slab track.

Keywords Mud pumping · Ballastless slab track · High-speed railway · In-situ investigation · Polyurethane grouting remediation method

Z. Wan · S. Li · X. Bian (✉) · Y. Chen
Department of Civil Engineering, MOE Key Laboratory of Soft Soils and Geo-Environmental Engineering, Zhejiang University, Hangzhou 310058, China
e-mail: bianxc@zju.edu.cn

Z. Wan
e-mail: zhangbowan@zju.edu.cn

S. Li
e-mail: lish@zju.edu.cn

Y. Chen
e-mail: chenyunmin@zju.edu.cn

363

1 Introduction

As a major mean of transportation in modern society, high-speed railway characterized by high speed and better safety provides fast and convenient services to transport both passengers and freights. Meanwhile, it also plays an increasingly leading role in economic development. As of October 1, 2019, the total mileages of high-speed railway in operation of the world had reached 47,560 km, of which the total mileages in China were as high as 31,043 km, accounting for 65.27% (latest data from UIC in 2019). As known to us all, the countries of the world are located in different regions, and the regional climatic conditions are diverse and complex. High speed, long mileage, and area-crossing are the main characteristics of ballastless slab track, therefore, as the main means of transportation connecting two and more cities, it will inevitably cross rainfall-intensive areas. In addition, the human activities are not so friendly, therefore, it will cause a large amount of damage to our environment, which results in continuous deterioration of the natural environment, and finally extreme precipitation occurs frequently. On the other hand, the drainage system of the railway was basically set for the surface drainage, and the infiltrated water into the roadbed and subgrade layer cannot be effectively drained, thereby, it was stored and finally formed the standing water at the interface, which eroded, softened and split the subgrade, and finally weakened the stiffness of roadbed and subgrade layer. Under the coupling action of train loads and precipitation, uneven settlement, mud pumping, and other subgrade distresses occurred more frequently. With the increasing need of train speed and axle load, the subgrade will further deteriorate, which threatens the driving safety of the railway lines.

Among all the subgrade distresses, mud pumping characterized by the upward migration of subgrade fine particles into ballast or roadbed layer was the most common one and was difficult to treat. Meanwhile, it has been commonly recognized in the highway, railway, and airfield pavements context [1–6]. Mud pumping was first academically defined in 1948 on the meeting of "Maintenance of concrete pavement as related to the pumping action of soil," which was defined as the ejection of water and subgrade soil through joints, cracks, and along the edges of pavements caused by downward actuated by the passage of heavy axle loads over the pavement after the accumulation of free water on or in the subgrade [1, 7]. As to the treatments for mud pumping, the traditional methods was to set geogrid-reinforced materials between ballast and subballast layer to prevent the further deterioration of track performance caused by mud pumping or fouled ballast, and the replacement of muddy ballast with fresh ballast also was used in serious mud pumping conditions [8]. Recently, polyurethane grouting method was adapted to treat the relative distresses caused by mud pumping. However, most of the researches and remediation methods mainly focused on mud pumping in ballasted railway [9]. The full-scale physical model was a very important means to study the subgrade distresses in high-speed railway. Based on the full-scale physical model testing apparatus, Bian and Jiang [10, 11] studied the dynamic characteristics of track structure after settlement remediation of ballastless slab track and the effects on the cumulative settlement of the track structure and the

dynamic stress of the subgrade as the water level of subgrade changes, showing that the polymer injection worked quite well in subgrade settlement remediation.

Unlike the conventional ballasted railway, ballastless slab track was a new type of track structure in high-speed railway. Therefore, in this paper, the in-situ investigation on mud pumping distress in ballastless slab track was conducted, and the two main affecting factors of mud pumping were put forward. In addition, a discussion of the traditional grouting remediation method was carried out. Based on the traditional shallow grouting repair method, a modified polyurethane grouting repair method (the deep grouting repair method) was put forward to treat mud pumping in ballastless slab track.

2 Mud Pumping in High-Speed Railway

2.1 Mud Pumping in Ballasted High-Speed Railway

As for ancient ballasted railway, ballast layer was directly laid on the subgrade layer, and under the action of train loads, an interlayer was naturally formed because of the inter-penetration of ballast and subgrade soil. In addition, in heavily rainy days, water infiltrated into the ballast layer and stored at the interlayer and finally formed the standing water. Under the coupling action of high-frequency dynamic train loads and the retained standing water, large numbers of fine particles migrated up into the ballast layer, which led to the formation of fouled ballast, and finally, mud pumping occurred with the continuous deterioration of subgrade. As is shown in Fig. 1, mud pumping can be considered as the final distress state of ballast fouling due to continuous deterioration of subgrade.

Fouled ballast caused hardening of ballast layer, which heavily affected the dynamic performance of track structure. Therefore, a 60 cm new layer called subballast layer was set between ballast and subgrade layer in ballasted high-speed railway
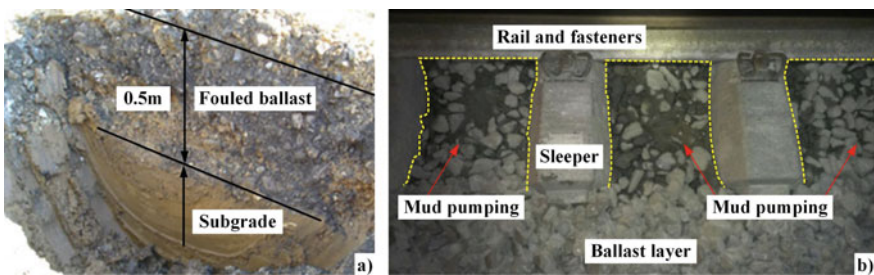
Fig. 1 Different kinds of subgrade distresses in ballasted railway: **a** geological section of fouled ballast [5]; **b** typical mud pumping [6]

so as to avoid the development of ballast fouling. Subballast layer effectively alleviated subgrade distresses to a certain degree; however, mud pumping still occurred for the increasing need of train speed and train capacity, meanwhile, the extreme precipitation also occurred frequently. A strict controlling of fine particles content in subballast layer and the compaction of subgrade layer will be a better means for treating mud pumping.

2.2 Mud Pumping in Ballastless High-Speed Railway

Ballastless high-speed railway was first built in Japan but highly developed all over the world, particularly in China. There are five main types of ballastless track in China, which are the CRTS-I, CRTS-II, CRTS-III slab track and CRTS-I, CRTS-II twin-block track (CRTS is short for China Railway Track System). As the economy in southeast coast area of China was highly developed, therefore, many high-speed railway lines were built in these areas (see Fig. 2, areas enclosed by yellow dotted line), most of which are ballastless high-speed railway, as is shown in Fig. 2b). Meanwhile, the shortest departure interval can reach less than 5 min, showing a busy railway traffic of ballastless track. In addition, precipitation was also abundant in those area. According to the precipitation statistics of the China Meteorological Administration in the past 30 years (1981–2010), it can be revealed that the intensive-precipitation areas mainly located in southeast coast area of China, and the maximum annual precipitation could reach as high as 3000 mm (Fig. 2a).

According to the latest investigation on subgrade distresses of the local railway administration in eastern coast area of China, mud pumping was the main distress suffered by the ballastless slab track. In April 2017, an in-situ investigation on mud pumping was conducted on a ballastless CRTS-I slab track of high-speed railway in eastern coast area of China. It can be found that mud pumping mainly occurred at
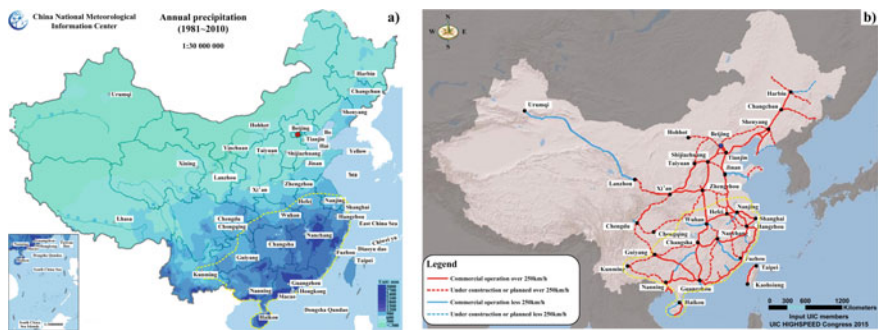
Fig. 2 **a** Annual precipitation of China from 1981 to 2010 (from China National Meteorological Information Center, 2019); **b** commercial operation and under construction or the planned high-speed railways of China in 2015 (from UIC, 2019)
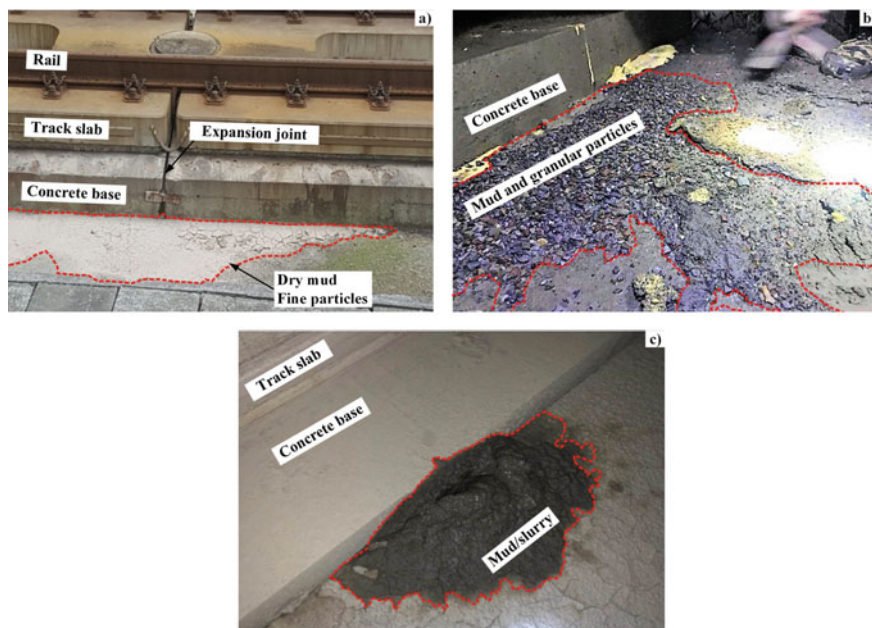
Fig. 3 Three main forms of mud pumping in ballastless slab track: **a** the typical mud pumping; **b** mud pumping with pumped-out granular particles (in serious conditions); **c** re-mud pumping

the expansion joint located at the end of concrete base, and gradually expanded to both sides of the expansion joint from 1 to 2 m. However, in the middle of concrete base, little and even no mud pumping occurred. After mud pumping occurred, large numbers of fine particles were pumped out and then accumulated around the expansion joint, as is shown in Fig. 3a, which showed the typical form of mud pumping in ballast track. In more serious precipitation conditions, part of coarse particles also can be pumped out, resulting in void areas under the concrete base (Fig. 3b). As the mixture of soil–water cannot be pumped out in a short time, the re-mud pumping even occurred frequently (Fig. 3c). The above cases were the three typical forms of mud pumping in ballastless slab track of high-speed railway.

Based on the existed researches on mud pumping in ballasted railway and the in-situ investigation on mud pumping in ballastless slab track, it can be observed that there are two main affecting factors that lead to mud pumping in ballastless slab track. One is the structure defects in concrete base. The existed expansion joint can lead to the free infiltration of rainwater and the higher vibration at the end of concrete base, which in turn further accelerates the infiltration speed of rainwater and the vibration of track structure. The other one is the standing water stored in the roadbed layer. The infiltrated rainwater was retained in the roadbed layer for the lower permeability of the naturally formed interface. Under the action of high frequency of dynamic train loads, fine particles and rainwater are mixed and finally pumped out to form mud pumping.

3 Remediation of Mud Pumping in Ballastless Slab Track of High-Speed Railway

For fouled ballast and mud pumping in ballasted railway, ballast stabilization was used to treat such kinds of subgrade distresses. Gundavaram [9] summarized three typical forms of polyurethane-based stabilization, namely XiTRACK, elastotrack, and polyurethane stabilized ballast, as is shown in Fig. 4.

This kind of polyurethane grouting method can also be borrowed to treat mud pumping in ballastless slab track of high-speed railway. Figure 5 shows the traditional chemical glue injection (CGI) remediation method in ballastless slab track. Two components are mixed and then grouted into the surface of roadbed layer to form a very thin polyurethane layer to prevent the continuous infiltration of rainwater.

However, this kind of remediation method was just the shallow injecting method, it can effectively improve the supporting condition of roadbed layer, and meanwhile prevent the deterioration of mud pumping to a certain degree. Unfortunately, there are still some defects that affected the long-term service performance of the remediation. Firstly, the grouting apparatus was too simple to accurately and completely mix the two components; secondly, the grouting pipes were randomly and densely distributed around the expansion joint, and some of the grouting pipes can be easily forgot to inject; thirdly, the grouting pressure was less than 0.3 MPa so as to avoid
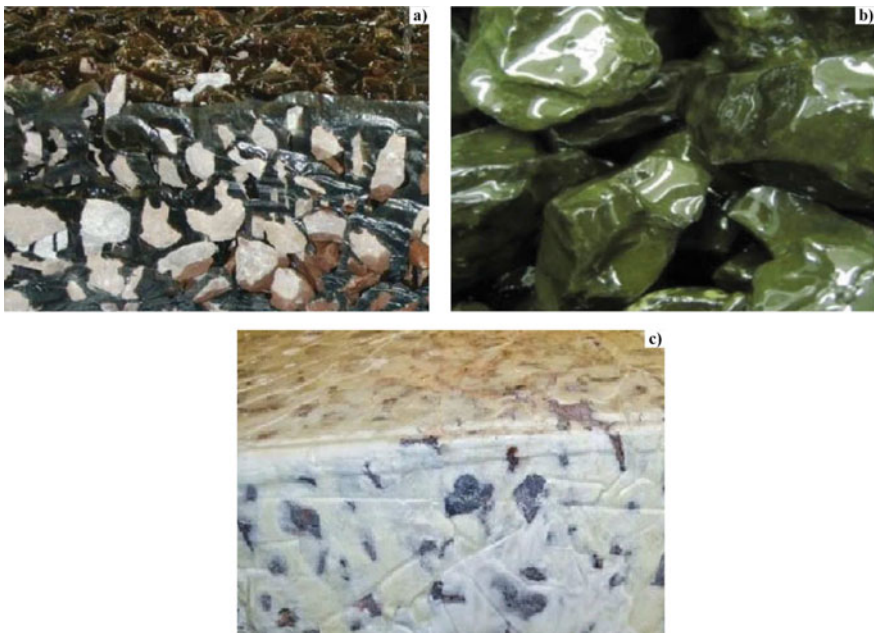
Fig. 4 Three main typical types of polyurethane-based stabilization: **a** XiTRACK; **b** Elastotrack-stabilized ballast; **c** polyurethane-stabilized ballast [9]
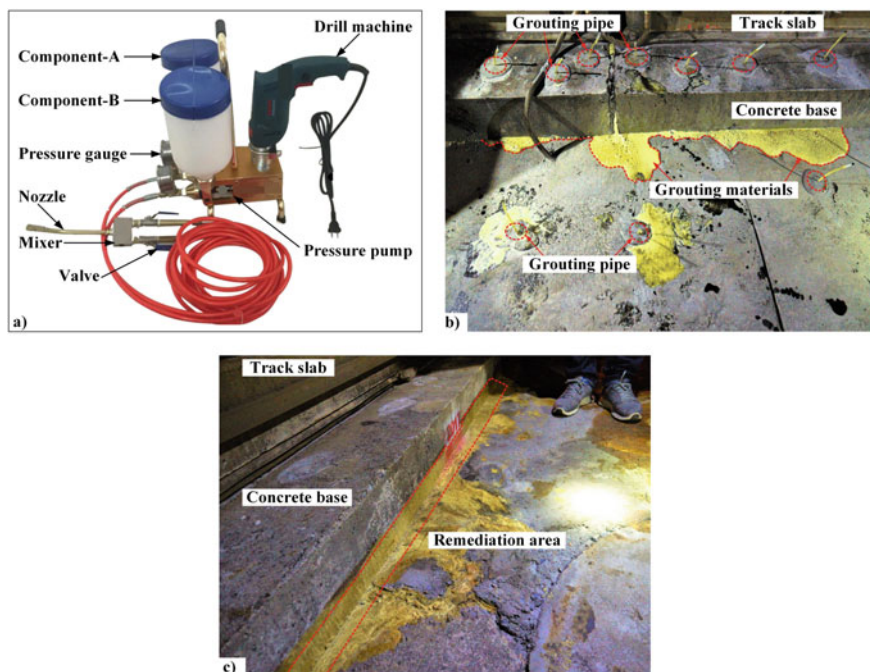
Fig. 5 Chemical glue injection (GUI) remediation method in ballastless slab track: **a** the grouting apparatus; **b** in-situ chemical grouting; **c** after remediation

over-uplift of the upper structure; therefore, the diffusion radius of the grouting materials was very limited. Therefore, the void between coarse particles and void areas under the concrete base was difficult to be completely filled. Meanwhile, the rainwater infiltration paths (expansion joint and side cracks) was left unsealed after CGI remediation, letting the thin polyurethane layer directly expose to rainwater, which further decreased the long-term performance of the grouting materials.

Having understood the leading formation causes of mud pumping, and based on the knowledge of polyurethane grouting in highway [12], a modified polyurethane grouting remediation method was put forward, which was a deep grouting repair method. As is shown in Fig. 6a, grouting holes are distributed around the expansion joint where mud pumping occurred. There are three rounds of chemical grouting. The first round of grouting can be used to drain the inner standing water, and the second round is to fill the void areas under the concrete base, and finally, the third round is left as auxiliary grouting for serious mud pumping conditions. Figure 6b shows the relative positions of grouting pipes, which can reach to the bottom of roadbed layer at an angle of 30–60°. During the grouting process, layered grouting and multiple-times grouting are used to ensure the fully filling of mud pumping areas at a relative high grouting pressure (the maximum pressure can reach to 3.0 MPa, ten times than that in CGI method). In addition, the water infiltration paths (the expansion joint and
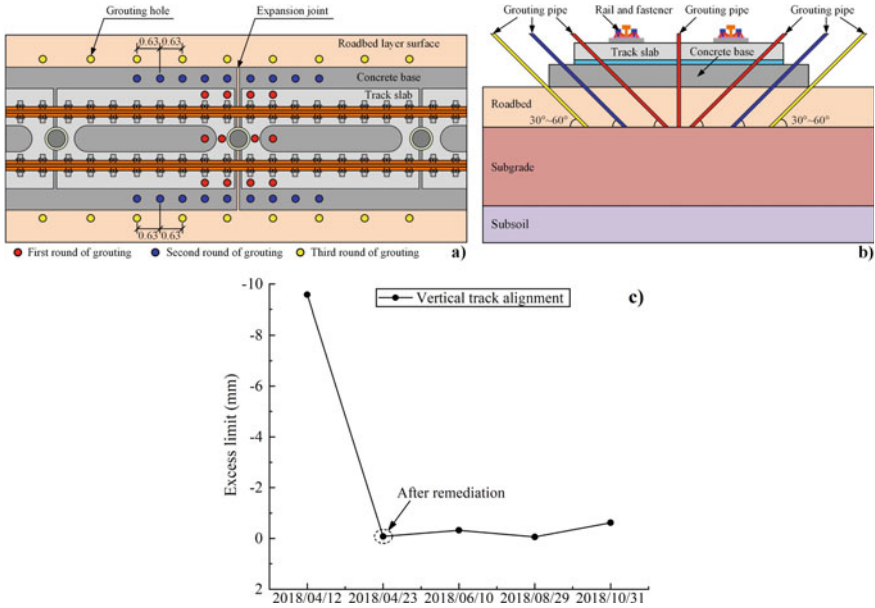
Fig. 6 Modified polyurethane grouting remediation method in ballastless slab track: **a** layouts of the grouting holes (unit: m); **b** relative positions of grouting pipes; **c** vertical track alignment before and after remediation

side cracks) is sealed with special sealant to prevent the continuous infiltration of rainwater, after the polyurethane grouting. This kind of deep grouting remediation was used in the in-situ grouting test, and Fig. 6c shows the vertical track alignment before and after modified polyurethane remediation, which indicated that this kind of deep grouting remediation method worked very well.

4 Conclusions

Mud pumping is an increasing subgrade distress both in ballasted and ballastless tracks. Compared to conventional ballasted railway, ballastless slab track is a new type of track structure in high-speed railways. Therefore, based on the in-situ distresses investigation and discussions on traditional grouting remediation method, the following conclusions may be made:

1. Mud pumping mainly occurred at the expansion joints located at the end of concrete base and then gradually expanded to both sides of the expansion joint from one to two meters.
2. The defects in the railway structure and the standing water stored in the roadbed layer were the two main factors affecting the formation of mud pumping.

3.   A modified polyurethane grouting remediation method was put forward for treating mud pumping in ballastless slab track.

References

1. Yoder EJ (1957) Pumping of highway and airfield pavements. Technical paper, Joint Highway Research Project. Purdue University, USA
2. Alobaidi I, Hoare DJ (1994) Factors affecting the pumping of fines at the subgrade subbase interface of highway pavements: a laboratory study. Geosynth Int 1(2):221–259
3. Duong TV, Cui YJ et al (2014) Physical model for studying the migration of fine particles in the railway substructure. Geotech Test J 37(5):895–906
4. Duong TV, Cui YJ et al (2014) Investigating the mud pumping and interlayer creation phenomena in railway sub-structure. Eng Geol 171:45–58
5. Cui YJ, Duong TV, Tang AM et al (2013) Investigation of the hydro-mechanical behavior of fouled ballast. J Zhejiang Univ Sci A (Appl Phys Eng) 14(4):244–255
6. Mehran S, Lu T et al (2020) Railway track degradation: the contribution of a spatially variant support stiffness-global variation. J Sound Vibr 464
7. Vogelgesang CE (1952) Effectiveness of granular bases for preventing pumping of rigid pavements. Highway Res Board Bull
8. Nakamura T et al (2014) Development of railway roadbed improvement method for existing lines by reusing deteriorated ballast. Quarterly Report of RTRI, vol 55, No. 1, pp 46–50
9. Gundavaram D, Hussaini SKK (2019) Polyurethane-based stabilization of railroad ballast–a critical review. Int J Rail Transp 7(3):219–240
10. Bian XC, Cheng C et al (2014) Experimental study on dynamic performance and long-term durability of high-speed railway subgrade rehabilitated by polymer injection technology. Chinese J Geotech Eng 36(3):562–568 (in Chinese)
11. Jiang HG, Bian XC et al (2015) Impact of water level rise on the behaviors of railway track structure and substructure full-scale experimental investigation. Transp Res Rec 15–22
12. Wei Y, Wang F, Gao X et al (2017) Microstructure and fatigue performance of polyurethane grout materials under compression. J Mater Civil Eng 29(9)

Geotechnical and Geophysical Railway Embankment Auscultation

Amine Dhemaied [iD], Robin Heraibi, Marine Dangeard, and Ludovic Bodet

Abstract As part of the understanding of the phenomena affecting tracks geometry on the Northern Europe high-speed line (LGV-Nord), a study was carried out on an area with occasional maintenance efforts. The goal is to identify the causes of structural disorders on railway embankment (RE). To better understand the origins of these issues, geotechnical characterization and bender elements (BE) tests were performed in the laboratory on soils collected on the field. Measurements of water content, density, and Atterberg limits cannot explain the anomalies observed along the tracks. However, when it comes to mechanical properties and more precisely to shear wave velocities (VS), we can clearly see strong contrasts between areas where the phenomena were observed and where it was not. Thus, VS obtained with BE tests seems to be a good indicator of the quality of soils constituting the RE. At the site scale, surface-wave methods were identified as a possible tool to estimate the mechanical properties of the RE. In this context, we dimensioned and designed specific acquisition setups. To estimate 1D profiles of shear wave velocities, we performed many tests to show the robustness of this method, when inversions are constrained by railway a priori. Those tests allowed us to determine the geometry of the platforms and to characterize the VS of the supporting soil. These results show a difference between the sections of RE with disorders and those without. The reliability of these results is also highlighted since they coincide with geotechnical data.

Keywords Railway embankment · Mechanical characterization · Geotechnical methods · Inverse problem · Seismic surface waves

A. Dhemaied (✉) · R. Heraibi · M. Dangeard
SNCF Réseau, 93574 La Plaine Saint-Denis Cedex, France
e-mail: amine.dhemaied@reseau.sncf.fr

R. Heraibi · M. Dangeard · L. Bodet
UMR 7619 METIS, Sorbonne Université, CNRS, EPHE, 75252 Cedex 05 Paris, France

1 Introduction

Railway embankments (RE) consist of several layers of thick materials constituting a base for the railway structure. The quality of the RE base is an important factor in deciding whether to regenerate this structure. This quality, bearing capacity, mainly depends on the mechanical properties of the materials constituting these structures and the soil support. Usually, we use conventional geotechnical and geophysical techniques: geotechnical soundings, coring, ground penetrating radar (GPR), etc. Some of these techniques are local, destructive, expensive, and with low yields. The non-destructive investigation techniques widely used for local diagnosis and monitoring are for great interest for enhancing the control of railway embankments. Ground penetrating radar is, for instance, used for the auscultation of the surface layers [1] but does not assess the mechanical properties of RE. This technique, widely used in low attenuating medium, suffers from its great sensitivity to metal components and conductive media (e.g., clay) and from three-dimensional (3D) effects due to local geometry. To characterize the RE, we also use micro-gravimetry to locate cavities and/or poorly compacted areas [2], but they also do not provide information about the mechanical properties of soils. In recent years, we have been developing a methodology based on the exploitation of the dispersion of surface waves.

Following the discovery of a disturbed area on the Northern Europe high-speed line (LGV-Nord), a geotechnical investigation mission was carried out. In order to provide some answers to the origins of these issues, geotechnical characterization and bender elements (BE) tests were performed in the laboratory on soils samples collected on the field. Seismic methods have also been proposed to estimate in situ mechanical parameters of near-surface layers (compression and shear moduli) below railway, with sufficient resolution while maintaining high yields in terms of auscultated linear. Seismic data sets aim to better define the characterization of the structural and mechanical properties of the layers above the track. The specific railway context, presence of 3D structures or velocity inversion, or difficulty in identifying the first arrivals because of the low signal to noise ratio, especially for S-wave studies, can limit the applicability of classical seismic methods for the characterization of RE.

As an alternative to shear-wave refraction seismic, surface-wave methods are now classically suggested (e.g., [3–5]). Surface-wave prospecting is less sensitive to strong 3D character of the structures usually encountered in civil engineering [6]. In addition, recent studies show an increasing interest for the use of surface-wave methods as a complement for geotechnical issues [7], even in railway context [8, 9].

2 Context

The track geometry on the Northern Europe high-speed line (LGV) showed a significant deterioration during the passage of the measurement trains. This degradation,
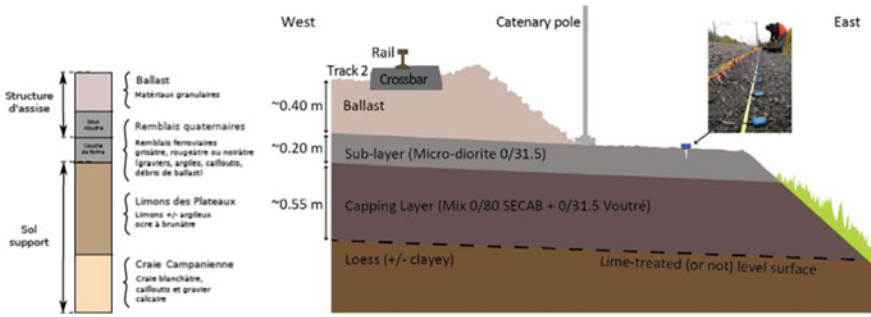
Fig. 1 Railway embankment corresponding to the LGV standards. Seismic devices used along the track for surface-wave acquisitions

more pronounced in track 2, is not linked to a fault in the track components but probably to a degradation of the platform and/or a faulty drainage system. To precisely identify the origin of this disorder, geological and geotechnical surveys have been proposed [10]. It showed that the structure of the platform is composed of backfilled loess mainly originating from the creation of the RE (less than 1 m thick); loess is characterized by beige silt with more clayey interval sand and Campanian chalk and whitish with low flint content, containing thin glauconitic intervals. As for the RE, it lies on the loess (the first cited layer) and presents the typical LGV structure (Fig. 1).

Eight core drilling, reaching 3 and 12 m deep (numbered SC1 to SC8), and five cone penetrometer tests (numbered PD 1 to PD 5), down to 12 m depth, were performed along the rail track. These field tests were supplemented by laboratory measurements of water content, Atterberg limits, methylene blue test, density, grain size distribution curve, and compressive strength on samples of core drillings. The results [10] don't identify any variation in the properties of the layers under ballast. The sub-ballast and capping layers appear more compact than the underlying loess. The latter is less compacted than the chalk located between 6 and 7 m deeper. Water content and density values are the same in loess for the different core drilling samples for different lateral positions and depths. Geotechnical tests show no significant variability in the structure of the RE along track 2, between the two tracks. Thus, considering these geotechnical investigations, we were not able to identify the origin of the phenomenon.

Bender element measurements were performed to estimate S-wave velocity in the loess layer [11]. Results illustrated with water content and density measurements showed that spatial VS variations, and therefore of shear modulus, are linked to the position of the observed phenomenon along track 2 [10]. For the same water content, the shear modulus turns out to be a good indicator of the quality of the loess layer. Such laboratory study cannot be deployed to diagnose large distances. Surface-wave seismic methods are thus proposed as an alternative to characterized mechanical properties, and more precisely appreciate shear modulus, along the whole track.

3   Seismic Acquisition and Results

Seven seismic profiles were implanted on the side path to ensure good geophone coupling with the medium and overcome specific acquisition conditions on ballast [10]. For each profile, we performed shots every 24 geophones and on both sides of the profile, one-half receiver spacing away from the first and last geophones. We used an aluminum plate vertically hit by a small hammer. To increase signal-to-noise ratio, we perform several hits at the same position. Profile P1 was carried in the area where the phenomenon was initially observed, while the profile P2 was centered on an area which never showed the disorder. Other profiles helped to complete the survey between these two profiles and slightly south of the maintenance area where the phenomenon was spotted during the campaign (Fig. 2). For data processing, surface-wave dispersion images were extracted from both direct and reverse shots. To obtain these images, the wavefield was transformed, after correction for geometrical spreading, to the frequency-phase velocity (f–c) domain in which maxima should correspond to Rayleigh wave propagation modes [12]. The dispersion images from direct and reserve shots were then stacked in order to increase the signal-to-noise ratio. The stacked dispersion data present a strong "effective character," with many propagation modes. On each dispersion image, the distinct propagation modes were identified with an estimated standard error in phase velocity: fundamental (0), first (1), and second (2) higher modes.

   1D inversion of dispersion data were performed for each profile. We assume we are in the presence of a 1D tabular medium below each spread. We used the neighborhood algorithm (NA) implemented for near-surface applications by [13], which performs a stochastic search of a pre-defined parameter space (namely VP, VS, density, and thickness of each layer).

Fig. 2 Schematic layout of the seismic profiles (P1–P7). The approximate positions of core drilling (SC#) and dynamic penetrometer tests (PD#) are given for information. Dashed lines indicate the locations of the observed phenomenon
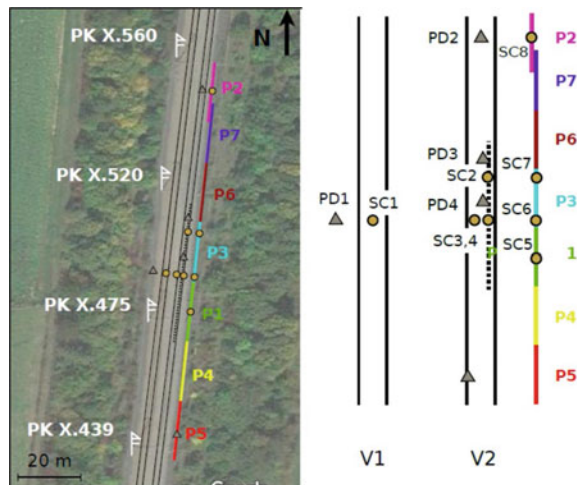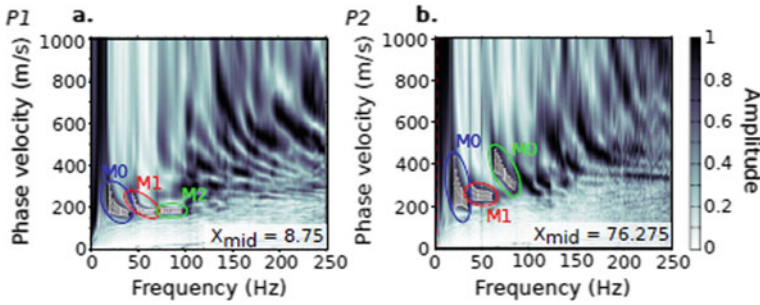
Fig. 3 Profile dispersion image **a** P1 and **b** P2. Identification of fundamental (0) first (1) and second (2) higher modes

We test different strategies of inversion taking into account the geotechnical a priori information's and the different higher modes. We used a parameterization with a stack of three layers overlaying the half-space. The half-space depth, of great importance since it depends on the poorly known depth of investigation of the method, was fixed to 9 m (half of the maximum observed wavelength).

For the first parametric study, the integration of the second higher mode (M2) further disperses the model and prevents a clear positioning between the zone without and without disorder. So, we have chosen to consider only the fundamental mode and the first higher mode in the data inversion (Fig. 3).

The second parametric study consisted of testing the influence of adjusting the degree of freedom offered to the parameters without adding additional data and with integrating a priori information (structural and geotechnical parameters). The valid parameters are presented in Fig. 4, and these correspond to a model where number of layers as well as thicknesses of the sub-layer and the capping layer are those of standard LGV structure.

The results combining geotechnical and geophysical results for P1 and P2 are presented in Fig. 5. Red and pink colors indicate, respectively, low and strong differences between data and forward models (misfit value). Results clearly show that for P1 (Fig. 5a) and P2 (Fig. 5b) S-wave velocities are not well defined for the two first layers, at a depth of less than 1 m, and do not suggest strong interface for the chalk. Between these two layers and the half-space, the "best models" (lower misfit values) present a third layer of at least 4 m thick with constant VS. The VS in loess. It is around 185 m/s for P1 and 310 m/s for P2. The resulting contrast is like the BE measurements.

Fig. 4 Parameterization with strong a priori

	épaiseur (m)	V_p (m/s)	V_S (m/s)	v	ρ (kg/m³)
Couche 1	0.1 à 0.5	20 à 2000	10 à 1200	0.1 à 0.5	2000
Couche 2	0.1 à 0.5	20 à 2000	10 à 1200	0.1 à 0.5	2000
Couche 3	0.1 à 10	20 à 2000	10 à 1200	0.1 à 0.5	2000
Couche 4	< 1	20 à 2000	10 à 1500	0.1 à 0.5	2000
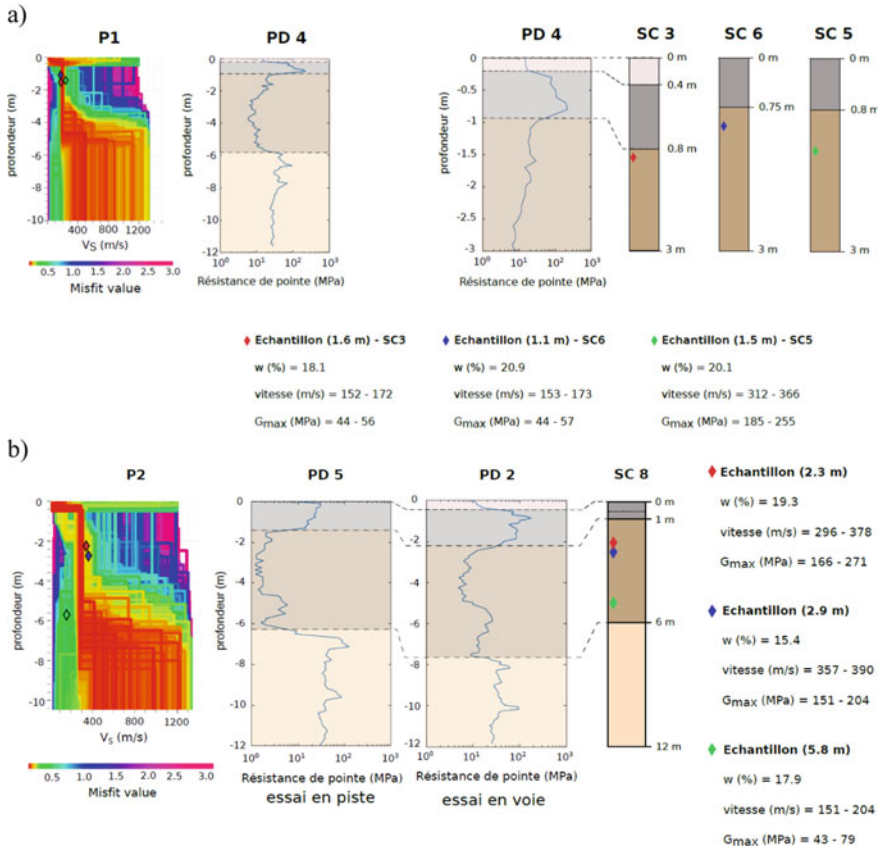
Fig. 5 VS models obtained from surface-wave dispersion inversion, geotechnical characterization, and bender element results on area where structural disorders are observed (**a**) and area where they are not (**b**)

Cone resistance (Qd) data obtained with dynamic penetrometer tests (PANDA®) is displayed according to the associated lithology from core drilling (Fig. 5a, b): ballast layer (pink), sub-ballast and capping layers (gray), loess layer (brown), and Campanian chalk (light brown). On the cone resistance graphs, the vertical line at 50 MPa corresponds to the critical limit under which maintenance action is occasionally necessary. The ballast thickness was removed when the method was realized on the sub-ballast layer. The gray diamond symbols visible on the VS models correspond to the bender element tests results. Locations of the profiles and the cone drilling and Panda tests are specified in Fig. 2. A comparison of the inversion results with cone resistance (Qd) data and the associated lithology for each area is presented on Fig. 5. Qd data reflect the lithology of the RE: the sub-ballast layer which has undergone high compaction has higher values than the compact loess layer. Qd values are also higher in the denser chalk. Cone resistance has an increasing trend in the sub-ballast

layer for the disturbed area and a decreasing trend in the healthy area. Theoretically, according to SNCF standards, the sub-ballast layer has a compaction objective higher than the capping layer. This observation on cone resistance test (PD4) could be consequently of lower VS values on the disturbed area resulting downward shift of compaction. The thicknesses obtained during the inversions corresponded to the geotechnical data of coring and cone resistance—around 4 m for profile 1 and close to 6 m for profile 2. This supports the relevant results of the inversions.

4 Conclusions

Previous studies showed, thanks to BE experiments and to geotechnical tests, and that VS was a good indicator of the quality of soils constituting the RE [10]. In the present study, strong a priori knowledge of the RE structure on this site allowed us to invert dispersion measurements for 1D VS models along the track. We showed that the results are more accurate where we simultaneously invert both the fundamental and first higher modes. Finally, geotechnical information validates the structure obtained by inversion (number and thickness of layers).

These results are interesting and need to be demonstrated in different contexts (other LGV and classic lines) before being generalized. In order to be used in an operational workflow, as a decision support tool, the parameter spaces need to be displayed in terms of probability with Bayesian formalism [13]. New tests are also necessary particularly concerning the inclusion of ballast and the inclusion of higher propagation modes from dispersion data to better describe the first meter of the embankment.

References

1. Hugenschmidt J, Kasa C, Kato H (2013) GPR for the inspection of industrial railway tracks. Near Surface Geophys 11(5):485–491
2. Nebieridze S, Leroux P (2012) Geotechnics, geophysics; a help to the earthworks diagnosis example: the excavation of Versigny. Journées internationales de Géotechnique et de Géologie de l'Ingénieur 2:12
3. Socco LV, Foti S, Boiero D (2010) Surface-wave analysis for building near-surface velocity models—established approaches and new perspectives. Geophysics 5:75A83–75A102
4. Bodet L, Pasquet S, Dhemaied A, Boisson-Gaboriau J, Cui YJ, Leroux P, Nebieridze S, Tang AM, Terpereau JM, Vitale Q (2015) Seismic surface-wave analysis for railway platform auscultation. In: Near surface geoscience 2015—21th European meeting of environmental and engineering geophysics. EAGE, Italy
5. Pasquet S, Bodet L (2017) SWIP: an integrated workflow for surface-wave dispersion inversion and profiling. Geophysics 82(6):WB47–WB61
6. Karl L, Fechner T, Schevenels M, François S, Degrande G (2011) Geotechnical characterization of a river dyke by surface waves. Near Surface Geophys 9(6):515–527

7. Heitor A, Indraratna B, Rujikiatkamjorn C, Golaszewski R (2012) Characterising compacted fills at Penrith lakes development site using shear wave velocity and matric suction. In: 2012 conference proceedings, pp 1262–1267
8. Donohue S, Gunn DA, Bergamo P, Hughes E, Dashwood B, Uhlemann S, Chambers J E, Ward D (2014) Assessing climate effects on railway earthworks using MASW. Near Surface Geosci 2014
9. Hwang H-J, Park H-C (2014) Evaluation of condition of gravel ballast layer on high-speed railway using surface wave method based on harmonic wavelet analysis of waves. NDT E Int 68:78–87
10. Dhemaied A, Cui Y-J, Tang A (2014) Étude de la sensibilité de la raideur mécanique des sols supports la variation de la teneur en eau. Technical report, ENPC/SNCF
11. Lee J, Santamarina J (2005) Bender elements: Performance and signal interpretation. J Geotech Geoenviron Eng 131(9):1063–1070
12. Mokhtar TA, Herrmann RB, Russell DR (1988) Seismic velocity and q model for the shallow structure of the Arabian shield from short-period Rayleigh waves. Geophysics 3(11):1379–1387
13. Wathelet M, Jongmans D, Ohrnberger M (2004) Surface-wave inversion using a direct search algorithm and its application to ambient vibration measurements. Near Surface Geophys 4:211–221

Evaluation on the Performance of Asphalt Concrete for the Railway Substructure

Liangwei Lou, Degou Cai, Jie Zhou, Xianhua Chen, and Yuefeng Shi

Abstract The dense-graded asphalt concrete has been a potential waterproofing material for the subgrade in high-speed railway in China. As a viscoelastic material, asphalt concrete can improve the bearing capacity and stability of the track structure. The main purpose of this paper is to evaluate the material performance of asphalt concrete substructure from different aspects. According to the environmental conditions and functional requirements, the mix design of asphalt concrete was completed based on the Marshall design method. The laboratory tests were conducted to evaluate the performance of asphalt concrete substructure, including rutting test, fatigue test, low-temperature bending test, immersion Marshall test, freeze–thaw split test, dynamic modulus test, and permeability test. The linear viscoelastic behavior of asphalt concrete at different temperatures and loading frequencies was then discussed, and it was observed that the asphalt concrete substructure had good energy dissipation capacity at the loading frequencies caused by the high-speed train. The tensile strain at the bottom of asphalt concrete substructure was analyzed by the finite element model. The results indicated that the service life increased as the thickness of asphalt concrete substructure increased. Therefore, the proposed asphalt concrete in this paper is a promising material for the sustainable substructure of high-speed railway.

Keywords Railway · Asphalt concrete · Linear viscoelasticity · Service life

L. Lou · D. Cai · Y. Shi
Railway Engineering Research Institute, China Academy of Railway Sciences Corporation Limited, Beijing 100081, China

Beijing Tieke Special Engineering Technology Corporation Limited, Beijing 100081, China

J. Zhou · X. Chen (✉)
School of Transportation, Southeast University, Nanjing 211189, China
e-mail: chenxh@seu.edu.cn

1 Introduction

As the foundation of the railway track structure, the stability and durability of the subgrade are extremely important for ensuring the safe operation of high-speed railways. The waterproofing layer set on the surface of subgrade plays an important role to ensure the long-term service performance of the subgrade. It can prevent the distresses in the subgrade, such as settlement, mud pumping, and frost heave [1, 2]. The hot mixed asphalt material has been proved to be a potential solution for the waterproofing layer of the subgrade [3]. The on-site test results showed that the water content inside the subgrade was very close to the optimum water content due to the presence of the asphalt concrete substructure, which ensured sufficient strength and durability of the entire track and subgrade structure [4]. The asphalt concrete substructure can also reduce the stress level and deformation of the subgrade and help to reduce the maintenance cost of the track structure [5, 6]. The asphalt concrete substructure has also been applied in Chinese high-speed railway, and the long-term monitoring results indicated that the self-compacted asphalt concrete was a sustainable waterproofing solution for the subgrade in cold regions [7].

Different kinds of asphalt mixtures have been selected as the material of asphalt concrete substructure around the world. Lee et al. reported that the crumb rubber-modified asphalt binder and styrene–butadiene–styrene (SBS)-modified asphalt binder were recommended to be used in railway substructure in terms of the water stability performance, resistance to permanent deformation, and anti-fatigue performance [8]. The crumb rubber modification for the asphalt concrete substructure effectively improved the fatigue life of the structure and had much better long-term performance [9]. The epoxy asphalt-based concrete for the railway substructure was evaluated by the laboratory tests, and the numerical simulation results demonstrated that the epoxy asphalt-based concrete had vibration attenuation performance for the ballastless track structure [10].

The objective of the paper is to evaluate the performance of asphalt concrete substructure for the high-speed railway. Considering the climate and engineering conditions in North China, raw materials were selected, and the mix design of asphalt mixture for the railway substructure was conducted. Then, the performance in different aspects of the designed asphalt mixture was investigated through a series of tests, and the technical indicators for the asphalt concrete substructure were also proposed. A 3D numerical finite element model was established to calculate the tensile strain at the bottom of asphalt concrete substructure, and the service life was also determined based on the fatigue function.

Fig. 1 The gradation curve of asphalt concrete substructure
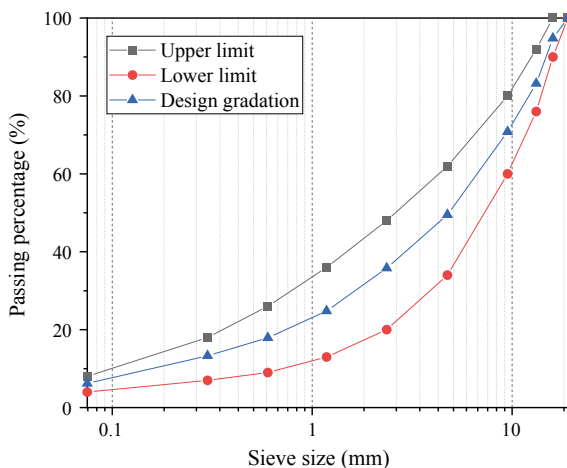
2 Materials and Laboratory Tests

2.1 Materials

At present, there is no clear design method and standard for the material composition design of railway asphalt concrete in China. This paper draws on the current asphalt pavement construction specification (JTG F40-2004) to design the material composition of the asphalt concrete substructure. The asphalt mixture consists of modified asphalt binder and basalt aggregate. Taking into account the climatic conditions in North China, the asphalt binder was modified by styrene–butadiene–styrene (SBS) and crumb rubber.

For asphalt concrete substructure in railway, the waterproofing and impermeability are its most basic performances. So the asphalt mixture was designed based on the dense gradation, and the nominal maximum aggregate size was 16 mm, as is shown in Fig. 1. According to Marshall design procedure, the optimal asphalt content in the asphalt mixture was 4.94% and the target void ratio was controlled at about 2–4%.

2.2 Laboratory Tests

According to the functional requirements of the asphalt concrete substructure, the test specimen was prepared by the above-mentioned gradation and asphalt content. The performance evaluation tests of asphalt concrete substructure mainly included the permeability test, high-temperature stability test, low-temperature bending test, fatigue test, dynamic modulus test, and water stability test.

2.2.1   Permeability Test

Good waterproofing performance is the basic function that asphalt concrete substructure should play. Under surface runoff or rainfall conditions, the asphalt concrete substructure should be substantially free of water seepage, and the surface water can be discharged from the surface by lateral or longitudinal drainage. The test specimen was prepared by the wheel rolling method and tested by the pavement water permeability meter. The water permeability coefficient was calculated by the amount of water passed in 3 min. The results show that the water permeability coefficient was 0 mL/min, which meant that the test specimen was impervious to water.

2.2.2   High-Temperature Stability Test

The rutting test was used to evaluate the ability of asphalt mixture to resist permanent deformation under high-temperature conditions. The corresponding index is the dynamic stability, that is, the number of walking times of the standard axle load that the asphalt mixture bears when the mixture is deformed by 1 mm under high temperature conditions. The test specimen (300 mm × 300 mm × 50 mm) was prepared by wheel rolling method, and the rutting test was carried out under the conditions of 60 °C and 0.7 MPa. The mean value of dynamic stability for the test specimens was 6403 cycle/mm.

2.2.3   Low-Temperature Bending Test

Under these circumstances, the asphalt concrete substructure should have good low-temperature crack resistance to avoid the effect of thermal cracks on impermeability. Therefore, at a temperature of -10° C and a loading rate of 50 mm/min, the prismatic specimen (250 mm × 30 mm × 35 mm) prepared by wheel rolling method was subjected to the low-temperature bending test. The specimen was placed on two supports, and the distance between the two supports was 200 mm. The load was applied to the mid-span position of the specimen, and the load-deformation data was recorded during the test. The mean value of flexural strength, failure strain, and flexural modulus for the test specimens was 12.4 MPa, 3279 $\mu\varepsilon$, and 3795 MPa, respectively.

2.2.4   Four-Point Bending Fatigue Test

The asphalt concrete substructure should have good fatigue performance and long service life under the long-term repetition of train load. The anti-fatigue properties of asphalt concrete substructure were evaluated by the four-point bending fatigue test. The test temperature was 15 °C, the loading frequency was 10 Hz, and the test was controlled by constant strain. The test specimen was a 380 mm × 50 mm × 63.5 mm
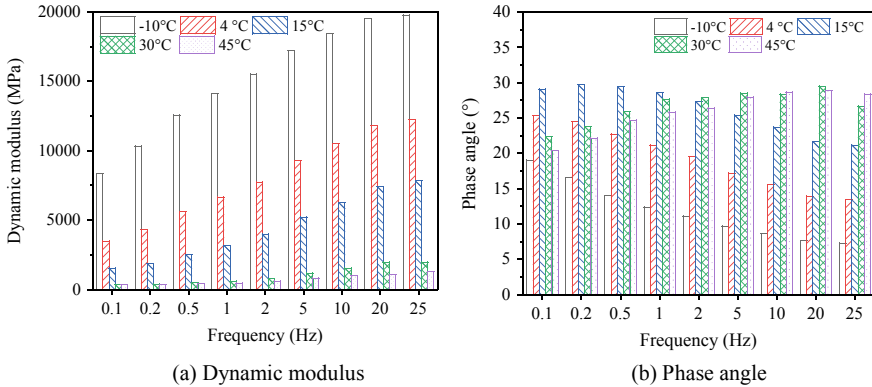
Fig. 2 Test results of dynamic modulus test

prism. When the stiffness modulus is reduced to 50% of the initial modulus, the corresponding number of loading cycles is the fatigue life. The fatigue life of the test sample was 2,610,000 cycles and 1,225,000 cycles under the strain level 400 $\mu\varepsilon$ and 500 $\mu\varepsilon$, respectively.

2.2.5 Dynamic Modulus Test

The dynamic modulus test was conducted to evaluate the modulus characteristics under dynamic loading. The test specimen prepared by the Superpave gyratory compactor had a diameter of 100 mm and a height of 150 mm. The test temperatures were − 10 °C, 4 °C, 15 °C, 30 °C, 45 °C, and the loading frequencies were 0.1 Hz, 0.2 Hz, 0.5 Hz, 1 Hz, 2 Hz, 5 Hz, 10 Hz, 20 Hz, 25 Hz, respectively. The results of dynamic modulus test were summarized in Fig. 2.

2.2.6 Water Stability Test

The asphalt concrete substructure should not only maintain good water resistance at high temperatures but also have excellent resistance to freezing and thawing at low temperatures. The immersion Marshall test and freeze–thaw split test were conducted to evaluate the water stability of asphalt concrete substructure. The detailed process of water stability test is illustrated in Fig. 3. The average residual stability of the immersion Marshall test was 92%, and the average tensile strength ratio of the freeze–thaw split test was 89%.

(a) Immersion Marshall test   (b) Freeze–thaw split test
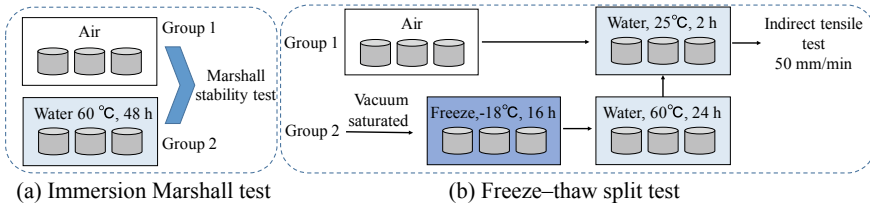
Fig. 3 Water stability test

3 Linear Viscoelastic Behavior of Asphalt Concrete Substructure

Asphalt concrete is a viscoelastic material, and its unique elastic hysteresis and energy dissipation characteristics are more conducive to the long-term stability of the high-speed railway track structure under train load compared to rigid cement concrete materials. In view of this, it is necessary to consider the viscoelastic mechanical behavior of asphalt concrete from the viscoelastic constitutive relationship of asphalt concrete. The test results of dynamic modulus test can be further used to analyze the linear viscoelastic behavior of asphalt concrete.

The 2S2P1D rheological model, consisting of two spring elements, two parabolic elements, and one dashpot element, has been proved to characterize the linear viscoelastic behavior of asphalt concrete over a very wide domain of frequencies and temperatures, as shown in Fig. 4 [11]. The complex modulus $E^*(i\omega\tau)$ of the 2S2P1D model is presented as follows:

$$E^*(i\omega\tau) = E_e + \frac{E_g - E_e}{1 + \delta(i\omega\tau)^{-k} + (i\omega\tau)^{-h} + (i\omega\beta\tau)^{-1}} \tag{1}$$

where ω is the angular frequency in rad/s; i is the complex number defined by $i^2 = -1$; E_e is the long-term equilibrium modulus and E_g is the instantaneous modulus; τ is the characteristic time which depends on the temperature; k and h are exponents defined such that $0 < k < h < 1$; δ and β are the model coefficients.

According to the time–temperature superposition principle, the characteristic time τ can be further expressed as follows:

Fig. 4 2S2P1D model
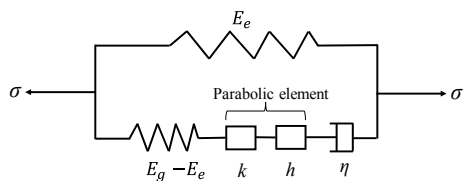
$$\tau(T) = a_T \times \tau(T_{\text{ref}}) \tag{2}$$

where T is the temperature and T_{ref} is the reference temperature; a_T is the shift factor and can be calculated based on the Williams-Landel-Ferry (WLF) equation:

$$\log(a_T) = \frac{-C_1(T - T_{\text{ref}})}{C_2 + T - T_{\text{ref}}} \tag{3}$$

where C_1 and C_2 are the equation constants.

The model coefficients in the 2S2P1D model at the reference temperature 20 °C were solved from the results of the dynamic modulus test, as listed in Table 1. Then the master curves of dynamic modulus and phase angle were established by the 2S2P1D model, as shown in Fig. 5. The fitted master curve indicated that the 2S2P1D model described the viscoelastic behavior of asphalt concrete substructure well.

The dissipated energy W that reflects the energy dissipated in a loading cycle is defined in Eq. (4). In addition, the damping D in geotechnics definition is shown in Eqs. (5) and [12].

$$W = \pi \cdot \sin(\varphi) \cdot |E^*| \cdot \varepsilon_0^2 \tag{4}$$

$$D = \frac{\sin(\varphi)}{2} \tag{5}$$

Table 1 Coefficients of 2S2P1D model

E_e (MPa)	E_g (MPa)	k	h	τ (s)	δ	β	C_1	C_2
166	31,684	0.19	0.43	0.000578	1.7	7895	11.5	117.9

(a) Dynamic modulus   (b) Phase angle
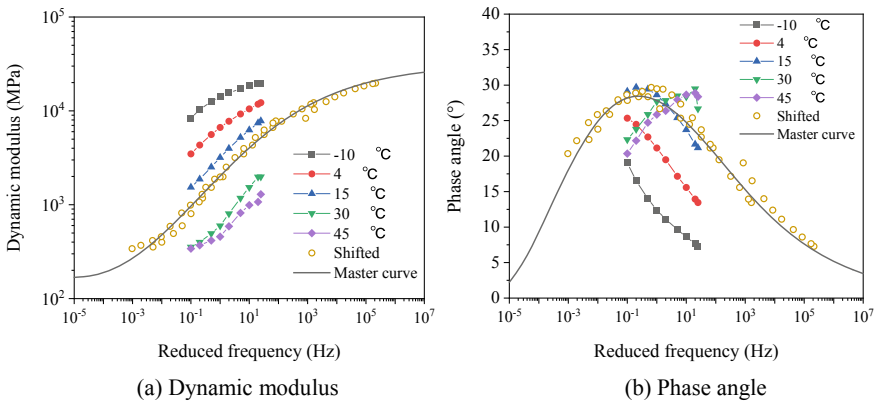
Fig. 5 Master curves at the reference temperature 20 °C

Fig. 6 Dissipated energy
curve and damping curve
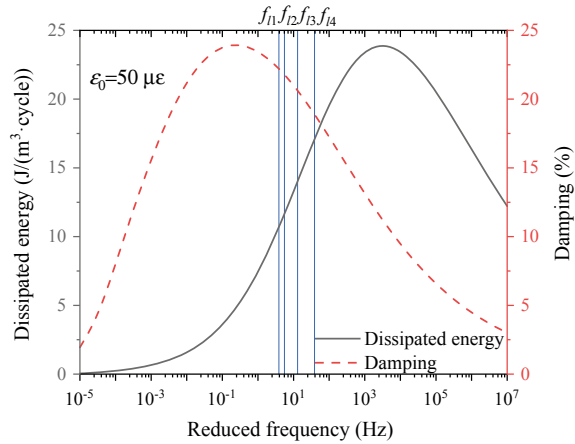
where $|E^*|$ is the dynamic modulus; φ is the phase angle; ε_0 is the strain level.

The change of dissipated energy and damping with loading frequency at the reference temperature under the strain level 50 µε is shown in Fig. 6. It can be observed that the dissipated energy and damping increased first and then decreased as the frequency increased.

For the asphalt concrete substructure, the frequency generated by the train load is related to the driving speed and vehicle component characteristics. The frequency can be expressed as:

$$f = v/l \tag{6}$$

where v is the driving speed; l is the disturbing wavelength of CRH380 train, as illustrated in Fig. 7. Furthermore, four frequencies corresponding to the four disturbing wavelengths as in Fig. 7 when the train speed was 350 km/h were marked as blue lines in Fig. 6. It can be observed that the dissipated energy in these four frequency ranges is about 10–17 J/(m³ cycle) and the damping is about 17–27%. The damping value of granular materials was about 1% within the small strain domain [12]. Compared to traditional granular materials, asphalt concrete materials have better energy dissipation capacity, which helps to reduce the vibration level of the track structure.

Fig. 7 CRH380 train model
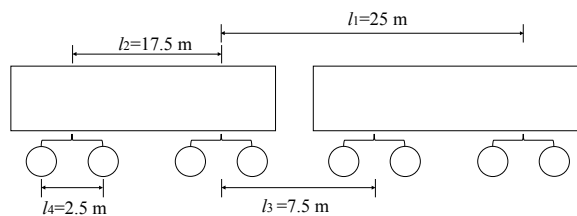
4 Structural Design

Due to the limited experience of the application of asphalt concrete structures on railways, the design of the fatigue failure of asphalt concrete substructures was carried out by referring to the mechanical experience method in the pavement engineering.

4.1 Finite Element Model

To calculate the tensile strain at the bottom of asphalt concrete substructure, a 3D finite element model of the track structure was established, as shown in Fig. 8. The track structure is CRTS III slab ballastless track structure. From bottom to top, it is subgrade, bottom layer of roadbed, surface layer of roadbed, asphalt concrete substructure, base plate, self-compacting concrete (SCC), track slab, fasteners, and rails. The detailed model parameters are listed in Table 2. The high-speed train load
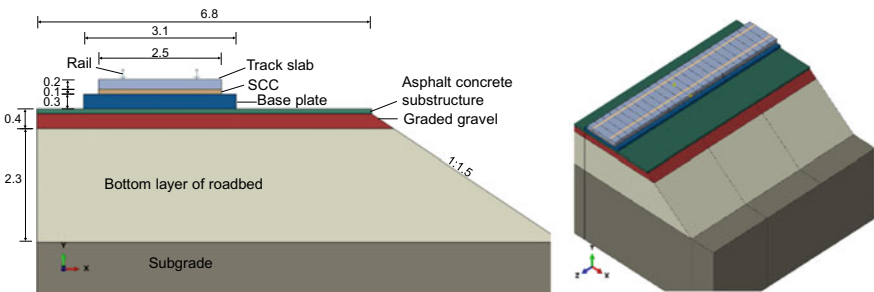
Fig. 8 Finite element model (Unit: m)

Table 2 Parameters of finite element model

Structure	Density (kg/m^3)	Modulus (MPa)	Poisson's ratio
Rail	7800	210,000	0.3
Track slab	2600	36,500	0.18
SCC and base plate	2400	34,000	0.18
Asphalt concrete substructure	2400	Viscoelastic	0.3
Surface layer of roadbed	2200	160	0.3
Bottom layer of roadbed	1900	100	0.3
Subgrade	1850	60	0.3

can be expressed as follows:

$$F(t) = k_1 k_2 (P_0 + P_1 \sin \omega_1 t + P_2 \sin \omega_2 t + P_3 \sin \omega_3 t) \tag{7}$$

where k_1 is the superposition coefficient between adjacent rails of the train, generally 1.2–1.7; k_2 is the dispersion coefficient of rail and sleeper to train load, generally 0.6–0.9; P_0 is the single-sided static wheel load and is considered as 85 kN in this paper; P_1, P_2, P_3 is the amplitude of the vibration load corresponding to a typical value of the low, medium, and high-frequency control conditions, and the expression is as follows:

$$P_i = M_0 a_i \omega_i^2 \tag{8}$$

where M_0 is the unsprung mass of the train, a_i is a typical vector height corresponding to the low, medium, and high frequency; ω_i is the circular frequency at the irregular vibration wavelength of low, medium, and high frequency under a certain vehicle speed and can be calculated as follows:

$$\omega_i = 2\pi \frac{v}{L_i} \tag{9}$$

where v is train speed; L_i is the typical wavelength corresponding to three cases of low, medium, and high frequency.

The parameters of CRH380 train were adopted in this paper to simulate the train load.

- $M_0 = 750$ kg
- $L_1 = 20$ m, $a_1 = 3.5$ mm; $L_2 = 2$ m, $a_2 = 0.4$ mm; $L_3 = 0.5$ m, $a_3 = 0.08$

4.2 Calculation of Service Life

The service life of fatigue failure of asphalt concrete substructure usually needs to be expressed according to the number of repeated actions of train load. To estimate the service life of the structure, firstly, the daily number of times of train load should be determined. In the calculation process, each cabin passing can be equivalent to four repetitions of the train load.

The material parameters of asphalt concrete are greatly affected by temperature, and the value of the modulus varies greatly in different seasons. Therefore, in the design process, the climate of different months in the design area should be considered, and the average temperature of each month should be obtained so that the viscoelastic parameters at different temperatures can be obtained according to the time–temperature equivalence principle. Then the finite element model can

be used to calculate the bottom tensile strain of asphalt concrete substructure in different months. According to the Japanese geotechnical specification [13], the standard calculation formula for fatigue failure of asphalt concrete substructure in the ballastless track structure is presented as follows:

$$N_A = 18.4 \times C \times 6.167 \times 10^{-5} \times \varepsilon_t^{-3.291} E_A^{-0.854} \tag{10}$$

where N_A is the allowable load times of fatigue failure of asphalt concrete layer; ε_t is the tensile strain at the bottom of asphalt concrete layer; E_A is the modulus of asphalt concrete layer; C is a function of void ratio V_v and asphalt content V_b.

$$C = 10^M \quad M = 4.84 \times \left(\frac{V_b}{V_v + V_b} - 0.69 \right) \tag{11}$$

Then, the service life of asphalt concrete substructure can be predicted as given below:

$$\text{Service life} = \frac{1}{\sum_{i=1}^{12} \frac{N_{pi}}{N_A}} \tag{12}$$

where N_{pi} is the predicted number of load repetitions each month.

5 Results and Discussion

5.1 Technical Requirements

Based on the asphalt concrete mix design, the performance of designed asphalt mixture was tested through various laboratory tests with Chinese standard; and combined with the engineering and climatic conditions in North China, the corresponding technical requirements of asphalt concrete substructure were proposed, as shown in Table 3.

5.2 Analysis of Service Life

In the process of life analysis, the paper selected the monthly mean temperature of a certain area in North China and calculated the bottom tensile strain of asphalt concrete substructure in different months through the finite element model, as shown in Fig. 9a. It was indicated that the bottom tensile strain was positively correlated with

Table 3 Technical requirements for the asphalt concrete substructure

Test	Test method	Technical indicator	Requirements
Permeability test	T 0730	Permeability coefficient	$\leq$ 60 mL/min
High-temperature stability test	T 0719	Dynamic stability (0.7 MPa, 60 °C)	$\geq$ 2400 cycle/mm
Low-temperature bending test	T 0715	Flexural strength (− 10 °C, 50 mm/min)	$\geq$ 8 MPa
		Flexural strain (− 10 °C, 50 mm/min)	$\geq$ 3000 $\mu\varepsilon$
Fatigue test	T 0739	Fatigue life (10 Hz, 15 °C, 500 $\mu\varepsilon$)	$\geq$ 200,000 cycle
Dynamic modulus test	T 0738	Dynamic modulus (10 Hz, 15 °C)	$\geq$ 6000 MPa
Water stability test	T 0709	Residual stability	$\geq$ 85%
	T 0729	Tensile strength ratio	$\geq$ 80%

(a) Tensile strain   (b) Service life
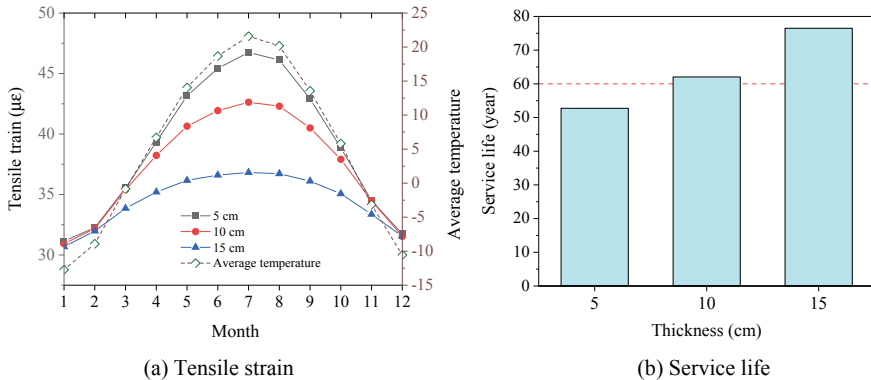
Fig. 9 Analysis of service life

the monthly mean temperature. The tensile strain of asphalt concrete substructure with different thickness is also compared in Fig. 9a. As the thickness of asphalt concrete substructure increased, the tensile strain showed a tendency to decrease. Moreover, the reduction of tensile strain at high temperatures was much greater than the reduction at low temperatures.

Referring to the departure frequency of the domestic railway, it was assumed that the daily train number is 96, and the number of train compartments is uniformly selected as 16. It can be concluded that the daily total number of train loads was 96 × 16 × 4 = 6144 times. The service life of different thicknesses of asphalt concrete substructure was shown in Fig. 9b. It can be observed that the greater the thickness of the asphalt layer, the longer the service life. If it is necessary to meet the requirements

of the current 60-year design period of high-speed railway subgrade, the thickness of the asphalt concrete substructure is recommended to be greater than 10 cm.

6 Conclusions

The paper is aimed to evaluate the performance of asphalt concrete substructure for the high-speed railway. The performance of asphalt mixtures was evaluated from the aspect of impermeability, fatigue resistance, water stability, and high- and low-temperature stability. The 2S2P1D model was adopted to describe the linear viscoelastic behavior of asphalt concrete substructure. A 3D finite element model of the track structure was developed to calculate the service life of asphalt concrete substructure.

The technical requirements for the asphalt concrete substructure were proposed for the application in North China according to the engineering and climatic conditions. Through the linear viscoelasticity analysis of asphalt concrete substructure, the asphalt materials showed better energy dissipation capacity compared with granular material in terms of damping. The results of numerical analysis indicated that the increase in the thickness of the asphalt concrete substructure helped to extend the service life. Based on the requirements for the service life of subgrade, the 10-cm-thick asphalt concrete substructure is suitable for the ballastless track structure in North China.

References

1. Abeywickrama A, Indraratna B, Rujikiatkamjorn C (2019) Excess pore-water pressure generation and mud pumping in railways under cyclic loading. Lecture Notes Civ Eng:371–383
2. Miao Q, Niu F, Lin Z, Luo J, Liu M (2020) Comparing frost heave characteristics in cut and embankment sections along a high-speed railway in seasonally frozen ground of Northeast China. Cold Reg Sci Technol 170:102921
3. Rose J, Teixeira P, Ridgway N (2010) Utilization of asphalt/bituminous layers and coatings in railway trackbeds: a compendium of international applications. In: 2010 joint rail conference, vol 1
4. Rose J, Brown E, Osborne M (2000) Asphalt trackbed technology development: the first 20 years. Transp Res Rec J Transp Res Board 1713:1–9
5. Teixeira P, López-Pita A, Casas C, Bachiller A, Robusté F (2006) Improvements in high-speed ballasted track design: benefits of bituminous subballast layers. Transp Res Rec J Transp Res Board 1943:43–49
6. Teixeira P, López Pita A, Ferreira P (2010) New possibilities to reduce track costs on high-speed lines using a bituminous sub-ballast layer. Int J Pavement Eng 11:301–307

7. Chen X, Tao T, Yang G, Yan H, Yang J (2018) Long-lasting waterproofing solution for the subgrade of high-speed railway in cold region. J Test Eval 47:20180046
8. Lee S, Lee J, Park D, Vo H (2014) Evaluation of asphalt concrete mixtures for railway track. Constr Build Mater 73:13–18
9. Asgharzadeh S, Sadeghi J, Peivast P, Pedram M (2018) Fatigue properties of crumb rubber asphalt mixtures used in railways. Constr Build Mater 184:248–257
10. Liu Y, Qian Z, Zheng D, Huang Q (2018) Evaluation of epoxy asphalt-based concrete substructure for high-speed railway ballastless track. Constr Build Mater 162:229–238
11. Mangiafico S, Sauzéat C, Di Benedetto H (2019) 2S2P1D model calibration error from user panel for one bitumen and one bituminous mixture. Adv Mater Sci Eng 2019:1–16
12. Ramirez Cardona D, Di Benedetto H, Sauzeat C, Calon N, Saussine G (2016) Use of a bituminous mixture layer in high-speed line trackbeds. Constr Build Mater 125:398–407
13. Momoya Y, Sekine E (2007) Performance-based design method for railway asphalt roadbed. Doboku Gakkai Ronbunshuu E. 63:608–619

Interface Test Study on Asphalt Concrete Full-Section Waterproof Sealing Structure of High-Speed Railway

Yang-Sheng Ye, De-Gou Cai, Hong-Ye Yan, Jian-Ping Yao, Liang-Wei Lou, Feng Chen, Yue-Feng Shi, Tai-Feng Li, and Song Lv

Abstract High-speed railways have extremely high requirements for smoothness and safety. The full-section asphalt concrete sealing layer is a new type of waterproof structure that can be used for high-speed railway subgrades. Therefore, higher requirements are put forward for the stability of the structural layer interface. In this paper, the interface relationship between the asphalt concrete layer and the base-slab of the track structure, the asphalt concrete layer and the surface layer of the subgrade, and the interface behavior of asphalt concrete layer with different engineering measures are studied through the interface test of the Beijing–Zhangjiakou high-speed railway. After compared with the interface effect of current high-speed railway concrete layer and graded gravel layer, the comparison results shown that the interface effect of asphalt concrete is sufficiently safe, which could provide an important reference for the application of full-section asphalt concrete in high-speed railways.

Keywords High-speed railway · Asphalt concrete · Waterproof sealing layer · Interface characteristic

By the end of 2018, the total mileage of China's high-speed railway has exceeded 28,000 km, and the overall quality is well controlled. However, some diseases such as mud-pumping, settlement, arching, and frost-heave occurred in some subgrade work points, which seriously affected the smoothness of the track [1–5]. The occurrence of these diseases is inseparable from the water content change in the subgrade itself, and

Y.-S. Ye
China Academy of Railway Sciences Corporation Limited, Beijing 100081, China

D.-G. Cai · H.-Y. Yan (✉) · J.-P. Yao · L.-W. Lou · F. Chen · Y.-F. Shi · T.-F. Li · S. Lv
Railway Engineering Research Institute, China Academy of Railway Sciences Corporation Limited, Beijing 100081, China
e-mail: yanhongye_2005@163.com

Y.-S. Ye · D.-G. Cai · H.-Y. Yan · J.-P. Yao · L.-W. Lou · F. Chen · Y.-F. Shi · T.-F. Li · S. Lv
State Key Laboratory for Track, Technology of High-Speed Railway, China Academy of Railway Sciences Corporation Limited, Beijing 100081, China

therefore, the anti-drainage work of high-speed railway subgrade is vital and essential [6]. At present, ordinary cement concrete and other materials are commonly used in the waterproof sealing layer of high-speed railway in China. The longitudinal and horizontal joints are filled with caulking materials. During long-term operation and service, it is easy to cause the separation between longitudinal or horizontal joints and caulking materials, so that rainfall water can penetrate into the subgrade. The using of full-section asphalt concrete can eliminate the existing longitudinal and transverse joints and avoids the separation between the sealing layer and the caulking material.

The full-section asphalt concrete sealing layer, as the waterproof and drainage and bearing structure, both material and mechanical properties of asphalt concrete layer are obvious different then the concrete layer and the graded gravel layer. The interlayer interaction relationship is complex, under the effect of train dynamic load, temperature load, etc, whether it can reach the design requirements of rail infrastructure under interface security is the key technical problem for the new ballastless track structure.

In this paper, full-scale and scaled push-slab tests are carried out through the foundation test section of Beijing–Zhangjiakou railway, and the characteristics of upper and lower interface of asphalt concrete layer are studied to evaluate stability and safety of asphalt concrete layer.

1 Test Scheme

1.1 Overview

The test section of asphalt concrete full-section waterproof sealing layer is located in the XiaHuaYuan Station of Beijing–Zhangjiakou high-speed railway, near the exit of DongJiaZhuang tunnel with the mileage from DK143 + 450 to DK143 + 870. The length of the full-section asphalt concrete sealing layer in the test section is 420 m. The average temperature of coldest month in the test section is − 9.6 °C, the monthly maximum precipitation is 243.9 mm, and the maximum freezing depth of the ground is 1.29 m.

1.2 Full-Scale Push-Slab Test

The full-size base-slab (19.2 m × 3.4 m × 0.3 m) was poured on the asphalt concrete layer. During the test, the hydraulic jack would be used to apply the horizontal load to the concrete base-slab, and the displacement was recorded by both the displacement meter and the total-station robot at the same time. The specific layout is shown in Fig. 1(mm).
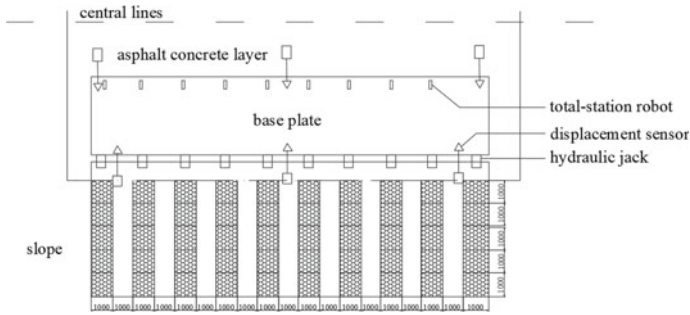
Fig. 1 Full-scale test layout

Fig. 2 Location of counter force pier and jack

The test equipment is mainly composed of base-slab, asphalt concrete layer, counter force pier, hydraulic jack, weighing sensor, displacement meter and the total-station robot, etc. The counter force can be supported with square concrete pier, which located at the side of asphalt concrete shoulder. There are ten rows of counter force pier have been set up totally. Jacks are located between the asphalt concrete and the counter force pier. The location of jacks and counter force piers has been shown in Fig. 2.

1.3 Scaled Push-Slab Test

In order to explore the bond strength and friction resistance characteristics differences between two interface cases, the following tests would be studied: Case 1, the interface of asphalt concrete and concrete base-slab. Case 2, the interface of concrete base-slab and graded gravel. Three-scale model (2 m × 2 m × 0.3 m) concrete blocks were poured in graded gravel layer and adjacent asphalt concrete layer, respectively, as comparison test.
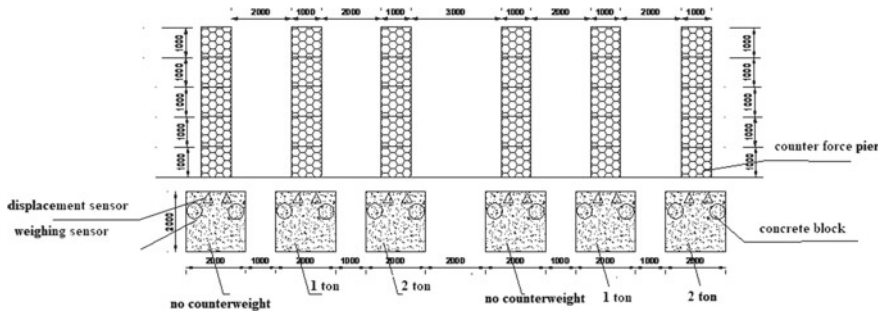
Fig. 3 Scaled test layout

Fig. 4 Counter force wall and jack site layout diagram

The test equipment is mainly composed of concrete block, asphalt concrete, graded gravel, counter force pier, hydraulic jack, weighing sensor and displacement meter, etc. Three concrete blocks of 1 m × 1 m (length × width) × 0.3 m (height) are poured on asphalt concrete layer and adjacent graded gravel layer, respectively.

The three concrete blocks are weighted with different additional weights, as the order of no counterweight, 1 and 2 tons of counterweight.

During the test, a hydraulic jack was used to apply transverse horizontal load on the concrete slab, and the displacement meter recorded the displacement at the same time, as shown in Fig. 3.

The wire displacement sensor is arranged along the shoulder side of the concrete block, and two wire displacement sensors are arranged on each side, and the pressure gauge is arranged next to the jack, as shown in Fig. 4.

1.4 Engineering Measures Interface Characteristics Test Plan

For the upper interface of asphalt concrete layer, the comparison test was carried out to explore the performance difference before and after laying composite geotextile.

For the lower interface of asphalt concrete layer, the performance difference before and after setting the notch groove, anti-slip nail, and spread emulsified asphalt is explored. The specific test arrangement is as follows.

1. The comparison test was carried out between the laying and without laying composite geotextile. Two pieces of 1 m × 1 m × 0.3 m base-slab are laid directly on the asphalt concrete layer on the site, one is provided with composite geotextile, one is not provided with composite geotextile, and then the push test is carried out, in order to find the interface parameters change before and after laying composite geotextile.

2. A comparison test was conducted with and without a notch groove. The groove depth, width, and spacing of notch groove were set as 2, 5 and 30 cm, respectively, in graded gravel layer to conduct push-slab test.

3. Followed with the comparison test of anti-slip nails and without anti-slip nails. Five anti-skid nails were set on one concrete block located at the graded gravel layer and the other concrete block without anti-slip nails to conduct push-slab test.

4. Another comparison test of emulsified asphalt and non-emulsified asphalt was carried out. The push-slab tests were conducted after the emulsified asphalt was spread on the graded gravel layer.

5. For the engineering measures of asphalt concrete upper interface, the wire displacement sensors are arranged on both of the concrete block and the asphalt concrete layer. For the lower interface, the wire displacement sensors are arranged in the center of the asphalt concrete layer, and the dynamometer is arranged next to the jack position.

During the loading process, the attention to paid to observe the change of the displacement gauge of the base-slab and the asphalt concrete layer, to recognize the displacement at each layer, and record the reading number of pressure gauge and wire displacement sensor.

2 Analysis of Push-Slab Test Results

2.1 Analysis of the Full-Scale Push-Slab Test Results

1. In order to explore the engineering effect of laying composite geotextile on asphalt concrete layer, the composite geotextiles were laid at the structural joints of the base-slab, and the center of the base-slab (unpaved geotextile) was directly poured on the asphalt concrete layer for comparison experiments. The relation between the dynamometer and displacement change in full-scale push-slab test is shown in Fig. 5.

It can be seen from Fig. 5 that the geotextile arrangement significantly reduces the interaction between the track base-slab and the asphalt concrete layer, which not only
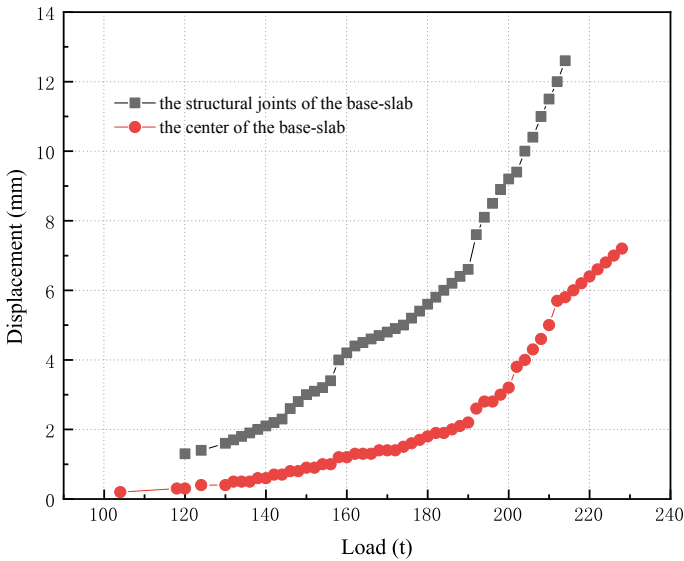
Fig. 5 Relationship between loading force and displacement of full-scale test (with or without geotextile)

reduces the negative effect of the asphalt concrete layer (restricting the stress release of the base-slab), but also reduces the additional stress of the base-slab expansion on the asphalt concrete layer, thereby reducing the probability of temperature stress cracking of the forced asphalt concrete. At the same time, the sliding layer is also prevented from appearing between the asphalt concrete layer and the graded gravel layer, which fully ensures the stability of the structure.

2. In order to explore the difference of the cohesive properties of the upper and lower interfaces of the asphalt concrete layer, a secondary push–pull test was carried out to record the relationship between the dynamometer and displacement of the asphalt concrete layer at the center of the base-slab. The relationship between the dynamometer and displacement in the full-scale push-slab test is shown in Fig. 6.

According to Fig. 6, when a 100 tons lateral load is applied, the base-slab starts to shift. With the load increases, the displacement of the base-slab under the lateral force includes two parts, the displacement of the base-slab itself and the displacement of the asphalt concrete layer.

When the lateral force applied is less than 180 tons, the asphalt concrete layer has no displacement. At this time, the total displacement is the displacement of the base-slab. When the lateral force is applied more than 180 tons, the total displacement of the base-slab includes its own displacement and additional displacement of the asphalt concrete layer.
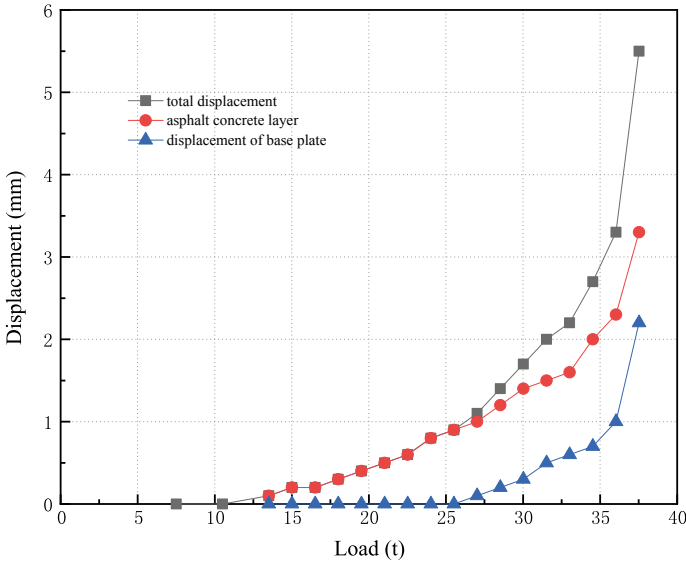
Fig. 6 Relationship between displacement and loading force at the center of the base-slab

2.2   Analysis of the Scaled Push-Slab Test Results

By comparing the cohesive strength and friction angle between the interface of the following three cases: (1) the interface of asphalt concrete layer and the concrete base-slab, (2) the interface of concrete base-slab and the graded gravel, (3) the interface of the asphalt concrete layer and the graded gravel. The scale push-slab test could reflect the interface characteristics among these cases.

The normal pressure is the weight of the concrete block plus additional weight, the normal stress is the normal pressure per unit area, the tangential pressure is the thrust load applied by the jack, and the tangential stress is the tangential load on the unit area of the concrete block. The cohesive strength and friction angle are calculated according to the formula of direct shear test of soil.

$$\tau_f = c + \sigma \tan\theta \tag{1}$$

τ_f tangential stress
σ normal stress
c cohesive strength
θ friction angle.

1. The test parameters and results of the scaled push-slab test between asphalt concrete and base-slab are shown in Fig. 7, Tables 1 and 2.

2. The test parameters and results of scaled push-slab test between graded gravel and base-slab are shown in Fig. 8, Tables 3 and 4.
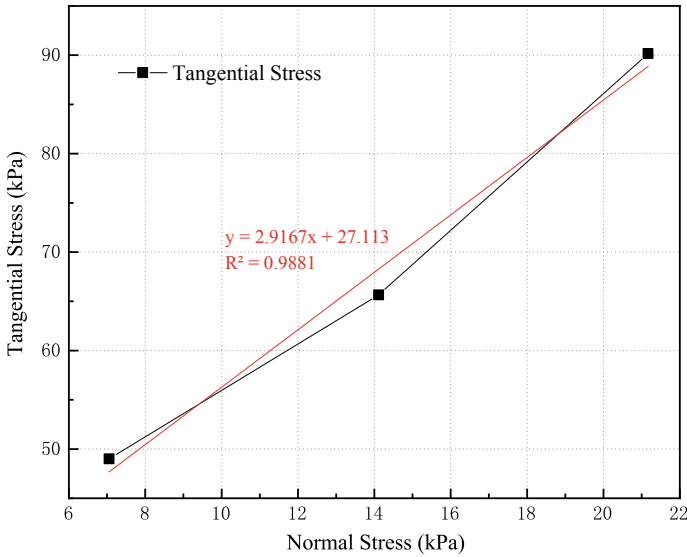
Fig. 7 Relationship between tangential stress and normal stress of asphalt concrete and concrete base-slab (shown cohesion and shear force behaviors)

Table 1 Scaled push-slab test between asphalt concrete and base-slab

No	Concrete block weight (tons)	Counterweight (tons)	Lateral Jack pressure (tons)	Bottom area
1	2.88	–	20	2 m × 2 m
2	2.88	2.90	20	2 m × 2 m
3	2.88	5.80	20	2 m × 2 m

Table 2 Test results of scaled push-slab between asphalt concrete and base-slab

No.	Normal pressure (kN)	Normal stress (kPa)	Tangential pressure (kN)	Tangential stress (kPa)	Cohesive strength (kPa)	Friction angle (°)
1	28.22	7.056	196	49	27	71
2	56.45	14.112	262.64	65.66		
3	84.67	21.168	360.64	90.16		

3.　The test parameters and results of the scaled push-slab test between asphalt concrete and graded gravel layer are shown in Fig. 9, Tables 5 and 6.

　　It can be seen from Tables 2, 4, and 6 that the cohesive strength between the asphalt concrete and the base-slab is 27 kPa for the upper interface of the asphalt
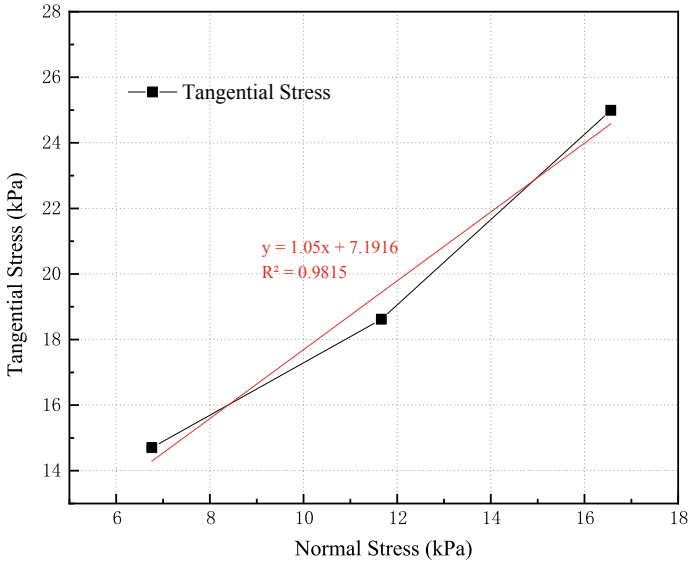
Fig. 8 Relationship between tangential stress and normal stress of graded gravel layer and concrete base-slab (shown cohesion and shear force behaviors)

Table 3 Scaled push-slab test between graded gravel and base-slab

No.	Concrete block weight (tons)	Counterweight (tons)	Lateral Jack pressure (tons)	Bottom area
1	2.88	–	20	2 m × 2 m
2	2.88	2.00	20	2 m × 2 m
3	2.88	4.00	20	2 m × 2 m

Table 4 Test results of scaled push-slab between graded gravel and base-slab

No.	Normal pressure (kN)	Normal stress (kPa)	Tangential pressure (kN)	Tangential stress (kPa)	Cohesive strength (kPa)	Friction angle (°)
1	28.22	6.762	58.80	14.7	7	44
2	47.82	11.662	74.48	18.62		
3	67.42	16.562	99.96	24.99		

concrete, and the cohesive strength between the graded gravel and the concrete base-slab is 7 kPa. Therefore, the asphalt concrete and the base-slab have better cohesive performance than the graded gravel; for the asphalt concrete lower interface, the cohesive strength between the asphalt concrete and the graded gravel is sticky with the concrete and the graded gravel. The junction strength is similar, both about 7 kPa.
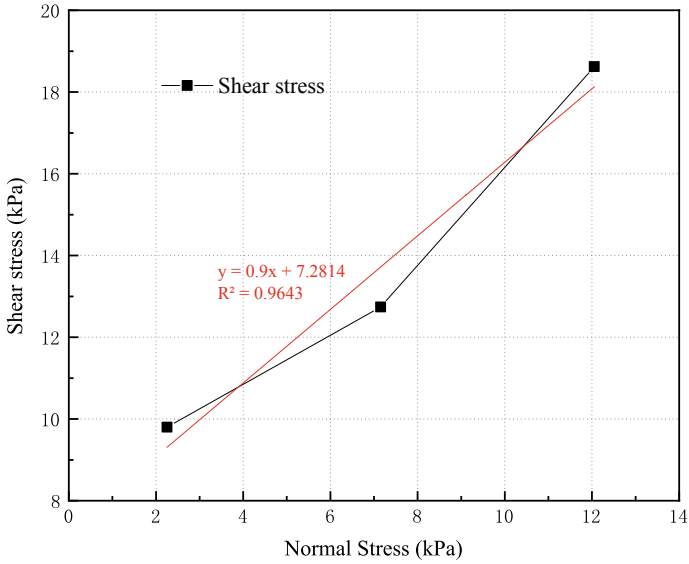
Fig. 9 Relationship between tangential stress and normal stress of graded gravel layer and asphalt concrete layer (shown cohesion and shear force behaviors)

Table 5 Scaled push-slab test between asphalt concrete and graded gravel layer

No.	Asphalt concrete block weight (tons)	Counterweight (tons)	Lateral Jack pressure (tons)	Bottom area
1	0.23	–	0.42	1 m × 1 m
2	0.23	0.15	0.50	1 m × 1 m
3	0.23	0.25	0.55	1 m × 1 m

Table 6 Test results of scaled push-slab test between asphalt concrete and graded gravel layer

No.	Normal pressure (kN)	Normal stress(kPa)	Tangential pressure (kN)	Tangential stress (kPa)	Cohesive strength (kPa)	Friction angle (°)
1	2.25	2.25	9.80	9.80	7.3	42
2	7.15	7.15	12.74	12.74		
3	12.05	12.05	18.62	18.62		

Therefore, the cohesive properties of asphalt concrete and graded gravel are not much different.

Table 7 Test results of push-slab test for treatment of base-slab and asphalt concrete layer

	Interface characteristics	Normal stress (kPa)	Lateral stress (kPa)	Sliding lateral stress (kPa)	Sliding friction coefficient
1	None	7.056	13.653	4.86	0.69
2	Geotextile	7.056	3.332	3.316	0.44

Note Working condition 1, concrete block weighs 2.88 tons, jack pressure is 20 tons, bottom area is 2 m × 2 m, and lateral jack pressure is 4 tons when sliding. Working condition 2, concrete block weighs 0.72 tons, the jack pressure is 20 tons, the bottom area is 1 m × 1 m, and the jack pressure during sliding is 0.32 tons

2.3 Analysis of Engineering Interface Characteristics Experimental Results

In view of the stability problem of the base-slab as a whole between the asphalt concrete and the graded gravel layer separation, it is necessary to study whether the engineering measures are taken between the asphalt concrete layer and the graded gravel layer. The mechanical properties of the structural components of the track before and after the engineering measures were taken to analyze the necessity. When the sliding occurs, the interface is de-bonded, and the sliding friction coefficient takes as the dynamic friction coefficient:

$$f = \frac{\sigma_f}{\tau_f} \tag{2}$$

σ_f Normal stress
τ_f Tangential Stress

It can be seen from Tables 7 and 8 that after laying composite geotextile, the lateral pressure changed at the start-up stage, the interface characteristics of the base, and the asphalt concrete layer is significantly reduced by 80%.

3 Conclusions and Recommendations

1. In the ballastless track structure system, the interface friction strength between the asphalt concrete and the base-slab is stronger than the interface strength between the graded gravel and the base-slab, and the asphalt concrete layer and the base interface have sufficient stability.
2. After laying composite geotextile, the cohesive force of the concrete between the base-slab and the asphalt concrete is obviously reduced. Laying composite geotextile at the expansion joint of the track slab can effectively reduce the influence of concrete temperature shrinkage on the asphalt concrete and improve the life of asphalt concrete.

Table 8 Test results of push-slab test for engineering measures of asphalt concrete layer and subgrade surface

	Interface characteristics	Normal stress (kPa)	Sliding lateral stress (kPa)	Sliding friction coefficient
1	None	2.25	1.76	0.78
2	Permeable asphalt oil	2.25	1.96	0.87
3	Surface layer is grooved	2.25	1.86	0.83
4	Anti-slip nails	2.25	–	0.00

Note Working condition 1, asphalt concrete block weighs 0.23 tons, lateral jack pressure is 1 ton, and the bottom area is 1 m × 1 m. Working condition 2, asphalt concrete block weighs 0.23 tons, lateral jack pressure is 0.3 tons, and the bottom area is 1 m × 1 m. Working condition 3, asphalt concrete block weighs 0.23 tons, lateral jack pressure is 0.42 tons, and the bottom area is 1 m × 1 m. Working condition 4, asphalt concrete block weighs 0.23 tons, and the bottom area is 1 m × 1 m

3. After the permeable asphalt oil is penetrated, the interface characteristics of the asphalt concrete layer and the surface layer of the subgrade have not been significantly improved.
4. After the surface layer is grooved, the interface characteristics of the asphalt concrete layer and the surface layer of the subgrade have not been significantly improved.
5. After the anti-slip nail, the asphalt concrete layer and the base the surface characteristics of the subgrade surface are significantly improved.

References

1. Zhao G (2005) High-speed railway ballastless track technology. China Railway Publishing House, Beijing
2. Peng H, Zhang H (2005) Types, mechanisms, detection and remediation technology of railway subgrade diseases. J Eng Geol 2:195–202
3. Shi G (2014) Research on frost-heave and engineering countermeasures of high-speed railway subgrade in severe cold area. Lanzhou University, Lanzhou
4. Wang Y (2010) Construction and maintenance of high-speed railway subgrade. Southwest Jiaotong University Press, Chengdu
5. Wang S (2015) Cause analysis and treatment measures of ballastless track diseases in Handan Railway. Subgrade Eng 6:217–221
6. Shi Y, Cai D, Yan H et al (2018) Overview of asphalt concrete waterproof sealing technology for high-speed railway subgrade. Railway Constr 58(1):33–36

The Settlement Characteristics of Ballast Bed Based on Variable Boundary Ballast Box

Liang Gao, Hao Yin, Yang Xu, Shunwei Shi, Hang Cai, and Xiangning Wang

Abstract The cumulative settlement of ballast bed greatly affects the service performance of railway lines. A discrete element method (DEM) model of ballast box with variable longitudinal force and accurate ballast shape was established in this study. The parameters of the simulation model were calibrated and validated by the self-developed experimental equipment of ballast box. Based on the validated DEM model, the mesoscopic effects of load frequency, load amplitude and longitudinal force of ballast bed on the settlement characteristics of ballast bed under cyclic loading were studied. The results show that the cumulative settlement of ballast bed includes initial settlement stage and stable settlement stage. The influence of longitudinal force on the settlement of ballast bed could not be neglected. The settlement decreases with the increase in the longitudinal force. When the longitudinal force increases from 5 to 8 kN, the settlement of ballast bed decreases by 68.2%. Besides, the settlement of ballast bed increases nonlinearly with the increase in load amplitude and frequency. When they increase from 60 to 80 kN and 32 Hz to 56 Hz, the settlement increases by 83.2% and 28.2%, respectively.

Keywords Ballast bed settlement · Ballast box · Variable boundary · Discrete element method

---

L. Gao (✉) · H. Yin · S. Shi · H. Cai · X. Wang
School of Civil Engineering, Beijing Jiaotong University, Beijing 100044, China
e-mail: lgao@bjtu.edu.cn

H. Yin
e-mail: yinhao@bjtu.edu.cn

S. Shi
e-mail: shunweishibjtu@gmail.com

H. Cai
e-mail: 18121218@bjtu.edu.cn

Y. Xu
Railway Engineering Research Institution, China Academy of Railway Science, Beijing 100081, China
e-mail: xuyangcars@qq.com

1 Introduction

Ballasted track plays an important role in the track structure of all countries in the world. It is widely used in high speed, heavy load and ordinary railway lines with its outstanding advantages of good applicability, low cost, and easy maintenance. As granular materials, ballasts are easy to be broken and moved under the effect of train load, thus causing the settlement of the ballast bed. When the settlement reaches a large value, the elasticity and drainage will decrease sharply, which further leads to the geometric irregularity of railway, increase in maintenance cost, as well as a deterioration of the level of operational safety. Researchers have done a lot of work on the settlement of ballast bed, mainly including experimental researches and numerical simulations.

In terms of experimental researches, most researchers have utilized triaxial apparatus and ballast box to study the settlement characteristics of ballast bed. Based on triaxial test, Diyaljee et al. [1] analyzed the effect of ballast materials on the settlement of ballasts, while Hu et al. [2] focused on the effect of ballast gradation and elasticity. Indraratna et al. [3–5] compared the difference of vertical settlement and lateral deformation between deteriorated and fresh ballast. To evaluate the settlement mechanism of ballast bed, Hirakawa et al. [6] studied the distribution of contact force in ballast aggregates and vertical deformation of sleeper under train load. Qian et al. [7, 8] explored the control measures of settlement, and proposed the reasonable parameters of geogrid. Other researchers used the ballast box to study the settlement of ballast bed, which is more accurate to simulate the interaction between sleeper and ballasts. Selig et al. [9] investigated the settlement characteristics of ballast under cyclic loading, and pointed out the most vulnerable area in ballast bed. Al-Saoudi et al. [10] analyzed the cumulative settlement, deformation modulus, as well as the deterioration state of ballasts, while loading. Lim et al. [11, 12] studied the effect of ballast gradation and wetting degree on ballasts settlement. In general, the macroscopic settlement characteristics are revealed better by experimental tests, such as the cumulative settlement and deterioration state. However, the mesoscopic settlement characteristics cannot be fully reviewed in experimental tests, like the contact state of ballasts, which is more important to determine the mechanism of settlement. Besides, it is difficult to unify the initial state of experimental tests due to the variation of ballast shape, size, and gradation et al. Therefore, it is not accurate enough to study the settlement characteristics of ballast bed only by experimental test.

Numerical simulations can effectively compensate for the shortcomings of experimental tests. Fu et al. [13] established a ballast bed model by two-dimensional DEM, and studied the effect of train load and subgrade deformation on the settlement of ballast bed. Xiao et al. [14] constructed the ballast bed model by three dimensional DEM, which had a higher simulation accuracy compared with the twodimensional DEM, and analyzed the mechanical properties and settlement characteristics of ballast bed under train load. In summary, the researches above simulated the ballast by ball element, neglecting the shape of ballast, and thus, the calculation accuracy was seriously affected. Lim et al. [12] used clump to simulate ballast with

different accuracy, which is composed of multiple balls. Xu et al. [15] established ballast box model based on the fine simulation of ballast, and investigated the effect of ballast gradation and shape on the settlement of ballast bed. The diffusion of internal stress could cause longitudinal deformation of ballast bed [16]. However, since all the existing researches used fixed boundary in ballast box model, the longitudinal deformation in ballast bed could not be revealed, correspondingly error in calculation being created.

To address the research gap in previous studies, a ballast box model with variable longitudinal force and accurate ballast shape was established by DEM at first in this study. Secondly, an experimental equipment of ballast box with movable boundary was innovatively developed, and the simulation model was verified by this equipment. Finally, the model was adopted to study the effect of longitudinal force in ballast bed, load amplitude and load frequency on ballast bed settlement. This paper can provide critical insights for the assessment and maintenance of ballast bed.

2 Discrete Element Modeling

2.1 Modeling Procedure

The shape of ballast has a great influence on the interaction of ballasts and the settlement characteristics of ballast bed [16]. Therefore, the complex shape of ballast was accurately captured by laser scanning, as shown in Fig. 1. Sixteen kinds of typical ballast particle shapes were determined by shape similarity analysis algorithm [17, 18], and the model generation subroutine was compiled to randomly extract them. Finally, the refined ballast models were simulated as clumps by filling the three dimensional outline shapes with sphere elements.

The train load is transmitted to the ballast bed through wheels, rails, and sleepers, causing the stress concentration of ballast bed under the rail groove [17]. Therefore, the research area of ballast box in this study is shown in Fig. 2.

(a)   (b)
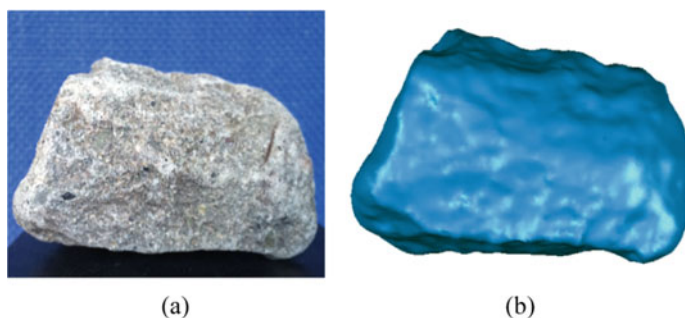
Fig. 1 Capture of ballast shape: **a** ballast sample, **b** capture results

Fig. 2 Research area of ballast box
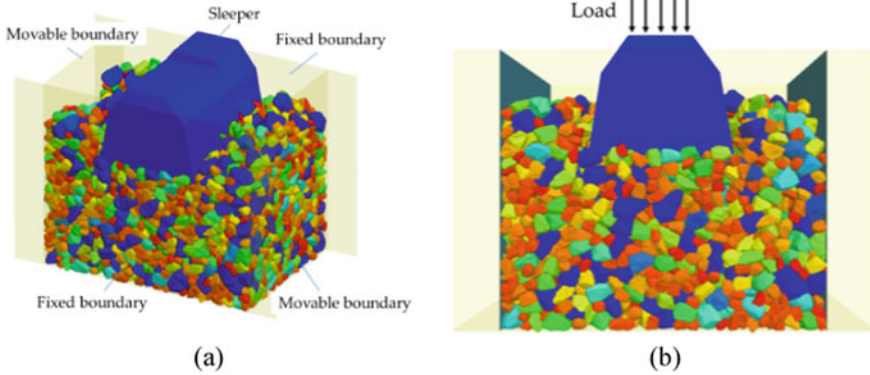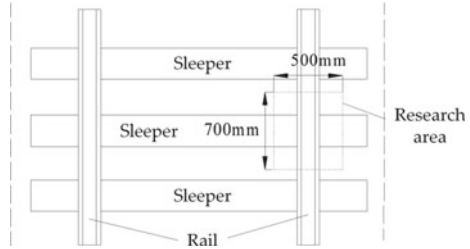
Fig. 3 Ballast box model with movable boundary

On the basis of fine simulation of ballast, the ballast box model with movable boundary was established by DEM, as presented in Fig. 3, whose gradation met the requirement of "Code for Design of High Speed Railway" [19]. The ballast models with different shapes were marked by different colors in this figure. The interaction between ballasts was calculated by Hertz-Mindlin contact model [20, 21]. The boundary in this model was moved by programming, which could reveal the longitudinal deformation of ballast bed, avoiding the analysis error of settlement caused by neglecting the varying of longitudinal force in ballast box with fixed boundary.

2.2 Load and Boundary Motion

The train load acting on the sleeper was simulated as a cosine function [11, 12], given by Eq. (1).

$$F(t) = F_0(\cos 2\pi f t - 1) \tag{1}$$

where $F(t)$ is the train load, t is the loading time, F_0 and f refer to the load amplitude and frequency, determined by axle load and running speed, respectively.

The model used a movable boundary to simulate the varying longitudinal force in ballast bed. In addition, the stress-displacement program module was innovatively developed to control the motion of boundary. The calculation process was as follows.

The velocity of moving boundary (v_t) is assumed to be invariable when the time step in DEM is short enough, and it can be calculated by Eq. (2).

$$v_t = v_{t-1} + w_a \Delta t \tag{2}$$

where Δt is the time step, v_{t-1} is the velocity of boundary in the last step, and w_a denotes the acceleration, presented in Eq. (3).

$$w_a = F_h / m_b \tag{3}$$

where m_b is the mass of moving steel wall, and F_h is the total force acting on it, as shown in Eq. (4).

$$F_h = \sum_{i=1}^{n} k_b \delta_{nb} - F_k(x) \tag{4}$$

where k_b is the normal stiffness of ballast, n is the number of ballast particles contacting with movable boundary, and δ_{nb} denotes the corresponding normal overlap. $F_k(x)$ is the longitudinal force, generated by the movable boundary, and it will be described later in this paper.

2.3 DEM Model Calibration and Validation

To calibrate the parameters of DEM model that we proposed, an experimental equipment of ballast box with movable boundary was innovatively developed, as shown in Fig. 4. The ballast box was loaded by large MTS fatigue testing machine. In addition, the ballasts were sieved to meet the requirement of "Code for Design of High Speed Railway" [19].

The mechanical parameters of DEM model were calibrated by comparing simulation and laboratory test results [15–18]. We take the contact stiffness as an example to analyze the calibration process, as shown in Fig. 5. It is clearly noticed that the simulation results are always in line with test results when the normal contact stiffness is 9.6×10^8 N/m, and the tangential contact stiffness is 6.3×10^8 N/m.

The mechanical parameters of DEM model were finally determined after dozens of tests, as presented in Table 1.

1-Counterforce crossbeam; 2-Ballast box; 3-Vertical displacement transducer; 4-Hydraulic servo loading device; 5-Vertical force transducer; 6-Rubber pad; 7-Sleeper; 8-Ballast; 9-Transparent plexiglass; 10-Biaxial bearing plate; 11-Biaxial bearing box; 12-Horizontal fixed rod; 13-Lateral displacement transducer; 14-Horizontal spring; 15-Horizonal force transducer; 16-Baseboard of ballast box; 17-Data collection system; 18-Laptop computer; 19-Counterforce column

(a)   (b)

Fig. 4 Laboratory test of ballast box: **a** sketch of ballast box, **b** experimental equipment of ballast box

Fig. 5 Comparison of simulation and test results

—— Laboratory test results
—●— Normal stiffness 5.0×10^9 N/m, tangential stiffness 3.0×10^9 N/m
—▲— Normal stiffness 3.0×10^9 N/m, tangential stiffness 2.0×10^9 N/m
—▼— Normal stiffness 9.6×10^8 N/m, tangential stiffness 6.3×10^8 N/m
—◆— Normal stiffness 6.0×10^8 N/m, tangential stiffness 3.0×10^8 N/m
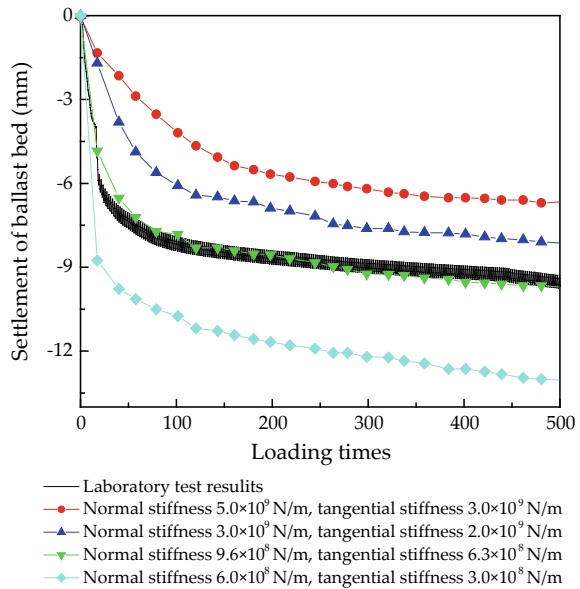
3   Results and Discussion

Based on the ballast box model with movable boundary, the effect of longitudinal force on the settlement of ballast bed is studied in this section at first. Then, the load with low frequency and high amplitude is used to analyze the effect of load amplitude

Table 1 Parameters of DEM model

Model parts	Parameters	Value
Sleeper	Normal contact stiffness (N/m)	1.0×10^9
	Tangential contact stiffness (N/m)	1.0×10^9
	Particle density (kg/m^3)	2.4×10^3
	Friction coefficient	5.0×10^{-1}
Ballast	Normal contact stiffness (N/m)	9.6×10^8
	Tangential contact stiffness (N/m)	6.3×10^8
	Particle density (kg/m^3)	2.7×10^3
	Density of ballasts (kg/m^3)	1.7×10^3
	Friction coefficient	6.0×10^{-1}
Boundary	Normal and tangential stiffness of box side (N/m)	1.0×10^9
	Normal and tangential stiffness of box bottom (N/m)	2.5×10^6
	Friction coefficient	2.0×10^{-1}

in heavy haul railway. Finally, the effect of load frequency in high speed railway is analyzed utilizing high frequency and low amplitude load.

3.1 Effect of Longitudinal Force

The longitudinal force of ballast bed is determined by the ballast compactness, contact states, etc., and it is linked to the confining pressure of ballast layer. The longitudinal could reveal the longitudinal stability of ballast bed. Therefore, it is valuable to figure out the effect of longitudinal force on the settlement of ballast bed, and this study can help to improve the maintenance and quality prediction of ballast bed.

To get the longitudinal force supplied by movable boundary, the boundary is moved at 1×10^{-4} m/s. In the simulation test, the longitudinal force and boundary displacement are recorded, as presented in Fig. 6. It is noticed that the variation of longitudinal force includes initial stage and stable stage. In initial stage (0–4 mm), the longitudinal force almost increases linearly with the increase in boundary displacement. In stable stage (4–14 mm), the longitudinal force keeps constant, due to the fact that shear failure happens in ballast bed. When the boundary displacement reaches 5 mm, the displacement trend of ballasts is presented in Fig. 7. The colors represent the displacement trend of ballasts, among which the red, green, and blue colors represent the fastest, second fastest, and slowest velocity, respectively. It is clearly seen that the ballasts in a certain distance ("d") from boundary are seriously affected, and the distance is determined by the quality of ballast bed. Besides, the ballasts move along the upper right slope, which is the shear failure surface. It indicates that shear strength is one of the most important factors affecting the mechanical properties of ballast bed.

Fig. 6 Variation of
longitudinal force with
boundary displacement
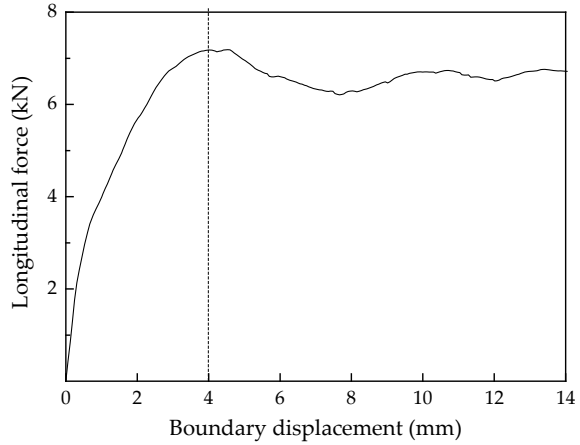
Fig. 7 Displacement trend
of ballasts
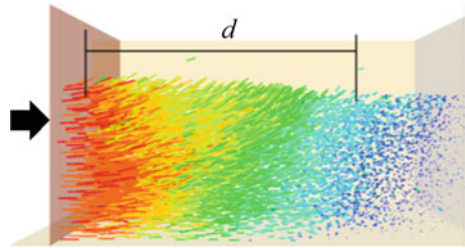
Based on the above analysis, the longitudinal force of ballast bed applied in simulation should be realized by programming, as shown in Fig. 8. In simulation test, the longitudinal force is assigned according to the corresponding curve in Fig. 8. The longitudinal force varies in every time step based on the displacement of movable boundary, thus realizing the settlement simulation of ballast bed under different longitudinal forces.

The ballast bed with different longitudinal forces is affected by train load, whose amplitude is 40 kN, and frequency is 44 Hz. The variation of settlement is shown in Fig. 9a. It is clearly noticed that the settlement process can be divided into initial settlement stage and stable settlement stage, respectively. In initial stage, the largest settlement is caused by the initial dozens of cyclic loads. The ballast bed becomes denser with the increase in loading times, leading to the decrease in settlement rate. When it comes to stable settlement stage, the settlement rate keeps constant. Moreover, the lager the longitudinal force is, the faster the stable settlement stage is reached.

When the loading times reach 1000, the variation of cumulative settlement with longitudinal force is presented in Fig. 9b. It is clearly seen that the cumulative settlement decreases with the increase in longitudinal force. When the longitudinal force

Fig. 8 Longitudinal force applied in simulation
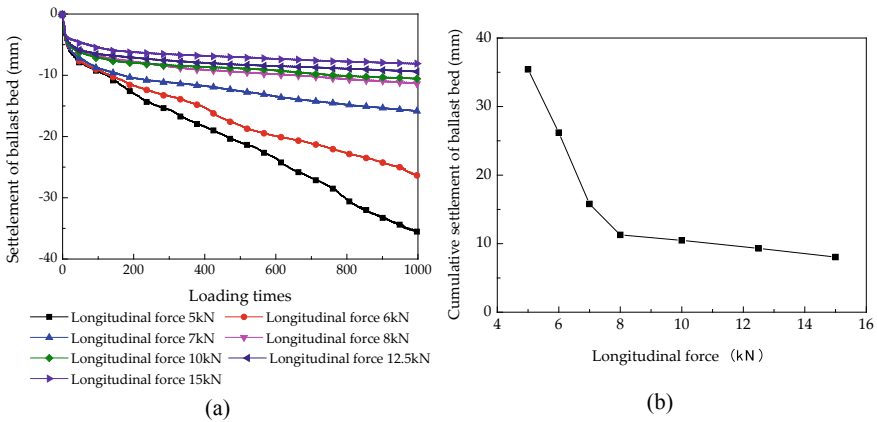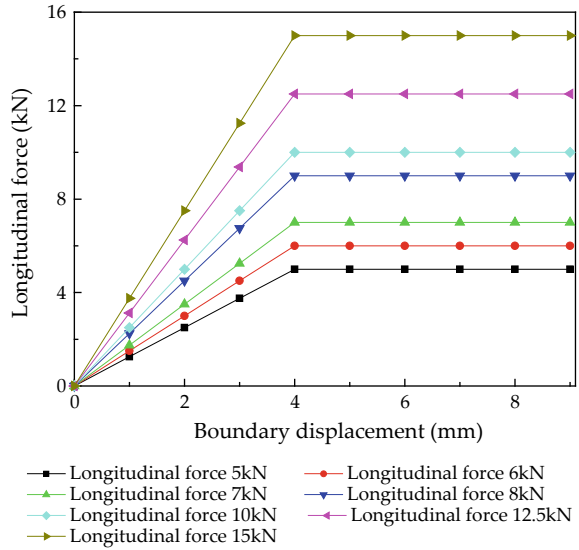
Fig. 9 Effect of longitudinal force on cumulative settlement of ballast bed: **a** settlement process while loading, **b** variation of cumulative settlement with longitudinal force

is less than 8 kN, it has a significant effect on the settlement of ballast bed. The settlement decreases by 68.2% when it ranges from 5 to 8 kN. However, the variation of settlement becomes slight when the longitudinal force is greater than 8 kN. The settlement decreases by 28.7% when it ranges from 8 to 15 kN. This is mainly because the movement of ballast particles is restricted by longitudinal force, thus controlling the settlement of ballast bed. When the longitudinal force is large enough, the ballasts are hard to be moved under the effect of train load, so its influence on the settlement gradually reduces.
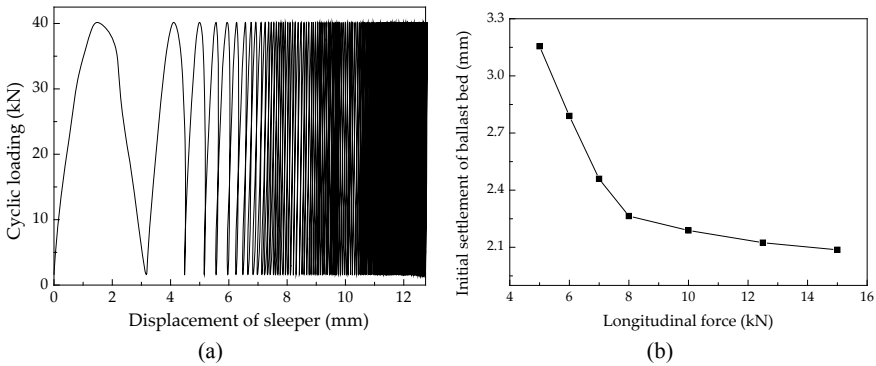
Fig. 10 Effect of longitudinal force on initial settlement of ballast bed: **a** dynamic displacement of sleeper while loading, **b** variation of initial settlement with longitudinal force

The initial settlement of ballast bed is one of the most important parameters in the prediction of settlement [22]. Therefore, the variation of initial settlement is analyzed in this section. When the longitudinal force is 5 kN, the dynamic displacement of sleeper in loading process is shown in Fig. 10a. It is noticed that the initial settlement is much larger than the settlement caused by later loads. The variation of initial settlement with longitudinal force is presented in Fig. 10b. As we can see, when the longitudinal force increases from 5 to 15 kN, the settlement decreases by 33.9%. To sum up, the longitudinal force has a great influence on the settlement characteristics of ballast bed. The longitudinal force is mainly determined by the compactness of ballast bed. Therefore, to maintain the geometry of ballasted track, the high compactness of ballast bed should be guaranteed.

3.2 Effect of Load Amplitude

The load axle has a great influence on the mechanical properties of ballast bed in heavy haul railway. Therefore, the effect of load amplitude on the settlement of ballast bed is necessary to be analyzed. In addition, the load frequency is 20 Hz, and the longitudinal force is 9 kN in this simulation. As seen from Fig. 11a, the settlement of ballast bed increases nonlinearly with the increase in load amplitude. The cumulative settlement of ballast bed when the loading cycle reaches 1000 is summarized in Fig. 11b. The settlement increases by 14% and 21% when the load amplitude ranges from 60 to 65 kN and 75 kN to 80 kN, respectively. It indicates that the maintenance workload of ballast bed increases nonlinearly with axle load in heavy haul railway.

The variation of initial settlement with load amplitude is shown in Fig. 12. It is clearly noticed that there is a significant positive correlation between them, which is similar to the variation of cumulative settlement. Therefore, excessive axle load will
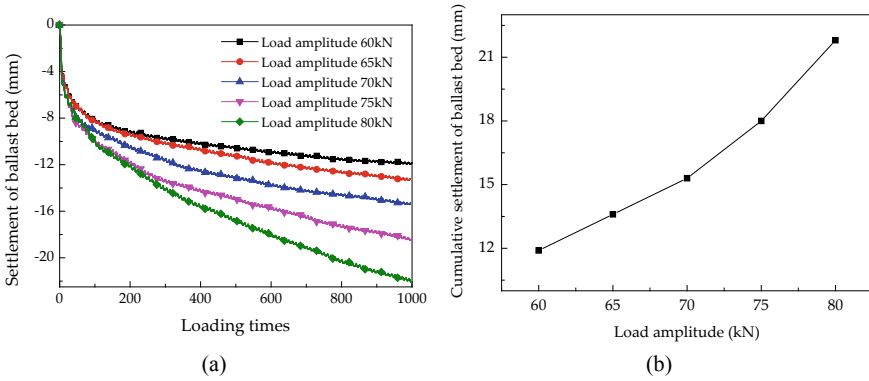
Fig. 11 Effect of load amplitude on cumulative settlement of ballast bed: **a** settlement process while loading, **b** variation of cumulative settlement with load amplitude

Fig. 12 Variation of initial settlement with load amplitude
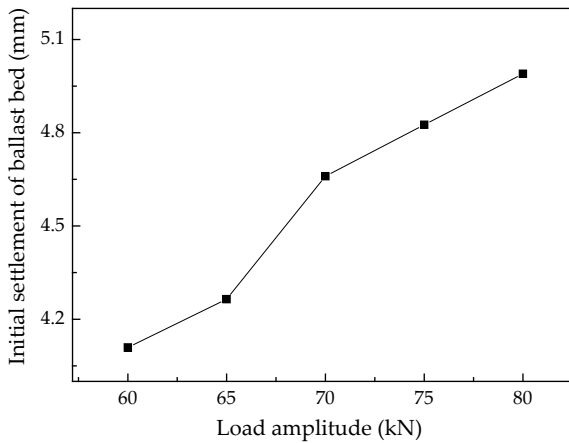
cause great damage to the quality of ballast bed, so it should be strictly limited in heavy haul railway.

3.3 Effect of Load Frequency

The mechanical properties of ballast bed are greatly affected by running speed in high speed railway. The load amplitude is 40 kN and the longitudinal force is 9 kN in this simulation. As shown in Fig. 13, the cumulative settlement of ballast bed increases with load frequency, ranging from 12.2 to 15.6 mm, and increasing by 27.87%. When the load frequency exceeds 40 Hz, there is a significant nonlinear
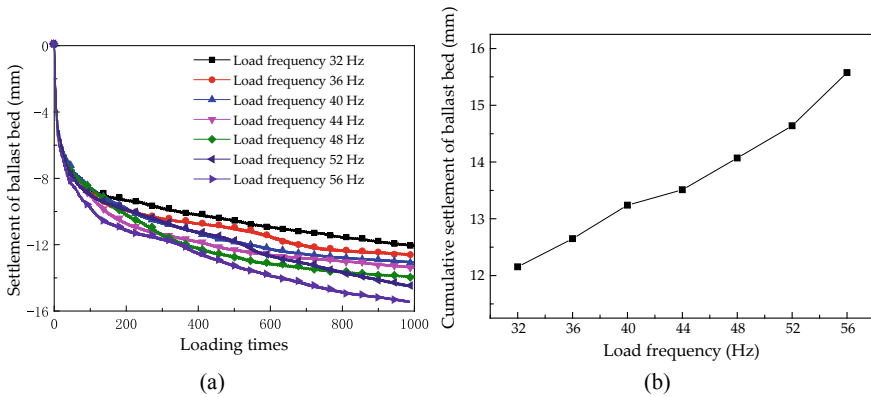
Fig. 13 Effect of load frequency on cumulative settlement of ballast bed: **a** settlement process while loading, **b** variation of cumulative settlement with load frequency

increase in settlement, which indicates that the increase in the train speed will cause damage to ballast bed.

The variation of initial settlement with load frequency is presented in Fig. 14. It is clearly seen that there is a negative correlation between them, which is contrary to the variation of cumulative settlement. In order to analyze the cause of this abnormal variation, the dynamic stress in ballast bed at different depths is analyzed.

The dynamic stress distribution under different load frequencies is presented in Fig. 15a, b, which are 32 Hz and 56 Hz, respectively. It is seen that the dynamic stress in ballast bed decreases with depth, but it varies a lot under different load frequencies. What is interesting is that the transmission depth of stress is deeper when the load frequency is smaller, as seen in Fig. 15. When the load frequency is 32 Hz, the average stress at 0.28 m from the bottom of sleeper is about 70% of that at 0.07 m. However, it is only 24% when the load frequency is 56 Hz. This indicates

Fig. 14 Variation of initial settlement with load frequency
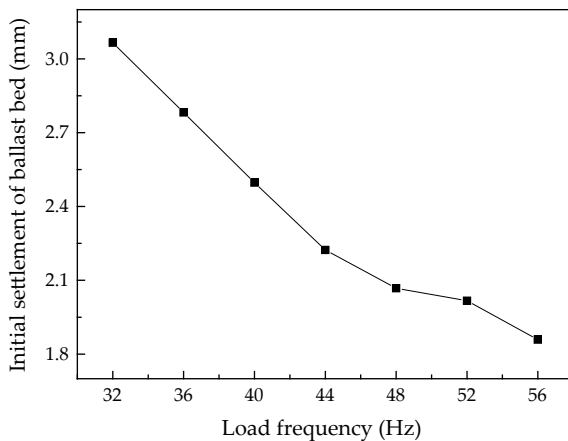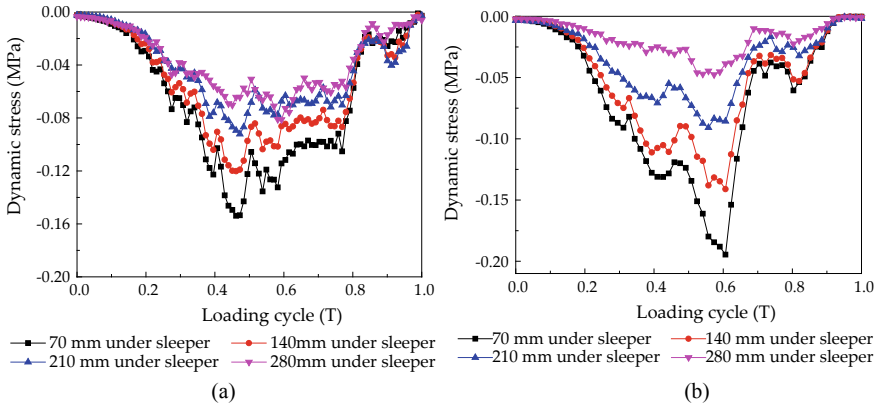
Fig. 15 Dynamic stress distribution under different load frequencies: **a** 32 Hz, **b** 56 Hz

that it is unlikely for dynamic stress caused by the first load to transmit to deep space of the ballast bed under the effect of high frequency load, so the initial settlement decreases with the increase in load frequency.

3.4 Regression Analysis of Settlement

On the basis of above analysis, it is discovered that there is a significant correlation between cumulative and initial settlement under the effect of longitudinal force, load frequency, and load amplitude. It is analyzed in this section, as illustrated in Fig. 16. As we can see, the cumulative settlement of ballast bed is positively proportional to initial settlement under the effect of longitudinal force and load amplitude. However, under the effect of high frequency load, the higher frequency will decrease the transmission depth of dynamic stress. Therefore, there is an abnormal negative correlation between the cumulative settlement and initial settlement.

4 Conclusions

In this study, the influence of longitudinal force, load amplitude, and load frequency on the settlement characteristics of ballast bed were researched, using a DEM model of ballast box with movable boundary. The main conclusions are as follows:

1. The settlement of the ballast bed under train load includes initial settlement and stable settlement stages. The settlement caused by the initial dozens of cyclic loads is the largest. The settlement of ballast bed is linear with the load repetitions
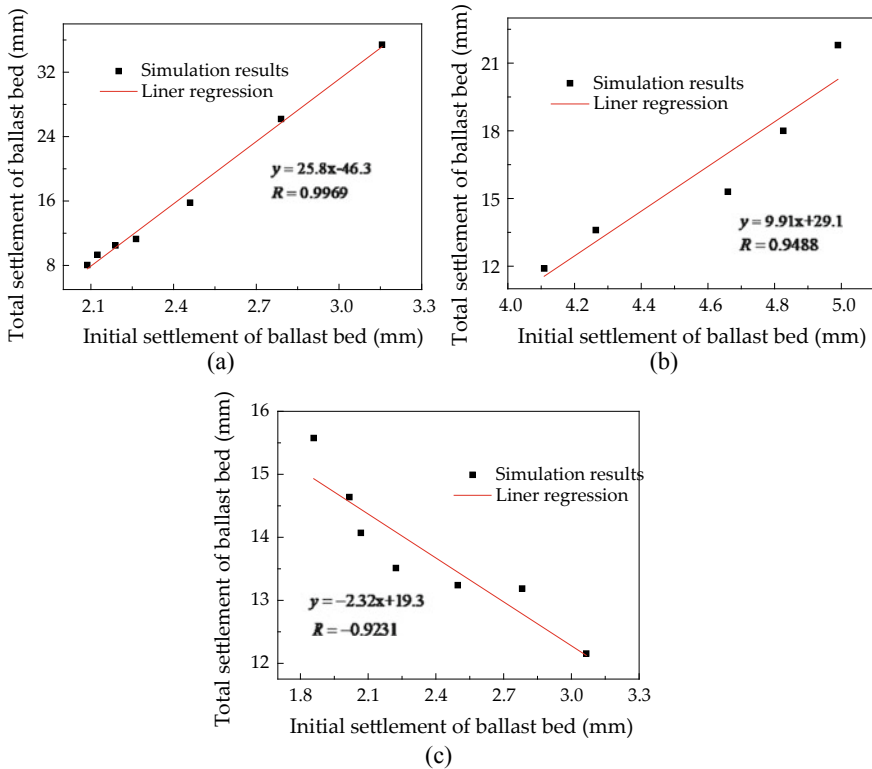
Fig. 16 Variation of cumulative settlement with initial settlement: **a** effect of longitudinal force, **b** effect of load amplitude, **c** effect of load frequency

in the stable settlement stage. More targeted maintenance plans should be made according to the settlement characteristics of ballast bed.

2. The insufficient longitudinal force will cause a large settlement of ballast bed. The larger the longitudinal force is, the faster the ballast bed will reach the stable settlement stage. When the longitudinal force is less than 8 kN, it has the most significant influence on the settlement of the ballast bed. The settlement decreases by 68.2% when the longitudinal force ranges from 5 to 8 kN. More attention should be paid to the longitudinal force of ballast bed in the detection and maintenance work of ballasted track.

3. The settlement of ballast bed increases nonlinearly with the load amplitude and frequency. When the load amplitude increases from 60 to 80 kN, the settlement increases by 83.2%. When the load frequency increases from 32 to 56 Hz, the settlement increases by 28.2%.

4. The initial settlement of ballast bed is proportional to the cumulative settlement under the effect of load amplitude and longitudinal force. However, the initial

settlement is inversely proportional to the cumulative settlement under high frequency load.

References

1. Diyaljee VA (2002) Repeated load aggregate degradation. In: Proceedings of the 6th international conference on the bearing capacity of roads and airfields
2. Renwei Hu, Hong W, Guotang Z (2001) Study on dynamic triaxial test and accumulated deformation of ballast. China Railway Sci 02:104–109
3. Indraratna B, Nimbalkar S (2013) Stress-strain degradation response of railway ballast stabilized with geosynthetics. J Geotech Geoenviron Eng 139(5):684–700
4. Indraratna B, Hussaini SKK, Vinod JS (2013) The lateral displacement response of geogrid-reinforced ballast under cyclic loading. Geotext Geomembr 39:20–29
5. Indraratna B, Navaratnarajah S, Nimbalkar S et al (2015) Use of shock mats for enhanced stability of railroad track foundation. Australian Geomech J 49(4):101–111
6. Hirakawa D, Kawasaki H, Tatsuoka F et al (2002) Effects of cyclic loading conditions on the behaviour of railway track in the laboratory model tests. In: Proceedings of the 6th international conference on the bearing capacity of roads and airfields
7. Qian Y, Tutumluer E, Mishra D et al (2013) Effect of geogrid reinforcement on railroad ballast performance evaluated through triaxial testing and discrete element modeling. In: International conference on soil mechanics and geotechnical engineering
8. Qian Y, Tutumluer E, Huang H (2011) A validated discrete element modeling approach for studying geogrid-aggregate reinforcement mechanisms. Geotechnical Special Publication
9. Selig ET, Waters JM (1994) Track geotechnology and substructure management. Thomas Telford, London
10. Al-saoudi NKS, Hassan KH (2014) Behaviour of track ballast under repeated loading. Geotech Geol Eng 32(1):167–178
11. Lim WL (2004) Mechanics of railway ballast behaviour. University of Nottingham, United Kingdom
12. Lim WL, Mcdowell GR (2005) Discrete element modelling of railway ballast. Granular Matter 7(1):19–29
13. Longlong Fu, Quanmei G, Shunhua Z et al (2013) Relationships between ballasted track settlement and differential subgrade settlement under train load. J Vibr Shock 32(14):23–28
14. Hong X, Liang G, Bowen H (2015) 3D discrete element analysis of selection of sleeper types on high-speed railway bridge. J Southwest Jiaotong Univ 05:811–816
15. Yang Xu, Liang G, Guotao Y et al (2014) Fine modelling of ballast grains and influence on mechanical properties of track bed. J China Railway Soc 36(9):73–78
16. Lu M, Mcdowell GR (2007) The importance of modelling ballast particle shape in the discrete element method. Granular Matter 9(1):69–80
17. Yang Xu, Liang G, Xiaopei C et al (2017) Influences of ballast gradation on railway ballast bed dynamic characteristics based on laser scanning and discrete element method. J Vibr Shock 36(5):20
18. Xu Y, Gao L, Zhang YR et al (2016) Discrete element method analysis of lateral resistance of fouled ballast bed. J Central South Univ 23(9):2373–2381
19. Code for design of high speed railway. TB 10621–2009. Beijing: China Railway Publishing House (2009)
20. Mindlin RD (1953) Elastic spheres in contact under varying oblique forces. Appl Mech 20:327–344

21. Johnson KL (1985) Contact mechanics. J Tribol 108(4):464
22. Ionescu D, Indraratna B, Christie HD (1998) Deformation of railway ballast under dynamic loads. In: Conference on railway engineering proceedings: engineering innovation for a competitive edge. Central Queensland University

Ballasted Track Maintenance Modelling Using DEM

Jean-Francois Ferellec, Eric Chapteuil, Nicolas Docquier, and Olivier Lantsoght

Abstract The ballast layer is a crucial component of railway tracks and it is hence essential to maintain it using adequate processes like tamping and stabilization. These will ensure that the density of the ballast layer is high enough to avoid shearing and settlement of the track under traffic. Ballasted tracks settle unevenly under the passage of trains. These geometrical defects are corrected by tamping which consists of lifting individually the sleepers and compacting the ballast underneath using vibrating tines. After tamping, the ballast layer is not homogeneous in terms of density along the track and requires stabilization before being commercially operational. This stabilization is performed either by regular trains at lower speeds for a given period hindering commercial operations, dynamic stabilization, or crib compaction. All these processes rely on vibrating the ballast layer using different approaches and have mainly been based on empirical observations. This paper describes an analysis of these ballasted track maintenance processes and their optimization using the discrete element numerical approach. This approach considers a granular material as an assembly of objects interacting through a specific contact law. In the present study, the code called LMGC90 has been used. The study includes a comparison of the processes in terms of ability to compact the ballast layer and lateral mechanical resistance of the track and their optimization. The final purpose of the project is to be able to specify optimal functioning parameters for all these processes.

J.-F. Ferellec (✉)
SNCF RESEAU, DGII-VA-CIR 6 Av. F. Mitterrand, 93574 La Plaine St Denis Cedex, France
e-mail: jean-francois.ferellec@reseau.sncf.fr

E. Chapteuil
VibraTeam, 28 chemin du Petit Bois, CS80210, 69134 Ecully, France
e-mail: eric.chapteuil@vibrateam.fr

N. Docquier · O. Lantsoght
Quandyga Engineering, Chemin du Cyclotron 6, 1348 Louvain-la-Neuve, Belgium
e-mail: nicolas.docquier@quandyga.com

O. Lantsoght
e-mail: olivier.lantsoght@quandyga.com

423

1 Introduction

Railway engineers struggle more and more maintaining ballasted tracks within their allowed budgets. Optimizing the maintenance operations became a challenge for many railway network owners in order to remain competitive in comparison with road or air transports. The principal maintenance operations are based on empirical observations and have barely changed for decades. Innovative numerical tools have emerged in parallel allowing a detailed analysis of their physical mechanisms and actions on ballast and hence their potential improvement.

The maintenance processes concerned are tamping, dynamic stabilization and crib compaction. The differential settlement of the track due to traffic is corrected by tamping which consists of repositioning the sleepers at their right location vertically and transversally and compacting the ballast underneath to keep them in place. After tamping the track requires stabilization of the ballast layer which is performed by letting regular trains roll on the track at lower speed hindering commercial traffic, by dynamic stabilization or crib compaction. Dynamic stabilization requires special equipment which simultaneously applies a load on the rails and vibrates them laterally and therefore also the sleepers and ballast surrounding them. The energy transmitted to the ballast is used to rearrange the grains and compact the ballast layer. In the crib compaction process, the ballast located between the sleepers and the shoulders is directly compressed using vertical compactors.

Analyzing experimentally these maintenance processes will quickly become costly in terms of time and budget. This paper describes the use of the numerical approach called discrete element method coupled with multibody system formalism to analyze and optimize tamping and, investigate crib compaction as an alternative to dynamic stabilization. The following sections explain this numerical approach and its application to reduce ballast fragmentation due to tamping and to compare the performance of crib compaction with that of dynamic stabilization.

2 Modelling via a MBS-DEM Coupling

On one hand, the Discrete Element Method (DEM) is a well-established approach to model granular material such as the ballast. It allows accounting for each grain of the media and its interactions with other particles. On the other hand, Multibody System (MBS) formalism enables to account for the dynamics of mechanical systems composed of several bodies connected by various kinds of joint. In particular, those methods are particularly adapted to study the dynamics of the maintenance machines (tamping machine, compacting machine or dynamic stabilizer).

Since the maintenance processes of the track imply dynamic interactions between the ballast and the machines, it is proposed to analyze and optimize their efficiency using a unified MBS-DEM modelling approach. This section gives a short summary of the two methods used for this paper. It then explains briefly how they are coupled. More details can be found in [1].

When considering DEM, the contact laws between the particles and the way they are handled deserve special attention. Classically, one can distinguish two main families. First, methods based on the «Molecular Dynamics» approach resort to regularized contact laws such as a spring-damper law and thus enable interpenetration between grains [2]. Estimating equivalent stiffness at the contact point is a tricky task. Furthermore, the equivalent stiffness may be very high, especially for ballast stones, requiring small time steps to avoid numerical instabilities. In contrast, the «Contact Dynamics» approaches consider a rigid contact and impose to solve at each time step the contact problem at the geometrical and dynamic levels for the whole set of particles. In particular, the method used in this paper is based on the Non-Smooth Contact Dynamics (NSCD) approach proposed by Moreau and Jean [3, 4]. This technique allows considering larger time steps but requires solving a complex contact problem which may be time-consuming. This second approach is used for the present work.

The NSCD method considers the equation of motion at the velocity level in terms of differential measure allowing for discontinuities of the velocity:

$$\mathbf{M}_G \mathrm{d}\mathbf{v}_G = \mathbf{f}_G(\mathbf{q}_G, \mathbf{v}_G, t)\mathrm{d}t + \mathbf{H}_G(\mathbf{q}_G)\mathrm{d}\mathbf{I}_U$$

where $\mathbf{q}_G$ is the vector of generalized coordinates describing the absolute position and the orientation of grains; $\mathbf{v}_G$ is the vector of generalized velocities of grains which is composed of the translation velocities $\mathbf{v}_i$ and the angular velocities $\boldsymbol{\omega}_i$ of each grain i; $\mathbf{M}_G$ is the mass matrix; $\mathbf{f}_G$ represents the non-linear dynamic terms and the force applied on the system; $\mathrm{d}\mathbf{v}_G$ is the differential measure associated with the velocity (it encompasses the continuous variation of the velocity and possible velocity jumps); t is the time, $\mathrm{d}t$ is the corresponding standard Lebesgue measure; $\mathrm{d}\mathbf{I}_U$ is the impulse measure associated with the contact reactions (it is composed of contributions of regular contact forces and possible impacts); $\mathbf{H}_G$ is a mapping operator between the global and contact local coordinates.

This set of equations must be completed by contact and impact laws. For the maintenance process application, Signorini-Coulomb is considered (see Fig. 1). The Signorini condition imposes a non-penetration condition while the Coulomb law corresponds to dry friction. In addition, impacts with null restitution are considered.

MBS formalisms are based on the same fundamental equations, i.e. the Newton–Euler equations. Several approaches exist, in particular for the description of the kinematics of the multibody chains. In the present work, relative coordinates are used [5]: the position and orientation of each body is defined with respect to a parent body (see Fig. 2). The variables of the system correspond to the degrees of freedom of the joints. In case of MBS presenting a tree-like structure (see Fig. 2a), i.e. there
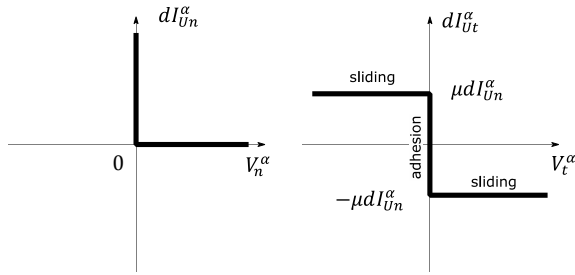
Fig. 1 Illustration of the Signorini-Coulomb law for a contact α between two particles. Left: in the normal direction, the Signorini condition imposes a complementarity relation between the normal component V_n^α of the relative velocity and the normal reaction dI_{Un}^α. Right: the Coulomb law defines sliding and adhesion zones for the relation between the tangential reaction dI_{Ut}^α and the tangential component V_n^α of the relative velocity depending on the normal reaction and the friction coefficient μ

a. Tree-like MBS   b. Closed-loop MBS
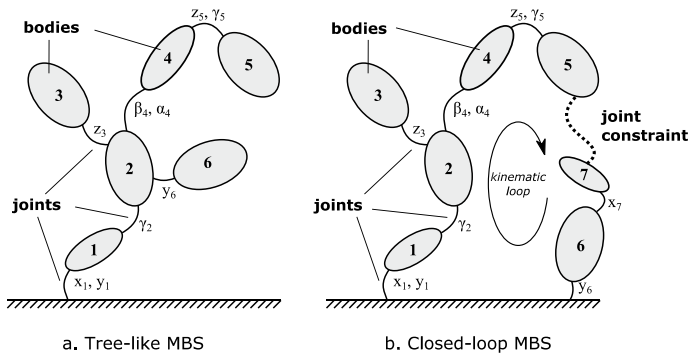
Fig. 2 Defining the kinematics of a multibody system (MBS) using relative coordinates. Left: a MBS with a tree-like structure: there is one path only between each body and the absolute frame. Right: a closed-loop MBS presenting a kinematic loop: one of the joints must be replaced by an algebraic constraint

is only one path from each body to the absolute frame, the equations of motion result in a system of ordinary differential equations (ODE). Formulated in terms of differential measure this set of equations can be written as follows:

$$\mathbf{M}_M(\mathbf{q}_M)d\mathbf{v}_M = \mathbf{f}_M(\mathbf{q}_M, \mathbf{v}_M, t)dt + \mathbf{H}_M(\mathbf{q}_G, \mathbf{q}_M)d\mathbf{I}_U$$

where $\mathbf{q}_M$ is the vector of joint position; $\mathbf{v}_M$ is the vector of joint velocities; $d\mathbf{v}_M$ is the differential measure associated with the multibody joint velocity; $\mathbf{M}_M$ is the mass matrix; $\mathbf{f}_M$ groups the non-linear dynamic terms, the forces/torques applied on the system and the joint forces/torques; $\mathbf{H}_M$ is the global–local mapping operator that links the multibody generalized coordinates to the contact coordinates.

Many MBS present kinematic loops (see Fig. 2b) which implies adding algebraic constraints, resulting in a set of differential–algebraic equations (DAE). In that case, the coordinate partitioning technique [5, 6] is used to reduce the DAE set to an ODE system presenting the same form as for tee-like MBS (See Ref. 1 for details).

The interaction between the machine and the ballast comes from the contact between ballast stones and some parts of the machine. Thus the dynamic coupling of the two-equation sets results from the contribution of the contact problem and leads to the following system:

$$
\begin{bmatrix} \mathbf{M}_G & 0 \\ 0 & \mathbf{M}_M(\mathbf{q}_M) \end{bmatrix} \begin{bmatrix} \mathrm{d}\mathbf{v}_G \\ \mathrm{d}\mathbf{v}_M \end{bmatrix} = \begin{bmatrix} \mathbf{f}_G(\mathbf{q}_G, \mathbf{v}_G, t) \\ \mathbf{f}_M(\mathbf{q}_M, \mathbf{v}_M, t) \end{bmatrix} \mathrm{d}t + \begin{bmatrix} \mathbf{H}_G(\mathbf{q}_G, \mathbf{q}_M) \\ \mathbf{H}_M(\mathbf{q}_G, \mathbf{q}_M) \end{bmatrix} \mathrm{d}\mathbf{I}_U
$$

This set of equations is discretized using a monolithic and implicit scheme, following the Moreau time-stepping method [2, 7]. The non-linear force vector $\mathbf{f}_M(\mathbf{q}_M, \mathbf{v}_M, t)$ is integrated explicitly. For the granular media, non-linearities of $\mathbf{f}_G(\mathbf{q}_G, \mathbf{v}_G, t)$ come from the angular velocity and require a specific treatment. The global–local mapping is used so as to formulate the dynamic equation in the local frame where the contact problem is solved. For this purpose, a Non-Linear Gauss-Seidl (NLGS) procedure is used. It consists of solving each contact one by one, assuming the others are solved. The operation is repeated several times until the algorithm converges to a solution.

The method is implemented by coupling two software programs: LMGC90[1] developed for the modelling of granular materials and ROBOTRAN[2] dedicated to MBS. On one hand, ROBOTRAN computes the kinematics and the dynamics of the multi-body chains [8]. It is based on a symbolic approach which enables it to easily give access to the equations of motion to LMGC90. On the other hand, LMGC90 calculates the dynamics of the ballast grains. Furthermore, LMGC90 gathers internal data with information coming from Robotran to perform a collision detection. Then, the NLGS algorithm of LMGC90 solves a monolithic contact problem accounting for the dynamics of both systems. The contribution of the contact problem solution is then accounted for in the dynamics of each system by the corresponding software.

The multibody model of the machine is illustrated in Fig. 3 is composed of 8 rigid bodies. It presents 2 kinematic loops. The mainframe is assumed to follow a vertical motion controlled by a joint force. Hydraulic actuators are modelled using two bodies connected by a prismatic joint where the squeezing force is applied. They are mounted on an eccentric shaft driven by a joint torque. This results in 4 degrees of freedom for the tamping unit. The ballast and the sleeper are modelled by convex polyhedra. The friction between the particles and between the particles and sleepers is set to 0.8, the restitution coefficient at contact to 0 and the rock density 2700 kg/m^3. The interaction of the two subsystems results from the contact of the tamping tool (arms and tines) with the ballast grains.

---

[1] https://git-xen.lmgc.univ-montp2.fr/lmgc90/lmgc90_user.

[2] http://www.robotran.eu.
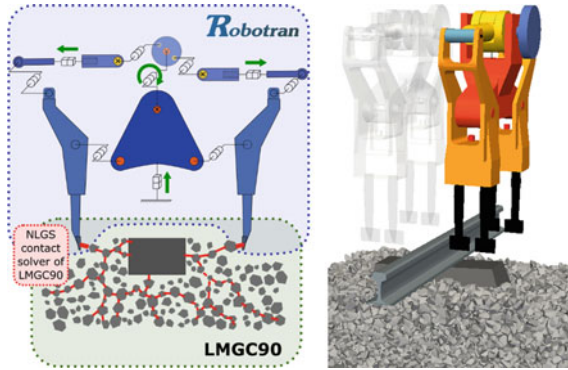
Fig. 3 Illustration of the strongly coupled MBS-DEM modelling of the tamping operation. Left: Schematic view of the model of one type of tamping machine modelled in Robotran interacting with a granular model of the track in LMGC90. The LMGC90 contact solver ensures the dynamic monolithic coupling between the two subsystems. Right: Screenshot of the 3D model before the machine enters the ballast

3 Maintenance Operations Modelling

3.1 Reduction of Ballast Fragmentation Due to Tamping

Tamping is a process used to put back into place the sleepers which have settled under traffic: each sleeper is lifted to its right position and the ballast under it is compacted in order to maintain it at that position. Tamping can be decomposed into two phases: insertion of the compacting tines on both sides of the sleeper and then squeezing of the ballast beneath that sleeper (Fig. 4). Although the tines are vibrating, the insertion phase can substantially damage the ballast hindering its shearing strength. One of the objectives of the present study was to reduce that degradation by measuring the
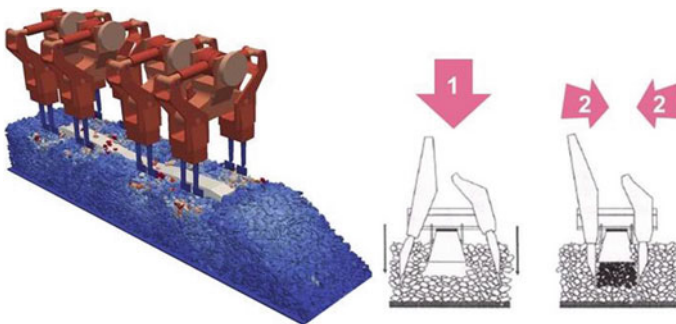
Fig. 4 Configuration of tamping simulations
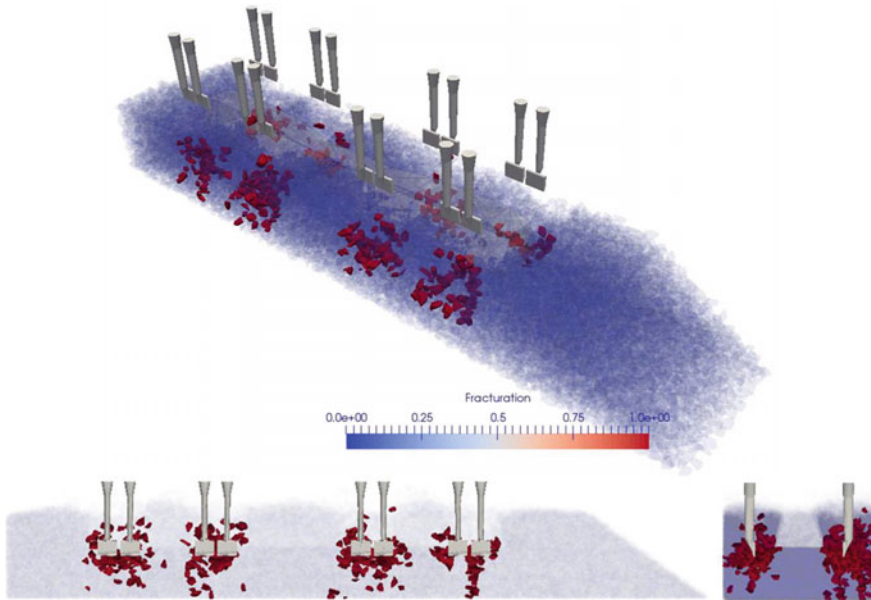
Fig. 5 Localization of fractured grains (in red) within the ballast layer

stress sustained by the ballast grains during tamping using the ability of the discrete element method to monitor the forces acting on each of them.

Figure 5 highlights in red the ballast grains which have sustained a pressure higher than the granite fragmentation threshold of 12 MPa (internal SNCF source) during tamping. Fragmentation is localized around the trajectory of the tines and occurs more significantly at the end of insertion. These results confirmed that tamping is very aggressive to ballast.

Different solutions have been analyzed to fluidize the ballast and hence temporarily reduce its shearing strength to facilitate the insertion of the tines but they have proved insufficient to reduce ballast fragmentation [9]. The present study explored the optimization of the insertion speed of the tines. The authors observed that the fragmentation of the ballast grains is higher at the end of the insertion and tried to decelerate the tines before they reach their final depth. In order not to increase the total tamping time, which can hinder maintenance operations, it was necessary to set the initial speed higher: in the end the longer the deceleration phase the higher the initial speed. Figure 6 (left) explains the tine insertion speed profiles analyzed: the conventional constant speed mode and additional profiles including a deceleration with initial speed between 1.7 and 2.5 m/s. Figure 6 (right) shows that even if the initial speed is higher the number of fractured ballast grains tends to decrease. A statistical analysis is necessary to confirm this tendency but because of the granular nature of ballast, deviation from this pattern can still be observed such as the one for 2.3 m/s.
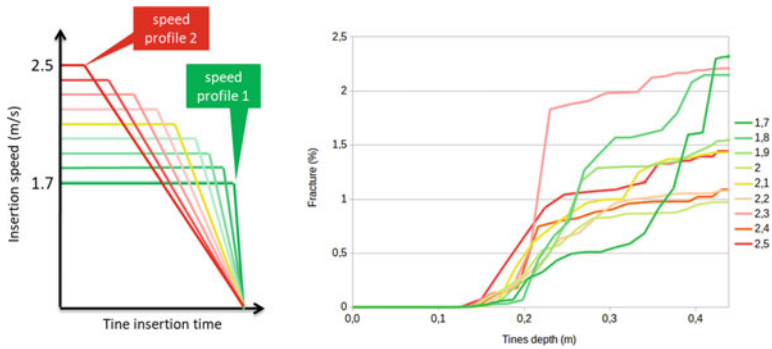
Fig. 6 Insertion speed profiles (left) and related fractured ballast grains numbers (right)
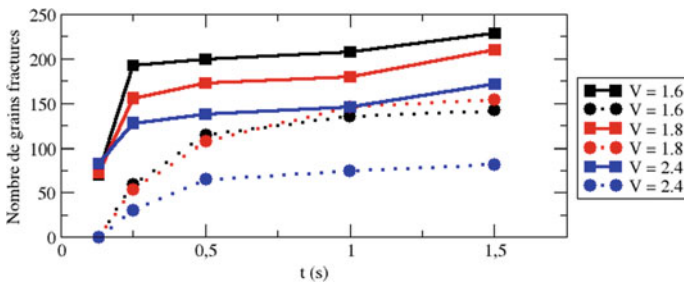
Fig. 7 Number of fractured ballast grains with (dot lines) and without (continuous lines) MBS

The DEM approach coupled with MBS (ROBOTRAN) has been used to model the same process. Figure 7 presents a comparison of the numbers of fractured ballast grains estimated from the stress on the grains at five different times of tamping simulation using MBS or not for three initial insertion speeds and taking into account a 12 MPa fracturing threshold. It shows that the non-MBS approach over-estimates the number of fractured grains as can be expected in a model where the trajectories of the tamping tines are fully defined. The results with MBS confirmed that prescribing a deceleration of the tines at the end of the insertion helps to decrease the fragmentation of the ballast grains.

3.2 Comparison of Crib Compaction with Dynamic Stabilization

Even if it corrects its geometry, tamping is not sufficient to restore the track to full operational conditions: the ballast layer density is not homogeneous anymore and the contacts with the sleeper are reduced impacting, in the same manner, the lateral resistance of the track crucial to prevent rail buckling during heat waves.

This condition after tamping impedes regular traffic and requires that trains travel at lower speeds completing a given tonnage high enough to stabilize the ballast layer. This stabilization corresponds to a denser rearrangement of the ballast grains under the vibrations created by the trains rolling on the track. This rearrangement can be accelerated by transferring directly mechanical energy to the ballast layer by vibrating the rails using dedicated equipment. This is the idea behind dynamic stabilization where the rails are vibrated laterally while a load is applied to them. This process is now systematically applied after tamping on the French railway network. However, there are situations where it cannot be applied, such as on steel bridges because of possible resonance phenomena. Crib compaction is a possible alternative to dynamic stabilization but is barely used in France. Before being implemented, it was assessed experimentally and numerically as in the present study by comparison to dynamic stabilization.

Both dynamic stabilization and crib compaction were compared numerically using a four sleeper section (Fig. 8). In dynamic stabilization, the lateral speed of the sleepers was set to a cyclic signal of 0.2 m/s at 25 Hz limited in amplitude by a 0.75 Hz sinusoidal envelope, repeated twice. Simultaneously a bell-shaped load of 60 kN was applied. In crib compaction, a vertical vibrating load of 50 Hz/45 kN was applied on the cribs and shoulders of the track for 2 s. These are typical values for both processes.

While in dynamic stabilization the ballast layer surface was barely modified, in the crib compaction process the shoulders of the track were heavily settled by the side compactor (Fig. 9) and in the end the ballast, profile did not comply anymore with the French standard. Figure 10 shows a comparison of the density along the track after tamping, dynamic stabilization and crib compaction. The initial layer of ballast was created by letting ballast grains settle under gravity leading to a homogeneous layer in terms of density around 55% (ratio between volume of rocks and volume of rocks + voids). After tamping, the layer was heterogeneous and presented peaks of density under the sleepers. After crib compaction, the layer was denser and more homogeneous. After dynamic stabilization, the layer was denser but still
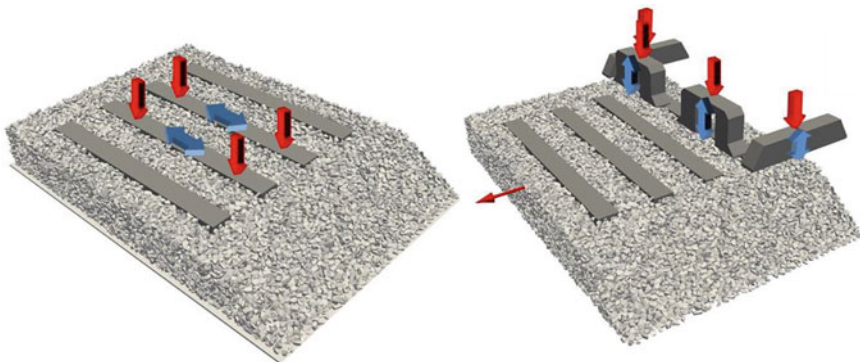
Fig. 8 Concepts of dynamic stabilization (left) and crib compaction (right) in simulations
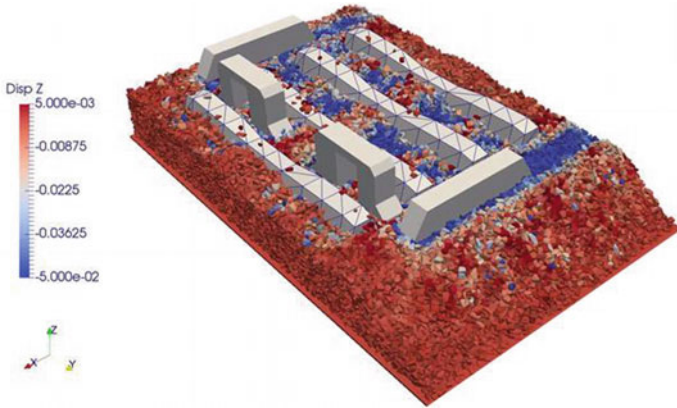
Fig. 9 Settlement of ballast after crib compaction in simulations
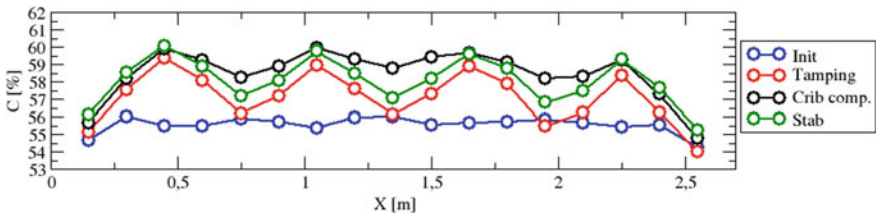
Fig. 10 Density of the ballast layer along the track

heterogeneous. Further simulations of crib compaction without side compactors are underway and seem promising in terms of compaction.

Figure 11 shows that the two processes worked in opposite ways. Crib compaction pushed the ballast grains of the cribs under the sleepers while dynamic stabilization moved them away from under the sleepers to the cribs leading to a settlement of the track.
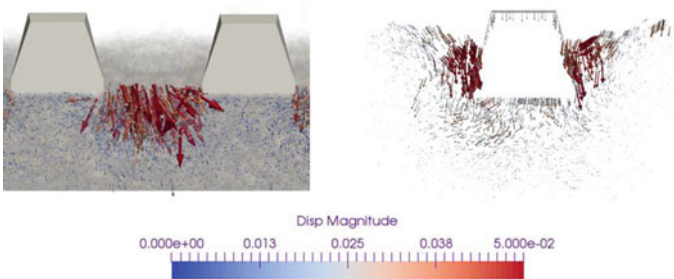
Fig. 11 Displacements of ballast grains in dynamic stabilization (left) and crib compaction (right)
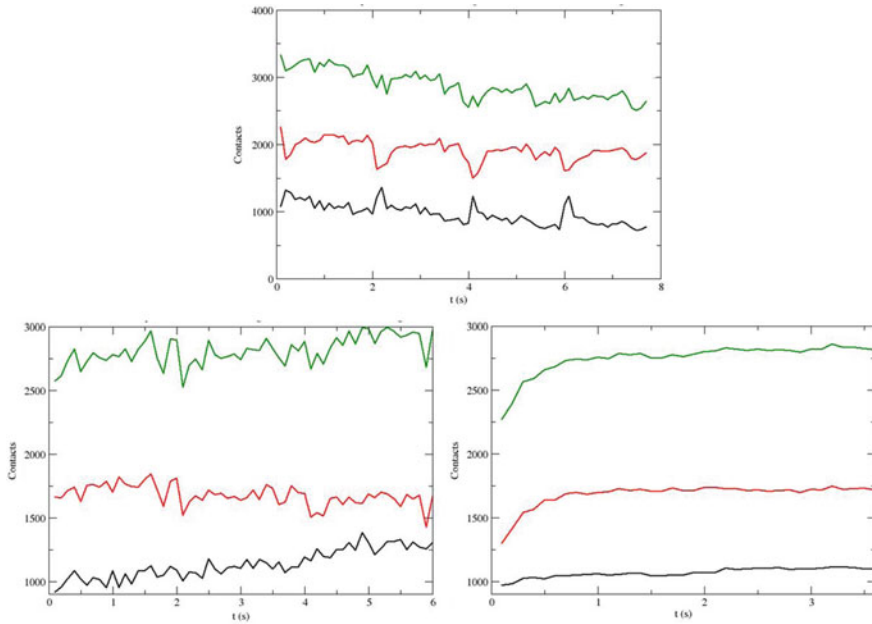
Fig. 12 Evolution of the number of contacts underneath the sleepers (in black) on the sides of the sleepers (in red) and all (in green) during tamping (top), during crib compaction (bottom left) and during dynamic stabilization (bottom right)

The performance of each process can be measured by the number of contacts created between the ballast grains and the sleepers because the more contacts the better the lateral resistance of the track for similar densities. Figure 12 shows the evolution of the number of contacts underneath the sleepers and on the sides of the sleepers during all processes. Tamping obviously decreased the number of contacts particularly under the sleeper confirming the instability of the layer after this process. Crib compaction increased the number of contacts under the sleepers while dynamic stabilization increased the number of contacts on the sides of the sleepers. Previous internal studies have shown that the bottom of the sleeper contributes at a higher level to the lateral resistance than the sides of that sleeper which means that a higher lateral stability can be expected after crib compaction than dynamic stabilization. Further simulations are underway to clarify this assumption.

4 Conclusions

The discrete element approach is an adequate method to analyze and optimize the maintenance processes of ballasted railway tracks and is even more efficient when coupled with the multibody system method.

The simulation results show that the fragmentation of ballast due to tamping can be reduced by controlling the insertion speed of the tines. They also confirm that crib compaction is an efficient alternative to dynamic stabilization in terms of compaction capability and potentially lateral resistance of the track.

Experimental tamping tests are underway to confirm and measure the effect of tamping on the degradation of ballast.

References

1. Docquier N, Lantsoght O, Dubois F, Brüls O. Modelling and simulation of coupled multibody systems and granular media using the non-smooth contact dynamics approach. Accepted for publication in Multibody System Dynamics
2. Cundall PA, Strack ODL (1979) Discrete numerical model for granular assemblies. Geotechnique 29(1):47–65
3. Moreau JJ (eds) (1988) Unilateral contact and dry friction in finite freedom dynamics Nonsmooth. Mechanics and applications, CISM 302. Spinger, pp 1–82
4. Jean M (1999) The non-smooth contact dynamics method. Comput Methods Appl Mech Eng 177:235–257
5. Samin J-C, Fisette P (2003) Symbolic modeling of multibody systems. Springer, p 483
6. Wehage RA, Haug EJ (1982) Generalized coordinate partitioning for dimension reduction. Anal Constr Dyn Syst J Mech Des 104:247–255
7. Dubois F, Acary V, Jean M (2018) The contact dynamics method: a non-smooth story. Comptes Rendus Mécanique 346:247–262
8. Docquier N, Poncelet A, Fisette P (2013) ROBOTRAN: a powerful symbolic generator of multibody models. Mech Sci 4:199–219
9. Ferellec JF (2019) Optimisation of ballasted tracks maintenance using DEM. In: 8th international conference on discrete element methods, 21st–26th July 2019. The Netherlands

Dynamic Behavior Modeling of Full-Scale High-Speed Ballasted Track Using Discrete Element Method

Zhongyi Liu, Bin Feng, Wei Li, Erol Tutumluer, Xuecheng Bian, and Youssef M. A. Hashash

Abstract Ballast layer dynamic behavior is critically important for railway track design and maintenance optimization. This paper presents findings on crosstie and ballast particle dynamic responses obtained from: (i) laboratory tests conducted at Zhejiang University innovative high-speed rail tester (ZJU-iHSRT) and (ii) discrete element method (DEM) simulations using algorithms with newly featured parallel computing capability developed at UIUC. Overall, more than 170,000 ballast particles and eight crossties were assembled in the DEM model. A proportional integral derivative (PID) controller was utilized to ensure realistic dynamic loads applied on crossties at three train speeds: (1) 108 km/h; (2) 252 km/h; (3) 300 km/h. Crosstie vibration velocities predicted using the DEM model matched closely with measurements from laboratory tests both in trends and in magnitudes. With Fourier transformation and Butterworth filter techniques implemented on ballast particle vibration velocities captured in the DEM model, inherent signal noise could be reduced, and as a result, the predicted ballast particle vibration trends matched closely with laboratory sensor measurements. However, individual ballast particle vibration magnitudes predicted by the DEM simulations revealed certain discrepancies with the measurements since velocity sensors used in the experiment only recorded vibration

---

Z. Liu · B. Feng · E. Tutumluer (✉) · Y. M. A. Hashash
University of Illinois At Urbana-Champaign, Urbana, IL 61801, USA
e-mail: tutumlue@illinois.edu

Z. Liu
e-mail: zhongyi3@illinois.edu

B. Feng
e-mail: binfeng2@illinois.edu

Y. M. A. Hashash
e-mail: hashash@illinois.edu

W. Li · X. Bian
Zhengjiang University, Hangzhou, China
e-mail: zjulw222@zju.edu.cn

X. Bian
e-mail: bianxc@zju.edu.cn

responses of an assembly of ballast particles. Further studies are necessary to reveal more detailed findings.

Keywords Railway · Crosstie · Ballast · Discrete element modeling · Dynamic response · Fourier transformation · Signal filtering

1   Introduction

Ballasted track is a common track type used in railway corridors in the USA Ballasted track consists of two parts: (1) superstructure, including rail, fastener and crosstie; (2) substructure, including ballast, subballast and subgrade. Compared to a ballast-less slab track, ballasted track can provide better drainage and flexible support to the track and is generally more economical to construct. Because of the significant infrastructure investments by freight companies in ballasted track, current U.S. high-speed railway (HSR) programs often need to share trackage with freight trains in joint rail corridors [1, 2]. As investigated in previous studies [3], higher train speed will routinely amplify crosstie movements and increase deformations of the particulate natured ballast layer, which presents challenges for constructing a safe, reliable and sustainable HSR infrastructure. To tackle such challenges in HSR construction where speed increases are introduced in joint lines, a better understanding of the dynamic behavior of crosstie and ballast components in a ballasted track system is important and necessary.

Discrete element method (DEM) is a numerical modeling approach widely used by researchers to investigate ballasted track deformation behavior due to its suitability to model individual ballast particle interactions under dynamic train loading scenarios. Tutumluer et al. developed crosstie-ballast DEM models to predict ballast settlement trends and validated the models with field measurements [4, 5]. Ngo et al. used DEM to simulate behavior of geogrid stabilized ballast fouled with coal in a shear box [6]. Huang et al. also achieved simulations of fouled ballast in a shear box by adjusting particle surface friction angles [7]. Hou et al. developed crosstie support condition models using DEM to study effects of crosstie support condition on ballasted track dynamic responses under static loading, and subsequently, Bin et al. introduced dynamic train loading patterns at different speeds into the crosstie support condition models for further investigating mixed train traffic effects [3, 8]. Previous studies mainly concentrated on modeling laboratory shear tests or one crosstie-ballast model under designed loading, and such models performed well in analyzing local ballasted track performance.

Note that there is a lack of research studies in the literature and therefore a gap in our understanding, when it comes to focusing on large-scale DEM simulations of ballasted track in relation to full-scale experiments involving multiple crossties and various dynamic loading scenarios associated with high-speed passenger trains. This study is intended to partially fill the current gap by constructing a full-scale, realistic

DEM ballasted track model with eight crossties and over 170,000 ballast particles and simulating the full-scale laboratory tests conducted at Zhejiang University (ZJU).

2 Full-Scale High-Speed Rail Tester (ZJU-IHSRT)

As shown in Fig. 1, the Zhejiang University innovative high-speed rail tester (ZJU-iHSRT) is a full-scale experimental facility equipped with eight actuators that can work in a specific sequential way to simulate train passages up to 360 km/h. The tie

Fig. 1 Full-scale high-speed railway tester (ZJU-iHSRT): **a** longitudinal cross-section view; **b** actual image of the ZJU-iHSRT

(a)
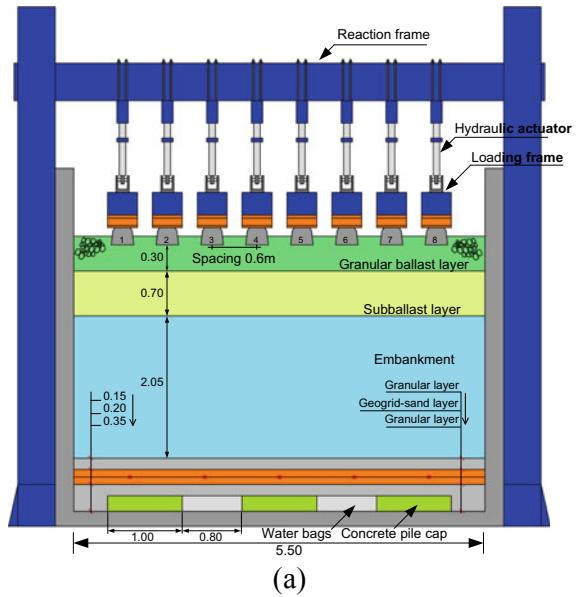
(b)

spacing is 0.6 m, and rail segments were installed on the crossties to transfer load from actuators downwards. The eight IIIc-type concrete crossties were placed on top of the physical model substructure, which consisted of a 0.3 m ballast layer, a 0.7 m subballast layer, a 2 m embankment and a 0.7 m piled foundation from the top down. Figure 2b shows the installation locations of vibration velocity meters on the surface of ballast layer and crossties in the physical model. Especially, records of velocity sensors V2 (at centerline of No. 5 crosstie surface) and V4 (at centerline between No. 5 and No. 6 crossties) were selected to verify the DEM model outputs in this study. The corresponding crosstie and ballast locations monitored in the DEM model are also labeled in Fig. 2a.

The resultant loadings on fasteners were analogous to field loadings as illustrated in a previous paper [9] based on Takemiya and Bian's train-track analysis model [10]. In total, three loading patterns were created to simulate three speeds: 108, 252 and 300 km/h. The speed effect on loading magnitude was not considered in this study. Therefore, the same loading magnitude, i.e. 80 kN, at each speed was used. The differences among loading patterns were reflected in different durations between two adjacent peaks.

(a)

(b)
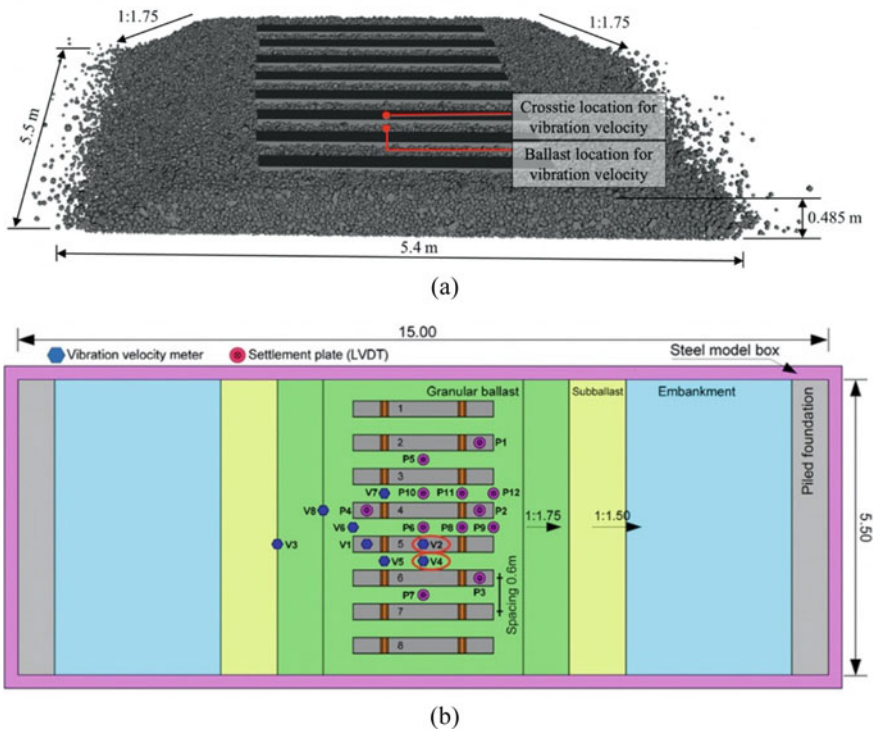
Fig. 2 **a** DEM model geometry and locations for vibration velocity analysis; **b** top view of the vibration velocity sensors installed in the full-scale physical model

3   DEM Simulation

3.1   Model Setup

BLOKS3D, a polyhedral 3D DEM code at the University of Illinois with parallel computation capability, was used to simulate the full-scale tests conducted at ZJU-iHSRT and establish a better understanding of the ballasted track dynamic response behavior. In accordance with the physical model at ZJU-iHSRT, the DEM model as shown in Fig. 2a placed eight crossties on over 170,000 ballast particles with overall model dimensions of 5.5 m × 5.4 m × 0.485 m. The ballast shoulder slopes at both sides were 1:1.75. Shape and angularity properties of ballast particles utilized in the DEM model were the same as those in the full-scale physical model analyzed with the Enhanced University of Illinois Aggregate Image Analyzer (E-UIAIA) [11, 12]. Gradation of ballast layer satisfied the requirement of No. 4A gradation of the American Railway Engineering and Maintenance-of-Way Association (AREMA). The bottom boundary under the ballast layer was modeled as a rigid plane with a contact normal stiffness of 20 MN/m. Note that particle breakage is not allowed in the BLOKS3D DEM model. However, Qian found that the gradation of limestone ballast aggregates was approximately identical to original after three permanent deformation tests (i.e. up to 30,000 repetitive loading cycles) which suggest negligible degradation [13]. Considering limited number of loading cycles in this study, it is reasonable to assume particle breakage was not predominant.

3.2   Loading Patterns with PID Controller

The three loading patterns acting on the fasteners in the physical model were used as input in the DEM simulation. To ensure reaction force reaching the same target force as applied in the physical model at ZJU-iHSRT, a validated PID controller was implemented in DEM simulation [9]. The controller generates force using feedback error as follows:

$$f(t) = k_p e(t) + k_i \int_0^t e(\tau) \mathrm{d}\tau + k_d \frac{\mathrm{d}e}{\mathrm{d}t}$$

where f is control force and e is the error between reaction force and target force. Thus, the control force is a sum of three terms: P-term (which is proportional to error) represents present value of error; I-term (which is proportional to integral of error) reflects historical error; and D-term (which is proportional to derivative of error) is interpreted as prediction of future error. At every time step in the DEM model, the resultant force acting on crossties is updated with the PID controller as illustrated in Fig. 3.
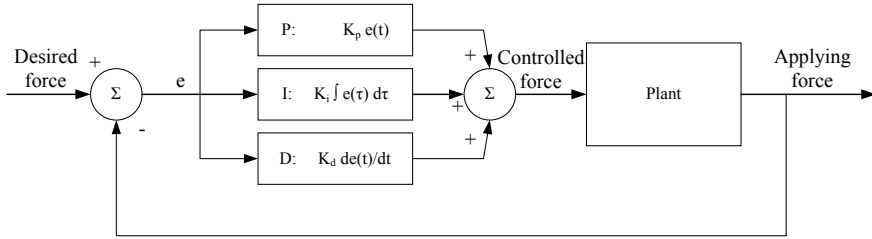
Fig. 3 A PID controller block diagram: a contact force feedback loop

4   Results and Discussion

With the large-scale DEM simulation model, dynamic responses such as velocities, forces and particle centroid coordinates were recorded at small time intervals of 1.62×10^{-4} seconds in the simulation of train passing. To validate the DEM model outputs with experimental results, crosstie and ballast layer vertical vibration velocities at the similar locations were investigated. Figure 2a labels the investigated crosstie and ballast layer surface locations in the DEM model, and the corresponding sensor V2 and V4 installation locations in the physical model are circled in Fig. 2b.

4.1   Comparisons of Crosstie Vibration Velocities

Figure 4 compares crosstie V2 sensor vibration velocities measured in the full-scale physical model and DEM model simulation data at three different speeds of 108, 252 and 300 km/h. The positive velocity in the figure indicates the crosstie moving upward, while the negative value means the crosstie is moving downward.

It is clearly shown in Fig. 4 that crosstie vibration velocities predicted from the DEM model match well with those measured from the full-scale physical model in both the vibration trends and magnitudes at the three investigated speeds. The magnitudes increasing with higher train speeds can be observed as well. The crosstie vibration velocities from the DEM model fluctuate obviously more than those from the physical model at the speed of 108 km/h. Such performance could possibly be explained as ballast particle abrasion, edge chipping and even breakage that may have happened in the physical model, whereas ballast particle sizes and shapes were kept unchanged with train loadings in the DEM model. With many train passes, the ballast particles underneath the tested crosstie would be denser and good shakedown achieved in the physical model. Better support condition underneath the crosstie in the physical model would lead to steadier vibrations. Note that at 252 and 300 km/h, the crosstie vibrates more smoothly than that at a speed of 182 km/h, and this can be caused by shorter rest period or free vibration time for the crosstie at speeds of 252 and 300 km/h.
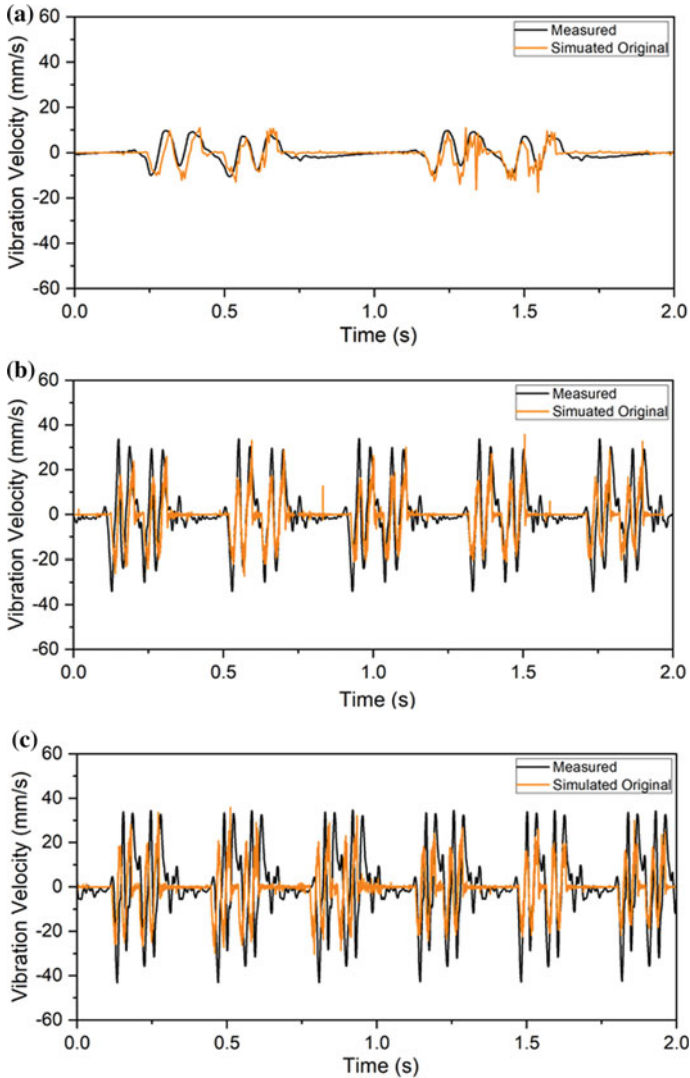
Fig. 4 Crosstie vibration velocity comparison between the experiment and DEM model: at speeds of **a** 108 km/h, **b** 252 km/h, **c** 300 km/h

Based on the study by Boler et al., the loading frequencies related to train configurations at the three investigated speeds are all under 30 Hz [14]. Therefore, ballast vibration frequencies should be in a range from 1 to 30 Hz. To eliminate the effect of vibrations for frequencies over 30 Hz, a proper signal filtering is required. Filtering is a common practice for removing some unwanted components of a signal so that component of interest in a measured signal can be emphasized. As for this study, Butterworth filter with order of 3 was implemented. The orange lines in Fig. 5c, d
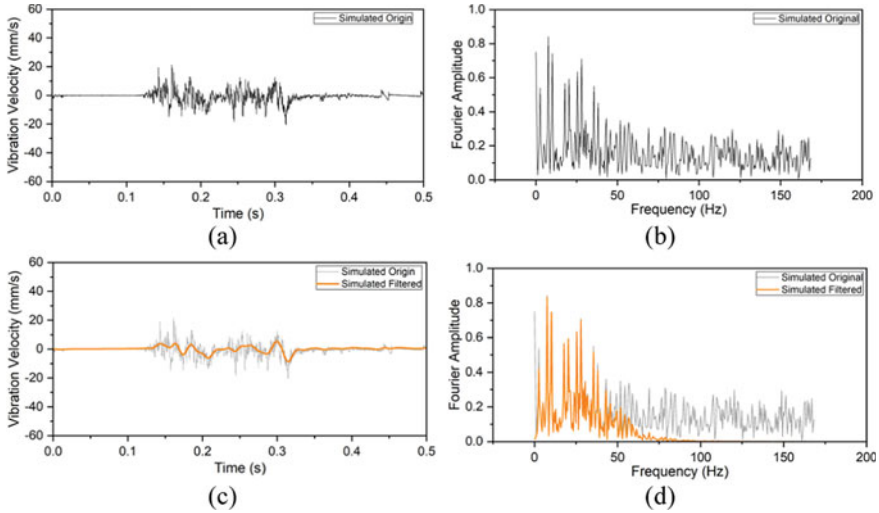
Fig. 5 Fourier transformation and Butterworth filter illustrations: **a** time domain, **b** frequency domain

display the selected ballast particle (#149091 in the DEM model) filtered vibration velocities in time and frequency domain, respectively. Black lines illustrate the unfiltered original data, the same as those in Fig. 5a, b. Figure 5d demonstrates that the Butterworth filter indeed decreased the vibrations for frequencies over 30 Hz and the dissipation rate was smooth from 30 to 100 Hz. After converting the filtered data to time domain, i.e., orange lines shown in Fig. 5c, noise was cut down dramatically and the vibration velocities display trends with the train passes more explicitly. Thus, using a Butterworth filter can efficiently clean noise and expose features of vibration velocities simulated in the DEM model. In this study, such a technique was applied to all ballast vibration velocities in the DEM model.

4.2 Comparisons of Ballast Vibration Velocities

The vibration sensor installed in the ballast layer in the ZJU-iHSRT consists of two parts: (1) the measurement sensor placed on top of the ballast layer, and (2) the 0.2 m long nail-like metal frame inserted into the ballast layer. Thus, not a specific individual ballast particle was detected by the sensors during dynamic loadings, and the recorded vibrations by such sensors might reflect combined dynamic responses of all surrounded ballast particles. To accurately compare the ballast layer vibrations at V4 (see Fig. 2b) between the physical model and the DEM model, vibration velocities of all ballast particles, located within a 0.30 m × 0.30 m × 0.30 m region around ballast vibration sensor, were monitored throughout the whole simulation. In total,

426 ballast particles in the DEM model were monitored and their vibration velocities were analyzed.

Figure 6 presents the ballast vibration velocities measured from V4 sensor in the full-scale physical model, and the original and filtered predictions from the DEM model at three different speeds: 108, 252 and 300 km/h. Positive value represents the ballast particles moving upwards, and negative value means the ballast particles
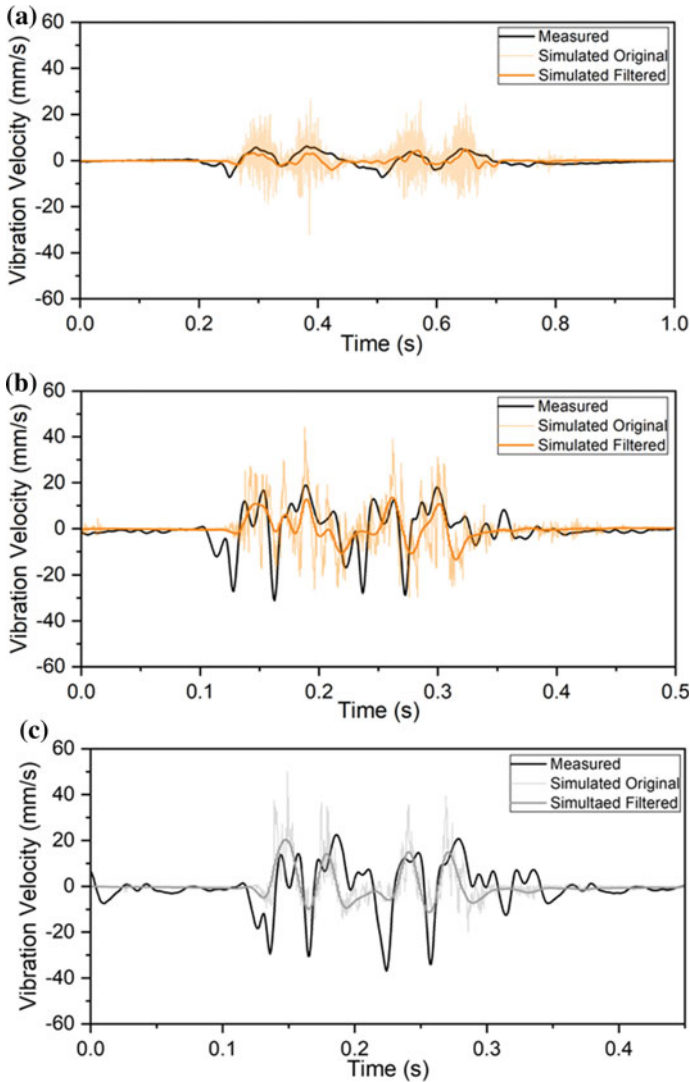
Fig. 6 Ballast vibration velocity comparisons between physical model and DEM model (original and filtered): at speeds of **a** 108 km/h, **b** 252 km/h, and **c** 300 km/h

moving downwards. Solid black lines are the vibration velocities collected from V4 sensor. The light orange lines and orange lines in one figure represent original and filtered vibration velocities of one particle out of the 426 monitored ballast particles, respectively. Note that the ballast particles selected in Fig. 6a–c are all different.

Overall, a good match can be observed in both trends and magnitudes between the filtered individual particle vibration velocities from the DEM model and the data collected from the sensor V4. With an increase in train speed, ballast will vibrate at higher magnitudes and frequencies. It seems difficult to make the same observations from the original simulation data when the velocities fluctuate more unsteadily than the filtered ones. Note that the filtered data do not match very accurately for negative values when compared to positive ones. As mentioned, what reflected by the sensor installed at V4 were complicated and included vibrations of an assembly of particles, and such behavior could not be represented by a single particle. Possibly, some particles had better matches with negative values and some with the positive ones and the sensor results are collected as a combined effect of all particle movements. More detailed research is needed to shed light on such combined effects of all neighboring particles on the sensor.

4.3   Individual Ballast Particle Behavior in the DEM Model

To further study the combined effects of all particle vibration velocities, individual particle vibration velocities need to be collected and analyzed. Figure 7 compares five representative ballast particle filtered vibration velocities in the DEM model. Figure 7a–d present four different particle filtered vibration velocities at their first loading cycle (four wheels passing). All four particles vibrated differently from one another. To be more specific, the first three particles in Fig. 7a–c have the same vibration trends with the experimental sensor data while the one in Fig. 7d vibrates with an opposite trend. In addition, among the three particle vibration velocities, the first one in Fig. 7a mostly consists of large positive values; the second one in Fig. 7b is dominated by large negative values; and only small vibrations are observed in Fig. 7c. As for the particle with the opposite trend in Fig. 7d, it displays large negative vibrations. Differences among all ballast particles within the same loading cycle can be quite intriguing in which ballast particles located at different places in the ballast layer undertake different load vibrations; and further, different masses and shapes may make particles react differently even under the same loading condition.

A typical filtered particle vibration velocity trend in first two loading cycles is recorded and compared with those measured from the physical model in Fig. 7e. The vibration velocities measured from the physical model seem identical, while those of the individual ballast particle perform differently between the two consecutive loading cycles. Different vibrations during the second loading cycle may be caused by a change of particle interlock status, which can change force directions and magnitudes acting on the ballast particle.

(a) Same trend; dominated by positive vibrations

(b) Same trend; dominated by negative vibrations

(c) Same trend; small vibrations

(d) Different trend; dominated by negative vibrations

(e) Particle vibration velocities in two loading cycles
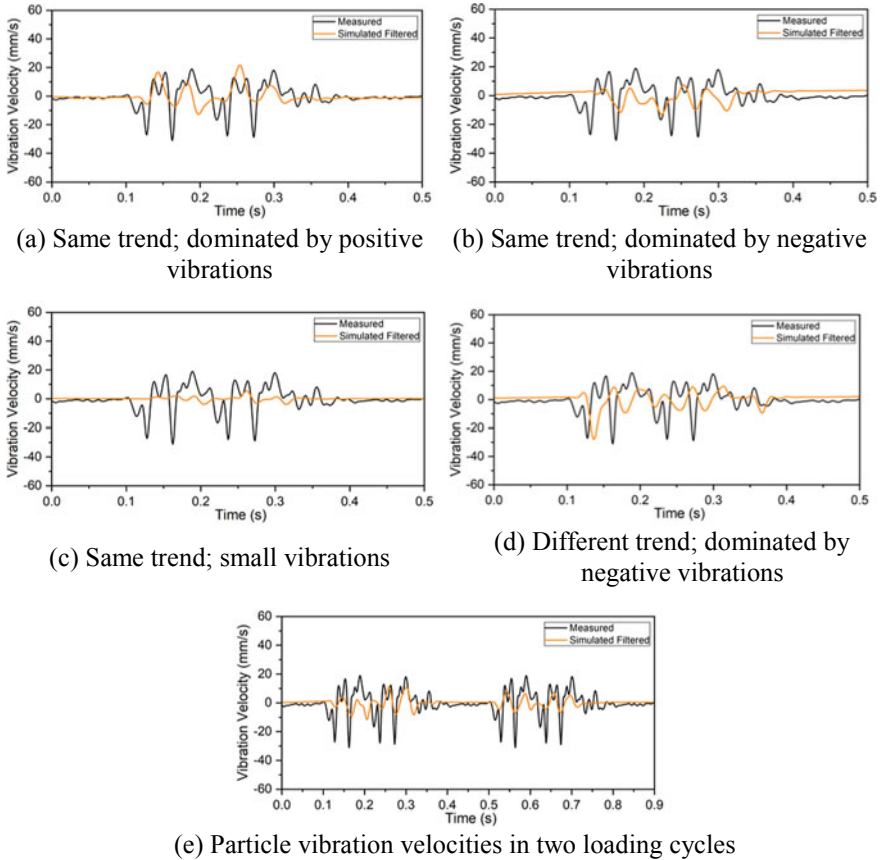
Fig. 7 Typical vibration velocities obtained from five ballast particles, parts (**a**)–(**e**)

To summarize, ballast particles around an inserted sensor in the physical model may vibrate differently in trend, magnitude or both. Therefore, the ballast vibration velocities recorded by the sensor in the physical model cannot be simply captured by an individual ballast particle in the DEM model. Some relationships between vibration velocities of individual particles and those measured by the sensor in the physical model in trend and magnitude have been exposed after filtering. Such observations would make it possible to study the combined effects of all neighboring ballast particles on the overall ballast vibration velocity sensor measurements.

5 Conclusions

A large-scale ballast layer model with over 170,000 ballast particles and eight crossties were set up using the University of Illinois polyhedral DEM code, BLOCK3D, to simulate the full-scale experiment conducted at ZJU-iHRST. Three train speeds, 108, 205 and 300 km/h, were simulated in the DEM model corresponding to the full-scale physical model tests. Vibration velocities of the same crosstie captured in the DEM model and measured in the physical model were in good agreement. To compare ballast layer vibration velocities, 426 ballast particles from the DEM model were studied in a location where a vibration velocity sensor was instrumented in the ballast layer physical model to record and monitor vibration velocities. The vibration velocities of the 426 ballast particles were filtered and compared with the results measured by the sensor in the physical model. Following conclusions can be drawn from this study:

- Crosstie vibration velocities captured in the DEM model matched closely with those measured in the physical model for both magnitude and trend. Higher velocities at higher speeds were captured both in the DEM model and the physical model.
- Fourier transformation can decompose ballast particle vibrations from time domain into frequency constitutions and Butterworth filter was proven to be effective to reduce signal noise. Filtered ballast particle vibration velocities can display clearer trends and magnitudes than the original ones. It is more accurate to compare filtered ballast vibration velocities from the DEM model with those measured in the physical model.
- Ballast layer vibration velocity measured by the sensor in the physical model was not the result of a ballast particle vibration, but instead it was a combined effect of many neighboring ballast particle vibrations. The vibration velocities measured by the sensor cannot be predicted by an individual ballast particle in the DEM model.
- The 426 ballast particles monitored in the DEM model around the same location where the sensor was installed in the physical model vibrated differently in either magnitude, trend or both. An individual ballast particle might also perform different vibrations due to different and sometimes consecutive loading cycles.

References

1. Frittelli J, Mallett W (2009) High speed rail (HSR) in the United States. Congressional Research Service
2. Peterman DR, Frittelli J, Mallett WJ (2012) The development of high speed rail in the United States: issues and recent events (No. R42584)
3. Feng B, Hou W, Tutumluer E (2019) Implications of field loading patterns on different tie support conditions using discrete element modeling: dynamic responses. Transp Res Rec. https://doi.org/10.1177/0361198118821936

4. Tutumluer E, Huang H, Hashash YMA, Ghaboussi J (2007, Sept) Discrete element modeling of railroad ballast settlement. In: AREMA 2007 annual conference

5. Tutumluer E, Qian Y, Hashash YM, Ghaboussi J, Davis DD (2013) Discrete element modelling of ballasted track deformation behavior. Int J Rail Transp 1(1–2):57–73

6. Ngo NT, Indraratna B, Rujikiatkamjorn C (2014) DEM simulation of the behavior of geogrid stabilized ballast fouled with coal. Comput Geotech 55:224–231

7. Huang H, Tutumluer E (2011) Discrete element modeling for fouled railroad ballast. Constr Building Mater 25(8):3306–3312

8. Hou W, Feng B, Li W, Tutumluer E (2018, Jan) Ballast support condition affecting crosstie performance investigated through discrete element method. In: 2018 joint rail conference. American Society of Mechanical Engineers Digital Collection

9. Feng B, Park EH, Huang H, Li W, Tutumluer E, Hashash YM, Bian X (2019) Discrete element modeling of full-scale ballasted track dynamic responses from an innovative high-speed rail testing facility. Transp Res Rec. https://doi.org/10.1177/0361198119846475

10. Takemiya H, Bian XC (2005) Substructure simulation of inhomogeneous track and layered ground dynamic interaction under train passage. J Eng Mech 131(7):699–711

11. Tutumluer E, Huang H, Hashash Y, Ghaboussi J (2006, Sept) Aggregate shape effects on ballast tamping and railroad track lateral stability. In: AREMA annual conference, Louisville, KY, Sept, pp 17–20

12. Moaveni M, Wang S, Hart JM, Tutumluer E, Ahuja N (2013) Evaluation of aggregate size and shape by means of segmentation techniques and aggregate image processing algorithms. Transp Res Rec J Transp Res Board 2335:50–59

13. Qian Y (2014) Integrated computational and experimental framework for the assessment of railroad ballast life-cycle behavior (Doctoral dissertation, University of Illinois at Urbana-Champaign)

14. Boler H, Mishra D, Hou W, Tutumluer E (2018) Understanding track substructure behavior: field instrumentation data analysis and development of numerical models. Transp Geotech 17:109–121

Steel Slag Aggregate Characteristics Evaluation as Railway Ballast

Guoqing Jing [ID]**, Peyman Aela** [ID]**, Qiang Zhou, and Wenli Jia**

Abstract The use of recycled materials is a new tendency in the field of railway engineering. Steel slag aggregates (SSA) are one of the recycled materials derived from the steel industry. The application of SSA in ballasted railway tracks requires mechanical examination. In the present paper, the shear behavior of the ballast layer constructed by SSA and basalt aggregates was considered to assess the use of SSA as a substitution for basalt. In this regard, a series of large-direct shear tests were performed on basalt and SSA under various normal stresses. Based on the results, basalt aggregates have higher shear resistance than SSA for all normal stress. However, steel slag has sufficient shear strength as well as particle abrasion resistance. Overall, it was proven that the SSA has suitable stability against shear forces that could be applied on railway ballast.

Keywords Shear resistance · Large-direct shear test · LA abrasion · SSA · Basalt

1 Introduction

In terms of the mitigation of environmental issues, the application of recycled materials in construction has grown considerably. The use of different types of recycled materials was reported by Prezzi [1], including tire rubber, fly and bottom ash, blast furnace slag, steel slag, cement kiln dust, glass, reclaimed asphalt pavement (RAP), and silica fume. Steel slag aggregates (SSAs) are one of the materials widely used in civil structures. Chemical properties of SSA were provided by Yildirim [2]. From a durability and economic perspective, the application of steel slag as fine aggregates in concrete and asphalt mixtures was a new approach investigated by many researchers [3–8]. On the other hand, due to the high density, better drainage properties, rough

G. Jing (✉) · P. Aela · Q. Zhou
School of Civil Engineering, Beijing Jiaotong University, Beijing 100044, China
e-mail: gqjing@bjtu.edu.cn

W. Jia
Faculty of Civil Engineering and Geosciences, Delft University of Technology, 2628 CN Delft, Netherlands

texture, and high resistance to changes in temperature, the SSA could also be used in railway superstructure applications [9].

Steel slag is a by-product of steel making formed during the separation of the molten steel from impurities in steel-making furnaces by one of the following methods:

- Basic Oxygen Furnace (BOF), where iron is transformed into steel, with the injection of oxygen to hot liquid metal, scrap, and fluxes.
- Electric Arc Furnace (EAF), where steel is produced by melting scrap steel, with melting the cold metal scrap.

In the process of BOF and EAF, 25%–35% and 100% old steel (scrap) is used for steel-making slag, respectively [10]. Although a massive amount of steel slag is utilized in the USA and European countries, only 22% of the produced slag is reused in the industry of China [11], and about 70 million tons of steel slag is released in China every year [12]. To produce SSA, firstly, the raw material (below 350 mm) enters the vibrating feeder (Fig. 1). Particles with a size of < 100 mm and > 100 mm are transferred to the cone crusher and jaw crusher, respectively. Afterward, material crushed in the jaw crusher move to the cone crusher for secondary crushing. Throughout this process, iron material is removed by the iron remover. Subsequently, the iron remover is screened by the vibrating screen, and the return cone crusher of more than 10 mm continues the aforementioned procedure, and particles with the size of lower than 10 mm are accumulated as the final product output [13].

CaO and SiO$_2$ are the main components of SSA for different processes of production, such as BOF, EAF, and Ladle slag [14]. As shown in Table 1, SSAs have approximately the same mechanical behavior as mineral aggregates [12, 15]. The higher density of particles could be a positive characteristic to enrich track stability. As mentioned earlier by Guo et al. [12], the type of treatment, including layer pouring,
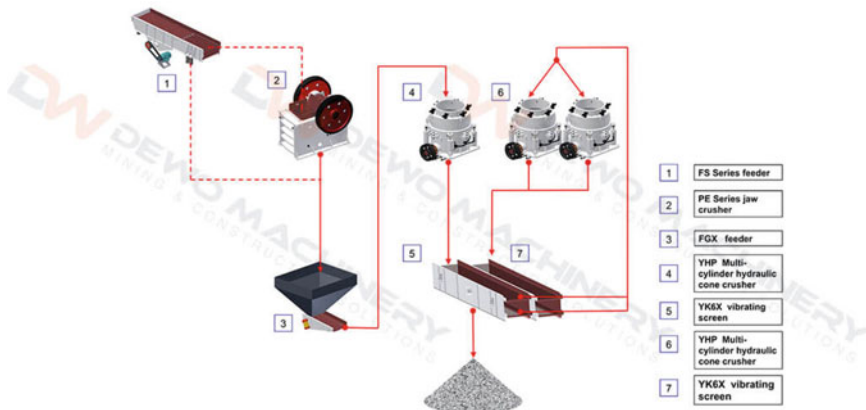
Fig. 1 Process of steel slag production [13]

Table 1 Mechanical properties of steel slags versus mineral aggregates [12]

Properties	Steel slag	Basalt	Granite	Greywacke
Particle density	3.1–3.7	2.8–3.1	2.6–2.8	2.7
Comprehensive strength	200	300	120	200
Impact value	17	17	–	20
Resistance to polishing (PSV)	54–57	50	45–55	56
Water absorption	0.2–1.0	< 1.0	0.3–1.2	< 0.5
Resistance to freezing	< 1.0	< 1.0	0.8–2.0	< 0.5

rotary cylinder, self-disintegrated by steam, and air-granulated, has a significant impact on the stability of steel slag production.

SSA is widely used in asphalt aggregate, cement, agriculture amendment, railroad, road base, and gabions [9, 16]. So far, SSAs have a high proportion of road construction by 67% [17]. In the current study, the application of steel slag was considered as a substitution of mineral aggregates in the ballast layer. The application of SSA in ballast tracks will contribute to sustainable development, decreasing the accumulation of waste material in the environment. However, less than 1% of SSA was used as ballast material in 1996–2001 [17]. From the environmental perspective, the radioactivity of slag does not influence the health condition of humans in case of using outdoor construction [18]. The hardness and rough surface of SSA are effective physical characteristics be likely to enrich ballast lateral resistance so that the angle of internal friction and hardness of SSA on the Mohs scale is in the range of 45–50 and 6–7, respectively [14]. However, the application of SSA as an unbound layer should fulfill the requirements of EN 13242-2013-05 [19]. On the other hand, in order to examine the stability of a layer constructed by SSA, volume expansion of the unbound granular material should be checked based on physical properties of a given slag according to the following formula:

$$F \leq k \frac{(\gamma_s - \gamma_0)}{\gamma_s^2} \times 100\% \tag{1}$$

where F is the hydratable oxide content of the slag; γ_s is the specific gravity of the slag; γ_0 is the bulk relative density of the slag, and k is a constant associated with the physical characteristics of the slag. If the hydratable oxide content (F) is lower than the right-hand term, aggregates will not extend in the case of using as granular material. It should be noted that the electrical resistance of SSA does not cause disturbance for the railway track circuit [20]. However, for the safety and reliability of railway operation, it is not recommended the furnace slag to be used in poor drainage or heavy rain conditions in case of track circuit problems.

The mechanical behavior of SSA should be assessed in order to apply to railway ballast tracks. Cyclic and monotonic triaxial tests on SSA with 1/3 of actual ballast size had higher strength and lower deformation than granite particles, as reported by

Delgado [21]. In other research, the lateral resistance of the ballast layer is another factor that should be considered in terms of track buckling. In this regard, different components influence the lateral resistance, such as sleepers, ballast, and fastening system [22]. The replacement of stone aggregates with SSA could be an economical and environmental solution. The field test result conducted by Esmaeili et al. [23] confirmed 27% growth in lateral resistance of track due to the replacement of limestone with SSA. In addition, the application of SSA could increase the rail support modulus by 64% in comparison with the limestone ballast track. There was a reduction in the contact stress between sleeper and slag ballast due to the high durability of SSA [24].

The shear behavior of the ballast layer is an important parameter that influences track lateral resistance. So far, several studies have been conducted on the shear behavior of ballast particles using the large-direct shear test. Large-direct shear tests carried out on clean and contaminated ballast with and without reinforcement were presented in Table 2. Due to the various sizes of the shear box, ballast gradation, and type of material, the shear resistance of ballast aggregates is variable.

So far, there is no experiment to evaluate the shear behavior of steel furnace slag using the large-direct shear test. Although adding 10% rubber crumb to the mixture of steel slag-coal wash (SFS-CW) causes an increase in the damping of ballast layer and consequential reduction in the ballast breakage, there is a reduction in the shear resistance of the mixture [33]. Therefore, the application of the steel slag without rubber crumb was preferred in this study in order to improve the shear behavior of ballast track. In this regard, the comparison between steel slag and basalt aggregates

Table 2 Different authors performed shear box tests

References	Test type	Box size (cm^3)	Material	Maximum normal stress (kPa)	Shear resistance (kPa)	Friction angle (°)
Huang [25]	Simulation	$30 \times 30 \times 20$	Granite	200	283	46.6
Dissanayake [26]	Experiment	40×30 (cylindrical)	Biotite gneiss	92	150	58 - 65
Liu [27]	Experiment	$30 \times 30 \times 20$	Granite	200	400	55 - 64
Jing [28]	Experiment	$30 \times 36 \times 24$	Basalt	200	230	–
Danesh [29]	Experiment	$31 \times 31 \times 21$	Andesite	183	280	55–65
Toloukian [30]	Experiment	$44 \times 44 \times 36$	Dolomite limestone	200	280	53
Indraratna [31]	Simulation	$30 \times 30 \times 20$	–	75	120	–
Sweta [32]	Experiment	$45 \times 45 \times 30$	Granite	70	126	64.7–66.5

was examined in terms of shear resistance by means of large-direct shear tests. In addition, the hardness of SSA was measured by the Los Angeles abrasion test in order to determine the actual physical parameters of SSA in this research. The range of LAA value for SSA is 15–20, as already proposed by Morata et al. [34].

2 Material Properties

In order to survey the use of SSA as a substitution of common ballast aggregates, Electric Arc Furnace (EAF) and basalt aggregates were tested (Fig. 2a). According to China National Standard TBT 2140, both types of material were provided with the same particle size distribution, as shown in Fig. 2b. In order to evaluate the durability of SSA, Los Angles Abrasion (LAA) test was conducted based on TB/T 2328.1 and ASTM C535-96 (Table 3). The results indicate that basalt and steel slag abrasion
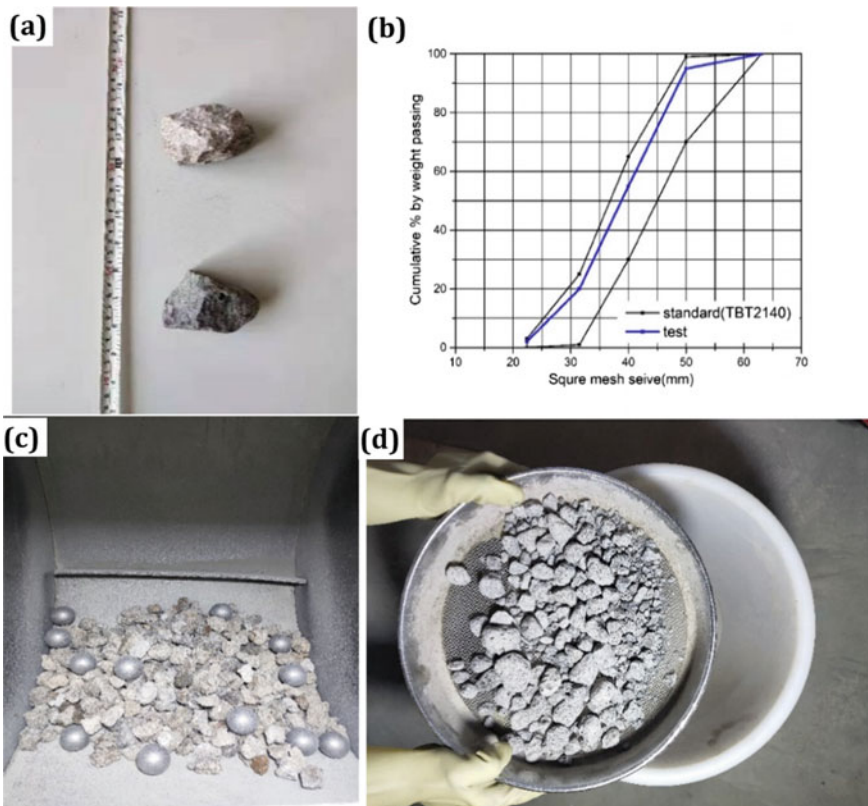
Fig. 2 **a** Sample of basalt and SSA, **b** particle size distribution, **c** particle abrasion after LAA test, **d** sieving particles

Table 3 Results of LAA tests on basalt and SSA

	China National Standard (20–40)		ASTM (31.5–50)	
	Basalt	SSA	Basalt	SSA
LAA (%)	6.0	29	4.93	24.4

resistance is in good agreement with the results of previous studies [14, 35] and meets the requirement of the American Railway Engineering and Maintenance of Way Association (AREMA) [36]. The lower LAA value of basalt could be attributed to the high strength of basalt material in comparison with SSA.

3 Test Procedure

Direct shear strength tests were performed on the reconstituted basalt and steel slag aggregates. Figure 3a shows the large shear box equipment comprised of two boxes
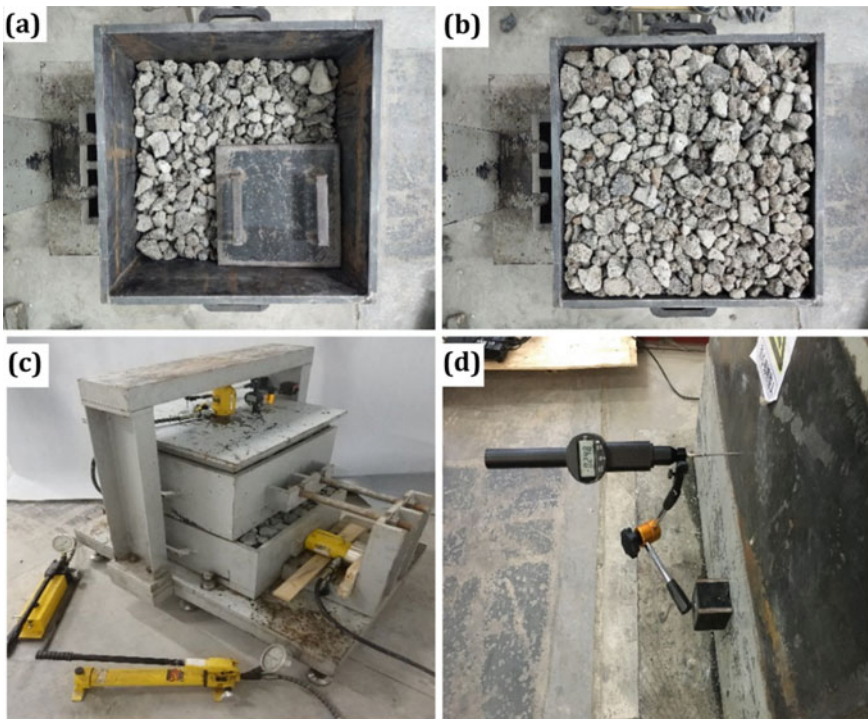
Fig. 3 **a** Compaction of samples, **b** full compacted sample, **c** instrumentation of shear test, **d** displacement gauge

with 600 mm, 600 mm, and 250 mm in length, width, and height, respectively. Ballast samples were prepared in five layers with a thickness of 10 cm along with the height of the shear box up to the top of the upper box. The bulk density of steel slag and basalt samples was 1570 kg/m³ and 1420 kg/m³, respectively, which were prepared by dropping the material into the box. Figure 3b shows the placement and compaction of samples in the lower box. The direct shear test was conducted for three normal pressures of 50, 100, and 200 kPa, and horizontal loading was applied by a hydraulic jack with a capacity of 100 kN to the bottom box. Simultaneously, the shear and vertical force were recorded using two digital indicators with a measurement course of 100 mm and 30 mm, respectively. Recording continued until the displacement of the bottom box reached 60 mm. This procedure was repeated three times to get the average value for each loading condition. It is noteworthy that the rate of applied force was 1 mm/min.

4 Test Results

4.1 Shear Strength of Fresh Ballast

The shear stress–displacement curve of basalt and SSA samples is presented in Fig. 4, which are approximately in the range of results reported by former studies [29, 37]. As shown in Fig. 4a, basalt samples had the highest shear strength at all normal stresses that can be attributed to the fact that basalt aggregates have a higher strength to bear applied stresses. In addition, with the increase of the normal stress, variation of strength between basalt and SSA became higher, so that the peak shear stress was 301.9 and 217.6 at 200 kPa normal stress, respectively (Fig. 4b). Since the recorded shear stress of SSA is in the range of ballast shear resistance reported by Estaire [37], SSA could be used as the substitution of rock material in ballasted railway tracks. As shown in Fig. 4c, the values of friction angle slightly decreased with the increase of normal stress for all samples. Due to the high vertical stress (200 kPa), the peak friction angle reduced about 19% in the case of using SSA as a substitution of basalt particles. As already reported by Estaire [37], parabolic curves could be precisely fitted on the variation of shear resistance and friction angle.

In order to make a comparison between the angle of repose and friction angle, samples of basalt and steel slag aggregates were selected and measured by a digital angle level device, as shown in Fig. 5. Although basalt aggregates have a higher friction angle than SSAs, the angle of repose of basalt is about 1° lower than SSA. As already mentioned by Al-Hashemi [38], the angle of repose could not be considered as the friction angle due to the different circumstances, such as moisture content, maximum dry density, and particle size. In the current test, the minor difference between the angle of repose of two samples could be attributed to the similar physical characteristic (e.g., static sliding friction coefficient) of SSA and basalt, whereas due
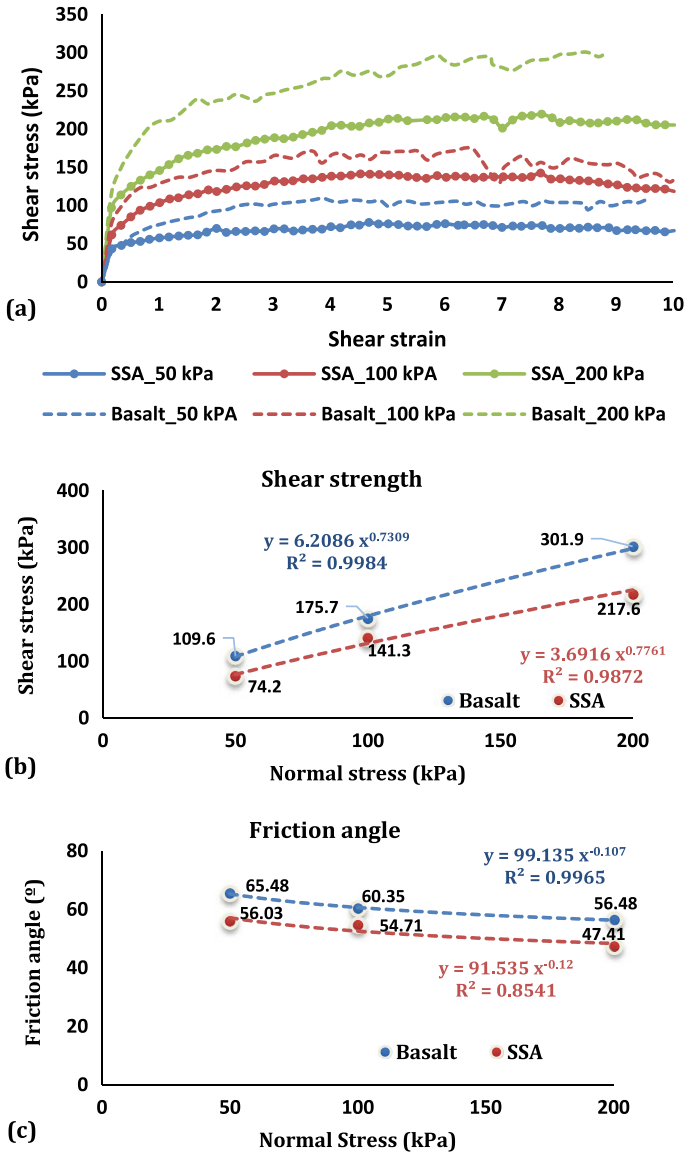
Fig. 4 **a** Shear stress–strain curves, **b** shear resistance of samples, **c** friction angle of samples

to the higher shear resistance of particles, the higher friction angle was obtained for basalt aggregates.
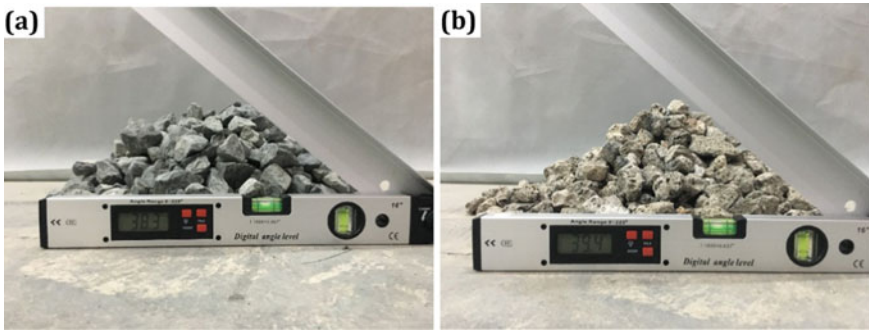
Fig. 5 Repose angle of **a** basalt and **b** SSA
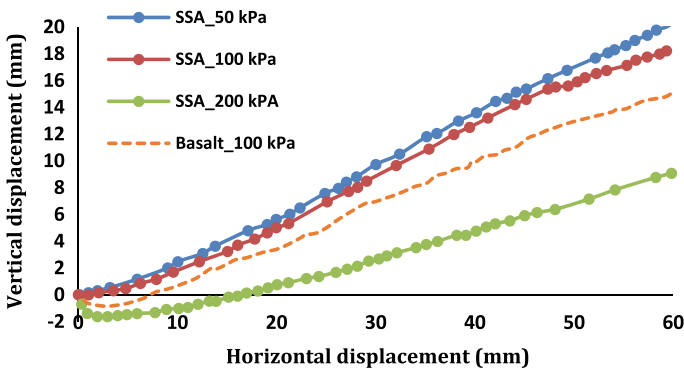
Fig. 6 Horizontal–vertical displacement during the shear test

4.2 Vertical–Horizontal Displacement Curves

Figure 6 shows the relation between the horizontal and vertical displacement. In all tests, the horizontal displacement caused growth in the vertical displacement. On the other hand, the dilation of the ballast increases with the reduction in the normal pressure. However, at 200 kPa normal stress, the contraction occurred in SSA sample up to the displacement of 17 mm. To compare the dilation of basalt and SSA, at 100 kPa normal stress, the dilatancy is higher for SSA specimens, in which the measured vertical displacement was about 20 mm, while in the specimen contained basalt aggregates, the vertical displacement was about 15 mm. It is noteworthy that the dilation of basalt samples was smaller than that reported by Estaire [37], which can be attributed to the application of the large size of the shear box (1 m × 1 m × 1.2 m).

5   Conclusion

The current study evaluates the mechanical behavior of steel slag aggregates derived from the steel industry as ballast aggregates. In this regard, a series of LA abrasion tests and large-direct shear tests were conducted on basalt and steel slag aggregates. The following results were achieved from this study:

- The physical properties of SSA fulfill the requirements of the Los Angeles abrasion test in order to be utilized as railway ballast materials.
- The shear resistance of basalt railway aggregates is higher than that of SSAs. The peak shear stress was 301.9 and 217.6, respectively, at 200 kPa normal stress.
- The increase of normal stress led to an increase and decrease in the values of shear strength and friction angle, respectively.
- The angle of repose could not be representative of the internal friction angle. Although the difference between the repose angle of basalt and SSA was insignificant, the internal friction angle of SSA was 19% lower than that of basalt aggregates.
- The dilatancy of SSAs was about 33% higher than basalt railway aggregates, and some reinforcement measures could be taken, such as geogrids, etc.

References

1. Prezzi M et al (2011) Use of recyclable materials in sustainable civil engineering applications. Hindawi
2. Yildirim IZ, Prezzi M (2011) Chemical, mineralogical, and morphological properties of steel slag. Adv Civ Eng
3. Zumrawi MM, Khalill FO (2015) Experimental study of steel slag used as aggregate in asphalt mixture. Int J Civ Environ Eng 9(6):753–758
4. Brand AS, Roesler JR (2014) Concrete with steel furnace slag and fractionated reclaimed asphalt pavement. Illinois Center for Transportation
5. Arabani M, Azarhoosh A (2012) The effect of recycled concrete aggregate and steel slag on the dynamic properties of asphalt mixtures. Constr Build Mater 35:1–7
6. Ahmedzade P, Sengoz BJJOHM (2009) Evaluation of steel slag coarse aggregate in hot mix asphalt concrete. J Hazardous Mater 165(1–3):300–305
7. Wang G (1992) Properties and utilization of steel slag in engineering applications. Wollongong. Ph. D. Thesis, University of Wollongong
8. Skaf M et al (2017) EAF slag in asphalt mixes: A brief review of its possible re-use. Resour Conserv Recycl 120:176–185
9. Association NS (2001) Steel furnace slag an ideal railroad ballast. NSA 173-3
10. Grubeša IN et al (2016) Characteristics and uses of steel slag in building construction. Woodhead Publishing
11. Dhoble YN, Ahmed S (2018) Review on the innovative uses of steel slag for waste minimization. J Mater Cycles Waste Manage 20(3):1373–1382

12. Guo J, Bao Y, Wang M (2018) Steel slag in China: treatment, recycling, and management. Waste Manage 78:318–330
13. Machinery D (2018) Steel slag processing
14. Wang GC (2016) The utilization of slag in civil infrastructure construction. Woodhead Publishing
15. Koh T et al (2018) A feasibility study on the application of basic oxygen furnace (BOF) steel slag for railway ballast material. Sustainability 10(2):284
16. Hainin MR et al (2012) Steel slag as an aggregate replacement in Malaysian hot mix asphalt. ISRN Civ Eng
17. Khan ZA et al (2002) Review of steel slag utilization in Saudi Arabia. In: The 6th Saudi engineering conference, KFUPM, Dhahran, Saudi Arabia
18. Wendling LA et al (2013) Geochemical and ecotoxicological assessment of iron-and steel-making slags for potential use in environmental applications. Environ Toxicol Chem 32(11):2602–2610
19. Standardization E.C.F. (2013) Aggregates for unbound and hydraulically bound materials for use in civil engineering work and road construction. EN 13242-2013-05
20. Kumar A (2014) Utilisation of wastes from integrated steel plant with special reference to India. Int J Eng Res Technol (IJERT) 3(1):47–52
21. Delgado BG et al (2019) Mechanical behavior of inert steel slag ballast for heavy haul rail track: laboratory evaluation. Transp Geotech 20:100243
22. Kish A, Samavedam G, Wormley D (2004) Fundamentals of track lateral shift for high-speed rail applications. National Technical Information Service
23. Esmaeili M, Nouri R, Yousefian K (2015) Experimental comparison of the lateral resistance of tracks with steel slag ballast and limestone ballast materials. Proc Inst Mech Eng Part F J Rail Rapid Transit 231(2):175–184
24. Esmaeili M, Yousefian K, Nouri R (2017) Vertical load distribution in ballasted railway tracks with steel slag and limestone ballasts. Int J Pavement Eng:1–8
25. Huang H, Tutumluer E, Dombrow W (2009) Laboratory characterization of fouled railroad ballast behavior. Transp Res Rec 2117(1):93–101
26. Dissanayake D, Kurukulasuriya L, Dissanayake P (2016) Evaluation of shear strength parameters of rail track ballast in Sri Lanka. J Nat Sci Found Sri Lanka 44(1)
27. Liu J, Wang P, Liu J (2015) Macro-and micro-mechanical characteristics of crushed rock aggregate subjected to direct shearing. Transp Geotech 2:10–19
28. Jing G et al (2015) Permeability and direct shear tests characteristics of railway subballast. Open Civ Eng J 9(1)
29. Danesh A, Palassi M, Mirghasemi AA (2018) Effect of sand and clay fouling on the shear strength of railway ballast for different ballast gradations. Granular Matter 20(3):51
30. TolouKian AR, Sadeghi J, Zakeri JA (2018) Large-scale direct shear tests on sand-contaminated ballast. Proc Inst Civ Eng Geotech Eng 171(5):451–461
31. Indraratna B et al (2016) Performance improvement of rail track substructure using artificial inclusions—experimental and numerical studies. Transp Geotech
32. Sweta K, Hussaini SKK (2018) Effect of shearing rate on the behavior of geogrid-reinforced railroad ballast under direct shear conditions. Geotext Geomembr 46(3):251–256
33. Indraratna B, Qi Y, Heitor A (2017) Evaluating the properties of mixtures of steel furnace slag, coal wash, and rubber crumbs used as subballast. J Mater Civ Eng 30(1):04017251
34. Morata M, Saborido C (2017) Recycled aggregates with enhanced performance for railways track bed and form layers. J Sustain Metallurgy 3(2):322–335
35. Kekec B et al (2017) Abrasion properties of some building stone wastes and usability for sustainability. Geo-Resour Environ Eng (GREE) 2:218–222
36. AREMA, American Railway Engineering and Maintenance of Way Association (2015) Roadway and ballast, Part 2, Chapter 1. Manual for railway engineering, 2015, vol 1
37. Estaire J, Santana M (2018) Large direct shear tests performed with fresh ballast. In: Railroad ballast testing and properties. ASTM International

38. Al- HMB, Al- OSB (2018) A review on the angle of repose of granular materials. Powder Technol 330:397–417

A Study on the Evolution of Ballast Particle Surface Damage

Akash Gupta ⓘ**, Madhusudhan B. N. Murthy** ⓘ**, Antonis Zervos** ⓘ**, and John Harkness** ⓘ

Abstract The role of railway ballast is to spread traffic loads to the underlying ground. The contact area between ballast particles is often very small, leading to high contact stresses and surface abrasion, which is considered to degrade ballast quality and eventually necessitating ballast replacement. It is desirable to recycle and reuse as much of this "life-expired" ballast as possible, in whole or in certain particle sizes, as it would lead to a more sustainable engineering practice. However, research on the effect that particle surface damage has on the mechanics of ballast is required to understand the differences in behavior between recycled and fresh ballast, with a view to improving performance and increasing the length of maintenance cycles. This paper presents a study of ballast particle surface damage in terms of surface roughness using variable focus microscopy. Nanometer-scale surface scans of fresh and recycled ballast particles were acquired at predetermined resolutions and preselected areas. Methods of evaluating surface roughness for railway ballast are proposed, which indicate significant differences in roughness between fresh and recycled ballast. Laboratory tests with a Micro-Deval apparatus were used to quantify damage and the corresponding link to surface roughness.

Keywords Railway ballast · Surface roughness · Ballast re-cycling · Particle shape · Contact mechanics

A. Gupta (✉) · M. B. N. Murthy · A. Zervos · J. Harkness
Infrastructure Research Group, School of Engineering, University of Southampton, Southampton SO16 7QF, UK
e-mail: akash.gupta@soton.ac.uk

M. B. N. Murthy
e-mail: M.Bangalore-Narasimha-Murthy@soton.ac.uk

A. Zervos
e-mail: az@soton.ac.uk

J. Harkness
e-mail: J.Harkness@soton.ac.uk

1 Introduction

Railway ballast undergoes damage and deterioration over a period of time due to traffic loading. This causes settlement of railway tracks and necessitates periodic maintenance, usually by tamping, which restores track geometry through reassembly of the ballast particle layer, creating new contacts between the particles. Maintenance of ballast to sustain optimum performance is, however, very costly.

The irregular shape of ballast grains provides strength to the aggregate through particle interlocking. Over a period of time and due to traffic, particle wear results in rounding of asperities and a reduction in strength of the ballast layer [1]. Eventually, the ballast needs to be replaced.

Various studies have been carried out in the areas of ballast shape categorization, quantification of damage in terms of the shape or the mechanical performance of spent ballast, measurement tools and techniques to quantify damage and effects of tamping on ballast. As concluded in [2], the mechanical response depends on (a) ballast shape and surface characteristics: texture, roundness, size, and shape and (b) particle deterioration. However, more understanding and insights are required to establish a definite relation between degradation and maintenance cycles of ballast in railway tracks [3–5]. This is even more important where high-speed railway lines are concerned, as there is evidence that particle wear is greater, due to both high-speed traffic and the accumulated effect of maintenance operations like tamping [6]. In the same context, it was observed that more angular asperities are relatively weak and disappear at the initial stage of a Micro-Deval test: either by progressive rounding or by breakage of the asperities [6].

In this study, we measure the roughness of (a) used ballast, (b) fresh ballast, and (c) fresh ballast progressively damaged using the Micro-Deval testing apparatus. A detailed illustration of ballast roughness determination is given. Our aim is to develop methods to replicate in the lab the damage suffered by ballast particles due to traffic, so that we can produce (from fresh ballast) equivalents of used ballast (i.e., a scaled version of used ballast) for systematic experimental testing in the lab, including triaxial testing to determine mechanical properties and parameters that control them.

2 Methods

2.1 Ballast Material

The ballast materials used in the past were from different origins, ranging from granite to limestone. In this study, we have selected granite ballast quarried from Mount Sorrel, East Midlands, England.

2.2 Ballast Surface Roughness

The surface roughness of ballast can vary with its mineralogical composition. Therefore, ballasts of the same granite mineralogy were selected for the comparison of surface roughness (texture) of fresh and used ballast.

Alicona G4 InfiniteFocus [7, 8] equipment was used to extract the topography data. The equipment inbuilt light and lens system and has auto-brightness ability that selects appropriate contrast and brightness to extract precise data. We selected 10 × lens for this operation which is optimum for our desired resolution of up to 3 µm lateral and 500 nm vertical resolution.

The roughness of ballast also varies with the scale of observation. In this work, wavelengths of a few millimeters are considered to correspond to the aspect of shape generally identified as "particle angularity," whereas wavelengths of a few microns are considered to relate to material roughness or texture.

The current study is concerned with the degradation and damage of ballast due to loading. The damage in such conditions occurs at a range of roughness wavelengths from millimeters to microns. From a discrete-element modeling perspective, a coarse-scale interlocking of the ballast particles is a function of particle form and angularity, whereas the inter-particle friction of ballast grains relates more to surface roughness or texture. Therefore, a full understanding of ballast shape and roughness requires consideration of the scale of observation or wavelength, as shown in Fig. 1. The measurement of surface roughness is affected by the local curvature of the scanned area. To reduce this effect low wavevectors were removed.

The power spectral density (PSD) of a surface is a representation of the roughness as a function of the spectral frequency (wavevector). PSD is the Fourier transformation of the autocorrelation function of the signal, which consists of just the power (not the phase) of the entire range of wavelengths [9]. Surface roughness measurement from PSD is widely used technique in a number of different disciplines [10–13]. In
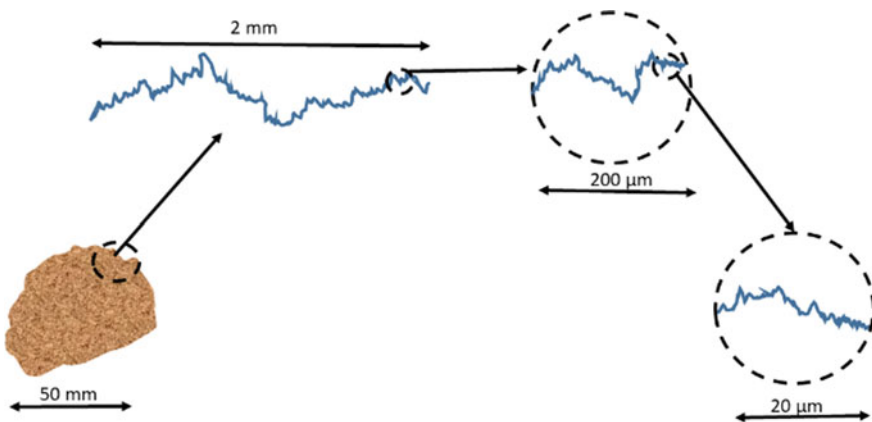
Fig. 1 Roughness of ballast at different scales (fractal in nature)

spatial frequency space, it is represented as a surface $C(q_x, q_y)$ the volume under which equals h_{rms}^2 which is defined in Eq. 1 where h_{rms} is root-mean-squared heights of the surface. The unit of $C(q_x, q_y)$ is L^4, whereas q_x and q_y represent the number of waves per unit length and the units are L^{-1}.

$$h_{rms}^2 = \frac{1}{4\pi^2} \int\limits_{-\infty}^{\infty} \int\limits_{-\infty}^{\infty} C(q_x, q_y) dq_x dq_y \qquad (1)$$

To determine the roughness of ballast, variable focus microscopy was used to obtain the 3-D profile of the selected area of ballast, utilizing an Alicona Infinite Focus apparatus. The machine is accurate up to few nanometers lateral resolution and combines dimensional metrology and a surface roughness measurement in one system.

2.3 Developing Used Ballast Using Micro-Deval

Micro-Deval is a standard apparatus for aggregate abrasion testing. The machine provides a measure of resistance against abrasion, toughness, and durability of aggregates when they are subjected to grinding in the presence of steel balls. In this study, the apparatus was used to abrade fresh ballast particles with the objective of replicating the surface roughness observed in used ballast recovered from the field after 30 years of service. Therefore, the procedure used in this study was different from the standard Micro-Deval testing procedure to determine the abrasion resistance and toughness of the aggregates.

Four random fresh ballast particles were loaded into the Micro-Deval machine together with some steel balls of diameter 10 mm. The machine was run at a speed of 100 rpm for durations of 5, 30, 60, and 90 min to abrade the particles. Six different patches were selected at random, and the PSD and roughness were determined at the end of each phase to investigate the evolution of damage and the corresponding values of roughness. After the tests were completed, the PSD and roughness were compared with those of the fresh and used ballast.

3 Results and Discussions

Figure 2 shows the PSD of fresh and used ballast. It can be seen that the roughness of the used ballast is lower than that of fresh ballast at all spectral frequencies. On a logarithmic scale, this difference increases with increasing wavenumber. However, the overall roughness, h_{rms} is largely governed by the lower frequency roughness because of the much larger C values in this range. It is therefore essential to compare the full PSD plot to understand the nature of the effects of ballast abrasion.
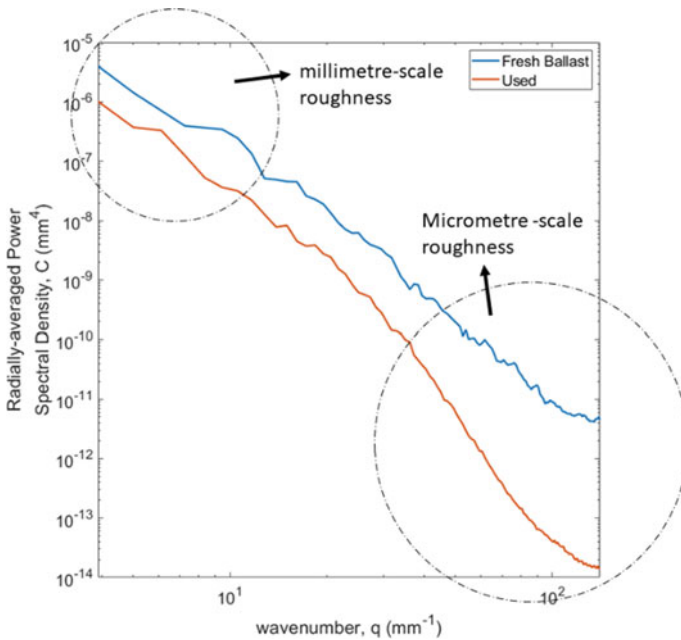
Fig. 2 Comparison of roughness: fresh and used ballast

The PSD range for fresh and used ballast abraded for 90 min in the Micro-Deval (abraded-90) is shown in Fig. 3. The range of PSD for abraded-90 is within the range of used ballast. The roughness of ballast corresponding to abraded-90 is therefore equivalent to the roughness of used ballast. The range of abraded-90 is, however, narrower than that of used ballast. The trend of how the PSD at the same location of the same particle evolves for increasing periods of abrasion in the Micro -Deval is shown in Fig. 4.

The values of roughness decrease with test duration over most of the spatial frequencies. More damage in the micro-scale is observed [i.e., lower values of C at higher wavenumbers (q)].

A summary of the roughness measurements is shown in the box plot of Fig. 5. After 90 min of particle abrasion, the values and range of roughness reported are quite close to those of used ballast. Some locations sustained more damage than others. This can be explained by the type of curvature at the selected locations. The locations with coarse-scale convex curvature showed more damage than those with a concave curvature, as shown in Fig. 6. In the case of ballast, we are concerned with the asperities or the roughness that are represented by wavevectors corresponding to about, or less than, the dimensions of a typical contact between the ballast. For fresh ballast, there is no reason to expect substantial non-uniformity in surface roughness. Evidence from visual observation of fresh ballast particles that have undergone loading suggests that degradation of their surface is more likely to occur at edges,

Fig. 3 PSD range for fresh, used and ballast abraded for 90 min in Micro-Deval
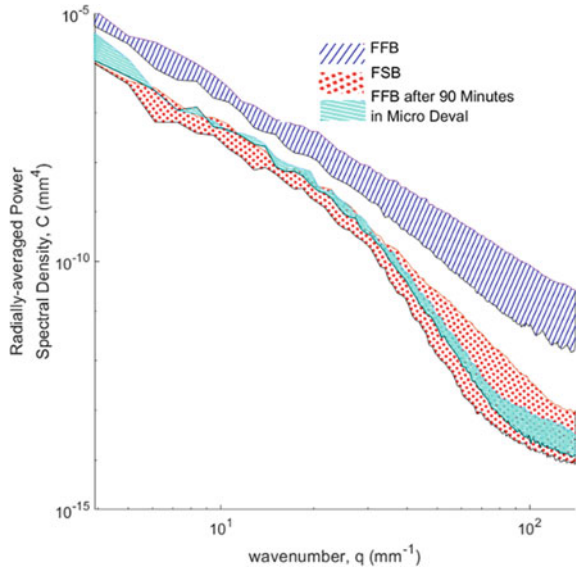
Fig. 4 Evolution of damage and comparison of roughness for the same location of the same particle for increasing periods of abrasion in the Micro-Deval
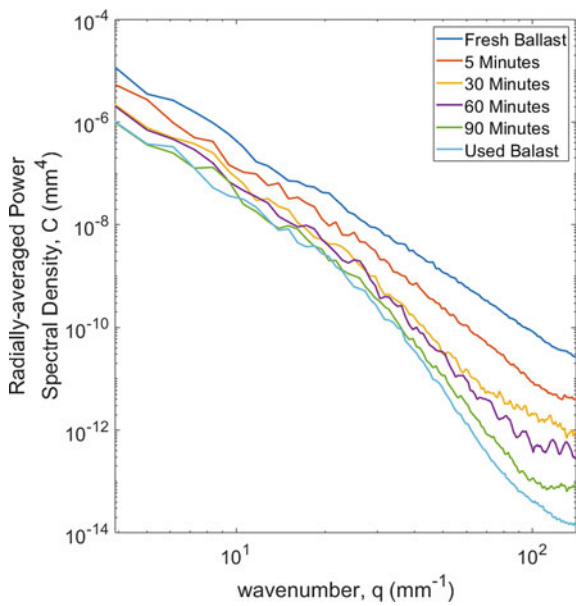
corners, and other convex parts of their surface. Concave parts of the surface are less likely to degrade at the same rate. A similar phenomenon was observed in [6]. With increased test duration, the particles become smoother.

Fig. 5 Roughness of ballast with Micro-Deval test per
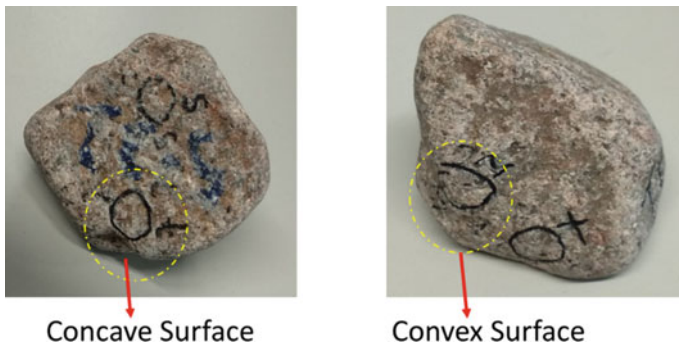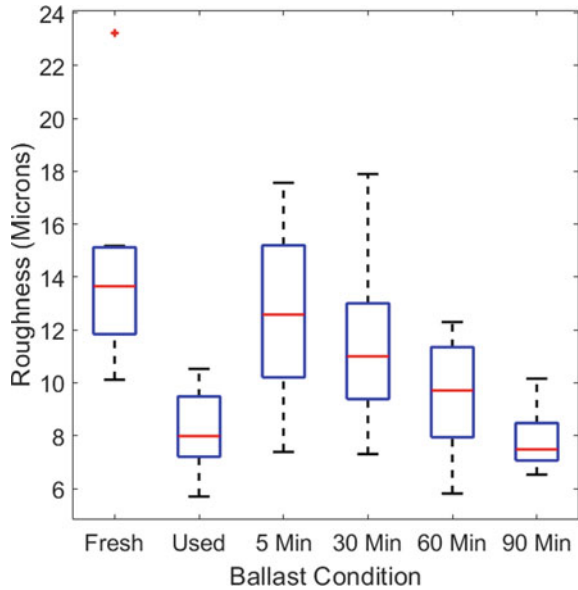
Fig. 6 Random patches selected for roughness measurement. Notice some patches are within concave surfaces that remain undamaged

Nevertheless, the mechanical behavior of ballast depends not only on particle roughness but also on particle form and angularity [14]. Apart from roughness, form and angularity of fresh and used ballast were also compared and the results are shown in Fig. 7 (form, in terms of particle platyness and elongation, was originally defined by [15]) and Fig. 8 (angularity). If L, I, and S the e's longest, intermediate, and shortest dimensions of a particle' best-fit scalene ellipsoid are considered to be coordinates in three-dimensional space, the overall shape of a particle can be represented as a vector f linking the origin of the axes to point (L, I, and S) as shown in Fig. 9. Particle form is then represented by the direction of f and the magnitude of f quantifies particle size. If we consider the intersection F of f with $L + I + S - 1 = 0$ 'deviatoric'

Fig. 7 Particle form of fresh and used ballast in terms of platyness (α) and elongation (ζ)
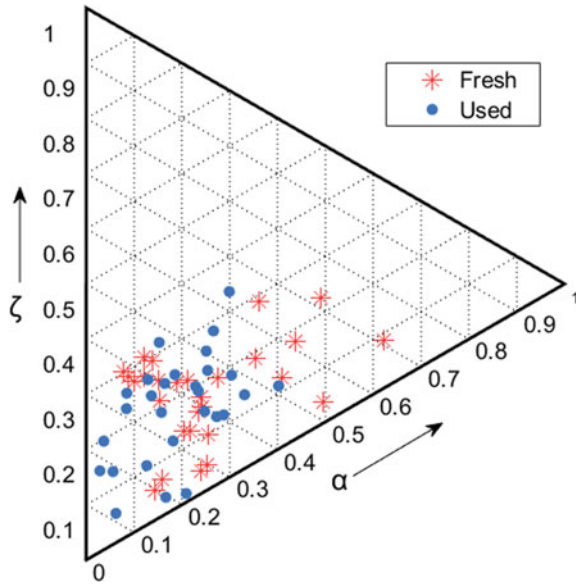
Fig. 8 Comparison of angularity: fresh and used ballast
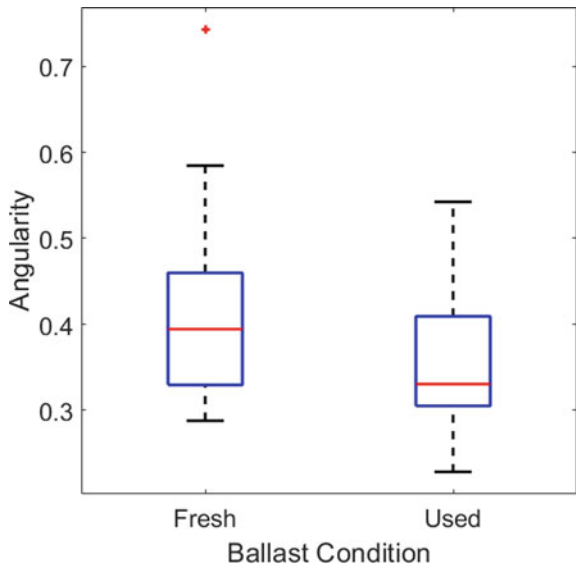
plane, normal to the spherical axis $L = I = S$, the form of each particle is uniquely defined by the two in-plane coordinates of F in a frame of reference centered at the intersection P of the spherical axis. The form is then essentially quantified as the deviation of particle's shape from that of a sphere. These two independent parameters of form are called platyness (α) and elongation (ζ) and are expressed by Eqs. 2 and
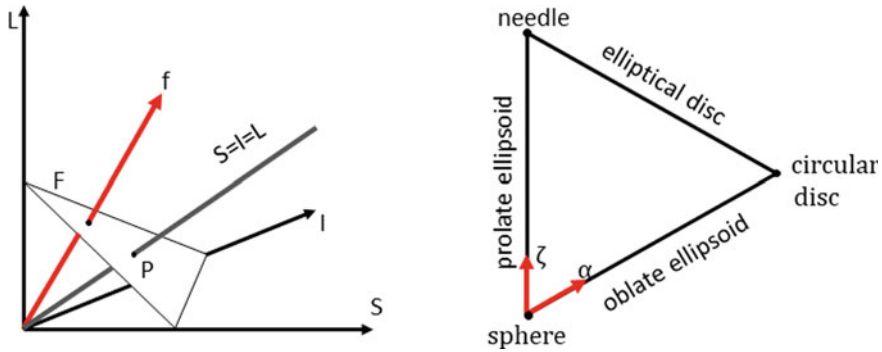
Fig. 9 Left: *L*, *I*, and *S* space; right: platyness and elongation space with form description [15]

3. Angularity is defined here as the volumetric difference between the actual shape and its equivalent scalene ellipsoid normalized by the original shape's volume.

$$\alpha = \frac{2(I - S)}{L + I + S} \tag{2}$$

$$\zeta = \frac{L - I}{L + I + S} \tag{3}$$

The effect of abrasion on the form of ballast particles was compared for four, randomly selected, fresh ballast particles before and after 90 min of abrasion in the Micro-Deval apparatus. The error margin for form determination is about 5% for repeatability. Therefore, any difference within this range would not be significant change of form. Although more rigorous statistical tests for larger populations of particles are in progress, plotting the results reveals no significant change in the particle form after 90 min in Micro-Deval test (Fig. 10), which provides, for now, some confidence that particle form is not significantly affected. The average platyness and elongation are also plotted for the same population before and after abrasion, further showing that changes in particle form are not significant. Also, no major breakage was observed. For all of the Micro-Deval tests, about 1% of particle weight was lost at the end of abrasion test as fine dust. The particle size distribution is unlikely to be significantly affected by the abrasion, but this could not be verified in this pilot study due to the relatively small number of particles tested.

4 Conclusion

- A method is proposed to determine the roughness of ballast ranging from a scale of millimeters to micrometers, i.e., scales relevant to the contact mechanics of ballast.
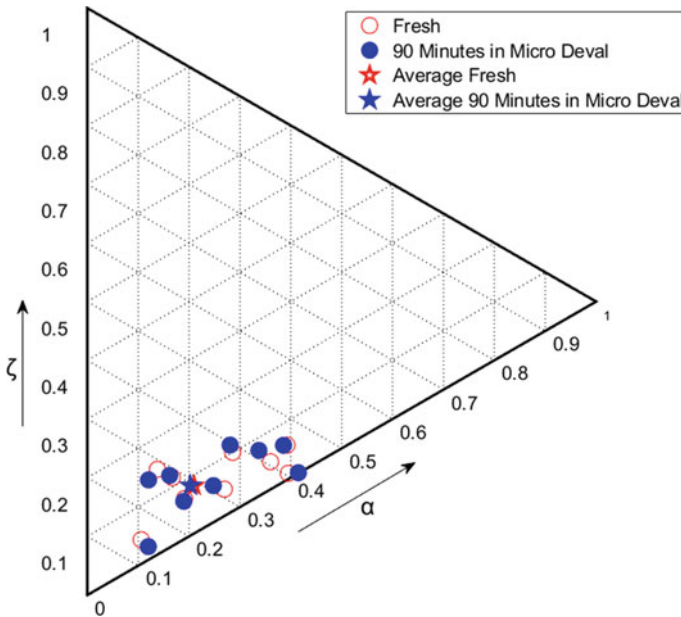
Fig. 10 Particle form of fresh and 'ballast abraded for 90 min in Micro-Deval' in terms of platyness (α) and elongation (ζ)

- Evolution of surface damage of ballast was studied and defined in terms of surface roughness using Micro-Deval apparatus.
- A 90-min Micro-Deval abrasion test reduced the roughness of fresh ballast to values very close to those of field used ballast.
- Because of the complexity in the shape, i.e., local convexity and concavity of ballast surfaces, there is uneven damage in ballast after Micro-Deval abrasion. Producing more evenly abraded particles requires different configurations of abrasives (i.e., smaller balls, coarse sand, etc.) and times of abrasion, which are currently being investigated.
- No significant changes in the angularity and shape were observed after the Micro-Deval operation as we lack major breakage. These findings are consistent with [6].

5   Future Works

- The data can be directly used for development of a scaled ballast with the same particle properties as used ballast, for laboratory testing purposes.
- The data can be used to inform the development of a discrete element contact model capable of capturing the effects of ballast aging.

References

1. N. Rail Infrastructure Limited (2019) Working for you Network Rail Infrastructure Limited
2. Buddhima Indraratna WS (2003) Deformation and degradation mechanics of recycled ballast stabalized with geosynthetics. Soils Found 43(4):35–46
3. Sahlin S (1993) Eleven thousand kilometres with a few millimetres tolerance—faster and heavier trains need better and more sophisticated railroad technique. J Vag Vattenbyggaren
4. Olsson E-L (1995) Testing of impact and abrasion properties of railroad ballast. Tekniska Hogskolan, Lulea
5. Peplow AT, Oscarsson J (1996) Review of research on ballast as track substructure
6. Deiros Quintanilla I (2018) Multi-scale study of the degradation of railway ballast
7. https://www.alicona.com/en/products/infinitefocus/
8. M. E. N. December, IF-MeasureSuite 43(316) (2013)
9. Jacobs TDB, Junge T, Pastewka L (2017) Quantitative characterization of surface topography using spectral analysis. Surf Topogr Metrol Prop 5(1)
10. Schwarz UD, Zwörner O, Köster P, Wiesendanger R (1997) Quantitative analysis of the frictional properties of solid materials at low loads. II. Mica and germanium sulfide. Phys Rev B Condens Matter Phys 56(11):6997–7000
11. Carpick RW, Agraït N, Ogletree DF, Salmeron M (1996) Variation of the interfacial shear strength and adhesion of a nanometer-sized contact. Langmuir 12(13):3334–3340
12. Holm R (1967) Electric contacts. Springer-Verlag, Berlin Heidelberg
13. Gotsmann B, Lantz MA (2013) Quantized thermal transport across contacts of rough surfaces. Nat Mater 12:59–65
14. Harkness J, Zervos A (2019) Some effects of particle shape on the mechanical behaviour of granular materials. Dem8, pp 1–11
15. Potticary M, Zervos A, Harkness J (2016) The effect of particle elongation on the strength of granular materials. 24th UK conference on association computational mechanics in engineering, pp 239–242

Investigations into the Critical Speeds in Ballasted and Ballastless Track

Jing Hu (id)**, Ying Wu, Xuecheng Bian, and Yunmin Chen**

Abstract The modern high-speed railway usually consists of track structure, subgrade and soil layers. The existence of track structure and subgrade can both improve the critical speed of railway especially when the railway is built on soft soil layers. However, the role that the track structure played hasn't been distinguished from subgrade. Therefore, further research is needed to investigate the difference of the critical speeds in ballasted and ballastless track. In this paper, two different types of track structures, ballasted and ballastless track, are built on the same subgrade-soil model using two-and-half-dimensional (2.5 D) finite element method to calculate the vibrations induced by the same high-speed trains. The rails, rail pads and ballast layer in ballasted track and rails, rail pads, slab, CA layer, concrete base in ballastless track are modelled as Euler–Bernoulli beams resting on the subgrade. The subgrade and soil layers are modelled by the 2.5D finite elements. The critical speeds in ballasted track and ballastless track are compared to reveal the consequence of track structure. It reveals that the critical speed in ballastless track is equal or greater than that in ballasted track. When the subgrade has enough stiffness, the critical speeds in both ballasted track and ballastless track can be the same. It can be concluded that the subgrade is more dominant than track structure in deciding the critical speed of railway.

Keywords Critical speed · Ballasted track · Ballastless track

1 Introduction

Since the high-speed railways have been developed rapidly all over the world, the dynamic responses of the railway track and ground along the railway line draw more

J. Hu (✉)
Department of Civil Engineering, Fuzhou University, Fuzhou 350108, China
e-mail: jingh@fzu.edu.cn

Y. Wu · X. Bian · Y. Chen
Department of Civil Engineering, Key Laboratory of Soft Soils and Geoenvironmental
Engineering, MOE, Zhejiang University, Hangzhou 310058, China

and more attention due to the significant amplification effect of the track-ground vibration.

According to the researches [1–12], the train-induced vibration of the track and ground is strongly affected by the relationship between the train speed and the corresponding propagating wave velocity of the underlying media. There exists a speed at which large amplification of the dynamic response will occur, and it is called 'critical speed'. At the critical speed, track structure may face the risk of train derailment and track structure damage. This phenomenon has been measured as a manifestation of the existence of the critical speed in the experience of the Swedish Rail Administration (SRA).

The modern high-speed railway is mainly composed of ballasted track and ballastless track. The main difference between these two track structures is that ballastless track adopts rigid concrete structures to replace the traditional ballast layers used for ballasted tracks. Recently, the study about critical speeds in ballasted track and ballastless track has been conducted separately. Sayeed and Shahin [12] built a three-dimensional (3D) finite element (FE) ballasted railway track model of the X-2000 HST to simulate the dynamic response of railway track foundations under true train moving loads, with special reference to the critical speed. Jing et al. [13] use a 2.5D finite element method to investigate the critical speed of ballastless track. Those researches revealed that the critical speed of track system is higher than the Rayleigh wave velocity of the underlying soil, attributed to the presence of the track structure and subgrade. However, the role that the track structure played hasn't been distinguished from subgrade.

Thus, this paper uses a same 2.5D subgrade-soil model to couple with ballasted track structure and ballastless track structure, respectively. The rails, rail pads and ballast layer in ballasted track and rails, rail pads, slab, CA layer, concrete base in ballastless track are modelled as Euler–Bernoulli beams resting on the subgrade. The subgrade and soil layers are modelled by the 2.5D finite elements. The critical speeds in ballasted track and ballastless track are compared to reveal the consequence of track structures.

2 Numerical Modelling

For the railway track, the material and geometry of the track structure and supporting ground can be treated as approximately constant in the longitudinal direction. Therefore, the wave propagation in this direction can be represented by the superposition of harmonic waves with a certain wavenumber. Based on this assumption, the 2D profile can be used to compute the 3D wave propagation under dynamic loading. This is referred to as the 2.5D method and has been applied to evaluate the dynamic response of solid structures due to traffic moving loads [2–4, 7, 9, 13–15]. In this section, the dynamic response of ballasted track and ballastless track due to train moving loads is investigated via 2.5D FEM modelling using the commercial software MATLAB. The detailed derivation can be found in [3].

China's high-speed railway is mainly composed of the ballasted track and the ballastless track. The main difference between the two track structures is that the ballastless track usually adopts the rigid concrete structure instead of the ballast layer in the ballasted track, as shown in Fig. 1. Due to the difference of track structure, the ballastless track has different dynamic characteristics such as transient response from the ballasted track. In this study, the critical speeds of the ballasted and ballastless track will be compared to find the function of track structure. To achieve this aim, these two types of track structures are built on the same subgrade-soil 2.5D finite element model. In the modelling, for the ballastless track, the rails, track slab, CA layer and concrete base are each modelled as a single Euler beam. Similarly, the ballast layer and sleepers in ballasted track are also modelled as a single Euler beam. As shown in Fig. 2, for both ballasted and ballastless tracks, they are built on the same subgrade and ground, which are discretized and modelled by 4-node quadrilateral elements for specific discrete wavenumbers in the transverse-vertical section. Each node of the element has three degrees of freedom allowing wave propagation in three-dimensional space to be taken into account faithfully.

The subgrade is divided into the sub-ballast layer and the embankment layer. The ground foundation consists of a single soil layer. The specific parameters of each layer are shown in Table 1. The loading represents an eight vehicles CRH2-type high-speed train with axle load of 140 kN, and its travelling speed was varied from 36 to 540 km/h (10–150 m/s). In this model, displacement response and stress response viewpoints are set along with the track centreline, marked in Fig. 2. Their locations are at the surface of the subgrade (node A), the midpoint of the embankment (node B), the surface of the ground (node C) and 3 m below the ground (node D).
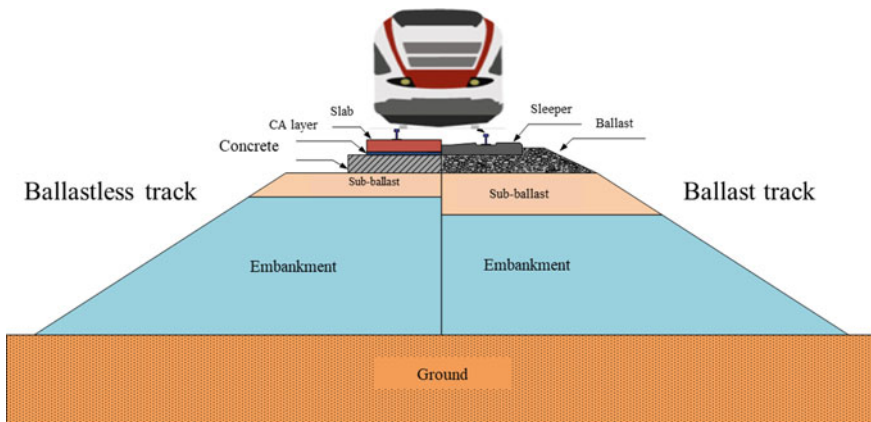
Fig. 1 Differences and links between the ballasted track and the ballastless track
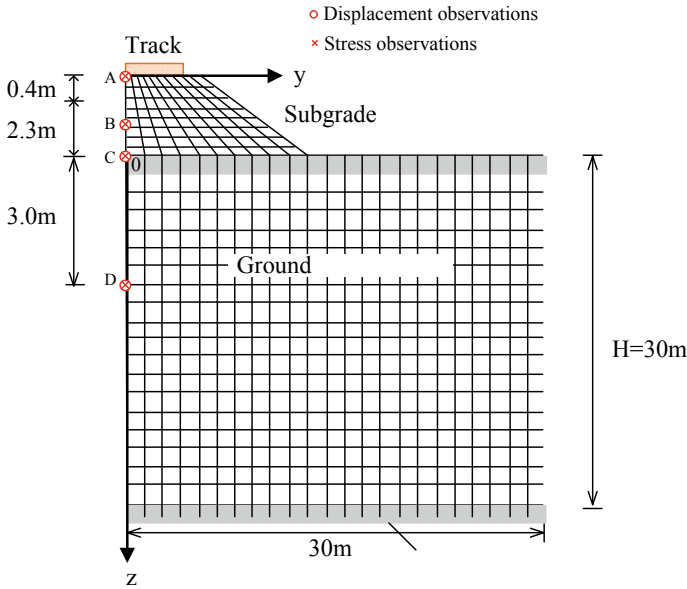
Fig. 2 Subgrade-soil model

Table 1 Parameters of the subgrade-soil model

	Sub-ballast	Embankment	Ground soil
Depth (m)	0.4	2.3	30
Density (kg/m^3)	2100	1900	1800
Shear wave velocity (m/s)	220	160	108
Rayleigh wave velocity (m/s)	202	147	101
Damping ratio	0.05	0.05	0.05
Poisson's ratio	0.3	0.3	0.33

3 Numerical Analysis

By coupling two different track structures on the same subgrade-soil finite element model and 2.5D FEM process, the dynamic displacement and stress responses of each viewpoint are obtained.

Figure 3 shows the maximum displacement under various train speeds at the surface of the subgrade of ballasted track and ballastless track, respectively. It can be seen that as the train speed increases, the maximum displacement amplitude of both two track structures starts to increase slowly from a static value about 1.05 mm. When the train speed keeps increasing and becomes close to the ground soil's Rayleigh wave velocity (363 km/h), the displacement response of both two track structures shows
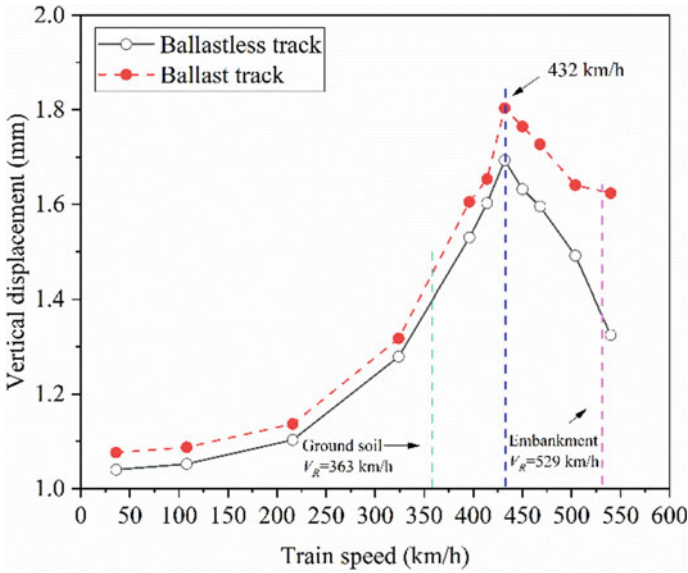
Fig. 3 Vertical displacement responses versus train speeds of ballasted track and ballastless track

sharply increase. After the train running speed exceeds the Rayleigh wave velocity of the ground soil, the displacement response reaches a peak value of 1.80 mm for ballasted track and 1.69 mm for ballastless track when train speed at 432 km/h, respectively. However, as the train speed increases continuously, the displacement response reduces gradually. Even the subsequent train speed reaches the Rayleigh wave velocity of the embankment, the displacement response is still in the downward trend. Thus, it can be concluded that the critical speed are 432 km/h for both the ballasted and ballastless tracks with the same subgrade-ground. This result means the track structures have no effect on the critical speed of the model built in Sect. 2. However, it is worth to note that the maximum displacement response of the ballasted track is always larger than that of the ballastless track.

Figure 4 is about the maximum dynamic stress response along with the train speed at the same position. It can be seen that the dynamic stress at the subgrade surface of ballasted track is much greater than that of the ballastless track. Although the dynamic stress responses do not appear at peak value showed in maximum displacement curves, the dynamic stresses are rapidly rising when the train speed is close to the Rayleigh wave velocity of the soil. At the critical speed of the displacement response (432 km/h), the dynamic stress value at the subgrade surface of ballasted track is 41.8 kPa, which is 1.5 times as much as that in quasi-static state. The dynamic stress value at subgrade surface of ballastless track is 27.1 kPa, which is 1.26 times as much as that in quasi-static state.

Figure 5 reveals the distribution of dynamic displacement along the depth. The response values are obtained at the time the maximum value occurs, which also
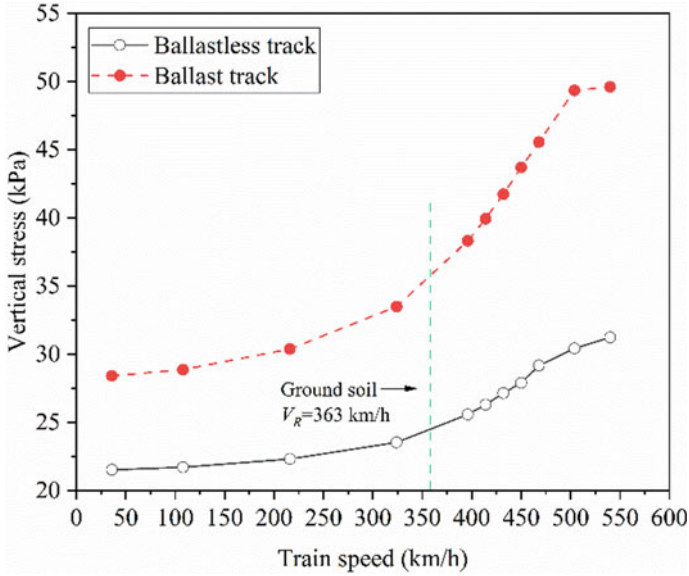
Fig. 4 Vertical stress responses versus train speeds of ballasted track and ballastless track
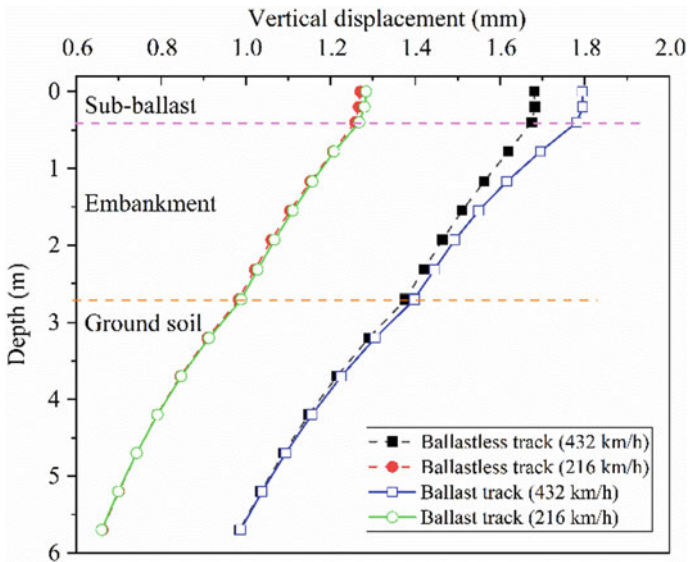
Fig. 5 Vertical displacement response along depth at different train speeds in ballasted track and ballastless track

corresponding to the time the wheels just arrive the observe position A. It shows that the displacement response along the depth of the two-track structures is mainly determined by the train running speed. The displacement values along the depth of ballasted track are quite close to that of ballastless track at low speed (216 km/h). When the train speed increases to the critical speed (432 km/h), the displacement responses in the subgrade of ballasted track are larger than that of ballastless track at each depth, however, the difference gradually reduces along the depth and becomes hard to tell in the ground soil layer. Briefly, the influence of track structure mainly affects the displacement response in subgrade.

Figure 6 reveals the distribution of corresponding dynamic stress response along with the depth. In the range of the subgrade, the dynamic stresses generated by same train speed in ballasted track are greater than that in ballastless track. The stress difference between two structures at subgrade surface is 10.2 kPa for train speed 432 km/h and 6.5 kPa for train speed 216 km/h; as the depth increases, the stress difference decreases; when it comes to the ground soil layer, the difference also becomes hard to tell. However, it is also worth to find that the dynamic stresses at lower train speed (216 km/h) generated in ballasted track are also larger than that in ballastless track induced by higher train speed (432 km/h). This means track structure is more dominant than train speed for dynamic stresses in this model.
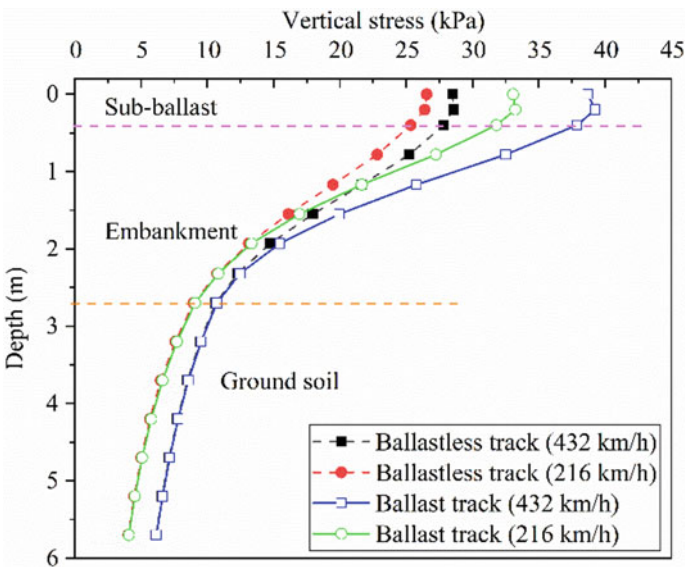
Fig. 6 Vertical stress response along depth at different train speeds in ballasted track and ballastless track

4   Conclusions

By coupling the ballasted and ballastless track structures on the same 2.5D FEM subgrade-soil model, respectively, the functions that the track structure played are revealed in this paper. The following conclusions are drawn from the current study:

1.   The existence of track structure and subgrade can improve the critical speed of the railway; however, the role that subgrade plays is more dominant because the ballasted track and ballastless track that were built on the same subgrade-soil model have the same value of critical speed.
2.   For the ballasted track and ballastless track built on the same subgrade-soil model, the displacement and stress responses in the subgrade range of ballasted track are larger than those in ballastless track.
3.   For the vibration responses in the range of subgrade, the train speed is the dominant factor; as for the stress responses, the track structure is more influential.

References

1.   Auersch L (2008) The effect of critically moving loads on the vibrations of soft soils and isolated railway tracks. J Sound Vibr 310(3): 587–607
2.   Bian X, Chen Y (2006) An explicit time domain solution for ground stratum response to harmonic moving load. Acta Mech Sin 22(5):469–478
3.   Bian X, Chen Y, Hu T (2008) Numerical simulation of high-speed train induced ground vibrations using 2.5D finite element approach. Sci China Ser G-Phys 51(6):632
4.   Bian X, Cheng C, Jiang J, Chen R, Chen Y (2016) Numerical analysis of soil vibrations due to trains moving at critical speed. Acta Geotech 11(2):281–294
5.   Bian X, Jiang H, Chang C, Hu J, Chen Y (2015) Track and ground vibrations generated by high-speed train running on ballastless railway with excitation of vertical track irregularities. Soil Dyn Earthquake 76:29–43
6.   Bian X, Jiang H, Cheng C, Chen Y, Chen R, Jiang J (2014) Full-scale model testing on a ballastless high-speed railway under simulated train moving loads. Soil Dyn Earthquake 66:368–384
7.   Costa PA, Colaço A, Calçada R, Cardoso AS (2015) Critical speed of railway tracks. Detailed and simplified approaches. Transp Geotech 2:30–46
8.   Grundmann H, Lieb M, Trommer E (1999) The response of a layered half-space to traffic loads moving along its surface. Arch Appl Mech 69(1):55–67
9.   Hu J, Bian X, Jiang J (2016) Critical velocity of high-speed train running on soft soil and induced dynamic soil response. Proc Eng 143:034–1042
10. Kaynia AM, Madshus C, Zackrisson P (2000) Ground vibration from high-speed trains: prediction and countermeasure. J Geotech Geoenviron Eng 126(6):531–537
11. Madshus C, Kaynia A (1999) Dynamic ground interaction; a critical issue for high speed train lines on soft soil interaction. J Geotech Eng Transp Infrastr 1829
12. Sayeed MA, Shahin MA (2016) Three-dimensional numerical modelling of ballasted railway track foundations for high-speed trains with special reference to critical speed. Transp Geotech 6:55–65
13. Costa PA, Calçada R, Cardoso AS, Bodare A (2010) Influence of soil non-linearity on the dynamic response of high-speed railway tracks. Soil Dyn Earthquake 30(4):221–235

14. Hu J, Bian X, Xu W, Thompson D (2019) Investigation into the critical speed of ballastless track. Transp Geotech 18:142–148
15. Yang Y-B, Hung H (2008) Soil vibrations caused by underground moving trains. J Geotech Geoenviron Eng 134(11):1633–1644

Measuring the Contact Stiffness at the Grain Scale of Fresh and Used Granite Ballast

Geoff Watson [iD]**, Jacapo Piazza, B. N. Madhusudhan** [iD]**, and Louis Le Pen** [iD]

Abstract Faster, heavier and more frequent use is placing greater demands than ever before on railways. These increased demands reduce the time available for maintenance without costly line closures. There is a need to improve the understanding of the performance of key materials used in railway construction to improve their specification and achieve greater durability. A key material is the source rock for railway ballast. It is known that different rock sources perform very differently as ballasts and there is a general consensus that igneous rock types perform the best. However, there can still be great variability in performance between alternate igneous rock ballasts and performance may vary with age/use. To better understand ballast behaviour, modern numerical tools such as the discrete element method (DEM) are able to model particles at the grain scale and can be used to assess how changes in ballast material and/or changes in performance with age/use may influence railway performance. However, a lack of understanding of inter-particle ballast contact mechanics mean that current DEM simulations lack the necessary input data to provide a high level of confidence in their outputs. To begin to address this, experiments were carried out to understand the normal contact behaviour of fresh and used granite type ballast grains under cycles of load at magnitudes representative of in-service use. The grains were tested using a uniaxial loading machine and the deflections measured using micro-photogrammetry and digital image correlation. The tests indicate significantly different load–deformation characteristics for fresh and used granite ballast and present a method for modelling the contact mechanics modified from Hertzian contact theory. Data also shows that used ballast shows less plastic deformation on first loading and could therefore be potentially re-used in track rather than down-cycled as is currently the case in some countries.

Keywords Ballast · Grain · Contact mechanics · Digital image correlation · Stiffness · Granite · Railway · Railroad · Trackbed · DEM · Testing · Uniaxial

G. Watson (✉) · J. Piazza · B. N. Madhusudhan · L. Le Pen
Infrastructure Research Group, School of Engineering, University of Southampton, Building 178, Burgess Road, Southampton SO16 7QF, UK
e-mail: g.watson@soton.ac.uk

1 Introduction

Ballasted track systems remain the most commonly used means of spreading the train vehicle load to the subgrade, providing lateral support and enabling trackbed drainage. They have key advantages over other track system forms in that they have lower upfront costs and the track alignment can be modified relatively easily. However, increased demands on modern railway infrastructure in many countries have led to more intensive use, with the effects of both increasing maintenance requirements and reducing the time available for them. Ideally, improvements to the specification for the components of ballasted track systems should be found that improve durability and reduce maintenance needs. One material with the potential to be specified better is the ballast itself.

Ballast grains are usually graded between 20 and 65 mm. For modern ballast, the rocks chosen will usually be strong, igneous or metamorphic rocks. The exact source material varies depending on region. In the UK, the regional geology has meant that granite is usually used. The preference for crushed igneous rocks rather than sedimentary rocks such as limestone is based on observations of improved performance and enforced through more onerous qualifying tests (e.g. fracture/abrasion resistance). However, although empirical observations may support the use of high specification ballasts, there is the potential for greater insights into the mechanisms for improved performance if representative models can be created, such models could potentially differentiate between ballast materials that would otherwise appear similar according to current specifications. Another issue is that in some countries, the UK included ballast is down-cycled at renewal based on a potentially outdated expectation that the material has lost its performance. This expectation is perhaps justified for sedimentary ballasts, but for modern igneous ballasts may be incorrect. To build models of railway system performance, material properties for soils and ballasts are traditionally obtained by carrying out tests on representative volumes, e.g. triaxial testing [1]. As ballasts have relatively large grain sizes, triaxial equipment has to be able to accommodate large diameter samples of 300 mm or more. Alternatively, specially prepared tests [2, 3] with larger volumes of material can be carried out. These tests are costly, especially if carried out at anything approaching track scale, so there is potential benefit from using numerical tools such as the discrete element method (DEM) to simulate results based on inter-grain tests. Railway ballast is, in principle, an ideal material to simulate using the discrete element method in which individual grains are modelled within an assembly; this is because there are relatively few particles to model compared with finer grained materials and the computational cost is therefore, in relative terms, more manageable. However, although models exist [4–6] and some inter-grain force deflection data is available for finer materials such as sands [7, 8], there is a lack of understanding of the ways in which coarse aggregate ballast grains interact at the grain scale and how responses may change with repeated loading.

This paper presents a uniaxial test method to determine contact mechanical behaviour between ballast grains. Tests are carried out on a fresh granite ballast and material recovered from the trackbed—termed 'used ballast'. The contact test

results are compared with Hertzian contact theory. Differences in behaviour from the theory are highlighted, and modifications to theory are suggested which could be used for assigning contact mechanical properties in numerical models. The data and analysis reported is a first step towards wider scale testing and modelling that could provide greater insights into which ballasts perform better and the potential for re-use of ballast recovered at track renewal.

2 Theoretical Basis for Contact Test Loading

Ballast layers typically support railway sleepers over a 2.5 m by 0.3 m footprint. The ballast layer typically has a depth of 300 mm. Peak ballast loading occurs on particles just below the sleeper beneath the rail positions (the railseats). Loads are then transferred down and outwards through the volume of ballast material attenuating with depth and horizontal offset. Measurements of the pressure on the underside of railway sleepers below the railseats have shown that peak vertical stress may be up to 250 kPa [9] for moderate loading which would be higher for heavy freight vehicles. Inter-particle contact forces are hard to calculate because load transfer through an irregular medium is nonuniform. However, if some simplifying assumptions are made about the arrangement and size of particles for a known/estimated vertical pressure, it is possible to calculate grain contact forces at, or near to, the railseat. The simplest model of grain packing is that of uniformly sized spherical particles in a cubic packing arrangement. In this idealized case, the contact force (F_c) induced by an applied vertical stress (σ_c) to a packing of particles of diameter (d) can be directly calculated using Eq. (1) to give the results shown in Table 1.

$$F_c = \sigma_c \bullet A_p = \sigma_c \bullet \frac{\pi d^2}{4} \tag{1}$$

More sophisticated modelling can also be used to estimate contact forces with perhaps more accurate outcomes. DEM simulations of monotonic failure triaxial tests on ballast [5] gave distributions of the grain normal contact forces with cell pressures of 15 and 200 kPa as shown in Fig. 1. For these confinement pressures, the vertical failure loads were of the order of 100 and 1600 kPa which fully envelopes the likely maximum vertical stress in the field. Figure 1 is plotted in terms of log of

Table 1 Calculated contact force for spherical particles of different diameters under different vertical stresses

Vertical stress, σ_c (kPa)	Sphere diameter, d (mm)	Contact force, F_c (N)
15	50	29
	25	7
200	50	393
	25	98
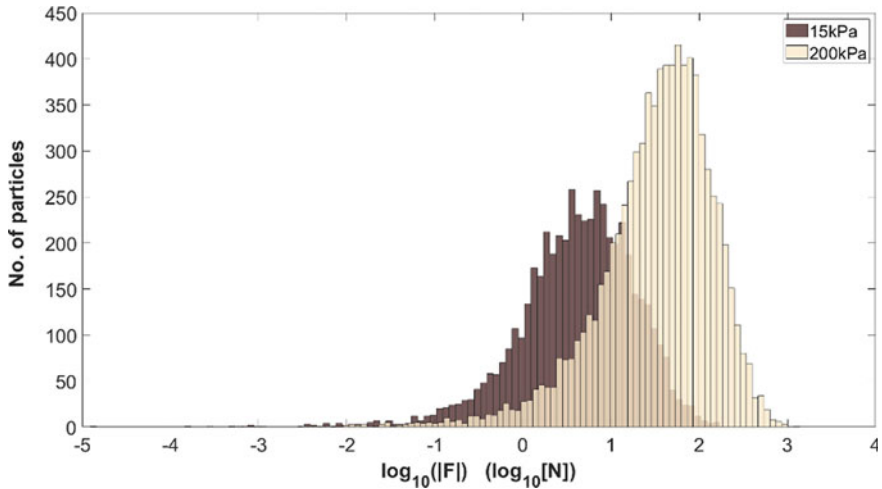
Fig. 1 Histograms of normal contact forces in simulated triaxial tests at cell pressures of 15 and 200 kPa (after [5])

normal force at peak strength versus frequency (number of grains). If the modal value (around the largest bar) for each test is eyed in, the log of force is approximately 0.697 and 1.76 corresponding to 5 kN–57 kN for the 15 kPa and 200 kPa cell pressure tests, respectively. However, there is a large range in contact forces through the population of grains in each test so that the grain contact force ranges from nearly zero to over 1000 N.

Based on consideration of the likely inter-particle contact force, a range for testing was selected of up to 200 N which is expected to be representative of field situations.

3   Methods

3.1   Materials

Ballast particles of two types were used for testing. Fresh ballast made of crushed granite was sourced from Cliffe Hill quarry (Leicestershire, UK). Used ballast was sourced from Network Rail. The used ballast was recovered from a trackbed during renewal. Normally, recovered trackbed material (at least in the UK), would be down-cycled and not returned to the railway. However, the recovered trackbed material contained a proportion of ballast in standard ballast particle sizes. The used material within ballast grade was separated from the finer materials at a processing centre and a sample of the used ballast was provided for testing. The used material is expected to have been in the trackbed for an estimated 30 years. Examination of the used ballast showed that it contained a mix of rock types which was predominantly (>

60%) granite but also contained some basalt and limestone grains. A subset of the granite grains were selected for testing. Young's modulus and Poisson's ratio of the ballast particles were taken as 64 GPa and 0.176, respectively, based on the literature [10–12].

3.2 Experiment

To test the contact behaviour of the ballast, the grains were placed into robust steel cup holders and roughly centred within the holder to have a locally pointed surface directed outwards. Once positioned, the grains were held in position with mounting putty, while an epoxy resin was poured in and allowed to set (Fig. 2). The use of the steel holder and resin was intended to provide a stable support to the particles although it is recognized that there will be some compliance of the assembly. Twenty-six tests were carried out on pairs of grains with repeats to confirm trends. Typical results from six pairs of particles are presented here representing fresh and used ballast grains in sizes retained on 50, 31.5 and 22.4 mm sieves. Each test consisted of a pair of particles from the same size category placed so that there was a local point-to-point contact. The particles were mounted in an Instron 5569 electromechanical uniaxial test machine and tested in staged load increments as shown in Table 2.
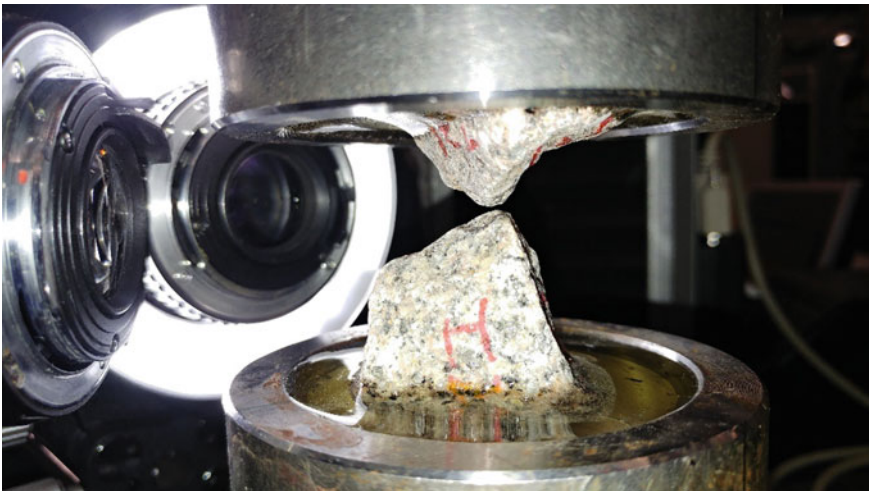
Fig. 2 Photograph showing the ballast particles embedded in resin and mounted in the test machine just prior to particle contact. The camera lenses and macro-lighting can be seen on the left

Table 2 Testing details

Stage	Loading
1	Apply initial load of 5 N at 1 N/s
2	Pause for 5 s on 5 N load to ensure contact stabilizes
3	Increase the load from 5 to 200 N at 4 N/s
4	Decrease the load from 200 to 5 N at 4 N/s
5	Repeat stages 3 and 4 ten times

3.3 Measurement System

Two cameras were set up focused on the inter-grain contact, with their line of sight normal to the contact and approximately at right angles from each other. The cameras used were Nikon D7100s, each attached to a Nikon bellows (PB-4 and PB-6 models) fitted with a reverse mounted Ricoh 50 mm F1.7 lens (Fig. 3a). The bellows are a means to obtain highly magnified images of the grain contact area. Those used permitted a magnification of up to 11 times. The camera measurement system was used to ensure the compliance of the resin/test apparatus was removed from the relative grain deflection. Each camera recorded images that included both the upper and lower particles. The inter-grain deflection was obtained by considering the change in position of pixel patterns on each grain calibrated to length units [13, 14].

A target, as shown in Fig. 3b, was used to calibrate the images. The cameras were both set to record high definition video (1920 × 1080 pixels) at 25 frames per second (fps).

Fig. 3 **a** Position of cameras relative to sample in test machine and **b** a calibration target. Each big square is 1.429 mm across meaning that in video mode, the resolution is ~ 200 pixels per mm or 5 μm per pixel

3.4 Theoretical Interpretation

According to Hertzian contact theory [15, 16], the normal displacement, δ, characterizing the stiffness of a solid body can be expressed as a function of the normal force, P; the relative Young's Modulus, E^*; and the relative radius of contact, R (Eq. (2))

$$\delta = \left(\frac{9P^2}{16RE^{*2}} \right)^{\frac{1}{3}}$$

(2)

where the relative radius of contact (R) is determined from R_1 and R_2 which are the radii of curvature of the contact area for each of the two particles [Eq. (3)] and the relative Young's Modulus E^* is determined from Young's Modulus (E_1 and E_2) and Poisson's ratio (v_1 and v_2) of each particle (Eq. 4).

$$R = \left(\frac{1}{R_1} + \frac{1}{R_2} \right)^{-1}$$

(3)

$$E^* = \left(\frac{1 - v_1^2}{E_1} + \frac{1 - v_2^2}{E_2} \right)^{-1}$$

(4)

However, Hertzian contact theory relies on two perfectly smooth spherical surfaces coming into contact and its ability to predict deflection from two angular grains coming into normal contact presents a difficulty in determining a radius of contact to assign even if Young's modulus and Poisson's ratio are known or can be estimated reliably. The effective radius of contacting regions may also not remain uniform with load. Nevertheless calculation of the Hertzian force/deflection provides a framework from which to interpret contact tests on ballast.

4 Results

4.1 Validation of Test Methods

To first understand whether the test arrangement and theory were reliable, spherical steel grains were tested (Fig. 4). These confirmed both that the resolution of spatial measurements and that Hertzian contact theory were reliable for accurately predicting deflection for known forces. Having proved the test concept, real ballast grains were tested.

4.2   Fresh and Used Ballast

Figure 5 shows the load–deflection results for tests on 50 mm fresh ballast; these
results are typical of trends seen in all the tests on fresh ballast. Figure 6 shows the
same curve but zoomed in so that the individual load/unload cycles are visible. There
is significant plastic deformation in the initial load cycles (usually the first and second)
which stabilizes with cycles so that during the 10th cycle the plastic deflection is a
small proportion of the elastic deflection. Figure 7 shows the corresponding test for
used ballast and is typical of trends seen in all the used ballast tests. In this test,
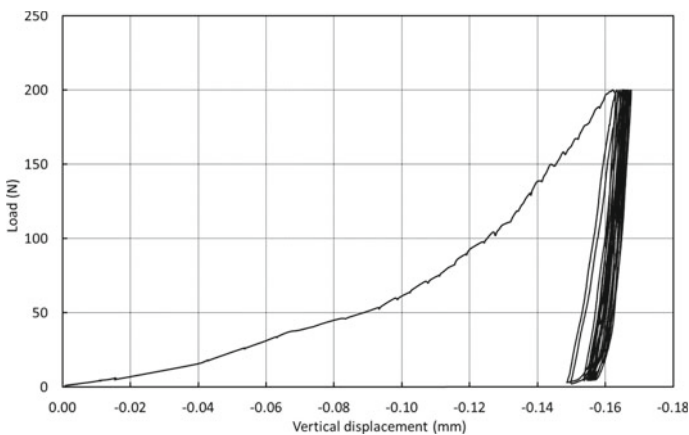
Fig. 5   Load–displacement curve for fresh ballast contact (50 mm)
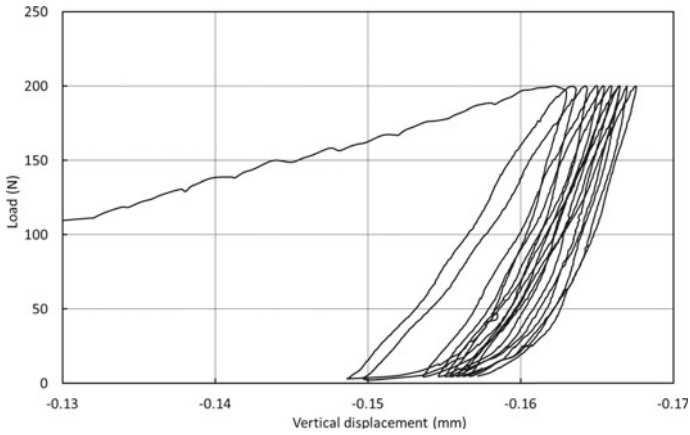
Fig. 6 Load–displacement curve for fresh ballast contact (50 mm)
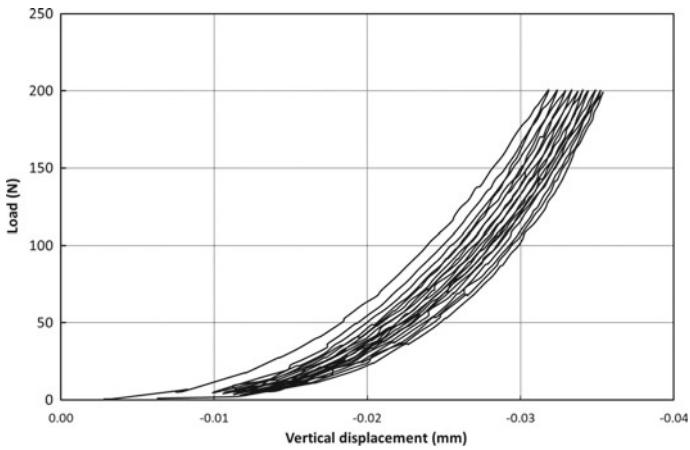
Fig. 7 Load–displacement curve for used ballast (50 mm)

there is very little plastic deformation and the load/unload cycles remain relatively constant with a small proportion of plastic settlement per cycle.

4.3   Comparison with Hertzian Contact Model

To evaluate the potential for Hertzian contact to predict the elastic load deflection behaviour of the tests, the 10th unload cycle was selected as this was considered to best represent the medium-term elastic response of the ballast. To assign parameters and apply Eq. (2), Young's Modulus and Poisson's ratio are required—they have

been taken from the literature as 64 GPa and 0.176, respectively. The remaining unknown is then the radius of contact for each particle. A simplifying assumption is that the radii of contact for each particle are equivalent; this then renders it possible to curve fit Eq. (2) to the measured behaviour by finding the value of R that gives the smallest difference between the measurements and the predicted curve. However, initial attempts at this showed that using a constant value of $R_1 = R_2$ throughout the cycle gave visually very poor agreement. A possible explanation for the poor agreement was that the effective radii of contact for the two particles were changing during loading due to their uneven local topography. This can be reasoned because the contact between two irregular surfaces is not a single contact but rather a series of smaller contacts that gradually merge and fuse together as the force is increased.

Given these considerations, an alternative for fitting the Hertzian contact theory was tried in which the experimental data was divided into six load steps (5–15, to 33.3, to 50, to 75, to 100 and to 200 N). The load steps are closer at the lower load values and over a larger range towards the higher loads. The ranges were selected in this way as it was thought that the contact would stabilize at higher loads. For these six load steps, the values of the local contact radii for a best fit to the Hertzian contact model were found using a minimal difference approach (as illustrated in Fig. 8).

Figures 9 and 10 show the final unload line for six particle pairs tested with the fitted modified Hertzian lines. Table 3 shows the values of the radii assigned.

Table 3 shows that there is quite some variability in the assignment of contact radii between the grains tested. However, some observations can be made. The best fit stepped load approach has given a consistent result of increasing contact radii needed to fit the Hertzian contact model with increasing load. This is consistent with the idea that the uneven contact area is developing as a fusion of locally rough topography. Visually Figs. 9 and 10 show that the stepped Hertzian curves match the measurements well and confirm that the effective contact radii stabilize at higher
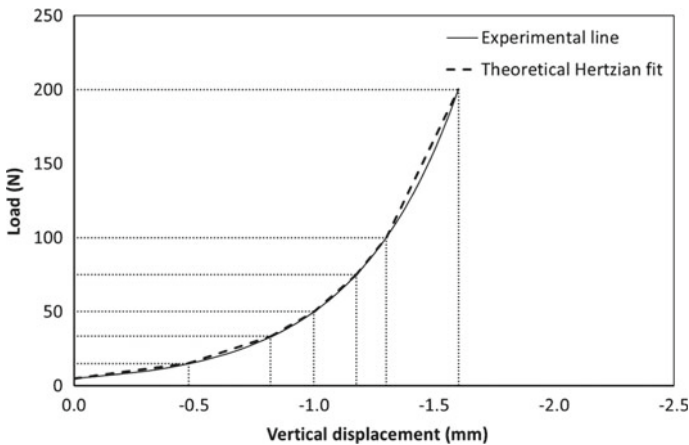
Fig. 8 Graph showing idealized fitting of Hertzian stepped approach to experimental data (schematic only, no real data present)
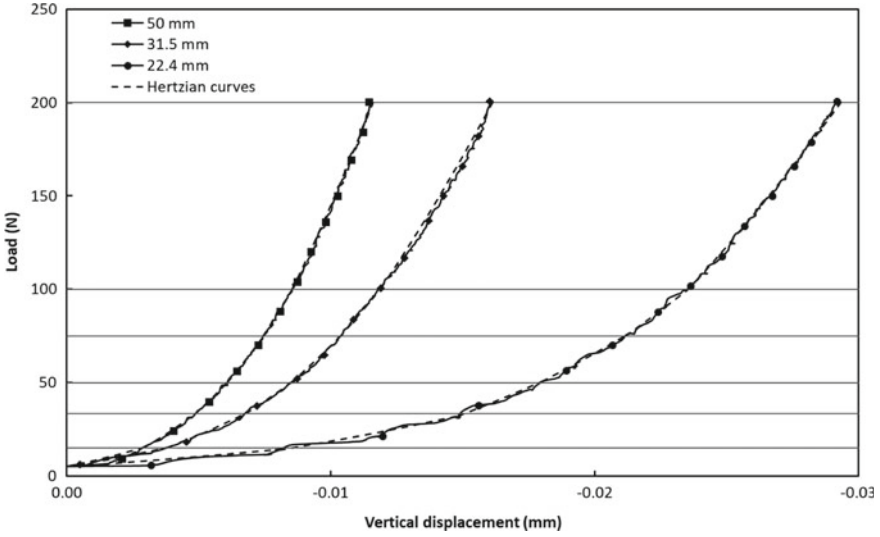
Fig. 9 Graph showing data from the 50, 31.5 and 22.4 mm fresh ballast tests with fitted Hertzian curves. The dashed horizontal lines show the load banding used for Hertzian radius calculation
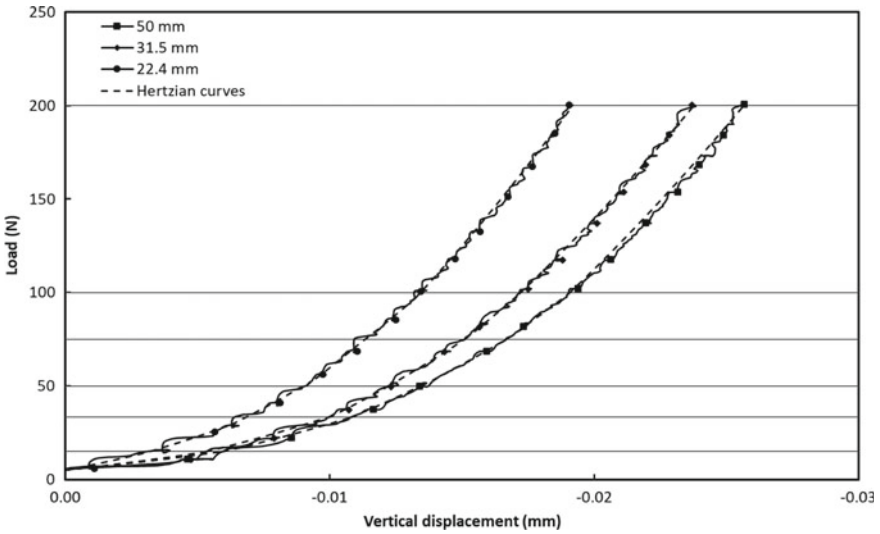
Fig. 10 Graph showing data from the 50, 31.5 and 22.4 mm used ballast tests with fitted Hertzian curves. The dashed horizontal lines show the load banding used for Hertzian radius calculation

Table 3 Nominal radii of Hertzian contact at the different load areas for each test

Label	Size (mm)	Hertzian contact radius (mm)					
		R_1	R_2	R_3	R_4	R_5	R_6
		to 200 N	to 100 N	to 75 N	to 50 N	to 33 N	to 15 N
Fresh	50	33	22	15	14	3.0	2.3
	31.5	14	8.1	5.8	3.1	1.6	0.31
	22.4	5.4	2.0	1.2	0.73	0.13	0.03
Used	50	3.6	1.9	1.2	0.98	0.36	0.08
	31.5	3.7	2.9	1.6	1.5	0.42	0.11
	22.4	5.4	3.6	2.7	1.5	0.72	0.50

loads. The larger grains may have been expected to produce stiffer responses; for the fresh ballast, this is the case for the 50 mm grain as the local contact radius (R_6–R_1) tends towards a final value (R_1) approaching the particle diameter. However, for the used ballast, the smaller particle is stiffer. Also, although the value of the local contact radius does increase with load step, the final value (R_1) remains a relatively small proportion of the grain diameter for the smaller fresh grain and the used grains so it can be said that the local angularity appears to dominate the results. This is perhaps an effect of scale and/or simply inhomogeneity from the parent population, and more tests are needed to evaluate more general trends.

5 Conclusions

These tests have shown that there are clear differences in contact behaviour between fresh and used particles, particularly the presence of large initial plastic deformations for the fresh material. Hertzian contact mechanics does not well match the tests if applied with constant radii of contact. However, modifying the approach by allowing the contact radii to change with steps in the load could offer a means to implement a DEM model. These results are a first step towards providing the input data needed to develop more realistic contact mechanics models for application in DEM simulations. They also demonstrate that used ballast has less plastic response compared with fresh ballast and could be suitable for re-use, although further work is required to confirm this.

References

1. Aursudkij B, McDowell GR, Collop AC (2009) Cyclic loading of railway ballast under triaxial conditions and in a railway test facility. Granular Matter 11:391–401

2. Abadi T, Le Pen L, Zervos A, Powrie W (2018) Improving the performance of railway tracks through ballast interventions. Proc Inst Mech Eng Part F J Rail Rapid Transit 232(2):337–355
3. McDowell GR, Lim WL, Collop AC, Armitage R, Thom NH (2005) Laboratory simulation of train loading and tamping on ballast. Proc Inst Civ Eng Transp 158(2):89
4. Lim WL, McDowell GR (2005) Discrete element modelling of railway ballast. Granular Matter 7(1):19–29
5. Harkness J, Zervos A, Le Pen L, Aingaran S, Powrie W (2016) Discrete element simulation of railway ballast: modelling cell pressure effects in triaxial tests. Granular Matter 18(3):65
6. Lu M, McDowell GR (2008) Discrete element modelling of railway ballast under triaxial conditions. Geomech Geoeng. 3:257
7. Cavarretta I, Coop M, O'Sullivan C (2010) The influence of particle characteristics on the behaviour of coarse-grained soils. Géotechnique 60(6):413–423
8. Cavarretta I, O'Sullivan C (2012) The mechanics of rigid irregular particles subject to uniaxial compression. Géotechnique 62(8):681–692
9. Shenton MJ (1975) Deformation of railway ballast under repeated loading conditions. In: Kerr (ed) Railroad track mechanics and technology. Proceedings of a symposium held at Princeton University, USA, pp 405–425
10. Christaras B, Auger F, Mosse E (1994) Determination of the moduli of elasticity of rocks. Comparison of the ultrasonic velocity and mechanical resonance frequency methods with direct static methods. Mater Struct 27(4):222–228
11. Martin CD, Chandler NA (1994) The progressive fracture of Lac du Bonnet granite. Int J Rock Mech Min Sci Geomech Abstr 31(6):643–659
12. Duevel B, Haimson B (1997) Mechanical characterization of pink lac du Bonnet granite: Evidence of nonlinearity and anisotropy. Int J Rock Mech Min Sci 34(3):117.e1-117.e18
13. White DJ, Take WA, Bolton MD (2003) Soil deformation measurement using particle image velocimetry (PIV) and photogrammetry. Géotechnique 53(7):619–631
14. Bhandari AR, Powrie W, Harkness RM (2011) A digital image-based deformation measurement system for triaxial tests. Geotech Test J 35(2):209–226
15. Hertz HR (1896) On the contact of rigid elastic bodies and on hardness (Verhandlungen des Vercins sur Beforderung des Gewerbefleisses, November 1882). In: Papers PL (ed) Miscellaneous. London, MacMillan and Co. Ltd, New York, Macmillan and Co.
16. Johnson KL (1985) Contact mechanics. Cambridge University Press

Geosynthetics in Transportation Applications

Numerical Study of Deformation Behavior of Geosynthetic Reinforced Soil Bridge Abutments Subjected to Longitudinal Shaking

Yewei Zheng [ID], **Patrick J. Fox** [ID], **and John S. McCartney** [ID]

Abstract This paper presents a numerical study on the deformation behavior of geosynthetic reinforced soil (GRS) bridge abutments subjected to longitudinal shaking using the finite difference program FLAC. The soil model characterizes the soil as an elastic–plastic material with hysteretic behavior. Numerical simulations were conducted for a single-span full-bridge system, including the bridge beam, two GRS abutments, and foundation soil, subjected to the 1940 Imperial Valley motion in the longitudinal direction. Simulation results show that the two front wall facings in each abutment moved in-phase during shaking and had different residual facing displacements at the end of shaking due to asymmetry of the earthquake motion with respect to the abutment geometry. Bridge seat settlements at the two ends of the bridge system were similar.

Keywords Geosynthetic reinforced soils · Bridge abutment · Earthquake

1 Introduction

Geosynthetic reinforced soil (GRS) bridge abutments are becoming widely used for transportation infrastructure in the USA. Although this technology offers substantial cost- and time-savings for construction, there are concerns regarding the use of GRS

Y. Zheng (✉)
School of Civil Engineering, Wuhan University, Wuhan 430072, Hubei, China
e-mail: yzheng@whu.edu.cn

P. J. Fox
Department of Civil and Environmental Engineering, Pennsylvania State University, University Park, PA 16802, USA
e-mail: pjfox@engr.psu.edu

J. S. McCartney
Department of Structural Engineering, University of California San Diego, La Jolla, CA 92093-0085, USA
e-mail: mccartney@ucsd.edu

bridge abutment technology in high seismic areas, and little information is available to guide designers on how to improve the seismic performance of these structures.

Post-earthquake reconnaissance for the 2010 Maule earthquake indicated that a GRS abutment exhibited no signs of lateral or vertical permanent displacements after shaking, while the bridge suffered minor damage that may have resulted from the bridge skew angle [1]. Shaking table tests have been conducted on GRS abutments for shaking in the longitudinal direction to the bridge beam [2–4]. Shaking table tests on a 3.6-m-high GRS abutment indicated no significant distress for longitudinal shaking with horizontal accelerations up to 1 g [2]. Results from a series of shaking table tests on 2.7-m-high half-scale GRS abutments subjected to scaled earthquake motions indicated that residual facing displacements and bridge seat settlements increased with larger reinforcement vertical spacing, reduced reinforcement stiffness, and lower surcharge stress under dynamic loading [3, 4].

Although these studies indicate good overall performance for GRS abutments under dynamic loading, the abutments specimens were limited by the size and payload capacity of the shaking table. Numerical modeling can be used to investigate potential seismic issues for GRS abutments with more realistic geometry and configuration. In this study, the two-dimensional finite difference program FLAC was used to simulate the deformation behavior of a single-span full-bridge system using two GRS abutments for earthquake shaking in the longitudinal direction.

2 Numerical Model

2.1 Model Configuration

The single-span full-bridge system investigated in this study consists of a bridge beam and two GRS abutments. Model geometry for the right-hand side of the bridge system is shown in Fig. 1 for simplicity, and the left-hand side is symmetric. The bridge system has a span $L_b = 30$ m and symmetrical structures on both ends, resting on foundation soil with a depth of 1 m. Each end structure consists of a lower GRS wall, bridge seat, and upper GRS wall. The lower GRS wall has height $h = 5$ m and 25 modular facing blocks with dimensions of 0.3 m (length) $\times$ 0.2 m (height). An L-shaped bridge seat with a vertical backwall rests on top of the lower GRS wall and has setback distance $a_b = 0.2$ m from the wall facing. The clear distance between the top facing block and bridge beam d_e is equal to the bridge seat thickness (0.4 m). The clearance height for the bridge beam above the foundation soil is 5.4 m, which satisfies the FHWA minimum requirement of 4.9 m for interstate highways [5]. The bridge seat has upper surface contact length $L_c = 1.0$ m with the bridge beam and lower surface contact length $L_s = 1.5$ m with the backfill soil. There is a 100-mm-wide vertical seismic joint between the bridge beam and the backwall of bridge seat. Assuming a ratio of bridge beam span to depth $R_{sd} = L_b/D = 20$, the depth of the bridge beam $D = 1.5$ m. A 1.9-m-high upper GRS wall lies behind the backwall of
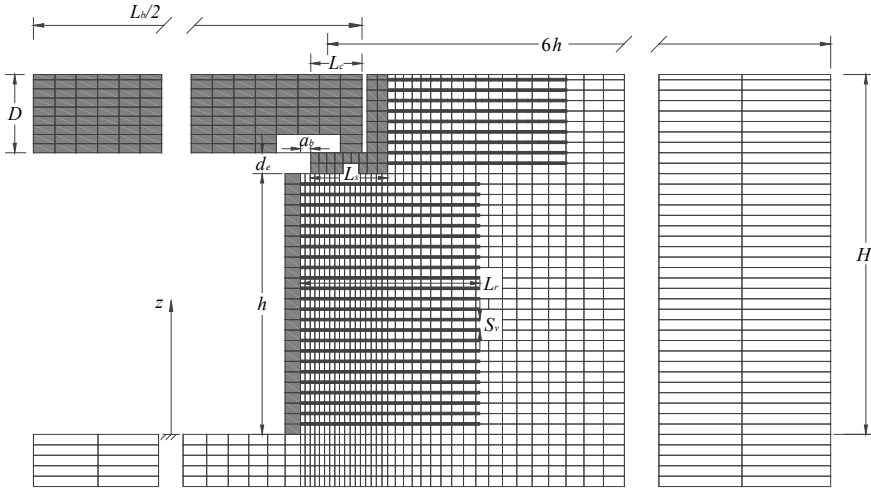
Fig. 1 Model geometry for the right-hand side of bridge system (left-hand side symmetric)

bridge seat. To minimize the influence of boundary conditions on system response, the lateral boundaries are located at a distance of 30 m (6 h) from the front wall facing on each end of the bridge. The vertical coordinate z is measured upward from the top surface of the foundation soil.

2.2 Material Model and Properties

Soils

The soil properties for this study are characterized of a well-graded sand. The angular sand has a high friction angle of 51.3° and zero cohesion according to results from drained triaxial compression tests on dry sand specimens. The foundation soil was assumed to be the same with the backfill soil and represented a dense sand foundation. For static analysis, the backfill soil and foundation soil were modeled as a nonlinear elastic–plastic material using the Duncan–Chang hyperbolic relationship [6] and the Mohr–Coulomb failure criterion. This model can capture the nonlinear stress–strain behavior before the peak shear strength and dilation behavior. Details of the soil model are reported by Zheng and Fox [7, 8].

For dynamic analysis, the UBCHYST model [9] was used in this study. This model can account for reduction in secant modulus with increasing shear strain. The tangent shear modulus is a function of the small strain shear modulus G_{max} times a reduction factor that is a function of the developed stress ratio and change in stress ratio to reach failure. In this study, the small strain shear modulus G_{max} is estimated using the empirical relationship proposed by Menq [10]. The model parameters, as summarized in Table 1, were calibrated by comparing cyclic simple

Table 1 UBCHYST model parameters

Parameter	Value
Friction angle, ϕ' (°)	51.3
Cohesion, c' (kPa)	0
Small strain shear modulus, G_{max} (MPa)	Stress-dependent
Bulk modulus, B (MPa)	$= G_{max}$
Atmospheric pressure, p_a (kPa)	101.3
Hysteretic parameter, H_n	6.0
Hysteretic parameter, H_{n1}	1.0
Hysteretic parameter, H_{rf}	0.98
Hysteretic parameter, H_{rm}	1.0
Hysteretic parameter, H_{dfac}	0

shear response to the modulus reduction curves and damping curves calculated using published empirical relationships [10, 11]. The shear stress–strain relationships from the numerical simulations for different mean effective stresses and cyclic shear strain amplitudes are shown in Fig. 2. The model exhibits hysteretic soil behavior that is consistent with that observed for sands [10].

Reinforcements

The geogrid layers in both the lower and upper GRS walls had a uniform length L_r = 3.5 m (0.7 h) and vertical spacing S_v = 0.2 m. No secondary (i.e., bearing bed) reinforcement layers were included under the bridge seat. The geogrid reinforcements were simulated using linearly elastic–plastic cable elements with tensile stiffness J = 1000 kN/m and yield tensile force T_y = 100 kN/m. The ultimate yield strength of 100 kN/m was selected as the yield tensile force for the geogrid.
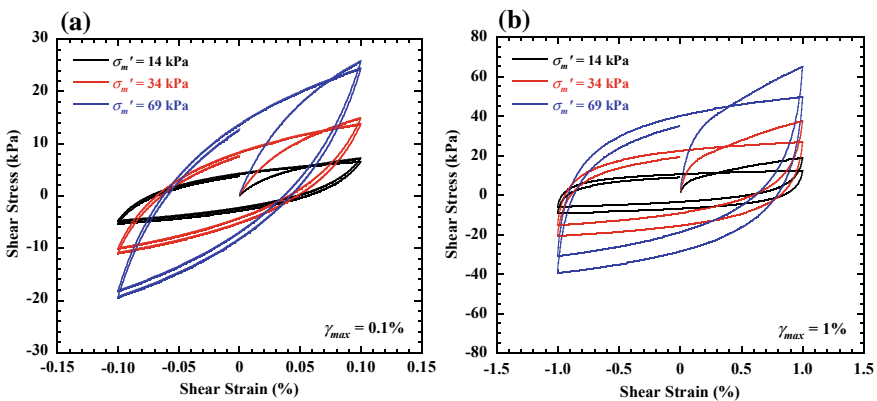
Fig. 2 Simulated shear stress versus shear strain: **a** γ_{max} = 0.1%; **b** γ_{max} = 1%

Structural Components

The concrete facing blocks and bridge seat were modeled as elastic materials with unit weight $\gamma = 23.5$ kN/m^3, elastic modulus $E = 20$ GPa, and Poisson's ratio $v = 0.2$. A longitudinal slice of the bridge beam with unit width was modeled as a solid block composed of elastic elements having an equivalent unit weight $\gamma_{eq} = 13.33$ kN/m^3 to produce an average vertical stress of 200 kPa on the lower GRS wall.

Interfaces

Various interfaces between soil, geogrids, blocks, and structures were simulated using interface elements with Coulomb sliding behavior. The bearing pads between the bridge beam and bridge seats on each end were simulated using interface elements with a friction coefficient of 0.4 [12].

2.3 Modeling Procedures

For static analysis, prior to dynamic loading, the GRS abutments were constructed in stages with the bottom boundary fixed in both horizontal and vertical directions and the lateral boundaries fixed in the horizontal direction. Details of numerical modeling of GRS abutments under static loading are provided by Zheng and Fox [7, 8]. For dynamic analysis, free-field conditions were applied at the lateral boundaries of the model to absorb energy and prevent seismic waves from reflecting back into the problem domain. The earthquake motion was the 1940 Imperial Valley motion (El Centro Station). The acceleration time history is shown in Fig. 3 and yields a peak horizontal acceleration (PHA) of 0.31 g and peak horizontal displacement (PHD) of 130.4 mm with a duration of 40 s. The earthquake motion was applied at the bottom boundary of the model in the longitudinal direction. In addition to the hysteretic
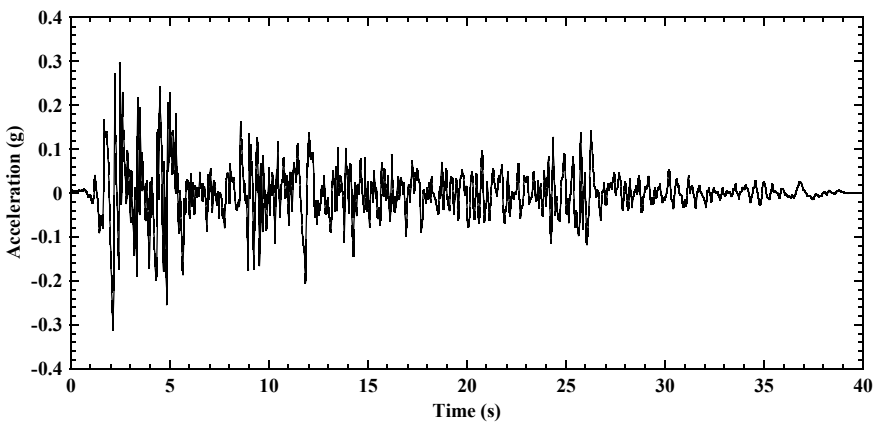
Fig. 3 Acceleration time history for the 1940 Imperial Valley motion (El Centro Station)

stress–strain behavior, a small amount of Rayleigh damping (0.8%) was specified for the soil.

3   Simulation Results

This study focuses on the deformation behavior of a bridge system using two GRS abutments subjected to longitudinal shaking, and the reinforcement tensile strains and forces are not included in the discussion. The seismic performance of GRS abutments is evaluated in terms of incremental facing displacements, abutment vertical compression, and width of the vertical seismic joint (i.e., gap) between the bridge beam and the backwall of bridge seat. The incremental facing displacement is taken relative to the initial facing displacements at the end of construction (i.e., before the start of shaking), with the outward displacements defined as positive. The abutment vertical compression is defined as the difference between the average bridge seat settlement and foundation soil settlement.

3.1   Facing Displacements

Time histories of incremental facing displacement at selected elevations for the left and right abutments are shown in Fig. 4. Each wall experienced larger facing displacements at higher elevations and permanent (i.e., residual) deformations by the end of the shaking. Results show that one facing moved outward when the other facing moved inward, which indicate the two wall facings moved approximately in-phase during shaking. Because the Imperial Valley earthquake motion shown in Fig. 3 is not symmetric, when it is applied longitudinally to the bridge beam, the abutments will experience the opposite motions. The simulated facing displacements for the right abutment are larger than those for the left abutment because the applied motion causes greater accelerations in the direction of the wall face for the right abutment.

Profiles of incremental maximum and residual facing displacements are shown in Fig. 5. The profiles display similar shapes with incremental displacements increasing with elevation and highest values at the top of the walls. The maximum facing displacements for each wall are slightly larger than the residual displacements, which indicates that only a small amount of recovery at the end of shaking. The maximum residual facing displacements were 44.4 mm and 92.2 mm at the top of the wall for the left and right abutments, respectively.
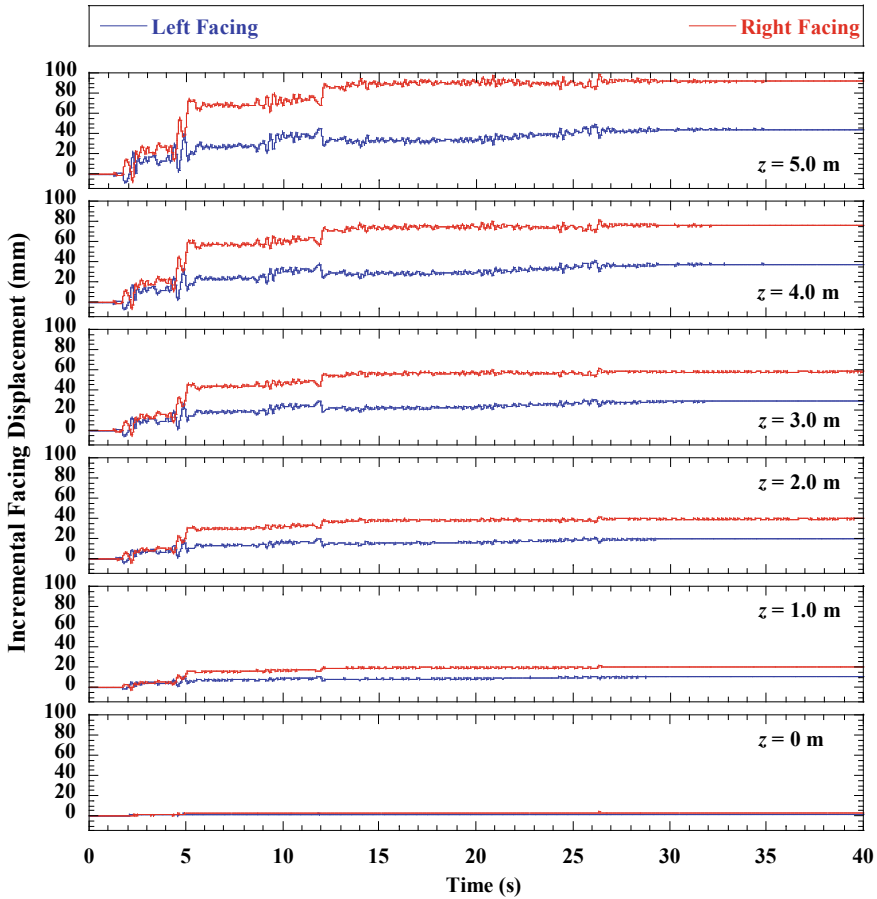
Fig. 4 Time histories of incremental facing displacements

3.2 Abutment Vertical Compressions

Time histories of vertical compression for the left and right abutments are shown in Fig. 6 and indicate similar shapes with respect to both magnitudes and trends. The abutment compressions increased significantly to approximately 4 mm at $t = 2$ s and to approximately 9 mm at $t = 5$ s, and then remained nearly constant thereafter. The residual vertical compressions were 9.2 mm and 9.8 mm for the left and right abutments, respectively, corresponding to vertical strains of 0.18% and 0.20% for the 5-m-high lower GRS walls. These magnitudes of vertical strain are relatively small and would not be expected to cause significant damage to most bridge structures.
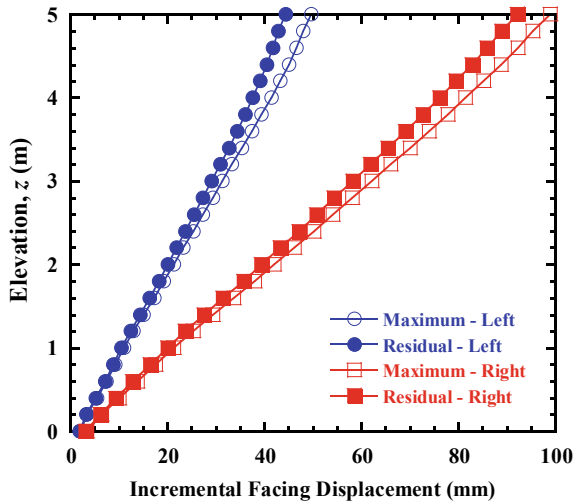
Fig. 5 Profiles of incremental facing displacements
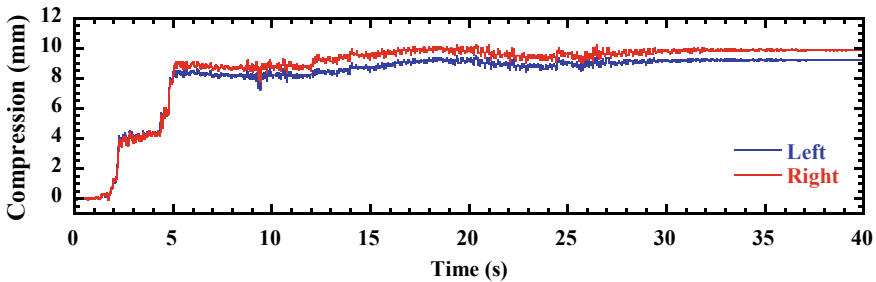
Fig. 6 Time histories of abutment vertical compression

3.3 Seismic Joint Widths

During shaking, the bridge beam interacted with the GRS abutments through friction developed on the bearing pad interfaces, and the bridge beam may potentially contact the backwall of bridge seat when the seismic joint closes. Time histories of seismic joint width on each side of the abutment are shown in Fig. 7. The initial width of the seismic joints was 92.5 mm before the shaking event and then decreased during shaking. Both seismic joints decreased in width because of the inward movement of the bridge abutments (i.e., toward the center of the bridge beam). The residual widths were 9.1 mm and 50.8 mm after shaking on the left and right sides of the bridge beam, respectively, which depended on the inward movement of the abutment and the horizontal displacement of the bridge beam. The inward movement of the abutment was different on either end of the bridge due to the asymmetric earthquake
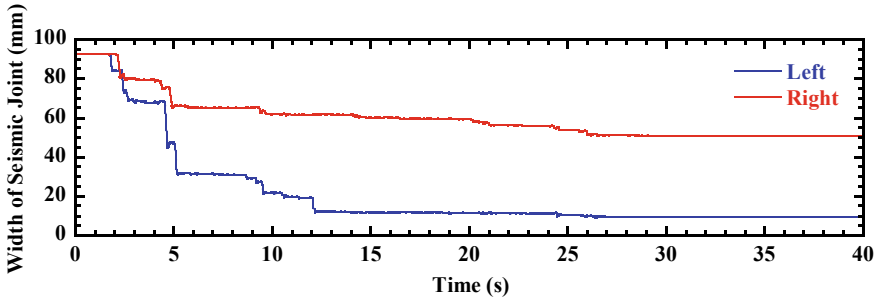
Fig. 7 Time histories of seismic joint width

motion applied in the in the direction longitudinal to the bridge beam. Joint closure did not occur during shaking at either end of the bridge abutment, and thus, no impact force occurred between the bridge beam and the backwall of bridge seat.

4 Conclusions

This paper presents a numerical study on the deformation behavior of geosynthetic reinforced soil (GRS) bridge abutments subjected to longitudinal shaking using the finite difference program FLAC. For the 1940 Imperial Valley motion in the longitudinal direction, simulation results indicate that the two wall facings of the bridge system moved in-phase during shaking, but had different residual facing displacements at the end of shaking due the inward movement of the abutment and the horizontal displacement of the bridge beam. This occurred due to asymmetry of the earthquake motion in the direction longitudinal to the bridge beam. Abutment vertical compressions on the two ends of the bridge beam are similar and relatively small, which would not be expected to cause significant damage to most bridge structures. Vertical seismic joints between the bridge beam and the backwall of bridge seat decreased in width because of the inward movement of the two GRS abutments (i.e., toward the center of the bridge beam), but did not close for this earthquake motion.

References

1. Yen W-HP, Chen G, Buckle I, Allen T, Alzamora D, Ger J, Arias JG (2011) Post-earthquake reconnaissance report on transportation infrastructure: impact of the February 27, 2010, offshore Maule Earthquake in Chile. FHWA-HRT-11-030, U.S. DOT, Washington, D.C.
2. Helwany SMB, Wu JTH, Meinholz P (2012) Seismic design of geosynthetic-reinforced soil bridge abutments with modular block facing. NCHRP Web-Only Document 187, Transportation Research Board, Washington, D.C.

3. Zheng Y, Sander AC, Rong W, Fox PJ, Shing PB, McCartney JS (2018) Shaking table test of a half-scale geosynthetic-reinforced soil bridge abutment. Geotech Test J 41(1):171–192

4. Zheng Y, McCartney JS, Shing PB, Fox PJ (2019) Physical model tests of half-scale geosynthetic reinforced soil bridge abutments. II: Dynamic loading. J Geotech Geoenviron Eng 145(11)

5. Stein WJ, Neuman TR (2007) Mitigation strategies for design exceptions. FHWA-SA-07-011, U.S. DOT, Washington, D.C.

6. Duncan JM, Byrne P, Wong KS, Mabry P (1980) Strength, stress-strain and bulk modulus parameters for finite element analysis of stresses and movements in soil masses. Report No. UCB/GT/80-01, University of California, Berkeley, CA, USA

7. Zheng Y, Fox PJ (2016) Numerical investigation of geosynthetic-reinforced soil bridge abutments under static loading. J Geotech Geoenviron Eng 142(5):04016004

8. Zheng Y, Fox PJ (2017) Numerical investigation of the geosynthetic reinforced soil-integrated bridge system under static loading. J Geotech Geoenviron Eng 143(6):04017008

9. Naesgaard E (2011) A hybrid effective stress—total stress procedure for analyzing soil embankments subjected to potential liquefaction and flow. Ph.D. thesis, The University of British Columbia

10. Menq F (2003) Dynamic properties of sandy and gravelly soils. PhD thesis, University of Texas, Austin

11. Darendeli IS (2001) Development of a new family of normalized modulus reduction and material damping curves. PhD thesis, University of Texas, Austin

12. Caltrans (2004) Section 5—Retaining walls. Bridge design specifications, August 2004

Coupled Analysis on Frost-Heaving Depression Effect of Geosynthetics Drainage Material for Road Pavement

Tomohisa Yasuoka, Tatsuya Ishikawa, Bin Luo, Yuwei Wu, Kimio Maruyama, and Chigusa Ueno

Abstract The frost heave of subgrade soil causes cracking and unevenness of pavement structure in cold region, which leads to uncomfortable driving and high maintenance cost. As one of the measures against frost heave damage, it has been considered to mitigate frost heave by draining water from the subgrade soil in road structure since soil moisture plays a critical role in ground heaving. The wicking fabric, a new type of geosynthetics drainage material, has been recently developed to drain water out of pavement and reduce the water content. Previous studies indicated that the wicking fabric has great promise as n effective means to solve the frost-heave-related problems on road systems. The purpose of this study is to verify the effectiveness of the wicking fabric for frost-heaving mitigation under local weather and soil conditions in Hokkaido by conducting the coupled thermo-hydro-mechanical (THM) analysis. The result of analysis indicates that wicking fabric has an excellent ability to drain water in road structure and that wicking fabric is an effective approach to mitigate frost heave.

Keywords Frost heave · Pavement structure · Coupled analysis

1 Introduction

In Hokkaido, a cold and snowy island in northern Japan, frost heaving of subgrade soil causes cracking and unevenness of pavement structure, which leads to extremely unsafe driving conditions and high maintenance cost. Water content reduction is an effective method to mitigate frost heave since it is well known that soil moisture plays a critical role in frost heaving. However, conventional geotextiles that have been used as drainage materials are not very effective in water absorption even though they are

T. Yasuoka · T. Ishikawa (✉) · B. Luo · Y. Wu
Hokkaido University, Sapporo 060-8628, Japan
e-mail: t-ishika@eng.hokudai.ac.jp

K. Maruyama · C. Ueno
Civil Engineering Research Institute for Cold Region, Sapporo 062-8602, Japan
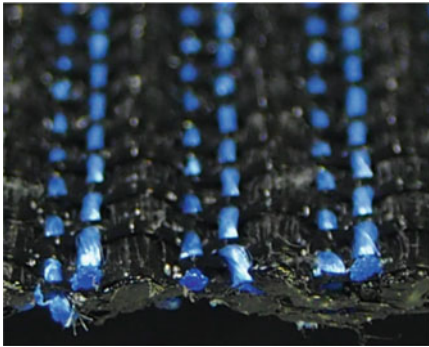
(a) Cross-section of wicking fabric   (b) Cross section of wicking fiber
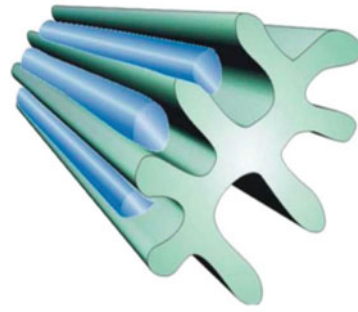
Fig. 1 Structures of wicking fabric (adapted from Lin et al. [4])

excellent in water permeability. Since frost-susceptible soils such as silt have high suction in the unsaturated state, conventional drainage materials are not effective in reducing water content and suppressing frost heaving. The wicking fabric, an advanced geotextile with wicking fibers, which has the capability to laterally drain the water in a roadway under unsaturated conditions, has been recently developed. As shown in Fig. 1a, the wicking fabric is composed of polyethylene yarns (black) for reinforcing purposes and specially designed hydrophilic and hygroscopic nylon fiber yarns (blue) for drainage purposes. These special hydrophilic and hygroscopic fibers give high wicking ability to geotextile. Figure 1b shows a cross section of each fiber, which has deep grooves and provides a larger surface area to hold and transfer larger amounts of water even in unsaturated conditions. Previous studies indicated that the wicking fabric has great promise to solve the frost-heave-related problems on road systems in the cold region, Alaska and Montana [1, 2]. However, the frost-heaving suppression effect of the wicking fabric has not been sufficiently discussed using quantitative data, such as frost-heaving displacement. Therefore, this study examines the effectiveness of the wicking fabric on frost-heaving mitigation under local weather and soil conditions in Hokkaido using numerical simulations, before conducting field research. In addition, before simulating models under local weather and soil conditions in Hokkaido, the simulations under the condition in Montana, where the effectiveness of the wicking fabric on frost-heaving mitigation was observed, are performed. Since the analysis on pavement subjected to freezing is a complex boundary value problem, which is related to moisture, heat and stress field, a numerical technique like the coupled thermo-hydro-mechanical (THM) analysis is required [3]. THM analysis, which can predict the freeze–thaw behavior of unsaturated soil, is conducted to reproduce the freezing behavior of pavement structure both with the wicking fabric and without wicking fabric to seek optimum buried depth for the wicking fabric under various conditions.

2 Governing Equations

The main formulation of coupled THM FE analysis in this study considers the interaction among water flow inside soils, heat conduction through soils and deformation of soil skeleton, as shown in Eqs. (1), (2) and (3). Also, to reproduce frost heave phenomenon of soils under saturated and unsaturated conditions, the strain of frost heave (ε_f) and strain of thaw contraction (ε_t) are considered in the constitutive model of the coupled THM FE analysis, as shown in Eqs. (4) and (5). Further details of the THM model can be found in Luo et al. [3].

Mass conservation of soil pore-water is given as:

$$\frac{\partial}{\partial x_i}\left[-k_{ij}\frac{\partial}{\partial x_j}\left(\frac{u_w}{\rho_w g}+z\right)\right] = \left(\frac{nS_e}{K_w}-n\frac{\partial S_e}{\partial u_w}\right)\frac{\partial u_w}{\partial t}+nS_e\alpha_T\frac{\partial T}{\partial t}-S_e\frac{\partial \varepsilon_v}{\partial t} \quad (1)$$

where x_i are Cartesian coordinates; k_{ij} is hydraulic conductivity of soil; u_w is pore-water pressure; ρ_w is mass density of water; g is gravitational acceleration; z is elevation head; n is porosity; S_e is the effective degree of saturation; K_w is bulk modulus of pore water; t is time; α_T is the thermal expansion coefficient of water; T is temperature; and ε_v is volumetric strain.

The heat transfer is expressed as:

$$C\rho\frac{\partial T}{\partial t} = -\frac{\partial}{\partial x_i}\left(\lambda_T\frac{\partial T}{\partial x_j}\right)+C_w\rho_w\frac{\partial (v_i T)}{\partial x_i} \quad (2)$$

where C is specific heat of wet soil at a constant volume; ρ is mass density of wet soil; λ_T is thermal conductivity of wet soil; C_w is specific heat of pore water at a constant volume; and v_i is average velocity of pore water in coordinate direction.

According to Bishop's effective stress theory, and considering the other two strain components caused by thermal expansion and frost expansion, volumetric strain is obtained as:

$$\frac{\partial \varepsilon_v}{\partial t} = \frac{1}{K_d}\frac{\partial \sigma_m}{\partial t}-\frac{S_e}{K_d}\frac{\partial u}{\partial t}+\beta_T\frac{\partial T}{\partial t}+\frac{\partial \varepsilon_f}{\partial t} \quad (3)$$

where σ_m is mean total stress; K_d is bulk modulus of drained soil; β_T is thermal expansion coefficient of soil; and ε is the strain of frost expansion.

From the results of the frost heave test, the strain of frost heave (ε_f) and strain of thaw contraction (ε_t) can be given as:

$$\varepsilon_f = \kappa\left(\frac{\varepsilon_{f\,max}S_{e0}}{\varsigma\sigma_n'+1}\Delta qbt/Q_1+1.09m_w\right) \quad (4)$$

$$\varepsilon_t = \omega\varepsilon_f \times \Delta q'bt/Q_1 = (c+d\ln\sigma_n)\varepsilon_f \times \Delta q'bt/Q_1 \quad (5)$$

where $\varepsilon_{f\,max}$ is maximum frost expansion strain of saturated soil without overburden pressure; S_{e0} is initial effective degree of saturation; σ'_n is effective stress at the direction of heat flow; Δq is the influx of heat added to an infinitesimal soil element per unit time; b is the ratio of latent heat to total outflow heat; Q_l is heat per unit volume of soil consumed for solidification of water; m_w is the ratio of water absorbed into an infinitesimal soil; κ and ς are constants; ω is the coefficient of thaw contraction; σ_n is total stress at the direction of heat flow; $\Delta q'$ is quantity of inflow heat in unit time; c and d are constants.

3 Numerical Simulations

3.1 Numerical Model

Figure 2 shows the transverse section of a simulated pavement structure as well as the boundary condition and finite element (FE) mesh. A pavement structure with wicking fabric was modeled which consists of surface layer, base course and subgrade. The pavement structure was based on in situ model test in past research as reference [2]. As for the placing conditions of wicking fabric, the three models for different buried depth from the top side of the subgrade (WWF model) and the models without wicking fabric (NWF model) were considered (Table 1). In addition, the conditions which only installing wicking fabric in initial and rainfall analysis (RWF model) were considered in order to examine the effect of suppressing frost heave by decreasing the water supply to the ice lenses during the freezing.

Fig. 2 Pavement structure profile and finite element mesh
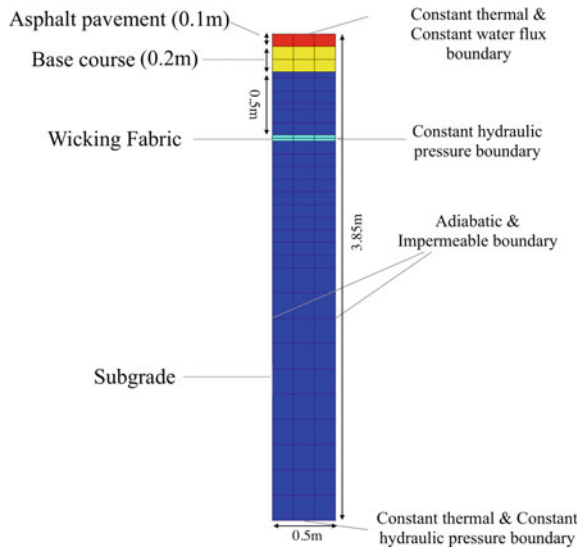
Table 1 Analytical conditions

Model	Buried depth for wicking fabric	Groundwater level
WWF	0.0/0.25/0.50 m	1.0/1.5/2.0 m
RWF	0.0/0.25/0.50 m	1.0/1.5/2.0 m
NWF	–	1.0/1.5/2.0 m

Boundary conditions of FE analysis were set as follows. As for the mechanical boundary condition, the base surface boundaries of the model were fixed in the vertical direction, and both lateral side boundaries were fixed in the horizontal direction. As for the hydraulic boundary condition, the impermeable boundary was imposed on both lateral sides, while the constant water flux boundary was set to the top surface of model. The constant hydraulic pressure boundary was employed at the base surface to achieve constant groundwater level. Three conditions were considered for the depth to groundwater level from top side of the subgrade (Table 1). In addition, the constant hydraulic pressure boundary was also set at the right side of the wicking fabric since the water seepage is in one direction in the wicking fabric. The constant hydraulic pressure was set with reference to literature as $s = 150$ kPa which can achieve the suction distribution similar to the actual measurement results [4]. In this analysis, the pore-water pressure was defined as negative; thus, the suction was considered to be positive. As for the thermal boundary condition, the adiabatic boundary was imposed on the both lateral sides, and the constant thermal boundary was imposed on the base surface and top surface.

3.2 Materials Properties

Table 2 summarizes the input parameters of FE simulation performed in this study. Parameters of wicking fabric are referenced from previous research [4]. For Montana conditions, the Montana silt was chosen as subgrade soil. The parameters of Montana soil, such as permeability of saturated soil (k_s), dry density (ρ_d) and specific heat of dry soil (C_d), were based on the past research [5]. For Hokkaido conditions, a representative fine-grained volcanic soil (Touryo soil) was chosen as subgrade soil. The input parameters of Touryo soil in this study were based on data from frost heave test and some common values used in previous research [6]. Since the other parameters for Montana silt were not available from the past research, the data of Touryo soil were used to as substitutes. The parameters of asphalt pavements and base courses were set with reference to some common values used in previous research [3].

Table 2 Input parameters of materials

Parameters	Unit	Wicking fabric	Subgrade		Base course	Asphalt
			Montana	Hokkaido		
Deformation modulus (E_0)	MPa	493	100	40	200	10,000
Final freezing temperature (T_f)	°C	−0.2	−0.2	−0.2	−0.2	−0.2
Poisson's ratio (υ)		0.001	0.33	0.33	0.35	0.35
Permeability of saturated soil (k_s)	m/h	2.232	4E−04	3.6E−05	2.3E−04	3.6E−06
Thermal conductivity (λ_T)	J/mhK	20,156	4320	4320	17,320	3600
Specific heat of dry soil (C_d)	J/m^{3}K	6.9E+01	1.2E+06	9.8E+05	2.8E+06	1.8E+06
Thermal expansion coefficient (α)	1/K	3.2E−06	1.2E−06	1.2E−06	1.2E−06	3E−05
Dry density of soil (ρ_d)	kg/m^3	9.8	1730	1400	2280	2200
Thaw contraction strain of soil (ε_{ft})		0	0.052	0.056	0	0
Porosity (n)		0.2126	0.361	0.45	0.154	0.03
Constant (α)	MPa^{-1}	129.7	102.5	102.5	846.6	0
Constant (λ)		2.5746	1.44	1.44	1.360	0

3.3 Simulation Procedure

A FE simulation for the pavement model was performed as follows.

1. Initial stability analysis: An initial distribution of moisture content and temperature inside FE model was calculated under a given groundwater level and a prescribed thermal boundary. The temperatures of all elements in the Montana model and the Hokkaido model were set at 8 and 9 °C, which are the in situ mean annual temperatures, respectively. The groundwater level from top side of the subgrade was set at the constant (1.0, 1.5, 2.0 m). The gravity force of 9.80 m/s^2 was applied to estimate the stress state of all elements.

2. Rainfall analysis: Considering the daily average precipitation in Montana and Hokkaido, rainfall intensity of 0.16 mm/h ($t = 24$ h) and 0.32 mm/h ($t = 24$ h) was given to the upper sides in the Montana model and Hokkaido model, respectively.

3. Freeze process analysis: The FE model was frozen under a prescribed thermal boundary condition from the ground surface while keeping the temperature of base surface at 8.0 °C in the Montana model and 9.0 °C in the Hokkaido model

as the temperatures of the constant-earth temperature layer. The temperature of ground surface in the Montana model and Hokkaido model was respectively set at −4 °C and 5 °C which are the in situ air mean-temperature during freezing period. The freeze process analysis was respectively performed for 2400 h in Montana model and 2600 h in Hokkaido model by referring to mean air temperature during winter season and freezing index observed measured at the testing point.

4. Thaw process analysis: The model was thawed under a prescribed thermal boundary condition from the ground surface. The temperature of ground surface in the Montana model and Hokkaido model was respectively set at 8.0 °C and 9.0 °C which is the in situ mean annual temperature. The thaw process analysis was performed for 2500 h in order to completely thaw all elements.

Note that the temperature and rainfall intensity were determined with reference to the field measurements with the AMeDAS or NOAA Online Weather Data in order to reproduce the in situ temperature and rainfall intensity in Hokkaido and Montana, respectively.

4 Results and Discussion

4.1 Water Content Change in the Pavement

Figure 3 illustrates the distribution of the degree of saturation after initial stability analysis under different models. The WWF model has less water content than the NWF model. Also, it shows that the water content of the soil above the drainage material is reduced. In other words, the water content of the soil after initial stability analysis is effectively reduced by installing wicking fabric in a deeper position of
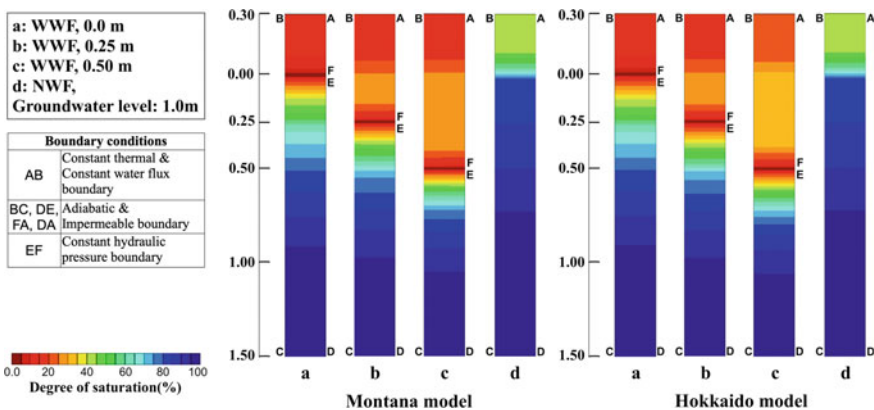
Fig. 3 Distribution of the degree of saturation after initial stability analysis
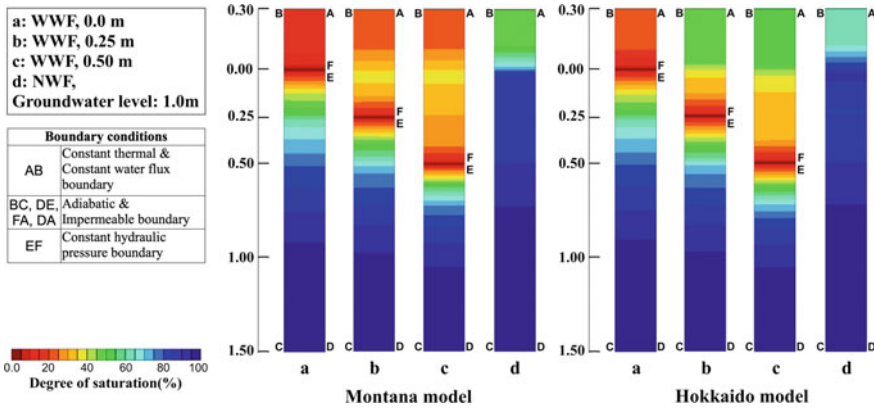
Fig. 4 Distribution of the degree of saturation after rainfall analysis

pavement. Figure 4 shows that the influence of rainfall is small in the model installing wicking fabric in the shallow position of pavement under different models. This result indicates that most waters did not penetrate the soil below the wicking fabric. Comparing the Hokkaido model with the Montana model (Fig. 4), it is also observed that the progress of drainage is slow since the hydraulic conductivity of the subgrade in the Hokkaido model is lower than the Montana model.

Figures 5 and 6 show the distribution of the degree of saturation after initial stability analysis and rainfall analysis under different groundwater level conditions, respectively. Below the wicking fabric, there is a difference in the distribution of the degree of saturation by the groundwater level condition. The deeper groundwater level, the less water content the model has. However, the distribution of the
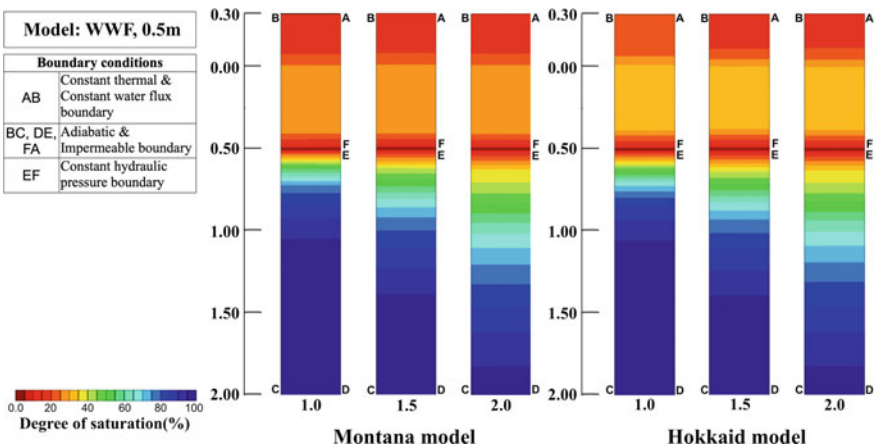
Fig. 5 Distribution of the degree of saturation after initial stability analysis under different groundwater level conditions
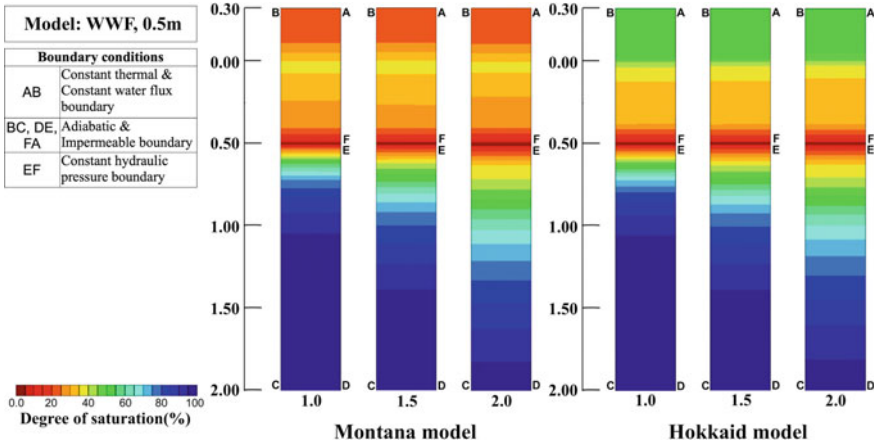
Fig. 6 Distribution of the degree of saturation after rainfall analysis under different groundwater level conditions

degree of saturation above the wicking fabric is the almost same. This is because the wicking fabric has the same suction in all models regardless of the groundwater level and suppresses the water supply to the soil above it by draining water from the groundwater.

4.2 Influence of Wicking Fabric on Frost Heave

Figure 7 shows the frost-heaving displacement and water supply to the soil above the wicking fabric under different models. The WWF model has a lower frost-heaving displacement than the NWF model and the RWF model. Also, the water supply to
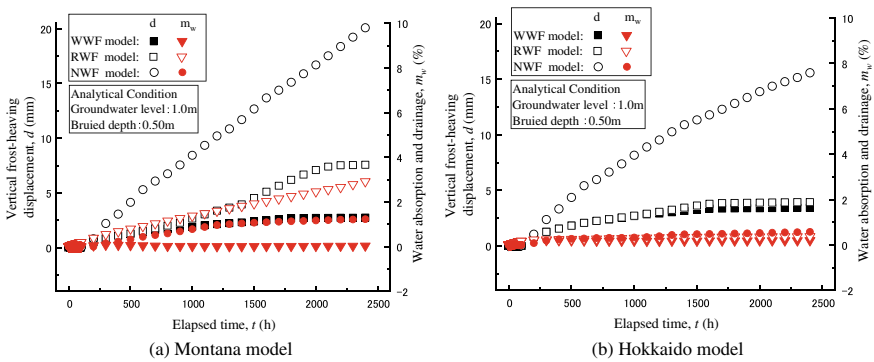
Fig. 7 Chang in frost heave and water supply to subgrade material above the wicking fabric
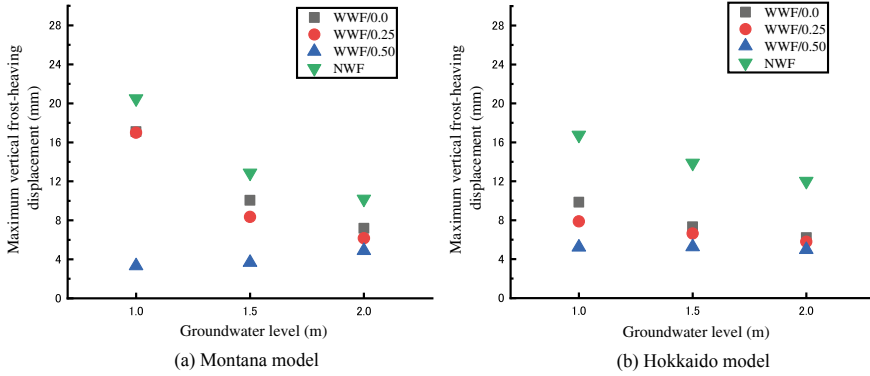
Fig. 8 Maximum vertical frost-heaving displacement under different buried depths for wicking fabric

the subgrade above the wicking fabric of the WWF model is more reduced than the NWF model and the RWF model. Figure 8 shows the maximum vertical frost-heaving displacement under different buried depths for wicking fabric during freezing analysis. The frost heave of the NWF model is larger than the other WWF models under the same groundwater level condition. This is because the all WWF model has less water content than the NWF model (Fig. 4). From Fig. 4, it is observed that the model installing wicking fabric in a deep position has less water content. As the results, when the buried depth for wicking fabric is deep in the WWF model, the frost heave is mitigated effectively. Also, the model under the deep groundwater level conditions has less water content below the wicking fabric (Fig. 6). Thus, the frost heave is reduced in the model under the deep groundwater level conditions. However, in the WWF/0.50 model, the frost heave is increased under the deep groundwater level conditions. This result is considered to be related to the increase of the frost penetration depth (Table 3). The frost heave in the WWF/0.50 model is greatly affected by whether or not the frost penetration depth penetrates the soil below the wicking fabric which has high water content. Thus, under the deep groundwater level conditions in the WWF/0.50 model, it can be considered that the frost penetration depth penetrates the soil with high water content below the wicking fabric and thereby

Table 3 Frost penetration depth

Buried depth for wicking fabric	Groundwater level					
	1.0 m	1.5 m	2.0 m	1.0 m	1.5 m	2.0 m
	Montana			Hokkaido		
WWF, 0.0 m	0.79 m	0.81 m	0.84 m	0.83 m	0.87 m	0.92 m
WWF, 0.25 m	0.81 m	0.85 m	0.90 m	0.91 m	0.93 m	0.94 m
WWF, 0.50 m	0.91 m	0.93 m	0.94 m	1.01 m	1.02 m	1.02 m
NWF	0.70 m	0.78 m	0.79 m	0.79 m	0.80 m	0.81 m
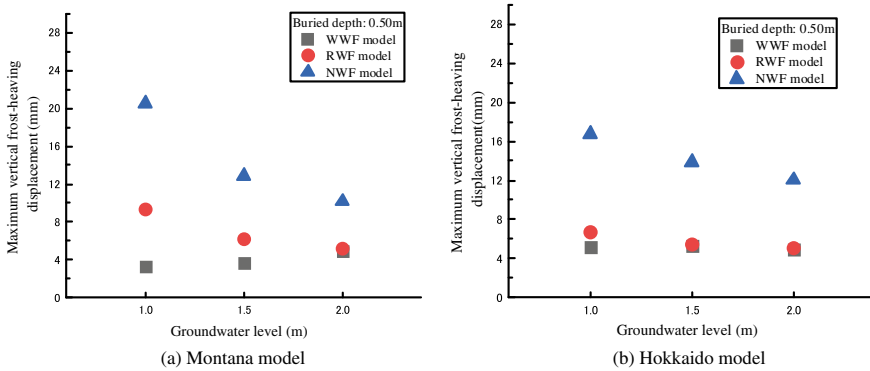
Fig. 9 Comparison of maximum vertical frost-heaving displacement for RWF model with the other models

frost heave is increased. In addition, the WWF model has a larger frost penetration depth than the NWF model. These results are considered to be related to the reduction of the latent heat in the freezing, which is caused by reducing the water content. These results also indicate that the decrease in frost heave of the WWF model is not due to the decrease in frost penetration depth.

Figure 9 compares the maximum vertical frost-heaving displacement for the RWF model with the other models. Under different groundwater level conditions, the RWF model has a smaller maximum vertical frost-heaving displacement than the NWF model. This result is considered to be related to the difference in the water content of the subgrade soil at the start of freezing. In addition, even if the water contents of the RWF model and WWF model are almost the same at the start of freezing, there is a difference in the maximum frost-heaving displacement, especially in the Montana model. From Fig. 7, the water supply to the subgrade above the wicking fabric is reduced and the frost heave is also mitigated in the WWF model. It can be observed more clearly in the Montana model, where the subgrade has a large hydraulic conductivity. This result indicates that water supply to the ice lenses above the wicking fabric is reduced by the capillary barrier during the freezing process in the WWF model. Comparing Figs. 7 and 9, it can be considered that the water supply to the subgrade above the wicking fabric affected maximum frost-heaving displacement of the model to some extent. In other words, it can be recognized that suppressing the water supply to the ice lens in the WWF model during the freezing process by the wicking fabric influences the reduction of frost heave.

5   Conclusion

This study examined the effectiveness of the wicking fabric on frost-heaving mitigation by conducting the coupled thermo-hydro-mechanical (THM) analysis. The following conclusions can be drawn from this study:

1.   Water content of the model was reduced by installing wicking fabric in the pavement. Since the wicking fabric effectively drains water from the soil above it, the water content was effectively reduced by installing it in the deep. It was also observed that moisture does not penetrate across the wicking fabric.
2.   Wicking fabric performed effectively to mitigate frost heave in both Montana model and Hokkaido model. Wicking fabric has two effects on suppressing frost heave. One is reducing the water content of the subgrade. The other is decreasing the water supply to the ice lenses during the freezing process. Decreasing the water supply to the ice lenses can be observed more clearly in the model, where the subgrade has a large hydraulic conductivity.

These findings need further validation based on future studies. Specifically, it is necessary to verify numerical results by comparing them with the results of laboratory tests and field research in Hokkaido. In addition, the model of this study, which is the simplified pavement structure in the transverse direction, may not be representative of a field condition because the soils at different transverse distances will have different drainage rates. Therefore, it is necessary to verify whether the characteristics of the wicking fabric found from the numerical results in this study can be also obtained from a model similar to the field conditions.

References

1.   Zhang X, Presler W, Li L, Jones D, Odgers B (2014) Use of wicking fabric to help prevent frost boils in Alaskan pavements. J Mater Civ Eng 26(4):728–740
2.   Zornberg JG, Azevedo M, Sikkema M, Odgers B (2017) Geosynthetics with enhanced lateral drainage capabilities in roadway systems. Transp Geotech 12:85–100
3.   Luo B, Ishikawa T, Tokoro T (2017) Coupled thermo-hydro-mechanical analysis of freeze–thaw behavior of pavement structure over a box culvert. Transp Res Rec J Transp Res Board 2656:12–22
4.   Lin C, Zhang X, Han J (2019) Comprehensive material characterizations of pavement structure installed with wicking fabric. J Mater Civ Eng 31(2):04018372
5.   Lay RD (2005) Development of a frost heave test apparatus. All theses and dissertations. 654, BYU Scholars Archive Citation
6.   Ishikawa T, Kijiya I, Tokoro T (2015) Evaluation of frost heave-thaw behavior of pavement with coupled thermo-hydro-mechanical analysis. J Jpn Soc Civ Eng Ser E1 (Pavement Eng) 71(3):I_185–I_192 (in Japanese)

Tension Behavior of Bituminous Mixture Samples Reinforced by Fiberglass Geogrids in Different Directions

Reuber Freire, Hervé Di Benedetto, Cédric Sauzéat, Simon Pouget, and Didier Lesueur

Abstract This work aims at presenting a new analysis methodology for interface mechanical characterization based on axial tension test, as well as verifying the effect of the fiberglass geogrid presence on interface behavior. Tests were performed on cylindrical samples vertically cored from slabs having horizontal interfaces. In addition, this investigation aims at verifying the geogrid contribution in the tension resistance of cylindrical samples horizontally cored also having horizontal interfaces. Two different bilayered asphalt slabs were prepared to conduct the investigation: one reinforced and one unreinforced. Both are composed of the same bituminous mixture, compacted in two layers glued by emulsion tack coat made with 160/220 pen grade bitumen. Afitexinov produced the coated geocomposites used in the study, based on a knitted fiberglass geogrid of 100 kN/m tensile strength in both directions, associated with a polyester veil. The characterization was conducted through tension test at a controlled axial strain rate (2% per minute) and at two temperatures (19 and 40 °C). Two tests were performed for each temperature and each type of sample (vertically and horizontally cored) resulting in sixteen test results. The proposed methodology is successfully able to characterize the interface behavior subjected to axial tension loading. The differences in the observed results are related to the variation of the interface thickness with and without fiberglass geogrids. Concerning the horizontally cored samples, a slight increase in the tension resistance was observed for the reinforced samples at 40 °C. This difference could be associated with the fiberglass geogrid contribution.

R. Freire (✉) · H. Di Benedetto · C. Sauzéat
Laboratory of Tribology and System Dynamics (LTDS) (UMR CNRS 5513), University of Lyon/ENTPE, 3 Rue Maurice Audin, 69518 Vaulx-en-Velin, France
e-mail: reuber.freire@entpe.fr

S. Pouget
Research & Innovation Department, EIFFAGE Infrastructures, 8 Rue du Dauphiné, 69964 Corbas, France

D. Lesueur
Afitexinov, 56 Route de Ferrossière, 38110 Saint-Didier-de-la-Tour, France

IMT Lille Douai, Institut Mines-Télécom, University of Lille, Lille, France

521

1 Introduction

The roadway reinforcement by geogrids has increased in the last decades in order to improve their serviceability by avoiding typical distresses occurring in these structures, such as cracking and rutting. In the flexible pavement structures, geogrids can be added in the unbound (granular) layers and/or in the bound layers (bituminous bases, surface and overlays) for reinforcement. They could be used for both rehabilitation and construction of new bituminous pavements [1, 2]. According to some authors, fiberglass geogrids are preferable for presenting high-tension resistance and flexibility at once [3]. It is also thermally and chemically stable at the mixing temperatures of bituminous mixtures [4] and easily removable by milling in the case of further pavement maintenances. Many works also indicated that fiberglass geogrids present a better performance to cracking resistance when compared to other types of geogrids [5–8].

Most studies in the literature related to geogrid reinforcement agreed with its benefits to limit reflective cracking development [6, 7, 9, 10]. The further step in the investigation of geogrid reinforcement benefits is the identification of other reinforcement mechanisms that can improve pavement performances. Some authors have been working on the pavement structural capacity increasing due to the reinforcement, specially the control of permanent vertical strain in pavement layers [11–14].

The presented work was performed within the framework of a collaboration between the companies Afitexinov, Eiffage and LTDS Laboratory from University of Lyon/ENTPE. This paper introduces a new analysis methodology for interface mechanical characterization using axial tension test. The investigation aims at verifying the effect of the fiberglass geogrid presence on interface mechanical behavior and especially the geogrid contribution to the tension resistance of reinforced specimens.

2 Specimen Preparation

A bituminous mixture, called *Béton Bitumineux Semi-Grenu* (BBSG) 0/10 according to the classification in French standards [15], was used to conduct the experimental campaign. It is a semi-coarse asphalt mixture designed for wearing course and composed of up to 10 mm size aggregates. The BBSG 0/10 gradation curve is presented in Fig. 1a. It is composed of mineral aggregates with rhyodactic and rhyolitic nature, limestone filler and 20% of recycled asphalt pavement (RAP) containing 4.75% of bituminous binder. These aggregates were mixed with 4.40% of 35/50 penetration grade bituminous binder [16]. The total bituminous binder content in the mixture was 5.53%.
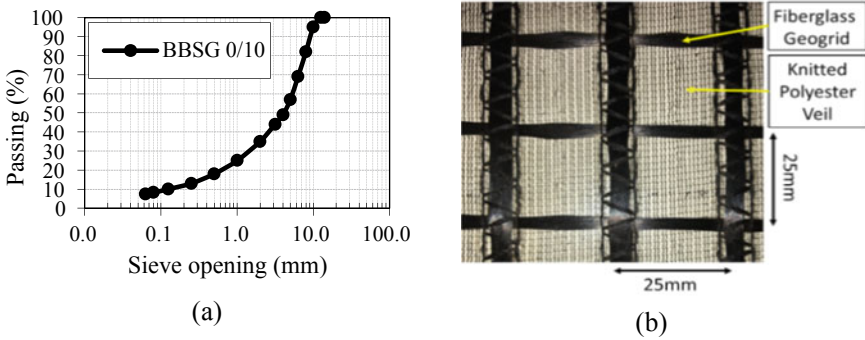
Fig. 1 Components of tested specimens: **a** bituminous mixture gradation curve and **b** fiberglass geogrid Notex Glass®

The geogrid used to reinforce the bituminous mixtures is Notex Glass®, presented in Fig. 1b, produced and provided by the French company Afitexinov. This geogrid is composed by coated fiberglass yarns and polyester knitted veil, both coated with bituminous emulsion. The grid has a square mesh opening of 25 mm and a maximum tensile strength of 100 kN in both directions.

Slabs of 600 × 400 × 150 mm were fabricated at the French company Eiffage Infrastructures using a French wheel compactor [17]. Slabs were composed of two layers having approximately the same thickness. In unreinforced slab (so-called B), the interface is only constituted of tack coat. For reinforced slab (so-called C), interface includes tack coat and geogrid. Emulsion made with 160/220 pen grade bitumen was used as tack coat for both unreinforced and reinforced slabs. For the unreinforced one, an amount of 290 g/m^2 of residual binder was used, while for the reinforced one, an amount of 800 g/m^2 was used, divided in two applications, one on each geogrid surface. The reinforced slab fabrication is conducted by first compacting half height slab (75 mm). Then, the first tack coat application is done (400 g/m^2), followed by the geogrid placement, then the second tack coat application is done (400 g/m^2) in the geogrid surface, and finally the second half height (75 mm) slab is compacted.

From each slab fabricated, cylindrical samples with 75 mm in diameter and 140 mm in height were cored. The coring was conducted in two directions, and the specimens were named H (horizontally cored) and V (vertically cored) depending on the direction they were cored. Figure 2 illustrates the specimen position within the slab and the interface position in each type. Detailed information of interface, air void content calculated in the bituminous mixture, testing temperature and testing strain rate are presented in Table 1.
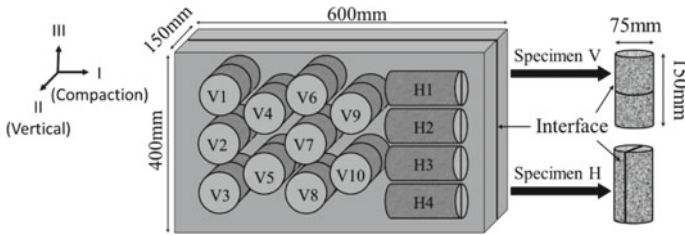
Fig. 2 Slab coring plan and interface (with or without geogrid) position illustration for specimens V and H

Table 1 Specimens' information concerning interface, emulsion, air voids, test temperature and strain rate for tension tests

Specimen	Interface		Emulsion: residual bitumen (g/m^2)	Air voids (mix) (%)	Temperature (°C)	Strain rate (%/min)
	Direction	Composition				
B-H1	Horizontal	Emulsion	290	6.1	19	2
B-H2	Horizontal	Emulsion	290	7.5	19	2
B-H3	Horizontal	Emulsion	290	7.0	40	2
B-H4	Horizontal	Emulsion	290	6.6	40	2
C-H1	Horizontal	Geogrid and emulsion	2 × 400	7.3	19	2
C-H2	Horizontal	Geogrid and emulsion	2 × 400	8.5	19	2
C-H3	Horizontal	Geogrid and emulsion	2 × 400	7.8	40	2
C-H4	Horizontal	Geogrid and emulsion	2 × 400	8.1	40	2
B-V1	Vertical	Emulsion	290	7.0	19	2
B-V2	Vertical	Emulsion	290	6.5	19	2
B-V3	Vertical	Emulsion	290	7.3	40	2
B-V4	Vertical	Emulsion	290	6.9	40	2
C-V1	Vertical	Geogrid and emulsion	2 × 400	7.1	19	2
C-V2	Vertical	Geogrid and emulsion	2 × 400	7.4	19	2
C-V3	Vertical	Geogrid and emulsion	2 × 400	8.3	40	2
C-V4	Vertical	Geogrid and emulsion	2 × 400	8.4	40	2

3 Experimental Device and Analysis Methodologies

Axial tension tests are performed with a servo-hydraulic press. This press has a maximum loading capacity of ± 25 kN. A thermal chamber is used for temperature control during the tests. The setup is the one which is classically used in experimental studies at LTDS/ENTPE laboratory [18–20]. However, the instrumentation is different and improved compared to mentioned works, to allow the interface characterization [21]. The axial strain measurements are performed by two couples of extensometers, both fixed in the middle height of the tested specimen. The first couple of extensometers has a 25 mm length (l_1), and they are disposed at 180° from one another. The other couple has a 90 mm length (l_2), and extensometers are disposed at 180° from one another (see Fig. 3a). The loading strain amplitude is controlled during the test from the average of the two smaller extensometers. The temperature is measured by a thermal gauge (PT100 temperature probe) fixed on the specimen surface. Figure 3a presents the instrumentation of specimen types H and V, and Fig. 3b presents the scheme of interface analysis performed for specimen V only.

Equations 1 and 2 can be written considering notation given in Fig. 3b. In this figure, the interface composed of tack coat only (for unreinforced slab B) or the interface composed of tack coat and geogrid (for reinforced slab C) is considered as an equivalent layer having a thickness (t). The strain values measured by each couple of extensometers could be expressed as in Eqs. (1) and (2):

$$\varepsilon_{m1} \cdot l_1 = \varepsilon_A \cdot (l_1 - t) + \varepsilon_G \cdot t \tag{1}$$

$$\varepsilon_{m2} \cdot l_2 = \varepsilon_A \cdot (l_2 - t) + \varepsilon_G \cdot t \tag{2}$$
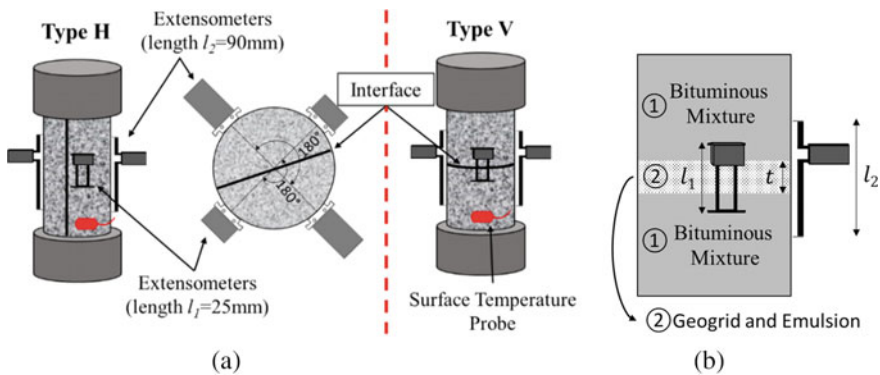
Fig. 3 Instrumental setup: **a** extensometers and temperature probe location, for specimen types H and V, and **b** scheme used for test analysis based on continuum mechanics for specimen type V (Eqs. 1 and 2)

where ε_{m1} and ε_{m2} are the measured strains (respectively, from couple 1 and 2 of extensometers), and l_1 and l_2 are the lengths of smaller (25 mm) and longer (90 mm) extensometers, respectively. (ε_A) is the axial strain of the mixture and (ε_G) the axial strain of the interface layer. From these equations, ε_A can be obtained as shown in Eq. 3 and it can be used to calculate as shown in Eq. 4. This strain ε_G depends on the interface thickness (t).

$$\varepsilon_A = \frac{\varepsilon_{m1} \cdot l_1 - \varepsilon_{m2} \cdot l_2}{l_1 - l_2} \tag{3}$$

$$\varepsilon_G(t) = \frac{\varepsilon_{m1} \cdot l_1 - \varepsilon_A \cdot (l_1 - t)}{t} \tag{4}$$

However, the interface strain can only be calculated by assuming an interface thickness value, which is another variable for the analysis. Considering that this interface thickness could not be easily and accurately determined, and in order to remove its influence, the interface has been assimilated to a surface. The parameter to be considered is not the strain in a layer but becomes the displacement gap (Δu) observed at the interface. The interface displacement gap (Δu) is calculated from Eq. 4 when considering t infinitively small (Eq. 5).

$$\Delta u = \varepsilon_{m1} \cdot l_1 - \varepsilon_A \cdot l_1 \tag{5}$$

The tests are performed at two temperatures: 19 and 40 °C. The loading path is divided into three steps: (i) initial tension loading until 0.1% strain with a constant strain rate of 2%/min; (ii) 10 s of relaxation (at 0.1% strain); and (iii) tension loading with a constant strain rate of 2%/min until specimen's failure. Figure 4a presents results obtained from sample B-V1, as an example. This figure shows the stress versus the strain obtained from the two extensometers and the strain values calculated for the bituminous mixture only. Figure 4b presents the stress as a function of the
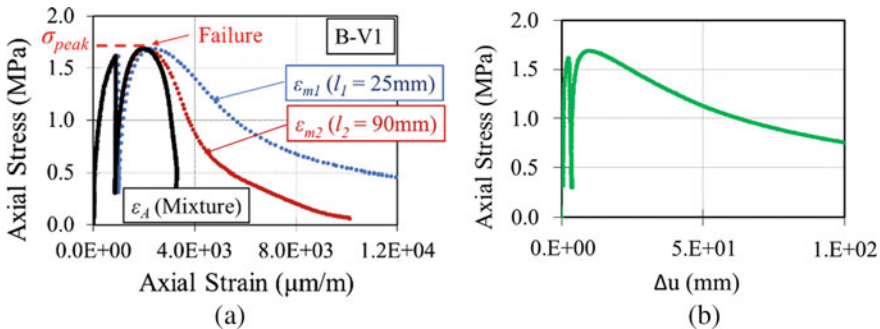
Fig. 4 Example of results obtained for specimen B-V1: **a** axial stress versus ε_{m1} (obtained from 25 mm extensometers), ε_{m2} (obtained from 90 mm extensometers) and calculated bituminous mixture strain (ε_A) (cf. Eq. 3), and **b** axial stress versus interface displacement gap (Δu) (cf. Eq. 5)

interface gap (Δu) calculated from Eq. 5. This last curve presents the interface behavior response to the tensile loading. Moreover, it can be used to compare all interfaces' behavior without depending on the thickness variable t.

The failure is determined for the maximum value of stress (σ_{peak}). From Fig. 4a, it can be observed that the bituminous mixture strain stops its progression after failure. This indicates that the failure is localized at the interface for this specimen of type V. This type of failure was obtained for all specimens of type V.

4 Results and Analysis

4.1 Interface Displacement Gap—Axial Stress Curves for Specimen Type V

Figure 5a presents the comparison between interface gaps for unreinforced specimens (slab B) and reinforced specimens (slab C) at 40 °C. The test repeatability appears to be quite good, since the curves for the two specimens in the same configuration were sufficiently close to each other. Same conclusion can be drawn from Fig. 5b, which presents the same comparison but at 19 °C. For repetition tests, it should be noticed that tested specimens were cored at two different positions in the slab. Thus, it is not possible to assure that the interfaces present exactly the same amount of emulsion and/or geogrid, and even surface, since the slab interface is not completely flat.

For both temperatures, 40 and 19 °C, a greater stress level is necessary for the unreinforced interface (B) than for the reinforced one (C) to obtain the same displacement gap. At 40 °C, approximately three times more stress was necessary before the specimen reaches failure, while at 19 °C, approximately 60% more stress was
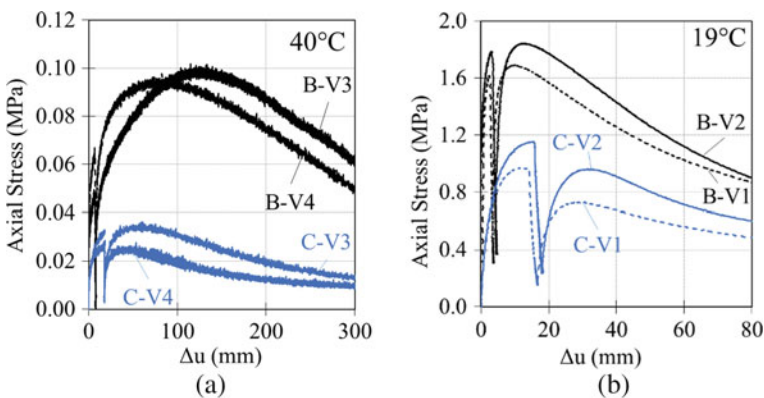
Fig. 5 Interface gap (Δu) versus axial stress measured during the tests for specimen V: **a** 40 °C and **b** 19 °C

necessary. However, the interface strength should be influenced by its real thickness. The reinforced specimens' interface presents 2.76 times more emulsion, besides the geogrid presence, compared to the unreinforced one. Thus, the reinforced speci- mens' interface is at least three times thicker, which could explain its lower strength resistance.

4.2 Specimen Type H

For specimen type H, the strain considered is the average of the four measure- ments obtained from the extensometers. In addition, the line from geogrid perfor- mance, representing its elastic behavior, according to its strength characterization performed by Afitexinov, is plotted with the results. This line represents the expected test response if the geogrid would have taken all the efforts alone (test of geogrid without mixture). For the results at 40 °C (Fig. 6a), the reinforced specimens (C) presented higher resistance when compared to the unreinforced ones (B), especially in the beginning of the test. This effect can be attributed to the geogrid presence. However, those curves are positioned below the geogrid characterization curve. This indicates that, at 40 °C, the geogrid is not entirely mobilized during the test. A possible reason could be a slipping effect occurring within the interface during the loading. Regarding Fig. 6b, which presents the results at 19 °C, similar results were obtained for reinforced and unreinforced specimens.
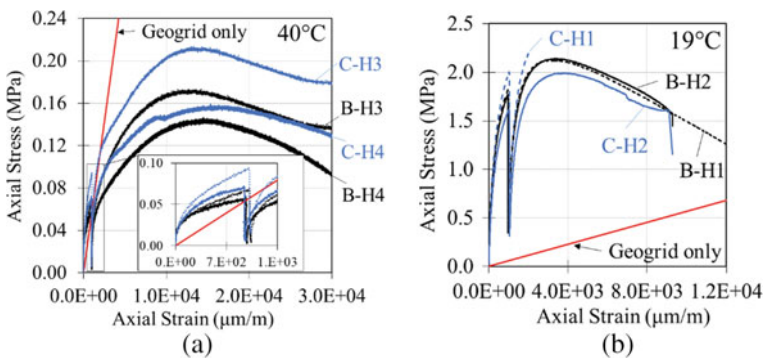
Fig. 6 Axial strain versus axial stress measured during the tests for specimen H plotted with the geogrid characterization curve: **a** 40 °C and **b** 19 °C
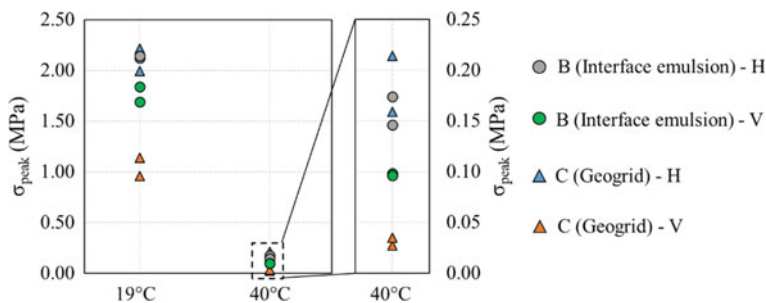
Fig. 7 Stress at failure (σ_{peak}) of all specimens for the two tested temperatures

4.3 Verification of Geogrid Influence in the Specimen Strength Resistance

Figure 7 presents the specimens' maximum stress (σ_{peak}) obtained through the tests for each tested sample. For the same temperature, specimen type H presented higher σ_{peak} than those obtained for specimen type V. Vertically cored specimens present a horizontal interface, which concentrates all the effort during loading and always causes failure in this region. Considering the average of the two samples tested in the same condition, for C (reinforced), type H, at 19 °C, σ_{peak} was approximately 11.3 times higher than those at 40 °C. Concerning the same specimens but type V, this ratio increases to 33.8. For B (unreinforced), type H, the ratio between 19 and 40 °C is 13.2, which is close to the value obtained for C type H. Finally, for B, type V, the ratio between 19 and 40 °C is 18.2. Therefore, a higher variation was obtained comparing temperatures and coring direction results, concerning the reinforced specimen. It is due to its greater heterogeneity, when compared to the unreinforced one.

5 Conclusions

From the presented test results, the following conclusions can be drawn.

- A new analysis methodology was successfully performed to measure interface mechanical behavior subjected to tensile loading of type V reinforced specimens.
- Unreinforced interfaces present higher strength resistances. It can probably be explained by the different thicknesses of the interface. As a matter of fact, the quantity of residual bitumen used to bond the two layers is higher when using geogrid.
- Good repeatability is observed for same specimens in the type V configuration, despite the adversities in sample's interface reproduction.
- In type H results, a slight increase in the tension resistance is observed for the reinforced samples at 40 °C which can be attributed to geogrid reinforcement.

References

1. Geosynthetic Material Association (2002) Handbook of geosynthetics, USA
2. Cost Action 348 (2006) Reinforcement of pavements with steel meshes and geosynthetics (REIPAS). Final report of a European Concerted Research Action Designated as COST Action 348
3. Nguyen ML, Blanca J, Kerzréhoa, JP, Hornych P (2013) Review of glass fibre grid use for pavement reinforcement and APT experiments at IFSTTAR. Road Mater Pavement 14(1):287–308. https://doi.org/10.1080/14680629.2013.774763
4. Darling JR, Woolstencroft JH (2004) Fibreglass pavement reinforcements used in dissimilar climatic zones for retarding reflective cracking in asphalt overlays. In: Proceedings of the 5th international RILEM conference on cracking in pavements, pp 435–442
5. Lytton RL (1988) Reinforcing fiberglass grids for asphalt overlays. Texas Transportation Institute Report for Bay Mills Limited, Texas A&M University, College Station, Texas
6. De Bondt AH (1999) Anti-reflective cracking design of reinforced asphaltic overlays. PhD thesis, Delft University of Technology, The Netherland
7. Brown SF, Thom NH, Sanders PJ (2001) A study of grid reinforced asphalt to combat reflective cracking. J Assoc Asphalt Paving Technol 70:543–571
8. Canestrari F, Belogi L, Ferrotti G, Graziani A (2013) Shear and flexural characterization of grid-reinforced asphalt pavements and relation with field distress evolution. Mater Struct 48(4):959–975. https://doi.org/10.1617/s11527-013-0207-1
9. Gonzalez-Torre I, Calzada-Perez MA, Vega-Zamanillo A, Castro-Fresno D (2015) Evaluation of reflective cracking in pavements using a new procedure that combine loads with different frequencies. Constr Build Mater 75:368–374. https://doi.org/10.1016/j.conbuildmat.2014.11.030
10. Nejad FM, Asadi S, Fallah S, Vadood M (2016) Statistical-experimental study of geosynthetics performance on reflection cracking phenomenon. Geotext Geomembr 44(2):178–187. https://doi.org/10.1016/j.geotexmem.2015.09.002
11. Laurinavicius A, Oginskas R (2006) Experimental research on the development of rutting in asphalt concrete pavements reinforced with geosynthetic materials. J Civ Eng Manag 12(4):311–317
12. Graziani A, Pasquini E, Ferrotti G, Virgili A, Canestrari F (2014) Structural response of grid-reinforced bituminous pavements. Mater Struct 18
13. Guler E, Atalay I (2016) The effects of geosynthetics on mitigation of rutting in flexible pavements. 6th Eurasphalt & Eurobitume congress, Berlin. https://doi.org/10.14311/EE.2016.101
14. Correia NS, Zornberg JG (2018) Strain distribution along geogrid-reinforced asphalt overlays under traffic loading. Geotext Geomembr 46:111–120. https://doi.org/10.1016/j.geotexmem.2017.10.002
15. Association Française de Normalisation (AFNOR) (2007) Spécifications des matériaux Partie 1: Enrobés bitumineux (in French), NF EN 13108-1, Paris
16. Association Française de Normalisation (AFNOR) (2018) Bitumes et liants bitumineux - Détermination de la pénétrabilité à l'aiguille (in French), NF EN 1426, Paris
17. Association Française de Normalisation (AFNOR) (2007) Mélange bitumineux - Méthodes d'essai pour mélange hydrocarboné à chaud - Partie 33: confection d'éprouvettes au compacteur de plaque (in French), NF EN 12697-33+A1, Paris
18. Gayte P, Di Benedetto H, Sauzeat C (2016) Visco-plastic behavior of bituminous mixtures: experiments and modeling. In: RILEM Bookseries, vol 13. Nantes, France, pp 47–52
19. Phan CV, Di Benedetto H, Sauzéat C, Lesueur D, Pouget S, Olard F, Dupriet S (2017) Complex modulus and fatigue resistance of bituminous mixtures containing hydrated lime. Constr Build Mater 139:24–33. https://doi.org/10.1016/j.conbuildmat.2017.02.042
20. Pedraza A, Di Benedetto H, Sauzéat C, Pouget S (2019) 3D Linear viscoelastic behaviour of bituminous mixtures containing high content of multi-recycled RAP. Road Mater Pavement Design 20(7):1709–1721. https://doi.org/10.1080/14680629.2019.1594054

21. Freire RA, Di Benedetto H, Sauzéat C, Pouget S, Lesueur D (2018) Linear viscoelastic behaviour of geogrids interface within bituminous mixtures. KSCE J Civ Eng 22(6):2082–2088. https://doi.org/10.1007/s12205-018-1696-9

Application of Wicking Geotextile for Pavement Infrastructure on Expansive Soil

Nripojyoti Biswas , **Md. Ashrafuzzaman Khan** , **Aritra Banerjee** , **Anand J. Puppala** , **and Sayantan Chakraborty**

Abstract Problematic soils cover a majority of North Texas, which are primarily characterized by high plasticity and expansive nature. Moisture intrusion plays a pivotal role in determining the long-term performance of such soils when subjected to repetitive axle loading. Highways constructed on such subgrade often fail to perform satisfactorily due to rutting, cracking, and differential movements during the seasonal moisture variation. Calcium-based stabilizers are traditionally used by existing practitioners to treat such problematic subgrade. However, treatment with calcium-based stabilizers fails to perform suitably over the pavement life due to durability and leaching problems. Besides, treatment with calcium-based stabilizers involves significant construction delay and has a detrimental impact on the environment. As an alternative to these shortcomings, a newly available geotextile with a wicking ability has been used to construct a test section in North Texas. The geotextile layer, installed at the interface of the base and subgrade layers, performs a two-fold function. Besides the primary function of providing separation and reinforcement to the subgrade, the wicking ability of this geotextile helps moisture redistribution within the pavement layers. The performance of the pavement section was closely monitored using several sensors. Initial observations suggest that the geotextile can suitably redistribute the moisture within the subgrade. The pavement section showed

N. Biswas · Md. A. Khan · A. J. Puppala (✉)
Texas A&M University, College Station, TX, USA
e-mail: anandp@tamu.edu

N. Biswas
e-mail: nripojyoti.biswas@tamu.edu

Md. A. Khan
e-mail: mak2019@tamu.edu

A. Banerjee
University of Delaware, Newark, DE, USA
e-mail: aritra@udel.edu

S. Chakraborty
Birla Institute of Technology and Science, Pilani, Rajasthan, India
e-mail: sayantan.chakraborty@pilani.bits-pilani.ac.in

an improved resilience to deformation from traffic load as compared to the control section.

1 Introduction and Background

Flexible pavements constructed on problematic soil suffer from different failures such as cracking, rutting, and depression. The reasons for such failure may be attributed to fatigue, temperature changes, moisture ingress, and softening caused by surface layer cracking [1–4]. Previous research studies have indicated that millions of dollars are spent annually for the maintenance and rehabilitation of such afflicted roads [5]. The performance of such pavement subgrades under normal conditions has been satisfactory to bear the repetitive axle load. However, most of the pavements in problematic soil show reduced strength, stiffness, and load-bearing capacity when subjected to moisture intrusion during and after rainfall events [6]. Several chemical treatment methods, such as cement and lime stabilizations, have been traditionally used for the treatment of such problematic soils [7–10]. However, chemical treatments have failed to maintain the durability over a long period when subjected to moisture intrusion and leaching of stabilizers [4, 7]. Some studies indicated that, if the subgrade soil has a soluble sulfate content of more than 3000 ppm, the available sulfates react with the calcium-based stabilizers to form a disruptive tri-sulfate hydrate product-Ettringite [8, 11]. The use of geotextile as a mechanical supporting layer to the existing subgrade may help the Departments of Transportation (DoTs) to eliminate the problems associated with the chemical-based stabilizers.

Geosynthetics have often found applications in different geotechnical systems such as dams, resistive barriers, coastal protection systems, foundation design, and pavement infrastructure, because of their versatility, ease of installation, cost-effectiveness, and ample mechanical and hydraulic properties [12–21]. Different types of woven and nonwoven geo synthetics have been used to reinforce and enhance the drainage in pavement infrastructures [22]. The use of conventional geotextile has been found to be effective in draining the moisture when the soil subgrade is in saturated condition [23]. However, pavements sections on the expansive subgrade undergo differential heaving, owing to seasonal moisture fluctuations and a variable degree of saturation [3]. Iryo and Rowe [23] showed that geotextiles have a steep hydraulic conductivity function that can cause a high hydraulic conductivity in saturated conditions that can drop to nearly impermeable conditions for a small increase in suction. Therefore, the use of conventional geotextiles for drainage under such variable suction conditions might not be sufficient to remove the subsurface moisture.

A new type of nylon wicking geotextile, developed by a geosynthetic manufacturer, combines various functions such as reinforcement, separation, and drainage through capillary action in a single geotextile layer [24]. This wicking geotextile is

made up of special hydrophilic and hygroscopic 4DG (DG-Deep Groove) fibers with a multichannel cross section (diameter ≈ 5.7–47.8 μ) [25]. The wicking geotextile possesses a high shape factor and a correspondingly higher number of channels per unit area. The presence of a high number of channels facilitates the development of capillary action in the wicking geotextile that helps in moisture migration under unsaturated conditions [22].

Azevedo and Zornberg [26] studied the influence of wicking geotextile on unsaturated properties of soil in a small-scale laboratory model. Laboratory studies were also performed to understand the maximum rate of removal of moisture from a saturated soil using the wicking fabrics [27]. Wang et al. [22] developed a laboratory-based physical model to understand the effectiveness of the wicking geotextile on pavement infrastructure. They concluded that wicking fibers could wick out moisture even when the water content was close to the optimum point. Furthermore, the wicking fibers helped to rapidly reduce the moisture content of the soil after rainfall to initial moisture percent. Zhang et al. [13] studied the influence of wicking geotextile on the field performance of pavements in Alaska. This was the first major field study undertaken to reduce the effect of freeze-thaw on pavement performance using wicking geotextiles.

In the context of the previous discussion, it is evident that to date, no major field implementation studies on the utilization of the wicking geotextile has been undertaken. Notably, no documented literature exists on field studies using the wicking geotextile on the expansive subgrade. Therefore, the primary objective of this paper is to study the benefits of the application of wicking geotextile for pavement infrastructure on an expansive subgrade. The document outlines the construction sequences involved for the implementation of the geotextile in the pavement layers. Furthermore, a detailed instrumentation plan has also been discussed. The performance of the pavement sections has been monitored for a certain period, and the initial results indicate that the inclusion of the wicking geotextile has a potential to improve the pavement performance.

2   Project Description

A 130 ft (40 m) long pavement section was constructed on a two-lane road in Venus, Texas. The locally available soil in this North Texas region is historically characterized as highly expansive in nature. The eastbound lane was used as a Test Section (TS) and reinforced with the wicking geotextile, whereas, the westbound lane was used as a Control Section (CS). This road section was of particular importance because a major rehabilitation activity was undertaken by the Texas Department of Transportation (TxDOT) in the Fall of 2017. However, the pavement section started showing rutting, cracking, and differential heaving within six months after the maintenance was completed. The subgrade of farm to market roads is generally constructed with locally available materials, in this case, the expansive soil. The differential heaving due to moisture migration, during and after a rainfall event, maybe attributed as the

principal reason for the occurrence of such failure in the early stages of its service life. The primary hypothesis for implementation of the wicking geotextile on such a road section was that, in addition to the reinforcement and separation action, the presence of wicking fibers would help in moisture redistribution through capillary action within the pavement layers. The moisture redistribution capacity of the wicking fibers would prevent differential heaving of the subgrade soil and subsequently increase the serviceability of the pavement.

3 Design, Construction and Instrumentation

3.1 Design of Test Section

The design of the test section was performed as per TxDOT design guidelines. TxDOT pavement design software FPS21, which is based on the AASHTO 1993 pavement design module, was used to predict the serviceability life of the newly constructed pavement. The traffic and standard design data for input were selected as per information provided by TxDOT design manuals for farm to market roads [28]. The subgrade soil properties corresponding to ASTM [29] standards and AASHTO guidelines are listed in Table 1. The resilient modulus was determined based on the repeated load triaxial test (AASHTO T-307-99) on the subgrade soil. The stresses on the subgrade was expected to be moderate from traffic loads, however for conservative design the resilient modulus value corresponding to the last loading sequence ($\sigma_3 = 13.8$ kPa and $\sigma_d = 68.9$ kPa) was adopted. Based on the design data, the pavement section was determined to be consisting of existing subgrade soil, followed by a layer of wicking geosynthetic, base course, and surface layer. The thickness of the base course was determined to be 15 in. (38 cm), followed by a 2 in. (5 cm) asphalt overlay. The base layer was constructed using flex-base material supplied by a local supplier conforming to Grade 1 (Type A) of the TxDOT material standard (Item #247). The control section consisted of a similar section design, except that it was not reinforced with a geotextile.

Table 1 Basic soil characterization test results

Property	Unit	Reference/Standard	Value
Liquid limit		ASTM D4318	58
Plasticity index		ASTM D4318	31
Optimum moisture content (OMC)	%	ASTM D698	23.5
Maximum dry unit weight (MDUW)	pcf (kN/m^3)	ASTM D698	89.9 (14.2)
Swell potential	%	ASTM D4546	8.5
Resilient modulus	ksi (MPa)	AASHTO T-307	9.0 (62.1)

3.2 Construction and Instrumentation

The construction started in early December of 2018 and was completed within a week. The construction of the sections was performed in the sequence, as discussed below. First, a trench of 17 in. (44 cm) depth in the CS (westbound lane) was made to install a 2 in. PVC pipe, which would be later used to accommodate the deflection sensor in it (Fig. 1). After the PVC pipe was laid, the trench was backfilled with 15 in. (38 cm) flexible base material and overlaid with a 2 in. (5 cm) asphalt layer. After the control section was completed, the construction of the test section was undertaken. The eastbound lane was excavated to the depth of 17 in. (44 cm) from the surface of the existing pavement using a cold planar machine. This enabled the exposure of the subgrade layer, from which soil samples were collected for laboratory studies. After the subgrade layer was properly leveled, a medium-duty pneumatic roller was used to
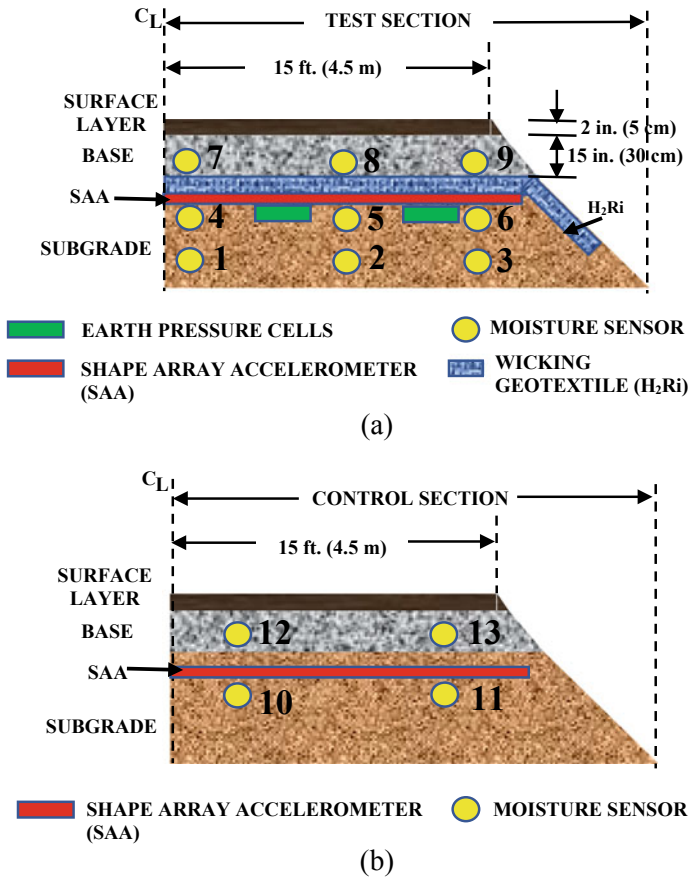
Fig. 1 Section details and instrumentation (not to scale)

compact the subgrade soil to reach the target MDUW and OMC. The sand-cone test was performed at regular intervals to ensure that the subgrade layer was adequately compacted.

After the subgrade soil was properly compacted, boreholes were made with hand-augers to insert the moisture sensors at different depths. A total of nine moisture sensors (1–9) were installed in the TS inside three boreholes at a depth of 12 in. (30 cm) (1, 2, and 3) and 6 in. (15 cm) (4, 5, and 6) below the geotextile and at 6 in. (15 cm) above the geotextile layer (7, 8, and 9). Similarly, a set of four moisture sensors (10–13) was installed in the CS at a depth of 6 in. (15 cm) below the geotextile and at 6 in. (15 cm) in the base layer above the geotextile (Fig. 1b). The boreholes were backfilled with soil, and proper care was taken to ensure that the wires from the sensors were protected adequately during construction. At the level of the subgrade, two earth pressure cells were installed at the distance of 2.5 ft. (0.75 m) and 8 ft. (2.45 m) from the center of the lane. Furthermore, a 2 in. PVC pipe was placed and connected to the pipe from the control section on top of the subgrade. The shape array accelerometers (SAAs) were inserted in the PVC pipes to measure the vertical movement in the subgrade layer due to the cumulative effect of moisture intrusion and axle loads. The SAA sensor consists of a micro-electro-mechanical system (MEMS) accelerometers for measuring the deflection. The wires from all the sensors were connected to the dataloggers, and the station was set up in the vicinity of the road.

The wicking capability of the fabric is highly directional; hence, proper care was taken, while installing the geotextile on top of the subgrade soil such that the wicking fabrics are always in a transverse direction to the pavement section. After the geotextile layer was laid over the subgrade, the base course was backfilled and compacted with the flex-base material to a height of 15 in. (38 cm) from the top of the subgrade.

The base course was compacted for another seven days when they were opened for regular traffic. Thereafter, a surface coating was performed using asphalt coats, and finally, an asphalt layer [15] was used to finish the surface course. The road became serviceable from the next day of the construction. The detailed representation of the construction sequence is shown in Fig. 2.

4 Analysis and Discussion

The pavement section was installed with different sensors, such as moisture sensors, deflection sensors, and pressure cells. The monitoring was performed on a bi-weekly basis, and the initial data was extracted, and pavement performance was analyzed for this initial period. Here, "initial" refers to the first year monitored data. Although the performance of pavement needs to be monitored over a longer period of time, before developing any design methodology, this analysis would help to envisage the initial response of the pavement.

Fig. 2 Construction sequence of flexible pavement using wicking geotextile: **a** milling, **b** excavation, **c** leveling, **d** compaction, **e** laying of the wicking geotextile (H$_2$Ri), **f** laying of base course, **g** asphalt overlay, and **h** final pavement section

4.1 Deflection Analysis

The SAA-MEMS was used to record the deflection of the subgrade layer in both the test section and the control section. Figure 3 shows the plot of the deflection data recorded by the SAA at four points along the pavement cross-section. The deflection

Fig. 3 Deflection of subgrade in test and control section
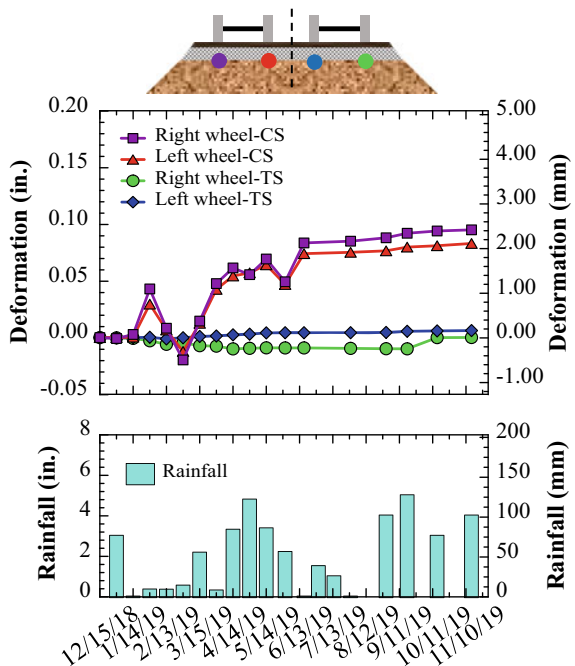
points selected below the wheel path provide a comprehensive understanding of the subgrade deflection due to the cumulative effect of axle load and subgrade movement due to moisture migration. The subgrade soil below the CS (red and purple dot) showed noticeable movements during the first few months after the construction phase. This movement may be attributed to the initial plastic deformation due to stresses acting on the subgrade. In the following months, there was a reduction of the subgrade fluctuations in the control section. However, the cumulative deformation of the points below the wheel path is much higher as compared to the reinforced section. The wicking geotextile has a wide width tensile strength of 5280 lb/ft (7.15 kN/m) (as per the manufacturer). Reinforcing the weak soil subgrade with the geotextile provides additional strength and stiffness to it through the process of stress distribution via membrane effect below the wheel path. Furthermore, the geotextile also provides additional strength to the subgrade by providing confinement to the soil layer. Therefore, from figure, it can be observed that the deflection of the points (green and blue dots) in the TS are almost negligible for the observation period.

The figure also shows the plot of measured rainfall in the region as obtained from a local rainfall recording station located at Venus, Texas. After a significant rainfall period (April–June 2019), the soil subgrade below the control section undergoes high swelling and permanent deformation due to moisture intrusion. However, the reinforced section shows no significant deformation during the same period. The presence of the wicking fiber might have been helpful in moisture redistribution to the pavement edges and within the pavement subgrade.

As the moisture is wicked out of the pavement subgrade, there is no loss of strength of the subgrade soils. Consequently, as there is a reduction in moisture content in the soil, there is minimal loss of strength and bearing capacity of the subgrade. Therefore, analyzing the deflection data shows that the inclusion of geotextile indeed improves pavement performance. Some additional observations using the moisture sensors are made to validate the utility of the geotextile in subgrade improvement.

4.2 Subgrade Moisture Analysis

The performance of the pavement may be affected due to seasonal fluctuations of the subgrade moisture. The presence of these wicking fibers might have been instrumental in the redistribution of the moisture within the pavement layers. Figure 4 shows the volumetric moisture variation (θ_V) within the pavement section for the period of August–September 2019. Furthermore, the rainfall data is also plotted in a tandem to provide a comprehensive analysis of the moisture migration inside the pavement layers.

After a typical rainfall event (late August), it could be observed that for the test section, there is an increase in moisture content within the soil subgrade (Sensor-6) and the base layer (Sensor-9) at the edge of the pavement. This could be due to moisture intrusion from the cracks between the pavement edges and the adjacent soil. However, over a period of a few days, there is a gradual reduction in the moisture

Fig. 4 Volumetric moisture variation within the pavement layers
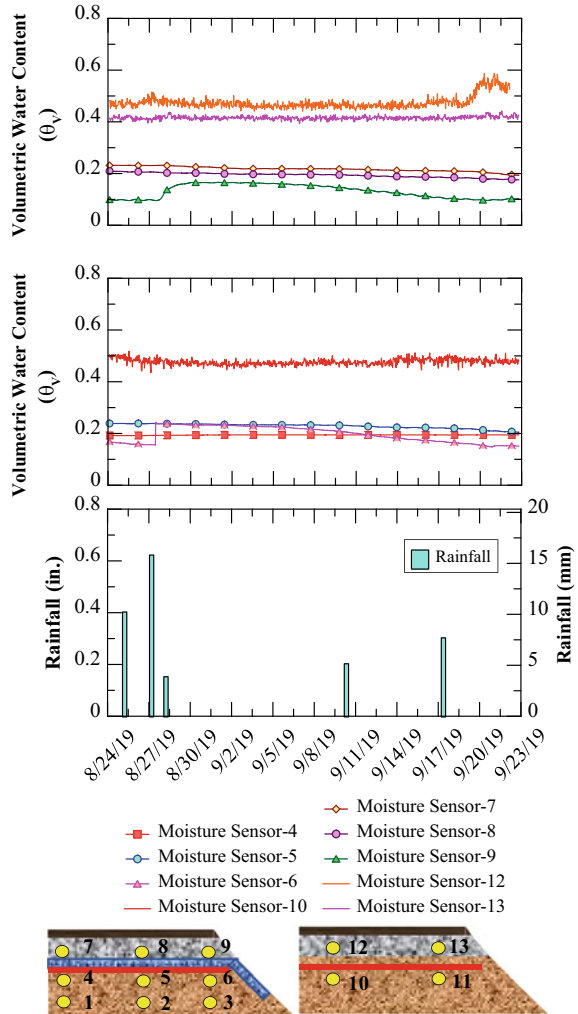
content until the soil moisture reduced to the initial state (before rainfall). As for the CS, the moisture content is observed to be noticeably high as compared to the test sections. The readings from moisture sensor-11 were discarded due to malfunctioning of the sensor. However, due to the absence of any wicking fiber, there is minimum moisture reduction in the subgrade at the control section edges.

The moisture sensors toward the center of the pavement sections in the subgrade (Sensors-4 and 5) and in the base layer (Sensor-7 and 8) shows minimum fluctuations in moisture content even after a period of rainfall. This could be attributed to the newly constructed pavement surface course. Since no cracks or fissures are present, no direct moisture migration from surface layers takes place.

However, it could be easily comprehended that the moisture content of the test section (Sensors 4, 5, and 6) is consistently low throughout the entire period as compared to the control section (Sensor-10). Because of the low moisture content, there is a negligible reduction in strength and stiffness of the soil subgrade in the reinforced section. As a result, the deformation of the reinforced section is also substantially reduced.

The installation of wicking geotextile was observed to improve the pavement performance by proving two-fold benefits, primarily through reinforcement of the subgrade layer, and followed by the enhancement of lateral drainage capacity through the capillary action of the wicking fibers.

5   Conclusions

The use of wicking geotextile has been found to be effective in moisture redistribution by several researchers for different laboratory-scale studies. However, very few studies on the field implementation and corresponding validations of the laboratory data have been documented. The present field study on expansive clay of North Texas and initial monitoring of the pavement performance provided us with valuable information regarding the effectiveness of the wicking fabrics. The initial observations from the monitoring of the test section could be summarized as follows.

1. The deflection data obtained from the SAA-MEMS indicated that there is a minimum movement in the test section due to the moisture fluctuations in the subgrade soil.
2. The moisture data recorded from the moisture sensors indicated that the moisture fluctuations are more prominent at the edges as compared to the center. Furthermore, the volumetric moisture content near the wicking geotextile in the pavement subgrade is less as compared to the control section. This indicates that the wicking geotextile is effective in redistributing the excess moisture from the subgrade soil.
3. The initial observations indicate that the pavement performance has improved due to the provision of the wicking geotextile in between the pavement subgrade and base course, as compared to the traditional pavement section.

Although there is an improvement in short-term performance due to the utilization of the wicking geotextile, long-term pavement monitoring is necessary to understand the pavement performance over the years. Data collected over a longer period will help the DOTs to understand the effectiveness of the wicking fiber on expansive soils. Furthermore, design charts could be developed after validating the field results and comparing them with the existing laboratory studies.

References

1. Barksdale RD (1972) Laboratory evaluation of rutting in base course materials. In: Third international conference on the structural design of Asphalt pavements, London
2. Puppala AJ (2008) Estimating stiffness of subgrade and unbound materials for pavement design. Transportation Research Board, Washington, D.C. https://doi.org/10.17226/13598
3. Puppala AJ, Saride S, Chomtid S (2009) Experimental and modeling studies of permanent strains of subgrade soils. J Geotech Geoenviron Eng 135(10):1379–1389. https://doi.org/10.1061/(ASCE)GT.1943-5606.0000163
4. Chakraborty S, Nair S (2020) Impact of curing time on moisture-induced damage in lime-treated soils. Int J Pavement Eng 21(2):215–217. https://doi.org/10.1080/10298436.2018.1453068
5. Bheemasetti TV, Chittoori B, Zou H, Puppala AJ, Thomey J (2017) Spatial mapping of soluble sulfate concentrations present in natural soils using geostatistics. J Geotech Geoenviron Eng 143(2):04016090. https://doi.org/10.1061/(ASCE)GT.1943-5606.0001590
6. Puppala AJ, Pedarla A (2017) Innovative ground improvement techniques for expansive soils. Innov Infrastruct Solut 2(1):24. https://doi.org/10.1007/s41062-017-0079-2
7. Little DN (1995) Handbook for stabilization of pavement subgrades and base courses with lime. National Lime Association, Kendall/Hunt Publishing Company, Iowa
8. Puppala AJ, Intharasombat N, Vempati RK (2005) Experimental studies on Ettringite-induced heaving in soils. J Geotech Geoenviron Eng 131(3):325–337. https://doi.org/10.1061/(ASCE)1090-0241(2005)131:3(325)
9. Puppala AJ, Congress SSC, Banerjee A (2019) Research advancements in expansive soil characterization, stabilization and geoinfrastructure monitoring. In: Madhavi Latha G (ed) Frontiers in geotechnical engineering. Springer Nature, Switzerland, pp 15–29. https://doi.org/10.1007/978-981-13-5871-5_2
10. Biswas N, Chakraborty S, Puppala AJ, Banerjee A (2021) A novel method to improve the durability of lime-treated expansive soil. In: Patel S, Solanki CH, Reddy KR, Shukla SK (eds) Proceedings of the Indian Geotechnical Conference 2019. Lecture Notes in Civil Engineering, vol 136. Springer, Singapore. https://doi.org/10.1007/978-981-33-6444-8_20
11. Nair S, Little DN (2011) mechanisms of distress associated with sulfate-induced heaving in lime-treated soils. Transp Res Rec J Transp Res Board 2212(1):82–90
12. George AM, Banerjee A, Puppala AJ, Saladhi M (2019) Performance evaluation of geocell-reinforced reclaimed asphalt pavement (RAP) bases in flexible pavements. Int J Pavement Eng 1–11. https://doi.org/10.1080/10298436.2019.1587437
13. Zhang X, Presler W, Li L, Jones D, Odgers B (2014) Use of wicking fabric to help prevent frost boils in Alaskan pavements. J Mater Civ Eng 26(4):728–740. https://doi.org/10.1061/(ASCE)MT.1943-5533.0000828
14. Khan MA, Biswas N, Banerjee A, Puppala AJ (2020) Performance of geocell-reinforced recycled Asphalt pavement (RAP) bases in flexible pavements built on expansive soils. Geo-Congr 2020:488–497. https://doi.org/10.1061/9780784482810.051
15. Khan MA, Biswas N, Banerjee A, Puppala AJ (2020) Field performance of geocell reinforced recycled asphalt pavement base layer. Transp Res Rec J Transp Res Board 2674(3):69–80. https://doi.org/10.1177/0361198120908861

16. Giroud JP (2010) Development of criteria for geotextile and granular filters. In: Proceedings of 9th international conference on geosynthetics, 4564, Guaruja, Brazil
17. Zornberg JG, Giroud JP (1997) Uplift of geomembranes by wind—extension of equations. Geosynth Int 4(2):187–207. https://doi.org/10.1680/gein.4.0093
18. Lawson CR (2008) Geotextile containment for hydraulic and environmental engineering. Geosynth Int 15(6):384–427. https://doi.org/10.1680/gein.2008.15.6.384
19. Biswas N, Ghosh P (2018) Interaction of adjacent strip footings on reinforced soil using upper-bound limit analysis. Geosynth Int 25(6):599–611. https://doi.org/10.1680/jgein.18.00020
20. Biswas N, Ghosh P (2019) Bearing capacity factors for isolated surface strip footing resting on multi-layered reinforced soil bed. Indian Geotech J 49(1):37–49. https://doi.org/10.1007/s40098-017-0293-z
21. Stormont JC, Ramos R, Henry KS (2001) Geocomposite capillary barrier drain system with fiberglass transport layer. Transp Res Rec J Transp Res Board 1772(1):131–136. https://doi.org/10.3141/1772-15
22. Wang F, Han J, Zhang X, Guo J (2017) Laboratory tests to evaluate effectiveness of wicking geotextile in soil moisture reduction. Geotext Geomembr 45(1):8–13. https://doi.org/10.1016/j.geotexmem.2016.08.002
23. Iryo T, Rowe RK (2003) On the hydraulic behavior of unsaturated nonwoven geotextiles. Geotext Geomembr 21(6):381–404. https://doi.org/10.1016/S0266-1144(03)00046-3
24. Zornberg JG, Bouazza A, McCartney JS (2010) Geosynthetic capillary barriers: current state of knowledge. Geosynth Int 17(5):273–300. https://doi.org/10.1680/gein.2010.17.5.273
25. Han J, Zhang X (2014) Recent advances in the use of geo synthetics to enhance sustainability of roadways. In: 20th International conference on advances in civil engineering for sustainable development. Ratchasima, Thailand, pp 29–39
26. Azevedo M, Zornberg JG (2013) Capillary barrier dissipation by new wicking geotextile. In: Panam. conference on unsaturated soils, pp 20–22
27. Guo J, Wang F, Zhang X, Han J (2017) Quantifying water removal rate of a wicking geotextile under controlled temperature and relative humidity. J Mater Civ Eng 29(1):04016181. https://doi.org/10.1061/(ASCE)MT.1943-5533.0001703
28. Stacks DL (2019) Pavement manual. Austin, TX
29. Annual book of ASTM (American Society for Testing and Materials) Standards ASTM International. West Conshohocken, PA (2019)

Performance Evaluation of Reinforced Expansive Soil Subgrade with Polypropylene Fiber and Geogrid

Nitin Tiwari and **Neelima Satyam**

Abstract The rapid development of infrastructure often encounters the loose soil subgrade and is becoming difficult to carry to construction activities. Various mechanical and chemical methods have been developed to reduce the impact of the expansive soil. Mechanical stabilization of expansive soils by reinforcing with polypropylene fibers and geogrid is one of the sustainable solutions. Geogrids and polypropylene fibers have been extensively used to reinforce the expansive soil subgrade and foundations as individuals. The polypropylene fiber reinforcement enhanced the tensile strength capacity of the reinforced expansive soil wherein the geogrid reinforcement is the quick fix mechanical stabilization technique, which reduces pavement failures. In this research, the combined effect of the polypropylene fiber and geogrid reinforcement has been evaluated to stabilize the pavement subgrades. Various mechanical strength tests such as unconfined compressive strength (UCS) and large direct shear box tests were conducted to evaluate the mechanical interaction between expansive soil subgrade, polypropylene fiber, triaxial geogrid, and biaxial geogrid at the interface. Polypropylene fiber of 12-mm length was used in the proportion of 0.25, 0.5, and 1.0% and single share geogrid layer at mid-depth. The result shows that the shear strength of reinforced subgrades with a layer of biaxial/triaxial geogrid and polypropylene fiber increases significantly. It is also observed that the unconfined compressive strength of the expansive soil increased with the inclusion of polypropylene fiber and geogrid. The combined reinforcement method shows an effective treatment methodology to improve the engineering property of expansive soil subgrades.

Keywords Expansive soil · Polypropylene fiber · Geogrid · Large direct shear · Unconfined compressive strength

N. Tiwari (✉) · N. Satyam
Department of Civil Engineering, Indian Institute of Technology Indore, Indore, India

545

1 Introduction

Expansive soil characterized by its nature of changing its volume with the change in water content. This change in volume known as swelling-shrinkage behavior of soil, and hence, this soil is also known as swell-shrink soil [1–4]. Pavement distresses in roadways are one of the impacts of the presence of expansive soil in the subgrade layer [5–7]. In a dry state, soil initiate shrinkage cracking, which propagates through the pavement system and leads to longitudinal, transverse, and fatigue cracking and rutting in the case of pavement surface [8]. Structures also suffer comparatively extensive damage when constructed on highly plastic clay subgrade as such soils undergo cycles of wetting and drying. Therefore, such characteristics of expansive fine-grained soil are one of the most significant reasons which lead to cracks, distress and most of the damage [9].

Expansive soil lies mostly in the central and the western part and covers more than 15–20% of the geographical area of India [10]. The expansive soil subgrade swells during rain and shear failure in the structure occurred. Various mechanical and chemical methods were lingering to mitigate the swelling pressure and heave phenomena of the expansive soil. Mechanical [11–13] and chemical [14–19] stabilization are the conventional methods used to improve the engineering properties of expansive soils; however, these methods are time-consuming and uneconomical. Geosynthetic has now emerged as one of the cost-effective and sustainable construction materials as separation, filtration, reinforcement, and stiffening are some of the primary function which can be used to enhance the engineering properties of the subgrade layer [20–25]. Installing geogrids led to the extension of the service life of the pavement due to its ability to minimize the development of reflective cracks and also reduce the chances of cracks by reducing the expansion and shrinking of the subgrade layer as indicated by various field evidence and theoretical studies of geotechnical engineers [26–31]. Among the different forms of Geosynthetic, geogrid has the special property of high tensile strength, to provide separation, frictional resistance to stabilize the soft soil subgrade.

There is also a rapid increase in the waste quantity of plastic fiber; if this waste can be utilized for the stabilization of soil, then a sustainable solution of the expansive soil can be achieved [32]. In recent years, the polymeric fibers have also been used to control the volume change behavior of expansive soil as well as to improve its strength. The performance of the reinforcement is persuaded by the properties of the fiber, volume fraction, modulus of elasticity, type of inclusion,, orientation, length, shape, grain size, gradation characteristics, and density [33] and also established that peak unconfined compressive strength of soil increased with the inclusion of fiber content and shown a meager reduction in shear capacity [34, 35]. Polypropylene fiber does not react with water and soil; hence can be used for the soil reinforcement [36].

The objective of this study is to evaluate the combined and individual effect of polypropylene fiber and biaxial/triaxial geogrid on geotechnical properties of the expansive soil. Single layer of geogrid at mid-depth and 0.25, 0.5, and 1.0% polypropylene fiber of 12-mm length were used to reinforce the expansive soil. To

Table 1 Index properties of expansive soil considered

Property	Value
Specific gravity	2.78
Liquid limit (%)	89
Plastic limit (%)	47
Plasticity index (%)	42
Shrinkage limit (%)	11
USCS soil classification	CH
Grain size distribution	
Clay (%)	71.5
Silt (%)	24.5
Sand (%)	4.0
Free swell index (%)	120

evaluate the effect of reinforcement a large size direct shear (300 mm × 300 mm × 150 mm) and unconfined compressive strength test has been carried out. The result shows that the shearing strength of expansive soil with a layer of biaxial/triaxial geogrid and polypropylene fiber increases significantly. It has also been observed that the stress–strain behavior of the expansive clay soil improved with the inclusion of polypropylene fiber with geogrid.

2 Properties of Material

2.1 Expansive Soil

The expansive clay soil used in this study was taken from Indore (India) at a depth of 1.5–2 m from the surface. The liquid limit (LL) and plastic limit (PL) of the soil were 89% and 47%, respectively. Because of which, this soil falls in the category of high plasticity clay (CH), as specified by the unified soil classification system (USCS). The free swelling index of the soil was 120%, which represents the high swelling potential of expansive soil. The various index properties of expansive soil considered in the study are shown below in Table 1.

2.2 Polypropylene Fiber

Polypropylene fibers have been used in the present study because they have several advantages, such as high strength, microfine reinforcement, chemically inert, non-corrosive, and availability in various lengths. For the present study, fibers with a

Table 2 Properties of polypropylene fiber considered

S. No.	Property	Value
1.	Specific gravity	0.91
2.	Tensile strength (kN/mm^2)	0.67
3.	Young's modulus (kN/mm^2)	4.0
4.	Melting point (°C)	165
5.	Ignition point (°C)	600
6.	Bulk density (kg/m^3)	910
7.	Loose density (kg/m^3)	250–430
8.	Fiber cut length (mm)	6 mm
9.	Dispersion	Excellent
10.	Acid and salt resistance	Chemical proof

length of 6 mm were used provided by Bajaj Reinforcements Nagpur India. The physical, chemical, and mechanical properties of PP fiber shown in Table 2.

2.3 Geogrid

Biaxial and triaxial polypropylene geogrid that is integrally formed by punch and drawn, and extrusion process as shown in Fig. 1 has been used in the study. Index properties of biaxial and triaxial geogrid are presented in Tables 3 and 4. The geogrid has been provided by Tensar® Geosynthetics India Pvt. Ltd.
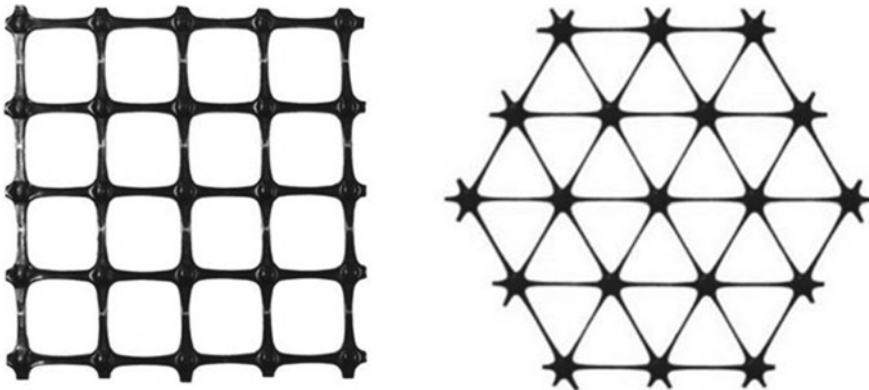
Fig. 1 Biaxial and triaxial geogrid

Table 3 Properties of biaxial geogrid considered

Characteristics			Units	MD	CD
Mechanical properties	Tensile strength ASTM 6626	@ 2% Strain	kN/m	4.1	6.6
		@ 5% Strain	kN/m	8.5	13.4
		Ultimate	kN/m	12.4	19
	Junction efficiency		%	93	–
	Flexural stiffness		mg cm	250,000	–
Geometric properties	Aperture dimensions		mm	25	33
	Minimum rib thickness		mm	0.76	0.76
	Rib width		mm	3.2	3.2
Polymer type			Polypropylene		
Manufacturing process			Integrally formed biaxial geogrid		

Table 4 Properties of triaxial geogrid considered

Characteristics			Unit	Value
Geometric properties	Rib pitch	Longitudinal	mm	40
		Diagonal	mm	40
	Mid-rib depth	Diagonal	mm	1.6
		Transverse	mm	1.4
	Mid-rib width	Diagonal	mm	1
		Transverse	mm	1.2
	Aperture shape		–	Triangular
Structural integrity	Junction efficiency		%	93
	Radial stiffness @ 0.5% strain		kN/m	300
Polymer type			Polypropylene	
Manufacturing process			Integrally formed triaxial geogrid	

3 Experimental Program

In this paper, the engineering properties of polypropylene fiber and geogrid reinforced expansive soil were investigated. Unconfined compressive strength and large size direct shear test have been conducted to investigate the shear strength and compressive strength of the reinforced soil specimen. The index properties, i.e., optimum moisture content (OMC), maximum dry density (MDD), liquid limit (LL), plastic limit (PL), grain size distribution (GSD), specific gravity, free swell index were carried out to characterize the expansive soil. In initial phase the expansive soil mechanically reinforced with 0.25, 0.50, and 1.00% polypropylene fiber content. The initial moisture content and dry unit weight are essential factors affecting the engineering behaviors of expansive soil. Hence, the specimen was prepared at the dry unit weight (17.65 kN/m^3) and optimum moisture content (19.2%) of expansive soil.

Table 5 Reinforced and unreinforced section considered

Polypropylene fiber (%)	Type of geogrid		
	No geogrid	Biaxial geogrid	Triaxial geogrid
0.00	BC	BC + BG	BC + TG
0.25	BC + 0.25% PP	BC + 0.25% PP + BG	BC + 0.25% PP + TG
0.50	BC + 0.50% PP	BC + 0.50% PP + BG	BC + 0.50% PP + TG
1.00	BC + 1.00% PP	BC + 1.00% PP + BG	BC + 1.00% PP + TG

The mix of polypropylene fiber and expansive soil kept in the environmental chamber at 27 ± 2 °C temperature and $65 \pm 5\%$ humidity to maintain the constant temperature and moisture condition. The required amount of clay and polypropylene fiber was compact statically using a lightweight proctor to achieve the field conditions. The test specimen was prepared in accordance with Indian Standard. To evaluate the shear strength parameter of reinforced and unreinforced soil subgrade, a large direct shear test has been conducted. The large direct shear box of 300 mm × 300 mm × 150 mm is used to evaluate the effect on soil geogrid interaction behavior. The lower box size kept large than the upper shear box to maintain the equal shear area during the experiment. The 287, 335, and 383 number of below applied to achieve the dry density using lightweight proctor method. The single layer geogrid was placed at mid-depth of a specimen to evaluate shear strength and applied 1.25 mm/min strain rate under 24.63, 49.27, and 98.54 kPa normal pressure. The maximum shear load and displacement during the experiment were recorded with LVDT and load cell of capacity 50 mm and 50 kN, respectively. The stress–strain behavior of the reinforced and unreinforced samples has been investigated by conducting the unconfined compressive strength test of 50 mm diameter. The samples were prepared as per the test sections mentioned in Table 5. The stress was calculated by applying the 1.25 mm/min constant strain rate up to deviator stress. The single layer geogrid placed at the mid-depth to evaluate the effect on unconfined compressive strength. In this paper the expansive soil, biaxial geogrid, triaxial geogrid, and polypropylene fiber referred as BC, BG, TG, and PP, respectively.

4   Results and Discussion

Figure 2 shows the effect of geogrid and polypropylene fiber on the shear strength of expansive soil. The large size direct shear test resembles the field condition up to a great extent. The large direct shear test result indicates a significant improvement in the expansive soil shear strength.

The shear strength with a single layer of a geogrid layer at a half depth of specimen increase from 55.56 to 101.11 kPa (82%), and 102.22 kPa (84%), while 68.33 kPa (23%), 84.05 kPa (51.29%), and 81.53 (46.75) with the inclusion of 0.25%, 0.50%, and 1.00% polypropylene at 24.63 kPa normal stress, respectively. The shear strength
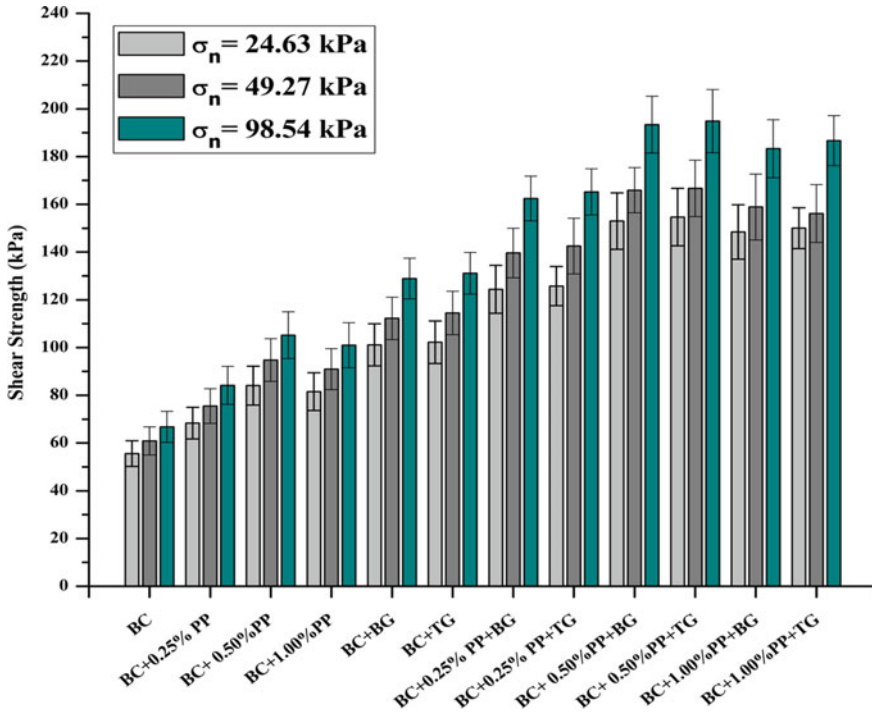
Fig. 2 Shearing strength of reinforced and unreinforced expansive soil

increased due to high frictional resistance between the soil particle and the geotextile layer. The interaction mechanism between polypropylene fiber and soil particles is based on dilation [37]. In the soil mass, randomly distributed polypropylene fiber act as a spatial network, interlocking with soil particles to form a unitary matrix. The soil matrix resists most of the applied load at relatively low strain levels. As the strain level increases, rearrangement or rotation of particles gradually mobilizes the tensile strength in the interlocked fibers, which will then contribute to resisting the applied shear force [38].

It has also observed that under normal stress 49.27 and 98.54 kPa the shear strength increases 60.88 kPa (9.60%), 112.22 kPa (10.99%), 114.44 kPa (11.96%) and 66.78 kPa (9.67%), 128.31 kPa (14.85%), 131.11 kPa (14.56%), respectively, for BC + BG and BC + TG section, respectively. Similar pattern has been observed with the inclusion of propylene fiber content (i.e., BC + 0.25% PP, BC + 0.50% PP, BC + 1.00% PP), shear strength increases between 10.5% and 12.5% under 49.27 kPa and 98.54 kPa normal stress. Under high normal stress, the restriction of particle rearrangement leads to slippage between particles and fibers and, consequently, to a reduction of stretching in the reinforcement. It indicates that with increasing the normal pressure, the soil particle got intact with each other and dominate with the particle cohesion than the frictional resistance between the geotextile layer. The

results also show the potential increment in the shearing strength with both geogrid and polypropylene fiber are used to reinforce the expansive soil. It can be noted that with the inclusion of fiber content with geogrid, the shear strength increases exponentially; however, the effect of biaxial and triaxial geogrid is similar.

The improvement in the behavior of soil–geogrid interfaces can be expressed in terms of the interface shear strength coefficient α, defined as

$$\alpha = \frac{\tau_{\text{reinforced}}}{\tau_{\text{unreinforced}}} \tag{1}$$

where $\tau_{\text{reinforced}}$ is the shear strength of expansive soil reinforced with polypropylene fiber and geogrid at the interface, and $\tau_{\text{unreinforced}}$ is the shear strength of expansive soil.

Table 6 summaries the measured peak interface shear strength coefficients for normal stresses of 24.69, 49.27 and 98.54 kPa with the average interface shear strength coefficients. The average peak interface shear strength coefficients of the soil with polypropylene fiber and geogrids used in this study range from 1.24 to 2.81. The average peak interface shear strength coefficients are lowest for BC + 0.25% PP interface and the highest for BC + 0.50% PP + TG interface. An interface shear strength coefficient exceeding unity represents the beneficial effect of geogrids in expansive soil reinforcement. Table 6 also show that the interface shear strength coefficient depends on the applied normal stress. At lower normal stresses, the materials are more dilative, while at higher normal stresses and larger shear strains, dilation is inhibited. Therefore, depending on the initial sample density, the

Table 6 Peak interface shear strength coefficients for normal stresses of 24.69, 49.27, and 98.54 kPa

Reinforced section	Peak interface shear strength coefficient α_{peak}			
	Normal stress (σ_n) kPa			Average α_{peak}
	24.69	49.27	98.54	
BC	1.00	1.00	1.00	1.00
BC + BG	1.82	1.84	1.93	1.86
BC + TG	1.84	1.88	1.96	1.89
BC + 0.25% PP	1.23	1.24	1.26	1.24
BC + 0.25% PP + BG	2.24	2.29	2.43	2.32
BC + 0.25% PP + TG	2.26	2.34	2.47	2.36
BC + 0.50% PP	1.51	1.56	1.57	1.55
BC + 0.50% PP + BG	2.75	2.72	2.90	2.79
BC + 0.50% PP + TG	2.78	2.74	2.92	2.81
BC + 1.00% PP	1.47	1.49	1.51	1.49
BC + 1.00% PP + BG	2.67	2.61	2.75	2.68
BC + 1.00% PP + TG	2.70	2.56	2.80	2.69

Reinforcement section	Angle of shearing resistance (Degree)	Cohesion (kPa)
BC	8.44	52.61
BC+0.25% PP	11.94	64.02
BC+ 0.50%PP	15.77	78.84
BC+1.00%PP	14.58	76.53
BC+BG	21.23	92.78
BC+TG	21.96	93.89
BC+0.25% PP+BG	29.06	112.97
BC+0.25% PP+TG	30.00	114.38
BC+ 0.50%PP+BG	31.41	139.24
BC+ 0.50%PP+TG	31.39	140.57
BC+1.00%PP+BG	27.28	136.16
BC+1.00%PP+TG	29.42	134.75
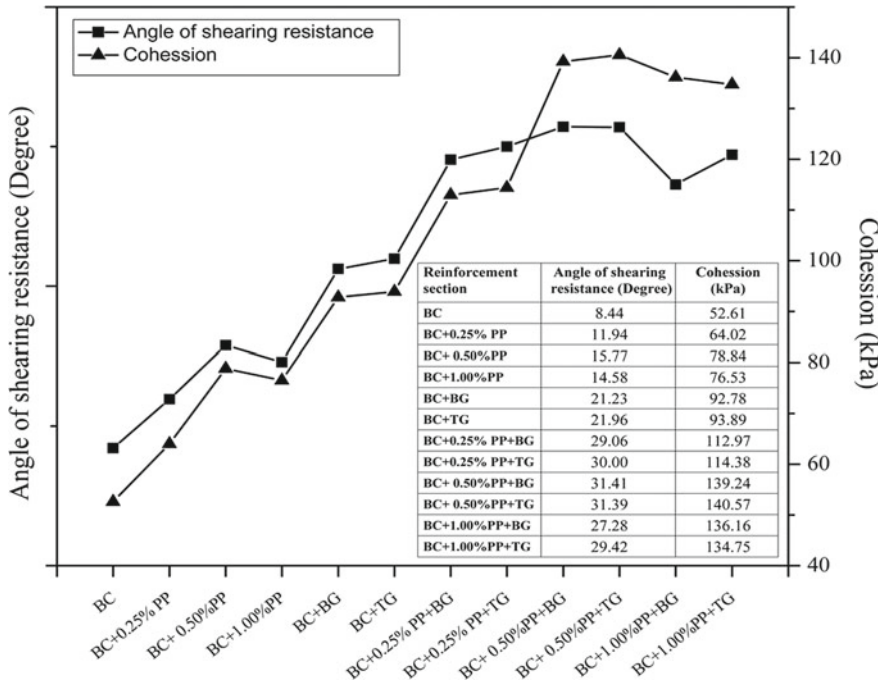
Fig. 3 Cohesion and angle of shearing resistance of reinforced and unreinforced expansive soil

normal stress and the degree of interlocking of particles within geogrid apertures, the interaction mechanism is expected to be different.

Figure 3 shows the cohesion and angle of shearing resistance of reinforced and unreinforced expansive soil. The angle of shearing resistance increases from 8.44° to 21.23°, 21.26°, and cohesion from 52.61 kPa to 92.78 kPa, 93.89 kPa with the reinforcement of BC + BG, and BC + TG, respectively. The cohesion of unreinforced expansive soil 52.61 kPa improved by 112.97–140.57 kPa for combined polypropylene fiber and geogrid reinforced expansive soil as a result reinforced soil falls under the category of very stiff clay soil as per Mohr's criteria and give higher shear resistance.

The unconfined compressive strength (UCS) curve of reinforced and unreinforced expansive soil shown in Fig. 4. Significant strength improvement has been observed with the inclusion of polypropylene fiber and geogrid. The UCS value of unreinforced section was observed as 139.7624 kPa which increase ranging 145.15–335 kPa. The maximum value of reinforced section BC + 0.50% PP + TG, which can be considered as the optimum percentage for reinforcement. The effect of geogrid do not affect much the strength of the material; however, the layer creates a strong base and separates the section into two part. With the inclusion of geogrid layer the *L/D* ratio of layers change, and as a result the increment in the UCS value observed. The UCS of the polypropylene fiber mix increased with the increment of the PP fiber
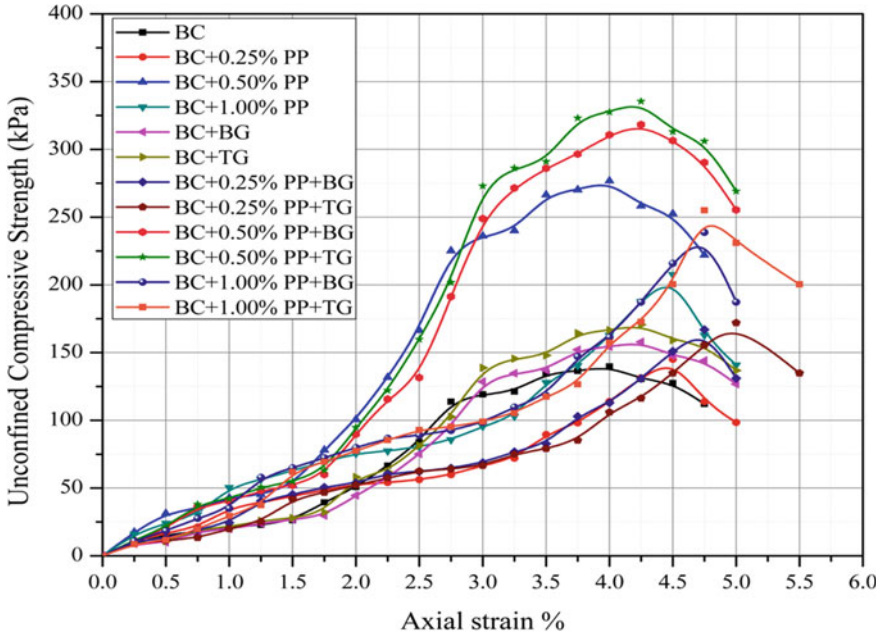
Fig. 4 Unconfined compressive strength of reinforced and unreinforced expansive soil

content; however, at higher amount of PP fiber content the axial strain capacity of the expansive soil reduces.

5 Conclusion

The inclusion of geogrid and polypropylene fiber shows a significant improvement in the property of expansive soil subgrade. The results of the study on the potential use of geogrid and polypropylene fiber to increase the shear strength and unconfined compressive strength of expansive soils are presented. The reinforced soil specimen can be used for controlling the shearing strength and stress–strain behavior of the expansive soil subgrade. Based on the results and discussion presented, the following conclusions were made.

- With the addition of geogrid and polypropylene fiber, the angle of shearing resistance increases from 8.44° to 21.23°, 21.26°, and cohesion from 52.61 kPa to 92.78 kPa, 93.89 kPa for BC + BG and BC + TG, respectively. The shear strength increased due to high frictional resistance between the soil particle, polypropylene fiber, and geogrid layer.
- The shearing strength of the expansive soil with the inclusion of polypropylene fiber and geogrid increase up to 154 kPa from 55.43 kPa. The 0.50% PP fiber

gives optimum results with biaxial and triaxial geogrids. However, the biaxial and triaxial geogrids performed similarly, no major improvement has been observed.
- The unconfined compressive strength of the reinforced section increases with the addition of geogrid and PP fiber. The UCS value of unreinforced section was observed as 139.76 kPa with increase ranging from 145.15 kPa to 335 kPa.

References

1. Jones LD, Survey BG, Jefferson I (1998) Expansive soils. In: Institution of civil engineers manuals series, ICE manuals, pp 1–46
2. Tiwari N, Satyam N, Kumar Shukla S (2020) An experimental study on micro-structural and geotechnical characteristics of expansive clay mixed with EPS granules. Soils Found 60:705–713. https://doi.org/10.1016/j.sandf.2020.03.012
3. Tiwari N, Satyam N (2020) An experimental study on the behavior of lime and silica fume treated coir geotextile reinforced expansive soil subgrade. Eng Sci Technol an Int J 23:1214–1222. https://doi.org/10.1016/j.jestch.2019.12.006
4. Sun S, Liu B, Wang T (2018) Improvement of expansive soil properties using sawdust. J Solid Waste Technol Manag 44:78–85. https://doi.org/10.5276/jswtm.2018.78
5. Samer D, Jeong HO, Mijia Y, Ilias M, Lee SI, Freeman T et al (2012) Pavement repair strategies for selected distresses in FM roadways. Austin, Texas
6. Marradi A, Pinori U, Betti G (2012) The use of lightweight materials in road embankment construction. Procedia Soc Behav Sci 53:1000–1009. https://doi.org/10.1016/j.sbspro.2012.09.949
7. Tiwari N, Satyam N, Singh K (2020) Effect of curing on micro-physical performance of polypropylene fiber reinforced and silica fume stabilized expansive soil under freezing thawing cycles. Sci Rep 10:7624. https://doi.org/10.1038/s41598-020-64658-1
8. Kermani B, Xiao M, Stoffels SM, Qiu T (2018) Reduction of subgrade fines migration into subbase of flexible pavement using geotextile. Geotext Geomembr 46:377–383. https://doi.org/10.1016/J.GEOTEXMEM.2018.03.006
9. Camacho-Tauta J, Reyes-Ortiz O, Da FAV, Rios S, Cruz N, Rodrigues C (2016) Full-scale evaluation in a fatigue track of a base course treated with geopolymers. Procedia Eng 143:18–25. https://doi.org/10.1016/j.proeng.2016.06.071
10. Thirumalai R, Babu SS, Naveennayak V, Nirmal R, Lokesh G (2017) A review on stabilization of expansive soil using industrial solid wastes. Engineering 09:1008–1017. https://doi.org/10.4236/eng.2017.912060
11. Punthutaecha K, Puppala AJ, Vanapalli SK, Inyang H (2006) Volume change behaviors of expansive soils stabilized with recycled ashes and fibers. J Mater Civ Eng 18:295–306. https://doi.org/10.1061/(ASCE)0899-1561(2006)18:2(295)
12. Hammouri NA, Husein Malkawi AI, Yamin MMA (2008) Stability analysis of slopes using the finite element method and limiting equilibrium approach. Bull Eng Geol Environ 67:471–478. https://doi.org/10.1007/s10064-008-0156-z
13. Tinoco J, António Alberto Santos C, Da Venda P, Correia AG, Lemos L (2016) A data-driven approach for qu prediction of laboratory soil-cement mixtures. Procedia Eng 143:566–573. https://doi.org/10.1016/j.proeng.2016.06.073
14. Krause Sternberg M (1977) DIURETIKA II. Monatskurse Fur Die Arztl Fortbildung. https://doi.org/10.1016/j.trgeo.2015.06.003

15. Estabragh AR, Rafatjo H, Javadi AA (2014) Treatment of an expansive soil by mechanical and chemical techniques. Geosynth Int 21:233–243. https://doi.org/10.1680/gein.14.00011
16. Tiwari N, Satyam N, Puppala AJ (2021) Effect of synthetic geotextile on stabilization of expansive subgrades: an experimental study. J Mater Civ Eng. https://doi.org/10.1061/(ASCE)MT.1943-5533.0003901
17. Sharma M, Satyam N, Reddy KR (2019) Investigation of various gram-positive bacteria for MICP in Narmada Sand, India. Int J Geotech Eng 1–15. https://doi.org/10.1080/19386362.2019.1691322
18. Phanikumar BR, Nagaraju TV (2018) Effect of fly ash and rice husk ash on index and engineering properties of expansive clays. Geotech Geol Eng 36:3425–3436. https://doi.org/10.1007/s10706-018-0544-5
19. Tiwari N, Satyam N, Patva J (2020) Engineering characteristics and performance of polypropylene fibre and silica fume treated expansive soil subgrade. Int J Geosynth Gr Eng 6:1–11. https://doi.org/10.1007/s40891-020-00199-x
20. Peng X, Zornberg JG (2017) Evaluation of load transfer in geogrids for base stabilization using transparent soil. Transp Geotech Geoecol 307–314. https://doi.org/10.1016/j.proeng.2017.05.049
21. Zornberg JG (2017) Functions and applications of geosynthetics in roadways. Procedia Eng 189:298–306. https://doi.org/10.1016/j.proeng.2017.05.048
22. Perkins SW, Ismeik M (1997) A synthesis and evaluation of geosynthetic-reinforced base layers in flexible pavements: part II. Geosynth Int 4:605–621. https://doi.org/10.1680/gein.4.0107
23. Vieira CS, Pereira PM (2016) Interface shear properties of geosynthetics and construction and demolition waste from large-scale direct shear tests. Geosynth Int 23:62–70. https://doi.org/10.1680/jgein.15.00030
24. Cristelo N, Vieira CS, De Lurdes LM (2016) Geotechnical and geoenvironmental assessment of recycled construction and demolition waste for road embankments. Procedia Eng 143:51–58. https://doi.org/10.1016/j.proeng.2016.06.007
25. Onur MI, Tuncan M, Evirgen B, Ozdemir B, Tuncan A (2016) Behavior of soil reinforcements in slopes. Procedia Eng 143:483–489. https://doi.org/10.1016/j.proeng.2016.06.061
26. Nejad FM, Noory A, Toolabi S, Fallah S (2008) Effect of using geosynthetics on reflective crack prevention. Geotext Geomembr 16:1–8. https://doi.org/10.1080/10298436.2014.943128
27. Mounes SM, Karim MR, Mahrez A, Khodaii A (2011) An overview on the use of geosynthetics in pavement structures. Sci Res Essays 6:2251–2258
28. Consoli NC, Lopes L da S, Prietto PDM, Festugato L, Cruz RC (2011) Variables controlling stiffness and strength of lime-stabilized soils. J Geotech Geoenviron Eng 137:628–632. https://doi.org/10.1061/(ASCE)GT.1943-5606.0000470
29. Zornberg JG (2012) Geosynthetic-reinforced pavement systems. In: 5th European geosynthetics congress, Valencia, pp 49–61
30. Mazzoni G, Stimilli A, Cardone F, Canestrari F (2017) Fatigue, self-healing and thixotropy of bituminous mastics including aged modified bitumens and different filler contents. Constr Build Mater 131:496–502. https://doi.org/10.1016/j.conbuildmat.2016.11.093
31. Tiwari N, Satyam N (2021) Experimental study on the swelling behavior of expansive soil reinforced with coir geotextile, lecture notes in civil engineering. In: Satyajit Patel et al (eds) Proceedings of the Indian Geotechnical Conference (Chapter 11), vol 138
32. Tiwari N, Satyam N (2021) The coupling effect of pond-ash and polypropylene fiber on strength and durability attributes of expansive subgrades: an integrated experimental and machine learning approach. J Rock Mech Geotech Eng
33. Liu J, Wang G, Kamai T, Zhang F, Yang J, Shi B (2011) Static liquefaction behavior of saturated fiber-reinforced sand in undrained ring-shear tests. Geotext Geomembr 29:462–471. https://doi.org/10.1016/j.geotexmem.2011.03.002
34. Ranjan G, Vasan RM, Charan HD (1994) Behavior of plastic-fiber-reinforced sand. Geotext Geomembr 13:555–565. https://doi.org/10.1016/0266-1144(94)90019-1
35. Tiwari N, Satyam N (2019) Experimental study on the influence of polypropylene fiber on the swelling pressure expansion attributes of silica fume stabilized clayey soil. Geosciences 9:377. https://doi.org/10.3390/GEOSCIENCES9090377

36. Tiwari N, Satyam N, Puppala AJ (2021) Strength and durability assessment of expansive soil stabilized with recycled ash and natural fibers. Transp Geotech 100556. https://doi.org/10.1016/j.trgeo.2021.100556
37. Anagnostopoulos CA, Tzetzis D, Berketis K (2014) Shear strength behavior of polypropylene fiber reinforced cohesive soils. Geomech Geoeng 9:241–251. https://doi.org/10.1080/17486025.2013.804213
38. Chunling L (2005) Mechanical response of fiber-reinforced soil. The University of Texas, Austin

Effects of Geogrid Encasement on Behavior of Stone Column-Improved Soft Clay

Meixiang Gu, Jie Cui, Yang Wu, Jie Yuan, and Yadong Li

Abstract Geosynthetic-encased stone columns (GESC) are commonly used to support embankments over soft clay. The load transfer mechanism and particle interactions have received little attention from researchers. This study presented some interesting results obtained from a numerical analysis using three-dimensional (3D) discrete element method (DEM). The aggregate, the geogrid encasement, and the soft clay were simulated using particles with different sizes and micromechanical properties. A validated DEM model was proposed to simulate the stone column-improved soft clay under a plate loading condition. Two important factors, the encasement length and the tensile stiffness of the geogrid, were investigated and showed different effects on the behavior of the stone column-improved soft clay. The encasement length had significant effects on the bearing capacity, the vertical and radial stresses of the column and the soft clay, and the tensile strain of the geogrid. The geogrid stiffness has negligible effect on the bearing capacity for partially encased stone column (e.g., the encasement length was twice the diameter of the column). The aggregate below the geogrid encasement was more likely to move laterally with the increase of the geogrid stiffness and caused bulging failure in the deep section.

Keywords Stone columns · Discrete element method · Load transfer mechanism · Particle interactions · Bulging zone

M. Gu · J. Cui (✉) · Y. Wu · J. Yuan · Y. Li
School of Civil Engineering, Guangzhou University, Guangzhou 510006, China
e-mail: jcui@gzhu.edu.cn

M. Gu
e-mail: mxgu@gzhu.edu.cn

Y. Wu
e-mail: yangwu@gzhu.edu.cn

J. Yuan
e-mail: yuanj@gzhu.edu.cn

Y. Li
e-mail: liyadong@gzhu.edu.cn

559

1 Introduction

Stone columns have been widely used to support embankments, highway facilities, bridge abutments, and building foundations over the soft ground [1, 2]. The bearing capacity of the stone column-improved soft clay depends on the lateral confining stress from the surrounding soils. In very soft clays (e.g., the undrained shear strength less than 15 kPa), stone columns may not achieve significant bearing capacity due to insufficient lateral confinement. The lower lateral confinement in the upper section of the column may cause large bulging deformation and significantly reduce its capacity [3]. In recent decades, fully or partially encasing individual stone columns with geosynthetic materials (e.g., geotextile and biaxial geogrid) were introduced, and extensively studies have conducted to understand the behavior of stone column-improved soft clay [4–10].

Hasan and Samadhiya [11] performed laboratory model tests and numerical analyses on reinforced granular piles installed in very soft clay. Significant improvement in ultimate load intensity and stiffness of the treated ground was achieved due to the inclusion of geosynthetic. Schnaid et al. [12] presented an instrumented case study of a full-scale bridge abutment on geotextile-encased columns supported soft soil. The results showed that the column reduced the horizontal earth pressure up to 50%. Chen et al. [13] performed large-scale triaxial tests on ordinary stone columns and uniaxial tests on geotextile-encased stone columns. The results showed the uniaxial compressive strength of the encased stone columns was mainly affected by the tensile strength of the geotextile. Yoo and Lee [14] investigated the load-carrying capacity and settlement reduction of geogrid-encased stone column by field-scale load tests. The performance was significantly improved even for partially encased stone columns. Gu et al. [15] conducted model tests on stone columns with different encasement lengths. The effective length of the encasement was suggested as three to four times of the diameter of the column based on the consideration of performance and economy.

However, most of the previous studies have focused on the macroscopic behavior (e.g., the bearing capacity and settlement) of stone columns, and there are limited results on the load transfer mechanism and particle interactions between the column and the surrounding soft clay. The discrete nature and large displacements of the granular material cannot be properly simulated by a continuum-based numerical approach (e.g., the finite element method) [16–22]. Discrete element method (DEM) can better model and give valuable insight into the behavior of stone column-improved soft clay in a microscopic perspective. Gu et al. [23, 24] proposed a three-dimensional DEM model for an axially-loaded geogrid-encased stone column under unconfined compression (without surround soil). The changes of vertical and radial stresses, the particle movements and contact-force distribution within the column, and tensile force in the geogrid encasement were investigated. The interlocking effects between the aggregate and the geogrid were observed from a microscopic view. Gu et al. [25] proposed a three-dimensional DEM model to simulate a partially encased stone column installed in a clay bed in the laboratory test under a plate loading condition.

The particle interaction and the interlocking effect between particles were investigated and showed different patterns in the encased and unreinforced sections due to the inclusion of the geogrid encasement.

Based on the previous study [23–25], validated three-dimensional DEM models were adopted in order to conduct a parametric study on influencing factors such as the encasement length and the geogrid stiffness. The load transfer mechanism and particle interactions between the column, the geogrid encasement, and the soft clay were investigated and are presented below.

2 Numerical Simulation

The three-dimensional particle flow code (PFC3D) [26] was employed in this study to simulate the stone column-improved soft clay under plate loading condition. Table 1 summarizes the variation of influencing factors used in the DEM models to investigate the effect of two important factors (i.e., encasement length and geogrid stiffness) on the behavior of stone column-improved soft clay. Models 1 and 2 simulated real laboratory tests on ordinary stone column and geosynthetic-encased stone column-improved soft clay, respectively. Details of the simulation process were presented in Gu et al. [25], and a brief introduction is presented below.

Figure 1 shows the three-dimensional DEM model for the geogrid-encased stone column-improved soft clay under a plate loading condition (i.e., model 2). The diameter of the column and its influenced soft clay were 200 and 800 mm, respectively, which represented an area replacement ratio of 0.0625 based on the unit-cell concept. The encasement length was 400 mm and represented the length of cylindrical encasement in the vertical direction from the ground surface. A cylindrical wall of 800 mm in diameter was created as the lateral boundary and its displacement was fixed in the radial direction. Two horizontal circular walls of 800 mm diameter were created as the upper and bottom boundaries, respectively, and their displacements were fixed in the vertical direction. Particles uniformly distributed between 18 and 20 mm were generated for the soft clay at an initial porosity of 0.40 using the radius-expansion method. Graded particles distributed between 30 and 50 mm were generated for the column at an initial porosity of 0.37 using the replacement method. Parallel-bonded particles with diameter of 3 mm were generated for the geogrid encasement with the real aperture size used in laboratory tests. The loading plate with diameter of 200 mm moved downward in a constant velocity of 0.008 m/s to apply vertical load on the top surface of the column during loading process. Thirty-six measurement spheres

Table 1 Summary of DEM model parameters

Parameters	Model 1	Model 2	Model 3	Model 4	Model 5
Encasement length (mm)	0	400	600	400	400
Geogrid stiffness (kN/m)	–	500	500	1000	1500
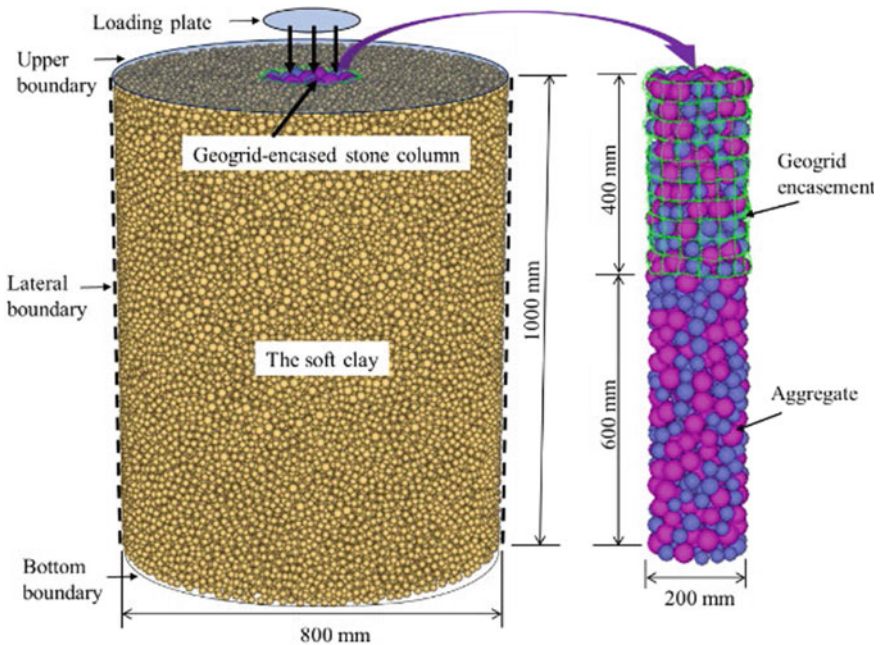
Fig. 1 DEM model for a geogrid-encased stone column-improved soft clay

were used to evaluate the microscopic behavior of the column and the soft clay, and their locations within the model were illustrated in Fig. 2.

The micromechanical properties of the column were determined by numerical triaxial tests at different confining stresses to calibrate its peak friction angle. The micromechanical properties of the soft clay were determined by numerical unconfined compression tests to calibrate its cohesion property. The linear increase of the undrained shear strength of the clay with depth was considered to simulate the construction sequence of the clay bed in laboratory tests in lifts. Small particles 18–20 mm in diameter with soft contact stiffness and weak contact bonds were generated to simulate the low shear strength of the soft clay. Unconfined compression tests were performed numerically in DEM to calibrate the shear strength of the clay under an unconsolidated undrained condition. The undrained shear strengths of the soft clay at depths of 0, 0.2, 0.4, 0.6, and 0.8 m was 3.4, 3.9, 4.4, 4.9, and 5.4 kPa, respectively, based on the Gibson soil model. The micromechanical properties of the geogrid encasement were determined by simulating multi-ribs tensile tests and flexural bending tests to calibrate its tensile properties and the flexural rigidity, respectively. The detailed determination and values of the micromechanical properties of the column, the soft clay, and the geogrid encasement can be found in Gu et al. [25] and are not presented herein for brevity purpose.

Figure 3 shows the key results for the validation of the numerical models against the laboratory tests. The load–displacement relationship obtained from the DEM

Fig. 2 Locations of measurement spheres within the model
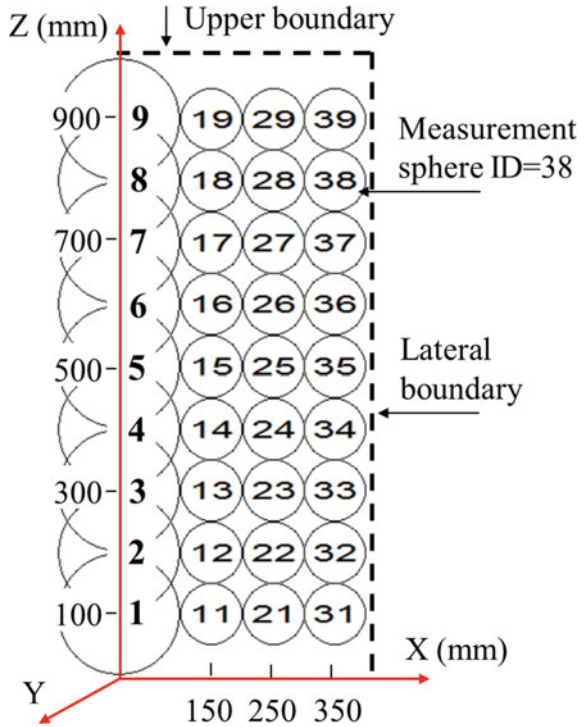
Fig. 3 Load–displacement curves from the DEM models and laboratory tests
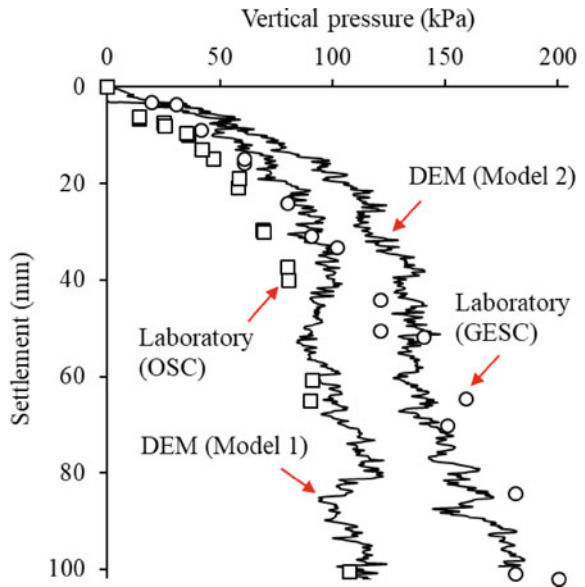
models (i.e., models 1 and 2) closely matched the laboratory results. Therefore, models 1 and 2 were treated as the baseline cases for the following parametric study.

Two important factors, the encasement length and the geogrid stiffness, were identified for a parametric study on the behavior of stone column-improved soft clay under plate loading condition based on the literature review. Three different encasement lengths were used in this study and the length varied from 0, 400, to 600 mm. Three different geogrid stiffness were used in this study, and their values were 500, 1000, and 1500 kN/m, which are typical for available geogrid products in the market. The simulation of higher tensile stiffness of the geogrid was achieved by increasing the particle stiffness and the parallel-bond stiffness simultaneously while other micromechanical properties were kept the same, which was proposed by Gu et al. [24].

3   Results and Discussion

3.1   Effect of Encasement Length

Three DEM models (i.e., models 1, 2, and 3) were conducted to investigate the effect of encasement length on the behavior of stone column-improved soft clay. Figure 4 shows the vertical pressure-settlement curves of axially-loaded stone column in soft clay with different encasement lengths. The bearing capacity of the column was significantly improved with the increase of encasement length. The ultimate bearing capacities of the columns with encasement lengths of 0, 400, and 600 mm were

Fig. 4 Vertical pressure-settlement curves for stone columns with different encasement lengths
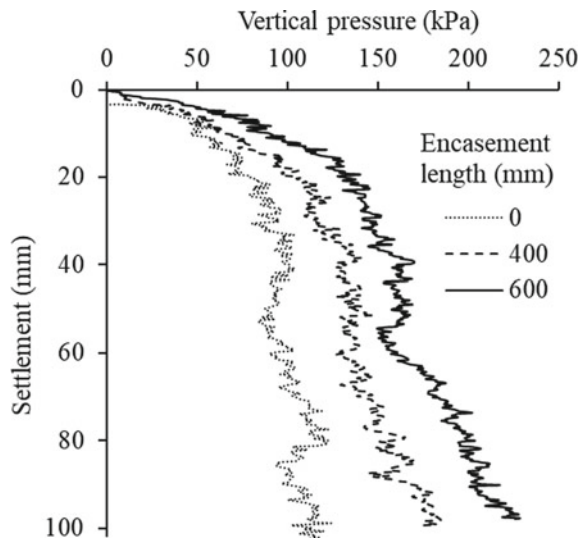
101 kPa, 131 kPa, and 162 kPa, respectively, which corresponded to the settlement of 40 mm (i.e., 20% the plate diameter). The improvement of the bearing capacity was primarily resulted from the confining stress developed in the geogrid encasement. Bulging deformation was the failure mechanism for ordinary stone columns (i.e., the encasement length was 0) and controlled the global behavior of stone column-improved soft clay. Upon applied vertical loads, the aggregate moved laterally to compress the surrounding soil in the radial direction. The column may fail due to the insufficient confinement provided by the soft clay in the shallow section. Geosynthetic encasement constrained the bulging deformation of the column in the shallow section and can provide additional confinement to the column. Therefore, the load transfer mechanism and particle movements of the stone column-improved soft clay became complicated due to the inclusion of the geosynthetic encasement.

Figure 5 shows the particle displacements of columns with different encasement lengths at the settlement of 40 mm (i.e., the column reached its ultimate bearing capacity). The position of each particle was evaluated by its elevation in the vertical direction and the radial strain in the horizontal plane. The radial strain was defined as the horizontal displacement of a particle divided by its initial position during loading process. A positive value of the radial strain represented that the particle moved outward to compress the surrounding soil and stretch the geogrid encasement. The particle position profiles clearly show different patterns with different lengths of the geogrid encasement. For ordinary stone column, large radial strains were observed at the top section of the column (i.e., high elevation) known as the bulging zone and the strain decreased sharply at the deep section of the column (i.e., elevation lower than 600 mm). For geosynthetic-encased stone column, the radial strain at the top section was relatively small and large radial strain was observed at the section below the base of the encasement. The bulging zone moved downward to the unreinforced section and developed large bulging deformation. A column section started from the base of the encasement (from the ground surface if the encasement length was 0 mm) and had a length of two times the diameter of the column (e.g., 400 mm in this case) can be identified as the bulging zone where significantly large radial strains were developed. The average radial strains in the bulging zone were 7.7, 7.4, and 9.3% for columns with the encasement length of 0, 400, and 600 mm, respectively. The average radial strains in the reinforced section were 0.5% and 0.2% for columns with the encasement length of 400 and 600 mm, respectively. The radial strain of the column in the shallow section was effectively constrained by the geogrid encasement; however, the large bulging deformation below the encasement was still the failure mechanism of the partially encased stone columns.

The vertical and radial stresses in the column and the soft clay were employed to investigate the load transfer mechanism between the column and the surrounding soft clay under vertical loading. Vertical and radial stresses at various locations were obtained by thirty-six measurement spheres (as shown in Fig. 2) during the loading process, which represented the average stress of particles contained within the measurement sphere. The stresses developed at the settlement of 40 mm were selected. Figure 6 shows the vertical stress distribution of columns with different encasement lengths. High vertical stresses were observed in the top section of the
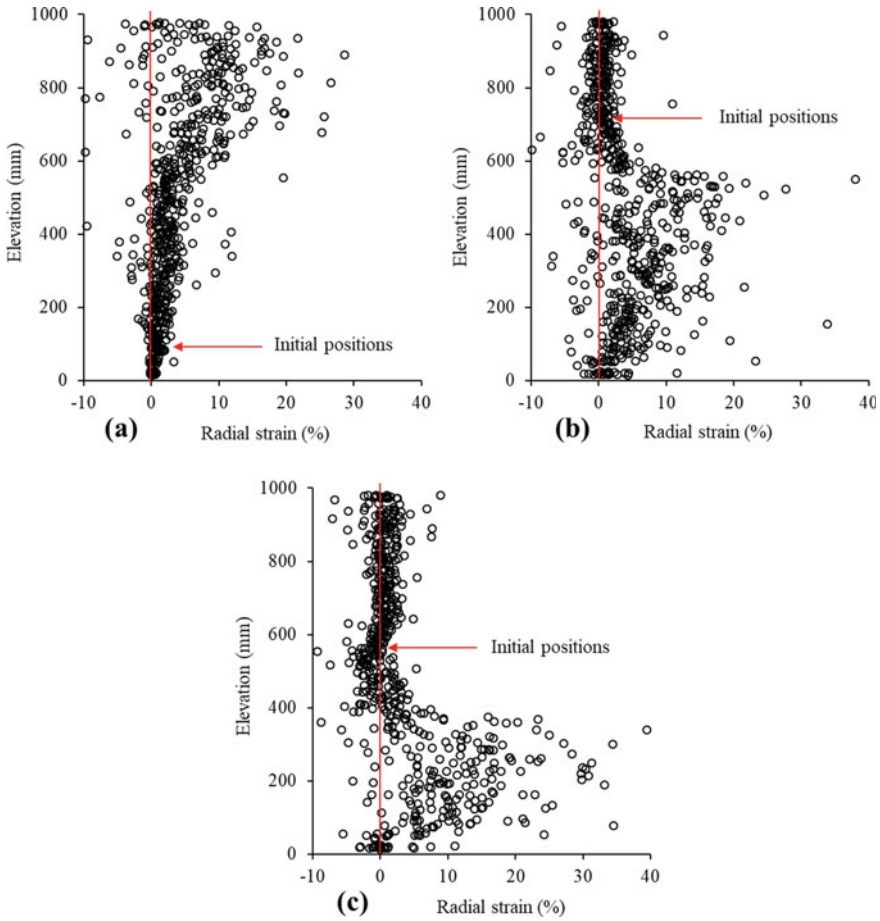
Fig. 5 Particle displacements of the column with the encasement length of: **a** 0 mm; **b** 400 mm; and **c** 600 mm

column in three cases. The vertical stress generally reduced along the column from the top to the bottom section. The reduction of vertical stress in the column was caused by the load transfer mechanism between the column and the soft clay. The applied vertical load was transferred from the column to the soft clay through strong particle interactions at the interface. Bulging deformation and side friction were mobilized and dominated within the bulging zone. The reduction ratio of the vertical stress (α_v) in the bulging zone was defined as follows:

$$\alpha_v = (\sigma_{v,1} - \sigma_{v,2})/\sigma_{v,1} \tag{1}$$

where $\sigma_{v,1}$ and $\sigma_{v,2}$ are vertical stresses at the top and the bottom planes of the bulging zone, respectively.

Fig. 6 Vertical stresses of the column with different encasement lengths
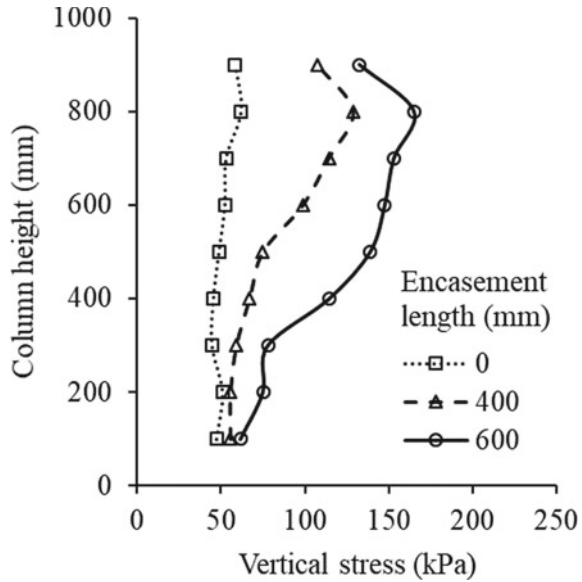
Table 2 summarizes the reduction ratio of the vertical stress in the column with different encasement lengths. 10% of the vertical stress was transferred to the soft clay in the bulging zone for the ordinary stone column-improved soft clay. 44 and 46% the vertical stresses were transferred to the soft clay in the bulging zone for cases with the encasement length of 400 and 600 mm, respectively.

Similar observations are made for the radial stress distribution of columns with different encasement lengths (Fig. 7). High radial stresses were observed in the top section of the column in three cases. The radial stress was significantly increased due to the inclusion of the geogrid encasement. The average values of the radial stress in the encased section were 58.9 and 71.0 kPa for columns with the encasement length of 400 and 600 mm, respectively. However, low radial stress was observed in the section below the base of the encasement (i.e., bulging zone). Radial stress in the bulging zone determined the ultimate bearing capacity of the stone column-improved soft clay. Table 3 summarizes the calculated and measured ultimate bearing capacities of columns with different encasement lengths. The ultimate bearing capacity of the column ($q_{u,c}$) can be calculated based on the limit equilibrium condition in the bulging zone as follows:

Table 2 Reduction ratio of vertical stress in the bulging zone

Encasement length (mm)	$\sigma_{v,1}$ (kPa)	$\sigma_{v,2}$ (kPa)	α_v (%)
0	58.4	52.3	10
400	99.1	55.4	44
600	114.6	61.6	46

Fig. 7 Radial stresses of the
column with different
encasement lengths
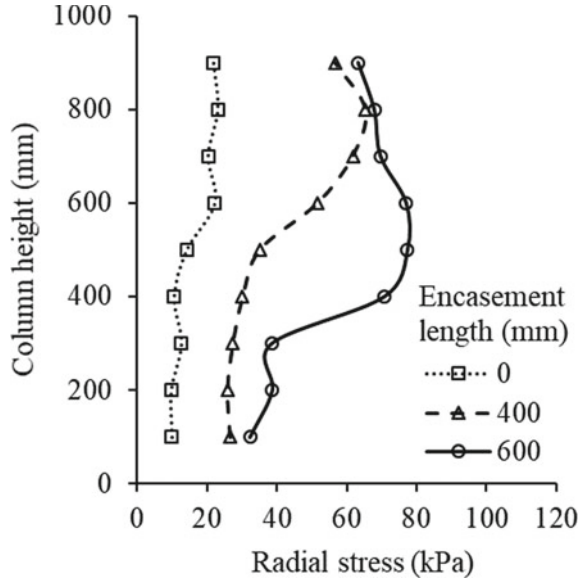
Table 3 Comparison between the calculated and measured bearing capacities

Encasement length (mm)	Average radial stress in the bulging zone (kPa)	Calculated bearing capacity (kPa)	Measured bearing capacity (kPa)	Error (%)
0	21.9	100.7	101	−0.3
400	29.5	135.7	131	3.6
600	36.5	167.9	162	3.6

$$q_{u,c} = K_p \sigma_{rf} \tag{2}$$

where K_p is the coefficient of passive earth pressure of the aggregate and σ_{rf} is the average radial stress of the column in the bulging zone.

The internal friction angle of the aggregate (φ) used in this study was 40.6° and $K_p = \tan^2\left(45° + \frac{\varphi}{2}\right) = 4.6$. The error was defined as follows:

$$e = \left(q_{u,c} - q_{u,m}\right)/q_{u,m} \tag{3}$$

where $q_{u,m}$ is the ultimate bearing capacity measured based on the vertical pressure-settlement curves (i.e., Fig. 4).

Table 3 illustrates the error between the calculated bearing capacity using Eq. (2) and the measured ultimate bearing capacity in DEM models. The good agreement between the calculated and measured bearing capacities demonstrated that the bulging deformation controlled the global behavior for both ordinary stone columns

and partially encased stone columns. The ultimate bearing capacity of the stone column-improved soft clay was depended on the radial stress of the column in the bulging zone.

The vertical and radial stresses developed in the surrounding soft clay were used to investigate the effect of encasement length on the stress distributions in the soft clay. In DEM models, the soft clay was divided into three zones with a thickness of 100 mm in the radial direction. The soft clay close to the column (i.e., at a horizontal distance of 150 mm away from the column center) directly contacted with the column and was likely to be affected by large particle movements of the column; therefore, the stresses of the soft clay in this zone were selected and analyzed. Figure 8 shows the vertical stress distribution of the soft clay for cases with different encasement lengths. The soft clay developed high vertical stress in the bulging zone due to large particle movements and strong particle interactions between the column and the soft clay. The average vertical stresses in the bulging zone were 10.4, 17.2, and 17.4 kPa for cases with the encasement length of 0, 400, and 600 mm, respectively. The vertical stress in the shallow section (e.g., the heights between 600 and 1000 mm) reduced due to the inclusion of the geogrid encasement. The average vertical stresses in the shallow section were 10.4, 3.8, and 3.8 kPa for cases with the encasement length of 0, 400, and 600 mm, respectively. The particle interactions between the column and the soft clay were constrained, and less vertical load can be transferred to the soft clay.

The radial stress distribution of the soft clay showed similar trend for cases with different encasement lengths (Fig. 9). High radial stresses were observed in the bulging zone for the soft clay. The average radial stresses in the bulging zone were 16.0, 19.1, and 21.3 kPa for cases with the encasement length of 0, 400, and 600 mm,

Fig. 8 Vertical stresses of the soft clay with different encasement lengths
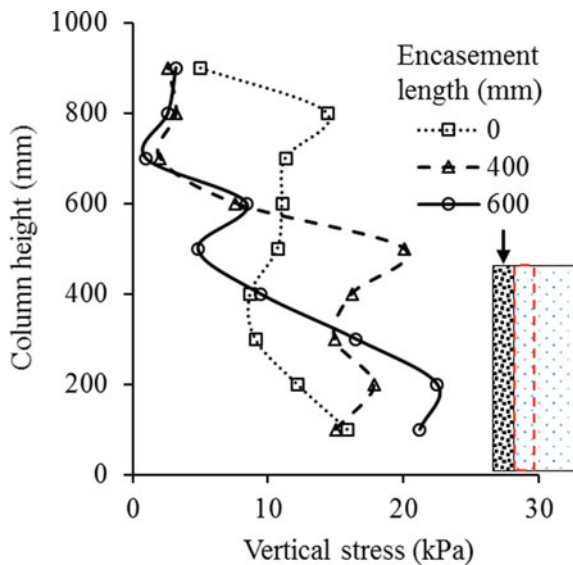
Fig. 9 Radial stresses of the soft clay with different encasement lengths
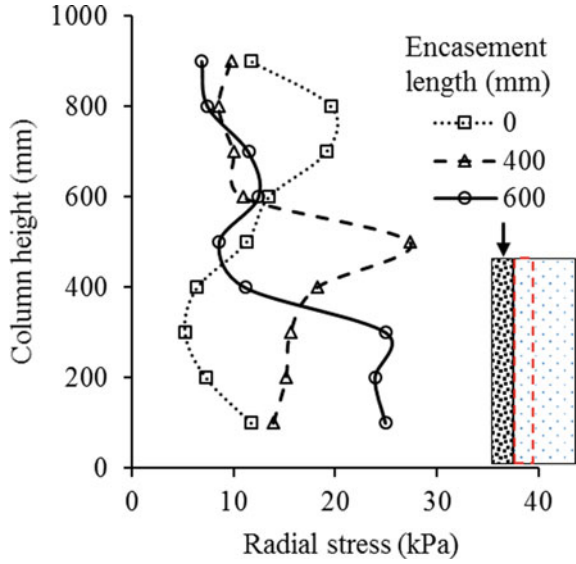
Fig. 10 Circumferential strains of the geogrid encasement
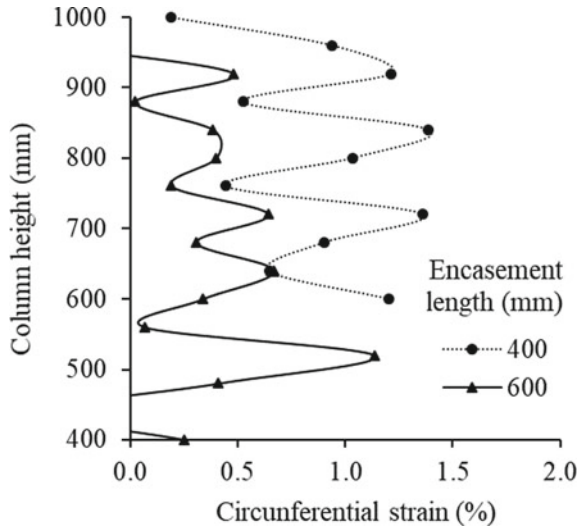
respectively. The column developed large radial displacement in the bulging zone and compressed the soft clay in the radial direction. The radial stress of the soft clay in the shallow section (e.g., the heights between 600 and 1000 mm) reduced due to the inclusion of the geogrid encasement. The average radial stresses in the shallow section were 16.0, 9.8, and 9.6 kPa for cases with the encasement length of 0, 400, and 600 mm, respectively.

Figure 10 illustrates the circumferential strains of the geogrid encasement with different encasement lengths after reaching ultimate bearing capacity at the settlement of 40 mm. The circumferential strain was defined as the ratio of the change in the circumferential length of the geogrid encasement to its original length. Larger circumferential strain was observed for the shorter geogrid encasement. Large circumferential strain indicated high confining stress provided by the geogrid encasement, which contributed to the improvement of the bearing capacity of the column. However, the bugling deformation of the column in the bulging zone controlled the global behavior of the stone column-improved soft clay. The soft soil in the deep section had high shear strength; therefore, the ultimate bearing capacity of the column with encasement length of 600 mm was higher than that for the case with encasement length of 400 mm.

3.2   Effect of Geogrid Stiffness

Three DEM models (i.e., models 2, 4, and 5) were conducted to investigate the effect of geogrid stiffness on the behavior of stone column-improved soft clay. The encasement length was 400 mm in these three models. Figure 11 shows the vertical pressure-settlement curves of axially-loaded stone column in soft clay with different geogrid stiffness. The improvement of the bearing capacity was less significant for cases with higher geogrid stiffness. Similar observations are made for the columns with the encasement length of 600 mm. The primary reason was the development of the bulging zone for partially encased stone columns during loading process. The column failed because large bulging deformations mobilized in the bulging zone and

Fig. 11 Vertical pressure-settlement curves for stone columns with different geogrid stiffness
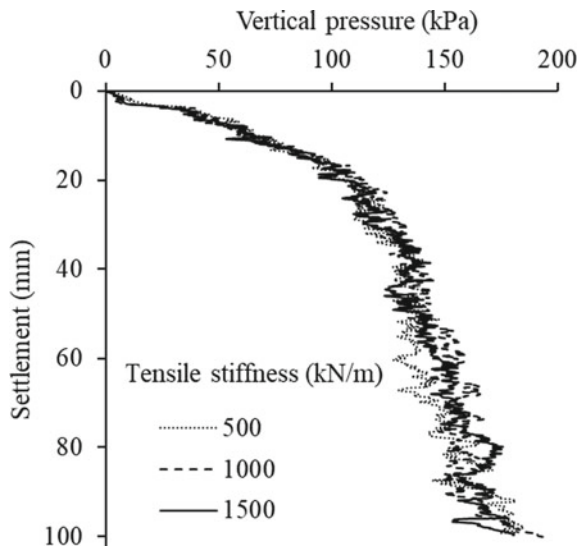
cannot carry more vertical loads even though the effective confining stress in the encased section.

4 Conclusions

Five three-dimensional discrete element method (DEM) models were adopted in this study to investigate the effects of two important factors (i.e., the encasement length and the geogrid stiffness) on the behavior of stone column-improved soft clay. Based on the numerical results obtained from this study, the following conclusions can be made:

1. The bearing capacity of the column was significantly improved with the increase of encasement length. The bulging zone was identified with a length of two times the diameter of the column based on the observation from the particle displacements of the column in DEM.
2. The applied vertical load transferred from the column to the soft clay through strong particle interactions. This phenomenon was significant within the bulging zone due to mobilized bulging deformation and side friction.
3. The ultimate bearing capacity of the stone column-improved soft clay was depended on the radial stress of the column in the bulging zone. The bulging failure controlled the global behavior for both ordinary stone columns and partially encased stone columns.
4. The soft clay developed high vertical and radial stress in the bulging zone due to large particle movements and strong particle interactions between the column and the soft clay. The shorter geogrid encasement mobilized larger circumferential strain.
5. The improvement of the bearing capacity was less significant for cases with higher geogrid stiffness. The partially encased stone column failed due to large bulging deformations in the bulging zone.

References

1. Barksdale RD, Bachus RC (1983) Design and construction of stone column, Report No. FHWA/RD-83/026. National Technical Information Service, Springfield, VA, USA
2. Han J, Ye SL (2001) A simplified method for consolidation rate of stone column reinforced foundations. J Geotech Geoenviron Eng 127(7):597–603

3. Yoo C (2010) Performance of geosynthetic-encased stone columns in embankment construction: numerical investigation. J Geotech Geoenviron Eng 136(8):1148–1160

4. Murugesan M, Rajagopal K (2007) Model tests on geosynthetic-encased stone columns. Geosynth Int 14(6):346–354

5. Pulko B, Majes B, Logar J (2011) Geosynthetic-encased stone columns: analytical calculation model. Geotext Geomembr 29(1):29–39

6. Chen JF, Li LY, Xue JF, Feng SZ (2015) Failure mechanism of geosynthetic-encased stone columns in soft soils under embankment. Geotext Geomembr 43(5):424–431

7. Han J (2015) Principles and practice of ground improvement. Wiley, Hoboken, NJ, USA

8. Zhang L, Zhao M (2015) Deformation analysis of geotextile-encased stone columns. Int J Geomech 15(3):198–210

9. Kadhim ST, Parsons RL, Han J (2018) Three-dimensional numerical analysis of individual geotextile-encased sand columns with surrounding loose sand. Geotext Geomembr 46(6):836–847

10. Kong G, Zhou Y, Liu H (2018) Nonlinear model analysis of radial bulging deformation of geosynthetic-encased stone columns. Int J Geomech 18(10):06018022

11. Hasan M, Samadhiya NK (2017) Performance of geosynthetic-reinforced granular piles in soft clays: model tests and numerical analysis. Comput Geotech 87:178–187

12. Schnaid F, Winter D, Silva AEF, Alexiew D, Küster V (2017) Geotextile encased columns (GEC) used as pressure-relief system. Instrumented bridge abutment case study on soft soil. Geotext Geomembr 45(3):227–236

13. Chen JF, Wang XT, Xue JF, Zeng Y, Feng SZ (2018) Uniaxial compression behavior of geotextile encased stone columns. Geotext Geomembr 46(3):277–283

14. Yoo C, Lee D (2012) Performance of geogrid-encased stone columns in soft ground: full-scale load tests. Geosynth Int 19(6):480–490

15. Gu M, Zhao M, Zhang L, Han J (2016) Effects of geogrid encasement on lateral and vertical deformations of stone columns in model tests. Geosynth Int 23(2):100–112

16. Cundall PA, Strack OD (1979) A discrete numerical model for granular assemblies. Geotechnique 29(1):47–65

17. Yao M, Anandarajah A (2003) Three-dimensional discrete element method of analysis of clays. J Eng Mech 129(6):585–596

18. Bhandari A, Han J (2010) Investigation of geotextile–soil interaction under a cyclic vertical load using the discrete element method. Geotext Geomembr 28(1):33–43

19. Han J, Bhandari A, Wang F (2011) DEM analysis of stresses and deformations of geogrid-reinforced embankments over piles. Int J Geomech 12(4):340–350

20. Indraratna B, Ngo NT, Rujikiatkamjorn C, Sloan SW (2015) Coupled discrete element finite difference method for analyzing the load-deformation behaviour of a single stone column in soft soil. Comput Geotech 63:267–278

21. Wang Z, Jacobs F, Ziegler M (2016) Experimental and DEM investigation of geogrid-soil interaction under pullout loads. Geotext Geomembr 44(3):230–246

22. Tan X, Zhao M, Chen W (2018) Numerical simulation of a single stone column in soft clay using the discrete-element method. Int J Geomech 18(12):04018176

23. Gu M, Han J, Zhao M (2017) Three-dimensional discrete-element method analysis of stresses and deformations of a single geogrid-encased stone column. Int J Geomech 17(9):04017070

24. Gu M, Han J, Zhao M (2017) Three-dimensional DEM analysis of single geogrid-encased stone columns under unconfined compression: a parametric study. Acta Geotech 12(3):559–572

25. Gu M, Han J, Zhao M (2020) Three-dimensional DEM analysis of axially-loaded geogrid-encased stone column in clay bed. Int J Geomech 20(3):04019180

26. PFC3D (Particle flow code in 3 dimensions) 3.10 [Computer software] (2005) Itasca Consulting Group, Minneapolis, USA

Finite Element Analyses of Geocell Reinforced Tracks Over Clayey Subgrade

Lalima Banerjee , **Sowmiya Chawla** , **and Sujit Kumar Dash**

Abstract Railways are an integral part of transportation sector of many countries like USA, China, and India. New tracks are being laid at a fast pace as well as existing tracks are being upgraded to meet the demands of the ever-increasing population. Geosynthetics in the form of geocells can be used as a reinforcement material in railways to reduce settlements and track deteriorations which can also reduce the maintenance costs involved. Upgrading tracks require parametric studies to evaluate the effect of various properties of track components on the track system. In the present study, three-dimensional geocell reinforced tracks are modeled using Midas GTS-NX, which is a commercial finite element analysis software. The displacement and vertical stress variations for the railway tracks over clayey subgrade under applied train load were obtained using finite element analyses. The parametric studies involved variation in subgrade modulus and infill modulus to show their effects on reduction in settlements as well as vertical stresses. The comparison of the geocell reinforced model with the unreinforced model showed improvement of railway tracks using geocell. The results of parametric studies show that increase in modulus of subgrade and infill material can effectively improve the performance of railway tracks.

Keywords FEM analyses · Geocell · Railways

L. Banerjee (✉) · S. Chawla
Indian Institute of Technology (Indian Schosol of Mines) Dhanbad, Dhanbad 826004, India

S. Chawla
e-mail: sowmiya@iitism.ac.in

L. Banerjee
KIIT Deemed to be University, Bhubaneswar 751024, India

S. K. Dash
Indian Institute of Technology Kharagpur, Kharagpur 721302, India
e-mail: sujit@civil.iitkgp.ac.in

1 Introduction

An increase in population has brought the need for better transportation systems to provide easier and faster travel means for people. This has resulted in laying of many new tracks, with upgradation of already existing ones. Deterioration of track hampers the movement of trains and also leads to passenger discomfort. Moreover, subgrade failures occurring in tracks as a result of heavy axle loads adopted nowadays have added to the increase in costs of maintenance for the railway authorities. Geosynthetics can be used to increase track stability. The effect of planar geosynthetics in reducing track deterioration has been studied extensively [1–4]. Geocells, a form of three dimensional geosynthetics, have shown better performance in comparison with planar ones for foundations [5, 6] and embankments [7, 8] mainly due to the confinement provided by it. In the present study, the advantage of using geocell in prototype tracks has been studied by varying the subgrade and sub-ballast modulus.

2 FEM Modeling

In the present study, FEM modeling and analysis of prototype tracks was carried out by Midas GTS NX, 2016 [9] software. A prototype track having subgrade height of 2 m was modeled. The height of prepared subgrade was fixed at 0.5 m. The height of sub-ballast and ballast was modeled as 0.6 m and 0.35 m, respectively, as per Indian Railways specifications [10]. The ballast and sub-ballast were modeled as Mohr–Coulomb drained model, while the subgrade was modeled as undrained model. The geocell was modeled within the sub-ballast layer to observe the improvement in vertical settlements and stresses that could be achieved by using it. The thickness of geocell was fixed as 0.002 m. The modeling was carried out considering total stress analyses.

2.1 Material Model

The prototype tracks were simulated as three-dimensional FEM models. One-half of the prototype track was modeled based on symmetry. Properties of the materials used for the entire modeling are given in Table 1. The rail, sleepers, and geocell were modeled as linear elastic material. Rail was considered as made of steel while sleepers of concrete. The material properties of track layers were based on values taken from [11]. The undrained Poisson's ratio value of subgrade and prepared subgrade was assumed to be 0.49. Pocket size of 0.5 m was used for modeling the geocell. The height of ballast, sub-ballast, prepared subgrade, and subgrade were modeled as 0.35 m, 0.6 m, 0.5 m, and 2 m, respectively. The geocell was modeled as a separate material type within the soil [12–15]. The geometry of the geocell layer of individual pocket

Table 1 Material properties

Properties	Rail	Sleepers	Ballast	Sub-ballast	Geocell	Prepared subgrade	Subgrade
Elastic modulus (MPa)	200,000	30,000	150	60, 80, 100	100	40	25, 30, 35
Poisson's ratio	0.27	0.2	0.35	0.32	0.35	0.49	0.49
Cohesion (kPa)	–	–	0.1	0.1	–	8	8
Friction angle (°)	–	–	47	41	–	0.1	0.1
Thickness (m)	0.136	0.21	0.35	0.6	0.002	0.5	2
Length (m)	4.55	1.375	–	–	–	–	–

size 0.5 m × 0.5 m was prepared with the required diamond shape over the surface of the foundation soil. It was then extruded as a solid element of required height. The small cohesion of the ballast and sub-ballast layers and the friction angle of the subgrade and prepared subgrade layers were only to avoid numerical instability. The modulus values of sub-ballast and subgrade were varied for parametric studies on prototype tracks.

2.2 Meshing and Boundary Conditions

The running length of track considered was 4.55 m. After modeling geometry, an auto-mesh generation option was used which generated mesh for the entire model. An
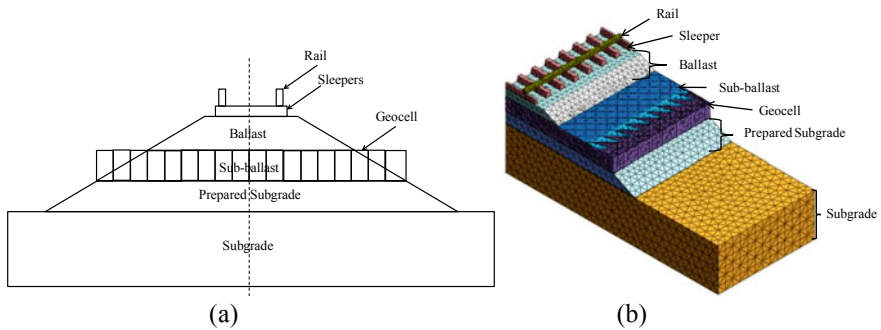
Fig. 1 **a** Cross-sectional diagram of the track **b** mesh generated for prototype model tracks

option of adaptive seeding was used for meshing which is available in [9]. Figure 1 shows the cross-sectional diagram of the track and the model track after meshing.

Roller supports were applied to the faces which were vertical while sloping faces were not assigned any boundary conditions. Bottom of the subgrade was assigned fixed support. A double-wheel load of 325 kN with dynamic magnification factor of 1.5 was applied, meaning that the load applied to each wheel was 243.75 kN. The other parameters controlling computation were left to their default values, except the displacement norm which was changed to 0.01.

3 Results and Discussions

3.1 Vertical Displacements

The load–displacement curves for the prototype tracks with varying sub-ballast modulus are shown in Fig. 2.

From Fig. 2, it can be observed that for the geocell reinforced track layer with same material properties as that of unreinforced track, a reduced displacement of 39% can be achieved for the same axle load applied. For the same model, increasing the sub-ballast modulus to 100 MPa further reduced the vertical displacement by 4.2%. When the sub-ballast modulus was decreased to 60 MPa for the geocell reinforced track, the reduction in displacement over unreinforced track also decreased to 31.8%. This clearly shows that improvement in vertical displacement depends on the sub-ballast modulus. The results also show that geocell reinforced tracks show a much-reduced vertical displacement as compared to the unreinforced track for the same axle load applied.

Figure 3 shows the load–displacement curves for the prototype tracks with varying subgrade modulus. It was observed that for the same applied axle load, using geocell for the track with same material properties, 39% reduction in vertical displacement

Fig. 2 Load–displacement curves for unreinforced and geocell reinforced tracks of varying sub-ballast modulus
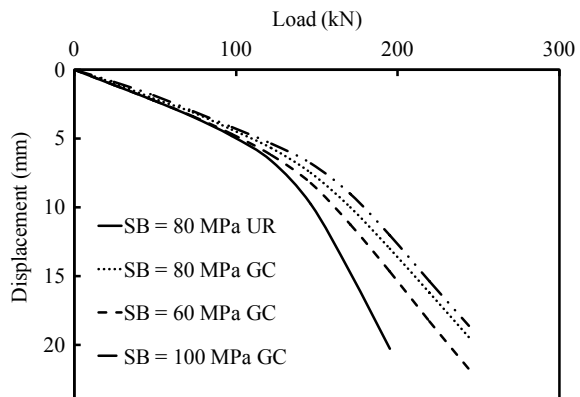
Fig. 3 Load–displacement curves for unreinforced and geocell reinforced tracks of varying subgrade modulus
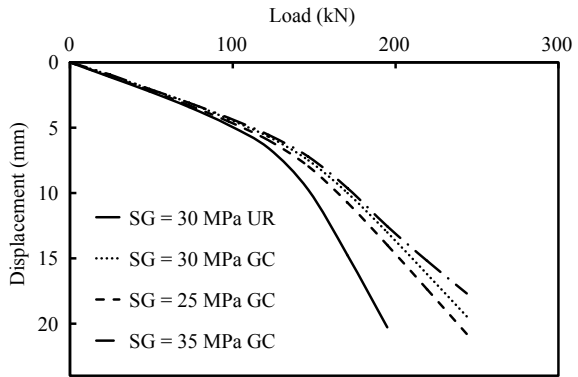
could be achieved over unreinforced track. For the geocell reinforced tracks, further 9% reduction in displacement could be achieved by increasing the subgrade modulus to 35 MPa. When the subgrade modulus of the geocell reinforced track was decreased to 25 MPa, reduction in displacement over unreinforced track also decreased to 35%. The vertical displacements are thus affected both by the subgrade and sub-ballast modulus, even for tracks reinforced with geocell of same material properties.

Figure 4 shows the vertical displacement contours obtained for the entire track model. These contours show that the extent of vertical displacement can be reduced to a great extent using geocell for the track with similar properties as that of unreinforced track.
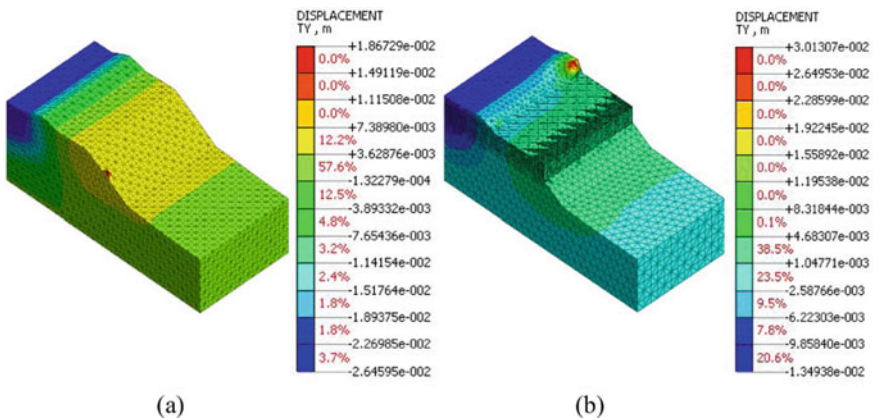
Fig. 4 Vertical displacement contours for **a** unreinforced and **b** geocell reinforced tracks of subgrade modulus = 30 MPa

3.2 Vertical Stresses

Figure 5 shows the vertical stresses with depth for the unreinforced as well as geocell reinforced tracks with varying sub-ballast modulus.

It can be observed that for geocell reinforced tracks with material properties similar to unreinforced tracks, 7% reduction in ballast vertical stresses could be achieved over unreinforced tracks. For sub-ballast layer, 28.2% reduction in vertical stress could be achieved. For prepared subgrade and subgrade layers, 44.5 and 66.9% reduction in vertical stress could be achieved. An increase in sub-ballast modulus further reduced the vertical stresses of individual track layers, while decrease in sub-ballast modulus increased the vertical stresses generated at the top of each layer.

Figure 6 shows the vertical stresses with depth for the unreinforced as well as geocell reinforced tracks with varying subgrade modulus. For geocell reinforced tracks with subgrade modulus of 35 MPa, 4.3% reduction in ballast stress was observed over tracks with subgrade modulus 30 MPa. Similarly, for sub-ballast,

Fig. 5 Vertical stress with depth curves for unreinforced and geocell reinforced tracks of varying sub-ballast modulus
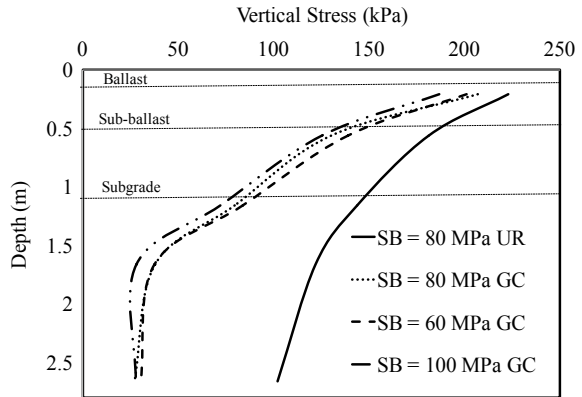
Fig. 6 Vertical stress with depth curves for unreinforced and geocell reinforced tracks of varying subgrade modulus
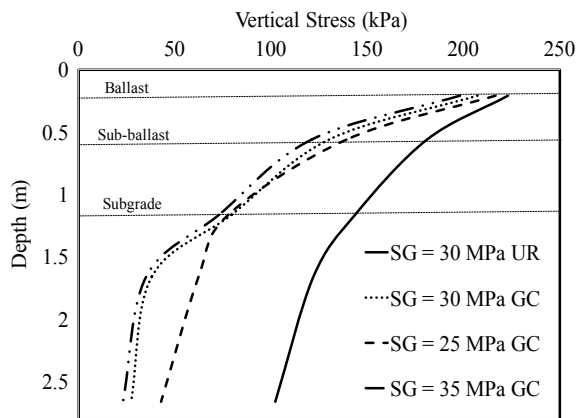
33.1% reduction in vertical stress was achieved. The prepared subgrade and subgrade layers showed further reduction in vertical stress of 49.2 and 71% when the subgrade modulus was increased from 30 to 35 MPa.

It was also observed that decreasing the subgrade modulus affected the stress on subgrade layer as when the subgrade modulus was lowered from 30 to 25 MPa, the subgrade stress increased by almost 39%. The stresses on other layers were much less affected in the range of 2–7%. Figure 7 shows the vertical stress contours for the entire track model for the same subgrade modulus with geocell can be improved as compared to unreinforced track.
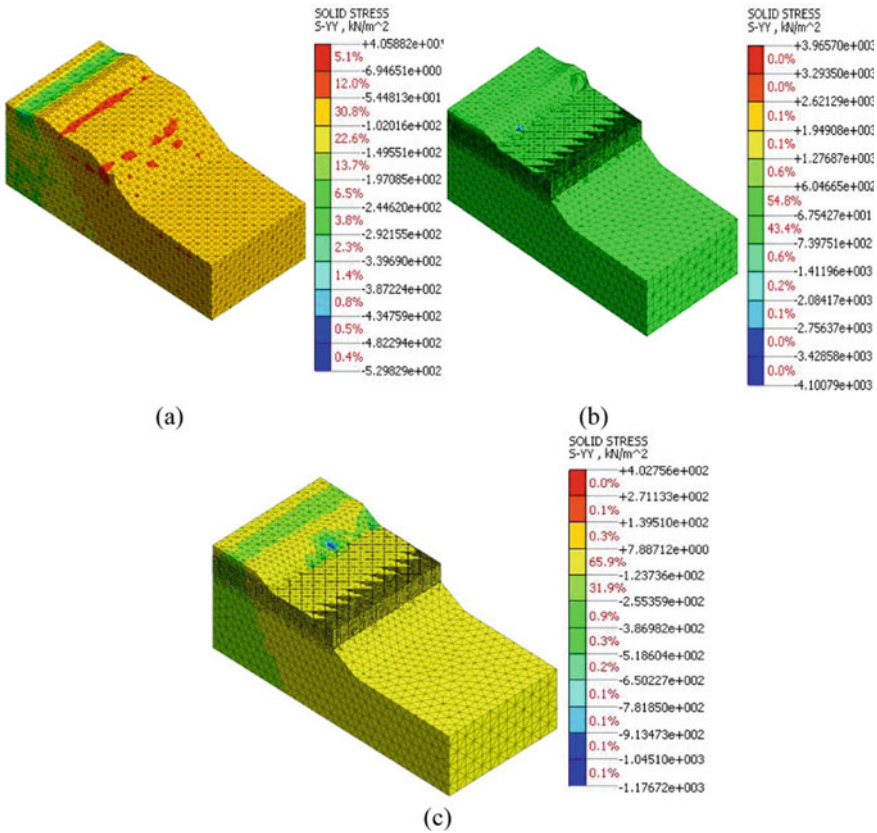
Fig. 7 Vertical stress contours for **a** unreinforced and **b** geocell reinforced tracks of subgrade modulus = 35 MPa **c** geocell reinforced tracks of subgrade modulus = 30 MPa

4   Conclusions

In the present study, the effectiveness of geocell in improving the vertical displacements and stresses were observed over unreinforced tracks using three-dimensional track models. The sub-ballast and subgrade modulus were varied to study the effect of these parameters on displacements and stresses. It was observed that increasing the sub-ballast or subgrade modulus of tracks with geocell having same material properties leads to reduction in vertical displacements and stresses of all the track layers. While a decrease in sub-ballast modulus increases the stresses on all track layers almost by equal margin, a decrease in subgrade modulus increases the stresses on subgrade more than that for other track layers.

References

1. Brown SF, Kwan J, Thom NH (2007) Identifying the key parameters that influence geogrid reinforcement of railway ballast. Geotext Geomembr 25(6):326–335
2. Chawla S, Shahu JT (2016) Reinforcement and mud-pumping benefits of geosynthetics in railway tracks: model tests. Geotext Geomembr 44(3):366–380
3. Fernandes G, Palmeira EM, Gomes RC (2008) Performance of geosynthetic reinforced alternative sub-ballast material in a railway track. Geosynth Int 15(5):311–321
4. Indraratna B, Nimbalkar S (2013) Stress-strain degradation response of railway ballast stabilized with geosynthetics. J Geotech Geoenviron Eng 139(5):684–700
5. Dash SK, Sireesh S, Sitharam TG (2003) Model studies on circular footing supported on geocell reinforced sand underlain by soft clay. Geotext Geomembr 21(4):197–219
6. Sitharam TG, Sireesh S (2005) Behavior of embedded footings supported on geocell reinforced foundation bed. Geotech Test J 28(5):452–463
7. Zhang L, Zhao M, Shi C, Zhao H (2010) Bearing capacity of geocell reinforcement in embankment engineering. Geotext Geomembr 28(5):475–482
8. Krishnaswamy NR, Rajagopal K, Madhavi Latha G (2000) Model studies on geocell supported embankments constructed over a soft clay foundation. Geotech Test J 23(1):45–54
9. Midas (2016) Midas/GTS-NX (geotechnical and tunnel analysis system) reference manual for modeling, integrated design and analysis. Midas Corporation
10. RDSO (2007) Guidelines for use of geosynthetics on railway formation including specifications. Indian Railways
11. Sowmiya LS (2013) Analysis and experimental investigations of railway tracks with and without geosynthetic reinforcement. Ph.D. thesis, Indian Institute of Technology, Delhi, India
12. Banerjee L, Chawla S, Dash SK (2018) Finite element modeling of geocell reinforced tracks. In: Advanced construction and computational tools in geotechniques—practice to theory. Indian Geotechnical Society, Kolkata Chapter, 27–28 July 2018
13. Banerjee L, Chawla S, Dash SK (2018) Three-dimensional finite element analyses of geocell reinforced railway tracks. In: Proceedings of Indian geotechnical conference, IGC-2018, IISC Bengaluru, 13–15 Dec 2018
14. Banerjee L, Chawla S, Bhandari G (2019) Experimental and 3-D finite element analyses on geocell-reinforced embankments. J Test Eval 47(3):1876–1899

15. Banerjee L, Chawla S, Bhandari G (2019) Performance of geocell reinforced embankment over soft soil deposit. In: Proceedings of the current geotechnical engineering aspects of civil infrastructures, China, pp 69–82

The Use of Draintube Drainage Geocomposites Under Railway Infrastructures

Stephan Fourmont and Mathilde Riot

Abstract Railway construction involves substantial earthworks (embankments and cuttings). Cuttings may reach the water table, and embankments may need preloading when on soft soils. Even during operation of the railway line, the ballast put into place under the railways undergoes densification and degradation over time which reduces the hydraulic conductivity of the material. This phenomenon may affect the durability of the structure if the ballast is not able to evacuate the water during heavy rainfall, flooding or snowmelt. Drainage systems for soil water were traditionally made with granular material layers and perforated collector pipes, one of the main reasons being the ability of that system to support heavy loads over time. As their flow capacity is not load or time-sensitive when confined in soil, drainage geocomposites with mini-pipes Draintube are often used instead of the granular drainage layers. At the different stages of the railway construction, it protects the cuttings against high water table, decreases the time for consolidation on soft soils and increases the overall drainage capacity of the system under ballast. It also allows the use of Hydraulically Bound Materials (HBMs) on top of it. This publication presents a case study for each application, along with the related laboratory study or on-site monitoring. Drainage geocomposites with mini-pipes have been successfully used for 30 years; the product is designed for each project function of the specific site conditions. It requires less machinery to install and reduces the Greenhouse Gas (GHG) emissions compared to a granular material solution.

Keywords Drainage · Geocomposite · Railways

S. Fourmont (✉)
Afitex-Texel Geosynthetics inc., 1300, 2e Rue Parc Industriel, Sainte-Marie, QC G6E 1G8, Canada
e-mail: sfourmont@afitextexel.com

M. Riot
Afitexinov, 13-15 Rue Louis Bleriot, 28300 Champhol, France
e-mail: mathilde.riot@afitex.com

1   Introduction

Drainage systems for soil water were traditionally made with granular material layers and perforated collector pipes. The use of drainage geocomposites becomes more common with the development of products that meets the specific requirements of each application. Moreover, the geosynthetic solution is cheaper than the granular material (for the same performances) in the majority of applications. It is faster to install, requires less machinery and reduces the Greenhouse Gas (GHG) emissions of the project [1]. Like any engineering solution, drainage geocomposites must be well selected and designed for the specific site conditions. In railway infrastructures, drainage geocomposites with mini-pipes are used as lateral drainage on vertical wick drains under preloading embankments, directly under the tracks to increase the drainage capacity of the ballast or in cuttings to intercept high water tables. These three applications will be developed in the following paragraphs based on case studies and laboratory tests.

2   Multi-linear Drainage Geocomposites

2.1   Geocomposite Description

Drainage geocomposites with mini-pipes Draintube have been used in civil engineering and more especially in earthworks projects for 30 years. They are multi-linear drainage geocomposites (terminology as per ASTM D4439 [2]) composed of non-woven geotextiles that are needle-punched together with perforated, corrugated polypropylene mini-pipes regularly spaced inside and running the length of the roll (see Fig. 1).
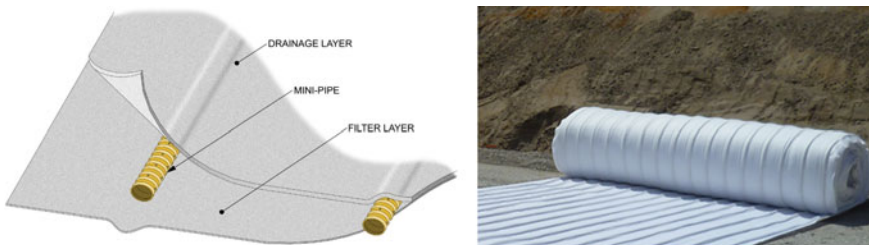
Fig. 1 Geocomposite description
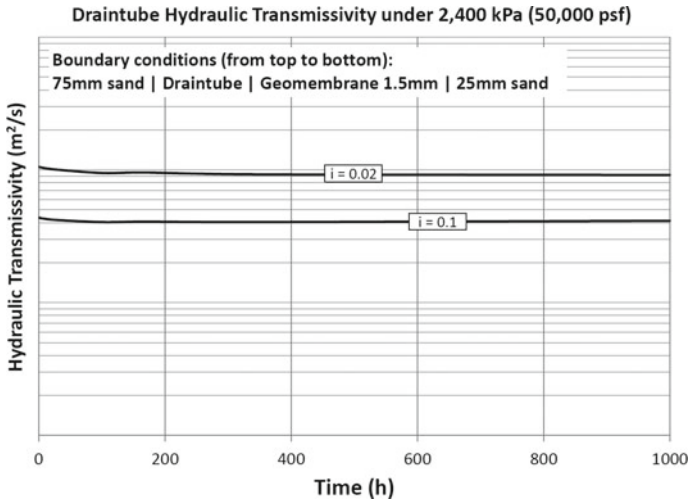
Fig. 2 Drainage capacity of the multi-linear drainage geocomposite over time

2.2 Hydraulic Characteristics

The drainage capacity of the product is driven by the number of mini-pipes within the product. There is a linear relationship between the distance between the mini-pipes and the transmissivity of the overall product [3, 4]. It has also been shown that the flow capacity of the multi-linear drainage geocomposite is not load or time-sensitive when confined in soil [5]. Figure 2 shows results of hydraulic transmissivity tests (ASTM D4716 [6]) carried out on the product compressed under a load of 2400 kPa (50,000 psf) which represents a 120 m (390 ft) high soil embankment.

2.3 Mechanical Characteristics

Mechanical properties of the drainage geocomposite must be selected as a function of the drainage application, the installation conditions and the soil in which the product is in contact. Draintube drainage geocomposite is made with adapted short-staple fibers geotextiles, from 200 g/m^2 (6 oz/sy) to 900 g/m^2 (26 oz/sy) or above. The elongation at break of the product is always greater than 50% (ASTM D4632 [7]), making the product flexible to provide a good connection with the subgrade soil when installed. The polypropylene mini-pipes have a pipe stiffness at 5% deflection over 3000 kPa (435 psi) (ASTM D2412 [8]).

3 Drainage Under Embankment on Soft Soils

3.1 Project Description

One of the High-Speed Lines (HSL) constructed in France in 2008 (LGV-Rhin Rhône), crossed numerous compressible areas as well as bridges that required the construction of preloading embankments in conjunction with surcharging to accelerate the expected settlements of the subgrade. These preloading embankments included vertical wick drains with a multi-linear drainage geocomposite on top as a horizontal drainage base layer. The major preloading embankments were 7.5 m (25 ft) high and more than 40 m (130 ft) wide. Subgrade was composed of loess on the first 4 m (13 ft), sandy soil from 4 m (13 ft) to 6.5 m (21 ft) then clayey soil from 6.5 m (21 ft) to 11 m (36 ft).

Expected settlements were estimated to be from 40 to 90 mm (1–1/2 to 3–1/2 in.) from geotechnical identification of the subgrade soil layers. The length of the vertical drains was set at 11 m (36 ft) with a square grid of 1.2 m × 1.2 m (4 ft × 4 ft). The multi-linear drainage geocomposite was unrolled directly on the wick drains.

3.2 Completion of Works

After the removal of the topsoil layer, the vertical wick drains were driven into the ground as required as described in Fig. 3.

The multi-linear drainage geocomposite was unrolled perpendicularly to the railway line and overlapped the wick drains (Fig. 4). The mini-pipes of the product have a spacing of 0.50 m (20 in.) center-to-center. The geocomposite collects the

Fig. 3 Installation of the vertical wick drains

Fig. 4 Drainage geocomposite installation

water from the wick drains and drains it to ditches on each side of the embankment. Backfilling soil was placed directly on the drainage geocomposite to the final level.

3.3 Monitoring and Results

The sub-base was monitored using profilometers to measure settlements over time and choose the right moment to remove the overload. Examples of settlement measurement values are indicated in Fig. 5.

The measured settlements did not exceed 40 mm (1–1/2 in.), which was lower than the estimated limit, and the effective consolidation time was about 3 months.

The use of a multi-linear drainage geocomposite for horizontal drainage instead of a granular layer offered consistent performances and reduced the cost of the preloading embankment construction as granular material should have been extracted and transported from the carrier to the site resulting in a heavy truck traffic in and around the worksite. In comparison, one full truck can carry enough multi-linear drainage geocomposite to cover an area of approximately 10,000 m^2 (approx. 100,000 sf).
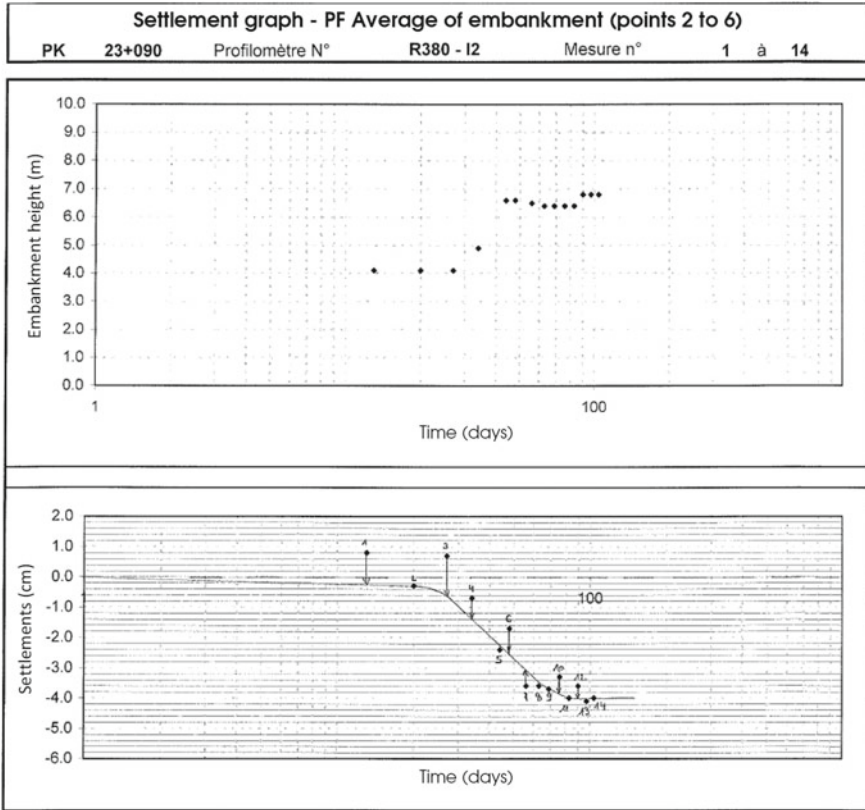
Fig. 5 Example of the subgrade settlements over time

4 Cut Sections

Cut sections involved large and high slopes to get stability and avoid landslides. In case of groundwater infiltrations or high water table, the use of drainage masks with granular material implies to carry and install a large amount of materials. The use of a drainage geocomposite for subsurface drainage reduces that need for granular material.

4.1 Installation

The Draintube drainage geocomposite is unrolled directly on the subgrade with the mini-pipes in the direction of the slope. It is anchored on top of the slope and

Fig. 6 Drainage mask construction with drainage geocomposite

connected to a French drain at the toe. The backfill is then placed on top of the product from the bottom to the top (Fig. 6).

The drainage geocomposite does not provide additional strength resistance for the stability of the slope. But due to the non-woven needle-punched geotextile layers of the product, the geocomposite/soil interface angle is generally the same as the internal friction angle of the soil in contact.

4.2 Monitoring and Results

On a new HSL constructed from 2013 in France (LGV Est), monitoring has been conducted to evaluate the two solutions: drainage layer made with granular material and made with multi-linear drainage geocomposite. Two areas of 525 m^2 (5650 sf.) each have been monitored with temperature sensors, water content gauges at the interface, and flowmeters [9]. Details are shown in Fig. 7. The mini-pipes of the product have a spacing of 0.50 m (20 in.) center-to-center.

The water content monitoring for both solutions is shown in Figs. 8 and 9. It can be observed that the water content remains stable between 20 and 40% at the gravel/soil interface and between 20 and 27% at the geocomposite/soil interface. Both drainage systems perform well, keeping the soil above unsaturated even during rain events.
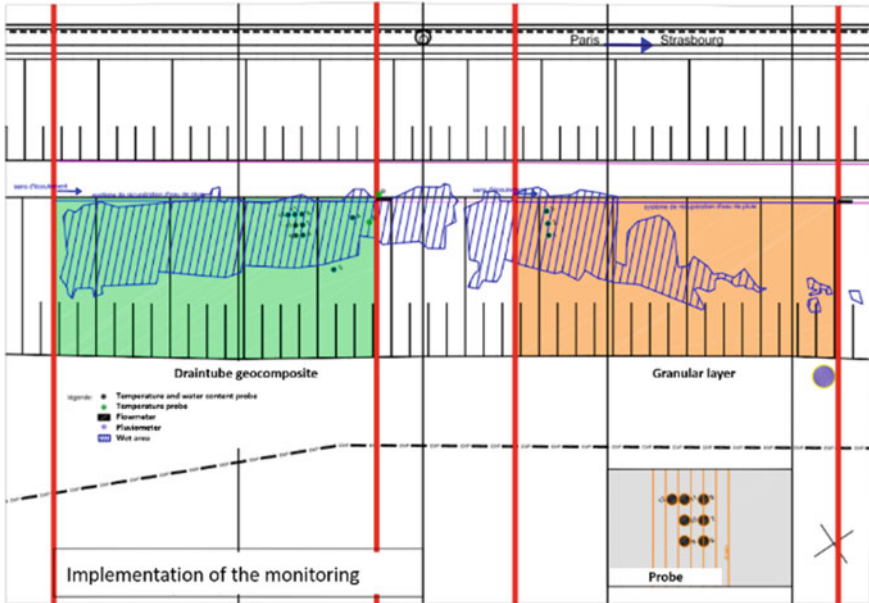
Fig. 7 Probes implementation (plan view)
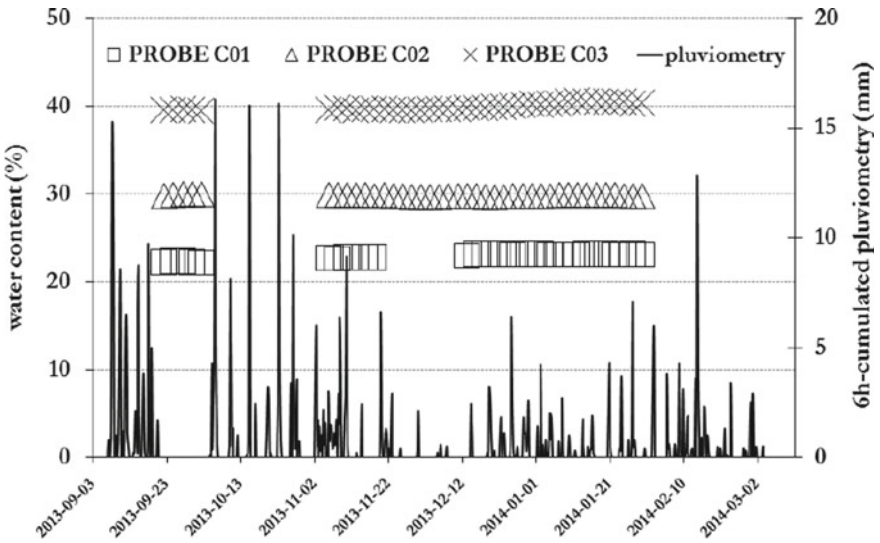
Fig. 8 Water content at gravel/soil interface
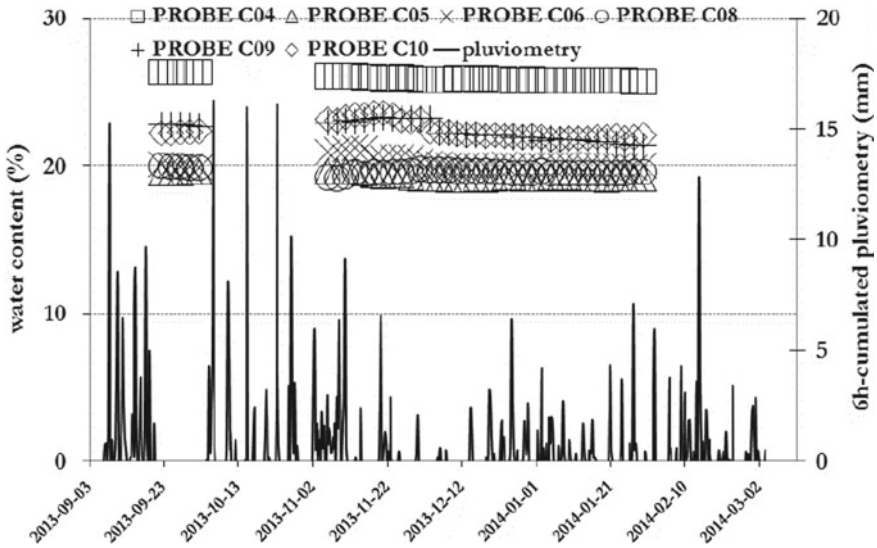
Fig. 9 Water content at geocomposite/soil interface

5 Drainage Improvement Under Railways

5.1 Project Description

Within the scope of work for some track reconfigurations, alternative drainage systems are used, given the limited space available in some track corridors. A drainage geocomposite with mini-pipes can be used in order to efficiently evacuate the water from below the tracks. The mini-pipes are brought to a ballast drain or an open ditch.

A Canadian National Railways project located in Quebec in 2016, required two tracks to be drained into either an open ditch or a ballast drain installed approximately 1 m (3 ft.) below track level. Without a proper drainage system, potential drainage problems and a shortened life for the ballast would occur. The multi-linear drainage geocomposite was placed directly under the ballast (Fig. 10). The mini-pipes in the product had a spacing of 0.25 m (10 in.) center-to-center.

5.2 Completion of Works

The multi-linear drainage geocomposite was unrolled perpendicular to the tracks directly on the MG-56 subgrade soil (Fig. 11). After which the ballast was installed in two layers of 150 mm (6 in.) each (Fig. 12).
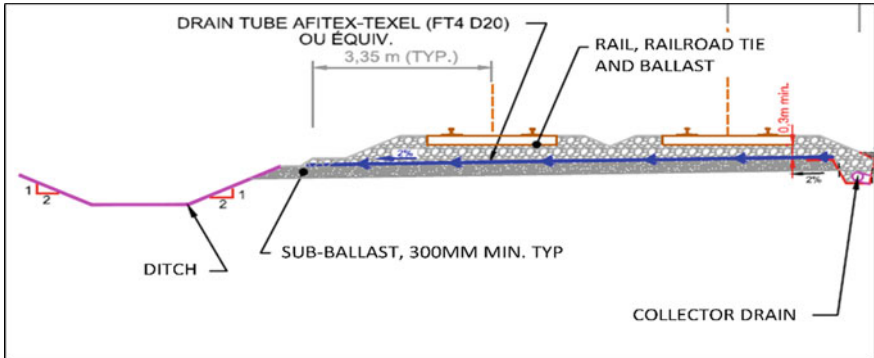
Fig. 10 Typical cross-section

Fig. 11 Installation of the draintube drainage geocomposite

The product was designed to have the ability to evacuate rainfall of 661 mm/day with the mini-pipes staying unsaturated [10]. The 100 years return period rainfall in Quebec is 156 mm/day. The drainage capacity of the drainage geocomposite is more than 4 times greater than what is required, taking into account the long-term hydraulic behavior of the geocomposite under the critical conditions of the application.

Fig. 12 Backfilling of the product with ballast

5.3 Laboratory Study

Using a 2.5 m (8 ft) long and 2 m (6–1/2 ft) wide inclinable open box with rainfall simulator on top (Fig. 13), it was shown that multi-linear drainage geocomposite Draintube enables rainfall to evacuate faster than a homogeneous drainage layer (Fig. 14) [11]. Due to the directional aspect of the product, the water is indeed

Fig. 13 Inclinable open box with a rainfall simulator

Response time Draintube vs Granular layer
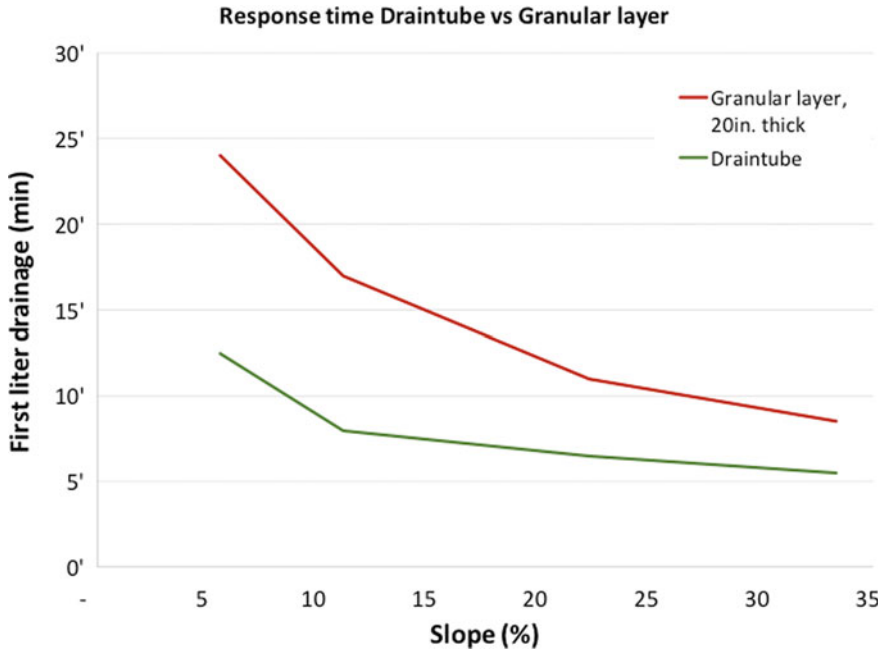
Fig. 14 Drainage response time drain tube versus granular layer

drained into the direction of the mini-pipes even in the situations when the slope is zero.

That behavior is significant for low slopes, where the rainfall water must be evacuated rapidly before building up into the overlying layer or infiltrating into the subgrade.

6 Conclusion

Multi-linear drainage geocomposites Draintube have been used successfully on many earthworks projects and more especially on railways construction projects. Depending on the project and the design consideration, it is used either for drainage under embankments and subsurface drainage on cut slopes as a replacement of the granular layers, or for drainage improvement under railway tracks.

Its useful characteristics, from an installation point of view, are its flexibility and robustness. The main benefits of using Multi-linear drainage geocomposite is that there is no creep or geotextile intrusion over time and under load. Its composition with a dense network of perforated mini-pipes between two geotextiles gives to the product a high drainage capacity, a short drainage response time even for low slopes and a high

mechanical resistance. All this makes the Draintube drainage geocomposite efficient and safe to use in replacement of drainage layers made with granular material.

References

1. Durkheim Y, Fourmont S (2010) Drainage geocomposites: a considerable potential for the reduction of greenhouse gas emission. In: 9th International conference on geosynthetics, Guaruja, Brazil
2. ASTM D4439. Standard terminology for geosynthetics. American Society for Testing and Materials, West Conshohocken, PA, USA
3. Blond E, Saunier P, Daqoune T, Fourmont S (2013) Assessment of the effect of specimens dimensions on the measured transmissivity of planar tubular drainage geocomposites. GeoMontreal 2013, Montreal, Canada
4. GRI Test Method GC15. Determining the flow rate per unit width of drainage geocomposites with discrete high flow components. Geosynthetic Institute, Folsom, PA USA
5. Saunier P, Ragen W, Blond E (2010) Assessment of the resistance of drain tube planar drainage geocomposites to high compressive loads. In: 9th International conference on geosynthetics, Guarujá, Brazil, vol 3
6. ASTM D4716. Standard test method for determining the (in-plane) flow rate per unit width and hydraulic transmissivity of a geosynthetic using a constant head. American Society for Testing and Materials, West Conshohocken, PA, USA
7. ASTM D4632. Standard test method for grab breaking load and elongation of geotextiles. American Society for Testing and Materials, West Conshohocken, PA, USA
8. ASTM D2412. Standard test method for determination of external loading characteristics of plastic pipe by parallel-plate loading. American Society for Testing and Materials, West Conshohocken, PA, USA
9. Heili V, Benamu D, Gendrin P, Godon V, Thomas D (2014) Experiment of the use of geosynthetics for the drainage in place of draining masks. In: Hydraulic properties and sustainability, 10 ICG, Berlin, Germany
10. Ruel M, Rodger D, Fourmont S (2018) Drainage improvement under CN railways with the use of a multi-linear drainage geocomposite. GeoEdmonton 2018, Edmonton, Canada
11. Del Greco O, Fey A, Oggeri C, Fourmont S (2012) Behaviour of drainage geosynthetics for landfill capping systems. In: 5th European geosynthetics congress, Valencia, Spain, vol 2, pp 114–118 (2012)

Rapid Pavement Roughness Measurement of Geogrid-Stabilized Roads

Prajwol Tamrakar, Mark H. Wayne, Garrett Fountain, Aaron Schlessinger, and Coady Cameron

Abstract Sophisticated computer-based pavement condition assessment methods are growing and replacing manual pavement condition assessment methods. The benefits of such computer-based pavement condition assessment methods are rapid data collection, efficient data management, wide coverage, repeatable measurements and low cost. The TotalPave system, a smartphone-based pavement roughness measurement system, uses the phone's accelerometer to record time histories of vehicle motion and estimates the pavement International Roughness Index (IRI). The aim of this study is to implement the TotalPave system for rapid IRI measurement of geogrid stabilized roads, to develop a georeferenced database of pavement IRI and to monitor the road performance over time. The TotalPave surveys were conducted on a section of West Hunt Highway in Arizona. The measured pavement IRI was evaluated and compared with the Standard IRI specified for such highways. Further, the predicted IRI from a numerical pavement model was also compared with the measured IRI.

Keywords Pavement roughness · IRI · Geogrid stabilization

1 Introduction

Aging effects on pavements, caused by extensive traffic loadings and climatic fluctuation, are reflected by the presence of different kinds of surface distresses. Such distresses are responsible for degrading the pavement condition and severely affecting pavement performance. Pavement condition assessment procedures offer an opportunity to access existing functional and structural characteristics of pavement [1]. A well-functioning pavement has smooth ride quality and is free of visual distress.

P. Tamrakar (✉) · M. H. Wayne · G. Fountain · A. Schlessinger
Tensar International Corporation, 2500 Northwinds Pkwy, Suite 500, Alpharetta, GA 30009, USA
e-mail: ptamrakar@tenarcorp.com

C. Cameron
Total Pave Inc., 2 Garland Court, Fredericton, NB, Canada

599

Road users, like drivers, are typically concerned with functional characteristics. On the other hand, the structural characteristics refer to the internal stability of the pavement system.

Transportation-related agencies, such as the State Department of Transportations (DOTs), local transit authorities, public works or street maintenance offices of cities, are concerned with both structural and functional pavement distresses. These agencies rely on pavement condition information for identifying and prioritizing transportation projects for maintenance and rehabilitation, allocating budgets and planning for new construction [2]. Similarly, the National Highway Performance Program (NHPP) utilizes pavement condition data such as International Roughness Index (IRI), percent cracking, rutting, and faulting for developing transportation plans.

Pavement management system (PMS), developed from pavement condition information, are also popular among transportation agencies for cost-effective management of a pavement system [3]. At the network level, the use of PMS provides an overall status of the existing road network. At the project level, the pavement condition assessment is a useful tool for in-detail evaluation of pavement sections. Regular pavement condition assessment helps in tracking pavement performance, identifying deteriorated pavement sections and providing necessary preventive measures. Other uses of pavement condition assessment are understanding the benefits of newly implemented technologies such as the use of new types of asphalt concrete mixes, composite pavement sections or geosynthetic stabilized sections [4].

The serviceability of any road network is directly influenced by the presence of distresses and the surface roughness. The most common types of pavement distress are cracks in different forms as described by Miller and Bellinger [5]. ASTM D6433 recommends using Pavement Condition Index (PCI) as an indicator of pavement performance based on the level of pavement distress. During traffic loadings, load-transfer mechanisms are disrupted due to the presence of cracks which result in the localized concentration of stresses. Additionally, the cracks allow moisture to penetrate the base/subbase layers and subgrade. Moisture has severe detrimental effects on the mechanical characteristic (stiffness) of bases and subgrade [6, 7]. The ultimate effect of pavement distresses can be experienced through the vehicle ride quality. The ride quality can be quantified in terms of pavement roughness such as Present Serviceability Rating (PSR) and IRI. American Association of State Highway Officials (AASHO) developed the PSR method in the 1960s whereas the World Bank introduced the IRI method in the 1980s.

ASTM E1926 describes the method for obtaining pavement IRI using the longitudinal road profiles. An IRI is a standardized measure of the reaction of a vehicle to roadway profile and roadway roughness that is expressed in "inches per mile" or "meters per kilometer". The typical IRI threshold limits [8] for different types of new pavement are shown in Table 1. Common devices used for measuring pavement roughness are Profilometer, Profilograph, Roughometer and Ridemeter [9].

In recent years, several sophisticated technologies were developed for automating pavement condition assessment procedures [10–12]. The use of advanced sensors for data collection and a complex computer algorithm for data analysis helped in

Table 1 Typical IRI threshold limits for new pavement

| | New pavement IRI (m/km) limits | | |
	Freeways	Arterials/Collectors	Local roads
Good	≤ 1.26	≤ 2.53	≤ 2.84
Acceptable	1.27–2.53	2.54–4.73	2.85–5.52

evaluating pavement condition cost-effectively and rapidly. The TotalPave system is one of the technologies for measuring pavement IRI.

This paper presents the result of TotalPave surveys conducted on the geogrid stabilized pavement and shows the spatial distribution of pavement IRI. Further, the measured IRI is also compared with the predicted IRI obtained from the numerical pavement model.

2 Project Location

The project site is located in Pinal County, Arizona, located about 50 km south-east of Phoenix Sky Harbor International Airport (see Fig. 1). The test section is about 10 km long, extending from Magma Rd to Thomson Rd. As per Arizona Department of Transportation's Transportation, the typical two-way Annual Average Daily Truck Traffic (AADTT) for the study site ranges between 3000 and 4000. The pavement was newly constructed in 2016 and was in service since then.

The pavement cross-section consisted of 125 mm of asphalt concrete and 150 mm of unbound granular base over subgrade. The base material was classified as GP-GM (USCS) and A-1-a (AASHTO). The maximum particle size of base material was 38 mm with about 5.7% fines (particles passing sieve 200). The subgrade modulus was about 103 MPa. The TX5 multi-axial geogrid was placed at the interface between base and subgrade (see Fig. 2). Table 2 presents the geogrid properties.

For this project, a multi-axial geogrid was selected based on the site condition and aggregate material type. The triangular apertures of multi-axial geogrids have much more uniform stress and strain distributions than the traditional biaxial geogrid with rectangular apertures [13]. Under traffic loadings, triaxial geogrid is more effective and efficient in distributing stresses in all directions [14–21]. Placing such multi-axial geogrids at the interface between base and subgrade creates a mechanically stabilized layer which improves the strength and stability of the pavement system. One of the benefits of such mechanical stabilization is the preservation of material stiffness for a longer period. The mechanical stabilization also offers an opportunity for pavement designers to optimize pavement layers to attain the same or higher targeted pavement performance [4].

Fig. 1 Study site

3 APLT Validation

Automated plate load testing (APLT, see Fig. 3) [17] was utilized to measure in-situ performance and confirm design requirements for this project during the construction phase. Using APLT, stress-dependent resilient modulus of unbound aggregate layers and composite modulus were measured at different locations. For the 1000 cycle APLT tests, results showed that the in-situ composite resilient modulus in the geogrid stabilized section was about 236 MPa at 330 kPa cyclic stress. The layered analysis results estimated that an average resilient modulus of 1073 MPa for the aggregate base layer and 111 MPa for the subgrade layer. These results indicated that the in-situ material stiffness exceeds the predicted (design) stiffness. Further, permanent deformation tests were also conducted to estimate the rutting resistance of the pavement. The pavement experienced about 2 mm permanent deformation after application of 10,000 load cycle at 330 kPa cyclic stress to increase at a slower rate. Based on a permanent deformation rate of 0.0025 mm/cycle the transition from plastic deformation accumulation to near-linear elastic occurs at $N^* = 8696$ cycles.

Fig. 2 Pavement construction

Table 2 Properties of geogrid

Parameter	Description
Geogrid	TX5 Multi-axial geogrid
Rib shape	Rectangular
Aperture shape	Triangular
Rib pitch	40 mm longitudinal and diagonal

Here N^* represents the cycle number at which the application of addition cyclic loadings results in very low accumulation of additional permanent deflection and the composite foundation layers are producing a resilient response. At N^* cycles and the associated permanent deformation, a stable equilibrium response from loading is anticipated [22].

4 TotalPave System

Currently available smartphones consist of several built-in sensitive sensors including an accelerometer. The accelerometer measures phone acceleration in x-, y- and z-directions, and determines motion and orientation of the phone. Such features are essential for map navigation, landscape or portrait display and so on. Several

Fig. 3 Automated plate load testing (APLT)

researchers [23, 24] had utilized smartphone-based acceleration data for capturing vehicle motion, estimating longitudinal road profile, and hence, measuring pavement IRI. As the manual steps involved in operating road profilers are replaced by the automated procedures through built-in functions of smartphones, the researchers had to overcome several challenges such as filtering unwanted signals due to vehicle damping, considering the effects of different models of phone and vehicles, adjusting the signal filtering window based on the sensitivity of the accelerometer and so on [25].

The IRI data collection technology for this project was developed by TotalPave Inc. The principles behind the TotalPave system are explained by Cameron [12]. This

system is calibrated against the standard profiler using different types of smartphones and vehicles [23]. The data collection process is fully automated. The user needs to mount a smartphone with a TotalPave IRI Calculator app to the vehicle's windshield. The mounting device should be sturdy so that the motion detected by the smartphone is totally from the vehicle. The TotalPave app allows users to level a smartphone vertically which helps to accurately detect motions in x-, y- and z-directions. The app collects data when the vehicle speed is more than 20 kmph. The app also collects GPS data along with the acceleration data for proper positioning and displaying of IRI data within the map. The system analyzes the raw acceleration data and estimates pavement IRI. Using the web portal, users can view the IRI data plotted on the map. Recently, several studies were conducted by utilizing TotalPave technology [26–28].

5 Presentation of Results

TotalPave surveys were conducted on both northbound lanes (left and right) of West Hunt Highway in 2019. The surveys were completed within 30 min which was significantly faster than the data collection procedure by a standard profiler. Figure 4 provides the average IRI of the pavement segments for both lanes through the color-coded map. Each segment is 50 m in length. The legend in the figure represents the IRI ranges. Such a map provides a spatial distribution of pavement IRI and shows the location of possible problematic area (i.e., the pavement segment with a high IRI value). The map shows that most of the pavement sections have an IRI value less than 1.5 m/km.
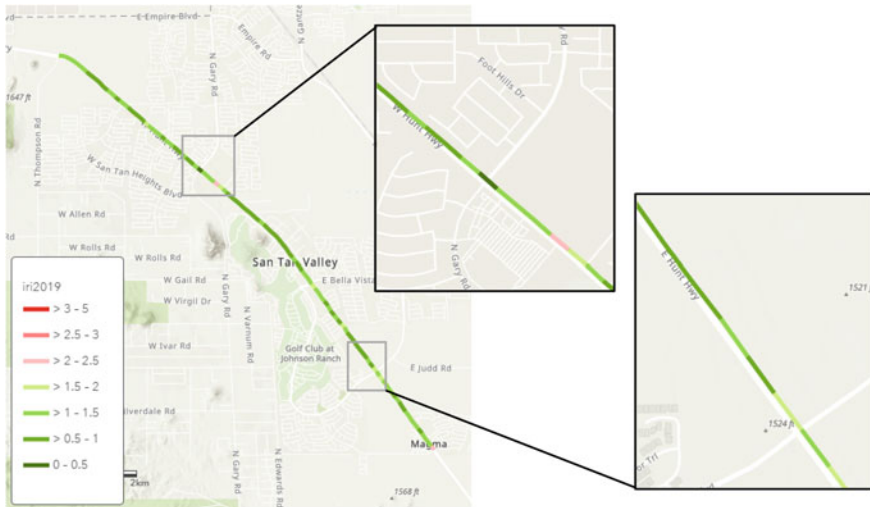
Fig. 4 IRI map
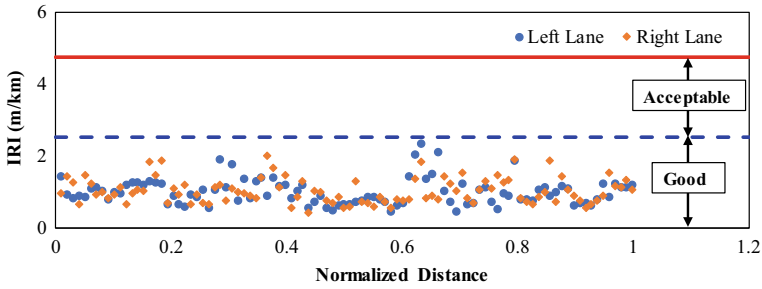
Fig. 5 Pavement IRI for left and right lanes

Figure 5 provides the distribution of pavement IRI based on the normalized distance. The normalized distance was computed using the actual distance of IRI measurement divided by the total survey distance. The starting location of the normalized distance was the intersection of West Hunt Highway and Magma Rd. Although the figure illustrates some variations in pavement IRI for left and right lanes, all IRI measurements are in the good range as specified by Arhin et al. [8].

To understand the overall condition of the pavement, the IRI values shown in Fig. 5 are averaged and presented in Fig. 6. The figure shows the distribution of IRI for each pavement section along the longitudinal direction of the roadway. Each pavement section is 1 km long (see Fig. 6). The IRI data were presented for an average of both lanes, left and right lanes. Sections 4, 7 and 8 consisted of moderately high IRI than the other sections. This may be due to the pavement distress or any existing utilities such as a sewer cover. In addition, Fig. 6 also shows the difference of pavement IRI in left and right lanes. This difference in the measured IRIs between two lanes is possible due to the effect of trafficking and existing pavement distresses.

On average, the overall IRI of north-bound lanes of West Hunt Highway was 1.04 m/km with a coefficient of variation (COV) of 18% (see Table 3). Further, the left and right lanes had an IRI of 1.02 m/km and 1.05 m/km with COVs of 20% and 17%, respectively.
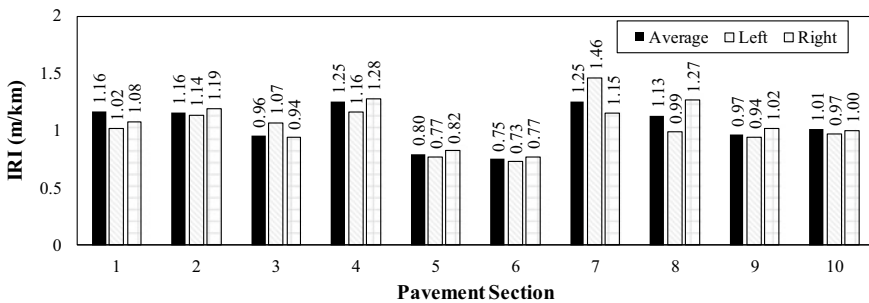
Fig. 6 Average IRI of pavement sections

Table 3 Basic statistics of IRI measurement

	Average (m/km)	Std. dev. (m/km)	COV (%)
Overall	1.04	0.19	18
Left lane	1.02	0.20	20
Right lane	1.05	0.17	17

In order to understand the variation of pavement IRI over time, a numerical model using AASHTOWare Pavement software was adopted. The software predicts several pavement performances, including pavement IRI, using mechanistic responses of pavement and the empirical prediction models developed from Long-Term Pavement Performance (LTPP) database. The major inputs required for the numerical model are shown in Table 4. The default calibration factors of the IRI model were adopted for the analysis. Due to the lack of initial pavement IRI information, it was assumed that the pavement had 1.0 m/km IRI at the beginning. As the initial IRI is a critical parameter affecting pavement performance prediction, two additional ranges of initial IRI were also selected by considering 20% variation in the initial assumption. Therefore, three AASHTOWare models were developed using the initial IRI of 0.8, 1.0 and 1.2 m/km. The pavement IRIs predicted by AASHTOWare are shown in Fig. 7. The figure shows a gradual increase in IRI with pavement life for all models. This represents a gradual decrease in the serviceability of the pavement, and the rate of serviceability reduction is affected by several parameters such as mechanical properties of pavement layers, foundation condition, environmental factors and traffic levels. The pavement is expected to have an IRI in between 1.0 and 1.4 m/km at the time of the TotalPave survey. The measured IRI of the pavement is 1.04 m/km which is in the lower range of the predicted IRI. This fact indicates that the mechanical stabilization provided by geogrid might have contributed to preserving the pavement IRI. Future IRI surveys will be needed for understanding the relationship between the measured and predicted pavement IRI. Besides, these numerical and experimental studies of pavement IRI predictions and measurements also suggest the need for calibrating the AASHTOWare pavement IRI model (distress model) for geogrid stabilized pavements.

Table 4 AASHTOWare inputs for numerical modelling

Category	Parameters	Input value
Traffic	Two-way AADTT	4000
Climate	Station ID	136,622
Pavement structure	HMA thickness (mm)	125
	Base layer thickness (mm)	150
Material properties	Asphalt binder	PG 76-34
	Base modulus (MPa)	206
	Subgrade modulus (MPa)	103
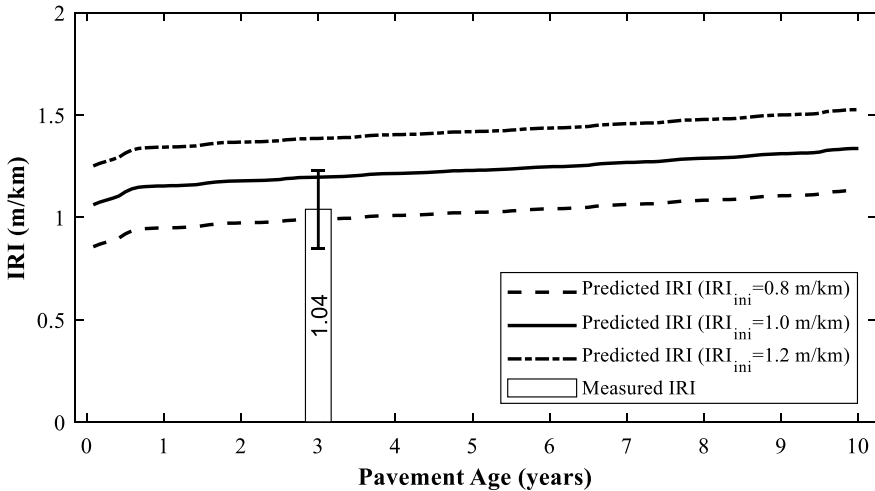
Fig. 7 Predicted and measured pavement IRI

6 Summary and Conclusion

Pavement roughness of geogrid stabilized roads was measured in terms of International Roughness Index (IRI) using a smartphone-based technology called Total-Pave. The TotalPave system collects IRI data rapidly. This enables users to develop an IRI database to monitor road performance over time. The IRI measurements were conducted on a section of West Hunt Highway in Arizona. The measured pavement IRI was evaluated and compared with the Standard IRI specified for such highways. Further, the IRI computed from numerical pavement models was also compared with the measured IRI.

The key findings of the study are:

- The overall IRI of geogrid stabilized pavement was measured as 1.04 m/km which indicates that the pavement is in a "good" condition.
- The right lane of geogrid stabilized pavement had slightly higher IRI than the left lane.
- The TotalPave system illustrated the variation in IRI along the longitudinal direction of the roadway for both (average) and each lane.
- The color-coded IRI map provided a spatial distribution of pavement IRI and helped in locating possible problematic areas.
- The TotalPave system allowed to collect IRI data rapidly and safely without interfering with traffic flow.
- The measured IRI of geogrid stabilized pavement was less than that predicted by the numerical model using AASHTOWare Pavement.

References

1. Bianchini A, Bandini P (2010) Prediction of pavement performance through neuro-fuzzy reasoning. Comput Civ Infrastruct Eng 25:39–54
2. Haas R (2001) Reinventing the (pavement management) wheel. In: 5th Annual conference on managing pavements. Seattle, Washington, USA
3. AASHTO (2012) Pavement management guide. American Association of State Highway and Transportation Officials, Washington, DC
4. Tamrakar P, Wayne MH, White DJ (2019) Permanent and resilient deformation behavior of geogrid-stabilized and unstabilized pavement bases. In: Geo-structural aspects of pavements, railways and airfield
5. Miller JS, Bellinger WY (2003) Distress identification manual for the long-term pavement performance program, 4th revised edn
6. Tamrakar P, Nazarian S (2017) Comparison of laboratory and field test results for granular bases. In: Geotechnical frontiers, pp 384–392
7. Tamrakar P, Nazarian S (2018) Evaluation of plate load based testing approaches in measuring stiffness parameters of pavement bases. Transp Geotech 16. https://doi.org/10.1016/j.trgeo.2018.06.005
8. Arhin SA, Noel EC, Ribbiso A (2015) Acceptable international roughness index thresholds based on present serviceability rating. J Civ Eng Res 5:90–96
9. Kelly LS, Leslie TG, Lynn DE (2002) Pavement smoothness index relationships: final report. Publ No FHWA-RD-02-057, US Dep Transp Fed Highw Adm Res Dev Technol Turner-Fairbank Highw Res Cent
10. Montoya K (2013) Improvements on manual pavement distress data collection to conform to state and federal requirements. University of New Mexico, Albuquerque, New Mexico
11. Dennis EP, Spulber A, Wallace R (2017) Innovative approaches to pavement condition data collection. Washington, DC
12. Cameron CA (2014) Innovative means of collecting international roughness index using smartphone technology. University of New Brunswick
13. Dong Y-L, Han J, Bai X-H (2011) Numerical analysis of tensile behavior of geogrids with rectangular and triangular apertures. Geotext Geomembr 29:83–91
14. Abu-Farsakh M, Hanandeh S, Mohammad L, Chen Q (2016) Performance of geosynthetic reinforced/stabilized paved roads built over soft soil under cyclic plate loads. Geotext Geomembr 44:845–853
15. Robinson WJ, Tingle JS, Norwood GJ (2017) Full-scale accelerated testing of multi-axial geogrid stabilized flexible pavements. ERDC-GSL Vicksburg United States
16. Gu F, Zhang Y, Luo X et al (2017) Characterization and prediction of permanent deformation properties of unbound granular materials for pavement ME design. Constr Build Mater 155:584–592
17. White DJ, Vennapusa PKR (2017) In situ resilient modulus for geogrid-stabilized aggregate layer: a case study using automated plate load testing. Transp Geotech 11:120–132
18. Roodi GH, Zornberg JG, Aboelwafa MM et al (2018) Soil-geosynthetic interaction test to develop specifications for geosynthetic-stabilized roadways
19. Vennapusa PKR, White DJ, Wayne MH et al (2018) In situ performance verification of geogrid-stabilized aggregate layer: Route-39 El Carbón–Bonito Oriental, Honduras case study. Int J Pavement Eng 1–12
20. Abu-Farsakh M, Hanandeh S, Mohammad L, Chen A (2019) Performance evaluation of geosynthetic reinforced pavement built over weak subgrade soil using cyclic plate load test. In: Geosynthetics conference
21. Wayne MH, Fountain G, Kwon J, Tamrakar P (2019) Impact of geogrids on concrete highway pavement performance. In: Geosynthetics conference
22. Collins IF, Wang AP, Saunders LR (1993) Shakedown theory and the design of unbound pavements. Road Transp Res 2

23. Hanson T, Cameron C, Hildebrand E (2014) Evaluation of low-cost consumer-level mobile phone technology for measuring international roughness index (IRI) values. Can J Civ Eng 41:819–827
24. Islam S, Buttlar WG, Aldunate RG, Vavrik WR (2014) Measurement of pavement roughness using android-based smartphone application. Transp Res Rec 2457:30–38
25. Forslöf L, Jones H (2015) Roadroid: continuous road condition monitoring with smart phones. J Civ Eng Archit 9:485–496
26. Ali A, Hossain K, Hussein A et al (2019) Towards development of PCI and IRI models for road networks in the City of St. John's. In: International airfield & highway pavements conference
27. Hossain MI, Tutumluer E (2019) Methodology for evaluation of seal-coated, gravel, and dirt roads
28. Tamrakar P, Wayne MH, Broadhead K (2019) Use of an innovative technology for measuring surface roughness of pavements. In: The 72nd Canadian geotechnical conference. St. John's, Newfoundland, Canada

Behavior of Asphalt Overlays with Geogrids and Geocomposite Interlayer Systems

V. Vinay Kumar (ID)**, Sireesh Saride** (ID)**, and Jorge G. Zornberg** (ID)

Abstract Geosynthetics in the form of geotextiles, geogrids, and geocomposites have been incorporated into pavement systems to enhance the service life of asphalt overlays by retarding reflective cracking. In this study, the performance of asphalt overlays reinforced with geogrids and geocomposite interlayer systems placed on pre-existing asphalt layer was evaluated. Specifically, both unreinforced and geosynthetic-reinforced, two-layered asphalt beam specimens prepared with a pre-existing 25 mm-deep notch (crack) in the bottom layer were tested under repeated four-point bending load conditions. The two-layered asphalt specimen consisted of a 45 mm-thick, old pavement layer collected from an existing highway as a bottom layer, a binder tack coat, the tested interlayer, and a 45 mm-thick hot mix asphalt (HMA) overlay. A glass-geogrid composite (GGC) involving a geotextile backing interlayer and two different types of geogrid interlayers, namely, a polyester geogrid (PET) and a polypropylene geogrid (PP) were used in this study. Repeated loading was applied to all specimens using a four-point bending configuration in a load-controlled mode at a frequency of 1 Hz. The performance of the different geosynthetic-reinforced specimens was compared against that of the control specimen (CS) and the improvement in fatigue life was estimated. Considering the specific products in this study, results indicate that all the geosynthetic-reinforced specimens resulted in extended fatigue life of overlays in relation to the CS, and among them, the best performance was obtained using the GGC.

Keywords Geogrid · Geocomposite · Asphalt overlay · Fatigue

V. V. Kumar (✉) · J. G. Zornberg
Department of Civil, Architectural and Environmental Engineering, University of Texas at Austin, Austin, TX 78712, USA

S. Saride
Department of Civil Engineering, Indian Institute of Technology Hyderabad, Kandi, Sangareddy, Telangana 502285, India

611

1 Introduction and Background

Hot mix asphalt (HMA) overlays are a widely adopted pavement rehabilitation approach due to their comparatively easy and expeditious construction. However, HMA overlays are frequently affected by a phenomenon known as reflective cracking, which has hindered the performance and service life of the rehabilitated pavement systems [1]. Reflective cracking is a complex phenomenon, which can be defined as a process of propagation of discontinuities and cracks from the existing, old distressed pavement layers into and through the new asphalt overlays [2–6]. The reflection cracks in the overlays often lead to moisture infiltration into the underlying layers, deteriorating the base and subgrade layers along with stripping of the asphalt layers [7, 8]. Previous research has evaluated the practice of restricting the reflection cracks into the overlays, including the possibility of adopting geosynthetics at the interface between the old distressed and the new pavement layers [2, 3, 9–11]. Geosynthetics have been reported to provide various functions in pavement systems such as separation, moisture barrier, reinforcement, filtration, and drainage [12].

Caltabiano [13] performed a series of asphalt beam tests to study the performance of geogrids and geotextile interlayers in restricting the crack growth into the overlays, concluding that geosynthetic interlayers extended the performance life of asphalt overlays. Cleveland et al. [1] reported that the geogrids were more effective than geotextiles and geocomposites in resisting the crack growth into the overlays. Barraza et al. [9] and Ogundipe et al. [14] evaluated the effectiveness of various anti-reflective cracking systems, including geosynthetics and stress-absorbing membrane interlayers (SAMI). They reported that all the anti-reflective cracking systems adopted in that study were effective in retarding reflective cracking and that geogrids outperformed the other systems. Besides, Walubita et al. [15] and Kumar and Saride [6] suggested that geosynthetic interlayers have the potential to improve the fracture characteristics of asphalt layers.

Virgili et al. [16], Ferrotti et al. [17], and Graziani et al. [10] conducted repeated four-point bending tests to study the influence of geosynthetics on the performance of asphalt overlays. They reported the geogrids could effectively retard crack propagation for a substantial performance period. Recently, Saride and Kumar [2, 5], Kumar and Saride [3, 4] performed beam fatigue tests to understand the influence of geosynthetics in asphalt overlays placed over existing, old deteriorated asphalt layer. They reported that the presence of geosynthetic interlayers at the interface of old and new pavement layers could effectively restrict crack growth into the overlays by redirecting them in the horizontal direction.

In summary, previous studies have generally considered geosynthetics placed within asphalt layers, instead of placing them at the interface of old and new pavement layers. In this regard, to better characterize the actual behavior of asphalt overlays reinforced with geogrids and geocomposite interlayers, a two-layered asphalt specimen with geogrid and geocomposite interlayers placed at the interface between old and new pavement layers was considered in the study presented in this paper. The primary goal of this study was to understand the behavior of asphalt overlays

with geogrid and geocomposite interlayer systems using repeated four-point bending tests.

2 Materials

2.1 Binder Tack Coat and Asphalt Concrete

The binder tack coat adopted in this study was a penetration grade 60/70 bitumen having a penetration value of 66. The tack coat had a specific gravity of 1.01 and a softening point of 52 °C. The flash-point and fire-point of the binder were found to be 340 °C and 365 °C, respectively. The viscosity of the binder was 460 cP at a temperature of 60 °C.

The asphalt concrete mix adopted in this study was prepared in a asphalt mixing plant and transported to the laboratory for specimen preparation. The asphalt mix involved maximum and nominal aggregate sizes of 25 mm and 13 mm, respectively, with a penetration grade 60/70 bitumen being adopted as a binder. Marshall Stability tests were performed on the asphalt concrete mix as per ASTM D6927 [18] to estimate the optimum binder content (OBC), which was determined to correspond to 5.5% (by weight of the aggregates). The maximum stability and flow value for the asphalt concrete mix with 5.5% OBC were found to be 14.25 kN and 2.5 mm, respectively.

2.2 Geogrids and Geocomposite Interlayers

This study aimed at understanding the behavior of asphalt overlays reinforced with geogrid and geocomposite interlayers under repeated four-point bending tests. In this regard, a glass-geogrid composite (GGC) interlayer, and two different types of geogrids, namely, a bi-axial polypropylene geogrid (PP) and a bi-axial polyester geogrid (PET) were adopted. The GGC interlayer consisted of a fiberglass geogrid with an aperture of 28 mm and continuous non-woven filaments mechanically bonded together. The GGC interlayer possessed an ultimate tensile strength of 28 kN/m (machine direction) reached at a strain of 2% and 25 kN/m (cross-machine direction) at a strain of 1.7%.

The bi-axial polypropylene (PP) geogrid was manufactured by extending the polypropylene material along the machine and cross-machine directions. The PP geogrids had a square aperture of 40 mm and an ultimate tensile strength of 30 kN/m at a strain of 10%, along both machine and cross-machine directions. The bi-axial polyester (PET) geogrid was manufactured by knitting together high molecular weight and high tenacity polyester yarns. The PET geogrids had a square aperture of 18 mm and an ultimate tensile strength of 40 kN/m at a strain of 20%, along both the machine and cross-machine directions.
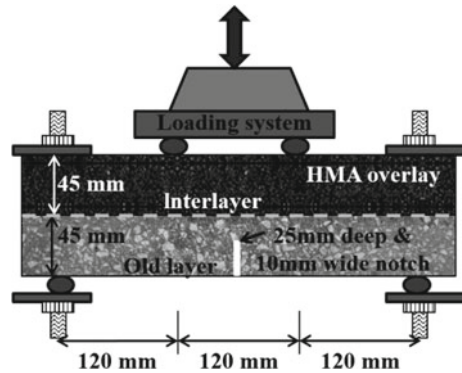
3 Experimental Program

3.1 Specimen Preparation

The specimens consisted of two asphalt layers, a tack coat, and a geosynthetic inter-
layer at the interface of two asphalt layers. The bottom layer, consisted of an old
pavement layer, which was extruded from an existing highway during the rehabili-
tation program and cut into a slab with dimensions of 400 mm in length, 300 mm
in width, and 45 mm in thickness. A penetration grade 60/70 binder tack coat was
applied over the bottom layer at a residual rate of 0.25 kg/m^2 as per India's ministry of
road transport and highways (MORTH) specifications [19]. The geosynthetic inter-
layer was then placed, as per experimental program, and finally, an HMA overlay
with a thickness of 45 mm was compacted using a 5 kg static weight compactor
having a height of fall of 500 mm. The two-layered asphalt slabs were then cut into
beam specimens with dimensions of 400 mm in length, 50 mm in width, and 90 mm
in thickness. To replicate a crack in the bottom layer, a notch of 25 mm deep (i.e.
55% of the layer thickness) was introduced in the bottom layer of the two-layered
asphalt beam specimens. Figure 1 presents a schematic of the two-layered asphalt
beam specimen adopted in this study. A detailed procedure of two-layered asphalt
specimen preparation for the repeated load tests is provided by Saride and Kumar
[2], and Kumar and Saride [3, 4].

3.2 Repeated Load Four-Point Bending Test

The behavior of asphalt overlays with geogrids and geocomposite interlayer systems
were studied using repeated load four-point bending tests performed on a two-layered
asphalt beam specimen under a load-controlled mode at a temperature of 30 ± 2 °C.
Figure 1 presents a schematic of the four-point bending test setup adopted in the study.

As shown in the figure, an asphalt beam specimen with a notch having dimensions of 25 mm in depth and 10 mm in width was made. Loads were applied on the specimens at a frequency of 1 Hz, and a typical load pattern was adopted to simulate a live moving traffic condition. In this regard, the maximum load corresponding to a contact pressure of 550 kPa was calculated using Eq. 1, per ASTM D7460 [20], as follows:

$$\sigma_f = \frac{Pl}{bh^2} \tag{1}$$

where σ_f is the maximum flexural stress in kPa (550 kPa), P is the maximum load applied in kN, l is the span length of the beam in m, b and h are the width and thickness of the beam in m.

Accordingly, a maximum load of 0.6 kN and a seating load of 0.06 kN was applied repeatedly to replicate the target live traffic condition. The loads were applied until complete specimen failure was reached, with the corresponding vertical deformation at mid-span length of the beam specimen being recorded at the end of each cycle.

4 Results and Discussion

The four-point bending tests performed in a load-controlled mode simulate the flexural fatigue behavior of the asphalt overlays with and without geogrid and geocomposite interlayers to understand their response as an anti-reflective cracking system in asphalt overlays. The repeated load four-point bending test results of the two-layered asphalt beam specimens are presented in Fig. 2, which depicts the change in vertical deformation (VD) with increasing number of load cycles (N). It can be observed that the control specimens (CS) failed after a comparatively small number of load repetitions, i.e. cracks propagated into the overlays and eventually failed after about 65 cycles. Instead, the specimens with geogrid and geocomposite interlayers could resist a comparatively larger number of load repetitions before failure. Specifically, the fatigue life of specimens with PP, PET, and GGC interlayers was about 750, 1250, and 3000, respectively. These results suggest that the presence of geogrids and geocomposites at the interface between old and new pavement layer has restricted the vertical deformation and, in turn, have delayed crack development for comparatively large performance periods. However, it is important to note that different geosynthetics have led to different responses. Specifically, the glass geogrid composite was found to delay crack development longer than PP and PET geogrids. This superior performance in GGC interlayers may be attributed to their ability to induce an ultimate tensile strength of 28 kN/m at a strain value as low as 2%. However, the geogrids were able to develop their ultimate tensile strengths of 40 kN/m (PET) and 30 kN/m (PP) at strain values as high as 18% (PET) and 12% (PP), respectively. Besides, among the specimens with geogrid interlayers, the geogrids with a relatively low initial stiffness (PET) showed a superior performance
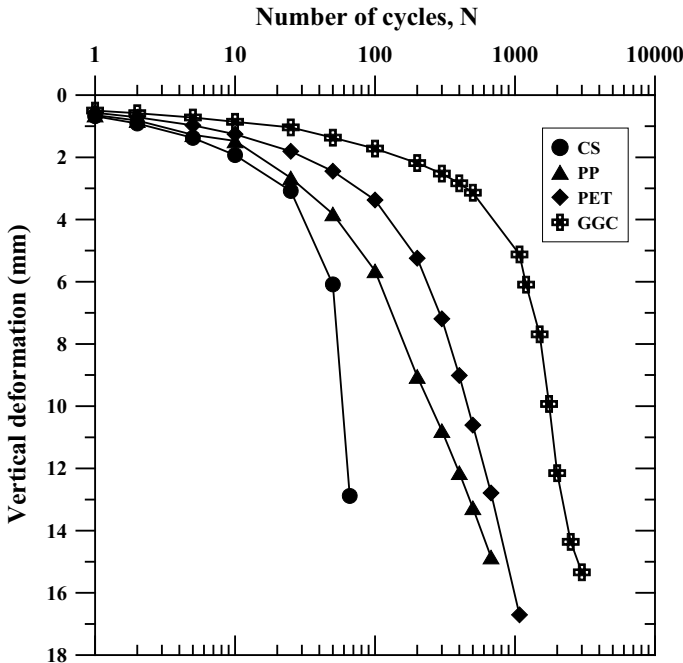
Fig. 2 Variation of vertical deflection (VD) with number of cycles (*N*)

than geogrids with a high initial stiffness (PP). This could be due to the enhanced interfacial bonding of the PET geogrids with the asphalt layers, resulting in a better load transfer to the layers below, in comparison with the PP geogrids [2]. Overall, the geosynthetic-interlayers placed at the interface zone restricted the crack growth into the overlays by distributing the strain energy (tensile) from the crack tip in the lateral direction at the interface zone. Hence, an extended fatigue life was achieved.

Further, to quantify the increase in fatigue life of the asphalt specimens with geogrids and geocomposite interlayers against the control specimens, an improvement ratio (I_R) is quantified. The improvement ratio (I_R) can be defined as the ratio between the number of load repetitions sustained by a specimen with geogrid or geocomposite interlayer to that sustained by a control specimen, at the same vertical deflections. The improvement ratio is expressed as:

$$I_R = \frac{N_R}{N_U} \tag{2}$$

where N_R and N_U are the number of cycles to fatigue failure of geosynthetic-reinforced and unreinforced specimens, respectively.

The differences in improvement ratio (I_R) with vertical deformation for the specimens with geogrid and geocomposite interlayers are plotted, as shown in Fig. 3. It
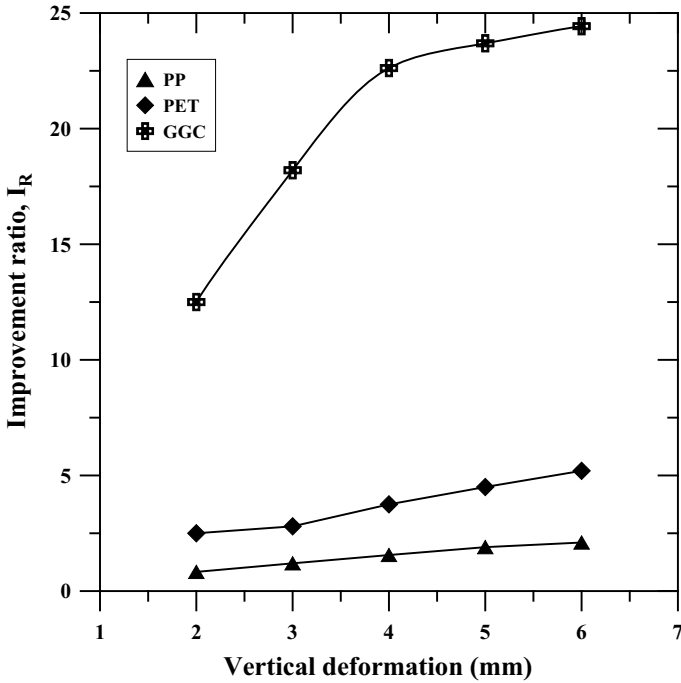
Fig. 3 Variation of improvement ratio (I_R) with vertical deformation (VD)

can be observed that I_R increases with increasing VD. The improvement in specimen with geocomposite interlayer is observed to be more prominent than that of specimens with geogrids. For instance, in the GGC specimen, a significant improvement in fatigue life can be observed as early as a VD of 2 mm is reached. Whereas, in specimens with geogrids, although improvement is observed at small VD, it is significant after a vertical deformation of 4 mm is reached.

A maximum I_R of 24 was obtained in GGC specimen, while a maximum I_R of 6 and 3 in PET and PP specimens, respectively, were obtained at a VD of 6 mm. These differences in the performances of geogrids and geocomposite interlayers may be attributed to their working tensile properties. The geocomposite interlayer (GGC) is expected to initiate a reinforcing effect at a vertical deformation of 2 mm and continue to provide a reinforcing function until failure. Besides, the reinforcing effect in specimens with geogrid interlayers is observed to be significant after reaching 4 mm vertical deformation, and hence, variation in the fatigue life improvements can be observed in the figure. Among the specimens with geogrid interlayers, the PET specimen has shown a better improvement than the PP specimen. This may be attributed to the ability of PET geogrids to achieve a better interfacial bonding between the asphalt layers resulting in a better load transfer and, in turn, enhanced performance.

5   Conclusions

The behavior of asphalt layers reinforced with geogrids and geocomposite interlayer systems was studied under repeated four-point bending tests, and the following conclusions can be drawn from the study:

- Both geogrids and geocomposite interlayer systems were found to successfully improve the fatigue performance of pre-cracked two-layered asphalt beam specimens by retarding reflective cracking. Among them, a superior performance was observed in the glass geogrid composite interlayer used in this study when compared with the tested geogrid interlayers.
- Fatigue life of 750, 1250, and 3000 was achieved in PP, PET, and GGC specimens, respectively, compared to a fatigue life of 65 in the control specimen. This accounts for an improvement in fatigue life of about 11-fold, 19-fold, and 45-fold in PP, PET, and GGC specimens, respectively.
- The geosynthetics (geogrids and geocomposite) placed at the interface between old and new pavement layers restrict the crack growth into the overlays, and as a result, the cracks were observed to spread along the horizontal direction in the interface zone.
- Overall, the geosynthetic (geogrids and geocomposite) interlayers were shown to improve the fatigue characteristics of the asphalt overlays before failure.

References

1. Cleveland GS, Button JW, Lytton RL (2002) Geosynthetic in flexible and rigid pavement overlay. Texas Transport Institute, Texas A&M University System, Report No. 1777-1
2. Saride S, Kumar VV (2017) Influence of geosynthetic-interlayers on the performance of asphalt overlays placed on pre-cracked pavements. Geotext Geomembr 45(3):184–196
3. Kumar VV, Saride S (2017) Use of digital image correlation for the evaluation of flexural fatigue behavior of asphalt beams with geosynthetic interlayers. Transp Res Rec J Transp Res Board 2631:55–64
4. Kumar VV, Saride S (2018) Influence of crack-depth on the performance of geosynthetic-reinforced asphalt overlays. In: Sundaram R, Shahu J, Havanagi V (eds) Geotechnics for transportation infrastructure. Lecture notes in civil engineering, vol 29. Springer, Singapore
5. Saride S, Kumar VV (2019) Estimation of service life of geosynthetic-reinforced asphalt overlays from beam and large-scale fatigue tests. J Test Eval 47(4):2693–2716
6. Kumar VV, Saride S (2018) Evaluation of cracking resistance potential of geosynthetic reinforced asphalt overlays using direct tensile strength tests. Constr Build Mater 162(20):37–47
7. Kumar VV, Saride S, Peddinti PRT (2017) Interfacial shear properties of geosynthetic interlayered asphalt overlays. In: Proceedings of geotechnical frontiers, GSP-277, Orlando, USA
8. Elseifi MA, Al-Qadi IL (2004) A simplified overlay design model against reflective cracking utilizing service life prediction. Road Mater Pavement Design 5(2):169–191
9. Barraza DZ, Peréz MAC, Fresno DC, Zamanillo AV (2010) Evaluation of anti-reflective cracking systems using geosynthetics in the interlayer zone. Geotext Geomembr 29(2):130–136
10. Graziani A, Pasquini E, Ferrotti G, Virgili A, Canestrari F (2014) Structural response of grid-reinforced bituminous pavements. Mater Struct 47(8):1391–1408

11. Correia NS, Zornberg JG (2016) Mechanical response of flexible pavements enhanced with geogrid-reinforced asphalt overlays. Geosynth Int 23(3):183–193
12. Khodaii A, Fallah S, Nejad FM (2009) Effects of geosynthetics on reduction of reflection cracking in asphalt overlay. Geotext Geomembr 27(1):131–140
13. Caltabiano MA (1990) Reflection cracking in asphalt overlays. M.Phil. thesis submitted to University of Nottingham
14. Ogundipe OM, Thom N, Collop A (2012) Investigation of crack resistance potential of stress absorbing membrane interlayers (SAMIs) under traffic loading. Constr Build Mater 38:658–666
15. Walubita LF, Faruk ANM, Zhang J, Hu X (2015) Characterizing the cracking and fracture properties of geosynthetic-interlayer reinforced HMA samples using the overlay tester (OT). Constr Build Mater 93:695–702
16. Virgili A, Canestrari F, Grilli A, Santagata FA (2009) Repeated load test on bituminous systems reinforced by geosynthetics. Geotext Geomembr 27(3):187–195
17. Ferrotti G, Canestrari F, Pasquini E, Virgili A (2012) Experimental evaluation of the influence of surface coating on fiberglass geogrid performance in asphalt pavements. Geotext Geomembr 34:11–18
18. ASTM D 6927. Standard test method for Marshall stability and flow of asphalt mixtures. American Society for Testing and Materials, Annual book of ASTM standards, ASTM International, West Conshohocken, PA
19. MORTH (2003) Specifications for road and bridge works. Ministry of Road Transport and Highways. Indian Road Congress (IRC), New Delhi
20. ASTM D7460. Standard test method for determining fatigue failure of compacted asphalt concrete subjected to repeated flexural bending. American Society for Testing and Materials, Annual Book of ASTM Standards, ASTM International, West Conshohocken, PA

Study of the Strained State of Bored Foundations for Weak Soils by Strengthening the Grillage with Geosynthetic Materials

Sergey Kudryavtcev, Tatiana Valtceva, Semyon Bugunov, Zhanna Kotenko, and Natalya Sokolova

Abstract Construction in northern regions of the Far East is always connected with a high degree of seasonal freezing risk. This is especially true for line transport structures which require a high level of reliability and responsibility. Such structures should provide permissible deformability and bearing capacity of the bases when exposed to moving loads in difficult geological and climatic conditions. The paper considered the development of bridge supports stabilizing structures using mathematical modeling methods and geosynthetic materials. The study used standard methods of engineering calculations using analytical approaches to determine the rational parameters of structural elements and the degree of their operational reliability and durability. In determining the behavior of structures as a whole, with the collaborative interaction of their individual elements with each other, nonlinear soil models of the base of the structures were used. Numerical modeling of bored foundations in an elastic–plastic soil mass allowed to work out effective structural solutions for reducing the deformability of the bridge and increasing the bearing capacity of the pile foundation due to reinforcing measures in the construction of the grillage and creating rational parameters of structures as a whole.

Keywords Stress–strain state · Foundation · Geosynthetic materials · Numerical modeling · Piles · Elastoplastic model · Weak base

1 Introduction

This paper described stabilization work performed for the bored foundations of a bridge. The bridge spans over a river 47.34 m long on the highway in the Sakhalin region of Russia. The bridge is located on a straight stretch of road crossing a swampy valley. The span beam is 42.0 m long, all-metal with an orthotropic steel plate of the

S. Kudryavtcev (✉) · T. Valtceva · S. Bugunov · Z. Kotenko
Far Eastern State Transport University, Khabarovsk, Russia

N. Sokolova
Financial University Under the Government of the Russian Federation, Moscow, Russia

carriageway and service passages on metal consoles. There is an expansion joint with rubber expansion joint. The foundations were made using bored posts with a diameter of 1020 mm with non-removable casing pipes with a wall thickness of 12 mm. The columns are arranged in two rows of 6 pieces in each row and are combined at the top with reinforced concrete monolithic slabs up to 1.0 m thick. The distance between the axes of the posts along the axis of the bridge is 2.70 m, across—2.10 m. The length of the pillars support No. 1 is 22.5 m, support No. 2—13.5 m.

On support No. 1 (right-bank), fixed tangential support parts are installed, and on support No. 2 (left-bank), movable tangential support parts are used. To keep the support nodes from tossing during earthquakes, the span is connected to the sub-truss plates by antiseismic anchor-type devices. During the construction, some additions were made to the project. In particular, support No. 2 was reinforced with an additional row of five bored posts with a diameter of 1220 mm and a length of 18.5 m in non-removable casing pipes. Reinforcement posts are included in the joint work with the previously constructed part of the support No. 2 due to the arrangement of a common sub-truss plate. At the same time, at a distance of 5 m from an additional row of columns to the side of the channel, a separate pile grillage was constructed from four bored columns in a row located in a row of 1220 mm in non-removable casing with a wall thickness of 18 mm. The grillage slab has dimensions $3.2 \times 9.5 \times 1.5$ m and is lower than the grillage slab of the support No. 2 by 1.0 m. The mentioned design is intended to reduce the landslide pressure of soft soils on the support No. 2.

2 Engineering and Geological Conditions of the Foundation

Silts are structurally unstable soils with specific properties. The structure of silty soils is determined by both the deposition conditions and the properties of mineral–colloidal particles and the composition of the aqueous medium. The structural features lead to the fact that the moisture content of natural sludges, as a rule, exceeds their yield strength in a bent state, and the porosity coefficient is often much greater than unity (porosity does not correspond to natural pressure). Structural bonds between particles and low water permeability interfere with the gravitational compaction of soils [1, 2].

Sludges are subject to thixotropic phenomena arising from dynamic influences. In this case, the occurrence of water films around the particles is noted, which significantly reduces the shear resistance. At the same time, during the transition of sludge to plastic clay, a gravitational compaction can be observed, which causes a partial violation of the initial coagulation structure, a decrease in porosity, an increase in strength properties and an increase in the concentration of the pore solution. An essential process that occurs in silty soils under the influence of an external load on them is the destruction of structural–colloidal bonds with the simultaneous emergence of new bonds due to the convergence of mineral particles during compaction under load. If the magnitude of the external load does not exceed the critical value, then sludge can be considered as soils with only adhesion [3, 4]. At a pressure exceeding

the structural strength, adhesion decreases sharply, silts pass into a liquefied state, easily squeezed out from under the structures.

In order to correctly take into account the properties of sludge during design, special laboratory tests are necessary, and the most important is field testing of sludge without violating their structure by stamping methods.

3 The Real State of the Construction of the Bridge Supports

Based on the above information on sludge, we can draw the following conclusions. The arrangement of bored piles of the bridge supports led to the appearance around the bored foundations of zones near the sludge with reduced strength characteristics and increased humidity due to thixotropic phenomena associated with the performance of work (dynamic impact). This fact did not affect the stability of the foundations of the supports in view of the fact that they are buried in the bedrock to a sufficient depth [5–7].

Further construction of approach sections of the embankment contributed to an increase in vertical stresses and, as a consequence, an increase in horizontal pressure on the support. The distance between the rows of piles and the presence of the second row in the support grill predetermined the formation of an arched effect that impedes the forcing of silt between piles. In addition, it is likely to assume that the feature of the sludge—low porosity—in the zone between piles under dynamic influences led to compaction of particles, which subsequently appeared on the surface in the form of cavities under the grillage.

The subsequent arrangement of an additional row of piles in close proximity to the support did not lead to stabilization of the soil, since it also provoked structural instability of silts around the piles. Obviously, thixotropic phenomena did not allow an additional row of piles to be included in the work, i.e., the soil being squeezed between these piles exerted pressure on the support-soil pile array that had already hardened and consolidated by that time.

The construction of stabilization of the soil base consists of several parts:

1. Lumps of coarse clastic unsorted soil up to 1–1.5 m in size are immersed in the foundation pit, at the foot of the pile holding structure.
2. After the construction of the reinforced soil structure to the level of the grillage of the pile holding structure, a stress distribution platform is arranged to redistribute the stresses from the weight of the embankment and transfer the load through the piles to strong primary soils.
3. Reinforcement with the geosynthetic materials of the embankment is performed by the wrapping method (Fig. 1).

A general view of the reinforced soil reinforcement design of the approach embankment is shown in Fig. 2.

Fig. 1 Scheme clips
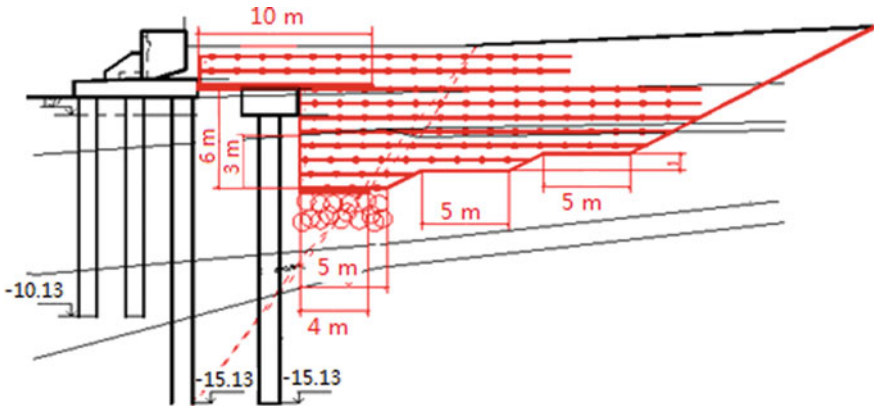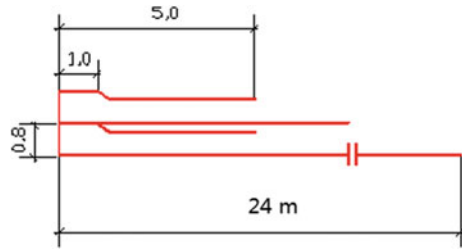
Fig. 2 General view of the reinforced soil reinforcement structure of the approach embankment

Figure 3 shows the facade of an armored structure. The design, located below the level of the day surface, is arranged with an overlap of rolls of 0.5 m. Located above—without overlaps.
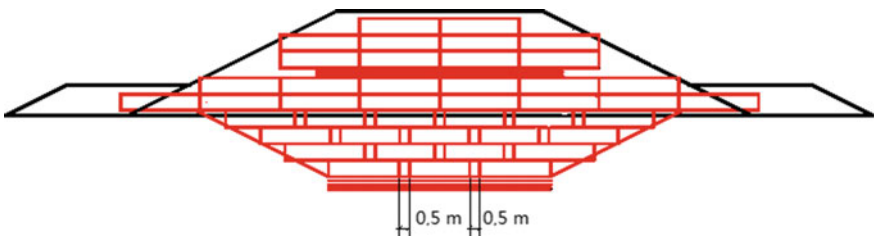
Fig. 3 Facade of armored construction

4 Geotechnical Modeling of the Work of Stabilization Structures of Bridge Supports

Geotechnical modeling of stabilization options for bridge supports was carried out to confirm the rationality of engineering solutions using the FEM models software package developed by geotechnicians of the Georekonstruktsiya-Fundamentproekt NGO of St. Petersburg under the guidance of Professor V. M. Ulitsky.

The software complex allows solving three-dimensional thermophysical and stress–strain state problems for structures and their foundations with dimensions of several million degrees of freedom at an acceptable time on a personal computer. In this regard, the complex has no domestic or European counterparts [8–10].

Based on the above-stated facts that affect the VAT of weak bases, the most reliable picture can be obtained when using discrete models in calculations, in particular, FEM in an elastoplastic setting. An elastoplastic model with a limiting surface was used to describe the operation of structures. The choice of this model is due to the fact that its parameters can be taken from existing materials from standard engineering and geological surveys. In this setting, numerical calculations are in good agreement with traditional engineering methods for calculating deformations and allow us to describe with sufficient accuracy the stress state and deformation of structures. The unit for solving problems allows solving systems of linear equations, as well as producing (if necessary) iterative solution of nonlinear problems. For solving systems of linear algebraic equations, direct methods can be used (Gauss method, Cholesky method), as well as iterative methods [11, 12]. To solve large systems of linear algebraic equations, the program developed an original iterative method based on the conjugate gradient method using a special pre-conditioner that guarantees an improvement in the conditionality of the solution matrix and accelerates the solution by the iterative method.

An iterative solution method allows you to achieve a user-specified solution accuracy. As a rule, calculations are performed with an accuracy of 10^{-8}.

The proposed methodology for the numerical simulation of the operation of an armored structure and foundation reinforced with geomaterials is an integral part of the FEM models modular program. The considered version of the program implements an elastoplastic solution of the FEM using the procedure of "initial stresses." The choice of interpolating polynomials and the construction of a rigidity matrix for a finite element, as well as the compilation and solution of a system of algebraic equations with respect to nodal values, is based on the FEM models software package. When developing the soil model, the authors made the following basic assumptions:

– Soil is considered as an ideal-elastic–plastic medium with the Coulomb strength criterion, obeying the laws of plastic flow;
– The reaction of the medium to volumetric deformations is elastic, and to shear elasto–plastic with an equal volume flow;
– Interpolating polynomials for each finite element are assumed linear, and stresses and strains in it are constant;

– The natural stress state is replaced by a hydrostatic compression tensor of the "characteristic volume" of the soil;
– There is a completeness of filtration consolidation and rheological processes in the foundation. Total deformations of the soil medium are presented as the sum of elastic and plastic deformations.

$$d\varepsilon_{ij} = d\varepsilon_{ij}^e + d\varepsilon_{ij}^p \tag{1}$$

To determine $d\varepsilon$ the theory of plastic flow is used in the form of an unassociated law:

$$d\varepsilon_{ij}^p = d\lambda \frac{\partial F}{\partial \sigma_{ij}} \tag{2}$$

where $d\lambda$ is the small scalar factor.

During the transition from an elastic state to a plastic vector, it passes through a plane tangent to the surface of the limiting state, and the end of the stress vector moves along this surface. In this case, the loading will be neutral, in which the laws of plasticity and elasticity coincide (only elastic deformations occur), which is a condition of continuity. When solving the elastoplastic problem (plane deformation), an ideal-plastic medium scheme with the Coulomb strength criterion is used

$$f = \sqrt{(\sigma_x - \sigma_y)^2 + 4\tau_{xy}^2} + (\sigma_X + \sigma_Y)\sin\varphi - 2c\cos\varphi = 0 \tag{3}$$

where σ_x; σ_y; τ_{xy}—axial stresses; φ—angle of internal friction; c—specific grip.

For the medium under consideration, the main parameters of the boundary of the limiting surface are constant and independent of the accumulated plastic deformation. When the limiting surface is reached, an equal volume flow occurs, and the plastic potential is parallel to the hydrostatic axis.

Geotechnical modeling took place in two stages: the first—modeling of the current situation, when unloading the embankment helps to stabilize deformations, the second—to determine the stress–strain state of the stabilization structure.

The pile holding structure during modeling was not taken into account in view of the fact that its deformations were not recorded and, presumably, due to the transition of silt around the piles into a fluid state, the soil is pressed between the piles. The presence of this design and its work is taken into stock [13, 14].

The design scheme of the foundation of the bridge support is shown in Fig. 4. At this step, the system is in a stable state, and there are no deformations of the support. The simulated situation corresponds to the current state of the support when a part of the embankment is disassembled.

The next steps consisted in sequential modeling of the construction of the approach embankment with the filling of the soil of the body of the approach embankment toward the location of the bridge. Figure 5 shows the zones of development of plastic
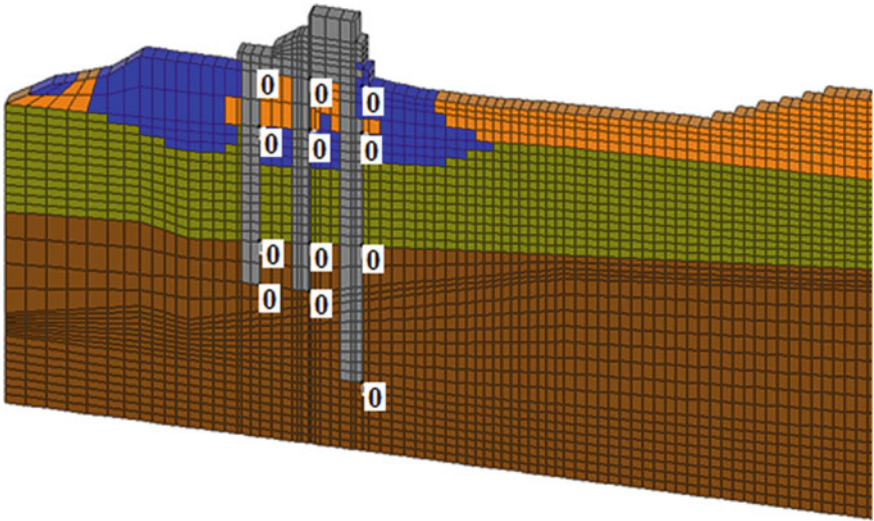
Fig. 4 Design scheme of the base of the foundations of the bridge support
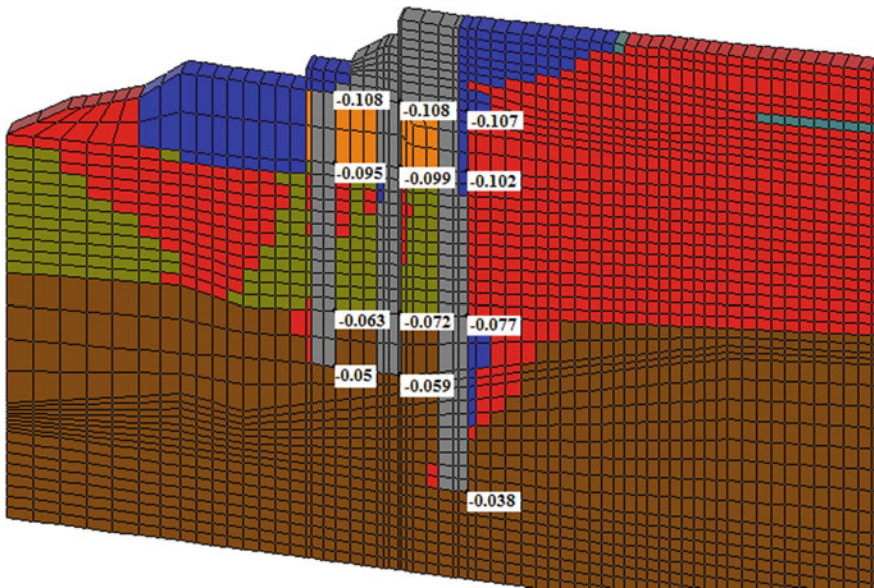
Fig. 5 Zones of plastic deformations and horizontal movements (m) at the stage of full filling of the embankment soil
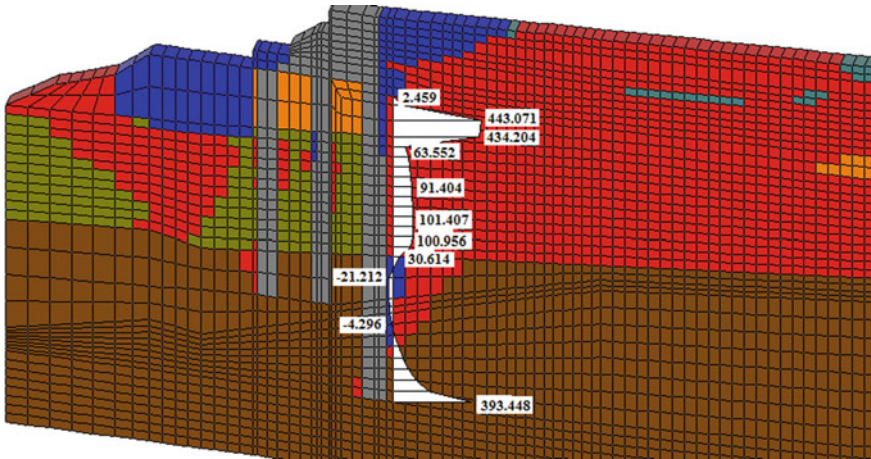
Fig. 6 Diagram of horizontal stresses without structural measures, kPa

deformations and horizontal movements at the time of the complete erection of the embankment. The magnitude of horizontal deformations reaches 110 mm.

As it can be seen in Fig. 8, plastic deformations are developed for the entire thickness of the sludge and partially in the clay loam. The nature of the development of zones in loam confirms the assumption that in this case the theory of soil pressure on the building envelope is applied. A moving clay wedge formed in loam is located in the sludge layer and in the soil of the body of the embankment. The horizontal displacements of the support were more than 10 cm (Fig. 6).

The simulation results of the stabilization design of the soil foundation of the bored foundations are presented in Fig. 7. The maximum horizontal deformations are up to 25 mm, i.e., 4 times; there was a decrease in horizontal deformations.

The horizontal pressure diagram is shown in Fig. 8. The maximum horizontal stresses under the sole of the grillage of bored foundations reach values up to 225 kPa. Those 2 times there was a decrease in horizontal stresses.

5   Conclusions

1. The design of the bored foundations for soil stabilization consisted of a pile armored structure to the level of grillage and reinforcing the body of the approaching embankment with geosynthetic materials by the method of wrapping.
2. Geotechnical modeling for the options considered for stabilizing the bridge supports, using FEM software package, was utilized to confirm the rationality of engineering solutions.
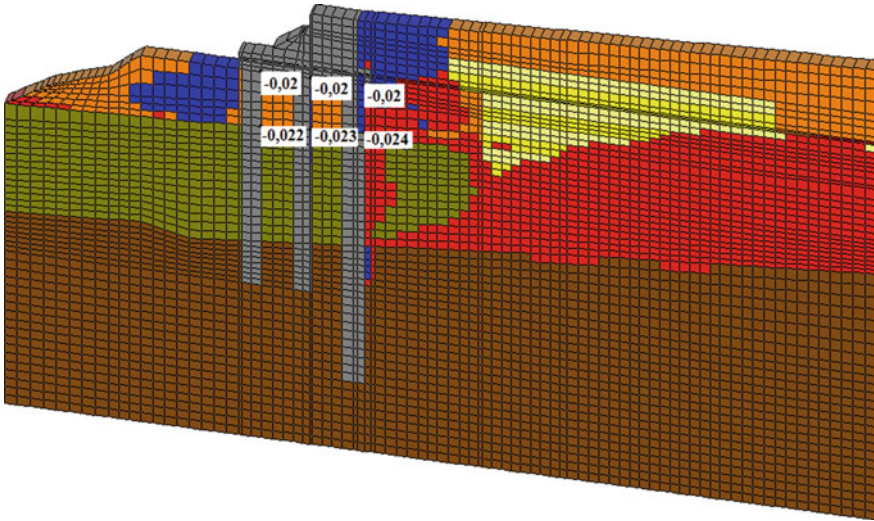
Fig. 7 Zone of plastic deformation and the magnitude of the horizontal deformation of the displacement of the structure (m)
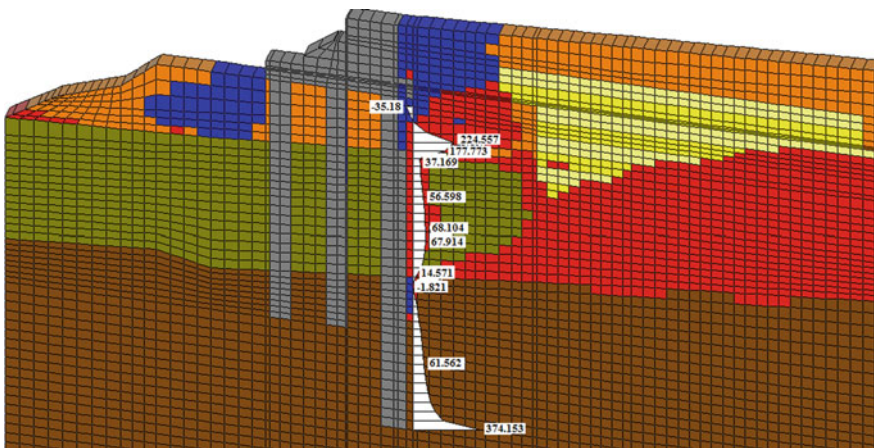
Fig. 8 Diagram of horizontal stresses along the length of the piles with the device of structural measures, kPa

3. Armored soil construction of the soil foundation of bored foundations reduces the horizontal stresses due to the self-weight of the soil in the body of the embankment to 50%, and the horizontal deformations to 25%. This indicates the effectiveness of the stabilization design.

4. A comparative analysis of the results of numerical modeling of the stress–strain state of the soil near the pile foundation of the bridge support shows a significant

reduction in the zones of plastic deformation in the soil base. This suggests that the shear stresses do not exceed the limit values of the strength characteristics of the soil.

5. The triangular view of the reinforced soil structure creates an additional advantage: When loading (filling the embankment), the vertical load will create lateral expansion of the soil, and due to the wedge-shaped form, the movement of soil will be directed away from the support.

6. Cyclic loading contributed to an increase in vertical stresses and, as a consequence, an increase in horizontal pressure on the support.

References

1. Ulitsky V, Sakharov I, Paramonov V (2018) Thermal-physical calculations as a basis of design solutions of buildings and structures in the permafrost zone. MATEC Web Conf 265:05009. EDP Sciences, France
2. Paramonov V, Sakharov I, Kudriavtcev S (2018) Forecast the processes of thawing of permafrost soils under the building with the large heat emission. MATEC Web Conf 73:05007. EDP Sciences, France
3. Ulitskii VM, Shashkin AG (2016) Successful construction of high-speed motorways: the geotechnical constituent. Transp Russ Feder 2–3:36–39
4. Kudruavtsev SA (2018) Evaluation of the carrying capacity of the building structures in the industrial heritage for its adaptation. MATEC Web Conf 146:02003. EDP Sciences, France
5. Valtseva TY, Kudruavtsev SA, Kazharsky AV, Goncharova ED (2017) Strengthening design for weak base using geomaterials on "Amur" automobile road section international. In: Murgul V, Popovic Z (eds) Scientific conference energy management of municipal transportation facilities transport EMMFT 2017. Advances in intelligent systems and computing. Springer, Cham, pp 145–153
6. Kudriavtsev S, Borisova A (2018) The research of the freezing and thawing process of the foundations with the use of season and cold-producing devices. MATEC Web Conf 193:03040. EDP Sciences, France
7. Kudryavtsev S, Paramonov V, Sakharov I (2016) Strengthening thawed permafrost base railway embankments cutting berms. MATEC Web Conf 73:05002. EDP Sciences, France
8. Kudryavtsev S, Maleev D, Tsvigunov D, Goncharova E (2016) Disalgnment of railroad poles as dynamic effect of rolling stock. Procedia Eng 165:1858–1865. Elsevier BV, Holland
9. Kudryavtsev S, Bugunov S, Pogulyaeva E, Peters A, Kotenko Z, Grigoryev D (2017) Construction of the high-rise buildings in the Far East of Russia. E3S Web Conf 33:02008. EDP Sciences, France
10. Kudriavtcev S, Kovshun V, Mut A (2017) The investigation of freezing and thawing processes of metal foundation ground of pipelines. In: Murgul V, Popovic Z (eds) Scientific conference energy management of municipal transportation facilities transport EMMFT 2017. Advances in intelligent systems and computing. Springer, Cham, pp 953–961
11. Kudriavtcev S, Valtseva T, Kotenko Z, Goncharova E (2016) Thermophysical feasibility of railway embankment design on permafrost when projecting side tracks. Procedia Eng 165:1080–1086. Elsevier BV, Holland
12. Paramonov VN, Sakharov II, Kudryavtsev SA (2016) Forecast the processes of thawing of permafrost soils under the building with the large heat emission. MATEC Web Conf 73:05007. EDP Sciences, France

13. Kudryavtsev S, Kazharssky A, Goncharova E, Kotenko Z, Grigoryev D (2017) Embankment on permafrost eastern polygon of Baikal-Amur mainline. Procedia Eng 189:774–782. Elsevier Ltd, Holland
14. Kudryavtsev S, Shvartcfeld V, Goncharova E, Mikhailin R, Kotenko Z, Grigoryev D (2016) Experimental researches on roadbed structural reinforcement with geogrid on automobile road. MATEC Web Conf 106:05003. EDP Sciences, France

Bearing Capacity Test with Small Soil Box Model on Reinforcement of Base Course Using Geotextile

Kenichi Sato, Takuro Fujikawa, Chikashi Koga, Takumi Kitamura, Yuichiro Wakabayashi, Junichi Hironaka, and Yusaku Isobe

Abstract In recent years, there has been a rapid increase in the number of road pavements that have exceeded 40 years of service life. As a result, it is anticipated that the number of pavements in need of repair, including the base course, will increase. In addition, the cost of repairing the pavement including the base course will be higher than if only the asphalt layers were repaired. Therefore, it is desirable to extend the service life of road pavements in order to reduce future maintenance costs. This study focuses on reinforcing the base course of road pavements and aimed to increase the durability and extend the service life of road pavements by laying geotextiles on the base course. The effect of different types of geotextiles on the reinforcement of the base course was reported from the results of bearing capacity tests using a small soil container.

Keywords Bearing capacity · Base course · Geotextile reinforcement

1 Introduction

In Japan, modern infrastructures were intensively constructed during the high economic growth period, which will reach the end of their service life after 2020. Thus, the aging of these infrastructures is becoming a social problem. After the beginning of operation, the durability of the pavement is impaired by heavy vehicle traffic and rainwater, and the pavement surface is subject to cracking and rutting. In

K. Sato (✉) · T. Fujikawa · C. Koga · T. Kitamura
Fukuoka University, Fukuoka, Japan
e-mail: sato@fukuoka-u.ac.jp

Y. Wakabayashi
Kiso-Jiban Consultants Co. Ltd., Tokyo, Japan

J. Hironaka
Mitsuichemicals, Tokyo, Japan

Y. Isobe
IMAGEi Consultant, Tokyo, Japan

particular, it has been reported that the bearing capacity of base course due to the ingress of rainwater from cracks has a significant impact on the durability of asphalt pavements. Thus, the base course has an important role in the service life of a road pavement. However, there are few cases in which the base course is replaced in the repair work because of maintenance cost reduction, increase in repair cost, and road closure due to construction.

In recent years, research and development has been focused on base course reinforcement, especially the reinforcement of base courses using geotextiles [1]. It is well known that geotextiles are very useful materials in the construction of soil structures, such as their function as tensile reinforcement [2, 3]. The use of geotextiles in pavement construction in Japan has been used as a countermeasure for soft base course in road pavements [4]. However, there are few examples of geotextiles being used to reinforce base courses. Thus, the research on the application of geotextiles to base courses has attracted a lot of attention. Hirakawa et al. showed that even a single layer of geogrid in the base course greatly suppressed the amount of residual subsidence in the base course. Furthermore, it was found that when used in conjunction with a high density of the base course, progressive residual settlements could be effectively restrained as well [5].

In this study, two types of loading tests, constant strain loading and cyclic loading, were conducted on a geotextile-reinforced base course. This study described the results of the investigation on the effect of geotextile type on bearing and deformation characteristics. The effect of geotextile laying depth and laying length on cyclic loading tests was also discussed.

2 Testing Procedure

2.1 Materials

A single grain size of Mikawa silica sand no. 5 was used in the soil test to check the deformation of the ground by loading. The physical properties of this silica sand are given in Table 1. Five types of geotextiles with different material properties such as stiffness and frictional force of geotextiles were used in this study: two types of woven fabrics, nonwoven fabrics and two types of geonets. Table 2 shows the geotextiles used and their physical properties. The woven fabric is a material that has a very large tensile strength compared to other geotextiles. Geonet is also a geotextile that can create an interlocking effect due to the continuity of soil particles.

Table 1 Physical property

Sample	Mikawa quartz sand no. 5
Photograph	
Soil particle density ρ_s (g/cm^3)	2.655
Maximum void ratio e_{max}	1.139
Minimum void ratio e_{min}	0.723
Uniformity coefficient U_c	1.766
Coefficient of curvature $U_c{'}$	1.052

Table 2 Geotextile

Reinforcement	Woven fabric A, B		Nonwoven	Geonet A	Geonet B
Photograph					
Tensile strength (kN/m)	A 89.0	B 74.0	11.7	5.6	3.6
Mesh size (mm)	–		–	2.5	10

2.2 Experimental Apparatus and Method

Figure 1 shows an outline of the small soil container (loading device) used in this experiment, which has a height of 90 cm, width of 120 cm, and depth of 20 cm. Six
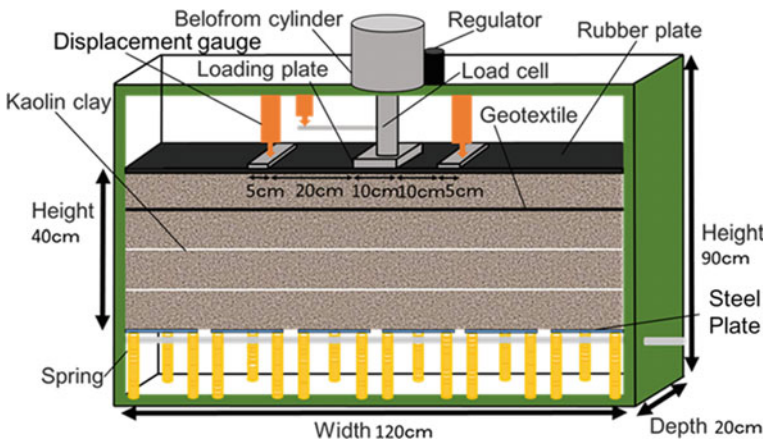
Fig. 1 Small soil container (loading apparatus)

steel plates and springs with a spring constant of 3.75 kN/mm were installed at the bottom of the box. This was designed to easily cause ground deformation during loading. The deformation of the model ground surface was measured by using a displacement gauge at three positions: at the loading position, 10 and 20 cm from the center of the loading. The relative density of the model ground was set at 80%.

The model ground was prepared by the tamping method with the moisture content of the samples adjusted to 5%. The bottom 30 cm of the model ground was made in three layers of 10 cm thickness. In particular, the upper 10 cm of the model ground was made in five layers with a thickness of 2 cm, because the geotextile was to be laid in a shallow area. After the preparation of the model ground, a 1 cm thick, 119 cm long, and 19.6 cm wide rubber plate was installed to simulate the asphalt pavement surface. Kaolin clay with a width of about 1 cm was placed at a depth of 20 and 30 cm from the top of the acrylic plate in order to visually capture the deformation of the model ground by the loading test.

Static loading was carried out at 1 mm/min, and the loading was terminated at a load stress of 5 kN/m^2. On the other hand, the cyclic loading was carried out under the sinusoidal stress control at a loading speed of 0.1 Hz with a maximum loading stress of 100 kN/m^2. In this test, the repetition rate $N = 360$ cycles (1 h) was set as the end condition. In this model test, the loading speed was set slower in order to see the reinforcing effect of the geotextile and the deformation of the ground by the loading test.

2.3   Experimental Conditions

Figure 2 shows the stress distribution when a loading stress of 100 kN/m^2 was applied to a 10 cm loading plate. It is considered that the stress distribution shown in Fig. 2 acts in the model ground, so the laying length L of a woven fabric A below the center of the loading plate was set to 15, 30, 60, and 120 cm. In addition, the rubber plate
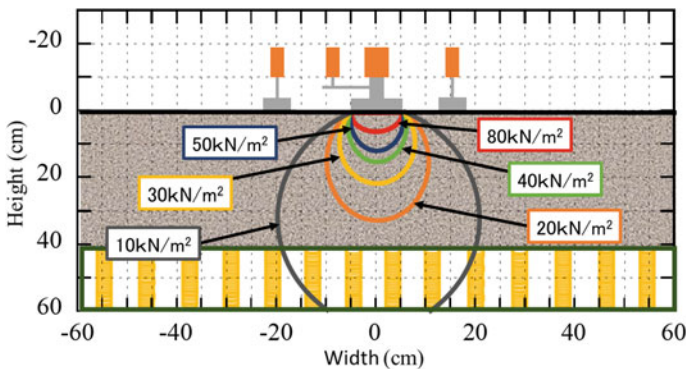
Fig. 2 Stress distribution when a loading stress of 100 kN/m^2

Table 3 Experimental conditions (static loading tests)

Relative density Dr (%)	Laying depth D (cm)	Laying length L (cm)	Loading method	Geotextile types
80	10	120	Static loading Cyclic loading	Woven fabric A, B
				Nonwoven
				Geonet A, B

Table 4 Experimental conditions (cyclic loading tests)

Relative density Dr (%)	Laying depth D (cm)	Laying length L (cm)	Loading method	Geotextile types
80	–	–	Cyclic loading	No laying
	2	15, 30, 60, 120		Woven fabric A
	4, 6, 8	60		
	10	30, 60, 120		

assumed as asphalt layer in this research was one fifth as thick as the real asphalt layer, so the experiment this time was considered as one fifth of the real condition in the scale. The base course rolling thickness in practical construction was 10–15 cm. But regarding the scale of the experiment, the laying depth is adjusted into 2, 4, 8, and 10 cm (assumed from 10, 20, 40, and 50 cm in practical terms).

As the test condition shown in Tables 3 and 4, the influence of laying position (depth), laying length, geotextile types, and loading method on reinforcement effect was discussed on the model ground with a relative density of 80%.

3　Results and Discussions

3.1　Effect of the Type of Geotextiles

Panels a and b of Fig. 3 show the relationship between loading displacement and loading stress of each geotextile by static loading test. By laying various geotextiles, loading displacement was suppressed due to an increase in loading stress. Moreover, about the types of geotextiles, the woven fabric A exhibited the most effective displacement-suppression effect. Figure 4 shows the relationship between the number of loadings in the cyclic loading test for each geotextile and the loading displacement at the center of the loading plate, and Fig. 5 shows the loading displacement after 360 times of repeated loading. Figures 4 and 5 show that all the reinforcing materials were deformed immediately after loading and then gradually changed in loading. Moreover, loading displacement was suppressed by laying in all the reinforcing materials, and the reinforcing effect was exhibited.
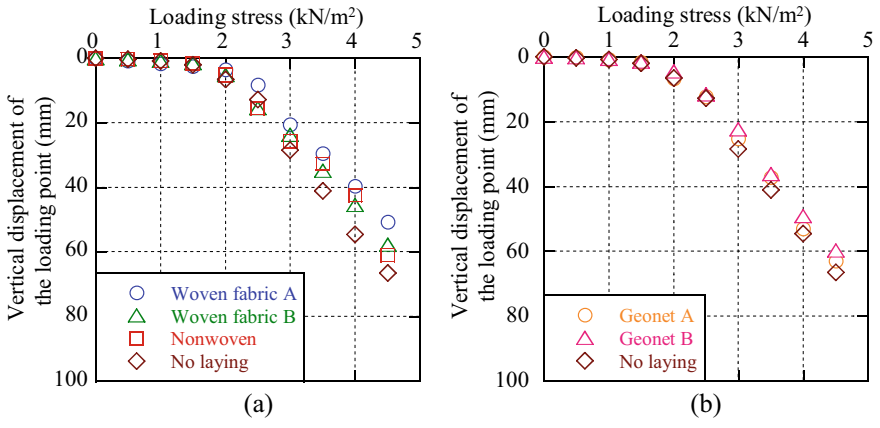
Fig. 3 Loading displacement and loading stress (static loading): **a** woven fabric, nonwoven and **b** geonet

Fig. 4 Number of loading times and loading displacement (cyclic loading)
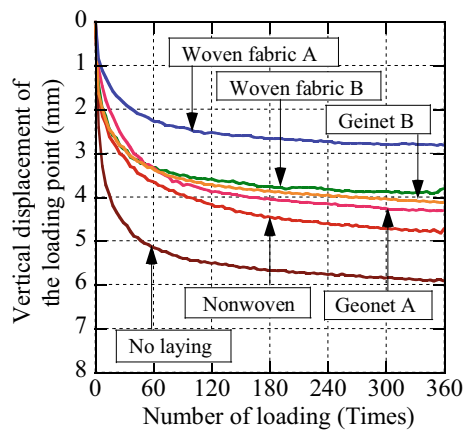
Fig. 5 Displacement after 360 loading cycles (cyclic loading)
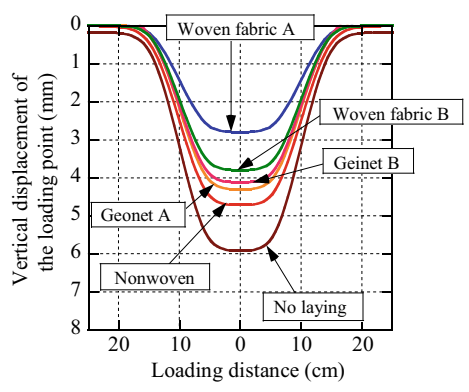
In terms of the difference in the types of geotextiles, the displacement-suppression effect was most exhibited in woven fabric A as in the case of static loading. In addition, when comparing the woven fabrics A and B, which are the same material, the load displacement was more suppressed in the woven fabric A which has a higher tensile strength, so. Thus, the tensile strength of each woven fabric affects the load displacement in the woven fabric. However, comparing two types of geonets with different strengths and shapes, the reinforcement effect was exerted more in geonets with larger meshes, although the strength was inferior. The reason was thought to be that the frictional force due to meshing with the ground material was more exhibited due to the large mesh. For this reason, the geonet is considered to be a reinforcing material that can be expected to have a friction effect due to the meshing effect with the base course material.

3.2 Effect of Geotextile Laying Depths and Lengths

Figure 6 shows the relationship between the number of loadings at each laying depth in the repeated loading test and the loading displacement at the center of the loading plate, and Fig. 7 shows the loading displacement after 360 times of repeated loading for woven fabrics A with cyclic loading. Both showed the results for $L = 60$ cm. The shallower the laying depth is, the better the reinforcement effect against displacement suppression becomes. The displacement was the smallest, and the reinforcement effect was greatest when $D = 2$ cm. This is considered to be due to the low geotextile laying depth, dispersion of the load, and increase of ground bearing capacity.

Figures 8 and 9 show the effect on the reinforcement effect because of the laying length at $D = 10$ cm. The loading displacement decreased in the order of $L = 30, 60,$ and 120 cm. This showed that the longer the laying length is, the more effective the reinforcement becomes. It is because the longer the laying length is, the greater the

Fig. 6 Number of loading times and loading displacement
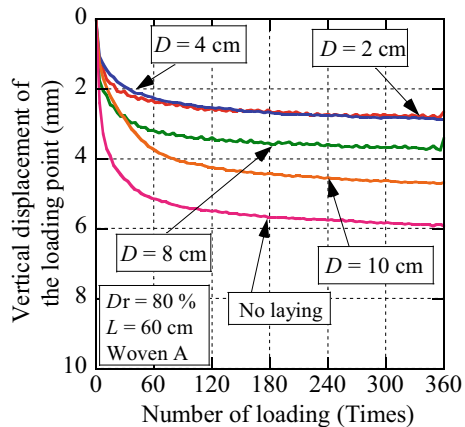
Fig. 7 Displacement after 360 loading cycles
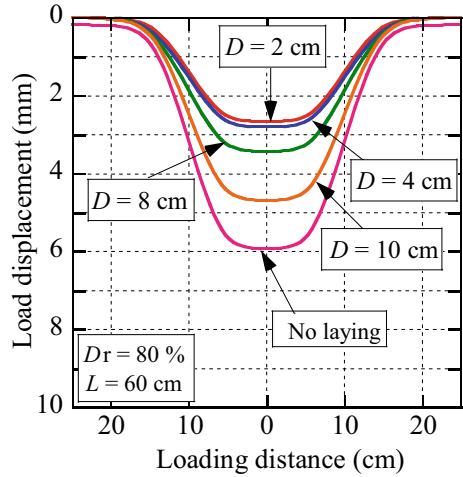
Fig. 8 Number of loading times and loading displacement
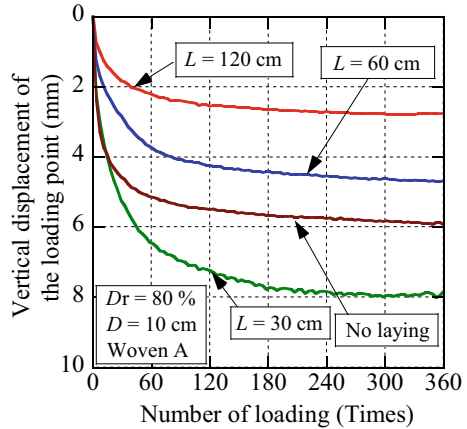
frictional force against the geotextile becomes through the increase of contact area between the geotextile and ground material. The frictional force will become greater with the increase of contact area, and the tensile force of the reinforcing material is generated by this frictional force. However, when $L = 30$ cm, the result shows a larger displacement than the condition without laying. From the stress distribution in Fig. 2, when $L = 30$ cm, the geotextile is within the range of the stress distribution, so it can be said that the tensile reinforcement effect of the geotextile is not enough in this condition. From those facts, it is shown that in practical road pavement, if the length extends beyond the range of the wheel load, the reinforcing effect can become better. Then, Figs. 10 and 11 show the effect on the reinforcement effect of the laying length at $D = 2$ cm. It shows the same effect as the case of $D = 10$ cm, which is that the loading displacement is becoming less with an increase of the laying length. In

Fig. 9 Displacement after 360 loading cycles
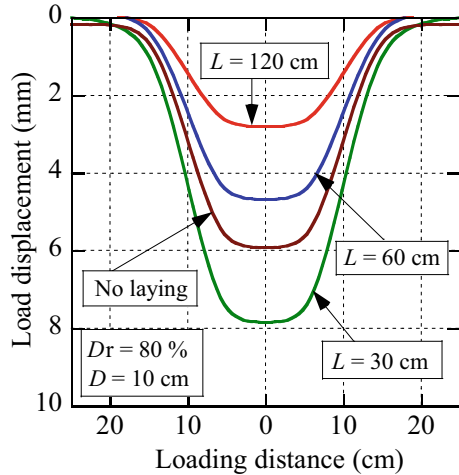
Fig. 10 Number of loading times and loading displacement
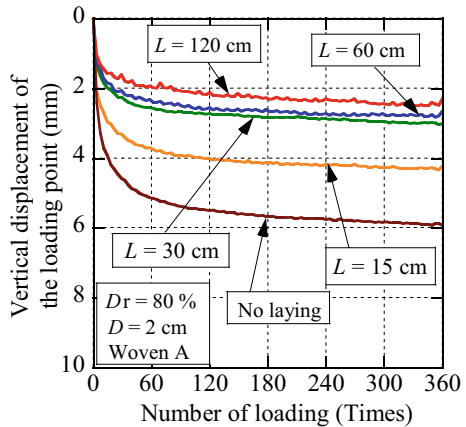
addition, compared with the case of $D = 10$ cm, the reinforcing effect can be good even when the laying length is short. This indicates that if the laying depth is reduced, the effect can be good even when the laying length of the geotextile is short.

Figure 12 shows the state of settlement of the loaded plate after repeated loading. In the state of settlement of the loading plate, it can be seen that there is almost no deformation when $D = 2$ cm and $L = 120$ cm. This also indicates that by reducing the geotextile laying depth and increasing the laying length, all the stress acting on the ground is dispersed at a shallow position. The frictional surface with the ground material and the reinforcement effect also increase. As mentioned above, when laying geotextiles on a road, it is important to make sure a low laying depth and determine the laying length considering the wheel load.

Fig. 11 Displacement after 360 loading cycles
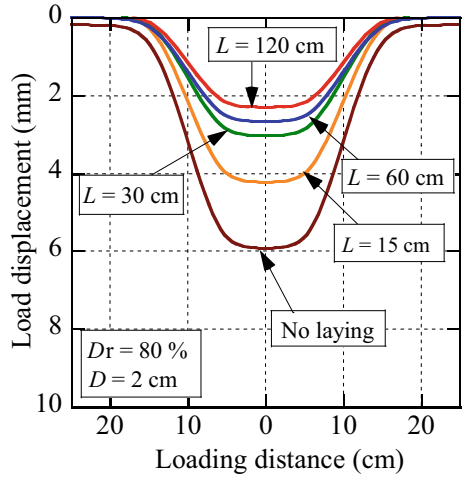
Fig. 12 State of settlement of the loaded plate after repeated loading: **a** $D = 10$ cm, $L = 30$ cm and **b** $D = 2$ cm, $L = 120$ cm

4 Conclusions

In this study, the importance of base course reinforcement in extending the service life of asphalt pavements was investigated by a model test using a small soil box. Therefore, the laying of geotextile was considered as a method of base course reinforcement. In the model test, the type of geotextile, its location, and length were investigated by static and cyclic loading tests. As a result, the following conclusions were obtained.

1. Geotextile is a material that can exhibit a friction effect due to a certain load displacement and can be expected to have a deformation suppressing effect when laid on the base course.
2. Geonet is a reinforcing material that can be expected to have a friction effect due to the meshing effect with the base course material.

3. Woven fabric with high tensile strength has the highest displacement-suppression effect, and it can be expected to suppress deformation due to traffic load on the base course material.
4. With the decrease of laying depth of the geotextile, the load is distributed more to the evenly distributed load, the ground supporting force is increased, and the reinforcing effect is better.
5. Regarding the geotextiles put in a low laying depth, with the increase of laying length, the reinforcement effect increases because of the frictional force against the ground material, because the tensile effect of the material is generated by the frictional force.
6. If the laying depth is reduced, the effect is good even when the laying length of the geotextile is short.

References

1. Zomberg JG, Roodi H, Sankaranarayanan S, Hernandez-Uribe L (2018) Geosynthetics in roadways: impact in sustainable development. In: Proceedings of the 11th international conference on geosynthetics
2. Yamauchi T (1986) Geotextiles—state of the art. J Jpn Soc Civ Eng 370(III-5):27–38 (in Japanese)
3. Takahashi Y, Hazama A, Tachibana T, Kaneko K, Kumagai K (2008) Experimental study on stability of reinforced soil wall using a high strength geotextile. Geosynth Eng J 23:155–160 (in Japanese)
4. Hirao K, Yasuhara K, Tanahashi Y, Takaoka K, Nishimura J (1992) Bearing capacity characteristics of model soft ground with reinforced geotextilies. Proc Geotext Symp 7:1–9 (in Japanese)
5. Hirakawa D, Miyata Y (2014) High stabilization of asphalt pavement by geogrid reinforcement. Geosynth Eng J 29:139–146 (in Japanese)

The Use of Microporous Membranes to Address Mud Pumping—UK Experience

Phil Sharpe and Andrew Leech

Abstract The UK has one of the most complex, most heavily trafficked rail networks in the world. In most areas, there is little time available for maintenance or track renewal; as a result, the installation of a completely new roadbed is seldom justifiable. Over the last 30 years, the need for time-consuming treatments requiring large volumes of excavation and imported sub-ballast has been gradually eliminated by maximising the use of geosynthetics to enhance the mechanical performance of the existing sub-ballast and subgrade. However, prior to the introduction of microporous membranes there was no treatment for a severe subgrade erosion problem that did not require installation of a new granular layer before placing new ballast. The paper summarises early roadbed treatments, subsequent research work on geosynthetics and the development of a suite of geosynthetic treatments. These would mitigate problems with existing sub-ballast or subgrade before placing new ballast. The development of microporous membranes is then described. Finally, the paper summarises the current methodology used by network rail (NR) to select an appropriate treatment for any given site.

Keywords Roadbed · Geosynthetics · Mud pumping

1 Roadbed Management Prior to Introduction of Geosynthetics

With increasing mechanisation of track renewal in the middle of last century came the realisation that in order to achieve good track geometry a deep layer of ballast was required. Therefore, it is NR policy to ensure that when track is renewed there was always an adequate depth of good clean ballast. However, it was recognised that

P. Sharpe (✉)
Phil Sharpe Limited, 17 Moor End, Spondon D21 7ED, UK

A. Leech
Geofabrics Ltd, Skelton Grange Rd, Leeds LS10 1RZ, UK
e-mail: aleech@geofabrics.com

re-ballasting alone could not solve problems associated with poor load distribution on a soft subgrade or erosion of a subgrade that has inadequate protection. It was also recognised that for a sub-ballast to perform well over a fine-grained subgrade it should have the correct filtering characteristics that would allow pore pressures in the subgrade to dissipate, while preventing any fine-grained particles from migrating upwards into the ballast layer. Excessive upwards migration of fine-grained material eroded from the subgrade would result in mud pumping; especially if lineside drainage was poor.

The presence of mud in the ballast causes track to become unstable; i.e. the track geometry deteriorates rapidly and requires frequent track surfacing. In order to restore track stability, it is necessary to determine the cause of mud pumping and install suitable remedial measures before installing new ballast. It was acknowledged that for good roadbed performance in the UK climate both ballast and sub-ballast layers had to have good lateral permeability, and the drainage system must be designed to prevent standing water in the roadbed.

1.1   Subgrade Erosion in the UK

The majority of soils in the UK are fine-grained, often soft and weathered, and as such are inclined to erode when ballast is placed directly above without the inclusion of a suitable interlayer. Historically a capping layer (or sub-ballast) was placed between the ballast and the subgrade, both to distribute load and prevent intermixing. The composition of the sub-ballast was dependent on the local materials available. Some of these layers were very effective; they had the correct grading to prevent the upwards migration of fines into the ballast. However, in many cases they were inadequate, and permitted fines to accumulate in the ballast as a result of subgrade erosion.

Another major cause of subgrade erosion in the UK has been the removal of effective sub-ballast layers. Many of the fine-grained soils are either stiff over-consolidated clays/silts or mudstone, so at the time of construction the roadbed thickness would have been minimum, sometimes consisting of a thin capping of ash separating ballast and subgrade. As a result, when installing a modern deep ballast layer, the thickness of residual capping is often inadequate or it is even removed completely, which results in the ballast being placed in direct contact with a susceptible subgrade. This can result in subgrade erosion, especially if the drainage is poor. In some cases, ballast life can be as little as 1 year, before the voids become totally filled with clay or silt slurry.

1.2   A Sand Blanket

The solution to subgrade erosion problems adopted circa 1960 by British Railways (BR)[1] was to install a "sand blanket". It was found that a well-graded coarse sand, with particle sizes largely in the range of fine sand to fine gravel, would perform adequately. It would normally be placed in layers of thickness between 200 and 300 mm, on a "one-size-fits-all" basis. It could be used to replace an existing, poorly performing blanket Additional thicknesses were installed as required to improve stiffness. The grading of this "Blanketing Sand" [1] was well-specified; it has a pore size which gives good permeability, while preventing the migration of clay and silt particles. Sand blankets are still used in certain circumstances today.

1.3   Use of Impermeable Membranes

At the same time, as the sand blanket was introduced there were various trials of impermeable membranes as separators. Polythene sheets were often included within sand blankets but were subsequently found to have little effect on their performance. Sprayed bitumen was also used to seal formations during undercutting work, but there is no documented evidence regarding its effectiveness.

Some years after geosynthetics were introduced an impermeable geocomposite was launched which claimed to prevent subgrade erosion. It was essentially a cuspoid-profiled stiff polyethylene membrane sandwiched between two layers of heat-treated geotextile. The product had some successes but was unsuitable for areas with poor drainage. It was found that slurry would pump sideways and find its way back into the ballast. The product was eventually discontinued due to inadequate overall performance.

2   Early Research into the Design of Roadbed

In 1964, the British Rail Research Division (BRR) was established in Derby, reporting directly to the Board of the nationalised "British Railways". The intention was to improve railway reliability and efficiency, while reducing costs and improving revenue. In the late 1970s, there was much research into the design of roadbed. However, the research was largely funded by the International Union of Railways (UIC) [2] in connection with the construction of new high-speed lines in various European Countries. For optimum performance, the new roadbeds required large thicknesses of granular capping layers and sub-ballast. However, with existing lines there was little opportunity to increase sub-ballast thickness as this would be time

---

[1] British Rail—former name of nationalised UK rail network, Privatised in 1994, Railtrack subsequently formed to manage infrastructure. Current ownership since 2003: Network Rail.

consuming. Design optimisation for existing formation therefore required a different approach.

It was accepted that new ballast was required to maximise track life and to enable track to be maintained, yet it was clear that re-ballasting alone could not correct inherent formation problems which might cause premature failure of the roadbed. Prior to the introduction of geosynthetics to enhance formation performance the only way to improve formation properties was to replace the old sub-ballast layers, e.g. with a sand blanket, which could only be considered in extreme cases.

Geosynthetics first became available in the 1970s, but their use was driven by manufacturers who made bold claims about the effectiveness of their products. There were various products trialled on the strength of claims that they could eliminate the need for sand blankets, but it wasn't until BR Research division carried out controlled studies that the effectiveness of geosynthetics could be realised. The broad objective was to determine how new construction techniques and materials could be used to enhance the properties of existing roadbeds. A programme of laboratory testing and associated site trials with suitable control sections was carried out, essentially to examine the use of non-woven geotextiles and stiff biaxial geogrids [3]. Woven geotextiles were included in these initial trials but were subsequently dismissed, as their filtering characteristics were poor, and their reinforcing characteristics were inferior to those of biaxial geogrids.

2.1 Non-woven Geotextiles

It was clear that there was no existing geotextile that could prevent the passage of clay slurry. The pore size of a geotextile was 30μ–50μ, whereas clay particles are less than 5μ, so a clay slurry would pass through easily. However, there was some indication that the use of thicker geotextiles was having some beneficial effects. A series of laboratory tests were undertaken by BR in an apparatus, referred to as a pulsator, that simulated the pumping action at track formation level [4]. The formation was modelled using a stiff over-consolidated clay on which the prepared geotextile test sample was placed. The ballast was simulated by a 25 mm layer of pea gravel. Cyclic loading was applied to simulate trafficking; the water level was maintained at height of 40 mm above geotextile under test. The main finding was that the efficiency in preventing the movement of a clay slurry was proportional to the mass/m^2 of the geotextile, irrespective of method of manufacture.

Other studies examined the effect of reducing sand thickness. Inspection of sand blankets that were successfully arresting the migration of clay slurry indicated that clay slurry had penetrated less than a quarter of an inch into the base of the sand, with the remaining sand being clean. The research trials described in [3] demonstrated that a 25-mm-thick layer of blanketing sand was enough to prevent the migration of clay slurry, provided that a geotextile was included as a separator between the sand and ballast. This led to the standard use by BR of geotextile as a separator between

sand and ballast, which allowed the sand blanket thickness to be reduced to 100 mm (25 mm was considered impracticable).

2.2 Biaxial Geogrids

Initial site measurements showed that elastic strain levels in ballast were very small, which suggested that geogrids may be unsuitable for use in roadbed [3]. However, both laboratory scale model trials and full-scale rolling load trials had shown that there were significant benefits to be gained by including a geogrid at the base of the ballast layer. The half scale model testing [5, 6] had shown the formation stiffness was critical in determining ballast settlement, with settlement rates over a soft formation being up to four times that of a stiff formation. Further testing showed that on soft formation ballast settlement could be reduced by more than 50% while on stiff formation there was very little effect. It was concluded that the presence of geogrid at the base of the ballast would allow the ballast to support tensile stress. Subsequent full-scale testing was undertaken in the "Rolling Load Rig" at BRR [7], which confirmed the reduction in ballast settlement under realistic loading conditions.

To investigate the durability of geogrids in the track, samples were taken in 2007 from a main line application installed 19 years earlier [8]. These samples were subjected to microscopic examination and testing of mechanical properties and were found to be still well within their original specified limits.

3 The Development of Anti-pumping Geocomposites (APGs)

The use of a 100 mm sand blanket with geotextile remained as the primary solution to a severe subgrade erosion for many years. Typically, 30 miles of sand blanket would be laid every year to satisfy BR's programme of domestic renewals. The long-term aim therefore remained to find a geosynthetic that could completely replace all the functions of the sand blanket as a sub-ballast layer, provided that the stiffness of the underlying formation was adequate. The first step in the development of alternatives was to set down the criteria that would need to be satisfied to permit the material to function successfully. The following criteria were identified:

- It must perform as a filter of fine soils, it must prevent the upwards migration of fines, yet it must aid desiccation of existing slurry. This means that the material cannot be impermeable to water and must have a pore size able to prevent the passage of particles as low as 2μ with surface pressure of approximately 70 kPa. This is relatively complex, as the material must be sufficiently open to allow the passage of water yet be closed enough to prevent the passage of clay particles.

Fig. 1 Installation of a 15 m roll of geosand

Fig. 1 Installation of a 15 m roll of geosand

- It must conform to the excavated formation, as any voids that may exist below the media would allow for the development of pockets of slurry resulting which would be undesirable.
- It must be durable to the dynamic environment encountered below ballast for the full duration of the required design life. There are two principal areas for concern, the material cannot suffer any potential failure as a result of fatigue, and the polymers used must also be suitable for the environment in relation to their long-term degradation.

3.1 Sand/Geotextile Composite

The first product to fully replace a traditional sand blanket essentially consisted of a 15-mm-thick layer of blanketing sand, loosely bonded to ensure its integrity while retaining its filtering properties [9]. The sand layer was protected top and bottom with a non-woven geotextile and was supplied either as pads or rolls. Figure 1 shows a 15 m roll of the product being rolled out manually; a specialised attachment was required to allow the roll to be craned into position. This product was discontinued in 2012.

3.2 Microporous Membrane

The first true anti-pumping geocomposite APG was launched in 2010 [10]. It consisted of a microporous membrane with a layer of needle punched geotextile above and below, as shown in Fig. 2. The pore size of the membrane was approximately 2μ which allowed the passage of water under pressure but would hold back fine silt and clay particles. The microporous membrane is effectively impermeable under low pressure, but it becomes permeable as pressure increases, which allows pore pressures to dissipate under traffic loading; initial testing demonstrated that

Fig. 2 TrackTex®—a geocomposite incorporating a microporous membrane
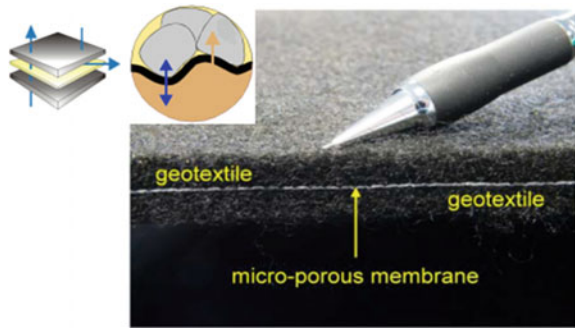
the threshold pressure was below 10 kN/m². The purpose of the upper and lower geotextile layers was purely to protect the central membrane.

Prior to launch the product had been trialled on a full-scale test rig with a series of actuators able to simulate realistic traffic loading as shown in Fig. 3. During earlier testing, the rig had been used to demonstrate both the mechanism of slurry production and how subgrade erosion could be prevented by the inclusion of a sand blanket [11]. It also demonstrated how ineffective a typical non-woven geotextile was at preventing subgrade erosion when compared to sand blanket.

In order to confirm the effectiveness of microporous membrane, a preparatory test was first undertaken to generate a severe pumping failure, as indicated in Fig. 4a. The subgrade used in the base of the rig was remoulded Oxford Clay, a grey slightly silty silicate mudstone which had weathered to a firm to stiff clay. The upper ballast was then removed to leave a 100-mm-thick layer of ballast contaminated with viscous clay slurry resulting from an ongoing subgrade erosion process, and the APG placed directly on top. Clean ballast and track were then replaced, and the water level was raised then maintained at 50 mm above the membrane to replicate conditions that would encourage the subgrade erosion to continue. Figure 4b shows the top of the
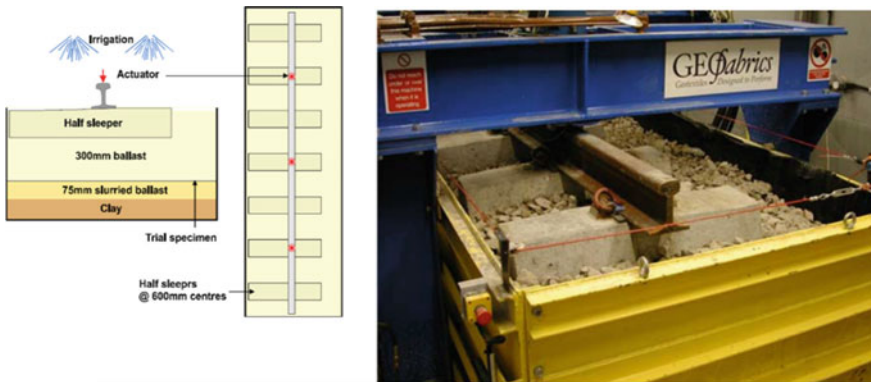
Fig. 3 Full-scale test rig—plan dimensions 2 m wide × 6 m long

(a)   (b)
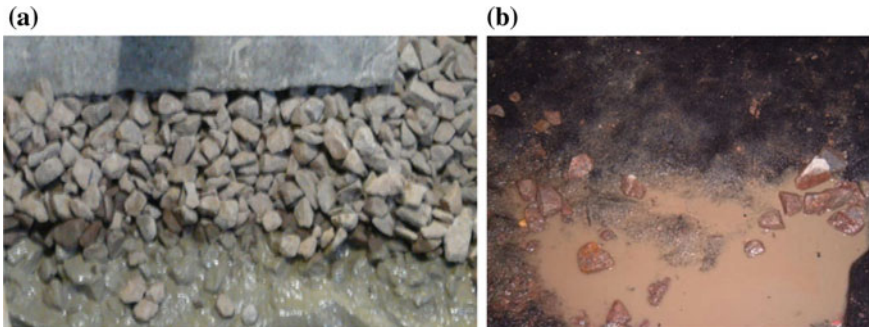
Fig. 4 **a** Generation of slurried formation, **b** APG after 70 mgt of loading.

APG after a simulated 70 million gross tonnes (mgt) of traffic. It was clear that no subgrade had migrated up through the membrane; the pink coloured wet residue above the APG was identified as fines derived from ballast breakdown.

APGs have now been in regular use in the UK now for almost ten years. The first installation by network rail was in September 2011 at Bradley Junction, a line that carried 6 mgt per annum of mixed traffic. The subgrade through much of this site was mudstone of the Lower Coal Measures, which had eroded and was present in the ballast as a light brown viscous clay slurry. A 100-mm-thick sand blanket had been proposed for this site, so the decision to use an APG over the part of the site with formation failure enabled the excavation depth to be reduced, giving valuable time savings. Figure 5 shows the installation. The APG was installed in conjunction with a biaxial geogrid to enhance the stiffness of the subgrade. Figure 6a shows the heavily slurried state of the formation at part of the site prior to installation. After six years in track NR commissioned trial holes on the site to assess the performance of the APG [12]. Figure 6b shows the base of a trial hole taken at the exact location of

Fig. 5 Installation of geogrid + APG at Bradley Junction

Fig. 6 **a** Formation prior to installation, **b** APG, 6 years post installation

the slurried formation shown in Fig. 6a; it was clear that no clay slurry had migrated upwards through the membrane.

4 Selection of the Correct Formation Treatment

In order to ensure a consistent approach to the process of investigation, design and construction of roadbed for an existing line a specification **NR/L2/TRK/4239** has been developed over the past 25 years. This now includes recommendations for where APGs are required. The process of determining if formation treatment is required begins when the track manager identifies the need to renew either the track or the roadbed or both. The first stage is to undertake a visual examination desk study of available information, from which a decision can be taken on whether an investigation is required. The following sections summarise the investigation and design of roadbed.

4.1 The Roadbed Logging Key

One of the first stages in standardising roadbed investigations was to propose a standard logging key for roadbed materials. This allows the nature and geotechnical properties of the various roadbed layers to be recorded and presented in a way that represents properties of the roadbed layers that relate to roadbed performance, rather than the general geotechnical parameters. The logs are particularly valuable in understanding deterioration modes and calibrating the GPR profiles. Figure 7 gives the current version of the Logging Key [13]. This logging key was customised for use on roadbed constructions commonly encountered in the UK, consequently some of the material descriptions and colour coding may not be universally applicable. However, it would be straightforward process to simplify the key to suit local conditions.

1 BALLAST

a) With no subgrade erosion

1 Clean Ballast
2 Slightly Dirty Ballast
3 Dirty Ballast
4 Very Dirty Ballast (non-cohesive)
5 Very Dirty Ballast (cohesive)
6 Very dirty ballast (slurried)

b) With subgrade erosion

7 Slurried Ballast < 10% fines
8 Slurried Ballast > 10% fines
9 Ballast – Voids filled with silt/fine sand
10 Ballast – Voids Filled with soft/firm clay

2 TRACKBED LAYERS/FILLS

a) Derived from naturally occurring Sands and Gravels.(% refers to clay/ silt content)

11 Fine/Medium Sand (<5%)
12 Coarse Sand (<5%)
13 Sand and Gravel (<5%)
14 Clayey/silty Sand and/or Gravel (5 to 20%)
15 Slurried Sand and/or Gravel (5 to 20%)

b) Quarry Products

16 Stone dust (<5%)
17 Coarse Crushed stone aggregate (<5%)
18 Clayey/silty Crushed Stone Aggregate (5 to 20%)
19 Slurried Crushed Stone Aggregate

c) Ash

20 Fine ash (sand sized) (<5%)
21 Coarse ash (gravel sized) (<5%) and
22 Clayey/silty Ash (5 to 20%)
23 Slurried Ash

d) Other granular trackbed materials

24 Fine grained, susceptible to erosion (<5%)
25 Coarse Granular Layer (<5%)
26 Clayey/silty Granular Layer (5 to 20%)
27 Slurried Granular Layer
28 Any of 2 a-d in a clay matrix (20 to 50%)

3 SUBGRADE

Use legends from section 2 where appropriate,
legend with bold outline indicates natural ground

a) Homogenous Fine Soils (Clay and Silt)

31 Organic/Very Soft
32 Soft $Cu < 40kN/m^2$
33 Firm $Cu = 40$ to $75kN/m^2$
34 Stiff $Cu = 75$ to $150kN/m^2$
35 Very Stiff / Hard / Very weak Mudstone $Cu > 150kN/m^2$

b) Mixed (Fine and Coarse) Soils

36 Unstratified (clayey/silty Coarse Soil OR sandy or gravely Fine Soil)
37 Interbedded or weathered/ weakly cemented fine grained rocks

c) Rock or Rockfill

38 Weak fine grained (mudstone, limestone, chalk, fine sandstone)
39 Moderately strong to hard rock

4 PITCHING LAYERS

29 Clean pitching
30 Slurried Pitching

5 SAMPLE LOSS IN ABS

0x   X   Soil penetrated by ABS, but not recovered
0d   D   Soil displaced by ABS – indicative of very soft soil

6 ADDITIONAL INFORMATION

g – permeable geotextile separator
c – permeable geocomposite
m – reinforcing mesh (geogrid)
p – impermeable membrane (polythene)
h – impermeable geocomposite
w – water level (wet samples)
ws – standing water (recorded in drill hole)
hs – historical slurrying
34 – shear strength kN/m^2
e – likely chemical contamination
L - >10 % limestone ballast

Fig. 7 Network rail logging key—version 3 (NR/L2/TRK/4239)

4.2 Investigation of Roadbed Condition

NR commonly use the automatic ballast sampler (ABS) as the main method of procuring good quality samples of the roadbed, which can penetrate to depths of up to 1.5 m below base of tie. Targeting of ABS and other methods of investigation is undertaken based on a desk study in which all available information on the site is

collated, including detailed track geometry records, work records and known geology. GPR data is also available for most sites as it is collected automatically at regular intervals on all main lines. Data is summarised on a schematic diagram of the track, which then facilitates targeting of investigation.

5   Design of Roadbed Treatments

Figure 8 shows an example of a design chart which allows the correct treatment to be selected based on the condition of the existing roadbed and subgrade. Figure 9 then gives an exampling of a longitudinal section of a roadbed with the proposed base of ballast superimposed. This allows the most suitable treatment to be selected.

Formation	NR Code	Good Drainage	Satisfactory Drainage	Poor Drainage
Coarse Granular. No erosion	3, 4, 13, 17, 21, 25, 29, 39			
New Blanket	12	green	green	green
Fine Granular. Potential for Intermixing	11, 16, 20, 24	green	green	green
Silty or clayey, coarse granular.	5, 9, 10, 14, 18, 22, 26, 36	green	green	yellow
Granular, Slurried	6, 7, 8, 15, 19, 23, 27, 28	yellow	yellow	yellow
Erosion/abrasion susceptible subgrade – Firm to hard	32-35, 37, 38	yellow	yellow	yellow
Erosion susceptible subgrade – soft or organic	30, 31	red	red	red

Key to Formation Treatments

white	No Formation Treatment Required
green	Separator / Robust Geotextile only
yellow	Blanket Replacement Geocomposite
red	Sand Blanket

Notes:

Geogrid may be specified with separator and Anti-pumping Geocomposite (Blanket Replacement Geocomposite), where required to improve the stiffness of the trackbed.

Decision to use separator or robust separator shall be based on the presence of coarse particles that could cause abrasion

Fig. 8   Example of design chart, based on NR logging key classifications
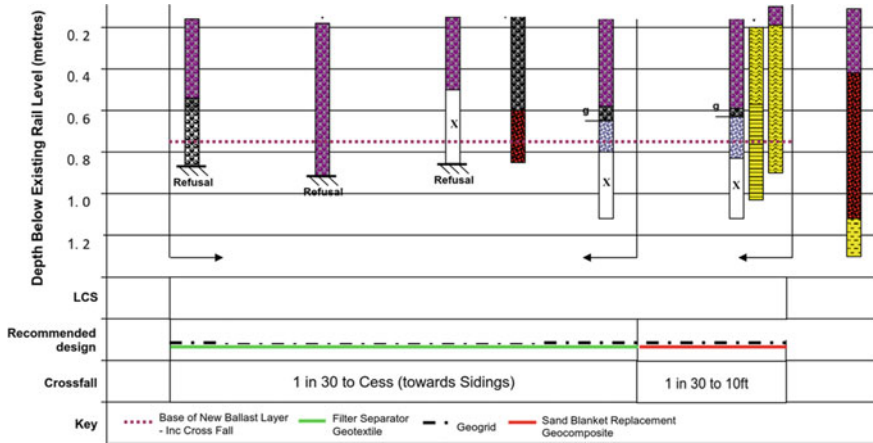
Fig. 9 Longitudinal section, showing proposed formation level and design

6 Conclusion

This paper has described the historical development of the use of geosynthetics on UK railways over the last 40 years and how, before 2007, there were no geosynthetic products that could successfully replace a granular sub-ballast (Sand Blanket). Geosand, the first successful APG, introduced in 2007, incorporated a fine granular layer, which made the product difficult to handle on site. Finally, in 2011 a geosynthetic incorporating a microporous membrane was introduced, which would eliminate the need for granular materials, providing the underlying ground was competent. APGs incorporating microporous membranes are now in regular use; approximately, 120 miles of track have now been treated in the UK since their introduction in 2010. They are now used in various countries including the USA, Canada, Australia and the Netherlands.

References

1. Network Rail Standard RT/CE/S/033. Track blanketing sand
2. UIC COMMITTEE—Question D 117. Optimum adaptation of the conventional track to future traffic, 1976–1982
3. Sharpe P (1988) Track foundation reinforcement—the performance of six experimental track foundations. BRR Technical Memorandum; TM - TM – 035
4. McMorrow J (1990) Filtering action of non-woven geotextiles under dynamic loading. British Rail Research, Derby
5. Hamed AH (1987) Geogrid reinforcement of ballasted track. MSc thesis, University of Birmingham
6. Sharpe P (2008) The use of geogrids on UK Railways. In: 4th forum of rail transport, Bratislava
7. Matharu SM (1994) Geogrids cut ballast settlement rates on soft sub-structures. Railway Gazette International, Mar 1994

8. Hall CD, Sharpe P (2007) Review of geogrid stabilisation of railway ballast. Railway Engineering, London
9. Burns B, Ghataora GS, Sharley P (2006) Development and testing of geosand composite layers using a pumping index test. In: Railfound 06—international conference on railway track foundations, pp 385–393
10. Sharpe P, Roskams T, Valero SN (2014) The development of a geocomposite to prevent mud pumping. In: CORE 2014, Adelaide
11. Sharpe P, Caddick VR (2004) Accelerated testing of geosynthetics in trackbed using Europe's largest full scale rail rig. Railway Engineering, London
12. D'Amico D (2017) Bradley Junction TBI report, Mar 2017. AECOM
13. NR/L2/TRK/4239 (2015) Trackbed investigation, design and installation

ASIRI+: French National Research Program on Soil Reinforcement with Rigid Inclusions

L. Briançon ⓘ **, L. Thorel** ⓘ **, and B. Simon** ⓘ

Abstract The ASIRI+ Project, initiated in April 2019, is presented with a special focus on rolling loads for the application to linear geotechnical infrastructures such as railways and roads. This type of loading needs to be taken into account for understanding and qualifying the efficiency of the load transfer for several geometrical configurations: loads following one-way, two-ways or random direction; load transfer platform reinforced with geosynthetics or not. Laboratory testing and centrifuge modeling devices are used for this research.

Keywords Soil reinforcement · Geosynthetics · Rigid Inclusions · Piled embankment · Rolling load

1 Introduction

The National Project ASIRI (Soil Improvement by Rigid Inclusions—www.asiri. irex.asso.fr) mobilized, from 2005 to 2011, thirty-nine partners (practitioners and academics) with a total budget of €2.9 million. This collective action received the support and direct funding from partners, the department in charge of the Transition Ecology and Solidarity (Commissariat Général au Développement Durable/Direction de la Recherche et de l'Innovation) and ongoing support from IREX (Institut for applied research and experimentation in civil engineering) for the management of

L. Briançon
GEOMAS, Université de Lyon, INSA-Lyon, 69621 Lyon, France
e-mail: laurent.briancon@insa-lyon.fr

L. Thorel (✉)
GERS, GMG, Université Gustave Eiffel, Allée des Ponts et Chaussées, CS4, 44344 Nantes, Bouguenais Cedex, France
e-mail: luc.thorel@univ-eiffel.fr

B. Simon
Terrasol, Paris, France
e-mail: bruno.simon@setec.com

the project. The NP ASIRI has worked to define, conduct, and interpret the experiments and modeling necessary to understand the mechanisms thanks to which this innovative composite foundation system works. This program of applied research has benefited from the range of expertise of the previous project; the valuable contribution of each partner and the material and human resources that each organization has made available. A very exceptional database of experimental data and numerical results was set up, supported by nine PhD theses carried out within the framework of the project. Observations and modeling could thus be compared for a wide variety of works. New perspectives have emerged, showing how the combination of such different elements (soft soil, inclusions, granular load transfer platform) leads to an efficient and particularly economical composite system. More than 70 scientific articles (journals and conferences) were published using the means developed within the ASIRI NP.

At the end of this study, the French version of the ASIRI *Recommendations for the Design, Construction and Control of Rigid Inclusion Ground Improvements* [1] was published in 2012 and the English version in 2013.

The work targeted by the ASIRI NP were mainly embankments, paving and shallow foundations subjected to static vertical loads and most often uniform. The good behavior of common structures on Rigid Inclusions (RI) has led to this technique being proposed for other works outside the field of application of ASIRI recommendations, or subject to demands that are more complex:

- Low-thickness embankments for which it is imperative to control differential settlement,
- Structures that transmit cyclic loads maintained on the reinforced soil (e.g., wind turbines) with a significant horizontal component,
- Foundations of structures that have to recover dynamic and not vertical efforts in seismic situations,
- Shallow foundations placed directly on RI, without load transfer platform (LTP).

The aim of the "ASIRI+ project," which has been launched by April 2019, is to extend the current ASIRI recommendations [1] to new applications:

- Roadways or railway tracks built on thin geosynthetics (GSY) reinforced piled embankments for which it is essential to be able to appreciate the load transfer mechanisms in the LTP, in order to optimize its thickness in relation to the expected service performance criteria;
- Works that transmit sustained cyclic loads to the reinforced soil mass (wind turbines for example), with a significant horizontal component;
- Foundations of geotechnical works that are exposed to dynamic general loads (that cannot be reduced to vertical force) in seismic situations and the number of which has greatly increased because of the new seismic hazard map applied in France since 2011;
- Foundations placed directly on RI without LTP.

A comprehensive state of the art [2] is available on the ASIRI technique used in this type of configuration, based largely on scientific and technical publications. The

Fig. 1 Principles of RI reinforcement (here the case of a slab) [1]
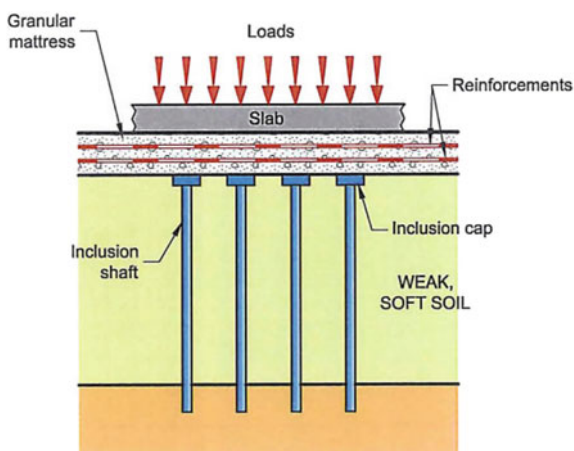
purpose of this paper is to present the main topics of this new French National research program which should gather around 40 partners both from the academic and the practitioner sides. A focus will be done on the application to linear geotechnical infrastructures such as railways and roads. The full-scale and laboratory experimentations will be presented.

2 Principles of Rigid Inclusions Reinforcement

As defined in the ASIRI recommendations [1], soil improvement by RI requires the installation of a LTP between the RI and the work (Fig. 1). This LTP sometimes referred to as "mattress" (granular or treated) may or may not be reinforced with horizontal reinforcements (GSY or welded mesh).

This type of composite foundation is often used for both road and railway applications.

3 Research Program

The research program [3] includes several topics that will be addressed through ten tasks (https://asiriplus.fr/):

- Task 1: Study of the mechanisms developed in the LTP—Experimental approach,
- Task 2: Real works instrumentation,
- Task 3: Laboratory tests to study the position of the reinforcements under the shallow embankments with traffic considerations,
- Task 4: Footings over RI,

- Task 5: Wind turbines on RI,
- Task 6: Behavior of soil reinforced by RI under dynamic loads,
- Task 7: Behavior of soil reinforced by RI under seismic loading,
- Task 8: Numerical modeling,
- Task 9: Environmental impact,
- Task 10: Promotion and transfer toward practice.

This comprehensive research program has been established by joining three different types of funding:

- A kind of joint venture, the French National Project ASIRI+,
- French Inter-ministries Unique Funding Project FUI25 FEDRE ("Fondations d'Eoliennes Durables avec REpowering") linked to task 5,
- French National Research Agency Project ANR ASIRI*plus*_SDS (Seismic and dynamic loadings) which covers both tasks 6 and 7 [4],
- The traffic consideration is mainly taken into account in task 3, and partly in tasks 8 and 6 (from a wave propagation point of view).

4 Experimental Work of Task 3

4.1 Laboratory Tests at Full Scale

An experimental device to test the effectiveness of GSY reinforcement layers on granular platforms subjected to rolling loads is available in the GEOMAS laboratory at INSA Lyon (Fig. 2). Test bench dimensions (1.8 m wide, 5 m long, and 1.2 m high) consider conducting LPT tests on RI on a scale of 1. An analogical compressible soil will be implemented: 50 cm RI, foam layers simulating the compressibility of a soft soil, instrumentation to control the load transfer and the settlement, granular layer reinforced or not by geosynthetics. The advantage of this laboratory experiment is that it is possible to multiply the configurations of the reinforcement of the granular

Fig. 2 Scheme of the experimental device for full-scale laboratory test
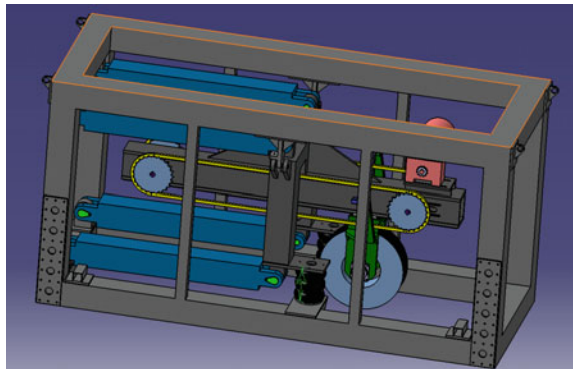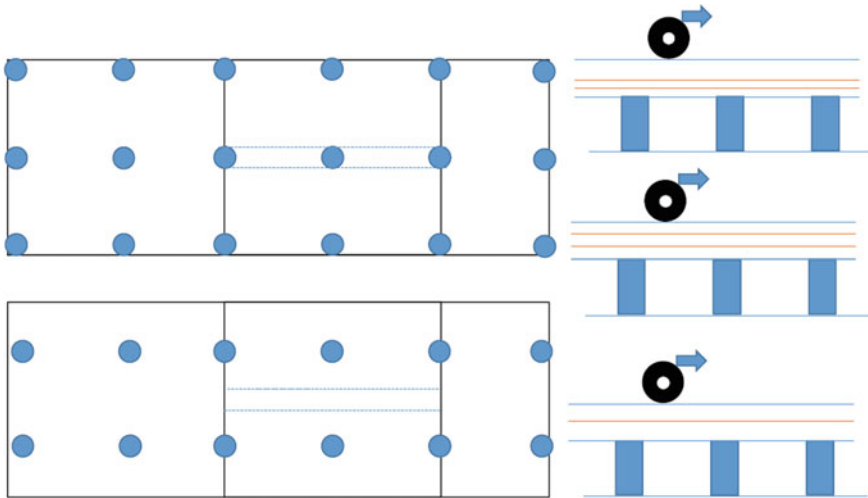
Fig. 3 Tests of rolling traffic

platform, of the RI's mesh and to apply traffic cycles. The device used to apply this load is a traffic accelerator simulator. This device was designed and developed within the framework of the Labcom PITAGOR of INSA Lyon. This apparatus simulates one-way or two-way traffic under a normal load of 40 kN which corresponds to the load of a half-axle with a wheel-to-surface stress of 566 kPa. This device was designed to provide an effective running length of two meters between buffer zones. The running speed of the wheel is set between 7 and 10 km/h.

Some modifications will need to be made to the existing device to install Rigid Inclusions and foam layers. Tests may be carried out on the right side of a line of inclusions or between two lines (Fig. 3) and on vertical loads. The configurations in task 1 will be tested on this equipment to verify the consistency of the results and identify the scale effects if they exist. The tests performed in task 3 will:

- compare the effectiveness of LTP reinforced or not;
- determine the settlement;
- determine the optimum configuration of horizontal reinforcement;
- compare the effect of a vertical cyclic load to a rolling load;
- analyze load transfer mechanisms.

4.2 Centrifuge Tests

A set of 2D centrifuge tests will be first performed in order to visualize through à window, with image analysis techniques, the soil deformation in the LTP during rolling type loading. A mono-size cylinder with several possible mass will be designed for applying the rolling load.

Fig. 4 Ifsttar's geotechnical centrifuge (radius 5.5 m, 2t of payload @ $100\times$ g)

A parametric study will be carried out in Ifsttar's geotechnical centrifuge (Fig. 4) using the 4-axis teleoperator robot *X*, *Y*, *Z*, θx [5] to take into account traffic loads. This will require the development of a specific tool to be adapted to the robot's head: a model wheel (e.g., a mono-wheel [6] or a four-wheels [7]), corresponding to a typical rolling load configuration. The reduced soil-IR-embankment model reinforced by GSY, or LTP in treated soil is pre-constructed and instrumented, with natural or analogue materials. The parametric study will focus on the nature of LTP, the presence or not of GSY, one-way or two-ways movement (similarly), or random displacement in the horizontal plane. The case of the ultimate hydraulic flood loading can also be addressed.

5 Conclusions

The French Research Program ASIRI+ will join the energy of about 40 partners (engineering consultancy, geosynthetic producers, ground improvement firms, and academics) to act for a better understanding of the behavior of the composite foundation that is a soft soil reinforced with vertical Rigid Inclusions (RI), surmounted with a load transfer platform (LTP) possibly horizontally reinforced with geosynthetics (GSY). Experimental approach on full-scale and small-scale models as well as numerical calculations will be used to take into account the rolling load, and its effect on the efficiency of the load transfer toward the RI.

References

1. ASIRI (French Research Project on Rigid Inclusions) (2013) Recommendations for the design, construction and control of rigid inclusion ground improvements. IREX, Presses des Ponts, Paris
2. Briancon L, Carpinteiro L, Cuira F, Dias D, Dubreucq T, Escoffier S, Girout R, Grange S, Lenoir T, Lopez-Caballero F, Racinais J, Simon B, Thorel L, Villard P (2018) ASIRI+, state of the art (in French). Report IREX, 204 p
3. Briançon L, Cuira F, Dias D, Grange S, Racinais J, Simon B, Thorel L, Villard P (2019) ASIRI+, research program (in French), 36 p
4. Thorel L (coord) (2019) Soil improvement by rigid inclusions: seismic and dynamic loading. ASIRIplus_SDS ANR project, 20 p
5. Gaudicheau P, Thorel L, Néel A, Audrain Ph, Lozada C, Monroy J (2014) Improvement of the IFSTTAR robot control system. In: 8th ICPMG international conference on physical modelling in geotechnics, Perth, 14–17 Jan 2014, pp 221–226
6. Lukiantchuki JA, Oliveira JRMS, Pessin J, Almeida MSS (2018) Centrifuge modelling of traffic simulation on a construction waste layer. Int J Phys Model Geotech 18(6):290–300. https://doi.org/10.1680/jphmg.17.00012
7. Kearsley EP, WJvdM Steyn, Jacobsz SW (2014) Centrifuge modelling of ultra thin continuously reinforced concrete pavements (UTCRCP). In: 8th ICPMG international conference on physical modelling in geotechnics, Perth, 14–17 Jan 2014, pp 1101–1106

Effect of Natural Reinforcement Aperture Shape on Bearing Capacity of Reinforced Soil

Sunil K. Ahirwar and **J. N. Mandal**

Abstract It is of interest, for a developing country like India, to use natural and low-cost reinforcement material in rural roads. Bamboo is a locally and cheaply available alternative as a reinforcement material in place of commercial geosynthetic materials. The tridirectional bamboo grid is a new innovative reinforcement of the limited life geotextiles (LLGs) family. The present paper reports the experimental results of plate load tests conducted on sand overlying a soft clay. The model plate load tests were carried out to study the influence of the tridirectional and bidirectional bamboo grid with jute geotextile on the bearing capacity of soft marine clay. A mild steel tank with dimensions of 0.7 m × 0.7 m × 0.6 m and a square model footing size of 100 mm × 100 mm were used for all laboratory model tests. It was observed that by making a suitable modification in the aperture shape of reinforcement, the bearing capacity and settlement resistance of soft clay could be improved. The model test results show that the tridirectional bamboo grid offers superior performance compared to the bidirectional bamboo grid.

Keywords Bamboo grid · Jute geotextile · Thickness ratio

1 Introduction

In various field conditions, the soft soil is replaced by a granular fill below a foundation for a very efficient and cost-effective solution for a stable base on soft clay. Such

S. K. Ahirwar (✉)
Assistant Professor, Civil Engineering and Applied Mechanics Department, Shri G. S. Institute of Technology and Science, Indore 452003, India
e-mail: skasgsits@gmail.com

Research Scholar, Civil Engineering Department, Indian Institute of Technology Bombay, Mumbai 400076, India

J. N. Mandal
Indian Institute of Technology Bombay, Mumbai 400076, India

solution is applied mainly in various geotechnical structures, including embankments and pavements (rail and roads), and large stabilized areas. The performance of the granular fill-soft subgrade system can be enhanced by using a geosynthetics material at the interface of granular fill-soft subgrade. Many researchers [1–7] have performed experimental studies to examine the pressure-settlement behavior of the geotextile-reinforced sand layer overlying soft clay. Numerous experimental studies [8–11] have been conducted to evaluate the bearing capacity-settlement responses of geogrid reinforced granular fill over weak clay with geogrid at the interface. Most of these studies have aimed to enhance the performance of soft subgrade and improvement in bearing capacity and reduction in the settlement. These experimental studies were performed on commercially available reinforcement materials (geotextiles and geogrids) under strip footing, square footing, and circular footing. Such existing petroleum-based products are not environmental friendly.

The ecological characteristics of natural reinforced materials (bamboo and jute) have motivated researchers to explore the effective and efficient use of these materials instead of commercial geotextile and geogrid. The very few investigators have conducted the laboratory model testing by using natural reinforced materials for firming up the foundations base. Akinmusuru and Akinbolade [12] examined the load settlement of the sand reinforced with rope fiber. Dixit [13] explored the possibility of using niwar tape and coir rope to reinforce clay under square footing through the plate load test. Mandal [14] presented the promising application of natural materials such as jute, coir, bamboo as soil reinforcement materials in small structures. Ramanatha Ayyar et al. [15] examined by the model plate load tests, use of coir-rope reinforcement with bamboo strip anchorages to improve the bearing capacity of the soil. The mesh pattern of reinforcement was found to be more effective than unidirectional alignments. Mandal and Manjunath [16] studied the influence of bamboo grid alignment and spacing on the bearing capacity of sand.

Datye and Gore [17] have reported a field study where natural geotextile, combined with bamboo strip reinforcement, has been used for improvement in the base of roads. The investigators were found that the bamboo grid mattress provided strengthened support for improving the bearing capacity. Khatib [18] performed an experimental study on the performance of bamboo poles for bearing capacity improvement of the soft subgrade. The laboratory test results indicated that the footing pressure increased approximately twice using bamboo poles. Hegde and Sitharam [19] observed the behavior of natural reinforced material and commercial geosynthetic material in the sand-clay system. The bearing capacity improvement of the sand-clay system reinforced with the bamboo grid and the bamboo cell was obtained 130% more than that of the sand-clay system reinforced with commercial geogrid and geocell. Dutta and Mandal [20] performed experimental studies on the efficacy of bamboo grid and geocell mattresses using fill material (fly ash) over the soft soil bed using laboratory plate load tests. Ye and Fu [21] explored the suitability of bamboo for reinforcing the highway embankment based on the physical and mechanical properties of fresh bamboo. Ahirwar and Mandal [22] conducted plate load tests to quantify the impact of geometry of the bamboo grid on reinforced

sand and found that the tridirectional bamboo grid is more efficient than that bidirectional bamboo grid. The durability of the jute geotextile and bamboo grid is a critical consideration for geotechnical engineers. When jute geotextile use as a separator in unpaved roads, the jute is weakened and blended in soil within one year [23]. The jute geotextile life depends upon the temperature, pH, and humidity, moisture content, and properties of the soil where it would be buried. The long-term durability of jute geotextile can be enhanced up to 3–4 years by bitumen coating [24]. Saha et al. [25] compared the performance of untreated and chemically treated jute geotextile under biological degradation conditions. The authors concluded that the treated jute geotextile retained 50% of initial tensile strength after 3–4 years. The long-term stability is the main problem for bamboo in the construction of civil engineering projects.

Gnanaharan [26] estimates that natural bamboo's longevity is up to five years in wet environments. As long-term stability issues, various chemical treatments may be implemented on bamboo to protect from fungi and insects attack. The conventional treatment methods are sap displacement, steeping, diffusion process, and pressure impregnation for the fresh bamboo. Hegde and Sitharam [19] conducted a detailed study on chemical treatment of bamboo strip with copper chrome-arsenic (CCA) for performance enhancement. The longevity of bamboo can also be enhanced by coating with cement and bitumen.

Prasad et al. [27] used bamboo geogrid with bitumen coating for examining the efficiency of granular sub-base strengthened layers. In the looking of past studies, it can be concluded that the long-term durability of bamboo can be enhanced by using various treatment methods. Most studies have been reported on the experimental test results of bearing capacity tests on the reinforced sand bed using the bamboo grid of square aperture. So far, the limited investigations have been reported by the investigators on the influence of the geometry of geogrid. A detailed investigation of the different geometry (aperture shape) of the bamboo grid is require for the cost-effective design of reinforcement. The present study explained the performance of the reinforced base-subgrade system using the bamboo grid of different aperture shapes.

2 Experimental Investigations

2.1 Soil Used

The river sand used in the base layer was collected from Vikroli, Mumbai, India. The grain size distribution plot of sand is shown in Fig. 1. The uniformity coefficient of the sand (C_u) is 1.46, and its coefficient of curvature (C_c) is 0.92. The base material is classified as poorly graded sand (SP) as per the unified soil classification system ASTM D2487-17. The maximum and minimum dry unit weights were determined from the test procedure as follows ASTM D4253-16 and D4254-16, and the values found 15.30 kN/m^3 and 13.24 kN/m^3, respectively. Direct shear test was performed

Fig. 1 Grain size distribution curve for sand and clay
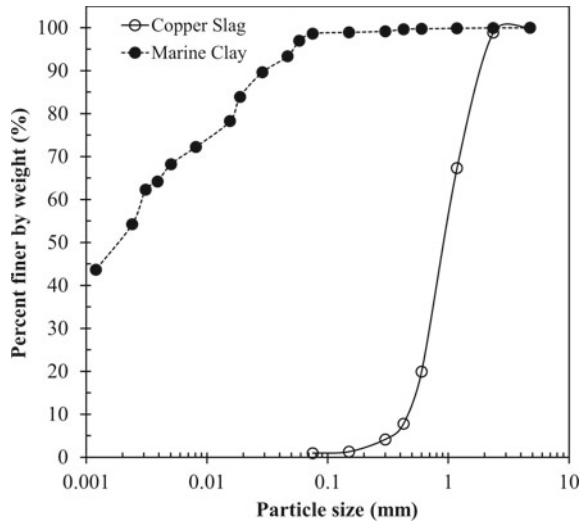
for obtaining the angle of internal friction of the sand. The average dry unit weight and the relative density of sand were maintained throughout the test program at 14.5 kN/m^3 and 65%, respectively. Marine clay used to prepare a subgrade layer was collected from Navi Mumbai, India. It contains sand 2%, silt 45%, and clay 53%. Atterberg's limits of marine clay are liquid limit 78% and plastic limit 44%. The clay is classified as CH (clay with high plasticity) as per the unified soil classification system ASTM D2487-17. The maximum dry unit weight and optimum moisture content (OMC) were obtained 14.8 kN/m^3 and 27% by standard Proctor test, according to ASTM D698-12e2.

2.2 Reinforcement

Jute geotextile was used at the interface of the subgrade bed (marine clay) and the base layer (sand) to provide a separator. The tensile strength properties were found 11 kN/m at the 6.8% failure strain as per ASTM D4595-17. The jute geotextile was 1.4 mm thick, measured according to the procedure given in ASTM D5199-12. The mass per unit area of jute geotextile was 0.8 kg/m^2, obtained from the test procedure mention in ASTM D5261-10. The fresh bamboo pole was used for preparing of bamboo strips. The bamboo strips of 3 mm wide and 1 mm thick were used to make a mat in the form of a grid. The length of the strip was chosen 650 mm. The bamboo strips were assembled in the planar form of bidirectional (square aperture) and tridirectional (hexagonal aperture) which are shown in Fig. 2. The tensile strength properties of the bamboo grid were evaluated 19 kN/m (bidirectional bamboo grid)

Fig. 2 Geometry of bidirectional and tridirectional bamboo grid

and 27 kN/m (tridirectional bamboo grid) according to the procedure given in ASTM D 4595-17.

2.3   Experimental Setup and Procedure

The bearing capacity tests were conducted on unreinforced and reinforced sand over marine clay bed in a square mild steel tank. The model test setup consists a square tank of inner dimensions 700 mm (length), 700 mm (width), 600 mm (depth), fabricated using 10 mm thick mild steel plates. A mild steel plate was used as a model footing of dimension as 100 mm × 100 mm × 15 mm. Two LVDTs were used to record the plate/footing settlement. A load cell of 10 kN capacity was used for measuring the footing pressure. Before making the soft clay bed in the tank, the inner walls of the tank were pasted a thin polythene sheet to prevent the friction between the soil and the inner wall. The required quantity of marine clay was weighed and placed in the tank. The marine clay was spread uniformly over the base area of the tank and then leveled it. The marine clay was well compacted in seven layers, and each layer was 50 mm thick. The quantity of damp soil required to form a layer was calculated based on maximum dry unit weight of 15.6 kN/m^3 and in situ moisture content of 67%. A modified proctor hammer was placed centrally in the grove of 70 mm diameter on this plate, and blows were imparted to it. After compaction, the clay surface was leveled, and pocket vane shear tests were performed to determine the unconfined shear strength. In series A, air-dried sand was allowed to fall from a height of 36 cm over the soft subgrade overlying soft subgrade to have a placement density of 1.45 g/cc. In series B1 and B2, the sand was placed over the soft subgrade after placing of jute geotextile and bamboo grid at the interface.

3   Results and Discussion

3.1   *Effect of Fill Thickness on Unreinforced and Reinforced Base Layer*

Initially, a model test was carried out on soft subgrade (marine clay) to determine the ultimate bearing capacity and settlement. Model test series A was conducted at a varying thickness ($H/B = 0.3, 0.6, 0.9, 1.2$) of the base layer (sand) over soft subgrade to investigate the effect of fill thickness on footing pressure-settlement behavior of the unreinforced base-subgrade system. Typical footing pressure-settlement curves for different fill thickness to footing width are shown in Fig. 3. From the curves, the bearing capacity improvement is observed with an increase in the thickness of the base layer over soft subgrade for the unreinforced case.

In series B1, the model tests were carried out on reinforced base-subgrade system by the varying thickness of sand to investigate the optimum fill thickness of sand. The jute geotextile ($b = 7B$) was placed at the interface of the base layer and soft subgrade, which acts as a separator. The bidirectional bamboo grid ($b = 4B$) of square aperture shape was also placed at the interface of sand and clay, which is acts as a geocomposite (jute geotextile and bamboo grid). In a reinforced model test, the thickness of the base layer was kept the same as the unreinforced case. The tests were performed separately for the bidirectional bamboo grid (square aperture) and a tridirectional bamboo grid (hexagonal aperture).

Typical footing pressure-settlement curves are shown in Fig. 4 for bidirectional and tridirectional bamboo grid reinforced base-subgrade system. It is seen from the curves that the ultimate bearing capacity of the reinforced base-subgrade system increases with the increase in H/B ratio from 0.3 to 0.6 and further increase in

Fig. 3 Footing pressure-settlement responses of unreinforced sand at different thickness ratio
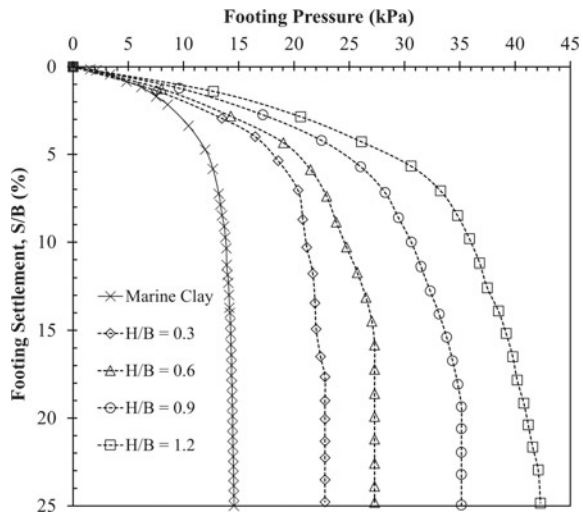
Fig. 4 Footing pressure-settlement responses of reinforced sand at different thickness ratio
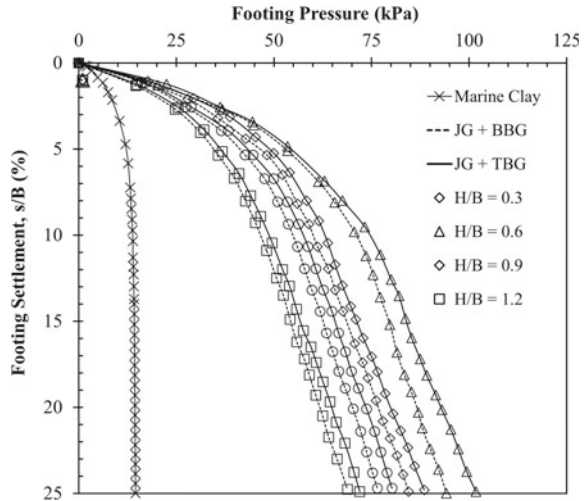
base thickness, the ultimate bearing capacity is decreased. The ultimate bearing capacity of 53 kPa is obtained at $H = 0.6B$ and it decreased to 35 kPa at $H = 1.2B$. The bearing capacity improvement due to the placement of jute geotextile and bidirectional bamboo grid (BBG) is attributed to geocomposite resistance. The jute geotextile offered membrane resistance, and the bamboo grid offered interlocking action at the limited thickness of the sand layer. As an increase in the thickness of the base layer ($H = 0.6B$), the placement of geocomposite beyond $H = 0.6B$ is not likely to improve the performance of the base-subgrade system. It indicates that the bamboo grid becomes less effective for greater thickness of base material since the influence zone is confined in the base layer.

Figure 4 also presents the footing pressure-settlement plots for a reinforced base-subgrade system using a tridirectional bamboo grid of the same size ($b = 4B$). The maximum footing pressure of the base-subgrade system using the tridirectional bamboo grid (TBG) reinforced base layer was found at $H/B = 0.6$, which is higher than that of footing pressure corresponding to reinforcement depth ratio $H/B = 0.3$, 0.9, and 1.2. The ultimate bearing capacity was reduced with an increase in sand layer thickness; the maximum ultimate bearing capacity of 61 kPa at $H/B = 0.6$ was reduced to 35 kPa. For the same size ($b = 4B$) of the tridirectional bamboo grid, the footing pressure improvement of the base-subgrade system was observed higher as compared to the bidirectional bamboo grid. It may be due to the effect of interlocking action, and surface friction resistance provides by the hexagonal aperture bamboo grid. The bearing capacity of the base-subgrade system is increased 53% with the provision of BBG (bidirectional bamboo grid) and whereas the provision of TBG increased it by as much as 60%. The results showed the appreciable influence of the TBG and BBG for the small thickness of the fill. The footing settlement of the base-subgrade system is also decreased by up to 29% and 16% using BBG and TBG, respectively, as compared to the unreinforced system.
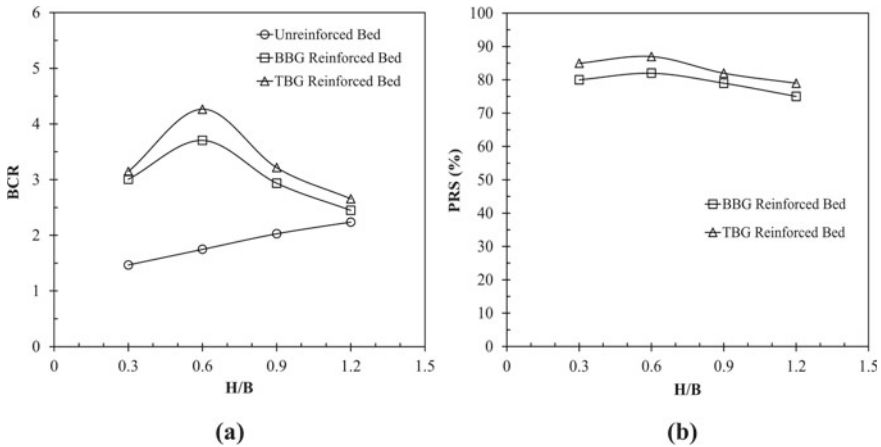
Fig. 5 Variation of **a** BCR with H/B, and **b** PRS with H/B

In the present study, bearing capacity ratio (BCR) term is used as the ratio of the ultimate bearing capacity of a reinforced base-subgrade system to the ultimate bearing capacity of the unreinforced subgrade. The plots between BCR and thickness ratio H/B are shown in Fig. 5a. It can be seen that the BCR value is 3.71 at $H/B = 0.6$, which reduces to 2.94 at $H/B = 0.9$ and further reduces to 2.45 when the $H/B = 1.2$. This trend of decrease in BCR value with an increase in H/B ratio indicates that the $H/B = 0.6$ is suitable fill thickness for achieving maximum BCR value for BBG reinforced base. A similar trend of results can be seen in the TBG reinforced base layer. The BCR values of the TBG are found to be higher than that of the BBG reinforced base-subgrade system.

The footing settlement behavior of the reinforced base-subgrade system is plotted between percentage reduction in footing settlement (PRS) and thickness ratio H/B. The percentage reduction in footing settlement defined as PRS = (Su − Sr)/Su × 100, where Su is the settlement ratio of non-reinforced subgrade corresponding to ultimate bearing capacity at a particular H/B ratio and Sr is the settlement ratio of reinforced base corresponding to the same value of the ultimate bearing capacity of unreinforced subgrade. Figure 5b shows the comparison of percentage settlement reduction and thickness ratio for the BBG and TBG reinforced base-subgrade system. It is observed that the PRS increases with an increase in thickness ratio up to the optimum value of the H/B ratio after that slightly decreases with an increase in thickness ratio H/B. The PRS values were found 72% and 78%, respectively, for BBG and TBG. It may be possible due to the better interlocking system developed through bamboo grid reinforcement and lateral and peripheral resistance during footing settlement.

4 Conclusion

The provision of jute geotextile and bamboo grids at the interface of soft subgrade and a stiffer base of sand material causes an appreciable gain in bearing capacity for the base-subgrade system. Based on the method of analysis and the experimental results presented in this investigation, it is found that higher the stiffness of the base then the higher is the degree of improvement, with the effect of geocomposite being more pronounced when the base layer thickness is less than 0.6 the footing width. For base thickness higher than $0.6B$, however, the effect of geocomposite becomes insignificant. The optimum fill thickness H/B of bamboo grid reinforced base layer is found 0.6 times the width of footing for the tridirectional and bidirectional bamboo grid and for achieving maximum bearing capacity. The ultimate bearing capacity can be improved by using natural geocomposite reinforcements by about 2.5–3 times. The BCR was found 3.71 and 4.27 for BBG and TBG, respectively. It appears that the observed improvement is mainly due to a higher tensile modulus of the tridirectional bamboo grid and their geometry, causing more interlocking action generated between base and reinforcement.

References

1. Gourc JP, Matichard Y, Perier H, Delmas P (1982) Capacite Portant d'un Bicouhe, Sable sur Sol Mou, Reinforce par Geotextile. In: Proceedings of the 2nd international conference on geotextiles, vol 2, pp 411–417
2. Sridharan A, Srinivasa Murthy BR, Bindumadhava F, Vasudervan AK (1988) Reinforced soil foundation on soft soil. In: Proceedings of the 1st Indian geotextiles conference, pp C.53–C.60
3. Das BM (1989) Foundation sand underlain by soft clay with geotextile at sand-clay interface. In: Proceedings of the geosynthetics '89 conference, vol 1, pp 203–214
4. Dembicki E, Alenowicz J (1990) Influence of geotextiles on bearing capacity of two-layer subsoil. Constr Build Mater 4(1):49–52
5. Alenowicz J, Dembicki E (1991) Recent laboratory research on unpaved road behaviour. Geotext Geomembr 10(1):21–34
6. Lee KM, Manjunath VR, Dewaikar DM (1999) Numerical and model studies of strip footing supported by a reinforced granular fill–soft soil system. Can Geotech J 36(5):793–806
7. Som N, Sahu RB (1999) Bearing capacity of a geotextile–reinforced unpaved road as a function of deformation: a model study. Geosynth Int 6(1):1–17
8. Mandal JN, Sah HS (1992) Bearing capacity tests on geogrid-reinforced clay. Geotext Geomembr 11(3):327–333
9. Khing KH, Das BM, Puri VK, Yen SC, Cook EE (1994) Foundation on strong sand underlain by weak clay with geogrid at the interface. Geotext Geomembr 13(3):199–206
10. Alawaji HA (2001) Settlement and bearing capacity of geogrid reinforced sand over collapsible soil. Geotext Geomembr 19(2):75–88
11. Demir A, Laman A, Yildiz A, Ornek M (2013) Large scale field tests on geogrid reinforced granular fill underlain by clay soil. Geotext Geomembr 38:1–15
12. Akinmusuru AM, Akinbolade JA (1981) Stability of loaded footings on reinforced soil. ASCE J Geotech Eng Div 107(GT6):819–827
13. Dixit RK (1985) Experimental investigations of model square footing in reinforced sand. M. Tech. thesis, IIT Bombay, Mumbai

14. Mandal JN (1987) Geotextiles in India. Geotext Geomembr 6(4):253–274
15. Ramanatha Ayyar TS, Joseph J, Beena KS (1988) Bearing capacity of sand reinforced with coir rope. In: Proceedings of the 1st Indian geotextiles conference, pp C.53–C.60
16. Mandal JN, Manjunath VR (1994) Bearing capacity of strip footing resting on reinforced sand subgrades. Constr Build Mater 9(1):35–38
17. Datye KR, Gore VN (1994) Geotextile bamboo fascine mattress for filling over very soft soils in Malaysia. Geotext Geomembr 13(6–7):371–388
18. Khatib A (2009) Bearing capacity of granular soil overlying soft clay reinforced with bamboo-geotextile composite at the interface. Ph.D. thesis, Dept. of Geotechnics and Transportation, Faculty of Civil Engineering, Univ. Teknologi Malaysia, Kuala Lumpur
19. Hegde A, Sitharam TG (2015) Use of bamboo in soft-ground engineering and its performance comparison with geosynthetics: experimental studies. J Mater Civ Eng 27(9):04014256
20. Dutta S, Mandal JN (2016) Model studies on geocell-reinforced fly ash bed overlying soft clay. J Mater Civ Eng 28(2):04015091
21. Ye F, Fu W (2017) Physical and mechanical characterization of fresh bamboo for infrastructure projects. J Mater Civ Eng 30(2). https://doi.org/10.1061/(ASCE)MT.1943-5533.0002132
22. Ahirwar SK, Mandal JN (2018) Behaviour of bamboo grid-reinforced soil bed. Int J Geotech Eng. https://doi.org/10.1080/19386362.2018.1550909
23. Basu G, Roy AN, Bhattacharyya SK, Ghosh SK (2009) Construction of unpaved rural road using jute–synthetic blended woven geotextile—a case study. Geotext Geomembr 27(6):506–512
24. Sanyal T, Chakraborty K (1994) Application of a bitumen-coated jute geotextile in bank-protection works in the Hooghly estuary. Geotext Geomembr 13(2):67–132
25. Saha P, Roy D, Manna S, Adhikari B, Sen R, Roy S (2012) Durability of transesterified jute geotextiles. Geotext Geomembr 35:69–75
26. Gnanaharan R (2000) Preservative treatment methods for bamboo: a review. KFRI research report, 177, pp 1–19
27. Prasad DSV, Kumar AM, Prasada Raju GVR (2010) Behavior of reinforced sub bases on expansive. Glob J Res Eng 10(1):2–8

Correlation of Geosynthetic Index Properties to Cyclic Plate Load Test Performance in Flexible Airfield Pavements

W. Jeremy Robinson and Jeb S. Tingle

Abstract Geosynthetics have been used in highway pavement applications for years; however, pertinent geosynthetic index properties and their correlation to pavement performance are not clear. Attempts have been made to correlate geosynthetic index properties to pavement performance; however, a single geosynthetic property or combination of properties has not been identified that definitively describe anticipated performance. This study was performed to evaluate the behavior of various geosynthetic properties in laboratory characterization tests and to investigate potential relationships to laboratory cyclic plate load testing of airfield flexible pavement structures. Geosynthetic characterization tests were conducted to measure physical dimensions, stiffness properties, and tensile strength properties. Statistical analyses were performed to determine index properties pertinent to pavement performance. It was found that a single test method was not capable of correctly categorizing pavement performance in terms of permanent surface deformation results; however, the combination of stiffness and tensile properties was an important factor in the performance of a reinforced pavement section.

Keywords Geosynthetics · Index property · Airfield pavement

1 Introduction

Geosynthetics have been used in highway pavement applications for years; however, pertinent geosynthetic index properties and their correlation to pavement performance are not clear. Attempts have been made to correlate specific geosynthetic properties to pavement performance with mixed success. For example, Webster [1] found that aperture stability showed good correlation with the performance of six

W. Jeremy Robinson (✉) · J. S. Tingle
USACE ERDC, Vicksburg, MS, USA
e-mail: Jeremy.Robinson@usace.army.mil

J. S. Tingle
e-mail: Jeb.S.Tingle@usace.army.mil

different geosynthetics in full-scale paved test sections. However, it was concluded that optimum geogrid properties to maximize performance were not fully understood, and that other properties such as stiffness and modulus may affect performance.

Berg et al. [2] suggested that geosynthetic modulus and soil–geosynthetic interaction should have the greatest impact on pavement performance; however, it was noted that evaluating performance properties is difficult due to the larger number of variables in pavement design. It was recommended that properties investigated should include 2 and 5% secant moduli, interaction coefficient, and interface friction from direct shear.

Tang et al. [3] attempted to correlate geogrid index properties to results of direct shear and pullout tests. Four geogrids were evaluated; three were considered flexible geogrids (generally manufactured with a series of yarns), and one was considered a stiff geogrid (extruded polypropylene sheet). It was found that the combination of geogrid tensile strength at 2% strain and junction strength had a good correlation with direct shear test results. Further, it was found that aperture size correlated well with pullout test results, suggesting that aperture size is important to base/subgrade interaction. Finally, it was noted that ultimate tensile strength did not correlate well with pullout tests and that junction strength showed some relationship with pullout test results.

Giroud and Han [4] utilized aperture stability as a geosynthetic input in a design methodology for geogrid-reinforced unpaved roads. The methodology accounted for interlock between geogrid and aggregate, aperture stability of the geogrid, and base course modulus, and it was indicated that these parameters were not accounted for in previous methods.

The literature suggests that a single geosynthetic index property or combination of properties has not been identified that definitively predict anticipated performance; therefore, it is important to investigate potential correlations between multiple geosynthetic index properties and accelerated load test performance. This paper presents the results of an effort to evaluate a number of geosynthetic properties and attempts to correlate a combination of properties to the performance results of laboratory cyclic plate load test.

2   Objectives and Scope

The primary objective of this study was to evaluate the behavior of various geosynthetic properties in laboratory characterization tests and to investigate potential relationships to laboratory cyclic plate load testing of flexible airfield pavement structures.

Geosynthetic characterization tests (Fig. 1 and Table 1) were performed to measure stiffness and tensile strength properties. While some characterization tests are generally applicable to only one geosynthetic type, i.e., individual junction strength is typically applicable to geosynthetics with integrated nodes, an attempt was made to conduct all testing on each geosynthetic in order to obtain a complete

(a) Tensile strength test

(b) Flexural rigidity test

(c) Aperture stability test

(d) ERDC puncture test
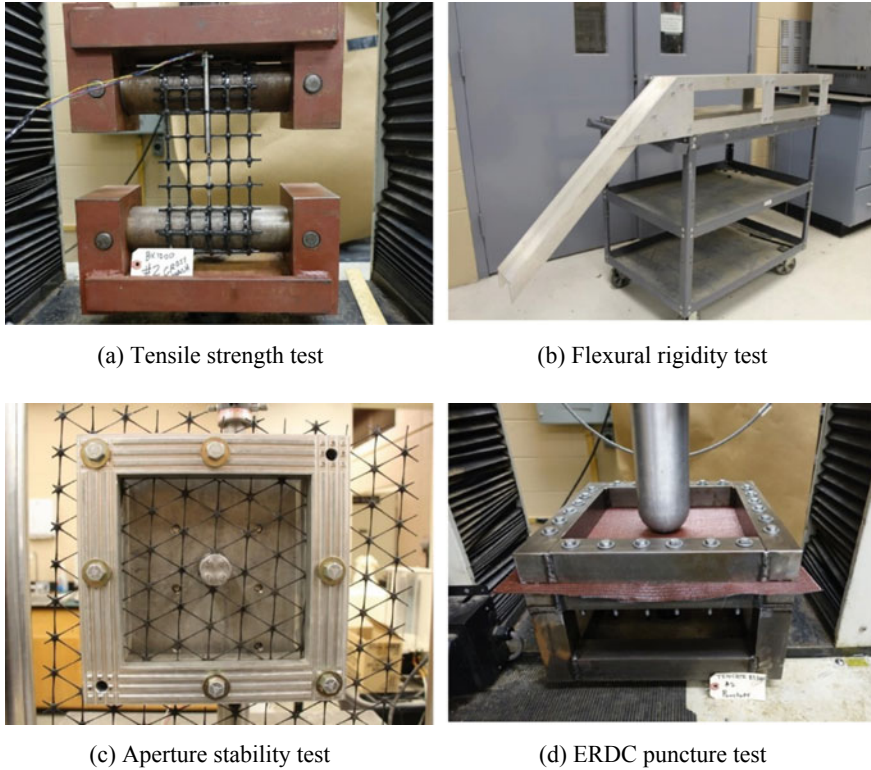
Fig. 1 Typical characterization test setup

Table 1 Laboratory characterization tests

Property	Standard
Tensile properties	ASTM D6637
Aperture stability	USACE method
Individual junction strength	ASTM D7737
Flexural rigidity	ASTM D7748
Puncture test	No standard

dataset of values. Tests were performed on a minimum of three randomly selected specimens from both the machine and cross-machine direction, where applicable. Results were evaluated using a Tukey test, which was used to compare all possible pairs of means to determine statistical significance; i.e., the difference in means was not equal to zero. The Tukey test assumes that observations are independent, values are normally distributed, and variances are equal across groups.

Four different geosynthetics (GEO1–GEO4) were evaluated during this suite of tests that represented a variety of geosynthetic types. GEO1 was a biaxial punched

Table 2 Geosynthetic properties as provided by manufacturer

Property	GEO1	GEO2	GEO3	GEO4
Geosynthetic type	Biaxial	Triaxial	Biaxial	Woven
Aperture size MD (mm)	25	–	25	–
Aperture size CMD (mm)	33	–	25	–
TS @ 2% strain MD (kN/m)	6.1	–	15.1	7.9
TS @ 2% strain CMD (kN/m)	9.1	–	15.1	31.5
TS @ 5% strain MD (kN/m)	11.8	–	32.1	22.8
TS @ 5% strain CMD (kN/m)	19.6	–	32.1	71.8
Ultimate TS MD (kN/m)	19.2	–	40.0	–
Ultimate TS CMD (kN/m)	28.8	–	40.0	–
Rib pitch-longitudinal (mm)	–	40	– 40	–
Rib pitch-transverse (mm)	–	40	–	–
Radial stiffness kN/m @ 0.5% strain	–	225	–	–

MD = machine direction; CMD = cross-machine direction; TS = tensile strength

and drawn polypropylene geogrid consisting of a series of rectangles. GEO2 was a multiaxial geogrid consisting of a series of concentric triangles forming a series of concentric hexagons. GEO3 was comprised of polypropylene yarns manufactured with an interlocking pattern and then coated with a polymer, and GEO4 was a woven geotextile manufactured from polypropylene filaments. A summary of geosynthetic properties as provided from the manufacturer are presented in Table 2.

3   Tensile Strength

Specimens were obtained of sufficient width to contain five intact ribs in the test direction and of sufficient length to allow for multiple complete wraps of the roller clamp assembly to minimize potential slippage. Prior to load application, an extensometer was firmly mounted with self-locking plastic bands to each geosynthetic to monitor elongation. A typical test setup was presented previously in Fig. 1a. Data were collected to determine tensile strength and modulus at 2% strain, tensile strength and modulus at 5% strain, and ultimate tensile strength and modulus in both the machine (MD) and cross-machine (CMD) direction.

In terms of tensile strength and modulus at 2% strain (MD), GEO3 was found to have the highest measured value (15.3 kN/m), followed by GEO1 (12.8 kN/m), and GEO4 (9.7 kN/m). GEO2 (1.8 kN/m) was found to have the lowest measured tensile strength and modulus. In the CMD, GEO4 (30 kN/m) had the highest tensile strength and modulus followed by GEO3 (14.3 kN/m), GEO1 (11.9 kN/m), and GEO2 (4.8 kN/m).

Table 3 Statistical comparison of tensile strength test results

Product	2% strain (kN/m)			5% strain (kN/m)				Ultimate strength (kN/m)			
GEO4	19.8	A		48.4	A			77.8	A		
GEO3	14.8	A		31.4	A	B		45.4		B	
GEO1	12.3	A	B	20.0		B	C	23.7			C
GEO2	3.3		B	6.1			C	15.5				D

Comparisons performed at $\alpha = 0.05$

GEO3 had the highest tensile strength and modulus (31.7 kN/m) at 5% strain (MD), followed by GEO4 (25.5 kN/m), GEO1 (20.5 kN/m), and GEO2 (2.1 kN/m). In the CMD, GEO4 (71.4 kN/m) had the highest tensile strength and modulus followed by GEO3 (31.2 kN/m), GEO1 (19.5 kN/m), and GEO2 (10.0 kN/m).

In terms of ultimate tensile strength and modulus (MD), GEO4 (72.1 kN/m) had the highest tensile strength and modulus, followed by GEO3 (49.4 kN/m), GEO1 (25.9 kN/m), and GEO2 (18.2 kN/m). Similar observations were made in the CMD.

CMD and MD results were combined to populate pairwise comparison procedures at a 95% confidence level (Tukey method) that were used to assess the statistical differences in each geosynthetic. Results are presented in Table 3, and results that do not share a letter are significantly different.

4 Flexural Rigidity

Flexural rigidity tests were performed to determine stiffness properties of each geosynthetic. Specimens were cut of sufficient width to include two apertures for the geogrids and a minimum 50-mm-width for the geosynthetic. All specimens were placed on a table, and weights were uniformly placed along the length of the specimen for a minimum of 24 h to minimize testing errors due to roll memory.

GEO1 had the highest flexural rigidity in both MD (1,259,540 mg cm) and CMD (1,246,400 mg cm). GEO3 and GEO2 had flexural rigidity in the CMD of 656,470 mg cm and 411,770 mg cm, respectively. GEO2 was found to be stiffer in the CMD (864,725 mg cm).

A statistical analysis (Table 4) indicated that GEO1 was significantly different from all other geosynthetics. GEO2 and GEO3 were not found to be statistically significant from each other, and GEO3 and GEO4 were not found to be statistically significant from each other.

Table 4 Statistical comparison of flexural rigidity test results

Product	Mean (mg cm)	Flexural rigidity (mg cm)		
GEO1	1,252,970	A		
GEO2	638,250		B	
GEO3	553,580		B	C
GEO4	271,840			C

Comparisons performed at $\alpha = 0.05$

5 Aperture Stability

Aperture stability test was performed to determine the in-plane rotational resistance of each geosynthetic and has been considered as a good indicator of anticipated performance [1, 3]. Three specimens were tested from each geosynthetic and average aperture stability modulus was calculated from the fifth test cycle at 2.0 N/m torque.

GEO4 was found to have the highest aperture stability (1.60 m N/°); however, it should be noted that this test is not generally applicable to geotextiles. The test assumes aggregate strikethrough and interlock that would not be present with a geotextile. To perform the test on a geotextile, slits were cut in the geotextile to facilitate placement of the bolts to secure the center clamping device. Thus, it is acknowledged that the geotextile results are not representative of actual performance. However, as mentioned previously, attempts were made to conduct all tests on all geosynthetics to fully populate a database of test results.

Of the geogrids, GEO3 had the highest aperture stability (0.54 m N/°) and GEO2 and GEO1 had comparable values (0.34 and 0.33 m N/°, respectively). A statistical analysis (Table 5) indicated that GEO4 was statistically different from all other geosynthetics as expected. When GEO4 was excluded from the pairwise comparison, it was found that none of the geogrids were statistically different.

Table 5 Statistical comparison of aperture stability test results

Product	Mean (m N/°)	Comparison including GEO4		Comparison excluding GEO4	
GEO4	1.604	A		–	–
GEO3	0.539		B	A	
GEO2	0.336		B	A	
GEO1	0.334		B	A	

Comparisons performed at $\alpha = 0.05$

6 ERDC Puncture Test

A modification of ASTM D6241 (Static Puncture Strength of Geotextiles) was performed to determine indirect tensile properties of each geosynthetic. A specimen retention frame was fabricated from 50-mm-square steel bar stock with overall dimensions of 406 mm by 406 mm. The upper portion of the specimen retention frame was attached to the lower portion of the retention frame with six bolts per side through slotted through-holes. Slotted holes were used to allow for minor adjustments due to different specimen geometries and aperture sizes. The inner bottom edge of the specimen retention frame was rounded to reduce the potential for stress concentrations at the edge of each specimen and to encourage failure to occur in the center of the specimen.

Loading was applied by a 101.6-mm-diameter semi-spherically shaped loading head. A semi-spherically shape was selected to reduce stress concentrations at the edge of the loading head during testing. Loading was maintained at a rate of 50 mm/min. until failure. Failure was defined as rupture of the specimen accompanied by a significant drop in measured load. A load rate of 50 mm/min. was selected to mimic load rates used in other test methods and to use a rate that is commonly available on most commercially available load frames. The puncture strength test setup is shown in Fig. 2.

This loading method was selected to engage the geosynthetic from all directions; i.e., effects from machine direction versus cross-machine direction could be observed simultaneously. Additionally, it was hypothesized that this method of loading, in theory, would be representative of the loading condition applied in the field, assuming a loaded tire applies a circular load to the pavement structure.

It is acknowledged that the test procedure does not account for the effects of aggregate/soil interaction of the geogrid. Therefore, the test results obtained, similar to other index tests, should be considered as a means to compare differing products.
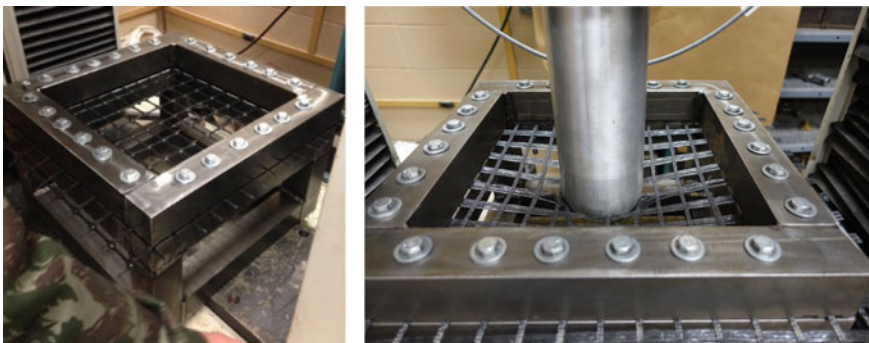
(a) Specimen retention frame   (b) Semi-spherical loading head

Fig. 2 ERDC puncture test apparatus

Table 6 Statistical comparison of ERDC-developed puncture test

Product	Mean (kN)	Puncture test			
GEO4	7.7	A			
GEO3	4.7		B		
GEO1	2.6			C	
GEO2	1.1				D

Comparisons performed at $\alpha = 0.05$

Table 7 Statistical comparison of individual junction strength

Product	Mean (kN)	Junction strength		
GEO1	0.60	A		
GEO2	0.48		B	
GEO3	0.03			C

GEO4 was found to have the highest puncture strength, followed by GEO3, GEO1, and GEO2. A statistical comparison (Table 6) indicated that all geosynthetics were significantly different from each other. This is encouraging in that it suggests that the test is capable of distinguishing between various types of geosynthetics. Further testing is recommended to investigate the effect of varying load rates and load head geometries.

7 Junction Strength

Tests were conducted to determine the individual junction strength of GEO1, GEO2, and GEO3; GEO4 was excluded from this particular test. It is noted that GEO1 and GEO2 are both manufactured from a punched and drawn polypropylene sheet, whereas GEO3 is manufactured from a series of intertwined polypropylene yarns; thus, the differences in junction strength were expected to be substantial. It was observed that GEO1 had the highest junction strength (0.58 kN in MD), followed by GEO2 (0.46 kN in MD), and GEO3 (0.04 kN in MD). The results of the statistical comparison (Table 7) indicated that all geogrids were statistically different from each other.

8 Correlation to Cyclic Plate Load Test Results

An attempt was made to correlate the results of geosynthetic laboratory characterization tests to airfield pavement performance observed under cyclic plate loading.

Table 8 Cycles to failure for cyclic plate load test

Product	Cycles at 25 mm Permanent deformation	Cycles at 50 mm Permanent deformation
GEO1	9720	44,960
GEO2	1460	9890
GEO3	4100	17,600
GEO4	2575	20,830

A series of cyclic plate load tests were conducted on airfield pavement structures that consisted of a 127-mm-thick asphalt layer, a 178-mm-thick base course layer, a 305-mm-thick subbase layer, and a 3 California bearing ratio (CBR) high plasticity clay subgrade. Geosynthetics were placed at the subgrade/subbase interface. Loading was applied via a 305-mm-diameter steel plate subjected to a 128 kN total load, resulting in a 1750 kPa contact pressure. A summary of cycles to 25 and 50 mm permanent deformation is presented in Table 8. More detailed information can be found in Robinson et al. [5].

In order to observe if individual geosynthetic test methods were capable of correctly categorizing pavement performance, test results were summarized as shown in Table 9. The results of each laboratory characterization test were assigned a ranking based on observed means with 1 being the highest mean value and 4 being the lowest mean value. Similarly, performance data (cycles to failure) were assigned a ranking with a value of 1 indicating the best performer and 4 being the lowest performer. It was observed that none of the laboratory characterization tests fully match the order of permanent deformation performance. It is noted that, based on pairwise comparison data, ultimate tensile strength, puncture test, and individual junction strength were the only test methods that differentiated between all geosynthetics; e.g., all products were found to be statistically different. Further, it is noted that tensile strength, puncture test, and flexural rigidity are the only tests that could be argued to be applicable to all products.

Table 9 Summary of ranking for each laboratory characterization test

Test	GEO1	GEO2	GEO3	GEO4
Wide width tensile @ 2% strain	3	4	2	1
Wide width tensile @ 5% strain	3	4	2	1
Wide width tensile @ ultimate	3	4	2	1
Flexural rigidity	1	2	3	4
Aperture stability	4	3	2	1
Puncture test	3	4	2	1
Individual junction strength	1	2	3	NA
Performance at 25 mm deformation	1	4	2	3
Performance at 50 mm deformation	1	4	3	2

NA = not applicable

A stepwise linear regression was performed to determine if a combination of geosynthetic characterization test results was capable of predicting deformation performance from laboratory cyclic plate load test summarized in Table 8. Predictive equations are based on the pavement structure and component layer properties contained in Robinson et al. [5], where geosynthetics were placed at the subbase/subgrade interface and should not be used for widespread prediction of pavement performance in other pavement structures under different loading conditions, component layer thicknesses, or layer properties. However, the predictive equations can give some general insight into material properties that may be pertinent to observed pavement performance.

Factors included in the stepwise linear regression for 25 mm permanent surface deformation were tensile strength at 2% strain, tensile strength at 5% strain, ultimate tensile strength, puncture strength, flexural rigidity, and aperture stability. A confidence level of 85% was selected as the threshold for a predictor to enter or exit the model. It was found that tensile strength at 2% strain and flexural rigidity were statistically significant at $\alpha = 0.15$. The predictive model is shown below.

$$\text{Deformation at 25 mm} = 278.6 * \text{Tensile Strength (2\% Strain)} \\ + 0.0093 * \text{Flexural Rigidity} - 5386$$

Similarly, a stepwise linear regression was performed for 50 mm permanent surface deformation. Initial analysis indicated that none of the factors were significant at an 85% confidence level; therefore, a confidence level of 75% was selected. It was found that ultimate tensile strength and flexural rigidity were statistically significant at the 75% confidence level. The predictive model is shown below.

$$\text{Deformation at 50 mm} = 476.0 * \text{Ultimate Tensile Strength} \\ + 0.05131 * \text{Flexural Rigidity} - 30,852$$

Review of both deformation predictive models based on permanent deformation results includes a stiffness term (flexural rigidity) and a tensile performance term (tensile strength at 2% strain or ultimate tensile strength). Further, the stiffness term (flexural rigidity) is observed in both models. The results of the predictive models suggest that geosynthetic stiffness is an important factor in geosynthetic airfield pavement performance and that an increase in stiffness contributes to the tensioned membrane mechanism, particularly at high levels of deformation. Similar observations can be made regarding tensile strength; i.e., as permanent deformation increases, tensile strength provides a greater contribution. It should be noted, however, that the cyclic plate load test were allowed to deform well beyond what would be expected on a typical operational airfield. Thus, the models presented herein should only be used as a means to identify properties that are potentially pertinent to performance.

9 Conclusions

A series of laboratory tests were performed to characterize physical properties of four different geosynthetics. While it is acknowledged that some tests are generally not applicable to some geosynthetics, an attempt was made to test all geosynthetics under all procedures. Statistical analyses were employed to observe the ability of each test to distinguish between products, and a stepwise linear regression was performed to investigate properties that may influence pavement performance. Based on the results of the testing described herein, the following conclusions can be made.

- Tensile strength tests, puncture test, and flexural rigidity were the only procedures that could be considered generally applicable to all geosynthetics evaluated.
- Ultimate tensile strength, puncture strength, and junction strength were capable of showing a statistical difference between all the geosynthetics.
- The puncture strength test showed some potential in being able to distinguish between different geosynthetics.
- A single test method was not capable of correctly ranking pavement performance for the permanent surface deformation results.
- Results of a stepwise linear regression suggest that stiffness and tensile properties were an important factor in the performance of a reinforced pavement section.

References

1. Webster SL (1993) Geogrid reinforced base courses for flexible pavements for light aircraft: test section construction, behavior under traffic, laboratory tests, and design criteria. No. WES/TR/GL-93-6. U.S. Army Engineer Waterways Experiment Station, Geotechnical Laboratory, Vicksburg, MS
2. Berg RR, Christopher BR, Perkins S (2000) Geosynthetic reinforcement of the aggregate base/subbase courses of pavement structures. GMA white paper II. Geosynthetic Materials Association, Roseville, MN. LNCS homepage. http://www.springer.com/lncs. Accessed 21 Nov 2016
3. Tang X, Chehab GR, Palomino AM, Allen SR, Sprague CJ (2008) Laboratory study on effects of geogrid properties on subgrade stabilization of flexible pavements. In: Proceedings of GeoCongress 2008: geosustainability and geohazard mitigation. ASCE, pp 1089–1096
4. Giroud JP, Han J (2004) Design method for geogrid-reinforced unpaved roads. J Geotech Geoenviron Eng 130(8):775–786
5. Robinson WJ, Mahaffey BJ, Howard IL, Norwood GJ (2019) Cyclic plate testing of geosynthetic-reinforced airfield pavements. Ground Improvement 172(4):229–243

Behavior of Geogrid-Reinforced Railway Ballast Under Train Traffic Loads

Qiusheng Gu, Kaihui Shi, Xuecheng Bian, and Sindy He

Abstract For the ballasted railway, under the action of dynamic load caused by the train traffic, the higher loading frequency and amplitude may eventually result in excessive settlement in the ballast, thereby reducing the passengers' comfort and even affecting the safety of train operation. To study the influence of train traffic load with higher frequency and amplitude imposed on the ballast and the employment of geogrid, ballasted railway model test on the cumulative settlement of geogrid-reinforced ballast under different train loads such as high-speed and heavy axle load and different types of geogrid reinforcement conditions, and triaxial test results of ballast specimens with and without geogrid under different confining pressures are discussed in this paper. The cumulative settlement and stress distribution of the ballast layer, the sleeper vibration, and the strain of geogrid of ballasted subgrade in the model tests under different train loads and geogrid reinforcement conditions are analyzed throughout the test, to explore the effect of geogrid and its working mechanism. Multiple groups of experimental results of axial strain, circumferential strain, and volumetric strain with various confining pressure in the triaxial tests are also compared and studied in this paper. These tests indicated that the installation of geogrid depresses the development of volumetric deformation and effectively increases the peak stress values in the ballast layer. The loading frequency and amplitude also play a vital role in the settlement development and degradation of ballasted subgrade at the same time.

Keywords Railway ballast · Train traffic load · Stabilization · Geogrid

Q. Gu · K. Shi · X. Bian (✉)
Key Laboratory of Soft Soils and Geoenvironmental Engineering, Department of Civil Engineering, MOE, Zhejiang University, Hangzhou 310058, China
e-mail: bianxc@zju.edu.cn

S. He
Tensar Corporation China, Wuhan 430056, China

1   Introduction

With the increase of train speed and axle load of modern railway, higher loading frequency and amplitude were put forward on the railway subgrade structure. For high-speed passenger trains, the train speed is higher, and a higher loading frequency is brought to the subgrade with the same axle load. Although heavy haul freight trains have a comparative lower train speed, higher dynamic loading amplitude is also caused due to the large axle load. Ballast layer endures higher dynamic load and vibration as the increase of loading frequency and amplitude in a traditional ballasted railway structure, which may result in excessive settlement and tremendous stress in the ballast layer consequently [1], thereby reducing the travel comfort and even threatening train operation. The development of axial and lateral stress in the ballast layer is also influenced significantly by the train traffic load, the compaction degree, and the restraint conditions. Seed et al. verified that the maximum vertical contact stress beneath the sleeper base of rail seats should be 200–270 kPa under a 200 kN wheel load [2]. Raymond and Davies demonstrated that the axial stresses at sleeper–ballast interfaces could hardly exceed 140 kPa under a static axle load of 150 kN [3]. Indraratna et al. [4] compared the effects of different confining pressures on the triaxial tests of ballast and found that the deformation and shear strength of ballast under different confining pressures are quite different. The in situ measurement [4] of stresses within the ballast layer indicated that the values of the maximum vertical and horizontal dynamic stresses varied in the ballast layer (as shown in Fig. 1).

Geogrid has been utilized to reinforce ballast layer to reduce track settlement and improve lateral stability successfully. Most previous studies [5–8] considered the deformation performance of ballast layer. However, few of them comprehensively explored the performance and reinforcement mechanism of reinforced ballast layer. Qian et al. studied the reinforcement effect of geogrids on well-graded and deteriorated ballast specimens using large triaxial test and found that the employment
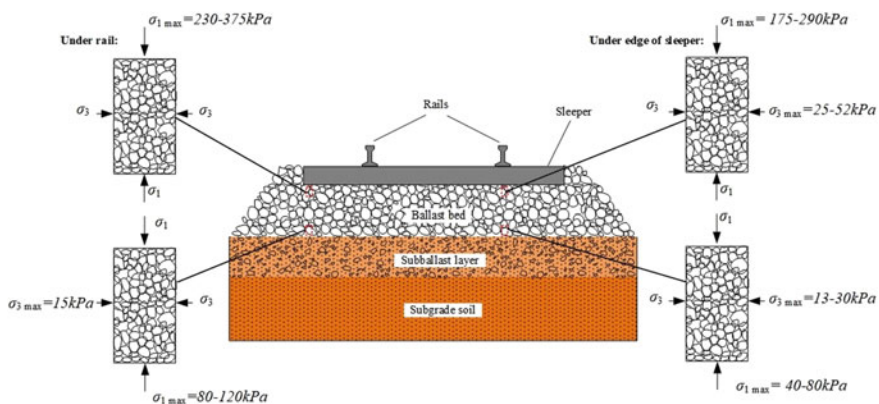
Fig. 1 Maximum vertical and horizontal stresses measured both under rail and sleeper edge

of geogrids can significantly increase the peak deviator stress value [9]. In order to study the reinforcement effect of geogrid on ballast materials, geogrid-reinforced ballast behavior was investigated utilizing large-diameter triaxial testing apparatus (LDTTA) under different confining pressures and physical model test under different train traffic load to explore the geogrid reinforcement effect and mechanism.

2 Geogrid Reinforcement Effect Under Different Confining Pressures

2.1 Triaxial Test of Geogrid-Reinforced Railway Ballast

The DSY-300 (as shown in Fig. 2) large-diameter triaxial testing apparatus (LDTTA) located in Zhejiang University could be used to apply axial load and confining pressure to the large specimens by an axial loading device and a confining pressure boosting system, respectively. A load cell and several confining pressure sensors were installed to monitor the stresses exerted on the specimen. The LDTTA adopted an electro-hydraulic servo program with a closed-loop control system to ensure the

Fig. 2 DSY-300 LDTTA

loading process accurate and stable. The axial strain of the specimen was calculated by the linear variable differential transformer (LVDT) at the top of the specimen, and the variation of the specimen's volume could be measured by the change of water volume in the triaxial chamber.

2.2 Experimental Procedure

Specimen Properties. The ballast material used in this study was tuff that taken from a railway construction site around Hangzhou, and the grain size distribution (as shown in Fig. 3) followed the requirements of the Chinese first-level railway ballast standard. The mechanical behaviors of granular material have been proved strongly depend on compacted condition, and the compaction degree of the ballast is defined as the ratio of the actual density to the most compacted density. The most compacted density of the tuff sample was 1642.67 kg/m^3 and the corresponding porosity ratio was 0.545. Therefore, the packing density of a 92% compaction degree of the specimens in this study was 1511.26 kg/m^3 and the corresponding porosity ratio was 0.679. The geogrid used in triaxial test was TriAx$^®$ TX150L, and the properties contributing to the performance of geogrid as a mechanically stabilized layer as shown in Tables 1 and 2.

Test Procedures. The ballast sample was poured into an iron split mold by four lifts, and each lift was compacted with a hammer carefully. After compaction of the first two lifts, one layer of geogrid was placed carefully in the middle of the test specimen
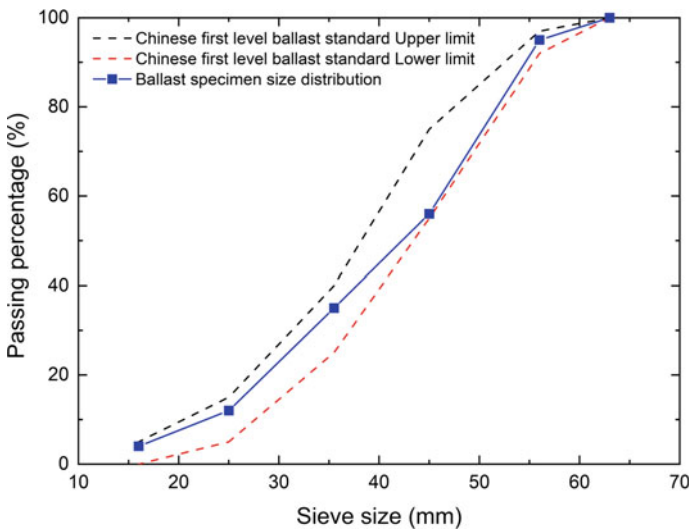
Fig. 3 Size distribution of ballast material

Table 1 Shape properties of TX150L/TX190L geogrid

Index properties	Longitudinal	Diagonal	General
Rib pitch (mm)	57/60	57/60	
Rib shape			Rectangular
Aperture shape			Triangular

Table 2 Structural properties of TX150L/TX190L geogrid

Structural integrity	General
Junction efficiency (%)	93
Isotropic stiffness ratio	0.6
Overall flexural rigidity (mg cm)	750,000/1,500,000
Radial stiffness at low strain (kN/m @ 0.5% strain)	325/350

for making a geogrid-reinforced ballast sample. A rubber pad (4 mm thick) was used to minimize the risk of breaking the ballast during compaction progress. The mean bulk packing density of the compacted specimens was determined to be around 1511.26 kg/m^3. Two 2.5-mm-thick rubber membranes were used to confine the cylindrical specimens and avoid being punctured by sharp corners and edges of the ballast during the test. Bishop and Henkel have proved that even thin rubber membranes can provide some confinement which increases the measured principal stresses [10]. Indraratna et al. proved rubber membranes with pressures higher than 120 kPa, the membrane corrections amounted to less than 2% of the measured principal stress, whereas at the lowest confining pressure 1 kPa, the maximum correction was below 8% [4]. Hence, the confinement provided by the rubber membranes has little effect on the data interpretation and the final conclusions. The geogrid was placed in the middle of the specimen in height. Different confining pressures were adopted in this study. By comparing and analyzing the test results under different confining pressures, the effects of geogrid reinforcement on the performance of ballast specimens were analyzed. The confining pressure remained stable during the test, and the axial loading was controlled by displacement and the shearing rate was 5 mm/min.

2.3　Results of Triaxial Test

Deviator Stress. Cylindrical specimens were used in ballast triaxial test. The specimen is subjected to the same circumferential pressure in three axes through the pressurized liquid in the pressure chamber and the whole test process remains unchanged. The specimen was then subjected to vertical axial pressure through the piston until the specimen was sheared. During the loading process of ballast specimens by actuators, the axial strain of the specimens and the variation of the axial load of the specimens were monitored through the vertical axial load sensor and the LVDT on the top. Figure 4 presents stress state from large-scale triaxial shear strength
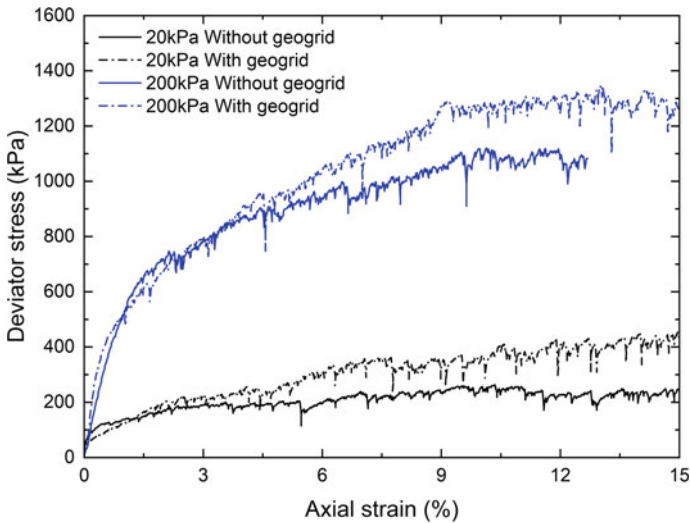
Fig. 4 Deviator stress–axial strain response under different confining pressure

tests conducted on the ballast specimen for up to 15% axial strain. Under the same confining pressure, the deviator stress of the specimens strengthened with geogrid was significantly greater than that of the specimens without geogrid at the same axial strain. The increase of deviator stress of the geogrid-reinforced specimens was mainly due to the lateral restraint provided by the geogrid. At the same time, with the increase of confining pressure, the deviator stress could be significantly increased.

Circumferential Strain and Volumetric Strain. The circumferential strain of the middle part of the ballast sample was monitored through a wire-drawn displacement sensor arranged in the middle part of the ballast sample. Figure 5 shows the circumferential strain of the specimens in this test. The circumferential strain in the middle of the specimen increased continuously in all the tests, and the geogrid would restrict the radial expansion of the specimen. Under high confining pressure, the confinement effect of geogrid on the circumferential strain in the middle of the specimen was less significant than that under low confining pressure. At the same time, under different confining conditions, the higher the confining pressure, the smaller the circumferential strain of the ballast specimen, and the later the restriction of geogrid on the circumferential strain of the specimen was exerted, and the less significant the effect was.

During the loading process of the tests, the volume change of ballast specimen was monitored through the volume change of confining water at the end of confining cylinder. Figure 6 presents the volumetric deformation of the specimens in tests. Under low confining pressure, the specimens dilated during the shear process, and the growth of specimen's volume was limited by geogrid. Under high confining pressure, the volume of the sample increased first and then decreased, while the radial expansion in the middle of the sample was limited by the geogrid.
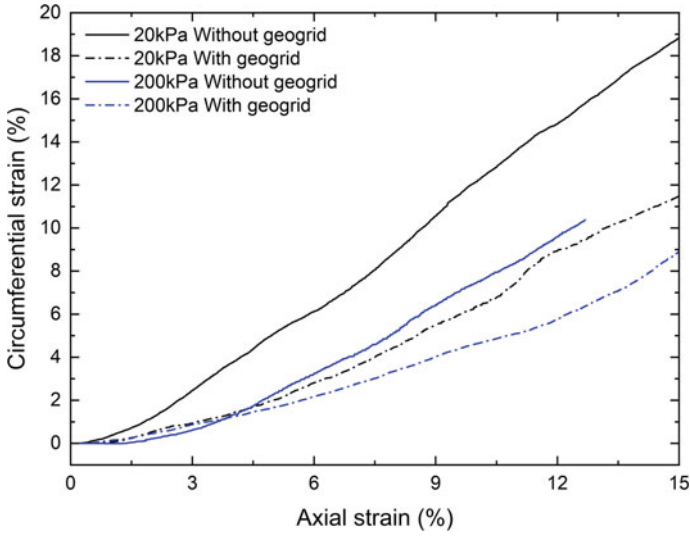
Fig. 5 Circumferential strain–axial strain response
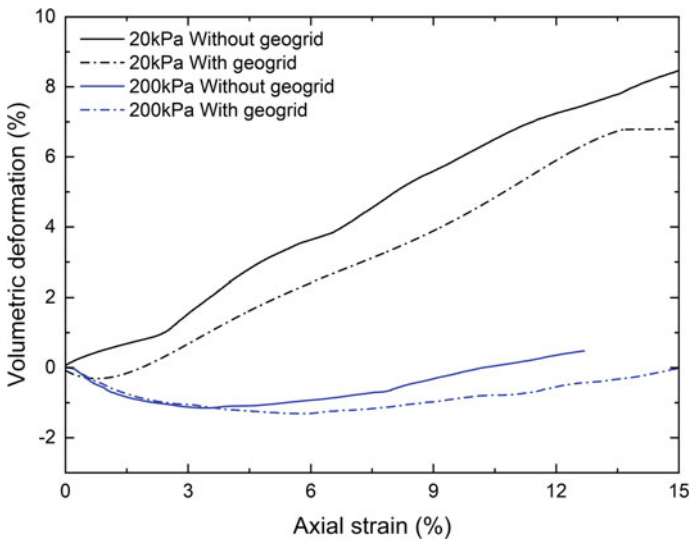
Fig. 6 Volumetric deformation–axial strain response

Geogrid Breakage. After the test, the geogrids were taken out for comparative analysis. Figure 7 shows the stress state of the specimens in this test, in which the deviating stress was included. The reinforcing effect of geogrids on ballast specimens was mainly due to restraining the lateral deformation of ballast specimens. With the increase of the axial strain during the test, the geogrid in the middle of the sample

<table>
<tr><td>(a) confining pressure 20kPa.</td><td>(b) confining pressure 200kPa.</td></tr>
</table>
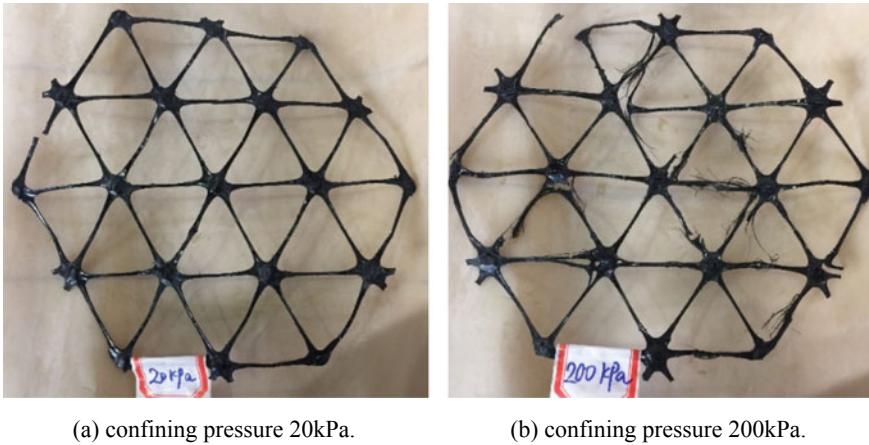
Fig. 7 Geogrid breakage under different confining pressure

would eventually be destroyed. Under low confining pressure, the ribs at the edge of the grill only fragmented slightly, and most of the area of the geogrid was intact. Under high confining pressure, the ribs at the edge of the geogrid were seriously broken, and almost all the ribs near the central area were broken. According to the experimental results, it can be found that with the increase of confining pressure, the breakage of the geogrid increased.

3   Geogrid Reinforcement Effect Under Different Train Traffic Loads

3.1   Model Test of Geogrid-Reinforced Railway Ballast Track Subgrade

The ballasted railway model test system developed by Zhejiang University was used in this test, which can not only apply vertical load to the test object but also lateral load simultaneously. The maximum loading force was up to 300 kN and the maximum frequency was 15 Hz, and different loading waveforms including sinusoidal wave can be selected. The system consists of a vertical loading host, lateral loading host, servo oil source and digital coordinated loading control system, and the corresponding data acquisition system. The testing machine relies on the closed-loop control of the computer program with electro-hydraulic servo, and automatic control was realized for the whole test loading process and data measurement. The axial load of the specimen during the test was applied by an axial loading device and was measured

by an axial force sensor, to ensure the consistency of the target force value and the applied force value.

3.2 Experimental Procedure

Physical Model Properties. In the test, the influence of the type of load, placement of geogrid, type of geogrid on the performance of ballasted layer was studied by establishing the model of ballasted track subgrade in different loading conditions. The layout structure of the model is shown in Fig. 8. The subgrade model was built in a ballast box which is 2060 mm * 860 mm * 950 mm (Length * Width * Height) inside. The box wall was made of organic glass with good surface flatness and moderate elastic modulus. The box bottom was made of steel with an 8-mm-thick rubber cushion to simulate the bottom boundary conditions of the actual subballast layer. The model consisted of the subballast layer, geogrid layer, ballast layer, sleeper, and rail. The model subgrade is filled following the construction process of ballasted subgrade during field construction. The ballast layer was laid above the subballast layer, and the thickness under the sleeper was 300 mm. The ballast layer was filled by referring to the actual railway construction method, and compaction was carried out for each laying of 120 mm, with three compacted parts in total during the filling progress; the layer was filled to the height of 300 mm. Finally, the compaction density of the ballast layer of each group was in a range of 1700–1740 kg/m^3 while the void ratio was in a range of 0.46–0.48 at the same time.

Test Procedures. Two loading conditions were set in this test, and the influences of three factors including the presence of geogrid, type of geogrid, and loading conditions on various performance parameters (as shown in Table 3) were studied by comparing and analyzing test results.
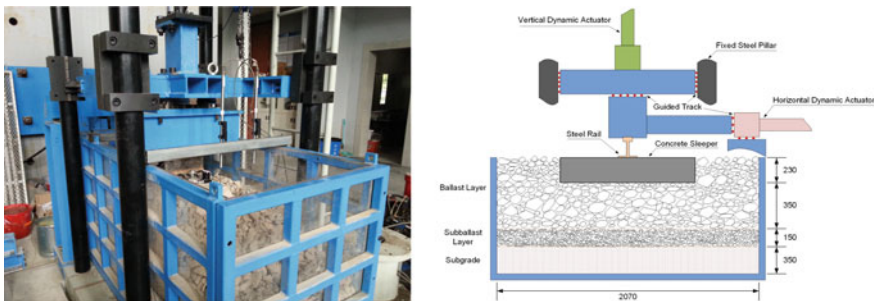
Fig. 8 Railway ballast track subgrade model layout

Table 3 Loading conditions of the model test

Group	Geogrid type	Placement of geogrid	Loading condition	Average contact pressure under the sleeper (kPa)	Peak load (kN)	Loading frequency (Hz)
①	No		High-speed train	82	21	3
②	TX190L	Ballast–subballast interface	High-speed train	82	21	3
③	TX190L	Ballast–subballast interface	Heavy haul train	121	31	2
④	TX150L	Ballast–subballast interface	Heavy haul train	121	31	2

3.3 Results of Model Test

Sleeper Vibration. Under the action of cyclic dynamic load, the vibration velocity of the sleeper was monitored in the whole process by the vibration velocity sensor fixed on the top surface of the sleeper. The vibration velocity of the sleeper with the loading times under different loading conditions is shown in Fig. 9.

By comparing these curves, the vibration velocity of the sleeper under 100,000 times of loading under four working conditions did not change much, and it can only be recognized that the amplitude was slightly reduced in the initial stage of loading. When the valley value was subtracted from the peak value of the 100,000 vibration waveform cycles, the average value of the amplitude of vibration velocity fluctuation during the loading of 100,000 cycles can be obtained, which could be used as an evaluation indicator of the vibration intensity of the sleeper in each working condition. It can be found through comparing the average amplitude of the vibration velocity of the first two groups of tests that after the geogrid was placed, the average amplitude of the vibration velocity of the sleeper surface in 100,000 loadings declined. The effect of the two different TriAx geogrid was not much different under heavy haul train load.

Soil Pressure. During the process of cyclic dynamic loading of the model by the actuator, soil pressure in the interface of the bottom of the ballast bed was monitored through the entire process through the soil pressure cell placed on the top surface of the subballast layer (as shown in Fig. 10).

The soil pressure behavior during the loading process under various loading conditions was different, which was supposed to be related to the change of the structure of granular mixtures. Under the group 1, the valley value and peak value of soil pressure at the bottom of the ballast layer decrease slightly under the cyclic loading, whether it was below the rail or the sleeper end. Under the loading conditions of group 2 and
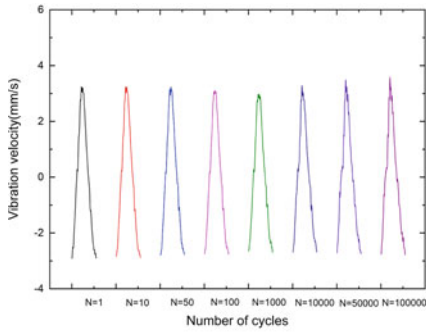
(a) High-speed train load No geogrid
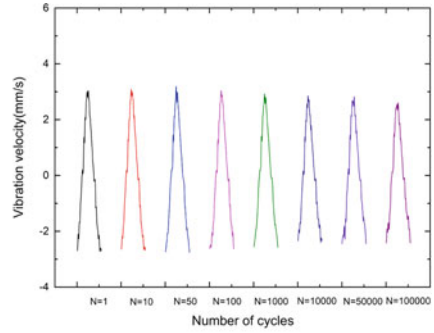
(b) High-speed train load TX190L
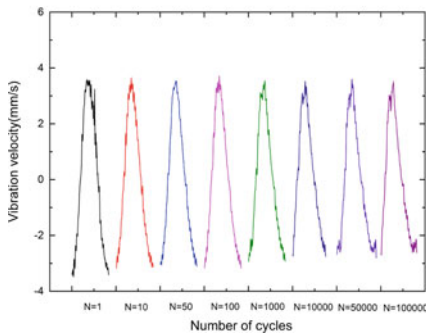
(c) Heavy-haul train load TX190L
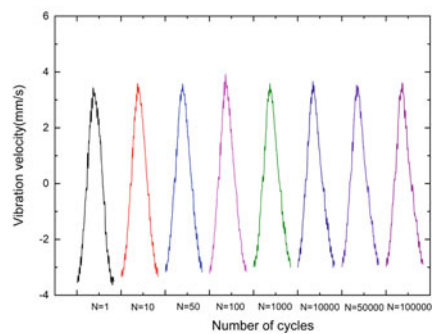
(d) Heavy-haul train load TX150

Fig. 9 Vibration of sleeper under different loading conditions

working condition 3, its change during loading was not particularly obvious. It can also be roughly judged from the figure that the additional soil pressure brought by the load was mainly concentrated below the loading point, and the soil pressure at the end of the sleeper was relatively low. The vertical soil pressure amplitude in group 4 decreased slowly after the first 50,000 loading cycles while the value in group 3 kept almost still, and a geogrid failure might occur in group 4.

4 Conclusions

The stabilization effect of geogrid on ballast was discussed in this paper based on both triaxial test and physical model test results, and the influence of confining pressure and train load in the ballast layer was analyzed. The main conclusions could be drawn below:

(a) High-speed train load No geogrid

(b) High-speed train load TX190L

(c) Heavy-haul train load TX190L

(d) Heavy-haul train load TX150L
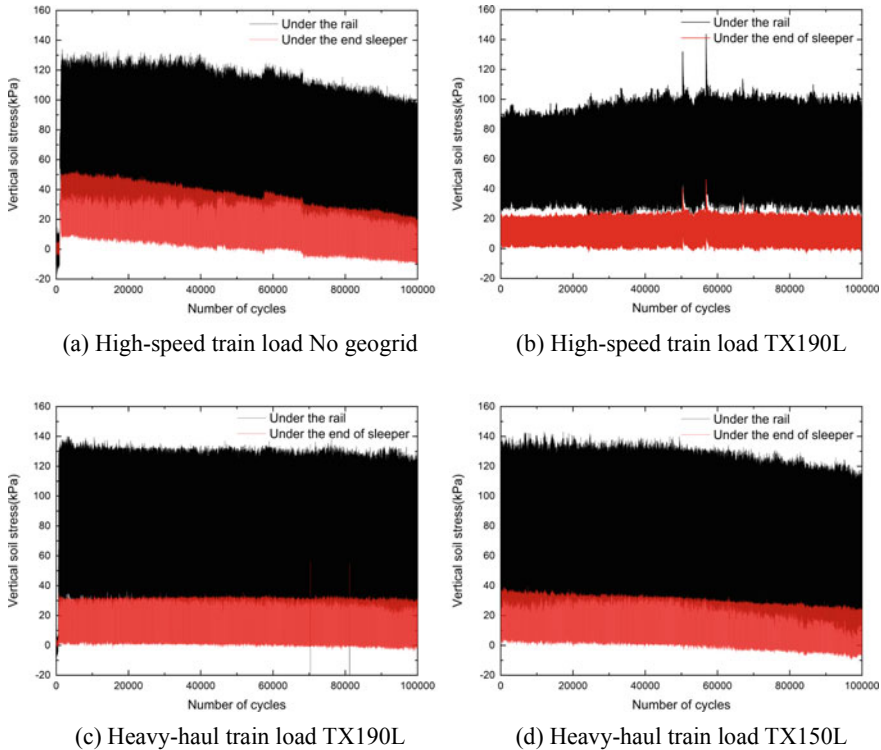
Fig. 10 Soil pressure at the bottom of the ballast bed below the rail and sleeper end

- The installation of geogrid could improve the bearing capacity of ballast significantly, and this performance improvement mainly due to the constrains of ballast particle movements in the lateral direction by the presence of geogrid. At the same time, with the increase of confining pressure, the strength of the ballast and breakage of the geogrid can be significantly enhanced.
- The circumferential strain of the ballast specimen increased all along with the tests, and the geogrid installation limited the radial expansion of the specimen. Geogrid showed stronger constrain on ballast's lateral deformation when the confining pressure is lower.
- The effect of geogrid on the ballast volumetric deformation was mainly due to the restriction of the radial expansion. Geogrid installation reduced volumetric dilation when the confining pressure is low, while facilitates volumetric reduction when the confining pressure was high.
- The geogrid could reduce the sleeper vibration velocity significantly and the dynamic displacement amplitude, thereby could improve the stabilization of ballast behavior. Geogrid had an effect of diffusing the soil pressure while the peak value at the bottom of the ballast layer under the rail was reduced.

References

1. Bian XC, Jiang HG, Cheng C, Chen YM, Chen RP, Jiang JJ (2014) Full-scale model testing on a ballastless high-speed railway under simulated train moving loads. J Soil Dyn Earthq Eng 66:368–384
2. Seed H, Chan C, Lee C (1962) Resilience characteristics of subgrade soils and their relation to fatigue failures in asphalt pavements
3. Raymond GP, Davies JR (1978) Triaxial test on dolomite railroad ballast. J Soil Mech Found Div ASCE 104(6):737751
4. Indraratna B, Ionescu D, Christie HD (1998) Shear behavior of railway ballast based on large scale triaxial testing. J Geotech Geoenviron Eng 124(5)
5. Aingaran S (2014) Experimental investigation of static and cyclic behavior of scaled railway ballast and the effect of stress reversal. PhD thesis, University of Southampton
6. Bathurst RJ, Raymond GP (1987) Geogrid reinforcement of ballasted track. Transp Res Rec 1153:8–14
7. Brown SF, Kwan J, Thom NH (2007) Identifying the key parameters that influence geogrid reinforcement of railway ballast. Geotext Geomembr 25(6):326–335
8. Indraratna B, Khabbaz H, Salim W, Christie D (2006) Geotechnical properties of ballast and the role of geosynthetics in rail track stabilization. J Ground Improv 10(3):91–102
9. Qian Y, Mishra D, Tutumluer E, Kazmee HA (2015) Characterization of geogrid reinforced ballast behavior at different levels of degradation through triaxial shear strength test and discrete element modeling. Geotext Geomembr 43(5):393–402
10. Bishop WA, Henkel DJ (1962) The measurement of soils properties in the triaxial test. Edward Arnold Ltd., London

Near Geogrid Stiffness Quantification in Airport Pavement Base Layers Using Bender Element Field Sensor

Mingu Kang, Issam I. A. Qamhia, Erol Tutumluer, Murphy Flynn, Navneet Garg, and Wilfredo Villafane

Abstract Geogrids are widely used for unbound aggregate base stabilization in flexible pavements. A new field evaluation methodology for quantifying the effects of geogrids on stiffness enhancement of unbound aggregate layers is demonstrated in this paper. The method utilizes a bender element field sensor, which measures the shear wave velocity transmitted between a source and receiver pair of bender element (BE) transducers and relates that to the localized stiffness. The paper introduces the new methodology and discusses the recent measurements obtained from a geogrid–aggregate system stiffened zone in the full-scale Construction Cycle 9 (CC9) pavement test sections constructed at the Federal Aviation Administration's (FAA's) National Airport Pavement Test Facility (NAPTF) in New Jersey. The aggregate materials used in the construction of the base and subbase layers were in accordance with the FAA-designated P-209 and P-154 specifications, respectively. A biaxial geogrid was placed at the interface between the subbase and base in the "North" test section. Two BE field sensors were installed in this "North" geogrid-stabilized section at 25 mm (1-in.) and 102 mm (4 in.) above the geogrid location. A third sensor was installed in the "South" control section with no geogrid at 25 mm (1 in.) above the bottom of the base layer. Shear wave signals were collected before and after base layer compaction, and shear wave velocities were calculated. The BE field sensor measurements clearly indicated that stiffness enhancement was achieved in the proximity of the geogrid, and that such effect of a stiffness enhancement diminished at about 102 mm (4 in.) away from the geogrid. The findings of this study are illustrated in this paper to quantify the magnitude and extent of the local stiffened zone near a geogrid.

Keywords Airport pavement · Bender element · Geogrid · Mechanical stabilization · Modulus · Shear wave · Monitoring

M. Kang · I. I. A. Qamhia · E. Tutumluer (✉)
University of Illinois at Urbana-Champaign, 205 N Mathews Ave, Urbana, IL 61801, USA
e-mail: tutumlue@illinois.edu

M. Flynn · N. Garg · W. Villafane
Federal Aviation Administration, Airport Technology R&D Branch, William J. Hughes Technical Center, Atlantic City, NJ 08045, USA

1 Introduction

Airfield pavements are designed and constructed to provide adequate support for the loads imposed by heavy aircraft and to produce a firm, stable, and smooth surface year-round. To fulfill such load-bearing and structural capacity requirements, pavement foundation layers should provide adequate strength and stiffness characteristics. Mechanical stabilization of the pavement base/subbase layer using geosynthetics enhances the load-bearing capacity and provides uniformity of support. With the recent FAA move toward the use of geosynthetics for airport pavements, as stated in the FAA Reauthorization Act of 2018 Section 558 Geosynthetics Materials, the evaluation of the layer modulus enhancement with stiff geogrids has gained much attention.

Many researchers to date have studied the geogrid–aggregate interaction and certain interlocking effects on mechanical stabilization using numerical methods, such as the Discrete Element Method (DEM) and finite element method (FEM), and reported that a stiffened zone was typically generated in the proximity of the geogrid [1–5]. Tirado et al. [6] evaluated the effect of geogrid enhancement in terms of traffic benefit ratio (TBR) for airport pavement designs with aircraft gear loading modeled using a 3D FEM approach and found significant influences of the base and subgrade layer moduli and the type of geogrid on the level of geogrid enhancement. Pullout tests have also been conducted to quantify the effect of interlocking and assess the resulting reduction in aggregate lateral movements with geogrids, which is due to the lateral restraint and considered as a key mechanism for mechanical stabilization [7–9]. Kwon and Tutumluer observed increased strength in depth profiles in the proximity of geogrids by using dynamic cone penetrometer (DCP) testing [10].

To quantify the stiffness increase due to a geogrid-stabilized aggregate layer, a recent research approach at the University of Illinois focused on determining such local stiffened zone characteristics through the shear modulus increase from measured shear wave velocities. Bender element (BE) pairs were utilized as shear wave transducers to measure the shear wave velocity profiles of geogrid-stabilized and geogrid-unstabilized aggregate samples. By installing BE pairs at different heights above the geogrid and measuring the shear wave velocities, the localized stiffness of a target area can be evaluated. From extensive studies using BEs and geogrid-stabilized aggregate specimens, stiffness enhancement in the vicinity of a geogrid was clearly observed [11–14]. Further, Byun et al. applied BE pairs to use as an embedded shear wave sensor in the pavement and measured shear wave velocities of as-constructed unbound aggregate base layers [15].

This paper demonstrates for the first time the utilization of a newly developed BE field sensor to measure shear wave velocities in order to quantify and monitor the shear modulus-based local stiffness characteristics of an airfield pavement base with and without geogrid. The dimensions and various components of the specially designed and manufactured BE field sensor including the BE protection casing module, BE field sensor frame, protection cover, and the coupling material are first described in detail. The shear wave measurement system and data acquisition process

are then highlighted. The installation of the field BE sensors and the shear wave measurements were conducted on an airport pavement test section constructed at FAA's National Airport Pavement Test Facility (NAPTF) at the William J. Hughes Technical Center near Atlantic City, New Jersey. The testing took place in the FAA NAPTF Construction Cycle 9 (CC 9) test sections. Shear wave velocities measured using the BE field sensors and the associated shear modulus properties obtained in the granular base were investigated to contrast effects of with and without geogrid cases.

2 Bender Element Field Sensor

2.1 Bender Element

Characterization of soils and aggregates using the propagation of small-strain elastic waves is a small perturbation phenomenon that can assess the state of a particulate medium without altering the structure of the soil or causing permanent effects [16]. A bender element (BE) is composed of two layers of piezoceramic plates bonded to a thin metal shim sandwiched in the middle. BE can be used as a shear wave actuator by converting an applied electrical voltage across the BE to a deformation of the BE. Further, the deformation of BE generates an electric voltage, and thus, the BE can be also utilized as a shear wave sensor. Due to the superiority of coupling between the transducer and soil or aggregates, bender elements have been widely used in laboratory applications to instrument soils [17]. There are two types of bender elements: series and parallel. In the series type, the poling directions of the two piezoelectric layers are opposite to each other, whereas the parallel type has the same poling direction for the two piezoelectric layers. In this study, the parallel type was used since it can provide a higher magnitude of shear wave signals. The dimensions of bender elements that were utilized in this study were 30.5 mm (1.2 in.) in length, 25.4 mm (1.0 in.) in width, and 0.5 mm (0.02 in.) in thickness.

2.2 Bender Element Field Sensor

Although bender elements have an exceptional coupling ability with dense-graded granular materials, these sensors have not been frequently used in the field due to their fragility. To protect a pair of bender elements and its cable connections from potential impacts or damage at a construction site, and to ensure that the BE sensors are directly facing each other during a shear wave signal propagation, a new BE field sensor has been recently developed for transportation geotechnics applications. Figure 1 shows a single bender element, a bender element sensor with a BE protection casing module, and the final design of the BE field sensor, which was utilized in this study. To
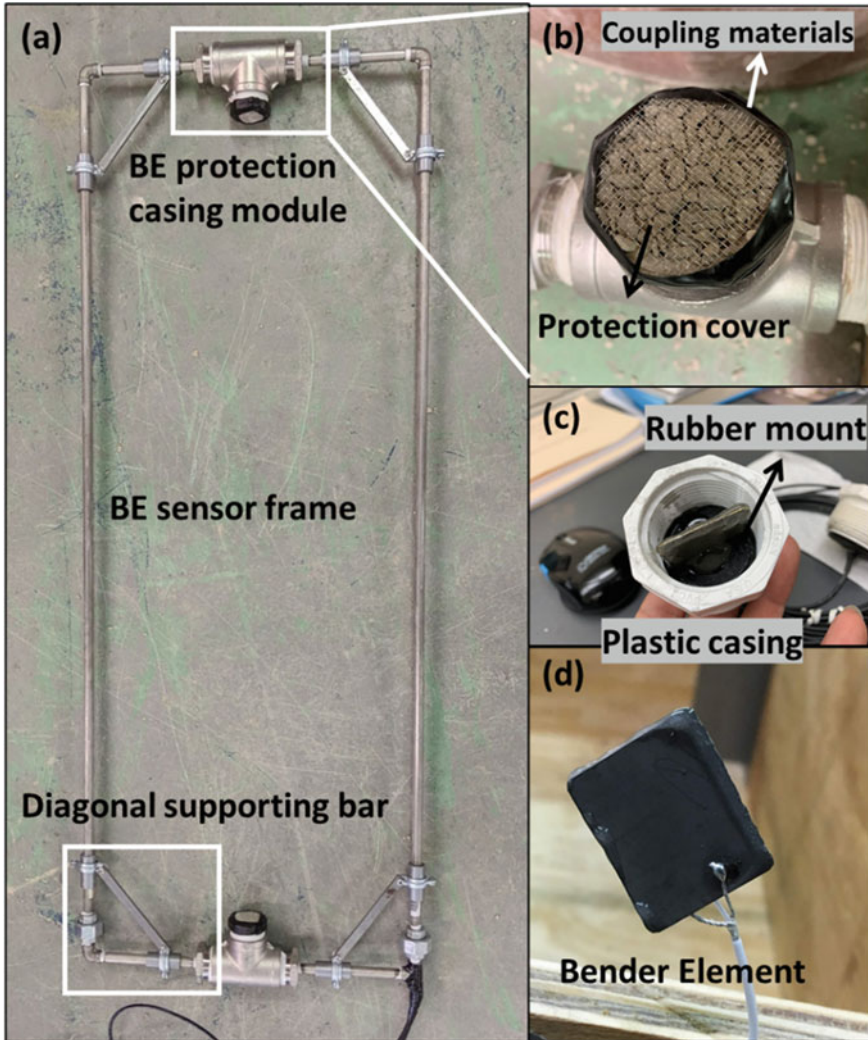
Fig. 1 Detailed view of bender element (BE) field sensor: **a** a photo of the BE field sensor, **b** BE protection casing module filled with coupling materials, **c** a plastic casing with a rubber mount and a BE inside, and **d** a BE that was installed in the casing module

protect the BE sensor, an aluminum mesh cover was used to cover the BE protection module. A stainless-steel frame enables the installation of the BE field sensor in a coarse aggregate base layer-type dense-grade material size and gradation without damaging the sensors and cables. The frame also maintains a fixed distance between the two pairs of BEs. The dimensions of the frame are 1219 mm (4 ft.) in length and 457 mm (1.5 ft.) in width. The length was designed to be longer than the width of the gears/tires used to traffic the pavement, and the width was optimized to ensure

that a clear shear wave could be generated and detected without any interference from the stainless-steel frame. The BE protection module was first filled with a coupling material engineered to be a uniform coarse sand so that shear waves could be propagated in a continuous medium. The thickness of the BE protection module was approximately 61 mm (2.4 in.). To minimize the possibility of a direct shear wave propagating through the frame, a rubber mount was attached to the BE protection module. Diagonal supporting bars were fitted at the four corners of the BE field sensor frame to prevent out-of-plane warping and to ensure each BE pair is in the same plane.

2.3　Shear Wave Measurement System

Figure 2 presents the BE field sensor configuration and the data acquisition devices used for the shear wave measurement. The signal generator provides the input signals
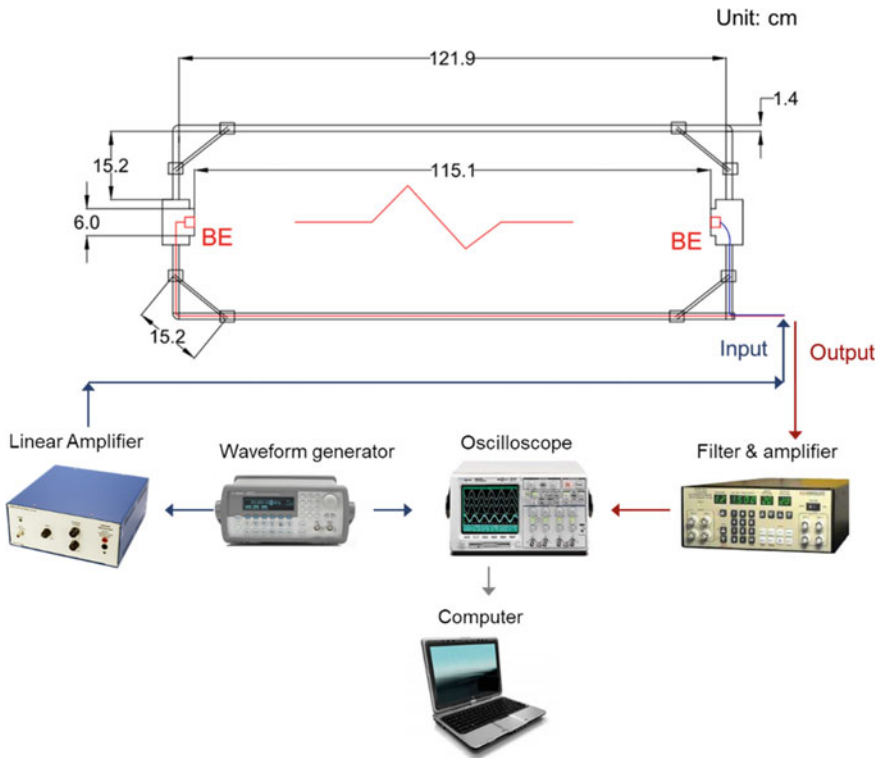
Fig. 2　BE field sensor and the shear wave measurement system configuration

to the "source" bender element with a magnitude of up to 10 V. The signal is intensified up to six times using a pre-amplifier. The input signal is delivered to the "source" BE transducer, and the waves propagating through the aggregate specimen are received by the "receiver" BE transducer. The output signals are filtered using the filter and amplifier and are displayed on the oscilloscope. For stable wave measurements, variable input sinusoidal signals with frequencies ranging from 300 to 1000 Hz are applied. The collected signals are compared after measurements. The stacking number of the signal is selected as 1024 to remove any uncorrected signal noises.

3 Sensor Installation Procedure

3.1 Field Test Sections

Three BE field sensors were installed in the full-scale pavement test sections constructed during the Construction Cycle 9 (CC9) flexible pavement test study at the FAA's NAPTF in New Jersey in 2019. The NAPTF aims to generate full-scale testing data to support the investigation of the response and performance of airport pavements subjected to complex gear loading configurations of new generation aircraft. At the NAPTF facility, carefully constructed and monitored test sections are used for evaluating new and effective pavement designs and construction technologies [18].

The CC9 pavement test sections consisted of 127 mm (5 in.) of P-401 asphalt surface course underlain by 203 mm (8 in.) of P-209 granular base. These instrumented test sections have substantially thick granular subbase layers of 737 mm (29 in.) of P-154 aggregate material. Figure 3b, c shows the profile views of the two pavement test sections where the three BE field sensors were embedded in the base layer. The P-209 base layer was constructed in two equal 4-in. (102 mm) lifts. In the "North" test section, an integrally formed, polypropylene biaxial geogrid with 25 mm (1.0 in.) × 33 mm (1.30 in.) rectangular aperture sizes was placed at the interface between the subbase and base layers. The installed direction of the 33-mm-rib of the geogrid was parallel to the gear path. Two BE field sensors were placed in the test section with geogrids (North section). The first field sensor (BE 1) was placed at 25 mm (1 in.) above the geogrid location, and the third BE field sensor (BE 3) was installed at 102 mm (4 in.) above the geogrid. The second sensor (BE 2) was installed in the "South" control section without geogrid again 25 mm (1 in.) above the bottom of the base layer. All three sensors were placed under the gear path of the National Airport Pavement Test Vehicle (NAPTV).

The base course aggregate material used in CC9 test section was a crushed stone from Birdsboro quarry, New Jersey. For the base course aggregate material, Fig. 4 shows the gradation curve, determined according to the ASTM C136 test procedure, and the moisture–density relationship. Figure 4a shows that the base course gradation met the lower and upper bound requirements of the FAA's P-209 granular base
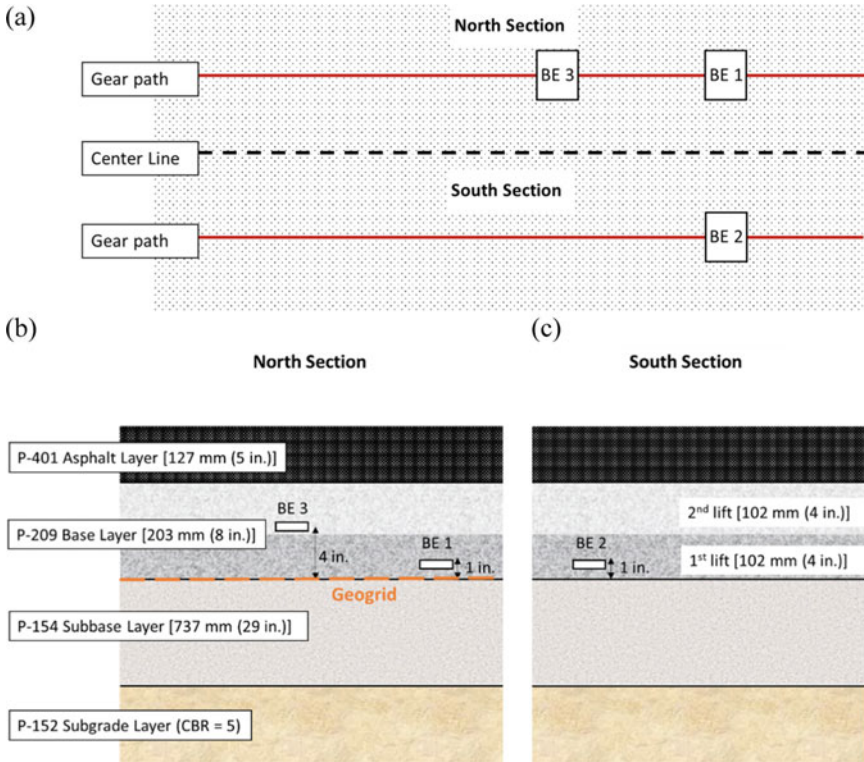
Fig. 3 Schematic drawing of NAPTF test sections: **a** plan view of the test section, **b** profile views of the BE sensors installed in the North (with geogrid), and **c** profile view of the BE sensor installed in the South (with no geogrid)

material specification. The aggregate material is classified A-1-a (stone fragments, gravel and sand) according to AASHTO soil classification, and as SP (poorly graded sand with gravel) according to the Unified Soil Classification System (USCS). D_{50} was 3.8 mm (0.15 in.) corresponding to 50% passing in a gradation chart, the top size was 25 mm (1 in.), and 3% were the percent passing No. 200 sieve size (0.075 mm). The modified Proctor (ASTM D1557) tests gave a maximum dry density (MDD) of 24.8 kN/m³ (158.0 pcf) at an optimum moisture content of 6.0%.

3.2 Sensor Installation and Test Procedure

The base layer was constructed in two 102-mm (4-in.) lifts. BE 1 and BE 2 were installed after the construction of the first layer, and BE 3 was placed after the construction of the second layer. The installation procedure for each BE field sensor was as follows: Once the first lift was placed and compacted, the location of the BE

Fig. 4 NAPTF CC-9 test sections P-209 base course aggregate material properties: **a** grain size distribution curve and **b** modified Proctor moisture–density curve
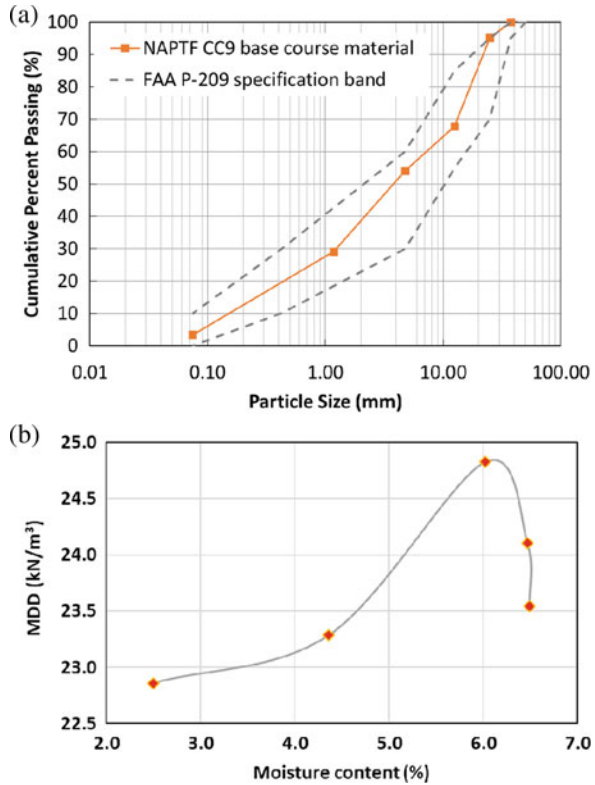
field sensor to be installed was marked and the base course materials were removed to bury the sensor frame as shown in Fig. 5.

The depth of placement of each BE sensor was carefully measured using a laser-level surveying equipment. The gap between the sensor frame and ground was filled and compacted properly to provide a uniform foundation to ensure sensor stability. To ensure contact between the BE sensors and the base course material, aggregates were gently placed in front of the sensors and initially compacted by hand tamping. The BE field sensors were then fully covered with the base course aggregates and compacted using a vibratory plate compactor. Both lifts were compacted with a vibratory roller compactor. Before the proper compaction with a vibratory roller, single lift density was assumed to be 18.9 kN/m^3 (120 pcf) for the purpose of calculating the shear modulus (see next section). The final dry density achieved after proper compaction was 23.8 kN/m^3 (151.3 pcf) which was measured using a nuclear density gauge. Figure 5 shows an installed BE field sensor in the aggregate base course and a zoomed-in view of BE 1 field sensor with the geogrid at the bottom.
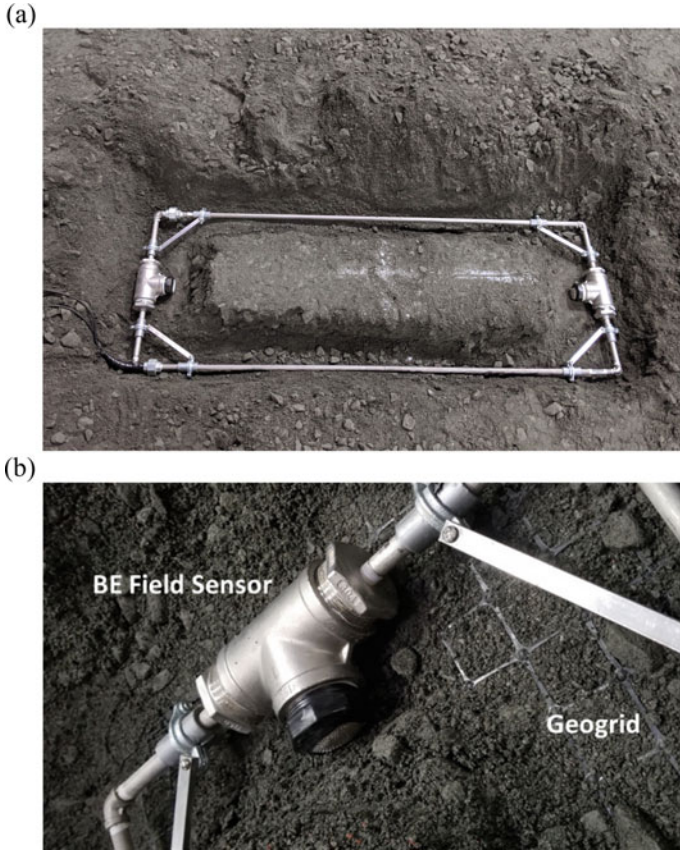
Fig. 5 BE field sensor base course installation; **a** BE field sensor placement during instrumentation and **b** BE 1 sensor protection casing module placed above the biaxial geogrid

4 BE Field Sensor Initial Results and Discussion

After installing the BE field sensors, shear wave signals were collected in two stages. The first measurements were taken after installing BE 1 and BE 2 in the first lift of the P-209 base layer. The measurement was made before the final compaction with a roller compactor; therefore, the density of the first lift was relatively low (assumed 18.9 kN/m^3 or 120 pcf). Figure 6a, b show the shear wave signals from BE 1 and BE 2, respectively, before placing the second lift and compacting with a vibratory roller. The red arrows indicate the first arrival time of the shear waves. The second measurement was performed after the placement and compaction of the second lift and the installation of BE 3 in the second lift. Figure 6c–e show the shear wave signals from BE 1, BE 2 and BE 3, respectively, during the second measurement. Shear wave velocity can be calculated as follows:
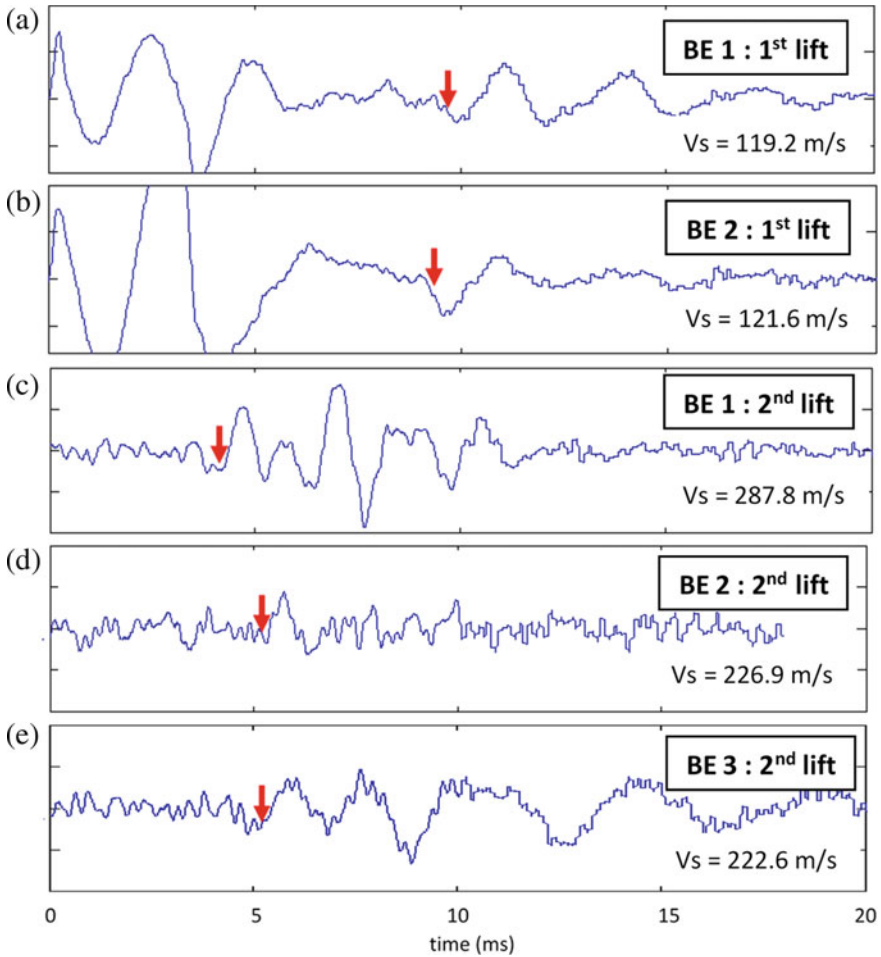
Fig. 6 Shear wave signal; **a** first measurement, BE 1, **b** first measurement, BE 2, **c** second measurement, BE 1, **d** second measurement, BE 2, and **e** second measurement, BE 3

$$V_S = \frac{L}{t_{\text{tip}-\text{tip}}} \tag{1}$$

where $t_{\text{tip}-\text{tip}}$ is the first arrival time and L is the distance between the two BE sensors.

The first arrival time of the shear waves was selected by finding the first break of the signal. The first break of the signal is considered as one of the best methods to get consistent results [19]. As shown in Fig. 6, the first arrival time of both signals from BE 1 and BE 2 in the first measurement is almost identical and does not show any enhanced stiffness from the geogrid. This is likely due to the low density and the relatively small overburden pressure. On the other hand, the first arrival times of the shear wave signals were significantly reduced in the second measurement

because of the higher density and the higher confinement from the overlying layer. As a small-strain stiffness, shear modulus can be estimated by using the following equation:

$$G_{\max} = \rho V_S^2 \tag{2}$$

where $G_{\max}$ is shear modulus and ρ is the bulk density of the aggregate material. Table 1 summarizes the shear wave velocities and shear modulus of the aggregate base layer from the first and second measurements. As mentioned above, shear modulus from BE 1 and BE 2 at the first measurement is comparable regardless of the presence of a geogrid. Considering that the lateral confinement of the aggregate materials is the key enhancement mechanism of the geogrid, it can be concluded that the lateral confinement was not sufficient at the first measurement due to the lack of compaction effort and low density, meaning that the geogrid enhancement was not fully utilized.

After the construction of the second lift and proper compaction, the shear modulus was dramatically increased for both BE 1 and BE 2. However, the shear modulus of BE 1, placed in the proximity of a geogrid, is significantly higher than that of BE 2 placed in the control section at the second measurement. After a high compaction effort was applied, the lateral confinement was successfully achieved due to the aggregate–geogrid interlocking which caused a significant stiffness enhancement. Further, it is notable that the shear modulus of BE 2 and BE 3 is comparable for the second measurement, which indicates that the geogrid enhancement effect was found to be diminished when measured at a 102 mm (4 in.) distance from the geogrid. It is thus clear that a stiffened zone is created in the proximity of the geogrid and that the range of the stiffened zone is approximately 102 mm (4 in.) above the geogrid.

Table 1 Shear wave velocity and shear modulus for the first and second measurements

Test condition	V_s [m/s]	$G_{\max}$ [MPa (ksi)]	Notes
First measurement, BE 1	119.2	27.3 (3.96)	
First measurement, BE 2	121.6	28.5 (4.13)	
Second measurement, BE 1	287.8	200.77 (29.12)	Near geogrid ⬅
Second measurement, BE 2	226.9	124.81 (18.10)	No geogrid
Second measurement, BE 3	222.6	120.15 (17.43)	10 m (4 in.) from geogrid

A similar conclusion that the stiffened zone ranges between 102 mm (4 in.) and 152 mm (6 in.) above and below the geogrid was reported in a previous study [20].

In conclusion, BE field sensors successfully measured small-strain stiffness from the field application and quantified the effect of geogrid enhancement. On top of that, the range of geogrid enhancement zone was successfully evaluated using the BE field sensors.

5   Conclusions

This study demonstrated recent findings from the new method to evaluate unbound layers in airport flexible pavements and discussed recent results on the stiffened zone quantified due to geogrid–aggregate system in the full-scale Construction Cycle 9 (CC9) pavement test sections constructed at the Federal Aviation Administration (FAA) National Airport Pavement Test Facility (NAPTF) in New Jersey. The FAA-designated P-209 and P-154 aggregate materials were used in the construction of the base and subbase layers, and a biaxial geogrid was placed at the interface between the sub-base and base layers in one of the test sections, while the other section was constructed as a control, i.e., having the same materials and layer thicknesses but no geogrid. Two bender element field sensors were installed in the geogrid-stabilized section at different depths of 25 mm (1 in.) and 102 mm (4 in.) from the geogrid location, and a third sensor was installed in the control section at a depth of 25 mm (1 in.) from the bottom of the base layer. Shear wave signals were collected in two measurement stages, and shear wave velocities and shear moduli were calculated.

The newly developed BE field sensor successfully collected shear wave velocities from the full-scale test sections and measured shear wave velocities. From the results of these experiments, a stiffness enhancement in the vicinity of the geogrid was clearly observed and quantified. The stiffness enhancement effect diminished when measured at about 102 mm (4 in.) away from the geogrid. Note that the testing results presented in this study are collected during the CC9 aggregate base course layer construction, i.e., before the stiffer asphalt concrete surface layer construction. The BE field sensors installed in the test sections will be further used to monitor the changes in the localized base course stiffness after the construction of the asphalt concrete layer and after certain increments/passes of trafficking the test sections with a moving wheel-gear loading.

References

1. McDowell GR, Harireche O, Konietzky H, Brown SF, Thom NH (2006) Discrete element modeling of geogrid-reinforced aggregates. Proc Inst Civ Eng Geotech Eng 159(1):35–48
2. Zhou J, Chen JF, Xue JF, Wang JQ (2012) Micro-mechanism of the interaction between sand and geogrid transverse ribs. Geosynth Int 19(6):426–437

3. Chen C, McDowell GR, Thom NH (2014) Investigating geogrid-reinforced ballast: experimental pull-out tests and discrete element modeling. Soils Found 54(1):1–11
4. Qian Y, Tutumluer E, Mishra D, Kazmee H (2015) Geogrid-aggregate interlocking mechanism investigated via discrete element modeling. In: Geosynthetics 2015, Portland, OR
5. Kim M, Lee JH (2013) Effects of geogrid reinforcement in low volume flexible pavement. J Civ Eng Manag 19(1):S14–S22
6. Tirado C, Carrasco C, Nazarian S, Norwood GJ, Tingle JS (2014) Benefits of inclusion of geosynthetic products in reinforcement of flexible airfield pavements using three-dimensional finite element modeling. In: 2014 FAA worldwide airport technology transfer conference, New Jersey
7. Sugimoto M, Alagiyawanna AMN (2003) Pullout behavior of geogrid by test and numerical analysis. J Geotech Geoenviron Eng 129(4):361–371
8. Moraci N, Recalcati P (2006) Factors affecting the pullout behavior of extruded geogrids embedded in a compacted granular soil. Geotext Geomembr 24(4):220–242
9. Peng X, Zornberg JG (2017) Evaluation of load transfer in geogrids for base stabilization using transparent soil. Procedia Eng 189:307–314
10. Kwon J, Tutumluer E (2009) Geogrid base reinforcement with aggregate interlock and modeling of associated stiffness enhancement in mechanistic pavement analysis. Transp Res Rec 2116:85–95
11. Byun YH, Tutumluer E (2017) Bender elements successfully quantified stiffness enhancement provided by geogrid-aggregate interlock. Transp Res Rec 2656:31–39
12. Byun YH, Tutumluer E, Feng B, Kim JH, Wayne MH (2019) Horizontal stiffness evaluation of geogrid-stabilized aggregate using shear wave transducers. Geotext Geomembr 47(2):177–186
13. Kim JH, Kang M, Byun YH, Qamhia IIA, Tutumluer E, Wayne MH (2020) Bender element shear wave measurement based local stiffness characteristics related to permanent deformation behavior of geogrid-stabilized aggregate specimens. In: Hambleton JH, Makhnenko R, Budge AS (eds) GEO-CONGRESS. ASCE, pp 517–526
14. Kang M, Kim JH, Qamhia IIA, Tutumluer E, Wayne MH (2020) Geogrid stabilization of unbound aggregates evaluated through bender element shear wave measurement in repeated load triaxial testing. Transp Res Rec 0361198120908230
15. Byun YH, Qamhia IIA, Feng B, Tutumluer E (2018) Embedded shear wave transducer for estimating stress and modulus of As-constructed unbound aggregate base layer. Constr Build Mater 183:465–471
16. Santamarina JC, Klein A, Fam MA (2001) Soils and waves. Wiley, Chichester
17. Lee JS, Santamarina JC (2005) Bender elements: performance and signal interpretation. J Geotech Geoenviron Eng 131(9):1063–1070
18. Kasthurirrangan G, Thompson MR (2007) Use of nondestructive test deflection data for predicting airport pavement performance. J Transp Eng 133(6):389–395
19. Clayton CRI (2011) Stiffness at small strain: research and practice. Géotechnique 61(1):5–37
20. Kwon J, Tutumluer E (2009) Geogrid base reinforcement with aggregate interlock and modeling of associated stiffness enhancement in mechanistic pavement analysis. Transp Res Rec 2116(1):85–95

Experimental Investigation of the Stabilization Performance of Geogrids for Unpaved Roads with Low Bearing Capacity Subgrade

**Süleyman Gökova , Mehmet Saltan , Serdal Terzi , Erol Tutumluer ,
Volkan Emre Uz , and Mustafa Karaşahin**

Abstract In this study, laboratory experiments were carried out on real sized samples to investigate the reinforcement performance of geogrids in highway pavements constructed on low bearing capacity subgrade (California Bearing Ratio, CBR = 3%). In all prepared samples, Hot Mix Asphalt (HMA) layer was not applied. A moving wheel load was applied with Accelerated Pavement Tester (APT) device on representative pavement samples with and without geogrids. Two types of geogrids were used to construct the pavement sample configurations. Resistance to plastic (permanent) deformation was recorded as a performance indicator to compare structural performance trends of the pavement samples. For this objective, surface deformations were measured after certain wheel load repetitions. Rut depths have been calculated from surface profiles measured with a laser profiler and were plotted versus number of load repetitions. As a result of this study, the use of geogrid over soft subgrade with low CBR values has been shown to extend the life of the pavement by reducing the rut depth.

Keywords Pavement · Geogrid · Geosynthetics · Wheel load simulator · CBR

S. Gökova
Mehmet Akif Ersoy University, 15030 Burdur, Turkey

M. Saltan · S. Terzi (✉)
Süleyman Demirel University, 32000 Isparta, Turkey
e-mail: serdalterzi@sdu.edu.tr

E. Tutumluer
University of Illinois at Urbana-Champaign, Urbana-Champaign, IL, USA

V. E. Uz
Department of Civil Engineering Izmir Institute of Technology, İzmir, Turkey

M. Karaşahin
İstanbul Gelişim University, İstanbul, Turkey

717

1 Introduction

According to ASTM D4439, a geosynthetic is a planar product manufactured from polymeric material used with soil, rock, earth, or other geotechnical engineering-related material as an integral part of a human-made project, structure, or system. There are many geosynthetic products in use, including geogrids, geotextiles, geomembranes, geosynthetic clay liners, geofoam, geonets, geocells, geobags, and geocomposites. The main geosynthetic types are permeable geotextiles and practically impermeable geomembranes. Types of geosynthetic materials include geogrid, geonet, geocell, geostrip, geomat, and geospacer under the permeable products called "geotextile-related products" [1]. Geomembranes can be polymeric (thermoplastic and elastomeric) and bituminous. Geosynthetic clay coatings containing clay (bentonite) are also impermeable products. Types produced using more than one geosynthetic are called geocomposites [2]. The International Geosynhetics Society (IGS) does not give a classification, but it also describes some other types, such as geomattress, geofoam, geoform, and geobar. Geosynthetics are successfully used to fulfill many of functions that improve performance on roadways, foundations, railway embankment, retaining walls and slopes [3–7]. The functions of geosynthetics are separation, filtration, reinforcement, stiffening, drainage, barrier, and protection, respectively [8]. In many applications, geosynthetics can perform one or more secondary functions at the same time, in addition to the prominent function. In almost all applications, for example, geosynthetics have the function of separation [9].

Geosynthetics are used either for new road construction or for repairing existing roads with separation, filtration, and/or reinforcement purposes. Cost-effective use of geosynthetics in these applications requires accurate analysis, research, and an experience-based approach.

In terms of applications of geosynthetics, roads can be treated in two categories as paved and unpaved ways [10]. It has been observed by Yang et al. [7] that a significant effect of the use of geosynthetics is in the provision of durability in unpaved roads and in reducing permanent deformations.

In pavement design, choosing the right layer thicknesses and the most suitable place to install the geogrid is important for reducing the rut depth that may occur in the pavement [10, 11].

When geosynthetics (geogrid and geotextile) are used between subgrade and base layers, it is possible to prevent the mixing of subgrade soil and granular base materials by providing the separation of the two layers. Furthermore, the geosynthetics used between the base layer and subgrade layer increase the bearing capacity of the subgrade and stiffen the base layer by strengthening the applied layers [12]. In addition, when the geogrid is used for strengthening the subgrade layer, economic benefits can be achieved by reducing the base and subbase layer thicknesses [13–15].

2 Materials Used in Experiments

In this part of the work, the physical and mechanical properties of the materials used to prepare the model test setups and the materials and methods used to determine these properties are available.

2.1 Subgrade Soil

In this study, the physical and mechanical properties of the subgrade soil were determined by conducting the following tests in the laboratory: Sieve analysis, Atterberg limits, standard Proctor compaction and CBR.

Table 1 lists the soil classification and Atterberg limits (liquid limit, plastic limit, and soil classification).

As a result of experiments on subgrade soil, low plastic inorganic clay (CL) was found as the soil classification.

A sample of 500 g taken from the subgrade soil was sieved with water in a 75 µm mesh sieve, and the remaining material on the sieve was placed in an oven and dried. After the sample was completely dry, its weight was found to be 218.98 g and the sieving process was continued with specific sieves. The results of sieve analysis (wet) for the subgrade soil are given in Table 2 and granulometry curve of subgrade material is shown in Fig. 1.

As a result of the standard Proctor test, the maximum dry density value was 1.83 g/cm^3 and the optimum water content value was found to be 15.3% (see Fig. 2).

The average value in the CBR test (ASTM D1883) on the samples prepared with optimum water content is 6.1%. But, since the CBR value of the subgrade sample to be used in the experiments is requested to be 3%, the water content of the subgrade material was determined as 19%.

Table 1 Atterberg limits and soil classification

Liquid limit	*46%*	*(TS 1900-1 AASHTO T-89)*
Plastic limit	17%	(TS 1900-1 AASHTO T-90)
Soil classification	CL	Unified soil classification

Table 2 Sieve analysis results of subgrade soil (ASTM D1140)

Sieve No	Sieve opening (mm)	Percent passing (%)
3/8″	9.53	100.00
No 4	4.760	99.48
No 10	2.000	99.18
No 40	0.425	94.93
No 200	0.075	56.35
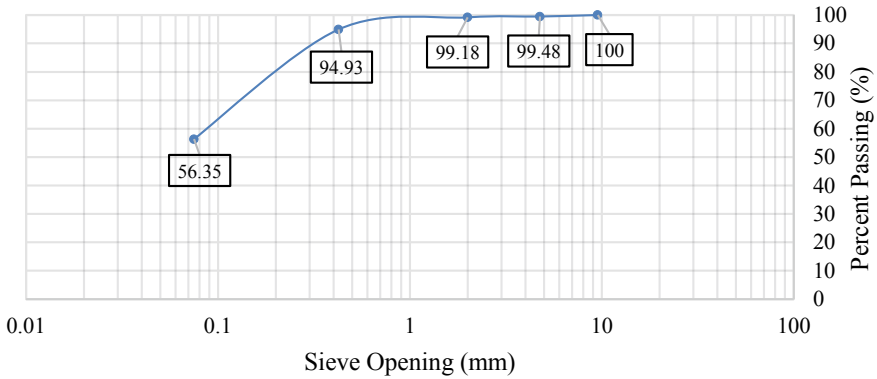
Fig. 1 Granulometry (particle size distribution curves) curve of subgrade material
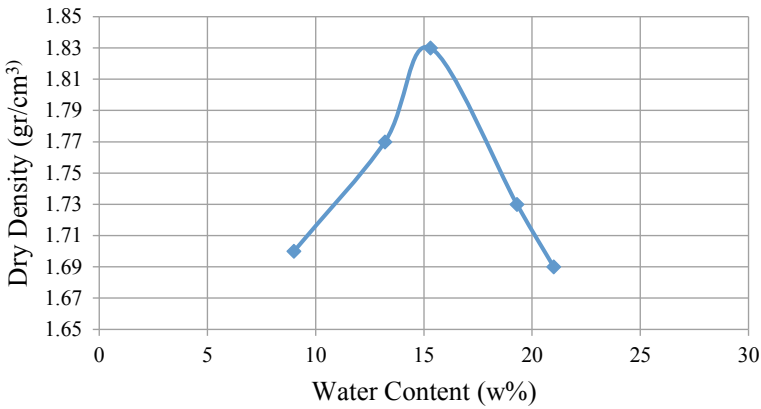
Fig. 2 Standard Proctor test chart for subgrade soil

2.2 Granular Base and Subbase Material

The materials to be used in the subbase and base layers are provided by KGM (Turkish General Directorate of Highways). The properties of the materials supplied by KGM are given in Tables 3, 4 and Fig. 3, respectively.

When the samples were being prepared, the results obtained from the modified Proctor experiment given in Table 3 were used. The results of the methylene blue test given in Table 3 show how much the clay is in the base and subbase materials. It has been observed that the clay ratios determined by the tests conducted are in accordance with the values determined in the KGM specifications. (Base MB ≤ 3.0—Subbase MB ≤ 4.0).

Table 3 Base and subbase course Proctor compaction test results

		Base	Subbase	Standard
Maximum dry density (t/m³)	Standard	–	–	–
	Modified	2.286	2.236	AASHTO T 180, TS 1900-1
	Vibrating	2.331	2.277	TS 1900-1, BS 1377
Optimum moisture content (%)	Standard	–	–	–
	Modified	5.1	5.0	AASHTO T 180, TS 1900-1
	Vibrating	3.7	3.7	TS 1900-1, BS 1377
Methylene blue test (%) max		1.75	2.25	TS EN 933-9

Table 4 Sieve analysis results of base and subbase course material

		Base	Subbase
Sieve No	Sieve opening (mm)	Percent passing (%)	Percent passing (%)
3″	75	–	–
2″	50	–	100
1 1/2″	37.50	100	97
1″	25.40	90.4	85
3/4″	19.05	78.2	75
3/8″	9.53	60.4	57
No 4	4.760	48.5	44
No 10	2.000	32.4	34
No 40	0.425	12.9	15
No 200	0.075	5.3	7
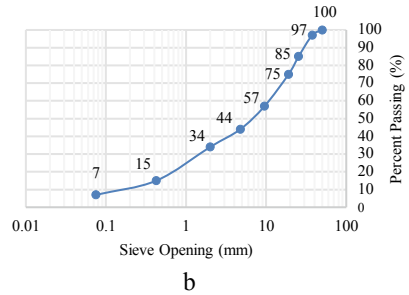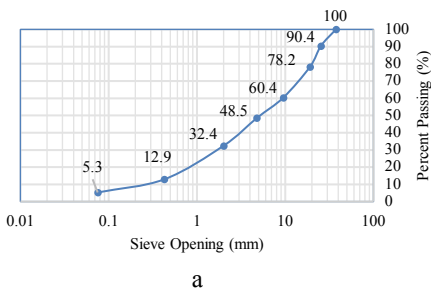
Fig. 3 Granulometry curve of base (**a**) and subbase (**b**) material

2.3   Geogrid Properties

The geogrids to be used in the study were selected by taking into account the grain sizes of the base layers to be placed on the location where they were placed, in order to perform the docking, separation and strengthening functions. The geogrids used were dual and multidirection geogrids with a 40 mm × 40 mm rib size. Type 1 and Type 2 geogrids used in this study were, respectively, biaxial and triaxial geogrids.

Tensile tests were performed on geogrids to determine their mechanical properties. The results obtained are as follows: Tensile strength, tensile elongation, tensile strength at 2% elongation and tensile strength at 5% elongation (see Tables 5 and 6, see Figs. 4 and 5).

3   Preparation of Samples

There are two sets of materials used in the experiments in which base course, subbase course, and subgrade materials were placed. (Model test setup dimensions is 140 cm longitudinally, 100 cm transverse, and 74 cm height.) These model test setups consist of interwoven walls of different heights. The fixed wall is 30 cm and the other removable walls are 20 cm and 12 cm high. The model test setups are prepared this way; it facilitates the placement of materials and offers the possibility to work at different heights (see Fig. 6).

The subgrade, subbase, and base course materials prepared at values of the predetermined moisture contents were compacted by placing them separately in the sample model test setup. Water content of 19% (determined moisture content), 5.1% (Opt. moisture content), and 5% (Opt. moisture content) was used in the subgrade, base and subbase materials respectively. The weights of the materials to be used in the experiments were found by using the determined density and the volume values. The subgrade sample was placed in three layers and compacted. Base and subbase materials were prepared and compacted in a single layer. After compaction, 95–99% compaction density was achieved using both a plate compactor and a hand compactor. In addition, the dynamic cone penetration (DCP) experiments had been performed at four pilot points on the subgrade and the obtained graphs were compared to observe whether the compactions of the samples were equal at each point. After each layer was compressed, it was kept for one day and the next layer was placed.

Layer thicknesses used in the experiments were as follows: Subgrade 50 cm, subbase 12 cm, and base 8 cm. The subgrade layer having a layer thickness of 50 cm was compressed into three layers separately so that it could not be compressed into a layer. The quantities of the materials to be used were calculated according to the mass density volume of the optimum water content. Three samples were prepared in this study. The first sample was prepared without geogrid, and on other samples, the two geogrid types were used (see Fig. 7).

Table 5 Longitudinal and transverse tensile test results for Type-1 geogrid (rib opening size 40 × 40 mm)

Nr	L0 (mm)	Tensile strength (kN/m)		Tensile elongation (%)		Force-F-%2		Force-F-%5 (kN/m)	
		Longitudinal	Transverse	Longitudinal	Transverse	Longitudinal	Transverse	Longitudinal	Transverse
1	100.0	23.50	19.75	12.00	11.12	8.03	7.14	15.09	13.41
2	100.0	23.31	20.30	13.31	12.13	7.90	7.22	14.57	13.45
3	100.0	23.16	20.75	12.07	15.52	8.43	7.32	15.47	13.34
4	100.0	22.87	20.55	12.40	14.08	8.63	7.59	15.42	13.79
5	100.0	23.37	19.95	13.97	13.46	7.45	6.64	13.75	13.41

Table 6 Longitudinal and transverse tensile test results for Type-2 geogrid (rib opening size 40 × 40 mm)

Nr	L0 (mm)	Tensile strength (kN/m)		Tensile elongation (%)		Force-F-%2 (kN/m)		Force-F-%5 (kN/m)		Force-F-%10 (kN/m)	
		Longitudinal	Transverse	Longitudinal	Transverse	Longitudinal	Transverse	Longitudinal	Transverse	Longitudinal	Transverse
1	100	17.26	16.95	12.29	10.63	4.68	5.66	9.52	11.63	15.44	16.73
2	100	17.15	17.38	11.77	11.56	4.64	5.67	9.40	11.49	15.88	16.93
3	100	17.15	17.75	11.88	11.03	4.60	5.68	9.35	12.10	15.73	17.41
4	100	17.07	17.79	11.82	11.65	4.79	5.79	9.52	12.05	15.87	17.26
5	100	17.20	17.55	10.71	10.68	4.72	5.16	10.04	11.67	16.55	17.27
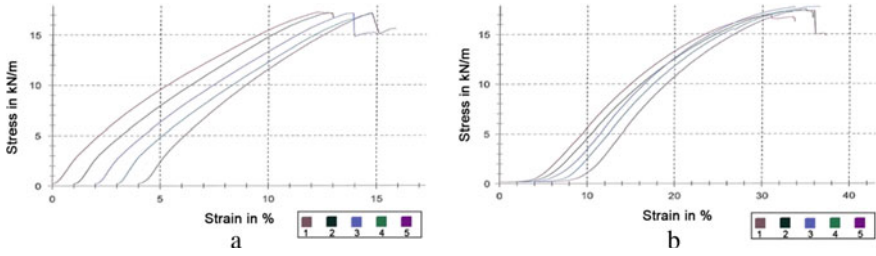
Fig. 4 Type-1 geogrid strain (%)—stress (kN/m). **a** Longitudinal, **b** transverse
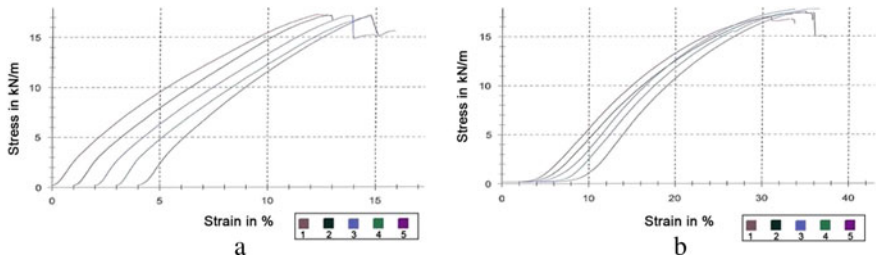
Fig. 5 Type-2 geogrid strain (%)—stress (kN/m). **a** Longitudinal, **b** transverse

Fig. 6 Model test setup used in experiments

With accelerated pavement testing (APT) shown in Fig. 6, desired wheel loads can be applied dynamically on the samples prepared using special model test setups. The amount of load to be applied, the lines on which the wheel is to be operated and the counts can be controlled from the control panel. The wheel positions can be controlled by the linear ruler on the device and the movement system of the device is hydraulic. The wheel load value applied in the tests was determined as 900 kg and the same load value was applied to all samples. Accelerated pavement testing

| Sample 1 (Without Geogrids) | Sample 2 and 3 (Type-1,Type-2 Geogrids) |
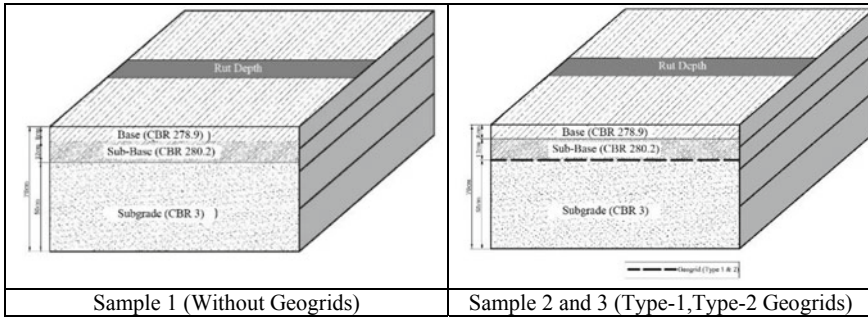
Fig. 7 Layers and their thicknesses used in the experiments

conditions: Temperature of test environment was 18–22 °C, velocity of wheel was 2.5 km/h, tire pressure was 524 kPa, tire diameter was 540 mm, and tire width was 170 mm.

4 Results

After each predetermined number of wheel repetitions, the rut depths were measured with the laser surface profiler tester and the data collected were transferred to a database on the computer. By using the generated database, the rut depth profiles formed on the surface were determined and various graphics were created.

4.1 Surface Profile Measurement Results

After the samples were prepared, the depths of the wheels were measured with the laser surface profiler before the test with the APT and after certain wheel pass numbers (50, 80, 120).

As a result of these tests, the surface profile measurements were recorded and the rut depths on the surface of the base layer were determined. It was observed that the rut depths formed in the samples subjected to tests, using geogrid, were less than those without geogrids. After the first 50 repetition, the formation of the rut depth has decreased thanks to aggregate interlocking (see Fig. 8). In the samples tested with using geogrid, it was seen that the formation of rut depths was almost the same amount after the first 50 cycles (see Table 7). The reason why the rut depth in the first 50 cycles of the sample using the Type-1 geogrid is lower than other sample with geogrid the tensile strength of the Type-1 geogrid is higher than the other geogrid.

As a result of the experiments, the changes in the rut depth values that occurred in the samples after a certain number of cycles have been compared among themselves
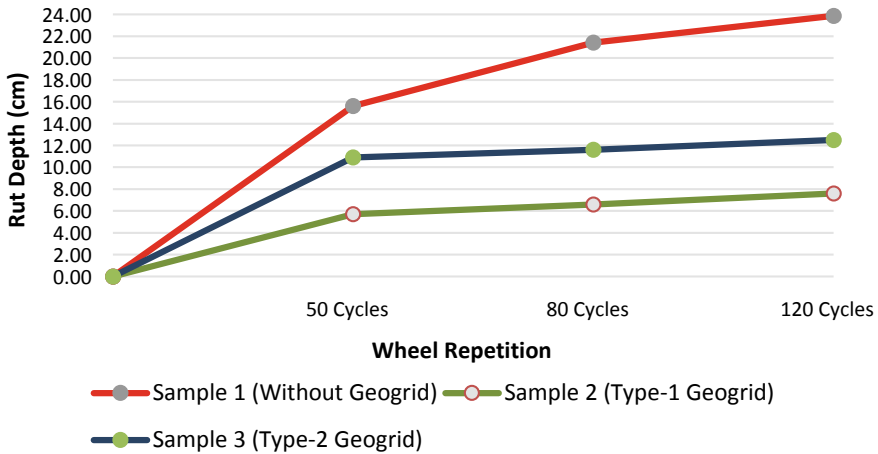
Fig. 8 Measured maximum rut depths formed on the surface of the base layers (cm)

Table 7 Change of surface profile measurement values between 50 and 120 cycles (cm)

Cycle ranges	0–50	50–80	80–120
Sample 1, without geogrid	15.5	5.92	2.45
Sample 2, Type-1 geogrid	5.7	0.9	1
Sample 3, Type-2 geogrid	10.9	0.7	0.9

and the differences are shown in Table 7. As shown in table, it has been observed that the rut depths occurring after 50 repetitions are more stable especially in samples with geogrid.

5　Conclusions

The effects of the use of geogrids to reduce the rut depth of pavements with low bearing capacity have been investigated in this study in which APT tests of samples with and without geogrids were carried out in the laboratory environment for this purpose. The main results are:

- The rut depths that are formed after repetitive wheel loads applied on the samples prepared using geogrid on the subgrade with low CBR value are lower than the samples prepared without using a geogrid. In addition, after a certain wheel repetition numbers, the rut depths increased more steadily and were lower than the samples without a geogrid. Along with the use of geogrids, in the remaining layers above the point where geogrid is placed, the elasticity increases and the formation process of the plastic deformations that can be formed by the applied loads can be delayed.

- As a result of certain wheel pass numbers applied to the samples prepared using geogrids with the same rib openings but different physical and mechanical properties, it was observed that the rut depth formed in the sample prepared using Type-1 was less than that of the sample prepared using Type-2. Among the samples tested with using geogrid, it was seen that the formation of rut depths and the rutting rates were similar after the first 50 wheel repetitions. On the other hand, the reason for the variation in the amount of rut depths occurring in the first 50 repetitions is due to the different tensile strengths of the two geogrid types used in the tests.

References

1. Shukla SK, Yin JH (2006) Fundamentals of geosynthetic engineering. CRC Press
2. Briaud JL (2013) Geotechnical engineering: unsaturated and saturated soils. Wiley, Canada
3. Benessalah I, Lambert S, Villard P, Arab A (2018) Effect of dynamics on the soil-geosynthetic interfaces used in reinforced rockfall embankments. Rock slope stability
4. Lambert S, Nicot F, Gotteland P (2011) Uniaxial compressive behavior of scrapped tire and sand-filled wire netted geocell with a geotextile envelope. Geotext Geomembr 29(5):483–490
5. Tafreshi SM, Dawson AR (2012) A comparison of static and cyclic loading responses of foundations on geocell-reinforced sand. Geotext Geomembr 32:55–68
6. Ahmadi H, Hajialilue-Bonab M (2012) Experimental and analytical investigations on bearing capacity of strip footing in reinforced sand backfills and flexible retaining wall. Acta Geotech 7(4):357–373
7. Yang X, Han J, Pokharel SK, Manandhar C, Parsons RL, Leshchinsky D, Halahmi I (2012) Accelerated pavement testing of unpaved roads with geocell-reinforced sand bases. Geotext Geomembr 32:95–103
8. Zornberg JG (2017) Functions and applications of geosynthetics in roadways. Procedia Eng 189:298–306
9. Wasti Y (2007) Geosynthetics—theory and application. Middle East Technical University, Ankara
10. Haas R, Walls J, Carrol RG (1988) Geogrid reinforcement of granular bases in flexible pavements. Transp Res Rec 1188:19–27
11. Soe AA, Kuwano J, Akram I, Kogure T (2018) Optimum use of geogrid in the unbound granular layer for the pavement construction. Int J GEOMATE 14(42):65–70
12. Giroud JP, Han J (2004) Design method for geogrid-reinforced unpaved roads—part I: theoretical development. ASCE J Geotech Geoenviron Eng 130(8):776–786
13. Carmo CD, D'ávila CA, Ruiz EF (2012) Deformation analysis of a geogrid-reinforced pavement. In: Second Pan American geosynthetics conference & exhibition. GeoAmericas, Lima
14. Kwon J, Tutumluer E (2009) Geogrid base reinforcement with aggregate interlock and modeling of associated stiffness enhancement in mechanistic pavement analysis. Transp Res Rec J Transp Res Board 2116:85–95
15. Kawalec J, Gołos M, Mazurowski P (2018) Environmental aspects of the implementation of geogrids for pavement optimisation. IOP Conf Ser Mater Sci Eng 356(1):012018. IOP Publishing

Subsurface Sensing for Transportation Infrastructure

Measuring the Performance of Railway Track Through Large-Scale Trackside Sensor Deployments

David Milne, Louis Le Pen, Geoff Watson, and William Powrie

Abstract Railway track performance is inherently variable along its length, even on straight plain line track. Current condition monitoring relies on snapshot train borne measurements of track geometry, which may be used to plan route level maintenance. Although this provides a global record of current track quality, it is difficult to infer the local condition of the trackbed and local mechanisms of deterioration that may be occurring. A more important indicator of local trackbed condition may be the trackbed support stiffness as seen by a train. The trackbed support stiffness influences the performance of the track and its variation could potentially be used to predict changes in longer term performance with trafficking by means of vehicle/track interaction models and settlement equations. Trackside measurements may be obtained using track mounted sensors such as accelerometers, geophones, deflectometers, high-speed video cameras or strain gauges. These may be interpreted to determine the trackbed support stiffness. However, many measurement locations are required to determine the variation in trackbed stiffness along a useful length of track. This requires a significant increase in the scale of typical trackside monitoring deployments, potentially generating large volumes of data and requiring a degree of automation for data processing. The availability of small, inexpensive, standalone micro-electromechanical systems (MEMS) accelerometers means that it is now practicable to instrument hundreds of sleeper-ends in a single deployment, covering far greater lengths of track than would be viable with more established and expensive trackside monitoring approaches. This paper shows how MEMS have been used to investigate the performance of longer sections of track. Data processing techniques are described, and insights into the actual variation of track system performance are discussed.

Keywords Rail track substructures · Including transition zones · Transportation geodynamics · Accelerometers · Ties · Sleepers · Trackbed stiffness · Support modulus

D. Milne (✉) · L. Le Pen · G. Watson · W. Powrie
University of Southampton, Southampton, UK
e-mail: d.milne@soton.ac.uk

1   Introduction

Route level maintenance of railway tracks is generally based on train borne measurements of track geometry [1]. Geometry parameters such as level or alignment are relative measures in that they describe the deviation from the average over a particular wavelength, rather than the absolute position of the track. Infrastructure managers use these data to plan trackbed maintenance, targeting both significant deviations in local geometry and high variability over fixed lengths of track. The implication of this is that differential settlement of the track will be a driver for trackbed maintenance. If differential behavior is important, variations in the track performance, loading (from vehicle track interaction) and track properties (stiffness) along the length of the track need to be understood. Taking an evidenced based, data rich approach to studying this will require large-scale monitoring with resolution at a local scale.

One approach for investigating the performance of railway track is lineside monitoring, in which different sensors placed at intervals along the track superstructure and used to record the response of the track under traffic, e.g., [2–6]. Typical lineside deployments tend to be small and highly localized owing to the costs of the instrumentation and analysis requirements. To investigate variability over longer lengths of track, the instrumentation, data acquisition and data processing/interpretation requirements will increase significantly. One implication of this is that lower cost instrumentation is needed to enable larger scale deployments; another is that data processing and basic interpretation will need to be automated to study the variability of the track from the trackside measurements. The same would likely be required for any long-term, pervasive monitoring of critical parts of the infrastructure.

This paper explores how large numbers of comparatively low-cost MEMS accelerometers can be deployed and the data obtained processed to provide insights into the variability of railway track performance. Criteria for the selection of accelerometers are discussed, processing techniques described and their application demonstrated.

2   Methods

2.1   Sensors

One of the most common lineside monitoring approaches is the use of inertial sensors to record track vibration. Displacement can be obtained by filtering then integrating once for velocity or twice for acceleration measurements [7]. Application of a high pass filter, necessary to avoid low frequency drift when integrating, results in startup transients and a shift in the apparent datum for the deflection data; a statistical method for correcting for this and assessing the range of deflection is described later.

Micro-electro mechanical systems (MEMS) accelerometers, often used in consumer electronics, are far less expensive than more conventional research-quality

devices (costing tens rather than hundreds of dollars), potentially enabling much larger deployments.

Deflection of railway track is a low frequency phenomenon [8]. This has implications for the selection of monitoring accelerometers, as the accelerations significant for deflection are likely to be of low amplitude and low frequency. Several facets of performance for both the transducer and the data acquisition system need to be considered, depending on where within the track system a sensor is to be deployed. For example, a sensor on the rail will experience higher amplitude, higher frequency vibration than a sensor on a sleeper or in the trackbed.

- **Accuracy** is limited by noise, as this affects the minimum acceleration that will be detectable at a given frequency, how accurately a change in acceleration can be resolved and whether acceleration data are likely to integrate to produce meaningful deflections. This is important in the current application because amplification of transducer noise is inversely proportional to the square of frequency of interest.
- **Range and resolution**—the range defines amplitude of acceleration over which a sensor can operate without saturating. The voltage range and/or bit depth over which this is discretized defines the precision of the monitoring system.
- **Sample rate** is controlled by which frequencies are of interest and the sensor bandwidth, i.e., the frequency range that a sensor can detect. The sensor should be able to detect all frequencies of interest and the data acquisition system must be capable of sample rates of twice the sensor bandwidth to satisfy the sampling theorem [9]. The bandwidth can be restricted by hard filtering the transducer outputs before analogue to digital conversion. Oversampling or similar signal conditioning can improve the effective bit depth or reduce noise.

Fairly inexpensive MEMS sensors have been shown capable of obtaining sleeper deflection from acceleration data, particularly at higher train speeds, producing reliable data for several months on end [10]. At higher train speeds, the frequencies and amplitudes of the acceleration signals are increased, improving the potential to detect them above sensor/system noise. MEMS sensors are available in variants that output both analogue and digital signals. Analogue sensor outputs require external analogue digital conversion (ADC) for data logging, whereas digital variants include this within the sensor's integrated circuit (IC). Digital sensors require a microcontroller to access, transfer and store the data; these can be combined at board level, giving low-cost standalone monitoring devices suited for monitoring infrastructure. An analogue sensor with an external ADC could, of course, be used with a microcontroller in a similar fashion.

The small size and IC form factor of MEMS sensors means that they can be assembled into a robust package. With appropriate power, communications systems/services and ruggedization these types of devices could form the basis of networked large-scale pervasive monitoring. This paper makes uses of a similar, but somewhat less sophisticated, standalone device, to demonstrate some potential applications of larger scale monitoring. The device used comprised an Analog Devices
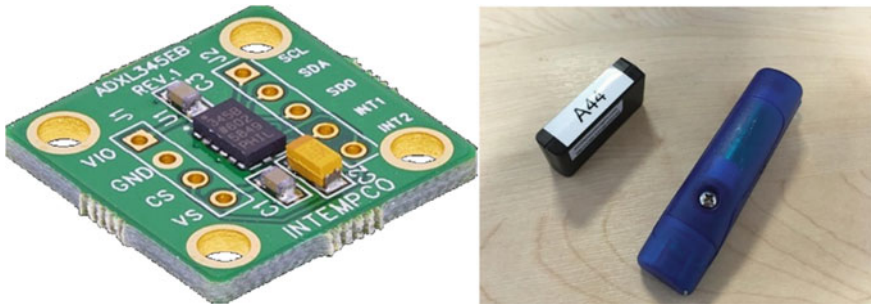
Fig. 1 MEMS accelerometer IC and standalone measurement devices (in two packaged equivalent variants)

ADLX 345 triaxial MEMS accelerometer, microcontroller, real-time clock, micro-SD card and lithium battery. This is a self-powered device, capable of sampling at 400 Hz (with $8\times$ over sampling and finite impulse response (FIR) filtering) for later download to a computer via a USB. These devices were manufactured by Gulf Coast Data Concepts and cost around \$100. The accelerometer chip and measurement devices are shown in Fig. 1.

Each device is independent and standalone; this means that in a deployment of multiple devices, measurements are simultaneous but not synchronous. Data are recorded continuously, as although the devices can be configured to start recording when a train is detected they do not buffer; thus, they cannot record the approach of the train, which is useful data for analysis.

2.2 Data Processing

In all the studies presented in this paper, the devices were placed on the track during a possession when no trains were able to pass. Devices were configured to start recording with the return of traffic, continuing until their batteries had depleted—usually between 4 and 8 h. Sensors were then recovered during another possession. In some deployments, the recovered sensors were recharged and transferred to a new location. Data were then downloaded to a computer via a USB. These devices functioned reliably for these short but repeated deployments.

This approach generates large volumes of data, from which the valuable train pass-by data need to be extracted. The pass-by events can be extracted by retrospectively applying a threshold acceleration at a suitable level to identify when trains were present on the track. If the sensor clocks are approximately synchronized, the timestamp can be used to group, but not align, the same pass-by event recorded by different devices.

Analysis often requires the type of train to be identified, enabling like with like comparison and association of the train set geometry and typical axle/wheel loads.

This is challenging as the monitoring systems tend to be unattended. It may be done by inspection, using prior knowledge of which train types operate on the line. For pervasive monitoring, route data of train passing times could be linked into the analysis system. An approach yet to be explored is using machine learning to identify trains from the sensor records.

Deflection

A common objective of lineside monitoring is to assess the movement of railway track under load from trains. Once individual pass-by events have been identified and extracted, the data must be processed to obtain deflections. For acceleration data, this is done by filtering and integrating twice. Generally, a high pass filter is used to prevent low frequency drift during integration, and a low pass filter used to remove higher frequency noise and vibration not relevant to the major trackbed motions. The filter cut on/off frequencies must be selected so that the frequencies relevant for deflection are in the passband.

Figure 2 shows acceleration data filtered and integrated to obtain deflection. The filtering affects the deflection trace obtained. There are transients at the start and end of the train passage and the data are averaged about zero, causing the apparent at rest position of the track to be shifted from zero.
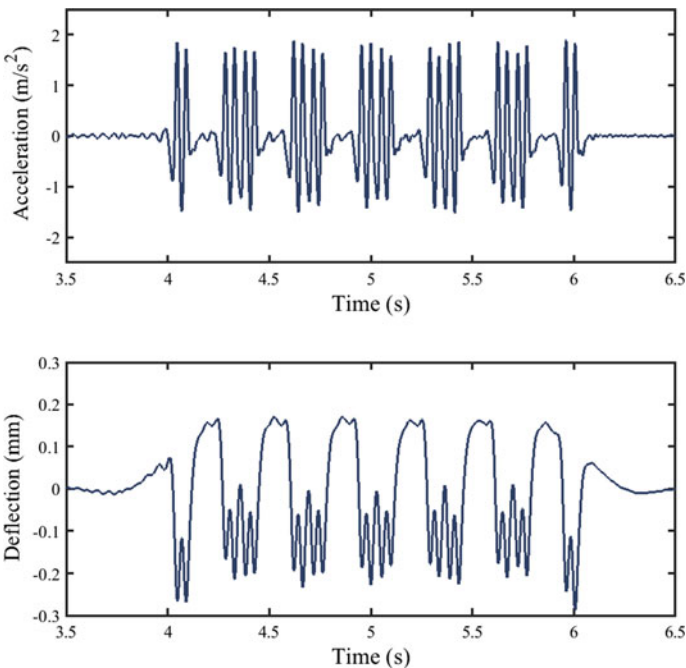
Fig. 2 Example acceleration signal integrated to obtain deflection

If the data are of good quality and have been processed appropriately, there will be a "stationary" region containing a repeating pattern due to the passing train, visible for the four pairs of internal vehicle ends. Milne et al. [11] present a statistical method using the cumulative distribution function for track deflection to calculate the proportion of the time that the track is expected to be above or below the rest position of the track. This can then be used to identify the at rest level of track and hence quantify the characteristic range of deflection, implicitly averaging over most of the train.

Figure 3 shows the acceleration and deflection spectra for the data in Fig. 2. The deflection spectrum shows that track deflection is a low frequency phenomenon, with the exact frequencies of interest dependent on the speed of the train. For passenger trains, repeating vehicles cause spectral peaks at multiples of the vehicle passing frequency (i.e., the length of the typical vehicle divided by the speed). The vehicle passing frequency can be considered to be the first frequency of interest for track deflection; the cut-off frequency for the high pass filter should be between $1/2$ and $1/3$ of this frequency. Powrie et al. [12] showed that including about 10 multiples of the vehicle passing frequency gives over 95% of the expected track deflection. The implication of this is that the cut-off on frequency for the low pass filter should be at least 10 multiples of the vehicle passing frequency to avoid filtering out information relevant for trackbed deflection.
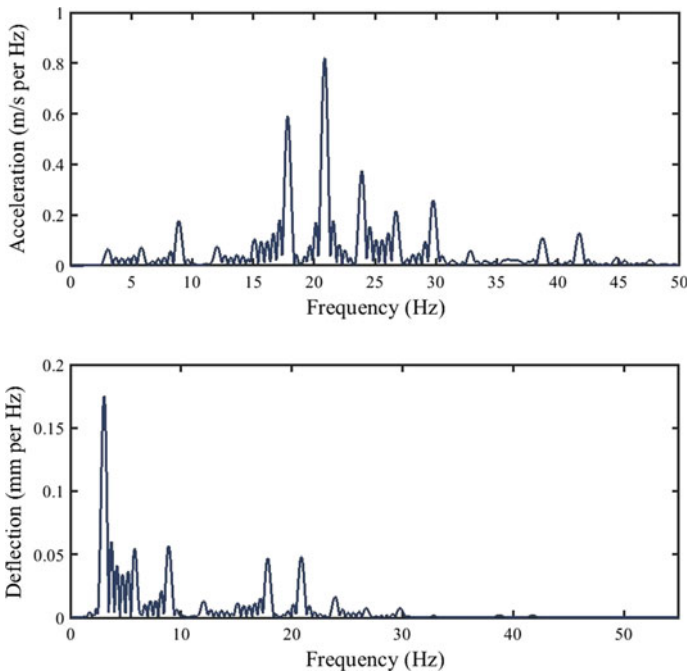
Fig. 3 Example acceleration and deflection spectra to 50 Hz

Stiffness

Another important performance indicator for different track systems is the stiffness, i.e., the amount it deflects for a given load. This may be defined in different ways, for example, as a spring stiffness per sleeper end or as a linear modulus per meter of track. Determining a support stiffness or modulus requires knowledge of the applied load, the track deflection and a mathematical framework to account for the bending stiffness of the rails [13–15]. On a live railway, the applied load is both uncertain and challenging to measure. Le Pen et al. [16] proposed a method for determining the support system modulus by analysis in the frequency domain, without knowledge or measurement of the load. The dominant train load frequencies occur at multiples of the vehicle passing frequency [17], as may be seen in Fig. 3. The magnitudes of these frequencies depend on the train geometry and the track stiffness. Le Pen et al. [16] used the Fourier transform of the simple beam on an elastic foundation model for track deflection to develop a closed form solution relating the ratio of magnitudes of pairs of these dominant frequencies to the track system support modulus. Certain pairs of frequencies are better suited for this analysis than others [18].

Along the Track

The techniques described above enable characterization of individual train passage in terms of deflection and stiffness at discrete locations. Once categorized by train type, these data need to be interpreted into a profile showing how deflection and stiffness vary along the track. This is an interesting problem, with some similarities to time series (or trend) analysis.

In a deployment of a sensor array, multiple observations for the same train type should be made at each location, and ideally some average of these observations should be used to assess how the deflection and stiffness vary along the track. Variable train occupancy, speed and wheel condition will cause the results obtained for deflection and stiffness to vary from train to train at each location and there may be outliers. Owing to limitations on the time available, it may not be possible to make enough measurements to obtain a robust average and understand the distribution of deflection at a measurement point.

Hence, the "best" (current) interpretation process for deflection and stiffness profiles is by a combination of curve fitting and inspection. In this process, every observation (for deflection or stiffness) for each sleeper is plotted along the track. A cubic "not-a-knot" spline is fitted to the data; this type of function suits rail deflection as it is continuous to its third derivative. Outliers are excluded by inspection, so that the curve is fitted to clusters of similar data at each measurement point. If enough observations are made, this stage is redundant. If data are missing or of low quality at some locations, curve fitting provides a way of estimating the likely performance, given the behavior of the surrounding track. A combination of clustering and curve fitting algorithms could be used to automate this process.

3   Studies

The techniques described above have recently been used to study the distribution of deflection and stiffness along different lengths of railway track in Europe [19, 20]. Two examples are presented here. These are a 200 m length of a ballasted high-speed railway track (site 1), with the aim of studying variation in performance, and a shorter length of track (site 2) where the techniques were used to measure the performance before and after a full trackbed renewal.

3.1   Site 1

Figure 4 shows downward deflection and support system modulus data obtained over 350 sleepers on a ballasted high-speed railway. The results are based on acceleration measurements for the same type of six-vehicle passenger trains, which generally passed the site at a speed of 60 m/s. Results were obtained in three consecutive deployments in which the sensors were moved along the track during a night time possession. The results shown were averaged from data for between 6 and 12 train passes at each monitoring point.

The data in Fig. 4 provide insights into the real variation of deflection and stiffness along the track. Both measures vary from sleeper to sleeper, and areas of good and poor performance are clear. For example, the track deflections are more significant and variable between sleepers 0 and 200, with discrete zones of increased deflection around sleeper numbers 50, 90–100, 120–130 and 180, likely due to voiding between the sleeper and trackbed. The support system modulus is also more variable in this section. Both are indicative of poor performance. In contrast, from sleeper
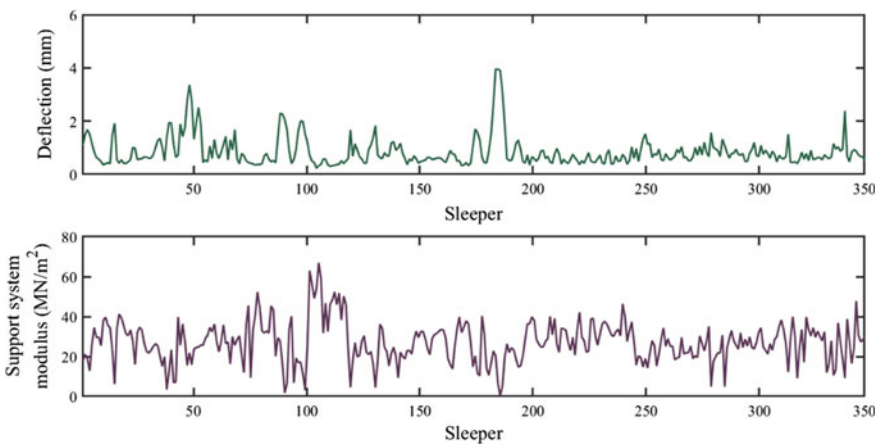
Fig. 4 Variation of deflection and support system modulus along 200 m of railway track [20]

200 onwards, the deflections are smaller and more consistent, with a deflection floor of around 0.4 mm indicative of good performance. The support system modulus is also less variable for these sleepers. Discussion with local track engineers revealed that sleeper 200 marks approximately the end location of a tamping run, and that the section of the site up to this location had been tamped more frequently than the latter part. This has interesting implications, and further work could usefully look at whether the increased tamping frequency was causal or symptomatic.

In addition to allowing intuitive visualization of performance along a track, these data have been used by [19] to study, quantify and better understand the distribution of stiffness and deflection along a railway, providing a framework for both assessing and comparing variation in track conditions and potentially synthesizing realistic variations in track properties for simulation and forecasting. Milne et al. [20] used the data in combination with a track level survey and a simple vehicle track interaction model to assess the significance of track level, track stiffness and geometric nonlinearity from voiding for measured and simulated track performance. For this site, the permanent differences in track level were more significant for wheel rail contact forces than differences in support conditions. The support conditions, including nonlinearity, were more important than initial level for determining track deflection.

3.2   Site 2

Figure 5 shows track deflection data recently obtained using a deployment of about 40 accelerometers over a section of track running along an embankment, before and after a track renewal. Sleepers were replaced during the renewal; hence, the sleeper numbers do not exactly correspond, and the data are not precisely aligned, although the two surveys are for the same section of track.

The data in Fig. 5 allow intuitive comparison of the condition of the track. Before the intervention, the performance was poor: deflections were large and variable (2–4 mm), and there was a distinct fault with probable voiding. After the renewal, performance improved. All deflections were reduced to below 1.5 mm. Sleepers 19–29 appear to be performing very well, achieving consistent performance with a deflection floor of around 0.6 mm. This was a significant improvement compared with the performance prior to renewal. It is attributable to an improvement in the trackbed and sleeper support conditions, as the underlying embankment did not feature in the remedial works.
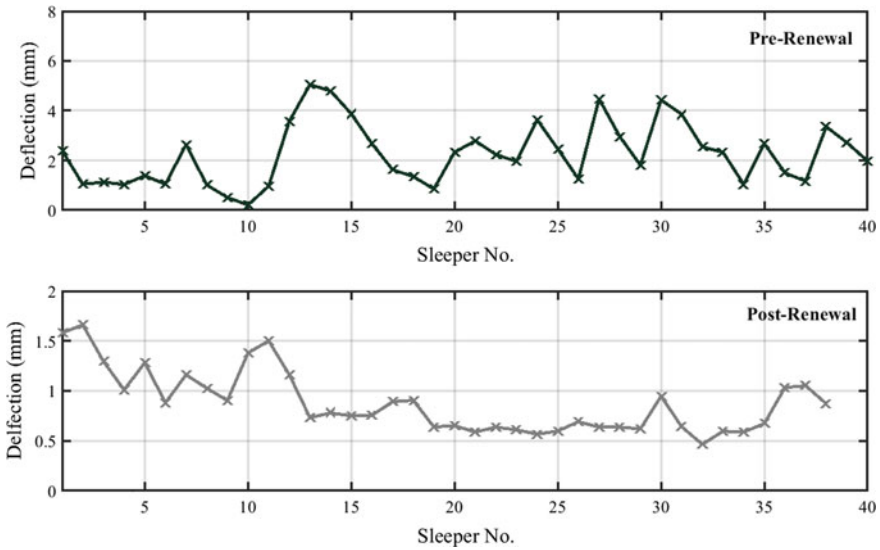
Fig. 5 Variation of deflection and system support modulus before and after a renewal

4 Summary

Evidence based large-scale and long-term studies of railway track infrastructure performance will require monitoring at an increased scale. Doing this from the infrastructure itself will necessitate the use of much lower cost monitoring equipment, and automation of data processing and interpretation. Low-cost MEMS accelerometers, read by microcontrollers, are suitably low noise and have the appropriate range, resolution and bandwidth to evaluate track deflection and stiffness from data of vibrations induced by passing trains. Using data from this type of device, this paper has demonstrated how existing (and automatable) techniques can be used to classify and interpret track vibration signals from larger scale deployments to study variations in track performance along a railway. Interpretation of the results from this type of analysis is intuitive; the performance and condition of the track are clear, and the effects of interventions can be evaluated directly.

References

1. British Standards Institution (2006) BS EN 13848. Railway applications—track—track geometry quality. In: Part 2: measuring systems—track recording vehicles. London
2. Auersch L (2005) The excitation of ground vibration by rail traffic: theory of vehicle–track–soil interaction and measurements on high-speed lines. J Sound Vib 284(1–2):103–132. https://doi.org/10.1016/j.jsv.2004.06.017
3. Cui Y-J et al (2014) Investigation of interlayer soil behaviour by field monitoring. Transp Geotech 1(3):91–105. https://doi.org/10.1016/j.trgeo.2014.04.002
4. Le Pen L et al (2017) Behaviour of under sleeper pads at switches and crossings—field measurements. Proc Inst Mech Eng Part F J Rail Rapid Transit 232(4):1049–1063. https://doi.org/10.1177/0954409717707400
5. Mishra D et al (2014) An integrated approach to dynamic analysis of railroad track transitions behavior. Transp Geotech 1(4):188–200. https://doi.org/10.1016/j.trgeo.2014.07.001
6. Paixão A, Fortunato E, Calçada R (2014) Transition zones to railway bridges: track measurements and numerical modelling. Eng Struct 80:435–443. https://doi.org/10.1016/j.engstruct.2014.09.024
7. Bowness D et al (2007) Monitoring the dynamic displacements of railway track. Proc Inst Mech Eng Part F J Rail Rapid Transit 221(1):13–22. https://doi.org/10.1243/0954409jrrt51
8. Thompson D (2009) Railway noise and vibration mechanisms, modelling and means of control. Elsevier, Oxford, p xv, 518 p
9. Oppenheim AV, Schafer RW (1975) Digital signal processing. Prentice-Hall
10. Milne D et al (2016) Proving MEMS technologies for smarter railway infrastructure. Procedia Eng 143:1077–1084. https://doi.org/10.1016/j.proeng.2016.06.222
11. Milne D et al (2018) Automated processing of railway track deflection signals obtained from velocity and acceleration measurements. Proc Inst Mech Eng Part F J Rail Rapid Transit
12. Powrie W et al (2019) Train loading effects in railway geotechnical engineering: ground response, analysis, measurement and interpretation. Transp Geotech 21:100261. https://doi.org/10.1016/j.trgeo.2019.100261
13. Priest J, Powrie W (2009) Determination of dynamic track modulus from measurement of track velocity during train passage. J Geotech Geoenviron Eng 135(11):1732–1740. https://doi.org/10.1061/(ASCE)GT.1943-5606.0000130
14. Timoshenko S, Langer BF (1932) Stresses in railroad track. ASME Trans 54:277–293
15. Esveld C (2001) Modern railway track, 2nd edn. MRT-Productions, Delft
16. Le Pen L et al (2016) Evaluating railway track support stiffness from trackside measurements in the absence of wheel load data. Can Geotech J 53(7):1156–1166. https://doi.org/10.1139/cgj-2015-0268
17. Ju S-H, Lin H-T, Huang J-Y (2009) Dominant frequencies of train-induced vibrations. J Sound Vib 319(1–2):247–259. https://doi.org/10.1016/j.jsv.2008.05.029
18. Milne D et al (2017) Properties of train load frequencies and their applications. J Sound Vib 397:123–140. https://doi.org/10.1016/j.jsv.2017.03.006
19. Le Pen L et al (2019) A model for the stochastic prediction of track support stiffness. Proc Inst Mech Eng Part F J Rail Rapid Transit. https://doi.org/10.1177/0954409719841800
20. Milne D et al (2019) The influence of variation in track level and support system stiffness over longer lengths of track for track performance and vehicle track interaction. Veh Syst Dyn 1–24. https://doi.org/10.1080/00423114.2019.1677920

Proposition for in Situ Evaluation of Geotechnical and Structural Aspects of a Heavy Haul Track

Robson Costa, José João Pires, Edson Moura, Rosângela Motta, Guilherme Castro, Liedi Bernucci, and Luciano Oliveira

Abstract Over time railroad tracks have their structural quality varying in function of traffic accumulation and maintenance. These changes can provoke different track responses in terms of unexpected stresses and deformations that, in turn, can bring on some loss of geometric quality and cause impact to the trafficability. Track condition monitoring can indicate the variation of geotechnical and structural characteristics in terms of traffic accumulation, maintenance, drainage, etc. The knowledge about these variations can provide information about the major factors that affect track behaviour and so support the maintenance planning of a railroad management operator. The aim of this paper is to propose a procedure for in situ evaluation by monitoring geotechnical and structural responses of typical sections of a heavy haul track (314 kN/axle) in the north region of Brazil. The implemented instrumentation was conceived using strain gauges for deformation measurements, vertical pressure cells for stresses monitoring and linear variable displacement transducer (LVDT) coupled to displacement measurement device (DMD) and tactile sensors. In addition, suction sensors were installed for measuring negative pore-pressure in the subgrade. From

R. Costa (✉) · J. J. Pires · E. Moura · R. Motta · G. Castro · L. Bernucci
Polytechnic School of University of São Paulo, Prof. Alm. Prado Ave. 83, São Paulo, Brazil
e-mail: robsoncosta@usp.br

J. J. Pires
e-mail: eng.josejoao@gmail.com

E. Moura
e-mail: edmoura@usp.br

R. Motta
e-mail: rosangela.motta@usp.br

G. Castro
e-mail: guilhermecastro@usp.br

L. Bernucci
e-mail: liedi@usp.br

L. Oliveira
Vale S.A, Dante Micheline Ave. 5500, Espírito Santo, Brazil
e-mail: oliveira.luciano@vale.com

the deformations in the web rail and considering an analytical model, it was possible to determine the wheel dynamic loads. It was observed the load factor values varying according to train speed and track quality, as well as the influence of the dynamic load in the stresses over the profile. Concerning the subgrade, the suction pressure presented slight variation (condition near saturation) during the period of analysis, so it could influence the track structural responses to the loads.

Keywords Railroads · In situ instrumentation · Heavy haul track · Geotechnical and structural responses

1 Introduction

The structural condition of the permanent way is related to the stresses and deformations acting on the track components (rails, sleepers, ballast, etc.). Normally, the methodology in structural analysis is based on the comparison of acting stresses with respective allowable materials, which should be superior to the allowable ones [1]. In heavy haul railroads, the pressure among competitors for larger world market shares requires company strategies to achieve better results [2]. In order to target these results, companies can speed up vehicles, carry larger volumes of cargo or even both combined. However, these factors contribute significantly to the increase of stresses acting on all components of the track over time, considering traffic accumulation and maintenance actions, especially on heavy haul tracks [3].

Along the traffic accumulation, geotechnical elements of the track, including the subgrade that crosses different soil horizons, influenced by weathering actions, thus being susceptible to resistance changes [4].

The function of the track components is to reduce the stresses transmitted by the dynamic passage of vehicles from the wheel-rail contact to the foundation. Magnitude of values generated at the interfaces is presented by Esveld [5] and Lichtberger [6]. Also, according to Selig and Waters [7], the loading imposed with the passage of trains added to the temperature changes generate stressing efforts on the track structure. These efforts can be classified according to the direction of operation (longitudinal, transverse and vertical).

Regarding the railroad track quality, it is known that through the track deflection measurements, it is possible to calculate the track modulus (u) and so obtain the elasticity and stiffness conditions of the substructure [8]. However, this condition may be influenced by the presence of voids between the base of the sleeper and the top of the ballast [9]. Related to geotechnical materials, studies conducted by Tutumluer [10] at the facility accelerated service testing (FAST) for high axle load in Pueblo (Colorado) indicated, in terms of vertical displacements in the evaluated section, that there is a greater contribution of the ballast layer compared to the subgrade (10% of the total displacement). On the other hand, evaluations performed by Selig and Waters [7] showed that the subgrade is one of the most important components of

the substructure, providing resilient support to the loading of the vehicles' wheels, besides contributing substantially to the elastic deflection of the rails.

The importance of the subgrade is due, among others, to the fact that in the different seasons of the year, the actions of weathering altering its bearing capacity. In this regard, Fredlund and Rahardjo [11] describe that variations in climatic conditions significantly influence the proximity of the soil surface. In arid and semi-arid climates, which have higher evaporation rates than precipitation, in addition to low water levels, cracks in the soil may occur. This phenomenon is caused when the pore suction stresses in all directions exceeds the confinement stresses to which the soil is subjected. In relation to the soil of the railroad subgrade, it is located in the unsaturated zone (above the water table), as well as most engineering structures designed with compacted soils, being very sensitive to local climatic conditions.

The objective of this study was to propose a procedure for in situ evaluation of structural and geotechnical aspects by adopting sensors between the track components measured over the dynamic passage of vehicles on a heavy haul track. This study contributes to the assessment of the increase in load per axle of the wagons through a better understanding of the efforts generated in the components of the permanent track dynamically and the subgrade conditions facing climate actions throughout the year.

2 In Situ Tests Using Devices and Sensors

Obtaining in situ parameters of a railroad track in operation is extremely relevant in the analysis of mechanical behaviour between the different superstructure and substructure components. According to Manda [15], the instrumentation in the railroad track using known loads allows the quantification of deformations, stresses and displacements. In addition, in order to better understanding the railroad behaviour, such studies are of great importance for improvements in the design of the individual elements (rail, sleepers, ballast, subballast), aiming to increase vehicle traffic safety and transported load capacity.

Concerning the materials that compose the subballast and subgrade, the water dynamics change the state of densification and stresses between the particles, causing changes in bearing capacity. The bearing capacity can be verified, for example, through light weight deflectometer, LWD [12, 13] and dynamic cone penetrometer, DCP [9, 14].

Data provided by such equipment concerning geotechnical materials is essential in the structural evaluation of the railroad track since the forces acting in the vertical direction are the ones that most impact the railroad structure, especially under dynamic loading [7]. They cause high stress levels and, if they are above the resistance of the track components, there is an acceleration of the deterioration of these track elements, which can even lead to rupture (concrete rails and sleepers), degradation (ballast) and permanent deformation (subballast and subgrade).
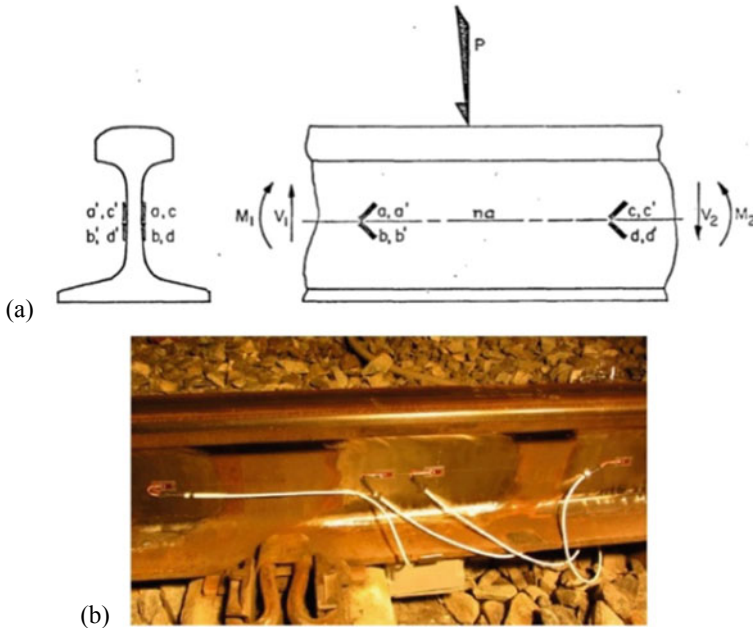
Fig. 1 (**a**) Sketch of the SG arranged on the rail web faces [16] and (**b**) fixed to the rail web [17]

Regarding the vertical load transmission with the dynamic passage of the vehicles, deformations measured from strain gauges (SG) fixed to the rail web [16–18] can be obtained, so the assembled circuit forms a Wheatstone bridge.

Figure 1 (a) and (b) shows, respectively, a sketch of the SG arranged on the faces of the rail web and oriented 45° with respect to their neutral axis [16] and (b) fixed in the rail web of the railroad [17], where the vertical load (P) is calculated by an analytical model [16], considering the (i) strain measurements in the SG, (ii) the difference between the shear forces (V_1 and V_2), and (iii) rail parameters: modulus of elasticity (E), moment of inertia (I), Poisson's ratio (v), rail thickness at neutral axis (t) and static moment of cross-sectional area (Q).

Regarding the efforts transmitted from rail to sleeper, it has been measured [18, 19] through the matrix-based tactile surface sensors (MBTSS) system. It consists of a triad composed of a thin-film pressure sensor and a sensor-attached data acquisition handle and connected via a USB cable to a computer that contains a dedicated software (I-Scan, Tekscan).

Concerning the tensions transmitted by the sleeper to the geotechnical materials, pressure cells have been employed to evaluate vertical and transverse stresses at different depths. Indraratna et al. [20] conducted in situ tests on a 60 m track section containing a ballast thickness of 300 mm and a subballast of 150 mm, divided into four railroad sections of 15 m (composed of recycled ballast; recycled ballast and geocomposite; new ballast and geocomposite and new ballast) in the city of Bulli

(Australia). The results showed vertical and horizontal tensions in the sleeper/ballast interfaces, respectively, close to 300 and 50 kPa (passing trains with 25 tons per axle). Considering the same directions at a depth of 300 mm, they were, respectively, close to 90 and 25 kPa.

In terms of assessing the contribution of the components underlying the rail, one parameter used on several railroads around the world as an indicator of elastic response [8] and rail quality is the track modulus (*u*). It requires the measurement of field displacements for an analysis of a particular railroad. In these, studies conducted in situ [4, 7, 20–30] employed different devices (Multidepth deflectometers—MDD; remoting video monitoring—RVM; laser dynamic deflectometer—LDD; and device for measurements of displacements—DMD) and sensors (linear variable displacement transducers—LVDTs; geophones and laser). It is noteworthy that some studies included the evaluation of displacements within the layers at different depths.

In the case of the subgrade, due to the fact that it serves as an elastic support to the acting stresses of the overlying components, it is of fundamental importance to the railroad track [31], so the soil must present geotechnical properties compatible with weathering actions (deformability, resistance and permeability).

Lu and Likos [32] explain that the variation of soil moisture and suction as a function of climate is a unique feature of unsaturated soils. According to Fredlund and Rahardjo [11] and Marinho [33], several methods have been proposed in order to determine the constitutive relationship between suction and soil moisture. Such methods can be classified as direct and indirect, which vary depending on the type of suction measured the measurement interval and the equilibrium time with the soil. In this case, the granular matrix sensor can be used for in situ evaluations (GMS 200SS) [34], which operates similarly to the porous gypsum block, based on the principle of electrical conductivity [11, 35]. This model was used by Castro [36] to evaluate the influence of geotechnical and climatic conditions on the hydro-mechanical behaviour of a railroad subgrade. After developing a numerical model of unsaturated infiltration and field monitoring, the author found that during the dry season, the suction values increase and, consequently, the subgrade soil present better behaviour.

Cui [37] monitored the variation of suction and water content throughout the seasons through suction sensors (tensiometers) installed on the interlayer (geotechnical layer formed by the mixture between ballast and subgrade soil) of a high-speed rail track. The devices were installed at a depth of 20, 30 and 50 cm, protected both under the track and at its ends. The results showed that the ballast, besides facilitating the presence of water in the subgrade, also hinders its evaporation, maintaining low suction values compared to the outside of the railroad.

3 Methodology

The methodology employed in this study aimed to propose an in situ procedure in order to measure structural and geotechnical aspects of the railroad track components. It was based on the use of sensors in two railroad track sections (rigid and elastic

foundation) of the Carajás Railway (EFC), which is 892 km long and located in the north of Brazil. Tests sections are, located at km 538 + 250 m (Açailândia—Maranhão State) and km 656 + 516 m (São Pedro da Água Branca—Maranhão State). Some characteristics of the EFC railroad are: 1600 mm gauge; TR-68 (RE 136) rail; Pandrol fastenings; concrete sleepers, 610 mm spacing between sleepers; crushed rock ballast of 300 mm thickness and subballast (executed in the 200 mm thickness design phase). Iron ore is the main product in the operations of the EFC railroad, and usually, each train has 330 wagons carrying 314 kN per axle (heavy haul).

In the track sections of this study, the following activities were performed: (i) in situ tests using light weight deflectometer (LWD) and dynamic cone penetrometer (DCP); (ii) strain measurements with strain gauges (SG) attached to the rail web; (iii) installation of matrix-based tactile surface sensors (MBTSS) between rail/pad and sleeper; (iv) installation of cells for measuring vertical stresses between sleeper-ballast (VSB) and ballast-subballast (VBSB); and transversal stresses underlying the sleeper-ballast (TSB) and sleeper edge (TSE); (v) installation of sensors to measure the suction stress; and (vi) measurements of displacements with DMD. It is noteworthy that in the study sections, geotechnical materials were sampled for laboratory characterization in addition to fresh (new) ballast stored in nearby areas.

The in situ characterization of the geotechnical layers of the track was performed using LWD and DCP, respectively, according to ASTM E2583 [38] and ASTM D6951/6951 M [39]. For this, it was performed near the rail/sleeper using the equipment's shown in Fig. 2 (a) LWD and (b) DCP. Regarding the laboratory characterization of the geotechnical materials, AREMA recommendations [40] were considered. Resilient modulus test was performed with the soil from the subgrade in accordance with AASHTO [47] and IPR [48].

(a)   (b)

Fig. 2 Characterization aspects at km 538 + 250 m with (**a**) LWD and (**b**) DCP
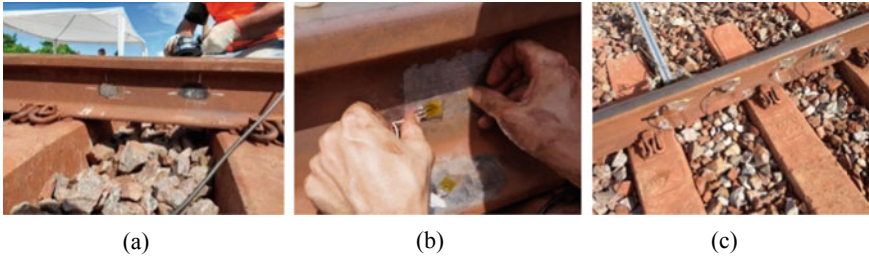
Fig. 3 Aspects of (**a**) preparation of the web rail; (**b**) gluing SG; (**c**) SG fixed between sleepers

3.1 Strain Gauges Installation

Rosette strain gauges (XY41—350 Ω, supplied by HBM) were employed and fixed to the rail web following the authors' recommendations [16–18] in order to measure the deformations and, from them, to calculate the dynamic load (*P*). So, initially it was necessary to sand the rail web, so that the surface was smooth and regular. Then, a template was used for marking the neutral line and fixing the SG. After cleaning the surface with solvent, the SG was fixed with appropriate glue to the rail web [Fig. 3 (a), (b) and (c)]. Regarding the acquisition of signal data, the HBM quantum system was adopted, which allows the use of frequencies above 2000 Hz.

3.2 MBTSS Installation

The stresses at the rail/pad-sleeper interface were measured using the MBTSS (model 5101), which is based on the ink resistivity change as the load is applied, sensitizing the sensels and generating what is called frame. The representation in 2D or 3D of all matrix sensels at a given moment is in Fig. 4. It is noteworthy that the sensor must be calibrated in the laboratory previously for an in situ use.
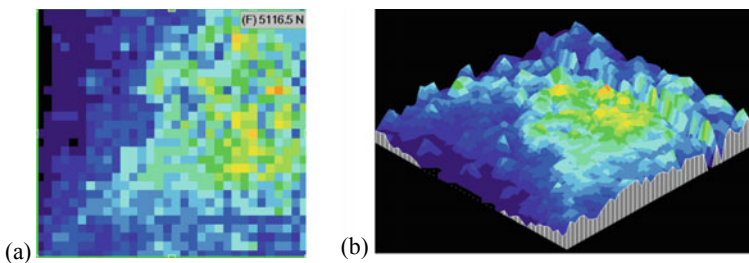
Fig. 4 (**a**) 2D and (**b**) 3D representation of the same frame of a MBTSS
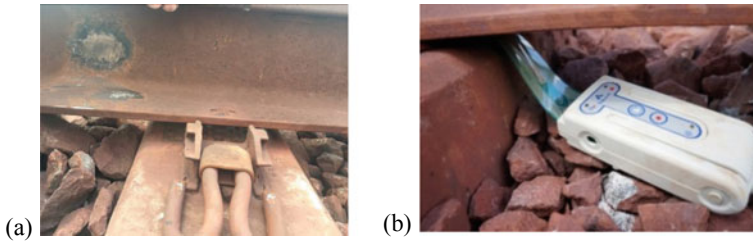
Fig. 5 (**a**) Aspects of the raised rail and (**b**) MBTSS positioned between the rail and top of the sleeper

When installing the sensor on the railroad track sections, it was necessary to remove the fixation of the sleeper and lift the rail a few millimetres with a hydraulic jack, in order to obtain adequate depth and thus the exact position of the MBTSS on the rail/pad-sleeper interface (Fig. 5). Then it was attached to the handle via an USB cable to a computer, thus logging the data through Tekscan's I-Scan software.

3.3 Pressure Cells Installation

The pressure cells used to measure the stresses at the different interfaces (VSB, VBSB, TSB and TSE) were model 3515 (capacities of 100, 250, 600 and 1000 kPa), supplied by Geokon. As previously mentioned, here also it is noteworthy that for in situ use, calibration must be previously performed in the laboratory. Figure 6 shows aspects of pressure cells installed in situ.

3.4 Displacements Measurement

With respect to vertical displacements within the layers, settlement pegs were positioned at the ballast-subballast and sleeper-ballast interfaces, shown, respectively, in Fig. 7 (a) and (b). Regarding to the displacements measured in the web rail, it was recorded through the displacement measuring device (DMD) developed by Costa [30]. It is a metal "arm" which contains at its extremity, linear variable displacement transducers (LVDTs) type sensors that are positioned in the rail base and at a little base connected to the settlement pegs located at different interfaces. The LVDTs, in turn, are connected to an acquisition system (HBM—PMX), which allows adopting frequencies above 2000 Hz of data, recording the displacements with the dynamic passage of vehicles. Figure 8 shows aspects related to DMDs positioned at points A (settlement pegs) and B (reference).
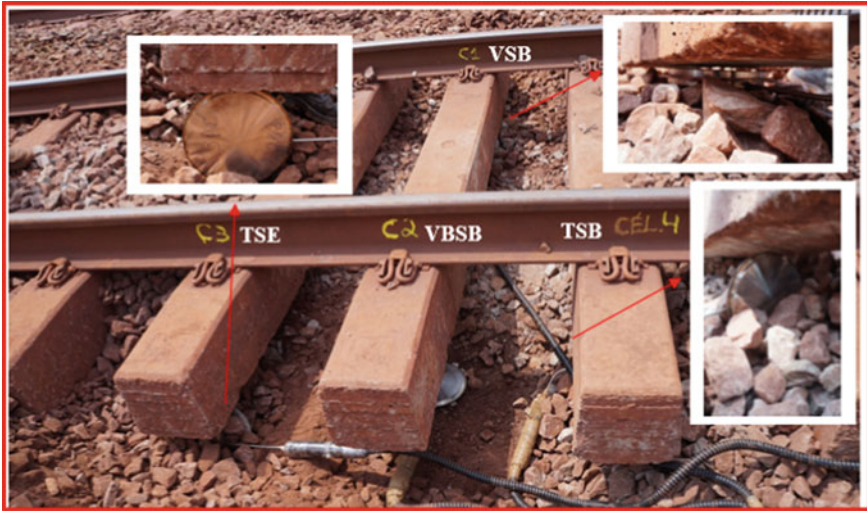
Fig. 6 Pressure cell aspects placed at different interfaces (VSB, VBSB, TSB and TSE)

(a)   (b)
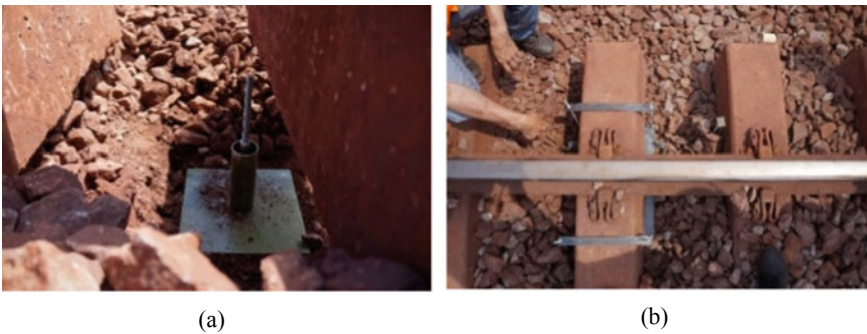
Fig. 7 Settlement pegs positioned at interfaces (**a**) ballast-subballast and (**b**) sleeper-ballast

3.5 Suction Sensor Installation

The measurement of the soil matrix potential (suction stresses) of the railroad track subgrade was performed through installation of 5 Watermark granular matrix sensors (GMS-type) at different depths, under a subballast of approximately 200 mm on average. GMS sensors are connected to a data logger for continuous monitoring of data over time with 2 h interval between each measurement. Figure 9 shows the location of each sensor in depth across the subgrade.
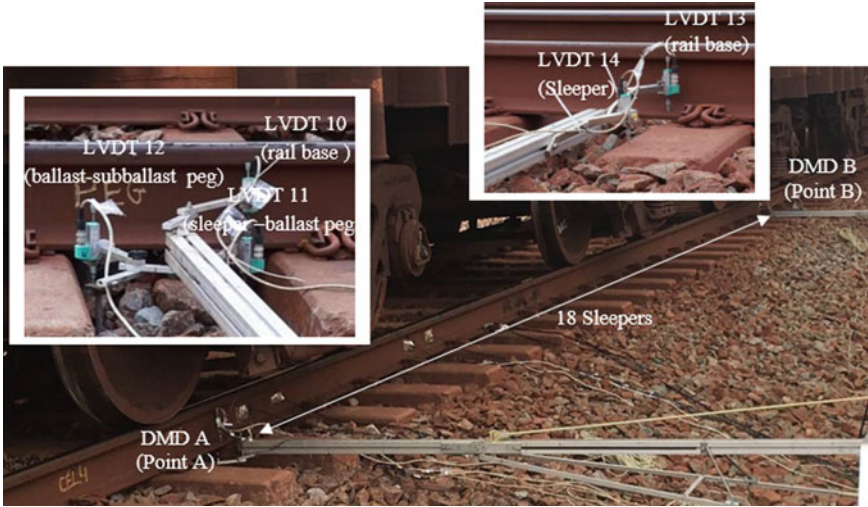
Fig. 8 General aspects of the DMDs positioned in the railroad and LVDTs details
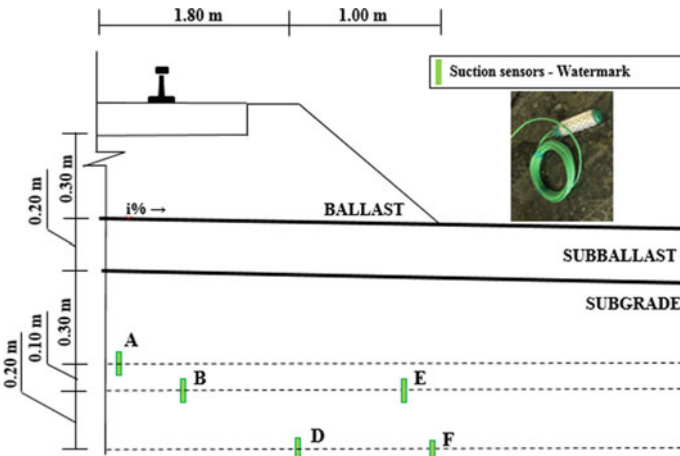
Fig. 9 Location of sensors on subgrade

4 Results and Discussion

4.1 In Situ Characterization

The resistance value measured at km $538 + 250$ m on the surface of the layer through the LWD was 104 MPa, indicative of high stiffness material. It is noteworthy that this parameter could not be obtained in km $656 + 516$ m, due to the presence of
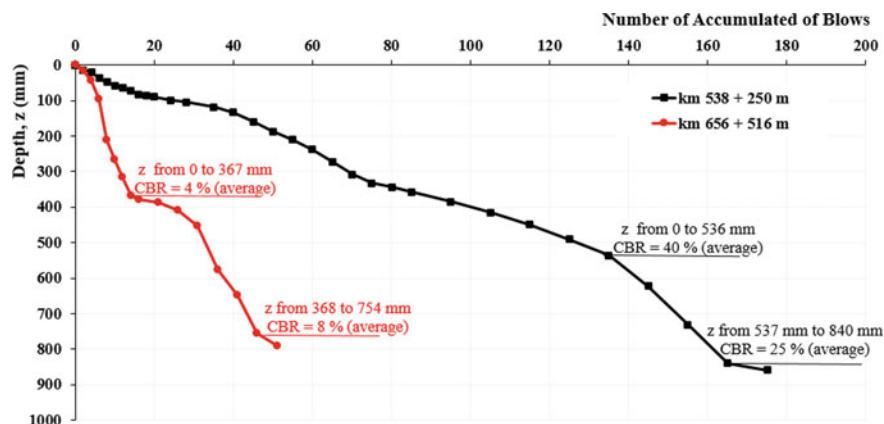
Fig. 10 In situ CBR results through DCP tests in the evaluated segments of EFC

surface water in the layer. The DCP and CBR values were calculated according to the ASTM standard equation results for the two segments evaluated in this study and the results are shown in Fig. 10. In general, it is observed that both segments present significant differences in terms of resistance of the materials underlying the ballast that increase with depth. The results showed good and low bearing capacity, respectively, at $538 + 250$ m (CBR value above project minimum, 20%) and km 656 $+ 516$ m (CBR value below project value).

Additionally, grain size distributions [41] of the ballast material are shown in Fig. 11 and compared to the limits of the AREMA N°. 24 grading [40]. Both track ballasts have been found to have slightly departed from the specification limits, while the fresh (new) ballast is slightly below the lower limit and is prone to uniformity.

Regarding the results of characterization of the material underlying the ballast, it was performed only for km 656 + 516 m, due to the low bearing capacity denoted "in situ". From the particle size distribution [42] and consistency limits [43], the soil classification according to TRB [44] was determined, indicating that it is A-2-6 material (excellent to good subgrade quality). Through the universal soil classification system (SUCS) [45], the classification was SC, denoting that it is a clay sand with gravels. In addition, by means of the expeditious method MCT [46], the classification was LG', showing that in the constituent materials, there are clays and sandy clays. The MCT classification was developed in Brazil addressing tropical soils.

Also, in order to evaluate the mechanical behaviour of the subballast material at different stress levels, resilient modulus test [47, 48] was performed. For this, it was necessary to obtain through the Proctor test [49] in the modified energy, the optimum moisture content ($W = 8.7\%$) and the dry bulk density ($\gamma s = 2.140$ g/cm^3). Figure 12 shows the results of resilient modulus as a function of the deviatoric stresses. As expected, it is observed that the increase of the deviatoric stresses influences the behaviour of the material, in order to decrease its resistance.
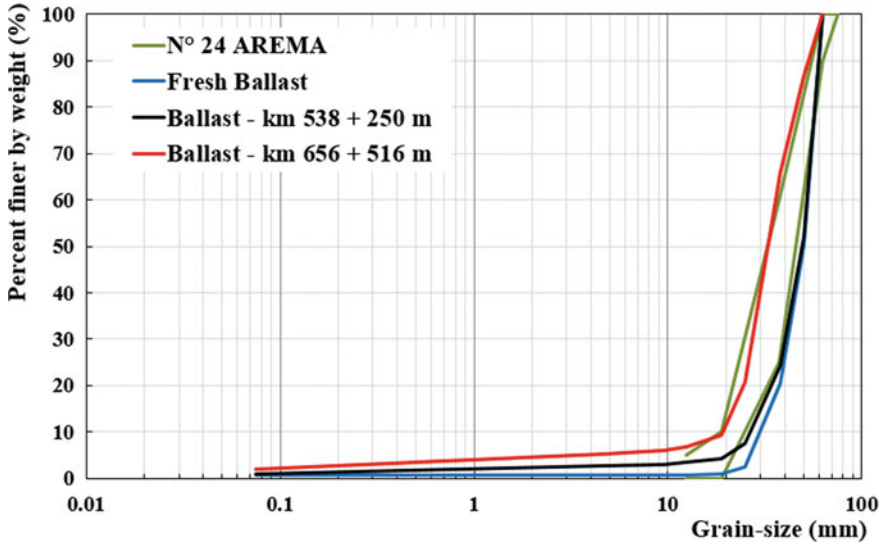
Fig. 11 Grain size distribution results for the sampled ballast
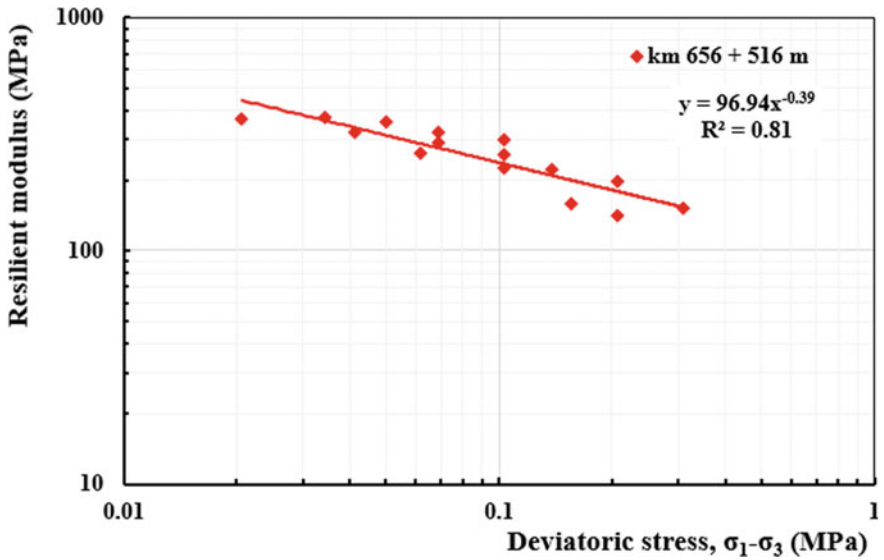
Fig. 12 Resilient modulus results of subballast material

4.2 Measurements Performed by Sensors

Through the SG fixed in the rail web, the deformations in both segments were measured, and through the calculation model mentioned in the item 2 [16], it was possible to determine the dynamic vertical wheel load (P). Signal results obtained in the 538 + 250 m segment with the passing of an empty vehicle (M005—average static wheel load wagons and speed, respectively, 24.5 kN and 65 km/h) and loaded (M818—average static wheel load wagons and speed, respectively, 155.0 kN and 42 km/h) are shown, respectively, in Fig. 13 (a) and (b). From the signals obtained in both trains, it is verified in the case of empty wagon that there is a definition between the peaks generated by the vertical wheel load of the locomotives and wagons, showing that the analytical model used [16] is valid for dynamic load determination (P). Comparing both cases, it was observed that there is a high concentration of points above static whell load, showing increases between 20 and 60% in signal levels in relation to the static load, and few that approach or even exceed 100% of that.

Still in the same railroad track section, considering the loaded wagon (M818), the tensions with the MBTSS on the rail/flexible pad-sleeper interface were recorded (Fig. 14). It is observed that there is a small variation between the maximum values of
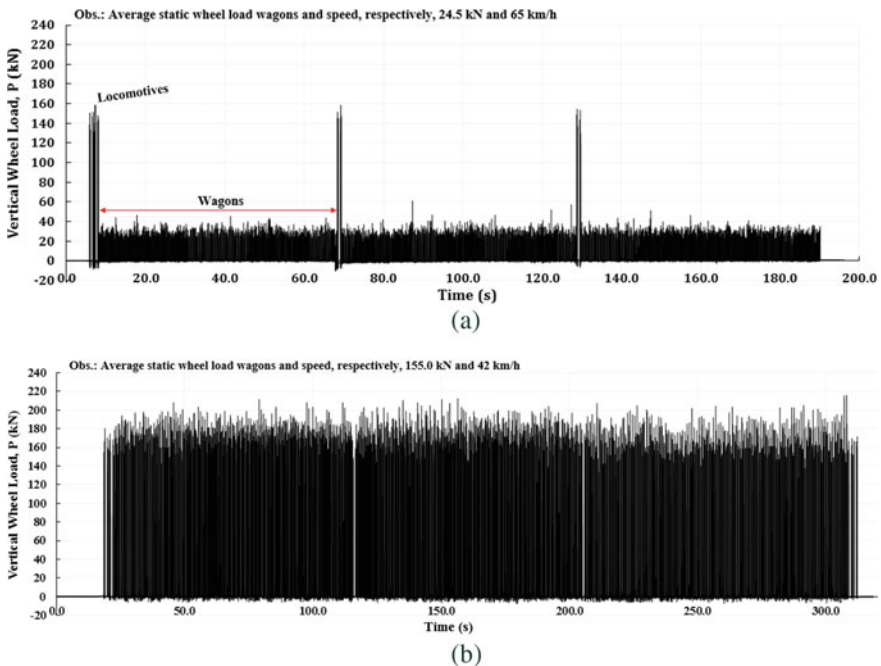
Fig. 13 Full load signal (P) obtained with SG with (a) an empty wagon and (b) a loaded vehicle
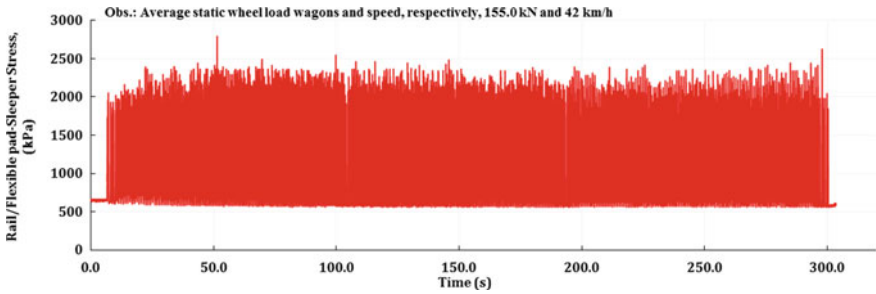
Fig. 14 Signals registered for a loaded vehicle with MBTSS
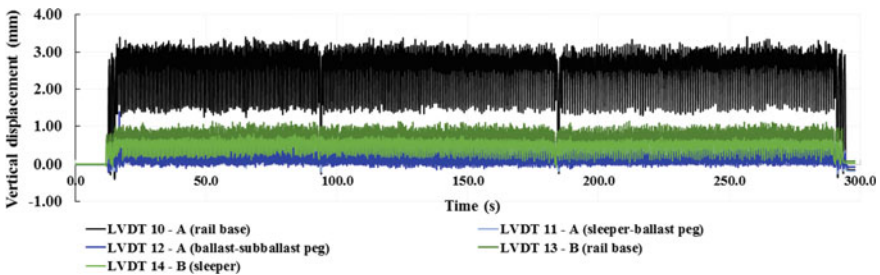
Fig. 15 Signals recorded with LVDTs in the DMDs

tensions measured at the top of the sleeper by the MBTSS with flexible pad (mostly between 2000 and 2500 kPa).

With respect to vertical displacements, considering loaded vehicle (M854 with average static wheel load wagons and speed, respectively, 157.0 kN and 44 km/h) at two points (as Fig. 8), the results were obtained through DMDs (Fig. 15). As previously observed, a slight variation in the maximum amplitude of the basins generated between the axles and trucks was verified. However, an important aspect in these measurements is the difference between the displacements generated in the sensor area (LVDT 10) and the reference (LVDT 13), where the maximum values were, respectively, 3.07 and 0.95 mm in average. This observation was due to the fact that the track structure under the LVDT 10 was disturbed for installation of pressure cells and settlement pegs, differently from the LVDT 13 place, which was not disturbed and so the track structure is presumed to be more consolidated.

In the railroad track section located at km 656 + 516 m, data were also obtained with the same types of sensors presented above. However, due to the low bearing capacity denoted "in situ", it will only be shown in Fig. 16 the results for pressure cells at different interfaces (VSB, VBSB, TSB and TSE) during the passage of the vehicle M706 (average static wheel load of 153.0 kN and 45 km/h). It is observed through the signals of vertical and transversal stresses that there is variation of what is transmitted by each wheel, generating maximum values at the interfaces VSB, VBSB, TSB and TSE, respectively, of 342, 93, 60 and 47 kPa.
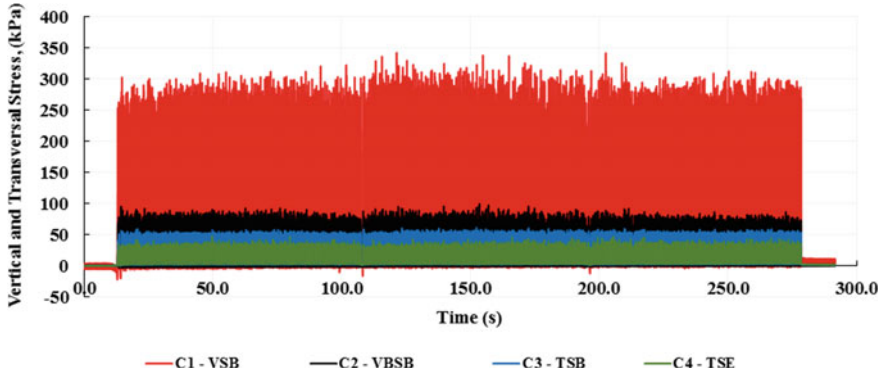
Fig. 16 Signal results from the pressure cells installed
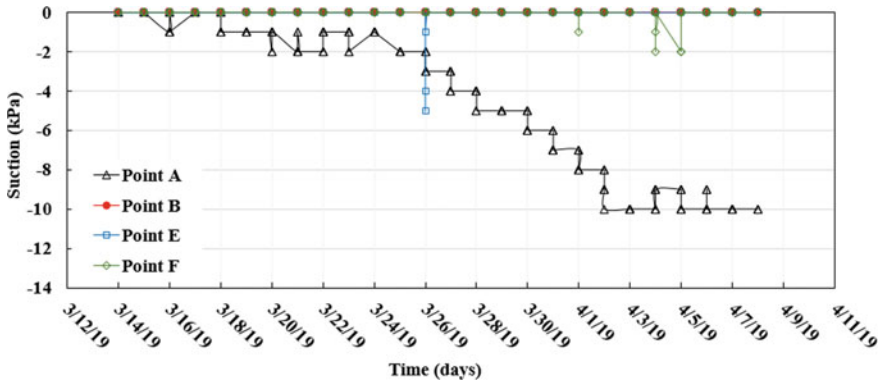
Fig. 17 Signal results of the suction sensors

In the same railroad track section (km 656 + 516 m), suction sensors were installed at different points and depths (A, B, E and F), and the results are shown in Fig. 17. Throughout a month, the suction stresses varied slightly (0–10 kPa), indicating that the materials are under high humidity, close to the saturation condition. However, for a better evaluation of the subgrade quality in terms of water content/suction pressure, it is needed to have more data, especially in different seasons where the variation on precipitation/evaporation could provide significant differences on that parameters and consequently to the mechanical behaviour of the platform.

5 Conclusions

The analytical model adopted for rail deformation using SG based on the literature for dynamic load calculation (P) can be evaluated by the passage of loaded and

empty wagons. The results of these compared to the static wheel load showed that there were significant increases in the load factor, showing that the analytical model is valid for load determination with the passing of vehicles.

MBTSS sensors showed a very little variation over time considering flexible pad while pressure cells revealed vertical stresses in the interface ballast-subballast of about 25% of that one in sleeper-ballast interface. On the other hand, horizontal stresses in the interface sleeper edge-ballast were found of about 60% of that one in sleeper-ballast interface.

Concerning to railroad displacements, there is a clear influence of material condition in terms of densification. Displacements in the undisturbed region were about 30% lower than the one on the disturbed track structure location.

Results from suction stresses varied slightly over a month period, indicating that the material is under a hydraulic condition very near to saturation. This corroborated with the in situ tests results (LWD and DCP) that showed a subgrade with low bearing capacity.

The signals recorded in all sensors (SG, MBTSS, LVDT, pressure cells and suction sensors), considering different foundations, were compatible with those presented in other studies.

The proposed in situ procedure using sensors is valid for the measurement of structural and geotechnical aspects in a heavy haul railroad track, considering the dynamic passage of loaded and empty vehicles.

In order to contribute for a better understanding of the railroad acting forces and, consequently of the general mechanical behaviour of the track, laboratory evaluations through triaxial tests on geotechnical materials, controls during construction and maintenance phase should be implemented.

References

1. Doyle NF (1980) Railway track design: a review of current practice. Occasional Paper No. 35, Bureau of Transport Economics, Commonwealth of Australia, Canberra
2. Profillidis VA (2006) Railway management and engineering. Third edn. Ashgate Publishing Limited
3. Pires J (2016) Integrated maintenance model for heavy haul tracks. École Polytechnique Fédérale de Lausanne, Switzerland, 189 p
4. Read D, Chrismer S, Ebersohn W, Selig E (1994) Track modulus measurements at the Pueblo soft subgrade site. Transportation research record 1470. Washington, D. C., p. 55–64. 1994
5. Esveld C (2001) Modern railway track, v. 2. Delft University of Technology, ZaltBommel, Netherlands, 632 pp
6. Lichtberger B (2005) Track compendium: formation maintenance. Econ Eurailpress Permanent Way 3-7771-0320-9, 374p
7. Selig ET, Waters JM (1994) Track geotechnology and substructures management. Thomas Telford Services Ltd., London, p 446p

8. Selig ET, Li D (1994) Track modulus: its meaning and factors influencing it. Transportation Research BoaRD 1470. Washington, D. C., pp 47–54
9. Li D, Hyslip J, Sussmann T, Chrismer S (2016) Railway geotechnics. CRC Press, Taylor & Francis Group, Boca Raton, FL, USA, p 584
10. Tutumluer E, Qian Y, Hashash YMA, Ghaboussi J, Davis D (2011) Field validated discrete element model for railroad ballast. In: Proceedings of AREMA annual conference. Minneapolis, Minnesota
11. Fredlund DG, Rahardjo H (1993) Soil mechanics for unsaturated soils. Wiley
12. Nazzal HD, Abu-Farkash MY, Khalid A, Mohamad L (2007) Evaluating the light falling weight deflectometer device for in situ measurement of elastic modulus of pavement layers. Trans Res Board 2016:13–22
13. Costa RC, Motta RS, Bernucci LLB, Moura E, Oliveira Filho JAP (2017) Bearing capacity evaluation of a subgrade in a heavy haul railway in Brazil. In: Proceedings of the 10th international conference on the bearing capacity of roads, Railways and Airfields (BCRRA 2017), June 28–30. Taylor & Francis Group, Athens, Greece, London. https://doi.org/10.1201/978131 5100333-280
14. Fortunato E, Pinelo A, Fernandes MM (2009) In situ characterization of an old railway platform with DCP. In: Proceedings of the 17th international conference on soil mechanics and geotechnical engineering
15. Manda KR (2014) Understanding the vertical load path under static and dynamic in concrete crosstie and fastening systems. University of Illinois at Urbana-Champaign, Urbana, Illinois, 62 pp
16. Ahlbeck DR, Johnson MR, Harrison HD, Prause RH (1976) Pilot study for the characterization and reduction of wheel/rail loads—field measurement and data reduction plan. U. S. Department of Transportation Federal Railroad Administration, Washington, D. C., 49 pp
17. Mishra D, Tutumluer E, Boler H, Hyslip JP, Sussman T, (2014) Instrumentation and performance monitoring of railroad track transitionsusing multidepth deflectometers and strain gauges. In: 93rd annual meeting of the transportation research board. Washington, D.C
18. Wei S (2017) Determination of load path through concrete crosstie and fastening system: a laboratory and field investigation. University of Illinois at Urbana-Champaign, Urbana, Illinois, 304 pp
19. Rose J, Stith J (2005) Pressure measurement in railraod trackbeds at the rail/tie interface using Tekscan sensors. University of Kentucky, Lexington, KY
20. Indraratna B, Salim W, Rujikiatkamjorn C (2011) Advanced rail geotechnology-ballasted. Taylor & Francis Group, London, UK
21. American Railway Engineering Association—AREA (1918) First progress report of the special committee on stresses in railroad track. Bull American Railway Eng Associat 19:875–1058
22. Kerr AD (1983) A method for determining the track modulus using a locomotive or car on multi-axle trucks. Bull American Railway Eng Associat 692 84:269–286
23. Gräbe PJ, Clayton CR, Shaw FJ (2005) Deformation measurement on a heavy haul track formation. In: Proceedings of the 8th international heavy haul conference. IHHA, Rio de Janeiro, pp 287–295
24. Silva FCM, Paiva CEL, Aguiar PR (2007) Evaluation of track/ballast behavior under increased axle load: measuring deflections on track. In: Proceedings of the international heavy haul conference. Specialist Technical Session. Kiruna. IHHA, Sweden, pp 31–38
25. Anderson JS, Rose JG (2008) In-situ test measurement techniques within railway track structures. In: IEEE/ASME/ASCE 2008 joint rail conference. Delaware, USA pp 187–207
26. Priest AJ, Powrie EW (2009) Determination of dynamic track modulus from measurement of track velocity during train passage. ASCE J Geotech Geoenviron Eng San Diego 135(11):1547–1778
27. Zakeri AJ, Abbasi R (2012) Field investigation on variation of rail modulus in ballasted railway tracks. Latin American J Solids Struct 9:643–656
28. Vorster DJ, Gräbe PJ (2013) The effect of axle load on track and foundation resilient deformation under heavy haul conditions. In: Proceedings of the 10th international heavy haul and innovation developments. IHHA, New Delhi, India

29. Nimbalkar S, Indraratna B (2016) Improved performance of ballasted rail track using geosynthetics and rubber shockmat. J Geotech Geoenviron Eng 142(8):04016031
30. Costa R, Motta RS, Moura , Oliveira Filho JAP, Bernucci LLB (2017) Measuring device for in situ determination of the track modulus in a heavy haul track. In: Proceedings of the 11th international heavy haul conference: advancing heavy haul technologies and operations in a changing world. Cape Town, South Africa
31. Hay WW (1982) Railroad engineering. Wiley
32. Lu N, Likos W (2004) Unsaturated soil mechanics, vol 19
33. Marinho FAM (1997) Medição de Sucção em Solos. In: Simpósio Brasileiro de Solos Não Saturados, 3, Rio de Janeiro, 373–397. [in Portuguese]
34. Irrometer Company website. http://www.irrometer.com/, acesso em 10/04/2018
35. Shock C, Barnum J, Seddigh M (1998) Calibration of watermark soil moisture sensors for irrigation management. In: Proceedings of the 1998 irrigation association conference on international irrigation show, pp 139–146
36. Castro GB (2019) Avaliação da Influência das Condições Geoténicas e Climáticas no Comportamento Hidromecânico de um Subleito Ferroviário. Master Dissertation. Escola Politécnica da Universidade de São Paulo. São Paulo. [in Portuguese]
37. Cui YJ (2016) Unsaturated railway track-bed materials. E3S Web of Conferences, v. 9, p 1001
38. ASTM. Standard test method for measuring deflections with a light weight Deflectometer (LWD), E2583—07 (Reapproved 2015)
39. ASTM. Standard test method for use of the dynamic cone penetrometer in shallow pavement applications, ASTM. D6951/D6951M—18
40. AREMA. American railway engineering and maintenance-of-way association. Manual Railway Eng (1–4):1-2-12
41. ASTM. Standard test methods for sieve analysis of fine and coarse aggregates, ASTM C136–06
42. ASTM. Standard test methods for particle-size distribution (gradation) of soils using sieve analysis ASTM 6913–04
43. ASTM. Standard methods for liquid limit, plastic limit, and plasticity index of soils, ASTM D4318–10
44. ASTM. Standard practice for classification of soils and soil-aggregate mixtures for highway construction purposes. ASTM D3282–15
45. ASTM. Standard practice for classification of sils for engineering purposes (unified soil classification system) ASTM D2487–11
46. Nogami J, Villibor D (1981) Um Novo Sistema de Classificação de Solos para Rodovias. In: Simpósio Brasileiro de Solos Tropicais em Engenharia, COPPE UFRJ, pp. 30–41. Rio de Janeiro BRA. [in Portuguese]
47. American Association of State Highway and Transportation Officials (AASHTO) (1999) T 307-99–Determining the Resilient Modulus of Soils and Aggregate Materials, USA. 37p
48. IPR. DNIT 134/2010—ME. 2010. Pavimentação—Solos—Determinação do Módulo de Resiliência—Método de Ensaio. Instituto de Pesquisas Rodoviárias—IPR, 1–11. [in Portuguese]
49. ASTM. Standard test methods for laboratory compaction characteristics of soil using standard effort. ASMT D698–12 (2012)

Evaluation Method of Deformation Modulus of Subgrade Soils Considering Drainage Condition

Hiroaki Wakatsuki, Yukihiro Kohata, Daisuke Tamayama, and Toshiyuki Mitachi

Abstract In order to improve the accuracy of pavement structural design, we examined a method to accurately estimate the deformation modulus of subgrade soils. When designing the pavement structure by the theoretical design method, if the deformation modulus of the subgrade can be accurately estimated, pavement structure thicknesses can be determined reasonably with a limited budget. For this purpose, we developed a new testing method "CTX-BE test" by combining the method of cyclic triaxial test (standardized by Japanese Geotechnical Society [JGS0542]) with that of bender element test ([JGS0544]). In this study, a series of CTX-BE tests were conducted on Toyoura sand to investigate the method of setting the deformation modulus E and Poisson's ratio v necessary for pavement structural analysis. The CTX-BE test was performed under undrained and drained conditions, and the shear wave velocity V_s was measured by bender element transducers after the change of effective stress with stepwise cyclic triaxial loading. Based on a series of test results, we proposed a new method for evaluating the deformation modulus and Poisson's ratio required for pavement structural design in consideration of drainage conditions of subgrade.

Keywords Subgrade soil · Drainage condition · Deformation modulus · Poisson's ratio · Cyclic triaxial test · Bender element test

H. Wakatsuki (✉) · D. Tamayama · T. Mitachi
Chiba Engineering Co. Ltd, Chiba, Japan
e-mail: h_wakatsuki@chiba-eng.co.jp

D. Tamayama
e-mail: d_tamayama@chiba-eng.co.jp

T. Mitachi
e-mail: mitachi@eng.hokudai.ac.jp

Y. Kohata
Muroran Institute of Technology, Muroran, Hokkaido, Japan
e-mail: kohata@mmm.murotan-it.ac.jp

761

1 Introduction

Resilient modulus (Mr) is usually used as a design value of the deformation modulus in the limit state design method with performance checking for pavement. Mr represents the deformation characteristics of the subgrade material, etc. and is measured assuming the effects of wheel load, etc. It has been known that Mr shows stress level and strain level dependency. According to the AASHTO T307 testing standard [1], resilient modulus test (hereafter, abbreviated as "Mr test") is conducted using unsaturated specimens and specimens are not consolidated, and stress loading is performed under undrained condition. Therefore, it is difficult to set up a material model that considers drainage conditions from the results of Mr test. In the case of using natural ground as a subgrade soil due to the restriction of the road formation, there are cases where drainage conditions should be considered in setting the material model for the pavement structure design because of the physical properties and sedimentary environment. An example of this is a road constructed on reclaimed land with a high groundwater level due to the restriction of location conditions. The subgrade may be submerged at airports built in coastal areas and container yards of port facilities. In addition, the moving speed of aircrafts and container handling heavy equipment is considerably low. In these circumstances, the subgrade deforms under the condition that drainage is allowed from the submerged subgrade. Therefore, if the deformation modulus of the subgrade considering drainage conditions can be accurately understood, it is considered that the pavement structure can be determined reasonably with a limited budget.

For this purpose, as an attempt to integrate pavement engineering with geotechnical engineering, a new testing method "CTX-BE test" is proposed in this study by combining the method of cyclic triaxial test standardized by Japanese Geotechnical Society (JGS 0542–2009 [2]) with that of bender element test (JGS 0944–2011 [3]). Then a series of CTX-BE test was conducted on Toyoura sand to investigate the method of setting the deformation modulus E and Poisson's ratio v necessary for pavement structure analysis. Toyoura sand which has been widely used in the previous studies was used in the test program, specimens of which were prepared as the relative density $D_r = 20\%$, 50%, and 80%. The CTX-BE test was performed under undrained and drained conditions, and the shear wave velocity V_s was measured by bender element after the change of effective stress with stepwise cyclic triaxial loading. Then the shear modulus G versus mean effective stress $\sigma_m{'}$ relationship was obtained. Based on a series of test results, we proposed a new setting method for evaluating the deformation modulus and Poisson's ratio required for pavement structural design in consideration of drainage conditions of subgrade.

2 Deformation Moduli of Undrained and Drained Conditions Based on Isotropic Elasticity

In order to examine the method of setting the design value of deformation moduli considering drainage conditions, the relationship among the elastic moduli under undrained and drained conditions was confirmed. Assuming that the soil specimen is an isotropic elastic body, the axial strain increment $\Delta\varepsilon_a$ and the lateral strain increment $\Delta\varepsilon_r$ in the axially symmetric triaxial compression test using the cylindrical specimen are expressed by Eqs. (1) and (2) with the axial effective stress increment $\Delta\sigma_a$', the lateral effective stress increment $\Delta\sigma_r$', Young's modulus E and Poisson's ratio ν.

$$\Delta\varepsilon_a = (\Delta\sigma_a' - 2\nu \cdot \Delta\sigma_r')/E \tag{1}$$

$$\Delta\varepsilon_r = \left\{(1 - \nu)\Delta\sigma_r' - \nu \cdot \Delta\sigma_a'\right\}/E \tag{2}$$

The relationship among the shear modulus G, Young's modulus E and Poisson's ratio ν is as shown in Eq. (3) with the maximum shear stress increment $\Delta\tau_{max}$ and the maximum shear strain increment $\Delta\gamma_{max}$.

$$G = \Delta\tau\,max\,/\Delta\gamma\,max = (\Delta\sigma_a' - \Delta\sigma_r')/2/(\Delta\varepsilon_a - \Delta\varepsilon_r)$$
$$= \left\{(\Delta\sigma_a' - \Delta\sigma_r')/2\right\}/\left\{(\Delta\sigma_a' - \Delta\sigma_r')(1 + \nu)/E\right\} = E/2(1 + \nu) \tag{3}$$

Young's Modulus E_u and Poisson's Ratio ν_u of Saturated Specimen under Undrained Condition. In the case of the triaxial compression test under undrained condition, $\nu_u = 0.5$ is obtained from Eqs. (1) and (2) since $\Delta\varepsilon_a + 2\Delta\varepsilon_r = 0$. Substitution of $\nu_u = 0.5$ into Eq. (1) gives Young's modulus E_u under undrained condition as in Eq. (4), and by substituting $\nu_u = 0.5$ into Eq. (3), undrained Young's modulus E_u versus shear modulus G relationship can be expressed by Eq. (5).

$$E_u = (\Delta\sigma_a' - \Delta\sigma_r')/\Delta\varepsilon_a = (\Delta\sigma_a - \Delta\sigma_r)/\Delta\varepsilon_a \tag{4}$$

$$G = E_u/3 \tag{5}$$

where $\Delta\sigma_a$ and $\Delta\sigma_r$ are axial total stress increment and lateral total stress increment, respectively.

Drained Young's Modulus E_d and Poisson's Ratio ν_d. Since $\Delta\sigma_a' = \Delta\sigma_a$ and $\Delta\sigma_r' = \Delta\sigma_r$ in drained condition, Young's modulus E_d for drained triaxial compression test under constant lateral stress is expressed by Eq. (6). As shown theoretically by Wood [4] and experimentally by Toki et al. [5], the shear modulus G is not dependent on the drainage conditions, and the following Eq. (7) is obtained based on Eq. (3).

$$E_d = \Delta\sigma_a / \Delta\varepsilon_a \tag{6}$$

$$G = E_u/2(1 + v_u) = E_d/2(1 + v_d) \tag{7}$$

Substituting $v_u = 0.5$ into Eq. (7), drained Poisson's ratio v_d can be expressed by Eq. (8) using E_d and E_u, and Eq. (9) is obtained from the Eq. (7).

$$vd = (3/2) \cdot (Ed/Eu) - 1 \tag{8}$$

$$Ed = 2G(1 + vd) \tag{9}$$

3 Measurement of Deformation Moduli by CTX-BE Test

3.1 Outline of CTX-BE Test

As mentioned previously in Chapter 1, CTX-BE test is composed of CTX test, which gives deformation modulus E, and BE test, which gives shear modulus G. Basic measurement procedure for the CTX-BE test is based on the JGS standard of CTX test, in which elastic shear wave velocity measurement (BE test) is performed during a cyclic stress loading stage (14 stages/sample) with a bender element inserted in advance at both ends of the specimen. The bender element is a vibrator that deforms when a voltage is applied, and its dimensions are 10 mm width and 0.5 mm thickness. It is coated with epoxy resin for insulation and waterproofing, and the dimensions, including the coating are 11 mm width and 1.5 mm thickness. These were attached to the upper and lower end surface of the specimen in the same direction. The length of insertion into the specimen was about 4 mm at both the upper and lower ends. The shear wave velocity can be measured by transmitting the shear wave at the upper end of the specimen and receiving the shear wave propagating at the lower end. Figure 1 shows the BE measurement system diagram.

Before inserting the bender element into the upper and lower end surfaces of the specimen, a groove slightly smaller than the thickness of the bender element was dug to reduce the influence of disturbance on the fabricated specimen. The shear wave velocity V_s is measured at a total of five times during a CTX-BE test for each sample: (a) Measurement of the initial V_s before first stage cyclic loading, (b) V_s measurement after any three stages in the middle of cyclic loading and (c) V_s measurement after the last stage cyclic loading. From these five measurement results of V_s, the shear modulus G is calculated by using Eq. (10) with the wet density ρ_t (g/cm^3) of the specimen.

$$G = \rho t \times V_s^2 \tag{10}$$

Fig. 1 BE measurement system diagram (Quoted from Japanese Geotechnical Society Standard: JGS0544)
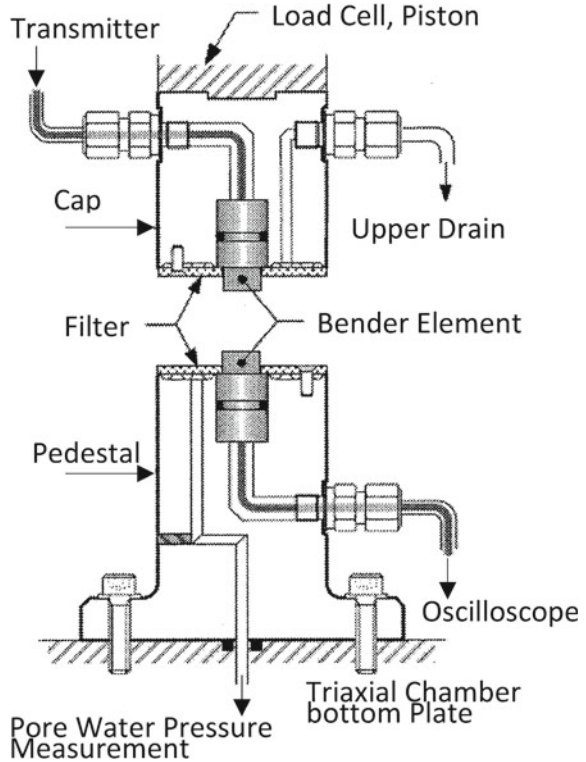
The drainage conditions during the CTXU-D and CTXD-D tests are explained below.

Undrained Condition, CTXU-D. Cyclic loading during a loading stage is performed under the undrained condition, and drainage is permitted in the intervals of the next loading stage. The drainage procedure is as follows: (a) After consolidation of the specimen, initial cyclic loading is performed under undrained condition with pore water pressure measurement, (b) drain valve is opened before next stage cyclic loading, (c) close the valve after confirming the rate of change in axial strain during drainage process, (d) undrained cyclic loading of the next stage is conducted, (e) repeat the procedure (b) to (d) until the last 14th stage.

Drained Condition, CTXD-D. CTXD-D is carried out with the drain valve open during the entire test.

Table 1 Differences between CTX test and Mr test

Test conditions	CTX test	Mr test
Cyclic loading waveform	Sine wave or Triangular wave	Haversine wave
Operation of consolidation before cyclic loading	Consolidated	Unconsolidated
Drainage conditions during cyclic loading	Drained or Undrained	Undrained

3.2 Comparison of CTX-BE Test with Mr Test

The main differences between the CTX test and the Mr test for determining the deformation modulus are the cyclic loading waveform, the operation of consolidation before cyclic loading, and the drainage conditions during cyclic loading, as shown in Table 1. As for the Mr test, it has been reported by Abe et al. [6] that the loading waveform by the haversine wave is compatible with the field condition, but the loading is limited to undrained conditions, and the strength and rigidity are remarkably reduced due to cyclic loading and it becomes to be a tough condition for the subgrade soils. Furthermore, if the test specimen is made incomplete contact with the cap and pedestal of the testing apparatus, the deformation modulus will be underestimated due to the bedding error effect as pointed out by Tatsuoka et al. [7]. Since the specimen of Mr test is not consolidated before loading, the degree of contact between the specimen and the cap and pedestal is lower than that in the CTX test, and more remarkable bedding error will be appeared. On the other hand, drained or undrained condition can be selected at the time of loading on the CTX test, and the measurement, considering the drainage conditions is possible, so that a highly accurate result can be obtained for the measurement of deformation modulus of subgrade soil. In addition, in the case study by Sugano et al. [8] in which the runway ground stiffness was evaluated using the BE test, a unique relationship between G and mean effective stress was suggested. Therefore, in this study, we conducted various CTX-BE test which is combining CTX test with the BE test in order to achieve the "elucidation of dependence of G on effective stress" and "acquisition of measured values considering the difference in drainage conditions." We considered that the design value according to the field conditions could be obtained reasonably through the practice of CTX-BE tests.

4 Index Properties of Sample and Test Conditions of CTX-BE Test

In order to evaluate the deformation moduli from the measurement data obtained by the CTX-BE test, the following laboratory tests and specimen conditions were set. Toyoura sand was used for a series of CTX-BE test in this study. The reason for this is that it is easy to handle because there is little variation in physical indices, and it

Table 2 Physical indices of Toyoura sand

Physical indices	Measured value
Density of soil particles, ρ_s (g/cm^3)	2.654
Average grain diameter, D_{50} (mm)	0.168
Minimum dry density, $\rho_{d\min}$ (g/cm^3)	1.363
Maximum dry density, $\rho_{d\max}$ (g/cm^3)	1.658
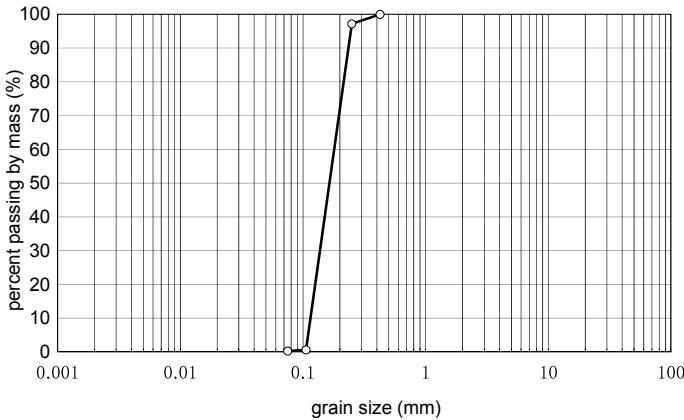
Fig. 2 Grain size accumulation curve of Toyoura sand

is convenient for comparison and examination of the results that the sand has been used in various experiments.

Test Sample and Physical Indices. Toyoura sand is a purchased material, and physical indices are as shown in Table 2 and Fig. 2.

Density Condition of Specimen. The specimens were prepared so that the relative density $Dr = 20\%$, 50%, and 80%, respectively, for the test series under undrained condition (CTXU-D) and drained condition (CTXD-D).

Preparation of Specimen. Specimens were produced by a method of statically compacting Toyoura sand in the mold. At this time, the specimen (volume $V \fallingdotseq 196.3$ cm^3, dimension φ5 cm × H10 cm) is divided into three layers, upper, middle, and lower, so that the variation in density in the specimen will be minimized.

Consolidation Stress of the Specimen. The consolidation stress σ_c' of the specimen was set of 3 cases of 100 kPa, 200 kPa, and 400 kPa.

5   Test Results

Table 3 shows a list of the deformation moduli obtained from a series of CTX-BE tests under undrained and drained conditions that are used to study the design value setting method.

CTXU-D test Results. The relationship between the shear modulus G and the mean effective stress σ_m' that changes at each stage of cyclic loading was obtained, considering sum of the principal stresses of the Mr model [9] (Mr $= k_1\theta^{k2}$, where k_1 and k_2 are regression constants, $\theta = \sigma_1 + \sigma_2 + \sigma_3$, σ_1: vertical stress, σ_2 and σ_3: horizontal stresses), since sandy soil (Toyoura sand) was used in this study.

From the results of BE test, $(G_{u0})_{BE}$ versus σ_m' and $(G_u)_{BE}$ versus σ_m' relationships (where, $(G_{u0})_{BE}$ is the measured shear modulus value G before cyclic loading, $(G_u)_{BE}$ is that after cyclic loading of each stage, respectively) are shown as Figs.3, 4 and 5. In calculating σ_m' in above relationships, the excess pore water pressure Δu of the specimen and the deviator stress σ_d remaining immediately before the BE test after cyclic loading of the CTX test were considered.

CTXD-D test Results and Setting Procedure of Design Values of Deformation Modulus E_d and Poisson's Ratio ν_d. Figure 6 shows how to set design values of deformation moduli for drained condition. First, substituting $(E_{u0})_{CTX}$ and $(E_{d0})_{CTX}$ obtained in the CTX test under undrained condition (CTXU-D) and drained condition (CTXD-D), respectively into Eq. (8), drained Poisson's ratio ν_d corresponding to

Table 3 List of the deformation moduli obtained from a series of CTX-BE test

Test conditions		Deformation moduli
CTXU-D	CTX test	$(E_{u0})_{CTX}$
	BE test	$(G_{u0})_{BE}$, $(G_u)_{BE}$
CTXD-D	CTX test	$(E_{d0})_{CTX}$
	BE test	$(G_{d0})_{BE}$

Fig. 3 $(G_{u0})_{BE}$ versus σ_m' and $(G_u)_{BE}$ versus σ_m' relationships obtained by CTX-BE tests ($D_r = 20\%$)
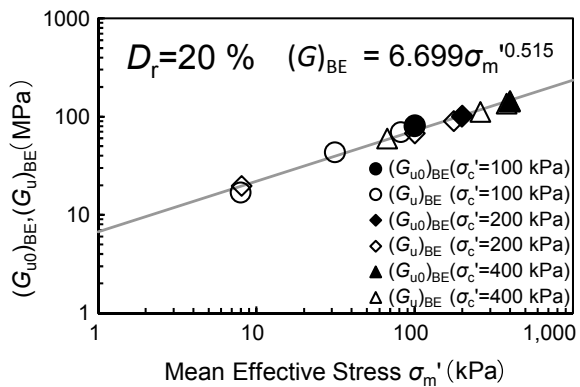
Fig. 4 $(G_{u0})_{BE}$ versus σ_m' and $(G_u)_{BE}$ versus σ_m' relationships obtained by CTX-BE tests ($D_r = 50\%$)
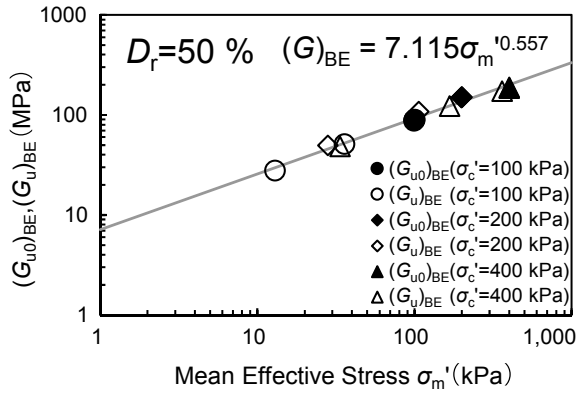
$D_r = 50\%$ $(G)_{BE} = 7.115\sigma_m'^{0.557}$

- ● $(G_{u0})_{BE}(\sigma_c'=100\ kPa)$
- ○ $(G_u)_{BE}\ (\sigma_c'=100\ kPa)$
- ◆ $(G_{u0})_{BE}(\sigma_c'=200\ kPa)$
- ◇ $(G_u)_{BE}\ (\sigma_c'=200\ kPa)$
- ▲ $(G_{u0})_{BE}(\sigma_c'=400\ kPa)$
- △ $(G_u)_{BE}\ (\sigma_c'=400\ kPa)$

Fig. 5 $(G_{u0})_{BE}$ versus σ_m' and $(G_u)_{BE}$ versus σ_m' relationships obtained by CTX-BE tests ($D_r = 80\%$)

$Dr = 80\%$ $(G)_{BE} = 11.027\sigma_m'^{0.514}$

- ● $(G_{u0})_{BE}(\sigma_c'=100\ kPa)$
- ○ $(G_u)_{BE}\ (\sigma_c'=100\ kPa)$
- ◆ $(G_{u0})_{BE}(\sigma_c'=200\ kPa)$
- ◇ $(G_u)_{BE}\ (\sigma_c'=200\ kPa)$
- ▲ $(G_{u0})_{BE}(\sigma_c'=400\ kPa)$
- △ $(G_u)_{BE}\ (\sigma_c'=400\ kPa)$
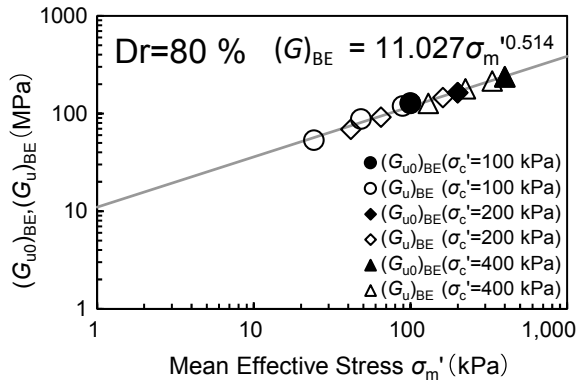
Fig. 6 Procedure for obtaining design values of deformation modulus E_d and Poisson's ratio ν_d
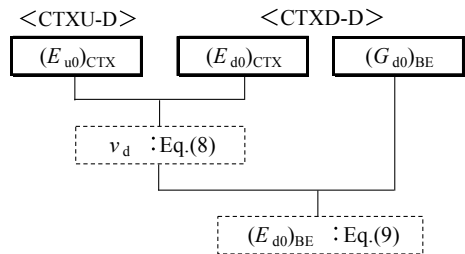
three cases of consolidation stress σ_c' are obtained. Subsequently, these values of ν_d and $(G_{d0})_{BE}$ values obtained by the BE test of CTXD-D are substituted into Eq. (9), then the relationship between the drained deformation modulus $(E_{d0})_{BE}$ and the effective confining stress σ_c' is obtained. $(E_{d0})_{BE}$ versus σ_c' and ν_d versus σ_c' relationships obtained by the procedure explained above are shown in Figs.7, 8 and 9.

Fig. 7 $(E_{d0})_B E$ versus $\sigma_c{}'$ and ν_d versus $\sigma_c{}'$ relationships obtained by the procedure illustrated in Fig. 6 with a series of CTX-BE tests ($D_r = 20\%$)
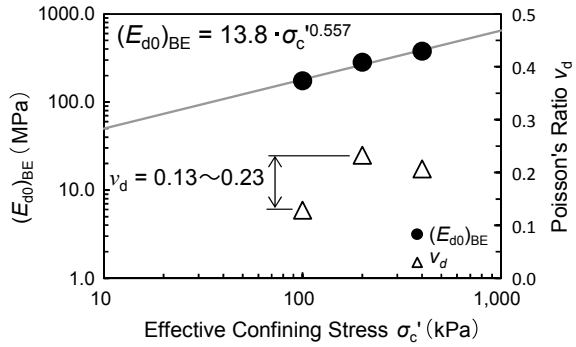
Fig. 8 $(E_{d0})_{BE}$ versus $\sigma_c{}'$ and ν_d versus $\sigma_c{}'$ relationships obtained by the procedure illustrated in Fig. 6 with a series of CTX-BE tests ($D_r = 50\%$)
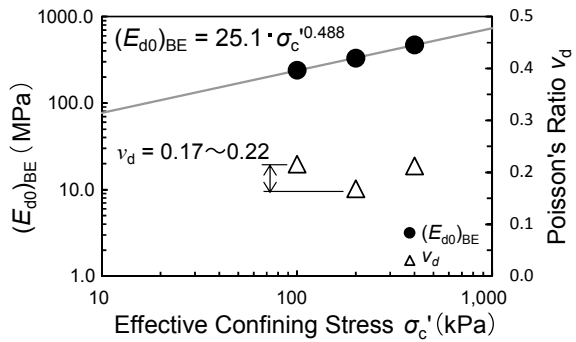
Fig. 9 $(E_{d0})_{BE}$ versus $\sigma_c{}'$ and ν_d versus $\sigma_c{}'$ relationships obtained by the procedure illustrated in Fig. 6 with a series of CTX-BE tests ($D_r = 80\%$)
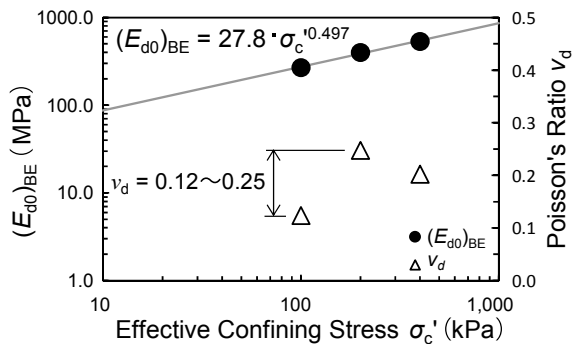
6 Setting Method for Design Values of Deformation Moduli Considering Drainage Conditions

Based on the above results, we examined the method for setting the deformation moduli used in the design of pavement structures that evaluated "effective stress dependency" and "difference in drainage conditions."

Table 4 Deformation moduli E and ν under drained and undrained conditions

Drainage conditions	D_r (%)		Deformation moduli for pavement structure design
Undrained	E_u(MPa)	20	$E_u = 20.1 \cdot \sigma_m'^{0.515}$
		50	$E_u = 21.3 \cdot \sigma_m'^{0.557}$
		80	$E_u = 33.1 \cdot \sigma_m'^{0.514}$
	ν_u		$\nu_u = 0.50$ (const.)
Drained	E_d(MPa)	20	$E_d = 13.8 \cdot \sigma_c'^{0.557}$
		50	$E_d = 25.1 \cdot \sigma_c'^{0.488}$
		80	$E_d = 27.8 \cdot \sigma_c'^{0.497}$
	ν_d		$\nu_d = 0.12 \sim 0.25$

(σ_m', σ_c': kPa)

Deformation Modulus E_u and Poisson's Ratio ν_u. The undrained deformation modulus E_u can be obtained as the equation of E_u versus σ_m' relationship by using $(G_{u0})_{BE}$ versus σ_m' and $(G_u)_{BE}$ versus σ_m' relationships obtained from CTX-BE test under the undrained condition and Eq. (5). Undrained Poisson's ratio ν_u is 0.5 (const.) as explained in Chap.s 2.

Deformation Modulus E_d and Poisson's Ratio ν_d. Figures 7, 8 and 9 show the drained Poisson's ratio ν_d obtained by the procedure as illustrated in Fig. 6, and it is seen that the values of ν_d as 0.12 to 0.25 in the range of $\sigma_c' = 100$ to 400 kPa. By substituting the values of ν_d and $(G_{d0})_{BE}$ into the Eq. (9), the drained deformation modulus E_d can be expressed as an E_d-σ_c' equation. Table 4 summarizes the above results.

7 Conclusions

1. A new test method CTX-BE was developed by combining the method of cyclic triaxial test CTX with that of bender element test BE, and a new method for evaluating the deformation moduli required for pavement structural design in consideration of drainage conditions of subgrade soils was proposed.
2. The design value of the deformation modulus E_u under undrained condition can be established from the $(G_{u0})_{BE}$ versus σ_m' and $(G_u)_{BE}$ versus σ_m' relationships and ν_u is 0.5 (const.) based on the CTX-BE test results.
3. Design values for the deformation modulus E_d and Poisson's ratio ν_d under drained condition can be established using the $(E_{d0})_{CTX}$, $(E_{u0})_{CTX}$, and $(G_{d0})_{BE}$ values obtained from the CTX-BE tests performed under drained and undrained conditions.

References

1. AASHTO (2003) Standard method of test for determining the resilient modulus of soils and aggregate materials T307–99
2. Japanese Geotechnical Society. Method for cyclic triaxial test to determine deformation properties of geomaterials, JGS 0542–2009
3. Japanese Geotechnical Society. Method for laboratory measurement of shear wave velocity of soils by bender element test, JGS 0544–2011
4. Wood DM (1990) Soil behavior and critical state soil mechanics. Cambridge University Press, pp37–46
5. Toki S, Shibuya S, Yamashita S (1995) Standardization of laboratory test methods to determine the cyclic deformation properties of geomaterials in Japan. Pre-failure Deformation of Geomaterials, Balkema, pp 741–784
6. Abe N, Masuyama Y, Ogasa Y, Minegishi J, Sugano S (1994) Determination method of deformation modulus for each layer of asphalt pavement. ASPHALT 36(179):53–72. (in Japanese).
7. Tatsuoka F, Teachavorasinskun S, Dong J, Kohata Y, Sato T (1994) Importance of measuring local strains in cyclic triaxial tests on granular materials. Dyn Geotech Testing II ASTM STP 1213:288–302
8. Sugano T, Nakazawa H, Ikeno K, Mitou M (2010) Study on countermeasure for liquefaction to runway ground by application of chemical grouting method. Technical Note of the Port and Airport Research Institute, No. 1206. (in Japanese)
9. AASHTO (1993) Guide for design of pavement structures

Validation of Photogrammetry-Based Method to Determine the Absolute Volume of Unsaturated Soils

Sara Fayek, Xiaolong Xia, and Xiong Zhang

Abstract Although many engineering practices are based upon a simplifying assumption that all soils are fully saturated, most pavement and geotechnical projects are typically constructed on compacted soils that are usually unsaturated. Triaxial tests are widely used to investigate the stress–strain behavior of both saturated and unsaturated soils. Many image-based methods have been developed to overcome the limitation of conventional triaxial testing methods. Recently, a photogrammetry-based method was proposed to measure the saturated and unsaturated soil volume change during triaxial tests. The triaxial test results and validation tests proved that this method is highly accurate, simple, and cost-effective. However, all previously suggested methods have a major limitation associated with their inability to determine top and bottom boundaries between the soil specimen, and the top and bottom pedestals. Although a simple and very precise approach has been proposed to determine the top and bottom boundaries in triaxial tests, the absolute soil volume calculation during triaxial testing included the volume of the membrane. This paper proposes a photogrammetry-based approach to overcome this limitation by developing a simple and precise method to calculate the membrane volume during triaxial testing and thus to accurately determine the absolute volume of soils. In this paper, the detailed procedures are presented, and the validation test was performed to demonstrate the accuracy of the proposed method. The results proved that the proposed method could determine the membrane volume for the calculation of the absolute volume of saturated and unsaturated soils with 0.062% error.

Keywords Photogrammetry-based method · Triaxial testing · Absolute volume

S. Fayek · X. Xia · X. Zhang (✉)
Missouri University of Science and Technology, Rolla, MO 65409, USA
e-mail: zhangxi@umsystem.edu

773

1 Introduction

Accurate local and total volume measurements are critical to determine strength and phase-relationship for soils. Soils behavior is generally described based on laboratory tests. Among laboratory tests, triaxial testing has been extensively used to characterize soil behavior due to its capability of providing controlled well-defined boundary, well-controlled drainage conditions, and uniform stresses within the soil. Many engineering practices are based upon simplifying assumptions such as all soils are fully saturated thus making projects susceptible to several uncertainties [1]. However, most infrastructures and structures, which are a vital part of a nation and one of the most important sectors [2, 3], are usually constructed on soils above water table and on compacted soils that are typically unsaturated soils. Volume measurements of unsaturated and saturated soils at any stage of triaxial testing are essential to determine the soil volumetric compression or dilation characteristics. For triaxial test on saturated soils, the soil volume change is equal to the water volume exchange since saturated soil is a two-phase system of water and soil solids. However, as unsaturated soil is a three-phase system of soil solids, water, and air, the soil volume change is not equal to the water volume exchange. Thus, conventional triaxial test methods for saturated soil cannot be applied for unsaturated soils. In the past few decades, researchers have employed various methods to determine volume measurement for unsaturated soils during triaxial testing [4–9]. The existing methods for volume change measurements for unsaturated soils can be classified into three main categories as suggested by Geiser et al. [10] and Laloui et al. [11]: measurement of the cell fluid, direct measurement of the air and water volumes, and the direct measurement of the soil specimen volume change. However, as summarized by Laloui et al. [11] and Zhang et al. [12], these methods had many disadvantages and limitations including the relative error and the complexity of the testing procedure. In addition, many of these methods measured the relative soil volume which is the final volume of soil during triaxial test contingent to the initial soil volume measurement in the air. The relative volume accuracy is highly dependent upon the accuracy of the initial soil volume measurement and the disturbance during the process of specimen preparation and triaxial testing. Many installation steps between the initial volume measurement in air and the initiation of triaxial testing including handling, preparing, and preserving the soil specimen can cause inevitable disturbances. In other words, if the initial soil measurement in the air is incorrect or the specimen is subjected to inevitable disturbance, all volume measurements at different stages of the triaxial test will diverge from its true values. For saturated soils, the error induced in the relative volume measurement cannot significantly change the interpretation of soil strength as the slopes of the specific volume versus effective stress remained constant. Fayek et al. [13] presented the error tendency resulted from considering the relative volume change and its potential misleading determination of unsaturated soil deformation and strength. For unsaturated soils with multiple influencing stress state variables, the imprecisions provoked from relative measurements could be problematic. From schematic plot of the void ratio, suction, and net mean stress, the yield curve can

imply expansive soil behavior for collapsible soil behavior. Accordingly, there is a great need to use or develop methods that can measure the absolute volume of unsaturated soils at any stage of the triaxial testing.

In recent years with the fast development of digital cameras, the popularity of photogrammetric-based methods has surpassed the previous developed methods because of their high accuracy, cost-effectiveness, and practicality [14–16]. The photogrammetry-based methods are to measure the local and total volume, volumetric strain localization, and shear band characterization. A multi-camera photogrammetric method was proposed by Salazar et al. [17] to measure the volume of soil by capturing a series of images for the soil specimen from within the triaxial cell. These cameras were placed inside the triaxial chamber to eliminate the effect of refractions. However, there are many drawbacks related to this photogrammetric method including the requirement of camera saturation, the replacement of multiple lenses, the use of special type triaxial cell, the need for special lighting, and the requirement to capture large number of pictures. So that, multi-camera photogrammetric methods are not extensively practical to determine volume change for unsaturated soil. Another photogrammetry method was developed by Zhang et al. [18] to determine the global and local deformations, strain localization, three-dimensional (3D) bulging, and shear plane evolution for both saturated and unsaturated soil [16, 18]. Only one commercial camera was placed at the exterior of a conventional triaxial cell apparatus to capture images around the soil specimen. Multiple ray-tracing processes and least-square optimization technique were used to consider the effect of refraction, cell deformation, and camera positions. The validation tests on stainless cylinder verified the high-accuracy level of methods with volume measurement accuracy of 0.25%. Many other image-based and photogrammetry-based techniques were developed that can potentially determine the absolute volume for unsaturated soil [19–22]. However, all these previously mentioned methods had one main limitation: their inability to determine the top and bottom boundaries between the soil specimens, and top cap and bottom pedestal, respectively. Recently, Fayek et al. [13, 23] proposed a new photogrammetry-based measurement technique to determine the absolute soil volume by back-calculating the top and bottom boundaries of the soil specimens. This method required posting measurement targets (high contrast dot) to the peripheral and surface planes of each the top and bottom pedestals separately, then taking pictures around each of the two pedestals. The top and bottom pedestals were then assembled with a soil specimen into a third model similar to placing the soil specimen in the unconfined compression test. This assembled model was then placed in a triaxial cell to duplicate the procedure of triaxial testing. Pictures were captured for each model of these four models, and then, photogrammetric analysis was performed. The surface plane equation of each the top and bottom pedestals, as well as the distance from each peripheral measurement target to the surface planes, was calculated using the top and bottom pedestal models. The top and bottom boundaries in the two models of unconfined compression test and triaxial tests were back-calculated using multiple ray-tracing and least-square optimization method. The method proposed by Fayek et al. [13] overcame one of the main limitations of previous image-based methods and proved to have very high accurate

absolute volume measurement from validation tests on stainless steel cylinder with
accuracy of 0.023% in unconfined compression test and 0.061% in the triaxial tests.
However, the aforementioned photogrammetry-based method did not consider the
membrane volume in calculating the absolute volume of soil specimens. This paper
proposed a photogrammetry-based measurement technique including a least-square
optimization method to determine the absolute volume of saturated and unsaturated
soils by considering the volume of the membrane.

2   Experiment

At present, all existing methods consider the membrane volume in the calculation
of the total and local volume measurements for soil specimens. However, consid-
ering the membrane volume can ultimately increase the accuracy of determining the
absolute volume of soil specimens during the triaxial testing at different deformation
and failure mode. This paper proposed a very simple and cost-effective method to
determine membrane volume. Only one calibrated commercially available camera
is needed to capture pictures around the soil specimen. The proposed procedure to
determine the membrane volume was demonstrated in Fig. 1. Measurements targets
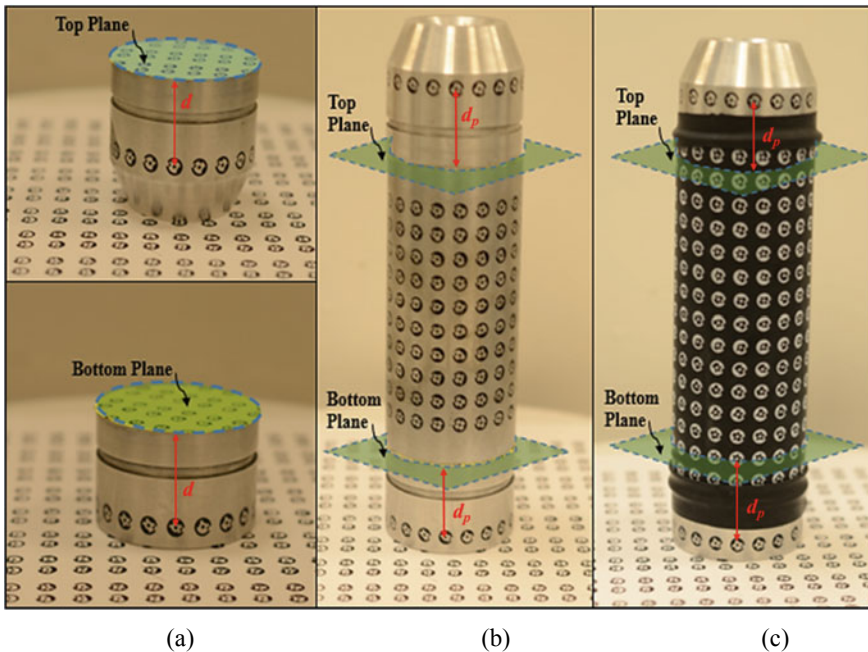
Fig. 1   Procedure setup **a** bottom and top pedestals, **b** Assembled model **c** assembled model with
the membrane

were printed directly on a stainless steel top and bottom pedestals (Fig. 1a), a stainless steel cylinder (Fig. 1b), and on the membrane (Fig. 1c). This method first determines the volume of cylinder restrained between the top and bottom pedestals without membrane (see Fig. 1b) and then that with membrane (Fig. 1c). The difference between the two volumes is equal to the membrane's volume. It is worth noting that the setup used is similar to the unconfined compression test with and without membrane to simplify the procedure compared with triaxial testing.

A technique similar to the one suggested by Fayek et al. [10] was used to determine the top and bottom boundaries. A series of pictures was taken for each of the top pedestal, the bottom pedestal, the assembled model without membrane, and the assembled model with the membrane. The photogrammetric analysis was then performed for each model independently to determine the coordinates of all measurement targets. This procedure can be divided into three main parts: (1) photogrammetric analysis of the pedestals separately to determine the surface planes equation and the distance from peripheral measurements targets to each of top and bottom surface separately, (2) photogrammetric analysis of the assembled model to back-calculate the top and bottom boundaries and to calculate the volume of the stainless steel without membrane, (3) photogrammetric analysis of the assembled model with membrane to back-calculate the top and bottom planes and to calculate the volume of the stainless steel cylinder covered with the membrane.

2.1 Step 1: Top and Bottom Pedestals Separately

After determining the coordinates of the measurement targets for the top and bottom pedestals models, the surface planes of each of the top and bottom pedestals were calculated by best fit all measurements targets to a plane equation. Then, the distance from each peripheral measurement target 'i' to the fitted plane was calculated and saved as a unique distance d_i to be used later in the next steps.

2.2 Step 2: Assembled Model Without Membrane

As each measurement target is unique (i.e., has unique identification number) and based on the fact that the distance from each periphery measurement target to the surface plane is fixed during the test, the bottom and top boundaries are back-calculated. A least-square optimization process was used to find the equation of the top and bottom boundaries in the new coordinate system of the assembled model. The concept is based on reducing the sum of the errors to zero which the difference of the measured distances d_i in 'Step 1' and the distances d_{pi} in 'Step 2' for all points on the peripheral. The top and bottom planes equation coefficients can be determined by minimizing the total error calculated using Eq. (1) as follows:

$$\sum_{i=1}^{n} d_i - d_{pi} \qquad\qquad (1)$$

where d_i is the distance from target 'i' to the surface plane in each of top and bottom pedestals' model; d_{pi} is the distance from target 'i' to the surface plane in the assembled model; n denotes the total number of measurements targets placed on the peripheral pedestal surface. Now, as the top and bottom boundaries equations are determined and the coordinates of the measurement targets on the stainless cylinder are recognized, a mesh can be generated to determine the volume of the stainless cylinder without membrane denoted by V_1.

2.3 Step 3: The Assembled Model with Membrane

A similar procedure to 'Step 2' was used for the assembled model with the membrane. The top and bottom boundaries in the new coordinate system was determined using Eq. (1). These two boundaries with the mesh consisted of the measurement targets form the boundary surface of the stainless steel cylinder with the membrane. Later, the volume of the cylinder covered with membrane, represented by V_2, was calculated using a self-developed Matlab program.

3 Results and Discussion

A stainless steel cylinder with identified dimensions was used for the validation test. To evaluate the accuracy of the proposed approach in this paper, a comparison was induced between the measured volumes at different steps. As the membrane is fabricated from an incompressible material, its thickness might change during trixial testing but its volume is considered unchangeable. The actual cylinder's volume measured by digital caliper was denoted by V_0. The initial volume of the stainless cylinder without membrane determined by photogrammetric analysis in the air was denoted by V_1 and that of the stainless cylinder with membrane represented by V_2. As the volumetric strain of stainless steel is negligible, the volumes V_0 and V_1 should be equal.

First, to prove the accuracy of this method, Table 1 represents the distance from the peripheral measurement targets to the surface plane of the bottom pedestal model and those after determining the bottom boundary equation. This table shows that the total error presented in Eq. (1) is insignificant which proves the high accuracy of the proposed procedure.

The 3D assembled model was reconstructed using a photogrammetry software, and then, both the top and bottom boundaries were back-calculated. Figure 2a shows

Table 1 Error induced from back-calculating the bottom plane equation

Target ID	d (mm)	d_p (mm)	Error (mm) = d-d_p
438	33.79804	33.80089	−0.00285
437	33.76774	33.77132	−0.00358
436	33.7352	33.73459	0.000619
435	33.70133	33.69331	0.008015
433	33.63748	33.63022	0.00726
429	33.53007	33.52008	0.008015
424	33.45754	33.45432	0.003215
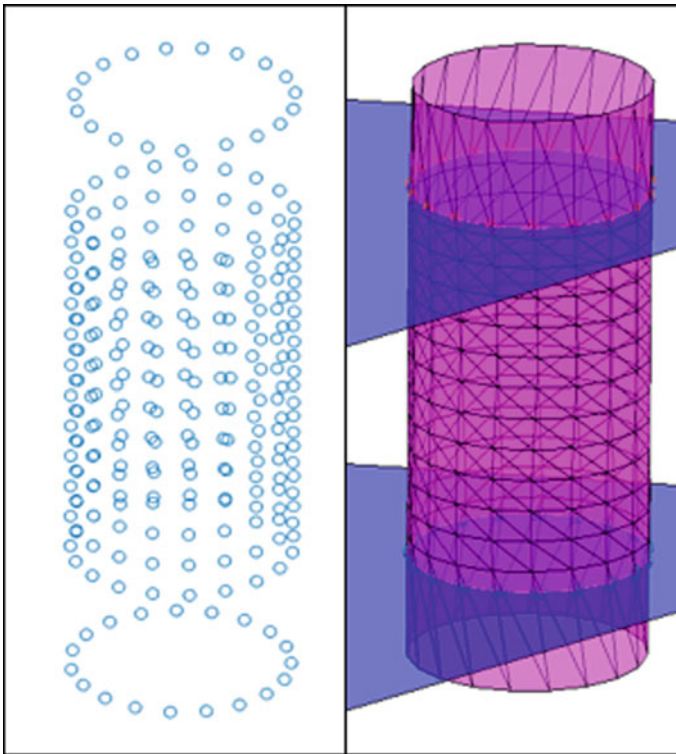
Fig. 2 Photogrammetry analysis results **a** Points cloud of the measurement targets **b** Intersection of the top and bottom boundaries with the cylinder mesh

the photogrammetry analysis results in determining the coordinates of the measurement targets of the assembled model. Using a developed software, a mesh is generated to connect the points and to form the cylinder. Then, the cylindrical volume can be determined by calculating the enclosed volume of the two planes with the hollow cylinder surface (see Fig. 2b). The calculated volume of the stainless steel cylinder represented by V_1 is equal to 378,403 mm³. Using a digital caliper, the cylinder's

diameter and height were measured and the volume V_0 was calculated as 378,403 mm^3. The difference between V_0 and V_1 is calculated to determine the accuracy of this procedure. The difference between the measured volume and the determined volume is 0.062%. This indicates that the proposed method is very accurate. In order to be able to precisely determine the absolute volume of the soil specimen, the volume of the membrane is calculated. The developed computer program was used to back-calculate the top and bottom planes and to determine stainless steel volume including the membrane. The volume of the stainless steel cylinder covered with the membrane is the restrained volume of the cylindrical hollow mesh and the two boundaries. This procedure determined the stainless steel cylinder volume covered with membrane, denoted by V_2, equal to 388,205.6 mm^3. The difference between V_1 and V_2 is equal to the membrane volume covering the stainless steel cylinder which is 9566.43 mm^3.

4   Conclusion

A photogrammetry-based approach was proposed to determine the absolute volume for saturated and unsaturated soils during triaxial test by considering the membrane volume. This proposed approach overcomes one of the main limitations associated with all existing image-based methods. The procedure is simple; it only requires using one commercially available camera, placing measurement targets on the surface plane and on the periphery of the top and base pedestals, and printing measurement targets on the membrane. Then, the captured pictures for each model are analyzed by a photogrammetry software to determine the 3D coordinates of the measurement targets. The top and bottom boundaries in the assembled model were back-calculated. This procedure was validated using a stainless steel cylinder to mimic the unconfined compression test with and without a membrane. The validation test proved the high accuracy associated with this proposed method with a 0.062% error. Then, the volume of the membrane covering the soil specimens can be determined by computing the difference between the cylindrical volume with and without membrane. The photogrammetry-based method proposed in this paper is a time-saving, cost-effective, and highly accurate technique to determine the membrane volume for the absolute volume calculation for both saturated and unsaturated soils at any stage during the triaxial testing.

References

1. Assaad R, El-Adaway IH, Abotaleb IS (2020) Predicting project performance in the construction industry. J Constr Eng Manag 146(5):04020030. https://doi.org/10.1061/(ASCE)CO.1943-7862.0001797
2. Assaad R, El-adaway IH (2020) Evaluation and prediction of the hazard potential level of dam infrastructures using computational artificial intelligence algorithms. J Manag Eng 36(5):04020051. https://doi.org/10.1061/(ASCE)ME.1943-5479.0000810

3. Assaad R, El-adaway IH (2020) Bridge infrastructure asset management system: comparative computational machine learning approach for evaluating and predicting deck deterioration conditions. J Infrastruct Syst 26(3):04020032. https://doi.org/10.1061/(ASCE)IS.1943-555X.0000572

4. Alshibli K, Sture S, Costes N, Lankton M, Batiste S, Swanson R (2000) Assessment of localized deformations in sand using X-ray computed tomography. Geotech Testing J 23(3):274–299

5. Bishop A, Donald I (1961) The experimental study of partly saturated soil in the triaxial apparatus. In: Proceedings of the 5th international conference on soils mechanic, vol 1. Paris, pp 13–21

6. Blatz J, Graham J (2003) Elastic-plastic modeling of unsaturated soil using results from a new triaxial test with controlled suction. Geotechnique 53(1):113–122

7. Bhandari A, Powrie W, Harkness RM (2012) A digital image-based deformation measurement system for triaxial tests. Geotech Testing J 35(2):209–226

8. Desrues J, Viggiani G (2004) Strain localization in sand: an overview of the experimental results obtained in Grenoble using stereophotogrammetry. Int J Numer Anal Methods Geomech 28(4):279–321

9. White D, Take W, Bolton M (2003) Measuring soil deformation in geotechnical models using digital images and PIV analysis. In: Proceedings of 10th international conference on computer methods and advances in geomechanics. Tuscon, Ariz., Balkema, Rotterdam, The Netherlands, pp 997–1002

10. Geiser F, Laloui L, Vulliet L (2000) On the volume measurement in unsaturated triaxial test. In: Rahardjo H, Toll DG, Leong EC, Balkema AA (eds) Unsaturated soils for Asia. Rotterdam, The Netherlands, pp 669–674

11. Laloui L, Peron H, Geiser F, Rifa A, Vulliet L (2006) Advances in volume measurement in unsaturated soil triaxial tests. Soils Found 46(3):341–349

12. Zhang X, Li L, Chen G, Lytton R (2015) A photogrammetry-based method to measure total and local volume changes of unsaturated soils during triaxial testing. Acta Geotech 10(1):55–82

13. Fayek S, Xia X, Li L, Zhang X (2020) Photogrammetry-based method to determine the absolute volume of soil specimen during triaxial testing. Transp Res Rec 0361198120928339

14. Li L, Zhang X (2015) A new triaxial testing system for unsaturated soil characterization. Geotech Testing J 38(6):823–839

15. Li L, Zhang X (2015) Modified unconfined compression testing system to characterize the stress-strain behavior of unsaturated soils at low confining stresses. Trans Res Record J Transp Res Board 2510:54–64

16. Li L, Zhang X, Chen G, Lytton R (2015) Measuring unsaturated soil deformations during triaxial testing using a photogrammetry-based method. Canadian Geotech J 53(3):472–489

17. Salazar S, Coffman R (2015) Consideration of internal board camera optics for triaxial testing applications. Geotech Testing J 38(1):40–49

18. Zhang X, Li L, Chen G, Lytton R (2015) A photogrammetry-based method to measure total and local volume changes of unsaturated soils during triaxial testing. Acta Geotech 10(1):55–82

19. Desrues J, Viggiani G (2004) Strain localization in the sand: an overview of the experimental results obtained in Grenoble using stereophotogrammetry. Int J Numer Anal Meth Geomech 28(4):279–321

20. Roscoe KH (1970) The influence of strains in soil mechanics. Geotechnique. 20(2):129–170

21. Parker J (1987) Image processing and analysis for the mechanics of granular materials experiment. In: ASME proceedings of the 19th SE symposium on system theory. Nashville, TN, March 2, ASME, New York

22. Lin H, Penumadu D (2006) Strain localization in combined axial-torsional testing on kaolin clay. J Eng Mech 132(5):555–564

23. Fayek S, Xia X, Zhang X (2020) A least square optimization approach for determining the soil boundary and absolute volume of unsaturated soils. In: Geo-congress 2020: geo-systems, sustainability, geoenvironmental engineering, and unsaturated soil mechanics. American Society of Civil Engineers, Reston, VA, pp 394–401

Development of In-Situ Modulus Detector for Transportation Substructure

Yong-Hoon Byun and Dong-Ju Kim

Abstract Resilient modulus of the subgrade is used for design and evaluation of transportation substructure. However, existing testing methods, e.g., falling weight deflectometer, can only provide the profile of resilient modulus of the substructure indirectly estimated from the measured deflection on the surface. The objective of this study is to develop a new testing device, so-called in-situ modulus detector (IMD), to evaluate the stiffness of subgrade along a depth. The IMD consists of a hammer, a guide, a driving rod, and a tip. At the bottom of the driving rod, a piezoelectric accelerometer and a load cell composed of four strain gauges are installed. To investigate and compare the penetration performance, three different shaped tips of the IMD are used. For dense and loose specimens, dynamic penetration tests are carried out by using eight different falling heights. The test results demonstrate that the penetration depths of cone-shaped tip are greater than those of wedge- and plane-shaped tips, regardless of soil density. The effect of buffer on penetration performance is significant for dense specimen. Based on the dynamic response, in-situ resilient modulus profiles are estimated along the penetration depth.

Keywords Dynamic penetration · In-situ test · Subgrade · Resilient modulus

1 Introduction

Resilient modulus of subgrade soil is one of the most important properties in the analysis and design of a flexible pavement structure. The resilient modulus can be determined from laboratory and field testing methods. In laboratory, a series of repeated load triaxial tests are conducted for evaluating the resilient modulus of soils. However, high cost of the testing system and the complexed test procedure are the disadvantages of the repeated load triaxial tests. Alternatively, field methods have been used for evaluating the resilient modulus.

Y.-H. Byun (✉) · D.-J. Kim
Kyungpook National University, Daegu 41566, South Korea
e-mail: yhbyun@knu.ac.kr

As an intrusive method, dynamic cone penetrometer (DCP) can be used for determining stiffness of soils, as well as strength. In previous studies, relationships between resilient modulus and DCP index were suggested [1–3]. Attempts to improve the DCP testing device have been done by several researchers [4–7]. Static cone penetration tests have been also used to predict the resilient modulus [8–11].

Nondestructive testing devices, such as falling weight deflectometer (FWD), light FWD (LFWD), and soil stiffness gauge (SSG), have been used to predict the resilient modulus of subgrade soils. The testing devices involve the measurement of both force and displacement. For pavement design, the relationships between the resilient modulus determined from laboratory tests and the modulus estimated from the nondestructive testing methods were reported [12–15]. Nevertheless, the measurement of using the nondestructive testing devices is still limited to the depth less than twice plate diameters.

In this paper, a new intrusive testing device for evaluating resilient modulus of subgrade soils is presented. A sandy soil is used for the preparation of dense and loose specimens. Using three different tips of the developed testing device, dynamic penetration tests are performed. The penetration performances of three different tips are compared, and the estimated resilient moduli along the depth are discussed.

2 Experimental Methods

2.1 *In-Situ Modulus Detector*

In-situ modulus detector (IMD) consists of a tip, rod, anvil, buffer, hammer, and guide, as shown in Fig. 1. In this study, three different tips shaped like plane, wedge, and cone were used. The dimensions of the three tips are summarized in Table 1. An ICP shock accelerometer with a maximum acceleration of 10,000 g (PCB Piezotronics, 350C03) was installed on the tip for the measurement of acceleration. A load cell configured with four strain gauges with an electrical resistance of 120 Ω was attached to the inner wall of lower part of rod for measuring force. A full Wheatstone bridge circuit can be used to efficiently convert a resistance change to an electric signal. In this study, the full-bridge circuit was designed to amplify the electrical resistance on the axial force and to simultaneously reduce the effects of temperature and bending of the rod [16]. A hollow rod with a length of ~ 1 m was connected to both tip and anvil. To minimize the side friction, the maximum diameters of tips were designed to be greater than the outer diameter of rod (24 mm). A rubber buffer was mounted on the anvil to adequately transfer the dynamic load to the rod. The hammer with the weight of 43 N can be dropped along the guide, and the falling height can be adjusted up to 685 mm. Using the hammer, the IMD can be driven into the soil, and dynamic responses can be measured from the accelerometer and load cell. More detailed information on the IMD was reported by Byun and Kim [17].

Fig. 1 In-situ modulus
detector
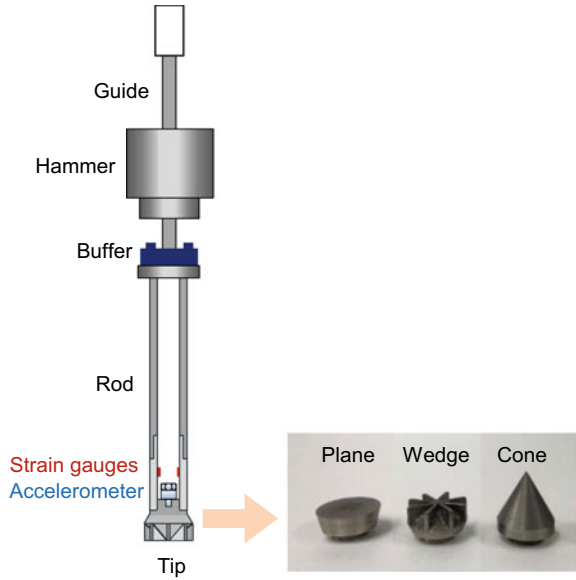
Table 1 Dimensions of three
tips

Type	Plane	Wedge	Cone
Maximum diameter	30	30	28
Height	10	15	29

Using the IMD, in-situ resilient modulus can be determined based on its definition as follows.

$$M_r = \frac{\sigma_d}{\varepsilon_r} \tag{1}$$

where σ_d and ε_r are deviator stress and recoverable strain, respectively. The deviator stress was set to a peak dynamic force obtained from the load cell divided by the projected area of the tip. Assuming that the contact stress on the tip is distributed along a parabolic function, the deviator stress was considered the average contact stress in the parabolic distribution. Similar to the strain response of a triaxial specimen under repeated loading, the dynamic displacement obtained from the accelerometer consists of the recoverable and permanent components. In this study, the recoverable strain was calculated from the recoverable displacement divided by the influence depth of dynamic load.

Table 2 Index properties of sandy soil

Specific gravity	Particle sizes [mm]				Gradation coefficient	Uniformity coefficient	Unified soil classification system
	D_{10}	D_{30}	D_{50}	D_{60}			
2.66	0.19	0.52	0.87	1.05	1.4	5.5	SP

2.2 Material

A sandy soil was used for the preparation of compacted specimens, and the index properties of the soil are summarized in Table 2. Using a rammer with the weight of 43.6 N, two different specimens were compacted with five different layers in a compaction mold with 168 mm in height and 150 mm in diameter. For loose and dense specimens, 9 and 56 blows were applied to each layer, respectively. After placing a donut type weight of 54 N on the top of the specimen, dynamic penetration tests using the IMD were conducted at the center of the specimen.

3 Experimental Results

3.1 Penetration Performance

The IMD penetrated into the compacted specimens by the hammer falling from eight different drop heights ranging from 5 to 57.5 cm. Figure 2 shows the penetration depths of three different tips along the drop heights without the buffer. For both
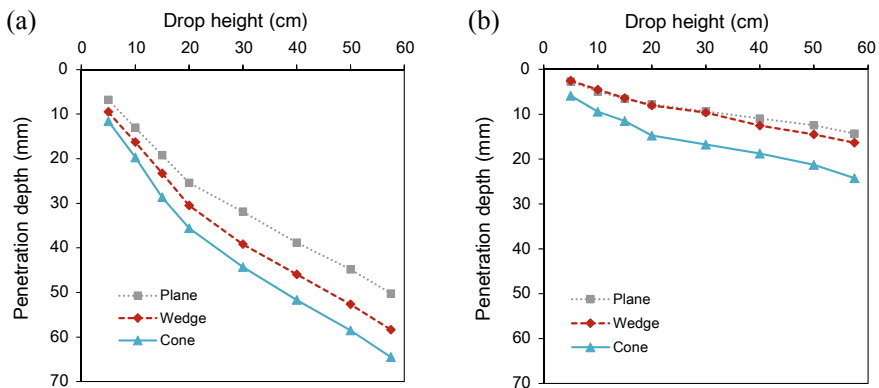
Fig. 2 Profiles of penetration without buffer: **a** loose specimen; **b** dense specimen. The penetration depth indicates the depth of penetration below the top of sample after one hammer drop
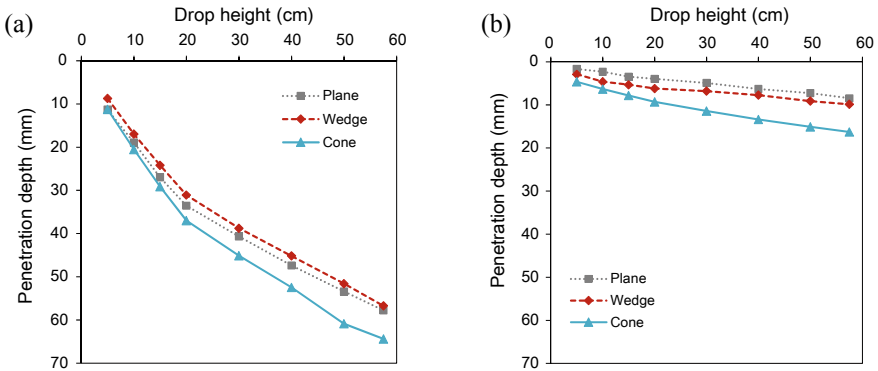
Fig. 3 Profiles of penetration with buffer: **a** loose specimen; **b** dense specimen

loose and dense specimens, the penetration depths of cone-shaped tip were greater than those of wedge- and plane-shaped tips.

Figure 3 shows the penetration depths along the drop heights with the buffer. Similar to the results without buffer, for both specimens, the penetration depths of cone-shaped tip were greater than those of wedge- and plane-shaped tips. For loose specimen, the final penetration depths of the three tips are less affected by buffer. In contrast, for dense specimen, the final penetration depths with buffer were significantly smaller than those without buffer. The cone-shaped tip showed the greatest final penetration depth.

3.2 Dynamic Response

Typical dynamic responses detected at the wedge-shaped tip are plotted in Fig. 4. After dropping the hammer, the impulse signals of force and displacement occurred almost simultaneously. Depending on the soil condition, the impulses were kept for 10–30 ms. The total displacement (d_t) at each response was composed of recoverable
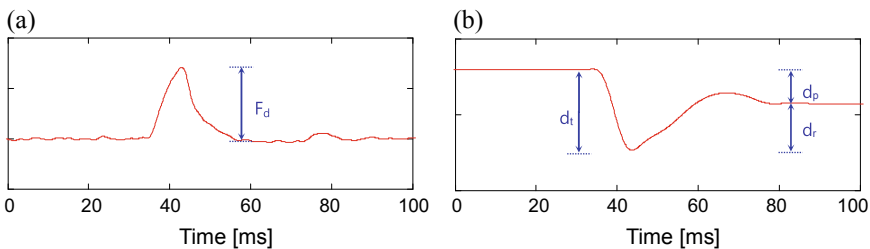
Fig. 4 Typical signals obtained from the IMD: **a** force; **b** displacement

Fig. 5 Resilient modulus profile along penetration depth. A "Set" consisted of a series of drop heights ranging from 5 to 50 cm, and the drop height was changed in ascending order. After finishing a set of drop heights, the following set of dropping the hammer was repeated.
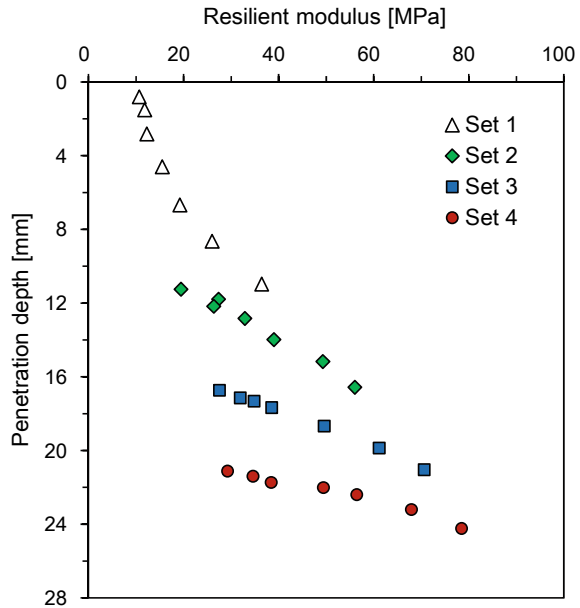
(d_r) and permanent displacements (d_p). Based on the maximum force (F_d) and recoverable displacement, resilient modulus was calculated.

Figure 5 shows the profiles of resilient moduli along the penetration depths obtained from a compacted specimen with a water content 10.8% reported by Byun and Kim [17]. Up to the depth of 24 mm, the resilient modulus ranged from 10 to 80 MPa. Generally, the resilient modulus increased with the drop height. For the same drop height, the resilient moduli at greater depths were higher than those at smaller depths. Furthermore, a resilient modulus of 40.7 MPa estimated from the CBR value of the specimen was in the range of resilient moduli estimated from the IMD.

4   Conclusions

The in-situ modulus detector (IMD) was developed for stiffness characterization of subgrade soils. The IMD had the components similar to dynamic cone penetrometer, but the shapes of tips were different. In addition, a load and an accelerometer were mounted at the tip to measure the dynamic response. On the compacted specimens, dynamic penetration tests were conducted by using the IMD with different shaped tips. The penetration depth per blow varied along the drop height of hammer. Furthermore, the penetration performance was also affected by the soil density, buffer application, and tip shape. Especially for dense specimen, the penetration performance significantly depended on buffer application. Regardless of soil density and

buffer application, the cone-shaped tip showed the greatest final penetration depth. Based on the measured dynamic force and displacement, the resilient modulus was estimated along the penetration depth. Considering the influencing factors on the resilient modulus, the IMD could be improved for subgrade characterization.

References

1. Chai G, Roslie N (1998) The structural response and behavior prediction of subgrade soils using falling weight deflectometer in pavement construction. In: Proceedings 3rd international conference on road and airfield pavement technology. Beijing, China
2. Hassan A (1996) The effect of material parameters on dynamic cone penetrometer results for fine-grained soils and granular materials. Ph.D. dissertation, Oklahoma State University, Stillwater
3. George KP, Uddin W (2000) Subgrade characterization for highway design. Final Report, University of Mississippi, in cooperation with the Mississippi Department of Transportation, US Department of Transportation, and Federal Highway Administration, Oxford
4. Langton D (1999) The Panda lightweight penetrometer for soil investigation and monitoring material compaction. Ground Eng 32(9):33–37
5. Byun YH, Lee JS (2013) Instrumented dynamic cone penetrometer corrected with transferred energy into a cone tip: a laboratory study. Geotech Test J 36(4):533–542
6. Byun YH, Hong WT, Lee JS (2015) Characterization of railway substructure using a hybrid cone penetrometer. J Smart Struct Syst 15(4):1085–1101
7. Lee JS, Kim SY, Hong WT, Byun YH (2019) Assessing subgrade strength using an instrumented dynamic cone penetrometer. Soils Found 59(4):930–941
8. Mohammad LN, Titi HH, Herath A (2000) Investigation of the applicability of intrusion technology to estimate the resilient modulus of subgrade soil. FHWA/LA-00/332, Louisiana Transportation Research Center, Baton Rouge
9. Mohammad LN, Titi HH, Herath A (2020) Effect of moisture content and dry unit weight on the resilient modulus of subgrade soils predicted by cone penetration test. FHWA/LA-00/355, Louisiana Transportation Research Center, Baton Rouge
10. Mohammad LN, Gaspard K, Herath A, Nazzal M (2007) Comparative evaluation of subgrade resilient modulus from non-destructive, in-situ and laboratory methods. FHWA/LA-06/417, Louisiana Transportation Research Center, Baton Rouge
11. Gudishala R (2004) Development of resilient modulus prediction models for base and subgrade pavement layers from in situ devices test results. Master's thesis, Louisiana State University, Baton Rouge
12. Choubane B, McNamara RL (2000) Flexible pavement embankment moduli using falling weight deflectometer (FWD) data. Research Report FL/DOT/SMO/00–442, State Materials Office, Florida Department of Transportation, Tallahassee
13. Rahim AA, George KP (2003) Falling weight deflectometer for estimating subgrade elastic moduli. J Transp Eng 129(1):100–107
14. White D, Thompson MR, Vennapusa P (2007) Validation of intelligent compaction monitoring technology for unbound materials. Center for Transportation Research and Education, Iowa State University, Ames, Minnesota Department of Transportation
15. Abu-Farsakh M, Alshibli K, Nazzal M, Seyman E (2004) Assessment of in situ test technology for construction control of base course and embankments. Final Report No. FHWA/LA.04/385, Louisiana Transportation Research Center, Baton Rouge

16. Byun YH, Yoon HK, Kim YS, Hong SS, Lee JS (2014) Active layer characterization by instrumented dynamic cone penetrometer in Ny-Alesund. Svalbard Cold Regions Sci Technol 104:45–53
17. Byun YH, Kim DJ (2020) In-situ modulus detector for subgrade characterization. Int J Pavement Eng 1–11

Evaluation of Various Spatial Interpolation Techniques for Generating Synthetic CPT Data Profile

Md Habibur Rahman and Murad Y. Abu-Farsakh

Abstract In order to incorporate the influence of collected in-situ data, the spatial correlation between the data and the foundation needs to be explored. Statistical information of the soil property can be estimated from available field data obtained from testing at discrete locations across the site. In this research, several well-established spatial interpolation methods like ordinary kriging (OK), simple kriging (SK), inverse distance weight (IDW), spline, natural neighbor (NaN), and universal kriging (UK) were incorporated to evaluate the best method for generating synthetic cone penetration test (CPT) data. To remove the spikes, continuous five points averaging was done to generate the smoothed tip resistance. For the analysis, the spatial interpolation was performed in each foot (depth wise). Six CPT cases were investigated in this study. According to the results, four out of six cases, if the first priority is given to bias factor followed by coefficient of variation (COV) and root mean square error (RMSE), the best three spatial interpolation techniques are IDW, OK, and SK sequentially, based on their performance. For the other two cases, in one case, the best three spatial interpolation techniques are OK, IDW, and SK, sequentially, and the other case shows SK, IDW, and OK sequentially are the best three spatial interpolation techniques.

1 Introduction

For comprehensive foundation design, geotechnical engineers preferably consider exclusive soil properties at different locations though achieving this goal can consume enormous amounts of investment, employment, ingredients, and time. It is fortunate that most of the soil properties are spatially correlated and can be connected to

Md Habibur Rahman
Department of Civil and Environmental Engineering, Louisiana State University, Baton Rouge, LA, USA

M. Y. Abu-Farsakh (✉)
Louisiana Transportation Research Center, Louisiana State University, 4101 Gourrier Ave., Baton Rouge, LA 70808, USA
e-mail: cefars@lsu.edu

many environmental concerns [1, 6, 9, 14, 15, 17]. For assessing the effects of uncertainties in geotechnical forecasts, probabilistic methods have been widely used in geotechnical engineering [16]. An in-situ testing like CPT can estimate different soil properties at the specific location. However, outside the tested locations, expected uncertainty and ambiguity are spatially varied.

Many researchers developed several correlations between the soil properties and the environment, and then incorporated these relationships with geostatistic techniques for additional soil mapping [8, 12]. The spatial variability of the random variable can be characterized by co-variance or semivariogram functions, which are the key elements in spatial estimation techniques [4]. The ArcGIS, which is a software, is used to provide a variety of tools (such as spatial analysts and geostatistical analysts) in order to explore spatial data, evaluates the prediction uncertainty, and creates surfaces for efficient decision making in geostatistics and that can be explored for geotechnical applications. There exist many spatial techniques that can be used to generate synthetic CPT profiles. Many researchers applied the principles of geostatistics and spatial interpolation using the kriging technique and described the assumptions of kriging [5, 7, 13]. Generally, the kriging technique is used widely to approximate the unknown values at specific points by using known points data. In this study, six spatial interpolation methods like ordinary kriging (OK), simple kriging (SK), universal kriging (UK), inverse distance weighted (IDW), spline, and natural neighbor (NaN) methods were investigated to evaluate the spatial variability of CPT data in the project sites.

The ordinary kriging (OK) technique is a geostatistical approach used for evaluating spatial variability. Instead of weighting nearby data points by some power of their inverted distance, the ordinary kriging relies on the spatial correlation structure of the data to determine the weighting values [11]. The simple kriging (SK) technique is another type of kriging that is generally adopted due to its simplicity and ability to evaluate the spatial variability. The universal kriging (UK) is applied when the regionalized variable exhibits in some form of a trend [5]. The inverse distance-weighted (IDW) interpolation technique can be categorized as a local, deterministic, and exact interpolation technique. Splines produce good results with gently varying surfaces and thus are often not appropriate when there are large changes in the surface values within a short horizontal distance. The natural neighbor (NaN) interpolation algorithm finds the closest subset of input samples to a query point and applies weights to them based on proportionate areas to interpolate a value. It is also known as Sibson or "area-stealing" interpolation.

2 Spatial Interpolation Techniques

The first step in the kriging interpolation method is the computation of an experimental semivariogram. The semivariance can be described by the following equation:

$$\gamma(h) = \frac{1}{2n} \sum_{i=1}^{n} (z(x_i) - z(x_i + h))^2 \tag{1}$$

where 'n' is the number of data points separated by distance 'h'; and $\gamma(h)$ is the semivariogram (commonly referred to as variogram) (Webster and Oliver 2001). However, all kind of kriging interpolation methods have a basic Eq. (2):

$$Z(x_0) - \mu = \sum_{i=1}^{n} \lambda_i [Z(x_i) - \mu(x_0)] \tag{2}$$

where 'μ.' is stationary known mean; 'λ_i' is the kriging weight, found from semivariogram, 'n' is the number of sampled points for the spatial interpolation and within the search window; '$\mu(x_0)$' is the mean of the sampled data. Step by step procedure of kriging interpolation methods were done by Clark and Harper [2].

The equation of the inverse distance weighted method is given as Eq. (3):

$$Z_0 = \frac{\sum_{i=1}^{n} Z_i \frac{1}{d_i^k}}{\sum_{i=1}^{n} \frac{1}{d_i^k}} \tag{3}$$

where 'Z_0' is the predicted value at the unsampled location; 'Z_i' is the observed value; 'd_i' is the distance between the prediction location and the measured location; and 'n' is the number of measured sample points within the neighborhood.

The algorithm used for the spline tool uses the following formula for the surface interpolation [10] by ArcMap 10.4:

$$S(x, y) = t(x, y) + \sum_{j=1}^{n} \lambda_j R(r_j) \tag{4}$$

where 'n' is the number of points; '$t(x, y)$' and 'λ_j' are coefficients found by the solution of a system of linear equations; 'r_j' is the distance from the interpolation point to the jth point; and 'R' is a distance dependent function.

The natural neighbors (NaN) method was introduced by Sibson (1981). We can represent this using the following formula:

$$\lambda_i = \frac{A_i}{\sum_{k=1}^{n} A_k} \tag{5}$$

In this study, ArcMap 10.4.1 software was used to perform the spatial interpolation.

3   Evaluation Criteria

Some statistical measures are built in ArcMap Software. While processing spatial interpolation techniques, these statistics are used. Cross-validation compares measured quantities with the value that would be predicted for a position given a dataset omitting the true value. Commonly used criteria such as the root mean square error (RMSE) and coefficient of effectiveness (COE) were done in this research. Bias factor and coefficient of variation of bias factor (COV_λ) were also computed and compared in this research. RMSE, COE, Bias factor (λ), and coefficient of variation of bias factor (COV_λ) is given by Eqs. (6)– (9), respectively:

$$\text{RMSE} = \sqrt[2]{\frac{1}{n} \sum_{i=1}^{n} (p_i - m_i)^2} \tag{6}$$

$$\text{COE} = 1 - \frac{\sum_{i=1}^{n}(p_i - m_i)^2}{\sum_{i=1}^{n}(m_i - \overline{m})^2} \tag{7}$$

$$\lambda = \frac{m_i}{p_i} \tag{8}$$

$$\text{COV}(\%) = \left(\frac{\text{Standard Deviation}}{\overline{\lambda}} \right) \times 100 \tag{9}$$

where 'n' is the number of samples or observations; 'p' is the predicted or estimated value and 'm' is the measured or observed value; '$\overline{m}$' is the arithmetic mean of the observation values; 'λ.' is each of the values of bias factor data; '$\overline{\lambda}$' is the mean of the values of bias factor data.

4   Description of CPT Sites

In this study, six different project sites with several CPT tests were used to evaluate the different spatial interpolation methods. The area being studied for Metairie site is a 0.50 km^2 area of Metairie (29°59′52″N and 90°10′39″W) situated at 0.9 m above the mean sea level (MSL). For the ALF site, the area being studied is about 0.002 km^2 of the accelerated loading facility (ALF) of the Louisiana Transportation Research Center (LTRC) (30°26′12.37″N and 91°14′39″W). For the US90 & LA85 site, the area being studied is about 0.125 km^2 (29°55′17″N and 91°′34″W). For the Hammond site, the area being studied is about 0.54 km^2 (30°28′50″N and 90°29′29″W). For the LA1 site, the area being studied is about 0.002 km^2 (30°26′00″N and 91°12′37.45″W). For the Bayou Lacassine site, the area being studied is about 0.01 km^2 (30°04′13″N and 92°52′52″W).
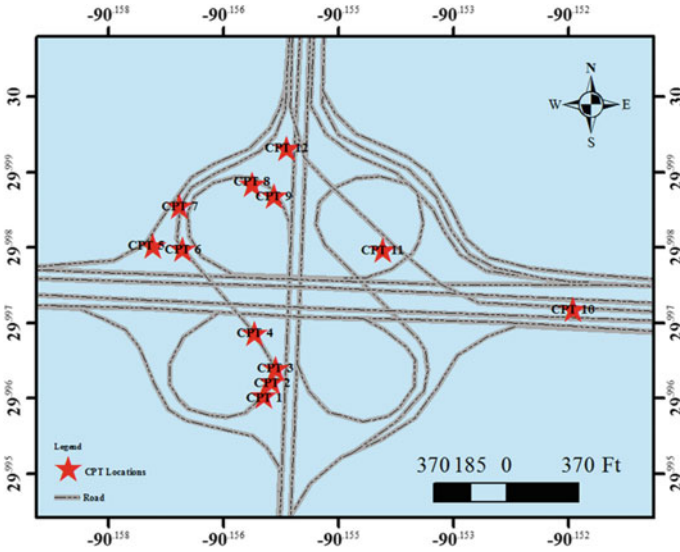
Fig. 1 Plan view of the locations for the Metairie site

For each site, several CPT locations were selected for analysis and evaluation of the synthetic CPT profiles generated using the different spatial interpolation techniques. For example, five CPT points, i.e., locations 3,6,8,9, and 11, were selected for Metairie site. For each selected CPT point, synthetic CPT profiles were generated using different spatial interpolation methods from the rest of CPlocations. Again, the synthetic CPT profiles were generated for every 1 ft. The predicted synthetic CPT profiles using different spatial interpolation methods were compared with the measured CPT profile at the selected location. The same approach was follower for the other selected CPT points. In Fig. 1, the plan view of Metairie site is schematically illustrated and black colored marker is used to indicate analyzed CPT points.

5 Subsurface Geotechnical Characterization

The subsurface soil conditions for all sites were characterized using the results of CPT tests. The profiles of CPT tip resistance, friction resistance, profile of smoothed tip resistance, estimated profile of average tip resistance per ft., in addition, to soil classification using the probabilistic region soil behavior estimation method [18]. For Metairie site, the maximum, minimum, and average COV of q_c values are 2.46, 0.00, and 0.74, respectively. The profile of CPT tests was used to classify the subsurface soil using Zhang and Tumay's (1999) probabilistic region estimation method (behavior-based classification) as shown in Fig. 2.
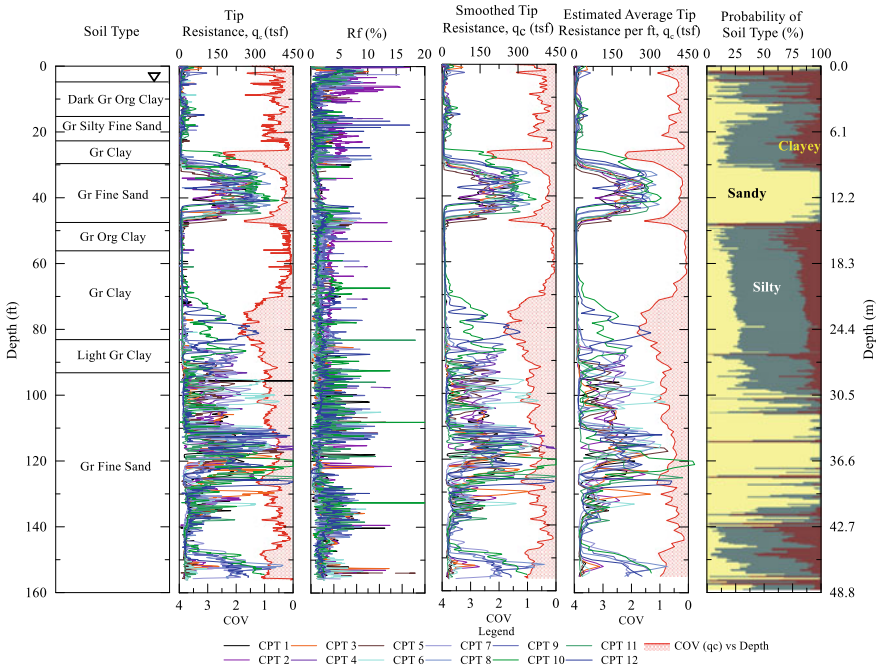
Fig. 2 CPT soil classification at Metairie site

6 Evaluation of Spatial Interpolation Methods

In this study, cross-validation techniques were performed to evaluate the performance of the different spatial interpolation techniques for generating synthetic CPT profiles, and to determine the methods that gives the best predictions. In Fig. 3, measured vs predicted cone tip resistance for different spatial interpolation methods like OK, SK, IDW, Spline, NaN, and UK were given for Metairie site.

Figure 4 presents the bar chart of RMSE (root mean squared error), COE (coefficient of effectiveness), bias factor (mean ratio of measured to predicted value), and COV (coefficient of variation) for the tip resistance predicted using OK, SK, IDW, Spline, NaN, and UK for Metairie site. Based on bias factor, in Fig. 4b, the IDW gives the best result followed by SK and OK. IDW gives 0.98 (average), which is very close to 1. On the other hand, the bias factor's average for OK, SK, Spline, NaN, and UK are 0.93, 0.97, 0.93, 0.90, and 0.93, respectively. In case of COV, Fig. 4d shows the IDW gives the least COV as compared to SK and OK. The average COV for IDW, OK, SK, Spline, NaN, and UK are 0.34, 0.36, 0.37, 0.53, 0.43, and 0.37, respectively. Based on COV, the IDW is the best method followed by OK and SK. Out of all estimated error parameters, the RMSE is the convenient tool that defines the best method. Based on RMSE in Fig. 4c, the IDW gives less average error than SK and OK. The average RMSE for IDW, OK, SK, Spline, NaN, and UK
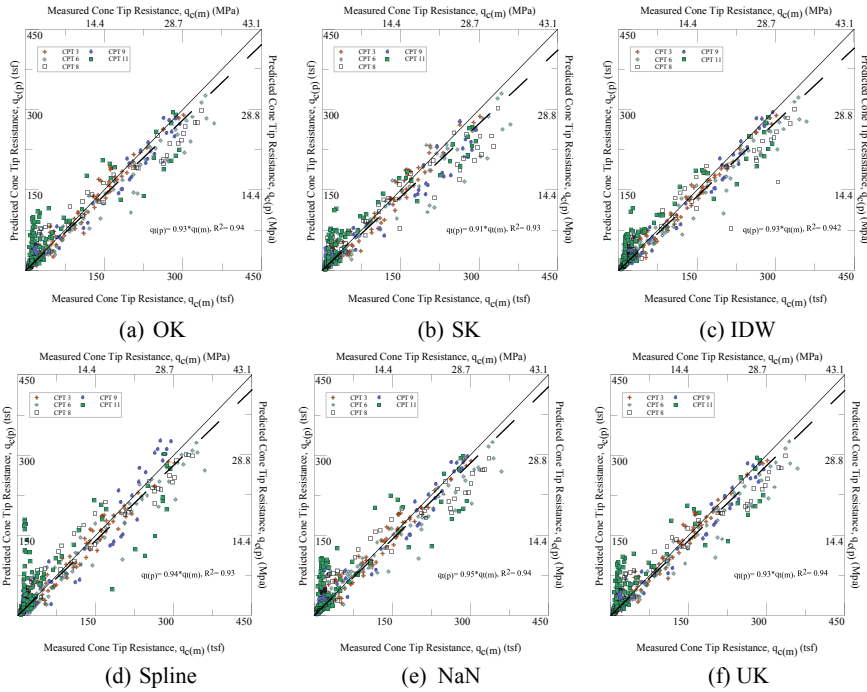
Fig. 3 Predicted versus measured plot of different spatial interpolations for Metairie site

are 22.37, 25.35, 28.68, 29.83. 30.57, and 25.37, respectively. Accordingly, the IDW is considered the best spatial interpolation method followed by OK and SK. Using COE criteria, the IDW is better than the other methods. From Fig. 4a, IDW gives 0.92 (average), which is very close to 1. On the other hand, the average COE for OK, SK, Spline, NaN, and UK are 0.90, 0.90, 0.86, 0.88, and 0.90, respectively.

The evaluation parameters of different Spatial interpolation techniques for generating synthetic CPT profiles at specified locations are given in Table 1.

7 Conclusions

This research study was conducted to investigate and evaluate the best spatial interpolation technique to incorporate site variability for generating synthetic CPT profiles in six CPT sites. Based on the results of statistical analyses for the six CPT sites, the following conclusions can be drawn:

- For Metairie, ALF, US90 & LA85, and Bayou Lacassine site, based on these results, if the first priority is given to best fit line of measured versus predicted, the bias factor, COV, and RMSE, the best three spatial interpolation techniques
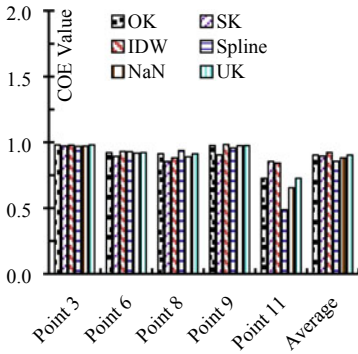
(a) COE
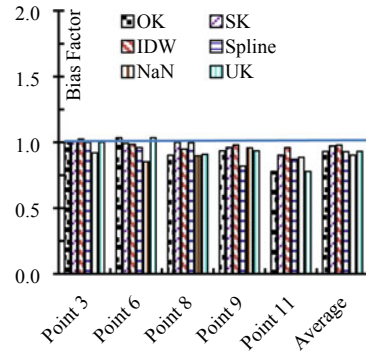
(b) Bias Factor
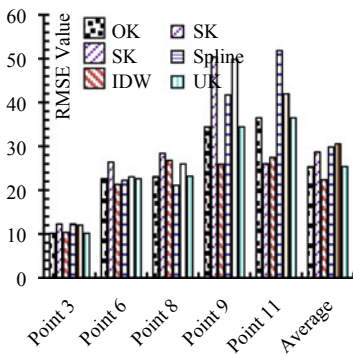
(c) RMSE
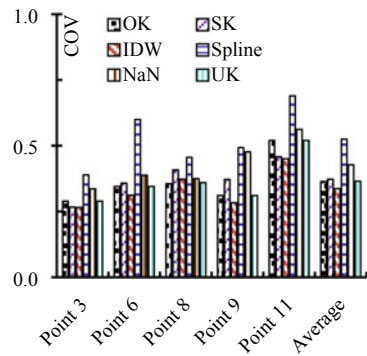
(d) COV

Fig. 4 Cross-validation techniques for Metairie site

are IDW, OK, and SK, based on their performance of generating synthetic CPT profiles.

- For Hammond site, based on these results, if the first priority is given to best fit line of measured versus predicted, the bias factor, COV, and RMSE, the best three spatial interpolation techniques are OK, IDW, and SK, based on their performance of generating synthetic CPT profiles.

- For LA1 site, based on these results, if the first priority is given to best fit line of measured versus predicted, the bias factor, COV, and RMSE, the best three spatial interpolation techniques are SK, IDW and OK, based on their performance of generating synthetic CPT profiles.

Overall, it can be concluded that for all cases considered in this study, if the first priority is given to best fit line of measured versus predicted, the bias factor, COV, and RMSE, the best three spatial interpolation techniques are IDW, OK, and SK, based on their performance of generating synthetic CPT profiles. The performance

Table 1 Evaluation parameters of different spatial interpolation techniques

Name of the site	Method	Parameters				
		Slope of the best fit line	RMSE	COE	Bias factor	COV
Metairie	OK	0.93	25.35	0.90	0.93	0.36
	SK	0.91	28.68	0.90	0.97	0.37
	IDW	0.93	22.37	0.92	0.98	0.34
	Spline	0.94	29.83	0.86	0.93	0.53
	NaN	0.95	30.57	0.88	0.90	0.43
	UK	0.93	25.37	0.90	0.93	0.37
ALF	OK	0.99	8.29	0.97	0.99	0.31
	SK	0.94	8.26	0.97	1.05	0.34
	IDW	0.98	8.13	0.97	1.00	0.31
	Spline	1.00	9.82	0.95	1.05	0.40
	NaN	0.99	9.25	0.96	1.01	0.34
	UK	0.99	8.29	0.97	0.99	0.31
US90 & LA85	OK	1.00	8.05	0.59	1.01	0.29
	SK	0.95	7.64	0.58	1.05	0.30
	IDW	0.99	7.63	0.62	1.02	0.29
	Spline	1.05	8.96	0.60	1.04	0.37
	NaN	1.03	7.93	0.65	1.02	0.31
	UK	1.00	8.05	0.60	1.01	0.29
Hammond	OK	0.91	19.30	0.97	1.04	0.20
	SK	0.82	38.09	0.81	1.15	0.29
	IDW	0.88	23.12	0.96	1.08	0.21
	Spline	0.89	37.14	0.88	1.10	0.31
	NaN	0.82	34.09	0.88	1.16	0.28
	UK	0.91	19.30	0.97	1.04	0.20
LA1	OK	1.00	7.81	0.08	0.98	0.40
	SK	0.95	7.37	0.01	1.03	0.37
	IDW	0.99	7.16	0.34	1.05	0.37
	Spline	0.99	7.86	0.03	1.02	0.47
	NaN	0.96	7.87	−0.18	1.02	0.43
	UK	1.00	7.81	0.08	0.98	0.40
Bayou Lacassine	OK	0.94	5.34	0.61	1.01	0.30
	SK	0.88	6.11	0.34	1.06	0.33
	IDW	0.92	5.18	0.62	1.02	0.29
	Spline	0.98	6.06	0.51	0.96	0.38
	NaN	0.94	5.74	0.51	0.98	0.36
	UK	0.94	5.34	0.61	1.01	0.30

of these methods is much better than the performance of Spline and NaN methods. Furthermore, in this study, the OK and UK methods gave same results.

References

1. Chai X, Shen C, Yuan X, Huang Y (2008) Spatial prediction of soil organic matter in the presence of different external trends with REML-EBLUP. Geoderma Elsevier BV 148(2):159–166
2. Clark I, Harper WV (2001) Practical Geostatistics 2000. Geostokos (Ecosse) Limited
3. Firouzianbandpey S, Ibsen LB, Griffiths DV, Vahdatirad MJ, Andersen LV, Sørensen JD (2015) Effect of spatial correlation length on the interpretation of normalized CPT data using a Kriging approach. J Geotech Geoenviron Eng 141(12):1–9
4. Gundogdu KS, Guney I (2007) Spatial analyses of groundwater levels using universal kriging. J Earth Syst Sci 116(1):49–55
5. Isaaks EH, Srivastava RM (1989) Applied geostatistics. New York
6. Kumar S, Lal R, Liu D (2012) A geographically weighted regression kriging approach for mapping soil organic carbon stock. Geoderma, Elsevier B.V., 189–190, 627–634
7. Matheron G (1971) The theory of regionalized variables and its applications. Les Cahiers du Centre de Morphlogie Mathematique
8. Miller DJ, Zhang Z, Ackerman AS, Platnick S, Baum BA (2016) The impact of cloud vertical profile on liquid water path retrieval based on the bi-spectral method: a theoretical study based on large-eddy simulations of shallow marine boundary-layer clouds. J Geophys Res Atmos 121(8):4122–4141
9. Minasny B, McBratney AB, Mendonça-Santos ML, Odeh IOA, Guyon B (2006) Prediction and digital mapping of soil carbon storage in the lower Namoi valley. Aust J Soil Res 44(3):233–244
10. Mitáš L, Mitášová H (1988) General variational approach to the interpolation problem. Comput Math Appl 16(12):983–992
11. Samui P, Sitharam TG (2010) Spatial variability of SPT data using ordinary and disjunctive kriging. Georisk 4(1):22–31
12. Somarathna PDSN, Malone BP, Minasny B (2016) Mapping soil organic carbon content over New South Wales, Australia using local regression kriging. Geoderma Regional Elsevier 7(1):38–48
13. Webster R, Oliver M (2001) Geostatistics for environmental scientists. Wiley, Chichester
14. Ye H, Shen C, Huang Y, Huang W, Zhang S, Jia X (2015) Spatial variability of available soil microelements in an ecological functional zone of Beijing. Environ Monit Assess 187(2).
15. Ye HC, Huang YF, Chen PF, Huang WJ, Zhang SW, Huang SY, Hou S (2016) Effects of land use change on the spatiotemporal variability of soil organic carbon in an urban-rural ecotone of Beijing, China. J Integrat Agricul Chinese Acad Agricul Sci 15(4):918–928
16. Zhang J, Zhang LM, Tang WH (2011) Kriging numerical models for geotechnical reliability analysis. Soils Found 51(6):1169–1177
17. Zhang S, Huang Y, Shen C, Ye H, Du Y (2012) Spatial prediction of soil organic matter using terrain indices and categorical variables as auxiliary information. Geoderma, Elsevier B.V., 171–172, 35–43.
18. Zhang Z, Tumay MT (1999) Statistical to fuzzy approach toward CPT soil classifcation. J Geotech Geoenviron Eng 125(3):179–186

Disturbance Deformation of Ground Induced by a Large-Area Piling: A Field Test

Limin Wei, Shuanglong Li, Qun He, Meng Du, and Hong Zhou

Abstract When a large-area piling is carried out on the ground adjacent to an existing railway line, the disturbance deformation caused by the piling construction may have an adverse effect on the existing railway foundation. In this paper, a field test with three pile types, consisting of prestressed pipe pile (PPP), micro-grouting pile (MGP), and cast-in-place bored pile (CBP), was carried out to investigate the disturbance response of ground induced by the large-area piling. A high-precision automatic monitoring system was established to measure the lateral displacement and ground surface uplift during the piling process. Test results show that under the same piling range, the disturbance effect caused by the piling of PPPs is significantly higher than that caused by the piling of MGPs and CBPs. The horizontal displacement decreases with the increase of soil depth, and the uplift displacement decreases exponentially with the increase of the distance between the test zone boundary and the measuring points. The maximum influence ranges of the horizontal and vertical displacements caused by the piling of PPPs are about 88d (d is pile diameter) and 30d, respectively, and the maximum influence ranges both of lateral and vertical deformation caused by MGPs and CBPs are less than 5.0 m. Under the same piling range, the maximum lateral displacement caused by PPPs with no pre-drilled hole is three times higher than that caused by PPPs with a pre-drilled hole of depth 15 m, indicating that the pre-drilled hole has a significant control effect on the soil squeezing deformation.

Keywords Link-line subgrade · Large-area piling · Soil squeezing deformation · Field test

1 Introduction

When a large-area piling construction is carried out on the ground of link-line subgrade adjacent to an existing railway line, the disturbance deformation during the

L. Wei · S. Li (✉) · Q. He · M. Du · H. Zhou
Central South University, No.22, Shaoshan South Road, Tianxin District, Changsha, Hunan 410075, China

piling process may affect the service performance of the existing subgrade. During the piling process, different types of piles would have a certain impact on the adjacent soil, which has been studied by many scholars.

The driving process of precast pile would cause additional deformation and excess pore water pressure of adjacent soil [1–3]. The increase of excess pore water pressure would reduce the undrained strength of soil [4, 5], and then affect the bearing capacity of adjacent soil. In addition, the process of precast pile intruding into the soil would produce soil squeezing deformation, which might cause the pile to float up and shift [6], and even cause the adjacent buildings to produce cracks or pipe deformation [7], or other engineering problems. Housel et al. [1] first reported the monitoring results of the piling process of precast concrete single pile with $d = 0.356$ m (d is the pile diameter) and $L = 24.0$ m (L is the pile length). They found that the deformation of soil around the pile was observed, while the measuring point at a distance of $2d$ from the pile axis was only slightly affected. Hwang et al. [8] studied the driving process of three precast concrete piles ($d = 0.8$ m). They found that the maximum radial displacement of the measuring point at a distance of $3d$ from the pile axis reached 29.0 mm, while the displacement of the measuring point at a distance of $9d$ was very small. Juan et al. [9] monitored the lateral horizontal displacement of ground at different depths during the driving process of a single steel pipe pile ($d = 0.61$ m and $L = 36.6$ m). The distribution of lateral displacement of each measuring point was in good agreement with the theoretical solution proposed by Vesic [10]. Xu et al. [11] studied the soil squeezing deformation during the driving process of single pile and double piles by model tests and obtained the qualitative characteristics of soil squeezing deformation around the pile. Lei et al. [12] carried out a field test of single PHC pile driving, and the monitoring data showed that the horizontal displacement of the measuring points at a distance of $(0.2–0.4)$ L from the pile axis was large.

Compared with precast pile, the impact of bored pile construction on adjacent soil is much smaller, but it cannot be ignored. Huang et al. [13] used the finite element method to study the influence of single bored pile on the adjacent tunnel. They found that the maximum displacement of the tunnel caused by the compression of the casing and the slurry was 5.5 mm when the bored pile was constructed at a distance of 1.5 m from the tunnel. Gao et al. [14] monitored the lateral displacement of soil caused by the Benoto construction of CBPs and found that Benoto construction had a greater impact on the soft soil.

From the above research, it can be found that regardless of the pile type, most of researches on soil squeezing deformation was focused on the process of single pile or group pile with few piles. However, the adverse effect of soil squeezing deformation on adjacent constructions usually occurs only in the case of large-area piling. In this case, the research on the distribution, influence range, and countermeasures of soil squeezing deformation caused by a large area piling should be further studied.

In this study, based on link-line subgrade engineering of Lunan High-speed Railway (LHR), a field test with 6 test zones that composed of prestressed pipe piles (PPPs), micro-grouting piles (MGPs), and cast-in-place bored piles (CBPs) was carried out to investigate the ground disturbance responses and the control effects of corresponding countermeasures.

2 Research Background

The LHR is the first railway line in China which performing the construction of the link-line in Qufudong railway station while the adjacent existing line is operating normally. The LHR adopts uplink-line and downlink-line to connect with Beijing-Shanghai High-speed Railway (BSHR) (see Fig. 1). Correspondingly, the subgrade of BSHR needs to be widened to meet the requirements of integration, and the foundation of link-line needs to be reinforced (see Fig. 2). However, the large-area piling in the foundation of link-line may have an adverse effect on the existing subgrade of BSHR. Therefore, it is necessary to carry out some tests to predict the squeezing deformation during the large-area piling on the foundation of BSHR subgrade.

The test area is located in the east of LHR, and its location is shown in Fig. 1. The test area belongs to alluvial proluvial plain landform with flat terrain. Figure 3 shows the distribution of the main strata and the mechanical parameters determined by the laboratory test. The strata mainly include artificial fill, silty clay layer (CL), and medium dense sand layer (SL). The buried depth of groundwater level is 11.2–13.5 m.
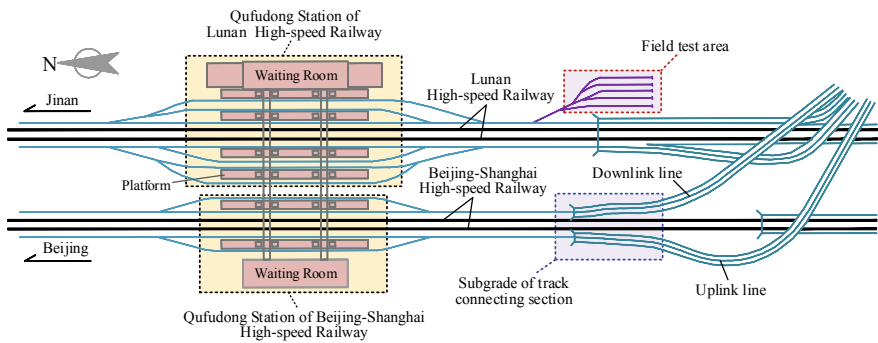
Fig. 1 Railway line layout of Qufudong station

Fig. 2 Profile of subgrade of track connecting section
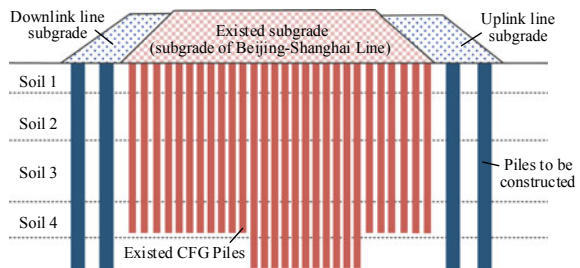
Fig. 3 Mechanical
properties of soils obtained
from laboratory tests
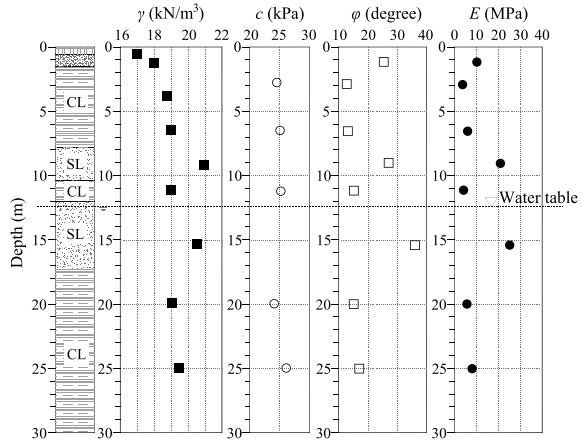
3 Field Test

3.1 Test Program Design

Three pile types including PPP, MGP, CBP were selected for comparative analysis, as shown in Fig. 4a. The test area was divided into 6 zones which named NO. I, NO. II, NO. III, NO. IV, NO. V and NO. VI. In NO. I, one row of CBPs were arranged, three in total, numbered 1#, 2#, 3#, respectively; in NO. II, 5 rows of MGPs were arranged; in NO. III, 5 rows of MGPs and 13 rows of PPPs without pre-drilled holes were arranged; in NO. IV, 14 rows of PPPs with pre-drilled holes with depth of 15 m were arranged; in NO. V, 8 rows of MGPs and 12 rows of PPPs without pre-drilled hole were arranged; in NO.VI, 5 rows of PPPs with pre-drilled hole with depth of 20 m and 9 rows of PPPs without pre-drilled hole were arranged, as shown in Fig. 4b. To investigate the control effect of different depth of pre-drilled hole on soil squeezing deformation, three kinds of depth including 0 m (without pre-drilled hole), 15 m, and 20 m were adopted. The piling order of each zone is shown in Fig. 4c.

3.2 Monitoring Instrument

A high-precision automatic monitoring system was established to monitor vertical and lateral displacement of the ground during the piling construction (see Fig. 5). The soil surface displacement was monitored by Leica Nova TS-60 with an accuracy of 0.6 mm and was automatically observed every 15 min, and the Leica Nova TS-60 is not within the scope of influence. The deep soil displacement of ground was monitored by inclinometer with an accuracy of 1.5 mm and was automatically

(a) Detailed structure of three types of piles

(b) Layout of test zones

(c) Piling order
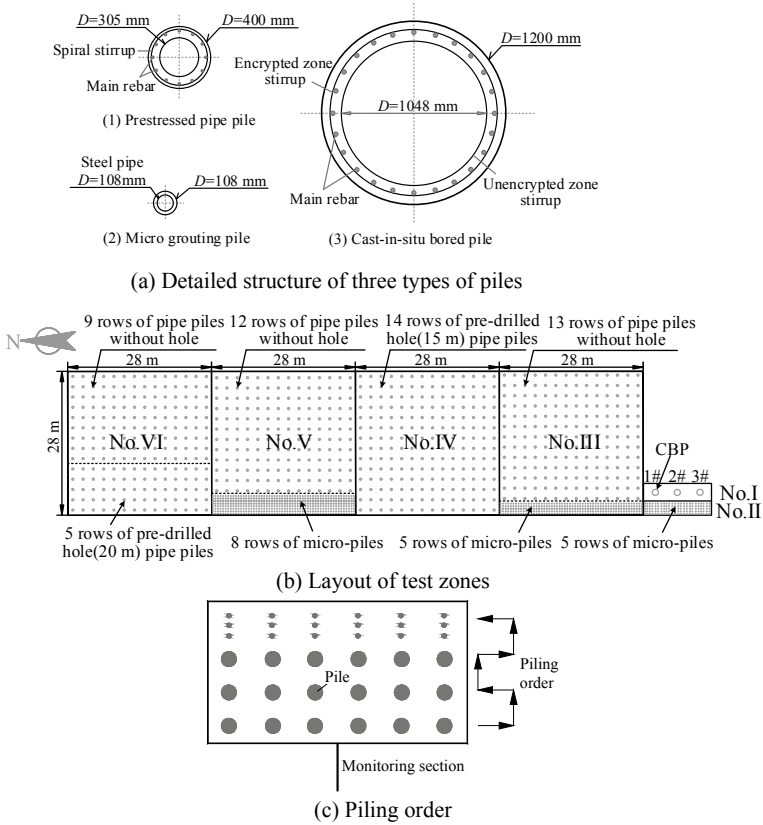
Fig. 4 Arrangement of piles in the test zones
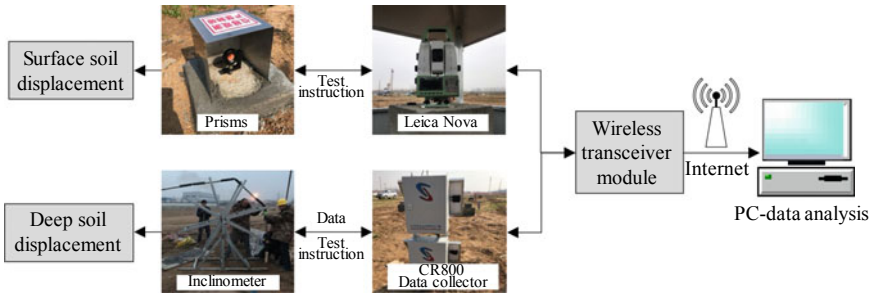
Fig. 5 A high precision automated monitoring system
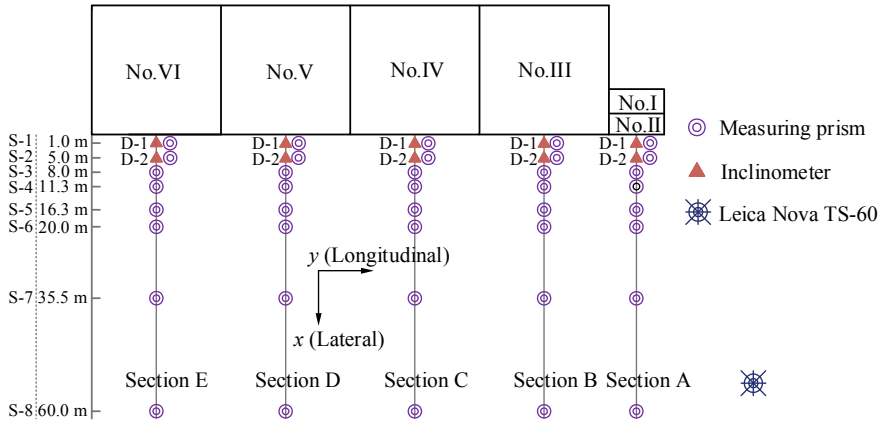
Fig. 6 Monitoring arrangements

Five typical monitoring sections (as shown in Fig. 6) were arranged at the central
line of 6 test zones, which were monitoring sections of A, B, C, D, and E, respectively.
Each monitoring section was equipped with 8 surface displacement measuring points,
which were 1.0 m, 5.0 m, 8.0 m, 11.3 m, 16.3 m, 20.0 m, 35.5 m, and 60.0 m away
from the boundary of the test zones, and the corresponding numbers were S-1 ~ S-8.
Two deep soil displacement measuring holes were set at 1.0 m and 5.0 m from the
boundary of the test zones, each hole was 30 m deep, and the corresponding numbers
were D-1 and D-2. In Fig. 6, x and y represent the horizontal displacement in the
lateral direction and the longitudinal direction, respectively.

4 Test Results and Analysis

4.1 Horizontal Ground Displacements

Figure 7 shows the distribution of lateral horizontal displacement along depth at
D-1 measuring hole in each monitoring section during the piling process. With the
increase of the number of PPP rows, the lateral horizontal displacement increases
gradually, and its development experiences rapid phase, slow phase, and stable phase,
successively. Take NO.VI as an example: during the piling process of the first seven
rows, the displacement develops fast and increases significantly because of the close
distance between the boundary of test zone and the measuring points; while during the
piling process of the 8th to 11th row, the distance between the boundary of test zone
and the measuring points increases gradually, and the soil stiffness increases with
the front pile, which has an isolation effect on the squeezing effect of the later pile,

(a) D-1 for NO.VI

(b) D-1 for NO.V

(c) D-1 for NO.IV

(d) D-1 for NO.III

(e) D-1 for NO.II and NO.I
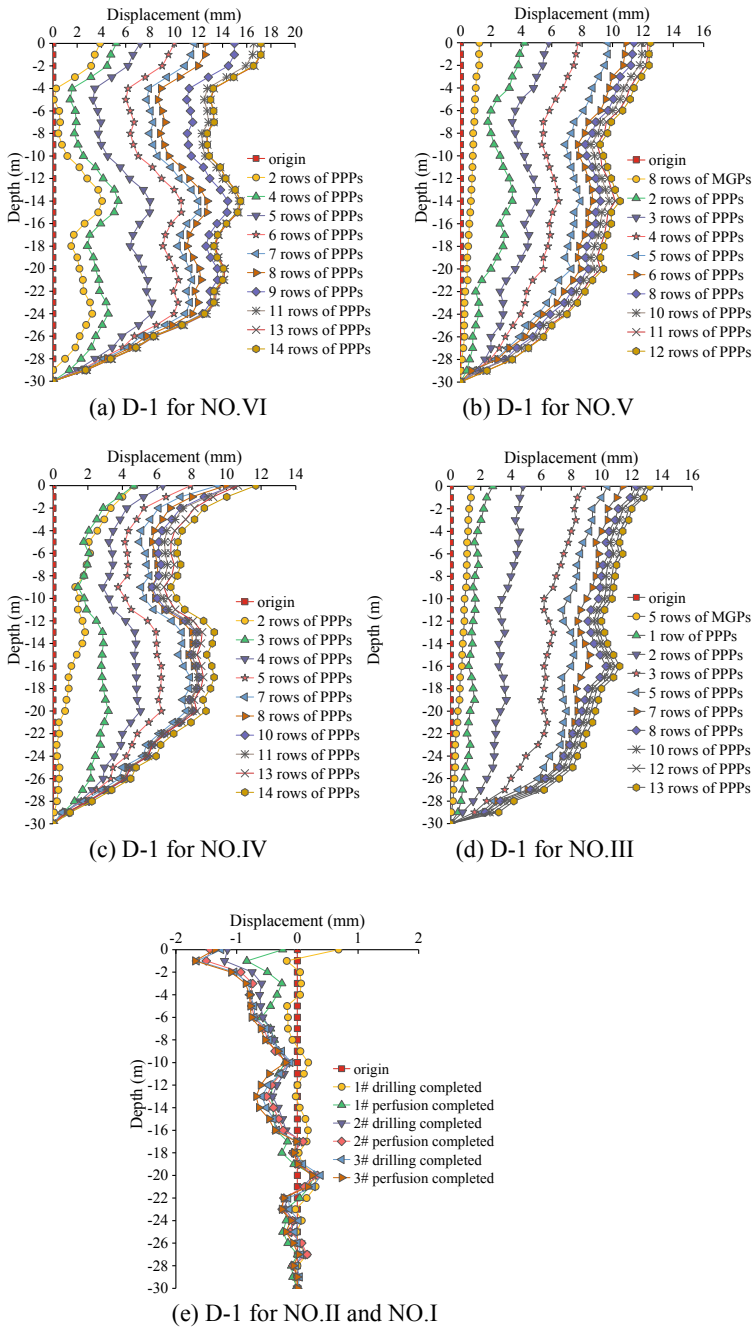
Fig. 7 Lateral horizontal displacement of ground

thus the displacement develops slowly. After the 11th row, affected by the distance and isolation effect, the measuring points gradually exceed the maximum range of soil squeezing deformation caused by pile driving, and the displacement increment is very small.

It should be noted that the distribution of horizontal displacement in depth varies greatly due to the different properties of soil layers at different depths. A coarse sand layer with the thickness of 5.3 m is distributed between 12 and 19 m depth (see Fig. 3), and the horizontal displacement of this layer is greater than that of other layers due to the low compressibility property of the coarse sand layer. Therefore, during the piling process, the problem of the deformation difference of adjacent piles along the depth caused by the difference in soil properties should be paid attention to in actual engineering.

The impact of MGPs piling on the ground is mainly reflected in two aspects: one is the disturbance to the soil during the drilling process, and the other is the pressure effect of grouting on soil. It can be seen from Fig. 7b and d that the lateral displacement of measuring hole caused by MGPs piling is very small, the maximum lateral displacement of NO.V is 1.2 mm, and that of NO.III is 1.4 mm, indicating that the impact of the piling construction of the MGPs on the adjacent ground is weak.

During the piling construction of CBPs, the rotation of the casing would drive the adjacent soil to deform due to the friction effect between the casing and the soil interface. In addition, the process of concrete pouring would squeeze the soil to deform on the sidewall of the CBP borehole. It can be seen from Fig. 7e that with the increase of the number of CBPs, the lateral horizontal displacement of ground develops in the negative direction of x. The main reason is that shrinkage occurs in the shallow soft silty clay during the drilling hole process, which causes the soil at the measuring point to move into the hole. Although the concrete compresses the soil during pouring, the displacement is not enough to cover the shrinkage deformation, resulting in the subsequent drilled to further increase the overall displacement in the negative direction. Therefore, for the piling construction of CBPs, the timely grouting of borehole is very important to prevent shrinkage deformation of adjacent soil.

4.2 Vertical Displacement of Ground Surface

Figure 8 shows the normalized relationship of the vertical displacement of ground surface with the distance between the boundary of test zone and the measuring points during the piling process. In the figure, S_Z is the vertical displacement of ground surface, r is the horizontal distance, d is diameter of pile. During the large-area piling of PPPs, the measuring points are obviously uplifted, and with the increase of the number of pile rows, the surface uplift displacement gradually increases, and its development trend is similar to the lateral horizontal displacement of measuring holes (see Fig. 7), experiencing rapid phase, slow phase, and stable phase, successively. With the horizontal distance between the boundary of test zone and measuring points

(a) Section E (*d* is diameter of PPP)

(b) Section D (*d* is diameter of PPP)

(c) Section C (*d* is diameter of PPP)

(d) Section B (*d* is diameter of PPP)

(e) Section A (*d* is diameter of CBP)
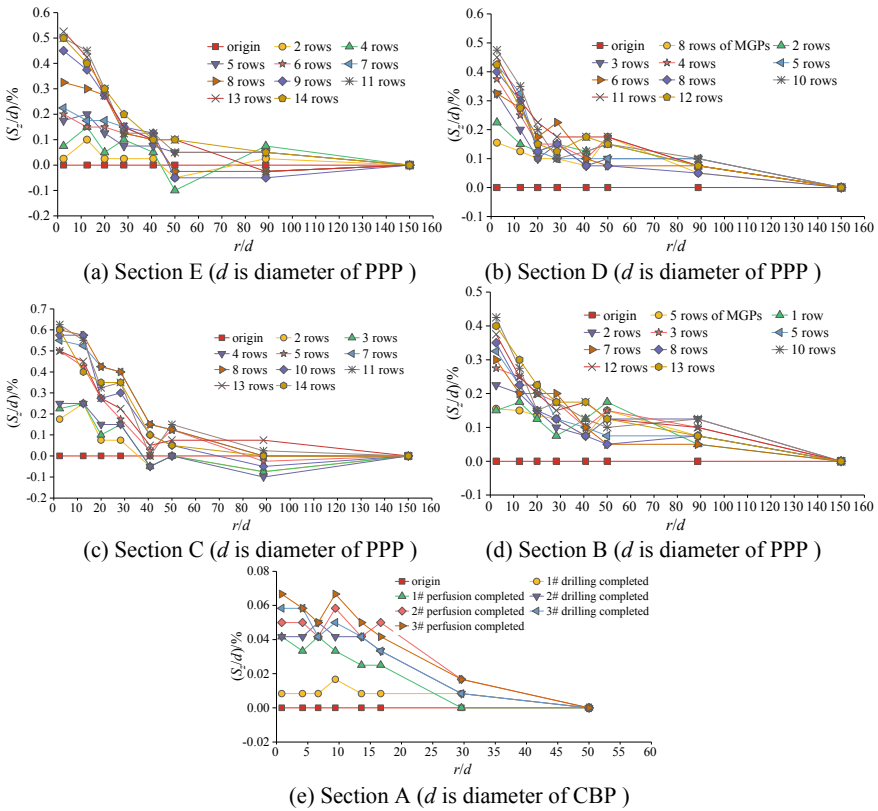
Fig. 8 Vertical displacement of ground surface

Table 1 Comparison of field test results with literature results

Literature	Pile diameter (mm)	Pile length (m)	Maximum uplift displacement	Influence range	Piling method	Number of piles
Xu[11]	45	1.0	7.1%*d*	(3–5)*d*	Top driving	Single
Present study	400	30.0	(0.6–0.8)%*d*	30*d*	Holding	Pile group
Zhou [16]	500	30.0	(2.5–4.5)%*d*	8*d*	Holding	Single
Hwang [8]	800	34.0	3.8%*d*	16*d*	Hammering	Three

increases, the surface uplift shows exponential attenuation, which is consistent with the distribution of numerical simulation results in Reference [15]. In addition, the horizontal influence range of vertical displacement caused by the piling of PPPs is about 30*d*, and the maximum uplift displacement is (0.6–0.8)%*d*.

Table 1 shows the comparison between the results of this test and the results of literature. Compared with the construction of group pile with few piles, the influence range of surface uplift deformation caused by the large area piling of PPPs is larger, but due to the effect of pre-drilled holes, the surface uplift is relatively smaller.

It can be seen from Fig. 8b and d that the vertical displacement of the ground surface is very small after the piling construction of MGPs, the maximum value is only 0.175%d (d is diameter of PPP). It can be seen from Fig. 8e that the influence of three CBPs on the vertical displacement of ground surface is weak, and the maximum value is only 0.067%d (d is diameter of CBP).

4.3 Effects of Pre-Drilled Hole on Soil Displacement

Pre-drilled hole can greatly reduce the volume of soil that needs to be removed during the process of pressing the pile into the soil, thereby reducing the surface uplift and horizontal deformation around the pile. Figure 9 compares the lateral horizontal displacement during the piling process between NO. VI and NO. IV. When the pile driving of first 5 rows are completed, the horizontal displacement of NO. VI at the D-1 measuring hole is basically the same as that of NO. IV.

After the pile driving is completed, the lateral horizontal displacement at the measuring holes caused by the driving of the last 9 rows without pre-drilled hole in NO. VI is higher than that in NO. IV (the last 9 rows were driven with pre-drilled hole with a depth of 15 m). The lateral horizontal displacement of the surface caused by the last 9 rows of piles in the two zones is extracted, as follows: in D-1 measuring
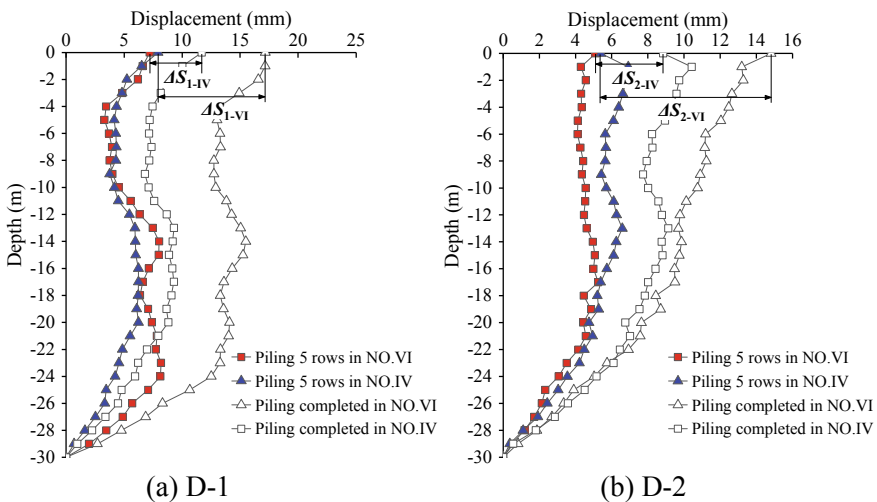
Fig. 9 Comparison of lateral horizontal displacement between NO. IV and NO. VI

hole, $\Delta S_{1\text{-VI}}$ of NO. VI is 10.0 mm, $\Delta S_{1\text{-IV}}$ of NO .IV is 3.8 mm (see Fig. 9a); in D-2 measuring hole, $\Delta S_{2\text{-VI}}$ of NO. VI is 9.6 mm, $\Delta S_{2\text{-IV}}$ of NO. IV is 3.5 mm (see Fig. 9b). It can be seen that the surface horizontal displacement caused by the last 9 rows of piles without pre-drilled hole is about 3 times the displacement caused by the last 9 rows with the pre-drilled hole of depth 15 m. It can be concluded that under the same piling range, the displacement caused by the piling with pre-drilled hole is more than three times smaller than the displacement caused by the piling without pre-drilled hole. To sum up, under the soil condition in the test of this study, the 15 or 20 m depth pre-drilled hole has a significant effect on the prevention and control of soil squeezing deformation, and the deeper the pre-drilled hole depth, the more significant the control effect.

4.4 Lateral Disturbance Influence Range

The influence range of adjacent soil deformation caused by the piling is a focus of attention of scholars [12, 16]. The determination of the influence range plays an important role in guiding adjacent buildings (structures) to take reasonable prevention and control measures. Figure 10 shows the influence range of horizontal displacement on the ground surface in each test zone during the piling process. It can be seen that with the number of pile rows increases, the maximum influence range increases in a stepped way. This is mainly because the number of measuring points in this paper is limited, and only the distance of measuring points is used to determine the maximum influence range. During the piling process, NO.VI and NO. IV reached the maximum influence range first than NO. V and NO. III. After the pile driving is completed, the maximum influence range of lateral horizontal disturbance in four test zones is 35.5 m, about 88 times of pile diameter.

Fig. 10 Comparison of lateral disturbance range of ground surface of each zone
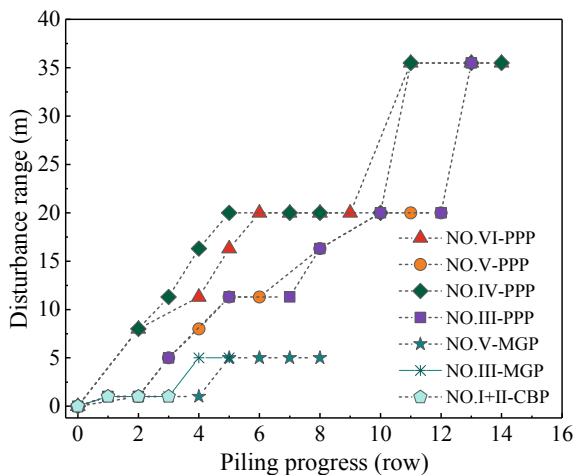
If the foundations in the uplink-line and downlink-line of BSHR are reinforced with PPPs with the same piling range as this test, then the existing foundation of BSHR is within the maximum range affected by soil squeezing deformation. Therefore, it is not recommended to use PPPs in this project. Compared with PPPs, the maximum influence range of soil squeezing deformation caused by MGPs or CBPs is smaller, not exceeding 5 m.

5 Conclusions

A field test was carried out to investigate the disturbance deformation of ground during the large-area piling process, and to guide the foundation reinforcement of new link-lines adjacent to existing lines, and the following conclusions were obtained:

(1) During the piling process, the lateral horizontal displacement decreases along the depth, and its distribution is related to the soil properties. The surface uplift displacement decreases exponentially with the increase of the distance between the boundary of test zone and the measuring points. Under the same piling range, the disturbance deformation caused by the PPPs is much larger than that caused by the MGPs and CBPs.

(2) The influence range of lateral horizontal displacement caused by the piling of PPPs is larger than that of vertical displacement. Under the soil condition of this study, the maximum influence range of lateral deformation is approximately $88d$ (d is the diameter of PPP), and the maximum influence range of vertical deformation is approximately $30d$. Affected by the pre-drilled hole, the maximum lateral horizontal displacement is 17.2 mm, and the maximum uplift displacement is $(0.6\text{–}0.8)\%d$. The maximum influence range both of lateral and vertical deformation caused by the piling construction of MGPs and CBPs are less than 5.0 m.

(3) Under the same piling range, the lateral horizontal displacement caused by the piling of PPPs with no pre-drilled hole is more than three times larger than that caused by the piling with a pre-drilled hole with depth of 15 m, indicating that the pre-drilled hole with a depth of 15 m has a significant control effect on the soil squeezing deformation. The control effect of the pre-drilled with a depth of 20 m is better than that with a depth of 15 m.

References

1. Housel WS, Burkey JR (1948) Investigation to determine the driving characteristics of piles in soft clay. In: proceedings of 2nd international conference on soil mechanics foundations engineering, Rotterdam, The Netherlands, 146–154

2. Fellenius BH, Samson L (1976) Testing of drivability of concrete piles and disturbance to sensitive clay. Can Geotech J 13(13):139–160
3. Randolph MF, Wroth CP (2010) An analytical solution for the consolidation around a driven pile. Int J Numer Anal Meth Geomech 3(3):217–229
4. Roy M, Blanchet R, Tavenas F et al (1981) Behaviour of a sensitive clay during pile driving. Can Geotech J 18(1):67–85
5. Li X, Cai G, Liu S et al (2019) Undrained shear strength and pore pressure changes due to prestress concrete pile installation in soft clay. Int J Civil Eng 17(2):193–203
6. Tho KK, Chen Z, Leung CF et al (2014) Enhanced analysis of pile flexural behavior due to installation of adjacent pile. Can Geotech J 51(6):705–711
7. Wang J, Xiao C, He C (2017) Numerical analysis of effect of jacked pile on performance of buried pipes. J Southwest Jiaotong Univ 53(2):322–329
8. Hwang JH, Liang N, Chen CH (2001) Ground response during pile driving. J Geotechn Geoenviron Eng 127(11):939–949
9. Pestana JM, Hunt CE, Bray JD (2002) Soil deformation and excess pore pressure field around. J Geotech Geoenviron Eng 128(1):1–12
10. Vesic AS (1972) Expansion of cavity in infinite soil mass. J Soil Mech Foundat Divis 98(3):265–289
11. Xu J, Zhou J, Xu C et al (2000) Model test research on pile driving effect of squeezing against soil. Rock Soil Mech 21(3):235–238
12. Lei H, Li X, Lu P et al (2012) Field test and numerical simulation of squeezing effect of pipe pile. Rock Soil Mech 33(04):1006–1012
13. Huang D, Zhou S, Liu C et al (2013) Analysis of small disturbing construction of protective jacket tube for cast-in-situ bored pile. Rock Soil Mech 34(4):1103–1108
14. Gao G, Zhuang Y, Wang K et al (2019) Influence of Benoto bored pile construction on nearby existing tunnel: A case study. Soils Found 59(2):544–555
15. Luo Z, Gong X, Wang J et al (2005) Numerical simulation and factor analysis of jacked pile compacting effects. J Zhejiang Univ (Eng Sci) 07:992–996
16. Zhou H, Shi J (2009) Test research on soil compacting effect of full scale jacked-in pile in saturated soft clay. RockSoil Mech 30(11):3291–3296

Simulating Water Balance of Road Embankment Lysimeters

Manuel Melsbach and **Emanuel Birle**

Abstract An alternative to dumping mineral materials containing moderate amounts of contaminants into landfills is to reuse them in road embankments and noise protection barriers. To ensure groundwater protection, seepage of precipitation water through these materials must be omitted or reduced to a minimum. Embankments consisting of both cohesive and coarse-grained soil materials under various designs of cover layers were investigated within six field lysimeters. To gain the understanding of the water balance, quantities of seepage water, as well as runoff in the cover layers and on the surface were monitored. When using moderately contaminated materials in earthworks, reliable prediction of the water balance is crucial. Thus, in this study 2.5 years of the lysimeter experiments were modeled using the finite element software Vadose/W. Results were compared to the experimental data. The unsaturated hydraulic characteristics of the core materials were known from experimental investigations. Those of the topsoil and the shoulder material were estimated from databases of similar soils. A climate boundary condition represented the daily mean of the actual climate data on-site including road runoff. The modeled water balances were in good agreement with the field data for the cohesive core material of low permeability. However, a tendency to overestimate of seepage water was observed, which was even higher in the lysimeters with coarse-grained materials. This is linked to the water-permeability of the shoulder material and demonstrates that the cover layers have a major influence on the water balance of the whole embankment.

Keywords Water balance · Seepage · Unsaturated soil · Lysimeter · Modeling · Groundwater protection · Road embankment

M. Melsbach (✉) · E. Birle
Technical University of Munich, Franz-Langinger-Str. 10, 81245 Munich, Germany
e-mail: m.melsbach@tum.de

E. Birle
e-mail: e.birle@tum.de

1 Introduction

A major challenge of the construction industry is to conserve natural resources and reduce the amounts of mineral waste being dumped into landfill as capacities are limited. Following this idea, an alternative to dumping excavation materials containing moderate amounts of contaminants and environmentally hazardous substances is to reuse them as construction or building material. Potential fields of application are road and railway embankments as well as noise protection barriers. To avoid the elution of contaminants from these materials, seepage water quantities must be reduced to a minimum to ensure groundwater protection over the whole lifespan of the earthwork. Prevention of seepage can be achieved by constructive measures, such as geo-membranes and other means of sealing. The design guideline MTSE [1], established by the German Association for Road Construction and Traffic Affairs (FGSV) suggests a variety of sealing design methods. Method E provides a special design, which uses mineral materials of low permeability (5 × 10^{-8} m/s) within the embankment core and avoids additional sealing elements as geo-membranes or clay liners. This design has been subject to closer investigation in field lysimeter tests to gain better understanding of the water balance of road embankments [2, 3]. Amounts of seepage water leaching from the core, interflow, and surface runoff were monitored over a period of several years.

A key to reuse contaminated materials in the future is a reliable prediction of their hydraulic behavior, which can be achieved by numerical modeling if models are well-calibrated [4]. Michaelides et al. [5] simulated the water balance of a large-scale test fill at Munich Airport. They found that the amount of infiltration notably depends on rainfall intensity amongst others. Modeling with mean values of precipitation and climate data over longer time periods like weeks or months, led to biased results. Yao et al. [6] compared the water content measurements from frequency domain reflectometry (FDR) probes within a road embankment to simulation results. Both data sets show that rainfall events mainly influence the water content in embankment sections close to the surface. This was also observed in numerical studies in soils with low conductivity [7].

Simulations of landfill cover tended to overestimate percolation from mineral sealing layers, despite the availability of laboratory data of the hydraulic material behavior [8]. Koukoulidou and Birle [7] simulated a significant reduction of seepage water when a drainage element was present above an embankment core of coarse material. Beyer et al. [9] also observed a capillary barrier effect of topsoil towards a coarse embankment material with a numerical analysis in GeoSys. This could also be shown in lysimeter tests under laboratory conditions [10].

Furthermore, it is essential to account for processes at the surface like evaporation and transpiration [11] and to correctly model properties of the shoulder material to gain reliable simulation results of the water balance [12].

Comparison between numerical models and actual monitoring data of seepage water quantities from traffic embankments have so far been rare.

1.1 Aims and Objectives

To gain knowledge about construction and design measures of embankments, the Federal Highway Research Institute (BASt) [2] investigated the water balance of road embankments in lysimeters adjacent to a road with two lanes in Augsburg/Germany. Three embankment sections consisted of soil with fine-grained material, covered with shoulder material on the verge, and topsoil in the sloped section, both with a grass cover. In lysimeters 2 and 3, a geo-composite drainage layer and a mineral drain were installed between topsoil and embankment material. Leachate from the cores of the embankment sections was collected in a pan with an impermeable base and quantified by tipping buckets. Surface runoff and intermediate flow from the top soil and a drainage layer (where present) were collected and quantified in the same way. Three lysimeters (6, 7, and 8) with a coarse embankment core were used as reference.

In this study, the water balances of these lysimeters were simulated by means of numerical modeling and the results compared to measurement data. The aim is to gain knowledge on reliability of the prediction of the water balance and which aspects have to be considered when modeling is utilized for design purposes in construction projects. Findings of this study can also help to optimize and enhance design methods.

2 The Numerical Model

The model was set up in Vadose/W supplied by GeoSlope International Ltd. The simulation period runs over 927 days from September 17, 2011 to March 31, 2013. Two-hour time steps were chosen, resulting in 11,124 steps. Differential water transport under unsaturated conditions is described by the nonlinear differential equation by Richards:

$$\frac{\partial}{\partial x}\left(k_x(\theta) \cdot \frac{\partial H_m}{\partial x}\right) + \frac{\partial}{\partial z}\left(k_z(\theta) \cdot \left(\frac{\partial H_m}{\partial z} + 1\right)\right) = C(H_m)\frac{\partial (H_m)}{\partial t} \qquad (1)$$

where x and z are the Cartesian coordinates for a two-dimensional model, k_x and k_z describe the hydraulic conductivity depending on θ. H_m is the matric potential and the capillary capacity $C(H_m)$ is defined as

$$C(H_m) = \frac{\partial \theta}{\partial H_m} \qquad (2)$$

Richards' equation is usually solved by numerical methods. To couple heat and mass transfer, Edlefsen and Anderson established a relationship between the parameters pressure, temperature, and vapor pressure [13]. Processes at the surface are

accounted for by atmospheric coupling with the relationship by Penman-Wilson [13].

2.1 Model Geometry

The model geometry was chosen according to the dimensions of the field lysimeters. Figure 1 shows the model geometries with boundary conditions and the sections, where seepage water as well as interflow and runoff were evaluated. Table 1 summarizes the soil classification of the core materials and the different setups of all lysimeters.

Additionally, two variations of lysimeter 6 were modeled. The saturated hydraulic conductivity of the shoulder material was reduced by two orders of magnitude to 1.5×10^{-5} m/s in variation 6.1 and three orders of magnitude to 1.5×10^{-6} m/s in variation 6.2.
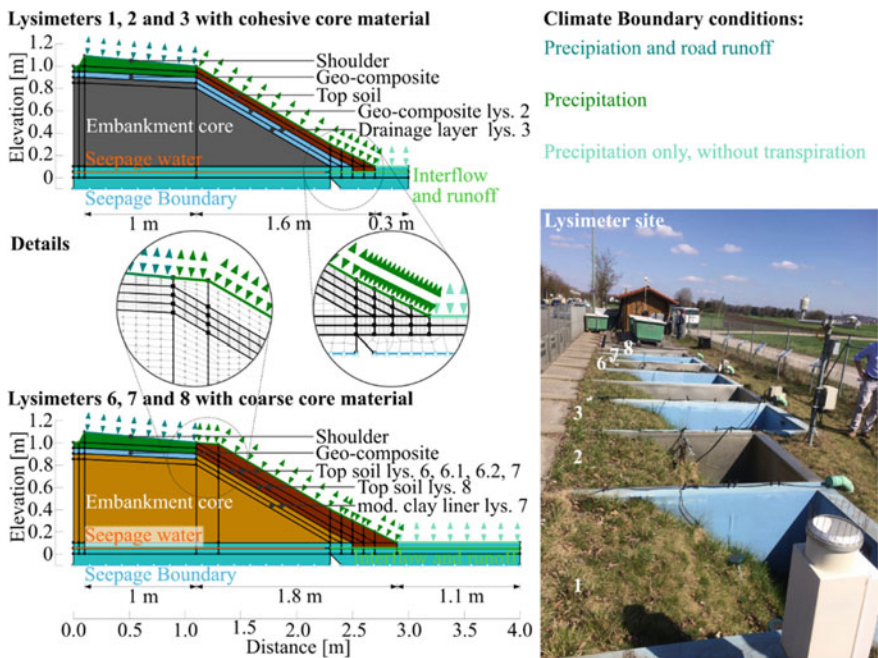
Fig. 1 Model geometry of the lysimeters with boundary conditions and mesh details. Sections of seepage water quantification (orange line) as well as interflow and surface runoff (green line) are marked. The collection pan is highlighted in turquoise. Right side: photo of the lysimeter site with lysimeter numbers

Table 1 Soil classification parameters of the core materials and overview on the setups of the different lysimeters according to the actual in-situ geometries [2]

Cohesive soil SC*								Coarse soil SW*							
Cl	Si	Sa	Gr	d_{10}	d_{60}	w_{pr}	ρ_{pr}	Cl	Si	Sa	Gr	d_{10}	d_{60}	w_{pr}	ρ_{pr}
[%]	[%]	[%]	[%]	[mm]	[mm]	[%]	[g/cm³]	[%]	[%]	[%]	[%]	[mm]	[mm]	[%]	[g/cm³]
2	25	49	24	0.01	0.36	9.0	2.02	0	3	40	57	0.30	4.78	7.7	2.25

Lysimeter	Slope	Lysimeter	Slope
1	Topsoil 10 cm	6, 6.1, 6.2	Topsoil 20 cm
2	Topsoil 10 cm, drainage geo-composite	7	Topsoil 20 cm, Mod. mineral clay liner 10 cm
3	Topsoil 10 cm, mineral drainage layer	8	Topsoil 10 cm

*According to the Unified Soil Classification System USCS, ASTM D-2487

2.2 Hydraulic Parameters of Embankment Materials

The embankment cores of lysimeters 1, 2, and 3 consisted of fine-grained material SC. Lysimeters 6, 7, and 8 contained coarse material SW in the embankment core. Their unsaturated hydraulic properties had been previously determined in the laboratory by Scharnagl and Durner [14] with the simplified evaporation method after Schindler [15]. The soil–water retention curve (SWRC) and the unsaturated hydraulic conductivity are shown in Fig. 2 As input data for the simulation, the actual laboratory results were directly fed into Vadose/W.

The hydraulic parameters of the layers at the surface (topsoil, shoulder material, and drainage layer) were unknown and had to be estimated according to their characteristics of classical soil mechanics. Grain size distribution and dry density were compared to soils from databases. For the topsoil on the slope section, the hydraulic characteristics of a loamy silt were sourced from the Soilvision database [16]. Those of a silty gravel from Ekblad and Isacsson [17] were applied to the shoulder material. Its saturated hydraulic conductivity was set to 1.5×10^{-3} m/s as determined in the laboratory on the actual material at proctor density.

Schanz et al. [18] determined hydraulic characteristics of the modified mineral sealing, a sand with bentonite and polymeric additives, used in lysimeter 7.

As the hydraulic characteristics of drainage geo-composites show very steep curves due to the uniformity of their pore system [19], numerical problems could be caused [13]. Thus, the hydraulic parameters of a coarse gravel were chosen from Ekblad and Isacsson [17]. The air-entry value of the material was adjusted according to Melsbach and Birle [20]. The same material was used for the gravel within the
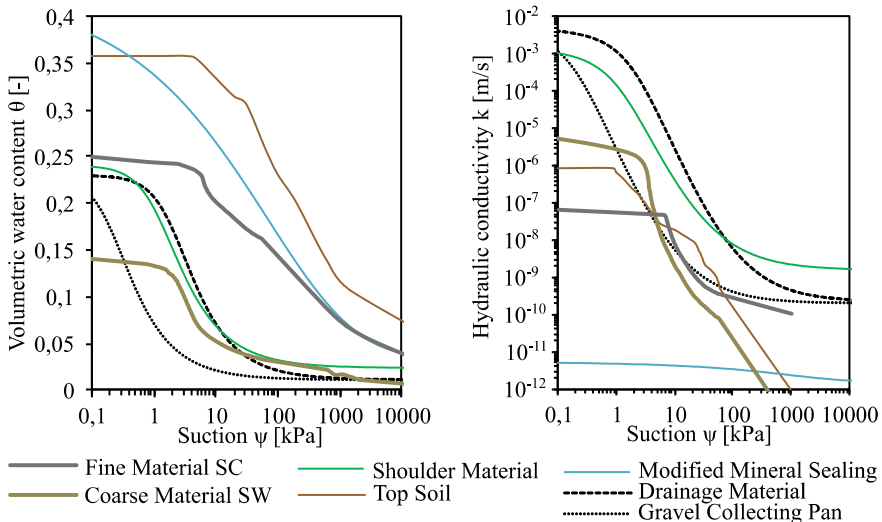
Fig. 2 SWRC and unsaturated hydraulic conductivity of the materials used in the simulation

Table 2 Hydraulic and thermal characteristics of the soil and drainage materials used in the simulation

Soil	Hydraulic						Thermal	
		van Genuchten Parameters						
	k_s	θ_s	θ_r	α	n	m	λ_{solids}	$c_{p\ solids}$
	[m/s]	[-]	[-]	[1/cm]			[J/s/m/°C]	[kJ/g/°C]
Coarse Material SW	1.0×10^{-5}	-	-	-	-	-	2.4	7.1×10^{-4}
Fine Material SC	6.6×10^{-8}	-	-	-	-	-	1.8	1.7×10^{-3}
Shoulder Material GW-GM	1.5×10^{-3}	0.24	0.02	0.085	1.73	0.42	2.4	7.1×10^{-4}
Topsoil SM	8.7×10^{-7}	-	-	-	-	-	1.8	1.7×10^{-3}
Modified Mineral Sealing	5.4×10^{-12}	0.42	0.03	5×10^{-7}	0.32	13.4	1.8	1.7×10^{-3}
Drainage Material (GP)	5.0×10^{-3}	0.23	0.01	0.05	1.79	0.44	2.4	7.1×10^{-4}
Gravel Collecting Pan GP	5.0×10^{-3}	0.23	0.01	0.5	1.79	0.44	2.4	7.1×10^{-4}

collection pan at the base of the lysimeter but with a lower air-entry value to avoid capillary rise. Hydraulic properties are shown in Fig. 2.

Thermal storage capacity and thermal conductivity were derived from the VDI table [21]. Table 2 shows the characteristics of all materials used in the simulation.

2.3 Boundary Conditions

Hydraulic boundaries. At the base of the model, a flux boundary of 0 m/s with potential seepage face review was applied. The boundary condition allows downward flux in case of a positive pressure head but prohibits upward flux that could occur in the model due to negative matric suction but would not be possible in-situ due to the collection of seepage water with the pan. The vertical sections at the sides of the model are water- and airtight.
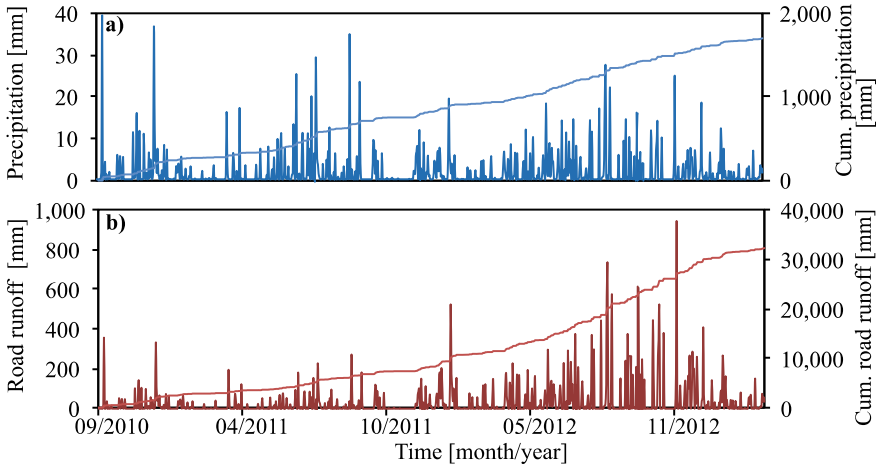
Fig. 3 Daily mean and cumulative water volume of **a** precipitation and **b** road runoff at lysimeter 1 (Data provided by BASt)

Climate Boundary Condition. A climate boundary condition represents processes at the surface by computing water and vapor flux depending on the current states of soil, atmosphere, and plant growth. This study used daily means of climate data.

Precipitation and Road Runoff. Figure 3 shows the rain regime for the simulation period and the road runoff on the example of lysimeter 1.

Precipitation data was recorded by a pluviometer adjacent to the lysimeters. Road runoff varied, as each lysimeter had a unique catchment area that differs depending on rain intensities. Catchment areas had thus to be estimated by a variety of approaches analyzing the measured fluxes and precipitations [2]. For the present simulation, the total influx to the lysimeter was determined by measurement of the total flux from the lysimeters during the winter months, when evaporation is low.

Handling high amounts of road runoff in addition to rainfall on the lysimeters is difficult in numerical models. Water, that cannot infiltrate in one section of the model, i.e. the shoulder, will be withdrawn from the model and computed as surface runoff. Thus, it is not automatically reallocated to another section, i.e. the slope, where there might be higher infiltration potential. To mitigate this problem, two consecutive calculation runs of the model were executed. The runoff in the shoulder section determined in the first calculation run was assigned to the slope section for the second run as illustrated in Fig. 4.

Evaporation and Transpiration. Other climate data for the simulation period was taken from a weather station of the German Meteorological Service (DWD) at Augsburg Airport, at a distance of approximately 4 km from the lysimeter site. The net radiation, which mainly controls transpiration was estimated from temperature and relative humidity according to the FAO [22] method. The data was compared and adjusted to data that was logged next to the lysimeters in 2015 after the simulation period. Therefore, net radiation in 2015 was calculated from temperature and relative
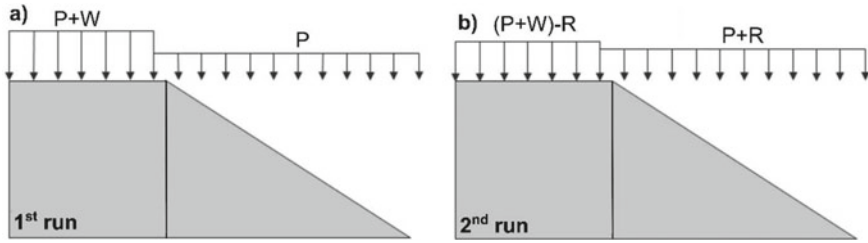
Fig. 4 Reallocation of runoff from **a** the shoulder section to **b**)the slope section in the second calculation run. P Precipitation, W road runoff, R Runoff in the shoulder section

humidity data from the DWD weather station and adjusted to data from the station at the lysimeters by least-square fitting.

A Leaf Area Index (LAI; ratio of leaf area to ground surface area) of 3 was estimated for the summer months, decreasing to 0 in winter [13]. The Plant Moisture Limiting Function (PML) describes the relation between actual and potential plant water uptake. It was set to 100% at field capacity ($\psi = 6.3$ kPa) with a linear decline to 0% at the permanent wilting point ($\psi = 1500$ kPa) [13].

2.4 Initial Conditions

Equilibrium of water potential within the model is derived from an initial water table at -1 m below the base of the dam core (hydrostatic initial condition). Although the actual water content at compaction is disregarded by this assumption, numerical problems due to differences in matric suction between the different layers can be avoided. Considering the large water quantities from precipitation and road runoff, the impact on the results is marginal.

3 Results and Discussion

Figure 5 shows the cumulative water balance of the lysimeters with fine material SC within the embankment core. Precipitation and road runoff result in interflow and surface runoff, seepage water, evaporation, and transpiration. Dashed lines show the results of the second calculation run.

The results show that seepage water quantities are low in proportion to the total amount of collected water at 17.5% in lysimeter 1. With the drainage geo-composite between topsoil and embankment core in lysimeter 2, seepage water is even lower at 8.6%. In lysimeter 3 however, the proportion of seepage water at 11.4% is higher than in lysimeter 2. Lysimeter 3 has a 10 cm drainage layer of coarse gravel, which was also adopted in the model. The drainage geo-composite in lysimeter 2 was modeled
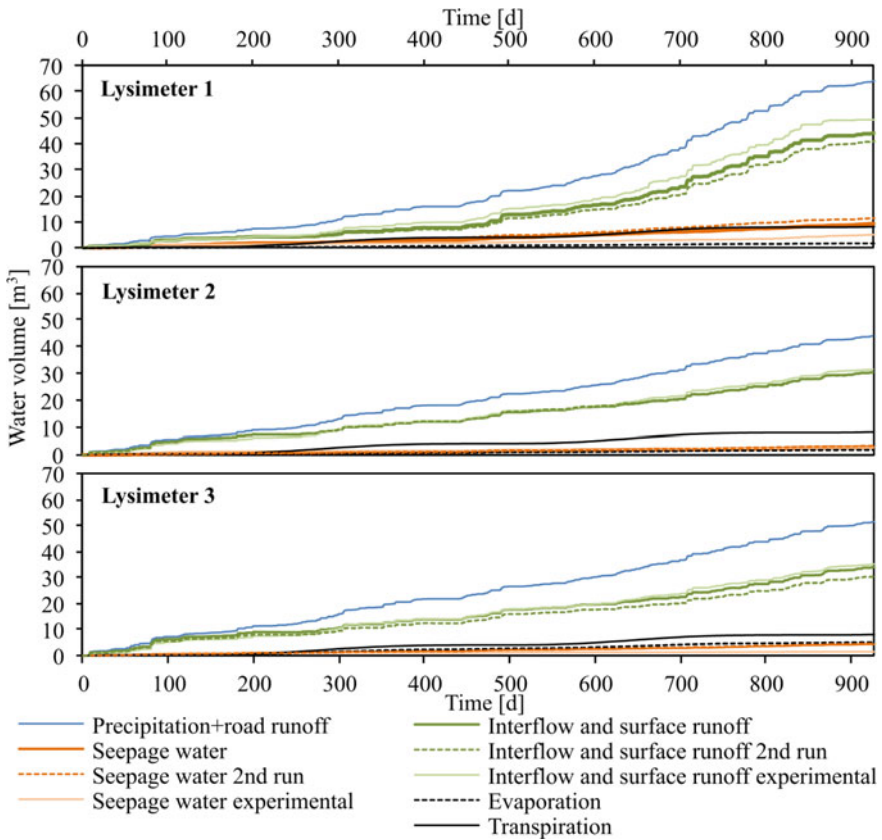
Fig. 5 Water balance of lysimeters with fine-grained material in the embankment core

with the same material properties but with a thickness of only 5 cm. This indicates that model geometry matters. The drainage layer in the model of lysimeter 3 is larger in volume, meaning it has a higher storage capacity and thus releases water to the core over a longer time after a rainfall event. Obviously, this enhances infiltration into the core, leading to an increase of seepage water in the model.

In comparison to the site data, seepage water quantities are overestimated by approximately 7.8% in lysimeters 1 and 3. In lysimeter 2, the overestimation is at 0.5% and thus, a very good result. As expected, overestimations of seepage water proportions in the second run increase in lysimeters 1–3 to 11.6%, 1.8% and 8.5%, respectively. This is due to more water being distributed on the slope section, where infiltration increases. In lysimeter 1, this increase is especially high, as there are no drainage elements to allow significant lateral flow. However, considering the distribution of road runoff on the surface, the second run is closer to reality.

In lysimeters with coarse-grained embankment material SW (Fig. 6), modeled results and site data tend to be more divergent than in the lysimeters with fine-grained material. Overestimation of seepage water-related to measured seepage water in lysimeters 6, 7 and 8 is at 28.8%, 32.6%, and 54.7%, respectively.

These results suggest that the shoulder material has a lower permeability than the value of $k = 1.5 \times 10^{-3}$ m/s. This could be caused by a self-densification and clogging of fine particles that were transported into the material by road runoff. Due to the geometry of the lysimeters, the geo-composite layer underneath the shoulder material cannot discharge significant volumes of water in lateral direction, neither in the field nor in the simulation. Thus, infiltrating water is stored within the geo-composite layer in the shoulder section and eventually percolates into the embankment core adding to the volume of seepage water.

Figure 7 gives an overview of the cumulative water balances of the simulated lysimeters including variations of lysimeter 6. In variation 6.1, where saturated
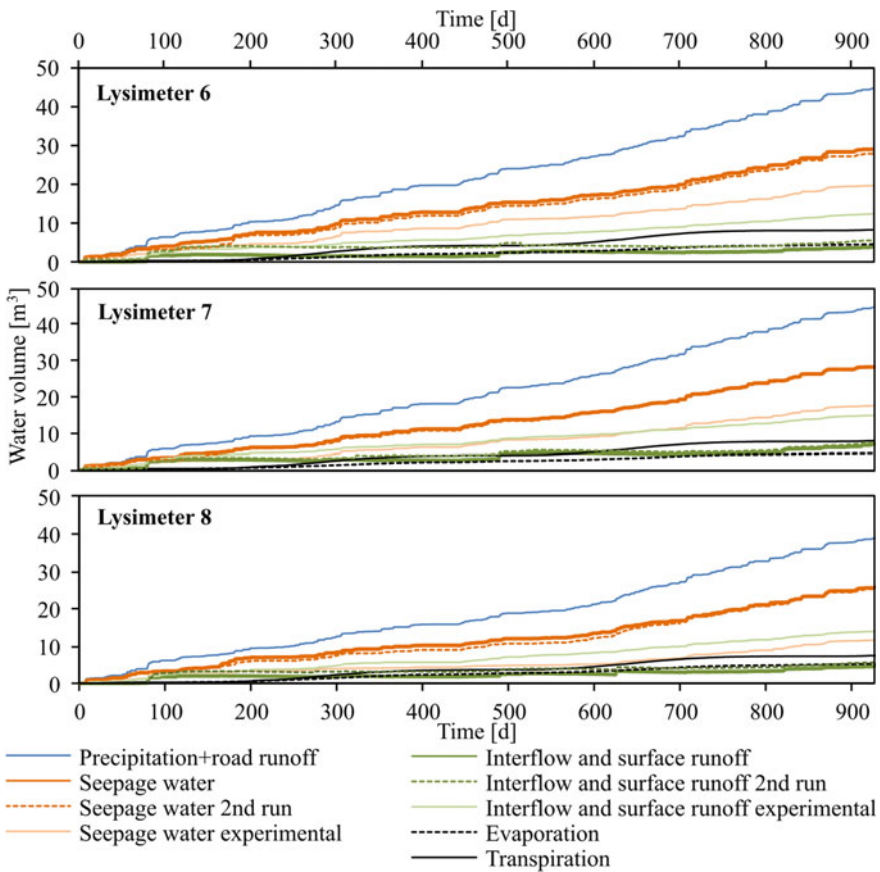
Fig. 6 Water balance of lysimeters with coarse-grained material in the embankment core
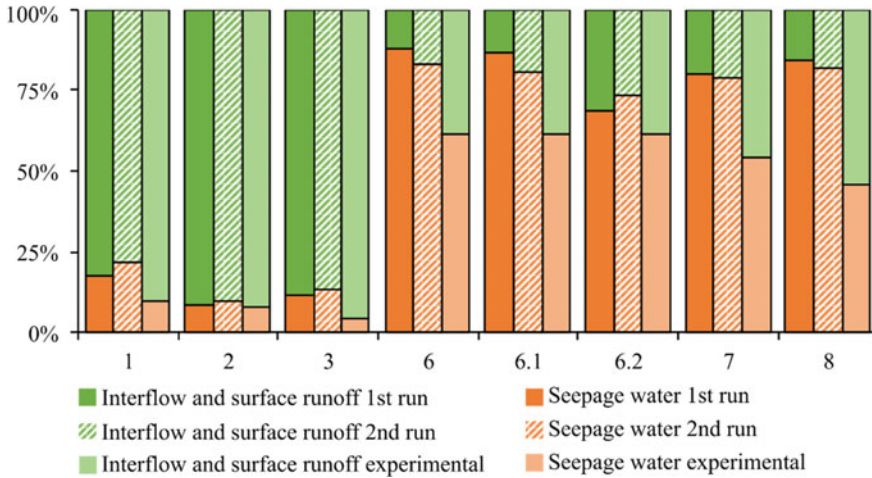
Fig. 7 Overview on the ratios of seepage water (orange) to interflow and surface runoff (green) of lysimeters 1, 2, 3, 6, 7, 8 and the variations of lysimeter 6 with reduced saturated conductivity of the shoulder material

conductivity of the shoulder material was reduced to $k = 1.5 \times 10^{-5}$ m/s, seepage did not decrease significantly. Only at $k = 1.5 \times 10^{-6}$ m/s in variation 6.2 a significant reduction of seepage water and thus an increase in surface runoff could be observed.

Reallocation of surface runoff from the shoulder section to the slope section in the second run did not return great differences. This could be expected due to the good saturated conductivity of shoulder material and top soil on the slope. Thus, runoff only happens at very few events of heavy rain and can mostly infiltrate in the slope section after reallocation.

4 Conclusions

Although hydraulic parameters of the soil layers at the surface had to be estimated, the numerical models of the lysimeters return water volumes in good accordance with the site data. However, in all setups, a tendency to overestimation of seepage water quantities can be observed. In lysimeters with fine material SC, overestimation is low, especially in lysimeters 2 and 3, which have drainage elements in the slope section. With respect to the aim of groundwater protection, these setups have the lowest amount of seepage water and are thus favorable designs.

Further, the results show, that the layers at the surface have a major influence on the total water balance. For the drainage geo-composite, the hydraulic properties of a gravel, adjusted to function as a drainage layer [20] provided good modeling results. However, this approach does not consider product-specific characteristics of different

geo-composites. This should be subject to further research to achieve a reliable basis for implementation of drainage geo-composites into a numerical model.

Overestimation of seepage water volumes was even higher in the lysimeters with coarse embankment materials SW. This can be partly linked to the saturated conductivity of the shoulder material, which seems to be lower than the laboratory value which might originate from subsequent densification. A reduction of the saturated conductivity in variations of lysimeter 6 gives evidence that the shoulder material has a high influence on the water balance, as seepage water quantities decrease. Reallocation of surface runoff from the embankment section to the slope section should be done, when hydraulic conductivity of shoulder material is low (e.g. $k \leq 1.5 \times 10^{-6}$ m/s) to avoid underestimation of seepage water. Software should be developed further to automatically shift surface runoff between sections.

The application of finite element simulation for seepage prediction in construction projects is feasible. As water volumes tend to be overestimated, the simulation can be considered a conservative approach.

References

1. FGSV (2017) Merkblatt über Bauweisen für technische Sicherungsmaßnahmen beim Einsatz von Böden und Baustoffen mit umweltrelevanten Inhaltsstoffen im Erdbau. FGSV Verlag, Köln
2. Brand M, Tiffert A, Endres M, Schnell M, Marks T, Kocher B (2016) Effizienz technischer Sicherungsmaßnahmen im Erdbau—Untersuchungen von Bauweisen in Freilandlysimetern. Teil 1 Untersuchungszeitraum 2010–2013. Berichte der BASt, Straßenbau Heft S 103. Bergisch Gladbach
3. Endres M, Brand M, Tiffert A, Schnell M, Kocher B, Marks T, Hilliges R (2016) Percolation and contaminant transport in road embankments with and without technical safeguards to reduce percolation—lysimeter experiments. Transp Res Procedia 14:2392–2401. Elsevier
4. Adu-Wusu C, Yanful EK, Lanteigne L, O'Kane M (2007) Prediction of the water balance of two soil cover systems. Geotech Geolog Eng 25:215–237. Springer Science+Business Media B.V
5. Michaelides G, Koukoulidou A, Birle E, Heyer D (2013) Strömungsmodelle zur Simulation der Durchsickerung von Straßenbauwerken mit Implementierung hydrologischer Parameter. Chair and Testing Institute of Soil Mechanics and Foundation Engineering, Rock Mechanics and Tunneling. Final report of R&D 84.105. BASt, Bergisch Gladbach (2013).
6. Yao Y-S, Zheng J-L, Chen Z-S, Zhang J-H, Li Y (2016) Field measurements and numerical simulations of temperature and moisture in highway engineering using a frequency domain reflectometry sensor. Sensors 16:857–874
7. Koukoulidou A, Birle E (2019) Untersuchungen zur Durchsickerung von RC-Baustoffen und industriellen Nebenprodukten bei Bauweisen für technische Sicherungsmaßnahmen. Final report of R&D 05.0192/2015/AGB. Chair and Testing Institute of Soil Mechanics and Foundation Engineering, Rock Mechanics and Tunneling. Technical University Munich
8. Khire M, Benson C, Bosscher J (1997) Water balance modeling of earthen final covers. J Geotech Environ Eng 123(8):744–754

9. Beyer C, Konrad W, Rügner H, Bauer S, Liedl R, Grathwohl P (2008) Model-based predictions of long-term leaching of contaminants from secondary materials in road constructions and noise protect dams. Waste Manage 23(2):839–850

10. Kellermann-Kinner Ch, Bürger M, Marks T (2016) Effizienz technischer Sicherungsmaßnahmen im Erdbau—Lysimeteruntersuchungen unter Laborbedingungen. Berichte der BASt. Bergisch Gladbach

11. Schweller G, Birle E, Heyer D (2009) Geohydraulische Bewertung technischer Sicherungsmaßnahmen beim Einsatz von Böden und Baustoffen mit umweltrelevanten Inhaltsstoffen im Erdbau. Chair and Testing Institute of Soil Mechanics and Foundation Engineering, Rock Mechanics and Tunneling. Final report of R&D 05.147/2007/CGB. Munich

12. Barbour SL, Fredlund DG, Gan JK-M, Wilson GW (1992) Prediction of moisture movement in highway subgrade soils. In: Proceedings of the 45th annual Canadian geotechnical conference. Toronto, Canada

13. Geo-Slope (2014) Vadose zone modeling with Vadose/W; April 2014 edn. Geo-Slope International Ltd. Calgary, Alberta, Canada

14. Scharnagl W, Durner B (2014) Bestimmung von Wassergehalts-Saugspannungsfunktionen für Böden, RC-Baustoffe und HMVA. Final report of R&D 05.0162/2011/LRB, BASt, Bergisch Gladbach

15. Schindler U (1980) Ein Schnellverfahren zur Messung der Wasserleitfähigkeit im teilgesättigten Boden an Stechzylinderproben. Forschungszentrum für Bodenfruchtbarkeit Münchberg der Akademie für Landwirtschaftswissenschaften der DDR

16. Fredlund M (2011) Soilvision user's manual. Soilvision Systems Ltd

17. Ekblad J, Isacsson U (2007) Time domain reflectometry measurements and soil-water characteristic curves of coarse granular materials used in road pavements. Can Geotech J 44(7):858–872

18. Schanz T, Agus SS, Tscheschlok G (2004) Hydraulisch-mechanische Eigenschaften einer polymerverbesserten Sand-Bentonit-Mischung beim Einsatz im Deponiebau. Geotechnik 2004(4):344–355

19. Bouazza A, Zornberg JG, McCartney JS, Nahlawi H (2006) Significance of unsaturated behaviour of geotextiles in Earthern structures. Australian Geomech 41(3):133–142

20. Melsbach M, Birle E (2019) Numerische Modellierung der Lysimeteruntersuchungen der BASt. Final report of R&D 05.0185/2014/CRB. Chair and Testing Institute of Soil Mechanics and Foundation Engineering, Rock Mechanics and Tunneling. Technical University Munich

21. VDI (2010) VDI-Richtlinie 4640 Blatt 1, Juni 2010: Thermische Nutzung des Untergrunds. Verein Deutscher Ingenieure—Gesellschaft Energie und Umwelt

22. Allen RG, Pereira LS, Raes D, Smith M (2018) Crop evapotranspiration—guidelines for computing crop water requirements. FAO irrigation and drainage paper 56, http://www.fao.org/docrep/x0490e/x0490e07.htm. Last Accessed 10 Aug 2018

Electrical Resistivity Changes in Wet and Dry Side of Optimum Moisture Content for Soils with Low to High Fines Content

Hamid Rostami and Abdolreza Osouli

Abstract Compacted soil is an essential element in the construction of geo-structures as not any soil site on its own is ideal for the intended construction. This research is an experimental study that investigates the interactional effect of moisture and fines contents on electrical resistivity (ER) of compacted soils. The soil type used in this study is sand with 0%, 30%, and 60% fines content. A non-conductive standard proctor mold is built and modified for measuring the electrical resistivity of soil samples with different dry densities and moisture contents. The electrical resistivity measurements are conducted using four electrodes; two electrodes for injecting the current and two electrodes for measuring the electrical potential difference. The soil specimens are tested under the same electrical setup in both dry and wet sides of the soil compaction curve. The results show that there is an inverse relationship between the electrical resistivity amount and both soil density and moisture content. The plot of electrical resistivity versus moisture content indicates that even though the electrical resistivity decreases with increasing the moisture content, the rate of electrical resistivity changes is different in wet and dry sides of optimum moisture content (OMC). In the dry side of OMC, the electrical resistivity decreases with a steep slope because of an increase in both soil density and moisture content. However, on the wet side of optimum moisture content, the soil density starts to decrease and electrical resistivity moves with a milder slope just because of an increase in moisture content.

Keywords Soil compaction · Electrical resistivity · Optimum moisture content · Fines content

1 Introduction

Electrical resistivity (ER) is an intrinsic characteristic of each material and is measured as the capability of contradicting the flow of electrical current. The basic

H. Rostami · A. Osouli (✉)
Southern Illinois University, Carbondale, IL 62901, USA
e-mail: aosouli@siue.edu

829

principle of the ER method is that when a constant current is injected in to the soil through the electrodes, the current that flows between the electrodes has an inverse relationship with the resistance of the soil [1]. ER is a geophysical testing method and is commonly used in geotechnical engineering, geology, and environmental studies [2–4]. The most important factors that influence the ER of soils are moisture content, porosity, particle sizes, bulk density, and plasticity [5]. Electrical current in soil is strongly dependent on the moisture content and degree of saturation. Therefore, they are the primary factors that affect the electrical resistivity of soils [6, 7].

ER can potentially be used to detect any difference in soil density because the electrical resistivity of soil materials increases with decreasing the soil density. The measurement of ER can be used as an alternative to traditional methods for quality control and estimation of soil density.

Conventionally, the soil compaction is usually estimated using the measurements of dry density and moisture contents of the soil [8]. However, there are often difficulties with traditional laboratory approaches when high accuracy is needed. The ER method is a non-destructive, fast, and cost-effective manner for investigating the subsurface materials without the need of sampling and laboratory tests. There have been several studies that investigate the measurement of soil compaction using the ER for practical engineering purposes. Kowalczyk et al. [9] investigated the relationship between ER and moisture content and the degree of compaction for non-cohesive soil. The results showed that the ER is a function of both moisture content and degree of compaction. Abidin et al. [10] explored the relationship between the ER, moisture content, and bulk density. They showed that the ER decreased with increasing the moisture content in a curvilinear form. Other research [11] proved that ER can be used as an indirect indicator of soil moisture content.

The correlation between ER, moisture content, and soil density is likely to depend on particular combinations of the ranges of moisture content and soil fines that may be encountered. It will then be necessary to study the effects of those combinations in order to develop reliable correlations to ER measurements. In this paper, there is an attempt to determine the moisture content range for various types soils in which ER measurement can be used as a reliable representation of soil density. In this research, the soil specimens are tested under the same electrical setup in both dry and wet sides of OMC for three different types of soils from coarse-grained to fine-grained soils with various amounts of fines content.

2   Material and Method

The soil samples were prepared with three different fines contents 0%, 30%, and 60%, which are called hereinafter Sample 1, Sample 2, and Sample 3, respectively. Figure 1 depicts the soil grain size distribution that was determined for these samples using sieve analysis. Table 1 shows the soil classification according to the Unified Soil Classification System (USCS).
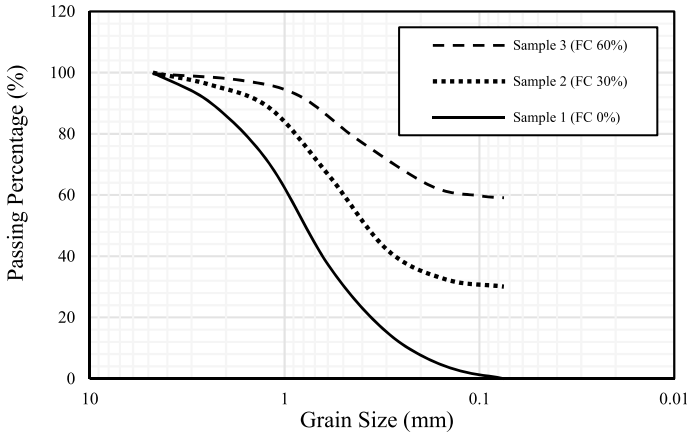
Fig. 1 Grading curves for soil samples

Table 1 Sample information and USCS classification

Sample no	Group symbol (USCS)	FC (%)	LL (%)	PI (%)	Description
1	SW	0	–	–	Clean and well-graded sands
2	SM	30	11.5	3	Silty sand
3	ML	60	21	7	Low-plastic silt

For the soil compaction, the standard proctor test was conducted according to the criteria of ASTM D-698. The only difference was using a mold machine from a 4-inch diameter PVC Schedule 80 pipe instead of regular steel mold for the standard proctor test. Fig. 2 shows the laboratory equipment used for ER measurement of compacted soils.

PVC was chosen because it was a good electrical insulator with resistivity of 1015 Ω-cm. It should be noted that, from geotechnical point of view, the plastic mold had no effect on results of moisture contents or soil density in comparison with regular proctor mold. Moreover, the plastic mold allowed insertion of two lateral electrodes (*M* and *N*) in the soil after its compaction. These electrodes were measuring the electrical potential, while the current was applied to the soil specimen through the top and bottom electrodes (*A* and *B*) (See Fig. 3).

The electrical resistivity of compacted soils was measured using SuperSting R1 and an Adapter Box. The SuperSting measures the resistance of material in Ohm Ω, which depends upon the shape and the size of specimen. In order to calculate the resistivity of soil material with the unit of Ohm Ω-cm, a correction factor was needed. This factor is derived by dividing the sample cross-sectional area by the distance between the electrodes A and B [12].

Fig. 2 Electrical laboratory test equipment

Fig. 3 A schematic view of PVC mold and four electrodes
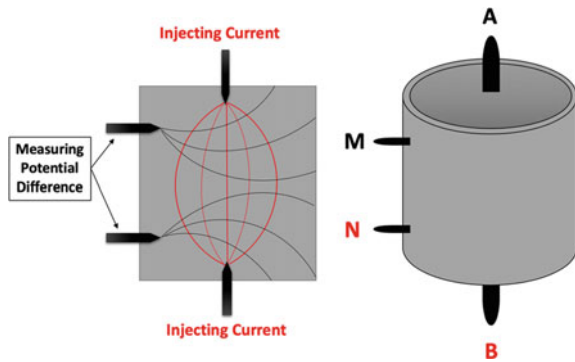
It should be noted that to assure repeatability of the results, 40% of the tests were repeated and the results of dry density, moisture content, and electrical resistivity were within ± 3.5% margin of error. Figure 3 illustrates a schematic view of the PVC mold, electrodes, and electrical current in soil sample.

3   Results and Discussion

The dry density versus moisture content curves for soil Samples 1 through 3 are presented in Fig. 4. This figure shows that Sample 1 with 0% fines content has the lowest optimum moisture content (OMC), while the Sample 2 with 60% fines
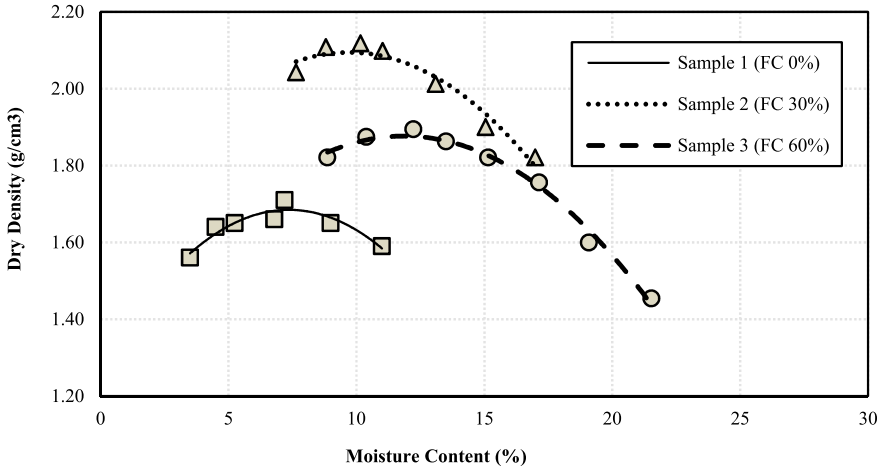
Fig. 4 Compaction curves for different soil samples

content has the highest OMC, which is compatible with typical behavior of well-graded sands [13]. These previous studies indicate that the addition of fines content with low plasticity to sandy soil up to a certain percentage, which varies from about 10% to 30% and depends upon the gradation of sand to be compacted, decreases the OMC and increases the Maximum Dry Density (MDD) of sand. With adding low-plastic fines content, OMC and MDD start to have an inverse trend.

Figure 5 illustrates electrical resistivity values versus moisture content for all soil samples tested. For the three types of samples, electrical resistivity values were found to decrease with increasing of moisture content. Resistivity values decrease with a
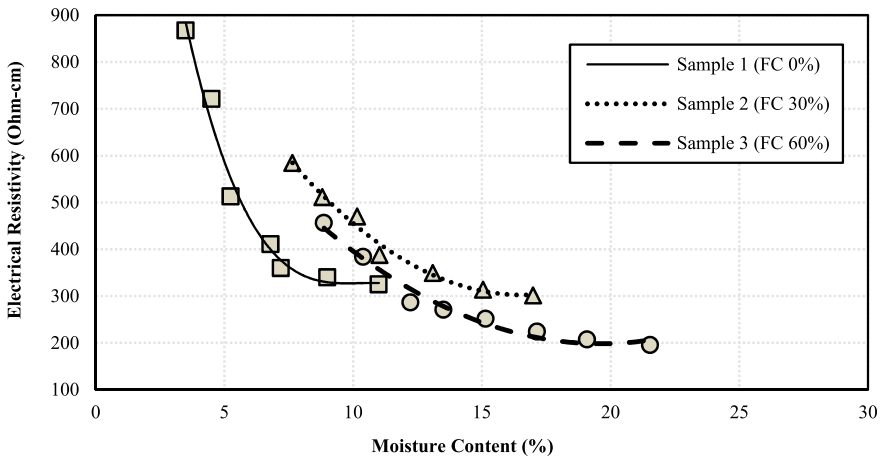
Fig. 5 Electrical resistivity versus moisture content

decreasing rate when moisture content increased up to 1–1.5 times the optimum moisture content, then electrical resistivity becomes almost constant with further increases in the moisture content. It indicates that when void spaces between grains fill and become connected to each other with fluid, adding more water to the soil has no considerable effect on the electrical conductivity of material. This is very similar to the variation of coefficient of permeability from dry to wet side of optimum moisture content.

Figure 5 also shows that in high moisture content ranges, the resistivity of individual soil samples decreases with increasing the percentage of fines content. In coarse granular soils, electrical resistivity is a function of the soil porosity, soil structure, and arrangement of the grains that provide different paths for the current. In fine-grained soils, however, it is mainly affected by the surface conductivity of the fine particles that considerably pave the way for electrical flow [14]. Furthermore, the increase of fines content results in filling the voids that exist between the particles and consequently minimize the volume of voids and connect the grains.

The relationship between electrical resistivity and soil density is more complicated. Figure 6a depicts the electrical resistivity values versus soil density on the dry side of OMC. According to this figure, the electrical resistivity has a decreasing trend for all three samples when the soil become denser, which is in agreement with conventional relationship between electrical resistivity and soil density. However, as shown by Fig. 6b, in wet side of OMC, the electrical resistivity continues to decrease with decreasing the soil density. It indicates that for Sample 1 (clean sand), soil density can be only detectable using electrical resistivity measurement up to OMC since the soil density has no considerable change versus electrical resistivity in wet side of compaction curve. However, for Samples 2 and 3 with 30% and 60% fines content, respectively, electrical resistivity can be used to detect the soil density change even in the wet side and up to 5% OMC.

4 Conclusion

This experimental study investigates the effect of moisture and fines contents on the relationship between electrical resistivity and soil density. Three different percentages of low-plastic (i.e., PI < 7%) fines content (i.e., 0%, 30%, and 60%) are compacted based on the standard proctor test procedure and using a PVC mold. The results clearly show that there is a relation between soil electrical resistivity and soil density that is affected by moisture content and fines content. The soil sample with zero percent fines content has a considerable high resistivity in low moisture content in comparison with two other samples. Regarding the moisture content, it should be noted that the OMC plays an important role in the soil resistivity-density relation, especially for clean sands. On the dry side of OMC, soil resistivity decreases with a steep gradient as a result of increase in soil density and moisture content. On the wet side of OMC, however, the electrical resistivity decreases with a decreasing rate when soil density starts to decrease. The moisture content gradually plays a
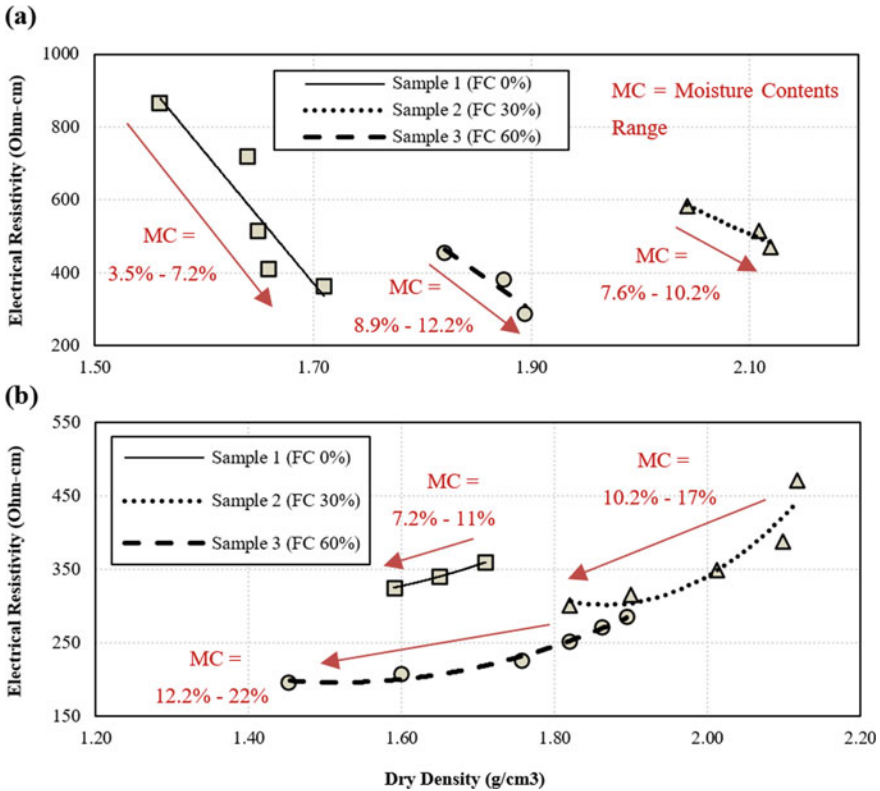
Fig. 6 Electrical resistivity versus soil dry density: **a** moisture content less than OMC (dry side); **b** moisture content greater than OMC (wet side)

more dominant role in this side for clean sands (Sample 1). Although electrical resistivity can be used as an effective method for measurement and quality control of field compaction, this study shows that two important parameters of soils, moisture content and fines content, must be considered if this approach is to be employed. The laboratory results show that in fine grained material and in more than 5% above optimum moisture content may lead to an incorrect soil density evaluation.

References

1. Kelleners TJ, Robinson DA, Shouse PJ, Ayars JE, Skaggs TH (2005) Frequency dependence of the complex permittivity and its impact on dielectric sensor calibration in soils. Soil Sci Soc Am J 69:67–76. http://soil.scijournals.org/cgi/content/abstract/69/1/67
2. Loke MH (1999) Electrical imaging surveys for environmental and engineering studies: a practical guide to 2-D and 3-D surveys

3. Dahlin T (2001) The development of DC resistivity imaging techniques. Comput Geosci 27(9):1019–1029
4. Zonge K, Wynn J, Urquhart S (2005) 9. Resistivity, induced polarization, and complex resistivity. In: Near-surface geophysics. Society of Exploration Geophysicistsm Tulsa, OK, pp 265–300
5. Zhou QY, Shimada J, Sato A (2001) Three-dimensional spatial and temporal monitoring of soil water content using electrical resistivity tomography. Water Resour Res 37(2):273–285
6. McCarter WJ (1984) The electrical resistivity characteristics of compacted clays. Geotechnique 34:263
7. Kibria G, Hossain MS (2012) Investigation of geotechnical parameters affecting electrical resistivity of compacted clays. J Geotech Geoenviron Eng 138(12):1520–1529
8. Avnimelech Y, Ritvo G, Meijer LE, Kochba M (2001) Water content, organic carbon and dry bulk density in flooded sediments. Aquacult Eng 25:25–33. https://doi.org/10.1016/S0144-860 9(01)00068-1
9. Kowalczyk S, Maslakowski M, Tucholka P (2014) Determination of the correlation between the electrical resistivity of non-cohesive soils and the degree of compaction. J Appl Geophys 110:43–50
10. Abidin M, Saad R, Ahmed F, Wijeyesekera D, Yahya A (2013) Soil moisture content and density prediction using laboratory resistivity experiment. IACSIT Int J Eng Technol 5(6):731–735
11. Bhatt S, Jain PK (2014) Correlation between electrical resistivity and water content of sand—a statistical approach. Am Int J Res Sci Technol Eng Math 6(2):115–121. ISSN (online) 2328–3580
12. Advanced Geosciences, Inc. (AGI) (2011) Instruction manual for supersting earth resistivity. IP & SP System
13. Deb K, Sawant V, Kiran A (2010) Effects of fines on compaction characteristics of poorly graded sands. Int J Geotech Eng 4(2):299–304. https://doi.org/10.3328/IJGE.2010.04.02.299-304
14. Mitchell J, Soga K (2005) Fundamentals of soil behavior, 3rd edn. Wiley, USA; Romero E, Gens Am Lloret A (1999) Water permeability, water retention curve and microstructure of unsaturated compacted Boom clay. Eng Geology 54:117–127

Characterizing the Effect of Fines Content on the Small Strain Shear Modulus of Sand-Silt Mixtures During Hydraulic Hysteresis

Mohammadreza Jebeli, S. Mohsen Haeri, and Ali Khosravi

Abstract Small strain shear modulus, G_{max}, is one of the most important parameters for the characterization of the behavior of earth structures subjected to static or dynamic loading conditions. This research presents an experimental laboratory study on the effect of non-plastic fines content and hydraulic hysteresis on the G_{max} of unsaturated sandy soils. In this regard, clean Firoozkuh No. 161 silica sand which is classified as poorly graded sand was mixed with different percentages of non-plastic Firoozkuh silt. A set of bender element tests were carried out using two modified triaxial devices. The modifications on these two apparatus were to add HAV ceramic discs for air–water control of unsaturated specimens, in addition to including piezoelectric bender elements to send and receive shear waves and measure their velocities within the unsaturated silt-sand mixtures. Axis translation technique was implemented for hydromechanical purposes and bender element for shear wave velocity measurements and calculating G_{max}.

Keywords Small strain shear modulus · Bender element test · Unsaturated sandy soils · Fines content · Hydraulic hysteresis

1 Introduction

Pavements, machines foundations, and shallow footings are usually exposed to low amplitude dynamic loads which in turn cause low strains in them. Also, earthquakes emit shear waves, which pass through the soil layers with different grain-size distributions. Analysis of the behavior of soil layers and overlaying structures in such loading conditions requires identifying dynamic characteristics of the soil layers in small strain situations. Shear modulus at small strains (less than $10^{-4}\%$), G_{max}, is considered as one of the most important dynamic characteristics of the soil. In addition, according to the recommendations of the seismic codes, engineers need

M. Jebeli (✉) · S. Mohsen Haeri · A. Khosravi
Sharif University of Technology, Azadi Avenue, Tehran, Iran

information about the soil stiffness for the design of geo-structures and classification of dynamic properties of the soils [15, 20]. Also, soil stiffness is utilized for the soil-structure interaction analyses. Moreover, shear wave velocity, which has a close correlation with G_{max}, is used to evaluate the susceptibility of the sediments to liquefaction. Researchers have tried to understand the behavior of silt-sand mixtures because of their liquefaction potential and compressibility. Moreover, silty sands may be used for the construction of road bases and embankments.

In recent decades, researchers have conducted numerous experiments to recognize factors that affect the small strain shear modulus of the soils. The result of these studies have shown that different parameters could affect G_{max}, such as effective confining stress, p', void ratio, e, percentage of fines content, FC, and over consolidation ratio, OCR [11, 12, 29, 30]. A significant decrease of G_{max} values with the increment of the fines content of silt-sand mixtures were reported in the previous studies as well [9, 26, 31].

Results of previous studies on the G_{max} of unsaturated fine soils have shown that maximum shear modulus increases with increasing matric suction in a nonlinear way. Meanwhile, the G_{max} of sandy soils varies in an up and down manner [18, 24, 25, 28]. On the other hand, the results of these studies on the G_{max} of unsaturated fine soils have demonstrated that fine soils possess greater G_{max} values during wetting paths than drying paths. In contrast, Khosravi et al. [18] reported that the G_{max} of some clean sand specimens during drying paths was lower than its values along wetting paths. They related this observation to the variation of suction stress along drying and wetting path. However, investigation on the small strain shear modulus of unsaturated silt-sand mixtures during hydraulic hysteresis is rare or nothing. In this study, the unsaturated shear modulus of an uniform clean silica sand which was mixed with different percentages of non-plastic silica silt was investigated under different matric suctions along both wetting and drying paths. The void ratio was kept constant for different mixtures during this study. In the following sections, some details of the tests and results are described.

2 Experimental Study

2.1 Tested Materials

In this study, standard Firoozkuh No 161 silica sand was used as clean sand. This angular sand is obtained from Firoozkuh mine in the northeast of Tehran province in Iran. Researchers in Iran use this sand as standard sand for geotechnical testing. Also, Firoozkuh silt from the same mine was used as non-plastic fines for the experiments. The corresponding grain size distribution curves obtained by performing sieve analysis according to ASTM D6913 [4] and hydrometer analysis according to ASTM D7928 [5] are shown in Fig. 1. According to USCS, this clean sand is classified as poorly graded sand. Additionally, the specific gravity test G_s was determined in
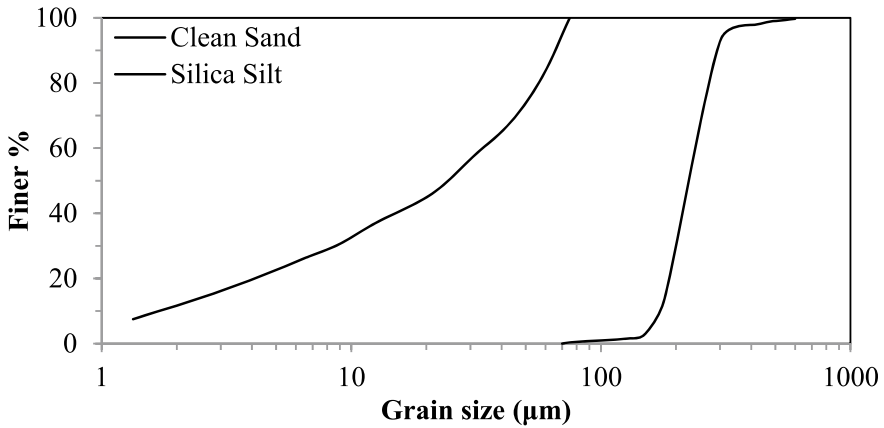
Fig. 1 Grain size distribution curves of tested materials

Firoozkuh Silt ML		No. 161 Firoozkuh Sand SP	
Table 1 Physical properties of tested materials			
Mineral	99%SiO$_2$	Mineral	99% SiO$_2$
D$_{50}$(mm)	0.025	D$_{50}$(mm)	0.226
PI	-	Cu	1.37
W$_{opt}$	19%		

accordance with ASTM D854 [6] to be 2.65. The physical properties of the clean sand and silt are demonstrated in Table 1.

The clean sand was mixed with different percentages of silt to investigate the effect of fines content respectively on maximum void ratio, e_{max}, according to ASTM 4254 [2] and minimum void ratio, and e_{min}, according to ASTM 4253[1] by using vibratory table. However, both methods are limited to soils that contain up to 15% fines content, so there is no standard method to obtain these parameters beyond these limitations. Despite these recommended limitations, these methods have been used to determine e_{max} and e_{max} in different studies [10, 14]. Figure 2 demonstrates the variation of maximum and minimum void ratio with adding non-plastic fines contents. According to this figure, the minimum and maximum void ratio of silt-sand mixtures decreased with the increase of fines content until they reached a minimum value at a threshold fines content, which is about 30%; after that, both values increased with the increment of fines content. These results are similar to the observations of other studies [27, 30]. It is argued that before the fines content threshold, the mechanical behavior of the mixtures is sand dominant, but by adding fines particles more than threshold fines content, the behavior changes to silt-dominant behavior.
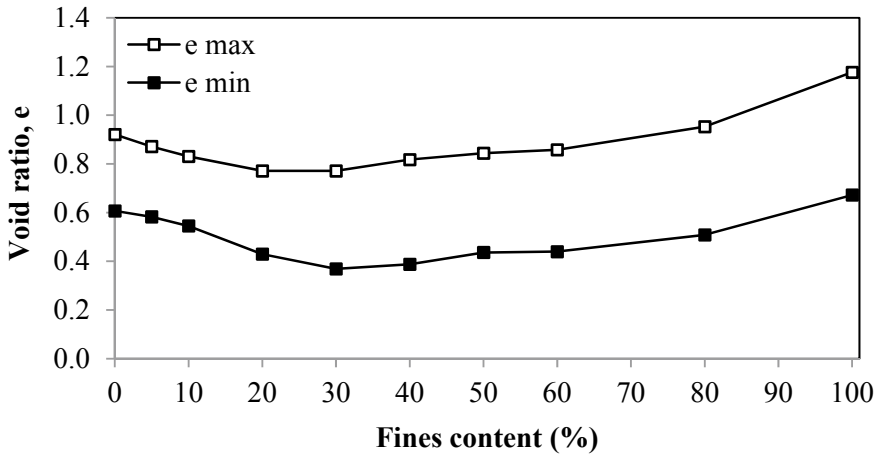
Fig. 2 Variation of maximum and minimum void ratio with the percentage of fines particles

2.2 Experimental Setup

Two triaxial cells equipped with bender elements and suction control system were used to measure the shear wave velocity and G_{max} of specimens during hydraulic hysteresis. Axis translation technique [13] was utilized to control and apply specific matric suctions. Each modified cells have a pair of bender elements in the bottom platen and top cap to send and receive shear waves, respectively. In this research, a signal generator was used to produce an input sinusoidal pulse. Also, the pulses were amplified up to 10 times of input signals in order to gain detectable responses while an oscilloscope, records both input and response signals.

Moreover, the changes in the level of water in graded burettes connected to the cells were recorded to measure the volume changes of specimens. These measurements were corrected according to the results of the several careful calibration tests to eliminate the errors caused by water evaporation, creep, and changes in the volume of the chambers, the pressure line tubing, and the burettes under various pressure. By the observation of graded burettes connected to the bottom of HAE ceramic disks, the variations of the volume of pore water were measured.

2.3 Specimen Preparation

The diameter and height of the tested cylindrical specimens were 60 mm and 120 mm, respectively. In order to prepare the sandy and silty samples in addition to samples with 10, 20, 30, 40, 60% non-plastic fines content, the clean sand was completely mixed with different percentages of the silts. Distilled water was added to the oven-dried soil mixtures and then was blended well. Static compaction was used to prepare

the specimens with an initial desirable void ratio, which was equal to 0.7. In this regard, specimens were prepared by tamping in ten layers with different heights using under-compaction technique in a split mold, according to Ladd [21]. This method prevents excessive compaction of lower layers during the compaction of the upper layers. Interfaces between the successive layers were scarified to establish a proper bond between layers.

2.4 Test Procedure

After placing the specimens in the cells, a vacuum was applied at the top cap to avoid deformation of the samples. A backpressure technique under 40 kPa mean net stress was used to saturate samples. In this regard, backpressure was increased in different water pressure steps, up to 340 kPa, accompanied by enough time span to dissolve air bubbles in the pore water. Skempton's B value greater than 0.95 was considered as a saturation criterion. After specimen saturation, the mean net stressed increased to 100 kPa, so the first bender element tests were carried out in different frequencies on saturated specimens after giving enough time to obtain volume change caused by the enhancement of mean net stress.

Desirable suctions were applied by means of adjusting air, water, and confining pressure at the boundaries of the specimens. Also, enough time was given until no detectable change of the water level in burettes was observed. The acceptable hydraulic equilibrium criterion was considered in the tests to be a water volume change of equal to or less than 0.1 mL in a day. Hydraulic equilibrium used to take 2–15 days, depending on the soil type and quantity of matric suction. Therefore, each test took more than 3 months. After equilibrium at each stage, bender element tests were carried out to obtain travel time by using peak to peak method. Shear wave velocity was obtained by dividing the distance between tips of bender elements into the travel time. Consequently, the small-strain shear modulus, G_{max}, was calculated by using Eq. (1) proposed in elasticity theory, in which ρ is the total density of a sample.

$$G_{max} = \rho \times V_s^2 \tag{1}$$

3 Results and Analysis

3.1 Effect of Fines Content on Soil Water Retention Curve

The soil water retention curves (SWRC) of the specimens during drying and wetting paths have been illustrated in Figs. 3 and 4, respectively. According to these figures,
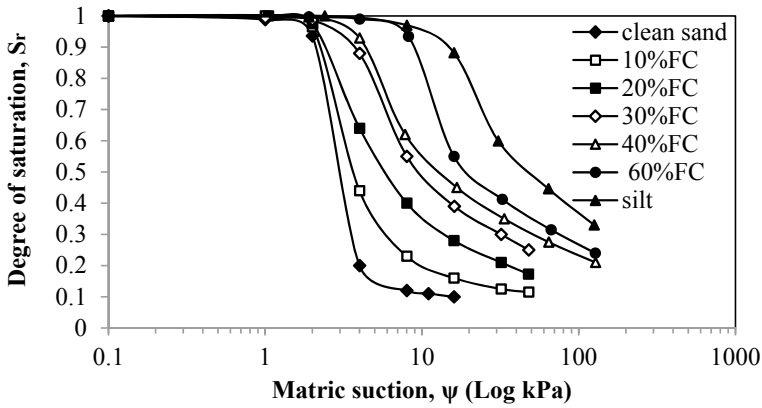
Fig. 3 Effect of fines content on the soil water retention curve of specimens during drying path
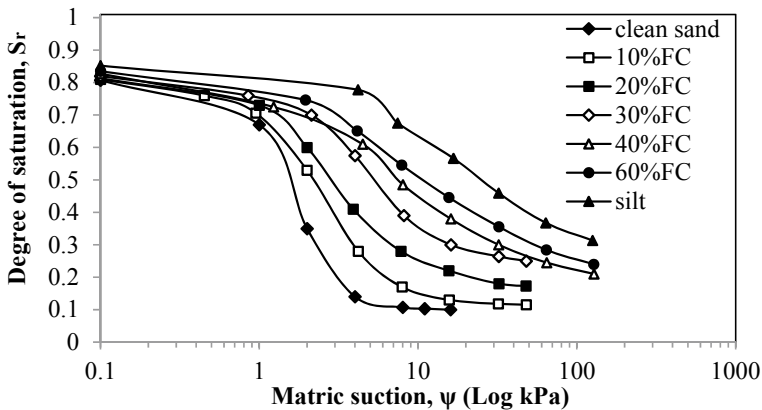
Fig. 4 Effect of fines content on the soil water retention curves of specimens during wetting path

adding fines content has significant effects on the soil water retention curves. As shown, by increasing fines content, the specimens retained more water at equal matric suctions, and this led to the enhancement of air entry values, residual matric suctions, and water entry values. This behavior can be attributed to the fact that fines particles replenish the void spaces of the sandy skeleton of specimens and decrease the average radius of void pores, so for a given degree of saturation, the level of matric suction increases with fines content. This observation is consistent with the observations of other researchers [7, 18] and is in a line with Young–Laplace equation. This equation establishes a correlation between matric suction and the dimension of pore space. As seen in Figs. 3 and 4, the slopes of soil water retention curve decreased with the enhancement of fines content. Not only did adding fines decrease the average radius of pores, but also it increased the distribution of pores with different radius. In other

words, adding fines led to decrease in the uniformity of the pores of the specimens. Moreover, as illustrated in these figures, adding fines had more profound effects on the bottom of the retention curves of the specimens. As mentioned by Lu and Likos [22], the primary mechanism which dominates suction at low degrees of saturation is short-range adsorption effects which depend on the surface of the solid particles. So, adding fines affected soil retention at relatively low values of water content more significant than retention at higher values of water content.

3.2 Effect of Fines Content on Small Strain Shear Modulus (G_{max})

Figure 5 represents the variations of G_{max} of the unsaturated specimens with suction along drying path. As shown in this figure, adding non-plastic fines content led to the reduction of G_{max} especially, at low matric suctions. The greatest decrease was for the specimen with low fines content (up to 20%). The given results are in harmony with the results of other studies [26, 30]. In other words, adding fines more than the threshold fines content led to the change of mechanical soil behavior and structure from sand dominant to silt dominant. On the other hand, pure silt with 0.7 initial void ratio had greater G_{max} than the other specimens with non-plastic fines content. This high value of modulus for silty specimen may be related to its high relative density (about 95%) for its 0.7 initial void ratio.

As seen in Fig. 5, the G_{max} value of sandy specimen increased with matric suction up to the proximity of air entry value, and then, decreased slightly with the further increment of matric suction and reached a constant value at residual matric suctions. This observation is consistent with the results reported by Khosravi et al. [18]. They
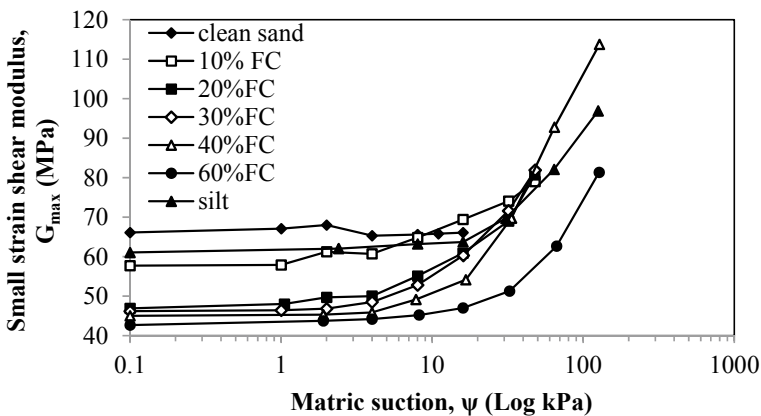
Fig. 5 Variation of small strain shear modulus of specimens with different non plastic fines content along drying path
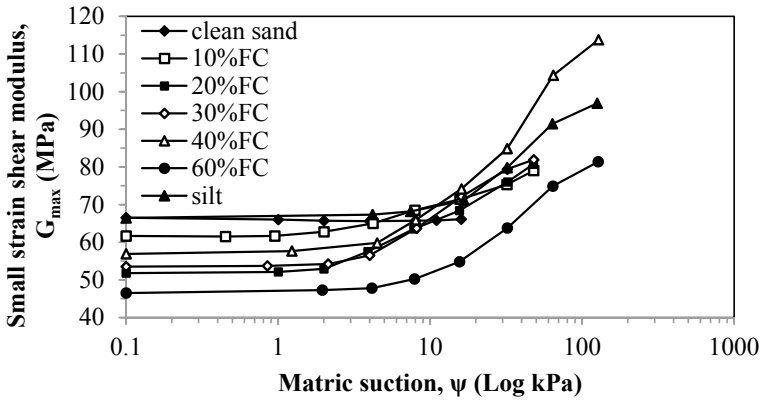
Fig. 6 Variation of the small strain shear modulus of specimens with different nonplastic fines content during wetting path

correlated this up and down trend with the variation of suction stress with the matric suction. In addition, this local maximum value of G_{max} at the proximity of air entry value can be observed for the specimens with 10 and 20% of fines content, although no local maximum exists for specimens with more than 30% of fines content. For higher values of matric suction, samples with fines content as low as 10% had different G_{max} behavior with suction from the sandy specimen. For these specimens, the variation of G_{max} values with matric suction consist of two parts; before the proximity of air entry value, in which G_{max} increased in a slightly linear manner, while at higher matric suctions values, G_{max} increased in a non-linear exponential manner.

The variation of G_{max} with matric suction during wetting path has been illustrated in Fig. 6. According to this figure, the G_{max} of the sandy specimen experienced few changes along wetting path, and its value increased slightly at the low values of matric suction. Despite the sandy specimen, other specimens had greater G_{max} quantities during wetting path than drying path. There is a consensus through literature about this behavior of fine soils [19, 24, 25]. Khosravi and McCartney [16] attributed this behavior to double hardening concept proposed by Wheeler et al. [33] and Tamagnini [32].

3.3 A New Model for Prediction of the Small Strain Shear Modulus of Sand-Silt Mixtures

Lu and Kaya [23] conducted compression tests on unsaturated sandy, silty, and clayey specimens and brought them to equilibrium at different degrees of saturation in order to measure finite-strain Young Moduli. Based on the results of this study, they concluded that finite strain shear modulus has an inverse relationship with a power of effective degree of saturation, as shown in Eq. (2).

$$G_{\max(\text{unsat})} \propto \left(\frac{1}{S_e}\right)^{\beta} \tag{2}$$

where $G_{\max(\text{unsat})}$ is small strain shear modulus at unsaturated state, β is an experimental fitting parameter, and S_e is considered as effective degree of saturation, which is defined in the following equation:

$$S_e = \frac{S_r - S_{r(\text{res})}}{S_{r(\text{sat})} - S_{r(\text{res})}} \tag{3}$$

where S_r is the current degree of saturation, $S_{r(\text{res})}$ and $S_{r(\text{sat})}$ are the values of degree of saturation at residual and saturated conditions, respectively.

Dong et al.[8] developed a new unified model for different types of soils reported in the literature based on Eq. (2). However, some other studies [16, 18, 28] reported that $G_{\max}$ is proportional to the product of degree of saturation and matric suction in terms of effective stress equation for unsaturated soils or suction stress definition proposed by Lu and Likos [22]. Based on these different reports in the literature, the product of effective stress and degree of saturation with separate exponents is considered proportional to $G_{\max}$ for the proposed model in this study.

In addition, applying hydromechanical loads may cause hardening/softening as well as irreversible changes in void ratio [32, 33]. In this study, specimens experienced maximum effective stress at the end of drying path; while, they tolerated less effective stresses along the wetting path. Besides, Hardin [12] reported that stress history (i.e., Over Consolidation Ratio) has significant effect on the measured values of small strain shear modulus. Based on the reported observations in the literature and the results of the experiments of this study, a new model was developed to predict the $G_{\max}$ of sand silt mixtures in terms of effective stress history, degree of saturation, and matric suction. In this regard, the over consolidation ratio was defined in terms of effective stress history, as follows:

$$\text{OCR} = \frac{P'_{\max}}{P'} \tag{4}$$

where P' is the current effective stress and $P'_{\max}$ is the maximum effective stress experienced during hydraulic hysteresis. In order to define effective stress, Eq. (5) proposed by Lu and Likos [22] was utilized.

$$P' = P_n + P_s \tag{5}$$

where P_n is mean net stress and P_s is suction stress which is defined in Eq. (6).

$$P_s = \chi \times \psi \tag{6}$$

where ψ is matric suction, and χ is effective stress parameter which can be defined by Khalili and Khabbaz's [10] proposed equation, as follows:

$$\chi = \left[\frac{\psi}{\psi_b}\right]^{-0.55} \tag{7}$$

where ψ_b is air entry value. Based on Eq. (4), specimens are considered normally consolidated along drying path, while they become over consolidated during wetting path because of experiencing maximum effective stress at the end of drying path. Therefore, Eq. (8) is proposed to predict small strain shear modulus of silt-sand mixtures during hydraulic hysteresis.

$$G_{\max(\text{unsat})} = G_{\max(\text{sat})}\left(\text{OCR}^K + \beta S_r^{-m}\left(\frac{\psi}{P_a}\right)^n\right) \tag{8}$$

where $G_{\max(\text{unsat})}$ and $G_{\max(\text{sat})}$ are small strain shear modulus at unsaturated and saturated states, respectively; P_a is atmospheric pressure (100 kPa), and K, β, m, and n are fitting parameters. This equation could be simplified to the model proposed by Oh and Vanapalli [28], by replacing $K = 1$ and $n = 1$. Also, this equation at saturated state is similar to the equation presented by Hardin [12] in order to predict the G_{max} of over consolidated fine soils. In this study, the measured values of G_{max} at saturated state are considered as $G_{\max(\text{sat})}$. Also, it is possible to use available models in literature rather than measuring of $G_{\max(\text{sat})}$.

Least square method was applied in order to determine these fitting parameters. Table 2 shows the variation of fitted parameters with fines percentages as well as coefficient of determination (R^2). Based on the obtained results and this table, the suggested relationship can predict small strain shear modulus of sand-silt mixtures during hydraulic hysteresis well. According to the variation of fitting parameters, G_{max} of the specimens is in inverse proportion to degree of saturation except for sandy soils, as suggested by Dong et al. [8]. Based on the determined parameters for the proposed equation, by adding fines content more than 40%, the matric suction fitting exponent (i.e. n) reached zero. In other words, when fines content was more than the threshold percentage, and the behavior of specimens became silty dominant, the effect of matric suction on soil stiffness vanished. So, degree of saturation mainly affected the variation of G_{max} for unsaturated silty soils instead of matric suction. This observation is in line with the reports of Dong et al. [8] indicating that the variations

Table 2 Variation of fitted parameters with fines content

Soil type	K	β	m	n	R^2
Clean Sand	0.12	1.601	−6.10	0.951	0.95
10%FC	0.78	0.239	0.36	0.461	0.99
20%FC	1.03	0.072	1.36	0.152	0.99
30%FC	1.07	0.060	1.90	0.060	0.99
40%FC	0.92	0.065	2.07	0.000	0.98
60%FC	0.45	0.035	2.31	0.000	0.98
Silt	0.12	0.039	2.49	0.000	0.98

Table 3 Equations for the prediction of the fitting parameters of the proposed model in terms of fines percentage

Parameter	K	β	m	n
Equation	$1.11e^{-\frac{(FC-30)^2}{776}}$	$\frac{1}{0.6249+0.4106FC}$	$\frac{-25.903+2.795FC^{1.049}}{4.246+FC^{1.049}}$	$\frac{182.02-0.016FC^{2.29}}{191.47+FC^{2.29}}$

of G_{max} with degree of saturation for silty soils are more sensitive than sandy ones. Based on these obtained values, four equations were developed to predict the fitting parameters in terms of non-plastic fines percentage for Firoozkuh sand-silt mixtures (Table 3). Further studies should be done to determine the relationship between these fitting parameters and other soil properties such as void ratio, plasticity index, etc.

4 Conclusion

In the current study, the small strain shear modulus of sand-silt mixtures during hydraulic hysteresis was studied by using two modified triaxial cells. These cells are equipped with bender elements to send and receive shear waves, and ceramic disks to implement axis translation technique. In order to investigate the variations of G_{max} along drying and wetting paths, 7 specimens with different non-plastic fines content were prepared with equal initial void ratio and tested under mean net stress of 100 kPa.

Results of this study have shown that adding fines content as low as 10% to poorly graded sands led to change in the manner of G_{max} variations with suction. Accordingly, the G_{max} of the specimens with fines content increased with the increment of matric suction in spite of up and down trend observed for clean sands. Moreover, these specimens had higher G_{max} values along wetting path compared to those for drying path, experiencing hardening during hydraulic hysteresis. Based on these observations, a new simple model was developed to predict the small strain shear modulus of silt-sand mixtures during drying and wetting paths. This model could predict different G_{max} trends of sands and silts in addition to considering double hardening during hydraulic hysteresis. According to this model, as fines percentage increases, the role of matric suction diminishes, and instead, the role of the degree of saturation on the stiffness of unsaturated soils increases during hydraulic hysteresis.

References

1. ASTM D4253–16 (2016) Standard test methods for maximum index density and unit weight of soils using a vibratory table. ASTM International, West Conshohocken, PA. www.astm.org
2. ASTM D4254–16 (2016) Standard test methods for minimum index density and unit weight of soils and calculation of relative density. ASTM International, West Conshohocken, PA. www.astm.org

3. ASTM D6836–16 (2016) Standard Test Methods for Determination of the Soil Water Characteristic Curve for Desorption Using Hanging Column, Pressure Extractor, Chilled Mirror Hygrometer, or Centrifuge, ASTM International, West Conshohocken, PA. www.astm.org

4. ASTM D6913/D6913M-17 (2017) standard test methods for particle-size distribution (gradation) of soils using sieve analysis. ASTM International, West Conshohocken, PA. www.astm.org

5. ASTM D7928–17 (2017) Standard test method for particle-size distribution (gradation) of fine-grained soils using the sedimentation (hydrometer) analysis. ASTM International, West Conshohocken, PA. www.astm.org

6. ASTM D854–14 (2014) Standard test methods for specific gravity of soil solids by water pycnometer, ASTM International, West Conshohocken, PA. www.astm.org

7. Benson CH, Chiang I, Chalermyanont T, Sawangsuriya A (2014) Estimating van Genuchten parameters α and n for clean sands from particle size distribution data. In: From soil behavior fundamentals to innovations in geotechnical engineering: Honoring Roy E. Olson, pp 410–427

8. Dong Y, Lu N, McCartney JS (2016) Unified model for small-strain shear modulus of variably saturated soil. J Geotech Geoenviron Eng 142(9):04016039

9. Goudarzy M, Rahman MM, Konig D, Schanz T (2016) Influence of nonplastic fines content on maximum shear modulus of granular materials. Soils Foundations

10. Haeri SM, Yasrebi SS (2016) Effect of amount and angularity of particles on undrained behavior of silty sands. Scientia Iranica 6(3):188–195

11. Hardin BO, Richart Jr FE (1963) Elastic wave velocities in granular soils. J Soil Mech Foundat Div, 89(Proc. Paper 3407)

12. Hardin BO (1978) The nature of stress strain behavior of soils. Earthquake Eng Soil Dyn 1:3–90

13. Hilf JW (1956) An investigation of pore-water pressure in compacted cohesive soils. Ph.D. Dissertation. University of Colorado, Boulder, CO, USA

14. Ishihara K (1993) Liquefaction and flow failure during earthquakes. Rankin Lecture Geotech 43(3):351–415

15. Ishihara K (1996) Soil behaviour in earthquake geotechnics. Oxford Science Publications

16. Khalili N, Khabbaz MH (1998) A unique relationship for χ for the determination of the shear strength of unsaturated soils. Geotechnique 48(5):681–687

17. Khosravi A, McCartney JS (1977) Impact of hydraulic hysteresis on the small strain shear modulus of low plasticity soils. J Geotech Geoenviron Eng 138(11)

18. Khosravi A, Shahbazan P, Pak A (2018) Impact of hydraulic hysteresis on the small strain shear modulus of unsaturated sand. Soils Found 58(2):344–354

19. Khosravi A, Rahimi M, Gheibi A, Shahrabi M (2018) Impact of plastic compression on the small strain shear modulus of unsaturated silts. Int J Geomech 18(2):04017138

20. Kramer SL (1996) Geotechnical earthquake engineering. Pearson Education, India

21. Ladd RS (1978) Preparing test specimens using undercompaction. Geotech Test J 1(1):16–23

22. Lu N, Likos WJ (2006) Suction stress characteristic curve for unsaturated soil. ASCE J Geotech Geoenviron Eng 132(2):131–142

23. Lu N, Kaya M (2013) Power law for elastic moduli of unsaturated soil. J Geotech Geoenviron Eng 140(1):46–56

24. Mancuso C, Vassallo R, d'Onofrio A (2002) Small strain behaviour of a silty sand in controlled-suction resonant column-torsional shear tests. Canadian Geotech J CGJ 39(1):22–31

25. Ng CWW, Xu J, Yung SY (2008) Determination of anisotropic shear stiffness of an unsaturated decomposed soil. Geotechnique 58(1):23–35

26. Payan M, Senetakis K, Khoshghalb A, Khalili N (2017) Characterization of the small-strain dynamic behaviour of silty sands; contribution of silica non-plastic fines content. Soil Dyn Earthq Eng 102:232–240

27. Phan VTA, Hsiao DH, Nguyen PTL (2016) Effects of fines contents on engineering properties of sand-fines mixtures. Procedia Eng 142:213–220

28. Oh WT, Vanapalli SK (2014) Semi-empirical model for estimating the small-strain shear modulus of unsaturated non-plastic sandy soils. Geotech Geol Eng 32(2):259–271

29. Qian X, Gray DH, Woods RD (1991) Resonant column tests on partially saturated sands. Geotech Test J 14(3):266–275
30. Ruan B, Miao Y, Cheng K, Yao EL (2018) Study on the small strain shear modulus of saturated sand-fines mixtures by bender element test. European J Environ Civil Eng 1–11
31. Salgado R, Bandini P, Karim A (2000) Shear strength and stiffness of silty sand. J Geotech Geoenviron Eng 126(5):451–462
32. Tamagnini R (2004) An extended Cam-clay model for unsaturated soils with hydraulic hysteresis. Géotechnique 54(3):223–228
33. Wheeler SJ, Sharma RS, Buisson MSR (2003) Coupling of hysteresis and stress–strain behaviour in unsaturated soil. Géotechnique 53(1):41–54
34. Wichtmann T, Hernández MN, Triantafyllidis T (2015) On the influence of a non-cohesive fines content on small strain stiffness, modulus degradation and damping of quartz sand. Soil Dyn Earthq Eng 69:103–114

Features of a Large-Scale Survey of Highways with Georadar

Alan Frid and Vladimir Frid 📧

Abstract The study is based on the results of a georadar study of the pavement substructure obtained during a large-scale geophysical project. The survey consisted of 6000 km investigation of highway pavements and underlying granular layers down to the depth of 0.9 m. It was carried out at high speed (not less than 80 km/h) in order to avoid interference with traffic and using air-coupled (horn) antennae (with center frequency of 1 and 2 GHz). The claim of the regulator for high-speed measurements on highways contradicts is its demand for the acquisition of high-quality data (the required inaccuracy in determining the layers' thickness had to be less than 8%). The reason for errors could be irregular changes in antennae height during surveying at high speed, changes in the pavement temperature and moisture content, variation in the properties of the pavement due to differences in age, design, and repair history. A common way to reduce the error is to correlate georadar data with the data obtained from control boreholes. However, this method makes the project very destructive, expensive, and time-consuming. In our case, the regulator allowed no more than 100 control wells implying one control borehole per each 60 km of highway pavement substructure. Here we present a methodology for correcting several causes of the inaccuracies in data processing noted above. This methodology includes compensation for irregular drift in antenna height that occurs during high-speed imaging, as well as changes in temperature and humidity. Our extensive study of asphalt cores has shown that the coefficient of dielectric constant can be used to compensate for changes in dielectric properties due to temperature variation. It was shown that the application of the Rayleigh model is very useful for compensating for changes in the moisture content of the pavement structure. The research results presented here make it possible to compensate for inaccuracies in the processing of georadar data and, hence, remain within the accuracy established by the regulator.

A. Frid
Department of Electrical and Electronics Engineering, Sami Shamoon College of Engineering, SCE, 56 Bialik st., 84100 Be'er Sheva, Israel

V. Frid (📧)
Department of Civil Engineering, Sami Shamoon College of Engineering, SCE, 84 Ja-botinsky st., 77245 Ashdod, Israel
e-mail: vladimirf@ac.sce.ac.il

851

1 Introduction

The georadar/ground penetrating radar (GPR) method consists of fast generation of electromagnetic (EM) "pulses" in the MHz to GHz range and registration of their reflections from the boundaries between adjacent layers due to differences in the layers' dielectric permittivity [1–11]. The asphalt mixture includes aggregates, water, asphalt, and air. The dielectric constant of aggregates usually ranges between 5 and 12 [3, 8, 11, 12] while its values for air and water are minor (1) and major (81), respectively [11]. That is the reason why air and water content essentially affects the value of dielectric constant of an asphalt layer [9, 13–17]. It is well known that the dielectric properties of materials strongly depend on their temperature, and that is correct for the asphalt mixtures too. Comparison of georadar data with borehole information enables one to reduce inaccuracy in layer thickness definition. However, big-scale georadar projects, consisting of measurements of hundreds or even thousands of kilometers, usually suffer from insufficient amount of control boreholes due to regulator requirements to decrease the pavement damage caused by borehole drilling, cost of survey, and time consumption. The article is based on the results of a georadar survey which consisted of 6000 km investigation of highway pavements and underlying granular layers down to the depth of 0.9 m. It was carried out at speeds higher than 80 km/h in order to avoid interference with traffic and using air-coupled (horn) antennae (with the center frequency of 1 and 2 GHz). Three causes of inaccuracy in layers thickness were revealed: a. irregular changes in antennae height when surveying at high speed, b. changes in pavement temperature, c. changes in pavement moisture content. Here we present the results of the study of these inaccuracies.

2 The Effect of Antenna Height Drift

The measured amplitude value of the georadar is known to be affected by the height of the antenna above the asphalt surface:

$$A_a = \frac{A_0\left(\sqrt{\varepsilon_a} - 1\right)}{\left(\sqrt{\varepsilon_a} + 1\right)} \tag{1}$$

where A_a, A_0, ε_a. are the amplitude of reflected signal from the asphalt surface (subscript 'a'), from the metal plate (subscript '0'), and asphalt dielectric constant, respectively. Let us denote reference height H^r to be the height of the antenna over the asphalt surface at a point before or/and after data acquisition while H^m. to be the height of the antenna different from the reference height (e.g. due to the antenna

height drift during data collection or bouncing test [18]). Then we define A_0^r and A_0^m to be the maximal value of georadar signal amplitude measured over maetal plate at a reference height H^r and at the height H^m different from the reference height, respectively. It was shown, [18] that the ratio between A_0^r and A_0^m values can be defined as follows:

$$\frac{A_0^r}{A_0^m} = e^{\alpha \Delta H} \tag{2}$$

where α is the coefficient of amplitude attenuation (1/m) equal to -1.1 for 1GHz and 2 GHz antennae in average [18], $\Delta H = H^r - H^m$ implying that for $\Delta H > 0$ the antenna is located below the reference height, and $\Delta H < 0$—the antenna height is greater than reference height. It is seen that the value of $e^{\alpha \Delta H}$ ranges from 0.8 (if the antenna places 20 cm below the reference height) to 1.25 (if the antenna is located 20 cm above the reference height).

Utilizing Eqs. (1) and (2) yields:

$$\begin{cases} A_a^r = \frac{A_0^r(\sqrt{\varepsilon_a^r}-1)}{(\sqrt{\varepsilon_a^r}+1)} \\ A_a^m = \frac{A_0^r(\sqrt{\varepsilon_a^r}-1)}{e^{\alpha \Delta H}(\sqrt{\varepsilon_a^r}+1)} \end{cases} \tag{3}$$

hence, the value of dielectric permittivity after height drift compensation $\varepsilon_{\Delta H}^m$:

$$\sqrt{\varepsilon_{\Delta H}^m} = \left(\frac{A_0^r + A_a^m e^{\alpha \Delta H}}{A_0^r - A_a^m e^{\alpha \Delta H}} \right) \tag{4}$$

Note that dielectric permittivity value without the height drift compensation ε^m can be found as follows:

$$\sqrt{\varepsilon^m} = \left(\frac{A_0^r + A_a^m}{A_0^r - A_a^m} \right) \tag{4'}$$

Since the pavement thickness is $L \sim \frac{1}{\sqrt{\varepsilon_a}}$, the relative error in the layer thickness calculation is $\varepsilon_{\Delta H} = \frac{L^m}{L_{\Delta H}^m} = \frac{\sqrt{\varepsilon_{\Delta H}^m}}{\sqrt{\varepsilon^m}}$. Hence the relative error caused by neglecting the antenna drift can be found as follows:

$$\varepsilon_{\Delta H} = \frac{\left(\frac{A_0^r + A_a^m e^{\alpha \Delta H}}{A_0^r - A_a^m e^{\alpha \Delta H}} \right)}{\left(\frac{A_0^r + A_a^m}{A_0^r - A_a^m} \right)} \tag{5}$$

Figure 1 shows the results of the error calculation. It is seen that the error is significant when the antenna is higher than the reference position. The same outcome is for small values of amplitude ratio $AR = A_0^r / A_a^m$ when the reflected georadar amplitude is quite big, e.g., for new asphalt pavement. The calculations were made
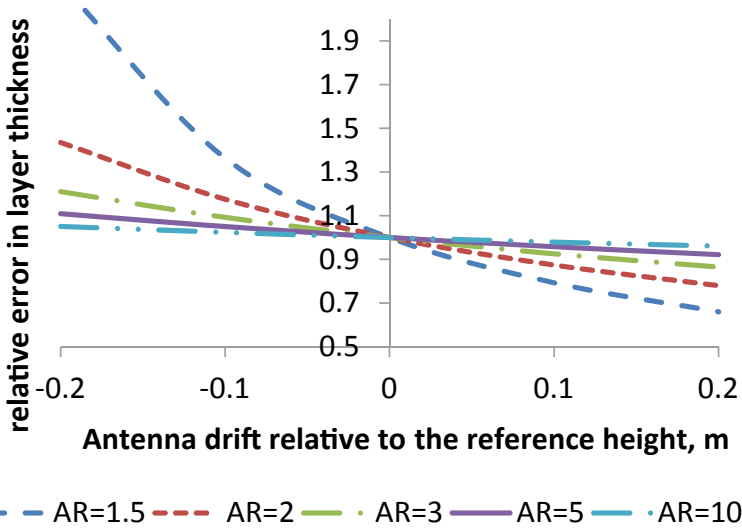
Fig. 1 The relative error in the layer thickness calculation $\varepsilon_{\Delta H}$ due to antenna height drift. Index AR means the value of amplitude ratio: (A_0^r/A_a^m)

for the reference height 0.3 m that is typical value of the antenna height without a drift. Note that the error does not depend on the specific value of the amplitudes A_0^r, A_a^m, but only on their ratio A_0^r/A_a^m.

3   The Effect of Pavement Temperature

The effect of temperature on the value of dielectric constant was studied using 40 asphalt core samples. The dielectric constant was determined for each core sample at five temperature values of 20, 30, 40, 50, and 60 °C that is the typical asphalt temperature range in Israel. Since the standard procedure of the rock/material drying is impossible for asphalt cores due to samples disintegration at temperature higher than 80 °C, the procedure similar to those described by Evans et al. [13, 15] was utilized as follows: after extracting the cores from the highway pavement, they were stored for several weeks at a temperature of 40–50 °C in outside conditions and then at room temperature. All cores were weighted to receive their dry mass M_{dry} and after each measurement of dielectric constant the values of dry mass M_{dry} was re-checked. The procedure of the dielectric constant measurement were performed in the following order: a. All 40 samples were placed in the drying oven at temperature of 20 °C for 24 h. b. One core was taken to measure the dielectric constant, while the others were left inside the oven at a temperature of 20 °C. c. The measurements were carried out using a Percometer probe [19] determining the real part of the relative dielectric permittivity based on the change in capacitance caused by the material

at the tip of the probe in the frequency range 40–50MHz. Note that difference in value of dielectric permittivity measured in this frequency range and in the range of georadar (1–2GHz) is insignificant for the aim of this study. d. The dry mass M_{dry} was re-checked. e. The steps a–d were repeated for all 40 samples for temperature 20 °C. Note that opening the oven door reduced the internal temperature, and the next measurement was carried out only when the internal temperature steadily returned to the desired value. f. The procedures a–f were repeated four times for the temperature values 30, 40, 50, and 60 °C.

Figure 2 shows the results of dielectric constant measurements while the temperature ranges 20–60 °C.

The results show the tendency of increase in dielectric permittivity value with increasing temperature, while the gradient of the rise is not the same for different samples and for different temperature ranges. It can be assumed that such changes can be associated with the inhomogeneity of the composition and structure of the samples. Understanding the phenomenon is a subject for future research.
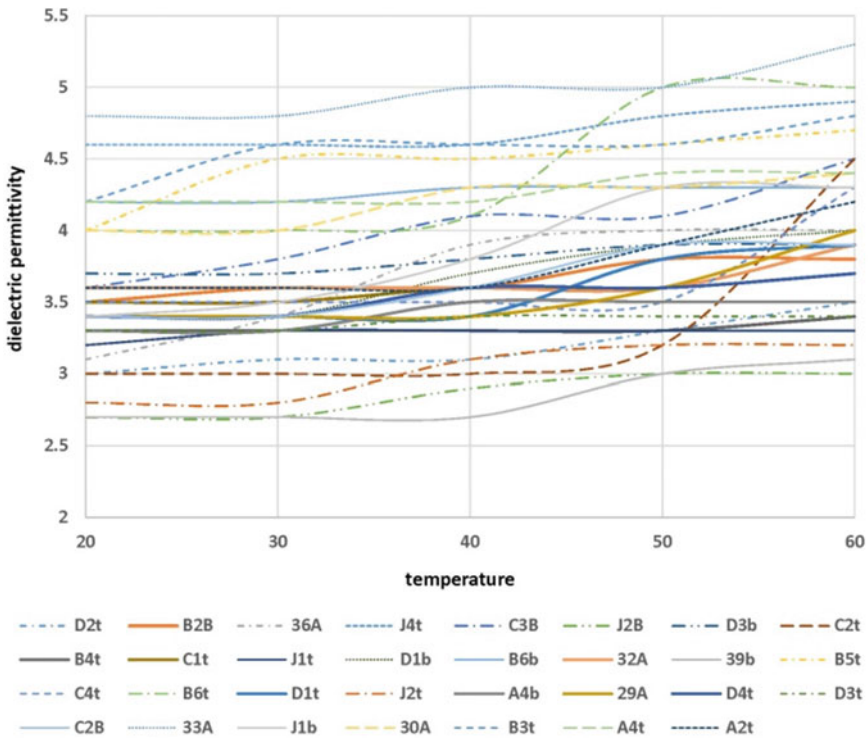
Fig. 2 Dielectric permittivity-temperature behavior of dry asphalt specimens. The *Y* axis is the value of dielectric permittivity. The *X*-axis is the value of temperature in degree of Celsius Symbols in the legend below the graph indicate the sample number and the corresponding curve

Fig. 3 The relationship between the relative error in asphalt thickness calculation due to temperature changes. The *Y* axis is the value of relative error Δ_{kT} see Eq. (7). The *X*-axis is the value of temperature in degree of Celsius
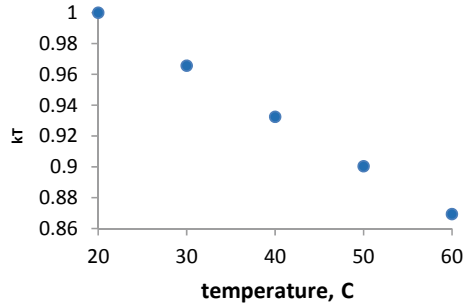
Currently, we propose to characterize the change in the value of the dielectric constant using the temperature coefficient '*k*' as follows:

$$\varepsilon_m = \varepsilon_{T=20} e^{k(T-20)} \tag{6}$$

where $\varepsilon_{T=20}$ and ε_m are the values of dielectric constant at temperature 20 °C and the temperature higher than 20 °C, respectively. T is the value of temperature in units of degree of Celsius. Our analysis showed that the average value of '*k*' for all measured asphalts cores is $7*10^{-3}$ (°C^{-1}). This result is consistent with those of Jeselskis et al. [20] and Evans et al [15], the average coefficient of dielectric constant in which was $2*10^{-3}$ (°C^{-1}). The relative error in calculating layer thickness $\Delta_{kT} = \frac{H_m}{H_{T=20}}$ due to ignoring changes in the asphalt temperature can be found as follows:

$$\Delta_{kT} = \frac{H_m}{H_{T=20}} = \sqrt{\frac{\varepsilon_{T=20}}{\varepsilon_m}} = e^{-0.5k(T-20)} \tag{7}$$

Figure 3 demonstrates the results of inaccuracy calculation using Eq. (7).

Analysis of Fig. 3 indicates that if the temperature changes significantly during the georadar survey the inaccuracy in asphalt thickness measurement can reach 10% or even more.

4 The Effect of Moisture Content

As we noted above, the values of dielectric constant of air ε_{air}, water ε_w and dry solids ε_s are 1, 81, and 5–12, respectively. Hence, the increase of water content within the pore space essentially affects the value of dielectric constant of the entire asphalt mixtures. The most comprehensive study of models for dry asphalts was performed by Leng et al. [21–23] and Al-Qadi et al. [6] who showed that their ALL model ensures the most accurate results for the density assessment than CRIM, Rayleigh, and Botcher models. Existing models of wet asphalt are mostly empirical. Their main

drawback is the lack of consistency between the relationships for dry and wet asphalt [24–31].

We developed novel equations for wet asphalt mixture for all four models and proved their consistency with the corresponding models for dry asphalts (volumetric water content is equal to zero). The analysis of these models was performed via simulation using Matlab software. The simulation of wet asphalt density G_{mb} and volumetric water content w_v showed that Rayleigh and ALL models yields quite similar results. Eq. (8) shows the developed relationships for Rayleigh and ALL models for wet asphalt.

$$
\begin{cases}
G_{mbR} = \dfrac{\frac{\varepsilon_{HMA}^{w}-b}{\varepsilon_{HMA}^{w}+2_b}+w_v\left[\frac{(1-P_b)}{G_{sb}}C+D-E\right]-nD}{\frac{(1-P_b)}{G_{sb}}C}; & \text{Rayleigh model}\\[3ex]
G_{mbALL} = \dfrac{\frac{\varepsilon_{HMA}^{w}-b}{\varepsilon_{HMA}^{w}-2.3_b}+w_v\left[\frac{(1-P_b)}{G_{sb}}F1_m+F2_m-F3_m\right]-nF2_m}{\frac{(1-P_b)}{G_{sb}}F1_m}; & \text{All model}
\end{cases}
\tag{8}
$$

where ε_{Asp}^{w}, ε_b are the dielectric constant of wet asphalt and binder, respectively. n is the asphalt porosity, C, D, E, $F1_m$, $F2_m$, $F3_m$ are the coefficients depending of asphalt properties as follows: $C = \frac{s-b}{s+2_b}$, $D = \frac{1-b}{1+2_b}$, $E = \frac{81-b}{81+2_b}$,

$$
F1m = \frac{s-b}{s-2.3_b+2\varepsilon_{Asp}^{w}},\; F2m = \frac{1-b}{1+2\varepsilon_{Asp}^{w}-2.3_b},\; F3m = \frac{81-b}{81-2.3_b+2\varepsilon_{Asp}^{w}}
$$

w_v is the value of volumetric water content, P_b is the binder content, G_{sb} is the specific gravity of the aggregate, calculated taking into account the binder absorption, s is the dielectric constant of aggregate. Note that substituting $w_v = 0$ turns out these relationships to be equal to corresponding ones developed for dry asphalts that indicate their self-consistency. Figure 4 shows the ratio of the value of wet asphalt density calculated using Rayleigh model G_{mbR} to the value of wet asphalt density calculated using ALL model G_{mbALL}. It can be seen that for porosity values in the range from 0.01 to 0.06, the discrepancy between these two models does not exceed 5% and it even decreases with the rise of volumetric water content. If the porosity of asphalt is relatively high (0.07–0.12), the discrepancy between the two models exceeds 5%, in the case of a low volumetric water content (less than 2–3%), but it decreases with an increase in the volumetric water content, as in the case of low porosity. Both models can be used for estimations of dielectric constant based on expected values of asphalt porosity and density, and vice versa for estimation of asphalt porosity and density based on measured values of dielectric constant. However, the Rayleigh model can be used for solving both direct and inverse problem while the ALL model application for inverse problem can be done only via simulation, e.g. using Matlab software.

Another conclusion, which inevitably follows from the analysis of Fig. 4, is that the relative error Δ_w in calculating the thickness of the asphalt layer, caused by neglecting water content for ordinary asphalt (4–6% in porosity), can reach 5%, but for highly porous or damaged/old asphalt, this error increases essentially.
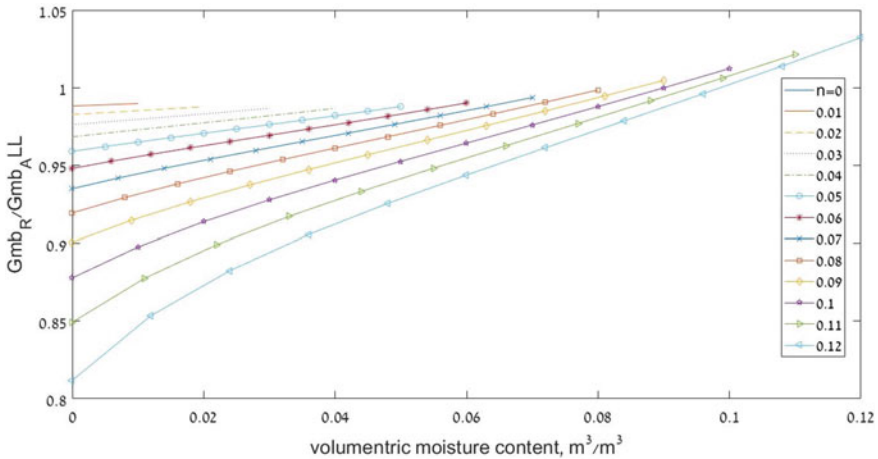
Fig. 4 Comparison values of wet density calculated using Rayleigh and ALL models for deferent values of volumetric water content and porosity

5 Conclusion

In this article, we present the results of a study of several causes of typical inaccuracies in calculating the thickness of asphalt in large-scale georadar surveys. It was shown that the total error in determining the thickness of the pavement layers due to neglect of the drift of antenna height, asphalt temperature, and moisture content can reach tens of percent. This is significantly higher than the error limit allowed by the regulator (less than 8%). The research results presented here make it possible to compensate for these inaccuracies in the processing of georadar data collected during large-scale road surveys, and, therefore, remain within the accuracy established by the regulator.

References

1. Benedetto A, Tosti F, Ciampoli LB, D'Amico F (2017) An overview of ground-penetrating radar signal processing techniques for road inspections. Signal Processing 132:201–209
2. Benedetto A, D'Amico F, Tosti F (2014) Improving safety of runway overrun through the correct numerical evaluation of rutting in cleared and graded areas. Saf Sci 62:326–338
3. Daniels DJ (2004) Ground penetrating radar. The Institution of Electrical Engineers, London
4. Saarenketo T, Scullion T (2000) Road evaluation with ground penetrating radar. J Appl Geophy 43:119–138
5. Al-Qadi IL, Lahouar S, Loulizi A (2003) Successful application of ground-penetrating radar for quality assurance-quality control of new pavements. Transp Res Rec 1861(1):86–97
6. Al-Qadi IL, Leng Z, Lahouar S, Baek J (2010) In-place hot-mix asphalt density estimation using ground-penetrating radar. Transp Res Rec 2152:19–27
7. Kassem E, Chowdhury A, Scullion T, Masad E (2016) Application of ground-penetrating radar in measuring the density of asphalt pavements and its relationship to mechanical properties. Int J Pavement Eng 17(6):503–516

8. Saarenketo T (2008) Ground penetrating radar: theory and applications, Part IV. Elsevier Science, Amsterdam, Netherland

9. Khamzin AK, Varnavina AV, Torgashov EV, Anderson NL (2017) Utilization of air-launched ground penetrating radar (GPR) for pavement condition assessment. Construct Building Mater 141:130–139

10. Joshaghani A (2019) Identifying the problematic areas with structural deficiencies of pavements using non-destructive tests (NDT). Int J Pavement Eng 20(11):1359–1369

11. ASTM D 4748—98. Standard test method for determining the thickness of bound pavement layers using short-pulse radar

12. Stryk J, Alani AM, Matula R, Pospisil K. Innovative inspection procedures for effective GPR surveying of critical transport infrastructures (pavements, bridges and tunnels). In: Andrea B, Lara P (eds) Civil engineering applications of ground penetrating radar. Springer 371

13. Evans R, Frost M, Stonecliffe-Jones M, Dixon N (2008) A review of pavement assessment using ground penetrating radar (GPR). In: 12th International conference on ground penetrating radar, June 16–19. Birmingham, UK

14. Maser K, Carmichael A (2015) Ground penetrating radar evaluation of new pavement density ground penetrating radar evaluation of new pavement density paving project. SR 539 in Lynden, WA

15. Evans R, Frost M, Stonecliffe-Jones M, Dixon N (2008) Assessment of in situ dielectric constant of pavement materials. Transp Res Rec 2037:128–135

16. Li Chunlin, Miao Linchang, Yue Jingchao (2010) Research on detection to moisture content of flexible pavement by GPR. Geotech Special Publicat 203:421–426

17. Soutsos MN, Bungey JH, Millard SG, Shaw MR, Patterson A (2001) Dielectric properties of concrete and their influence on radar testing. NDT&E Int 34:419–425

18. Frid A, Frid V (2018) Irregular changes in antenna height during high speed scanning as a source of essential errors in measuring the thickness of asphalt. In: 17th international conference on ground penetrating radar. GPR 2018. Rapperswil, Switzerland, 772–775

19. Saarenketo T (2006) Electrical properties of road materials and subgrade soils and the use of Ground Penetrating Radar in traffic infrastructure surveys. Faculty of Science, Department of Geosciences, University of Oulu, P.O.Box 3000, FI-90014 University of Oulu, Finland, Acta Univ. Oul. A 471 (2006)

20. Jeselskis EJ, ASCE AM, Grigas J, Brilingas A (2003) Dielectric properties of asphalt pavement. J Mater Civ Eng 15(5):427–434

21. Leng Z, Baek J (2008–2009) In-place hot mixture asphalt density estimation using ground penetrating radar for airport pavement quality control and assurance activities

22. Leng Z, Al-Qadi IL, Lahouar S (2011) Development and validation for in-situ asphalt mixtureture density prediction models. NDT & E Int 44(4):369–375

23. Leng Z, Al-Qadi I, Shangguan P (2012) Field application of ground penetrating radar for asphalt mixtureture density measurement: a case study of Illinois route 72 overlay. In: Transportation research board 91st annual meeting. Washington D.C. 15 pp

24. Maser KR, Scullion T (1992) Automated pavement subsurface profiling using radar: case studies of four experimental field sites. Transp Res Rec 1344:148–54

25. Li Ch, Miao L, Yue J (2010) Research on detection to moisture content of flexible pavement by GPR. Geotech Special Publicat 203:420–426

26. Benedetto A, De Blasiis MR (2010) Application of ground penetrating radar to road pavements. State of the art and novelties. Geotech Special Publicat 203:412–419

27. Grote K, Hubbard S, Harvey J, Rubin Y (2005) Evaluation of infiltration in layered pavements using surface GPR reflection techniques. J Appl Geophys 57(2):129–153

28. Leucci G (2007) Geoscientific investigations for mapping the subsidence risk in an urban area. J. Geophys. Eng. 4:317–331

29. Plati C, Loizos A (2013) Estimation of in-situ density and moisture content in HMA pavements based on GPR trace reflection amplitude using different frequencies. J Appl Geophys 97:3–10

30. Baran E (1994) Use of time domain reflectometry for monitoring moisture changes in crushed rock pavements. In: Proceedings, symposium and workshop on time domain reflectometry in environmental, infrastructure, and mining application. Evanston, Illinois, Spec. Publ. 19–94, 349–356

31. Benedetto A, Pensa S (2007) Indirect diagnosis of pavement structural damages using surface GPR reflection techniques. J Appl Geophys 62:107–123

Bender Element Field Sensors for Base Course Stiffness Measurements in Airport Pavements

Mingu Kang, Issam I. A. Qamhia, Erol Tutumluer, Won-Taek Hong, Jesse D. Doyle, Harold T. Carr, Wayne D. Hodo, Ben C. Cox, and Jeb S. Tingle

Abstract This paper presents the field installation in an airport pavement and early results of a bender element (BE) field sensor recently developed at the University of Illinois for direct in situ local stiffness measurement and assessment of layer moduli of pavement base/subbase layers. The BE field sensors were installed in a 'Smart Runway' pavement; an extensively instrumented and monitored runway at Hill Air Force Base in Utah. The instrumentation project was undertaken by the US Army Engineer Research and Development Center (ERDC) for monitoring responses of in-service airport pavements subjected to aircraft loadings. Three BE field sensors were installed at different depths in the base layer along the gear path of a heavy cargo aircraft, and a fourth BE sensor was placed in a non-trafficked area of the pavement for comparison. Shear wave velocities were measured immediately after sensor installation in the base and after the construction of the asphalt surfacing. The modulus of the aggregate base was estimated from the measured shear wave velocities. Test results indicated a significant increase in shear wave velocities after proper compaction of the base layer and the placement of the asphalt surface course. The stiffening of the base due to higher confinement could be reliably determined by the shear wave measurement method. In addition, heavy weight deflectometer (HWD) and dynamic cone penetrometer (DCP) tests were also conducted on the test pavement. Comparisons between the moduli obtained from HWD backcalculation, the DCP-based assessment, and those measured by the innovative BE field sensors indicated that the layer moduli from the BE field sensors and DCP testing were relatively similar; whereas the modulus values backcalculated from HWD tests were notably higher.

M. Kang · I. I. A. Qamhia · E. Tutumluer (✉)
University of Illinois at Urbana-Champaign, 205 N Mathews Ave, Urbana, IL 61801, USA
e-mail: tutumlue@illinois.edu

W.-T. Hong
Gachon University, 1342 Seongnam-daero, Sujeong-gu, Seongnam-si, Gyeonggi-do 13120, Republic of Korea

J. D. Doyle · H. T. Carr · W. D. Hodo · B. C. Cox · J. S. Tingle
US Army, Engineer Research and Development Center, 3909 Halls Ferry Road, Vicksburg, MS 39180, USA

861

1 Introduction

Unbound aggregate layers serve as a major structural component of flexible pavements by supporting and distributing vehicular loading. The resilient modulus of unbound aggregate bases/subbases is a mechanistic layer property for analysis, design, and construction quality control of pavements. Most of the pavement design procedures including FAA's Advisory Circulars for Airport Pavement Design and Evaluation, AASHTO's Pavement ME (Mechanistic-Empirical) Design Guide, and many other guidelines used by individual state Department of Transportation (DOTs) recommend using the resilient modulus to characterize unbound aggregate base and subbase layers [1].

Resilient modulus values of aggregate materials are typically determined by performing repeated load triaxial tests in the laboratory. With the goal to simulate construction and traffic loading conditions, most repeated load triaxial test procedures include conditioning and load cycles with different combinations of confining and deviatoric stresses applied on test specimens when determining resilient moduli, whereas the actual stress states in the field for modulus estimation are typically unknown. Resonant column tests and simple shear tests can also be used for modulus estimation, but there are concerns about differences in the stress states and stress path [2]. Field assessment methods are also utilized for layer stiffness estimation. Nondestructive field test methods such as falling weight deflectometer (FWD) and heavy weight deflectometer (HWD) are commonly used to estimate moduli of the aggregate base, subbase and subgrade layers from measured surface deflections [1, 3, 4]. FWD and HWD methods involve a backcalculation/forward calculation procedure for the estimation of the base course modulus with non-standardized software [5]. Other nondestructive techniques include seismic methods, such as spectral analysis of surface waves (SASW), for the modulus estimation but require the use of an inversion method [6, 7]. GeoGauge, a nondestructive method for modulus estimation, has a limitation of considering only a shallow depth of influence [8]. Further, empirical correlations are commonly used to estimate resilient modulus from engineering properties such as the California Bearing Ratio (CBR) or unconfined compressive strength (UCS), but empirical methods lack accuracy.

For accurate and direct estimation of unbound aggregate base layer stiffness, a recent research initiative at the University of Illinois focused on the development of innovative bender element (BE) field sensors that can be installed in pavement layers. By installing BE pairs in the target layer, the local stiffness can be evaluated through shear wave velocity measurement. From extensive studies involving the use of BEs during repeated load triaxial testing in the laboratory, the ability of BEs to measure the localized stiffness of unbound aggregate specimens was verified [9–11]. Moreover, Byun et al. [12] managed to apply BE embedded shear wave transducers for

measuring shear wave velocities and estimating modulus of as-constructed unbound aggregate base layers.

This paper describes the field application of a newly developed BE sensor that is intended to monitor local stiffness characteristics and assess layer modulus of an airfield pavement base course from measured shear wave velocities. The instrumentation project was managed by the US Army Engineer Research and Development Center (ERDC) for monitoring the mechanistic responses of an in-service airport runway pavement subjected to mixed aircraft traffic. The design and manufacture of the BE field sensor and the function of each component including the BE protection module, BE field sensor frame, protection cover, and the coupling material are described in depth. The data acquisition process and shear wave measurement device configuration are then provided. The detailed information of the instrumented 'Smart Runway' pavement where the BE sensors were installed, and the installation and testing procedure of the BE field sensors are described. The modulus characteristics of the unbound base course evaluated using the installed BE field sensors before and after compaction and asphalt surface course construction are then compared to the layer stiffness evaluations from HWD and DCP test data.

2 Development of Bender Element Field Sensor

In this study, pairs of bender element (BE) transducers were used to evaluate the stiffness characteristics of an aggregate base layer constructed in the 'Smart Runway,' an extensively instrumented pavement section at US Hill Air Force Base in Utah. BE shear wave transducers have outstanding coupling ability with granular materials and are cost-effective, but they have not been frequently used in field applications due to issues with fragility. To overcome the fragility of BE sensors, a novel BE field sensor was carefully designed for in situ applications and installed in a constructed pavement layer.

2.1 Bender Element

Piezoelectricity is a property of certain dielectric materials to physically deform in the presence of an electric field, or conversely, to produce an electrical charge when mechanically deformed [13]. A BE is composed of two layers of piezoceramics bonded to a thin metal shim sandwiched in the middle. The application of a voltage across the BE forces one layer to expand and the other to contract, which can generate a detectable shear wave. Thus, BE pairs can be embedded within an aggregate layer to measure modulus and change in modulus. BE sensors can be installed in the field at any depth and orientation [12]. In this study, parallel-type BEs with 30.5 mm (1.2 in.) length and 25.4 mm (1.0 in.) width were utilized. To minimize the internal low-pass filtering effect in granular materials, it is known that the wavelength should be

longer than twice the median particle size [14]. Considering the median aggregate particle size of 10.1 mm in this study, the 30.5 mm length of BE was selected to minimize the internal low-pass filtering effect. Parallel-type BEs were chosen since they provide a higher magnitude of shear wave signal compared to the serial type BEs.

2.2 Bender Element Field Sensor

Bender element field sensors developed for field applications must ensure a reliable and robust design to overcome any possible issues due to the fragility of the piezo-electric material or the coupling with the unbound aggregate materials. The BE field sensor developed in this study consisted of a stainless-steel frame, BE protection modules, and diagonal supporting bars. Figure 1a shows a schematic drawing of a BE field sensor. The stainless-steel sensor frame protects both the BE sensors and the cable connections from potential impact or damage at a construction site and maintains a constant distance between BE sensor pairs. Further, it ensures that the source and receiver transducers directly face each other during shear wave signal propagation. The dimensions of the frame developed herein are 121.9 cm (4 ft) in length and 45.7 cm (1.5 ft) in width. The length was designed to be longer than the width of the gears/tires used to traffic the pavement, and the width was selected to enable collecting a clear shear wave signal without any interference from the stainless-steel frame. The BE protection module, which consists of PVC casing, coupling material (uniform coarse sand) and aluminum mesh protection cover, was designed to protect the BE sensors and propagate shear wave in a continuous medium. The thickness of the BE protection module is 6.0 cm (2.4 in.). A rubber mount is attached to the BE protection module to minimize the possibility of a shear wave propagating through the frame. Diagonal supporting bars were fitted at the four corners of the BE field sensor frame to prevent out-of-plane warping and ensure the pair of BEs are on the same plane. A detailed view of the different components of the developed BE field sensor is shown in Fig. 1b.

2.3 Shear Wave Measurement System

Figure 2 presents a schematic drawing of an embedded BE field sensor in an airport pavement aggregate base layer under traffic loading. The devices utilized for shear wave measurement and the procedure for shear wave measurement are presented in Fig. 2. The measurement system consists of a linear amplifier, a signal generator, an oscilloscope, and a filter and amplifier. Depending on the connections, one of the BEs becomes a source of shear waves and the other becomes a receiver. The input signal with a magnitude of up to 10 V is produced by the signal generator and delivered to the pre-amplifier. The signal is intensified approximately 6-times, which triggers the
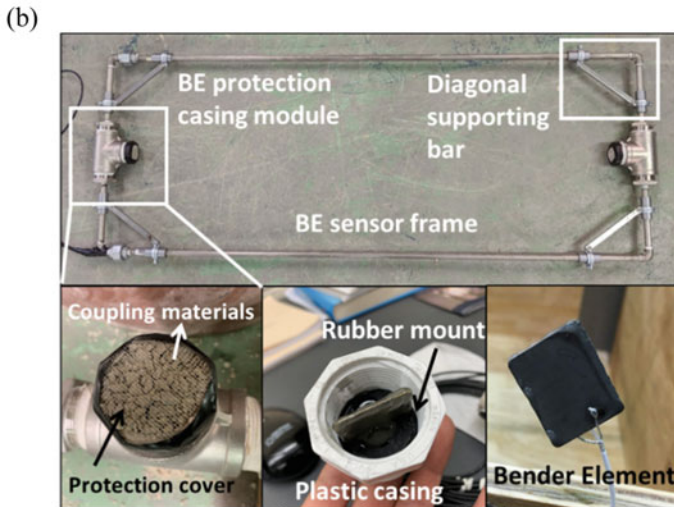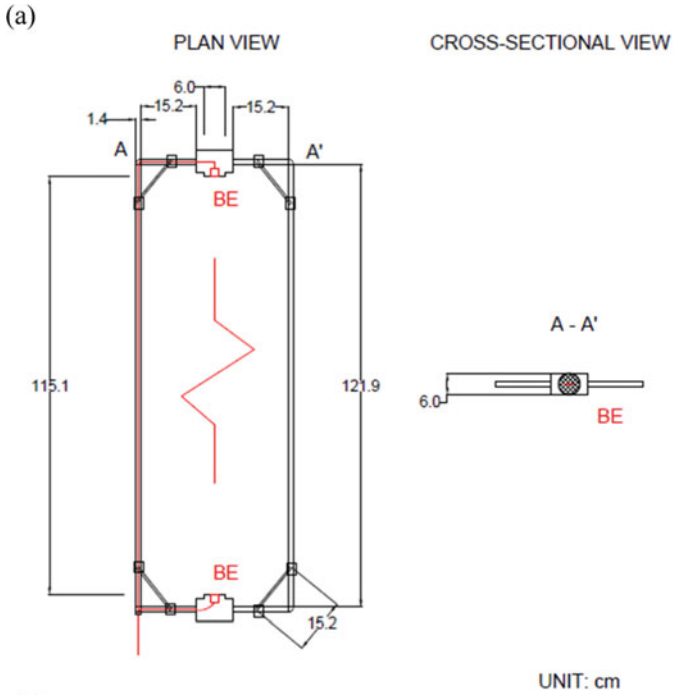
Fig. 1 Bender element (BE) field sensor: **a** schematic drawing showing the dimensions of a BE field sensor; and **b** a detailed view of the BE field sensor and its components
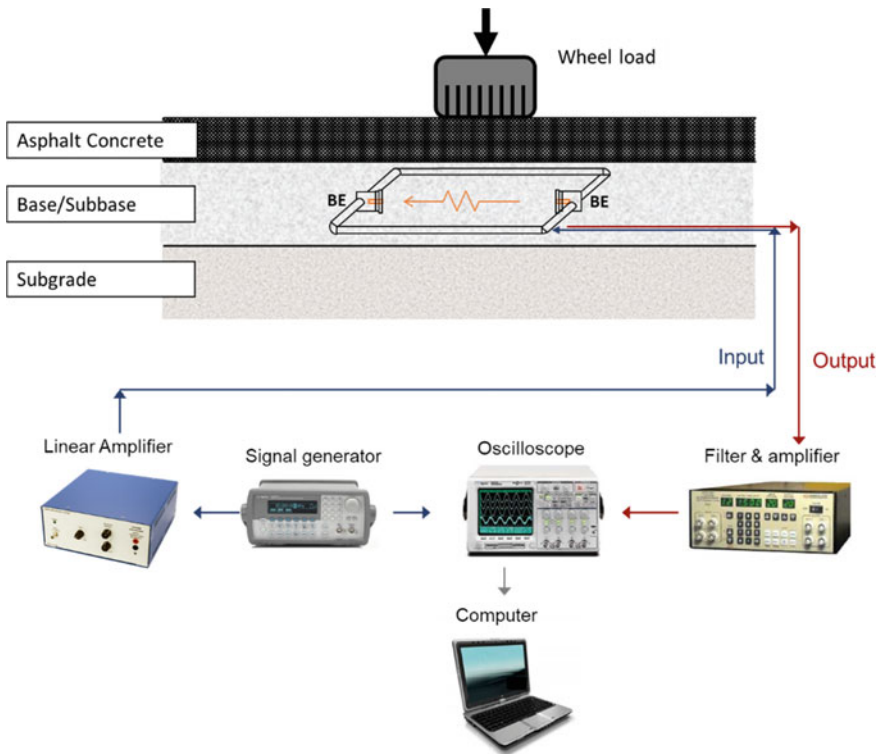
Fig. 2 Schematic drawing of the embedded BE field sensor and the configuration of the shear wave measurement system

'source' BE transducer, and the shear waves that propagate through the aggregate specimen are received by the 'receiver' BE transducer. The output signals are filtered and amplified using the filter and amplifier and are displayed on the oscilloscope. The 1024 signals are stacked and averaged to remove any uncorrected signal noise.

3 Field Application of BE Field Sensors

Four BE field sensors were installed in the Smart Runway pavement at Hill Air Force Base, Utah. The instrumentation effort was undertaken by the US Army Engineer Research and Development Center (ERDC) for monitoring the mechanistic responses of the in-service runway pavement subjected to mixed aircraft loadings. The runway pavement test section consisted of 216 mm (8.5 in.) of hot mix asphalt underlain by 300 mm (11.8 in.) of unbound aggregate base and a 445 mm (17.5 in.) subbase.

3.1 Material Properties

Figure 3 shows the grain size distribution curve and the moisture–density relationship of the aggregate material used to construct the base course layer of the Smart Runway. The grain size distribution was determined according to the ASTM C136 test procedure. The aggregate base material used in the field test section was classified as an A-1-a (stone fragments, gravel, and sand) according to AASHTO soil classification and as a GP-GM (poorly graded gravel with silt) according to the Unified Soil Classification System (USCS). For this aggregate material, 10.1 mm (0.4 in.) was
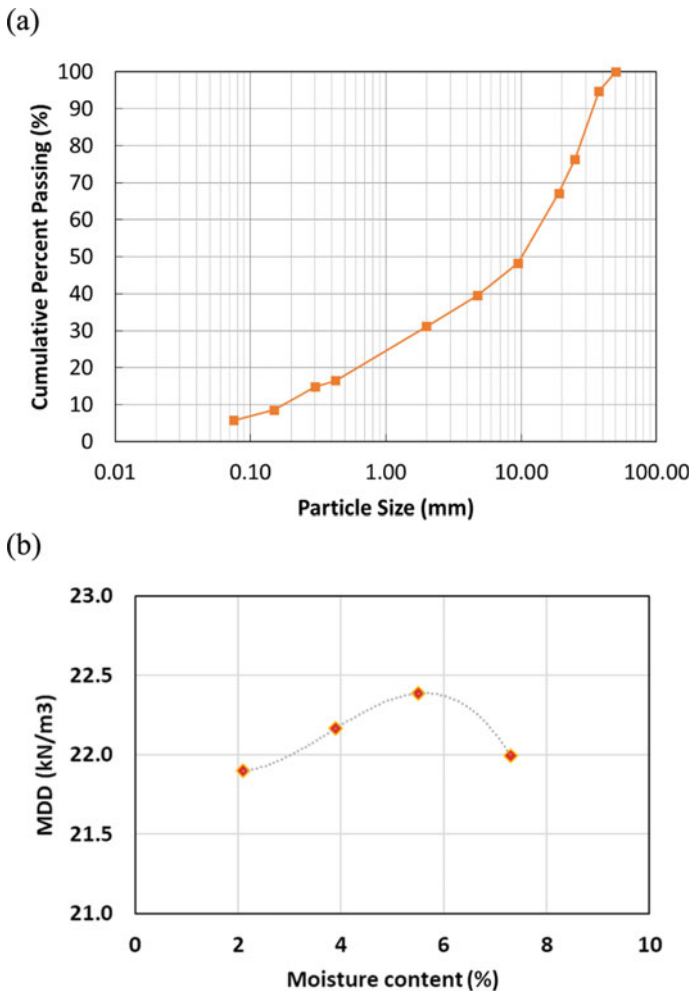
Fig. 3 Material properties for the aggregate base course: **a** grain size distribution; and **b** moisture–density relationship from the modified Proctor (ASTM D1557) tests

the D_{50} size corresponding to 50% passing in a gradation chart, 37.5 mm (1.5 in.) was the top size, and the percentage passing the No. 200 sieve size (0.075 mm) was 6%. The modified Proctor (ASTM D1557) tests produced a maximum dry density (MDD) of 22.4 kN/m^3 (142.5 pcf) at an optimum moisture content (OMC) of 5.7%. Both the subbase and subgrade were classified as a silty sand (SM) according to USCS classification. The maximum dry densities of the subbase and subgrade were 21.5 kN/m^3 (136.7 pcf) and 19.3 kN/m^3 (122.9 pcf), respectively.

3.2 Field Test Sections

Figure 4 shows the depth profile and plan views of the Smart Runway pavement section with exact elevations of the four BE field sensors embedded in the base course above the subbase and subgrade. The first BE field sensor (BE 1) was placed in a non-traffic area of the test section, 239 mm (9.4 in.) above the bottom of the base layer. On the other hand, three other BE field sensors were placed in the Smart Runway section under the probable gear path of the C-17 cargo aircraft. The second BE field sensor (BE 2) was placed at 81 mm (3.2 in.) above the bottom of the base layer, the third BE field sensor (BE 3) was installed at 198 mm (7.8 in.) above the
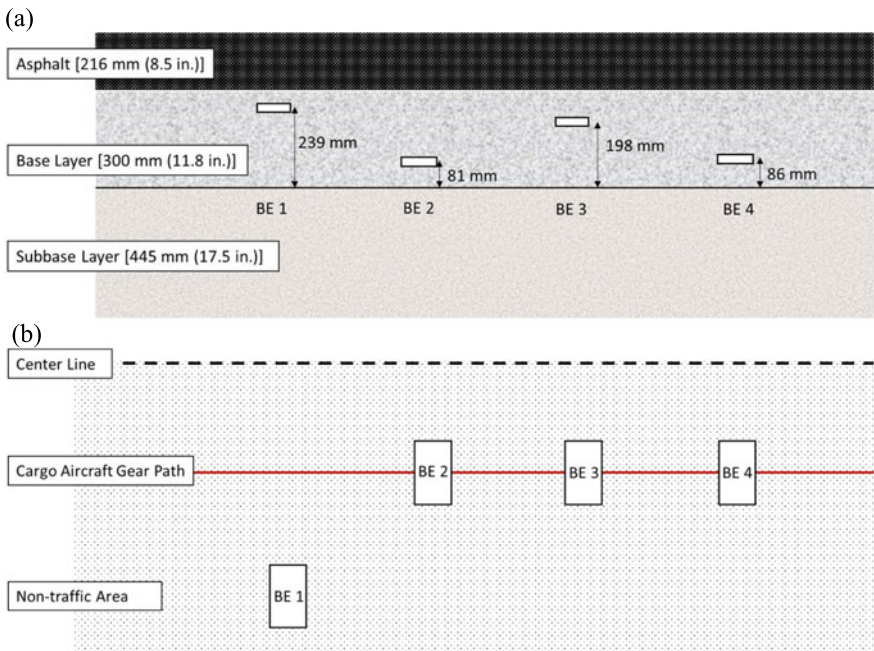
Fig. 4 Constructed Smart Runway pavement test section showing the locations of the BE field sensors: **a** cross-sectional view; and **b** plan view

bottom of the base layer, while the fourth sensor (BE 4) was installed at 86 mm (3.4 in.) above the bottom of the base layer. In short, BE 1 and BE 3 were placed near the top of the base layer, whereas BE 2 and BE 4 were installed near the bottom of the base layer for comparison (see Fig. 4).

3.3 BE Field Sensor Installation Procedure

Installation of the BE field sensors was performed after the construction of the aggregate base layer. After construction and compaction of the aggregate base course layer, the location of the BE field sensor installation was carefully marked, and the base course materials were removed to place the sensor frame as shown in Fig. 5. To bring the sensor cables to the data acquisition box placed at the shoulder, a narrow trench was dug, and uniformly graded fine sand was placed as a padding material to protect the cables. After installing the BE field sensors in the base layer, the depth of placement of each BE sensor was carefully measured using a robotic total station. Any gaps between the sensor frame and the ground were filled and compacted properly to provide a uniform foundation for sensor stability. Aggregates were placed in front of the sensors and compacted by hand tamping to ensure proper contact between the BE sensors and the base course material. The BE field sensors were then covered with the base course aggregates and compacted using a vibratory plate compactor within the excavated trench, followed by a large self-propelled vibratory roller at the final base course surface elevation. The achieved average dry density of the aggregate base course measured using a nuclear density gauge was 22.05 kN/m^3 (141.5 pcf).

4 Experimental Results and Discussion

After the BE sensor installation, shear wave signals were collected on two different occasions. The first measurements were taken after installing BE field sensors in the aggregate base course and before the hot mix asphalt layer construction. Figure 6 shows the shear wave signals from this first measurement. The installation of the BE field sensors and the first measurements took place in May 2019, after two weeks of continuous heavy rain. Thus, the aggregate base layer was extremely wet. Shear wave signals from the first measurement show relatively low signal-to-noise ratio. The high water content in the granular base led to a significant attenuation of the transmitted shear waves, which led to poor quality of the recorded signals due to the extremely wet aggregate base condition [14, 15]. The red arrows in Fig. 6 indicate the estimated first arrival time of the shear waves. As shown earlier in Fig. 4a, BE 2 and BE 4 were placed at the bottom of the base layer, whereas BE 1 and BE 3 were installed at the top of the base layer. The first arrival times of the shear waves of BE 2 and BE 4 are relatively shorter because of the higher confinement pressure applied from the overlying base material.

Fig. 5 BE field sensor installation procedure: **a** marking sensor location; **b** removing constructed aggregates and placing BE field sensor; **c** preparing the trench for cables; **d** measuring the depth of placement of BE field sensor; **e** preliminary compaction using a plate compactor; and **f** final compaction after sensor installation using a vibratory roller compactor
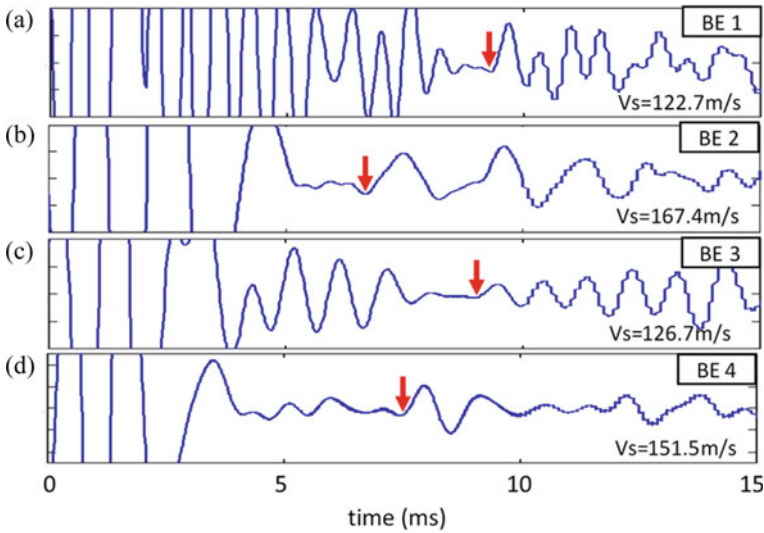
Fig. 6 Shear wave signals recorded after the compaction of the aggregate base for **a** BE 1; **b** BE 2; **c** BE 3; and **d** BE 4

The second measurement was performed in July 2019, a few days after the construction of the HMA layer. Figure 7 shows the shear wave signals recorded from the second measurement. The quality of shear wave signals was clearly improved after the placement of the asphalt surface layer, which led to increased confinement, and the reduction in the moisture content in the aggregate base, which had stabilized with proper drainage for approximately two months.

From the recorded shear wave signals, shear wave velocities can be calculated as follows:

$$V_S = \frac{L}{t_{\text{tip}-\text{tip}}} \tag{1}$$

where $t_{\text{tip}-\text{tip}}$ is the first arrival time and L is the distance between the two BE sensors.

The first arrival time of the shear waves was chosen by finding the first break of the signal. The first break of the signal is considered as one of the best methods to get consistent results [16]. The accuracy of the shear wave velocity from the bender element test was reported as ±2% [17, 18]. As shown in Figs. 6 and 7, the first arrival times of shear wave signals from the BE field sensors in the first measurement sequence were relatively higher and more scattered. On the other hand, the first arrival times from the second measurement sequence were significantly lower and the values were more uniform. From previous experimental research studies, it is well-known that the modulus of the aggregate material is stress-dependent [19, 20]. The shear wave velocity can be expressed as a function of confining stress as follows:
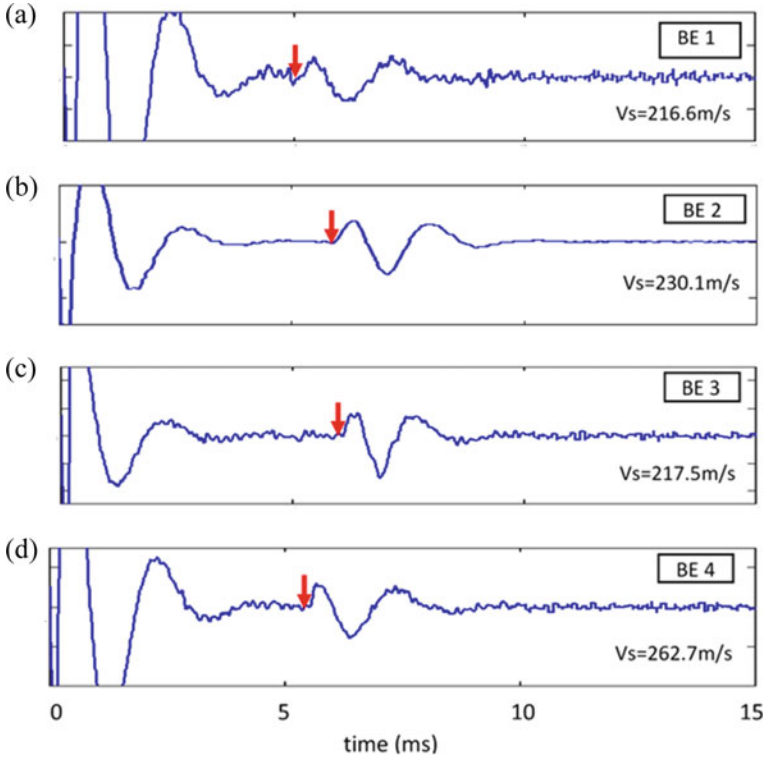
Fig. 7 Shear wave signals from the second measurements; **a** BE 1, **b** BE 2, **c** BE 3, and **d** BE 4

$$V_S = \alpha \sigma_c{}^\beta \tag{2}$$

where α and β are the model parameters obtained from regression analysis using the test results and σ_c is a confining pressure.

After the construction of the HMA layer, relatively uniform confining pressure was achieved due to the weight of overlying asphalt layer. As a small-strain stiffness, shear modulus can be calculated by using the following equation:

$$G_{\max} = \rho V_S^2 \tag{3}$$

where $G_{\max}$ is small-strain shear modulus, and ρ is the bulk density of the aggregate material.

Based on the theory of elasticity, the elastic modulus in a small-strain range can be estimated as follows:

$$E_{\mathrm{BE}} = 2G(1 + \upsilon) \tag{4}$$

Table 1 Summary of modulus measurements from BE field sensors, and HWD and DCP tests

Sensor No.	1st Measurement		2nd Measurement		HWD	DCP
	V_s (m/s)	E_{BE} (MPa)	V_s (m/s)	E_{BE} (MPa)	E_{HWD} (MPa)	M_R (MPa)
BE 1	122.7	92.2	216.6	287.0	506.1	328.9
BE 2	167.4	171.4	193.9	230.1		
BE 3	126.7	98.1	188.5	217.5		
BE 4	151.5	140.5	207.2	262.7		

where E_{BE} is the elastic modulus from BE sensor in small-strain range, and υ is Poisson's ratio of the aggregate material.

Poisson's ratio of the base layer was assumed to be 0.35, which is a typical value commonly assumed for an unbound aggregate base layer. Table 1 summarizes the shear wave velocities and small-strain elastic moduli of the aggregate base layer calculated from the first and second measurement sequences.

On the same day that the second shear wave measurements were performed, HWD tests were also performed on the newly paved instrumented Smart Runway pavement. The utilized HWD device was a Dynatest 8082 heavy weight deflectometer. The applied impulse loads ranged from 157 kN (35,300 lbs.) to 252 kN (56,650 lbs.). The HWD moduli were estimated through backcalculation using the PCASE software and BAKFAA software. PCASE stands for Pavement-Transportation Computer Assisted Structural Engineering, which is the US Army ERDC pavement evaluation and design software, and BAKFAA software was developed by the Federal Aviation Administration (FAA) to perform backcalculation of pavement layer moduli. Both software programs have been widely used for the analyses of the HWD and FWD data [21, 22]. The estimated HWD moduli of the surface course, base course, subbase course, and subgrade were 333.0 MPa (48.3 ksi), 506.1 MPa (73.4 ksi), 344.7 MPa (50.0 ksi), and 177.2 MPa (25.7 ksi), respectively. The HWD moduli of the surface course was lower than the base and subbase layers, and this low measurement was expected because the HWD testing was conducted a few days after the surface course construction before the asphalt mixture had fully cured.

Before the HMA surface course construction, DCP tests were also conducted with the goal of determining the strength profiles of the runway pavement structure. The DCP penetration rate was converted to California Bearing Ratio (CBR) using the following equation:

$$\log(\text{CBR}) = 2.46 - 1.12\log(DCP_{(\text{mm})}) \qquad (5)$$

where DCP is the penetration rate (mm/blow).

A representative set of CBR values was selected using the 85th-percentile method for the base material to characterize the constructed pavement section according to the US Army Corps of Engineers procedure [23]. From the obtained CBR data, layer modulus values were estimated using the empirical equation as follows [24]:

$$M_R = 17.6 \times CBR^{0.64} \tag{6}$$

where M_R is the resilient modulus.

The resilient modulus of the aggregate base course from the DCP test data was approximately 328.9 MPa (47.7 ksi). Note that the estimated CBR of the base layer was 97%, which is a considerably high CBR value, whereas Eq. 6 is more applicable to low or medium CBR ranges.

Table 1 summarizes the shear wave velocities and modulus values measured/calculated from BE field sensors, the HWD and the DCP tests. As discussed earlier, the small-strain elastic modulus E_{BE} of the base layer not only increased significantly but also became less variable after the HMA surface layer construction owing to the uniform overburden pressure applied. Also, note that the modulus values calculated from the BE field sensor and DCP testing were relatively close, whereas the modulus values estimated from HWD test data were somewhat higher. Considering the heavy dynamic loads applied during HWD tests, a higher stress state developed in the aggregate base would cause a stress-hardening effect, and that would result in high modulus values backcalculated in the base layer during the HWD tests. Furthermore, a modulus degradation curve-based conversion should also be investigated in the future studies to adequately relate small-strain E_{BE} modulus to the larger-strain modulus, i.e. resilient modulus, for comparison purposes. This will help to determine a more realistic modulus of the base and subbase layers under traffic loading, i.e. large strain/stress excursions, when using the data from BE field sensors.

In conclusion, BE field sensors installed in the runway pavement test site successfully measured the shear wave velocities. The calculated small-strain elastic moduli were within a reasonable range. The BE field sensors embedded in the Smart Runway section will further enable long-term monitoring of the small-strain modulus during the use phase of the runway under repeated loading with aircraft landing gears.

5   Summary and Conclusions

This study established early research results for direct shear wave velocity measurements and pavement layer modulus estimations from innovative bender element (BE) field sensors, which were newly developed at the University of Illinois for a direct and accurate assessment of the moduli of base and subbase pavement layers. The BE field sensors were installed in an extensively instrumented Smart Runway pavement section at Hill Air Force Base in Utah. This research initiative was carried out by the US Army Engineer Research and Development Center (ERDC) to collect data from an instrumented airport pavement section exposed to repeated loadings from military and civilian aircraft. The Smart Runway section consisted of 216 mm (8.5 in.) of HMA layer underlain by 300 mm (11.8 in.) of unbound aggregate base and a 445 mm (17.5 in.) subbase. Three BE field sensors were installed at different depths

in the base layer under the probable gear path of a heavy cargo aircraft, and the fourth sensor was placed in a non-trafficked area for comparison. Shear wave velocities were measured on two different occasions: immediately after sensor installation and after the construction of the asphalt surface course. The modulus of the aggregate base layer was estimated from the measured shear wave velocities. Finally, the moduli values estimated from the shear wave velocities were compared with the moduli calculated from heavy weight deflectometer (HWD) displacements and dynamic cone penetrometer (DCP) penetration rates.

The BE field sensors installed in the runway test section successfully measured shear wave velocities before and after the asphalt layer construction. Immediately after the sensor installation, the small-strain elastic modulus, E_{BE}, from the BE sensors at the bottom of the base layer were relatively larger than those closer to the top because of the higher magnitude of confinement pressure. The small-strain elastic modulus E_{BE} not only increased significantly, but also became less variable after the HMA surface layer construction owing to the uniform overburden pressure applied. The moduli values from the BE field sensors and DCP testing were relatively similar, whereas the modulus values backcalculated from HWD tests were notably greater possibly due to the higher stress states that may have caused stress-hardening effect in the backcalculated moduli. The BE field sensors installed in the runway test sections will be further studied to monitor the changes in moduli of the base course after trafficking with various aircraft landing gear loads.

References

1. Puppala AJ (2008) Estimating stiffness of subgrade and unbound materials for pavement design, vol 382. Transportation Research Board
2. Barksdale RD, Alba J, Khosla PN, Kim R, Lambe PC, Rahman MS (1997) Laboratory determination of resilient modulus for flexible pavement design. NCHRP Web Document 14, Federal Highway Administration, Washington, D.C., 486 pp
3. Choubane B, McNamara RL (2000) Flexible pavement embankment moduli using falling weight deflectometer (FWD) data. Research Report FL/DOT/SMO/00-442, State Materials Office, Florida Department of Transportation, Tallahassee
4. Ping WV, Yang Z, Gao Z (2002) Field and laboratory determination of granular subgrade moduli. J Perform Constr Facil 16(4):149–159
5. Sharma S, Das A (2008) Backcalculation of pavement layer moduli from falling weight deflectometer data using an artificial neural network. Can J Civ Eng 35(1):57–66
6. Heisey JS, Stokoe KH, Hudson WR, Meyer AH (1981) Determination of in situ shear wave velocities from spectral analysis of surface waves. Master's thesis, University of Texas at Austin
7. Nazarian S, Desai M (1993) Automated surface wave testing: field testing. J Geotech Eng 119(7):1094–1112
8. Lenke LR, McKeen RG, Grush MP (2003) Laboratory evaluation of the geogauge for compaction control. Transp Res Rec 1849:20–30
9. Byun YH, Tutumluer E (2017) Bender elements successfully quantified stiffness enhancement provided by geogrid-aggregate interlock. Transp Res Rec 2656:31–39
10. Byun YH, Tutumluer E, Feng B, Kim JH, Wayne MH (2019) Horizontal stiffness evaluation of geogrid-stabilized aggregate using shear wave transducers. Geotext Geomembr 47(2):177–186

11. Kang M, Kim JH, Qamhia IIA, Tutumluer E, Wayne MH (2020) Geogrid stabilization of unbound aggregates evaluated through bender element shear wave measurement in repeated load triaxial testing. Transp Res Rec 2674(3):113–125
12. Byun YH, Qamhia II, Feng B, Tutumluer E (2018) Embedded shear wave transducer for estimating stress and modulus of As-constructed unbound aggregate base layer. Constr Build Mater 183:465–471
13. Carter R, Kensley R, Introduction to piezoelectric transducers. Midé Technology Corp., Woburn, MA, USA
14. Santamarina JC, Klein A, Fam MA (2001) Soils and waves. Wiley, Chichester
15. Oelze ML, O'Brien WD, Darmody RG (2002) Measurement of attenuation and speed of sound in soils. Soil Sci Soc Am J 66(3):788–796
16. Clayton CRI (2011) Stiffness at small strain: research and practice. Géotechnique 61(1):5–37
17. Hight DW, Bennell JD, Chana B, Davis PD, Jardine RJ, Porovic E (1997) Wave velocity and stiffness measurements of the Crag and Lower London Tertiaries at Sizewell. Geotechnique 47(3):451–474
18. Pennington DS, Nash DFT, Lings ML (1997) Anisotropy of G_0 shear stiffness in Gault Clay. Geotechnique 47(3):391–398
19. Rada G, Witczak MW (1981) Comprehensive evaluation of laboratory resilient moduli results for granular materials. Transp Res Rec 810:23–33
20. Uzan J (1985) Characterization of granular material. Transp Res Rec 1022(1):52–59
21. Adolf M (2010) PCASE 2.09. User manual. US Army Corps of Engineers. Transportation System Center & Engineering Research and Development
22. Priddy LP, Bianchini A, Gonzalez CR, Dossett CS (2015) Evaluation of procedures for back-calculation of airfield pavement moduli, research report ERDC/GSL-TR-15–31, Engineer Research and Development Center Geotechnical and Structures Lab, Vicksburg, MS
23. Pavement Design for Airfields (2008) UFC (Unified Facilities Criteria), 3-260-02
24. Lister NW, Powell WD (1987) Design practice for bituminous pavements in the United Kingdom. In: Proceedings, sixth international conference on the structural design of asphalt pavements, vol 1, pp 220–231

Monitoring and Modeling of Soil Thermal and Hydraulic Behavior Beneath a Granular-Surfaced Roadway

Derya Genc, Jeramy C. Ashlock, Bora Cetin, Kristen Cetin, Masrur Mahedi, Robert Horton, and Halil Ceylan

Abstract Annual freeze–thaw cycles reduce the overall performance and ride quality of granular-surfaced roadways by causing significant damage in the roadbed system during spring thaw periods. The severity of the damage depends on the subgrade properties and external environmental factors. Field monitoring can play an important role in quantifying these factors as well as the roadbed subgrade responses to further our understanding of the resulting moisture transport and freeze–thaw mechanisms. Field monitoring can also be used to assess the effectiveness of computational models that use measurements of the environmental factors to predict the subgrade response. In this study, an extensive sensor network was installed up to a depth of 213 cm (7 ft) under a granular-surfaced roadway in Hamilton County, Iowa, for continuous measurement of soil temperature and water content. Soil index properties and hydraulic properties of the subgrade soils were determined by laboratory testing of disturbed and intact soil samples. This paper presents and compares the collected data on in-situ soil temperature and soil moisture distributions with those of preliminary computational modeling of the soil response using the SHAW Model. Laboratory-assessed soil properties and weather station measurements were used as inputs for the computational predictive models. The computational models give promising results, particularly for prediction of the subgrade temperature profiles.

Keywords Soil temperature · Soil moisture content · Soil matric potential · Field monitoring · Granular-surfaced roads · Computational modeling · Precipitation

D. Genc · J. C. Ashlock (✉) · M. Mahedi · R. Horton · H. Ceylan
Iowa State University, Ames, IA 50011, USA
e-mail: jashlock@iastate.edu

B. Cetin · K. Cetin
Michigan State University, East Lansing, MI 48824, USA

1 Introduction

1.1 *Freeze–thaw Processes Under Granular Roads*

Granular-surfaced roadways play a significant role in the economy and rural life in the Midwestern states of the USA. These roadways can be damaged severely due to annual freeze–thaw cycles, as in other cold regions, due to the presence of water, frost-susceptible soils, and freezing temperatures [1, 2]. This damage can easily affect the condition and performance of the roadway and may require additional maintenance or even new construction.

One of the primary causes of freeze–thaw damage to granular-surfaced roadways is water migration and phase change during the freeze–thaw cycles. As the air temperature decreases, the temperature gradient between the unfrozen water and the frozen zone in the subgrade causes an increase in the velocity of the frost front. A matric potential gradient also develops between the frozen and unfrozen zones depending on the temperature gradient and size distributions of voids and soil particles. Therefore, water migrates from the unfrozen soil to the frozen soil in response to both thermal gradients and matric potential gradients. As the frost front slows down, the temperature gradient is reduced, and water can accumulate at a certain depth and freeze to form ice lenses [3].

As the water freezes and turns to ice, its volume increases. As the amount of water increases in the frozen zone, the overall change in volume will thus be greater. Due to the volume increase, internal pressure is applied to the subgrade. As thawing occurs, the ice within the soil melts and the internal pressure decreases. The stiffness of the soil also decreases as the water in the soil changes its phase from solid to liquid. This process causes frost heave problems and weakening of the subgrade material, particularly during thawing. Therefore, the severity of the freeze–thaw damage depends on the subgrade soil properties including frost-susceptibility, hydraulic and thermal conductivities, and pore size distribution, in addition to environmental factors such as precipitation and groundwater table level [1]. Subgrade soils have been monitored in many studies over long periods to understand the effects of freeze–thaw cycles on soil structure. Field monitoring data can provide continuous and accurate representations of the thermal and hydraulic dynamic processes during freeze–thaw cycles [2].

Long-term subgrade measurements are also useful for examining the accuracy, sensitivity, and effectiveness of computational models [4–6]. Since some models are only valid for specific soil types, temperature ranges, or environmental conditions, the measured data can be used to calibrate or enhance the capabilities of existing models. For example, Zhao et al. [4] conducted a study to evaluate a computational model of soil freezing by using field data collected from Inner Mongolia. In another study, hydrothermal transfer processes during soil freezing and thawing were simulated using a coupled heat and water transfer model, and the results were compared with the observed temperature profile from a site in the Qinghai–Tibet Plateau [5]. In a

similar study, the coupled heat and water transfer model SHAW was compared with data from sensors at depths of 0.05, 0.15, and 0.30 m in the soil [6].

Nevertheless, there are limited studies that target freeze–thaw cycles under granular-surfaced roadways and the resulting damage they cause. In this study, the subgrade beneath a granular-surfaced roadway was monitored for one complete seasonal winter–spring freeze–thaw period to collect data on temperature and moisture content variations. The seasonal temperature and moisture variations were calculated for the same soil profile by using the computational model SHAW with the inputs obtained from atmospheric conditions and laboratory-measured soil index properties. Then the monitoring data were compared to the preliminary modeling results generated by SHAW to understand the overall consistency and differences. The procedure described herein can be used to calibrate freeze–thaw models to improve their prediction accuracy, which could be used to help control damage to granular-surfaced roads, for example, by identifying the critical thawing period during which frost embargos should be imposed.

1.2 SHAW Model

The simultaneous heat and water (SHAW) software program is a one-dimensional computational model used to simulate freezing and thawing vertically in soils. It accounts for the transfer of heat, water and solute from the top of a plant canopy, snow cover, residue, or soil surface to a chosen depth within the soil [6–8]. Due to its capability of simulating the combined effects of residue, snow and soil, it is widely used by researchers in Agronomy studying vegetation [9]. However, it may also be a beneficial resource for geotechnical engineering applications.

In SHAW, the simultaneous heat and water transfer within the system is defined from the water and heat fluxes into the system using boundary conditions determined from user-specified inputs of initial soil temperature and water content conditions, atmospheric conditions at the upper boundary, and soil conditions at the lower boundary. Heat and water transfer in the SHAW model is calculated for a node located at the center of each soil layer such that thermal and hydraulic equilibrium are achieved. The transient heat transfer within the system is defined through the following partial differential equation [10, 11]:

$$\frac{\partial}{\partial z}\left(\lambda_s \frac{\partial T}{\partial z}\right) + \rho_l c_l \frac{\partial (q_l T)}{\partial z} + S = C_s \frac{\partial T}{\partial t} - \rho_i L_f \frac{\partial \theta_i}{\partial t} + L_v \left(\frac{\partial \rho_v}{\partial t} + \frac{\partial q_v}{\partial z}\right) \quad (1)$$

where λ_s is the thermal conductivity of soil (W/m/°C), c_l is the specific heat capacity of water (J/kg/°C), q_l is the liquid water flux (m/s), S is the a source term source (W/m^3), T is the temperature (°C), C_s is the volumetric heat capacity of soil (W/m^3/°C), L_f is the latent heat of fusion (J/kg), and L_v is the latent heat of vaporization (J/kg).

Water flow within the system is defined by the following partial differential equation [7, 10, 11]:

$$\frac{\partial}{\partial z}\left[k\left(\frac{\partial \psi}{\partial z}+1\right)\right] + \frac{1}{\rho_l}\frac{\partial q_v}{\partial z} + U = \frac{\partial \theta_l}{\partial t} + \frac{\rho_i}{\rho_l}\frac{\partial \theta_i}{\partial t} \qquad (2)$$

where k is the unsaturated hydraulic conductivity (m/s), ψ is the matric potential (m), z is the vertical coordinate (m), ρ_l is the density of liquid water (g/cm^3), ρ_i is the density of ice (g/cm^3), θ_l is the volumetric liquid water content (cm^3/cm^3), θ_i is the volumetric ice content (cm^3/cm^3), q_v is the water vapor flux (m/s), U is a source/sink term (cm^3/cm^3/s), and t is time (s).

Some of the parameters such as matric potential at unsaturated conditions and unsaturated hydraulic conductivity in Eqs. (1) and (2) were interpreted from soil density and soil constituent fractions of sand, silt, clay, water, ice, and air in the soil layer. The density and soil particle size distribution were measured in the laboratory. To predict the matric potential and unsaturated hydraulic conductivity of soil, the Campbell equations were used in the SHAW model as follows:

$$\psi = \psi_e\left(\frac{\theta}{\theta_s}\right)^{-b} \qquad (3)$$

where ψ is matric potential (m), ψ_e is air entry potential (m), b is a pore size distribution parameter, θ is volumetric liquid water content, θ_s is saturated water content, and

$$K = K_s\left(\frac{\psi_e}{\psi}\right)^{(2+3/b)} \quad \text{for} \quad \psi < \psi_e, \qquad (4)$$

where K_s is saturated hydraulic conductivity (m/s).

Atmospheric conditions from a weather station were also used as inputs, specified in the form of air temperature, wind speed, precipitation, relative humidity, and solar radiation. These variables should be collected either daily or hourly to run the SHAW model. In the present study, hourly weather data were used. In addition, the granular roadway surface was represented by specifying an additional soil layer on top of the subgrade; the residue and canopy layers were not used in the analysis.

2   Field Instrumentation and Data Collection

Field data were collected from the subgrade of a granular-surfaced roadway within a 500-ft long test section on Vail Avenue in Hamilton County, Iowa. This test section was designed to have an extensive sensor network system consisting of 80 soil sensors
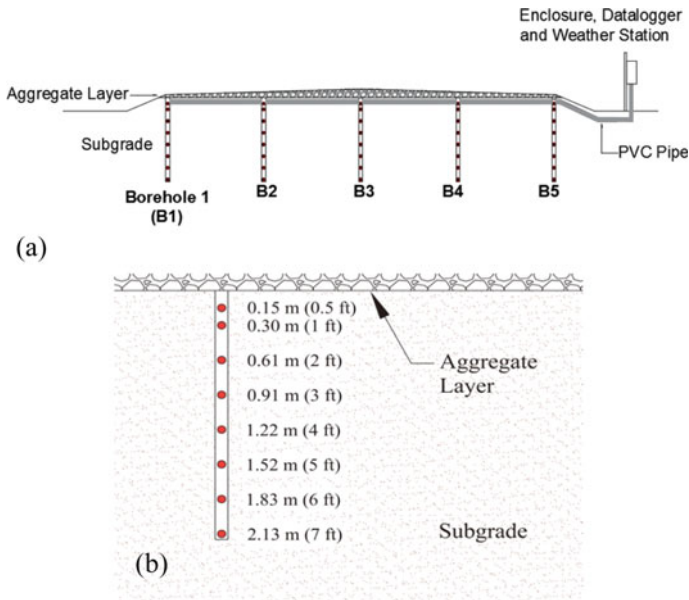
Fig. 1 **a** Cross section of the granular-surfaced road test section in Hamilton County, IA, **b** sensor depths below the aggregate–soil interface

forming a grid across the roadway cross section, with a weather station installed adjacent to the site. The subgrade of the test section was instrumented with soil moisture content, temperature, and matric potential sensors installed in five boreholes located at the shoulders, quarter points and centerline of the roadway (Fig. 1a). Sensors were installed at eight different depths within these boreholes as shown in Fig. 1b, which ranged from 0.15 to 2.13 m below the subgrade surface. The array of sensors was used to study lateral as well as vertical variations in soil temperature and moisture throughout the roadway cross section.

A weather station was also installed adjacent to the roadway to capture the atmospheric conditions simultaneously with the changes occurring in the soil. The weather station was used to measure the following variables: (1) precipitation, (2) wind speed and direction, (3) solar radiation, (4) air temperature, and (5) relative humidity. These variables were chosen so that the weather data were comparable to those of the existing Road Weather Information System (RWIS) network [9]. In addition, these values were required for specifying inputs to the SHAW model, as discussed previously. For this purpose, a composite weather station was selected which had the benefits of being compact, lightweight, and easily integrated with the datalogger selected for the site.

Observations from the 80 subgrade sensors and the weather station were obtained by a multipurpose measurement and control datalogger at 10-min intervals. This interval was chosen for consistency with the RWIS data. Because of the large number of sensors in the system, two multiplexers were also used to connect all of the sensors

to the single datalogger. A cellular modem was also installed to enable remote data downloading and troubleshooting [10].

Data collection was initiated in late August 2018. However, some unstable and out-of-range measurements were observed through mid-November 2018, which required troubleshooting to resolve. The measured data presented in this study were from November 20, 2018, to September 23, 2019, covering a total duration of 10 months. The groundwater table was estimated to be 1.20–1.52 m (4–5 ft) deep based on the volumetric water content measurements during the period.

3   Laboratory Testing of Soil Properties

Continuous intact soil cores were taken from the test section for laboratory tests to determine the in-situ index and hydraulic properties of the soil layers, which were later used as input values for modeling. The cores were collected at the centerline (Borehole B3) and one shoulder (Borehole B5) using 76 mm (3 in.) diameter thin-walled tubes to depths of 2.13 m (7ft). Samples were divided into 0.3 m (1 ft) long segments for testing. SHAW requires input values of percent clay, percent sand, percent silt, percent organic material, bulk density, saturated hydraulic conductivity, and saturated water content. Therefore, particle size distribution tests (ASTM D6913 and ASTM D7928) were conducted along with saturated hydraulic conductivity tests using a Shelby Tube Permeameter (ASTM D2434). For soil classification, the Unified Soil Classification System (USCS) particle size limits were used, which are 4.75 mm, 0.075 mm, and 0.002 mm for the demarcations between gravel–sand, sand–silt, and silt–clay, respectively.

Pressure cell tests were performed to measure soil water retention curves and to determine saturated water contents. The soil samples were first saturated for 2–3 weeks depending on the soil type. The obtained saturated water contents were compared with the maximum values measured in-situ. For depths of 0.91 m (3 ft) and deeper, the laboratory saturated water content values were lower than the in-situ maximum soil water contents measured by the sensors. This discrepancy may have been a result of sample disturbance. Therefore, the measured in-situ maximum water contents were used in the SHAW models for these depths. The bulk density of soil samples was also measured as part of the soil water retention curve tests. However, the SHAW model did not accept bulk density values larger than 2.0 g/cm^3, so the upper limit of 2.0 g/cm^3 was used for samples whose measured values exceeded this limit. It is important to note that for soil science studies and the SHAW program, bulk density is commonly defined as the mass of dry soil per total volume of soil (i.e., dry density), whereas in geotechnical engineering bulk density commonly refers to the ratio of the wet total mass to the total volume (i.e., moist density) [12, 13]. The user of the model should be aware of which value to enter. The percent organic material was assumed to be zero for all of the layers. Finally, percent fraction of gravel, sand, silt, and clay was entered according to the particle size distribution analysis results.

Table 1 Soil properties of centerline borehole (B3) entered as inputs to the SHAW model

Soil Layer Depth[a] (m)	Gravel (%)	Clay (%)	Sand (%)	Silt (%)	Bulk Density[b] (g/cm³)	θ_{sat}[c] (cm³/cm³)	k_{sat}[d] (cm/h)
Aggregate	31.1	6.2	54.5	8.2	2.00	0.150	36.0
0.00–0.30	0.0	42.5	27.1	30.4	1.41	0.467	0.001
0.30–0.61	0.0	22.4	35.3	42.3	1.13	0.573	0.022
0.61–0.91	0.0	48.3	20.1	31.6	1.53	0.422	0.006
0.91–1.22	2.6	31.6	41.9	23.9	1.39	0.475	0.001
1.22–1.52	3.1	25.5	43.9	27.5	1.43	0.461	0.002
1.52–1.83	2.4	25.5	41.5	30.6	1.33	0.497	0.005
1.83–2.13	0.9	23.3	45.7	30.1	1.46	0.448	0.002

[a]Depths are measured from the bottom of the aggregate layer
[b]Dry soil mass per total volume
[c]Saturated volumetric water content
[d]Saturated hydraulic conductivity

The input values used in the SHAW modeling of the soil profile at Borehole B3 are given in Table 1.

An aggregate layer with 10 cm (4 in.) thickness was created on top of the soil layers to simulate the granular roadway conditions of the test site. In SHAW, the top of the aggregate layer is at the surface (0 m depth) and the soil layers start at 10 cm depth. For plotting purposes, the corresponding field sensor depths measured from the bottom of the aggregate layer, as denoted in Fig. 1b, are used in the comparison of results. Particle size distribution tests were also conducted for the aggregate surface material.

4 Results and Discussion

Coupled heat and water transfer SHAW analyses were conducted for the borehole at the centerline (Borehole B3) for the monitoring period of November 20, 2018, to September 23, 2019. The results are compared to the field measurements for all sensor depths in Figs. 2 and 3. For the atmospheric data input, the weather station measurements of air temperature, precipitation, solar radiation, relative humidity, and wind speed collected within the simulation period were used. The field measurements taken at 10-min intervals were averaged to obtain the hourly inputs required by SHAW. Snow, residue and vegetation cover were specified as absent, so no input values were necessary for these parameters, as previously mentioned.

The dielectric water content sensors were only capable of measuring the liquid water content in the soil. This was because water in the liquid phase had a higher dielectric constant ($\kappa_{water} \approx 80$) than the air and solids ($\kappa_{air} \approx 1$, $\kappa_{solids} \approx 4$ to 16), whereas frozen water had a dielectric constant close to that of the solids ($\kappa_{ice} \approx$
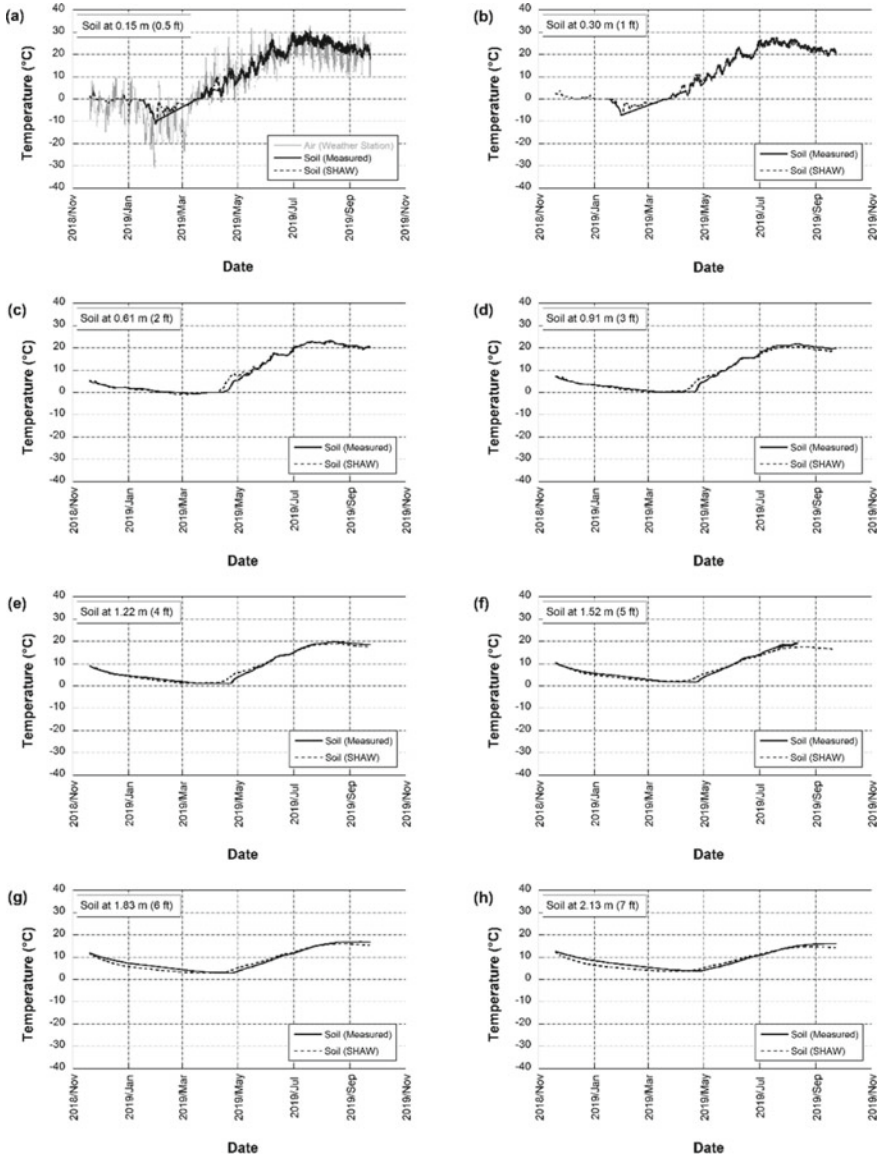
Fig. 2 Measured and modeled data for soil temperature at depth of **a** 0.15 m (along with air temperature from weather station), **b** 0.30 m, **c** 0.61 m, **d** 0.91 m, **e** 1.22 m, **f** 1.52 m, **g** 1.83 m, and **h** 2.13 m
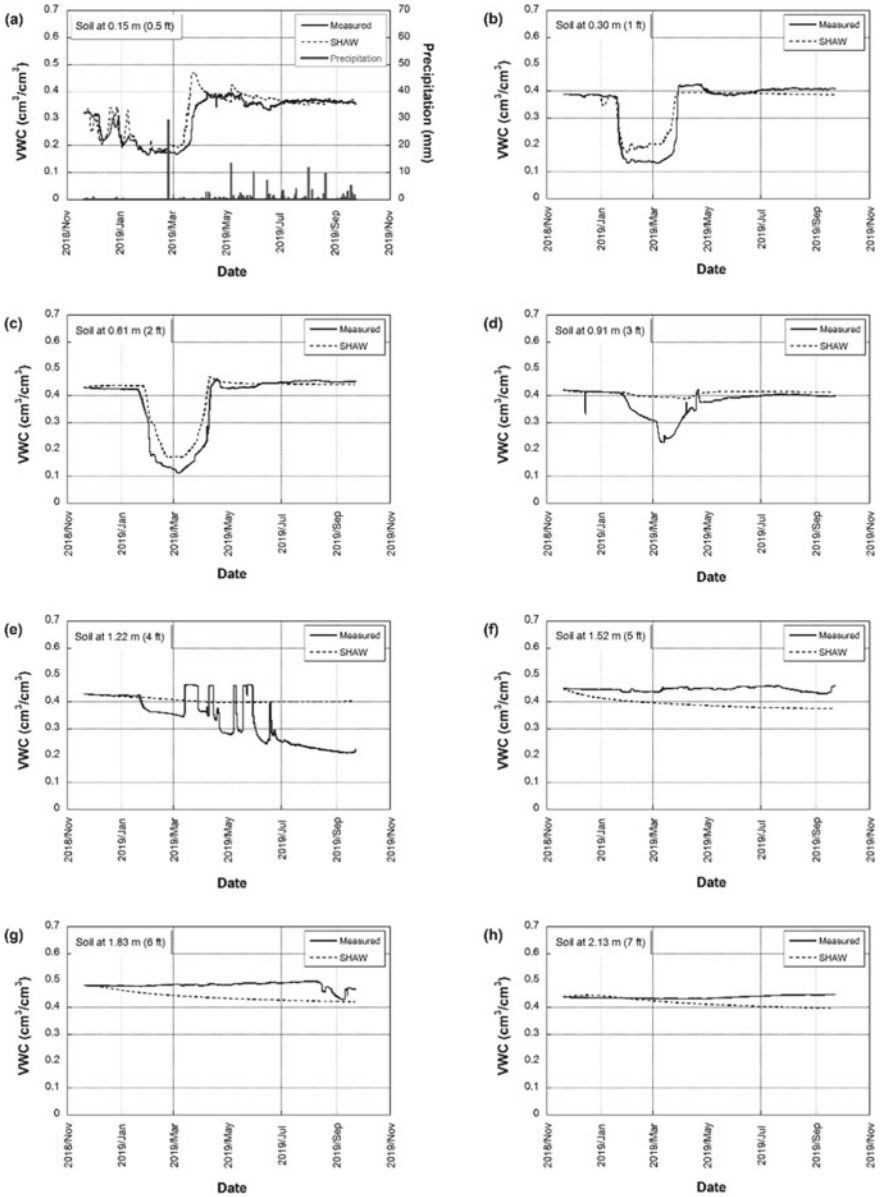
Fig. 3 Measured and modeled data for soil volumetric water content at depth of **a** 0.15 m (along with precipitation from weather station), **b** 0.30 m, **c** 0.61 m, **d** 0.91 m, **e** 1.22 m, **f** 1.52 m, **g** 1.83 m, and **h** 2.13 m

3.2) [14–17]. Therefore, the frozen soil water could not be distinguished from that of dry soil by the sensors. However, sudden decreases in the liquid water content values were observed in late January 2019 as the soil water partially froze (Fig. 3). This sudden transition was also consistent with soil temperatures decreasing to 0 °C or lower (Fig. 2). Therefore, although the dielectric water content sensors did not provide measurements of the frozen water content, the sudden drop in liquid water content at temperatures at or below 0 °C did indicate the onset of freezing.

The modeling results agreed reasonably well with the trends of the measured data. As can be seen in Fig. 2a, the soil temperature was directly affected by the air temperature changes, with an increasing time lag and diminishing amplitude with depth, as expected. The SHAW model results were able to capture the general trends of the measured temperatures for all depths with reasonable accuracy. The model was able to predict the freezing and thawing periods accurately. For the top two depths of 0.15 m (0.5 ft) and 0.30 m (1 ft), the model predicted a slightly higher soil temperature during the freezing period, but matched the measured temperatures much more closely during thawing, whereas for the deeper points the freezing period was predicted correctly and thawing started slightly earlier than recorded by the sensors.

For the volumetric liquid water content (VWC) results, there was relatively good agreement between the modeling results and the measured data. First, the effect of precipitation and thawing was observed at the shallowest depth of 0.15 m (0.5 ft) as a sudden increase in the measured VWC after the soil thawed. However, precipitation did not seem to have a significant impact on measured VWC at 0.30 m (1 ft) or deeper. To a depth of 0.91 m (3 ft), the freezing of soil water could be observed from both the measured and predicted VWC data. SHAW was able to capture the timing of freezing and thawing at these shallow depths. Although SHAW predicted the occurrence of freezing at 0.91 m (3 ft), it did not well predict the decrease in VWC (i.e., frozen water content). The in-situ measurements at 1.22 m (4 ft) showed irregular readings with several increases and decreases in VWC. This instability could have been triggered by seasonal groundwater level fluctuations. For the deeper layers, the measured VWC values become relatively constant between 0.4 and 0.5, which is likely due to these sensors being below the water table. For the depths of 1.22 m (4 ft) and greater, the VWC values predicted by SHAW did not fluctuate, but decreased slightly over time. The water table was not specified in the SHAW model calculations, so the slight decreases in VWC at the lower depths were due to the imposed unit-gradient lower boundary condition; i.e., the matric potential gradient was set at zero and gravity was the only driving force for water drainage. Therefore, accounting for the groundwater table in SHAW could help to improve the VWC predictions at the deeper points.

5 Conclusions

In this study, soil temperature and water content simulation results obtained using the simultaneous heat and water (SHAW) model were compared to in-situ data measured

below a granular road test section. Because the model requires in-situ soil properties as inputs, the soil index and hydraulic properties were determined from laboratory tests on intact soil cores collected from the field or were specified by the SHAW model. However, some of the laboratory-measured saturated water content values were not in agreement with the field observations and were therefore replaced by the maximum water contents measured in the field. SHAW is a detailed model for coupled heat and water transfer calculations, which has been used for several agronomic applications. This study is one of the first evaluations of SHAW for a geotechnical application. Several limitations were identified in this study associated with its application to geotechnical problems.

Overall, the preliminary SHAW model predictions provided promising results for simulating the temperature and water content variations and freeze–thaw cycles over a 10-month period for this specific site. The modeled soil temperatures closely matched the measured data except during soil freezing at depths shallower than 0.61 m (2 ft) and during thawing periods below this depth. The predicted water contents did not always match well the measured data, partially due to the sensor's inability to measure VWC in the frozen state and possibly due to a fluctuating water table not accounted for in the SHAW model. Water content in the frozen state can be studied further and supplemented by nuclear gauge measurements of the frozen soil's water content in the future studies. Based on the results presented herein, such further refinements of the SHAW model and its inputs may be able to improve the agreement between the measured and predicted results.

References

1. White D, Vennapusa P (2013) Low-cost rural surface alternatives: literature review and recommendations (IHRB Project TR-632)
2. Saarenketo T, Aho S (2005) Managing spring thaw weakening on low volume roads problem description, load restriction policies, monitoring and rehabilitation
3. Konrad JM, Morgenstern NR (1980) A mechanistic theory of ice lens formation in fine-grained soils. Can Geotech J 17(4):473–486. https://doi.org/10.1139/t80-056
4. Zhao Y, Si B, He H, Xu J, Peth S, Horn R (2016) Modeling of Coupled Water and Heat Transfer in Freezing and Thawing Soils, Inner Mongolia. Water (Switzerland) 8(10):1–18. https://doi.org/10.3390/w8100424
5. Hu G, Zhao L, Li R, Wu T, Wu X, Pang Q, Xiao Y, Qiao Y, Shi J (2015) Modeling hydrothermal transfer processes in permafrost regions of Qinghai-Tibet Plateau in China. Chin Geogra Sci 25(6):713–727. https://doi.org/10.1007/s11769-015-0733-6
6. Hymer DC, Moran MS, Keefer TO (2000) Soil water evaluation using a hydrologic model and calibrated sensor network. Soil Sci Soc Am J 64:319–326
7. Flerchinger GN (2017) The simultaneous heat and water (SHAW) model: technical documentation, Boise, Idaho
8. U.S. Department of Agriculture (USDA) Agricultural Research Service: SHAW Model. https://www.ars.usda.gov/pacific-west-area/boise-id/watershed-management-research/docs/shaw-model/. Accessed 11 Nov 2019
9. Li R, Shi H, Flerchinger GN, Akae T, Wang C (2012) Simulation of freezing and thawing soils in Inner Mongolia Hetao Irrigation Distinct, China. Geoderma 173–174:28–33. https://doi.org/10.1016/j.geoderma.2012.01.009

10. Flerchinger GN, Saxton KE (1989) Simultaneous heat and water model of a freezing snow residue soil system I. Theory and development. Trans ASAE 32(2):565–571
11. Nassar IN, Horton R, Flerchinger GN (2000) Simultaneous heat and mass transfer in soil columns exposed to freezing/thawing conditions. Soil Sci 165(3):208–216
12. Jury, W.,Horton, R.: Soil physics: 6th ed. Hoboken, NJ: J. Wiley, 29 (2004).
13. Knappett JA, Craig RF (2012) Craig's soil mechanics, 8th edn. Spon Press, Abingdon, p 23
14. Genc D, Ashlock JC, Cetin B, Kremer P (2019) Development and pilot installation of a scalable environmental sensor monitoring system for freeze-thaw monitoring under granular-surfaced roadways. Transp Res Rec 1(11). https://doi.org/10.1177/0361198119854076
15. Bittelli M (2011) Measuring soil water content: a review
16. Genc D (2019) Development, installation and preliminary data collection of an environmental sensor system for freeze–thaw monitoring under granular-surfaced roadways. Graduate Theses and Dissertations. 17450. https://lib.dr.iastate.edu/etd/17450
17. Patterson DE, Smith MW (1980) The use of time domain reflectometry for in frozen soils. Cold Reg Sci Technol 3:205–210

Risk Evaluation of Unbound Pavement Layers to Extreme Weather Events Using Remote Sensing

Joe Rosalez , **Sonya Lopez, and Mehran Mazari**

Abstract The resilience of transportation infrastructure during and after extreme weather events, such as flash floods, sea-level rise, and hurricanes, is critical. A disruption in transportation and road networks during and after such events can delay emergency services and may disrupt the evacuation process. Studying the resilience of the transportation networks with a comprehensive data source can enhance the resiliency of infrastructure and assess the risks associated with a natural disaster. In this study, open-source satellite observations were used to investigate the impact of Hurricane Harvey on the performance of the pavement network in the State of Texas in 2017. Using volumetric moisture content, the environmental stress factor was calculated before, during, and after the hurricane to estimate the changes in the strength of geomaterial pavement layers. A preliminary risk assessment parameter was developed to evaluate and compare the resiliency of roads in the network. The results of this study can be further extended to other coastal regions with the incorporation of more in situ data and an extended version of the risk factor.

Keywords Extreme weather events · Resilience · Transportation infrastructure · Unbound pavement layers · Satellite data

1 Introduction

Extreme weather events such as flash floods and hurricanes could damage the transportation infrastructure and road pavements, specifically the unbound geomaterial layers (e.g., subgrade soil and granular base layer), due to excessive inundation, which

---

J. Rosalez · S. Lopez · M. Mazari (✉)
California State University Los Angeles, Los Angeles, CA 90032, USA
e-mail: mmazari2@calstatela.edu

J. Rosalez
e-mail: jrosal51@calstatela.edu

S. Lopez
e-mail: slope188@calstatela.edu

    889

increases the water content. Moreover, the groundwater table is mainly affected by the rising sea level in coastal regions. High tides and sea-level rise can potentially inundate pavement infrastructures along coastlines [1, 2]. The intrusion of excess water into pavement geomaterial layers negatively impacts the strength of those layers and affects the structural performance and load-bearing capacity of the pavement system. Such changes are not always visible and may lead to the failure of road infrastructure under traffic loads. Estimating the performance of pavements under flooded conditions can help to prevent future structural failures. One approach to evaluating the impact of moisture variations during flooding is through the concept of environmental conditions as introduced in the Mechanistic-Empirical Pavement Design Guide (MEPDG). The proposed guidelines incorporate the variation of moisture in terms of the degree of saturation as part of the Enhanced Integrated Climate Model (EICM), which simulates the impact of environmental conditions on pavement structural response [3]. However, the uncertainties associated with the construction process should also be considered.

The design guide for new pavement structures recommends the placement and compaction of unbound pavement layers at or near the optimum moisture condition that is achieved at the maximum dry density in laboratory conditions. Any variation in moisture content from optimum conditions can lead to a change in the strength of compacted geomaterials. The variation of moisture content in pavement materials is categorized as follows [4]: variation of moisture content from initial or optimum value of the equilibrium condition, seasonal variation of moisture content that could happen due to precipitation, flash storms, sea-level rise and groundwater table rise, and variation of moisture content due to freeze/thaw cycles during cold seasons. The main objective of this study was to evaluate the impact of moisture variation, due to an extreme weather event such as a flash flood, on the strength of pavement geomaterial layers in terms of failure risk. The following sections summarize the research efforts in the literature related to the main objective of the current study, followed by the explanation of the data collection and analysis process.

Several studies in the literature showed that increasing moisture content in compacted geomaterials results in a reduction of strength in terms of resilient modulus (MR) and stiffness [5–11]. Evaluating the short-term and long-term structural capacity of pavement structures during and after weather events can help decision-makers decide when to resume traffic on a flooded section of a highway [12–15]. Knott et al. [16] presented an adaptation plan to mitigate pavement damage from groundwater triggered by sea-level rise in a coastal region. They performed two case studies of coastal roads subject to elevated groundwater due to different sea-level rise scenarios. A layered elastic model was employed to evaluate the performance of various pavement structures under the expected inundations. They showed that modification of pavement structure could delay the inundation by 20 years and can eliminate the expected reduction in service life as a result of sea-level rise. That study showed that an adequate unbound geomaterial pavement layer combined with a simple top layer modification could avoid the premature failure of the inundated pavement structure.

Qiao et al. [17] developed a decision tree model to estimate post-flood pavement operations to maintain the serviceability of inundated roads. They applied the developed strategy to evaluate a case study using falling weight deflectometer (FWD) data to evaluate the structural performance of the flooded pavement system. Their study showed that the post-flood decision-making process is affected by uncertainties in the actual structural performance of the inundated pavement, variability of in situ data collection devices, and estimation of maintenance and repair costs. Zhang et al. [18] evaluated the pavement structural damage caused by flooding during Hurricane Katrina. They also used an FWD along with other in situ field tests to evaluate the performance of post-flood pavement systems. By comparing the before and after data for resilient modulus and structural number (SN) of the flooded pavement sections, they concluded that inundation reduces the structural capacity of both surface layers and underlying unbound geomaterial layers. The failure was significantly higher for roads with thin pavement layers. Sultana et al. [19] presented a deterministic model to predict the short-term performance of flexible pavement systems after a major flooding event. They showed that the flooded pavement section deteriorated at a faster rate compared to the predicted deterioration rate for an unflooded pavement structure. The developed structural strength ratio is a function of time after flooding. The authors concluded that resurfacing and rehabilitation strategies based on predicted post-flood deterioration is critical in maintaining the structural integrity of inundated pavement sections.

In this study, the network-level performance of road infrastructure after a significant flooding event was evaluated using satellite data and remote-sensing products. The impact of flooding on the strength of unbound geomaterial pavement layers was estimated based on the extracted satellite data during and after the case study. We also explored the development of a preliminary risk assessment methodology. The following sections include the details of data extraction, processing, and model development.

2 Methodology

Multiple satellite data sources were collected in this study to estimate the environmental factor that affects the strength of pavement foundation layers for a case study of the state of Texas road network before and after Hurricane Harvey. The disruption in transportation and road networks during and after this event caused delays for the emergency services and interrupted the evacuation process. By utilizing the National Aeronautics and Space Administration (NASA) open-access Soil Moisture Active Passive (SMAP) satellite Version 3 dataset, we were able to collect the volumetric moisture content (cm^3/cm^3) before, during, and after Hurricane Harvey. Using this and other datasets from the Texas Department of Transportation (TxDOT), we were able to identify areas at risk of damage due to extreme weather events. The daily observations of soil moisture from the SMAP satellite for geolocations along with the Texas road network from August 1, 2017, through September 30, 2017,

were extracted. We mainly focused on the hurricane period, which was August 17 to September 3, 2017. This study incorporated statistical and geospatial analysis methods to process the complex satellite data and determine how the storm affected the road network.

We have employed the concept of environmental factor, that was introduced in the initial version of Mechanistic-Empirical Pavement Design Guide, to estimate the variations of resilient modulus of pavement structures due to moisture fluctuations, in terms of the degree of saturation, as shown in Eq. 1:

$$MR = F_{env} \times MR_{opt} \tag{1}$$

where F_{env} is the composite environmental adjustment factor that considers changes in moisture, density, and freeze/thaw conditions, and MR_{opt} is the resilient modulus at optimum conditions. When F_{env} is less than 1.0, the corresponding resilient modulus is less than the resilient modulus at optimum conditions, which shows a higher moisture level in the form of degree of saturation. In this study, we also employed Eqs. 2 and 3 to calculate the environmental factor for the unbound pavement layers in the road network. Equation 2, defined by Witczak et al. [3], is used for both fine- and coarse-grained unbound pavement materials.

$$\log(F_{env}) = \log\left(\frac{MR}{MR_{opt}}\right) = a + \frac{b - a}{1 + e^{\left(\ln \frac{-b}{a} + k_m \times (S - S_{opt})\right)}} \tag{2}$$

where MR is the modulus at a degree of saturation S (in decimal), S_{opt} is the degree of saturation (in decimal) at the maximum dry density, and optimum moisture content and a, b, and k_m are regression parameters. Volumetric moisture content, extracted from the satellite data, is a measurement of the volume of water in the volume of a porous medium (in cm^3/cm^3), while the degree of saturation (S) is defined as the ratio of volumetric water content to porosity.

Cary and Zapata [7] developed an empirical equation that further evaluated the impact of moisture variation. Their model used a more specific set of parameters by incorporating additional geomaterial properties, including the percent finer than No. 200 sieve (w, in decimals) and the plasticity index of the geomaterials (PI, in percent) as follows:

$$\log(F_{env}) = \left(\alpha + \beta \times e^{-wPI}\right)$$
$$+ \frac{\left(\delta + \gamma \times wPI^{0.5}\right) - \left(\alpha + \beta \times e^{-wPI}\right)^{-1}}{1 + e^{\left(\ln\left(\frac{-\left(\delta + \gamma \times wPI^{0.5}\right)}{\left(\alpha + \beta \times e^{-wPI}\right)^{-1}}\right) + \left(\rho + \omega \times e^{-wPI}\right)^{0.5} \times \left(\frac{S - S_{opt}}{100}\right)\right)}} \tag{3}$$

Table 1 summarizes the model parameters for both Eqs. 2 and 3. To further simplify Eq. 3, we followed the approach proposed by Nazarian et al. [9] and Mazari and

Table 1 F_{env} model parameter summary for Eq. 2 and 3

Equation 2	Coarse-grained	Fine-grained	Equation 3	Values	Equation 3	Values
a	−0.3123	-0.5934	α	−0.6000	γ	0.08000
b	0.3010	0.3979	β	−1.8719	ρ	11.9652
k_m	6.8157	6.1324	δ	0.8000	ω	−10.1911

$F_{env} = MR/MR_{opt}$, the ratio of MR at a given time to a resilient modulus at optimum conditions MR_{opt}, a = minimum of $\log F_{env}$, b = maximum of $\log F_{env}$, k_m = regression parameter, $\alpha, \beta, \delta, \gamma, \rho, \omega$ = regression parameters

Nazarian [11] that suggested assuming $wPI = 0$ in Eq. 3 could represent a wide range of geomaterials.

2.1 Remote Sensing of Soil Moisture Data

This study used NASA's Soil Moisture Active Passive (SMAP) measurements that provide global soil moisture estimates up to 5 cm depth [20]. The SMAP satellite, which was launched in January 2015, combines the advantage of both active (radar) and passive (radiometer) microwave remote sensing to estimate soil moisture with specific accuracy and resolution [21]. The Level-3 product has a 0.1-degree spatial resolution with daily observations. Global volumetric soil moisture maps (in cm^3/cm^3) have an unbiased root mean squared error no greater than 0.04 cm^3/cm^3 [21, 22]. The combination of orbital spin and antenna movement generates a 1000 km gap every eight days, as shown in Fig. 1. An upgraded product with no data gap is expected from NASA in the near future.
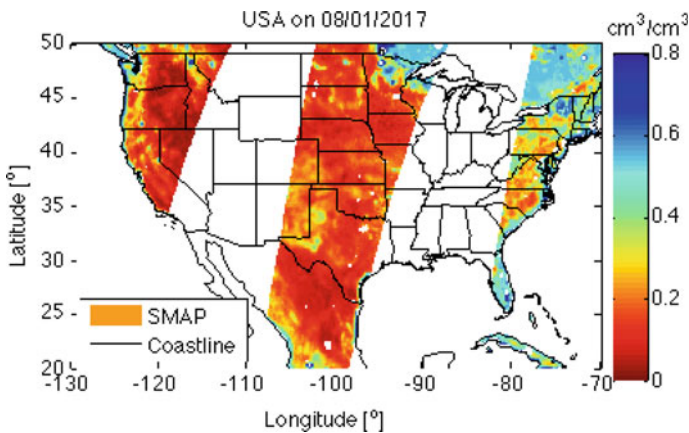

Fig. 1 SMAP swath over the State of Texas on August 1, 2017

To evaluate the performance of pavement structures in the road network during flooding, we extracted major highway and roadway polylines from the Texas Department of Transportation database for the year of the hurricane [23]. Polylines represent the centerline of the road or highway. Both SMAP and transportation datasets were georeferenced using the North American Datum 1983 (NAD83) coordinate system. SMAP data was superimposed onto a map subset using user-defined north, east, west, and south coordinate boundaries. In this study, the subset coordinates ranged from 25.70° N to 36.66° N latitude and 92.0° W to 106.7° W longitude, which spanned the entire state of Texas.

The minimum distance, as defined in Eq. 4, was used to identify the nearest neighbor between the road or highway centerline point and a SMAP data point.

$$\min D = \sqrt{(x_s - x_T)^2 + (y_s - y_T)^2} \tag{4}$$

x and y are longitudinal and latitudinal coordinates, respectively, for SMAP (s subscript) and TxDOT (T subscript). We extracted daily soil moisture data for each road segment during the observation period and performed statistical analyses to estimate the impact of traffic and flooding in terms of a risk factor that can represent the risk of pavement structural failure due to flooding. The following section includes the details of extracting traffic data and developing the preliminary risk factor.

2.2 Preliminary Risk Assessment

Pavement structures are designed to withstand traffic loads from different vehicle types. However, to combine and superimpose the damage incurred by traffic load impacts, a unified scale is required. The 18,000-lb (or 18 kips) equivalent single axle load (ESAL) is commonly used in pavement studies to evaluate the impact of traffic loads. The traffic data were extracted from the TxDOT online database. The ESAL values were then used to calculate the traffic index (TI) for each road network using Eq. 5. Traffic Index is an estimation of the number of ESALs to be expected during the service life of the pavement structure in the design lane and is calculated as follows [24]:

$$TI = 9\left(\frac{\text{ESALs} \times \text{LDF}}{10^6}\right)^{0.119} \tag{5}$$

where TI is the traffic index and LDF is the lane distribution factor. Considering the impact of changes in the degree of saturation, due to flooding, on the strength of pavement layers, the preliminary risk factor (RISK) was defined as the ratio of the traffic index to the F_{env} value (Eq. 6). Larger values of risk parameter identify the roads at higher risk of structural damage or failure due to moisture intrusion.

$$\text{RISK} = \frac{\text{TI}}{F_{\text{env}}} \tag{6}$$

3 Results and Discussion

From the TxDOT roadway inventory, we were able to study over 16,000 lane miles of state highways and roads, which accumulated more than 1 million points of interest. The SMAP radar data were georeferenced on the points of interest to calculate the environmental factor using the soil moisture content values. Figure 2 shows the daily mean of the degree of saturation and the environmental factor for coarse- and fine-grained pavement geomaterials using Eqs. 2 and 3. The highlighted section is the inundation period from Hurricane Harvey. The hurricane caused surface inundation resulting in a significant decrease in the magnitude of the environmental factor. This triggered a drop in overall geomaterial pavement layer strength.

Equation 3 provided the highest variability in F_{env} calculation in comparison to the fine-grained and coarse-grained calculations. However, all equations matched with the daily low values. Lower values of F_{env} are of more significant concern since they represent lower strength of the pavement structure. The difference in F_{env} calculation between coarse-grained and fine-grained soils is due to soil porosity. Recall, the degree of saturation is the ratio of volumetric water content to porosity, and an increase in porosity for a given water content increases the degree of saturation. A high saturation level decreases the F_{env} value, as shown in Fig. 2 for fine-grained soils.
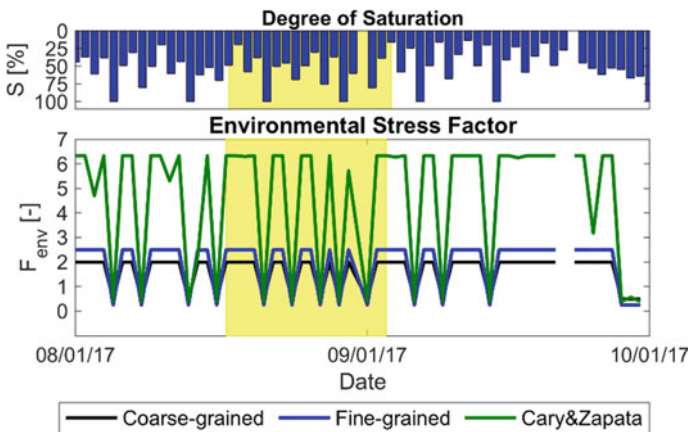

Fig. 2 Variation of degree of saturation based on satellite data, and variation of pavement layer strength for different geomaterial types before, during (yellow shaded region), and after Hurricane Harvey

F_{env} calculations, using Eq. 3, for selected days within the study period are illustrated in Fig. 3. Those sections of the road network shown in gray are the locations missing from the daily SMAP observations. The environmental factor is low for pavements near the coastline during early August, then moves further inland when the Hurricane period begins. Locations in blue experienced the highest stress under the inundated conditions. When the hurricane period ends, the levels of saturation does not immediately decline, which leaves homes, roadways, and highways remain flooded for several days. The impact of the hurricane is still visible on September 17 in Fig. 3.

The ESAL database for 2017 is shown in Fig. 4. The mean values of flexible ESALs for the state of Texas were around 3100. Approximately 75% of the state streets and highways experienced less than or equal to 1000 equivalent numbers of 18,000-lb. single axle loads summed over that period. About 18% of the road networks had ESALs in the range within 1001–11,000, and 7% exceeded 11,000. The higher the traffic load, the higher the risk of damage coupled with the environmental stress factor.
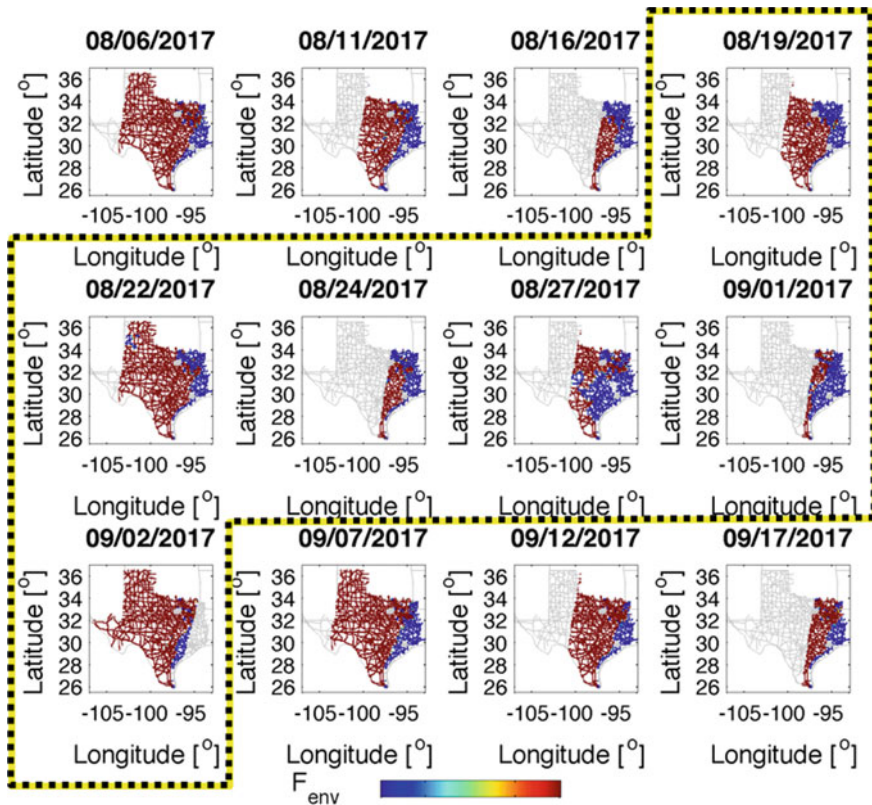

Fig. 3 Environmental stress factor, F_{env}, using Eq. 3 for the Texas road network (dotted outline shows the Hurricane Harvey period)
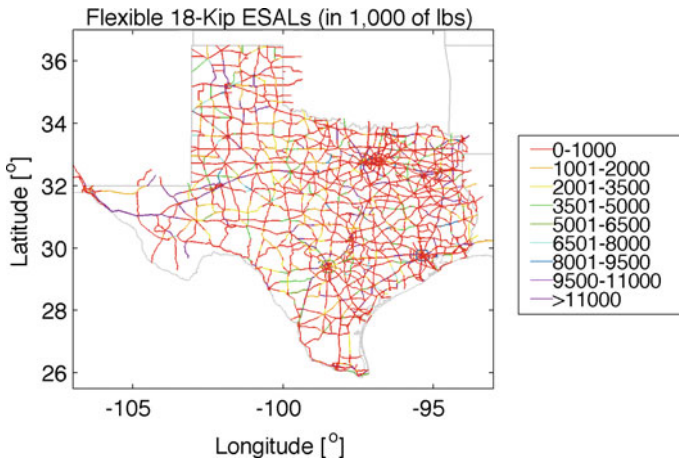
Fig. 4 Daily 18,000 lb (or 18-kip) equivalent single axle loads (ESALs) for the Texas road network

Although many other variables, including the number of truck traffic and magnitude of heavy traffic loads, may impact the performance of a flooded pavement, we have only considered the effect of ESAL for this preliminary risk assessment.

Figure 5 shows the RISK values for corresponding environmental factors based on the simplified version of Eq. 3. The illustrated results are representing the Hurricane period only (8/21 and 8/26 had low swath coverage). Once again, we see more variability in the results using Eq. 3. There is a clear trend in the high-risk road networks moving inland as the hurricane progresses, and both major and minor road networks are affected. According to the Hurricane Harvey cyclone report [25], as of August 26th, the rainfall was not heavy yet, although 2–3 inches of rain per hour was experienced in the Houston area. The heaviest rain occurred during August 28th–30th, and these trends are clearly seen as more roads experience an increase in the *RISK* parameter on those dates. The hurricane begins to recede back toward the coastline on September 2nd.

Figure 6 summarizes the daily percentage of road lane miles (out of the total 16,000) that fell within risk ranges 0–1, 1–5, 5–10, and greater than 10. The fine- and coarse-grained equations provided similar results during the hurricane period. Those equations provided a more binary solution of risk categories. However, Cary and Zapata's equation provided more sensitivity to the risk assessment process [26]. Moving forward with the next phase of this study, we rely more on Eq. 3 in calibrating the risk assessment framework.
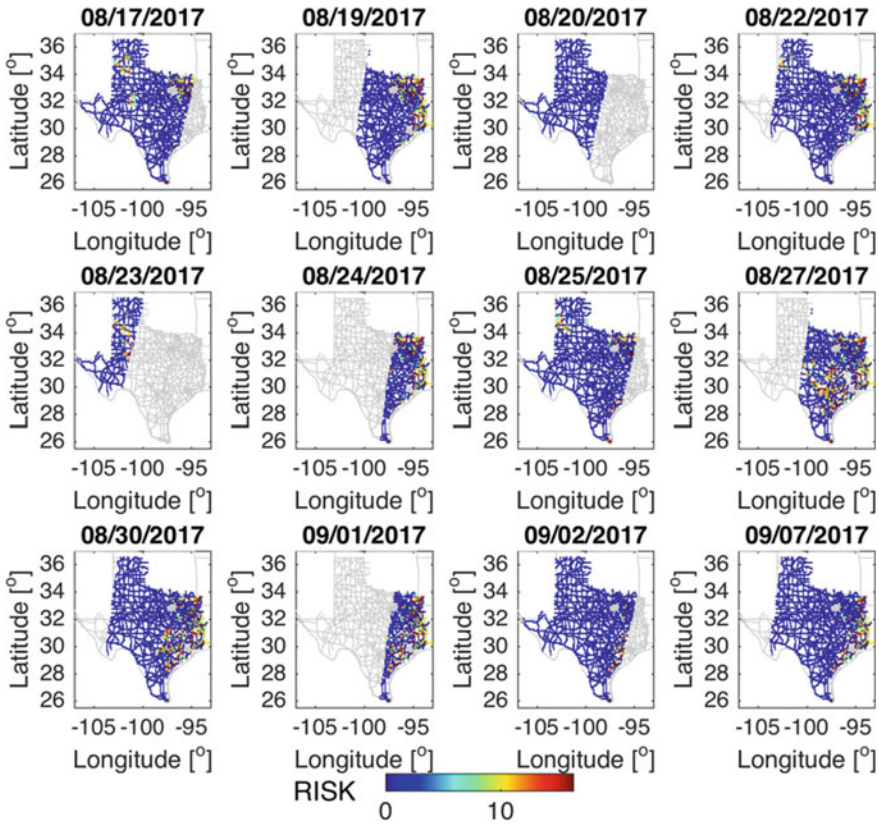
Fig. 5 RISK calculations for road network using F_{env} from Eq. 3

4   Summary and Conclusions

Transportation infrastructure in coastal regions is subject to significant damage during extreme weather events [27]. Those events include sea-level rise, high tides, flash floods, and storms that increase the vulnerability of transportation systems. It is essential to evaluate the resilience of transportation systems for post-hazard management, emergency preparedness, and maintenance procedures. In this study, we were able to use open-access remote sensing observations and the road network axle load database to develop a risk assessment framework for transportation infrastructures in the State of Texas post-hurricane Harvey. This work is a preliminary step toward developing better tools to estimate the risk of preventing damage and high infrastructure maintenance costs.

The results of this study are summarized as follows:

- Soil saturation values were extracted to demonstrate progression before, during, and after the hurricane. It should be mentioned that due to the proximity of these
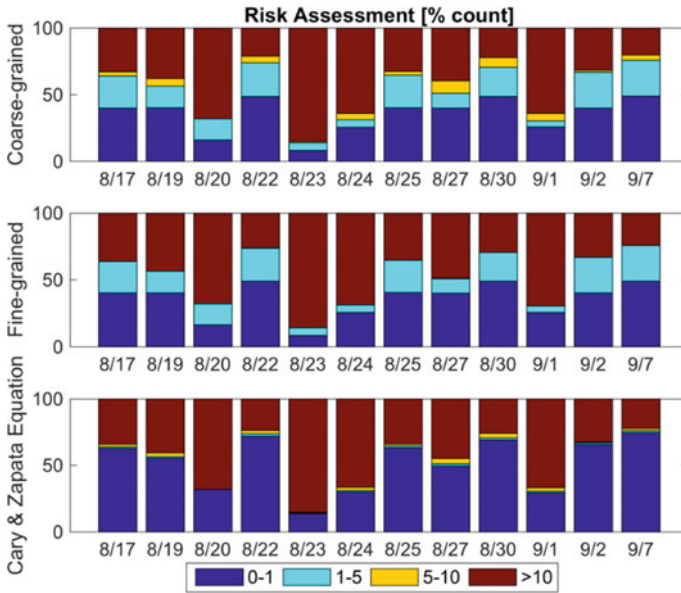
Fig. 6 Percent of roads within each risk category by day

data points relative to the centerline of the road network and also the limited resolution of the satellite data, this type of analysis can be applied at the network level for decision-making purposes. More detailed analyses require field data collections and evaluation of pavement structural capacity after the flooding event.

- The environmental factor, F_{env}, decreased during the hurricane period, which shows lower strength, in terms of modulus, of geomaterial pavement layers compared to the optimum moisture conditions.
- A preliminary risk assessment factor that only considered the impact of saturation level in terms of environmental factor and traffic in terms of equivalent single axle loads and was developed. Based on the definition of risk factor in this study, higher risk values were associated with lower environmental factors and a higher number of traffic axle loads.

The next phase of this work entails calibrating these results with damage observations from the post-event reconnaissance studies.

References

1. Packman S, Lopez S, Mazari M (2018) Evaluating the feasibility of using soil-moisture active passive satellite data to evaluate resilience of transportation infrastructures. In: International conference on transportation and development, p 314
2. Packman S, Lopez S, Fathi A, Mazari M (2019) Using soil-moisture active passive satellite data to evaluate the performance of transportation infrastructure foundations—a feasibility study. In: Eighth international conference on case histories in geotechnical engineering, geo-congress 2019, ASCE
3. Witczak MW (2004) Laboratory determination of resilient modulus for flexible pavement design. Project 1-28A Research Results Digest Number 285, Transportation Research Board, National Research Council, Washington, DC
4. Zapata CE, Houston WN (2008) Calibration and validation of the enhanced integrated climatic model for pavement design. NCHRP Report 602, National Cooperative Highway Research Program, Transportation Research Board of the National Academies
5. Khoury NN, Zaman MM (2004) Correlation between resilient modulus, moisture variation, and soil suction for subgrade soils. Transp Res Rec 1874(1):99–107
6. Liang RY, Rabab'ah S, Khasawneh M (2008) Predicting moisture-dependent resilient modulus of cohesive soils using soil suction concept. J Transp Eng 134(1):34–40
7. Cary CE, Zapata CE (2010) Enhanced model for resilient response of soils resulting from seasonal changes as implemented in mechanistic-empirical pavement design guide. Trans Res Rec TRB 2170:36–44
8. Sotelo MJ, Mazari M, Garibay J, Nazarian S (2014) Variability of moisture content measurement devices on subgrade soils. In: Geo-congress 2014: geo-characterization and modeling for sustainability, pp 1425–1432
9. Nazarian S, Mazari M, Abdallah I, Puppala A, Mohammad L, Abu-Farsakh M (2015) Modulus-based construction specification for compaction of earthwork and unbound aggregate. NCHRP Project 10-84, National Cooperative Highway Research Program, Transportation Research Board, Washington, DC
10. Mazari M, Garibay J, Abdallah I, Nazarian S (2015) Effects of moisture variation on resilient and seismic moduli of unbound fine-grained materials. Airfield Highway Pavements 2015:885–895
11. Mazari M, Nazarian S (2017) Mechanistic approach for construction quality management of compacted geomaterials. Transp Geotech 13:92–102
12. Daniel JS, Jacobs JM, Douglas E, Mallick B, Hayhoe K (2014) Impact of climate change on pavement performance: preliminary lessons learned through the infrastructure and climate network (ICNet). In: Climatic effects on pavement and geotechnical infrastructure, pp 1–9
13. Mallick RB, Tao M, Daniel J, Jacobs J, Veeraragavan A (2017) Development of a methodology and a tool for the assessment of vulnerability of roadways to flood-induced damage. J Flood Risk Manage 10(3):301–313
14. Valenzuela YB, Rosas RS, Mazari M, Risse M, Rodriguez-Nikl T (2017) Resilience of road infrastructure in response to extreme weather events. In: International conference on sustainable infrastructure 2017, pp 349–360
15. Elshaer M, Ghayoomi M, Daniel JS (2019) Impact of subsurface water on structural performance of inundated flexible pavements. Int J Pavement Eng 20(8):947–957
16. Knott JF, Daniel JS, Jacobs JM, Kirshen P (2018) Adaptation planning to mitigate coastal-road pavement damage from groundwater rise caused by sea-level rise. Transp Res Rec 2672(2):11–22
17. Qiao Y, Medina RA, McCarthy LM, Mallick RB, Daniel JS (2017) Decision tree for postflooding roadway operations. Transp Res Rec 2604(1):120–130
18. Zhang Z, Wu Z, Martinez M, Gaspard K (2008) Pavement structures damage caused by Hurricane Katrina flooding. J Geotech Geoenviron Eng 134(5):633–643
19. Sultana M, Cahi G, Chowdhury S, Martin T (2016) Rapid deterioration of pavements due to flooding event in Australia. In: 26th ARRB conference, Australian Road board, Australia

20. Panciera R, Walker JP, Jackson TJ, Gray DA, Tanase MA, Ryu D, Monerris A, Yardley H, Rüdiger C, Wu X, Gao Y (2014) The soil moisture active passive experiments (SMAPEx): toward soil moisture retrieval from the SMAP mission. IEEE Trans Geosci Remote Sens 52(1)
21. Entekhabi D, Yueh S, O'Neill PE, Kellogg KH, Allen A, Bindlish R, Brown M (2014) SMAP handbook–soil moisture active passive: mapping soil moisture and freeze/thaw from space. NASA Jet Propulsion Laboratory
22. Kerr YH, Waldteufel P, Wigneron JP, Delwart S, Cabot F, Boutin J, Escorihuela MJ, Font J, Reul N, Gruhier C, Juglea SE (2010) The SMOS mission: new tool for monitoring key elements of the global water cycle. Proc IEEE 98(5):666–687
23. Texas Department of Transportation Roadway Inventory. https://www.txdot.gov/inside-txdot/division/transportation-planning/roadway-inventory.html. Last Accessed 29 Jan 2019
24. California Department of Transportation (2017) Highway Design Manual (HDM), Sacramento, CA
25. Blake ES, Zelinsky DA (2018) NOAA—National Hurricane Center Tropical Cyclone Report Hurricane Harvey, National Hurricane Center
26. Mazari M, Velarde J, Lopez AL, Nazarian S (2017) Impact of moisture variation on stiffness properties of compacted geomaterials. In: Proceedings of the 19th international conference on soil mechanics and geotechnical engineerings, Seoul
27. Martinez E, Hernandez J, Rodriguez-Nikl T, Mazari M (2018) Resilience of underground transportation infrastructure in coastal regions: a case study. In: International conference on transportation and development, p 223

Riprap Stockpile Size and Shape Analyses Using Computer Vision

Jiayi Luo, Haohang Huang , **Issam Qamhia** , **John M. Hart, and Erol Tutumluer**

Abstract Riprap rocks and large-sized aggregates are being used extensively in geotechnical and hydraulic engineering applications. Knowing the particle size and morphological/shape properties ensures the reliable and sustainable use of aggregate materials at both quarry production lines and construction sites. Traditional methods for assessing aggregates geometric properties involve subjective visual inspection and time-consuming hand measurements, while the use of computer vision analysis techniques is restricted primarily due to the unwieldiness of large-sized aggregates. This paper presents the use of a computer vision system for in-place size and shape evaluation of large aggregates in a stockpile using images of stockpiles conveniently collected using smartphone cameras. The automated image analysis software is comprised of an image segmentation kernel and a morphological analysis module. Comprehensive analyses are conducted on a sample stockpile with multiple view inspections. Based on the findings of this study, the stockpile aggregate image analysis program has great potential as an efficient and innovative application for field-scale and in-place evaluations of aggregate materials.

1 Introduction

Riprap and large-sized aggregates are being widely used in geotechnical and hydraulic applications. Particle size and morphological properties are among the

---

J. Luo · H. Huang · I. Qamhia · E. Tutumluer (✉)
Department of Civil and Environmental Engineering, University of Illinois At
Urbana-Champaign, 205 N Mathews, Urbana, IL 61801, USA
e-mail: tutumlue@illinois.edu

J. M. Hart
Beckman Institute for Advanced Science and Technology, University of Illinois At
Urbana-Champaign, 405 N Mathews, Urbana, IL 61801, USA

primary factors that determine the performance and characteristics of the aggregate skeleton in various types of structures such as Portland cement concrete layers [1], unbound or bound pavement layers [2], ballast layer in railway tracks [3], and riprap materials for slope stability and erosion control in hydraulic applications [4]. Knowing the size and shape properties of each single particle in a stockpile facilitates the quality assurance/quality control (QA/QC) process and helps to understand the behavior of aggregate material [5]. In practice, QA/QC tasks are time-consuming due to the uncertainty introduced by the varying rock mineralogy and quarrying procedure. Therefore, convenient and efficient aggregate stockpile analyses throughout the production line and mix design are essential for material selection and construction.

In this regard, several existing aggregate imaging systems were devised for analyzing aggregate materials under different forms of placement (manually separated or densely stacked) and different conditions (i.e., under laboratory or field conditions). Masad et al. [6] developed and Gates et al. [7] improved the prototype of a laboratory imaging system, aggregate imaging system (AIMS), that can analyze multiple aggregates manually separated and placed. Tutumluer et al. [8] developed and Moaveni et al. [9] improved a laboratory imaging system, Enhanced-University of Illinois Aggregate Image Analyzer (E-UIAIA), which captures individual aggregates sequentially from orthogonal views. AIMS and E-UIAIA imaging systems both provide an efficient analysis for separated aggregates in laboratory conditions. For field conditions where the random arrangement of aggregates often presents a challenge to image analysis, Huang et al. [10, 11] recently developed a field imaging system for individual large-sized aggregates and a deep learning-based field imaging system for aggregates in a densely stacked stockpile.

2   Objective and Methodology

The objective of this paper is to apply a deep learning-based computer vision system, recently established by the authors [11], to an aggregate stockpile for the analysis of the size and shape properties of the individual particles in the stockpile. The accuracy and robustness of the system were validated in the previous work of the authors. The system operates on field aggregate images collected using smartphone cameras and conducts analysis based on an automated stockpile image segmentation kernel and a morphological analysis module. In this paper, comprehensive analyses are conducted on a sequence of multi-view images of the stockpile, which demonstrates the practical application of the system on aggregate stockpile analysis.

3   Stockpile Aggregate Imaging System

The utilized computer vision system consists of three main components: an image acquisition module, an image segmentation module, and a morphological analysis

module. The innovative field imaging system is intended for automated and user-independent analyses of aggregate stockpile images.

3.1 Image Acquisition Procedure

To obtain multi-view representation of the stockpile, a sequence of images should be taken with the camera of a handheld smartphone from different locations around the stockpile. Photos were taken while ensuring the image sequence forms a continuous panorama with minimal boundary overlap between adjacent images. Note that images are recommended to be taken from a nearly perpendicular viewing angle against the stockpile slope to minimize the perspective and distortion effect. Additionally, to determine the unit of length in an image, a calibration object is often used as a scale (reference) in the image acquisition procedure.

3.2 Image Segmentation Kernel

Aggregate image analysis typically consists of two sequential stages: an image segmentation kernel followed by a morphological analysis module. The image segmentation step detects and delineates each target particle of interest appearing in the given image. The morphological analysis step quantifies the size and shape properties of the segmented particle regions. Accordingly, the system consists of an image segmentation kernel based on a deep learning framework and a morphological analysis module for particle size and shape characterization.

An image segmentation kernel based on deep learning requires a high-quality labeled training dataset for extracting and learning important image features. Stockpile aggregate images were collected and manually labeled as training data. A state-of-the-art deep learning framework for object detection and segmentation, mask region-based convolutional neural network (Mask R-CNN) [12], was followed to conduct image segmentation in an automated manner. Training parameters were carefully tested and tuned to achieve optimal performance of the final image segmentation kernel, and an efficient segmentation kernel was trained and validated in a previous work by the authors [11]. Upon input of a stockpile aggregate image, the segmentation kernel will output the segmented image with the detected aggregates delineated in different colors.

The image segmentation task is divided into an object detection step followed by a semantic segmentation step. Accordingly, the image segmentation kernel is composed of two neural networks: R-CNN for object detection and fully convolutional network (FCN) for semantic segmentation. The model architecture of the neural network is illustrated in Fig. 1.

Object detection precisely estimates the content and location of objects contained in an image. As one of the fundamental topics in computer vision, object detection
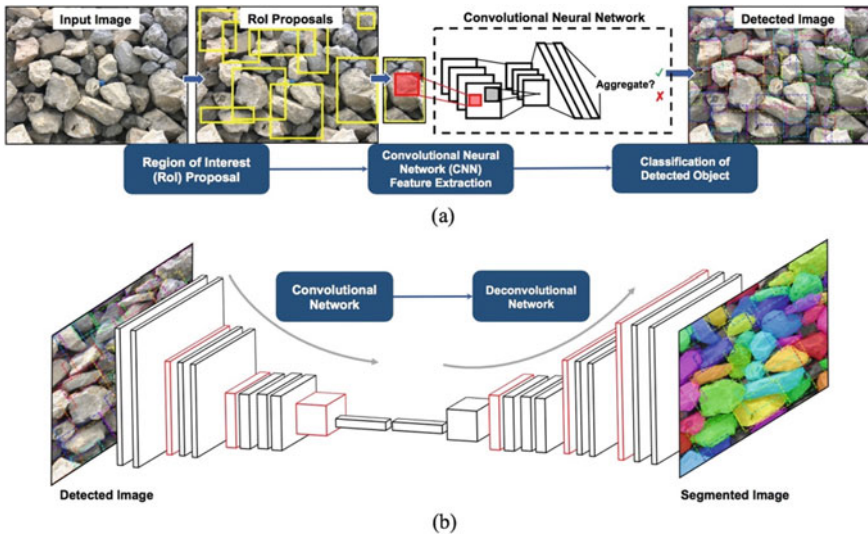
Fig. 1 Flowchart of **a** region-based convolutional neural network (R-CNN) for object detection and **b** fully convolutional network (FCN) for semantic segmentation

provides comprehensive information for semantic understanding of the target image. For the stockpile aggregate image segmentation, aggregate particles are specified as the target category of objects to be detected. Traditionally, this task involves three stages: region selection, feature extraction, and object classification [13]. Following this pipeline, the kernel adopts an R-CNN architecture that consists of a region proposal scheme and an object classification scheme, as shown in Fig. 1a.

Following object detection, semantic segmentation is needed to further extract the valid aggregate pixels inside each bounding box in order to obtain the effective regions used to determine particle size and shape information. FCN is one of the most powerful models for semantic segmentation, which associates each pixel with an object class description [14]. FCN is a network with pure convolutional and pooling layers and thereby requires fewer model parameters while preserving high accuracy. The network is composed of a convolutional network followed by a symmetric deconvolutional network. Through the forward inference and backward propagation mechanism, the trained network can take an input image of any arbitrary size and output localized object regions for the designated class. At the pixel level, the network will screen out the invalid non-aggregate pixels and extract the aggregate surfaces inside the detected bounding box. This semantic segmentation process is illustrated in Fig. 1b.

3.3 Morphological Analysis Module

For the morphological analysis module, the size and shape of each aggregate detected and segmented in the image segmentation module should be determined with reference to a calibration object. Then, the collective statistics of the particle properties in the stockpile image can be illustrated in the form of a histogram and a cumulative distribution, as illustrated in Fig. 2. Note that the following morphological analyses on the size and shape are both 2D analyses based on the images.

The equivalent sizes and flat and elongated (F&E) ratios are calculated for the segmented particles. The equivalent size of a particle follows the definition of the equivalent spherical diameter (ESD), which is commonly used to characterize the size of an irregularly shaped object as follows:

$$ESD = 2 \cdot \sqrt{\frac{A}{\pi}} \tag{1}$$

where 'A' is the measured area of the irregularly shaped object.

Other size metrics such as longest, shortest, or intermediate dimension can be also used at the users' discretion. For the F&E ratio, the maximum or longest Feret dimension, $L_{\max}$, is first determined by searching for the longest intercept with the particle region in all possible directions. Next, by searching the intercepts along the orthogonal directions against the $L_{\max}$, the minimum or shortest Feret dimension, $L_{\min}$, is obtained. The F&E ratio is then defined as follows:

$$F \cdot E = \frac{L_{\max}}{L_{\min}} \tag{2}$$

With the image segmentation module and morphological analysis modules, the imaging system can be applied to a single image or to a sequence of multi-view images to conduct in-place size and shape evaluation of aggregate stockpiles. The detailed description, performance evaluation, comparison, and validation study of the aggregate imaging system can be found in Huang et al. [11].
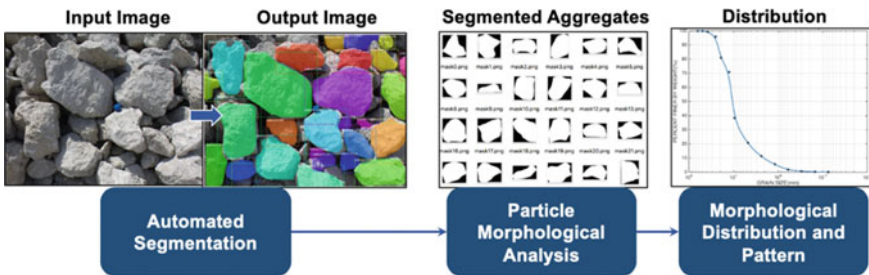

Fig. 2 Flowchart of the morphological analysis module for size and shape properties determination

4 Stockpile Analysis Results and Discussion

4.1 Stockpile Description

Comprehensive analyses are conducted on a selected stockpile located at an aggregate quarry in Kankakee, IL. This aggregate stockpile comprises aggregates of the largest size category that is being permitted for use in Illinois, called RR7 as per the Illinois Department of Transportation (IDOT) specification [15]. The weight of the aggregates in this category typically ranges between 136 kg (300 lbs.) and 454 kg (1000 lbs.). For the selected stockpile, images were taken from three views as shown in the first column of Fig. 3. Segmentation analysis was conducted using the stockpile aggregate imaging system, and the segmented images are shown in the second column of Fig. 3. As mentioned in the image acquisition procedure, a 5.7-cm (2.25-in.) blue calibration ball was used as the calibration object, as illustrated in the third column of Fig. 3. Before the morphological analysis step, the calibration ball was first identified and manually delineated; then, its pixel region was used to compute the calibration factor for size and shape analyses.

4.2 Segmentation and Morphological Analysis Results

For the stockpile image segmentation, results were achieved by detecting and segmenting 51, 55, and 53 aggregate particles from the three views, respectively. From the segmentation results shown in Fig. 3, most of the identifiable aggregate particles were successfully detected and segmented with acceptable accuracy. Each of these segmented particle regions was then processed by the morphological analysis module to determine the size and shape of each aggregate particle as well as the overall stockpile statistics. Note that some highly occluded particles or small fragments were not captured by the imaging system, which was because these irregularly shaped regions were not recognized as typical aggregate particles from the manual labeling phase.

For the morphological analysis module, each of the single-view images was first evaluated. The size and shape statistics for each view are presented in Fig. 4. The results show that for each of the three views, the sizes of all the aggregate particles ranged between 12.7 cm (5 in.) and 63.5 cm (25 in.), with around 60% of the particle sizes ranging from 19.0 cm (7.5 in.) to 38.1 cm (15 in.). This size distribution is consistent with the Illinois DOT's practice that the largest aggregate particle could weigh up to 522 kg (1150 lbs.) with nominal size up to 61.0 cm (24 in.) [15]. From the F&E ratio analysis results in Fig. 4, the F&E ratios for all particles range from 1.0 to 3.0, and more than 90% of the particles have F&E ratios less than 2.5.

During the image acquisition process, the multi-view representation of the stockpile was captured from three different views with minimal overlap between adjacent images. Ignoring the duplication of particles, the overall size and shape properties of
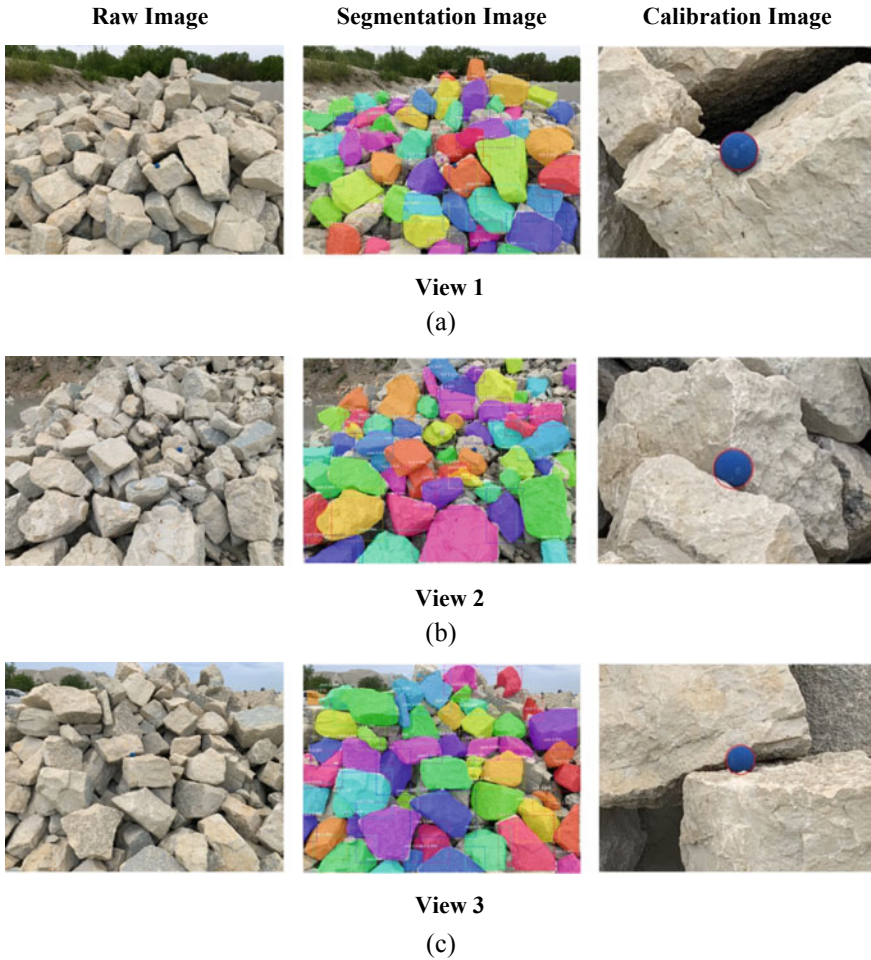
Raw Image　　　**Segmentation Image**　　　**Calibration Image**

View 1

(a)

View 2

(b)

View 3

(c)

Fig. 3 Raw images, segmentation results, and calibration results of **a** first view; **b** second view; and **c** third view in aggregate stockpile analysis

the entire stockpile can be further analyzed by combining the results from the multi-view representations together. The combined distribution results in a total of 159 detected particles that are plotted together with each view's contribution in Fig. 5.

Both analyses show reasonable statistical distributions for the morphological properties of a typical aggregate stockpile. The particle size distribution curve implies the uniform gradation of the selected stockpile, while the F&E ratio distribution generally indicates rounded shape and small angularity for the particles in the selected stockpile.

It is observed that the single-view results slightly differ from each other, but the combined results can serve as a more accurate representation of the stockpile being
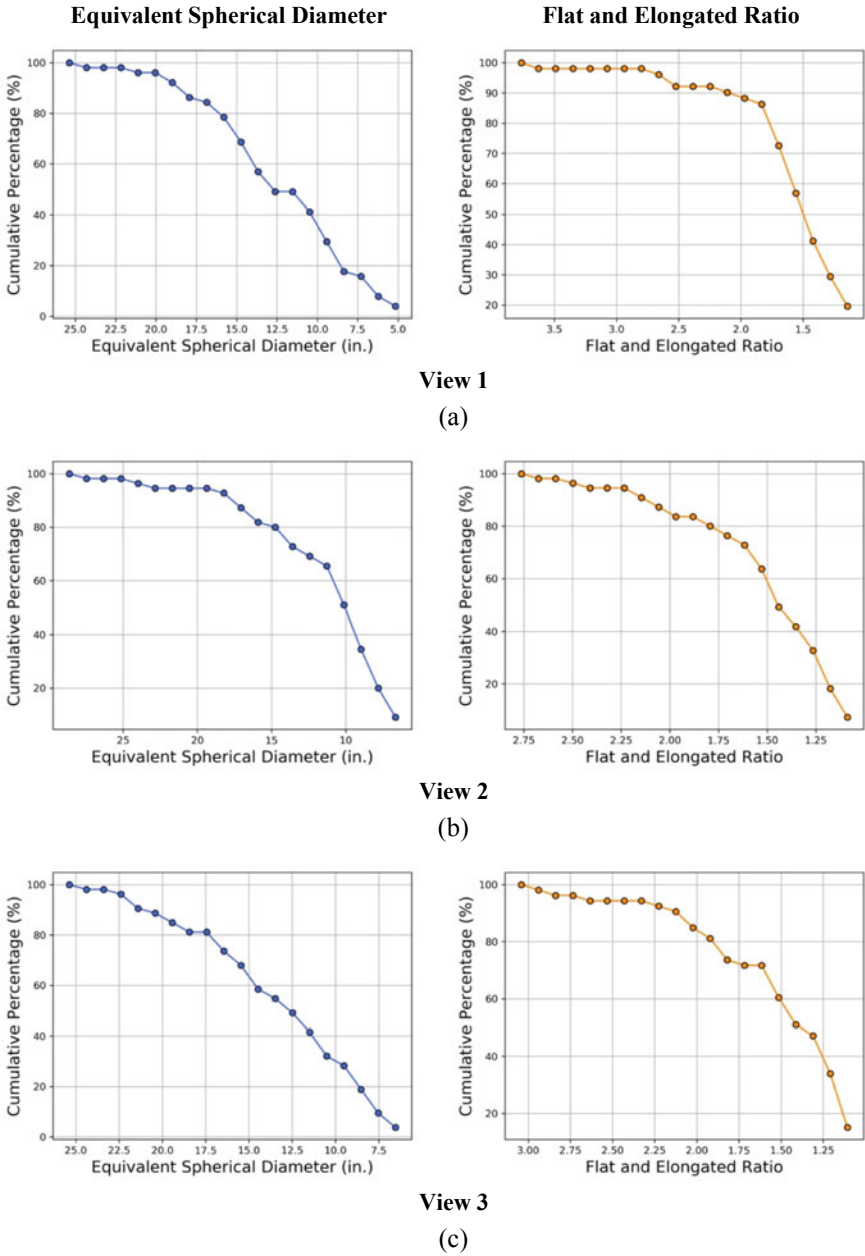
Fig. 4 Size and shape distribution curves of **a** first view; **b** second view; and **c** third view based on morphological analysis (1 in. = 25.4 mm)

Fig. 5 **a** Size and **b** shape distribution curves from the multi-view stockpile analyses and the combined results (1 in. = 25.4 mm)
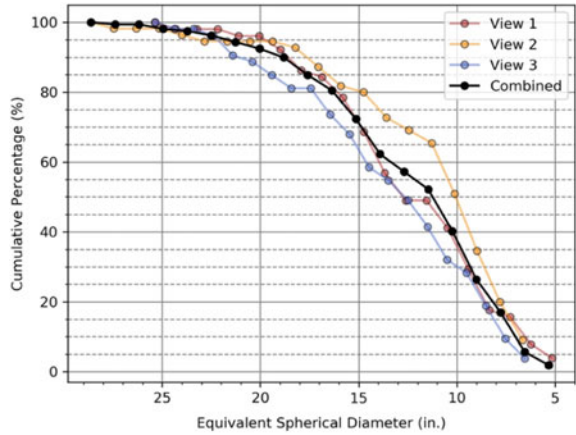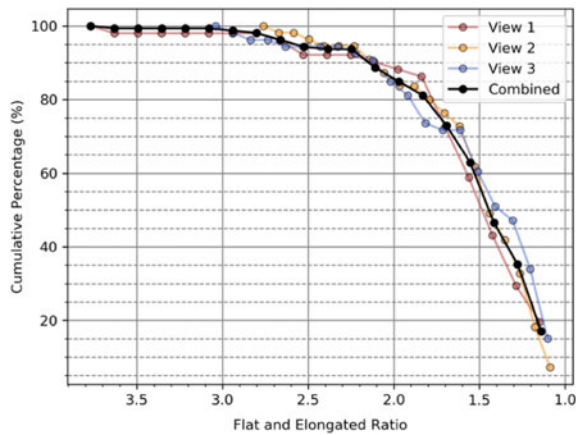
inspected. This is due to the fact that each view only consists of a partial section of
the stockpile, while the size and shape statistics should cover the panoramic stockpile
surface. Similarly, the combined results show the same trend as single-view results
where the sizes of the aggregate particles are between 12.7 cm (5 in.) and 63.5 cm
(25 in.) with over 60% of the particle sizes ranging from 19.0 cm (7.5 in.) to 38.1 cm
(15 in.), and the F&E ratios range from 1.0 to 3.0 with more than 90% of the particles
have F&E ratios less than 2.5.

4.3 Discussion

The segmentation and morphological analysis results demonstrate the convenient application of the developed computer vision system for aggregate stockpile analysis, whereby the users can obtain the in-place size and shape statistics of a stockpile. The system can be used to analyze the particle size and shape information from a single-view image. With standardized image acquisition procedure, the system can be further utilized to derive the gradation and typical particle shape pattern for a batch of aggregate products with multi-view representation.

Nevertheless, since only the stockpile surface is visible to the users, it should be noted that the segmentation and morphological analyses results presented herein only represent the size and shape statistics of the stockpile surface. This is typically the case when manual QA/QC inspection procedures are utilized. Additionally, duplication of the particles across image boundaries could be another source of inaccuracy due to the coverage overlap during the data acquisition procedure.

5 Conclusions

A computer vision system, developed based on deep learning techniques, is applied to determine in-place size and shape properties of aggregate stockpiles in the field. The system involves using a smartphone camera to capture multi-view images of a stockpile for estimating the morphological size and shape properties of the aggregates contained in the stockpile. Based on the findings of this study, the computer vision-based system for stockpile assessment demonstrates its use as a convenient and efficient application for field and in-place evaluation of aggregate morphological properties. The system has the capability to provide reliable and sustainable solutions for performing onsite QA/QC tasks related to riprap rock and large-sized aggregates in the field.

References

1. Quiroga PN, Fowler DW (2004) ICAR Research Report No. 104-1F: the effects of aggregate characteristics on the performance of Portland Cement Concrete. International Center for Aggregates Research

2. Tutumluer E, Pan T (2008) Aggregate morphology affecting strength and permanent deformation behavior of unbound aggregate materials. J Mater Civ Eng 20(9):617–627
3. Wnek MA, Tutumluer E, Moaveni M, Gehringer E (2013) Investigation of aggregate properties influencing railroad ballast performance. Transp Res Rec: J Transp Res Board 2374:180–190
4. Lagasse PF, Clopper PE, Zevenbergen LW, Ruff JF (2006) NCHRP Report 568: riprap design criteria, recommended specifications, and quality control. Transportation Research Board, Washington, DC
5. Barrett PJ (1980) The shape of rock particles, a critical review. Sedimentology 27
6. Masad E, Al-Rousan T, Bathina M, McGahan J, Spiegelman C (2007) Analysis of aggregate shape characteristics and its relationship to hot mix asphalt performance. Int J Road Mater Pavement Des 8(2):317–350
7. Gates L, Masad E, Pyle R, Bushee D (2011) FHWA-HIF-11-030 report: aggregate imaging measurement system 2 (AIMS2). Highways for LIFE Program Office, Federal Highway Administration, Pine Instrument Company
8. Tutumluer E, Rao C, Stefanski JA (2000) FHWA-IL-UI-278 report: video image analysis of aggregates. University of Illinois Urbana-Champaign, Urbana, Illinois
9. Moaveni M, Wang S, Hart JM, Tutumluer E, Ahuja N (2013) Evaluation of aggregate size and shape by means of segmentation techniques and aggregate image processing algorithms. Transp Res Rec: J Transp Res Board 2335:50–59
10. Huang H, Luo J, Moaveni M, Tutumluer E, Hart JM, Beshears S, Stolba AJ (2019) Field imaging and volumetric reconstruction of riprap rock and large-sized aggregates: algorithms and application. Transp Res Rec: J Transp Res Board. https://doi.org/10.1177/0361198119848704
11. Huang H, Luo J, Tutumluer E, Hart JM, Stolba AJ (2020) Automated segmentation and morphological analyses of stockpile aggregate images using deep convolutional neural networks. Transp Res Rec: J Transp Res Board. https://doi.org/10.1177/0361198120943887
12. He K, Gkioxari G, Dollár P, Girshick R (2017) Mask R-CNN. In: Proceedings of IEEE international conference on computer vision, Venice, Italy, pp 2961–2969
13. Zhao ZQ, Zheng P, Xu ST, Wu X (2019) Object detection with deep learning: a review. IEEE Trans Neural Netw Learn Syst 1–21
14. Long J, Shelhamer E, Darrell T (2015) Fully convolutional networks for semantic segmentation. In: Proceedings of IEEE conference on computer vision and pattern recognition, Boston, Massachusetts, pp 3431–3440
15. Illinois Department of Transportation (IDOT) (2016) Standard Specifications for Road and Bridge Construction. Illinois Department of Transportation, pp 759–761
16. Huang H, Luo J, Tutumluer E, Hart JM, Qamhia I (2020) FHWA-ICT-20-002 report: size and shape determination of riprap and large-sized aggregates using field imaging. University of Illinois Urbana-Champaign, Urbana, Illinois

Statistical Analysis of the Influence of Ballast Fouling on Penetrometer and Geoendoscope Data

Jorge Rojas Vivanco ⓘ **, Sébastien Barbier** ⓘ **,**
Miguel-Angel Benz Navarrete ⓘ **, and Pierre Breul** ⓘ

Abstract Fouling and deterioration of the ballast are major problem in operation of railway tracks. Its characterization is fundamental to optimize decision making in maintenance programs. This study aims to characterize the fouled ballast by dynamic penetrometer (PANDA) and geoendoscope test (This method, hereafter PANDA and geoendoscope test, is known as Pandoscope® [17]). The methodology presented consists in analyzing the dynamic cone resistance (q_d) of each layer and then performing a geoendoscope test to obtain borehole images. Statistical analysis of cone resistance and image parameters (texture and colorimetry) shows their dependence on the degree and of fouling material. As ballast fouling increases, the *average cone resistance* initially increases and then decreases. Image features also depend on the proportion of fouling but especially allow to distinguish different contents of fine particles in the fouling material. Nevertheless, each of the measurements taken separately is not enough to determine a ballast fouling amount. In this way, data fusion has been carried out and shows an improvement in the quantification of the fouling index [1].

Keywords Laboratory test · Penetrometer · Geoendoscope · Railway · Ballasted track · Fouling index · Statistical analysis · Data fusion

1 Introduction

Most of rail networks around the world are often composed of ballasted tracks, where the main component is the "ballast," which is a coarse grained and uniformly graded crushed rock aggregate placed between and immediately underneath the sleepers. The main purposes of ballast are as follows: to provide an efficient drainage of the

J. R. Vivanco · S. Barbier (✉) · M.-A. B. Navarrete
Sol Solution, 63204 Riom Cedex, France
e-mail: sbarbier@sol-solution.com

J. R. Vivanco · P. Breul
Institut Pascal, UMR CNRS 6602, Université Clermont Auvergne, 63100 Clermont-Ferrand, France

track; to maintain tracks vertical and horizontal geometry; to distribute traffic loading from sleeper to a level allowed by lower structural layers; and to enable correction of track geometry errors.

Over time and as a result of repeated and increasing heavy loads, the railway track ages, and the ballast deteriorates deviating from its original standard specifications. The results: Fouling materials is created, and ballast layer is progressively fouled with materials finer than aggregate particles, filling the void spaces. Consequently, fouled ballast impacts the track performance by changing the mechanical properties of substructure layers. Maintenance of railways is needed, and its frequency is linked to the ballast quality, which as seen, changes over time due to the generation of fouling materials. Field characterization of ballast fouling degree, as well as its mechanical behavior, is an important task to optimize decision making in maintenance programs.

The French lightweight dynamic penetrometer, known as PANDA [2, 3], coupled with geoendoscope [4–8] offers the opportunity to reach this purpose by measuring the dynamic cone resistance (q_d) and image features continuously in depth (Fig. 1). This method has been widely studied to evaluate the bearing capacity as well as to assess mechanical properties of the soil. However, none of these studies focused on establishing a relationship between (q_d) images parameters and ballast fouling index (FI).

This article presents the first results obtained from a laboratory study aimed at establishing a database to correlate dynamic penetrometer values, images features as well as ground-penetrating radar (GPR) data in order to improve railroad surveys by means of data fusion. This study is particularly interested in the effects of fouling index, and nature of fouling material, on the cone resistance and images features.
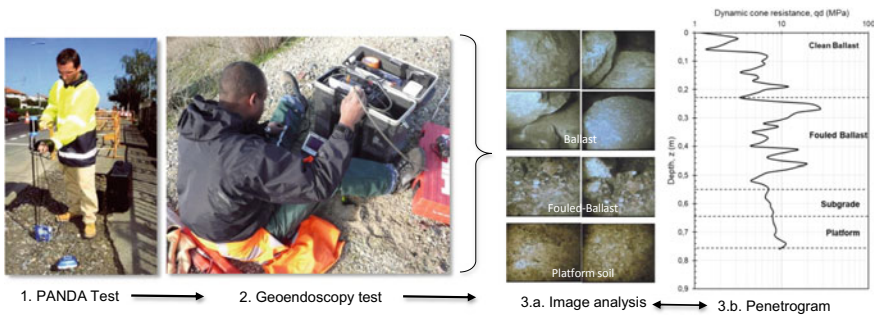

Fig. 1 Principle of lightweight dynamic penetrometer PANDA and geoendoscope tests

2 Lightweight Dynamic Penetrometer and Geoendoscope Test

The methodology for railway tracks survey involving PANDA penetrometer and geoendoscope test was born at the beginning of the 2000s in France, when the SNCF (French railway company) started looking for a new methodology, not engine based, that would provide at least the layer identification of the coring machine (that was used at the time) as well as a mechanical characterization of the trackbed. The fusion of data from PANDA penetrometer and geoendoscope test is currently employed in France to assess the substructure of railway tracks [5, 6, 9, 10] (Fig. 1).

PANDA is a lightweight variable energy dynamic penetration test that is standardized in France. The test consists in driving a set of steel rods equipped with a conical tip into the soil by manual or automatic hammering. For each blow, drive energy is measured in the instrumented anvil. Other sensors measure simultaneously the penetration of the cone. Both data are immediately transmitted to the acquisition unit, and cone resistance (q_d) is directly calculated by the Dutch formula. The log of sounding, called penetrogram, plots the almost continuously in depth (z) the evolution of q_d. PANDA is a versatile equipment (weight < 20 kg), and in the context of railway investigations, adaptations have been made to make it even lighter and more rugged [6, 10, 11].

Geondoscope test consists of introducing an endoscope probe in the borehole previously made by the dynamic penetrometer. After the penetration test, a windowed hollow tube is placed in the same borehole. A 6 mm diameter endoscopic camera is lowered into that guiding tube. The endoscope continuously records 5 mm wide images of the borehole wall with a high resolution (640 × 480 pixels at least). A depth recorder is added so that the video and depth are simultaneously recorded on a rugged laptop, thanks to a custom acquisition software. Images extracted from each video are then processed using automatic image analysis algorithms to provide qualitative and quantitative information for each soil layer (thickness, nature, humidity…). In addition, each image is analyzed to obtain image parameters (i.e., moment, volume, area mask…) [7, 8]. This imaging technique has already been successfully implemented in railway geotechnics as well as in substructure integrity assessment.

3 Ballast Fouling Characterization

Fouling material in ballast has been traditionally considered not favorable for ballasted track performance. Ballast fouling is caused by a number of mechanisms: (i) fracturing, abrasion and particle attrition of ballast; (ii) infiltration of sub-ballast under cyclic loading or from underlying clay subgrade; and (ii) spillage and contamination from surface sources are some of different mechanism of fouling [12]. Fouled ballast has different physical and strength properties than those of clean ballast. The fouling material increases the contact surface of the ballast generating losses

of mechanical resistance and drainage performance, and this leads to a degradation deformability and strength properties of resulting material. Regardless of the generating process, fouled ballast can be characterized by several indexes: fouling index, percentage void contamination, void contamination index or relative ballast fouling ratio. In this work, the (Selig and Waters, 1994) definition is employed [1], where fouling index (FI) has been identified as small particles in the matrix of large ballast particles (Eq. 1), where P_4 and P_{200} are, respectively, the percentage in mass less than 4.75 mm and 75 µm.

$$FI = P_4 + P_{200} \tag{1}$$

Previous studies have shown the effects of the FI on the strength properties of fouled ballast [13–16]. It was observed that strength properties increase (from clean ballast state) when FI rise. Beyond a threshold of FI, the strengths properties decrease for higher quantities of FI. This threshold depends on the nature of fouling material, as well as its water content. In this way, the same phenomenon should be observed for measured dynamic cone resistance (q_d) and observable from the image's features.

Although in most practical cases the fouling material is sand and silt produced by ballast abrasion, in this work, it was chosen to reproduce fouled ballast using sand and clay. The main purpose is to evaluate the effects of the nature of fouling material on dynamic penetration and geoendoscope tests.

4 Laboratory Test and Data Collection

In the laboratory, parallelepipedic specimens of soil (800 × 600 × 1000 mm) were prepared (Fig. 2). The main purpose is to reproduce a multi-layer structure representative of a railway track, where the lower part is the subgrade, and the upper part simulates the ballasted layer. Subgrade was designed by two different layers (sand, silty, and clay) that remain unchanged in terms of nature as well as compaction degree. For each sample, ballasted upper layer changes in nature and content of fouling material. Fouled ballast was created by mixing different quantities of clean ballast, sand, and clay.

Dynamic penetration and geoendoscope test, as well as GPR measurements, were conducted for each sample. At the end of the tests, the healthy ballast layer is dismantled, and in the contaminated ballast layer, the humidity and granulometry controls are carried out. The aim of these experiments was to create different simple cases to evaluate the effects of the fouling index on the values measured by PANDA as well as image features obtained by geoendoscope test.
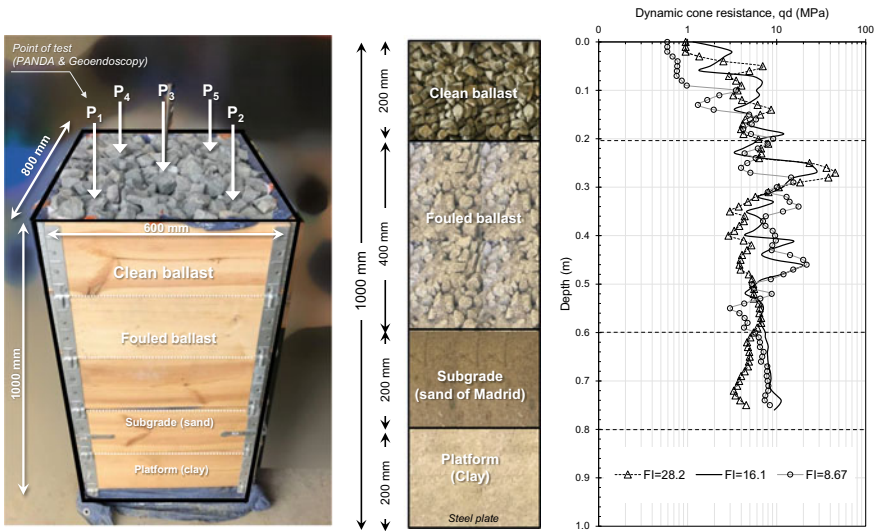
Fig. 2 Laboratory experiences: (left) dimensions of specimens and test position; (middle) vertical profile of specimens tested; and (right) example of dynamic penetration test results

4.1 Samples Construction

Different samples were constructed in a parallelipedic wooden structure (Fig. 2). Each specimen is composed of four different thickness layers: (i) clean ballast of 200 mm, (ii) 400 mm of fouled ballast, and (ii) 400 mm sand and clay layers (subgrade). General properties of materials employed are presented (Table 1). Moreover, vertical stress resulting from the weight applied by the superstructure of the railway (rail, sleepers…) is not simulated in these experiences.

Sample construction begins with the manual compaction of a 100 mm thick subgrade soil layer. Geotextile is placed between each layer, and the construction proceeds with the placement of each layer until the top layer (clean ballast) is reached. Once the tests are carried out, the specimen is completely emptied, and another sample is later built.

Fouled ballast was obtained by mixing different proportions of clean ballast and finer material (sand, clay, or both). Fouled ballast was prepared thanks to a concrete mixer, and the mixture was placed inside the specimen in compacted layers (analysis is only done on ballasted layers). Quantity of materials W_{ratio} required to obtain the desired fouled ballast samples was calculated according to:

$$W_{\text{ratio}} = \frac{M_c}{M_c + M_b} * 100\% \tag{2}$$

Table 1 Main properties of soils employed in this study

Material	D_{max}	Pass. 80 μm	Pass. 2 mm	γ_{OPN} (kN/m³)	W_{OPN} (%)	CBR (%)	Classification		
							NF EN 13,450	GTR	AASHTO
Ballast	50	0.0	0.0	–	–	–	C	D3	A-1-a
Sand Madrid	5.0	18.7	83.2	1.96	9	34.5	–	B6	A-2-6
Sand Izeaux	5.0	12.9	78.2	1.95	19	14.2	–	B5	A-2-4
Clay Lornage	1.0	50.6	97.6	2.03	18.2	7.0	–	A1	A4

D_{max} = maximum size; γ_{OPN} = optimum density; W_{OPN} = optimal humidity; CBR = California bearing ratio; GTR = guides to road terracing (France)

where M_c and M_b are, respectively, the total weight of the fouling material and ballast. This equation was used to construct samples with the same mass of material. This is to highlight the effects of the different levels of fine elements. In Table 2, W_{FM} is equivalent to P_4 sieving results. A total of 20 different mixtures (cases) of fouled ballast have been prepared. Figure 3 shows the particle size distribution of each sample.

In all cases, the percentage of material passing the P_4 sieve is 100%. Indeed, to reproduce different fouled ballast samples, only the quantity of material passing through the P_{200} sieve was changed.

4.2 Tests Performed and Cases Studied

A total of 21 specimens with different ratio of fouling index were produced. They are mainly grouped in five cases, which differ in the nature of the fouling material. For each case, five different fouled ballast mixtures were tested. All studied cases and the main characteristics of fouled ballast samples are presented in Table 2. Fouling index and its classification, as well as the average cone resistance measured in the fouled ballast layer, are also summarized.

For each sample, the following tests were performed: (i) lightweight dynamic penetrometer PANDA ($\times 5$) and (ii) geoendoscope test ($\times 10$). An example of one of the specimens performed is shown in Fig. 2 where the position of each test is represented. Dynamic penetrometer and geoendoscope results are presented in Figs. 2 and 4.

5 Results and Discussion

Results obtained in the fouled ballast layers were analyzed to evaluate the effects of the fouling index (FI), and its nature, on the dynamic cone resistance values obtained by means of PANDA test as well as images features measured by geoendoscope. Figure 2 shows an example of cone resistance q_d penetrogram obtained on different specimens. Figure 4 presents some representative images obtained from the 21 tested samples. As FI increases, the images are saturated with fine material until it is impossible to identify the ballast grain.

5.1 Fouling Index Effects on Dynamic Cone Resistance

For each specimen, five penetration tests were carried out. From each penetrogram obtained (log of cone resistance, $q_d(z)$), only the part of the signal obtained in the ballasted layer is analyzed. Based on all signals obtained on each specimen, average

Table 2 Summary of different cases: fouling index (FI) and q_d average values

Case	Fouling material		$W_{Ballast}$ (kg)	W_{ratio} (%)	Passing sieve P_4/P_{200}	FI (%)	Class FI	$(\overline{q_d})$ (MPa)	Stdev (Mpa)	W%
	Type	W_{FM} (kg)								
0	–	0	290	0.00	0/0	0	C	5.6	4.71	0
1	Sand (Izeaux)	23.8	285	7.7	7.7/1	8.7	MC	8.1	4.43	5.98
		47.5	285	14.3	14.3/1.8	16.1	MF	9.3	5.57	5.80
		95.0	285	25	25.0/3.2	28.2	F	8.8	6.80	6.12
		125.8	252	33.2	33.3/4.3	37.6	F	6.9	4.30	5.30
		192.9	232	45.4	45.4/5.9	51.2	HF	3.9	3.28	5.72
2	Clay (Lornage)	23.8	285	7.7	7.7/4	11.56	MF	7.3	4.77	6.10
		47.5	285	14.3	14.3/7.2	21.5	F	7.8	5.58	5.86
		95.0	285	25	25.0/12.7	37.6	F	5.1	3.86	6.12
		125.8	252	33.3	33.3/16.9	50.2	HF	4.8	3.81	5.55
		192.9	232	45.4	45.4/23	68.46	HF	3.3	2.05	5.36
3	50% sand and 50% clay	23.8	285	7.7	7.7/2.4	10.1	MF	8.3	7.02	5.78
		47.5	285	14.3	14.3/4.5	18.8	MF	8.9	8.25	5.99
		95.0	285	25	25.0/8.0	32.9	F	5.2	3.04	6.21
		125.8	252	33.3	33.3/10.6	43.9	HF	5.6	3.82	5.34
		192.9	232	45.4	45.4/14.4	59.9	HF	5.1	2.63	5.91
4	75% sand and 25% clay	23.8	285	7.7	7.7/1.7	9.4	MC	8.5	6.60	5.36
		47.5	285	14.27	14.3/3.2	17.5	MF	7.7	6.12	5.59
		95.0	285	24.97	25.0/5.6	30.6	F	6.8	5.40	5.78
		125.8	252	33.29	33.3/7.4	40.7	HF	5.2	2.62	5.97

Table 2 (continued)

Case	Fouling material		$W_{Ballast}$ (kg)	W_{ratio} (%)	Passing sieve P_4/P_{200}	FI (%)	Class FI	$\overline{q_d}$ (MPa)	Stdev (Mpa)	W%
	Type	W_{FM} (kg)								
		192.9	232	45.40	45.4/10.2	55.5	HF	5.0	3.46	6.01

C clean; *MC* moderately clean; *MF* moderately fouled; *F* fouled; and *HF* highly fouled
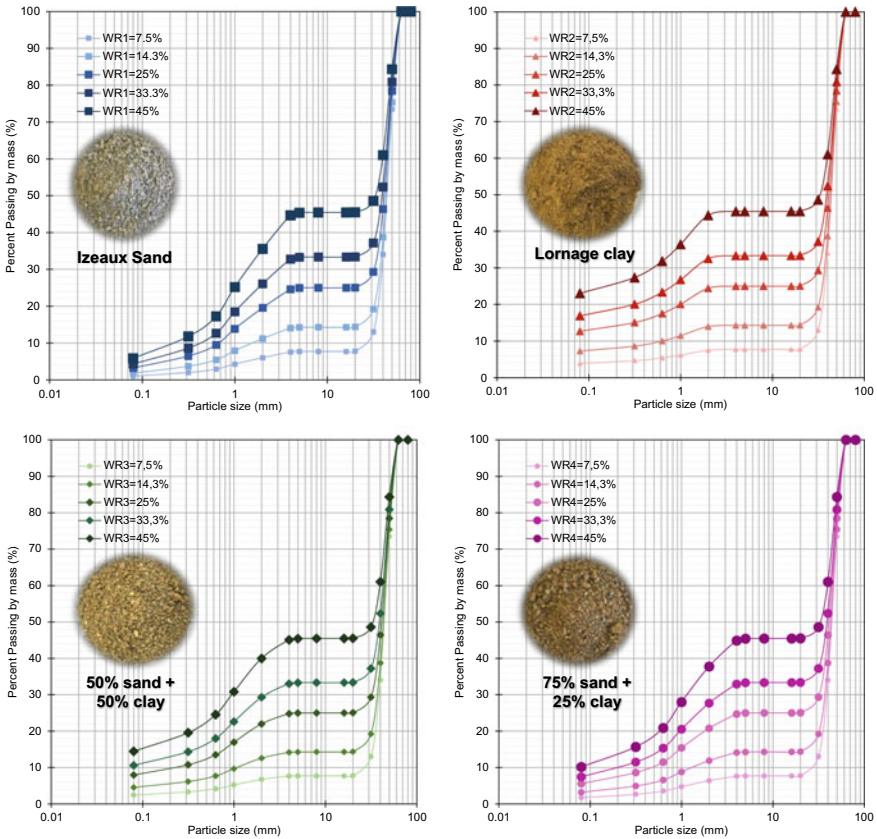
Fig. 3 Particle size distribution of different fouled ballast samples tested in this study. Mixtures of clean ballast and **a** sand, **b** clay, **c** 50% sand—50% clay, and **d** 75% sand—25% clay

value of cone resistance q_d and its standard deviation are calculated for clean ballast and fouled ballast layers. The variation of these indicators is then studied according to the fouling index (FI) and nature of fouling material (Fig. 5).

It should be noted that the cone resistance q_d values presented thereafter are much lower than those measured in practice [4, 5, 8–10]. Indeed, as mentioned above, the effects of overburden pressure (due to the track load) as well as rod's skin friction—which considerably amplifies the value of q_d measured in the field—have been neglected.

Figure 5a shows a general trend. The average q_d increases with FI values and later decreases after approximately 20% FI. This is because the particles initially increase the stability of the granular medium.

As the quantity of material increases, the contact between the ballast grains is eliminated, reducing the tip resistance. The standard deviation is also reduced because the granular medium has a more continuous behavior. Figure 5b illustrates the similarity
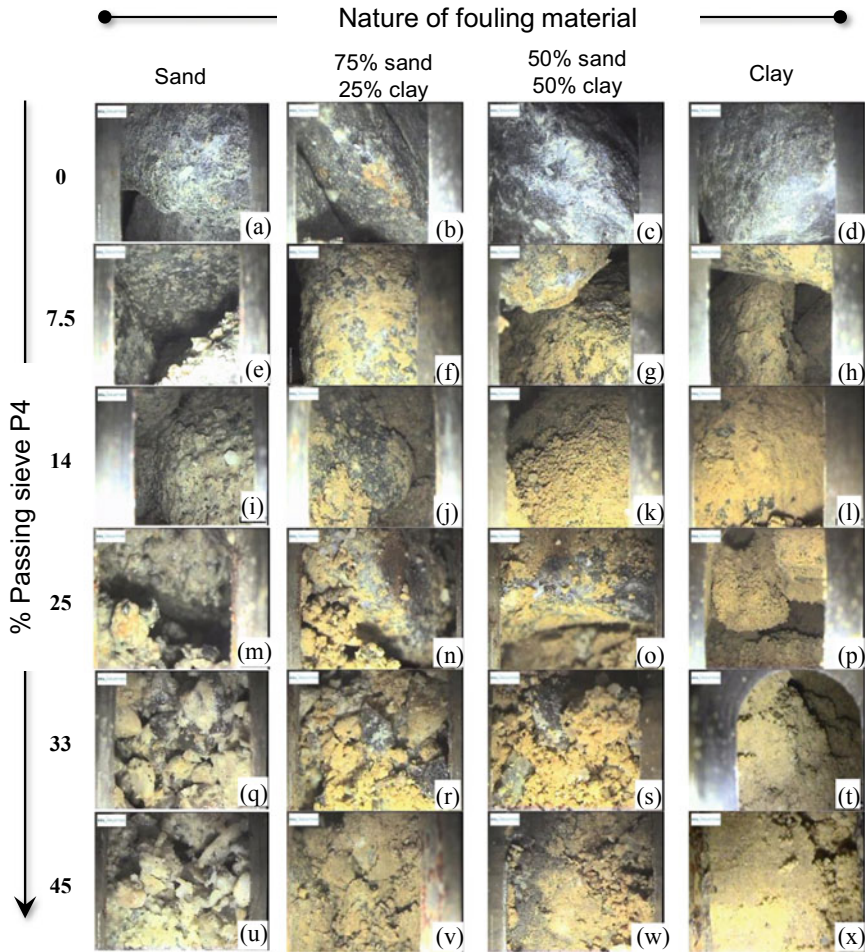
Fig. 4 Example of images according to the nature of fouling material versus passing P4 sieve

in behavior for each type of fouling material. The average dynamic cone resistance increases and reaches a maximum for distinct FI values. Then, it decreases reaching values lower than clean ballast around 40% FI.

The particle size distribution of the fouling material has a great impact on the results. In Fig. 6, the behavior is analyzed according to the amount of material passing through the P_4 and P_{200} sieve. The one that generates the greatest variability in results is P_4, while P_{200} is an enhancer. In Fig. 6a, it is easy to visually identify a correlation, where there is an increase and later a decrease in cone resistance. As for Fig. 6b, it is very difficult to establish a direct relationship because at different values of P_{200}, a similar average resistance is obtained. Case 1 (sand) contains a small amount of fines. It has a parabolic behavior: q_d increases then decreases depending
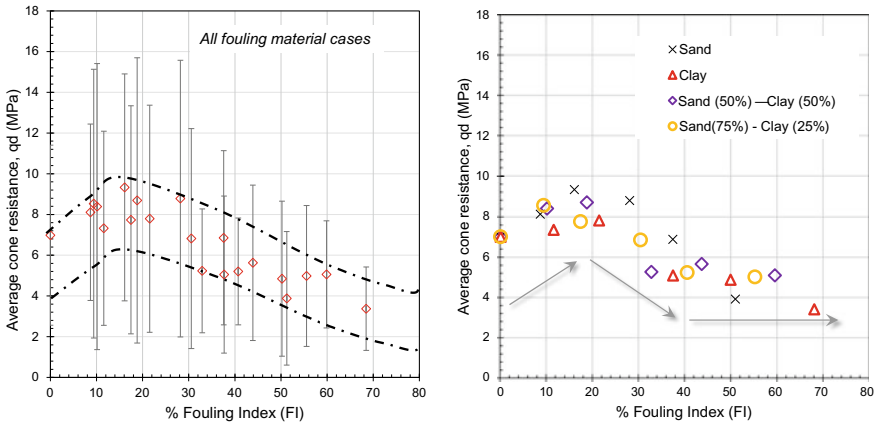
Fig. 5 Effects of fouling index (FI) on average dynamic cone resistance (q_d) values. Evolution of q_d for **a** all tested cases and **b** for different nature of fouling material
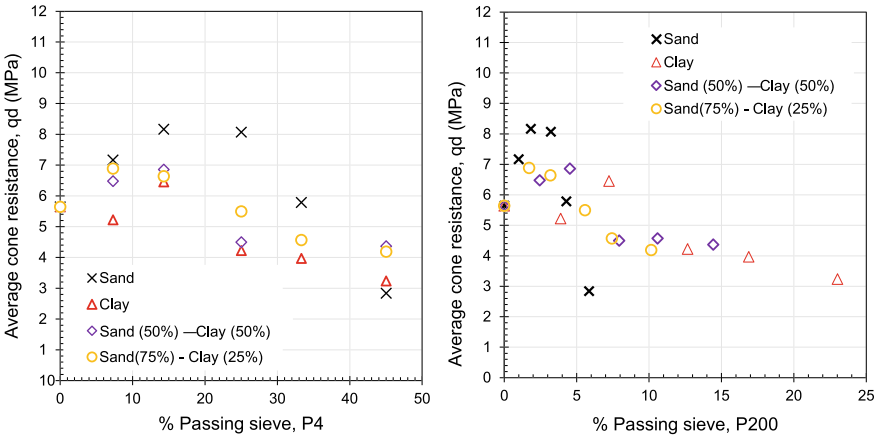
Fig. 6 Evolution of dynamic cone resistance q_d according to fines content, **a** passing the sieve P_4 and **b** passing the sieve P_{200}

on the quantity of material. Case 2 (clay) has a linear behavior with, unlike the other cases, only one value higher than that of the healthy ballast. The third (50% sand—50% clay) and the fourth (75% sand—25% clay) cases are intermediate to the previous two. These are similar to sand for small values of FI and similar to clay for large values.

5.2 Fouling Index Effects on Geoendoscope Images Features

Regarding geoendoscope results, for each sample, a total of ten tests were carried out. Only the images obtained from the videos recorded in the top ballasted layers are analyzed. Image analysis consists of first measuring the colorimetry and texture parameters of the images obtained in the fouled ballast layer. The image analysis is then performed for different values of fouling index (FI). Different algorithms were applied to obtain a vector of image's features that allow to quantify colorimetry and texture. In this study, we are mainly interested to analyze variations of average moment and average saturation (Fig. 7).

The first parameter, moment, is related to the image texture, and it is calculated in the frequency domain. It increases with small patterns in texture. Only sand has a different value from the others, but the ascending behavior in function of the amount of material is identical (Fig. 7a). The behavior and values of the other cases are similar. This parameter is highly influenced by the presence of clay in the fouling material.

The second parameter, saturation, is related to colorimetry, measured in Hue, saturation and brightness color space. The same conclusions as for the moment parameter can be made. However, on Fig. 7b, it is possible to distinguish the different fouling material cases. The curves are aligned in function of the clay content. The higher the clay content, the higher the values.
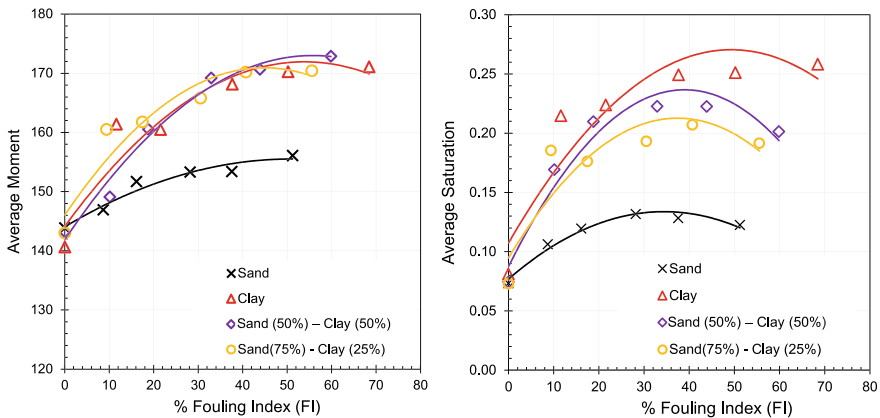

Fig. 7 Effects of fouling index (FI) and nature of fouling material on geoendoscope image features, **a** texture feature: moment and **b** colorimetry feature: saturation
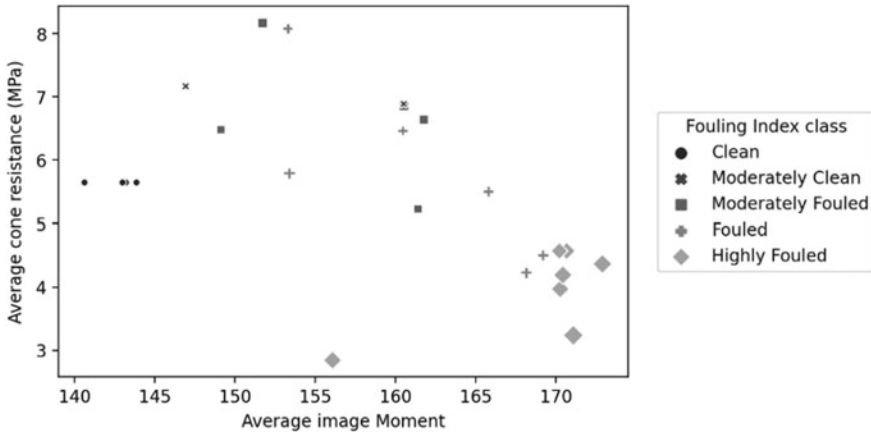
Fig. 8 Average cone resistance as a function of average image moment parameter for each tested case grouped by fouling index class

5.3 Fouling Index Characterization with Data Fusion

The cone resistance average and standard deviation values are different for each fouling index measured during the experiment. But this variation is not simply proportional. For a measured cone resistance, different FI can correspond. In this study, this variation is related to the proportion of fouling material of each class: sand or clay. The highlighted relation may change with variations in structure compaction degrees.

Sandy or clayey materials have different aspects on geoendoscope test images. According to this study, the variation of a texture and a colorimetric parameter seems to reflect the variation in fouling material composition. Moreover, the stability of the colorimetric parameters between different acquisition devices or fouling material is poor.

The fusion of both measurement techniques could improve the determination of ballast FI. In Fig. 8, the fouling index variation is represented for a combination of two calculated parameters, one from penetrometer test and the other from geoendoscope image processing.

This representation (Fig. 8), given here only for illustration, is an example of the remaining work that will be done on data fusion: assemble the mechanical behavior and the physical aspect of the fouling material for a better fouling index assessment.

6 Conclusion

Fouling in the ballast layers changes the mechanical behavior of the railway tracks. In this study, the influence of ballast fouling quantity and material type on dynamic penetrometer and geoendoscope tests results is analyzed.

The cone resistance (q_d) initially increases with fouling index, highlighting the mechanical resistance to penetration improvement of the ballasted layer. Then, when the ballast is fouled, this mechanical resistance is smaller than that of the clean ballast. The nature of the fouling material changes the degree of the above effects: In the case of sandy soils, the resistance is higher than that of clayey soils.

Texture and colorimetry parameters obtained from geoendoscope images are sensitive to variations in fouling index. The two studied parameters, moment and saturation, increase with increasing fouling content. Above all, these parameters show great sensitivity to the variation in the proportion of fine elements.

Combining dynamic penetrometer and geoendoscope tests results could describe the mechanical and physical changes caused by ballast fouling. This study covers only one case of compaction as well as only two fouling materials and therefore cannot be generalized as it is. Moreover, the effects of overburden pressure due to the track load as well as rod's skin friction, which considerably amplifies the value of q_d measured in the field, have been neglected. Further experiments and a study on the data fusion should be carried out and could improve this railway tracks problem quantification.

References

1. Selig JM, Water ET (1995) Track geotechnology, pp 12–19
2. Gourvès R, Barjot R (1995) Le pénétromètre dynamique léger PANDA. In: 11ème Congrès Européens de Mécanique des sols et des travaux de fondations, pp 83–88
3. Gourvès R (2002) Pénétromètre dynamique à énergie variable, FR2817344
4. Kazmee H, Tutumluer E, Beshears S (2017) Evaluating constructed aggregate layers of working platforms and flexible pavements: adequacy of in-place quality control and quality assurance techniques. Transp Res Rec J Transp Res Board 2655(1):1–12
5. Haddani Y et al (2016) High yield geotechnical characterization of existing railway tracks. Civ-Comp Proc 110
6. Haddani Y, Breul P, Saussine G, Navarrete MAB, Ranvier F, Gourvès R (2016) Trackbed mechanical and physical characterization using PANDA®/geoendoscopy coupling. Procedia Eng 143(Ictg):1201–1209
7. Breul P, Gourvès R (2000) Caractérisation endoscopique des milieux granulaires couplée à l'essai de pénétration. Rev Française Géotechnique 91(91):27–35
8. Breul P, Gourves R, Haddani Y (2002) Geoendoscopie - Application à la reconnaissance et au diagnostic en site urbain. Rev Française Géotechnique 101:47–55
9. Saussine G, Dhemaied A, Delforge Q, Benfeddoul S (2017) Statistical analysis of cone penetration resistance of railway ballast. EPJ Web Conf 140:2–5
10. Lamas-Lopez F, Cui YJ, Costa dAguiar S, Calon N (2016) Geotechnical auscultation of a French conventional railway track-bed for maintenance purposes. Soils Found 56(2):240–250
11. Kazmee H, Tutumluer E, Haddani Y, Benz Navarrete MA, Gourves R (2016) Use of a variable energy penetrometer and geo-endoscopic imaging in the performance assessment of working platforms constructed with large size unconventional aggregates. In: International conference on transportation and development 2016: projects and practices for prosperity—proceedings of the 2016 international conference on transportation and development, pp 1227–1238
12. Anbazhagan P, Bharatha TP, Amarajeevi G (2012) Study of ballast fouling in railway track formations. Indian Geotech. J. 42(2):87–99

13. Tutumluer E, Dombrow W, Huang H (2008) Laboratory characterization of fouled railroad ballast behavior. In: AREMA 2008 annual conference, p 32
14. Huang H, Tutumluer E, Dombrow W (2009) Laboratory characterization of fouled railroad ballast behavior. Transp Res Rec 2117:93–101
15. Ebrahimi A, Tinjum JM, Edil TB (2015) Deformational behavior of fouled railway ballast. Can Geotech J 52(3):344–355
16. Neupane M, Parsons RL, Han J (2018) Rapid estimation of fouled railroad ballast mechanical properties. Geotech Test J 41(4):777–786
17. Gourvès R, Haddani Y (2014) Méthode de caractérisation de l'assise d'une voie ferrée, dispositif pour visualiser l'intérieur d'un sol et ensemble de caractérisation de l'assise d'une voie ferrée comprenant un tel dispositif

A Back-Analysis Technique for Condition Assessment of Ballasted Railway Tracks

Shadi Fathi and **Moura Mehravar**

Abstract Track substructure is a key component of railway transportation systems. Similar to the built environment of other surface transportation systems, track substructures are subjected to ageing and deterioration. This frequently leads to failure and collapse of systems and imposing costly repairs and maintenance. Further, limited knowledge about the substructure condition leads to employing inefficient, time-consuming, and expensive maintenance. As the importance of time and budget limitation, there is a need to develop more time and cost-efficient techniques for frequent condition assessment of the existing railway substructures. Falling weight deflectometer (FWD) is recognised as an effective non-destructive test (NDT) for surveying the ballasted railway substructures through the back-analysis process, including a forward analysis of track substructure and an optimisation method. This paper presents a novel hybrid back-analysis technique, including artificial neural network (ANN) and ant colony optimisation for the continuous domain (ACO_R) to backcalculate substructure layer moduli of railway track. To this aim, a dynamic finite element (FE) model is developed to generate a reliable dataset which is covering various layer moduli for ANN training. ACO_R is employed as an optimisation tool to optimise estimated layer moduli (ANN's input). Furthermore, a validation study has been conducted using the developed FE model with back-analysed layer moduli values to evaluate the developed technique's performance. The validation study results show that use of ANNs incorporates ACO_R results in excellent performance and robustness of the developed back-analysis technique. The hybrid ANN-ACO_R back-analysis technique is a computationally efficient method with no dependency on seed modulus values.

Keywords Back-analysis · Railway · Hybrid neural network · Ant colony optimisation

S. Fathi (✉) · M. Mehravar
College of Engineering and Physical Science, School of Infrastructure and Sustainable Engineering, Aston University, Birmingham, UK
e-mail: fathis@aston.ac.uk

M. Mehravar
e-mail: m.mehravar@aston.ac.uk

1 Introduction

Several non-destructive testing (NDT) methods have been developed for condition assessment of railway track substructure. Among all of the NDTs, falling weight deflectometer (FWD) test, which is a widely used and well established one for frequent condition assessment of in-service pavements and highways [1–3], has recently been employed in railway industry with some minor modifications [4]. Deflection basins obtained from the FWD test are interpreted through back-analysis technique, as a technique for substructure layer moduli estimation, which is commonly used for in-service pavement condition assessment [5].

Over the past few years, different back-analysis techniques have been developed for condition assessment of highways. Most of these techniques are different in terms of forward analysis method used to model the pavement structure, range of the layer moduli, seed modulus values, and convergence requirement. Most of the previously developed back-analysis techniques were based on an iterative process. This process starts with predicting surface deflections considering an initial set of (seed) moduli for each layer, then comparing calculated deflections with the measured deflections, and finally, defining an error function to evaluate the estimated results. However, this method suffers from different limitations as such different sets of seed moduli need to be assumed per each iteration to minimise the error function. Moreover, long computational time and dependency on the seed moduli in each iteration, which increases the possibility of trapping in the local minima of the results, can be mentioned as the iterative method's limitations [6].

In the past two decades, artificial neural network (ANN) as a robust and fast soft computation tool has been successfully employed as an alternative to conventional pavement structure forward models in several research studies [7–14]. Moreover, various metaheuristic optimisation algorithms such as genetic algorithm (GA), particle swarm optimisation (PSO) [15, 16], differential evolution (DE) [17], shuffled complex evolution (SCE) [18], levy ant colony optimisation (ACO_{RL}) [19], and combination of ANN as a soft computation tool and metaheuristic search methods [7–9, 20–26] were employed to backcalculate layer moduli and layer thicknesses of pavement structures more accurately and faster when compared to the conventional techniques. Among the abovementioned metaheuristic optimisation techniques, ant colony optimisation for the continuous domain (ACO_R), as a robust modern metaheuristic optimisation algorithm with proven ability in various engineering optimisation problems, has been used to develop the back-analysis technique for pavements. This method shows higher accuracy and less computation time compared with other metaheuristic back-analysis techniques such as GA-based methods [19, 27–29].

Few studies have been conducted to assess the performance of railway track systems using different back-analysis techniques [30, 31]. These techniques were developed for a limited number of layers (up to three layers) and were based on an iterative method in which seed moduli for layers need to be assumed in each iteration, which increases the inaccuracy possibility and analysis time.

In this paper, for the first time, a hybrid back-analysis technique based on integrating ANN and ACO_R was developed as a tool to estimate railway track substructure layer moduli. This technique addresses the shortcomings of the previous methods including computational time, the limitations associated with number of track layers, and dependency on the seed moduli. ANN was employed in the proposed ANN-ACO_R hybrid technique to calculate surface deflections. Firstly, a dynamic finite element simulation of the FWD test, which was conducted on a railway section near the Leominster station (UK), was developed using COMSOL-Multiphysics. In this model, the railway track substructure was composed of five layers, and the results were validated against experimental data. The ANN model was trained using a synthetic database generated using the FE model. On the other hand, ACO_R was employed as an optimisation tool to estimate optimised values of layer moduli (ANN's input). Finally, the back-analysed layer moduli were implemented in the FE model, and the obtained deflections were compared with the measured experimental data. The comparison shows great performance, robustness, and efficiency of the developed hybrid back-analysis technique.

2 Methodology

2.1 Finite Element Analysis of the FWD Test

A three-dimensional dynamic finite element analysis (FEA) of the FWD test on a railway section near Leominster station in Herefordshire, UK, was conducted using COMSOL-Multiphysics. The cone penetration test (CPT) data of this track section have been used to define each substructure layer thickness as inputs for the finite element (FE) model [32]. Taking advantage of symmetrical nature of the problem, including both geometry and loading conditions, a quarter of the railway track was modelled as shown in Fig. 1. The model includes a loaded sleeper, two ballast layers, two clay layers (subgrade 1 and 2), and a sand/gravel layer (subgrade 3). Deflections in all three directions (x, y, and z) were fixed at the bottom of the model. Only one sleeper has been modelled since the FWD test procedure had the loaded sleeper disconnected from the rails. Perpendicular to the track direction, near-end boundary is located where it passes across the middle of the loaded sleeper. The model had a dimension of 10 m × 10 m × 10 m to prevent reflecting the wave from outer boundaries. Figure 1 also shows the typical finite element mesh employed in this study for the railway track.

A 31.25-kN dynamic load pulse, which is a quarter of the FWD load specified in the UK's standard (i.e., $\frac{1}{4} \times 125$ kN), was idealised using a haversine function of duration 40 ms. The load was assumed to be applied over the circular load plate at 0.55 m from sleeper's centre where sensor D_0 is located (see Fig. 2). The arrangements of four sensors (geophones) employed for the FWD test [30], including their distances from the loading point, are shown in Fig. 2. In this figure, D is the displacement
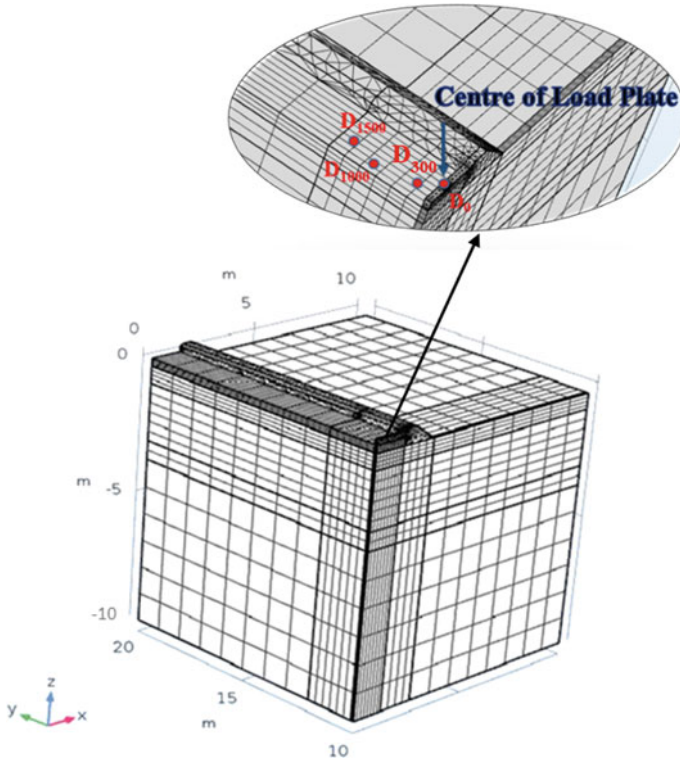
Fig. 1 3D COMSOL FE model geometry of a quarter of the railway track section near Leominster station, UK
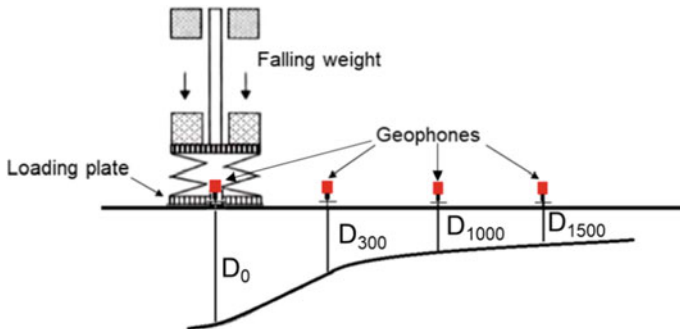

Fig. 2 Schematic drawing of FWD test including geophone arrangements

measured at the indicated horizontal offset distance (provided in the figure in mm) between the sensor and the centre of load cell.

The ballast, sub-ballast, and subgrade layers were modelled using quadratic brick elements, and tetrahedral elements were employed for the slope side of the ballast layer. In this study, a linear elastic material model was employed to describe the soil layers due to the small deflection values recorded by the geophones, which reduce the computation time [30, 33].

2.2 Finite Element Analysis Results and Validation

This section presents a validation that was carried out to evaluate the performance of the developed FE model. Figure 3 shows the peak deflections of four different geophones predicted by the developed FE model as well as recorded by the FWD test [30]. It can be observed that the predicted deflection time history basins and the experimental data presented by Burrow et al. [30] follow similar trend. On the other hand, a good agreement between the peak deflections predicted by the FE model and measured from the FWD test data can be observed. Additionally, the differences between the predicted and measured peak deflections at four different geophones were calculated and presented as percentage errors in Table 1. It can be seen that the error value for each individual geophone and also an average error for all geophones are less than 10%, which confirms the accuracy of the FE model predictions [34].
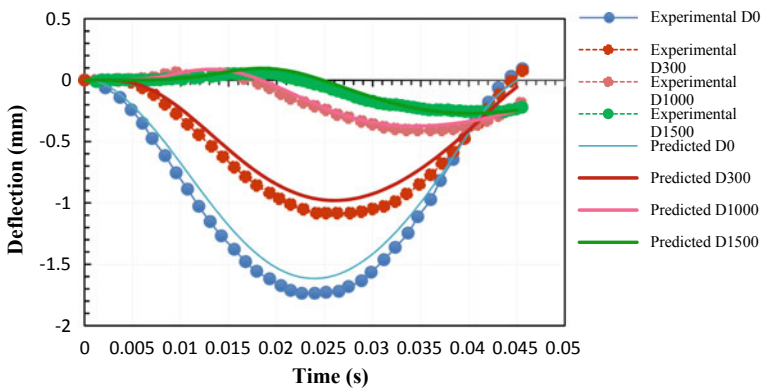

Fig. 3 Comparisons between the measured (FWD) and predicted (FE model) deflection time history at different geophones (D_0, D_{300}, D_{1000}, and D_{1500}) for railway section near Leominster station, UK

Table 1 Comparisons of FWD measured and predicted deflections of the railway section near Leominster station, UK at four geophones

Geophones	Surface deflection (mm)		Percentage error
	Experimental	Predicted (FE model)	
D_0	−1.73658	−1.616	6.961
D_{300}	−1.08288	−0.980	9.473
D_{1000}	−0.40584	−0.374	7.821
D_{1500}	−0.2566	−0.270	5.378

2.3 Development of a Hybrid ANN-ACO$_R$ Back-Analysis Technique and Results

This section presents the proposed hybrid back-analysis technique consisting of ANN and ACO$_R$ method for condition assessment of railway tracks. To this aim, a multi-layered feed-forward neural network was trained using an error back-propagation algorithm. The database was generated based on the various scenarios obtained from the developed FE model by changing each layer modulus over a range of values that reflect realistic field conditions. The ANN model served as a surrogate forward analysis model to replace the FE model. The ANN captured the behaviour of deflection basin based on the predicted moduli of five layers of the railway track substructure.

The multilayer feed-forward network has been employed in this study which is including one input layer, at least one hidden layer, and one output layer. Each layer is composed of basic particles called artificial neurons which are set up in different layers. The optimal network architecture of 19-6-5-4-4 was selected for the five-layer track system via trial and error. The number of neurons in the input layer (nineteen neurons) was correspondence with the number of each layer's material properties (layers' moduli and Poisson's ratio), layers' thicknesses, and the FWD load magnitude. While, the output layer was including four neurons which are correspond to the peak deflections at the predefined geophones at different offsets from the load point in the FWD test (presented in Fig. 2). Meanwhile, three hidden layers with six, five, and four neurons were considered in these layers. The coefficient of correlation (R) value of defined network at D_0, D_{300}, D_{1000}, and D_{1500} geophones is 0.99999, 0.99998, 0.99997, and 0.99995, respectively. Moreover, the root mean square error (RMSE) values are 0.0003503, 0.00041986, 0.00024929, and 0.00025117 at D_0, D_{300}, D_{1000}, and D_{1500} geophones, respectively. The high value of R and low values of RMSE at D_0, D_{300}, D_{1000}, and D_{1500} geophones proved the satisfactory performance of the ANN model for track surface deflection predictions.

Next, the ANN model was integrated with the ACO$_R$ optimisation method to determine the optimum values of the substructure layer moduli. This hybrid back-analysis technique code was implemented in MATLAB. To solve the current optimisation problem, a deflection-based objective function shown in Eq. (1) was chosen [17].

$$\text{Cost Function} = \sqrt{\frac{1}{n}\sum_{i=1}^{n}((D_i - d_i)/d_i)^2} \times 100 \tag{1}$$

Then, the ACO_R optimisation process was started with pheromone representation. In this step, the solution archive, which has k solutions and n decision variables (corresponding with the layer moduli), was defined. Moreover, solutions were sorted in this step based on the calculated objective function (ANN's output). The next step was probabilistic solution construction where during each iteration, the new solution was generated based on the chosen solution from the archive and its probability. By generating new solutions, pheromone was updated. New solutions in m size were added to the solution archive ($m + k$ size), sorted, and the worst solutions (m) were removed. In this way, the solution archive was updated, and the solution archive size was remained the same as initial.

An important user-defined parameter, ξ, was responsible in this algorithm to control the speed of convergence conversely and make a balance between exploitation and exploration. The higher value of ξ decreases the convergence speed of the algorithm to the solution due to the increase of the worst solution forgotten rate [19]. Moreover, q is a parameter of algorithm that affects optimisation performance.

A parametric study was conducted to adopt the best value of archive size (k). Figure 4 shows the effect of various archive sizes on the model error. It can be observed that the algorithm with $k = 200$ has the lowest value of RMSE. The ACO_R parameter values, including q, ξ, and iteration number, were considered 0.1, 0.85, 50, respectively, based on the literature [19, 35].

The back-analysed layer moduli from the ANN-ACO_R technique are compared to cone penetration testing (CPT)-based moduli in Table 2.

Moreover, the performance and accuracy of the developed back-analysis technique were evaluated using the developed FE model. Table 3 presents details of the performance evaluation of the ANN-ACO_R back-analysis technique. It can be
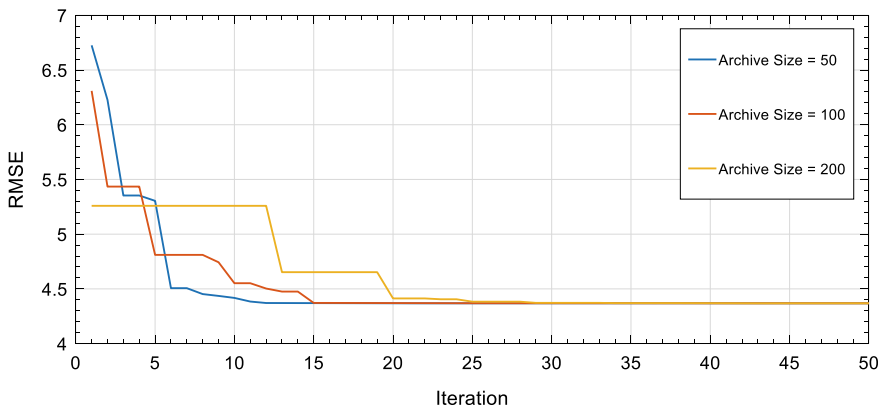

Fig. 4 Effect of archive size variation on the developed ANN-ACO_R back-analysis technique

Table 2 ANN-ACO$_R$ back-analysed layer moduli compared to cone penetration testing (CPT)-based moduli for railway section near Leominster station, UK

Layer	CPT-based layer modulus (MPa)	Back-analysed layer modulus (MPa)
Clean ballast	110.000	107.376
Contaminated ballast	32.500	27.500
Subgrade 1	71.829	66.633
Subgrade 2	33.956	50.000
Subgrade 3	362.100	400.000

Table 3 FE model results verified with the predictions of the ANN-ACO$_R$ back-analysis technique for railway section near Leominster station, UK

Geophones	Measured deflection (mm)	Predicted deflection (mm)	Percentage error	Absolute per cent error
D_0	−1.737	−1.758	1.209	2.100
D_{300}	−1.083	−1.085	0.185	0.200
D_{1000}	−0.406	−0.408	0.493	0.200
D_{1500}	−0.257	−0.293	14.010	3.600
			Sum	6.100

observed that the predicted (FE model) deflections based on the back-analysed data are in good agreement with the experimental FWD data.

In terms of the computational time, ANN-ACO$_R$ shows fast convergence (around 45 s on an i7-8750H CPU) which was obtained.

3 Conclusion

In this research, an attempt has been made to develop a time-efficient, reliable, and accurate back-analysis technique for railway track application, with no dependency on the seed moduli and number of track substructure layers. To this aim, firstly, a finite element (FE) analysis model was developed to simulate the FWD test of the railway track section near the Leominster station in the UK. The predicted surface deflections at four different horizontal offsets (D_0, D_{300}, D_{1000}, D_{1500}) from the FE model were used to generate a database to train an ANN surrogate forward model. The ANN model with a 19-6-5-4-4 network architecture was next developed to replace the FE model in order to accurately map the relationship between substructure layer moduli and the surface deflections. Afterwards, an ant colony optimisation for the continuous domain (ACO$_R$) was integrated into the forward ANN model to determine the optimum values of the layer moduli as ANN inputs.

The results of the developed ANN-ACO$_R$ back-analysis technique as a computational framework for railway track section showed excellent performance in terms of the accuracy as well as time efficiency. It is worth mentioning that using the developed hybrid back-analysis technique, ANN-ACO$_R$ in this study is computationally efficient.

References

1. Ellis T (2008) A comparison of nondestructive testing backcalculation techniques for rigid and flexible pavements
2. Berggren E (2009) Railway track stiffness: dynamic measurements and evaluation for efficient maintenance
3. Tang X, Yang X (2013) Inverse analysis of pavement structural properties based on dynamic finite element modeling and genetic algorithm. Int J Transp Sci Technol 2:15–30. https://doi.org/10.1260/2046-0430.2.1.15
4. Sharpe P (2000) Trackbed investigation. J Rep Proc-Permanent Way Inst, Permanent Way Inst 118:238–255
5. Kargah-Ostadi N, Stoffels S (2015) Backcalculation of flexible pavement structural properties using a restart covariance matrix adaptation evolution strategy. J Comput Civ Eng 29:04014035. https://doi.org/10.1061/(ASCE)cp.1943-5487.0000309
6. Chou Y, Lytton R (1991) Accuracy and consistency of backcalculated pavement layer moduli. Transp Res Rec 1293:72–85
7. Ceylan H, Guclu A, Tutumluer E, Thompson M (2005) Backcalculation of full-depth asphalt pavement layer moduli considering nonlinear stress-dependent subgrade behavior. Int J Pavement Eng 6:171–182. https://doi.org/10.1080/10298430500150981
8. Ceylan H, Gopalakrishnan K, Guclu A (2007) Advanced approaches to characterizing nonlinear pavement system responses. Transp Res Rec: J Transp Res Board 2005:86–94. https://doi.org/10.3141/2005-10
9. Gopalakrishnan K, Thompson M, Manik A (2006) Rapid Finite Element Based Airport Pavement Moduli Solutions Using Neural Networks. Int J Comput Intell 3:63–71
10. Ceylan H, Gopalakrishnan K, Bayrak M (2008) Neural networks based concrete airfield pavement layer moduli backcalculation. Civ Eng Environ Syst 25:185–199. https://doi.org/10.1080/10286600701838667
11. Bayrak M, Ceylan H (2008) Neural network-based approach for analysis of rigid pavement systems using deflection data. Transp Res Rec: J Transp Res Board 2068:61–70. https://doi.org/10.3141/2068-07
12. Beltran G, Romo M (2014) Assessing artificial neural network performance in estimating the layer properties of pavements. Ingeniería e Investigación 34:11–16. https://doi.org/10.15446/ing.investig.v34n2.42158
13. Leiva-Villacorta F, Vargas-Nordcbeck A, Timm D (2017) Non-destructive evaluation of sustainable pavement technologies using artificial neural networks. Int J Pavement Res Technol 10:139–147. https://doi.org/10.1016/j.ijprt.2016.11.006
14. Saric A, Pozder M (2017) Artificial neural networks application in the backcalculation process of flexible pavement layers elasticity modulus. In: International symposium on innovative and interdisciplinary applications of advanced technologies, pp 549–559
15. Gopalakrishnan K (2009) Backcalculation of non-linear pavement moduli using finite-element based neuro-genetic hybrid optimization. Open Civ Eng J 3:83–92. https://doi.org/10.2174/1874149500903010083
16. Öcal A (2014) Backcalculation of pavement layer properties using artificial neural network based gravitational search algorithm

17. Gopalakrishnan K, Khaitan S (2010) Development of an intelligent pavement analysis toolbox. In: Proceedings of the Institution of Civil Engineers—Transport. Thomas Telford Ltd., pp 211–221. https://doi.org/10.1680/tran.2010.163.4.211

18. Gopalakrishnan K (2009) Backcalculation of pavement moduli using bio-inspired hybrid metaheuristics and cooperative strategies. 2009 Mid-Continent Transportation Research Symposium

19. Fileccia Scimemi G, Turetta T, Celauro C (2016) Backcalculation of airport pavement moduli and thickness using the Lévy Ant Colony Optimization Algorithm. Constr Build Mater 119:288–295. https://doi.org/10.1016/j.conbuildmat.2016.05.072

20. Gopalakrishnan K (2012) Instantaneous pavement condition evaluation using non-destructive neuro-evolutionary approach. Struct Infrastruct Eng 8:857–872. https://doi.org/10.1080/15732471003653009

21. Li M, Wang H (2017) Development of ANN-GA program for backcalculation of pavement moduli under FWD testing with viscoelastic and nonlinear parameters. Int J Pavement Eng 20:490–498. https://doi.org/10.1080/10298436.2017.1309197

22. Saltan M, Uz V, Aktas B (2012) Artificial neural networks–based backcalculation of the structural properties of a typical flexible pavement. Neural Comput Appl 23:1703–1710. https://doi.org/10.1007/s00521-012-1131-y

23. Rakesh N, Jain A, Reddy M, Reddy K (2006) Artificial neural networks—genetic algorithm based model for backcalculation of pavement layer moduli. Int J Pavement Eng 7:221–230. https://doi.org/10.1080/10298430500495113

24. Pekcan O (2011) Soft computing based parameter identification in pavements and geomechanical systems

25. Ghorbani B, Arulrajah A, Narsilio G, Horpibulsuk S, Bo M (2020) Development of genetic-based models for predicting the resilient modulus of cohesive pavement subgrade soils. Soils Found 60:398–412. https://doi.org/10.1016/j.sandf.2020.02.010

26. Nazzal M, Tatari O (2013) Evaluating the use of neural networks and genetic algorithms for prediction of subgrade resilient modulus. Int J Pavement Eng 14:364–373. https://doi.org/10.1080/10298436.2012.671944

27. Gao W (2020) Comparison study on nature-inspired optimization algorithms for optimization back analysis of underground engineering. Eng Comput. https://doi.org/10.1007/s00366-019-00918-7

28. Conti C, Roisenberg M, Neto G, Porsani M (2013) Fast seismic inversion methods using ant colony optimization algorithm. IEEE Geosci Remote Sens Lett 10:1119–1123. https://doi.org/10.1109/lgrs.2012.2231397

29. Yuan S, Wang S, Tian N (2009) Swarm intelligence optimization and its application in geophysical data inversion. Appl Geophys 6:166–174. https://doi.org/10.1007/s11770-009-0018-x

30. Burrow M, Chan A, Shein A (2007) Deflectometer-based analysis of ballasted railway tracks. Proc Institution Civ Eng-Geotech Eng 160:169–177. https://doi.org/10.1680/geng.2007.160.3.169

31. Haji Abdulrazagh P, Farzaneh O, Behnia C (2018) Evaluation of railway trackbed moduli using the rail falling weight test method and its backcalculation model. Proc Inst Mech Eng, Part F: J Rail Rapid Transit 233:431–447. https://doi.org/10.1177/0954409718799800

32. Brough M, Stirling A, Ghataora G, Madelin K (2003) Evaluation of railway trackbed and formation: a case study. NDT E Int 36:145–156. https://doi.org/10.1016/s0963-8695(02)00053-1

33. Sadrossadat E, Ghorbani B, Zohourian B, Kaboutari M, Rahimzadeh Oskooei P (2018) Predictive modelling of the MR of subgrade cohesive soils incorporating CPT-related parameters through a soft-computing approach. Road Mater Pavement Des 21:701–719. https://doi.org/10.1080/14680629.2018.1527241

34. Rabbi M, Mishra D (2019) Using FWD deflection basin parameters for network-level assessment of flexible pavements. Int J Pavement Eng 22:147–161. https://doi.org/10.1080/10298436.2019.1580366
35. Cottone G, Pirrotta A, Scimemi G, Sanseverino E (2010) Damage identification by Lévy ant colony optimization. In: Reliability and optimization of structural systems, pp 37–44

Retaining Walls

Numerical Simulation of Compaction Load on Stress-Deformation Behavior of Soil Geosynthetic Composite Mass

Truc T. T. Phan, Meen W. Gui, and Thang Q. Pham

Abstract Fill compaction in the construction of soil geosynthetic composite (SGC) walls is typically carried out by operating a compactor. Due to the multiple passes of a compactor, the compaction-induced stress (CIS) at any given section can be evaluated by considering the compaction load applied directly above the section under consideration. The compaction load can be modeled as a distribution load on top of each soil layer (Type I), or as a distribution load at the top and bottom of each layer (Type II). This paper aimed to evaluate and compare the effect of the above two compaction simulation methods on the stress and deformation behavior of a full-scale instrumented SGC mass, which is under the working stress condition. Results are evaluated in the form of compaction-induced stresses, stress and strain developed in the reinforcements, and volumetric strain of the SGC mass.

Keywords Soil geosynthetic-reinforced soil · Compaction-induced stresses · Volumetric strain

1 Introduction

Over the past two decades, geosynthetic-reinforced soil (GRS) structures, including retaining walls, slopes, embankments, roadways, and load-bearing foundations, have gained increasing popularity in the US and abroad [2, 3, 6, 8, 9, 15–17]. In actual construction, GRS structures have demonstrated a number of distinct advantages over

T. T. T. Phan (✉) · M. W. Gui
Department of Civil Engineering, National Taipei University of Technology, No 1, Sec 3, ZhongXiao E Rd, Taipei 10608, Taiwan
e-mail: t107429402@ntut.org.tw; phantranthanhtruc@muce.edu.vn

M. W. Gui
e-mail: mwgui@ntut.edu.tw

T. Q. Pham
Department of Civil Engineering, University of Texas Rio Grande Valley, Edinburg, TX 78539, USA
e-mail: thang.pham@utrgv.edu

their conventional counterparts. GRS structures are generally more ductile, more flexible, more adaptable to low permeability backfill, easier to construct, require less over-excavation, and more economical than conventional earth structures [18]. These reinforced soil walls are designed by using methods such as AASHTO specifications [1], FHWA guidelines [4], and NCMA method [11].

Figure 1 schematically shows the compaction load moving away from the section II. When a soil mass is subjected to an increase in vertical load (Fig. 1a), there will generally be an increase in the vertical and horizontal stresses in the soil mass (Fig. 1b). When the compaction load is directly above II, the stresses at depth z would follow the stress path AF (Fig. 1b), as the compaction load leaves II, the ground stresses reduce following the stress path FG. AG denotes the increment of the horizontal stress after removing the compaction load. The increase in the horizontal stress and, hence, the confining pressure will lead to an increase in the stiffness and strength of the soil mass. The net increase in the horizontal stress that will "remain" in the soil mass is commonly referred to as the "residual" or "lock-in" lateral stress.
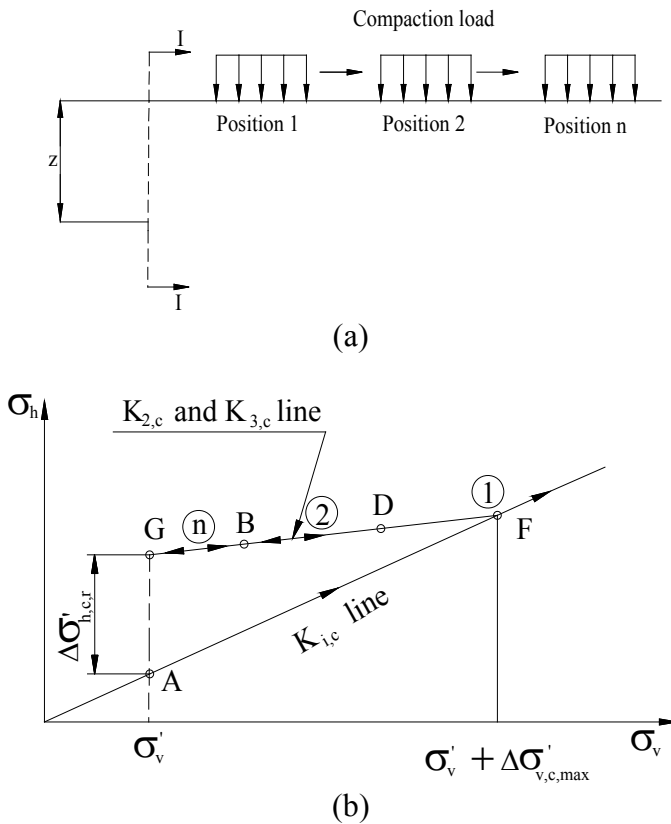

Fig. 1 **a** Positions of compaction load and **b** stress paths at depth z along section II as compaction load moves away the section [12]

(a) Type I (Pham, 2009)
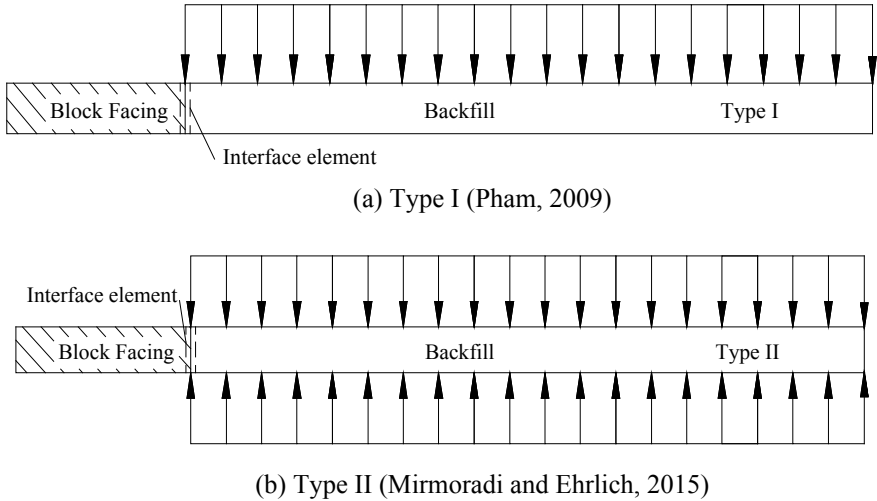

(b) Type II (Mirmoradi and Ehrlich, 2015)

Fig. 2 Type I and Type II compaction simulation procedures

An increase in vertical load followed by subsequent removal of the load is a typical phenomenon in fill compaction during construction. The residual lateral stress due to compaction is referred to as the "compaction-induced stress (CIS)" [5].

The effect of the induced stresses due to backfill soil compaction on the behavior of GRS walls has rarely been numerically modeled. For examples, Mirmoradi and Ehrlich [10], Pham [12], and Phan et al. [13] numerically investigated the stress-deformation behavior of soil-geosynthetic composite mass. Issues such as compaction-induced stresses, stress and strain in reinforcements, and angle of dilation of a soil-geosynthetic composite by using a uniform vertical stress applied only to the top of each backfill soil layer (Fig. 2a), while Ehrlich and Mitchell [7] and Mirmoradi and Ehrlich [10] simulated the compaction-induced stress by applying an equal distribution load at the top and bottom of each soil layer (Fig. 2b). It is therefore intriguing to evaluate whether there are any significant effect of these two vastly different compaction mechanisms on the mechanical behavior of the SGC masses.

In this study, the effect of the two different types of compaction simulation procedures: Type I and Type II on the induced CIS and the mechanical behavior of a field-scale instrumented SGC masses would be investigated and discussed.

Table 1 Test conditions of one unreinforced test (Test 1 and SGC test (Test 2))

Test designation	Geosynthetic reinforcement	Confining pressure (kPa)	Wide-width strength reinforcement	Reinforcement, spacing, S
Test 1	None	34	N/A	N/A
Test 2	Geotex 4×4	34	$T = 140$ kN/m	$Sv = 0.2$ m

2   Numerical Modeling

2.1   Test Characteristics and Material Used

Pham [12] conducted two field-scale test with various monitoring instrumentation on the SGC masses. One of the tests was installed with Geotex, arranged in a vertical spacing of 0.2 m, while the other test was without any geosynthetic material. The dimension of the soil-geosynthetic composite specimens used in Pham [12] tests was 2.0 m high and 1.4 m wide and in a plane strain condition. Details of the SGC tests: Test 1 and Test 2 as conducted by Pham [12] are shown in Table 1.

2.2   Numerical Modeling

Finite element (FE) method of analysis was employed to simulate the field-scale SGC experiments described behavior of SGC mass. The analysis was conducted by using the finite element program Plaxis 2D [14]. Figure 3 illustrates some of the main characteristics of the typical geometric, loading condition of a SGC mass, and FE modeling in Plaxis 2D.

In this analysis, geosynthetic reinforcement was simulated by a linear elastic model that input parameters are shown in Table 2. The values of interface property between soil reinforcement ($R_i = 0.8$) are valuable in this research. The hardening soil model was selected for simulation of the behavior of the fill material in the SGC tests. The soil parameters of the hardening soil model are determined from drained triaxial. The input parameters of FE modeling are shown in Table 2.

2.3   Compaction Simulation

Two different methods of compaction simulation, which involved applying (i) a uniform vertical stress to the top of each backfill soil layer only (Type I) and (ii) an equal distribution load at the top and bottom of each backfill soil layer (Type II), were modeled in this study. Figure 4 below shows that each backfill soil layer has been compacted in thin increments (<0.3 m), and that the compactive effort throughout
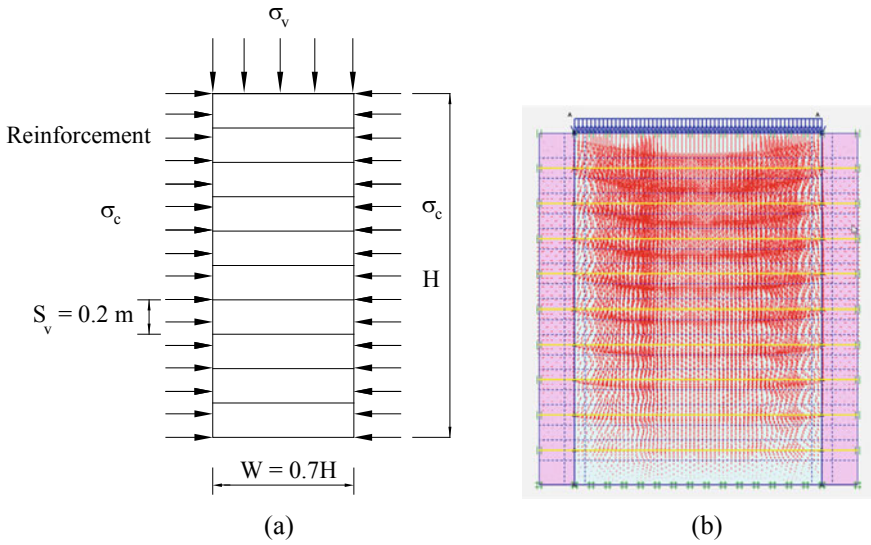
Fig. 3 **a** Typical geometric and loading conditions of an SGC mass; **b** FE model

the layer is equal. This method does not take into account instances in which heavier compaction induces additional compactive effort in the lower layers. The difference between the two approaches on representation of the actual field behavior is presented and discussed in this research.

3 Results and Discussion

3.1 Compaction-Induced Stresses (CIS)

The global stress–strain relationships as obtained from FE analysis and the SGC Test 2 are shown in Fig. 5. The relative difference between cases with CIS and no CIS is about 9.10% and 10.4% simulated using Type I and Type II, respectively. These results suggested that CIS in SGC mass should not be neglected in analyses. However, Fig. 5 also shows that using the different compaction simulation procedures of Type I and II did not significantly affect the strength of the SGC masses, and the variation in terms of deviatoric stress is found to be approximately 5%.

Table 2 Input parameters for the numerical analysis

Material	Value
Soil properties	
Model	Hardening soil
Peak plane strain friction angle, ϕ (°)	50
Apparent cohesion, c (kN/m^2)	70
Dilation angle, Ψ (°)[a]	19
Unit weight, γ (kN/m^3)	25
E_{ref}^{50a} (kN/m^2)	62,374
$E_{\text{ur}}^{50} = 3 * E_{\text{ref}}^{50}$ (kN/m^2)	187,122
Stress dependence exponent, m	0.5
Failure ratio, R	0.9
Poisson's ratio, υ	0.2
P_{ref} (kN/m^2)	100
Reinforcement (single-sheet Geotex 4 × 4)	
Elastic axial stiffness (kN/m)	1000
Reinforcement spacing (m)	0.2
Modular block properties	
Model	Model linear elastic
Stiffness modulus (kN/m^2)	$3 * 10^6$
Unit weight, γ (kN/m^3)	12.5
Poisson's ratio, υ	0
Block-Block interface[b]	
Model	Mohr–Coulomb
Stiffness modulus (kN/m^2)	$3 * 10^6$
Poisson's ratio, υ	0.45
Angle of internal friction, ϕ (°)	33
Apparent cohesion, c (kN/m^2)	2
Soil-Block interface[b]	
Model	Mohr–Coulomb
Poisson's ratio, υ	0.45
Angle of internal friction, ϕ (°)	33.33
Apparent cohesion, c (kN/m^2)	46.67
Stiffness modulus (kN/m^2)	74,829.711
Soil-Soil interface[b]	
Model	Mohr–Coulomb
Poisson's ratio, υ	0.45
Angle of internal friction, ϕ (°)	45
Cohesion, c (kN/m^2)	56

(continued)

Table 2 (continued)

Material	Value
Stiffness modulus (kN/m^2)	106,685.26

[a]Based on drained triaxial testing
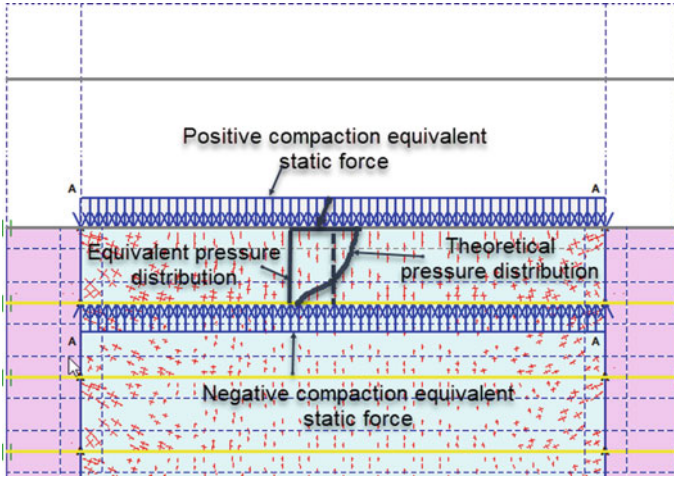[b]Defined interface elements with zero thickness in Plaxis

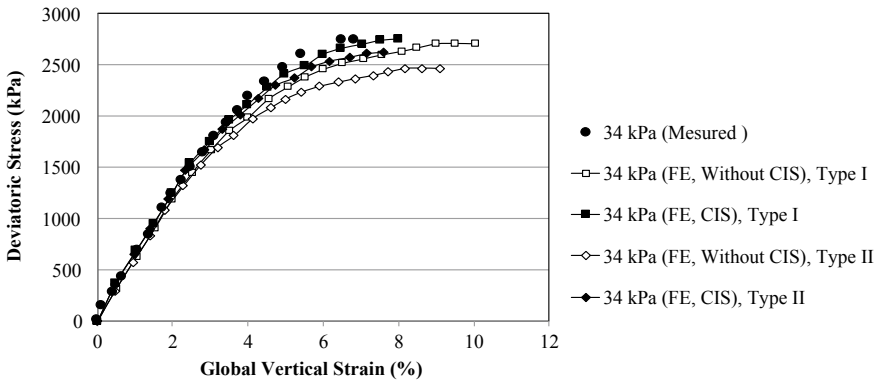**Fig. 4** Simulation of Type II compaction load distribution

Fig. 5 Comparison of global stress–strain relationship of SGC Tests 2

3.2 Stress and Strength of Reinforcement

Figure 6 and Table 3 show the lateral displacements on the open faces of the specimen under applied pressures of 400 kPa, 1000 kPa, 2000 kPa, and 2500 kPa. At the applied pressure of 2500 kPa, the pressure was close to the failure condition, and
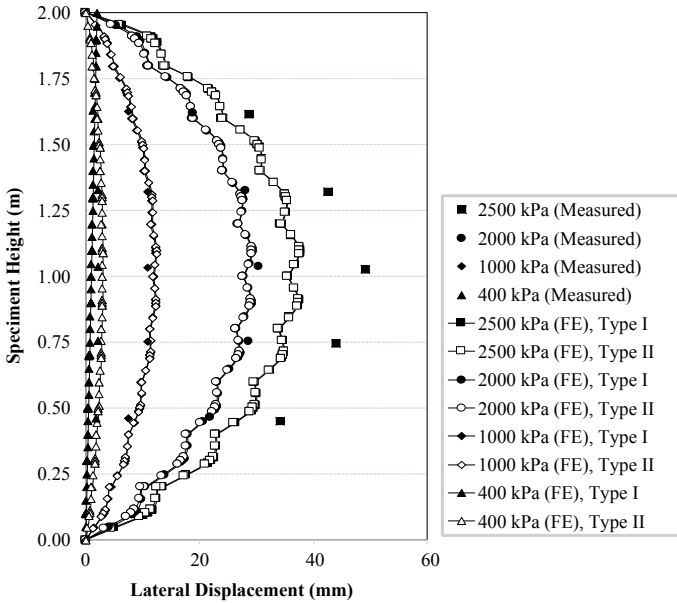
Fig. 6 Comparison of lateral displacement at open face of SGC Test 2

Table 3 Numerical results from lateral displacement of at open face of SGC Test 2 for compaction procedure of Type I and Type II with applied surcharge load of $p = 400$ kPa, 1000 kPa, 2000 kPa, and 2500 kPa

Applied surcharge load p (kPa)	Maximum lateral displacement (mm)	
	Type I	Type II
$p = 400$	2.95	3.01
$p = 1000$	12.41	12.45
$p = 2000$	29.45	29.29
$p = 2500$	37.72	37.76

the values near failure may be unstable. That is why the values from the measure data were higher than the numerical results. At other applied pressures, smaller the failure pressure, the FE and measured data were in good agreement. In addition, it is seen that the effect of the different compaction simulation procedures on the lateral displacement is minimal. The maximum variation between the numerical results of the two compaction procedures and the measured data is very small, only about 2%. This result may also imply that the interface property between the soil reinforcement might be insignificant to the stress-deformation behavior of this SGC mass.

A comparison between the FEM analyses and the measured data of the distribution of reinforcements strains in the SGC Test 2 is shown in Fig. 7 and Table 4. It is seen that the simulated strains for both the two cases of compaction simulation procedures are in good agreement with the measured data for reinforcement layers located at 1.6 m and 0.8 m from the base, with a variation of only about 2%. The results thus
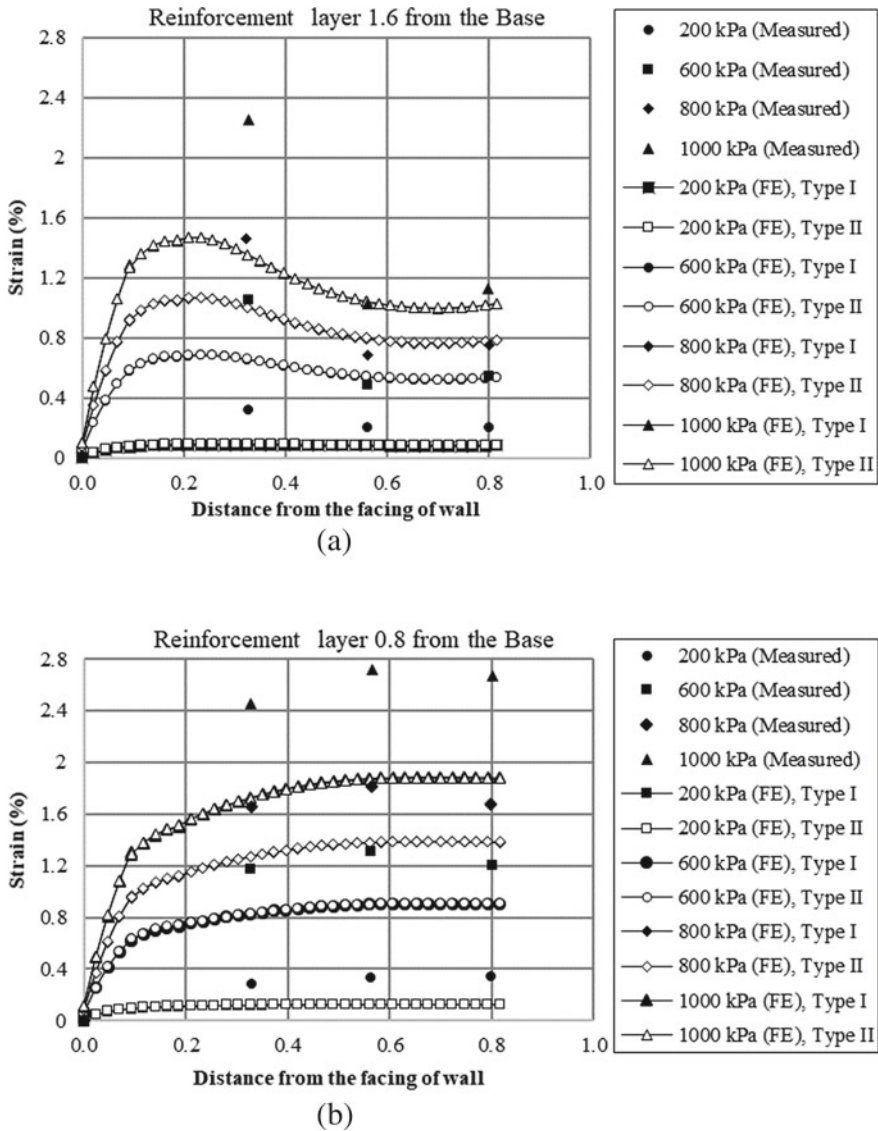
Reinforcement layer 1.6 from the Base

(a)

Reinforcement layer 0.8 from the Base

(b)

Fig. 7 Comparison of reinforcement strains of SGC Test 2: **a** at reinforcement layer 1.6 m from the base; **b** at reinforcement layer 0.8 m from the base

suggested that the consideration of different compaction simulation procedures on the lateral displacements in SGC mass could be neglected in the future numerical simulation.

Table 4 Numerical results from reinforcement strain of SGC Test 2 mass at reinforcement layer 0.8 m and 1.6 m from the base for compaction procedure of Type I and Type II with applied surcharge load of $p = 200$ kPa, 600 kPa, 800 kPa, and 1000 kPa

Applied surcharge load p (kPa)	Maximum reinforcement strain (%)			
	Layer 0.8 m from the base		Layer 1.6 m from the base	
	Type I	Type II	Type I	Type II
$p = 200$	0.129	0.128	0.089	0.091
$p = 600$	0.908	0.904	0.684	0.678
$p = 800$	1.378	1.389	1.069	1.067
$p = 1000$	1.885	1.881	1.468	1.467

3.3   Volumetric Strain of SGC Mass

Figure 8 shows the comparison of the global stress–strain and volume strain relationships of the SGC Test 1 and Test 2 as obtained from the FE analysis and the measured data. The SGC Test 2 was conducted under a confining pressure of 34 kPa, and additional simulations under different confining pressures of 100 kPa and 200 kPa have also been conducted. It is seen that the global stress–strain and volume change relationships under the confining pressure of 34 kPa obtained numerically are in good agreement with the measured data. The variation between the measured and the numerical results was found to be no more than 4%. These results suggested that the consideration of different compaction procedures on the induced volumetric strain of reinforced and unreinforced SGC mass might also be neglected. It is also found that the volumetric strain behavior involved in the geosynthetic-reinforced soil mass and that of an unreinforced soil mass is totally different.
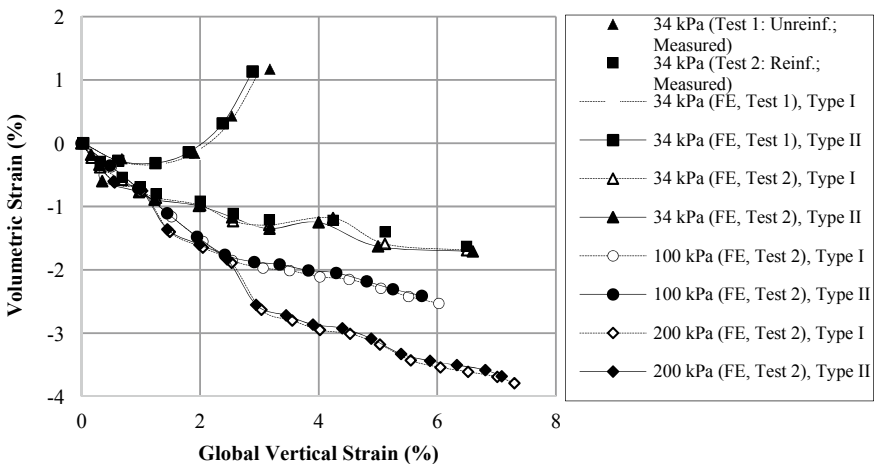

Fig. 8 Volume change behaviors of SGC mass

4   Conclusions

In this study, the effect of the two different types of compaction simulation procedures, (i) by applying a uniform vertical pressure to the top of each backfill layer (compaction procedure type I) as well as (ii) applying uniform vertical pressures at the top and bottom of each soil layer (compaction procedure type II), on the induced CIS and the mechanical behavior of a field-scale instrumented SGC masses, has been investigated. The results from the FE analyses of this study and the field-scale instrumented tests obtained by Pham [12] were in good agreement. Including the CIS in the analysis of GRS structures increased the strength of the GRS mass by about 10% and should not be neglected in analysis. Numerical analysis results showed that the compaction modeled using simulation procedures Type I and Type II both agreed well with the measured data. The variation of results between these two cases of compaction simulation procedures was found to be insignificant on the stress-deformation behavior of this SGC mass.

References

1. AASHTO (2014) American association of state highway and transportation officials: LRFD bridge design specifications, 7th edn.
2. Adams MT, Schlatter W, Stabile T (2007) Geosynthetic-reinforced soil integrated abutments at the bowman road bridge in defiance county, Ohio. Geotechnical Special Publication No. 172: Proceedings of Geo-Denver 2007, ASCE, Denver, Colorado
3. Allen TM, Bathurst RJ (2001) Application of K0-stiffness method to reinforced soil wall limit state design. Final Research Report to Washington State Department of Transportation, Seattle, Washington State
4. Berg RR, Christopher BR, Samtani NC (2009) Design of mechanically stabilized earth walls and reinforced soil slopes, Publication No. FHWA-NHI-10-024, Volume No 1, Federal Highway Administration, McLean, p 332
5. Duncan JM, Seed RB (1986) Compaction-induced earth pressure under Ko conditions. J Geotech Eng Div ASCE 112(1):1–22
6. Elton DJ, Patawaran MAB (2005) Mechanically Stabilized Earth (MSE) reinforcement tensile strength from tests of geotextile reinforced soil. Technical Report, Alabama Highway Research Center, Auburn University.
7. Ehrlich M, Mitchell JK (1994) Working stress design method for reinforced soil walls. J Geotech Eng ASCE 120(4):625–645
8. Holtz RD (2010) Reinforced soil technology: from experimental to the familiar. Terzaghi Lecture, Geo-Florida, Palm Beach
9. Holtz RD, Lee WF (2002) Internal stability analyses of geosynthetic reinforced retaining walls. Report No. WA-RD 532.1, Washington State Department of Transportation, Washington, DC
10. Mirmoradi SH, Ehrlich M (2015) Modeling of the compaction-induced stress on reinforced soil walls. Geotext Geomembr 43(1):82–88
11. NCMA (2009) Design manual for segmental retaining walls, 3rd edn., TR 127B, National Concrete Masonry Association, Herndon, VA, p 302
12. Pham TQ (2009) Investigating composite behavior of geosynthetic-reinforced soil (GRS) mass. Ph.D. dissertation, University of Colorado Denver

13. Phan TTT, Gui MW, Pham QT (2019) Numerical simulation analysis of stress-deformation behavior of soil and geosynthetic composite mass: a case study. In: Proceedings of 3rd international conference on transportation infrastructure and sustainable development, Danang, Vietnam, p 211
14. Plaxis BV (2002) Plaxis 2D—Version 8 Manual. Balkema, Rotterdam
15. Wu JTH (2001) Revising the AASHTO guidelines for design and construction of GRS walls. Report CDOT-DTD-R-2001-6, Colorado Department of Transportation, University of Colorado Denver, p 148
16. Wu JTH, Pham TQ (2013) Load carrying capacity and required reinforcement strength of closely spaced soil-geosynthetic composites. J Geotech Geoenviron ASCE 139(9):1468–1476
17. Wu JTH, Tung CY, Adams MT, Nicks JE (2018) Analysis of stress-deformation behavior of soil-geosynthetic composites in plane strain condition. Transp Infrastruct Geotechnol 5(3):210–230
18. Wu JTH (1994) Design and construction of simple, easy and low-cost retaining walls. Colorado Transportation Institute, Report CTI-UCD-1-94

Geotechnical Centrifuge and Full-Scale Laboratory Testing for Performance Evaluation of Conventional and High-Speed Railway Track Structures

Peter K. Woodward, Andrew Brennan, Omar Laghrouche, Ahmet Esen, David Connolly, and Tina Mariot

Abstract The development of high-speed railways is progressing at a very rapid pace worldwide. For example, in the UK, the construction of Phase 1 (225 km) of the HS2 line has now begun, and it will have a maximum operational speed of 360 km/h. In this paper, the performance of a geosynthetic-reinforced soil retaining wall (GRS-RW) is presented for both ballasted track and concrete slab track using full-scale laboratory testing and geotechnical centrifuge modelling. In the full-scale testing, the geo-pavement and railways accelerated fatigue testing (GRAFT II) facility at Heriot-Watt University is used. It operates using six independent hydraulic actuators over three full-size sleepers to simulate the passage of a moving train. The tested GRS-RW structures consist of well-compacted subgrade and a frost protection layer designed to HS2 standards. Results are recorded in terms of deflections, accelerations, total settlement and transient stresses at various locations of the structure model. Whilst the full-scale GRAFT II testing elucidates behaviour of the track and wall, in order to study how the foundation subsoil may interact with the structure, a series of small-scale experiments were carried out in the geotechnical centrifuge by the University of Dundee. By creating small-scale physical models of the GRS-RW and foundation and by increasing gravity, the centrifuge was used to simulate the large induced stresses. Short- and long-term deformations of the wall and foundation were also monitored. Comparisons between the full-scale and centrifuge modelling are presented.

P. K. Woodward (✉) · D. Connolly
Institute for High Speed Rail and System Integration, University of Leeds, Leeds, UK
e-mail: p.k.woodward@leeds.ac.uk

A. Brennan
Department of Civil Engineering, University of Dundee, Dundee, UK

O. Laghrouche · A. Esen
School of Energy, Geoscience, Infrastructure and Society, Heriot-Watt University, Edinburgh, UK

T. Mariot
Faculty of Engineering and Technology, Liverpool John Moores University, Liverpool, UK

1   Introduction

High-speed rail lines, at ever-increasing speeds and distances, are in development both in the UK and worldwide, but up-front capital expenditure remains a major inhibiting factor both to the client and also in the eyes of the public. Embankments have primarily been used as the principal means of supporting the railway track for nearly 200 years. Indeed, modern high-speed railway lines still typically use traditional sloping embankments for track support over flood plains and for alignment and track geometry considerations. However, in Japan, the application of GRS-RW systems has gained popularity as alternative to conventional embankments, particularly for high-speed lines like the Hokkaido Shinkansen [1]. These structures are used because they are cost effective, both in terms of construction and maintenance costs. The technique requires less ground stabilization/improvement and land take than a conventional embankment, as it has a much smaller base area. In addition, embankment protection is not required (e.g., under flooding conditions) and is therefore a significant step forward in high-speed track structure design.

To investigate the performance of these structures in the laboratory, the UK Engineering and Physical Sciences Research Council (EPSRC) awarded research funding for GRS-RW structures to be tested in the GRAFT II test facility at Heriot-Watt University and for scaled-down versions to be tested in the Centrifuge Test Facility at the University of Dundee. The project was called LOCORPS, and this paper presents early experimental test data from these studies.

2   GRS Structures

Geosynethic-reinforced structures (GRS) have been used extensively for highways and bridge abutments all over the world [2–8]. Field studies of GRS-RW (retaining wall) structures have been reported in the literature by authors such as Tatsuoka and Tateyama [1, 9]. Their performance has been reported as excellent; however, in the UK (and many countries across the World), these structures have to date not been used. The LOCORPS project was developed to look at how these types of structures could be adopted in the UK through proven laboratory-controlled testing programs. GRS-RW structures (Fig. 1) use geosynthetics wrapped around gravel bags to provide stability prior to the formation of a rigid concrete facing.

One of the principal benefits of the GRS-RW technique is its ability to accommodate ground movement during construction. In addition, unlike a cantilevered retaining structure, it does not require piled foundations to resist the active lateral thrust developed by the backfill; *this active thrust normally leads to large overturning*
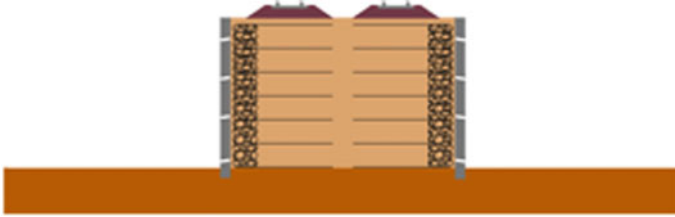
Fig. 1 Example GRS-RW structure

moments in the cantilevered wall requiring large civil engineering works for the piled foundations.

When compared to embankments, the amount of land take and soil movement (to construct the embankment slopes) is significantly reduced. If the structure is to be built over poor ground the amount of in situ ground (foundation), improvement required is also significantly reduced when compared to traditional embankments.

3 GRAFT II Testing by Heriot-Watt University

The full-scale geo-pavement and railways accelerated fatigue testing (GRAFT II) facility located at Heriot-Watt University (Fig. 2) was used to test the GRS-RW structures for both ballasted and concrete slab track types. Testing in GRAFT II for non-GRS walls (as the benchmark) has also been performed as part of the LOCORPS project [10].

GRAFT II primarily provides the settlement performance of the track and its associated upper subgrade layers. In particular, it tests the short- and long-term performance of the track/formation interface for a variety of subgrade structures. The accelerated testing approach means that many years of train loading (at full scale) can be applied within a relatively short period of time (a few days or weeks). GRAFT II applies loading through six independent hydraulic actuators situated over three full-sized sleepers to simulate the passage of a moving train. This loading pattern is also used for concrete slab track with three built-in sleepers. It is important to note that GRAFT II is not a full dynamic test facility, i.e., it cannot be used to simulate effects such as critical velocity or other ground vibration phenomena.

3.1 Track Test Setup and Loading

Full details about how the LOCORPS track was set up in GRAFT II can be found in [10]. For the GRS-RW, the procedure described by Yonezawa et al. [1] was adopted.
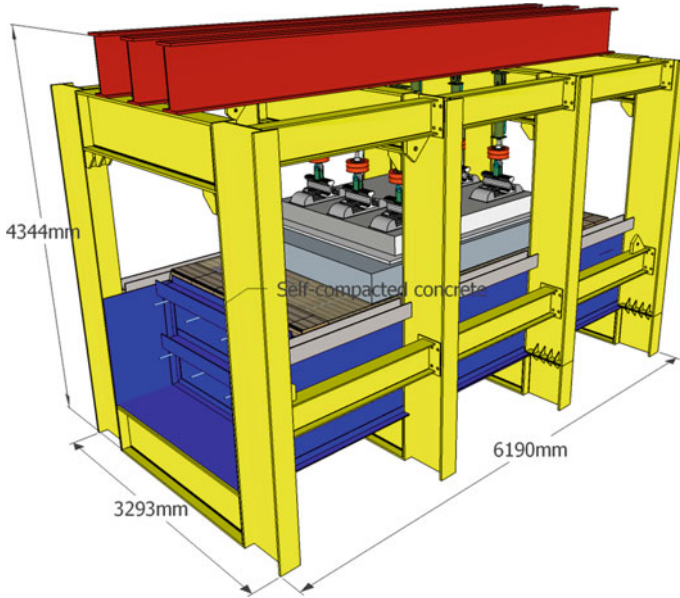
Fig. 2 GRAFT II test facility at Heriot-Watt University

The substructure consisted of a 0.1 m very well-compacted base layer on top of which a 1.2 m high GRS-RW wall was constructed in multiple layers using geogrids.

At certain locations within the fill layers, embedded rods/bolts, connected to perpendicular angular sections, were located to form the wall supports. Each geogrid was placed over the base layer and then wrapped over the gravel bags positioned at the fill ends to form the wall facing. The layer depth was 0.3 m in height, and two layers of 0.15 m of sand were compacted in stages to form a granular layer. The geogrid was tightened over the bags and pinned to the compacted soil to provide a relatively small geosynthetic pre-stress. At the end of construction, the preformed wall (steel) was connected to the rods/bolts. The wall was not restrained by the test frame (i.e., it was free to move laterally). Grout was then poured in the gap between the wall and the geosynthetic reinforced bags. Once the grout had cured, the upper track structure was then formed in accordance with the procedure given in [10].

The experimental procedure was to first construct and test a concrete slab track section (Fig. 3) in both static and cyclic conditions. The concrete track was then removed and replaced by a ballasted section and subsequently subjected to the same static and cyclic loading regime.

Fig. 3 **a** Construction of the GRS-RW test specimen and **b** completed structure prior to cyclic loading for concrete slab track

3.2 Experimental Results for Ballasted and Concrete Slab Tracks

The cyclic loading sequence is shown in Fig. 4. To ensure principal stress rotation conditions were simulated, the loading from the actuators was phased. The phase calculation was based on the loading sequence provided by a train travelling at 100 m/s (phased loading of 0.0065 s from one sleeper to the adjacent one at a distance of 0.65 m away).

Two different frequencies and cyclic loads were modelled:

- 1.17 million cycles at 5.6 Hz at a peak actuator load of 58.9 kN, followed by,
- A further 2.2 million cycles at 2.5 Hz at a peak actuator load of 83.4 kN.

Table 1 shows the overall (average) final settlement values after the two stages of testing for both the ballasted and concrete slab track tests. Despite being the first track type tested, the superior low settlement characteristics of the concrete slab track can be clearly seen.
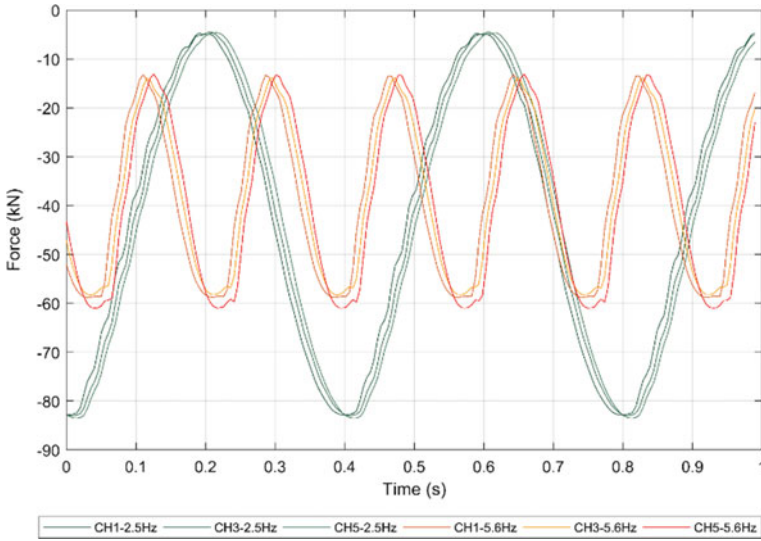
Fig. 4 Example phase loading for the cyclic tests

Table 1 Accumulated cyclic displacements

Accumulated displacement	Ballasted track (mm)	Concrete slab track (mm)
After first 1.2 million load cycles at 5.6 Hz	5.6	0.36
Total after a further 2.2 million load cycles at 2.5 Hz	10.0	0.7

4 Centrifuge Testing by the University of Dundee

To complement the measurements of the settlements from the full-scale GRAFT II tests, small-scale tests were undertaken in the centrifuge to quantify the settlements expected as a result of the stress transfer to the subsoil foundation. Analysis of the results is however still at the very early stages as these results have only just become available.

Small-scale models of the walls on thick sub-soil layers were created at a scale of 1:50. In order to match the self-weight stresses in the full-scale wall and subsoil, gravity was increased by a factor of 50 by spinning the model on the 3 m radius geotechnical centrifuge at the University of Dundee (Fig. 5a). This has the effect of increasing the stress underneath the 25 mm high model wall from 0.4 to 20.2 kPa, equivalent to the stress applied by the 1.2 m high full-scale version as tested using the GRAFT II simulator.

The small-scale model is created by depositing the subsoil using air pluviation (described in detail in [11]) in a strongbox (Fig. 5b). The model ends at the Perspex wall of a viewing chamber through which a GoPro Hero 4 camera was able to observe

Fig. 5 **a** 3 m radius geotechnical centrifuge at the University of Dundee with the railway testing apparatus in place and **b** the model container and actuation system

a cross section of the wall and subsoil, recording still images 40 times per cycle in order to allow settlement patterns to be mapped using digital image correlation through PIV.

For the case described in this paper, the subsoil used was dry, air-pluviated sand prepared at a relative density of $D_r = 70\%$. HST95 sand was used, which is an even graded fine silica sand with $D_{50} = 0.15$ mm and an internal friction angle of $\varphi' = 32°$. Further details and material properties may be found in [11]. Miniature thin-film capacitive total stress sensors (Singletact S8-10N) with a diameter of 8 mm and a thickness of 300 μm were placed on the soil surface directly beneath the structures to measure the changes in total stress in an array of five sensors located in a line from the centre to the facing wall at the edge. The walls (and/or embankments) are then placed onto the subsoil (and sensors). Miniature vertical displacement sensors were installed close to the total stress sensors to measure settlements including the vertical displacement of the track itself.

4.1 GRS-RW Construction

The model GRS-RW structures consisted of several components; layers of geogrid, compacted fill, gravel bags and facing walls. Each of these was required to be correctly scaled and miniaturized, both in terms of their size and engineering behaviour, in order to ensure the behaviour of the model is representative of the full-scale problem. In the case of the geogrid, a miniature HDPE mesh (manufactured by Suregreen Ltd., with a 2 mm × 2 mm grid size) was selected from a range of materials tested as it closely matched the required scaled tensile stiffness based on tests of a sample of the geogrid used in the full-scale GRAFT II model tests, as well as having a similar open area. The model fill is comprised of HST95 sand, which is a fine silica sand

[11]. The mesh was also used as the fixing system for the wall facings (it was not possible to model the wall anchor rods/bolts).

The HST95 sand has a comparable scaled particle size distribution to the crushed limestone fill used in the full-scale tests, which has the effect of ensuring a similar ratio of particle size to geogrid opening size. A model scale gravel for the gravel bags was also prepared by washing, sieving and regrading locally available Cotside sand. Cotside sand has a highly open grading such that sands with a wide range of particle size distributions (PSD) can be created to match the specific PSD required by simply removing any unnecessary fractions. Tests indicated that the model gravel mix had similar properties to full-scale rail ballast (UK Network Rail specification) in terms of its PSD, as well as exhibiting similar oedometric stress–strain response.

The facing walls were simulated by 2 mm × 25 mm aluminium flats, selected to match the required scaled longitudinal bending stiffness of the full-scale steel plate and section used in the GRAFT II tests (also adjusting for the differing modulus of the aluminium compared to the steel used at full-scale), whereas the GRAFT II steel plate wall (which was held in place by the anchoring system) was bonded to the sides of the compacted embankment by a 50 mm thick layer of top flow grout; at the model scale, the aluminium (with one side sand-blasted to ensure full adhesion) was fixed by a layer of R-KEM II rapid hardening polyester resin.

To construct the walls, a former (90 wide × 215 mm long) was used to ensure precise control over the final dimensions (Fig. 6a). The layers of geogrid (6 mm high, 300 mm at full scale) were pre-prepared with the gravel bags at the edges secured in place with thin stainless-steel wire ties, mimicking the fixing pins used at full scale. Each layer was placed in the mould individually, and the fill was compacted in place using a modified compaction hammer (750 g mass, 300 mm fall height) fitted with

Fig. 6 **a** Single model geogrid and gravel bag layer in the wall former, **b** the fill compaction process, **c** a compacted 25 mm GRS-RW with four layers and **d** the full completed model

a square end plate the width of the required fill (Fig. 6b). The fill (HST95 sand) was partially saturated at its optimal moisture content ($w = 8\%$) and compacted with 40 blows of the compaction hammer per layer. The process was found to provide a fill (dry) density of 1652 kg/m^3, which corresponds to a degree of compaction greater than 98%, exceeding the recommendations of [2].

The layer was scraped level using a 3D printed levelling tool to provide a perfectly flat surface for the next layer of geogrid. The process was repeated until each of the four layers was in place, before the sides of the wall former were removed (Fig. 6c), and the aluminium flats representing the facing walls were secured using the polyester resin and allowed to set for 10 min. The partially saturated fill had the advantage of making the walls sufficiently handleable to place them onto the subsoil (Fig. 6d) after removal from the former.

4.2 Track Setup

A model, simulating the rail, slab and track arrangement, was placed onto the wall. The model train weighed 0.56 kg (70 tonnes at full scale) with its weight evenly distributed across four bearings (two at each end, 280 mm apart) running on the track such that each pair of bearings simulates one bogie (equivalent of two 17 tonne axle loads per bogie).

The train was attached to a horizontal actuation system such that it was free to move vertically. Following construction, the centrifuge was accelerated to 50 g, and the train was cyclically pulled along the track forwards and backwards (passing the instrumented section in the centre of the model each time) such that approximately, 800 train passes (1600 bogie passes) were made.

4.3 Early Centrifuge Results

Figure 7 shows the recorded settlements of the wall and the slab track over the course of the cyclic testing. As can be seen, the track settlement rapidly increases before the rate of settlement slows with an increasing number of cycles, reaching a final vertical displacement of 0.57 mm. However, when the scaling laws are applied this corresponds to a settlement of 28.5 mm at full scale which, even when the wall foundation settlement is removed, is significant and much larger than the GRAFT II measurements. The settlement of the wall foundation (on this dense sand subsoil) was 0.12 mm which is equivalent to 6 mm displacement once the scaling laws are applied.

Figure 8 shows the response of the slab track and embankment over one (typical) cycle of loading which encompasses two train passes.
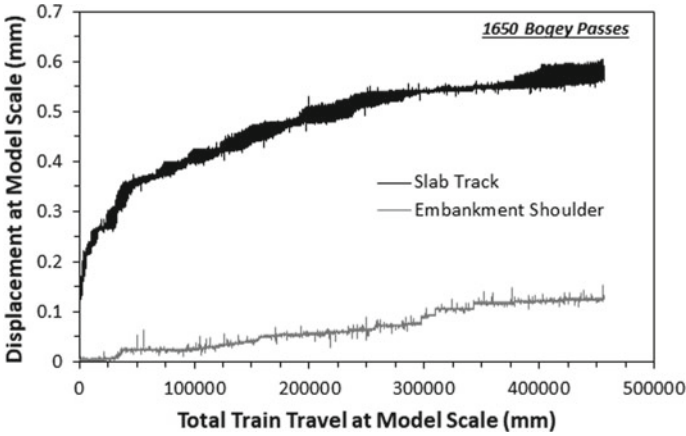
Fig. 7 Settlement of the slab track and embankment with 1650 bogie passes
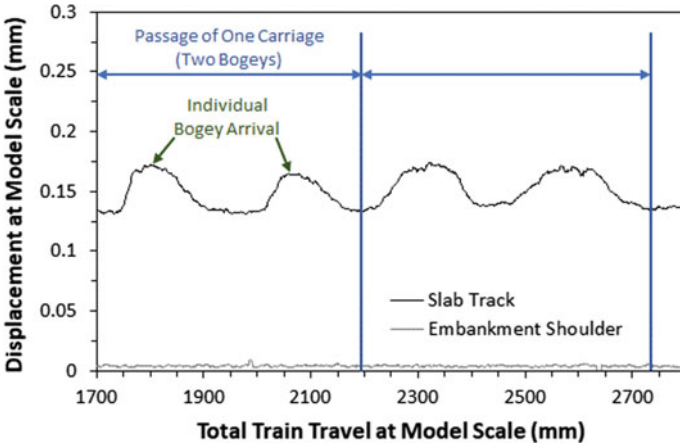

Fig. 8 Vertical displacement of the slab track and embankment for one cycle (two train passes)

This shows that centrifuge measurement of the deflection of the slab track under each bogie pass is approximately 0.04 mm (2 mm at full scale), and that the majority of this deflection is elastic (recoverable).

5   Discussion of the Results

At the time of writing, this paper analysis of the results from the two different track testing methods is still very much in its infancy. However, initial observations suggest that this particular centrifuge test appeared to produce larger settlements to those

measured in GRAFT II once the scaling laws were applied. The reasons for this are currently being investigated, but may be related to the method used to form the wall facing in the centrifuge, i.e., the wall fixing system. The GRAFT II tests are full scale so represent the true displacement of the structure under the laboratory conditions applied. It is clear that very small changes to the settlements measured during the centrifuge test lead to large variations in the scaled displacements. This perhaps highlights some of the challenges associated with modelling complex structures and construction processes in the centrifuge with regard to railway applications. In reality, the GRS-RW wall would be much higher than the one built-in GRAFT II.

The next task is to look at consistency across the testing methodologies to ensure like for like comparisons. To the authors knowledge, the LOCORPS project is one of the first occasions where a centrifuge has been used and compared to full-scale testing for railway track settlement analysis of a GRS-RW system. From this study, it is clear that much more research work is required in order for centrifuge studies of railway track behaviour to be realized. In particular, the challenges associated with increasing train speed are yet to be fully simulated in the centrifuge, especially if the train is passes 50% of the critical velocity resulting in ground wave propagation. Future research will look in more detail at the construction methods used to form the wall to ensure that they represent the as-built structure more closely, in an attempt to bridge the gap between real-life behaviour and that simulated in the centrifuge.

References

1. Yonezawa T, Yamazaki T, Tateyama M, Tatsuoka F (2014) Design and construction of geosynthetic-reinforced soil structures for Hokkaido high-speed train line. Transp Geotech 1(1). https://doi.org/10.1016/j.trgeo.2013.12.001
2. Tatsuoka F, Tateyama M, Koseki J, Yonezawa T (2014) Geosynthetic-reinforced soil structures for railways in Japan. Transp Infrastruct Geotechnol 1(1):5–53
3. Lee K, Wu JT (2004) A synthesis of case histories on GRS bridge supporting structures with flexible facing. Geotext Geomembr 181–204
4. Lenart S, Kralj M, Medved S, Šuler J (2016) Design and construction of the first GRS integrated bridge with FHR facings in Europe. Transp Geotech 8:26–34
5. Berg R, Christopher B, Samtani N (2009) Design of mechanically stabilized earth walls and reinforced soil slopes-volume II. Report No. FHWA-NHI-10-025, Washington, DC: National Highway Institute, Federal Highway Administration
6. Wu JT (2018) Geosynthetic reinforced soil (GRS) walls. Wiley, s.l.
7. Skinner GD, Rowe RK (2005) Design behaviour of geosynthetic reinforced retaining wall and bridge abutment on yielding foundation. Geotext Geomembr 234–260
8. Kim D, Kim U (2016) Performance evaluation of a new type of abutment with geosynthetics. Civil-Comp Press, Stirlingshire, p 33
9. Tatsuoka F (2019) Geosynthetic-reinforced soil structures for transportation: from walls to bridges. Australia, s.n

10. Čebašek TM, Esen AF, Woodward PK, Laghrouche O, Connolly DP (2018) Full scale laboratory testing of ballast and concrete slab tracks under phased cyclic loading. Transp Geotech 17:33–40
11. Robinson S, Brown MJ, Matsui H, Brennan AJ, Augarde CE, Coombs WM, Cortis M (2019) Centrifuge testing to verify scaling of offshore pipeline ploughs. Int J Phys Model Geotech 19(6):305–317

Numerical and Experimental Analysis of Internal Stability of Back-to-Back Mechanically Stabilized Earth Walls Supporting the Rail Embankment System

Shilpa S. Vadavadagi and Sowmiya Chawla

Abstract Back-to-back mechanically stabilized earth walls (BBMSEWs) have been increasingly used for the bridge approaches where there is an elevation from the ground level to the bridge level. Their usage has been increased because of continuing expansion of high-occupancy vehicle (HOV) lane and railways in urban areas. More precisely, their applications are in narrow ramps and turning lanes. These walls are constructed on the lanes of existing medians. So such back-to-back walls have small aspect ratios. FHWA design guidelines available for numerical modeling of BBMSEWs are limited when the distance between two opposing walls interacts with each other. So a numerical and an experimental study has been carried out for the case when the two opposing walls interact with each other. In the analysis, rigid and flexible facing panels, geo-synthetic materials as reinforcements have been used. Stiffness of the reinforcing material has been varied. A parametric study has been carried to analyze the effect of them in the reduction of the distance between two opposing walls. Also the tensile stress distribution for varying distance between two opposing walls has been carried out.

Keywords Back-to-back mechanically stabilized earth wall · Numerical modeling · Rigid and flexible panels

1 Introduction

Mechanically stabilized earth walls (MSEWs) are used worldwide because of their ease of construction, economic effectiveness, and tolerance to deformations. When the MSE walls are used for the bridge approaches from ground level to the bridge elevation, such walls are said to be back-to-back mechanically stabilized earth walls [1]. In order for the MSE wall to have resistance against collapse (ultimate strength), it

S. S. Vadavadagi (✉) · S. Chawla
Indian Institute of Technology (Indian School of Mines) Dhanbad, Dhanbad, India

S. Chawla
e-mail: sowmiya@iitism.ac.in

is necessary to consider the internal and external stability in the design. Earth pressure during the service leads to determination of internal stability which is characterized by maximum reinforcement loading, designing against reinforcement rupture and pullout failure. Thus, the maximum tension, T_{max}, in each reinforcement is dependent on the lateral earth pressure. In the past decade, BBMSEWs were used progressively for the bridge approaches. Studies on the behavior of BBMSEWs are very limited.

Federal Highway Administration (FHWA) design guideline gives two conditions for its behavior [2]. Case 1: the distance between two walls, D, is far enough that they are designed independently. Thus, each wall is designed independently. Case 2: two walls interact with each other with reinforcements from both the walls that connect at the center by overlapping. For the case 1, the distance between two walls measured from the ends of the reinforcements, D, is H tan (450-ϕ/2). 'H' indicates height of wall, and ϕ indicates friction angle of soil.

For case 2, they are still assumed to be designed independently for internal stability. Active thrust to the reinforced zone is not assumed from the backfill. In other words, for external stability, no active thrust is assumed, and the two walls are assumed to act as a whole structure individually.

2   Numerical Analysis

A finite element analysis has been carried out for back-to-back mechanically stabilized earth walls. Analysis has been carried out in Midas GTS NX software.

2.1   Geometry

The geometry has been drawn in 2D. Analysis of wall in 2D and 3D would yield same results [3]. And all results which are necessary to analyze a wall say suppose, stress distribution, lateral earth pressure behind the wall, wall deformation, and axial forces and many more are available directly in 2D analysis. Dimensions of the geometry are shown in Fig. 1.

Length of the panel is 1.5 m. LR is the overlapping length of geogrid. Overlapping length of geogrid is decided based on the ratio of height of the wall into 0.3. In other words, it has been decided as (LR/H = 0.3) out of LR/H = 0.1, 0.2, 0.4, and 0. In the present study anyway, a portion of the work for LR/H = 0.3 has been discussed further.

Material properties considered for panel, reinforced fill, and foundation soil are Mohr–Coulomb, whereas geogrid is considered as elastic with elastic modulus of 1000 MPA. Material properties are given in Table 1.
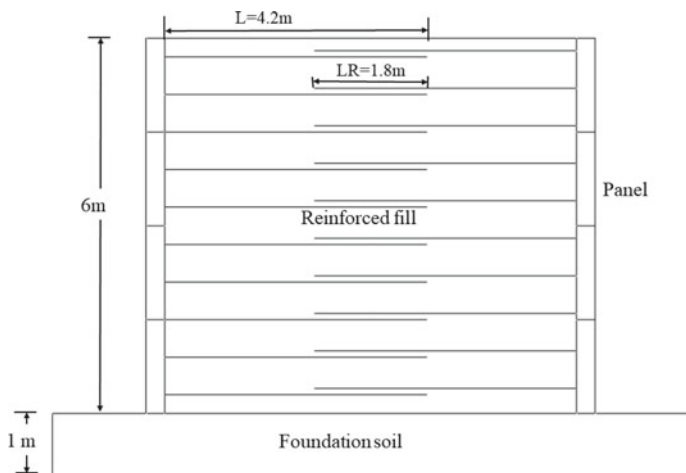
Fig. 1 Dimensions of line diagram

Table 1 Material properties

Material	Reinforced fill	Foundation soil	Panel wall
Elastic modulus (kPa)	10,000	10,000	100,000
Poison's ratio	0.3	0.3	0.3
Friction angle	25	1	34
Cohesion	1	100	100

2.2 Modeling

Size control was given at the top of reinforced fill, at the inner side of the panel where panel is contact with reinforced fill, at the bottom of both right and left side panels where they are in contact with foundation soil and also in between the reinforced fill and foundation soil. The number of divisions given in size control varied for all was different. Geogrids were imprinted on the plane of reinforced fill using imprint option. Meshing was first done to all geogrids from top to bottom for the two overlapping geogrids at once. 1D mesh element was used to mesh geogrids. 2D meshing was done to reinforced fill, panel, and foundation soil. For 2D meshing, auto face option was chosen. The size method for reinforced fill, panel, and foundation was different depending upon the fineness of the mesh needed. Anyway for all the three, element type used for meshing was triangular. Meshed model is shown in Fig. 2.

Interfaces were given between panel-reinforced fill and geogrid-reinforced fill. The line of interface was chosen to give interface between panel-reinforced fill. From mesh set, (T-X cross type) was chosen as a type or method of interface. However, for geogrid-reinforced fill, truss/beam was chosen. Further for both the cases, interface properties were given by wizard. Strength reduction factor(R) 1 was given. Additional
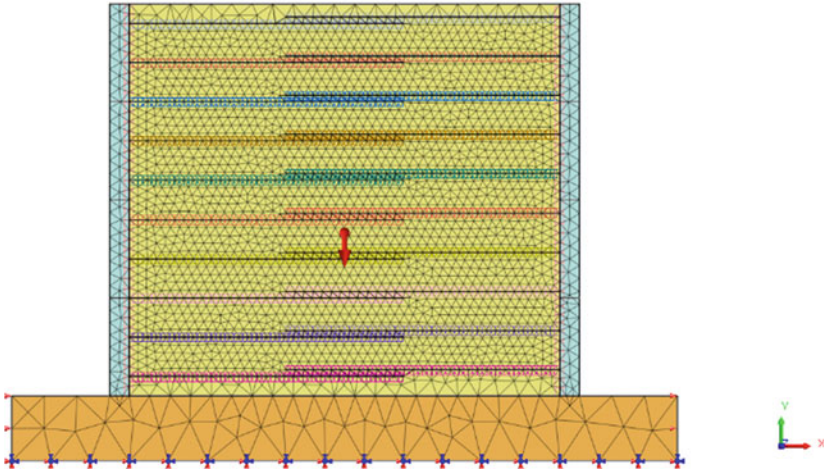
Fig. 2 Meshed diagram of the model

rigid links were created along with interface between panel-reinforced fill. However, for geogrid-reinforced fill, each single node connected geogrid and reinforced fill were merged in order to have connectivity between them. For boundary conditions, horizontal fixity was given at both sides foundation edges. And fixed boundary condition was given at the bottom. Self-weight of the model is also considered.

Strength reduction method was chosen for the analysis case. All the meshes and boundary conditions were activated in active sets. And the analysis was performed.

3   Results and Conclusions

3.1   *Displacement of the Wall*

Figure 3 shows the punching failure which took for rigid wall. Wall has failed as a rigid whole structure in both the walls. Deformation at the wall bottom is found to be more which has failed by its self-weight (punching failure).

The analysis was further carried for flexible walls as a comparison for rigid wall. They have shown completely different failure pattern.

The parametric study has been carried out by varying elastic modulus of geogrid. The varied values were 500, 1000, 2000, and 3000 MPA. Walls were found to deform maximum almost at one-third distance from the bottom of wall height. Figure 4 shows the wall displacement for flexible wall with elastic modulus as 500 MPA.
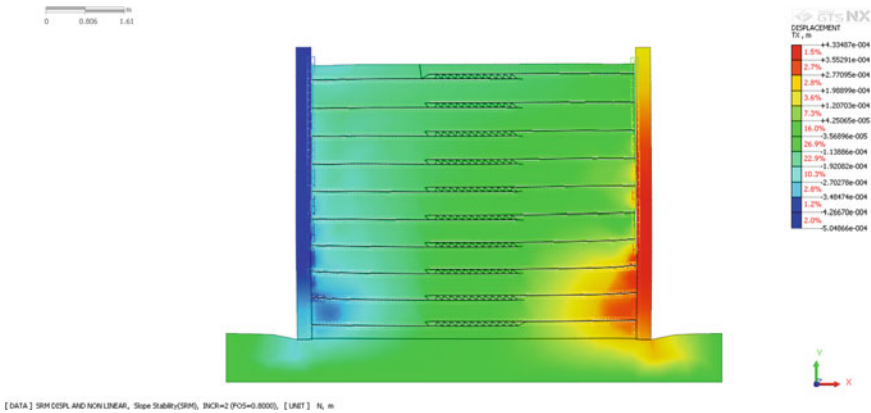
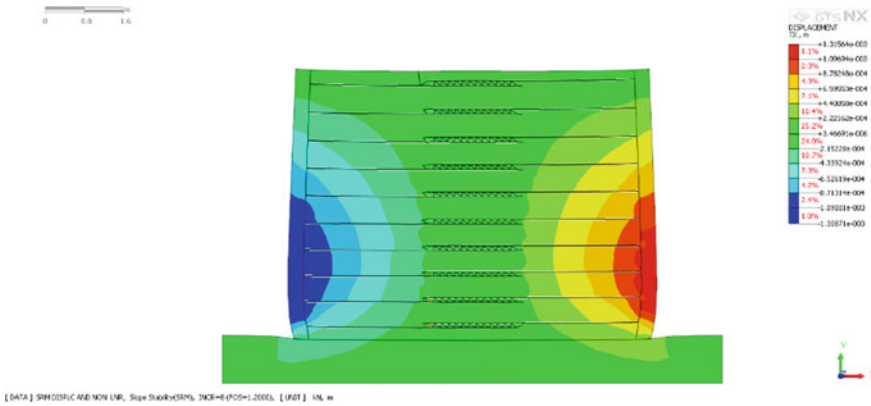**Fig. 3** Horizontal displacement of rigid wall (punching failure)

Fig. 4 Displacement of flexible wall with geogrid elastic modulus 500 MPA

All the models have shown the same deformation pattern with maximum deformation at one-third from the bottom of wall height. But there was no much difference in maximum deformation of the wall. Figure 5 shows the displacement of the wall with geogrid elastic modulus 1000 MPA. In all the cases, critical failure surfaces were not developed fully, but some shear zones were observed [4]. The deformation pattern of wall well developed as like [5].

Factor of safety was found to increase as the elastic modulus of geogrid was increased. Further it was also observed that the maximum displacement of the wall was found to decrease with in geogrid modulus given in Table 2.
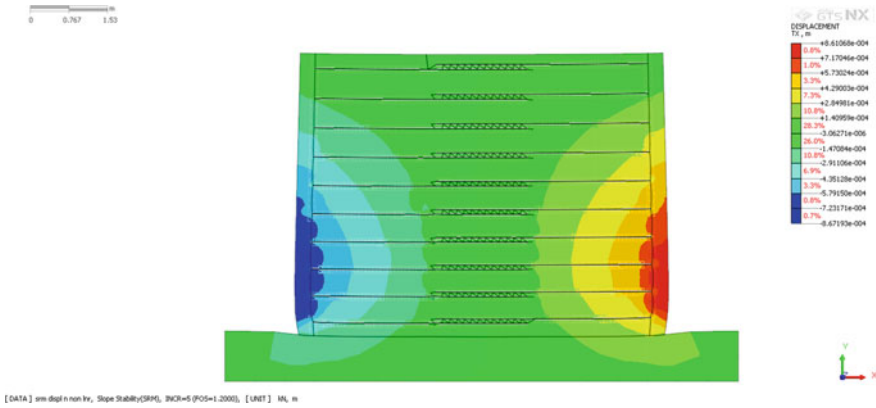
Fig. 5 Displacement of flexible wall with geogrid elastic modulus 1000 MPA

Table 2 Factor safety, maximum displacement of wall, and maximum axial force of geogrid

Elastic modulus of geogrid (kPa)	Max. displacement (mm)	Max. axial force of geogrid (kN)	FOS
500	3.97	8.975	1.12
1000	3.81	9.34	1.21
2000	3.72	9.76	1.31
3000	3.67	10	1.45

3.2   Axial Force of Geogrid

Figure 6 shows the plot of axial force of geogrid for elastic modulus of geogrid 500 MPA. It was found that from the second bottom layer of geogrid, axial force increased. Axial force of third layer of geogrid was almost same that of second layer. From fourth layer till the last of geogrid, axial force was fund to decrease. Similar kind of patter was observed by Yu et al. [6] when they did parametric study varying elastic modulus of backfill soil. Results of axial force followed the same pattern in all parametric study carried out. Figure 7 shows the axial force distribution for elastic modulus of geogrid 1000 MPA. The remaining 2000 and 3000 MPA also showed the same pattern of axial force distribution. But all have showed different values of axial force. Their maximum axial forces were also different as given in Table 2. Lateral earth pressure has been ignored if over lapping length is greater than 0.3H [7].

As the elastic modulus of geogrid is increased, displacement of soil is directly affected and maximum axial force of geogrid is inversely affected. At the same time, factor of safety of whole system is increasing.
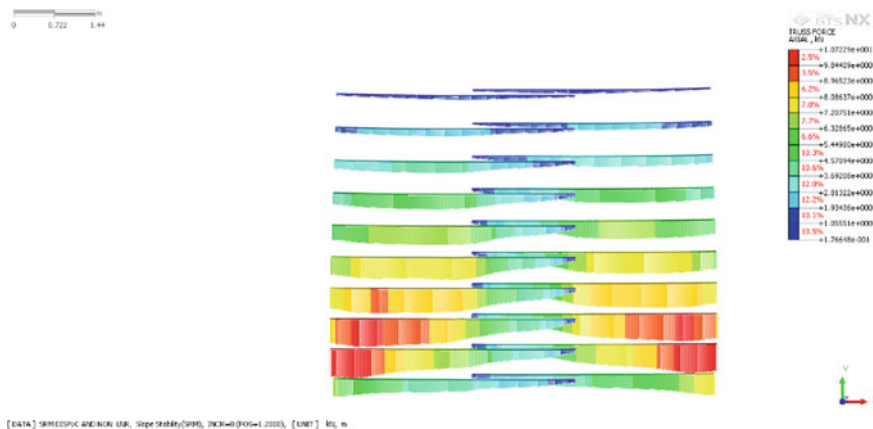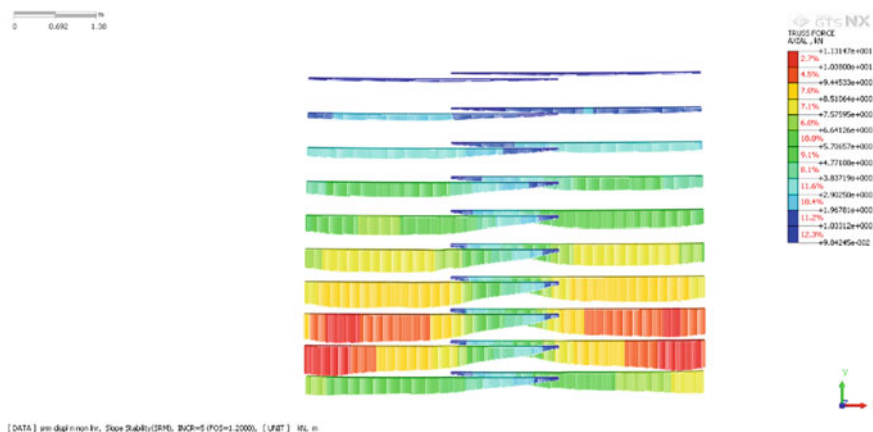
Fig. 6 Axial force of geogrid-500 MPA

Fig. 7 Axial force of geogrid-1000 MPA

References

1. Han J, Leshchinsky D (2010) Analysis of back-to-back mechanically stabilized earth walls. Geotext Geomembr 28(3):262–267
2. Berg RR, Christopher BR, Samtani NC (2010) Design and construction of mechanically stabilized earth walls and reinforced soil slopes—volume I, Report No. FHWA-NHI-10-024, Federal Highway Administration, U.S. Department of Transportation, Washington, DC
3. Skejic A, Medic S, Dolarevic S (2018) Influence of wire mesh characteristics on reinforced soil model wall failure mechanisms-physical and numerical modelling. Geotext Geomembr 46(6):726–738
4. Benmebarek S, Djabri M (2017) FEM to investigate the effect of overlapping-reinforcement on the performance of back-to-back embankment bridge approaches under self-weight. Transp Geotech 11:17–26

5. Leshchinsky D, Han J (2004) Geosynthetic reinforced multitiered walls. J Geotech Geoenviron Eng 130(12):1225–1235
6. Yu Y, Bathurst RJ, Miyata Y (2015) Numerical analysis of a mechanically stabilized earth wall reinforced with steel strips. Soils Found 55(3):536–547
7. Benmebarek S, Attallaoui S, Benmebarek N (2016) Interaction analysis of back-to-back mechanically stabilized earth walls. J Rock Mech Geotech Eng 8(5):697–702